Copyrighted Material

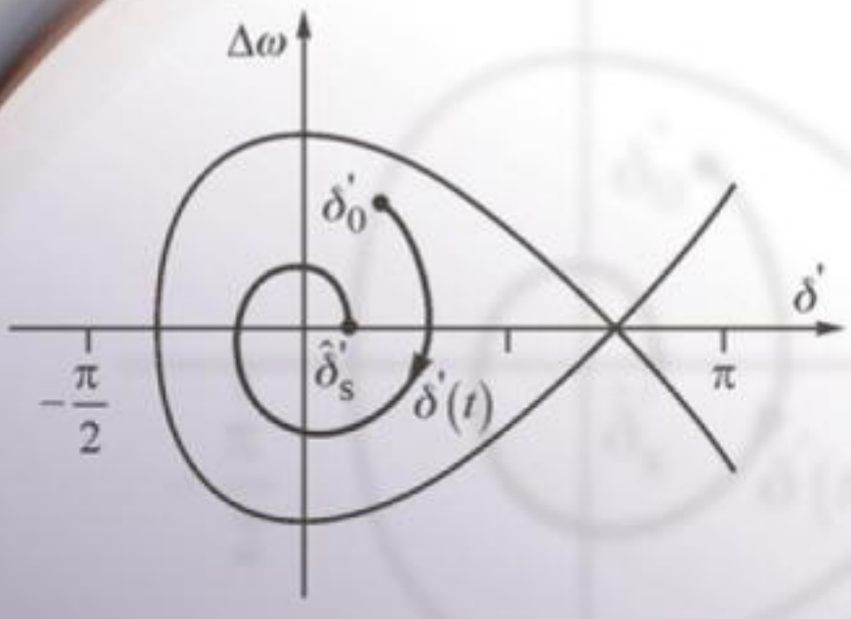

Second Edition

POWER SYSTEM DYNAMICS: STABILITY AND CONTROL

Jan Machowski
Janusz W. Bialek
James R. Bumby

WILEY

Copyrighted Material

VISIT…

POWER SYSTEM DYNAMICS

Stability and Control

Second Edition

Jan Machowski

Warsaw University of Technology, Poland

Janusz W. Bialek

The University of Edinburgh, UK

James R. Bumby

Durham University, UK

John Wiley & Sons, Ltd

POWER SYSTEM DYNAMICS

POWER SYSTEM DYNAMICS

Stability and Control

Second Edition

Jan Machowski

Warsaw University of Technology, Poland

Janusz W. Bialek

The University of Edinburgh, UK

James R. Bumby

Durham University, UK

John Wiley & Sons, Ltd

This edition first published 2008
© 2008 John Wiley & Sons, Ltd.

Registered office
John Wiley & Sons Ltd, The Atrium, Southern Gate, Chichester, West Sussex, PO19 8SQ, United Kingdom

For details of our global editorial offices, for customer services and for information about how to apply for permission to reuse the copyright material in this book please see our website at www.wiley.com.

The right of the author to be identified as the author of this work has been asserted in accordance with the Copyright, Designs and Patents Act 1988.

All rights reserved. No part of this publication may be reproduced, stored in a retrieval system, or transmitted, in any form or by any means, electronic, mechanical, photocopying, recording or otherwise, except as permitted by the UK Copyright, Designs and Patents Act 1988, without the prior permission of the publisher.

Wiley also publishes its books in a variety of electronic formats. Some content that appears in print may not be available in electronic books.

Designations used by companies to distinguish their products are often claimed as trademarks. All brand names and product names used in this book are trade names, service marks, trademarks or registered trademarks of their respective owners. The publisher is not associated with any product or vendor mentioned in this book. This publication is designed to provide accurate and authoritative information in regard to the subject matter covered. It is sold on the understanding that the publisher is not engaged in rendering professional services. If professional advice or other expert assistance is required, the services of a competent professional should be sought.

Library of Congress Cataloging-in-Publication Data

Machowski, Jan.
Power system dynamics: stability and control / Jan Machowski, Janusz W. Bialek, James R. Bumby. – 2nd ed.
p. cm.
Rev. ed. of: Power system dynamics and stability / Jan Machowski, Janusz W. Bialek, James R. Bumby. 1997.
Includes bibliographical references and index.
ISBN 978-0-470-72558-0 (cloth)
1. Electric power system stability. 2. Electric power systems–Control. I. Bialek, Janusz W. II. Bumby, J. R. (James Richard) III. Title.
TK1010.M33 2008
621.319′1–dc22
2008032220

A catalogue record for this book is available from the British Library.

ISBN 978-0-470-72558-0

Typeset in 9/11pt Times New Roman by Aptara Inc., New Delhi, India.
Printed in Great Britain by Antony Rowe Ltd, Chippenham, Wiltshire

Contents

About the Authors **xiii**
Preface **xv**
Acknowledgements **xix**
List of Symbols **xxi**

PART I INTRODUCTION TO POWER SYSTEMS

1 Introduction **3**
1.1 Stability and Control of a Dynamic System 3
1.2 Classification of Power System Dynamics 5
1.3 Two Pairs of Important Quantities: Reactive Power/Voltage and Real Power/Frequency 7
1.4 Stability of a Power System 9
1.5 Security of a Power System 9
1.6 Brief Historical Overview 12

2 Power System Components **15**
2.1 Introduction 15
2.1.1 Reliability of Supply 15
2.1.2 Supplying Electrical Energy of Good Quality 16
2.1.3 Economic Generation and Transmission 16
2.1.4 Environmental Issues 16
2.2 Structure of the Electrical Power System 16
2.2.1 Generation 18
2.2.2 Transmission 18
2.2.3 Distribution 19
2.2.4 Demand 19
2.3 Generating Units 19
2.3.1 Synchronous Generators 20
2.3.2 Exciters and Automatic Voltage Regulators 21
2.3.3 Turbines and their Governing Systems 25
2.4 Substations 35
2.5 Transmission and Distribution Network 35
2.5.1 Overhead Lines and Underground Cables 35
2.5.2 Transformers 36
2.5.3 Shunt and Series Elements 41
2.5.4 FACTS Devices 43

2.6 Protection 54
2.6.1 Protection of Transmission Lines 54
2.6.2 Protection of Transformers 56
2.6.3 Protection of Busbars 57
2.6.4 Protection of Generating Units 57
2.7 Wide Area Measurement Systems 58
2.7.1 WAMS and WAMPAC Based on GPS Signal 58
2.7.2 Phasors 59
2.7.3 Phasor Measurement Unit 61
2.7.4 Structures of WAMS and WAMPAC 62

3 The Power System in the Steady State **65**
3.1 Transmission Lines 65
3.1.1 Line Equations and the π-Equivalent Circuit 66
3.1.2 Performance of the Transmission Line 67
3.1.3 Underground Cables 72
3.2 Transformers 72
3.2.1 Equivalent Circuit 72
3.2.2 Off-Nominal Transformation Ratio 74
3.3 Synchronous Generators 76
3.3.1 Round-Rotor Machines 76
3.3.2 Salient-Pole Machines 83
3.3.3 Synchronous Generator as a Power Source 89
3.3.4 Reactive Power Capability Curve of a Round-Rotor Generator 91
3.3.5 Voltage–Reactive Power Capability Characteristic $V(Q)$ 95
3.3.6 Including the Equivalent Network Impedance 100
3.4 Power System Loads 104
3.4.1 Lighting and Heating 105
3.4.2 Induction Motors 106
3.4.3 Static Characteristics of the Load 110
3.4.4 Load Models 111
3.5 Network Equations 113
3.6 Power Flows in Transmission Networks 118
3.6.1 Control of Power Flows 118
3.6.2 Calculation of Power Flows 122

PART II INTRODUCTION TO POWER SYSTEM DYNAMICS

4 Electromagnetic Phenomena **127**
4.1 Fundamentals 127
4.2 Three-Phase Short Circuit on a Synchronous Generator 129
4.2.1 Three-Phase Short Circuit with the Generator on No Load and Winding Resistance Neglected 129
4.2.2 Including the Effect of Winding Resistance 133
4.2.3 Armature Flux Paths and the Equivalent Reactances 134
4.2.4 Generator Electromotive Forces and Equivalent Circuits 140
4.2.5 Short-Circuit Currents with the Generator Initially on No Load 146
4.2.6 Short-Circuit Currents in the Loaded Generator 149
4.2.7 Subtransient Torque 150

4.3 Phase-to-Phase Short Circuit 152
4.3.1 Short-Circuit Current and Flux with Winding Resistance Neglected 153
4.3.2 Influence of the Subtransient Saliency 156
4.3.3 Positive- and Negative-Sequence Reactances 159
4.3.4 Influence of Winding Resistance 160
4.3.5 Subtransient Torque 162
4.4 Synchronization 163
4.4.1 Currents and Torques 164
4.5 Short-Circuit in a Network and its Clearing 166

5 Electromechanical Dynamics – Small Disturbances 169
5.1 Swing Equation 169
5.2 Damping Power 172
5.2.1 Damping Power at Large Speed Deviations 175
5.3 Equilibrium Points 176
5.4 Steady-State Stability of Unregulated System 177
5.4.1 Pull-Out Power 177
5.4.2 Transient Power–Angle Characteristics 179
5.4.3 Rotor Swings and Equal Area Criterion 184
5.4.4 Effect of Damper Windings 186
5.4.5 Effect of Rotor Flux Linkage Variation 187
5.4.6 Analysis of Rotor Swings Around the Equilibrium Point 191
5.4.7 Mechanical Analogues of the Generator–Infinite Busbar System 195
5.5 Steady-State Stability of the Regulated System 196
5.5.1 Steady-State Power–Angle Characteristic of Regulated Generator 196
5.5.2 Transient Power–Angle Characteristic of the Regulated Generator 200
5.5.3 Effect of Rotor Flux Linkage Variation 202
5.5.4 Effect of AVR Action on the Damper Windings 205
5.5.5 Compensating the Negative Damping Components 206

6 Electromechanical Dynamics – Large Disturbances 207
6.1 Transient Stability 207
6.1.1 Fault Cleared Without a Change in the Equivalent Network Impedance 207
6.1.2 Short-Circuit Cleared with/without Auto-Reclosing 212
6.1.3 Power Swings 215
6.1.4 Effect of Flux Decrement 215
6.1.5 Effect of the AVR 216
6.2 Swings in Multi-Machine Systems 220
6.3 Direct Method for Stability Assessment 222
6.3.1 Mathematical Background 223
6.3.2 Energy-Type Lyapunov Function 225
6.3.3 Transient Stability Area 227
6.3.4 Equal Area Criterion 228
6.3.5 Lyapunov Direct Method for a Multi-Machine System 230
6.4 Synchronization 237
6.5 Asynchronous Operation and Resynchronization 239
6.5.1 Transition to Asynchronous Operation 240
6.5.2 Asynchronous Operation 241
6.5.3 Possibility of Resynchronization 242

6.6 Out-of-Step Protection Systems 244
6.6.1 Impedance Loci During Power Swings 245
6.6.2 Power Swing Blocking 248
6.6.3 Pole-Slip Protection of Synchronous Generator 249
6.6.4 Out-of-Step Tripping in a Network 251
6.6.5 Example of a Blackout 253
6.7 Torsional Oscillations in the Drive Shaft 253
6.7.1 The Torsional Natural Frequencies of the Turbine–Generator Rotor 253
6.7.2 Effect of System Faults 259
6.7.3 Subsynchronous Resonance 261

7 Wind Power 265
7.1 Wind Turbines 265
7.1.1 Generator Systems 269
7.2 Induction Machine Equivalent Circuit 274
7.3 Induction Generator Coupled to the Grid 277
7.4 Induction Generators with Slightly Increased Speed Range via External Rotor Resistance 280
7.5 Induction Generators with Significantly Increased Speed Range: DFIGs 282
7.5.1 Operation with the Injected Voltage in Phase with the Rotor Current 284
7.5.2 Operation with the Injected Voltage out of Phase with the Rotor Current 286
7.5.3 The DFIG as a Synchronous Generator 287
7.5.4 Control Strategy for a DFIG 289
7.6 Fully Rated Converter Systems: Wide Speed Control 290
7.6.1 Machine-Side Inverter 291
7.6.2 Grid-Side Inverter 292
7.7 Peak Power Tracking of Variable Speed Wind Turbines 293
7.8 Connections of Wind Farms 294
7.9 Fault Behaviour of Induction Generators 294
7.9.1 Fixed-Speed Induction Generators 294
7.9.2 Variable-Speed Induction Generators 296
7.10 Influence of Wind Generators on Power System Stability 296

8 Voltage Stability 299
8.1 Network Feasibility 299
8.1.1 Ideally Stiff Load 300
8.1.2 Influence of the Load Characteristics 303
8.2 Stability Criteria 305
8.2.1 The $\mathrm{d}\Delta Q/dV$ *Criterion* 305
8.2.2 The dE/dV *Criterion* 308
8.2.3 The $dQ_{\mathrm{G}}/\mathrm{d}\,Q_{\mathrm{L}}$ *Criterion* 309
8.3 Critical Load Demand and Voltage Collapse 310
8.3.1 Effects of Increasing Demand 311
8.3.2 Effect of Network Outages 314
8.3.3 Influence of the Shape of the Load Characteristics 315
8.3.4 Influence of the Voltage Control 317
8.4 Static Analysis 318
8.4.1 Voltage Stability and Load Flow 318
8.4.2 Voltage Stability Indices 320

8.5 Dynamic Analysis 321
8.5.1 The Dynamics of Voltage Collapse 321
8.5.2 Examples of Power System Blackouts 323
8.5.3 Computer Simulation of Voltage Collapse 326
8.6 Prevention of Voltage Collapse 327
8.7 Self-Excitation of a Generator Operating on a Capacitive Load 329
8.7.1 Parametric Resonance in RLC Circuits 329
8.7.2 Self-Excitation of a Generator with Open-Circuited Field Winding 330
8.7.3 Self-Excitation of a Generator with Closed Field Winding 332
8.7.4 Practical Possibility of Self-Excitation 334

9 Frequency Stability and Control 335
9.1 Automatic Generation Control 336
9.1.1 Generation Characteristic 336
9.1.2 Primary Control 339
9.1.3 Secondary Control 341
9.1.4 Tertiary Control 345
9.1.5 AGC as a Multi-Level Control 346
9.1.6 Defence Plan Against Frequency Instability 347
9.1.7 Quality Assessment of Frequency Control 349
9.2 Stage I – Rotor Swings in the Generators 350
9.3 Stage II – Frequency Drop 353
9.4 Stage III – Primary Control 354
9.4.1 The Importance of the Spinning Reserve 356
9.4.2 Frequency Collapse 358
9.4.3 Underfrequency Load Shedding 360
9.5 Stage IV – Secondary Control 360
9.5.1 Islanded Systems 361
9.5.2 Interconnected Systems and Tie-Line Oscillations 364
9.6 FACTS Devices in Tie-Lines 370
9.6.1 Incremental Model of a Multi-Machine System 371
9.6.2 State-Variable Control Based on Lyapunov Method 375
9.6.3 Example of Simulation Results 378
9.6.4 Coordination Between AGC and Series FACTS Devices in Tie-Lines 379

10 Stability Enhancement 383
10.1 Power System Stabilizers 383
10.1.1 PSS Applied to the Excitation System 384
10.1.2 PSS Applied to the Turbine Governor 387
10.2 Fast Valving 387
10.3 Braking Resistors 391
10.4 Generator Tripping 392
10.4.1 Preventive Tripping 393
10.4.2 Restitutive Tripping 394
10.5 Shunt FACTS Devices 395
10.5.1 Power–Angle Characteristic 395
10.5.2 State-Variable Control 397
10.5.3 Control Based on Local Measurements 400
10.5.4 Examples of Controllable Shunt Elements 404
10.5.5 Generalization to Multi-Machine Systems 406
10.5.6 Example of Simulation Results 414

10.6 Series Compensators 416
10.6.1 State-Variable Control 417
10.6.2 Interpretation Using the Equal Area Criterion 419
10.6.3 Control Strategy Based on the Squared Current 420
10.6.4 Control Based on Other Local Measurements 421
10.6.5 Simulation Results 423
10.7 Unified Power Flow Controller 423
10.7.1 Power–Angle Characteristic 424
10.7.2 State-Variable Control 426
10.7.3 Control Based on Local Measurements 428
10.7.4 Examples of Simulation Results 429

PART III ADVANCED TOPICS IN POWER SYSTEM DYNAMICS

11 Advanced Power System Modelling 433
11.1 Synchronous Generator 433
11.1.1 Assumptions 434
11.1.2 The Flux Linkage Equations in the Stator Reference Frame 434
11.1.3 The Flux Linkage Equations in the Rotor Reference Frame 436
11.1.4 Voltage Equations 440
11.1.5 Generator Reactances in Terms of Circuit Quantities 443
11.1.6 Synchronous Generator Equations 446
11.1.7 Synchronous Generator Models 453
11.1.8 Saturation Effects 458
11.2 Excitation Systems 462
11.2.1 Transducer and Comparator Model 462
11.2.2 Exciters and Regulators 463
11.2.3 Power System Stabilizer (PSS) 470
11.3 Turbines and Turbine Governors 470
11.3.1 Steam Turbines 471
11.3.2 Hydraulic Turbines 476
11.3.3 Wind Turbines 481
11.4 Dynamic Load Models 485
11.5 FACTS Devices 488
11.5.1 Shunt FACTS Devices 488
11.5.2 Series FACTS Devices 488

12 Steady-State Stability of Multi-Machine System 491
12.1 Mathematical Background 491
12.1.1 Eigenvalues and Eigenvectors 491
12.1.2 Diagonalization of a Square Real Matrix 496
12.1.3 Solution of Matrix Differential Equations 500
12.1.4 Modal and Sensitivity Analysis 509
12.1.5 Modal Form of the State Equation with Inputs 512
12.1.6 Nonlinear System 513
12.2 Steady-State Stability of Unregulated System 514
12.2.1 State-Space Equation 515
12.2.2 Simplified Steady-State Stability Conditions 517
12.2.3 Including the Voltage Characteristics of the Loads 521
12.2.4 Transfer Capability of the Network 522

12.3 Steady-State Stability of the Regulated System 523
12.3.1 Generator and Network 523
12.3.2 Including Excitation System Model and Voltage Control 525
12.3.3 Linear State Equation of the System 528
12.3.4 Examples 528

13 Power System Dynamic Simulation 535
13.1 Numerical Integration Methods 536
13.2 The Partitioned Solution 541
13.2.1 Partial Matrix Inversion 543
13.2.2 Matrix Factorization 547
13.2.3 Newton's Method 548
13.2.4 Ways of Avoiding Iterations and Multiple Network Solutions 551
13.3 The Simultaneous Solution Methods 553
13.4 Comparison Between the Methods 554

14 Power System Model Reduction – Equivalents 557
14.1 Types of Equivalents 557
14.2 Network Transformation 559
14.2.1 Elimination of Nodes 559
14.2.2 Aggregation of Nodes Using Dimo's Method 562
14.2.3 Aggregation of Nodes Using Zhukov's Method 563
14.2.4 Coherency 565
14.3 Aggregation of Generating Units 567
14.4 Equivalent Model of External Subsystem 568
14.5 Coherency Recognition 569
14.6 Properties of Coherency-Based Equivalents 573
14.6.1 Electrical Interpretation of Zhukov's Aggregation 573
14.6.2 Incremental Equivalent Model 575
14.6.3 Modal Interpretation of Exact Coherency 579
14.6.4 Eigenvalues and Eigenvectors of the Equivalent Model 582
14.6.5 Equilibrium Points of the Equivalent Model 589

Appendix 593

References 613

Index 623

About the Authors

Professor Jan Machowski received his MSc and PhD degrees in Electrical Engineering from Warsaw University of Technology in 1974 and 1979, respectively. After obtaining field experience in the Dispatching Centre and several power plants, he joined the Electrical Faculty of Warsaw University of Technology where presently he is employed as a Professor and Director of the Power Engineering Institute. His areas of interest are electrical power systems, power system protection and control.

In 1989–93 Professor Machowski was a Visiting Professor at Kaiserslautern University in Germany where he carried out two research projects on power swing blocking algorithms for distance protection and optimal control of FACTS devices.

Professor Machowski is the co-author of three books published in Polish: *Power System Stability* (WNT, 1989), *Short Circuits in Power Systems* (WNT, 2002) and *Power System Control and Stability* (WPW, 2007). He is also a co-author of *Power System Dynamics and Stability* published by John Wiley & Sons, Ltd (1997).

Professor Machowski is the author and co-author of 42 papers published in English in international fora. He has carried out many projects on electrical power systems, power system stability and power system protection commissioned by the Polish Power Grid Company, Electric Power Research Institute in the United States, Electrinstitut Milan Vidmar in Slovenia and Ministry of Science and Higher Education of Poland.

Professor Janusz Bialek received his MEng and PhD degrees in Electrical Engineering from Warsaw University of Technology in 1977 and 1981, respectively. From 1981 to 1989 he was a lecturer with Warsaw University of Technology. In 1989 he moved to the University of Durham, United Kingdom, and since 2003 he has been at the University of Edinburgh where he currently holds the Bert Whittington Chair of Electrical Engineering. His main research interests are in sustainable energy systems, security of supply, liberalization of the electricity supply industry and power system dynamics and control.

Professor Bialek has co-authored two books and over 100 research papers. He has been a consultant to the Department of Trade and Industry (DTI) of the UK government, Scottish Executive, Elexon, Polish Power Grid Company, Scottish Power, Enron and Electrical Power Research Institute (EPRI). He was the Principal Investigator of a number of major research grants funded by the Engineering and Physical Sciences Research Council and the DTI.

Professor Bialek is a member of the Advisory Board of Electricity Policy Research Group, Cambridge University, a member of the Dispute Resolution Panel for the Single Electricity Market Operator, Ireland, and Honorary Professor of Heriot-Watt University, Scotland.

Dr Jim Bumby received his BSc and PhD degrees in Engineering from Durham University, United Kingdom, in 1970 and 1974, respectively. From 1973 to 1978 he worked for the International Research and Development Company, Newcastle-upon-Tyne, on superconducting machines, hybrid vehicles and sea-wave energy. Since 1978 he has worked in the School of Engineering at Durham University where he is currently Reader in Electrical Engineering. He has worked in the area of electrical machines and systems for over 30 years, first in industry and then in academia.

Dr Bumby is the author or co-author of over 100 technical papers and two books in the general area of electrical machines/power systems and control. He has also written numerous technical reports for industrial clients. These papers and books have led to the award of a number of national and international prizes including the Institute of Measurement and Control prize for the best transactions paper in 1988 for work on hybrid electric vehicles and the IEE Power Division Premium in 1997 for work on direct drive permanent magnet generators for wind turbine applications. His current research interests are in novel generator technologies and their associated control for new and renewable energy systems.

Preface

In 1997 the authors of this book, J. Machowski, J.W. Bialek and J.R. Bumby, published a book entitled *Power System Dynamics and Stability*. That book was well received by readers who told us that it was used regularly as a standard reference text both in academia and in industry. Some 10 years after publication of that book we started work on a second edition. However, we quickly realized that the developments in the power systems industry over the intervening years required a large amount of new material. Consequently the book has been expanded by about a third and the word *Control* in the new title, *Power System Dynamics: Stability and Control*, reflects the fact that a large part of the new material concerns power system control: flexible AC transmission systems (FACTS), wide area measurement systems (WAMS), frequency control, voltage control, etc. The new title also reflects a slight shift in focus from solely describing power system dynamics to the means of dealing with them. For example, we believe that the new WAMS technology is likely to revolutionize power system control. One of the main obstacles to a wider embrace of WAMS by power system operators is an acknowledged lack of algorithms which could be utilized to control a system in real time. This book tries to fill this gap by developing a number of algorithms for WAMS-based real-time control.

The second reason for adding so much new material is the unprecedented change that has been sweeping the power systems industry since the 1990s. In particular the rapid growth of renewable generation, driven by global warming concerns, is changing the fundamental characteristics of the system. Currently wind power is the dominant renewable energy source and wind generators usually use induction, rather than synchronous, machines. As a significant penetration of such generation will change the system dynamics, the new material in Chapter 7 is devoted entirely to wind generation.

The third factor to be taken into account is the fallout from a number of highly publicized blackouts that happened in the early years of the new millennium. Of particular concern were the autumn 2003 blackouts in the United States/Canada, Italy, Sweden/Denmark and the United Kingdom, the 2004 blackout in Athens and the European disturbance on 4 November 2006. These blackouts have exposed a number of critical issues, especially those regarding power system behaviour at depressed voltages. Consequently, the book has been extended to cover these phenomena together with an illustration of some of the blackouts.

It is important to emphasize that the new book is based on the same philosophy as the previous one. We try to answer some of the concerns about the education of power system engineers. With the widespread access to powerful computers running evermore sophisticated simulation packages, there is a tendency to treat simulation as a substitute for understanding. This tendency is especially dangerous for students and young researchers who think that simulation is a panacea for everything and always provides a true answer. What they do not realize is that, without a physical understanding of the underlying principles, they cannot be confident in understanding, or validating, the simulation results. It is by no means bad practice to treat the initial results of any computer software with a healthy pinch of scepticism.

Power system dynamics are not easy to understand. There are a number of good textbooks which deal with this topic and some of these are reviewed in Chapter 1. As the synchronous machine plays a decisive role in determining the dynamic response of the system, many of these books start with a detailed mathematical treatment of the synchronous generator in order to introduce Park's equations and produce a mathematical model of the generator. However, it is our experience that to begin a topic with such a detailed mathematical treatment can put many students off further study because they often find it difficult to see any practical relevance for the mathematics. This can be a major obstacle for those readers who are more practically inclined and who want to understand what is happening in the system without having to refer continuously to a complicated mathematical model of the generator.

Our approach is different. We first try to give a qualitative explanation of the underlying physical phenomena of power system dynamics using a simple model of the generator, coupled with the basic physical laws of electrical engineering. Having provided the student with a physical understanding of power system dynamics, we then introduce the full mathematical model of the generator, followed by more advanced topics such as system reduction, dynamic simulation and eigenvalue analysis. In this way we hope that the material is made more accessible to the reader who wishes to understand the system operation without first tackling Park's equations.

All our considerations are richly illustrated by diagrams. We strongly believe in the old adage that an illustration is worth a thousand words. In fact, our book contains over 400 diagrams.

The book is conveniently divided into three major parts. The first part (Chapters 1–3) reviews the background for studying power system dynamics. The second part (Chapters 4–10) attempts to explain the basic phenomena underlying power system dynamics using the classical model of the generator–infinite busbar system. The third part (Chapters 11–14) tackles some of the more advanced topics suitable for the modelling and dynamic simulation of large-scale power systems.

Examining the chapters and the new material added in more detail, Chapter 1 classifies power system dynamics and provides a brief historical overview. The new material expands on the definitions of power system stability and security assessment and introduces some important concepts used in later chapters. Chapter 2 contains a brief description of the major power system components, including modern FACTS devices. The main additions here provide a more comprehensive treatment of FACTS devices and a whole new section on WAMS. Chapter 3 introduces steady-state models and their use in analysing the performance of the power system. The new material covers enhanced treatment of the generator as the reactive power source introducing voltage–reactive power capability characteristics. We believe that this is a novel treatment of those concepts since we have not seen it anywhere else. The importance of understanding how the generator and its controls behave under depressed voltages has been emphasized by the wide area blackouts mentioned above. The chapter also includes a new section on controlling power flows in the network.

Chapter 4 analyses the dynamics following a disturbance and introduces models suitable for analysing the dynamic performance of the synchronous generator. Chapter 5 explains the power system dynamics following a small disturbance (steady-state stability) while Chapter 6 examines the system dynamics following a large disturbance (transient stability). There are new sections on using the Lyapunov direct method to analyse the stability of a multi-machine power system and on out-of-step relaying. Chapter 7 is all new and covers the fundamentals of wind power generation. Chapter 8 has been greatly expanded and provides an explanation of voltage stability together with some of the methods used for stability assessment. The new material includes examples of power system blackouts, methods of preventing voltage collapse and a large new section on self-excitation of the generator. Chapter 9 contains a largely enhanced treatment of frequency stability and control including defence plans against frequency instability and quality assessment of frequency control. There is a large new section which covers a novel treatment of interaction between automatic generation control (AGC) and FACTS devices installed in tie-lines that control the flow of power between systems in an interconnected network. Chapter 10 provides an overview of the main methods of stability enhancement, both conventional and using FACTS devices. The new material

includes the use of braking resistors and a novel generalization of earlier derived stabilization algorithms to a multi-machine power system.

Chapter 11 introduces advanced models of the different power system elements. The new material includes models of the wind turbine and generator and models of FACTS devices. Chapter 12 contains a largely expanded treatment of the steady-state stability of multi-machine power systems using eigenvalue analysis. We have added a comprehensive explanation of the meaning of eigenvalues and eigenvectors including a fuller treatment of the mathematical background. As the subject matter is highly mathematical and may be difficult to understand, we have added a large number of numerical examples. Chapter 13 contains a description of numerical methods used for power system dynamic simulation. Chapter 14 explains how to reduce the size of the simulation problem by using equivalents. The chapter has been significantly expanded by adding novel material on the modal analysis of equivalents and a number of examples.

The Appendix covers the per-unit system and new material on the mathematical fundamentals of solving ordinary differential equations.

It is important to emphasize that, while most of the book is a teaching textbook written with final-year undergraduate and postgraduate students in mind, there are also large parts of material which constitute cutting-edge research, some of it never published before. This includes the use of the Lyapunov direct method to derive algorithms for the stabilization of a multi-machine power system (Chapters 6, 9 and 10) and derivation of modal-analysis-based power system dynamic equivalents (Chapter 14).

J. Machowski, J.W. Bialek and J.R. Bumby
Warsaw, Edinburgh and Durham

Acknowledgements

We would like to acknowledge the financial support of Supergen FutureNet (www.supergennetworks.org.uk). Supergen is funded by the Research Councils' Energy Programme, United Kingdom. We would also like to acknowledge the financial support of the Ministry of Science and Higher Education of Poland (grant number 3 T10B 010 29). Both grants have made possible the cooperation between the Polish and British co-authors. Last but not least, we are grateful as ever for the patience shown by our wives and families during the torturous writing of yet another book.

List of Symbols

Notation

Italic type denotes scalar physical quantity (e.g. R, L, C) or numerical variable (e.g. x, y).
Phasor or complex quantity or numerical variable is underlined (e.g. $\underline{I}$, $\underline{V}$, $\underline{S}$).
Italic with arrow on top of a symbol denotes a spatial vector (e.g. $\vec{F}$).
Italic boldface denotes a matrix or a vector (e.g. $\boldsymbol{A}$, $\boldsymbol{B}$, $\boldsymbol{x}$, $\boldsymbol{y}$).
Unit symbols are written using roman type (e.g. Hz, A, kV).
Standard mathematical functions are written using roman type (e.g. e, sin, cos, arctan).
Numbers are written using roman type (e.g. 5, 6).
Mathematical operators are written using roman type (e.g. s, Laplace operator; T, matrix transposition; j, angular shift by 90°; a, angular shift by 120°).
Differentials and partial differentials are written using roman type (e.g. $\mathrm{d}f/\mathrm{d}x$, $\partial f/\partial x$).
Symbols describing objects are written using roman type (e.g. TRAFO, LINE).
Subscripts relating to objects are written using roman type (e.g. $\underline{I}_{\mathrm{TRAFO}}$, $\underline{I}_{\mathrm{LINE}}$).
Subscripts relating to physical quantities or numerical variables are written using italic type (e.g. A_{ij}, x_k).
Subscripts A, B, C refer to the three-phase axes of a generator.
Subscripts d, q refer to the direct- and quadrature-axis components.
Lower case symbols normally denote instantaneous values (e.g. v, i).
Upper case symbols normally denote rms or peak values (e.g. V, I).

Symbols

$\underline{a}$ and $\underline{a}^2$	operators shifting the angle by 120° and 240°, respectively.
B_μ	magnetizing susceptance of a transformer.
B_{sh}	susceptance of a shunt element.
D	damping coefficient.
E_{k}	kinetic energy of the rotor relative to the synchronous speed.
E_{p}	potential energy of the rotor with respect to the equilibrium point.
e_{f}	field voltage referred to the fictitious q-axis armature coil.
e_{q}	steady-state emf induced in the fictitious q-axis armature coil proportional to the field winding self-flux linkages.
e'_{d}	transient emf induced in the fictitious d-axis armature coil proportional to the flux linkages of the q-axis coil representing the solid steel rotor body (round-rotor generators only).
e'_{q}	transient emf induced in the fictitious q-axis armature coil proportional to the field winding flux linkages.
e''_{d}	subtransient emf induced in the fictitious d-axis armature coil proportional to the total q-axis rotor flux linkages (q-axis damper winding and q-axis solid steel rotor body).

e''_{q}	subtransient emf induced in the fictitious q-axis armature coil proportional to the total d-axis rotor flux linkages (d-axis damper winding and field winding).
$\underline{E}$	steady-state internal emf.
$\underline{E}_{\mathrm{f}}$	excitation emf proportional to the excitation voltage V_{f}.
E_{fm}	peak value of the excitation emf.
E_{d}	d-axis component of the steady-state internal emf proportional to the rotor self-linkages due to currents induced in the q-axis solid steel rotor body (round-rotor generators only).
E_{q}	q-axis component of the steady-state internal emf proportional to the field winding self-flux linkages (i.e. proportional to the field current itself).
$\underline{E}'$	transient internal emf proportional to the flux linkages of the field winding and solid steel rotor body (includes armature reaction).
E'_{d}	d-axis component of the transient internal emf proportional to flux linkages in the q-axis solid steel rotor body (round-rotor generators only).
E'_{q}	q-axis component of the transient internal emf proportional to the field winding flux linkages.
$\underline{E}''$	subtransient internal emf proportional to the total rotor flux linkages (includes armature reaction).
E''_{d}	d-axis component of the subtransient internal emf proportional to the total flux linkages in the q-axis damper winding and q-axis solid steel rotor body.
E''_{q}	q-axis component of the subtransient internal emf proportional to the total flux linkages in the d-axis damper winding and the field winding.
$\underline{E}_{\mathrm{r}}$	resultant air-gap emf.
E_{rm}	amplitude of the resultant air-gap emf.
$\boldsymbol{E}_{\mathrm{G}}$	vector of the generator emfs.
f	mains frequency.
f_{n}	rated frequency.
$\vec{F}$	magnetomotive force (mmf) due to the field winding.
$\vec{F}_{\mathrm{a}}$	armature reaction mmf.
$F_{\mathrm{a\,AC}}$	AC armature reaction mmf (rotating).
$F_{\mathrm{a\,DC}}$	DC armature reaction mmf (stationary).
$\vec{F}_{\mathrm{ad}},\ \vec{F}_{\mathrm{aq}}$	d- and q-axis components of the armature reaction mmf.
$\vec{F}_{\mathrm{f}}$	resultant mmf.
G_{Fe}	core loss conductance of a transformer.
G_{sh}	conductance of a shunt element.
$H_{ii},\ H_{ij}$	self- and mutual synchronizing power.
$i_{\mathrm{A}}, i_{\mathrm{B}}, i_{\mathrm{C}}$	instantaneous currents in phases A, B and C.
$i_{\mathrm{A\,DC}}, i_{\mathrm{B\,DC}}, i_{\mathrm{C\,DC}}$	DC component of the current in phases A, B, C.
$i_{\mathrm{A\,AC}}, i_{\mathrm{B\,AC}}, i_{\mathrm{C\,AC}}$	AC component of the current in phases A, B, C.
$i_{\mathrm{d}}, i_{\mathrm{q}}$	currents flowing in the fictitious d- and q-axis armature coils.
$i_{\mathrm{D}}, i_{\mathrm{Q}}$	instantaneous d- and q-axis damper winding current.
i_{f}	instantaneous field current of a generator.
$\boldsymbol{i}_{\mathrm{ABC}}$	vector of instantaneous phase currents.
$\boldsymbol{i}_{\mathrm{fDQ}}$	vector of instantaneous currents in the field winding and the d- and q-axis damper windings.
$\boldsymbol{i}_{\mathrm{0dq}}$	vector of armature currents in the rotor reference frame.
$\underline{I}$	armature current.
$I_{\mathrm{d}},\ I_{\mathrm{q}}$	d- and q-axis component of the armature current.
$\underline{I}_{\mathrm{S}}, \underline{I}_{\mathrm{R}}$	currents at the sending and receiving end of a transmission line.
$\underline{\boldsymbol{I}}_{\mathrm{R}}, \underline{\boldsymbol{I}}_{\mathrm{E}}$	vector of complex current injections to the retained and eliminated nodes.

$\underline{\boldsymbol{I}}_{\mathrm{G}}, \underline{\boldsymbol{I}}_{\mathrm{L}}$	vector of complex generator and load currents.
$\Delta\underline{\boldsymbol{I}}_{\mathrm{L}}$	vector of load corrective complex currents.
J	moment of inertia.
j	operator shifting the angle by 90°.
$k_{\mathrm{PV}}, k_{\mathrm{QV}}$	voltage sensitivities of the load (the slopes of the real and reactive power demand characteristics as a function of voltage).
$k_{\mathrm{Pf}}, k_{\mathrm{Qf}}$	frequency sensitivities of the load (the slopes of the real and reactive power demand characteristics as a function of frequency).
$K_{E_{\mathrm{q}}}$	steady-state synchronizing power coefficient (the slope of the steady-state power angle curve $P_{E_{\mathrm{q}}}(\delta)$).
$K_{E'_{\mathrm{q}}}$	transient synchronizing power coefficient (the slope of the transient power angle curve $P_{E'_{\mathrm{q}}}(\delta')$).
$K_{E'}$	transient synchronizing power coefficient (the slope of the transient power angle curve $P_{E'}(\delta')$).
K_i	reciprocal of droop for the ith generating unit.
K_{L}	frequency sensitivity coefficient of the system real power demand.
K_{T}	reciprocal of droop for the total system generation characteristic.
l	length of a transmission line.
$L_{\mathrm{AA}}, L_{\mathrm{BB}}, L_{\mathrm{CC}}, L_{\mathrm{ff}}, L_{\mathrm{DD}}, L_{\mathrm{QQ}}$	self-inductances of the windings of the phase windings A, B, C, the field winding, and the d-and the q-axis damper winding.
$L_{\mathrm{d}}, L_{\mathrm{q}}$	inductances of the fictitious d- and q-axis armature windings.
$L'_{\mathrm{d}}, L'_{\mathrm{q}}, L''_{\mathrm{d}}, L''_{\mathrm{q}}$	d- and q-axis transient and subtransient inductances.
L_{S}	minimum value of the self-inductance of a phase winding.
L_{xy}	where $x, y \in \{\mathrm{A}, \mathrm{B}, \mathrm{C}, \mathrm{D}, \mathrm{Q}, \mathrm{f}\}$ and $x \neq y$, are the mutual inductances between the windings denoted by the indices as described above.
ΔL_{S}	amplitude of the variable part of the self-inductance of a phase winding.
$\boldsymbol{L}_{\mathrm{R}}$	submatrix of the rotor self- and mutual inductances.
$\boldsymbol{L}_{\mathrm{S}}$	submatrix of the stator self- and mutual inductances.
$\boldsymbol{L}_{\mathrm{SR}}, \boldsymbol{L}_{\mathrm{RS}}$	submatrices of the stator-to-rotor and rotor-to-stator mutual inductances.
M	coefficient of inertia.
$M_{\mathrm{f}}, M_{\mathrm{D}}, M_{\mathrm{Q}}$	amplitude of the mutual inductance between a phase winding and, respectively, the field winding and the d- and the q-axis damper winding.
N	generally, number of any objects.
p	number of poles.
P_{acc}	accelerating power.
P_{D}	damping power.
P_{e}	electromagnetic air-gap power.
$P_{E_{\mathrm{q}}\,\mathrm{cr}}$	critical (pull-out) air-gap power developed by a generator.
$P_{E_{\mathrm{q}}}(\delta), P_{E'}(\delta'), P_{E'_{\mathrm{q}}}(\delta')$	air-gap power curves assuming $E_{\mathrm{q}} =$ constant, $E' =$ constant and $E'_{\mathrm{q}} =$ constant.
P_{g}	in induction machine, real power supplied from the grid (motoring mode), or supplied to the grid (generating mode).
P_{L}	real power absorbed by a load or total system load.
P_{m}	mechanical power supplied by a prime mover to a generator; also mechanical power supplied by a motor to a load (induction machine in motoring mode).
P_{n}	real power demand at rated voltage.
P_{R}	real power at the receiving end of a transmission line.
$P_{\mathrm{rI}}, P_{\mathrm{rII}}, P_{\mathrm{rIII}}, P_{\mathrm{rIV}}$	contribution of the generating units remaining in operation to covering the real power imbalance during the first, second, third and fourth stages of load frequency control.

P_{sI}, P_{sII}, P_{sIII}, P_{sIV}	contribution of the system to covering the real power imbalance during the first, second, third and fourth stages of load frequency control.
P_s	stator power of induction machine or power supplied by the system.
P_S	real power at the sending end of a transmission line or real power supplied by a source to a load or real power supplied to an infinite busbar.
P_{SIL}	surge impedance (natural) load.
$P_{sE_q}(\delta)$	curve of real power supplied to an infinite busbar assuming $E_q =$ constant.
P_T	total power generated in a system.
P_{tie}	net tie-line interchange power.
$P_{V_g}(\delta)$	air-gap power curve assuming $V_g =$ constant.
$P_{V_g\,cr}$	critical value of $P_{V_g}(\delta)$.
Q_L	reactive power absorbed by a load.
Q_G	reactive power generated by a source (the sum of Q_L and the reactive power loss in the network).
Q_n	reactive power demand at rated voltage.
Q_R	reactive power at the receiving end of a transmission line.
Q_S	reactive power at the sending end of a transmission line or reactive power supplied by a source to a load.
R	resistance of the armature winding of a generator.
r	total resistance between (and including) a generator and an infinite busbar.
R_A, R_B, R_C, R_D, R_Q, R_f	resistances of the phase windings A, B, C, the d- and q-axis damper winding, and the field winding.
$\boldsymbol{R}_{ABC}$	diagonal matrix of phase winding resistances.
$\boldsymbol{R}_{fDQ}$	diagonal matrix of resistances of the field winding and the d- and q-axis damper windings.
s	Laplace operator.
s	slip of induction motor.
s_{cr}	critical slip of induction motor.
S_n	rated apparent power.
S_{SHC}	short-circuit power.
t	time.
T'_d, T''_d	short-circuit d-axis transient and subtransient time constants.
T'_{do}, T''_{do}	open-circuit d-axis transient and subtransient time constants.
T'_q, T''_q	short-circuit q-axis transient and subtransient time constants.
T'_{qo}, T''_{qo}	open-circuit q-axis transient and subtransient time constants.
T_a	armature winding time constant.
$\boldsymbol{T}$	transformation matrix between network (a, b) and generator (d, q) coordinates.
v_A, v_B, v_C, v_f	instantaneous voltages across phases A, B, C and the field winding.
v_d, v_q	voltages across the fictitious d- and q-axis armature coils.
v_w	wind speed.
$\boldsymbol{v}_{ABC}$	vector of instantaneous voltages across phases A, B, C.
$\boldsymbol{v}_{fDQ}$	vector of instantaneous voltages across the field winding and the d- and q-axis damper windings.
V	Lyapunov function.
V_{cr}	critical value of the voltage.
V_d, V_q	direct- and quadrature-axis component of the generator terminal voltage.
V_f	voltage applied to the field winding.
$\underline{V}_g$	voltage at the generator terminals.

$\underline{V}_s$	infinite busbar voltage.
V_{sd}, V_{sq}	direct- and quadrature-axis component of the infinite busbar voltage.
$\underline{V}_S$, $\underline{V}_R$	voltage at the sending and receiving end of a transmission line.
V_{sh}	local voltage at the point of installation of a shunt element.
$\underline{V}_i = V_i \angle \delta_i$	complex voltage at node i.
$\underline{\boldsymbol{V}}_R$, $\underline{\boldsymbol{V}}_E$	vector of complex voltages at the retained and eliminated nodes.
W	work.
$\boldsymbol{W}$	Park's modified transformation matrix.
$\boldsymbol{W}$, $\boldsymbol{U}$	modal matrices of right and left eigenvectors.
X_a	armature reaction reactance (round-rotor generator).
X_C	reactance of a series compensator.
X_D	reactance corresponding to the flux path around the damper winding.
X_d, X'_d, X''_d	d-axis synchronous, transient and subtransient reactance.
x_d, x'_d, x''_d	total d-axis synchronous, transient and subtransient reactance between (and including) a generator and an infinite busbar.
$x'_{d\,PRE}$, $x'_{d\,F}$, $x'_{d\,POST}$	prefault, fault and postfault value of x'_d.
X_f	reactance corresponding to the flux path around the field winding.
X_l	armature leakage reactance of a generator.
X_q, X'_q, X''_q	q-axis synchronous, transient and subtransient reactance.
x_q, x'_q, x''_q	total q-axis synchronous, transient and subtransient reactance between (and including) a generator and an infinite busbar.
X_{SHC}	short-circuit reactance of a system as seen from a node.
Y_T	admittance of a transformer.
$\underline{\boldsymbol{Y}}$	admittance matrix.
$\underline{\boldsymbol{Y}}_{GG}$, $\underline{\boldsymbol{Y}}_{LL}$, $\underline{\boldsymbol{Y}}_{LG}$, $\underline{\boldsymbol{Y}}_{LG}$	admittance submatrices where subscript G corresponds to fictitious generator nodes and subscript L corresponds to all the other nodes (including generator terminal nodes).
$\underline{Y}_{ij} = G_{ij} + \mathrm{j}B_{ij}$	element of the admittance matrix.
$\underline{\boldsymbol{Y}}_{RR}$, $\underline{\boldsymbol{Y}}_{EE}$, $\underline{\boldsymbol{Y}}_{RE}$, $\underline{\boldsymbol{Y}}_{ER}$	complex admittance submatrices where subscript E refers to eliminated nodes and subscript R to retained nodes.
Z_c	characteristic impedance of a transmission line.
$\underline{Z}_s = R_s + \mathrm{j}X_s$	internal impedance of an infinite busbar.
$\underline{Z}_T = R_T + \mathrm{j}X_T$	series impedance of a transformer.
β	phase constant of a transmission line.
γ	instantaneous position of the generator d-axis relative to phase A; propagation constant of a transmission line.
γ_0	position of the generator d-axis at the instant of fault.
δ	power (or rotor) angle with respect to an infinite busbar.
δ_g	power (or rotor) angle with respect to the voltage at the generator terminals.
$\hat{\delta}_s$	stable equilibrium value of the rotor angle.
δ'	transient power (or rotor) angle between E' and V_s.
δ_{fr}	angle between the resultant and field mmfs.
$\Delta\omega$	rotor speed deviation equal to $(\omega - \omega_s)$.
ε	rotor acceleration.
ζ	damping ratio.
ϑ	transformation ratio.
λ_R	frequency bias factor.
$\lambda_i = \alpha_i + \mathrm{j}\Omega_i$	eigenvalue.
ρ	static droop of the turbine–governor characteristic.
ρ_T	droop of the total system generation characteristic.

τ_e	electromagnetic torque.
τ_m	mechanical torque.
τ_ω	fundamental-frequency subtransient electromagnetic torque.
$\tau_{2\omega}$	double-frequency subtransient electromagnetic torque.
τ_d, τ_q	direct- and quadrature-axis component of the electromagnetic torque.
τ_R, τ_r	subtransient electromagnetic torque due to stator and rotor resistances.
φ_g	power factor angle at the generator terminals.
Φ_a	armature reaction flux.
Φ_{ad}, Φ_{aq}	d- and q-axis component of the armature reaction flux.
$\Phi_{a\,AC}$	AC armature reaction flux (rotating).
$\Phi_{a\,DC}$	DC armature reaction flux (stationary).
Φ_f	excitation (field) flux.
Ψ_A, Ψ_B, Ψ_C	total flux linkage of phases A, B, C.
Ψ_{AA}, Ψ_{BB}, Ψ_B	self-flux linkage of phases A, B, C.
$\Psi_{a\,AC\,r}$	rotor flux linkages produced by $\Phi_{a\,AC}$.
$\Psi_{a\,DC\,r}$	rotor flux linkages produced by $\Phi_{a\,DC}$.
$\Psi_{a\,r}$	rotor flux linkages produced by the total armature reaction flux.
Ψ_D, Ψ_Q	total flux linkage of damper windings in axes d and q.
Ψ_d, Ψ_q	total d- and q-axis flux linkages.
Ψ_f	total flux linkage of the field winding.
Ψ_{fa}	excitation flux linkage with armature winding.
Ψ_{fA}, Ψ_{fB}, Ψ_{fC}	excitation flux linkage with phases A, B and C.
$\boldsymbol{\Psi}_{ABC}$	vector of phase flux linkages.
$\boldsymbol{\Psi}_{fDQ}$	vector of flux linkages of the field winding and the d- and q-axis damper windings.
$\boldsymbol{\Psi}_{0dq}$	vector of armature flux linkages in the rotor reference frame.
ω	angular velocity of the generator (in electrical radians).
ω_s	synchronous angular velocity in electrical radians (equal to $2\pi f$).
ω_T	rotor speed of wind turbine (in rad/s)
Ω	frequency of rotor swings (in rad/s)
Ω	rotation matrix.
$\Re$	reluctance.
$\Re_d$, $\Re_q$	reluctance along the direct- and quadrature-axis.

Abbreviations

AC	alternating current
ACE	area control error
AGC	Automatic Generation Control
AVR	Automatic Voltage Regulator
BEES	Battery Energy Storage System
d	direct axis of a generator
DC	direct current
DFIG	Doubly Fed Induction Generator
DFIM	Double Fed Induction Machine
DSA	Dynamic Security Assessment
emf	electro-motive force
EMS	Energy Management System
FACTS	Flexible AC Transmission Systems
HV	high voltage
HAWT	Horizontal-Axis Wind Turbine

IGTB	insulated gate bipolar transistor
IGTC	integrated gate-commutated thyristor
LFC	load frequency control
mmf	magneto-motive force
MAWS	mean annual wind speed
PMU	Phasor Measurement Unit
PSS	power system stabiliser
pu	per unit
q	quadrature axis of a generator
rms	root-mean-square
rpm	revolutions per minute
rhs	right-hand-side
SCADA	Supervisory Control and Data Acquisition
SIL	surge impedance load
SMES	superconducting magnetic energy storage
SSSC	Static Synchronous Series Compensator
STATCOM	static compensator
SVC	Static VAR Compensator
TCBR	Thyristor Controlled Braking Resistor
TCPAR	Thyristor Controlled Phase Angle Regulator
TSO	Transmission System Operator
VAWT	Vertical-Axis Wind Turbine
UPFC	unified power flow controller
WAMS	Wide Area Measurement System
WAMPAC	Wide Area Measurement, Protection and Control

Part I

Introduction to Power Systems

1

Introduction

1.1 Stability and Control of a Dynamic System

In engineering, a *system* is understood to be a set of physical elements acting together and realizing a common goal. An important role in the analysis of the system is played by its *mathematical model*. It is created using the system structure and fundamental physical laws governing the system elements. In the case of complicated systems, mathematical models usually do not have a universal character but rather reflect some characteristic phenomena which are of interest. Because of mathematical complications, practically used system models are usually a compromise between a required accuracy of modelling and a degree of complication.

When formulating a system model, important terms are the *system state* and the *state variables*. The system state describes the system's operating conditions. The state variables are the minimum set of variables $x_1, x_2, \ldots, x_n$ uniquely defining the system state. State variables written as a vector $\boldsymbol{x} = [x_1, x_2, \ldots, x_n]^{\mathrm{T}}$ are referred to as the *state vector*. A normalized space of coordinates corresponding to the state variables is referred to as the *state space*. In the state space, each system state corresponds to a point defined by the state vector. Hence, a term 'system state' often refers also to a point in the state space.

A system may be *static*, when its state variables $x_1, x_2, \ldots, x_n$ are time invariant, or *dynamic*, when they are functions of time, that is $x_1(t), x_2(t), \ldots, x_n(t)$.

This book is devoted to the analysis of dynamic systems modelled by ordinary differential equations of the form

$$\dot{\boldsymbol{x}} = \boldsymbol{F}(\boldsymbol{x}) \quad \text{or} \quad \dot{\boldsymbol{x}} = \boldsymbol{A}\,\boldsymbol{x}, \tag{1.1}$$

where the first of the equations above describes a *nonlinear system* and the second describes a *linear system*. $\boldsymbol{F}(\boldsymbol{x})$ is just a vector of nonlinear functions and $\boldsymbol{A}$ is a square matrix.

A curve $\boldsymbol{x}(t)$ in the state space containing system states (points) in consecutive time instants is referred to as the *system trajectory*. A trivial one-point trajectory $\boldsymbol{x}(t) = \hat{\boldsymbol{x}} =$ constant is referred to as the *equilibrium point* (*state*), if in that point all the partial derivatives are zero (no movement), that is $\dot{\boldsymbol{x}} = 0$. According to Equation (1.1), the coordinates of the point satisfy the following equations:

$$\boldsymbol{F}(\hat{\boldsymbol{x}}) = 0 \quad \text{or} \quad \boldsymbol{A}\,\hat{\boldsymbol{x}} = 0. \tag{1.2}$$

A nonlinear system may have more than one equilibrium point because nonlinear equations may have generally more than one solution. In the case of linear systems, according to the Cramer theorem concerning linear equations, there exists only one uniquely specified equilibrium point $\hat{\boldsymbol{x}} = 0$ if and only if the matrix $\boldsymbol{A}$ is non-singular ($\det \boldsymbol{A} \neq 0$).

Power System Dynamics: Stability and Control, Second Edition Jan Machowski, Janusz W. Bialek and James R. Bumby
© 2008 John Wiley & Sons, Ltd

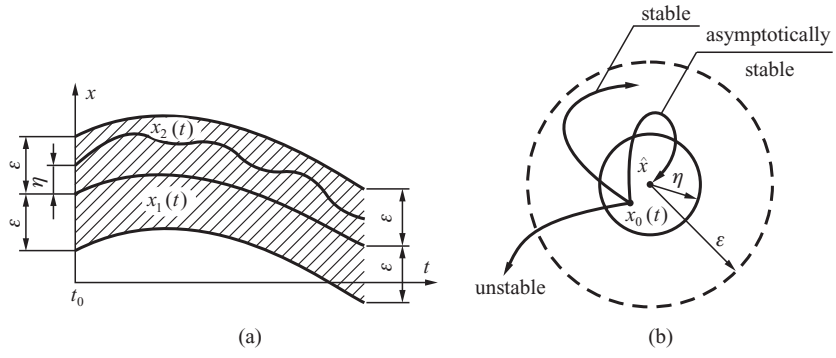

Figure 1.1 Illustration of the definition of stability: (a) when the initial conditions are different but close; (b) in a vicinity of the equilibrium point.

All the states of a dynamic system, apart from equilibrium states, are dynamic states because the derivatives $\dot{\boldsymbol{x}} \neq 0$ for those states are non-zero, which means a movement. *Disturbance* means a random (usually unintentional) event affecting the system. Disturbances affecting dynamic systems are modelled by changes in their coefficients (parameters) or by non-zero initial conditions of differential equations.

Let $\boldsymbol{x}_1(t)$ be a trajectory of a dynamic system, see Figure 1.1a, corresponding to some initial conditions. The system is considered *stable in a Lyapunov sense* if for any t_0 it is possible to choose a number η such that for all the other initial conditions satisfying the constraint $\|\boldsymbol{x}_2(t_0) - \boldsymbol{x}_1(t_0)\| < \eta$, the expression $\|\boldsymbol{x}_2(t) - \boldsymbol{x}_1(t)\| < \varepsilon$ holds for $t_0 \leq t < \infty$. In other words, stability means that if the trajectory $\boldsymbol{x}_2(t)$ starts close enough (as defined by η) to the trajectory $\boldsymbol{x}_1(t)$ then it remains close to it (number ε). Moreover, if the trajectory $\boldsymbol{x}_2(t)$ tends with time towards the trajectory $\boldsymbol{x}_1(t)$, that is $\lim_{t\to\infty} \|\boldsymbol{x}_2(t) - \boldsymbol{x}_1(t)\| = 0$, then the dynamic system is *asymptotically stable*.

The above definition concerns any trajectory of a dynamic system. Hence it must also be valid for a trivial trajectory such as the equilibrium point $\hat{\boldsymbol{x}}$. In this particular case, see Figure 1.1b, the trajectory $\boldsymbol{x}_1(t)$ is a point $\hat{\boldsymbol{x}}$ and the initial condition $\boldsymbol{x}_2(t_0)$ of trajectory $\boldsymbol{x}_2(t)$ lies in the vicinity of the point defined by η. The dynamic system is stable in the equilibrium point $\hat{\boldsymbol{x}}$ if for $t_0 \leq t < \infty$ the trajectory $\boldsymbol{x}_2(t)$ does not leave an area defined by the number ε. Moreover, if the trajectory $\boldsymbol{x}_2(t)$ tends with time towards the equilibrium point $\hat{\boldsymbol{x}}$, that is $\lim_{t\to\infty} \|\boldsymbol{x}_2(t) - \hat{\boldsymbol{x}}\| = 0$, then the system is said to be asymptotically stable at the equilibrium point $\hat{\boldsymbol{x}}$. On the other hand, if the trajectory $\boldsymbol{x}_2(t)$ tends with time to leave the area defined by ε, then the dynamic system is said to be unstable at the equilibrium point $\hat{\boldsymbol{x}}$.

It can be shown that stability of a linear system does not depend on the size of a disturbance. Hence if a linear system is stable for a small disturbance then it is also globally stable for any large disturbance.

The situation is different with nonlinear systems as their stability generally depends on the size of a disturbance. A nonlinear system may be stable for a small disturbance but unstable for a large disturbance. The largest disturbance for which a nonlinear system is still stable is referred to as a *critical disturbance*.

Dynamic systems are designed and constructed with a particular task in mind and assuming that they will behave in a particular way following a disturbance. A purposeful action affecting a dynamic system which aims to achieve a particular behaviour is referred to as a *control*. The definition of control is illustrated in Figure 1.2. The following signals have been defined:

- $\boldsymbol{u}(t)$ – a control signal which affects the system to achieve a desired behaviour;
- $\boldsymbol{y}(t)$ – an output signal which serves to assess whether or not the control achieved the desired goal;

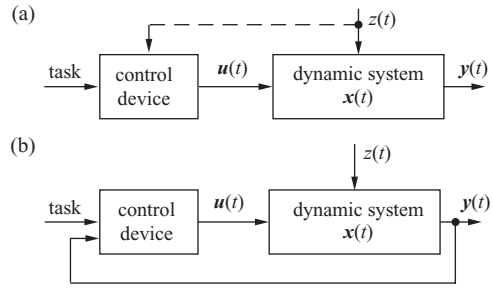

Figure 1.2 Illustration of the definition of: (a) open-loop control; (b) closed-loop control.

- $\boldsymbol{x}(t)$ – system state variables;
- $\boldsymbol{z}(t)$ – disturbances.

Control can be open loop or closed loop. In the case of open-loop control, see Figure 1.2a, control signals are created by a control device which tries to achieve a desired system behaviour without obtaining any information about the output signals. Such control makes sense only when it is possible to predict the shape of output signals from the control signals. However, if there are additional disturbances which are not a part of the control, then their action may lead to the control objective not being achieved.

In the case of closed-loop control, see Figure 1.2b, control signals are chosen based on the control task and knowledge of the system output signals describing whether the control task has been achieved. Hence the control is a function of its effects and acts until the control task has been achieved.

Closed-loop control is referred to as *feedback control* or *regulation*. The control device is then called a *regulator* and the path connecting the output signals with the control device (regulator) is called the *feedback loop*.

A nonlinear dynamic system with its control can be generally described by the following set of algebraic and differential equations:

$$\dot{\boldsymbol{x}} = \boldsymbol{F}(\boldsymbol{x}, \boldsymbol{u}) \quad \text{and} \quad \boldsymbol{y} = \boldsymbol{G}(\boldsymbol{x}, \boldsymbol{u}), \tag{1.3}$$

while a linear dynamic system model is

$$\dot{\boldsymbol{x}} = \boldsymbol{A}\,\boldsymbol{x} + \boldsymbol{B}\,\boldsymbol{u} \quad \text{and} \quad \boldsymbol{y} = \boldsymbol{C}\,\boldsymbol{x} + \boldsymbol{D}\,\boldsymbol{u}. \tag{1.4}$$

It is easy to show that, for small changes in state variables and output and control signals, Equations (1.4) are linear approximations of nonlinear equations (1.3). In other words, linearization of (1.3) leads to the equations

$$\Delta\dot{\boldsymbol{x}} = \boldsymbol{A}\,\Delta\boldsymbol{x} + \boldsymbol{B}\,\Delta\boldsymbol{u} \quad \text{and} \quad \Delta\boldsymbol{y} = \boldsymbol{C}\,\Delta\boldsymbol{x} + \boldsymbol{D}\,\Delta\boldsymbol{u}, \tag{1.5}$$

where $\boldsymbol{A}$, $\boldsymbol{B}$, $\boldsymbol{C}$, $\boldsymbol{D}$ are the matrices of derivatives of functions $\boldsymbol{F}$, $\boldsymbol{G}$ with respect to $\boldsymbol{x}$ and $\boldsymbol{u}$.

1.2 Classification of Power System Dynamics

An electrical power system consists of many individual elements connected together to form a large, complex and dynamic system capable of generating, transmitting and distributing electrical energy over a large geographical area. Because of this interconnection of elements, a large variety of dynamic interactions are possible, some of which will only affect some of the elements, others

are fragments of the system, while others may affect the system as a whole. As each dynamic effect displays certain unique features. Power system dynamics can be conveniently divided into groups characterized by their cause, consequence, time frame, physical character or the place in the system where they occur.

Of prime concern is the way the power system will respond to both a changing power demand and to various types of disturbance, the two main causes of power system dynamics. A changing power demand introduces a wide spectrum of dynamic changes into the system each of which occurs on a different time scale. In this context the fastest dynamics are due to sudden changes in demand and are associated with the transfer of energy between the rotating masses in the generators and the loads. Slightly slower are the voltage and frequency control actions needed to maintain system operating conditions until finally the very slow dynamics corresponding to the way in which the generation is adjusted to meet the slow daily demand variations take effect. Similarly, the way in which the system responds to disturbances also covers a wide spectrum of dynamics and associated time frames. In this case the fastest dynamics are those associated with the very fast wave phenomena that occur in high-voltage transmission lines. These are followed by fast electromagnetic changes in the electrical machines themselves before the relatively slow electromechanical rotor oscillations occur. Finally the very slow prime mover and automatic generation control actions take effect.

Based on their physical character, the different power system dynamics may be divided into four groups defined as: *wave*, *electromagnetic*, *electromechanical* and *thermodynamic*. This classification also corresponds to the time frame involved and is shown in Figure 1.3. Although this broad classification is convenient, it is by no means absolute, with some of the dynamics belonging to two or more groups while others lie on the boundary between groups. Figure 1.3 shows the fastest dynamics to be the wave effects, or surges, in high-voltage transmission lines and correspond to the propagation of electromagnetic waves caused by lightning strikes or switching operations. The time frame of these dynamics is from microseconds to milliseconds. Much slower are the electromagnetic dynamics that take place in the machine windings following a disturbance, operation of the protection system or the interaction between the electrical machines and the network. Their time frame is from milliseconds to a second. Slower still are the electromechanical dynamics due to the oscillation of the rotating masses of the generators and motors that occur following a disturbance, operation of the protection system and voltage and prime mover control. The time frame of these dynamics is from seconds to several seconds. The slowest dynamics are the thermodynamic changes which result from boiler control action in steam power plants as the demands of the automatic generation control are implemented.

Careful inspection of Figure 1.3 shows the classification of power system dynamics with respect to time frame to be closely related to where the dynamics occur within the system. For example, moving from the left to right along the time scale in Figure 1.3 corresponds to moving through the power system from the electrical *RLC* circuits of the transmission network, through the generator

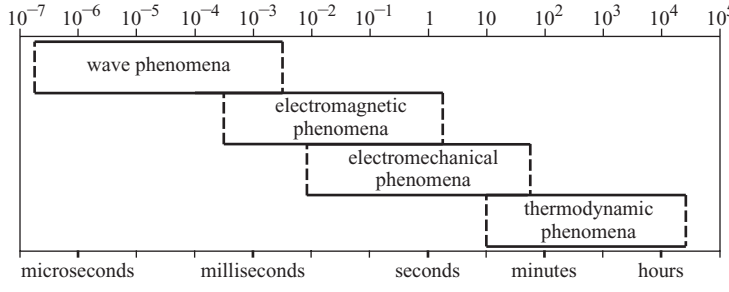

Figure 1.3 Time frame of the basic power system dynamic phenomena.

armature windings to the field and damper winding, then along the generator rotor to the turbine until finally the boiler is reached.

The fast wave phenomena, due to lightning and switching overvoltages, occur almost exclusively in the network and basically do not propagate beyond the transformer windings. The electromagnetic phenomena mainly involve the generator armature and damper windings and partly the network. These electromechanical phenomena, namely the rotor oscillations and accompanying network power swings, mainly involve the rotor field and damper windings and the rotor inertia. As the power system network connects the generators together, this enables interactions between swinging generator rotors to take place. An important role is played here by the automatic voltage control and the prime mover control. Slightly slower than the electromechanical phenomena are the frequency oscillations, in which the rotor dynamics still play an important part, but are influenced to a much greater extent by the action of the turbine governing systems and the automatic generation control. Automatic generation control also influences the thermodynamic changes due to boiler control action in steam power plants.

The fact that the time frame of the dynamic phenomena is closely related to where it occurs within the power system has important consequences for the modelling of the system elements. In particular, moving from left to right along Figure 1.3 corresponds to a reduction in the accuracy required in the models used to represent the network elements, but an increase in the accuracy in the models used first to represent the electrical components of the generating unit and then, further to the right, the mechanical and thermal parts of the unit. This important fact is taken into account in the general structure of this book when later chapters describe the different power system dynamic phenomena.

1.3 Two Pairs of Important Quantities: Reactive Power/Voltage and Real Power/Frequency

This book is devoted to the analysis of electromechanical phenomena and control processes in power systems. The main elements of electrical power networks are transmission lines and transformers which are usually modelled by four-terminal (two-port) *RLC* elements. Those models are connected together according to the network configuration to form a network diagram.

For further use in this book, some general relationships will be derived below for a two-port π-equivalent circuit in which the series branch consists of only an inductance and the shunt branch is completely neglected. The equivalent circuit and the phasor diagram of such an element are shown in Figure 1.4a. The voltages V and E are phase voltages while P and Q are single-phase powers. The phasor $\underline{E}$ has been obtained by adding voltage drop $\mathrm{j}X\underline{I}$, perpendicular to $\underline{I}$, to the voltage $\underline{V}$. The triangles OAD and BAC are similar. Analysing triangles BAC and OBC gives

$$|\mathrm{BC}| = XI\cos\varphi = E\sin\delta \quad \text{hence} \quad I\cos\varphi = \frac{E}{X}\sin\delta, \tag{1.6}$$

$$|\mathrm{AC}| = XI\sin\varphi = E\cos\delta - V \quad \text{hence} \quad I\sin\varphi = \frac{E}{X}\cos\delta - \frac{V}{X}. \tag{1.7}$$

Real power leaving the element is expressed as $P = VI\cos\varphi$. Substituting (1.6) into that equation gives

$$P = \frac{EV}{X}\sin\delta. \tag{1.8}$$

This equation shows that real power P depends on the product of phase voltages and the sine of the angle δ between their phasors. In power networks, node voltages must be within a small percentage of their nominal values. Hence such small variations cannot influence the value of real power. The conclusion is that large changes of real power, from negative to positive values, correspond to

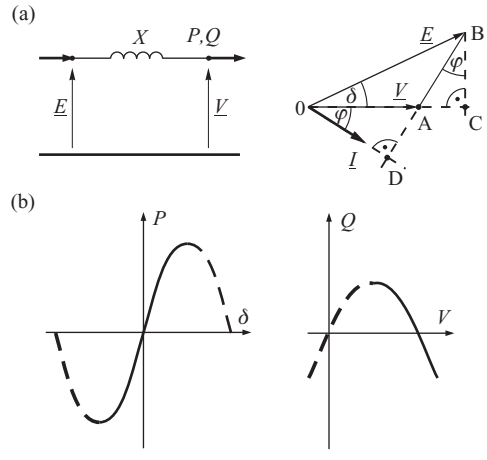

Figure 1.4 A simplified model of a network element: (a) equivalent diagram and phasor diagram; (b) real power and reactive power characteristics.

changes in the sine of the angle δ. The characteristic $P(\delta)$ is therefore sinusoidal[1] and is referred to as the *power–angle characteristic*, while the angle δ is referred to as the *power angle* or the *load angle*. Because of the stability considerations discussed in Chapter 5, the system can operate only in that part of the characteristic which is shown by a solid line in Figure 1.4b. The smaller the reactance X, the higher the amplitude of the characteristic.

The per-phase reactive power leaving the element is expressed as $Q = VI \sin\varphi$. Substituting (1.7) into that equation gives

$$Q = \frac{EV}{X}\cos\delta - \frac{V^2}{X}. \tag{1.9}$$

The term $\cos\delta$ is determined by the value of real power because the relationship between the sine and cosine is $\cos\delta = \sqrt{1 - \sin^2\delta}$. Using that equation and (1.8) gives

$$Q = \sqrt{\left(\frac{EV}{X}\right)^2 - P^2} - \frac{V^2}{X}. \tag{1.10}$$

The characteristic $Q(V)$ corresponds to an inverted parabola (Figure 1.4b). Because of the stability considerations discussed in Chapter 8, the system can operate only in that part of the characteristic which is shown by a solid line.

The smaller the reactance X, the steeper the parabola, and even small changes in V cause large changes in reactive power. Obviously the inverse relationship also takes place: a change in reactive power causes a change in voltage.

The above analysis points out that Q, V and P, δ form two pairs of strongly connected variables. Hence one should always remember that voltage control strongly influences reactive power flows and vice versa. Similarly, when talking about real power P one should remember that it is connected with angle δ. That angle is also strongly connected with system frequency f, as discussed later in the book. Hence the pair P, f is also strongly connected and important for understanding power system operation.

[1] For a real transmission line or transformer the characteristic will be approximately sinusoidal as discussed in Chapter 3.

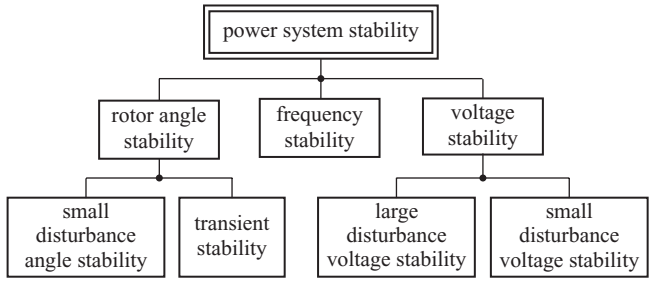

Figure 1.5 Classification of power system stability (based on CIGRE Report No. 325). Reproduced by permission of CIGRE

1.4 Stability of a Power System

Power system stability is understood as the ability to regain an equilibrium state after being subjected to a physical disturbance. Section 1.3 showed that three quantities are important for power system operation: (i) angles of nodal voltages δ, also called power or load angles; (ii) frequency f; and (iii) nodal voltage magnitudes V. These quantities are especially important from the point of view of defining and classifying power system stability. Hence power system stability can be divided (Figure 1.5) into: (i) rotor (or power) angle stability; (ii) frequency stability; and (iii) voltage stability.

As power systems are nonlinear, their stability depends on both the initial conditions and the size of a disturbance. Consequently, angle and voltage stability can be divided into small- and large-disturbance stability.

Power system stability is mainly connected with electromechanical phenomena – see Figure 1.3. However, it is also affected by fast electromagnetic phenomena and slow thermodynamic phenomena. Hence, depending on the type of phenomena, one can refer to *short-term stability* and *long-term stability*. All of them will be discussed in detail in this book.

1.5 Security of a Power System

A set of imminent disturbances is referred to as *contingencies*. *Power system security* is understood as the ability of the power system to survive plausible contingencies without interruption to customer service. Power system security and power system stability are related terms. Stability is an important factor of power system security, but security is a wider term than stability. Security not only includes stability, but also encompasses the integrity of a power system and assessment of the equilibrium state from the point of view of overloads, under- or overvoltages and underfrequency.

From the point of view of power system security, the operating states may be classified as in Figure 1.6. Most authors credit Dy Liacco (1968) for defining and classifying these states.

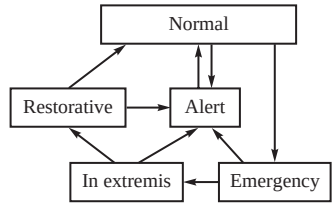

Figure 1.6 Classification of power system operating states (based on CIGRE Report No. 325). Reproduced by permission of CIGRE

In the *normal state*, a power system satisfies the power demand of all the customers, all the quantities important for power system operation assume values within their technical constraints, and the system is able to withstand any plausible contingencies.

The *alert state* arises when some quantities that are important for power system operation (e.g. line currents or nodal voltages) exceed their technical constraints due to an unexpected rise in demand or a severe contingency, but the power system is still intact and supplies its customers. In that state a further increase in demand or another contingency may threaten power system operation and preventive actions must be undertaken to restore the system to its normal state.

In the *emergency state* the power system is still intact and supplies its customers, but the violation of constraints is more severe. The emergency state usually follows the alert state when preventive actions have not been undertaken or have not been successful. A power system may assume the emergency state directly from the normal state following unusually severe contingencies like multiple faults. When a system is in the emergency state, it is necessary to undertake effective corrective actions leading first to the alert state and then to the normal state.

A power system can transpose to the *in extremis state* from the emergency state if no corrective actions have been undertaken and the system is already not intact due to a reduction of power supply following load shedding or when generators were tripped because of a lack of synchronism. The extreme variant of that state is a partial or complete blackout.

To return a power system from an *in extremis* state to an alert or normal state, a *restorative state* is necessary in which power system operators perform control actions in order to reconnect all the facilities and restore all system loads.

Assessment of power system security can be divided into static and dynamic security. Static security assessment (SSA) includes the following computational methods:

- for the pre-contingency states, determine the available transfer capability of transmission links and identify network congestion;
- for the post-contingency states, verify the bus voltages and line power flow limits.

Those tasks of SSA have always been the subject of great interest for power dispatching centres. However, when the industry was still vertically integrated (see Chapter 2), security management was relatively easy to execute because any decisions affecting the outputs or control settings of power plants could be implemented internally within a utility controlling both generation and transmission. Security management is not that easy to execute in the unbundled industry structure when the system operator has no direct control of generation. Any decisions affecting outputs or control settings of power plants have to be implemented using commercial agreements with power plants or enforced through the Grid Code. Especially, the analysis of available transfer capacity and congestion management have important implications for power plants as they directly affect their outputs, and therefore revenues.

SSA methods assume that every transition from the pre- to post-contingency state takes place without suffering any instability phenomena. Dynamic security assessment (DSA) includes methods to evaluate stability and quality of the transition from the pre- to post-contingency state. Typical criteria for DSA include:

(i) rotor (power) angle stability, voltage stability, frequency stability;
(ii) frequency excursion during the dynamic state (dip or rise) beyond specified threshold levels;
(iii) voltage excursion during the dynamic state (dip or rise) beyond specified threshold levels;
(iv) damping of power swings inside subsystems and between subsystems on an interconnected network.

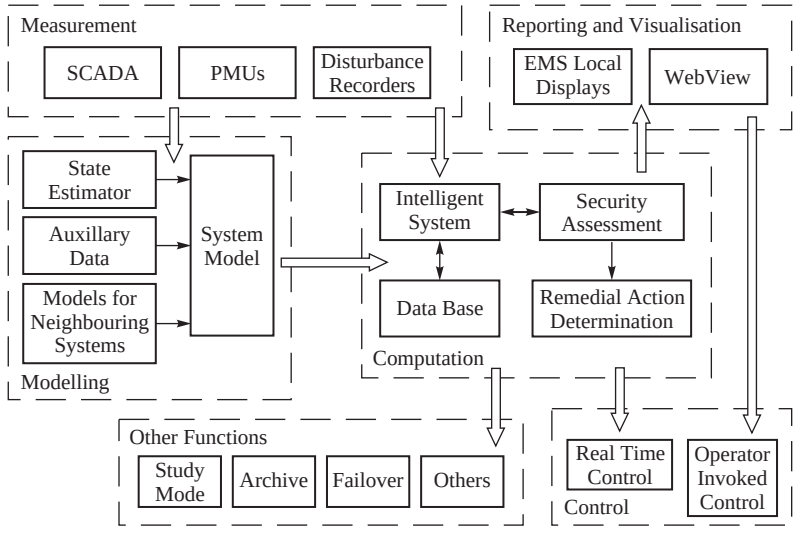

Figure 1.7 Components of DSA according to CIGRE Report No. 325. Reproduced by permission of CIGRE

Criteria (i) and (ii) are assessed using computer programs executing *transient security assessment* (TSA). Criteria (iii) are assessed by programs executing *voltage security assessment* (VSA), and criteria (iv) are assessed using programs executing *small-signal stability assessment* (SSSA).

Recent years have seen a number of total and partial blackouts in many countries of the world. These events have spurred a renewed interest among system operators in the tools for SSA and DSA. There are a variety of online DSA architectures. Figure 1.7 shows an example of the DSA architecture. The main components are denoted by boxes drawn with dashed lines.

The task of the component 'measurement' is online data acquisition and taking a snapshot of power system conditions. Supervisory control and data acquisition (SCADA) systems usually collect measurements of real and reactive power in network branches, busbar voltages, frequency at a few locations in the system, status of switchgear and the position of tap changers of transformers. As will be shown in Section 2.6, new SCADA systems are often augmented by phasor measurement units (PMUs) collecting synchronized voltage phasor measurements.

The 'modelling' component uses online data from the 'measurement' component and augments them with offline data, obtained from a database, describing the parameters of power system elements and contingencies to be analysed. The task of the 'modelling' component is to create an online power system model using the identification of the power system configuration and state estimation. That component may also contain computer programs for the creation of equivalent models of neighbouring systems. Contingencies vary according to the type of security being examined and in general need to be able to cater for a variety of events like short circuits at any location, opening any line or transformer, loss of the largest generating unit or largest load in a region, multiple faults (when considered to be credible) and so on.

The next important component is 'computation'. Its task is system model validation and security assessment. The accuracy of the security assessment depends on the quality of the system model. Offline data delivered to the 'modelling' component are validated through field testing of devices. Online data of the network configuration and system state obtained from the 'measuring' component are validated using bad measurement data identification and removal which is made possible by redundancy of measurements. The best methodology for power system model validation is via a comparison of simulation results of the dynamic response of the power system with recorded

responses following some disturbances. To achieve this, the 'measurement' component sends data from disturbance recorders to the 'computation' component. The tools for the security assessment consist of a number of computer programs executing voltage stability analysis, small-signal stability analysis, transient stability analysis by hybrid methods combining system simulation, and the Lyapunov direct method described in the textbook by Pavella, Ernst and Ruiz-Vega (2000). Intelligent systems are also used, employing learning from the situations previously seen.

The 'reporting and visualization' component is very important for a system operator employing the described architecture. Computer programs of the 'computation' component process a huge amount of data and analyse a large number of variants. On the other hand, the operator must receive a minimum number of results displayed in the most synthetic, preferably graphic, way. Some DSA displays have been shown in CIGRE Report No. 325. If the power system is in a normal state, the synthetic results should report how close the system is to an insecure state to give the operator an idea of what might happen. If the system moves to an alert state or to an emergency state, the displayed result should also contain information about preventive or corrective action. This information is passed on to the 'control' component. This component assists the operator in preventive and corrective actions that are executed to improve power system operation. Some information produced by security assessment programs may be used to produce remedial control actions, which can be automatically executed by real-time control.

The description of the current state of the art in DSA can be found in CIGRE Report No. 325.

1.6 Brief Historical Overview

The first articles on power systems dynamics began to appear in conference proceedings and technical journals at about the same time as the first interconnected power systems were constructed. As power systems developed, interest in their behaviour grew until power system dynamics became a scientific discipline in its own right.

Perhaps the greatest contribution in developing the theoretical foundations of power system dynamics was made by research workers in those countries whose power systems cover large geographical areas, most notably the United States, Canada and the former Soviet Union. However, much excellent work has also been contributed by research workers in many other countries. With the mountain of research papers and books now available it is difficult to attempt to give a short historical overview of all the literature on power system dynamics, so, out of necessity, the following overview is restricted to what the authors regard as some of the most important books dealing with power system dynamics.

Some of the first monographs on power system dynamics published in English were the books by Dahl (1938), a two-volume textbook by Crary (1945, 1947) and a large, three-volume, monograph by Kimbark (1948, 1950, 1956; reprinted 1995). In all these books the main emphasis was on electromechanical phenomena. At the same time a Russian text was published by Zdanov (1948) also dealing mainly with electromechanical phenomena. Zdanov's work was later continued by Venikov, who published about a dozen books in Russian between 1958 and 1985 and one of these books, again dealing mainly with electromechanical phenomena, was published in English by Pergamon Press (Venikov, 1964). An extended and modified version of this book was published in Russian in 1978 (Venikov, 1978a) and then later in the same year translated into English (Venikov, 1978b). The main feature of Venikov's books is the emphasis placed on the physical interpretation of the dynamic phenomena.

One of the first books devoted to the general description of power system dynamics was written in Germany by Rüdenberg (1923). This book was later translated into many languages with an English edition appearing in 1950. Other important books that have dealt generally with power system dynamics have been written by Yao-nan Yu (1983), Racz and Bokay (1988) and Kundur (1994). The comprehensive text by Kundur contains an excellent overview of modelling and analysis of power

systems and constitutes the basic monograph on power system dynamics. Fast electromagnetic phenomena, like wave and switching transients, are described by Greenwood (1971).

From the 1940s until the 1960s power system dynamics were generally studied using physical (analogue) models of the system. However, rapid developments in computer technology brought about an ever-increasing interest in mathematical modelling of power systems with the main monographs on this topics being written by Anderson and Fouad (1977, 2003), Arrillaga, Arnold and Harker (1983), Arrillaga and Arnold (1990), Kundur (1994), Ilić and Zaborszky (2000) and Saccomanno (2003).

Another category of books uses the Lyapunov direct method to analyse the electromechanical stability of power systems. The main texts here are those written by Pai (1981, 1989), Fouad and Vittal (1992), Pavella and Murthy (1994) and Pavella, Ernst and Ruiz-Vega (2000). It is worth stressing that a large number of excellent books on the Lyapunov direct method have been published in Russia (Lyapunov's homeland) but were not translated into English.

A brief overview of the large number of papers published over the last 20–30 years shows the main emphasis of power system research to have been on the effective use of computers in power system analysis. Given the rapid developments in computer technology, and its fundamental importance in power system analysis, this is perhaps to be expected and understood. However, there is a danger that young engineers and researchers become more concerned with the computer technology than in understanding the difficult underlying physical principles of the power system dynamics themselves. In time this may endanger progress in the field. To try and combat this problem, this book first describes the underlying physical process of the particular power system dynamic phenomena and only after a thorough understanding has been reached is a more rigorous mathematical treatment attempted. Once the mathematical treatment has been completed, computers can then be used to obtain the necessary quantitative results. For these reasons this book concentrates on developing a basic analysis of the different problem areas and often refers to more specialized publications.

2

Power System Components

2.1 Introduction

Modern-day society requires a large amount of energy for use in industry, commerce, agriculture, transportation, communications, domestic households and so on. The total energy required during one year is called the *annual energy demand* and is satisfied using naturally occurring primary energy resources, principally fossil fuels such as coal, oil, natural gas and uranium. In the current world energy scene these fossil fuels are also the main fuels used in the generation of electrical energy with the renewable energy resources such as hydro, biogas, solar, wind, geothermal, wave and tidal energy being used to a lesser extent. In the future it is likely that the share of the energy market taken by renewables will increase as environmental issues play a more dominant role on the political agenda.

Perhaps the most important, and unique, feature of an electrical power system is that *electrical energy cannot easily and conveniently be stored in large quantities*. This means that at any instant in time the energy demand has to be met by corresponding generation. Fortunately the combined load pattern of a power system normally changes in a relatively predictable manner even though individual consumer loads may vary quite rapidly and unpredictably. Such a predictable system demand pattern goes some way in allowing the daily generation schedule to be planned and controlled in a predetermined manner.

If a power utility is to provide an acceptable supply of electrical energy to its consumers it must address the following issues.

2.1.1 Reliability of Supply

High reliability of supply is of fundamental importance as any major interruption of supply causes, at the very least, major inconvenience to the consumer, can lead to life-threatening situations and, for the industrial consumer, may pose severe technical and production problems. Invariably in such situations the electrical supply utility also incurs a large loss in financial revenue. High reliability of supply can be ensured by:

- high quality of installed elements;
- the provision of reserve generation;
- employing large interconnected power systems capable of supplying each consumer via alternative routes;
- a high level of system security.

Power System Dynamics: Stability and Control, Second Edition Jan Machowski, Janusz W. Bialek and James R. Bumby
© 2008 John Wiley & Sons, Ltd

2.1.2 Supplying Electrical Energy of Good Quality

Electrical energy of good quality is provided by:

- regulated and defined voltage levels with low fluctuations;
- a regulated and defined value of frequency with low fluctuations;
- low harmonic content.

Two basic methods can be used to ensure a high quality of electrical supply. Firstly the proper use of automatic voltage and frequency control methods and, secondly, by employing large, interconnected, power systems which, by their very nature, are less susceptible to load variations and other disturbances.

2.1.3 Economic Generation and Transmission

The majority of electricity is generated by first converting the thermal energy stored in the fossil fuel into mechanical energy and then converting this mechanical energy into electrical energy for transmission through the power system to the consumer. Unfortunately the efficiency of this overall process is relatively low, particularly the first-stage conversion of thermal energy into mechanical energy. It is therefore vital that operation of the overall system is optimized by minimizing the generation and the transmission costs. Once again some saving can be achieved by connecting, and operating, a number of smaller systems as one larger, interconnected, system.

2.1.4 Environmental Issues

Modern society demands careful planning of generation and transmission to ensure as little effect as possible on the natural environment while meeting society's expectations for a secure electrical supply. Consequently air and water pollution produced by power generation plants are limited to prescribed quantities while the pathways for transmission lines are planned so as to cause minimal disturbance to the environment. In addition, new plans for power stations and transmission lines are subject to close public scrutiny.

Environmental issues are now playing an ever-increasing important role on the political agenda. Power generation has always been a major sources of air pollution and much effort has been devoted to developing cleaner generation technologies. However, the relatively recent concerns about global warming and sustainability have started to change the way power systems operate and expand. It is estimated that power generation contributes about one-third of the global CO_2 emissions so that many countries in the world have set a target for renewable generation to contribute 20% or more of their total energy production by about 2020. The consequences of this for the power industry will be discussed later in this chapter.

Another consequence of the environmental pressure is that power utilities must continually seek ways of making better use of their existing system. Obtaining planning permission for new transmission lines and generation sites has become more difficult and stringent.

It is within this political and operational framework that an electrical power utility generates, transmits and distributes electrical energy to its consumers. Consequently the purpose of this chapter is to describe how the different elements of a power system function and the effect they have on both power system operation and control.

2.2 Structure of the Electrical Power System

The basic structure of a contemporary electrical power system is illustrated schematically in Figure 2.1 and shows the power system to be divided into three parts: generation, transmission and

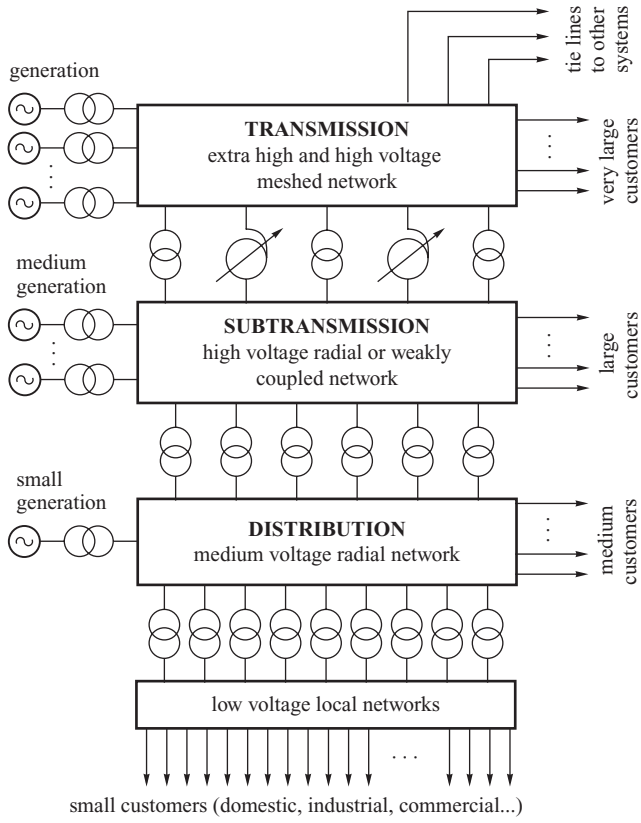

Figure 2.1 Structure of an electrical power system.

distribution. Historically the power supply industry tended to be vertically integrated with each utility responsible for generation and transmission and, in many cases, also distribution in its own service (or control) area. The main justification for this was economies of scale and scope. It was also thought that in order to optimize the overall power system planning and operation, a utility should be able to have full control of both transmission and generation, and sometimes also distribution. This situation has changed since the 1990s. In order to improve the overall efficiency of the industry, many countries have decided to introduce a liberalized competitive market for the industry. That has required *unbundling*, that is splitting, the vertically integrated utilities. In a typical liberalized model, the generation sector is divided into an number of private companies each owning individual power stations and competing with each other. The transmission tends to be operated by one monopoly company, referred to as the *system operator*, which is independent of the generation and regulated by an industry regulator. The distribution is also often split into separate distribution companies (*wires businesses*) which own and manage the distribution network in a given area, while retail, that is buying power on the wholesale markets and selling it to final customers, is handled by a number of competing *supply companies*. Customers are free to choose their suppliers, although in many countries that is restricted to industrial and commercial, but not domestic, customers.

That reorganization of the industry has created many challenges to the way power systems are being planned and operated. This book, however, focuses on the technical aspects of power system operation and will not discuss in detail the challenges brought about by liberalization.

Different parts of the power system operate at different voltages. Generally voltages can be considered to be *low voltages* if they are below the 1 kV mark, while *medium voltages*, used in distribution systems, are typically between 1 and 100 kV. The *high voltages* used in subtransmission networks are between 100 and 300 kV and the *extra-high voltages* used in transmission networks are above 300 kV. This classification is loose and by no means strict.

2.2.1 Generation

Traditionally power system operation has been based around a relatively small number of large power plants connected to the transmission system. Those plants are usually thermal or hydro plants in which electricity is produced by converting the mechanical energy appearing on the output shaft of an engine, or more usually a turbine, into electrical energy. The main thermal energy resources used commercially are coal, natural gas, nuclear fuel and oil.

The conversion of mechanical to electrical energy in traditional thermal or hydro plants is almost universally achieved by the use of a synchronous generator. The synchronous generator feeds its electrical power into the transmission system via a step-up transformer (Figure 2.1) in order to increase the voltage from the generation level (10–20 kV) to the transmission level (hundreds of kilovolts).

As mentioned earlier, concerns about global warming and sustainability have recently spurned interest in renewable generation. Generally there are three main ways the industry can reduce its CO_2 emissions: (i) by moving from the traditional coal/gas/oil-based generation to renewable generation (wind, solar, marine); (ii) by moving towards increased nuclear generation which is largely CO_2-free; (iii) by removing CO_2 from exhaust gases of traditional thermal generation using for example carbon capture and storage technology. Discussing the relative merits of those three options is not the subject of this book. However, it is important to appreciate that the last two options retain the traditional structure of the power system, as that based around a relatively few large generating units, and would therefore not require major changes to the way power systems are designed and operated. The first option, however, would require a major shift to the current practices as generation would be increasingly based around a large number of small renewable plants. This is because renewable energy has a low energy density so that renewable power stations tend to be small with capacities of individual plants being between hundreds of kilowatts and a few megawatts. Such small plants are often connected at the distribution, rather than transmission, network due to the lower cost of connection. Such plants are referred to as *distributed*, or *embedded*, generation. Wind plants usually use induction generators, fixed speed or double fed, in order to transform wind energy into electricity, although sometimes inverter-fed synchronous generators may be used. Solar plants can be either thermal or photovoltaic (PV) with an inverter feeding a synchronous generator. Renewable generation is treated in more detail in Chapter 7.

2.2.2 Transmission

One significant advantage of electrical energy is that large traditional plants can be constructed near the primary fossil fuel energy resource or water reservoirs and the electrical energy produced can be transmitted over long distances to the load centres. Since the energy lost in a transmission line is proportional to the current squared, transmission lines operate at high or very high voltages. The electrical network connects all the power stations into one system, and transmits and distributes power to the load centres in an optimal way. Usually the transmission network has a mesh structure in order to provide many possible routes for electrical power to flow from individual generators to individual consumers thereby improving the flexibility and reliability of the system.

One cannot overemphasize the importance of transmission for overall power system integrity. The transmission network makes the power system a highly interacting, complicated mechanism,

in which an action of any individual component (a power plant or a load) influences all the other components in the system. This is the main reason why transmission remains a monopoly business, even under the liberalized market structure, and is managed by a single system operator. The system operator is responsible for maintaining power system security and for optimizing power system operation.

As the electrical energy gets closer to the load centre, it is directed from the transmission network into a subtransmission network. When a power system expands with the addition of new, high-voltage transmission lines some of the older, lower voltage lines may become part of the subtransmission network. There is no strict division of the network into transmission and subtransmission networks and smaller power generation plants may feed directly into the subtransmission network while bulk power consumers may be fed directly from the transmission or subtransmission network (Figure 2.1).

2.2.3 Distribution

Most of the electrical energy is transferred from the transmission, or subtransmission, network to distribution high-voltage and medium-voltage networks in order to bring it directly to the consumer. The distribution network is generally connected in a radial structure as opposed to the mesh structure used in the transmission system. Large consumers may be supplied from a weakly coupled, meshed, distribution network or, alternatively, they may be supplied from two radial feeders with a possibility of automatic switching between feeders in case of a power cut. Some industrial consumers may have their own on-site generation as a reserve or as a by-product of a technological process (e.g. steam generation). Ultimately power is transformed to a low voltage and distributed directly to consumers.

Traditionally, distribution networks have been passive, that is there was little generation connected to them. Recently the rapid growth in distributed and renewable generation has changed that picture. Power flows in distribution networks may no longer be unidirectional, that is from the point of connection with the transmission network down to customers. In many cases the flows may reverse direction when the wind is strong and wind generation high, with distribution networks even becoming net exporters of power. That situation has created many technical problems with respect to settings of protection systems, voltage drops, congestion management and so on.

Typically about 8–10% of the electrical energy appearing at the generator terminals will be lost on its way to the consumers in the transmission and distribution level.

2.2.4 Demand

The demand for electrical power is never constant and changes continuously throughout the day and night. The changes in demand of individual consumers may be fast and frequent, but as one moves up the power system structure (Figure 2.1) from individual consumers, through the distribution network, to the transmission level, the changes in demand become smaller and smoother as individual demands are aggregated. Consequently the total power demand at the transmission level changes in a more or less predictable way that depends on the season, weather conditions, way of life of a particular society and so on. Fast global power demand changes on the generation level are usually small and are referred to as *load fluctuations*.

2.3 Generating Units

The block diagram of a generating unit is shown in Figure 2.2. Electrical energy is produced by a synchronous generator driven by a prime mover, usually a turbine or a diesel engine. The turbine is equipped with a *turbine governor* which controls either the speed or the output power according to a preset power–frequency characteristic. The generated power is fed into the transmission

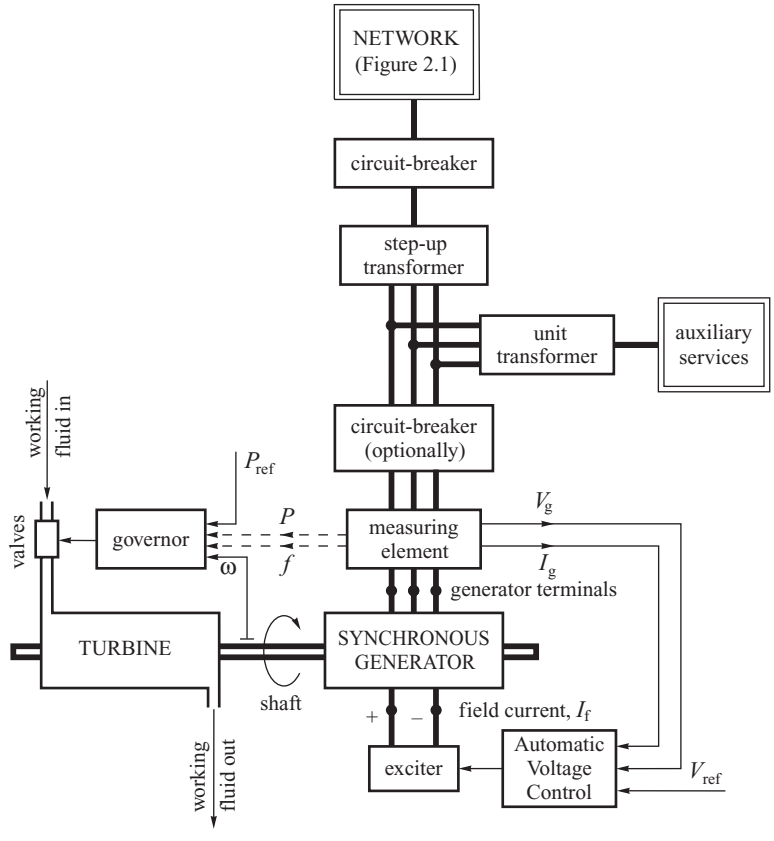

Figure 2.2 Block diagram of a power generation unit.

network via a step-up transformer. The DC excitation (or field) current, required to produce the magnetic field inside the generator, is provided by the *exciter*. The excitation current, and consequently the generator's terminal voltage, is controlled by an *automatic voltage regulator* (AVR). An additional *unit transformer* may be connected to the busbar between the generator and the step-up transformer in order to supply the power station's auxiliary services comprising motors, pumps, the exciter and so on. The generating unit is equipped with a *main circuit-breaker* on the high-voltage side and sometimes also with a *generator circuit-breaker* on the generator side. Such a configuration is quite convenient because, in case of a maintenance outage or a fault, the generator circuit-breaker may be opened while the auxiliary services can be fed from the grid. On the other hand, with the main circuit-breaker open, the generator may supply its own auxiliary services.

2.3.1 Synchronous Generators

Synchronous generators can be loosely classified as either high-speed generators, driven by steam or gas turbines (and often called *turbogenerators*), or low-speed generators, driven by water turbines. To reduce centrifugal forces, high-speed turbogenerators have relatively low diameter but large axial length and are mounted horizontally. Typically they will have two or four electrical poles so that in a 50 Hz system a generator would be driven at 3000 or 1500 rpm respectively. In contrast, low-speed

generators operate at typically 500 rpm and below, have a large number of electrical poles, large diameter and shorter axial length. The actual number of magnetic poles depends on the required speed and nominal frequency of the power system.

All generators have two main magnetic parts termed the *stator* and the *rotor*, both of which are manufactured from magnetic steel. The *armature winding*, which carries the load current and supplies power to the system, is placed in equidistant slots on the inner surface of the stator and consists of three identical phase windings. The rotor of a high-speed generator also contains slots for the DC excitation winding while the excitation winding for low-speed generators is wound on the salient poles of the rotor. The rotor also has additional short-circuited damper*, or* amortisseur*,* windings, to help damp mechanical oscillations of the rotor. In high-speed, non-salient pole generators the damper windings are usually in the form of conductive wedges mounted in the same slots as the excitation winding. In low-speed generators the damper windings are mounted in axial slots in the pole face.

The rotor excitation winding is supplied with a direct current to produce a rotating magnetic flux the strength of which is proportional to the excitation current. This rotating magnetic flux then induces an electromotive force (emf) in each phase of the three-phase stator armature winding which forces alternating currents to flow out to the power system. The combined effect of these AC armature currents is to produce their own *armature reaction* magnetic flux which is of constant magnitude but rotates at the same speed as the rotor. The excitation flux and the armature reaction flux then produce a resultant flux that is stationary with respect to the rotor but rotates at synchronous speed with respect to the stator. As the resultant flux rotates relative to the stator it is necessary to laminate the stator iron core axially in the shaft direction to limit the iron losses due to eddy currents. However, as the magnetic flux is stationary with respect to the rotor, the rotor is normally constructed from a solid steel forging.

If, for some reason, the rotor speed deviates from synchronous, the flux will not be stationary with respect to the rotor and currents will be induced in the damper windings. According to Lenz's law, these currents will oppose the flux change that has produced them and so help restore synchronous speed and damp the rotor oscillations.

Historically there has been a universal tendency to increase the rated power of new power stations and individual generators as capital cost and operating cost (per-unit megawatt) decrease with increased megawatt rating. This economy of scale results in lower generator mass per-unit megawatt, smaller buildings and power station area, and lower auxiliary equipment and staffing costs. However, the increased use of natural gas since the 1990s has halted the trend of increasing rated power of power stations with combined cycle gas turbine plant utilizing air-cooled generators up to typically 250 MW becoming the norm. Consequently, modern synchronous generators have ratings ranging from about 100 MW to more than 1300 MW and operate at voltages of between 10 and 32 kV.

Generally a synchronous generator is connected to the transmission network via a step-up transformer. In the case of a small unit the generator and transformer are connected by cables while a large, high-power generator may be connected to its transformer by a number of single-phase screened busbars. The generator transformer is usually located outdoors and is of the tank type. Power from the transformer is fed to the substation busbars via high-voltage cables or a short overhead line.

2.3.2 Exciters and Automatic Voltage Regulators

The generator excitation system consists of an exciter and an AVR and is necessary to supply the generator with DC field current as shown in Figure 2.2. The power rating of the exciter is usually in the range 0.2–0.8% of the generator's megawatt rating. In the case of a large generator this power is quite high, in the range of several megawatts. The voltage rating of the exciter will not normally exceed 1000 V as any higher voltage would require additional insulation of the field winding.

2.3.2.1 Excitation Systems

Generally exciters can be classified as either rotating or static. Figure 2.3 shows some typical systems. In the rotating exciters of Figure 2.3a–c, the excitation current is supplied either by a DC generator or by an AC generator with rectifiers. As DC generators usually have relatively low power ratings, they are cascaded to obtain the necessary output, Figure 2.3a. Because of commutation problems with DC generators this type of exciter cannot be used for large generators which require large excitation currents.

As the number of cascaded DC generators increases, the dynamic properties of the exciter deteriorate, resulting in an increase in the equivalent time constant. Nowadays DC generators have been almost entirely replaced by alternators, which are simpler and more reliable. This change to alternators has been possible because of advances in power electronics which allow cheap, high-power rectifiers to be used in conjunction with the AC exciter.

The exciter shown in Figure 2.3b is a reluctance machine (inductor generator) operating at about 500–600 Hz so that the rectified current requires little smoothing. With this exciter both windings (AC and DC) are on the stator side. One disadvantage of this system is that slip rings are required to feed the rectified excitation current to the rotating field winding of the main generator. A further disadvantage is that the exciter itself tends to be quite large. This is a direct result of the way in which the sinusoidal flux changes, necessary to induce the alternating emf in the armature, are produced solely by the changes in reluctance due to the rotation of the salient rotor teeth.

The exciter shown in Figure 2.3c has neither commutator nor slip rings. The principal excitation source is an inside-out synchronous machine with the field winding on the stator and armature winding on the rotor. The induced current is rectified by diodes, which are also mounted on the rotor, and fed directly to the excitation winding of the main generator. One limitation of this type of exciter is that the current supplied to the main generator can only be controlled indirectly via field control of the exciter. This tends to introduce a time constant of about 0.5 to 1 s into the exciter

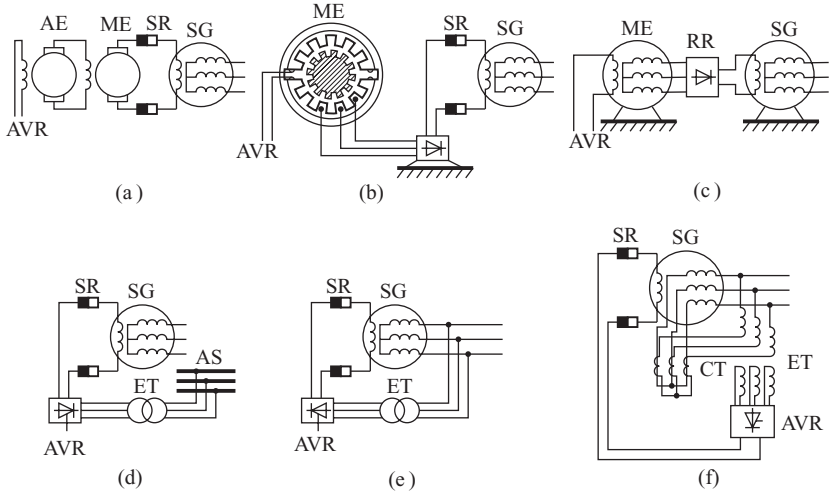

Figure 2.3 Typical exciter systems: (a) cascaded DC generators; (b) reluctance machine with rectifier; (c) inside-out synchronous generator with rotating rectifier; (d) controlled rectifier fed from the auxiliary supply; (e) controlled rectifier fed from the generator terminals; (f) controlled rectifier fed by the generator's voltage and current. SG, synchronous generator; SR, slip rings; ME, main exciter; AE, auxiliary exciter; RR, rotating rectifier; ET, excitation transformer; AS, auxiliary service busbars; CT, current transformer; AVR, automatic voltage regulator.

control system. One solution to this problem is to use rotating thyristors, rather than diodes, and control the exciter output via the firing angle of the thyristors. Unfortunately, controlling the firing angle of a rotating thyristor is not easy and the reliability of such systems tends to be compromised by stray fields causing unscheduled thyristor firing.

Some alternative exciter systems using static thyristor converters are shown in Figure 2.3d–f. In these exciters the thyristor rectifiers are controlled directly by a voltage regulator. The main differences between the systems is in the type of supply used. Figure 2.3d shows an exciter supplied by an additional auxiliary service transformer. Figure 2.3e shows an alternative, and simpler, solution in which the exciter is fed from the generator output via a transformer. However, should a short circuit occur, particularly one close to the generator terminals, the decrease in the generator terminal voltage will result in a possible loss of excitation. With careful design the exciter can operate when the short circuit is further away from the generator terminals, for example at the high-voltage terminals of the step-up transformer. More flexibility can be obtained by modifying the supply to the rectifier as shown in the exciter design of Figure 2.3f. In this system the generator does not lose excitation because its supply voltage is augmented, or compounded, by a component derived from the generator load current.

The main disadvantage of all static exciters is the necessity of using slip rings to feed current to the rotor of the main generator. This is offset to a large extent by the rapid speed with which they can react to control signals. As the cost of high-power rectifiers decreases, and reliability increases, static exciters are becoming the main source of excitation for high-power generators.

2.3.2.2 Automatic Voltage Regulators

The AVR regulates the generator terminal voltage by controlling the amount of current supplied to the generator field winding by the exciter. The general block diagram of the AVR subsystem is shown in Figure 2.4. The measuring element senses the current, power, terminal voltage and frequency of the generator. The measured generator terminal voltage V_g is compensated for the load current I_g and compared with the desired reference voltage V_{ref} to produce the voltage error ΔV. This error is then amplified and used to alter the exciter output, and consequently the generator field current, so that the voltage error is eliminated. This represents a typical closed-loop control system. The regulation process is stabilized using a negative feedback loop taken directly from either the amplifier or the exciter.

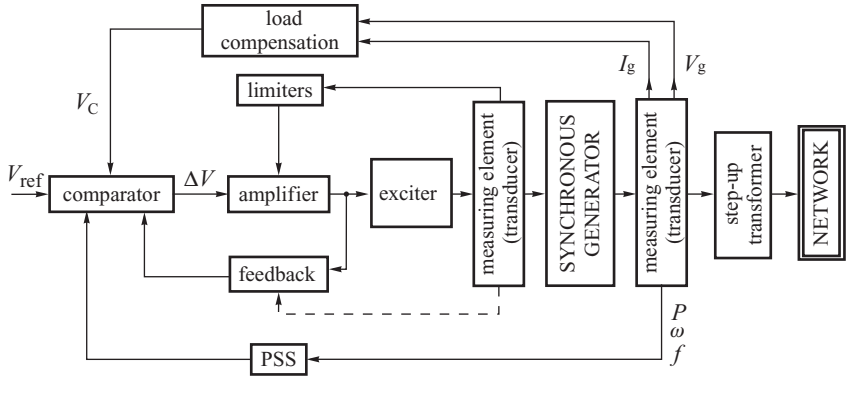

Figure 2.4 Block diagram of the excitation and AVR system. PSS, power system stabilizer.

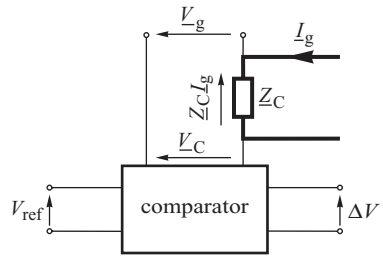

Figure 2.5 Load compensation element together with the comparator.

The load compensation element, together with the comparator, is shown in Figure 2.5. The voltage drop across the compensation impedance $\underline{Z}_C = R_C + jX_C$ due to the generator current $\underline{I}_g$ is added to the generator voltage $\underline{V}_g$ to produce the compensated voltage V_C according to the function

$$V_C = \left|\underline{V}_C\right| = \left|\underline{V}_g + (R_C + jX_C)\,\underline{I}_g\right|. \tag{2.1}$$

If the load compensation is not employed, $\underline{Z}_C = \underline{0}$, then $V_C = V_g$ and the AVR subsystem maintains constant generator terminal voltage. The use of load compensation ($\underline{Z}_C \neq \underline{0}$) effectively means that the point at which constant voltage is maintained is 'pushed' into the network by a distance that is electrically equal to the compensation impedance. The assumed direction of the phasors in Figure 2.5 means that moving the voltage regulation point towards the grid corresponds to a negative compensation impedance.

In the case of parallel generators supplying a common busbar the compensation impedance must be smaller than the impedance of the step-up transformer in order to maintain stable reactive power dispatch between the parallel generators. Usually $X_C \approx -0.85X_T$, where X_T is the reactance of the step-up transformer. In this case the regulator maintains a constant voltage value at a distance of $0.85X_T$ from the generator terminals towards the network or at a distance of $0.15X_T$ from the high-voltage terminal towards the generator.

The AVR subsystem also includes a number of limiters whose function is to protect the AVR, exciter and generator from excessive voltages and currents. They do this by maintaining the AVR signals between preset limits. Thus the amplifier is protected against excessively high input signals, the exciter and the generator against too high a field current, and the generator against too high an armature current and too high a power angle. The last three limiters have built-in time delays to reflect the thermal time constant associated with the temperature rise in the winding.

A power system stabilizer (PSS) is sometimes added to the AVR subsystem to help damp power swings in the system. PSS is typically a differentiating element with phase shifting corrective elements. Its input signals may be proportional to rotor speed, generator output frequency or the electrical real power output of the generator.

The AVR parameters have to be chosen in such a way that an appropriate quality of voltage regulation is maintained. For small disturbances, that quality can be assessed by observing the dynamic voltage response of a generator to a step change in the reference value. This is illustrated in Figure 2.6 for a step change of reference value by $\Delta V = V_{ref+} - V_{ref-}$. Three indices assess the quality of regulation: (i) settling time t_ε; (ii) overshoot ε_p; and (iii) rise time t_r. These indices are defined as follows:

- Settling time t_ε is the time necessary for the signal to reach its steady-state value with a tolerance of ε.

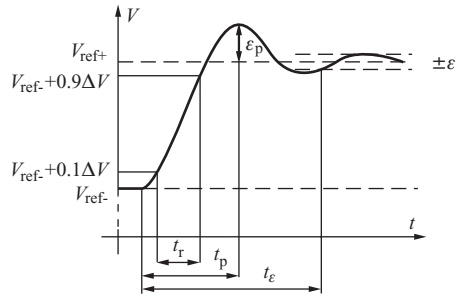

Figure 2.6 Dynamic voltage response to the step change in reference value.

- Overshoot ε_p is the difference between the peak value of the voltage and a reference value, usually expressed as a percentage of the reference value.
- The time to reach the peak value is denoted as t_p.
- Rise time t_r is the time taken for the voltage to rise from 10 to 90% of $\Delta V = V_{ref+} - V_{ref-}$. In this interval the speed at which the voltage increases is about $0.8\Delta V/t_r$.

Usually it is assumed that with an accuracy of regulation $\varepsilon \leq 0.5\%$ and with 10% step change of the voltage reference value, the settling time is $t_\varepsilon \leq 0.3$ s for static exciters and $t_\varepsilon \leq 1.0$ s for rotating exciters. The overshoot is usually required to be $\varepsilon_p \leq 10\%$ for step changes of the reference value when the generator is off load. The speed of voltage increase should not be less than $1.5U_{ref}$ per second.

2.3.3 Turbines and their Governing Systems

In a power system, the synchronous generators are normally driven by either steam turbines, gas turbines or hydro turbines as shown in Figure 2.2. Each turbine is equipped with a governing system to provide a means by which the turbine can be started, run up to the operating speed and operate on load with the required power output.

2.3.3.1 Steam Turbines

In coal-burn, oil-burn and nuclear power plants the energy contained in the fuel is used to produce high-pressure, high-temperature steam in the boiler. The energy in the steam is then converted to mechanical energy in axial flow steam turbines. Each turbine consists of a number of stationary and rotating blades concentrated into groups, or stages. As the high-pressure steam enters the fixed set of stationary blades it is accelerated and acquires increased kinetic energy as it expands to a lower pressure. The stream of fluid is then guided onto the rotating blades where it experiences a change in momentum and direction thereby exerting a tangential force on the turbine blade and output torque on the turbine shaft. As the steam passes axially along the turbine shaft its pressure reduces, so its volume increases and the length of the blades must increase from the steam entrance to the exhaust to accommodate this change. Typically a complete steam turbine will be divided into three or more stages, with each turbine stage being connected in *tandem* on a common shaft. Dividing the turbine into stages in this way allows the steam to be reheated between stages to increase its enthalpy and consequently increase the overall efficiency of the steam cycle. Modern coal-fired steam turbines have thermal efficiency reaching 45%.

Steam turbines can be classified as *non-reheat, single-reheat or double-reheat systems*. Non-reheat turbines have one turbine stage and are usually built for use in units of below 100 MW. The most

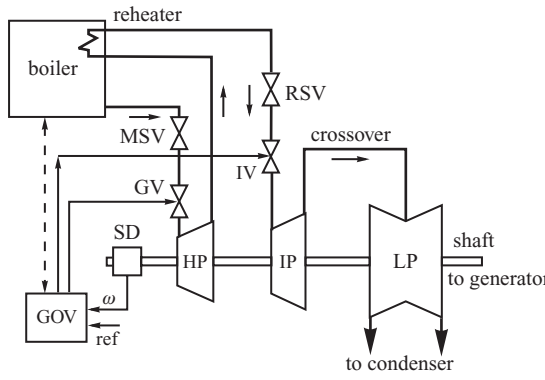

Figure 2.7 Steam configuration of a tandem compound single-reheat turbine.

common turbine configuration used for large steam turbines is the single tandem reheat arrangement shown diagrammatically in Figure 2.7. In this arrangement the turbine has three sections: the *high-pressure* (HP), *intermediate-pressure* (IP) and *low-pressure* (LP) stages. Steam leaving the boiler enters the steam chest and flows through the *main emergency stop valve* (MSV) and the *governor control valve* (GV) to the HP turbine[1]. After partial expansion the steam is directed back to the boiler to be reheated in the *heat-exchanger* to increase its enthalpy. The steam then flows through the *reheat emergency stop valve* (RSV) and the *intercept control valve* (IV) to the IP turbine where it is again expanded and made to do work. On leaving the IP stage the steam flows through the crossover piping for final expansion in the LP turbine. Finally the steam flows to the *condenser* to complete the cycle. Typically the individual turbine stages contribute to the total turbine torque in the ratio 30% (HP) : 40% (IP) : 30% (LP).

The steam flow in the turbine is controlled by the *governing system* (GOV). When the generator is synchronized the emergency stop valves are kept fully open and the turbine speed and power regulated by controlling the position of the GV and the IV. The speed signal to the governor is provided by the *speed measuring device* (SD). The main amplifier of the governing system and the valve mover is an *oil servomotor* controlled by the *pilot valve*. When the generator is synchronized the emergency stop valves are only used to stop the generator under emergency conditions, although they are often used to control the initial start-up of the turbine.

Besides the tandem compound single-reheat turbine shown in Figure 2.7, other turbine arrangements are also used. Double-reheat turbines have their first HP section divided into the very high-pressure (VHP) turbine and the HP turbine with reheat between them. In this arrangement the individual turbines typically contribute to the total torque in the ratio : 20% (VHP) : 20% (HP) : 30% (IP) : 30% (LP). Control valves are mounted after each of the reheaters and before the VHP section. In contrast to the single-shaft arrangements just described, cross-compound, two-shaft turbines are sometimes used where one of the shafts rotates at half the speed of the other. These turbines may have single- or double-reheat steam cycles.

2.3.3.2 Gas Turbines

Unlike steam turbines, gas turbines do not require an intermediate working fluid and instead the fuel thermal energy is converted into mechanical energy using the hot turbine exhaust gases. Air is

[1] The governor valves are also referred to as the main control valves or the HP control valves, while the intercept valves are also referred to as the IP intercept valves or simply the IP control valves.

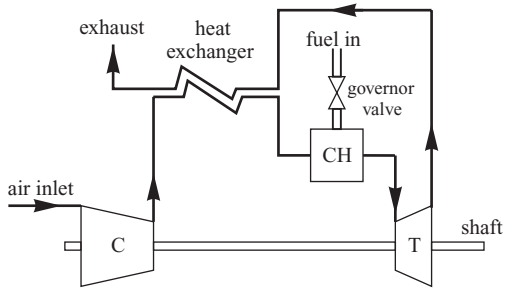

Figure 2.8 Open regenerative cycle of the gas turbine.

normally used as the working fluid with the fuel being natural gas or heavy/medium fuel oil. The most popular system for gas turbines is the open regenerative cycle shown in Figure 2.8 and consists of a compressor C, combustion chamber CH and turbine T. The fuel is supplied through the governor valve to the combustion chamber to be burnt in the presence of air supplied by the compressor. The hot, compressed air, mixed with the combustion products, is then directed into the turbine where it expands and transfers its energy to the moving blades in much the same way as in the steam turbine. The exhaust gases are then used to heat the air delivered by the compressor. There are also other, more complicated cycles that use either compressor intercooling and reheating, or intercooling with regeneration and reheating. The typical efficiency of a gas turbine plant is about 35%.

2.3.3.3 Combined Cycle Gas Turbines

A significant technological step forward in the use of gas turbines came with the introduction of the combined cycle gas turbine (CCGT) illustrated in Figure 2.9. In this system the exhaust heat from the gas turbine is directed into a heat-recovery boiler (HRB) to raise steam, which is then used to generate more electricity in a steam-driven generating unit. Generally the temperature of the gas turbine exhaust gases is quite high, typically around 535 °C, so by adding a steam turbine cycle at the bottom end of the gas cycle the otherwise wasted heat can be utilized and the overall cycle efficiency significantly increased. Modern CCGT plant can have an efficiency approaching, or even exceeding, 60%. Usually CCGT power stations utilize the exhaust gases from two or three gas

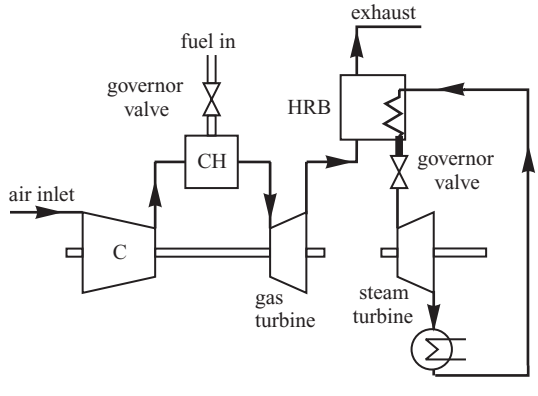

Figure 2.9 Example of a combined cycle gas turbine.

turbines to raise steam for one steam turbine with both types of turbines driving separate generators. More recently *single-shaft modes* have become popular where both the gas and the steam turbines are mounted on the same shaft and drive the same generator. In some CCGT designs the HRB may be equipped with supplementary firing to increase the temperature of the HP steam. In addition, some combined cycle plants are designed to produce steam for district heating or for use in the process industry.

CCGT plants, apart from higher thermal efficiency, also have other important advantages over more traditional coal-fired plants. They have a short construction time and low capital construction cost, both about half that of the equivalent coal-fired plant, they are relatively clean with almost no SO_2 emission, they require little staffing, and the materials handling problem of gas versus coal and ash is much simpler.

2.3.3.4 Hydro Turbines

The oldest form of power generation is by the use of water power. Hydraulic turbines derive power from the force exerted by water as it falls from an upper to a lower reservoir. The vertical distance between the upper reservoir and the level of the turbine is called the *head*. The size of the head is used to classify hydroelectric power plants as high-head, medium-head *and* low-head *(*run-of-river*) plants*, although there is no strict demarcation line.

Low- and medium-head hydro-electric plant is built using *reaction turbines* such as the *Francis turbine* shown in Figure 2.10a. Because of the relatively LP head reaction, turbines typically use a large volume of water, require large water passages and operate at low speed. Because of the low rotational speed, the generators have a large diameter. In operation, water enters the turbine from the intake passage or *penstock* through a spiral case, passes through the stay ring and the movable *wicket gates* onto the *runner*. On leaving the runner, the water flows through the *draft tube* into the *tail-water reservoir*. The movable wicket gates, with their axes parallel to the main shaft, control the

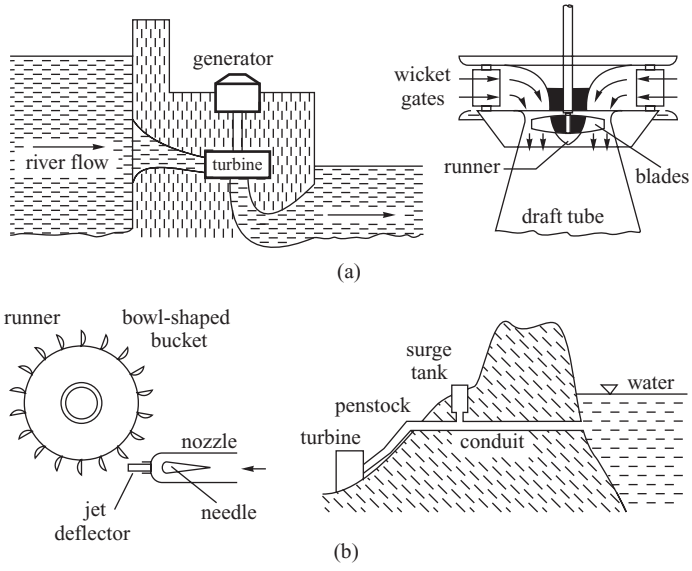

Figure 2.10 Hydro turbines: (a) low- and medium-head reaction turbine; (b) high-head Pelton wheel.

power output of the turbine. Francis turbine runners have the upper ends of their blades attached to a crown and the lower ends attached to a band. For low-head operation the runner has no crown or band so that the blades are unshrouded. The blades themselves may be either fixed or adjustable. For adjustable-blade runners the governor can change both the blade angle and the wicket gate opening (*Kaplan-type turbine*). The blades are adjusted by means of an oil-operated piston located within the main shaft.

In high-head hydro-electric power plants *Pelton wheel* impulse turbines, shown in Figure 2.10b, are used. In these turbines the HP water is converted into high-velocity jets of water by a set of fixed nozzles. The high-velocity water jets impact on a set of bowl-shaped buckets attached around the periphery of the runner which turn back the water so impacting the full effect of the water jet to the runner. The size of the jet, and thus the power output of the turbine, is controlled by a needle in the centre of the nozzle. The movement of the needle is controlled by the governor. A jet deflector is located just outside the nozzle tip to deflect the jet from the buckets in the event of sudden load reduction.

2.3.3.5 Turbine Governing Systems

For many years turbine governing systems were of a mechanical–hydraulic type and used the *Watt centrifugal mechanism* as the speed governor. The original Watt mechanism used two *flyballs* as the speed-responsive device, but on new machines the Watt governor has been replaced by an electro-hydraulic governor. However, it is useful to understand the operation of the traditional mechanical–hydraulic system, shown in Figure 2.11, as it is still in use in various forms on older machines and it is a good way to illustrate the general principle of turbine control.

The pair of spring-loaded weights in the centrifugal governor is driven by a motor that receives its power from the turbine shaft such that the height of the weights depends on the speed. When the turbine mechanical torque is equal to the counteracting generator electromagnetic torque, the rotational speed of the turbine–generator is constant and the position of the weights does not

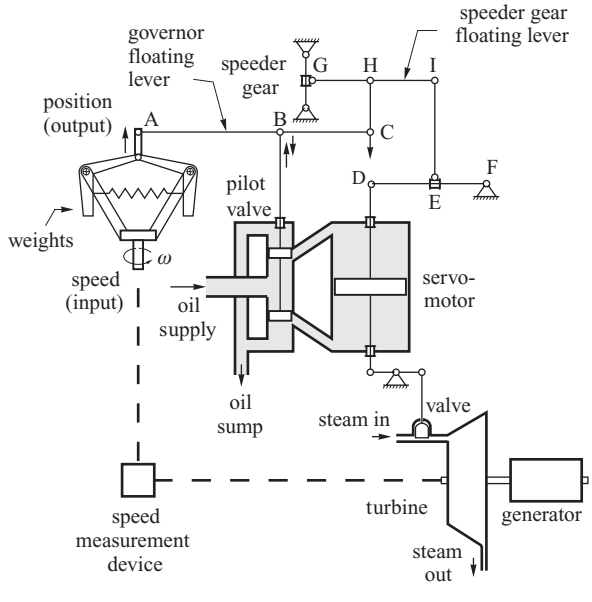

Figure 2.11 Mechanical–hydraulic governing system of the steam turbine.

change. If the electrical torque increases, due to a change in load, so that it is greater than the mechanical driving torque, the rotational speed ω decreases and the weights move radially inwards under centrifugal action. This causes point A on the governor floating lever to rise and the floating lever A–B–C rotates around point C. This rotation results in point B and the pilot valve moving upwards so allowing HP oil to flow into the upper chamber of the main servomotor. The differential pressure across the piston now forces the piston to move downwards so partially opening the turbine valve and increasing the turbine power. The displacement of the main servomotor piston downwards causes points D, E, I and H to lower and the speeder gear floating lever to rotate downwards about point G. This lowers point C, around which the lever A–B–C rotates, and partially closes the pilot valve to reduce the oil flow into the upper chamber.

This governing system has two negative feedback loops: the main speed feedback loop through the turbine speed measuring device and the centrifugal governor, and the second valve position feedback loop through the steam valve, piston and points D, E, I, H and C. This latter feedback loop ensures that the static speed–power characteristic of the turbine has a negative slope. As will be explained later in this section, such a characteristic is fundamental to turbine control as it ensures that any speed increase will be met by a corresponding reduction in turbine torque and vice versa. The slope, or gain, of the characteristic may be changed by moving point E horizontally on the lever D–E–F.

The purpose of the *speeder gear* is twofold. Firstly it controls the speed of the unsynchronized generator and, secondly, it controls the power output of the synchronized generator. To see how the speeder gear works, assume that the generator is synchronized and that it is required to increase the power output. As the generator is synchronized its speed will be constant and equal to synchronous speed. If the speeder gear is used to raise point G then points C and B and the pilot valve will also rise. HP oil will then enter the upper chamber of the main servomotor, the piston will fall and the steam valve will be opened thereby increasing the steam flow through the turbine and the power output. As the servomotor piston falls, so too do points D, E, I and H. This movement lowers point C and returns the pilot valve to its equilibrium position. The schematic diagram of the mechanical–hydraulic governor is shown in Figure 2.12a with the position of the speeder gear setting the *load reference set point*.

The main disadvantages of the Watt centrifugal governor are the presence of deadbands and a relatively low accuracy. The size of the deadbands also tends to increase with time due to wear in the moving mechanical elements. Newer solutions replace the Watt centrifugal mechanism with an electronic regulator. In these systems the turbine rotor speed is measured electronically, with high accuracy, using a toothed wheel and a probe. The resulting electrical signal is amplified and acts on the pilot valve via an electro-hydraulic converter. The schematic diagram of the electro-hydraulic system in Figure 2.12b shows that its operation does not differ much from that of the mechanical–hydraulic system shown in Figure 2.12a, but the flexibility of electronic regulators enables additional control loops to be introduced that link the boiler and the turbine control systems. The dashed line in Figure 2.12b symbolizes the steam flow feedback and its function is to prevent the valves being opened by the speed regulator when the steam inlet pressure is too low. The reference speed is set electronically in the *speed reference set point*. It is also possible to change the turbine power using an additional signal that is added to the control circuit at the load reference set point.

Higher forces are required to move the control gates in hydro turbines than the valves in steam turbines and, as a result, hydro turbine governing systems usually employ two cascaded servomotors. The first, low-power, *pilot servomotor* operates the *distributor or relay valve* of the second, high-power, *main gate servomotor*. Just as in the steam turbine, the pilot servomotor has a pilot valve which is controlled either by a mechanical Watt-type governor or by an electronic regulator via an electro-hydraulic converter. The turbine governing system is similar to that used in steam turbines (Figure 2.12) but the number of servomotors is higher and the feedback loop has an additional dashpot for reasons described in Chapter 11 (Section 11.3).

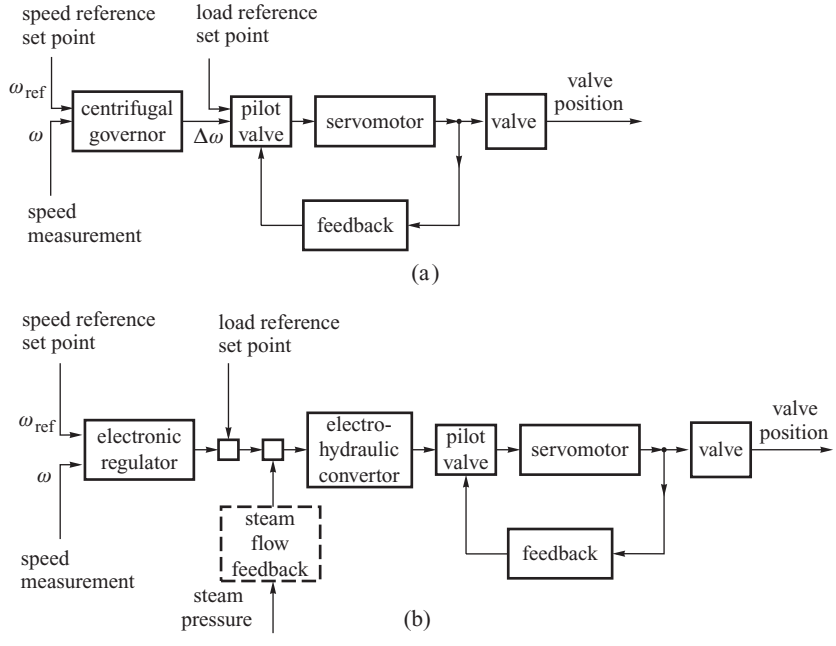

Figure 2.12 Schematic diagram of the governing system: (a) mechanical–hydraulic; (b) electro-hydraulic.

2.3.3.6 Turbine Characteristics

For stable operation the turbine must have a power–speed characteristic such that as the speed increases the mechanical input power reduces. Similarly, a decrease in speed should result in an increase in the mechanical power. This will restore the balance between the electrical output power and mechanical input power.

To examine how such a characteristic can be achieved, Figure 2.13 shows the idealized power–speed characteristics for an unregulated and a regulated turbine. Point A is the rated point which corresponds to the optimal steam flow through the turbine, as determined by the turbine designers. Consider first the unregulated characteristic and assume that the turbine is initially operating at point A with the turbine control valve fully open. The generator is assumed to be synchronized with the system and its speed can only change if the system frequency changes. If, for some reason, the system frequency rises, then so too does the speed of the rotor. As the main valve is fully open the speed increase causes additional losses in the turbine and the

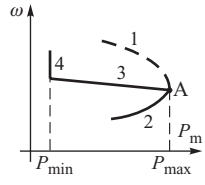

Figure 2.13 Turbine power–speed characteristic for the unregulated turbine (lines 1, 2) and the regulated turbine (lines 3, 2, 4).

efficiency of the steam flow drops (with respect to the optimal point A) with a corresponding reduction in power as shown by the dashed curve 1. Similarly, a decrease in the system frequency causes the rotor speed to drop with a corresponding drop in power as shown by curve 2. The rapid reduction in turbine power with reduction in system frequency can be explained as follows. The steam flow through the turbine depends on the performance of the boiler and the boiler feed pumps. As the performance of these pumps is strongly dependent on frequency, a reduction in system frequency (and rotor speed) reduces their performance. This causes a decrease in the amount of steam flowing through the turbine and a further drop in the turbine torque.

The task of the turbine governor is to set a characteristic corresponding to line 3 which has a small droop. As explained below, such a characteristic is necessary to achieve stable operation of the turbine.

Let us consider the governor functional diagrams in Figure 2.12. If the steam flow feedback in the electro-hydraulic governing system is neglected and the governor response assumed to be dominated by the time constant of the servomotor, both the mechanical–hydraulic and the electro-hydraulic governors shown in Figure 2.12 may be represented by the simplified block diagram shown in Figure 2.14. The coefficient K_A in Figure 2.14a corresponds to the amplification gain of the servomotor, while coefficient R corresponds to the gain of the feedback loop. Transformation of the block diagram allows R to be eliminated from the feedback loop by moving it into the main loop to obtain the block diagram shown in Figure 2.14b where $T_G = 1/(K_A R)$ and is the effective governor time constant.

The block diagram of Figure 2.14b allows an approximate analysis of the static and dynamic properties of the turbine–governor system. In the steady state $t \to \infty$, $s \to 0$ and the turbine block diagram can be simplified to that shown in Figure 2.14c where P_{ref} is the load reference set point expressed as a fraction of the nominal or rated power, P_n. If the valve position c is assumed to vary between 0 (fully closed) and 1 (fully open) then a small change in turbine speed $\Delta\omega = \omega - \omega_{ref}$ will produce a corresponding change in valve position $\Delta c = -\Delta\omega/R$. Normally $\Delta\omega$ is expressed as a fraction of rated speed ω_n so that

$$\Delta c = -\frac{1}{\rho}\frac{\Delta\omega}{\omega_n} \quad \text{or} \quad \frac{\Delta\omega}{\omega_n} = -\rho\Delta c, \tag{2.2}$$

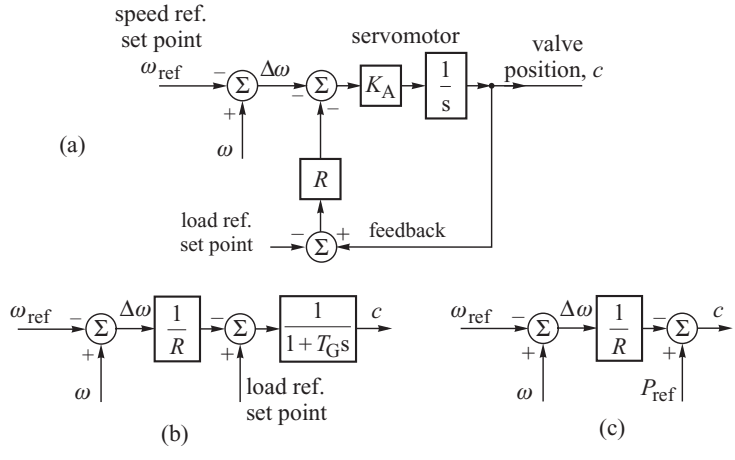

Figure 2.14 Simplified model of the steam turbine governing system : (a) block diagram with negative feedback; (b) equivalent block diagram; (c) equivalent block diagram for the steady state.

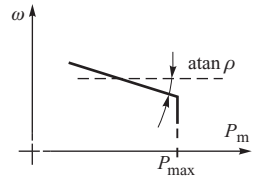

Figure 2.15 Illustration of the definition of the speed–droop coefficient.

where $\rho = R/\omega_n$ is referred to as the *speed–droop coefficient* or simply the *droop*. The reciprocal of droop $K = 1/\rho$ is the *effective gain* of the governing system. The definition of ρ is illustrated in Figure 2.15.

Physically droop can be interpreted as the percentage change in speed required to move the valves from fully open to fully closed. If a linear relationship is assumed between the valve position and mechanical power then the turbine power output ΔP_m expressed as a fraction of the nominal or rated power output P_n is given by $\Delta P_m/P_n = \Delta c$ and

$$\frac{\Delta\omega}{\omega_n} = -\rho\frac{\Delta P_m}{P_n} \quad \text{or} \quad \frac{\Delta P_m}{P_n} = -K\frac{\Delta\omega}{\omega_n}. \tag{2.3}$$

Equation (2.3) describes an idealized turbine power–speed characteristic. In (P_m, ω) coordinates this gives a straight line of gradient ρ shown in Figure 2.13 by line 2. However, it is important to realize that once the steam valves are fully open, no more control can be exerted over the turbine so that should the speed drop, the turbine would follow characteristic 4 in the same way as the unregulated turbine.

A good control system should ensure that any load fluctuation ΔP_m would only produce a small speed change $\Delta\omega$. This is achieved by making the droop ρ small. However, it should be emphasized that the droop cannot be zero or negative. Figure 2.16 illustrates this point. The system demand is dominated by electrical loads for which an increment in the active power ΔP_{load} is weakly dependent on the change in the system frequency and therefore on the change in the rotational speed of the synchronous generators. As a result the static load characteristic $\omega(P_{load})$ is almost a vertical line in the (P, ω) plane but with a slight positive slope that reflects the frequency dependence. The point of intersection of the load characteristic $\omega(P_{load})$ and the turbine characteristic $\omega(P_m)$ is the equilibrium point where the opposing electromagnetic and mechanical torque acting on the shaft are equal in magnitude and the rotational speed is constant.

Figure 2.16a shows the case where the droop is positive ($\rho > 0$) so that, according to Equation (2.3), the turbine power increases when its rotational speed decreases. In this case a small disturbance in frequency (turbine speed) causes the system to return automatically to the equilibrium point. For

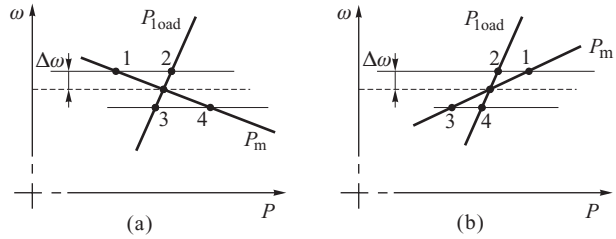

Figure 2.16 The equilibrium point between the turbine power and the load power: (a) stable point; (b) unstable point.

example, if there is a momentary increase in frequency, then the disturbed load power (point 2) is greater than the disturbed turbine power (point 1). This means that the opposing electromagnetic torque is greater than the driving torque and the system is forced to return to the equilibrium point. Similarly, if the frequency decreases then the load power (point 3) is less than the turbine power (point 4) and this excess mechanical power causes the turbine speed to increase and the system to return to the equilibrium point.

On the other hand, Figure 2.16b shows a case where the droop is assumed to be negative ($\rho > 0$). The situation is then reversed as any increase in frequency will cause the turbine power (point 1) to be greater than the load power (point 2). This would result in an increase in turbine speed and a further increase in the power imbalance. Similarly, a decrease in frequency would result in the turbine power (point 3) being less than the load power (point 4) with further movement away from the equilibrium point. Such a droop characteristic is not resistant to disturbances and the system is unstable.

The case when $\rho = 0$ is the marginal stability case and corresponds to the absence of the negative feedback loop on valve position. For the Watt regulator of Figure 2.11 this corresponds to the absence of the lever H–E which realizes the position feedback between the servomotor piston and the pilot valve. Neglecting the steady-state error, the governing system without this negative feedback would be of the constant speed type. Such a governor cannot be used if two or more generators are electrically connected to the same system since each generator would be required to have precisely the same speed setting (which is technically impossible) or they would 'fight' each other, each trying to pull the system frequency to its own setting. If generators connected to the system have speed–droop characteristics with $\rho > 0$, then there will always be a unique frequency at which they will share load. This will be described in Chapter 9.

Typical values of the speed–droop coefficient (per unit) are between 0.04 and 0.09 with the lower value corresponding to turbogenerators and the higher to hydrogenerators. This is connected with the relative ease, and speed, with which a hydro plant can accept a change in load compared with a thermal plant.

2.3.3.7 Governor Control Functions

Having established the basic workings of the governor, it is now prudent to look at the overall control functions required of a practical turbine governor. These control functions can be subdivided into run-up control, load/frequency control, overspeed control and emergency overspeed trip. *Run-up control* of the unsynchronized generator is not considered further other than to comment that this is one area where control may be carried out using the main stop valves with both sets of control valves and the interceptor stop valves fully open. Primary *load/speed control* and secondary *frequency/tie-line power control* are achieved via the GVs with the IVs fully open. This control action is fundamental to turbine operation and is discussed in more detail in Chapter 9. If a severe disturbance occurs then the turbine speed may increase quickly and the aim of the *overspeed control* is to limit the maximum overspeed to about 110%. If overspeed control were possible only via the governor control valves then, depending on the droop setting, the generator speed would increase to, say, 105% (5% droop) before the main valves were shut. Although this would quickly reduce the HP torque, the entrapped steam in the reheater would reduce only slowly, typically with a time constant of 5 s or more, resulting in a slow decay of both the IP and the LP torque. As these typically contribute 70% of the torque, the turbine speed would continue to increase until the steam flow had time to reduce. Consequently the purpose of the overspeed control is to shut the IVs and, as these are at the inlet to the IP turbine, they have an immediate effect on reducing the IP and LP torque so limiting the overspeed. Typically the IVs will be kept fully open until the generator speed has reached an overspeed of, say, 104%, when the IVs will be closed.

In addition to IV closure, electro-hydraulic governors may also be equipped with additional *fast-valving* control logic which uses auxiliary control signals such as acceleration, electrical power, generator current, and so on, to fast-close the control valves when a large disturbance close to the generator is sensed. These fast-valving control functions are discussed in more detail in Section 10.2. The final stage of protection, the *emergency overspeed trip*, is independent of the overspeed control. If this trip function is activated both sets of control valves and the emergency stop valves are shut and the boiler tripped to ensure that the turbine is quickly stopped.

2.4 Substations

A substation can be regarded as a point of electrical connection where the transmission lines, transformers, generating units, system monitoring and control equipment are connected together. Consequently, it is at substations that the flow of electrical power is controlled, voltages are transformed from one level to another and system security is provided by automatic protective devices.

All substations consist of a number of incoming and outgoing circuits located in *bays*. These incoming and outgoing circuits are connected to a common busbar system and are equipped with apparatus to switch electrical currents, conduct measurements and protect against lightning. Each electrical circuit can be divided into a *primary* circuit and a *secondary* circuit. The primary circuit includes the transmission line, power transformer, busbars, and so on, and the high-voltage side of voltage and current transformers. The secondary circuit consists of the measurement circuits on the low-voltage side of the voltage and current transformers and the control circuits for the circuit-breakers and isolators, protection circuits.

The busbar constitutes a point of electrical contact for individual lines and transformers. In indoor substations the busbar consists of flat conductors made of aluminium or copper and supported by insulators, while in outdoor substations the busbars are stranded conductors made of steel and aluminium and suspended on insulators. A number of different busbar arrangements are possible, each of which differs in the flexibility of possible electrical connections and the ease with which maintenance can be carried out without disturbing either the operation of the substation or system security. The type of busbar system used will depend on the role and importance of the substation in the power system, the voltage level, installed capacity and on the expected reliability of network operation. Bigger substations tend to use more elaborate busbar systems requiring higher capital investment and operating cost. A description of different types of substation layout can be found in Giles (1970) and McDonald (2003).

2.5 Transmission and Distribution Network

The transmission and distribution network connects all the power stations into one supplying system and transmits and distributes power to individual consumers. The basic elements of the network are the overhead power lines, underground cables, transformers and substations. Auxiliary elements are the series reactors, shunt reactors and compensators, switching elements, metering elements and protection equipment.

2.5.1 Overhead Lines and Underground Cables

Overhead lines are universally used to transmit electrical energy in high-voltage transmission systems while underground cables are normally only used in low- and medium-voltage urban distribution networks. Because of their high cost, and the technical problems associated with the capacitive charging current, high-voltage underground cables can only be used under special circumstances such as in densely populated urban areas, wide river crossings or areas of major environmental concern. For example, short-distance cables are sometimes used to connect a power station to a substation.

Whenever current flows through any network element, real power is lost. As this power loss is proportional to the square of the current, transmission lines operate at high voltage and low current. Generally the more power that is sent over a transmission line, the higher will be its voltage. For practical reasons there is a standardization of voltage levels within different regions of the world. Unfortunately these standard voltages tend to vary slightly between regions but are not too dissimilar. Typical transmission voltage levels are 110, 220, 400, 750 kV for Continental Europe, 132, 275, 400 kV for the United Kingdom and 115, 230, 345, 500, 765 kV for the United States.

The maximum theoretical voltage value at which an overhead transmission line can be built is limited by the electrical strength of air and is estimated to be about 2400 kV. Currently the maximum voltage at which commercial lines have been built is 765 kV (Canada) and 750 kV (former Soviet Union). Experimental lines have been built to operate at 1100 kV in Japan and 1200 kV in the former Soviet Union (CIGRE, 1994).

Because of the high right-of-way costs associated with overhead lines, multi-circuit lines are usually built where more than one three-phase circuit is supported on the same tower. If a large increase in transmitted power is predicted for the future, space may be left on the transmission towers for extra circuits to be added later.

Distribution networks generally operate at lower voltages than the transmission network. Here the voltage standards used, both by different countries and by different areas in one country, can be quite varied, partly because of the way the system has developed. Historically, different parts of a network may have belonged to different private companies each of which would have followed its own standardization procedures. For example, there are 12 different standard distribution voltages in the United States, in the range between 2.4 and 69 kV. In the United Kingdom the distribution voltages are 6.6, 11, 33 and 66 kV.

2.5.2 Transformers

Transformers are necessary to link parts of the power systems that operate at different voltage levels. In addition to changing voltage levels, transformers are also used to control voltage and are almost invariably equipped with taps on one or more windings to allow the turns ratio to be changed. Power system transformers can be classified by their function into three general categories:

- *generator step-up transformers* (which connect the generator to the transmission network) and *unit transformers* (which supply the auxiliary service – Figure 2.2);
- *transmission transformers*, which are used to connect different parts of the transmission network, usually at different voltage levels, or connect the transmission and distribution networks;
- *distribution transformers*, which reduce the voltage at load centres to a low voltage level required by the consumer.

Generator and transmission transformers have ratings from several tens of megavolt-amperes to more than 1000 MVA and are usually oil cooled. The transformer core is placed inside a tank filled with oil which acts as both a coolant and insulator for the transformer windings. Heat, due to core loss and ohmic loss in the transformer windings themselves, is removed from the oil through external radiators. The circulation of oil inside the transformer is either natural or forced. The air circulation outside the transformer is usually forced using fans. Because of transportation problems, large, high-power transformers are usually constructed as three separate single-phase transformers. Smaller power transformers are usually of an integrated three-phase design.

Generator transformers step up the voltage from the generator level of typically 10–20 kV to the transmission or subtransmission voltage. In a power station employing large generators of typically 200–500 MW and above, each generator may have its own transformer consisting of three interconnected *two-winding transformers*. In contrast to this the generators in a smaller power station may operate with two generators connected to one *three-winding*, three-phase transformer.

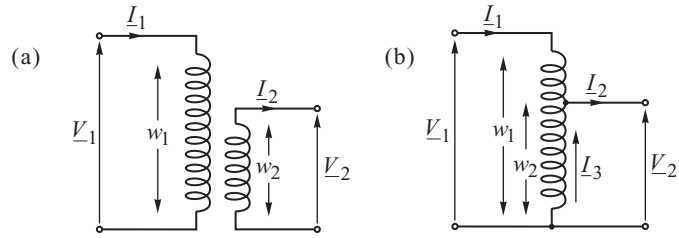

Figure 2.17 Transmission transformers: (a) two-winding transformer; (b) autotransformer.

Generator step-up transformers are usually Δ–Y connected with the neutral grounded. The delta low-voltage winding closes the path for the circulating current resulting from asymmetrical loading and the undesirable third-harmonic magnetizing current, caused by the nonlinear *B*–*H* characteristic of the transformer core, so that these currents remain trapped inside it. In a large power station with many generating units some of the transformer neutrals may not be grounded to limit the single-phase short-circuit currents in the transmission network.

Transmission transformers connect different parts of the transmission and subtransmission networks operating at different voltage levels, supply distribution networks and connect large industrial consumers directly to the transmission network as shown in Figure 2.1. The windings of the transformers tying transmission and subtransmission networks are normally Y–Y connected with the neutral grounded. These transformers often also have a low-power, medium-voltage, Δ-connected tertiary winding to provide a path for the circulating current when the high-voltage winding is asymmetrically loaded. This additional winding can also be used to supply local loads inside a substation or to connect a reactive power compensator.

If the required transformation ratio is not too high the two-winding transformer shown in Figure 2.17a can be replaced by the one-winding *autotransformer* shown in Figure 2.17b. In the autotransformer, parts of the primary winding, w_1, and the secondary winding, w_2, are common giving an obvious economy. Autotransformers are normally used to connect networks at consecutive voltage levels: for example, 132/275, 275/400 kV in the United Kingdom, 138/230, 230/345, 345/500 kV in the United States and 110/220, 220/400 kV in Continental Europe.

Distribution networks are normally supplied from transmission and subtransmission networks by transformers with the high-voltage side connected in star and the medium-voltage side connected in delta to help minimize any possible load asymmetry. Autotransformers linking parts of distribution networks operating at different, but close, voltage levels are usually star connected with the neutral grounded.

Each of the above transformers can be made with a controllable voltage transformation ratio and with, or without, phase shift control. The former is used for voltage or reactive power flow control while the latter controls the flow of real power.

2.5.2.1 Tap-Changing Transformers

Controlling the voltage transformation ratio without phase shift control is used for generator step-up transformers as well as for transmission and distribution transformers. The easiest way to achieve this task is by using tap changers to change the transformation ratio.

Control of the transformation ratio without phase shift control is usually achieved by using taps on one of the windings. In this way the transformation ratio is changed stepwise, rather than continuously. Tap-changing facilities can be made to operate either off load or on load.

The off-load tap changer requires the transformer to be de-energized while tap changing takes place. A typical range of regulation is ±5%. This method is used for low-rating transformers

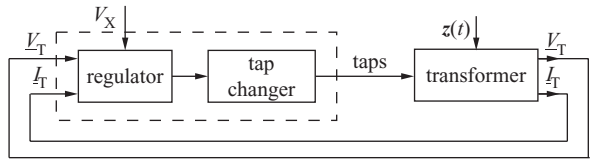

Figure 2.18 Block diagram of the transformation ratio control system.

operating in medium- and low-voltage distribution networks. Change of the transformer ratio is usually done manually according to season – typically two times a year.

The *underload tap-changing transformer* (ULTC), also called the *on-load tap changer* (OLTC) or *load tap changer* (LTC), allows the taps to be changed while the transformer is energized. A typical range of regulation is ±20%.

A simplified block diagram of the control system of a regulating transformer is shown in Figure 2.18. The transformer is subject to disturbances $\boldsymbol{z}(t)$ which could be network loading changes or network configuration changes. The regulator acts on the transformer via a tap changer. The regulator receives signals of measurements of the voltage $\underline{V}_T$ and current $\underline{I}_T$ on a chosen side of the transformer. By comparing these with a reference value, it forms a control signal and executes a required control task. The regulator may additionally obtain external control signals V_x from, for example, a supervisory controller.

Depending on the point of installation of the transformer and its function in the system, the controlled variables may be the voltage at a certain point in the network or reactive power flowing through the transformer. When controlling the voltage at a desired location, the control signal is obtained using current compensation: that is, by adding the voltage drop on the assumed compensation impedance to the transformer voltage, as in Figure 2.5.

Transformer taps may be situated in the same tank as the main winding. The taps are usually installed on the high-voltage side of the transformer (because of the lower current) and near the neutral end of the winding (where the voltage with respect to ground is smallest). In autotransformers taps are also on the high-voltage side but near the common part of the winding. The regulator of the tap changer usually tries to minimize the number, or frequency, of tap changes per day in order to prolong the life of the tap changer.

The principle of operation of the OLTC is shown in Figure 2.19. For simplicity, only five taps and a part of the winding have been shown. The choice of taps selected for operation is done by two tap selectors S1 and S2.

In the first solution, Figure 2.19a, both tap selectors are set on the same tap during normal operation. The load current of the transformer flows through both parallel chokes X. This causes an increase in the reactance by the value $X/2$, which is a disadvantage of the solution. When the tap is to be changed, first selector S1 is moved while selector S2 remains at the initial position.

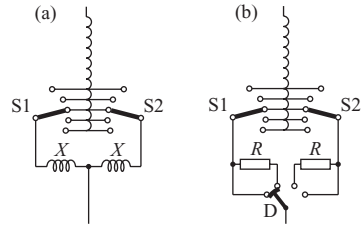

Figure 2.19 Principle of operation of the on-load tap changer: (a) with reactors; (b) with resistors.

During that time, the part of the windings between the taps is short-circuited by reactance $2X$. This reactance reduces the short-circuit current and it is an advantage of the solution. Then selector S2 is moved so that both selectors are in a new position on the chosen tap. An appropriate tap drive system is necessary to ensure that the selectors are moved without creating a gap in the circuit.

In the second solution, Figure 2.19b, two resistors R and a diverter switch D are used. During normal operation on a chosen tap, the diverter switch D is at the extreme position, that is the left position in the diagram. The load current flows through the conductor short-circuiting the resistor. Just before the switching sequence is started, the diverter switch D is moved to the middle position. The current then flows through two parallel resistors and the circuit resistance is increased by $R/2$. The selector S1 is moved to the new position and the part of the winding between the taps is momentarily short-circuited by resistance $2R$. This resistance limits the short-circuit current which is an advantage of the solution. Then selector S2 is moved so that both selectors are in a new position on the chosen tap. Finally the diverter switch D returns to its extreme left position.

Both elements (diverter switch and the selectors) may be parts of one mechanism but they operate in two separate compartments. Both selectors and resistors are located in the lower compartment, which is in the transformer's tank. The diverter switch is in the upper compartment with its own oil, outside the transformer's tank. Thanks to this separation, oil used during tap changes (i.e. during breaking the circuit) does not contaminate oil in the transformer's tank. Oil in the small diverter compartment is replaced more often than oil in the big transformer's tank. The resistors are used only momentarily and if the switching mechanism blocks when the resistors are operating, the transformer must be disconnected.

Sometimes the tap selectors and diverter switch are combined into one switch as shown in Figure 2.20. That switch is made up of several fixed contacts spread in a circle and one triple moving contact. For simplification, only the left side of the fixed contacts has been shown together with corresponding taps. An important role for the switching sequence is played by the empty space between the fixed contacts. The moving contact consist of the main (middle) contact and two side contacts. There are resistors in the circuit of those contacts. Movement of this triple contact is executed in the following way. The width of the contacts and of the empty space is selected such that, before the main moving contact leaves a given fixed contact, side contacts move from the neighbouring empty spaces into neighbouring fixed contacts. This causes a momentary short circuit, through resistors, of the neighbouring fixed contacts. Further movement of the triple contact causes a connection of the main contact with the fixed contact and movement of the side contacts into empty space. The short circuit is interrupted and normal operation through a new fixed contact, and on a new tap, is restored.

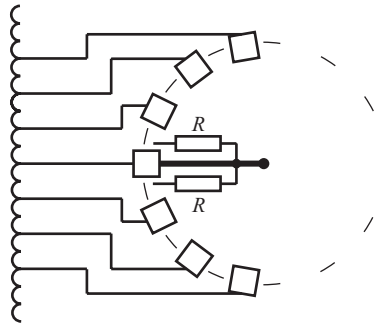

Figure 2.20 Principle of operation of the selector-type tap changer.

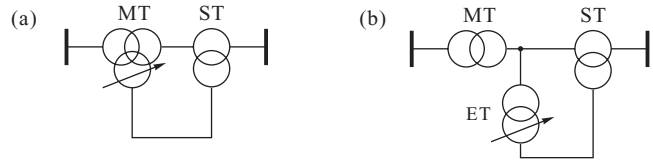

Figure 2.21 Two ways of supplying the series transformer: (a) from the tertiary winding of the main transformer; (b) from a separate excitation transformer. MT, main transformer; ST, series (booster) transformer; ET, excitation transformer.

2.5.2.2 Phase Shifting Transformer

Phase shifting transformers control the voltage transformation ratio together with voltage phase angle in order to control real power flows in transmission networks. The regulation is executed using a series transformer referred to as a *booster transformer* which is fed by an *excitation transformer*. Examples of connecting booster and excitation transformers are shown in Figure 2.21.

With the transformer connections shown in Figure 2.21, the voltage can be regulated in both magnitude and phase with the degree of regulation depending on the connection made between the tertiary winding of the main transformer MT (or the excitation transformer ET) and the series transformer ST. A number of possible schemes are illustrated Figure 2.22.

Figure 2.22a shows the series transformer windings where $\Delta\underline{V}_A$, $\Delta\underline{V}_B$, $\Delta\underline{V}_C$ are the voltages supplied from the excitation transformer (not shown) to be injected into each phase of the main circuit. Figure 2.22b shows the phase relationship of the phase and phase-to-phase voltages used to supply the excitation transformer. The same voltages are also on the primary side of the series transformer. If the excitation transformer is constructed so that the voltages $\Delta\underline{V}_A$, $\Delta\underline{V}_B$ and $\Delta\underline{V}_C$ are proportional to, and in phase with, the primary-side phase voltages $\Delta\underline{V}_A$, $\Delta\underline{V}_B$ and $\Delta\underline{V}_C$ then

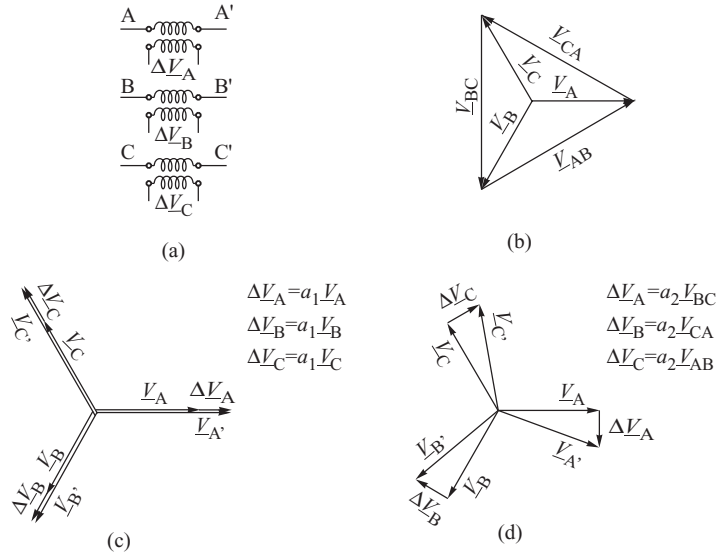

Figure 2.22 Complex transformation ratio: (a) windings of the series transformer; (b) the triangle of phase and line voltages; (c) in-phase booster voltages; (d) quadrature booster voltages.

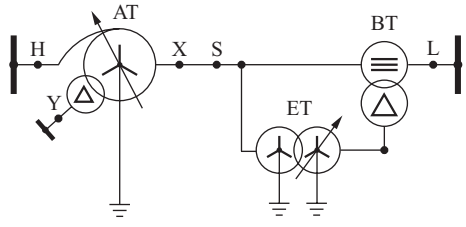

Figure 2.23 Transformer combination for independent in-phase and quadrature regulation.

the series transformer will produce a change in the voltage magnitude as shown in Figure 2.22c. The secondary voltages of the series transformer are $\underline{V}_{A'}$, $\underline{V}_{B'}$ and $\underline{V}_{C'}$.

Alternatively, as shown in Figure 2.22d, the excitation transformer can be constructed so that the voltages $\Delta\underline{V}_A$, $\Delta\underline{V}_B$ and $\Delta\underline{V}_C$ are proportional to the phase-to-phase values $\Delta\underline{V}_{BC}$, $\Delta\underline{V}_{CA}$ and $\Delta\underline{V}_{AB}$ of the primary-side voltages. As the line voltage between two phases in a three-phase system is always in quadrature with the voltage of the third phase, the series transformer will introduce a change in the voltage angle and a small change in voltage magnitude. This type of booster transformer is referred to as a *quadrature booster transformer*.

Generally the excitation transformer can be constructed so that it supplies the series transformer with a net voltage made up of an in-phase component and a quadrature component. The voltage change in all three phases can be then expressed as

$$\Delta\underline{V}_A = a_1\underline{V}_A + a_2\underline{V}_{BC}, \quad \Delta\underline{V}_B = a_1\underline{V}_B + a_2\underline{V}_{CA}, \quad \Delta\underline{V}_C = a_1\underline{V}_C + a_2\underline{V}_{AB}, \tag{2.4}$$

where a_1 and a_2 are the voltage transformation ratios associated with the in-phase component and quadrature component respectively. Both these voltage ratios can be adjusted to allow control of both the voltage magnitude and angle. In this case the transformation ratio is a complex number, $\underline{\vartheta} = \underline{V}_{A'}/\underline{V}_A = \underline{V}_{B'}/\underline{V}_B = \underline{V}_{C'}/\underline{V}_C = \vartheta e^{j\theta}$, where θ is a phase shift angle.

It is possible to construct a single transformer in which both in-phase and quadrature regulation are done in the same tank. In practice, the two modes of regulation tend to be executed in separate transformers as shown in Figure 2.23. Quadrature regulation is executed using the booster transformer BT and the excitation transformer ET situated in a common tank. In-phase regulation is executed independently in the main autotransformer AT which has its own tank. The main advantage of this solution is operational flexibility. In the case of a maintenance outage or failure of the tap changer of the excitation transformer ET, the autotransformer AT may operate after a bypass is inserted between terminals S and L – see Figure 2.23.

2.5.3 Shunt and Series Elements

Shunt and series elements, such as series capacitors and shunt compensators (static and rotating), are used in transmission networks for a number of purposes. From the point of view of this book their use will be considered for the purposes of reactive power compensation and stability improvement.

2.5.3.1 Shunt Elements

Section 3.1 will show how the ever-changing real and reactive power demand may cause large variations in the network voltage profile. Generally, reactive power cannot be transmitted over long distances and should be compensated for close to the point of consumption. The simplest, and cheapest, way of achieving this is by providing *shunt compensation*, that is by installing capacitors and/or inductors connected either directly to a busbar or to the tertiary winding of a transformer.

Shunt elements may also be located along the transmission route to minimize losses and voltage drops. Traditionally, static shunt elements are breaker switched either manually or automatically by a voltage relay. Modern solutions, involving the use of thyristors, will be described in the next subsection.

When the system power demand is low, reactive power produced by the transmission line capacitance may prevail over the reactive power consumed by the inductance and the transmission line may be a net source of reactive power (Section 3.1.2). The effect of this may be to boost the network voltages to unacceptably high values. In such circumstances *shunt reactors* can be used to consume the surplus reactive power and depress the voltages. Usually shunt reactors are required for transmission lines longer than about 200 km. During heavy loading conditions some of the reactors may have to be disconnected and *shunt capacitors* used to supply reactive power and boost local voltages.

Another traditional means of providing shunt compensation is by the use of a *synchronous compensator*. This is a salient-pole synchronous motor running at no load and whose field is controlled so as to generate or absorb reactive power. When overexcited the synchronous compensator is a source of reactive power; when underexcited it absorbs reactive power. Although relatively expensive synchronous compensators play an important role in the control of voltage and reactive power at the transmission, and especially subtransmission, voltage levels. They are used in order to improve stability and maintain voltages within desired limits under varying load conditions and contingency situations. When used in new substations, synchronous compensators are often supplemented by switched shunt capacitor banks and reactors so as to reduce installation and operating costs. The majority of synchronous compensator installations are designed for outdoor operation and operate unattended with automatic control of start-up and shutdown. Small synchronous compensators of several megavolt-amperes are usually connected to the tertiary winding of the transmission transformer while larger units of up to a few hundred megavolt-amperes are connected by individual step-up transformers to the busbars of a high-voltage substation. The small units are generally air cooled while the bigger units are either water cooled or hydrogen cooled.

2.5.3.2 Series Elements

Series capacitors are connected in series with transmission line conductors in order to offset the inductive reactance of the line. This tends to improve electromechanical and voltage stability, limit voltage dips at network nodes and minimize the real and reactive power loss. Typically the inductive reactance of a transmission line is compensated to between 25 and 70%. Full 100% compensation is never considered as it would make the line flows extremely sensitive to changes in angle between the voltages at the line terminals and the circuit would be series resonant at the fundamental frequency. Moreover, high compensation increases the complexity of protection equipment and increases the probability of subsynchronous resonance as discussed in Section 6.7.3.

Normally series capacitors are located either at the line terminals or at the middle of the line. Although fault currents are lower, and line protection easier, when the capacitors are located at the mid-point, the access necessary for maintenance, control and monitoring is significantly eased if the capacitor banks are positioned at the line terminals. For this reason the compensating capacitors and associated shunt reactors are usually split into two equal banks positioned at each end of the line Typically each bank will be capable of compensating the line to a maximum of 30%. A detailed discussion of the benefits and problems of locating series capacitors at different points along the line can be found in Ashok Kumar *et al.* (1970) and Iliceto and Cinieri (1970).

Sometimes during power swings or heavy power transfers the line reactive current is high and the voltage may rise excessively on one side of the series capacitor. In this case the system must be designed to limit the voltage to acceptable levels or capacitors of appropriately high-voltage rating must be used. Normally the voltage drop across a series capacitor is only a small percentage of the rated line voltage. A short circuit on one side of the capacitor may, however, produce a temporary

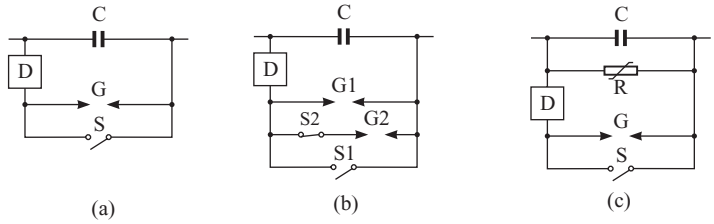

Figure 2.24 Series capacitor protective schemes: (a) single-gap scheme; (b) dual-gap scheme; (c) zinc oxide scheme.

voltage across the element approximately equal to the line rated voltage. As such a fault is rare, it is uneconomical to design the element to withstand such a high voltage so that normally provision is made for the capacitor to be bypassed during such a fault and reinserted after fault clearing.

The traditional way of bypassing the capacitor is to include a spark gap across either the capacitor bank itself or each module of the bank. A better solution is to use nonlinear zinc oxide resistors which provide almost instantaneous reinsertion. Figure 2.24 shows some alternative bypass schemes (ABB, 1991). The single-gap protective scheme in Figure 2.24a uses a single spark gap G which bypasses the capacitor if the voltage exceeds a preset value, normally equal to about 3–4 times the rated voltage of the capacitor. The short-circuit current flowing through the capacitor is damped in the damper D. When the gap current is detected the bypass breaker S is closed diverting the current from the gap. When the line current returns to normal the bypass breaker opens within 200–400 ms and the capacitor is reinserted.

A faster reinsertion time, around 80 ms, is provided by the dual-gap scheme in Figure 2.24b. When the fault occurs the spark gap G2, which is set lower than G1, sparks over first bypassing the capacitor. Breaker S2, which is normally closed, opens immediately upon sensing the normal line current and reinserts the capacitor. In this way capacitor reinsertion is not delayed by deionization time. The other gap G1 and the bypass breaker S1 serve as back-up protection.

Due to its nonlinear properties the zinc oxide resistor shown in Figure 2.24c limits the voltage across the capacitor bank during a fault and reinserts the bank immediately when the current returns to normal. The spark gap G does not normally operate and is provided only as back-up overvoltage protection for the resistor.

2.5.4 FACTS Devices

Traditionally the main control actions in a power system, such as transformer tap changers, have been achieved using mechanical devices and were therefore rather slow. However, continuing progress in the development of power electronics has enabled a number of devices to be developed which provide the same functions but with much faster operation and with fewer technical problems. Transmission networks equipped with such devices are referred to as FACTS (Flexible AC Transmission Systems) while the electronic devices themselves are referred to as *FACTS devices*. At the heart of FACTS devices is a controlled semiconductor, the *thyristor*.

The first thyristor developed in the early 1970s was the *silicon-controlled rectifier* (SCR), which had turn-on but no turn-off capability. Such a thyristor is now referred to as a *conventional thyristor*. It was at the heart of a rapid expansion of power electronics. It was also used to construct the first FACTS devices using thyristor valves. A thyristor valve is constructed using conventional thyristors and may be a circuit-breaker or a current controller (Figure 2.25).

Figure 2.25a shows a thyristor valve consisting of two thyristors that allow regulation of the current flowing through a shunt reactor. Regulation of alternating current is executed by cutting

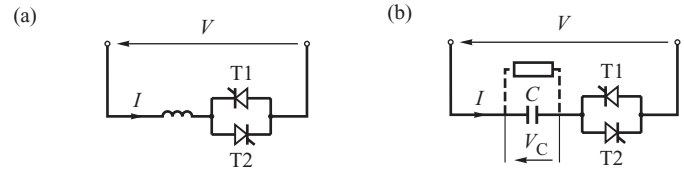

Figure 2.25 Two applications of thyristor valves: (a) thyristor-controlled reactor; (b) thyristor-switched capacitor.

out a part of the sine waveform. The resulting alternating current contains harmonics. Hence any FACTS device using this type of regulation must be equipped with additional harmonic filters to help smooth the current waveform. Such filters are quite expensive and constitute a substantial part of the overall cost.

In the case of the capacitor it is not possible to obtain smooth control of the current due to the long time constant associated with the capacitor charge/discharge cycle so that the thyristor valve can only switch the capacitor on or off as shown in Figure 2.25b. When the flow of the current is blocked, the capacitor is discharged via the discharge resistor.

The next stage in the development of power electronics was the invention of the *gate turn-off thyristor* (GTO), which has both turn-on and turn-off capability. GTOs have found application in a number of more advanced FACTS devices based on voltage source converters and current source converters. The basic principle of these converters is shown in Figure 2.26. To differentiate it from the conventional thyristor, the GTO is denoted by an additional slanted line.

The voltage source converter (Figure 2.26) connects a DC system with an AC three-phase system (the three slanted lines on the right denote a three-phase system). Generally, power can flow in either direction; that is, the DC system can either send or receive power. The DC voltage always has one polarity and power reversal takes place through reversal of the polarity of the direct current. Therefore the converter valve has to be bidirectional and is made up of an asymmetric turn-off GTO device with a parallel diode connected in reverse. The capacitor on the DC side must be large enough to handle a sustained charge/discharge current that accompanies the switching sequence of the converter valve. On the AC side, the voltage source converter is connected with the AC system through a small reactance (usually a transformer) in order to ensure that the DC capacitor is not short-circuited and discharged rapidly into a capacitive load such as transmission lines of the AC system. In a particular case the DC side may consist of only a capacitor and then the real power of the DC system is equal to zero. In that case there is only reactive power on the AC side.

Current source converters used in low-voltage power electronic devices tend not to be used in high-voltage power electronics as they would require AC filters on the AC side, which is expensive. Hence they will not be discussed here.

The main disadvantages of GTOs are their bulky gate drivers, slow turn-off and costly snubbers. Research continues to overcome those problems. It is likely that in coming years GTOs will be

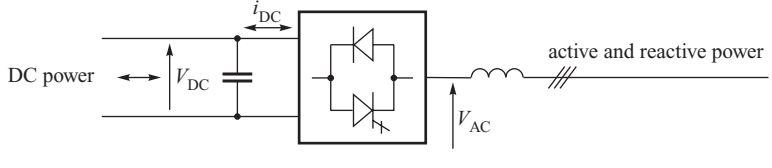

Figure 2.26 Basic principle of voltage source converter.

replaced in FACTS devices by new, more advanced thyristors such as the *integrated gate-commutated thyristor* (IGCT) or *MOS-controlled thyristor* (MCT).

Detailed description of thyristor-based FACTS devices can be found in Hingorani and Gyugyi (2000) and Akagi, Watanabe and Aredes (2007). Below only a short description will be given, necessary for understanding the rest of this book.

Depending on the way FACTS devices are connected to a power system, they can be divided into shunt and series devices. Main shunt FACTS *devices* are reactive power compensators, energy storage (e.g. superconducting or battery-based) and braking resistors. Among various *series FACTS devices* are series compensators, phase angle regulators and power controllers.

2.5.4.1 Static VAR Compensator

Static VAR compensators (SVCs) based on conventional thyristors have been used in power systems since the 1970s, long before the concept of FACTS was formulated. The role of the SVC is to adjust the amount of reactive power compensation to the actual system needs. A flexible and continuous reactive power compensation scheme that operates in both the capacitive and inductive regions can be constructed using the thyristor-switched and/or thyristor-controlled shunt elements shown in Figure 2.25. Using these elements it is possible to design a variety of SVC systems. Some typical configurations are shown in Figure 2.27.

In Figure 2.27a one reactor is thyristor controlled and the other is thyristor switched. When the inductive VAR demand is low, only the thyristor-controlled reactor operates. When demand increases, both reactors are switched on with the thyristor-controlled reactor being used to control the actual amount of reactive power needed.

Figure 2.27b shows a thyristor-switched bank of capacitors. The reactive power control (in the capacitive region only) can be accomplished in steps by switching consecutive capacitors in or out.

The SVC shown in Figure 2.27c consists of a bank of shunt capacitors connected in parallel with a thyristor-controlled shunt reactor. The thyristor valve enables smooth control of the lagging VARs produced by the reactor. With the reactors switched fully on, the parallel reactor–capacitor bank appears to be net inductive, but with the reactors fully off, the bank is net capacitive. By controlling the reactor current it is possible to achieve a full control range between these two extremes. A similar principle is used in the system shown in Figure 2.27d which additionally contains a bank of thyristor-switched capacitors.

Each of the above systems can be associated with a static voltage–reactive power characteristic $V(Q)$. This will be discussed using the TSC/TCR compensator as an example.

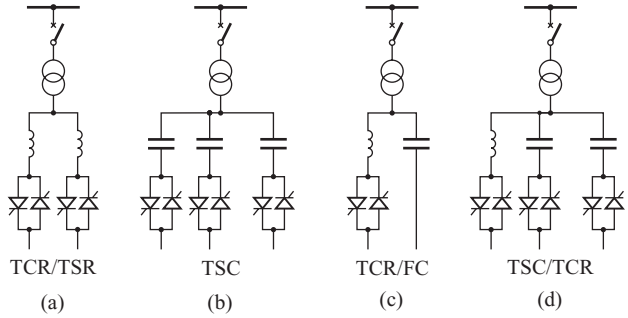

Figure 2.27 Types of SVCs. TCR, thyristor-controlled reactor; TSR, thyristor-switched reactor; TSC, thyristor-switched capacitor; FC, fixed capacitor.

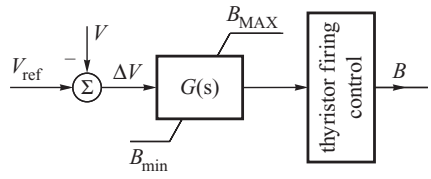

Figure 2.28 Simplified block diagram of SVC.

The thyristor firing circuits used in SVCs are usually controlled by a voltage regulator (Figure 2.28) which attempts to keep the busbar voltage constant by controlling the amount and polarity of the reactive power injected into the busbar. The TSCs and the TCRs are equipped with a controller, shown on the right hand side of the diagram, enforcing a required total value of the equivalent compensator susceptance B. This susceptance controller executes the overall control strategy and is very important for operation of the whole system. The regulator, shown on the left hand side of the diagram, creates a signal dependent on the controller transfer function and a voltage error in the node where the compensator is connected. Obviously the value of the total susceptance is between the total susceptance of the capacitor bank and the reactor susceptance when the capacitors are switched off. In the steady state, the regulator's transfer function $G(s)$ is such that for $t \to \infty$, that is $s \to 0$, it is equal to

$$G(s)|_{s=0} = K, \tag{2.5}$$

namely a gain. Hence in the steady state, $\Delta B = K \cdot \Delta U$; that is, the change of susceptance is proportional to the voltage change. For voltages close to the rated voltage it may be assumed that $V \cong V_{ref}$, that is $\Delta Q = \Delta B \cdot V^2 \cong \Delta B \cdot V_{ref}^2$. Hence

$$\Delta Q \cong \left(K \cdot V_{ref}^2\right) \cdot \Delta V. \tag{2.6}$$

Figure 2.29 shows a voltage–reactive power characteristic of the device. The part of the $V(Q)$ characteristic corresponding to (2.6) is denoted by I. This characteristic has a small droop, that is the tangent is equal to $1/K$, the reciprocal of the regulator gain. The voltage at the point of intersection with the vertical axis is equal to V_{ref}.

The part of the characteristic denoted by II corresponds to a parabola $Q = B_{MAX} \cdot V^2$, that is the maximum value of the capacitive susceptance when all the capacitors are switched on and the reactors switched off. The part of the characteristic denoted by III corresponds to a parabola $Q = B_{min} \cdot V^2$, that is the minimum value of the susceptance when all the reactors are switched on and all the capacitors switched off.

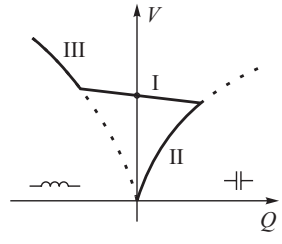

Figure 2.29 Static characteristic of SVC equipped with voltage regulator.

The SVC can operate in transmission networks as a voltage regulator with an additional PSS regulator added to damp power oscillations. This will be discussed in Chapter 11.

Nowadays SVCs based on conventional thyristors are regarded as old technology. Particularly troublesome and expensive is the necessity to smooth the current deformed by TCRs. The cost of such an SVC is typically several times that of an uncontrolled bank of shunt reactors or fixed capacitors and a considerable part of that cost is due to the filters. A modern solution to the same problem of thyristor-based reactive power compensation is the static compensator based on a voltage source converter.

2.5.4.2 Static Compensator

The *static compensator* (STATCOM), also called the *static VAR generator* (SVG), provides shunt compensation in a similar way as the SVCs but utilizes the voltage source converter. Consequently it incorporates a very high content of power electronics but its conventional components are reduced to only a transformer and a capacitor.

The operating principle of the STATCOM is illustrated in Figure 2.30. On the DC side of the voltage source converter, there is only a capacitor. Compared with the block diagram in Figure 2.26, there is no source or demand of real power. The voltage source converter is equipped with a pulse-width modulation (PWM) controller operating with two control parameters m and ψ. The AC voltage produced by this converter is given by

$$\underline{V}_{\mathrm{AC}} = mkV_{\mathrm{DC}}(\cos\psi + \mathrm{j}\cos\psi)\,. \tag{2.7}$$

A change in m enables the converter to change the magnitude of the AC voltage and therefore it influences a change of alternating current flowing through the transformer reactance X:

$$\underline{I}_{\mathrm{AC}} = \left(\underline{V}_i - \underline{V}_{\mathrm{AC}}\right)/\mathrm{j}X. \tag{2.8}$$

If $V_{\mathrm{AC}} > V_i$ then $\underline{I}_{\mathrm{AC}}$ leads $\underline{V}_i$ and reactive power is delivered to the busbar. The compensator acts like a capacitor. Conversely if $V_{\mathrm{AC}} < V_i$ then $\underline{I}_{\mathrm{AC}}$ lags $\underline{V}_i$ and reactive power is drawn from the busbar. The compensator acts like a reactor. For a transformer reactance of 0.1 pu, a $\pm 10\%$ change in V_{AC} produces a ± 1 pu change in the inserted reactive power.

Changing ψ, responsible for the phase of AC voltage, see (2.7), makes it possible to control the active power fed to the capacitor, which is necessary to keep a constant value of the DC voltage.

To compensate reactive power in a power system, the STATCOM must be equipped with an AVR. Its function is to enforce appropriate reactive power changes by affecting the regulation parameters m and ψ of the converter controller.

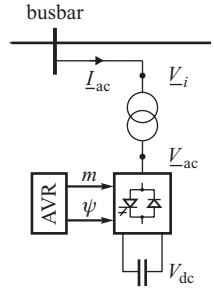

Figure 2.30 STATCOM based on voltage source converter.

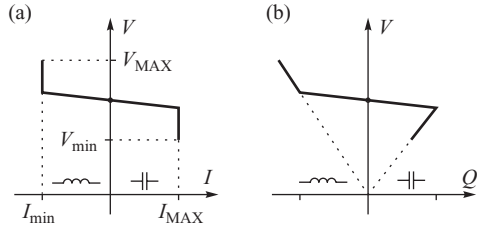

Figure 2.31 Static characteristics of STATCOM equipped with voltage regulator: (a) voltage vs current; (b) voltage vs power.

The transfer function of the voltage controller, as for the SVC, enforces a required small droop around the reference voltage V_{ref} in the static voltage–reactive power characteristic. The regulator has a stabilizing feedback loop fed from the compensator current. The regulator also has voltage and current limiters. Current limiters stop regulation after a maximum value of the current is reached. They correspond to vertical lines I_{min} and I_{MAX} in Figure 2.31a, and diagonal lines $Q = VI_{min}$ and $Q = VI_{MAX}$ in Figure 2.31b. Voltage limiters switch off the device when allowed values have been exceeded. The limiters correspond to a break in the characteristics at values V_{min} and V_{MAX}.

The STATCOM can operate in transmission networks as a voltage regulator with an additional PSS regulator added to damp power oscillations. This will be discussed in Chapter 10.

2.5.4.3 Energy Storage System

Figure 2.26 shows that a voltage source converter may operate with a DC device sending or receiving power. That power will appear on the AC side as real power sent to, or received from, a power system.

The *battery energy storage system* (BESS) shown in Figure 2.32 has a chemical battery connected to its DC side. The battery voltage V_{DC} may be considered to be constant so that, according to (2.7), changes in parameters m and ψ allow the magnitude and phase of the AC voltage $\underline{V}_{AC}$ to be regulated and therefore a regulation of real and reactive power flows. Regulation of m and ψ is executed by a *power conditioning system* (PCS). That regulator enforces a required real power flow discharging or charging the battery at an acceptable rate. Depending on needs, BESS can also control reactive power flows just like the STATCOM.

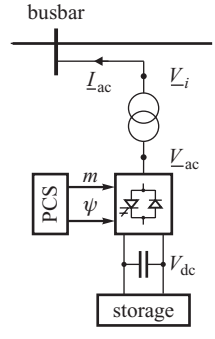

Figure 2.32 Battery energy storage system.

BESSs connected at the distribution level range in size from less than 1 MW to over 20 MW and find many applications. One of them is smoothing of power flows due to intermittent loads or renewable generators.

In transmission networks, BESSs with ratings of several tens of megawatts or higher may potentially find an application for spinning reserve or frequency control in the first instance after a large power unit is lost – see Chapter 9. Real power of BESS could also be used for the damping of power swings and stability enhancement (Chapter 10).

Superconducting magnetic energy storage (SMES) is functionally similar to BESS but with a superconducting coil used to store energy in the magnetic field of the coil. The active and reactive power available from SMES depends on the direct current stored in the coil. For a given direct current, the SMES power can be regulated in four quadrants of the complex power domain within a circular range limited by

$$[P_s(t)]^2 + [Q_s(t)]^2 \leq |S_{MAX}|^2 , \tag{2.9}$$

where S_{MAX} is the maximum available apparent power. Applications of SMES are similar to those of BESS.

2.5.4.4 Thyristor-Controlled Braking Resistor

The braking resistor is used exclusively for transient stability enhancement. It acts as an additional resistive load capable of absorbing some of the surplus generation in case a severe fault occurs near a generator, thus preventing loss of synchronism.

Traditionally, braking resistors were made as cast-iron resistors switched on by a mechanical circuit-breaker for a short time after clearing the fault. Because of the restricted lifetime of the mechanical circuit-breaker, the resistor would be switched on and off only once after a fault.

In newer solutions, the mechanical circuit-breaker can be replaced by an electronic switch made of conventional thyristors connected back to back – see Figure 2.33. Such a device is referred to as a *thyristor-switched braking resistor* (TSBR). The number of switches allowed is no longer restricted and it is possible to apply bang–bang control with a number of switches on and off after a fault occurs.

Theoretically, it is possible to use voltage source converters to control the braking resistor. In that case the resistor may be connected on the DC side, similar to BESS. The voltage source converter may smoothly control real power absorbed by the resistor from the AC system. Such a device could be referred to as a *thyristor-controlled braking resistor* (TCBR). Like BESS, reactive power could also be controlled within the capacity of the converter.

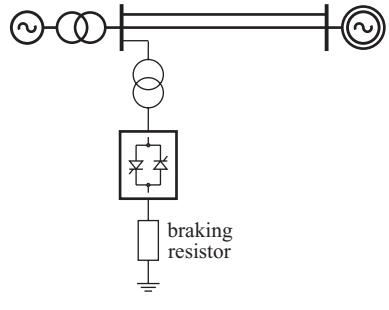

Figure 2.33 Thyristor-switched braking resistor.

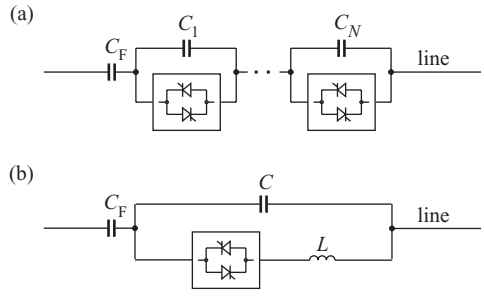

Figure 2.34 Series compensators based on conventional thyristors: (a) thyristor-switched series capacitor; (b) thyristor-controlled series capacitor.

2.5.4.5 Series Compensators

Traditional series condensers are switched by mechanical circuit-breakers. Consequently their control properties are limited and they usually operate with a constant capacitance.

Modern FACTS series compensators, apart from traditional compensation of the series line reactance, can also be used to regulate the total reactance of the transmission system and therefore they can provide regulation of real power flows. Such compensators can be made using conventional thyristors or voltage source converters.

Figure 2.34 shows two examples of series compensators based on traditional thyristors. In the first device shown in Figure 2.34a, referred to as the *switched series capacitor* (SSC), the series condensers consist of fixed capacitor C_F and a bank of series capacitors $C_1, C_2, \ldots, C_N$. The thyristor control system can short-circuit or open-circuit a number of capacitors. Thus the total series capacitance inserted into the network can change stepwise with the step equal to the capacitance of one series compensator. The thyristors are protected against overvoltages by nonlinear zinc oxide resistors as shown in Figure 2.24.

In the second device shown in Figure 2.34b, referred to as the *controlled series capacitor* (CSC), a condenser of capacitance C is bypassed using a TCR. The condenser current is compensated by the reactor current. Consequently the reactor current control is equivalent to controlling the resultant reactance of a parallel-connected condenser and reactor. The control is smooth but a disadvantage is the thyristor control of the reactor current as it deforms the sine waveform by cutting out a part of it. This leads to harmonics and the need to use smoothing filters.

Modern series compensators use thyristor converters. Figure 2.35 illustrates the *static synchronous series compensator* (SSSC). The source of the AC voltage is a voltage source converter loaded by a condenser on the DC side. The capacitance of the condenser is such that it maintains a constant DC voltage. The converter operates as a voltage source synchronous with the AC network. The AC voltage $\Delta \underline{V}$ produced by the converter is inserted in the transmission link by the series (booster) transformer ST. Construction of the SSSC is similar to the STATCOM. Hence the SSSC is sometimes referred to as the series STATCOM.

As in the STATCOM, the voltage source converter is controlled using two parameters m and ψ responsible for the magnitude and phase of the AC voltage. Those parameters are controlled using PCS.

The SSSC compensates the reactance of a transmission line if its regulator ensures that the series booster voltage is always proportional to the current flowing in that line. This can be proved using Figure 2.36. Let us assume that the booster voltage is given by

$$\Delta \underline{V} \equiv -\mathrm{j}\Delta X \underline{I}. \tag{2.10}$$

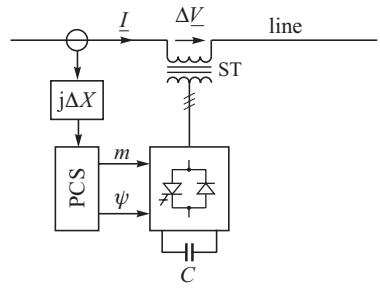

Figure 2.35 Static synchronous series compensator.

Using the equivalent diagram of the transmission link including the booster transformer (Figure 2.36a) gives

$$\underline{V}_k - \underline{V}_j = \mathrm{j}X_\mathrm{L}\underline{I}, \tag{2.11}$$

$$\underline{V}_k = \underline{V}_i - \underline{\Delta V}, \tag{2.12}$$

or $\underline{V}_i - \underline{V}_j = \mathrm{j}X_\mathrm{L}\underline{I} + \Delta\underline{V} = \mathrm{j}X_\mathrm{L}\underline{I} - \mathrm{j}\Delta X\underline{I} = \mathrm{j}(X_\mathrm{L} - \Delta X)\underline{I}$. Hence finally

$$\underline{V}_i - \underline{V}_j = \mathrm{j}(X_\mathrm{L} - \Delta X)\underline{I}. \tag{2.13}$$

The last equation corresponds to the equivalent diagram shown in Figure 2.36b in which the equivalent line reactance is equal to $(X_\mathrm{L} - \Delta X)$. This means that adding the voltage expressed by (2.10) in parallel with the line is equivalent to compensating the line reactance X_L by ΔX. In the phasor diagram shown in Figure 2.36c, the voltage inserted in series with the line compensates the voltage drop on the line reactance.

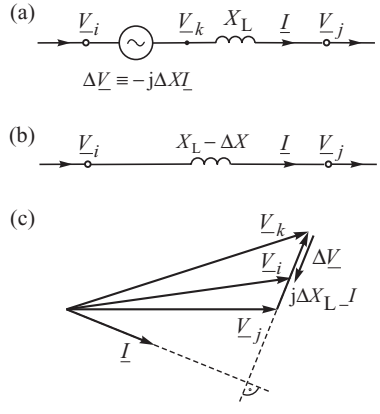

Figure 2.36 Compensation of the transmission line reactance using a current-controlled voltage source: (a) transmission line with a series-connected voltage source; (b) equivalent reactance; (c) phasor diagram.

It should be remembered that the SSSC compensates the reactance only if the voltage source is controlled using (2.10). That condition must be enforced by the regulator of the device.

Reactive power losses on the equivalent reactance ($X_L - \Delta X$) are smaller than the reactive power losses on the transmission line reactance X_L. It follows then that the source $\Delta \underline{V}$ must deliver the capacitive reactive power necessary to compensate the difference between reactive power losses in the transmission line reactance and the equivalent reactance. That power must come from the condenser loading the converter on the DC side.

Series condensers may be used to regulate power flows in the steady state. Their speed of operation may also be used for the damping of power swings and that application will be discussed in Chapter 10.

2.5.4.6 Thyristor-Controlled Phase Angle Regulator

Mechanical tap changers for the quadrature voltage regulation previously shown in Figure 2.22 can be replaced by FACTS technology. Figure 2.37 shows the *thyristor-controlled phase angle regulator* (*TCPAR*) where thyristor valves are used as electronic switches to replace the traditional mechanical tap changers. The number of electronic switches is restricted to three because the supply (excitation) transformer ET has three sets of windings on the secondary with a turns ratio of 1 : 3 : 9. The thyristor-switched system allows any one of these three sets of windings to be switched in series with the series transformer ST in either a positive or negative direction. Consequently each of these sets of windings can therefore be in one of three states giving $3^3 = 27$ possible values of the voltage supplying the series transformer. This corresponds to 27 taps in a traditional quadrature booster. For example, the booster value 1 is obtained by inserting only winding 1 in the supply circuit. The booster value $2 = 3 - 1$ is obtained if winding 3 is inserted in the opposite direction to winding 1. The booster value $4 = 3 + 1$ is obtained if windings 3 and 1 are connected in the same direction. The other ± 13 values are obtained in a similar way.

2.5.4.7 Unified Power Flow Controller

The unified power flow controller (UPFC), shown in Figure 2.38, consists of a shunt and series part. The shunt part consists of an ET and a voltage source converter CONV 1. The series part consists of a voltage source converter CONV 2 and an ST. Both voltage source converters CONV 1 and CONV 2 are connected back to back through the common DC link with a capacitor. Each converter has its own PWM controller which uses two control parameters, respectively m_1, ψ_1 and m_2, ψ_2, as shown in Figure 2.38.

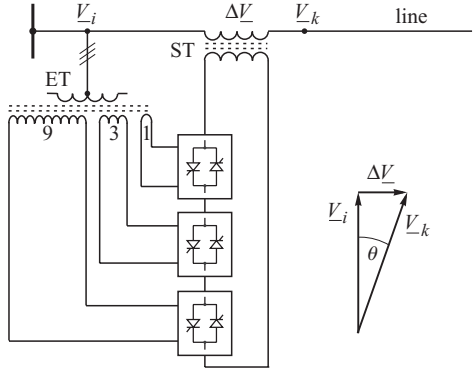

Figure 2.37 Thyristor-controlled phase angle regulator.

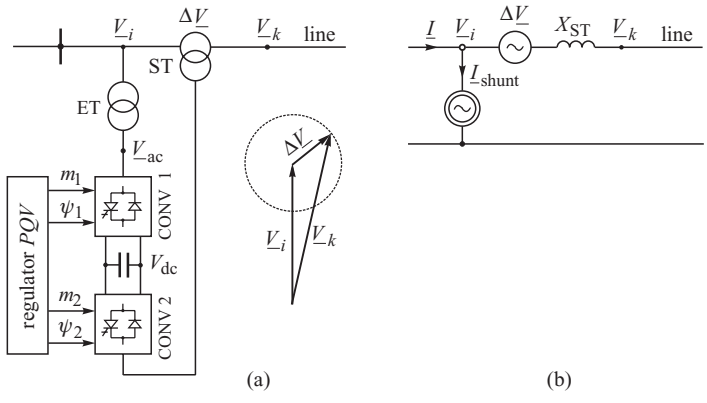

Figure 2.38 Unified power flow controller: (a) functional diagram and the phasor diagram; (b) equivalent circuit.

The shunt part of the UPFC works similarly to the STATCOM (Figure 2.30). Converter CONV 1 regulates voltage $\underline{V}_{AC}$ and thereby also the current received by the UPFC from the network. The voltage is expressed by

$$\underline{V}_{AC} = m_1 k V_{DC} (\cos\psi_1 + \mathrm{j}\cos\psi_1) . \tag{2.14}$$

The controller enforces a required value $\underline{V}_{AC}$ by choosing appropriate values of m_1 and ψ_1.

The series part of the UPFC works similarly to the SSSC (Figure 2.35). Converter CONV 2 regulates both the magnitude and the phase of the AC voltage $\Delta\underline{V}$ supplying the booster (series) transformer. That voltage is expressed by

$$\Delta\underline{V} = m_2 k V_{DC} (\cos\psi_2 + \mathrm{j}\cos\psi_2) . \tag{2.15}$$

The controller enforces the required value of $\Delta\underline{V}$ by choosing appropriate values of m_2 and ψ_2. Thanks to the control of both the magnitude and phase of the booster (series) voltage, the voltage $\underline{V}_k$ at the beginning of the transmission line may assume any values within the circle created by the phasor $\underline{V}_i$. This is illustrated on the phasor diagram in Figure 2.38.

Regulation of the magnitude and phase of the booster voltage corresponds to operation of the phase shifting transformer shown in Figure 2.23. The main constraints of the regulation are the allowed voltage ΔV and the allowed current flowing through the BT.

The simplified steady-state equivalent circuit of the UPFC shown in Figure 2.38 contains a series voltage source $\Delta\underline{V}$, reactance of the booster transformer X_{ST} and shunt current source $\underline{I}_{shunt}$ responsible for the reactive power consumption by the shunt part necessary to maintain a constant value of the DC voltage. Obviously the model must also include the limiters described above for both the series and shunt parts.

The UPFC can execute the following control functions:

1. Control of real power flows P by controlling the quadrature component Im ($\Delta\underline{V}$) of the booster voltage in the series part.
2. Control of reactive power flows Q by controlling the direct component Re ($\Delta\underline{V}$) of the booster voltage in the series part.
3. Control of the voltage V_i in the connection node by controlling the reactive current Im ($\underline{I}_{shunt}$) supplied by the network to the shunt part.

The UPFC can also work similarly as the series compensator SSSC (Figure 2.35). In this case, the direct and quadrature components of the booster voltage must be chosen by the regulator in such a way that the booster voltage phasor is perpendicular to the current phasor so that condition (2.10) is satisfied and therefore the reactance of the transmission element is compensated.

As with other FACTS devices, the fast-acting UPFC can also be used for the damping of power swings discussed in Chapter 9 and Chapter 10.

2.6 Protection

No system element is completely reliable and can be damaged by some internal or external fault. If the damaged element is not immediately disconnected, it may suffer further damage and be completely destroyed. A damaged element may also disturb operation of the neighbouring elements so as to threaten the operation of the whole power system and the continuity of energy supply to the consumer. Protective equipment is therefore needed to detect a fault and disconnect the faulty element. Typically, power system protective equipment consists of current and/or voltage transformers, relays, secondary circuits supplying the relays and controlling the circuit-breakers, and auxiliary power supplies for the relays.

Operation of the protection must be fast, reliable and selective. A fast *speed of response* and *high reliability* are vital to limit the damage that could be caused by a fault. In addition the protection must be *selective* so that only the faulty element is switched off. Reliability is achieved by using high-quality equipment and by using two different protection schemes for each element called the *main protection* and the *back-up protection*. The main protection should operate according to different physical principles than its back-up. If back-up protection is placed in the same substation bay as the main protection then it is termed *local back-up*. If the main protection of a neighbouring element is used as the back-up protection of the given element then it is called *remote back-up*.

There are a number of books available which deal in detail with power system protection (Phadke and Thorap, 1988; Wright and Christopoulos, 1993; Ungrad, Winkler and Wisniewski, 1995). This section will contain only a brief overview of some of the main protection schemes and will introduce terms necessary for the remainder of the book.

2.6.1 Protection of Transmission Lines

The main faults on transmission lines are short circuits. Overhead transmission lines are shielded from lightning stroke by ground wires, hung above the phase conductors, and surge diverters connected to the conductors themselves. Nevertheless, lightning is still the most common cause of faults on overhead transmission lines, with single-phase faults contributing 75–90% of all faults. In contrast, multiple phase-to-ground faults constitute 5–15% of faults while multi-phase faults with no ground connection are the rarest at 5–10%. Other rare causes of faults are insulator breakages, swinging of wires caused by strong winds and temporary contact with other objects.

The majority (80–90%) of the faults on overhead lines are of a temporary nature and are caused by flashovers between phase conductors, or between one or more of the phase conductors and earthed metal or the ground caused by, for example, lightning stroke. The remaining 10–20% of faults are either semi-temporary or permanent. Temporary faults can be dealt with by switching off the line until the arc or arcs are extinguished, and then switching it on again after a certain period, termed the *dead time*. The whole procedure is referred to as *auto-reclosing* and significantly improves the continuity of energy supply. Obviously in the case of a permanent fault the re-energized line will be tripped again by its protection. There may be two or three such attempts, but usually only a single-shot reclosure is used in high-voltage transmission networks.

The oldest type of protection is the *differential-current protection* based on Kirchhoff's current law stating that the sum of currents flowing into and out of a circuit is equal to zero. Figure 2.39 shows the basic differential-current protection scheme where the current transformers installed at

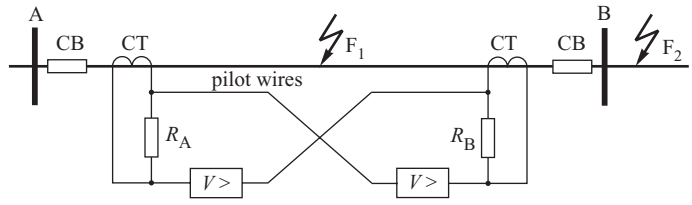

Figure 2.39 Differential-current protection. A, B, substation busbars; CB, circuit-breaker; CT, current transformer; V>, overvoltage relay; F_1, F_2, internal and external faults.

both terminals of a line are connected via resistors and pilot wires so as to oppose each other. Under healthy conditions or external faults (like F_2 in Figure 2.39), no current flows in the interconnecting cables. A fault occurring within the protected zone (fault F_1) creates a potential difference between the resistors and a small circulating current flows through the pilot wires energizing the overvoltage relays and operating the circuit-breakers.

Because of the need to transmit signals continuously with fairly high accuracy between the ends of the protected line, the differential scheme with pilot wires is only used to protect short transmission lines with a maximum length of about 20–30 km. For longer lines the *interlock scheme* is used which employs directional relays sited at each end of the protected zone. These relays initiate the opening of the circuit-breakers at each end of a line if both sets of relays indicate that currents are flowing into the line. The information which must be transmitted between the relays is a logical yes or no, as opposed to the analogue signals used in the differential scheme. To avoid the expense of the pilot cables, the logic signal is usually transmitted over the conductors of the protected line using high-frequency signals and is called the *power line carrier*.

Another, more popular, protection scheme utilizing the power line carrier is the phase comparison scheme in which the phase of the current at the two ends of the protected circuit is compared. Under normal operating conditions, or in case of an external fault, the currents at the opposite ends of the line are almost in phase with each other, whereas they are displaced by large angles when internal faults are present.

The frequency used in the power line carriers is typically in the range 20–200 kHz. Lower frequencies increase the cost of the carrier, while higher frequencies cause too high an attenuation of the signal. The lines must be equipped with *line traps*, which are tuned circuits to block the high-frequency signals so that they do not enter other lines.

The *directional comparison* protection scheme utilizes the travelling waves which accompany the short circuit. Any short circuit produces voltage and current travelling waves which travel in both directions from the point of fault. The fault is detected by comparing the direction of the travelling waves at both ends of the line. An internal fault will cause the waves to travel in opposite directions, while an external fault will result in waves travelling in the same direction through the protected zone.

The development of optical-fibre technology has opened new possibilities for transmitting information over long distances. Optical-fibre links placed inside ground wires of transmission lines are currently used in directional comparison and phase comparison schemes, replacing pilot wires or power line carriers.

The most popular scheme for protecting transmission lines is *distance protection*. Its main advantage is that it does not require pilot wires or power line carriers. An additional advantage is that it may provide back-up protection for neighbouring network elements (lines and transformers). The principle of operation recognizes that the impedance of a high-voltage transmission line is approximately proportional to its length. This means that the apparent impedance measured during a fault by the relay is proportional to the distance between the point of fault and the relay. If this

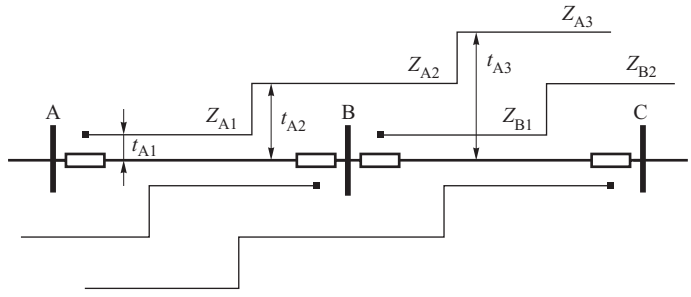

Figure 2.40 Distance protection zones of two neighbouring lines.

impedance is less than the series impedance of the line then it may be concluded that a fault has occurred inside the protected zone and the line should be tripped. Unfortunately, measurement of the apparent impedance has low accuracy due to the errors introduced by the current and voltage transformers, the relay itself and other factors such as the impedance of the fault. Consequently the relay must have a time characteristic with a few zones corresponding to different impedance settings and tripping times, as shown in Figure 2.40. Distance protection of line A–B at busbar A (marked by the small solid rectangle) has three zones, Z_{A1}, Z_{A2} and Z_{A3}, with tripping times t_{A1}, t_{A2} and t_{A3}, respectively. To make sure that a distance relay will not overreach the protected zone, that is unnecessarily trip for faults outside the zone, the first protection zone is usually set between 85 and 90% of the line length. As this first zone, Z_{A1}, cannot protect the entire line, the distance relay is equipped with a second zone, Z_{A2}, which deliberately reaches beyond the remote terminal of the transmission line. The second zone is slowed down in order that, for faults in the next line B–C, the protection of the next line (located at B) will operate before the second zone of the distance relay at A. The second zone of A also partially backs up the distance relay of the neighbouring line B–C. In order to extend this back-up as much as possible into neighbouring lines, it is customary to provide yet another zone, Z_{A3}. The third protection zone is obviously the slowest.

Choosing the maximum reach of the third zone requires great care and analysis of the relay operation under heavy load, especially during an emergency state with depressed voltages. With high line currents and depressed voltages, the apparent impedance measured by the relay may approach the characteristic of the distance relay and even encroach into the third tripping zone. This may cause unnecessary tripping of the transmission line and further stressing of an already weakened system, possibly leading to a blackout. Examples of such blackouts are discussed in Chapter 8.

A distance relay may also cause unnecessary tripping of a transmission line during power swings. To prevent this, the relays must be equipped with power swing blocking relays or power swing blocking functions. This will be further discussed in Section 6.6.

2.6.2 Protection of Transformers

Power transformers are an important link in high-voltage transmission networks and must be protected against both external and internal faults. Internal faults may be due to earth faults on windings, interphase faults, interturn faults and interwinding faults. This classification is important as it also corresponds to the different types of protection used.

The main form of transformer protection is differential-current protection. Its principle of operation is similar to the current differential protection used to protect a transmission line, Figure 2.39. The transformer protection scheme has, however, some special features because the magnitude

and phase of the current are different on the primary and the secondary sides. The transformer protection scheme must also cope with the possible presence of a large *magnetizing inrush current*. Depending on the instant when an unloaded transformer is energized, a magnetising current several times the rated current of the transformer may flow and, because the losses in the transformer are small, it will decay slowly with a time constant of several seconds to its normal small value. Because of the nonlinearity of the magnetizing characteristic, this inrush current has a high second harmonic and this distortion can be used to distinguish it from a normal fault current.

Differential protection, despite its sensitivity, is not able to detect interturn faults. The transformer is protected against these faults by the *Buchholz protection* installed in the pipe between the main tank of the oil-filled transformer and the conservator. Localized heating or arcing associated with interturn or interwinding faults decomposes the oil and produces gases such as hydrogen and carbon monoxide. The gases rise from the transformer and pass up the sloping pipe through the Buchholz relay, filled with oil, towards the conservator. On their way they rise inside the Buchholz relay and become trapped in the top of the casing, so displacing oil. As a result a pivoted float or bucket falls and, depending on the amount of gas released, causes an alarm or trips the relay.

Large transformers are also equipped with two distance protection devices, one on each side of the transformer. The first and third zones of both relays are directed towards the impedance of the transformer and their tripping signals are passed to the trip-coil circuits of both circuit-breakers. This constitutes a local back-up of the transformer's differential protection. The second zone is directed in the opposite direction towards the network. This constitutes the main protection from external faults and the local back-up for busbar protection.

In addition, transformers may also be equipped with earth fault protection (supplied with zero-sequence currents), combined differential and restricted earth fault protection, overload protection in the form of an overcurrent relay (supplied from the current transformers) and a thermal relay reacting to the temperature inside the transformer tank.

2.6.3 Protection of Busbars

Faults on substation busbars are relatively rare compared with those on overhead transmission lines. The most common cause of busbar faults is flashover on the insulators, power apparatus failure and, quite often, human error due, for example, to opening or earthing the isolator when on load. The consequences of a fault on a substation busbar may be far more severe than for a fault on a transmission line. The busbars of less important substations, in which all the outgoing circuits are protected with distance protection, are themselves protected by the second zone of the distance protection at neighbouring stations. This is illustrated in Figure 2.40 where the busbars at substation B are protected by the distance protection at substations A and C. An obvious drawback of this scheme is the long fault clearing time associated with second zone of the distance protection. This cannot be tolerated for more important substations so they are normally equipped with differential-current protection for each of their circuits, or with modern phase comparison protection schemes. In this case the distance protection of outgoing circuits constitutes a remote back-up for the busbar protection.

2.6.4 Protection of Generating Units

As shown in Figure 2.2, a generating unit is a complex system comprising the generator, exciter, prime mover, step-up transformer and often a unit transformer supplying the auxiliary services. As the generating unit may be subject to a variety of faults or disturbances, it is normally protected by a number of protection systems. The most important is the differential protection against faults inside the generator and transformer. This normally consists of three differential protection systems: one for the generator, a second for the unit transformer and a third for the generator with its step-up transformer (or for the generator with both step-up and unit transformers). Large generating

units are protected from external faults by the distance protection directed towards the network, in a similar manner as for transformers. The unit transformer is usually protected from external faults by an overcurrent relay. Similar overcurrent protection is used to protect the stator winding from both overloading and load asymmetry, and the rotor winding from overloading. Additional protection systems are used to protect the generator from loss of excitation, loss of synchronism (pole-slip protection), faults in stator windings (underimpedance protection), earth faults in the rotor windings and from failure of the prime mover (motoring protection).

The generator is also equipped with protection from non-electrical disturbances due to low vacuum, lubrication oil failure, loss of boiler fire, overspeeding, rotor distortion, excessive vibration and difference in expansion between rotating and stationary parts.

2.7 Wide Area Measurement Systems

Wide area measurement systems (WAMS) are measurement systems based on the transmission of analogue and/or digital information using telecommunication systems and allowing synchronization (time stamping) of the measurements using a common time reference.

Measuring devices used by WAMS have their own clocks synchronized with the common time reference using synchronizing devices. This concept is not new and for many years radio signals sent from ground stations have been used. As the reference, UTC (Universal Time Coordinated) has been used as specified by the BIMP (Bureau International des Poids et Mesures) located in France. UTC is specified using time obtained from about 200 atomic clocks located in various places around the globe. A number of ground radio stations have been constructed to transmit the UTC signals. In Europe the DCF77 transmitter is used. It is located in Mainflingen near Frankfurt in Germany. Many supervisory control and data acquisition (SCADA) systems, which are used for monitoring and control of power system operation, utilize the DCF77 signals for synchronization. The accuracy of the time reference obtained using DCF77 is 1–10 ms. Such accuracy is good enough from the point of view of SCADA systems which measure magnitudes of current and voltages and corresponding real and reactive powers. Currently much better accuracy, at least 1μs, is obtained using satellite GPS (Global Positioning System).

2.7.1 WAMS and WAMPAC Based on GPS Signal

The satellite GPS system is the result of many years of research undertaken by US civil and military institutions aiming to develop a very accurate navigation system. The system has been made available for civil users around the world. The system consists of a space segment, a ground segment and users.

The space segment comprises a constellation of 24 satellites located in six orbits, that is with four satellites per orbit. The location of the orbits and the satellites is such that at any time 4–10 satellites can be seen from any point on the Earth. Access to a number of satellites is necessary to determine the location of any receiver using three coordinates (longitude, latitude and altitude) and the reference time. Each satellite transmits to the Earth a coded message about the time of transmission and actual coordinates of the satellite with respect to the Earth. The message also contains a pulse of 1PPS (i.e. 1 pulse per second) informing about the beginning of each second of the universal time. That signal is very important for WAMS as it is used for synchronising WAMS devices.

The ground segment of GPS consists of six radio stations located near the equator. One of those stations, in Colorado Springs in the United States, is the master station while the remaining ones are the monitoring stations. The latter monitor the correctness of operation of the satellites and send information to the main station. The areas of observation of neighbouring monitoring stations overlap, which makes it possible to observe the same satellite from two stations. The main station communicates with all the monitoring stations and with the satellites. The main station sends to the

satellites corrections to their orbits and a correction to the time of satellite clocks. As the reference time, UTC is used and it is transmitted from a space observatory of the US Navy.

In the GPS system, the users are only receivers of satellite messages and do not send any information to the system. Consequently the number of users is not restricted. Calculation of the coordinates of a given receiver and the time is executed in the receiver based on messages received from a few satellites. This means that the receiver is equipped with an algorithm solving an equation in which the message data (the location of a satellite and the reference time) are treated as known data while the receiver coordinates and the reference time are treated as unknown data. The reference time is implicit in the solved equations because the equations are set up in such a way as to eliminate the transmission time of messages from the satellites to the receiver.

The accuracy of the GPS reference time of about 1μs is good enough to measure AC phasors with a frequency of 50 or 60 Hz. For a 50 Hz system, the period time corresponding to a full rotation corresponding to 360° is 20 ms $= 20 \cdot 10^3$ μs. The time error of 1 μs corresponds to the angle error of $360^\circ/20 \cdot 10^3 = 0.018^\circ$, that is 0.005%. Such an error is small enough from the point of view of phasor measurement.

The possibility of measuring voltage and current phasors in a power system has created new control possibilities:

(a) Monitoring of operation of a large power system from the point of view of voltage angles and magnitudes and frequency. This is referred to as *wide area monitoring* (WAM).
(b) Application of special power system protection based on measuring phasors in large parts of a power system. Such protection is referred to as *wide area protection* (WAP).
(c) Application of control systems based on measuring phasors in large parts of a power system. Such control is referred to as *wide area control* (WAC).

WAMS integrated with WAM, WAP and WAC is referred to as *wide area measurement, protection and control* (WAMPAC).

Recent years have seen a dynamic expansion of WAMPAC systems. Measurement techniques and telecommunication techniques have made rapid progress, but the main barrier for the expansion of WAMPAC systems is a lack of WAP and WAC control algorithms based on the use of phasors. There has been a lot of research devoted to that problem but the state of knowledge cannot be regarded as satisfactory.

2.7.2 Phasors

The definition of a phasor is closely connected to the representation of a periodic waveform as a rotating vector. This is illustrated in Figure 2.41. A vector $\vec{V}_\mathrm{m}$ is rotating with angular velocity ω with respect to a stationary reference axis. Its position at any instant of time is given by

$$\vec{V}(t) = V_\mathrm{m} \mathrm{e}^{\mathrm{j}(\omega t + \delta)}, \tag{2.16}$$

where V_m is the amplitude and δ is the phase shift with respect to the reference frame Re. This reference frame together with an orthogonal axis Im constitute the rotating complex plane Re–Im.

Projection of vector $\vec{V}(t)$ onto the horizontal axis is periodically time varying (see Figure 2.41b), and is expressed as $v(t) = V_\mathrm{m} \cos(\omega t + \delta)$. Frequency f of the periodic changes is related to the angular velocity by $\omega = 2\pi f = 2\pi/T$, where T is the period of rotation. The effective value of the sine waveform is given by $V = V_\mathrm{m}/\sqrt{2}$. Equation (2.16) can be transformed in the following way:

$$\vec{V}(t) = V_\mathrm{m} \mathrm{e}^{\mathrm{j}(\omega t + \delta)} = \sqrt{2} \frac{V_\mathrm{m}}{\sqrt{2}} \mathrm{e}^{\mathrm{j}\delta}\, \mathrm{e}^{\mathrm{j}\omega t} = \sqrt{2}\, V \mathrm{e}^{\mathrm{j}\delta}\, \mathrm{e}^{\mathrm{j}\omega t} = \sqrt{2}\, \underline{V}\, \mathrm{e}^{\mathrm{j}\omega t}. \tag{2.17}$$

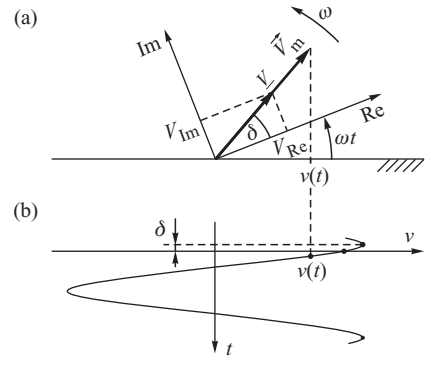

Figure 2.41 Illustration of the definition of phasors: (a) a rotating vector; (b) a corresponding time-domain signal.

Vector $\underline{V} = V\mathrm{e}^{\mathrm{j}\delta}$ is referred to as the *phasor*. Its length (magnitude) is V and it is equal to the effective value of the periodic waveform $v(t)$. Its angle δ is defined by the location of the rotating vector with respect to the axis Re. The phasor components in the complex plane Re–Im can be determined from

$$\underline{V} = V_{\mathrm{Re}} + \mathrm{j}V_{\mathrm{Im}} = V\mathrm{e}^{\mathrm{j}\phi} = V(\cos\phi + \mathrm{j}\sin\phi)\,. \tag{2.18}$$

The phasor contains information about both the effective value and the phase shift with respect to the reference frame. Knowing the components V_{Re}, V_{Im} of the phasor, it is easy to calculate its length V and the phase shift δ.

The above definition assumes that the reference frame Re and the complex plane Re–Im rotate with the same velocity ω as the vector $\vec{V}_{\mathrm{m}}$. Generally those two velocities may be different, that is vector $\vec{V}_{\mathrm{m}}$ may rotate with velocity ω while the reference frame may rotate with velocity $\omega_{\mathrm{ref}} \neq \omega$. In that case the phase shift δ is not constant but changes with a velocity equal to the difference between the two velocities $\mathrm{d}\delta/\mathrm{d}t = \Delta\omega$ where $\Delta\omega = \omega - \omega_{\mathrm{ref}}$. In a special case when ω oscillates around ω_{ref}, the movement of the phasor in the complex plane is referred to as *swinging*.

An electrical network has generally $i = 1,\ 2, \ldots,\ n$ nodes. The phasors of all the nodal voltages can be placed in common complex coordinates Re–Im as shown in Figure 2.42. The voltage at node i can be then expressed as

$$\underline{V}_i = V_i\,\mathrm{e}^{\mathrm{j}\delta_i} = V_i(\cos\delta_i + \mathrm{j}\sin\delta_i)\,, \tag{2.19}$$

where V_i and δ_i are the effective value (magnitude) and the phase angle of the voltage, respectively. Section 3.5 will show that the electrical state of a network is determined by the voltage magnitudes and differences between the voltage angles. This means that the common coordinates can be changed

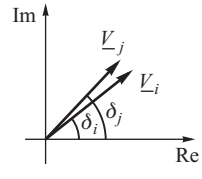

Figure 2.42 Two phasors in the complex plane.

by rotating them by an angle, because adding the same value to all the phase angles does not change the differences $(\delta_i - \delta_j)$. This leads to an important conclusion that, in order to measure voltage phasors, one can assume any, but common, coordinates (any common reference frame).

2.7.3 Phasor Measurement Unit

The freedom to choose any common coordinates for a power system is important for the methodology of phasor measurement using WAMS. The common coordinates for the whole WAMS are obtained by synchronizing the measurements using the 1 PPS signal obtained from the GPS. The GPS signal is received at any point on the Earth, and therefore at any measurement system. Thus assuming the same 1 PPS signal as the time base ensures common coordinates for all the measurements in WAMS.

A measurement system allowing measurement of the phasors of voltages and currents in a power system is referred to as the *phasor measurement unit* (PMU) and is shown schematically in Figure 2.43.

Voltages and currents for which phasors are to be determined are measured, using current and voltage transformers, as three-phase analogue signals and delivered to the PMU. Each analogue signal is filtered using an anti-aliasing filter and sent to an analogue–digital converter (A/C). Here the signal is sampled: that is, converted into digital samples. The sampler impulses are generated by an oscillator operating with the GPS receiver in the phase-locked loop system. Consequent data samples are sent to a microprocessor together with their time stamps. The microprocessor sends to its memory the sequence of N subsequent data samples corresponding to a whole AC period. The samples are then used to calculate the orthogonal components of each phasor using the discrete Fourier transform (DFT):

$$\underline{V} = V_{\mathrm{Re}} + \mathrm{j}\,V_{\mathrm{Im}} = \frac{\sqrt{2}}{N}\sum_{k=1}^{N} v_k \mathrm{e}^{-\mathrm{j}k2\pi/N} = \frac{\sqrt{2}}{N}\sum_{k=1}^{N} u_k \left[\cos\left(k\frac{2\pi}{N}\right) - \mathrm{j}\sin\left(k\frac{2\pi}{N}\right)\right]. \tag{2.20}$$

The advantage of this measurement algorithm is that, apart from calculating the orthogonal components of a phasor, it also filters both components using two orthogonal filters based on sine and cosine functions. Consequently the calculated orthogonal components of the phasor are those of the first (fundamental) harmonic. The higher harmonics and the DC component are washed out.

Each phasor calculated from N samples is time stamped using the time stamp of the first sample. Then the three-phase phasors of voltages and currents are replaced by their positive sequence components:

$$\underline{V}_{1k} = \frac{1}{3}\left(\underline{V}_{\mathrm{L}1k} + \underline{\mathrm{a}}\,\underline{V}_{\mathrm{L}2k} + \underline{\mathrm{a}}^2\,\underline{V}_{\mathrm{L}3k}\right), \tag{2.21}$$

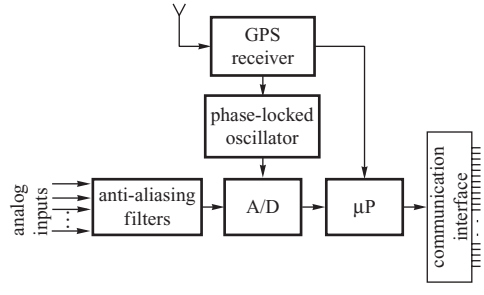

Figure 2.43 Functional diagram of PMU.

where $\underline{V}_{L1k}$, $\underline{V}_{L2k}$, $\underline{V}_{L3k}$ are the three-phase phasors and $\underline{a} = e^{j120^\circ}$ is the phase shift operator used in the theory of symmetrical components.

The positive-sequence phasor of each measured quantity is stored, together with its time stamp, every 40 ms (25 measurements per second) or every 100 ms (10 measurements per second) depending on the needs. For storing, a data format is used appropriate for the telecommunication port of the PMU. Then the telecommunication port transmits data to other WAMS devices.

Some PMU devices may also calculate the frequency of the measured voltage, perform harmonic analysis and send data to SCADA systems.

Increasingly, manufacturers of other microprocessor devices, such as disturbance recorders, equip their devices with software functions executing PMU tasks.

2.7.4 Structures of WAMS and WAMPAC

WAMS, and constructed on their basis WAMPAC, may have different structures depending on the telecommunication media used. With point-to-point connections, the structure may be multi-layer when PMU data are sent to phasor data concentrators (PDCs). One concentrator may service 20–30 PMUs. Data from the concentrators are then sent to computers executing SCADA/EMS functions or WAP/WAC phasor-based functions. An example of a three-layer structure is shown in Figure 2.44.

In each stage of data transmission, delays are incurred. Concentrators in the lowest layer service PMUs. As the delays are smallest at that stage, the concentrators may supply data not only for monitoring (WAM) but also for protection (WAP) and control (WAC).

The middle-layer concentrators combine data from individual areas of a power system. The data may be used for monitoring and for some WAP or WAC functions.

The top, central concentrator services the area concentrators. Since at that stage the delays are longest, the central layer may be used mainly for monitoring and for those SCADA/EMS functions that do not require a high speed of data transmission.

The main advantage of the layered structure is the lack of direct connections between area concentrators. Such connections may make it difficult, or even impossible, to execute those WAP or WAC functions that require data from a number of areas. The only way to get access to data from another area is via the central concentrator, which incurs additional delays. That problem may be solved by adding additional communication between area concentrators. This leads to more complicated communication structures as more links are introduced.

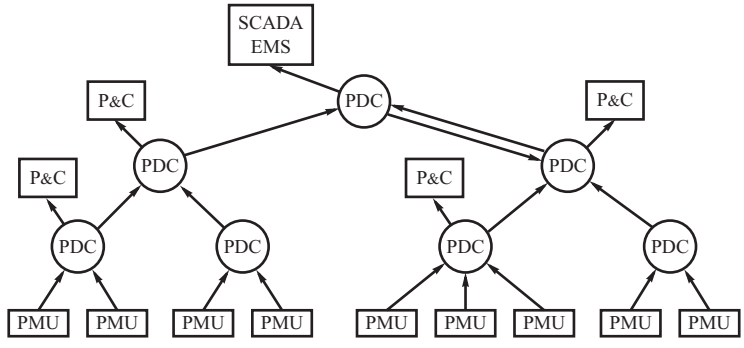

Figure 2.44 An example of a three-layer structure of WAMPAC. PMU, phasor measurement unit; PDC, phasor data concentrator; P&C, protection and control based on phasors.

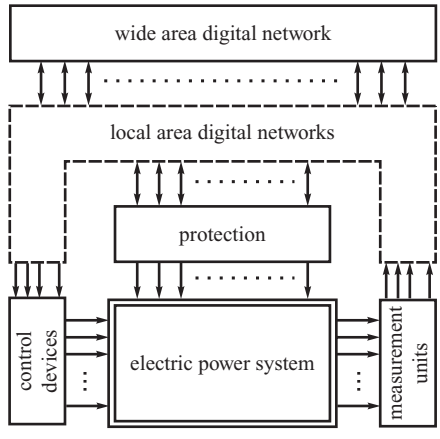

Figure 2.45 WAMPAC structure based on a flexible communication platform.

Computer networks consisting of many local area networks (LANs) and one wide area network (WAN) offer the best possibilities of further WAMPAC development and application. Such a structure is illustrated in Figure 2.45. The digital LAN services all measurement units and protection and control devices in individual substations. The connecting digital WAN creates a flexible communication platform. Individual devices can communicate with each other directly. Such a flexible platform may be used to create special protection and control systems locally, for each area and centrally. The platform could also be used to provide data for local and central SCADA/EMS systems.

3

The Power System in the Steady State

One of the characteristic features of power system operation is the continual need to adjust system operating conditions in order to meet the ever-changing load demand. Although the demand from any particular load can vary quite significantly, the total demand, consisting of a very large number of individual loads, changes rather more slowly and in a predictable manner. This characteristic is important as it means that within any small time period the transmission and subtransmission systems (shown in Figure 2.1) can be regarded as being in the steady state and, as time progresses, considered to move slowly from one steady-state condition to another.

To help describe and quantify the system behaviour under these steady-state conditions this chapter develops steady-state mathematical models of all the main system elements such as transmission lines, transmission cables, transformers, generators and so on. The behaviour of the main types of system loads is also considered so that the way in which the demand may change with both voltage and frequency is understood. Having established such component models, the way they can be linked together to form the full set of network equations is described.

3.1 Transmission Lines

Figure 3.1 shows the single-phase equivalent circuit of a transmission line suitable for analysing its symmetrical three-phase operation. In this circuit the voltages and the currents at the line terminals are the variables while the line parameters are assumed to be uniformly distributed over the line length.

The parameters describing this circuit are:

r	series resistance per unit length per phase (Ω/km);
$x = \omega L$	series reactance per unit length per phase (Ω/km) and L is the series inductance per phase (H/km);
g	shunt conductance per unit length per phase (S/km);
$b = \omega C$	shunt susceptance per unit length per phase (S/km) and C is the shunt capacitance per phase (F/km);
l	line length (km);

Power System Dynamics: Stability and Control, Second Edition Jan Machowski, Janusz W. Bialek and James R. Bumby
© 2008 John Wiley & Sons, Ltd

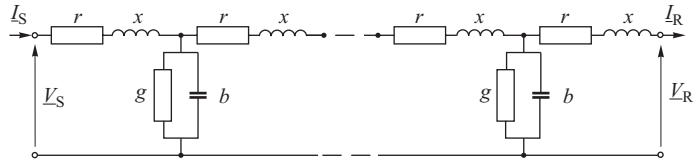

Figure 3.1 Single-phase equivalent circuit of a transmission line with distributed parameters.

where $\omega = 2\pi f$ and f is the frequency. The series impedance and shunt admittance per phase per unit length are defined as $\underline{z} = r + \mathrm{j}x$ and $\underline{y} = g + \mathrm{j}b$. Each of the parameters in the equivalent circuit has a physical meaning and is linked with a particular aspect of the transmission line behaviour. Thus the resistance r represents the Joule (heating) loss that occurs due to current flow and depends on the type, construction and diameter of the conductor used. The series inductance L depends on the partial flux linkages within the conductor cross-section itself and the external flux linkages with the other conductors. The shunt conductance g represents the corona loss and the leakage current on the insulators. This value is not usually constant as the corona loss depends on air humidity while the leakage current depends on dirt and salt contamination on the surface of insulators. In power lines g is small and is usually neglected. The shunt capacitance C is due to the potential difference between the conductors. As the voltages are AC voltages this shunt capacitance is alternately charged and discharged resulting in the flow of the *line charging current*.

3.1.1 Line Equations and the π-Equivalent Circuit

For steady-state analysis the variables of interest are the voltages and currents at the line terminals $\underline{V}_R$, $\underline{I}_R$, $\underline{V}_S$, $\underline{I}_S$ where the subscripts 'R' and 'S' signify the receiving end and sending end of the line, respectively. The voltages and currents are linked by the *long-line equation*:

$$\begin{bmatrix} \underline{V}_S \\ \underline{I}_S \end{bmatrix} = \begin{bmatrix} \cosh \underline{\gamma} l & \underline{Z}_C \sinh \underline{\gamma} l \\ \sinh \underline{\gamma} l / \underline{Z}_C & \cosh \underline{\gamma} l \end{bmatrix} \begin{bmatrix} \underline{V}_R \\ \underline{I}_R \end{bmatrix}, \tag{3.1}$$

where $\underline{Z}_C = \sqrt{\underline{z}/\underline{y}}$ is the characteristic *(or* surge*)* impedance of the line and $\underline{\gamma} = \sqrt{\underline{z}\underline{y}}$ is the *propagation constant*. As both the constants $\underline{\gamma}$ and $\underline{Z}_C$ are complex quantities the propagation constant can be expressed as $\underline{\gamma} = \alpha + \mathrm{j}\beta$ where α is termed the *attenuation constant* and β the *phase constant*. The four elements of the matrix linking the sending-end and the receiving-end voltages and currents are often referred to as the *ABCD* constants where $\underline{A} = \underline{D} = \cosh \underline{\gamma} l$, $\underline{B} = \underline{Z}_C \sinh \underline{\gamma} l$ and $\underline{C} = \sinh \underline{\gamma} l / \underline{Z}_C$. Interested readers are referred to Grainger and Stevenson (1994) or Gross (1986) for the detailed derivation of Equation (3.1).

As power system networks consist of many lines, the use of Equation (3.1) for analysis purposes is very inconvenient and a simpler way is to replace each line by its π-equivalent shown in Figure 3.2. A little circuit analysis shows that the π-equivalent parameters $\underline{Z}_L$ and $\underline{Y}_L$ are given by

$$\underline{Z}_L = \underline{Z} \frac{\sinh \underline{\gamma} l}{\underline{\gamma} l}, \quad \underline{Y}_L = \underline{Y} \frac{\tanh\left(\underline{\gamma} l/2\right)}{\underline{\gamma} l/2}, \tag{3.2}$$

where $\underline{Z} = \underline{z} l$ is the line total series impedance per phase and $\underline{Y} = \underline{y} l$ the total shunt admittance per phase.

It should be emphasized that the π-equivalent parameters $\underline{Z}_L$ and $\underline{Y}_L$ are generally not equal to the total impedance and admittance of the line, that is $\underline{Z}_L \neq \underline{Z} = \underline{z} l$ and $\underline{Y}_L \neq \underline{Y} = \underline{y} l$. However, for

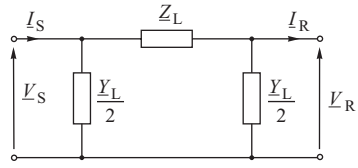

Figure 3.2 The π-equivalent circuit of a transmission line.

a typical power line $\underline{\gamma} l$ is small and the hyperbolic functions can be approximated as $\sinh(\underline{\gamma} l) \approx \underline{\gamma} l$ and $\tanh(\underline{\gamma} l/2) \approx \underline{\gamma} l/2$. Substituting these values into Equation (3.2) gives the *medium-length line* (l between 80 and about 200 km) parameters

$$\underline{Z}_L = \underline{Z}, \quad \underline{Y}_L = \underline{Y}. \tag{3.3}$$

For a *short-length line* ($l < 80$ km) the charging current (and the capacitance C) may be neglected when the parameters are

$$\underline{Z}_L = \underline{Z}, \quad \underline{Y}_L = 0. \tag{3.4}$$

Nowadays, with the wide use of computers, such approximations have limited practical value as the parameters can be easily calculated using Equation (3.2). For manual calculations the most convenient, and practical, formulae to use are those of the medium-length line, Equation (3.3), when the parameters in the nominal π-equivalent circuit represent the total series impedance $\underline{Z}$ and the total shunt admittance $\underline{Y}$.

3.1.2 Performance of the Transmission Line

For a typical high-voltage transmission line g can be neglected while $r \ll x$. An additional insight into line performance may be obtained by considering the *lossless line*, that is by neglecting r altogether. With r and g neglected, the characteristic impedance is purely resistive

$$\underline{Z}_C = Z_C = \sqrt{\underline{z}/\underline{y}} = \sqrt{L/C}, \tag{3.5}$$

and the propagation constant $\underline{\gamma}$ is purely imaginary

$$\underline{\gamma} = \sqrt{\underline{z}\underline{y}} = \mathrm{j}\omega\sqrt{LC}, \tag{3.6}$$

so that $\alpha = 0$ and $\beta = \omega\sqrt{LC}$. With these values of Z_C and γ the hyperbolic functions become $\sinh \underline{\gamma} l = \mathrm{j} \sin \beta l$ and $\cosh \underline{\gamma} l = \cos \beta l$ so that Equation (3.1) simplifies to

$$\begin{aligned} \underline{V}_S &= \underline{V}_R \cos\beta l + \mathrm{j} Z_C \underline{I}_R \sin\beta l \\ \underline{I}_S &= \underline{I}_R \cos\beta l + \mathrm{j}\left(\underline{V}_R / Z_C\right) \sin\beta l, \end{aligned} \tag{3.7}$$

and the voltage and current are seen to vary harmonically along the line length. The *wavelength* of the full cycle can be calculated as $\lambda = 2\pi/\beta$. For 50 Hz lines the wavelength is nearly 6000 km, while for 60 Hz lines it is $60/50 = 1.2$ times shorter and is equal to about 5000 km.

Power engineers often find it convenient to compare the actual loading on the line with the *natural load*, or *surge impedance load* (SIL), where SIL is defined as the power delivered at rated voltage to

Table 3.1 Examples of overhead lines parameters (NGC, 1994; Kundur, 1994)

f_n (Hz)	V_n (kV)	r (Ω/km)	$x = \omega L$ (Ω/km)	$b = \omega C$ (μS/km)	β (rad/km)	Z_C (Ω)	P_{SIL} (MW)
50 (UK)	275	0.067	0.304	4.14	0.00112	271	279
	400	0.018	0.265	5.36	0.00119	222	720
	230	0.05	0.488	3.371	0.00128	380	140
60 (USA)	345	0.037	0.367	4.518	0.00129	285	420
	500	0.028	0.325	5.2	0.0013	250	1000
	765	0.012	0.329	4.978	0.00128	257	2280
	1100	0.005	0.292	5.544	0.00127	230	5260

a load impedance equal to Z_C. That is,

$$P_{SIL} = \frac{V_n^2}{Z_C}. \tag{3.8}$$

Substituting $\underline{I}_R = \underline{V}_R / Z_C$ into the first, and $\underline{V}_R = Z_C \underline{I}_R$ into the second, of the equations in (3.7) shows that when a lossless transmission line is loaded at SIL

$$\underline{V}_S = \underline{V}_R e^{j\beta l} \quad \text{and} \quad \underline{I}_S = \underline{I}_R e^{j\beta l}, \tag{3.9}$$

indicating that:

- the voltage and current profiles are flat, $V_S = V_R$ and $I_S = I_R$;
- the voltage and current at both ends (and at any point along the line) are in phase so that the reactive power loss in the line is zero (in other words, the reactive power generated by C is compensated by the reactive power absorbed by L).

As the reactive power loss of the line is zero, the natural impedance loading is an optimum condition with respect to voltage and reactive power control.

Table 3.1 shows typical values of SIL and other characteristic parameters of overhead lines.

Unfortunately the loading on the power line is rarely equal to the natural load. At night the loading may be a small fraction of SIL, whereas during peak load periods the loading may be significantly greater than SIL. To examine the effect this has on the line voltage Figure 3.3 shows three plots of the sending-end voltage V_S required to deliver power P_R at rated voltage and unity power factor at the receiving end, each plotted as a function of line length. These calculations have been done using the full line model described by Equation (3.1) (with resistance included) assuming the parameters of the 400 kV line given in Table 3.1. When the delivered power P_R is less than SIL then V_S is smaller than V_R, while $P_R > P_{SIL}$ requires V_S to be larger than V_R. Delivering $P_R = P_{SIL}$ does not actually result in the voltage along the line being constant but it is seen to increase slightly towards the sending end. This is due to including the line resistance in the calculation. Note the harmonic variation of the voltage with length.

3.1.2.1 Real Power Transmission

In Chapter 1, approximate Equations (1.8) and (1.9) were derived for real and reactive power transmission in a line represented by just its series reactance $X = xl$. Now the equation for real and reactive power transmission will be derived using the full π-equivalent model of the line.

Let $\underline{V}_R$ be the reference phasor and assume that $\underline{V}_S$ leads $\underline{V}_R$ by angle δ_{SR}, that is $\underline{V}_R = V_R$ and $\underline{V}_S = V_S e^{j\delta_{SR}}$. The angle δ_{SR} is referred to as the *load angle* or *transmission angle*. Assuming a lossless

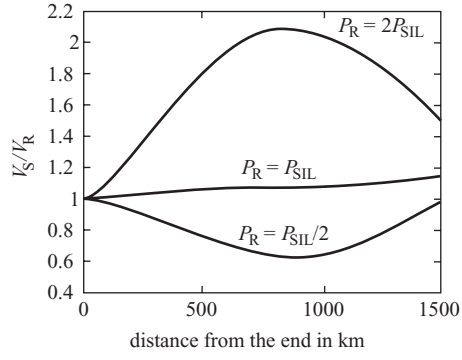

Figure 3.3 Sending-end voltage required to supply a given real power load at rated voltage and at unity power.

line, the receiving-end current can be calculated from Equation (3.7) as

$$\underline{I}_R = \frac{\underline{V}_S - \underline{V}_R \cos \beta l}{\mathrm{j} Z_C \sin \beta l} = \frac{V_S}{Z_C \sin \beta l} \mathrm{e}^{\mathrm{j}(\delta_{SR} - \pi/2)} - \frac{V_R \cos \beta l}{Z_C \sin \beta l} \mathrm{e}^{-\mathrm{j}\pi/2}, \tag{3.10}$$

allowing the complex apparent power at the receiving end to be calculated as

$$\underline{S}_R = \underline{V}_R \underline{I}_R^* = \frac{V_R V_S}{Z_C \sin \beta l} \mathrm{e}^{\mathrm{j}(\pi/2 - \delta_{SR})} - \frac{V_R^2 \cos \beta l}{Z_C \sin \beta l} \mathrm{e}^{\mathrm{j}\pi/2}. \tag{3.11}$$

The real power at the receiving end P_R can be now obtained as

$$P_R = \mathrm{Re}[\underline{S}] = \frac{V_S V_R}{Z_C \sin \beta l} \sin \delta_{SR}, \tag{3.12}$$

showing that for sending-end and receiving-end voltages of specified magnitude, *an increase in the receiving-end power P_R leads to an increase in the load angle δ_{SR}* while the maximum power transfer occurs when $\delta_{SR} = \pi/2$ and is equal to

$$P_{R,\max} = \frac{V_S V_R}{Z_C \sin \beta l} \approx \frac{P_{SIL}}{\sin \beta l}. \tag{3.13}$$

Table 3.1 shows that βl is small for medium-length lines (l less than about 200 km). Thus, it can be assumed that the following simplifications hold:

$$\sin \beta l \cong \beta l, \quad \cos \beta l \approx 1, \quad Z_C \sin \beta l \cong \sqrt{\frac{L}{C}} \omega \sqrt{LC}\, l = \omega L l = X, \tag{3.14}$$

where X is the total inductive reactance of the line. In this case Equation (3.12) simplifies to

$$P_R \cong \frac{V_S V_R}{X} \sin \delta_{SR}, \tag{3.15}$$

showing that the power transfer limit is approximately inversely proportional to the line series inductance and the length. Any attempt to increase power transfer above $P_{R,\max}$ will result in instability and is connected with *steady-state stability* discussed in detail in Chapter 5. Note that Equation (3.15) corresponds to Equation (1.8) derived for a simplified line model.

It is worth noting that a transmission line constitutes only part of the transmission link that connects a generator with the system or connects two parts of a system together. This means that it is the equivalent voltages of the generator and the system which should be considered to be constant and used in Equation (3.12), not the terminal voltages of the line itself. Obviously the equivalent impedance of the generator and the system will then have to be added to the line impedance. As a result δ_{SR} is smaller than the angle between the equivalent voltages and, in practice, the power transfer limit occurs at $\delta_{SR} < \pi/2$. In addition, when transient stability effects, discussed in Chapter 6, are taken into account the practical limit on δ_{SR} is significantly less than $\pi/2$.

Although Equation (3.13) suggests that the maximum line loading is due to the power transfer limit set by the load angle δ_{SR}, this is not always the case and other effects such as the thermal rating of the line and the maximum allowable voltage drop between the ends of the line must also be considered. For short lines, less than about 100 km, the maximum line loading is usually limited by the thermal rating rather than the maximum power transfer limit. On the other hand, for lines longer than about 300 km, the maximum line loading is determined by the power transfer limit which may be substantially below the limit set by thermal considerations. Typically utilities will give the maximum power loading of a line as a fraction (or multiple) of P_{SIL}.

3.1.2.2 Reactive Power Considerations

If for this discussion the sending-end voltage is assumed constant, the question then arises as to what happens to the receiving-end voltage if (i) the reactive power Q_R at the receiving end changes and (ii) the real power P_R at the receiving end changes.

Changes in Q_R will be considered first. The reactive power at the receiving end may be found from the imaginary part of Equation (3.11) as

$$Q_R = \mathrm{Im}\left[\underline{V}_R \underline{I}_R^*\right] = \frac{V_S V_R}{Z_C \sin \beta l} \cos \delta_{SR} - \frac{V_R^2 \cos \beta l}{Z_C \sin \beta l} = \frac{V_R}{Z_C \sin \beta l} \left(V_S \cos \delta_{SR} - V_R \cos \beta l\right). \quad (3.16)$$

The simplifications of Equation (3.14) allow Equation (3.16) to be approximated as

$$Q_R \cong \frac{V_R}{X} \left(V_S \cos \delta_{SR} - V_R\right). \quad (3.17)$$

This equation corresponds to Equation (1.8) derived for a simplified line model. Normally, for the stability reasons considered earlier, the angle δ_{SR} is kept small so that $\cos \delta_{SR} \approx 1$. Strictly speaking, this assumption corresponds to considering the reactive power transfer only so that $P_R = 0$ and, according to Equation (3.12), $\delta_{SR} = 0$. This simplification gives

$$Q_R \approx \frac{V_R(V_S - V_R)}{X}, \quad (3.18)$$

and shows very clearly that the reactive power, Q_R, is strongly dependent on the magnitude of the voltage at both the sending end and the receiving end of the line and that it flows from the higher voltage to the lower voltage. Assuming that V_S = constant and plotting the variation of Q_R against the receiving-end voltage V_R produces the parabolic relationship shown in Figure 3.4a with a maximum at $V_R = V_S/2$. As system voltages must be kept close to V_n, the operating point is always to the right of this peak with the condition $V_R > V_S/2$ always being satisfied. Thus, an *increase in* Q_R *leads to a decrease in* V_R while *a decrease in* Q_R *leads to an increase in* V_R. This observation has important repercussions regarding the introduction of reactive power compensation.

The sending-end reactive power Q_S can be calculated using a similar derivation as in Equation (3.16) to give

$$Q_S = \frac{V_S}{Z_C \sin \beta l} \left(V_S \cos \beta l - V_R \cos \delta_{SR}\right), \quad (3.19)$$

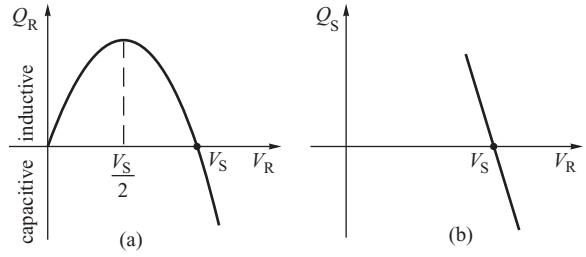

Figure 3.4 The approximate effect on receiving-end voltage of: (a) changes in Q_R and (b) changes in Q_S, when the influence of the real power flow is neglected.

which, assuming that βl is small, gives

$$Q_S \cong \frac{V_S}{X}(V_S - V_R \cos \delta_{SR}). \tag{3.20}$$

Assuming δ_{SR} is also small gives

$$Q_S \approx \frac{V_S}{X}(V_S - V_R). \tag{3.21}$$

Again the strong dependence of reactive power with voltage magnitude is apparent and, as V_S is assumed constant, the approximate variation of Q_S with V_R is linear as shown in Figure 3.4b.

Now consider how the inclusion of the real power transfer ($P_R \neq 0$ and hence $\delta_{SR} \neq 0$) modifies the above considerations. To investigate this, consider the reactive power loss in the line itself due to flow of P_R. Generally the reactive line loss can be positive or negative so that the line can be a net source or sink of reactive power. The reactive power is generated in the line capacitance and depends on the voltage which is normally kept close to the rated value. This relatively constant reactive power generation is offset by the consumption in the line inductance. This consumption varies as the square function of the line current ($Q = I^2 X$) and strongly depends on the actual loading of the line. To quantify this effect the reactive power loss $\Delta Q = Q_S - Q_R$ can be calculated from Equations (3.16) and (3.19) as

$$\Delta Q = Q_S - Q_R = \frac{V_S^2 \cos \beta l - 2 V_S V_R \cos \delta_{SR} + V_R^2 \cos \beta l}{Z_C \sin \beta l}. \tag{3.22}$$

Assuming $V_S \approx V_R \approx V_n$ and eliminating $\cos \delta_{SR}$ using Equation (3.12) gives

$$\Delta Q(P_R) \approx \frac{2 P_{SIL}}{\sin \beta l}\left[\cos \beta l - \sqrt{1 - \left(\frac{P_R \sin \beta l}{P_{SIL}}\right)^2}\right]. \tag{3.23}$$

The characteristics produced by Equation (3.23) are shown in Figure 3.5 for transmission lines that operate at different voltage levels. The reactive power loss is zero only when $P_R = P_{SIL}$. If $P_R < P_{SIL}$ then the line is a net source of reactive power and if $P_R > P_{SIL}$ the situation is reversed and the line is a net sink of reactive power.

The consequence of Figures 3.4 and 3.5 is profound. According to Figure 3.5, as the real power increases, the reactive power loss in the line also increases. This loss must be supplied from the sending end giving an increase in Q_S. Figure 3.4b then shows that for this to occur with V_S constant then V_R must reduce. If the resulting reduction in V_R is unacceptable then, according to Figure 3.4a, this can be compensated by reducing Q_R in some way, perhaps by the introduction of some form of reactive power compensation, see Section 2.4.3.

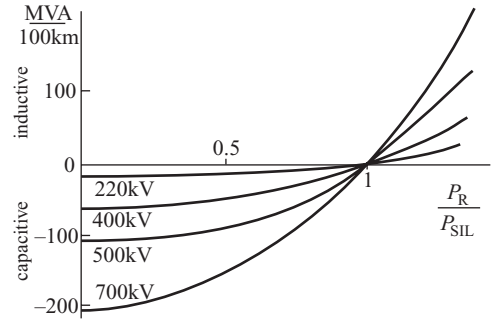

Figure 3.5 Examples of reactive power absorbed by a lossless line as a function of its real load for various voltage ratings.

3.1.3 Underground Cables

From a mathematical point of view an underground cable can be modelled exactly the same way as an overhead transmission line. The only difference is in the values of the characteristic parameters. Because there are many methods of cable construction the parameters of these different cables can also be quite different. In particular the shunt capacitance of the cable depends strongly on whether the three-phase conductors are screened or constitute separate single-phase cables. Typically the per-unit-length series reactance of a cable is about half that of a similarly rated overhead line. On the other hand, the per-unit-length charging current is about 30 times more. This means that even for a short cable run of several tens of kilometres the charging current in the cable constitutes a substantial portion of its thermally admissible maximum current and severely limits its transmission capacity. In the extreme case of a critically long cable the charging current would be equal to the maximum current and there would be no capacity left for any power transmission. The charging current barrier is the main obstacle for practical application of AC cables in power transmission networks.

3.2 Transformers

The main types of transformers were discussed in Section 2.4.2. In this section the equivalent circuit of the transformer will be derived together with a method for dealing with off-nominal transformation ratio.

3.2.1 Equivalent Circuit

The equivalent circuit of a transformer is shown in Figure 3.6a. The main element of the circuit is the *ideal transformer* with transformation ratio $\vartheta = N_1/N_2$, where N_1 and N_2 are respectively the number of turns on the primary and secondary winding. The resistances R_1 and R_2 account for the I^2R loss in the primary and secondary winding while the reactances X_1 and X_2 account for the *leakage flux*, that is the flux component that does not link the two windings but only the primary or the secondary winding. The sinusoidal changes in the supply voltage cause cyclic remagnetization of the transformer core as determined by the hysteresis curve of the core steel. This results in the flow of a *magnetization current* I_μ even at no load. I_μ is in phase with the flux and is therefore delayed with respect to the induced emf E_1 by $\pi/2$. This current is modelled by the shunt susceptance B_μ. The cyclic changes of the core flux also dissipate a certain amount of energy in the form of heat in the transformer core. This component of the core loss is referred to as the *hysteresis loss*. As the core

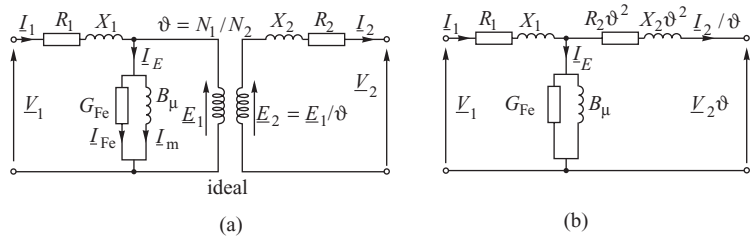

Figure 3.6 Single-phase, two-winding transformer: (a) equivalent circuit; (b) equivalent circuit with secondary referred to the primary.

itself is an electrical conductor, the flux changes induce emfs which result in the flow of circulating *eddy currents*. These eddy currents produce a thermal energy loss called the *eddy-current loss*. The sum of the eddy-current loss and the hysteresis loss is the *core loss* P_{Fe}. This energy loss in the core is provided for by an additional current I_{Fe} flowing in the primary but this time in phase with the induced emf. This is modelled by inserting a shunt conductance G_{Fe} in the equivalent circuit of Figure 3.6a. At no load the primary-side current is equal to the phasor sum of the magnetization current and the core loss current and is referred to as the *excitation current* I_E. When the transformer is loaded, the excitation current is superimposed on the load current.

The transformation ratio ϑ can be eliminated from the diagram if all the quantities in the equivalent circuit are referred to either the primary or secondary side of the transformer. For example, Figure 3.6b shows the case when all voltages, currents and impedances of the circuit of Figure 3.6a are referred to the primary. To produce this model of the transformer, the secondary voltage is multiplied by ϑ while the secondary current is divided by ϑ. Consequently the secondary impedance must be multiplied by ϑ^2.

The equivalent circuit shown is of the T type but it is often more convenient in network analysis to deal with π-type circuits. If the shunt element in the transformer equivalent circuit cannot be neglected then the circuit of Figure 3.6b can be transformed into the π form using the standard star–delta transformation. However, the π circuit will not be symmetrical if the series impedances of the primary and the secondary branches in Figure 3.6b are not equal. To avoid this, the following approximations are usually made:

- the secondary series impedance referred to the primary ($\underline{Z}_2 = R_2\vartheta^2 + \mathrm{j}X_2\vartheta^2$) is equal to the primary series impedance ($\underline{Z}_1 = R_1 + \mathrm{j}X_1$);
- the shunt impedance $1/(G_{Fe} + \mathrm{j}B_\mu)$ is much greater than the total series impedance $\underline{Z}_T = \underline{Z}_1 + \underline{Z}_2$.

With these assumptions the parameters of the π-equivalent circuit, shown in Figure 3.7, are given by

$$\underline{Z}_T = \underline{Z}_1 + \underline{Z}_2 = R + \mathrm{j}X, \quad Y_E = G_{FE} + \mathrm{j}B_\mu. \tag{3.24}$$

The value of the parameters in the transformer equivalent circuit can be determined from the no-load test and the short-circuit test. In both of these tests the supply voltage, current and real power are measured. Table 3.2 shows some examples of test data.

On no load the secondary winding of the transformer is open-circuited and the primary supplied with rated voltage $V_1 = V_n$. In this condition the series winding impedance is small compared with the shunt admittance and can be neglected so that the measured current and power correspond entirely to the shunt branch and relate to the excitation current I_E and iron loss P_{Fe}. Parameters of

Table 3.2 Typical values of transformer parameters in pu on unit ratings

S_n (MVA)	V_{SHC} (pu)	P_{Cu} (pu)	I_E, (pu)	P_{Fe} (pu)
150	0.11	0.0031	0.003	0.001
240	0.15	0.0030	0.0025	0.0006
426	0.145	0.0029	0.002	0.0006
630	0.143	0.0028	0.004	0.0007

the shunt branch can then be computed, per unit to the unit rating, from

$$G_{Fe} = P_{Fe(pu)}, \quad Y_E = I_{E(pu)}, \quad B_\mu = \sqrt{Y_E^2 - G_{Fe}^2}, \tag{3.25}$$

where $P_{Fe(pu)}$ and $I_{E(pu)}$ are also expressed in pu.

During the short-circuit test the secondary winding is short-circuited. The primary winding is supplied with a voltage that is of sufficient magnitude to circulate a current in the short-circuited secondary that is equal to the rated load current ($I_2 = I_n$). This primary voltage is usually referred to as the short-circuit voltage V_{SHC} and is much smaller than the rated voltage $V_{SHC} \ll V_n$. Small primary voltage means that the excitation current I_E is much smaller than $I_2 = I_n$ and can be neglected. Hence, the parameters of the series branch, per unit to the unit rating, can be found from

$$Z_T = V_{SHC(pu)}, \quad R_T = P_{Cu(pu)}, \quad X_T = \sqrt{Z_T^2 - R_T^2}, \tag{3.26}$$

where $V_{SHC(pu)}$ and $P_{Cu(pu)}$ are given in pu.

The equivalent circuit for a multi-winding transformer is formed in a similar way. For example, the equivalent circuit of a three-winding transformer consists of three winding impedances connected in star with the shunt admittances connected to the star point.

3.2.2 Off-Nominal Transformation Ratio

A power system usually operates at a number of voltage levels. The equivalent circuit shown in Figure 3.7 is not very convenient as the secondary voltage must be referred to the primary, resulting in the equivalent circuit including the transformer turns ratio. If the parameters of the equivalent circuit are expressed in pu then, as explained in Section A.6, the transformation ratio ϑ must be related to the nominal network voltages on both sides of the transformer. If the transformer rated voltages are equal to the nominal network voltages then the pu nominal transformation ratio is equal to unity, $\vartheta = 1$, and may be neglected in the transformer equivalent circuit shown in Figure 3.6a. However, the pu transformation ratio may not be unity for two reasons: (i) the rated transformer voltages are slightly different to the nominal network voltages and (ii) the tap changer adjusts the turns ratio away from the nominal setting thereby changing the transformation ratio.

A convenient way to account for the off-nominal turns ratio is to replace the actual turns ratio by some fictitious reactive shunt elements in such a way that these elements change the voltage up

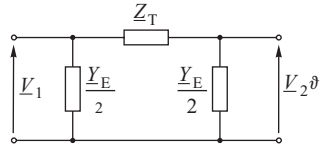

Figure 3.7 The approximate, symmetrical, equivalent π-circuit of a two-winding transformer.

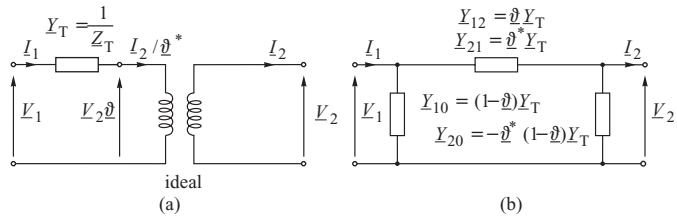

Figure 3.8 Equivalent circuit of a two-winding transformer: (a) using the ideal transformer; (b) using fictitious shunt elements.

or down, as required. As an example consider the transformer from Figure 3.6a with the shunt branch neglected and the secondary series impedance referred to the primary, as shown in Figure 3.8a. The series impedance $\underline{Z}_T$ has been replaced by its reciprocal $\underline{Y}_T$ in order to use nodal analysis. The transformer turns ratio will be taken as a complex number since this allows the general case of the phase shifting transformer to be considered.

For the ideal part of the transformer equivalent circuit shown in Figure 3.8a the apparent power on both sides is the same and the current in the primary is equal to the secondary current divided by the conjugate of the turns ratio, that is $\underline{I}_2/\underline{\vartheta}^*$. The two-port network corresponding to the branch with admittance $\underline{Y}_T$ can be described by the following nodal equation:

$$\begin{bmatrix} \underline{I}_1 \\ -\underline{I}_2/\underline{\vartheta}^* \end{bmatrix} = \begin{bmatrix} \underline{Y}_T & -\underline{Y}_T \\ -\underline{Y}_T & \underline{Y}_T \end{bmatrix} \begin{bmatrix} \underline{V}_1 \\ \underline{\vartheta}\,\underline{V}_2 \end{bmatrix}. \tag{3.27}$$

Eliminating the turns ratio $\underline{\vartheta}$ from the voltage and current vectors gives

$$\begin{bmatrix} \underline{I}_1 \\ -\underline{I}_2 \end{bmatrix} = \begin{bmatrix} \underline{Y}_T & -\underline{\vartheta}\,\underline{Y}_T \\ -\underline{\vartheta}^*\underline{Y}_T & \underline{\vartheta}^*\underline{\vartheta}\,\underline{Y}_T \end{bmatrix} \begin{bmatrix} \underline{V}_1 \\ \underline{V}_2 \end{bmatrix}. \tag{3.28}$$

This equation can be interpreted as a nodal voltage equation $\underline{I} = \underline{Y}\underline{V}$ describing a π-equivalent network. The admittance of the series branch of this network is equal to the off-diagonal element (with the sign inverted) in the nodal admittance matrix, that is

$$\underline{Y}_{12} = \underline{\vartheta}\underline{Y}_T, \quad \underline{Y}_{21} = \underline{\vartheta}^*\underline{Y}_T, \tag{3.29}$$

while the admittances of the shunt branches are equal to the sum of elements in corresponding rows of the nodal admittance matrix, that is

$$\underline{Y}_{10} = (1 - \underline{\vartheta})\underline{Y}_T, \quad \underline{Y}_{20} = \underline{\vartheta}^*(1 - \underline{\vartheta})\underline{Y}_T. \tag{3.30}$$

The equivalent network corresponding to this nodal admittance matrix is shown in Figure 3.8b. It may not be symmetric because generally $\underline{\vartheta} \neq 1$. In the case of a phase shifting transformer, the transformer turns ratio $\underline{\vartheta}$ is a complex number and the series branch of the equivalent network is *anisotropic*, that is as $\underline{Y}_{12} \neq \underline{Y}_{21}$ it has a different impedance value depending on which side the transformer is viewed from. The transformer ratio in the circuit diagram of Figure 3.8b is modelled by the shunt elements. Flow of current in these elements causes a change in the voltages in the series branch that corresponds to the voltage transformation in a real transformer.

If it is necessary to include the shunt branch corresponding to the exciting current then the equivalent circuit must be modified slightly by the addition of two shunt admittances to the circuit (as in Figure 3.7): shunt admittance $\underline{Y}_E/2$ to the left hand side of the circuit and shunt admittance $\vartheta^2\underline{Y}_E/2$ to the right hand side.

3.3 Synchronous Generators

Chapter 2 described how a synchronous generator consists of a stator, on which the three-phase armature winding is normally wound, and a rotor, on which the DC field winding is wound. The rotor damper windings do not affect steady-state operation of the generator and will not be considered in this chapter. The rotor is on the same shaft as the prime mover and may have salient or non-salient magnetic poles.

The steady-state performance of a synchronous machine with a non-salient round rotor will be analysed first before generalizing the analysis to include the effects of rotor saliency. Of particular importance in this analysis is the way the rotor magnetic field interacts with the stator magnetic field to produce electromagnetic torque. An understanding of this interaction is more important than the detailed equations themselves. Having established the mechanisms by which torque and emf are created, the role of the generator in the power system as a source of both active and reactive power will be analysed.

3.3.1 Round-Rotor Machines

The schematic diagram of a two-pole generator on no load is shown in Figure 3.9. For simplicity, only the centre conductor of each of the distributed windings is shown. The beginning and end of the field winding are denoted by f_1 and f_2, while the beginning and end of each of the phase windings are denoted by a_1 and a_2 (phase A), b_1 and b_2 (phase B) and c_1 and c_2 (phase C). The stator has three axes A, B and C, each corresponding to one of the phase windings. The rotor has two axes: the direct axis (d-axis), which is the main magnetic axis of the field winding, and the quadrature axis (q-axis), $\pi/2$ electrical radians behind the d-axis. The dashed lines show the path taken by the rotating field (or excitation) flux, Φ_f, produced by the field winding, and the field leakage flux, Φ_{fl}. $\vec{F}_f$ shows the direction (or the peak value) of the *magnetomotive force* (mmf) wave produced by the field current. The angle $\gamma = \omega_m t$, where ω_m is the rotor angular velocity, defines the instantaneous position of the rotor d-axis with respect to the stationary reference assumed here to be along the A-axis.

For a two-pole machine one complete mechanical revolution corresponds to one electrical cycle and one electrical radian is equal to one mechanical radian. However, if the generator has p poles then one mechanical revolution corresponds to $p/2$ electrical cycles. In this general case one

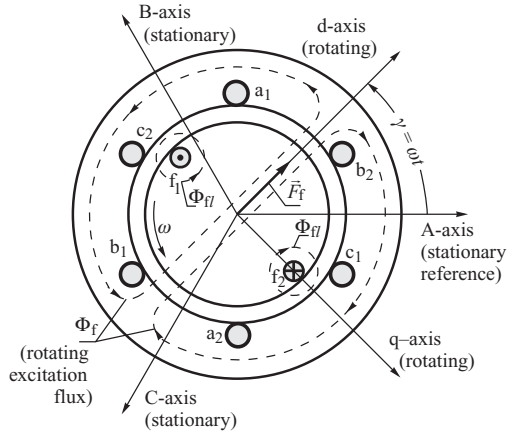

Figure 3.9 Symbolic representation of the generator and its fluxes at no load.

mechanical radian is equal to $p/2$ electrical radians and

$$\gamma_e = \frac{p}{2}\gamma_m, \tag{3.31}$$

where γ_m is the angle γ expressed in mechanical radians (or degrees) and γ_e is the same angle expressed in electrical radians (or degrees). Similarly the rotor speed ω_e expressed in electrical radians per second can be related to the rotor speed in mechanical radians per second ω_m by

$$\omega_e = 2\pi f = \frac{p}{2}\omega_m, \tag{3.32}$$

where f is the system nominal frequency (50 Hz in Europe, 60 Hz in the United States). Often the rotor speed is expressed in revolutions per minute (rpm) when the relation between the rotor speed n and the system frequency is $n = 120f/p$.

For simplicity the generator equations will be developed by reference to the two-pole machine shown in Figure 3.9 when both the speed and the angle are the same in electrical and mechanical units and the subscripts 'e' and 'm' can be dropped. The generator will be analysed using only the fundamental component of the stator and rotor spatial mmf waves. Although the equations will be developed for a two-pole generator, they are equally applicable to a p-pole machine when all angles and speeds are expressed in electrical units. All the equations are valid whether expressed in SI or per-unit notation. If SI units are used it must be remembered that any power expression refers to the power per phase. In per-unit notation they can be interpreted as generator power (see Appendix A.1).

3.3.1.1 The Generator on No Load

To begin the analysis assume that the generator is on no load, that is it is not generating any power and the current in the armature is zero. The DC field current i_f produces an mmf wave which is approximately sinusoidally distributed around the circumference of the stator. The peak value of the mmf

$$F_f = N_f i_f \tag{3.33}$$

lies along the d-axis and is shown in Figure 3.9 by the vector $\vec{F}_f$. In this equation N_f is the effective number of field winding turns per pole and is smaller than the actual number of turns N_F in order to account for the winding geometry and the actual trapezoidal mmf distribution of the field winding. It can be shown (McPherson and Laramore, 1990) that $N_f = (1/p)(4/\pi)\, N_F k_{wF}$ where the winding geometry is accounted for by the winding factor k_{wF} and the mmf distribution by the factor $4/\pi$.

The field winding mmf drives the excitation (or field) flux Φ_f around the magnetic circuit. The flux per pole is

$$\Phi_f = \frac{F_f}{\Re} = \frac{N_f i_f}{\Re}, \tag{3.34}$$

where $\Re$ is the *reluctance* of the path per pole. As the reluctance of the path in iron is negligibly small compared with that in air, $\Re$ is approximately directly proportional to the width of the air gap.

The flux density produced by the field mmf is sinusoidally distributed around the circumference of the stator and, for a round-rotor machine, its peak coincides with the peak of the mmf wave. As the rotor rotates at synchronous speed, the excitation flux rotates with it and produces a time-varying flux linkage with each phase of the armature winding. Each of the phase flux linkages Ψ_{fA}, Ψ_{fB} and Ψ_{fC} reaches a maximum when the d-axis of the rotor aligns with the magnetic axis of the

respective phase winding. Taking phase A as the reference gives

$$\begin{aligned}\Psi_{\mathrm{fA}}(t) &= \Psi_{\mathrm{fa}}\cos\omega t = N_\phi\Phi_{\mathrm{f}}\cos\omega t = N_\phi\frac{N_{\mathrm{f}}i_{\mathrm{f}}}{\Re}\cos\omega t = M_{\mathrm{f}}i_{\mathrm{f}}\cos\omega t\\ \Psi_{\mathrm{fB}}(t) &= M_{\mathrm{f}}i_{\mathrm{f}}\cos\left(\omega t-\frac{2\pi}{3}\right), \qquad \Psi_{\mathrm{fC}}(t) = M_{\mathrm{f}}i_{\mathrm{f}}\cos\left(\omega t-\frac{4\pi}{3}\right).\end{aligned} \tag{3.35}$$

In these equations $\Psi_{\mathrm{fa}} = N_\phi\Phi_{\mathrm{f}}$ is the amplitude of the excitation flux linkage of an armature phase winding, $M_{\mathrm{f}} = N_\phi N_{\mathrm{f}}/\Re$ is the *mutual inductance* between the field and the armature winding, and $N_\phi = k_{\mathrm{w}}N$ where N is the number of turns in series in each phase winding and k_{w} is the armature winding factor.

The time-varying flux linkages induce an *excitation emf* (also called the *internal voltage*) in each of the phase windings. Faraday's law gives

$$\begin{aligned}e_{\mathrm{fA}} &= -\frac{\mathrm{d}\Psi_{\mathrm{fA}}(t)}{\mathrm{d}t} = \omega M_{\mathrm{f}}i_{\mathrm{f}}\sin\omega t, \qquad e_{\mathrm{fB}} = -\frac{\mathrm{d}\Psi_{\mathrm{fB}}(t)}{\mathrm{d}t} = \omega M_{\mathrm{f}}i_{\mathrm{f}}\sin\left(\omega t-\frac{2\pi}{3}\right)\\ e_{\mathrm{fC}} &= -\frac{\mathrm{d}\Psi_{\mathrm{fC}}(t)}{\mathrm{d}t} = \omega M_{\mathrm{f}}i_{\mathrm{f}}\sin\left(\omega t-\frac{4\pi}{3}\right).\end{aligned} \tag{3.36}$$

In the absence of any armature current these emfs appear at the generator terminals as the *no-load terminal voltage*. Figure 3.10a shows the time variation of the phase flux linkages and the reference emf e_{fA} as a function of $\gamma = \omega t$ while the phasor representation of the flux linkages $\underline{\Psi}_{\mathrm{fA}}$, $\underline{\Psi}_{\mathrm{fB}}$ and $\underline{\Psi}_{\mathrm{fC}}$ and the emfs $\underline{E}_{\mathrm{fA}}$, $\underline{E}_{\mathrm{fB}}$ and $\underline{E}_{\mathrm{fC}}$ induced by them are shown in Figure 3.10b. The root-mean-square (rms) value of each of these emfs (or the length of the phasors $\underline{E}_{\mathrm{fA}}$, $\underline{E}_{\mathrm{fB}}$, $\underline{E}_{\mathrm{fC}}$) is

$$E_{\mathrm{f}} = \frac{1}{\sqrt{2}}\omega\Psi_{\mathrm{fa}} = \frac{1}{\sqrt{2}}\omega N_\phi\Phi_{\mathrm{f}} = \frac{1}{\sqrt{2}}\omega M_{\mathrm{f}}i_{\mathrm{f}} \cong 4.44\,f\,M_{\mathrm{f}}i_{\mathrm{f}}. \tag{3.37}$$

This equation is the well-known *transformer equation* and illustrates how the primary (field) winding current induces an emf in the secondary (armature) winding. The emf is proportional to both the frequency and the field current i_{f}. The mutual inductance M_{f} is in practice not constant but depends on the saturation of the magnetic circuit.

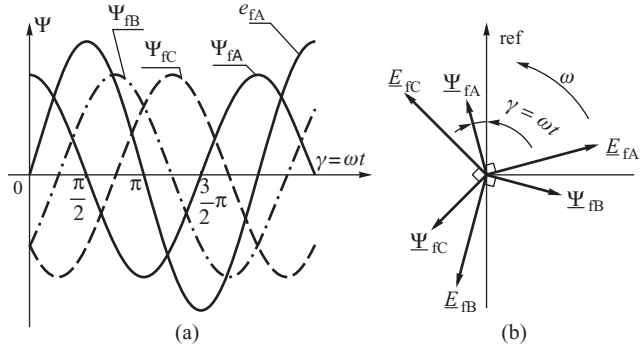

Figure 3.10 The phase excitation flux linkages and the emfs induced by them shown as: (a) time-varying waveforms; (b) rotating phasors.

3.3.1.2 Armature Reaction and the Air-Gap Flux

Now consider the effect of loading the generator when an *armature current* flows in each phase of the stator winding. As the three phase windings are magnetically coupled, Chapter 11 will show how the equivalent circuit can be developed by considering their self- and mutual inductances. In this chapter another, simpler, approach will be followed when the combined magnetic effect of all three phase windings is considered. This is referred to as the *armature reaction*.

Generally the stator phase currents will be delayed by an angle λ with respect to the reference flux linkages $\Psi_{fA}(t)$ and may be written as

$$i_A = I_m \cos(\omega t - \lambda), \quad i_B = I_m \cos\left(\omega t - \lambda - \frac{2\pi}{3}\right), \quad i_C = I_m \cos\left(\omega t - \lambda - \frac{4\pi}{3}\right), \tag{3.38}$$

where I_m is the maximum (peak) value of the armature current. Each of the phase currents produces a pulsating phase mmf per pole:

$$\begin{aligned} F_A(t) &= N_a I_m \cos(\omega t - \lambda), \quad F_B(t) = N_a I_m \cos\left(\omega t - \lambda - \frac{2\pi}{3}\right), \\ F_C(t) &= N_a I_m \cos\left(\omega t - \lambda - \frac{4\pi}{3}\right), \end{aligned} \tag{3.39}$$

where $N_a = (1/p)(4/\pi) N_\phi$ is the effective number of turns per phase per pole and, as before, $N_\phi = k_w N$.

Because the magnetic axes of the phase windings are shifted in space from each other by $2\pi/3$ electrical radians, the phase mmfs are shifted in both space and time. A convenient way to account for the shift in space is to represent the mmfs as *space vectors* directed along their respective phase axes with instantaneous values given by Equations (3.39). A space vector will be denoted by an arrow on top of the symbol. The vector of the resultant *armature reaction mmf* $\vec{F}_a$ can then be obtained by adding the component phase vectors.

A neat way to analyse the space position of the phase mmfs is to introduce a complex plane which has its real axis directed along the A-axis and its imaginary axis $\pi/2$ ahead (counterclockwise). The space operator $e^{j\theta}$ then introduces a phase shift in the complex plane which, when multiplied by the value of the phase mmf, will direct it in space along the magnetic axes of the winding. Axis B is at an angle $2\pi/3$ with respect to A, while axis C is at an angle $4\pi/3$. The value of F_B must be multiplied by $e^{j2\pi/3}$ to obtain a vector directed along the B-axis, while the value of F_C must be multiplied by $e^{j4\pi/3}$ to obtain a vector directed along the C-axis. The vector of the resulting armature mmf per pole $\vec{F}_a$ is then

$$\begin{aligned} \vec{F}_a &= \vec{F}_A + \vec{F}_B + \vec{F}_C = N_a i_A e^{j0} + N_a i_B e^{j2\pi/3} + N_a i_C e^{j4\pi/3} \\ &= N_a I_m \left[\cos(\omega t - \lambda) + \cos\left(\omega t - \lambda - \frac{2\pi}{3}\right) e^{j2\pi/3} + \cos\left(\omega t - \lambda - \frac{4\pi}{3}\right) e^{j4\pi/3}\right]. \end{aligned} \tag{3.40}$$

Using the identity

$$\cos(\alpha - \beta) = \cos\alpha \cos\beta + \sin\alpha \sin\beta \tag{3.41}$$

gives

$$\begin{aligned} \vec{F}_a &= N_a I_m \{\cos(\omega t - \lambda) + [-0.5\cos(\omega t - \lambda) + 0.866\sin(\omega t - \beta)](-0.5 + j0.866) \\ &\quad + [-0.5\cos(\omega t - \lambda) - 0.866\sin(\omega t - \lambda)](-0.5 - j0.866)\} \\ &= N_a I_m [1.5\cos(\omega t - \lambda) + 1.5j\sin(\omega t - \lambda)] = 1.5 N_a I_m e^{j(\omega t - \lambda)}. \end{aligned} \tag{3.42}$$

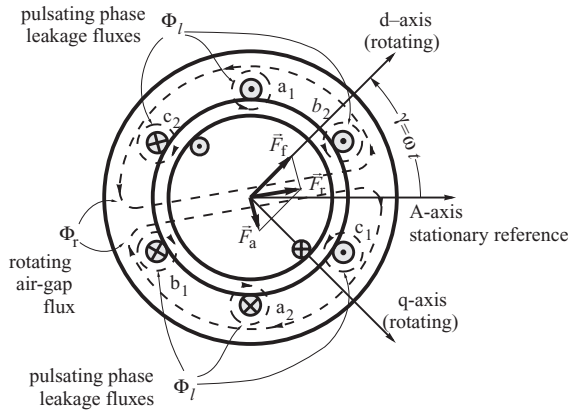

Figure 3.11 Resultant flux in the round-rotor generator operating at lagging power factor.

This equation shows that $\vec{F}_a$ is a vector of constant magnitude $F_a = 1.5 N_a I_m$ which rotates in the complex plane with an angular velocity ω. As this is also the rotational speed of the generator, the rotor and stator mmfs are stationary with respect to each other. To find the relative spatial position of the mmfs, recall that the angle λ was defined as a time delay with respect to the linkages $\Psi_{fA}(t)$. As $\vec{F}_f$ is in phase with $\Psi_{fA}(t)$ (i.e. Ψ_{fA} reaches the maximum when $\vec{F}_f$ aligns with A-axis), Equation (3.42) shows that $\vec{F}_a$ must lag $\vec{F}_f$ by the spatial angle λ.

As the two rotating mmfs $\vec{F}_a$ and $\vec{F}_f$ are stationary with respect to each other, they can be combined to give a *resultant mmf* $\vec{F}_r = \vec{F}_f + \vec{F}_a$ which drives the resultant *air-gap flux* Φ_r. This is shown in Figure 3.11. It is important to realize that the magnetic circuit does not 'see' $\vec{F}_a$ or $\vec{F}_f$ alone but $\vec{F}_r = \vec{F}_f + \vec{F}_a$. The peak flux density in the air gap of a round-rotor generator coincides with the peak of $\vec{F}_r$ and it is in the same direction. Figure 3.11 shows the typical relative position of the mmfs with $\pi/2 < \lambda < \pi$. It can be seen that the armature reaction field demagnetizes the generator and the resultant mmf is smaller than the excitation mmf alone.

As the resultant mmf is the sum of two rotating, sinusoidally distributed mmfs, both the resultant mmf per pole and the density of the air-gap flux driven by it are sinusoidally distributed around the air gap. In practice, magnetic saturation will cause a slight flattening of the flux density wave which results in third-harmonic voltages being induced in the armature winding. Connecting the generator windings in Δ or Y with the star point not earthed prevents the third-harmonic currents appearing at the generator terminals.

3.3.1.3 Equivalent Circuit and the Phasor Diagram

The rotating air-gap flux produces sinusoidally changing flux linkages with each of the stator phase windings. The linkages with phase A, F_{rA}, can be calculated by projecting the component rotor and stator mmf waves onto the A-axis in order to obtain the resultant mmf along this axis. Recall that F_f is assumed to align with the A-axis at $t = 0$ and that F_a is delayed with respect to F_f by λ. This gives

$$F_{rA}(t) = F_f \cos \omega t + F_a \cos(\omega t - \lambda) = N_f i_f \cos \omega t + 1.5 N_a I_m \cos(\omega t - \lambda). \tag{3.43}$$

This resultant mmf must be divided by the reluctance, $\Re$, and multiplied by the number of armature turns N_ϕ to obtain the resultant flux linkages with phase A:

$$\Psi_{\mathrm{rA}}(t) = N_\phi \frac{F_{\mathrm{rA}}(t)}{\Re} = M_{\mathrm{f}} i_{\mathrm{f}} \cos\omega t + L_{\mathrm{a}} I_{\mathrm{m}} \cos(\omega t - \lambda), \tag{3.44}$$

where $M_{\mathrm{f}} = N_\phi N_{\mathrm{f}}/\Re$ is the mutual inductance between the field and the armature winding and $L_{\mathrm{a}} = 1.5 N_{\mathrm{a}} N_\phi/\Re$ is the *armature reaction inductance* or *magnetizing inductance*. In the round-rotor machines with a uniform air gap the reluctance $\Re$ does not depend on the flux position.

The linkages $\Psi_{\mathrm{rA}}(t)$ induce the *air-gap emf* in phase A equal to

$$e_{\mathrm{rA}} = -\frac{\mathrm{d}\Psi_{\mathrm{rA}}}{\mathrm{d}t} = \omega M_{\mathrm{f}} i_{\mathrm{f}} \sin\omega t + \omega L_{\mathrm{a}} I_{\mathrm{m}} \sin(\omega t - \lambda) = e_{\mathrm{fA}}(t) + e_{\mathrm{aA}}(t), \tag{3.45}$$

where $e_{\mathrm{fA}}(t) = \omega M_{\mathrm{f}} i_{\mathrm{f}} \sin\omega t$ and $e_{\mathrm{aA}}(t) = \omega L_{\mathrm{a}} I_{\mathrm{m}} \sin(\omega t - \lambda)$. Equation (3.45) shows that the trick in modelling the synchronous generator is to represent the resultant air-gap emf by a sum of two fictitious emfs. The first is the *excitation* (or *internal*) *emf* $e_{\mathrm{fA}}(t)$ due to the rotor field and is equal to the no-load terminal voltage, Equation (3.36). The second is the *armature reaction emf* $e_{\mathrm{aA}}(t)$ due to the armature reaction field, which lags the A-phase current by $\pi/2$ (compare Equation (3.45) with Equation (3.38)). Using phasor notation this corresponds to multiplying the current phasor by $-\mathrm{j}$ so that the armature reaction emf phasor is $\underline{E}_{\mathrm{a}} = -\mathrm{j}X_{\mathrm{a}}\underline{I}$ where $X_{\mathrm{a}} = \omega L_{\mathrm{a}}$ is the *armature reaction reactance* or *magnetising reactance* and $\underline{I}$ is the current phasor of magnitude $I = I_{\mathrm{m}}/\sqrt{2}$. The phasor of the air-gap emf can therefore be expressed as

$$\underline{E}_{\mathrm{r}} = \underline{E}_{\mathrm{f}} + \underline{E}_{\mathrm{a}} = \underline{E}_{\mathrm{f}} - \mathrm{j}X_{\mathrm{a}}\underline{I}, \tag{3.46}$$

where $\underline{E}_{\mathrm{f}}$ is the phasor of the internal emf with magnitude E_{f} given by Equation (3.37). Thus $-\underline{E}_{\mathrm{a}} = \mathrm{j}X_{\mathrm{a}}\underline{I}$ has the properties of a reactance drop resulting from the effect of the armature current. When $-\underline{E}_{\mathrm{a}}$ is replaced by the reactance voltage drop $\mathrm{j}X_{\mathrm{a}}\underline{I}$, the circuit model becomes that to the left of the phasor $\underline{E}_{\mathrm{r}}$ in Figure 3.12.

Figure 3.12a shows how the full equivalent circuit can be obtained by accounting for electrical and magnetic imperfections of the machine. Firstly, each armature winding has some resistance R which produces the voltage drop $R\underline{I}$. In the case of the synchronous generator this armature resistance is very small and can often be neglected. Secondly, although most of the magnetic flux produced by the armature crosses the air gap to link with the rotor winding, a part of it, called the *leakage flux*, does not. This pulsating leakage flux is shown as Φ_l in Figure 3.11 and only links with the armature winding. The leakage flux can be accounted for by inserting a *leakage reactance* X_l into the circuit. As the leakage flux closes its path largely through air, $X_l \ll X_{\mathrm{a}}$.

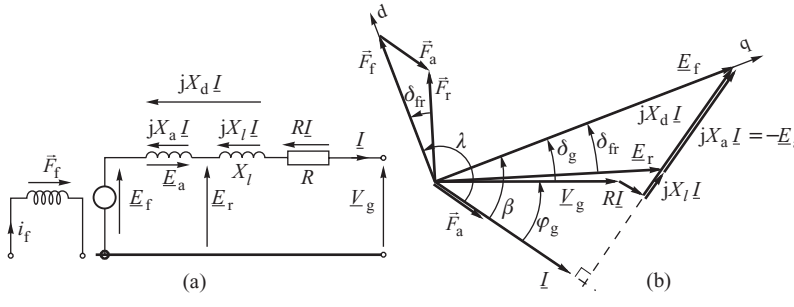

Figure 3.12 Round-rotor synchronous generator: (a) equivalent circuit diagram; (b) phasor/vector diagram for operation at lagging power factor.

Figure 3.12a shows the total equivalent circuit of the round-rotor synchronous machine with all the imperfections included. The terminal voltage $\underline{V}_g$ is

$$\underline{V}_g = \underline{E}_f - j X_a \underline{I} - j X_l \underline{I} - R\underline{I} = \underline{E}_f - j X_d \underline{I} - R\underline{I}, \tag{3.47}$$

where $X_d = X_a + X_l$ is the *synchronous reactance*, or more precisely the *direct-axis synchronous reactance*. As $L_l \ll L_a$, $X_l \ll X_a$ and to all practical purposes $X_d \approx X_a$. The internal emf E_f is sometimes referred to as the *voltage behind the synchronous reactance*. The phasor diagram resulting from Equation (3.47) is shown in Figure 3.12b for a generator operating at lagging power factor.

The phasor diagram is normally constructed knowing only the generator voltage V_g and its per-phase active and reactive load powers P and Q. From these the current and the power factor angle are calculated:

$$I = \frac{\sqrt{P^2 + Q^2}}{V_g}, \quad \varphi_g = \arctan \frac{Q}{P}. \tag{3.48}$$

Knowing the length and the direction of the current phasor relative to the reference voltage V_g, the length and direction of the voltage drops $\underline{I}R$, $j\underline{I}X_l$ and $j\underline{I}X_a$ can be found and the phasor diagram constructed.

Apart from the usual voltage and current phasors, Figure 3.12b also shows the space vectors of the mmfs and the position of the d- and q-axes. Combining both space vectors and phasors on the same diagram is very useful and is accomplished by drawing the voltage (and current) *phasors* and the mmf *vectors* on the same complex plane at $t = 0$, taking phase A as the reference.

To find the relative displacement between the phasors and the vectors on the diagram, consider the relative position of the armature current I and the armature mmf $\vec{F}_a$. At $t = 0$ the space angle of $\vec{F}_a$ is $(-\lambda)$ with respect to the A-axis, Equation (3.42). At the same time the phase angle of the A-axis current is also $(-\lambda)$, Equation (3.38), indicating that the current phasor $\underline{I}$ and the mmf vector $\vec{F}_a$ are in phase on the phasor/vector diagram. As $\underline{E}_a = -j X_a \underline{I}$, it follows that $\underline{E}_a$ lags $\vec{F}_a$ by $\pi/2$. A similar argument shows that all the emfs must lag their mmfs by $\pi/2$.

The phasor diagram of Figure 3.12b provides additional insight into the meaning of all the angles on it. As all the emfs are perpendicular to their mmfs, the mmf triangle (F_f, F_a, F_r) is similar to the voltage triangle (E_f, E_a, E_r) and all the angles shown in Figure 3.12 have a dual meaning: they are, at the same time, the spatial angles between the rotating mmfs and the phase shifts between the AC voltages. For example, the angle δ_{fr}, which is the space angle between the field and the resultant air-gap mmf, is at the same time the phase shift between $\underline{E}_f$ and $\underline{E}_r$.

3.3.1.4 The Torque Creation Mechanism

The rotor of the synchronous generator is driven by a prime mover which exerts a mechanical torque τ_m on it. For the speed of the rotor to remain constant, the machine must develop an equal, but opposing, electromagnetic torque τ_e. Resolution of the air-gap mmf into the stator and rotor component mmfs provides a means of understanding how the electromagnetic torque is developed. The component stator and rotor mmfs can be compared with two magnets rotating at the same speed and trying to co-align, with the north magnetic pole of one attracting the south pole of the other and vice versa. The torque produced by these attractive forces can be calculated from the three-phase air-gap power P_{ag}, which in its electrical form is equal to

$$P_{ag} = 3 E_f I \cos\beta, \tag{3.49}$$

where β is the angle between $\underline{E}_f$ and $\underline{I}$ and is referred to as the *internal power factor angle* (see Figure 3.12b). Neglecting mechanical losses, P_{ag} must be equal to the mechanical power $\tau_m \omega_m$ supplied

by the prime mover so that for a p-pole machine

$$\tau = \frac{1}{\omega_m} P_{ag} = \frac{p}{2} \frac{1}{\omega} P_{ag}. \tag{3.50}$$

Substituting for E_f from Equation (3.37) and noting that $I = I_m/\sqrt{2}$ gives

$$\tau = \frac{3}{4} p \Phi_f N_\phi I_m \cos\beta. \tag{3.51}$$

This equation can be written in terms of the angle λ and the armature mmf F_a by noting that

$$N_a = \frac{1}{p} \frac{4}{\pi} N_\phi$$

when, from Equation (3.42),

$$F_a = \frac{3}{2} N_a I_m = \frac{3}{2} \left(\frac{1}{p} \frac{4}{\pi} N_\phi \right) I_m. \tag{3.52}$$

Figure 3.12b shows that $\lambda = \pi/2 + \beta$ so that $\sin\lambda = \cos\beta$ and

$$\tau = \frac{\pi}{8} p^2 \Phi_f F_a \sin\lambda = \frac{\pi}{8} p^2 \frac{F_f F_a}{\Re} \sin\lambda, \tag{3.53}$$

where λ is the angle between F_f and F_a. Inspection of Figure 3.12b shows that $F_a \sin\lambda = F_r \sin\delta_{fr}$ and Equation (3.53) can be rewritten as

$$\tau = \frac{\pi}{8} p^2 F_r \frac{F_f}{\Re} \sin\delta_{fr} = \frac{\pi}{8} p^2 F_r \Phi_f \sin\delta_{fr}, \tag{3.54}$$

where the angle δ_{fr} is referred to as the *torque angle*. For a two-pole machine this equation simplifies to

$$\tau = \frac{\pi}{2} F_r \Phi_f \sin\delta_{fr}. \tag{3.55}$$

If the rotor field leads the air-gap field, as in Figure 3.11, then the electromagnetic torque acts in the opposite direction to the rotation and opposes the mechanical driving torque so the machine acts as a generator. On the other hand, if the rotor field lags the air-gap field, then the electromagnetic torque acts in the direction of rotation and the machine acts as a motor.

3.3.2 Salient-Pole Machines

Because of the relative ease of balancing round rotors, and their ability to withstand high centrifugal forces, round-rotor generators are normally used for turbo units driven by high-speed steam or gas turbines. Generators operating at a lower speed, such as those driven by hydro turbines, need many magnetic poles in order to operate at 50 or 60 Hz. As the centrifugal forces experienced by the rotors of these low-speed machines are lower than in the corresponding turbogenerators, salient poles can be used and the rotor diameter increased. Normally salient-pole rotors have more than two poles and the angles (and speed) expressed in mechanical units are related to those expressed in electrical units by Equations (3.31) and (3.32). To simplify considerations a two-pole salient generator will be considered here so that the angles expressed in electrical and mechanical radians are the same. The simplified cross-section of such a generator is shown in Figure 3.13.

The main problem with modelling a salient-pole machine is that the width of the air gap varies circumferentially around the generator with the narrowest gap being along the d-axis and the widest along the q-axis. Consequently the reluctance of the air-gap flux is not uniform but varies between

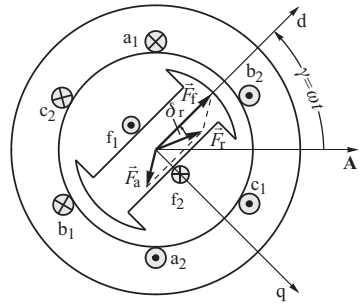

Figure 3.13 A simplified salient-pole generator.

its minimum value $\Re_d$ and its maximum value $\Re_q$ as shown by the approximated function in Figure 3.14. This creates a problem as one of the fundamental assumptions for modelling the uniform-gap, round-rotor generator was that the peak density of the flux wave coincides with the peak density of the mmf wave or, in other words, the mmf and the flux vectors are in phase. It is important to realize that this assumption is no longer valid for salient-rotor machines. As flux tends to take the path of least reluctance, the flux vector is shifted towards the d-axis (where reluctance is least) when compared with the mmf vector. The only instance when the two vectors are in phase is when the mmf vector lies along either the d-axis (which is the position of minimum reluctance) or the q-axis (when the attractive forces that tend to shift the flux towards the d-axis balance each other). At any other position the flux and mmf are out of phase and the simple analysis used for the round-rotor machine is no longer valid. To overcome this problem, A. Blondel developed his *two-reaction theory* which resolves the mmfs acting in the machine along the d- and q-axes. The emfs due to these component mmfs are then considered separately, assigning different, but constant, values of reactances to the fluxes acting along these axes.

This concept is illustrated in Figure 3.15. The armature mmf $\vec{F}_a$ and the armature current $\underline{I}$ are resolved into two components, one acting along the d-axis ($\vec{F}_{ad}$, $\underline{I}_d$) and the other acting along the q-axis ($\vec{F}_{aq}$, $\underline{I}_q$). There is no need to resolve the excitation mmf $\vec{F}_f$ as this always acts only along the d-axis. The resultant mmf $\vec{F}_r$ may then be expressed as

$$\vec{F}_r = \vec{F}_d + \vec{F}_q, \tag{3.56}$$

where $\vec{F}_d = \vec{F}_f + \vec{F}_{ad}$ and $\vec{F}_q = \vec{F}_{aq}$. Similarly the current $\underline{I}$ may be expressed as

$$\underline{I} = \underline{I}_d + \underline{I}_q. \tag{3.57}$$

Similarly, as for the round-rotor generator, the resultant air-gap emf is equal to the sum of the component emfs, each of which is due to a corresponding mmf. In this case the resultant emf is assumed to be equal to the sum of three components due to $\vec{F}_f$, $\vec{F}_{ad}$ and $\vec{F}_{aq}$ respectively. Because the excitation mmf $\vec{F}_f$ always acts along the d-axis, the internal emf E_f due to $\vec{F}_f$ depends only on

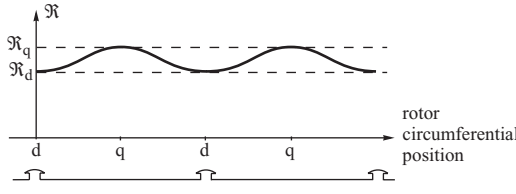

Figure 3.14 Approximate variation of reluctance with circumferential position.

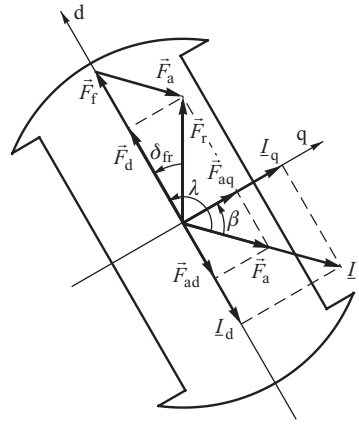

Figure 3.15 Resolution of the mmfs and the current into d- and q-components.

the d-axis reluctance $\Re_d$ and is constant for a given value of field current. As the emfs lag their mmfs by $\pi/2$, $\underline{E}_f$ is directed along the q-axis.

The emf due to the d-axis armature mmf $\vec{F}_{ad}$ is proportional to $\underline{I}_d$ and delayed by $\pi/2$ with respect to it. This emf is therefore directed along the q-axis and may be expressed as

$$\underline{E}_{aq} = -\mathrm{j}X_{ad}\underline{I}_d \tag{3.58}$$

where X_{ad} is the *direct-axis armature reaction reactance*. As $\vec{F}_{ad}$ acts across the shortest gap, X_{ad} is inversely proportional to $\Re_d$.

The emf due to the q-axis armature mmf $\vec{F}_{aq}$ is proportional to I_q and delayed by $\pi/2$. This emf is therefore directed along the d-axis and may be expressed as

$$\underline{E}_{ad} = -\mathrm{j}X_{aq}\underline{I}_q, \tag{3.59}$$

where X_{aq} is the *quadrature-axis armature reaction reactance*. As $\vec{F}_{aq}$ acts across the widest gap, X_{aq} is inversely proportional to $\Re_q$. The resultant air-gap emf is then

$$\underline{E}_r = \underline{E}_f + \underline{E}_{aq} + \underline{E}_{ad} = \underline{E}_f - \mathrm{j}X_{ad}\underline{I}_d - \mathrm{j}X_{aq}\underline{I}_q. \tag{3.60}$$

The terminal voltage $\underline{V}_g$ is obtained by subtracting from this emf the voltage drops due to the armature leakage reactance and resistance to give

$$\begin{aligned}\underline{V}_g &= \underline{E}_r - \mathrm{j}X_l\underline{I} - R\underline{I} = \underline{E}_f - \mathrm{j}X_{ad}\underline{I}_d - \mathrm{j}X_{aq}\underline{I}_q - \mathrm{j}X_l(\underline{I}_d + \underline{I}_q) - R\underline{I} \\ &= \underline{E}_f - \mathrm{j}(X_{ad} + X_l)\underline{I}_d - \mathrm{j}(X_{aq} + X_l)\underline{I}_q - R\underline{I},\end{aligned} \tag{3.61}$$

or

$$\underline{E}_f = \underline{V}_g + \mathrm{j}X_d\underline{I}_d + \mathrm{j}X_q\underline{I}_q + R\underline{I}, \tag{3.62}$$

where $X_d = X_{ad} + X_l$ is the *direct-axis synchronous reactance* and $X_q = X_{aq} + X_l$ is the *quadrature-axis synchronous reactance*. As the reluctance along the q-axis is the highest (because the gap is the widest), $X_d > X_q$.

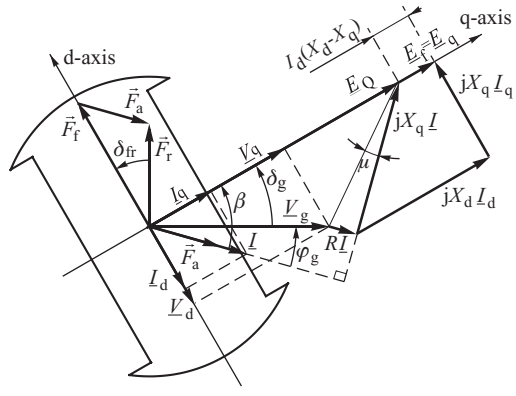

Figure 3.16 Phasor diagram for a salient-pole generator.

3.3.2.1 Phasor Diagram and the Equivalent Circuit

Figure 3.16 shows the phasor diagram resulting from Equation (3.62). Its construction is more complicated than that for the round-rotor generator shown in Figure 3.12. In order to determine $\underline{I}_d$ and $\underline{I}_q$, it is necessary first to determine the angle δ_g so as to locate the q-axis relative to $\underline{V}_g$. To solve this problem, recall that the emf $\underline{E}_f$ lies along the q-axis. Rearranging Equation (3.62) gives

$$\underline{E}_f = \underline{V}_g + R\underline{I} + jX_q\underline{I} + j(X_d - X_q)\underline{I}_d = \underline{E}_Q + j(X_d - X_q)\underline{I}_d, \tag{3.63}$$

where

$$\underline{E}_Q = \underline{V}_g + (R + jX_q)\underline{I}. \tag{3.64}$$

Because multiplication of $\underline{I}_d$ by j shifts the resultant phasor $\pi/2$ ahead, the second term in Equation (3.63), equal to $j(X_d - X_q)\underline{I}_d$, is directed along the q-axis. As $\underline{E}_f$ itself lies on the q-axis, $\underline{E}_Q$ must also lie on the q-axis. Knowing $\underline{V}_g$ and $\underline{I}$, the phasor $(R+jX_q)\underline{I}$ can be added to $\underline{V}_g$ to obtain $\underline{E}_Q$. This determines the direction of the q-axis and the angle δ_g. Once the location of the q-axis is known, $\underline{I}$ can be resolved into its components $\underline{I}_d$ and $\underline{I}_q$ and the phasor diagram completed. For the round-rotor generator, $X_d = X_q$ and $\underline{E}_Q$ becomes equal to $\underline{E}_f$ (and $\underline{E}_q$).

Resolving Equation (3.62) into its d- and q-components allows the generator equivalent circuit to be constructed. As multiplication of a phasor by j gives a phasor shifted $\pi/2$ counterclockwise, the phasor $(jX_q\underline{I}_q)$ is directed along the d-axis. Similarly the phasor $(jX_d\underline{I}_d)$ is $\pi/2$ ahead of the d-axis; that is, it is directed in the opposite direction to the q-axis so that its q-axis component is negative.[1] Consequently, the d- and q-components of Equation (3.62) are

$$\begin{aligned} &\text{d-axis:} \quad E_d = V_d + RI_d + X_q I_q = 0 \\ &\text{q-axis:} \quad E_q = V_q + RI_q - X_d I_d = E_f. \end{aligned} \tag{3.65}$$

These equations can be written in matrix form as

$$\begin{bmatrix} E_d \\ E_q \end{bmatrix} = \begin{bmatrix} 0 \\ E_f \end{bmatrix} = \begin{bmatrix} V_{gd} \\ V_{gq} \end{bmatrix} + \begin{bmatrix} R & +X_q \\ -X_d & R \end{bmatrix} \begin{bmatrix} I_d \\ I_q \end{bmatrix}. \tag{3.66}$$

[1] Figure 3.16 shows the phasor of $(jX_d\underline{I}_d)$ to be along the q-axis. This is because I_d is negative.

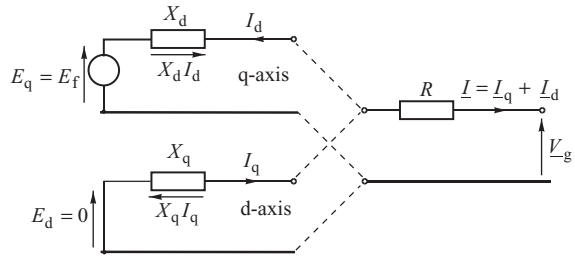

Figure 3.17 Equivalent d- and q-axis circuit diagrams of the salient-pole generator.

It is important to realize that all the variables in each of these equations are in phase with each other and are real (not complex) numbers. The d- and q-components of the terminal voltage and current are

$$\begin{aligned} V_d &= -V_g \sin\delta_g, \qquad V_q = V_g \cos\delta_g \\ I_d &= -I \sin\beta, \qquad I_q = I \cos\beta \end{aligned} \tag{3.67}$$

and $\beta = \delta_g + \varphi_g$. The minus sign in the d-components of the voltage and the current indicates the fact that they are directed in the opposite direction to the d-axis. The equivalent circuit for the salient-pole generator can now be drawn in two parts, one corresponding to the d-axis and the other to the q-axis, as shown in Figure 3.17. As all the variables in each of the Equations (3.65) are in phase, the reactances X_d and X_q are shown using the symbol of resistance, rather than reactance, to give a voltage drop that is in phase with the current.

A slightly misleading feature of the equivalent circuit shown in Figure 3.17 is that the d-axis current flows into, rather than out of, the generator. This is a consequence of assuming that the d-axis leads the q-axis. As δ_g is assumed to be positive for generator action, this assumption gives negative values for the d-components of the terminal voltage and current, see Equation (3.67). The selection of the d-axis leading the q-axis is purely arbitrary and is recommended by IEEE (1969) on the grounds that the d-axis current usually causes demagnetization of the machine and should be negative in the generator reference frame. Many authors, however, assume the d-axis to lag the q-axis, which removes the minus sign from Equation (3.67) and changes the sign of the reactive terms in Equations (3.65).

3.3.2.2 The d- and q-axis Armature Coils

As will be seen in later chapters, it is often helpful to consider the effect of the three-phase armature winding to be produced by two equivalent windings phase displaced by 90°. If one of these equivalent armature coils is located along the d-axis and the other along the q-axis then the equivalent circuit of Figure 3.17 can be seen to take on a more direct physical meaning. These two equivalent armature coils are known as the d- and q- axis armature coils and are assumed to have the same number of turns as an actual armature phase winding.[2] To account for the DC nature of the equations in (3.65) these two equivalent armature coils are also assumed to rotate with the generator rotor, with the voltages $E_q = E_f$ and E_d being injected into the respective armature coil. As E_f and E_d are proportional to the rotational speed ω, these voltages are known as *rotational voltages*. This concept of d- and q-axis armature coils will be examined in detail in Chapter 11.

[2] This assumption is not strictly necessary but is the assumption made in this book. A fuller explanation of this is given in Chapter 11.

3.3.2.3 Torque in the Salient-Pole Machine

The mechanism by which electromagnetic torque is produced was explained earlier with regard to the round-rotor generator when it was shown that torque was proportional to the product of the stator mmf and rotor flux and the sine of the angle between them, Equation (3.53). In the case of the salient-pole generator a similar torque creation mechanism applies but now the d- and q-axis components of the mmf must be considered. Resolution of the armature mmf gives

$$F_{ad} = F_a \cos\lambda; \quad F_{aq} = F_a \sin\lambda. \tag{3.68}$$

As the angle between Φ_f and F_{aq} is $\pi/2$, application of Equation (3.53) leads to the electromagnetic torque in a two-pole generator being equal to

$$\tau_q = \frac{\pi}{2}\Phi_f F_{aq}. \tag{3.69}$$

This equation represents only part of the tangential force on the armature as there will be other forces due to the interaction of other components of the d-axis flux with the q-axis mmf. The effect of these other d-axis flux components is included by algebraically adding all the d-axis fluxes before multiplying by the q-axis mmf. In the steady state the only other flux along the d-axis is the flux produced by the d-axis mmf itself so that the torque expression becomes

$$\tau_q = \frac{\pi}{2}(\Phi_f + \Phi_{ad})F_{aq}, \tag{3.70}$$

where $\Phi_{ad} = F_{ad}/\Re_d$. There will also be a similar interaction between any q-axis flux and the d-axis mmf that will produce an additional torque component

$$\tau_d = \frac{\pi}{2}(\Phi_{aq})F_{ad}, \tag{3.71}$$

where $\Phi_{aq} = F_{aq}/\Re_q$. As F_{ad} is produced by the d-axis current which flows into, rather than out of, the generator (see Figure 3.17) the torque τ_d acts in the opposite direction to τ_q. The total torque is equal to the difference between the two components giving

$$\tau = \tau_q - \tau_d = \frac{\pi}{2}(\Phi_f + \Phi_{ad})F_{aq} - \frac{\pi}{2}(\Phi_{aq})F_{ad}. \tag{3.72}$$

Regrouping the terms and substituting $\Phi_{ad} = F_{ad}/\Re_d$, $\Phi_{aq} = F_{aq}/\Re_q$, $F_{aq} = F_a \sin\lambda = F_r \sin\delta_{fr}$ and $F_{ad} = F_a \cos\lambda = F_r \cos\delta_{fr}$ finally gives

$$\tau = \frac{\pi}{2}\Phi_f F_r \sin\delta_{fr} + \frac{\pi}{4}F_r^2 \frac{\Re_q - \Re_d}{\Re_q \Re_d} \sin 2\delta_{fr}. \tag{3.73}$$

This equation shows that the torque developed in a salient-pole generator consists of two components. The first component, proportional to $\sin\delta_{fr}$, is identical to the torque expressed by Equation (3.55) for a round-rotor generator and is termed the *synchronous torque*. The second component, termed the *reluctance torque*, arises as the rotor tries to assume a position of minimum magnetic reluctance by moving towards the air-gap mmf. This additional torque is due to the non-uniform air gap and is a direct consequence of the air-gap mmf and flux not being in phase. The reluctance torque is present even without any field excitation and is proportional to $\sin 2\delta_{fr}$. It vanishes for both $\delta_{fr} = 0$ and $\delta_{fr} = \pi/2$. In both these positions the air-gap mmf and flux are in phase and the tangential forces acting on both poles balance each other. In the round-rotor generator, $\Re_d = \Re_q$ and the torque expression reverts to that given in Equation (3.55).

3.3.3 Synchronous Generator as a Power Source

The synchronous generator is connected to the high-voltage transmission network via a step-up transformer (Figure 2.2) and together they form a *generator–transformer unit*. From the power system point of view, the unit is a source of real and reactive power. This subsection contains a description of the mathematical model of the unit together with its main characteristics.

3.3.3.1 Equivalent Circuit of the Generator–Transformer Unit

The equivalent steady-state circuit diagram and phasor diagram of a unit consisting of a round-rotor generator and a step-up transformer is shown in Figure 3.18. The transformer is modelled using the impedance $R_T + jX_T$. The phasor diagram of the generator alone is the same as that shown in Figure 3.12 but with a voltage drop on the transformer impedance added to the voltage $\underline{V}_g$ in order to get the terminal voltage $\underline{V}$. The following equation can be formed similar to (3.47):

$$\underline{V} = \underline{E}_f - jX_d\underline{I} - R\underline{I} - jX_T\underline{I} - R_T\underline{I} = \underline{E}_f - j(X_d + X_T)\underline{I} - (R + R_T)\underline{I}, \tag{3.74}$$

or simply

$$\underline{V} = \underline{E}_f - jx_d\underline{I} - r\underline{I}, \tag{3.75}$$

where $x_d = X_d + X_T$ is the generator reactance increased by the transformer reactance and $r = R + R_T$ is the generator resistor increased by the transformer resistor.

In the case of a salient-pole generator, the block diagram for the generator–transformer unit is similar to that for the generator alone (Figure 3.16) but, similar to Figure 3.18, it is necessary to subtract a voltage drop on the transformer impedance from the generator voltage $\underline{V}_g$ in order to

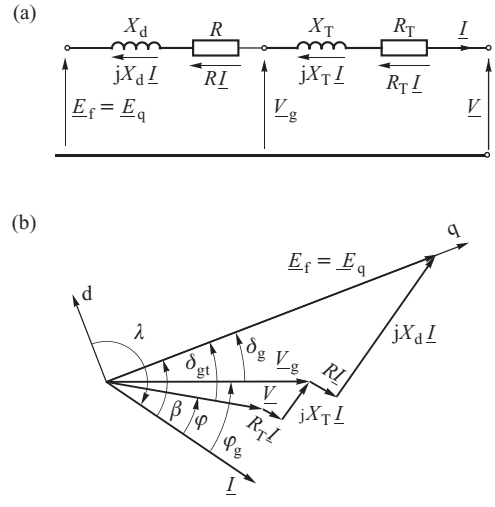

Figure 3.18 Equivalent steady-state circuit diagram and phasor diagram of the round-rotor generator with a step-up transformer.

get the voltage $\underline{V}$ on the transformer terminals. For the salient-pole generator, an equation similar to (3.63) can be derived:

$$\begin{aligned}\underline{V}_g &= \underline{E}_f - j X_d \underline{I}_d - j X_q \underline{I}_q - R\underline{I} - X_T \underline{I} - R_T \underline{I} \\ &= \underline{E}_f - j X_d \underline{I}_d - j X_q \underline{I}_q - R\underline{I} - X_T \left(\underline{I}_d + \underline{I}_q\right) - R_T \underline{I}.\end{aligned} \tag{3.76}$$

Or in the compact form

$$\underline{V}_g = \underline{E}_f - j x_d \underline{I}_d - j x_q \underline{I}_q - r\,\underline{I}, \tag{3.77}$$

where $x_d = X_d + X_T$, $x_q = X_q + X_T$ and $r = R + R_T$. Hence, as in (3.66),

$$E_q = V_q + r I_q - x_d I_d = E_f, \tag{78a}$$

$$E_d = V_d + r I_d + x_q I_q = 0, \tag{78b}$$

where

$$I_d = -I \sin\beta \quad \text{and} \quad I_q = I \cos\beta, \tag{79a}$$

$$V_d = -V \sin\delta_{gt} \quad \text{and} \quad V_q = V \cos\delta_{gt}, \tag{79b}$$

where δ_{gt} is the angle of the generator emf with respect to the voltage at the terminals of the generator–transformer unit.

Similar to (3.66), Equations (3.78) may be written in matrix form as

$$\begin{bmatrix} E_d \\ E_q \end{bmatrix} = \begin{bmatrix} V_d \\ V_q \end{bmatrix} + \begin{bmatrix} r & +x_q \\ -x_d & r \end{bmatrix} \begin{bmatrix} I_d \\ I_q \end{bmatrix} = \begin{bmatrix} 0 \\ E_f \end{bmatrix}. \tag{3.80}$$

In the rest of the book, the total reactances and resistances of the generator–transformer unit will be denoted by lower case letters. It should be remembered that the phase angle between the voltage and the current is different for the generator terminal voltage $\underline{V}_g$ and the high-voltage side of the transformer $\underline{V}$. Consequently powers measured on both sides of the transformer differ by the value of power losses on the transformer.

3.3.3.2 Real and Reactive Power of the Generator–Transformer Unit

From the power system point of view, the values of interest are the voltage and powers on the high-voltage side of the generator–transformer. Single-phase power measured on the generator terminals can be calculated from the general expression $P = VI\cos\varphi$. Figure 3.18 shows that $\varphi = \beta - \delta_{gt}$. Hence

$$P = VI\cos\varphi = VI\cos(\beta - \delta_{gt}) = VI\sin\beta\sin\delta_{gt} + VI\cos\beta\cos\delta_{gt}. \tag{3.81}$$

Substituting into Equations (3.79) gives

$$P = V_d I_d + V_q I_q. \tag{3.82}$$

The current components I_d and I_q can be calculated by solving Equations (3.78):

$$I_d = \frac{1}{z^2}\left[r\left(E_d - V_d\right) - x_q\left(E_q - V_q\right)\right], \qquad I_q = \frac{1}{z^2}\left[r\left(E_q - V_q\right) + x_d\left(E_d - V_d\right)\right], \tag{3.83}$$

where $z^2 = r^2 + x_d x_q$.

Equations (3.83) can also be written in matrix form. Solving the matrix equation (3.80) yields

$$\begin{bmatrix} I_d \\ I_q \end{bmatrix} = \frac{1}{z^2} \begin{bmatrix} r & -x_q \\ +x_d & r \end{bmatrix} \begin{bmatrix} E_d - V_d \\ E_q - V_q \end{bmatrix}. \tag{3.84}$$

Taking into account that in the steady state $E_d = 0$, and substituting (3.83) into (3.82), gives

$$P = \frac{1}{z^2} \left[-r \left(V_q^2 + V_d^2 \right) - \left(x_d - x_q \right) V_d V_q + E_q \left(r V_q - x_q V_d \right) \right]. \tag{3.85}$$

Substituting (3.79b) into (3.83) yields

$$P = \frac{E_q V}{z} \frac{x_q}{z} \sin \delta_{gt} + \frac{1}{2} \frac{V^2}{z} \frac{x_d - x_q}{z} \sin 2\delta_{gt} + \frac{E_q V}{z} \frac{r}{z} \cos \delta_{gt} - \frac{V^2}{z} \frac{r}{z}. \tag{3.86}$$

The resistance of the stator and transformer windings is quite small, so for approximate calculations the last two components may be neglected. Assuming $r \cong 0$ and $z^2 \cong x_d x_q$, the above equation simplifies to

$$P = \frac{E_q V}{x_d} \sin \delta_{gt} + \frac{V^2}{2} \frac{x_d - x_q}{x_d x_q} \sin 2\delta_{gt}. \tag{3.87}$$

The first component is dominant and depends on the sine of the angle δ_{gt} between the voltage and the generator emf. The second component, referred to as the *reluctance power*, exists only in salient-pole generators ($x_d > x_q$). For round-rotor generators ($x_d = x_q$), the reluctance power vanishes and the above equation further simplifies to

$$P = \frac{E_q V}{x_d} \sin \delta_{gt}. \tag{3.88}$$

Equations for the reactive power can be derived in a similar way. The expression $\varphi = \beta - \delta_{gt}$ is substituted into the general equation $Q = VI \sin \varphi$. Taking into account Equations (3.79) gives

$$Q = -V_q I_d + V_d I_q. \tag{3.89}$$

Using Equations (3.83) and (3.79b) gives

$$Q = \frac{E_q V}{z} \frac{x_q}{z} \cos \delta_{gt} - \frac{V^2}{z} \frac{x_d \sin^2 \delta_{gt} + x_q \cos^2 \delta_{gt}}{z} - \frac{E_q V}{z} \frac{r}{z} \sin \delta_{gt}. \tag{3.90}$$

For the round-rotor generators and when neglecting the resistance ($r = 0$), the above equation simplifies to

$$Q = \frac{E_q V}{x_d} \cos \delta_{gt} - \frac{V^2}{x_d}. \tag{3.91}$$

All the equations in this chapter are valid for per-unit calculations. If phase voltages are used in Equations (3.88) and (3.91) then the resulting real and reactive powers are per-phase. If line voltages ($\sqrt{3}$ higher than the phase voltages) are used in (3.88) and (3.91) then the resulting real and reactive powers are totals for all three phases.

3.3.4 Reactive Power Capability Curve of a Round-Rotor Generator

The synchronous generator is a source of real and reactive power which can be conveniently regulated over a wide range of values. This can be shown using the equations derived above for real

and reactive power. Equations (3.88) and (3.91) show that, assuming a given value of the generator reactance, the real and reactive power produced by the generator depends on:

- the emf $E_q = E_f$ which is proportional to the generator field current I_f;
- voltage V on the terminals of the step-up transformer;
- the power angle δ_{gt}.

The voltage of a generator operating in a power system cannot change much and must be held within typically 10 % of the network rated voltage. Consequently a wide range of real power changes P (see (3.88)) corresponds to changes in δ_{gt}. Note that mechanical power produced by the turbine must appear as the electrical power P of the generator (minus small losses). Hence, in the steady state, any change in the turbine power corresponds to an almost equal change in P and therefore an almost proportional change in $\sin\delta_{gt}$. When the angle is δ_{gt} and the required power is P, the field current I_f can be used to control the emf $E_q = E_f$ and therefore the reactive power Q that the generator produces (Equation (3.91)).

Limits in the real and reactive power control of the generator are the result of the following constructional and operational constraints:

(i) Stator (armature) current I must not cause overheating of the armature winding. Hence it must be smaller than a certain maximum value I_{MAX}, that is $I \le I_{MAX}$.
(ii) Rotor (field) current I_f must not cause overheating of the field winding. Hence it must be smaller than a certain maximum value I_{fMAX}, that is $I_f \le I_{fMAX}$ or $E_q \le E_{qMAX}$.
(iii) The power angle must not be higher than a maximum value due to stable generator operation $\delta_{gt} \le \delta_{MAX}$ (steady-state stability is explained in Chapter 5).
(iv) The temperature in the end region of the stator magnetic circuit must not exceed a maximum value.
(v) The generator real power must be within the limits set by the turbine power, that is $P_{min} \le P \le P_{MAX}$.

The area of allowed generator loading due to those constraints is illustrated in Figure 3.19 Individual elements of that diagram will be discussed below.

Condition (i) concerns the stator current. In the P–Q plane, it corresponds to a circle with a radius and centre determined as follows. The real and reactive power are given by $P = VI\cos\varphi$ and $Q = VI\sin\varphi$. Squaring these equations and adding gives $P^2 + Q^2 = (VI)^2$, as $\sin^2\varphi + \cos^2\varphi = 1$. In the P–Q plane, this equation corresponds to a circle with radius VI and centre at the origin. Assuming a given voltage V and loading $I = I_{MAX}$ yields

$$P^2 + Q^2 = (VI_{MAX})^2, \tag{3.92}$$

which corresponds to a circle of radius VI_{MAX} and which is shown in Figure 3.19 using a dotted line. All the points inside the circle correspond to powers P, Q for which the condition $I \le I_{MAX}$ is satisfied.

Condition (ii) concerns the rotor current. In the P–Q plane, it corresponds to a circle with centre and radius determined as follows. Equations (3.88) and (3.91) can be written as

$$P = \frac{E_q V}{x_d}\sin\delta_{gt} \quad \text{and} \quad Q + \frac{V^2}{x_d} = \frac{E_q V}{x_d}\cos\delta_{gt}. \tag{3.93}$$

Squaring both equations and adding gives

$$P^2 + \left(Q + \frac{V^2}{x_d}\right)^2 = \left(\frac{E_q V}{x_d}\right)^2. \tag{3.94}$$

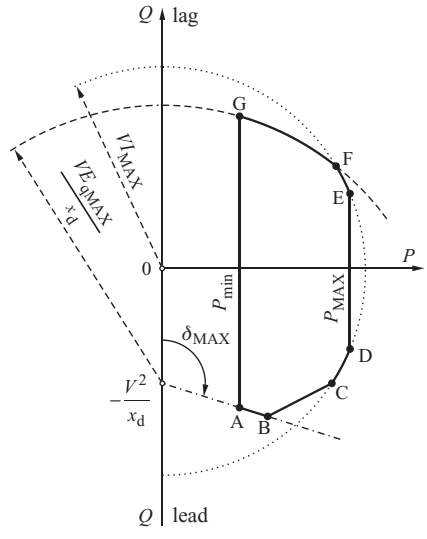

Figure 3.19 Reactive power capability curve assuming a given voltage.

For $E_q = E_{qMAX}$, the above equation becomes

$$P^2 + \left(Q + \frac{V^2}{x_d}\right)^2 = \left(\frac{E_{qMAX}\,V}{x_d}\right)^2 \tag{3.95}$$

which corresponds to a circle of radius $E_{qMAX}V/x_d$ and with a centre displaced from the origin along the reactive power axis Q by the value $-V^2/x_d$. The relevant fragment of that circle is shown by the dashed line along points G and F in Figure 3.19.

Condition (iii), concerning the maximum value of the power angle, corresponds to a straight line. The position and tangent of the line can be derived in the following way. Dividing both sides of (3.93) by each other gives

$$P = \left(Q + \frac{V^2}{x_d}\right) \cdot \tan\delta_{gt}. \tag{3.96}$$

Substituting $\delta = \delta_{MAX}$ leads to

$$P = mQ + c \quad \text{where} \quad m = \tan\delta_{MAX} \quad \text{and} \quad c = \frac{V^2}{x_d}\tan\delta_{MAX}. \tag{3.97}$$

In the P–Q plane, this equation describes a straight line intersecting the reactive power axis at the angle δ_{MAX} and at the point $P = 0$ or $Q = -c/m = -V^2/x_d$. In Figure 3.19, this line is drawn with a dot–dashed line from A to B.

There is no simple mathematical formulation describing constraint (iv) corresponding to the end region heating limit. The relevant curve has to be determined experimentally by the manufacturer. This constraint manifests itself when the generator loading is high and capacitive and is shown in Figure 3.19 by line B–C.

Constraint (iv) is concerned with turbine power and depends on the type of turbine. For steam turbines, the upper constraint P_{MAX} is due to the maximum (rated) output of the turbine while the lower constraint P_{min} is due to the stable operation of burners at a low turbine output. In Figure 3.19, the upper and lower limits correspond to straight vertical lines P_{MAX} and P_{min}.

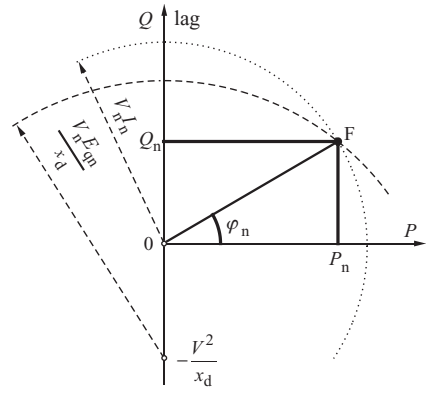

Figure 3.20 Determination of the rated operating point of the synchronous generator.

The border line of the allowed generation, that is when no constraint is breached, is shown in Figure 3.19 by a bold line. It is the polygon ABCDEFG in which each of the sides corresponds to one the discussed constraints.

It should be noted that all three electrical constraints (i), (ii) and (iii) depend on the terminal generator voltage V. The value of the voltage influences the radius of the circle (3.92), the radius and displacement of the circle (3.95) and also the position of the straight line (3.97). The higher the value of V, the wider the area of the polygon ABCDEFG. Hence the characteristic $Q(P)$ shown in Figure 3.19 is always determined assuming a given voltage, usually rated.

Of particular interest is the range of allowed powers P and Q corresponding to the rated voltage $V = V_n$ and under the assumption that the stator and rotor windings are not overloaded, that is the maximum currents in those windings are equal to their rated currents: $I_{MAX} = I_n$ and $I_{fMAX} = I_{fn}$ or $E_{qMAX} = E_{qn}$. Figure 3.20 illustrates this. The dotted line shows a circle corresponding to the rated stator current I_n. The dashed line shows a circle corresponding to the rated rotor current $I_f = I_{fn}$. Point F, lying on the intersection between the two circles, is the rated operating point of the generator as at that point all the quantities are rated, that is $V = V_n$, $I = I_n$, $I_f = I_{fn}$. Figure 3.20 also shows the values of P_n, Q_n and φ_n which are, respectively, the rated powers and the rated phase angle.

Generator nameplate data are usually V_n, P_n and φ_n. For further consideration it is useful to determine the value of $E_{qMAX} = E_{qn}$ as a function of V_n, P_n and φ_n. That relationship can be derived from (3.95). Simple algebra gives

$$E_q^2 = V^2 \left[\left(1 + x_d \frac{Q}{V^2} \right)^2 + \left(x_d \frac{P}{V^2} \right)^2 \right]. \tag{3.98}$$

For the rated values

$$E_{qn}^2 = V_n^2 \left[\left(1 + x_d \frac{Q_n}{V_n^2} \right)^2 + \left(x_d \frac{P_n}{V_n^2} \right)^2 \right]. \tag{3.99}$$

Substituting $x_d = x_{d\,pu} V_n^2 / S_n$, where $x_{d\,pu}$ is in per-unit form, and using $\sin \varphi_n = Q_n / S_n$ and $\cos \varphi_n = P_n / S_n$ (see Figure 3.20), gives

$$E_{qn}^2 = V_n^2 \left[\left(1 + x_{d\,pu} \sin \varphi_n \right)^2 + \left(x_{d\,pu} \cos \varphi_n \right)^2 \right], \tag{3.100}$$

Simple transformations result in

$$E_{\mathrm{qn}} = k_{\mathrm{fn}} V_{\mathrm{n}} \quad \text{where} \quad k_{\mathrm{fn}} = \sqrt{1 + x_{\mathrm{d\,pu}}(x_{\mathrm{d\,pu}} + 2 \cdot \sin \varphi_{\mathrm{n}})}. \tag{3.101}$$

This means that E_{qn} is proportional to V_{n} with the reactance $x_{\mathrm{d\,pu}}$ and $\sin \varphi_{\mathrm{n}}$ as parameters.

3.3.5 Voltage–Reactive Power Capability Characteristic $V(Q)$

The capability curve $Q(P)$ shown in Figure 3.19 characterizes the generator–transformer unit as a source of real and reactive power while taking into account the constraints and assuming that the transformer terminal voltage is a parameter. When assessing the generator as a voltage and reactive power source, it is important to consider a capability characteristic $V(Q)$ of the unit equipped with the automatic voltage regulator (AVR) discussed in Section 2.2.2 and assuming that real power P is a parameter. The task of the AVR is to maintain a required value of the voltage at a given point in the network while observing the constraints.

According to Figure 2.5, the AVR maintains a measured voltage

$$\underline{V}_{\mathrm{C}} = \underline{V}_{\mathrm{g}} + \underline{Z}_{\mathrm{C}} \underline{I}, \tag{3.102}$$

which is the generator terminal voltage with added voltage drop on the compensator impedance $\underline{Z}_{\mathrm{C}} = (R_{\mathrm{C}} + \mathrm{j} X_{\mathrm{C}})$. It is equal to the voltage at a fictitious point inside the transmission network displaced from the generator terminals by the impedance $\underline{Z}_{\mathrm{C}}$. The task of the AVR is to maintain the voltage $\underline{V}_{\mathrm{C}}$ at that fictitious measurement point.

Figure 3.21 shows a simplified equivalent circuit and a phasor diagram to illustrate the principle of voltage regulation. The resistance of the generator and transformer has been neglected. The compensation resistance has also been neglected, $R_{\mathrm{C}} \cong 0$, so that $\underline{Z}_{\mathrm{C}} \cong -\mathrm{j} X_{\mathrm{C}}$, where $X_{\mathrm{C}} = (1 - \kappa)\, X_{\mathrm{T}}$. Hence the fictitious measurement point is assumed to be located at a distance $\kappa\, X_{\mathrm{T}}$ from the transformer terminals and at a distance $X_{\mathrm{k}} = (1 - \kappa)\, X_{\mathrm{T}}$ from the generator terminals, see Figure 3.21. $\underline{V}_{\mathrm{g}}$ is the generator terminal voltage and $\underline{V}$ is the transformer terminal voltage.

The characteristic $V(Q)$ of the generator as a reactive power source, with real power P as a parameter, will be determined by considering four characteristic operating regimes:

(i) The field current is less that its limit, $I_{\mathrm{f}} < I_{\mathrm{fMAX}}$, and the generator controls the voltage at a given point in the transmission network.
(ii) The field current I_{f} is at maximum, $I_{\mathrm{f}} = I_{\mathrm{fMAX}}$, so that the generator operates with a constant emf $E_{\mathrm{q}} = E_{\mathrm{qMAX}}$.

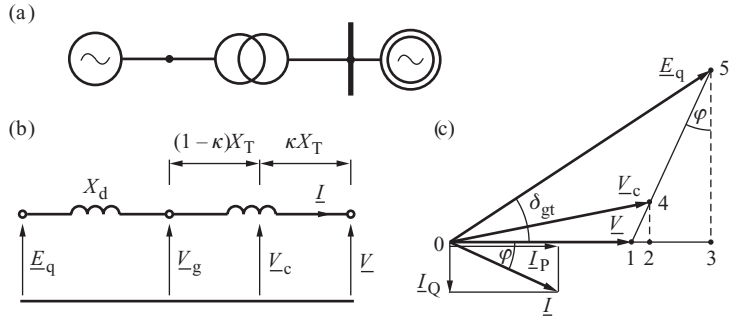

Figure 3.21 The choice of the voltage regulation point for a generator–transformer unit: (a) block diagram; (b) simplified equivalent circuit; (c) phasor diagram.

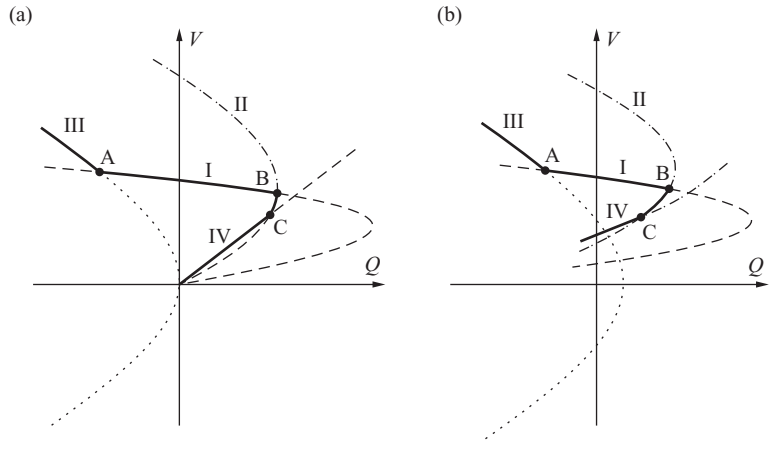

Figure 3.22 Characteristic $V(Q)$ and its elements when: (a) $P = 0$ and (b) $P \neq 0$.

(iii) The power angle δ is at its maximum, $\delta = \delta_{MAX}$, and the reactive power Q is controlled within the limits.
(iv) The stator current I is at its maximum, $I = I_{MAX}$, and the reactive power Q is controlled within the limits.

Each of the four operating conditions can be described by a separate characteristic $V(Q)$ which will be combined to form the overall $V(Q)$ characteristic of the generator–transformer unit shown in Figure 3.22.

3.3.5.1 $I_f < I_{fMAX}$ and AVR Controls the Voltage

For this operating regime, the characteristic $V(Q)$ is determined by the position of the voltage regulation point. When $\kappa = 1$, the AVR controls the voltage at the generator terminals, and when $\kappa = 0$, the AVR controls the voltage at the transformer terminals (Figure 3.21). In practice, a small positive value of κ is chosen so that the voltage regulation point is located inside the transformer, close to its high-voltage terminals.

The voltages on both sides of the transformer are $\underline{V}_C$ and $\underline{V}$, see Figure 3.21. For a reactance κX_T between the generator transformer and the voltage regulation point, a relationship similar to (3.94) can be derived:

$$P^2 + \left(Q + \frac{V^2}{\kappa X_T}\right)^2 = \left(\frac{V_p V}{\kappa X_T}\right)^2, \tag{3.103}$$

When the field current limit is not exceeded, the regulator maintains a reference voltage value $V_C = V_{C\,ref}$, where $V_{C\,ref}$ is the set value of the voltage at the regulation point. Simple algebra transforms the above equation to

$$Q = \sqrt{\left(\frac{V_{C\,ref} V}{\kappa X_T}\right)^2 - P^2} - \frac{V^2}{\kappa X_T}. \tag{3.104}$$

When $P = 0$, this equation simplifies to

$$Q = \frac{V}{\kappa X_T}(V_{C\,ref} - V). \tag{3.105}$$

The resulting characteristic $Q(V)$ is denoted by Roman numeral I in Figure 3.22 and shown using a dashed line. It is an inverted parabola crossing the V-axis at $V = 0$ and $V = V_{C\,ref}$. The peak of the parabola reaches the value $Q_{MAX} = V_{C\,ref}^2/4\kappa X_T$ when $V = V_{C\,ref}/2$. The smaller the value of κ, the higher the value of Q_{MAX} and the parabola becomes slimmer. When $P \neq 0$, the parabola moves along the V-axis towards positive values and its peak Q_{MAX} becomes smaller.

3.3.5.2 Maximum Field Current

When the field current is maximum, $I_f = I_{fMAX}$, the generator becomes a voltage source with constant emf $E_q = E_{qMAX}$ behind the reactance $x_d = X_d + X_T$. After simple algebra, an equation similar to (3.95) is obtained:

$$Q = \sqrt{\left(\frac{E_{qMAX}V}{x_d}\right)^2 - P^2} - \frac{V^2}{x_d}. \tag{3.106}$$

The resulting characteristic $Q(V)$ is denoted by Roman numeral II in Figure 3.22 and shown using a dot–dashed line. It is also an inverted parabola. For $P = 0$ the parabola crosses the V-axis at $V = 0$ and $V = E_{qMAX}$, while its peak reaches the value $Q_{MAX} = E_{qMAX}^2/4x_d$ when $V = E_{qMAX}/2$. For $P \neq 0$, the parabola moves along the V-axis towards positive values and its peak Q_{MAX} becomes smaller.

3.3.5.3 Maximum Power Angle

When $\delta_{gt} = \delta_{MAX}$, Equation (3.96) can be transformed to

$$Q = P \cdot \arctan\delta_{MAX} - \frac{V^2}{x_d}. \tag{3.107}$$

The resulting characteristic $Q(V)$ is denoted by Roman numeral III in Figure 3.22 and shown using a dotted line. It is an inverted parabola symmetrical with respect to the V-axis. Its peak is at $Q_{MAX} = P \cdot \arctan\delta_{MAX}$ while its roots are at $V = \pm\sqrt{P \cdot x_d \cdot \arctan\delta_{MAX}}$.

3.3.5.4 Maximum Stator Current

Now Equation (3.91) can be transformed to

$$V = \frac{\sqrt{P^2 + Q^2}}{I_{MAX}}. \tag{3.108}$$

The resulting characteristic $Q(V)$ is denoted by Roman numeral IV in Figure 3.22 and shown using a double-dot–dashed line. When $P = 0$ the equation simplifies to $V = Q/I_{MAX}$ and the characteristic $V(Q)$ becomes a straight line crossing the origin ($V = 0$, $Q = 0$). When $P \neq 0$ a curved line crosses the V-axis at $V = P/I_{MAX}$.

3.3.5.5 Combined Characteristic

The combined characteristic taking into account all the constraints consists of the four segments I, II, III, IV and is shown in Figure 3.22 using a bold line. The left hand side of the characteristic

corresponds to a capacitive loading of the generator. In the area limited by segment III, regulator operation is constrained by the power angle and the voltage depends strongly on reactive power. Increasing capacitive loading causes a strong voltage rise. The middle part of the characteristic between points A and B corresponds to segment I when the regulator can change the field current while controlling the voltage. Changing reactive loading hardly influences the transformer terminal voltage. The slope of the characteristic depends on how slim the characteristic is as explained below.

When point B is reached, the generator starts to operate with a maximum field current and cannot produce more reactive power. When the voltage drops, the reactive power produced decreases according to segment II until it reaches point C. Further reduction in the voltage results in the stator current becoming the limiting factor as shown by segment IV.

These considerations show that a synchronous generator operating as the reactive power source has a quite complicated nonlinear characteristic due to the limits imposed by the AVR. It is important to appreciate the following:

1. Along segment I, when the voltage drops, the generator produces more reactive power. When the constraints are reached the generator behaves the other way around: that is, when the voltage drops, the generator produces less reactive power moving along segments II and IV. This may cause worsening of the reactive power balance leading to voltage instability (Chapter 8).
2. The influence of real power on the shape of the characteristic is very strong as revealed by comparing both diagrams in Figure 3.22. When real power production is small, the distance between points A and B is large. When real power production increases, points A and B get closer to each other so that the stabilizing action of the AVR is possible for only a small range of reactive power changes. Moreover, when real power output is high, the curvature of the characteristic is stronger, which means that falling voltage causes a faster drop in reactive power output and therefore is more dangerous from the voltage stability point of view.

The slope of parabola (3.104) or (3.105) in the segment A–B depends on the value of κX_T, that is on the choice of the voltage regulation point – see Figure 3.21. This can be proved by deriving the derivative $\mathrm{d}V/\mathrm{d}Q$ under a simplifying assumption that $P = 0$ when (3.105) holds. For the upper part of the parabola, the voltage can be calculated from (3.105) as

$$V = \frac{1}{2} V_{C\,\mathrm{ref}} + \frac{1}{2}\sqrt{V_{C\,\mathrm{ref}}^2 - 4\kappa X_T Q}. \tag{3.109}$$

After differentiation,

$$\frac{\mathrm{d}V}{\mathrm{d}Q} = -\frac{\kappa X_T}{\sqrt{V_{C\,\mathrm{ref}}^2 - 4\kappa X_T Q}}. \tag{3.110}$$

The square root in the denominator can be eliminated using (3.109) leading to

$$\frac{\mathrm{d}V}{\mathrm{d}Q} = -\frac{\kappa X_T}{2V - V_{C\,\mathrm{ref}}}. \tag{3.111}$$

If $V = V_{C\,\mathrm{ref}}$ then

$$\left.\frac{\mathrm{d}V}{\mathrm{d}Q}\right|_{V = V_{C\,\mathrm{ref}}} = -\frac{\kappa X_T}{V_{C\,\mathrm{ref}}}. \tag{3.112}$$

This equation shows that the smaller is κX_T, the smaller is the slope of the voltage capability characteristic shown in Figure 3.21, segment A–B. If κX_T is small then the parabola denoted by I is slim and with a peak far away from the vertical axis, that is Q_{MAX} is large. When the slope is small, the changes in reactive power hardly influence the transformer terminal voltage V. This

is understandable because, for small values of κX_T, the voltage regulation point is close to the transformer terminals.

The minus sign in (3.112) means that increased reactive power causes a reduction in the voltage – see Figure 3.22.

A general equation for dV/dQ when $P \neq 0$ could also be derived using (3.104). This is, however, more complicated and would not illustrate so clearly the underlying mechanisms.

3.3.5.6 Voltage–Current Regulation Characteristic $V(I_Q)$

In practice, engineers use much simpler equations to describe a voltage–current regulation characteristic $V(I_Q)$ where I_Q denotes the reactive component of the current. The relevant equations can be derived using the phasor diagram shown in Figure 3.21. The distance between points 1 and 4 corresponds to the voltage drop on the reactance κX_T, so it is equal to $|1-4| = \kappa X_T I$. Hence the distance between point 1 and 2 is $|1-2| = \kappa X_T I \sin\varphi = \kappa X_T I_Q$ and the distance between points 0 and 2 is $|0-2| = V + \kappa X_T I_Q$. It can be assumed that that the distance between points 0 and 4 is approximately the same as the distance between points 0 and 2. Hence $V_C = |0-4| \cong |0-2| = V + \kappa X_T I_Q$ so that

$$V \cong V_C - \kappa X_T I_Q. \tag{3.113}$$

A similar analysis can be applied to the distances between points 1, 5, 3 and 0. Taking into account that the distance between points 1 and 4 corresponds to the voltage drop on the reactance $x_d = X_d + X_T$, one gets $E_q = |0-5| \cong |0-3| = V + (X_d + X_T) I_Q$. Hence

$$V \cong E_q - (X_d + X_T) I_Q. \tag{3.114}$$

Equations (3.113) and (3.114) correspond to two characteristics shown in Figure 3.23. The characteristic shown in Figure 3.23a is valid when the AVR is active and it is a rough approximation of the linear characteristic I from Figure 3.22. The slope of that characteristic corresponds to an angle α where $\tan\alpha = \kappa X_T$. This matches Equation (3.112) but with an additional requirement that $V_{C\,ref}$ is used, as (3.112) was concerned with reactive power while (3.113) is concerned with the reactive component of the current.

The tangent of the angle α is referred to as the droop of that characteristic. It depends on the coefficient κ defining the value κX_T and the position of the voltage regulation point.

The characteristic shown in Figure 3.23b is valid when the AVR is not active and the synchronous emf of the generator is constant. It is a rough linear approximation of characteristic II from

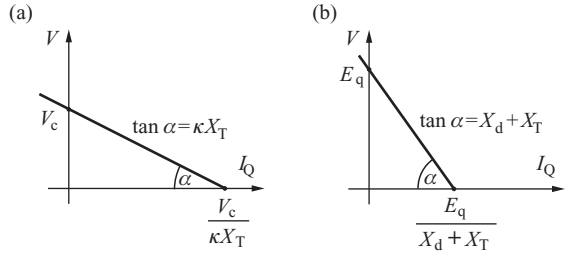

Figure 3.23 Voltage–current characteristics with: (a) acting AVR controlling V_C; (b) constant generator synchronous emf E_q.

Figure 3.22. The slope of the characteristic corresponds to angle α for which

$$\tan\alpha = x_d = X_d + X_T. \tag{3.115}$$

The slope is steeper as $(X_d + X_T) \gg \kappa X_T$. A steeper slope means that when the AVR is not acting, changes in the generator reactive power loading cause large changes in the transformer terminal voltage.

Generally the compensation impedance does not have to match the position of the measurement point inside the step-up transformer, see Figure 3.21. When a generator is connected to the transmission via a radial transmission line, $\underline{Z}_C$ may encroach into the line.

The main aim of using current compensation in the AVR is to make the power station terminal voltage insensitive to reactive power loading. The droop of the regulator characteristic depends on the compensation reactance. Equations (3.112), (3.113) and Figure 3.23 show that the smaller the droop of the characteristic, the smaller the sensitivity of the terminal voltage to the reactive power.

3.3.6 Including the Equivalent Network Impedance

Synchronous generators are rarely used to supply individual loads but are connected to a power system that consists of a large number of other synchronous generators and loads linked by the transmission network (Figure 2.1). The power rating of an individual generator is usually many times smaller than the sum of the power ratings of all the remaining generators in the system. Therefore, for a simplified analysis, these remaining generators in the system can be treated as one equivalent, very large, generating unit with an infinite power rating. This equivalent generating unit is referred to as the *infinite busbar* and can be represented on a circuit diagram as an ideal voltage source behind an equivalent system impedance. The infinite busbar maintains a constant terminal voltage and is capable of absorbing all the active and reactive power output of the generator in question.

This concept is illustrated in Figure 3.24 where the generator is connected to the system via a step-up transformer, represented by the series impedance $\underline{Z}_T = R_T + jX_T$ (the shunt admittance is neglected). It is assumed that the ideal transformer has been eliminated from the circuit diagram by either using per units or recalculating all the quantities using a common voltage level. The rest of the power system is represented by the infinite busbar, that is by the ideal voltage source $\underline{V}_s$ behind the equivalent system impedance $\underline{Z}_s = R_s + jX_s$ (again the shunt admittance is neglected). The impedance $\underline{Z}_s$ combines the transmission network and remaining generators in the system.

The infinite busbar is assumed to have constant voltage and frequency, neither of which is influenced by the action of an individual generator. This means that the voltage $\underline{V}_s$ can be used as a reference and the phase angles of all the other voltages and currents in the circuit measured with respect to it. Of particular importance is the power angle δ, which defines the phase shift

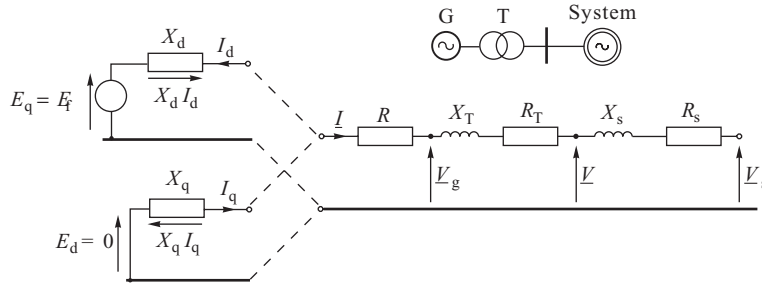

Figure 3.24 Equivalent circuit of the generator operating on an infinite busbar.

between $\underline{E}_f$ and $\underline{V}_s$. As all the angles in the phasor diagram have a dual time/space meaning, δ is also the *spatial* angle between the two synchronously rotating rotors: that of the generator under consideration and that of the fictitious generator replacing the power system. This spatial angle is referred to as the rotor angle and has the same numerical value (in electrical radians) as the power angle. As the 'rotor' of the infinite busbar is not affected by an individual generator, this 'rotor' also provides a synchronously rotating reference axis with respect to which the *space position* of all the rotors may be defined. This dual meaning of rotor/power angle is very important and will be used extensively throughout this book.

The elements of the equivalent circuit may be combined to give the total parameters

$$x_d = X_d + X_T + X_s; \quad x_q = X_q + X_T + X_s; \quad r = R + R_T + R_s. \tag{3.116}$$

All the equations derived earlier in this chapter and the phasor diagram shown in Figure 3.16 can still be used by replacing X_d by x_d, X_q by x_q, R by r and $\underline{V}_g$ by $\underline{V}_s$. Also the angle δ_g must be replaced by the phase shift δ between $\underline{E}_f$ and $\underline{V}_s$. With these modifications the round-rotor generator can be described by the following equation (corresponding to Equation (3.47)):

$$\underline{E}_f = \underline{V}_s + r\underline{I} + \mathrm{j}x_d\underline{I}, \tag{3.117}$$

while the salient-pole generator can be described by an equation similar to Equation (3.62):

$$\underline{E}_f = \underline{V}_s + r\underline{I} + \mathrm{j}x_d\underline{I}_d + \mathrm{j}x_q\underline{I}_q. \tag{3.118}$$

This equation can be broken down into its d- and q-axes components to obtain equations similar to Equation (3.65)

$$\begin{aligned} E_d &= V_{sd} + r I_d + x_q I_q = 0 \\ E_q &= E_f = V_{sq} + r I_q - x_d I_d, \end{aligned} \tag{3.119}$$

which can be expressed in matrix form as

$$\begin{bmatrix} E_d \\ E_q \end{bmatrix} = \begin{bmatrix} 0 \\ E_f \end{bmatrix} = \begin{bmatrix} V_{sd} \\ V_{sq} \end{bmatrix} + \begin{bmatrix} r & x_q \\ -x_d & r \end{bmatrix} \begin{bmatrix} I_d \\ I_q \end{bmatrix} \quad \text{or} \quad \boldsymbol{E}_{dq} = \boldsymbol{V}_{sdq} + \boldsymbol{Z}_{dq}\boldsymbol{I}_{dq}, \tag{3.120}$$

where

$$\begin{aligned} V_{sd} &= -V_s \sin\delta, \qquad V_{sq} = V_s \cos\delta \\ I_d &= -I \sin\beta, \qquad I_q = I \cos\beta \end{aligned} \tag{3.121}$$

and $\beta = \delta + \varphi$.

Equations (3.120) and (3.121) allow formulae for the active and reactive power supplied by the generator to the system to be derived.

3.3.6.1 Real Power

Solving Equation (3.120) with respect to the currents gives

$$\begin{bmatrix} I_d \\ I_q \end{bmatrix} = \frac{1}{Z^2} \begin{bmatrix} r & -x_q \\ x_d & r \end{bmatrix} \begin{bmatrix} 0 - V_{sd} \\ E_q - V_{sq} \end{bmatrix}, \tag{3.122}$$

where $Z^2 = \det Z_{dq} = r^2 + x_d x_q$.

The real power supplied by each phase of the generator to the network (the infinite busbar in Figure 3.24) is given by

$$\begin{aligned} P_s &= V_s I\cos\varphi = V_s I\cos(\beta-\delta) = V_s I\sin\beta\sin\delta + V_s I\cos\beta\cos\delta \\ &= V_{sd}I_d + V_{sq}I_q = \frac{1}{Z^2}\left\{V_{sd}\left[-r\,V_{sd} - x_q\left(E_q - V_{sq}\right)\right] + V_{sq}\left[-x_d V_{sd} + r\left(E_q - V_{sq}\right)\right]\right\} \\ &= \frac{1}{Z^2}\left[-r(V_{sq}^2 + V_{sd}^2) - (x_d - x_q)V_{sd}V_{sq} + E_q(r\,V_{sq} - x_q V_{sd})\right], \end{aligned} \tag{3.123}$$

which, after substituting for V_{sq} and V_{sd} from Equation (3.121), gives

$$P_s = \frac{E_q V_s}{Z}\frac{x_q}{Z}\sin\delta + \frac{V_s^2}{2}\frac{x_d - x_q}{Z^2}\sin 2\delta + \frac{E_q V_s}{Z}\frac{r}{Z}\cos\delta - \frac{V_s^2}{Z}\frac{r}{Z}. \tag{3.124}$$

The second component in Equation (3.124) is referred to as the reluctance power and corresponds to the reluctance torque in the salient-pole generator. It depends on $\sin 2\delta$, vanishes for $\delta = 0^\circ$ and $\delta = 90^\circ$ and is proportional to $x_d - x_q = X_d - X_q$ and inversely proportional to Z^2. As $x_d - x_q = X_d - X_q$ is independent of X_s the Z^2 term tends to dominate this expression so that the reluctance power of a generator connected to the system through a long transmission link (large X_s and Z) can often be neglected.

For round-rotor generators $X_d = X_q$ and the reluctance term vanishes irrespective of the value of the power angle δ. For such generators $Z^2 = r^2 + x_d^2$ and Equation (3.124) can be rearranged as

$$\begin{aligned} P_s &= \frac{E_q V_s}{Z}\cos\mu\sin\delta + \frac{E_q V_s}{Z}\sin\mu\cos\delta - \frac{V_s^2}{Z}\sin\mu \\ &= \frac{E_q V_s}{Z}\sin(\delta+\mu) - \frac{V_s^2}{Z}\sin\mu, \end{aligned} \tag{3.125}$$

where $\sin\mu = r/Z$ and $\cos\mu = x_d/Z$. The active power load on the generator is larger than the real power supplied to the system because of the $I^2 r$ loss in the resistance. If the resistance of the generator and the network is neglected ($r \ll Z$), P_s is equal to the real power load on the generator. In this case, for the salient-pole generator

$$P_s = \frac{E_q V_s}{x_d}\sin\delta + \frac{V_s^2}{2}\frac{x_d - x_q}{x_d x_q}\sin 2\delta, \tag{3.126}$$

while for the round-rotor generator the real power is

$$P_s = \frac{E_q V_s}{x_d}\sin\delta. \tag{3.127}$$

In per units these equations can also be used to express the generator air-gap torque.

3.3.6.2 Reactive Power

The reactive power supplied to the network is given by

$$\begin{aligned} Q_s &= V_s I\sin\varphi = V_s I\sin(\beta-\delta) = V_s I\sin\beta\cos\delta - V_s I\cos\beta\sin\delta \\ &= -V_{sq}I_d + V_{sd}I_q = \frac{1}{Z^2}\left\{V_{sq}\left[r\,V_{sd} + x_q\left(E_q - V_{sq}\right)\right] + V_{sd}\left[-x_d V_{sd} + r\left(E_q - V_{sq}\right)\right]\right\} \\ &= \frac{1}{Z^2}\left(E_q V_{sq} x_q - V_{sq}^2 x_q - V_{sd}^2 x_d + E_q V_{sd} r\right), \end{aligned} \tag{3.128}$$

which, after substituting for V_{sq} and V_{sd} from Equation (3.121), gives

$$Q_s = \frac{E_q V_s}{Z}\frac{x_q}{Z}\cos\delta - \frac{V_s^2}{Z}\frac{x_d \sin^2\delta + x_q \cos^2\delta}{Z} - \frac{E_q V_s}{Z}\frac{r}{Z}\sin\delta. \tag{3.129}$$

For the round-rotor generator $x_d = x_q$ and the second term is independent of δ. Equation (3.129) can then be written as

$$Q_s = \frac{E_q V_s}{Z}\cos(\delta - \mu) - \frac{V_s^2}{Z}\cos\mu. \tag{3.130}$$

If the resistance r is neglected then $Z = x_d$, $\mu = 0$, $\cos\mu = 1$ and this equation simplifies to

$$Q_s = \frac{E_q V_s}{x_d}\cos\delta - \frac{V_s^2}{x_d}. \tag{3.131}$$

A generator supplies reactive power to the system, and operates at a lagging power factor, when the field current, and consequently E_q, is high enough to make the first component in Equation (3.131) larger than the second. This state of operation is referred to as *overexcitation*.

On the other hand, a low value of the field current, and E_q, will make the second component of Equation (3.131) larger than the first; the generator will then supply negative reactive power to the system and will operate at a leading power factor. This state of operation is referred to as *underexcitation*.

As will be explained in Section 3.5, a typical power system load contains a high proportion of induction motors. Such a load operates at a lagging power factor and consumes positive reactive power. For this reason generators are usually overexcited, operate at lagging power factor and supply positive reactive power to the system. Overexcited generators operate at a high value of E_q, which is also important for stability reasons as explained in Chapters 5 and 6.

3.3.6.3 Steady-State Power–Angle Characteristic

Figure 3.16 shows the phasor diagram of a generator operating under a particular load as defined by the length and direction of the current phasor $\underline{I}$. Obviously the diagram will change if the load is changed. However, the way in which the diagram will change depends on whether the AVR is active or not. When the AVR is active it will try to maintain a constant voltage at some point after the generator terminals by changing the excitation (see Section 2.2.2). This mode of operation is closely related to steady-state stability and will be considered in Chapter 5. In the present chapter, only the case when the AVR is inactive will be considered. The excitation is then constant, $E_f = E_q$ = constant, and any change in load will change the generator terminal voltage V_g, the angle δ_g and the power angle δ. If the resistance r is neglected then the real power supplied by the generator to the system is given by Equation (3.126) which is repeated here for convenience:

$$P_{sE_q} = \frac{E_q V_s}{x_d}\sin\delta + \frac{V_s^2}{2}\frac{x_d - x_q}{x_d x_q}\sin 2\delta. \tag{3.132}$$

In this equation the subscript E_q in P_{sE_q} has been added to emphasize that this formula is valid for the case E_q = constant. Note that P_{sE_q} is a function of the power angle δ only. Function $P_{sE_q}(\delta)$ is referred to as the *power–angle characteristic* of the generator operating on the infinite busbar and is shown in Figure 3.25.

The reluctance power term deforms the sinusoidal characteristic so that the maximum of $P_{sE_q}(\delta)$ occur at $\delta < \pi/2$. For the round-rotor generators the maximum of $P_{sE_q}(\delta)$ occurs at $\delta = \pi/2$.

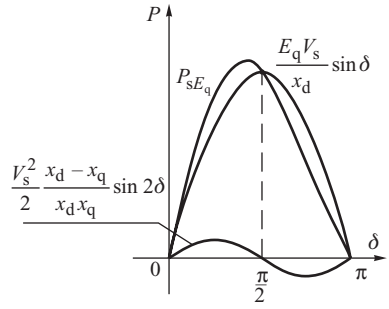

Figure 3.25 Power–angle characteristic $P_{sE_q}(\delta)$ for E_q = constant.

3.4 Power System Loads

The word 'load' can have several meanings in power system engineering, including:

- a device connected to the power system that consumes power;
- the total active and/or reactive power consumed by all devices connected to the power system;
- the power output of a particular generator or plant;
- a portion of the system that is not explicitly represented in the system model, but treated as if it were a single power-consuming device.

This section deals with loads that conform to the last definition. Chapter 2 explained that electrical power systems are large, complex structures consisting of power sources, transmission and subtransmission networks, distribution networks and a variety of energy consumers. As the transmission and subtransmission networks connect the main generation and load centres, they are quite sparse, but as the distribution networks must reach every consumer in their service area, they are very dense. This means that a typical power system may consist of several hundred nodes at the transmission and subtransmission levels, but there could be a hundred thousand nodes at the distribution level. Consequently, when power systems are analysed only the transmission and subtransmission levels are considered and the distribution networks are not usually modelled as such, but replaced by equivalent loads, sometimes referred to as *composite loads*. Usually each composite load represents a relatively large fragment of the system typically comprising low- and medium-voltage distribution networks, small power sources operating at distribution levels, reactive power compensators, distribution voltage regulators, and so on, and includes a large number of different component loads such as motors, lighting and electrical appliances. Determining a simple and valid composite load model is therefore not an easy problem and is still the subject of intensive research (IEEE Task Force, 1995). In this chapter, only a simple static composite load model will be described while dynamic models will be described in Chapter 11.

In the steady state the demand of the composite load depends on the busbar voltage V and the system frequency f. The functions describing the dependence of the active and reactive load demand on the voltage and frequency $P(V, f)$ and $Q(V, f)$ are called the *static load characteristics*. The characteristics $P(V)$ and $Q(V)$, taken at constant frequency, are called the *voltage characteristics* while the characteristics $P(f)$ and $Q(f)$, taken at constant voltage, are called the *frequency characteristics*.

The slope of the voltage or frequency characteristic is referred to as the *voltage (or frequency) sensitivity* of the load. Figure 3.26 illustrates this concept with respect to voltage sensitivities. Frequency sensitivities are defined in a similar way.

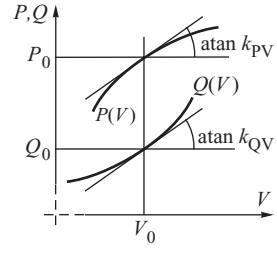

Figure 3.26 Illustration of the definition of voltage sensitivities.

The voltage sensitivities k_{PV} and k_{QV} and the frequency sensitivities k_{Pf} and k_{Qf} are usually expressed in per units with respect to the given operating point:

$$k_{PV} = \frac{\Delta P/P_0}{\Delta V/V_0}, \quad k_{QV} = \frac{\Delta Q/Q_0}{\Delta V/V_0}, \quad k_{Pf} = \frac{\Delta P/P_0}{\Delta f/f_0}, \quad k_{Qf} = \frac{\Delta Q/Q_0}{\Delta f/f_0}, \tag{3.133}$$

where P_0, Q_0, V_0 and f_0 are the real power, reactive power, voltage and frequency at a given operating point.

A load is considered to be *stiff* if, at a given operating point, its voltage sensitivities are small. If the voltage sensitivities are equal to zero then the load is *ideally stiff* and the power demand of that load does not depend on the voltage. A load is voltage sensitive if the voltage sensitivities are high and small changes in the voltage cause high changes in the demand. Usually voltage sensitivity of real power demand is less than voltage sensitivity of reactive power demand.

As the characteristics of the composite load depend on the characteristics of its individual components, it is first of all necessary to examine the characteristics of some of the more important individual loads. This will then be developed into a more general composite load model.

3.4.1 Lighting and Heating

About one-third of electricity consumption is on lighting and heating. Traditional bulb lighting prevails in residential areas while discharge lights (fluorescent, mercury vapour, sodium vapour) dominate in commercial and industrial premises. Traditional electric bulbs consume no reactive power and their power demand is frequency independent but, as the temperature of the filament depends on the voltage, the bulb cannot be treated as a constant impedance. Figure 3.27a shows the relevant characteristic.

Fluorescent and discharge lighting depends heavily on the supply voltage. When the voltage drops to below 65–80 % of the rated value the discharge lights extinguish and will restart with a 1–2 second delay only when the voltage recovers to a value above the extinguish level. When the voltage

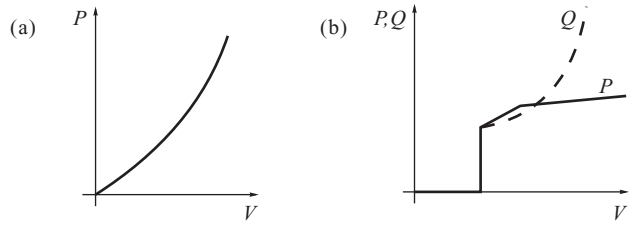

Figure 3.27 Voltage characteristics of: (a) electric bulbs; (b) discharge lighting.

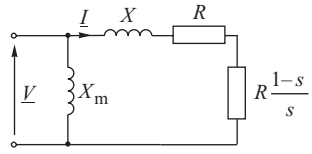

Figure 3.28 Simplified equivalent circuit of induction motor.

is above the extinguish level, the real and reactive power vary nonlinearly with voltage as shown in Figure 3.27b.

Heating loads basically constitute a constant resistance. If a heater is equipped with a thermostat, the thermostat will maintain constant temperature and power output despite any variations in voltage. In such cases the load can be modelled as a constant power rather than a constant resistance.

3.4.2 Induction Motors

About 50–70 % of all electricity is consumed by electric motors with about 90 % of this being used by induction motors. Generally such motors dominate industrial loads to a far greater degree than they do commercial or residential loads.

Figure 3.28 shows the well-known simplified equivalent circuit of the induction motor where X is the equivalent reactance of the stator and rotor windings, R is the rotor resistance, X_m is the magnetizing reactance and s is the *motor slip* defined as $s = (\omega_s - \omega)/\omega_s$. This equivalent circuit will be discussed in detail in Chapter 7. Here it is used to derive the reactive power–voltage characteristic of an induction motor as the load in power system.

3.4.2.1 Power–Slip Characteristic

The square of the current flowing through the series branch is $I^2 = V^2/\left[X^2 + (R/s)^2\right]$ where V is the supply voltage. The real power demand due to this current is then

$$P_e = I^2 \frac{R}{s} = V^2 \frac{Rs}{R^2 + (Xs)^2}. \tag{3.134}$$

The solid lines in Figure 3.29a show the variation of P_e with slip for different values of V. By differentiating the power expression it can be shown that the maximum loading $P_{max} = V^2/2X$ is reached at the *critical slip* $s = s_{cr} = R/X$. Note that s_{cr} does not depend on the voltage.

The stable operating part of the induction motor characteristic is to the left of the peak, where $s < s_{cr}$. To prove this, consider point 1′ lying to the right of the peak on the highest characteristic. Ignoring for the moment any losses, if point 1′ is an equilibrium point then the electrical power supplied P_e is equal to the mechanical power P_m shown on the diagram as P_0. Now assume that the motor experiences a momentary disturbance causing a decrease in slip (i.e. an increase in speed). This will cause the supplied electrical power to increase. As P_m can be assumed to remain unchanged, the motor draws more power than the load can absorb ($P_e > P_m$) and the excess power accelerates the rotor so that the speed increases further. This increase in speed results in the operating point moving further to the left away from point 1′. Now consider another momentary disturbance causing an increase in slip (drop in speed). This will cause P_e to drop, resulting in a deficit of power and further slowing down of the rotor. The slip increases further and the motor finally stops at $s = 1$.

The situation is reversed at the stable equilibrium point 1. At this point any disturbance causing a decrease in slip (i.e. an increase in speed) will result in a decrease in the power supplied to the

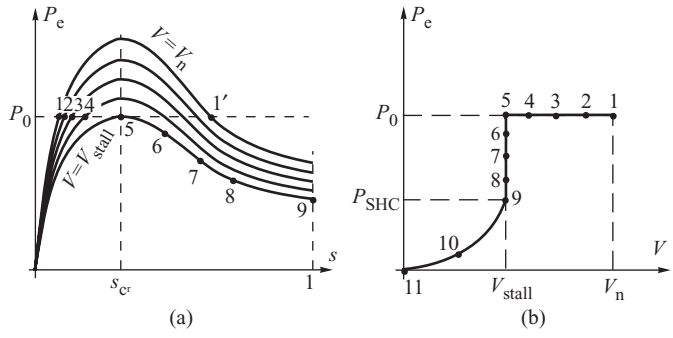

Figure 3.29 Induction motor characteristics: (a) family of $P_e\,(s)$ characteristics for different values of V; (b) $P_e\,(V)$ characteristic of the motor loaded with a constant torque.

motor. This deficit of power ($P_e < P_m$) will result in the motor slowing down (increasing the slip) until it returns to point 1. In a similar way the motor will return to point 1 when subjected to a disturbance causing an increase in slip.

3.4.2.2 Real Power–Voltage Characteristic

The motor's operating point corresponds to the intersection of the motor characteristic $P_e(s)$ with that of the mechanical load $P_m(s)$. Mechanical loads can be categorized as either *easy starting* (zero torque at starting) or *heavy starting* (a non-zero torque at starting). For further analysis the special case of a heavy starting load with a constant mechanical torque τ_m will be considered. This type of load will allow the voltage characteristics of the motor to be derived. These characteristics will then be generalized to include other types of mechanical load.

If τ_m is constant then the mechanical power developed by the motor is $P_m = \tau_m\omega = \tau_m\omega_s(1-s) = P_0(1-s)$ where $P_0 = \tau_m\omega_s$ and is represented in the equivalent circuit by the power loss in the resistance $R(1-s)/s$. The total motor power demand P_d is obtained by adding P_m to the power loss in the rotor resistance where $P_{loss} = I^2R$, that is

$$P_d = P_m + P_{loss} = P_0(1-s) + I^2R = P_0(1-s) + \frac{V^2Rs^2}{(Xs)^2 + R^2}. \tag{3.135}$$

The value of the operating slip is given by the intersection of the $P_e(s)$ and $P_d(s)$ characteristics. Equation $P_e(s) = P_d(s)$ gives

$$\frac{V^2Rs}{(Xs)^2 + R^2} = P_0(1-s) + \frac{V^2Rs^2}{(Xs)^2 + R^2}, \tag{3.136}$$

which, assuming that the motor is not stalled ($s \neq 1$), gives the following equation after some simple algebra:

$$s^2 - 2as_{cr}s + s_{cr}^2 = 0, \tag{3.137}$$

where $a = V^2/(2P_0X)$ and $s_{cr} = R/X$. The roots of this equation are

$$s_{1,2} = s_{cr}\left[a \pm \sqrt{a^2 - 1}\right]. \tag{3.138}$$

The roots are real only if $|a| \geq 1$, that is $V \geq \sqrt{2P_0X}$. Hence the minimum supply voltage for which the motor can still operate, referred to as the *stalling voltage*, is $V_{stall} = \sqrt{2P_0X}$. For $V > V_{stall}$

there are two different roots s_1 and s_2 with the smaller root corresponding to the stable operating point (i.e. that part of the characteristic to the left of the peak). Substituting this root into Equation (3.134) gives

$$P_e|_{s=s_{1,2}} = \frac{V^2}{X} \frac{Rs_{cr}\left(a \pm \sqrt{a^2-1}\right)}{R^2 + X^2 s_{cr}^2 \left(a \pm \sqrt{a^2-1}\right)^2} = \frac{V^2}{X} \frac{a \pm \sqrt{a^2-1}}{1 + \left(a \pm \sqrt{a^2-1}\right)^2} = \frac{V^2}{2aX} = P_0. \quad (3.139)$$

This shows that for a heavy-starting load with τ_m = constant the real power demand is independent of both the supply voltage and the slip. This is shown in Figure 3.29a by the dashed horizontal line $P = P_0$. Figure 3.29b shows the resulting $P_e(V)$ characteristic obtained in the following way.

Assume that the motor initially operates at rated voltage ($V = V_n$) so that the equilibrium point corresponds to point 1 on the top characteristic. A decrease in the supply voltage will lower the power–slip characteristic and shift the operating point to the right, as shown by points 2, 3 and 4 in Figure 3.29a. As real power demand is constant, the $P_e(V)$ characteristic corresponding to points 1, 2, 3 and 4 is horizontal as shown in Figure 3.29b. The lowest characteristic in Figure 3.29a corresponds to the stalling voltage $V = V_{stall}$. The operating point is at point 5 and the slip is critical ($s = s_{cr}$). Any further slight decrease in voltage will result in the motor slip increasing along the lowest, unstable, characteristic (points 6, 7 and 8) until the motor finally stalls ($s = 1$) at point 9. As the motor moves along this stalling characteristic, the real power decreases while the voltage is constant and slip increases. Consequently the $P_e(V)$ characteristic for points 6, 7 and 8 is vertical as shown in Figure 3.29b. At point 9 the slip is $s = 1$ and the motor consumes its short-circuit power, $P_{SHC} = V^2 R/(X^2 + R^2)$. Any further decrease in voltage will cause a decrease in the real power demand which can be calculated from Equation (3.135) as

$$P_e(s)|_{s=1} = \frac{V^2 R}{X^2 + R^2}. \quad (3.140)$$

This is shown by the parabola 9, 10, 11 in Figure 3.29b.

3.4.2.3 Reactive Power–Voltage Characteristic

The reactive power consumed by each phase of the motor is made up of two components corresponding to each of the two parallel branches shown in Figure 3.28b:

$$Q_m = \frac{V^2}{X_m} \quad \text{and} \quad Q_s = I^2 X = \frac{P_e s}{R} X = P_e \frac{s}{s_{cr}}. \quad (3.141)$$

The component Q_m is associated with the motor magnetizing reactance while the component Q_s depends on the motor load. For a heavy-starting load, with τ_m = constant, the real power demand is $P_e = P_0$ and the slip corresponding to the stable operating point is $s = s_{cr}\left[a - \sqrt{a^2-1}\right]$ (Equation (3.138)). Substituting these values into the expression for Q_s gives

$$Q_s = \frac{V^2}{2X} - \sqrt{\left(\frac{V^2}{2X}\right)^2 - P_0^2} \quad \text{for} \quad V > V_{stall}. \quad (3.142)$$

Figure 3.30 shows Q_m, Q_s and $Q = Q_m + Q_s$ as a function of the voltage. The component $Q_m(V)$ is a parabola starting from the origin and increasing to infinity. The component $Q_s(V)$ tends to zero as $V \to \infty$. As V decreases, $Q_s(V)$ increases until at $V = V_{stall}$ it reaches a value corresponding to point 5. Any decrease in voltage will cause $Q_s(V)$ to move along the unstable part defined by the vertical line 5, 6, 7, 8, 9. At point 9 the motor stalls ($s = 1$). Any further decrease in voltage causes $Q_s(V)$ to decrease along a parabola 9, 10, 11 describing the short-circuit characteristic.

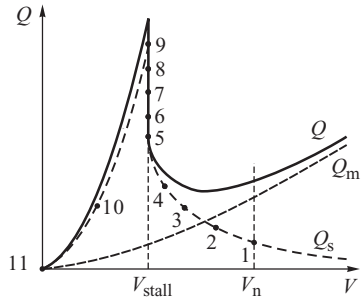

Figure 3.30 Reactive power–voltage characteristics of an induction motor.

The resulting characteristic, $Q(V) = Q_m(V) + Q_s(V)$, is shown by the continuous line in Figure 3.30. Inspection of this characteristic leads to the following conclusions:

- for voltages close to the rated voltage V_n the slope of the characteristic is positive;
- as voltage decreases, the characteristic first becomes flatter (indicating a reduced voltage sensitivity) and then, with a further reduction in voltage, the reactive power increases rapidly to a large value when the motor stalls.

Although a heavy-starting load has been considered here, the actual stalling voltage depends on the type of mechanical load that is being driven by the motor. For heavily loaded motors, driving heavy-starting loads, it can be quite close to the rated voltage. For lightly loaded motors, especially those driving easy-starting mechanical loads, the stalling voltage can be quite small.

3.4.2.4 Influence of Motor Protection and Starter Control

The above considerations do not take into account motor protection or starter control. Many industrial motors have starter controls with electromechanically held AC contactors. If the voltage is too low, such contactors immediately drop out, tripping the motor supply. The dropout voltage ranges from about 0.3 to 0.7 per unit. The effect of this can be modelled by assuming zero real and reactive power demand for voltages lower than the dropout voltage as shown in Figure 3.31. Only heavily loaded motors may stall above the dropout voltage and give a large increase in the reactive power demand, Figure 3.31a. When the stalling voltage is smaller than the dropout voltage, the motor will not stall or exhibit a rapid increase in reactive power demand, Figure 3.31b.

When operating at a low voltage the motor may also be tripped by the overcurrent protection. This usually involves some time delay.

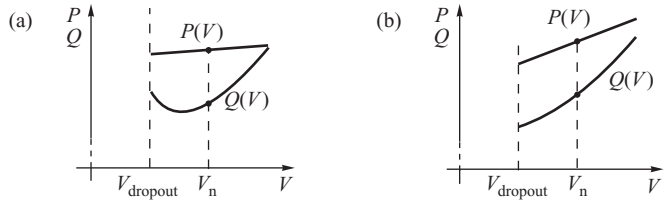

Figure 3.31 Examples of induction motor characteristics with starter control: (a) heavy-starting load; (b) easy-starting load.

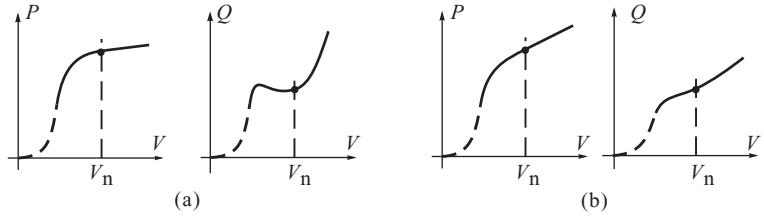

Figure 3.32 Examples of the voltage characteristics of a load: (a) dominated by large, heavily loaded induction motors; (b) dominated by lighting and heating.

Motors operating under residential and commercial loads are usually oversized, operate at less than 60% of rated power, and therefore have characteristics similar to those shown in Figure 3.31b. On the other hand, large industrial motors are usually properly sized and, when driving heavy-starting mechanical loads, may have characteristics similar to those shown in Figure 3.31a.

3.4.3 Static Characteristics of the Load

The aggregate characteristic of the load depends on the characteristics of its individual components. A rough estimate of the aggregate characteristic, viewed from the medium-voltage side (the secondary of the feeder transformer), can be obtained by summing the individual load characteristics. Figure 3.32 shows two examples of load characteristics obtained by this technique. Figure 3.32a shows an industrial load characteristic with a predominance of heavily loaded induction motors and discharge lighting. Near the nominal operating point (voltage V_n), the $P(V)$ curve is flat while the $Q(V)$ curve is steeper with a positive slope. As the voltage decreases, the $Q(V)$ curve becomes flatter and even rises due to the increased reactive power demand of the stalled motors. When the voltage drops below about 0.7 per unit, the $P(V)$ and $Q(V)$ curves rapidly decrease due to tripping of the induction motors and extinguishing of the discharge lighting.

Figure 3.32b shows an example of a residential/commercial load that is dominated by traditional bulb lighting and heating. Near the nominal voltage both the $P(V)$ and $Q(V)$ curves are quite steep. Again the real and reactive power demand drops rapidly at about 0.7 per unit. As the induction motor's stall voltage is now below the dropout voltage, dropout is not preceded by an increase in the reactive power demand.

The curves shown in Figure 3.32 can only give an indication of the kind of shape a load voltage characteristic may have. They cannot be treated in a general manner because the characteristic of a particular load may be quite different. For example, reactive power compensation can cause the $Q(V)$ curve to be flatter near the nominal voltage. Also relatively small, non-utility generation embedded in the load area will significantly affect the load characteristic.

There is also a difference in the characteristic as seen from the primary and secondary sides of the feeder transformer. Firstly, the real and reactive power loss in the transformer must be added to the load demand. Secondly, the feeder transformer is usually equipped with an on-load tap changer to help control the voltage in the distribution network and this also affects the characteristic as illustrated in Figure 3.33.

In Figure 3.33 the middle dashed bold line represents the load voltage characteristic at the nominal transformation ratio. Tap changing is controlled in discrete steps so that if the transformer tap setting is changed, the voltage characteristic moves to the left or right in discrete steps as shown by the dotted lines. The extreme left and right characteristics represent the tap-changer limits. A dead zone is also present in the regulator in order to prevent any tap changes if the voltage variations are within limits. The resulting voltage characteristic is shown by the bold line and is quite flat within the regulation range, as can be seen by sketching an average line through the resulting characteristic.

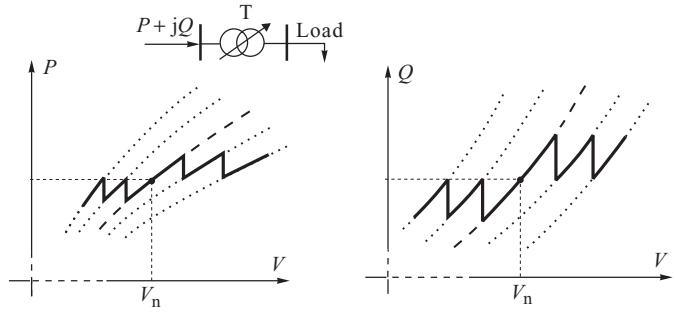

Figure 3.33 Influence of a tap-changing transformer on the voltage characteristic of a composite load.

3.4.4 Load Models

The last subsection described how the real and reactive power of particular types of load depends on the load voltage but did not explain how these could be represented by a mathematical model. Since all power system analysis programs, for example load flow or dynamic simulation, require such a load model, this subsection describes some of the most popular models currently in use.

3.4.4.1 Constant Power/Current/Impedance

The simplest load models assume one of the following features:

- a constant power demand (P)
- a constant current demand (I)
- a constant impedance (Z).

A constant power model is voltage invariant and allows loads with a stiff voltage characteristics $k_{PV} \approx k_{QV} \approx 0$ to be represented. This model is often used in load flow calculations, Section 3.7, but is generally unsatisfactory for other types of analysis, like transient stability analysis, in the presence of large voltage variations. The constant current model gives a load demand that changes linearly with voltage $k_{PV} \approx 1$ and is a reasonable representation of the real power demand of a mix of resistive and motor devices. When modelling the load by a constant impedance the load power changes proportionally to the voltage squared $k_{PV} \approx k_{QV} \approx 2$ and represents some lighting loads well but does not model stiff loads at all well. To obtain a more general voltage characteristic the benefits of each of these characteristics can be combined by using the so-called *polynomial or ZIP model* consisting of the sum of the constant impedance (Z), constant current (I) and constant power (P) terms:

$$\begin{aligned} P &= P_0 \left[a_1 \left(\frac{V}{V_0} \right)^2 + a_2 \left(\frac{V}{V_0} \right) + a_3 \right] \\ Q &= Q_0 \left[a_4 \left(\frac{V}{V_0} \right)^2 + a_5 \left(\frac{V}{V_0} \right) + a_6 \right], \end{aligned} \tag{3.143}$$

where V_0, P_0 and Q_0 are normally taken as the values at the initial operating conditions. The parameters of this polynomial model are the coefficients (a_1 to a_6) and the power factor of the load.

In the absence of any detailed information on the load composition, the real power is usually represented by the constant current model while the reactive power is represented by a constant impedance.

3.4.4.2 Exponential Load Model

In this model the power is related to the voltage by

$$P = P_0 \left(\frac{V}{V_0}\right)^{n_p} \quad \text{and} \quad Q = Q_0 \left(\frac{V}{V_0}\right)^{n_q}, \tag{3.144}$$

where n_p and n_q are the parameters of the model. Note that by setting the parameters to 0, 1, 2, the load can be represented by constant power, constant current or constant impedance, respectively.

The slope of the characteristics given by Equation (3.144) depends on the parameters n_p and n_q. By linearizing these characteristics it can be shown that n_p and n_q are equal to the voltage sensitivities given by Equation (3.133), that is $n_p = k_{PV}$ and $n_q = k_{QV}$.

3.4.4.3 Piecewise Approximation

None of the models described so far will correctly model the rapid drop in load that occurs when the voltage drops below about 0.7 per unit. This can be remedied by using a two-tier representation with the exponential, or polynomial, model being used for voltages close to rated and the constant impedance model being used at voltages below 0.3–0.7 per unit. Figure 3.34 shows an example of such an approximation which gives similar characteristics to those shown in Figure 3.32.

3.4.4.4 Frequency-Dependent Load Model

Frequency dependence is usually represented by multiplying either a polynomial or an exponential load model by a factor $[1 + a_f (f - f_0)]$ where f is the actual frequency, f_0 is the rated frequency and a_f is the model frequency sensitivity parameter. Using the exponential model this gives

$$\begin{aligned} P &= P(V)\left[1 + k_{Pf}\frac{\Delta f}{f_0}\right] \\ Q &= Q(V)\left[1 + k_{Qf}\frac{\Delta f}{f_0})\right], \end{aligned} \tag{3.145}$$

where $P(V)$ and $Q(V)$ represent any type of the voltage characteristic and k_{Pf}, k_{Qf} are the frequency sensitivity parameters, $\Delta f = f - f_0$.

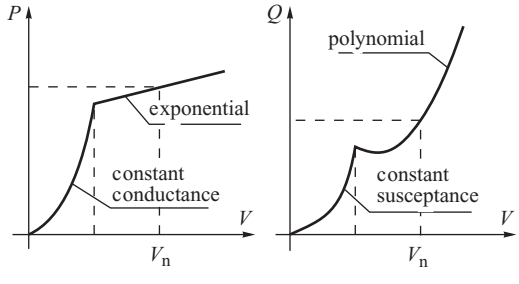

Figure 3.34 Example of a two-tier approximation of the voltage characteristics.

Table 3.3 Typical load model parameters (IEEE, 1993)

Type of load	Power factor	k_{PV}	k_{QV}	k_{Pf}	k_{Qf}
Residential	0.87–0.99	0.9–1.7	2.4–3.1	0.7–1	−1.3 to −2.3
Commercial	0.85–0.9	0.5–0.8	2.4–2.5	1.2–1.7	−0.9 to −1.6
Industrial	0.8–0.9	0.1–1.8	0.6–2.2	−0.3–2.9	0.6–1.8

3.4.4.5 Test Results

A number of papers have been published that describe the results of field tests used to identify the parameter values for different load models; a survey of such papers can be found in Concordia and Ihara (1982) and Vaahedi *et al.* (1987). An alternative to having to conduct field tests is to use a *component-based approach* (IEEE, 1993) where the composite load model is constructed by aggregating individual components. With this technique the component characteristics are determined for particular classes of loads, for example residential, commercial or industrial, either by theoretical analysis or laboratory experiment. The composite load model is then constructed by aggregating the fraction of the load consumed by each particular class of load. This approach has the advantage of not requiring field measurements and of being adaptable to different systems and conditions. Table 3.3 shows some typical voltage and frequency sensitivity coefficients obtained in this way.

3.5 Network Equations

All electrical networks consist of interlinked transmission lines and transformers, each of which can be modelled by the π-equivalent circuits described in Sections 3.1 and 3.2. These individual models are combined to model the whole network by forming the *nodal network equation*:

$$\begin{bmatrix} \underline{I}_1 \\ \vdots \\ \underline{I}_i \\ \vdots \\ \underline{I}_N \end{bmatrix} = \begin{bmatrix} \underline{Y}_{11} & \cdots & \underline{Y}_{1i} & \cdots & \underline{Y}_{1N} \\ \vdots & \ddots & \vdots & & \vdots \\ \underline{Y}_{i1} & \cdots & \underline{Y}_{ii} & \cdots & \underline{Y}_{iN} \\ \vdots & & \vdots & & \vdots \\ \underline{Y}_{N1} & \cdots & \underline{Y}_{Ni} & \cdots & \underline{Y}_{NN} \end{bmatrix} \begin{bmatrix} \underline{V}_1 \\ \vdots \\ \underline{V}_i \\ \vdots \\ \underline{V}_N \end{bmatrix} \quad \text{or} \quad \underline{\boldsymbol{I}} = \underline{\boldsymbol{Y}}\underline{\boldsymbol{V}}. \tag{3.146}$$

The suffices i, j represent node numbers so that $\underline{V}_i$ is the voltage at node i, $\underline{I}_i$ is the *current injection* at node i and is equal to the algebraic sum of the currents in all the branches that terminate on node i, $\underline{Y}_{ij}$ is the *mutual admittance* between nodes i and j and is equal to the negative of the branch series admittance $\underline{Y}_{ij}$ that links nodes i and j, $\underline{Y}_{ii} = \sum_{i=1}^{N} \underline{Y}_{ij}$ is the *self-admittance* of node i and is equal to the sum of all the admittances terminating on node i (including any shunt admittance $\underline{Y}_{i0}$) and N is the number of nodes in the network.

The matrix $\underline{\boldsymbol{Y}}$ is called *the nodal admittance matrix*. Within this matrix, the algebraic sum of all the elements in any row i is equal to the shunt admittance Y_{i0} connecting node i to the reference node (ground), that is $\underline{Y}_{i0} = \sum_{j=1}^{N} \underline{Y}_{ij}$. The nodal admittance matrix is singular if it does not have any shunt branches. In this case the sum of the elements in all rows is zero and $\det \underline{\boldsymbol{Y}} = 0$. If the matrix is not singular then its inverse $\underline{\boldsymbol{Z}} = \underline{\boldsymbol{Y}}^{-1}$ exists and Equation (3.146) can be

rewritten as

$$\begin{bmatrix} \underline{V}_1 \\ \vdots \\ \underline{V}_i \\ \vdots \\ \underline{V}_N \end{bmatrix} = \begin{bmatrix} \underline{Z}_{11} & \cdots & \underline{Z}_{1i} & \cdots & \underline{Z}_{1N} \\ \vdots & \ddots & \vdots & & \vdots \\ \underline{Z}_{i1} & \cdots & \underline{Z}_{ii} & \cdots & \underline{Z}_{iN} \\ \vdots & & \vdots & & \vdots \\ \underline{Z}_{N1} & \cdots & \underline{Z}_{Ni} & \cdots & \underline{Z}_{NN} \end{bmatrix} \begin{bmatrix} \underline{I}_1 \\ \vdots \\ \underline{I}_i \\ \vdots \\ \underline{I}_N \end{bmatrix} \quad \text{or} \quad \underline{\boldsymbol{V}} = \underline{\boldsymbol{ZI}}, \tag{3.147}$$

where $\underline{\boldsymbol{Z}}$ is the *nodal impedance matrix*.

Any off-diagonal element $\underline{Y}_{ij}$ is non-zero only if there is a branch linking nodes i and j. If there are L branches in the system then $k = L/N$ is the ratio of the number of branches to the number of nodes and $\underline{\boldsymbol{Y}}$ has N^2 elements, $(2k+1)N$ of which are non-zero. The ratio of the number of non-zero elements to the total number of elements is $\alpha = (2k+1)/N$. High-voltage transmission networks are rather sparse so that typically k has a value of between 1 and 3. Thus, for example, if a network has 100 nodes, then only 3 to 7 % of the elements in the admittance may be non-zero. Such a matrix is referred to as a *sparse matrix*. Power network matrices are usually sparse and, to save computer memory, only non-zero elements are stored with additional indices being used to define their position in the matrix. All matrix manipulations are performed only on the non-zero elements using *sparse matrix techniques*. The description of such techniques is beyond the scope of this book but can be found in Tewerson (1973) or Brameller, Allan and Hamam (1976). As the principal objective of the present text is to describe power system dynamics and stability from an engineering point of view, full, formal matrix notation will be used.

For any node i, the current injection at the node can be extracted from Equation (3.146) as

$$\underline{I}_i = \underline{Y}_{ii}\underline{V}_i + \sum_{j=1;j\neq i}^{N} \underline{Y}_{ij}\underline{V}_j, \tag{3.148}$$

where the complex voltage and admittance can be generally written as $\underline{V}_i = V_i\angle\delta_i$ and $\underline{Y}_i = Y_{ij}\angle\theta_{ij}$. Using polar notation the apparent power injected at any node i is expressed as

$$\begin{aligned} \underline{S}_i &= P_i + \mathrm{j}Q_i = \underline{V}_i\underline{I}_i^* = V_i\mathrm{e}^{\mathrm{j}\delta_i}\left[Y_{ii}V_i\mathrm{e}^{-\mathrm{j}(\delta_i+\theta_{ii})} + \sum_{j=1;j\neq i}^{N} V_j Y_{ij}\mathrm{e}^{-\mathrm{j}(\delta_j+\theta_{ij})} \right] \\ &= V_i^2 Y_{ii}\mathrm{e}^{-\mathrm{j}\theta_{ii}} + V_i \sum_{j=1;j\neq i}^{N} V_j Y_{ij}\mathrm{e}^{\mathrm{j}(\delta_i-\delta_j-\theta_{ij})}. \end{aligned} \tag{3.149}$$

Separating the real and imaginary parts gives

$$\begin{aligned} P_i &= V_i^2 Y_{ii}\cos\theta_{ii} + \sum_{j=1;j\neq i}^{N} V_i V_j Y_{ij}\cos(\delta_i - \delta_j - \theta_{ij}) \\ Q_i &= -V_i^2 Y_{ii}\sin\theta_{ii} + \sum_{j=1;j\neq i}^{N} V_i V_j Y_{ij}\sin(\delta_i - \delta_j - \theta_{ij}). \end{aligned} \tag{3.150}$$

Alternatively the rectangular coordinate system (a, b) shown in Figure 3.35 can be used when the apparent power injected at a node is written as

$$\underline{S}_i = P_i + \mathrm{j}Q_i = \underline{V}_i\underline{I}_i^* = (V_{\mathrm{a}i} + \mathrm{j}V_{\mathrm{b}i})(I_{\mathrm{a}i} - \mathrm{j}I_{\mathrm{b}i})$$

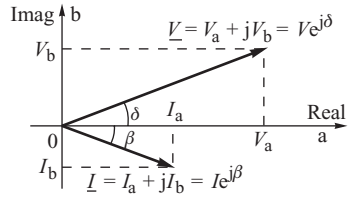

Figure 3.35 Voltage and current in the complex plane; a, b, rectangular coordinates.

and

$$P_i = V_{ai} I_{ai} + V_{bi} I_{bi}, \quad Q_i = V_{bi} I_{ai} - V_{ai} I_{bi}. \tag{3.151}$$

Expressing the admittance in rectangular coordinates as $\underline{Y}_{ij} = G_{ij} + jB_{ij}$, the current injection at each node i, given by Equation (3.146), can be written as

$$\underline{I}_i = I_{ai} + jI_{bi} = \sum_{j=1}^{N} \underline{Y}_{ij}\underline{V}_j = \sum_{j=1}^{N} \left(G_{ij} + jB_{ij}\right)\left(V_{aj} + jV_{bj}\right). \tag{3.152}$$

Separating real and imaginary parts gives

$$I_{ai} = \sum_{j=1}^{N} \left(G_{ij} V_{aj} - B_{ij} V_{bj}\right), \quad I_{bi} = \sum_{j=1}^{N} \left(B_{ij} V_{aj} + G_{ij} V_{bj}\right). \tag{3.153}$$

With this notation the complex network Equation (3.146) can be transformed into the real-number domain to give

$$\begin{bmatrix} \boldsymbol{I}_1 \\ \vdots \\ \boldsymbol{I}_i \\ \vdots \\ \boldsymbol{I}_N \end{bmatrix} = \begin{bmatrix} \boldsymbol{Y}_{11} & \cdots & \boldsymbol{Y}_{1i} & \cdots & \boldsymbol{Y}_{1N} \\ \vdots & & \vdots & & \vdots \\ \boldsymbol{Y}_{i1} & \cdots & \boldsymbol{Y}_{ii} & \cdots & \boldsymbol{Y}_{iN} \\ \vdots & & \vdots & & \vdots \\ \boldsymbol{Y}_{N1} & \cdots & \boldsymbol{Y}_{Ni} & \cdots & \boldsymbol{Y}_{NN} \end{bmatrix} \begin{bmatrix} \boldsymbol{V}_1 \\ \vdots \\ \boldsymbol{V}_i \\ \vdots \\ \boldsymbol{V}_N \end{bmatrix} \quad \text{or} \quad \boldsymbol{I} = \boldsymbol{Y}\boldsymbol{V}, \tag{3.154}$$

where all the elements are now real submatrices of the form

$$\boldsymbol{I}_i = \begin{bmatrix} I_{ai} \\ I_{bi} \end{bmatrix}, \quad \boldsymbol{V}_i = \begin{bmatrix} V_{ai} \\ V_{bi} \end{bmatrix}, \quad \boldsymbol{Y}_{ij} = \begin{bmatrix} G_{ij} & -B_{ij} \\ B_{ij} & G_{ij} \end{bmatrix}, \tag{3.155}$$

with dimension (2×1) and (2×2), respectively.

Quite often it is convenient to 'mix' the coordinate systems so that the voltages are expressed in polar coordinates as $\underline{V}_i = V_i \angle \delta_i$ while the admittances are expressed in rectangular coordinates as $\underline{Y}_{ij} = G_{ij} + jB_{ij}$. Equations (3.150) then take the form

$$\begin{aligned} P_i &= V_i^2 G_{ii} + \sum_{j=1;j\neq i}^{N} V_i V_j \left[B_{ij} \sin(\delta_i - \delta_j) + G_{ij} \cos(\delta_i - \delta_j)\right] \\ Q_i &= -V_i^2 B_{ii} + \sum_{j=1;j\neq i}^{N} V_i V_j \left[G_{ij} \sin(\delta_i - \delta_j) - B_{ij} \cos(\delta_i - \delta_j)\right]. \end{aligned} \tag{3.156}$$

Because of the mixing of complex variables in both the polar and rectangular coordinate systems, the above equations are called the *hybrid network equations*.

3.5.1.1 Linearization of Power Network Equations

The real and reactive power injection at each node is a nonlinear function of the system voltages, that is $P = P(V, \delta)$ and $Q = Q(V, \delta)$, and it is often both convenient and necessary to linearize these functions in the vicinity of the operating point. This linearization is carried out using a first-order Taylor expansion and neglecting the higher order terms. The change in the real and reactive power injection at all the system nodes can then be written, using matrix algebra and the hybrid network equations, as

$$\begin{bmatrix} \Delta \boldsymbol{P} \\ \Delta \boldsymbol{Q} \end{bmatrix} = \begin{bmatrix} \boldsymbol{H} & \boldsymbol{M} \\ \boldsymbol{N} & \boldsymbol{K} \end{bmatrix} \begin{bmatrix} \Delta \boldsymbol{\delta} \\ \Delta \boldsymbol{V} \end{bmatrix}, \tag{3.157}$$

where $\Delta \boldsymbol{P}$ is the vector of the real power changes at all the system nodes, $\Delta \boldsymbol{Q}$ is the vector of reactive power changes, $\Delta \boldsymbol{V}$ is the vector of voltage magnitude increments and $\Delta \boldsymbol{\delta}$ is the vector of voltage angle increments. The elements of the Jacobian submatrices $\boldsymbol{H}$, $\boldsymbol{M}$, $\boldsymbol{N}$, $\boldsymbol{K}$ are the partial derivatives of the functions in (3.156), that is

$$H_{ij} = \frac{\partial P_i}{\partial \delta_j}, \quad M_{ij} = \frac{\partial P_i}{\partial V_j}, \quad N_{ij} = \frac{\partial Q_i}{\partial \delta_j}, \quad K_{ij} = \frac{\partial Q_i}{\partial V_j}. \tag{3.158}$$

In order to obtain simpler and more symmetrical Jacobian submatrices, Equation (3.157) is often modified by multiplying the submatrices $\boldsymbol{M}$ and $\boldsymbol{K}$ by the nodal voltage magnitude. This then requires the voltage increments $\Delta \boldsymbol{V}$ to be divided by the voltage magnitude and Equation (3.157) takes the form

$$\begin{bmatrix} \Delta P_1 \\ \vdots \\ \Delta P_N \\ \hline \Delta Q_1 \\ \vdots \\ \Delta Q_N \end{bmatrix} = \left[\begin{array}{ccc:ccc} \frac{\partial P_1}{\partial \delta_1} & \cdots & \frac{\partial P_1}{\partial \delta_N} & V_1 \frac{\partial P_1}{\partial V_1} & \cdots & V_N \frac{\partial P_1}{\partial V_N} \\ \vdots & \ddots & \vdots & \vdots & \ddots & \vdots \\ \frac{\partial P_N}{\partial \delta_1} & \cdots & \frac{\partial P_N}{\partial \delta_N} & V_1 \frac{\partial P_N}{\partial V_1} & \cdots & V_N \frac{\partial P_N}{\partial V_N} \\ \hdashline \frac{\partial Q_1}{\partial \delta_1} & \cdots & \frac{\partial Q_1}{\partial \delta_N} & V_1 \frac{\partial Q_1}{\partial V_1} & \cdots & V_N \frac{\partial Q_1}{\partial V_N} \\ \vdots & \ddots & \vdots & \vdots & \ddots & \vdots \\ \frac{\partial Q_N}{\partial \delta_1} & \cdots & \frac{\partial Q_N}{\partial \delta_N} & V_1 \frac{\partial Q_N}{\partial V_1} & \cdots & V_N \frac{\partial Q_N}{\partial V_N} \end{array}\right] \begin{bmatrix} \Delta \delta_1 \\ \vdots \\ \Delta \delta_N \\ \hline \Delta V_1 / V_1 \\ \vdots \\ \Delta V_N / V_N \end{bmatrix} \tag{3.159}$$

or $$\begin{bmatrix} \Delta \boldsymbol{P} \\ \Delta \boldsymbol{Q} \end{bmatrix} = \begin{bmatrix} \boldsymbol{H} & \boldsymbol{M}' \\ \boldsymbol{N} & \boldsymbol{K}' \end{bmatrix} \begin{bmatrix} \Delta \boldsymbol{\delta} \\ \Delta \boldsymbol{V} / \boldsymbol{V} \end{bmatrix},$$

with the elements of the Jacobian being

$$\begin{aligned} H_{ij} &= \frac{\partial P_i}{\partial \delta_j} = -V_i V_j \left[B_{ij} \cos(\delta_i - \delta_j) - G_{ij} \sin(\delta_i - \delta_j) \right] \qquad \text{for} \quad i \neq j \\ H_{ii} &= \frac{\partial P_i}{\partial \delta_i} = \sum_{\substack{j=1 \\ j \neq i}}^{N} V_i V_j \left[B_{ij} \cos(\delta_i - \delta_j) - G_{ij} \sin(\delta_i - \delta_j) \right] = -Q_i - V_i^2 B_{ii}, \end{aligned} \tag{3.160}$$

$$
\begin{aligned}
N_{ij} &= \frac{\partial Q_i}{\partial \delta_j} = -V_i V_j \left[G_{ij} \cos(\delta_i - \delta_j) + B_{ij} \sin(\delta_i - \delta_j) \right] \qquad \text{for} \quad i \neq j \\
N_{ii} &= \frac{\partial Q_i}{\partial \delta_i} = \sum_{\substack{j=1 \\ j \neq i}}^{N} V_i V_j \left[G_{ij} \cos(\delta_i - \delta_j) + B_{ij} \sin(\delta_i - \delta_j) \right] = P_i - V_i^2 G_{ii},
\end{aligned}
\tag{3.161}
$$

$$
\begin{aligned}
M'_{ij} &= V_j \frac{\partial P_i}{\partial V_j} = V_i V_j \left[G_{ij} \cos(\delta_i - \delta_j) + B_{ij} \sin(\delta_i - \delta_j) \right] \qquad \text{for} \quad i \neq j \\
M'_{ii} &= V_i \frac{\partial P_i}{\partial V_i} = 2V_i^2 G_{ii} + \sum_{\substack{j=1 \\ j \neq i}}^{N} V_i V_j \left[G_{ij} \cos(\delta_i - \delta_j) + B_{ij} \sin(\delta_i - \delta_j) \right] = P_i + V_i^2 G_{ii},
\end{aligned}
\tag{3.162}
$$

$$
\begin{aligned}
K'_{ij} &= V_j \frac{\partial Q_i}{\partial V_j} = V_i V_j \left[G_{ij} \sin(\delta_i - \delta_j) - B_{ij} \cos(\delta_i - \delta_j) \right] \quad \text{for} \quad i \neq j \\
K'_{ii} &= V_i \frac{\partial Q_i}{\partial V_i} = -2V_i^2 B_{ii} + \sum_{\substack{j=1 \\ j \neq i}}^{N} V_i V_j \left[G_{ij} \sin(\delta_i - \delta_j) - B_{ij} \cos(\delta_i - \delta_j) \right] = Q_i - V_i^2 B_{ii}.
\end{aligned}
\tag{3.163}
$$

Note that Equations (3.160) show an important property of matrices $\boldsymbol{H}$ and $\boldsymbol{N}$. The diagonal elements of those matrices are equal to the negative sum of all the off-diagonal elements. Consequently, the sum of all the elements in a row is equal to zero:

$$
H_{ii} = \sum_{\substack{j=1 \\ j \neq i}}^{N} H_{ij} \quad \text{and} \quad \sum_{j=1}^{N} H_{ij} = 0, \tag{3.164}
$$

$$
N_{ii} = \sum_{\substack{j=1 \\ j \neq i}}^{N} N_{ij} \quad \text{and} \quad \sum_{j=1}^{N} N_{ij} = 0. \tag{3.165}
$$

That property generally does not hold for the submatrices $\boldsymbol{M}'$ and $\boldsymbol{K}'$ due to the presence of shunt admittances in the network. These admittances are added to the diagonal, but not off-diagonal, elements of the matrices.

3.5.1.2 Change of Reference Frame

The network equations, namely Equations (3.146) and (3.154), are in network's complex coordinates (a, b) while the generator equations, namely Equations (3.120), are in the generator's (d, q) orthogonal coordinates. Figure 3.36 shows the relative position of the two systems of coordinates. The q-axis of a given generator is shifted with respect to the network's real axis by the rotor angle δ. The relationship between the two systems of coordinates is

$$
\begin{bmatrix} E_\mathrm{a} \\ E_\mathrm{b} \end{bmatrix} = \begin{bmatrix} -\sin\delta & \cos\delta \\ \cos\delta & \sin\delta \end{bmatrix} \begin{bmatrix} E_\mathrm{d} \\ E_\mathrm{q} \end{bmatrix} \quad \text{or} \quad \boldsymbol{E}_{ab} = \boldsymbol{T}\ \boldsymbol{E}_\mathrm{dq}. \tag{3.166}
$$

The transformation matrix $\boldsymbol{T}$ is unitary because $\boldsymbol{T}^{-1} = \boldsymbol{T}$. The inverse transformation is governed by the same matrix

$$
\begin{bmatrix} E_\mathrm{d} \\ E_\mathrm{q} \end{bmatrix} = \begin{bmatrix} -\sin\delta & \cos\delta \\ \cos\delta & \sin\delta \end{bmatrix} \begin{bmatrix} E_\mathrm{a} \\ E_\mathrm{b} \end{bmatrix} \quad \text{or} \quad \boldsymbol{E}_{\mathrm{dq}-} = \boldsymbol{T}\ \boldsymbol{E}_\mathrm{ab}. \tag{3.167}
$$

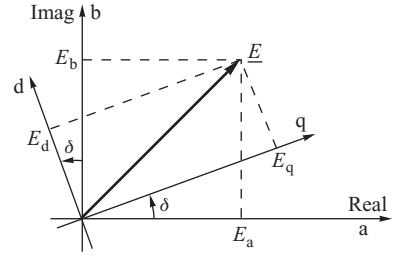

Figure 3.36 Relative position of the generator's rectangular (d, q) coordinates with respect to the network's complex (a, b) coordinates.

All the other current and voltage phasors can be transformed in a similar way. Obviously, each generator may operate at a different rotor angle δ which gives as many (d, q) systems of coordinates as there are generators in the network.

3.6 Power Flows in Transmission Networks

Transmission networks have a meshed structure and there are a very large number of possible parallel routes between generators and loads. The actual flow of power through each network element is determined by Kirchhoff's and Ohm's laws and given by Equations (3.150). Generally the flow in each line and transformer cannot be directly controlled as it is a function of generations and demands in all network nodes. There are only limited possibilities of directly controlling the flow of power in transmission lines as discussed later in this section.

Predicting future power flows plays a major role in planning the future expansion of a power system as well as in helping to run the existing system in the best possible way. In this book two problems will be discussed: (i) the power (or load) flow problem, that is calculation of power flows determining the steady state of power system; and (ii) control of power flow in the network in both the steady state and dynamic state.

3.6.1 Control of Power Flows

Real and reactive power flows in a network can be modified to some extent by using controllable network elements without changing the overall generation and demand pattern. Generation control will be discussed in Chapter 9.

Figure 1.4 and the simplified power flow equations, Equations (1.8) and (1.9), show that the flow of real and reactive power through a network element (i.e. a line or a transformer) is mainly a function of:

- voltage magnitudes at both ends of the element;
- the load (or power) angle, that is the difference between the terminal voltage angles;
- the series reactance of the element.

Real power and reactive power are two strongly connected quantities in AC transmission networks. However, as discussed in Section 1.3, real power flow is mainly affected by the load angle while reactive power flow is mainly affected by the voltage magnitudes. Hence reactive power flow control is executed by changing voltage magnitudes through: (i) changing generator voltages; (ii) changing transformation ratios; and (iii) changing reactive power consumed/generated by reactive

power compensation elements discussed in Section 2.4.3. As reactive power cannot be transmitted over long distances, see Section 3.1.2, reactive power control is a local problem.

Control of real power flows is executed using the remaining two quantities, for example the load angle and the series reactance. Such regulation can be implemented using: (i) quadrature booster transformers, (ii) series compensators such as SSSCs; and (iii) series FACTS devices such as UPFCs or TCPARs (see Section 2.4.4). The control of the load angle using a quadrature booster transformers or a FACTS device, such as UPFC or TCPAR, will be discussed below.

The dependence of real power flow on the load angle was illustrated in Figure 1.4. It was shown that the load angle can change a real power flow over a wide range from negative to positive values. The way that a change in the load angle can be enforced is illustrated in Figure 3.37. To simplify considerations, a case is considered of two parallel transmission lines I and II with identical parameters. The terminal voltages are $\underline{V}_i$ and $\underline{V}_j$ and the load angle (i.e. the difference between the voltage angles) is δ.

The phasor diagram for line I is shown in Figure 3.37b. The line current is $\underline{I}_{\mathrm{I}}$ while the real power flow is given by $P_{\mathrm{I}} = (V_i V_j / X) \sin\delta$. The phasor diagram for line II is shown in Figure 3.37c. The line has an installed quadrature booster and the terminal voltages, the same as for line I and II, are equal to $\underline{V}_i$ and $\underline{V}_j$. The diagram shows that booster voltage $\underline{\Delta V}_k$, in quadrature with $\underline{V}_i$, is added to $\underline{V}_i$. Consequently the voltage at the beginning of line II but after the quadrature booster is $\underline{V}_k = \underline{V}_i + \underline{\Delta V}_k$. The load angle for line II is $(\delta + \Delta\delta)$ while the line current is $\underline{I}_{\mathrm{II}}$ and the real power flow is given by $P_{\mathrm{II}} = (V_k V_j / X) \sin(\delta + \Delta\delta)$. Since $(\delta + \Delta\delta) > \delta$, power P_{II} is greater than P_{I}. The total power entering both lines is $P = P_{\mathrm{I}} + P_{\mathrm{II}}$.

Changing the booster voltage $\underline{\Delta V}_k$ causes a change in the load angle $\Delta\delta$ and therefore also a change in the line flow P_{II}. The booster voltage $\underline{\Delta V}_k$ can be controlled from negative to positive values. When $\underline{\Delta V}_k$ is negative, the load angle is decreased and therefore the flow P_{II} is reduced. When $\underline{\Delta V}_k = 0$, that is the quadrature booster is not acting, the power entering both lines is divided equally between them, that is $P_{\mathrm{I}} = P_{\mathrm{II}} = P/2$. The conclusion is that changing the booster voltage

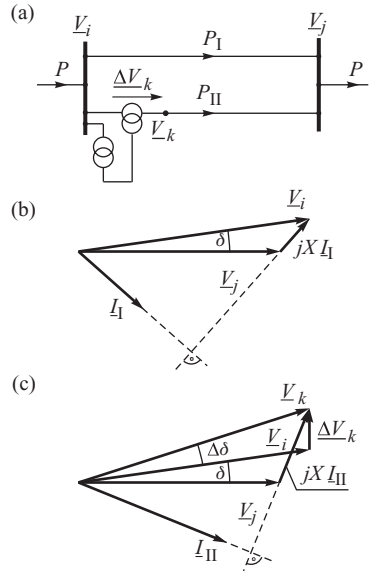

Figure 3.37 Controlling the real power flow by changing the load angle: (a) circuit diagram; (b) phasor diagram for line I; (b) phasor diagram for line II.

$\underline{\Delta V_k}$ changes the proportions between power flows P_{I} and P_{II} in parallel lines. Obviously the booster transformer cannot change the total power flow in the network.

The discussed principle of power flow control in parallel lines can also be used for flow control in more complicated network configurations, and in particular in parallel transmission corridors in meshed networks. Usually quadrature boosters are used for:

- increasing loading on underloaded, or decreasing loading on overloaded, parallel transmission corridors;
- elimination of circulating power in meshed networks;
- changing import (or export) direction in interconnected power systems;
- prevention of unwanted loop flows entering subsystems in interconnected power systems.

Each of these options will now be briefly discussed.

A transmission network is usually meshed and parallel transmission corridors are loaded in inverse proportion to the reactances of the corridors, assuming no quadrature boosters are present. Hence it may occur that short transmission links are overloaded while long ones are underloaded. If that happens, a desired loading of lines can be enforced using quadrature boosters. Reducing the flow on overloaded lines and increasing the flow on underloaded lines has the effect of increasing a transfer capacity between areas.

Large interconnected networks may suffer from *circulation of power* between subsystems when power enters a subsystem through one transmission corridor and returns through another. This means that there may be large power transfers between regions while net power exchanges, when circulating power is taken away, are small. Quadrature boosters may eliminate or significantly reduce circulation of power. This usually results in reduced load on some transmission corridors at the cost of a small increase in transmission losses.

Figure 3.38 illustrates the application of a quadrature booster to a change of import (or export) direction in an interconnected system. It is assumed that system A has a surplus of power and exports it to systems B and C. The operator of system A would like to enforce an increased export to system B at the cost of reducing export to system C. This can be achieved by installing a quadrature booster or a FACTS device in one of the tie-lines, say line A–B. The total export from an area is equal to the difference between generation and demand, that is the total export from

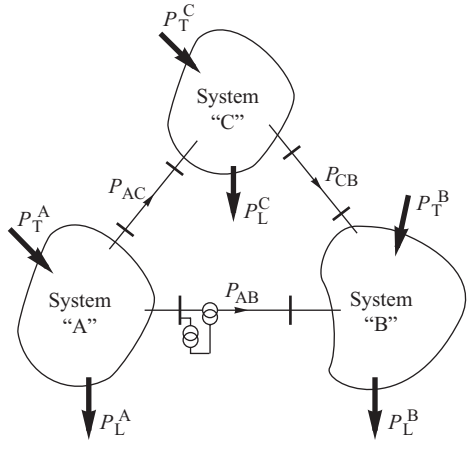

Figure 3.38 Power exchanges between three control areas: P_{T}, power generation; P_{L}, power demand.

system A is $(P_{AB} + P_{AC}) = (P_T^A - P_L^A)$. Obviously no quadrature booster or FACTS device can change the total value of export from an area. The device only changes the distribution among imported areas, that is it changes the proportions between P_{AB} and P_{AC} while keeping the total $(P_{AB} + P_{AC})$ constant. It should be appreciated that installation of a quadrature booster has to be agreed between all partners. Unilateral action of one system operator against the will of other system operators may be futile since the other system operators might install a similar quadrature booster acting in the opposite direction with the net effect of no change of flows and at a significant cost of installation of the devices.

Section 2.1 discussed briefly the recent liberalization of electricity markets. One of the effects of liberalization was a significant increase in cross-border (or interarea) trades in interconnected networks. The problem with cross-border trades is that a trade does not travel along an agreed 'contract path' between a seller and a buyer but flows over many parallel routes, as discussed earlier in this section. The flows outside the agreed contract path are referred to as *parallel flows*, or *loop flows*. For example, Figure 3.39 shows the different routes through which an assumed 1000 MW trade between northern France and Italy would flow (Haubrich and Fritz, 1999). Only 38 % of the power would flow directly from France to Italy; the remaining 62 % would flow through different parallel routes loading the transit networks. Note that 15 % of the power would even flow in a round-about way via Belgium and the Netherlands.

Parallel flows did not cause major problems before 1990, as interarea exchanges were usually agreed well in advance by system operators and were relatively small. Since 1990, interarea trades have not only increased significantly in volume, but also started to be arranged by independent agents, rather than system operators. Consequently, system operators often find their networks loaded with power transfers they have little idea about as they were not notified about the trades, causing loop flows. Such a situation endangers secure power system operation and actually led to a few blackouts that were just avoided in Belgium in the late 1990s. In recent years the situation was made worse by increased penetration of renewable generation, mostly wind. Wind is an intermittent energy source and the actual wind generation may be different from the one predicted a day ahead. A changed wind generation may strongly affect power flows in a network endangering secure

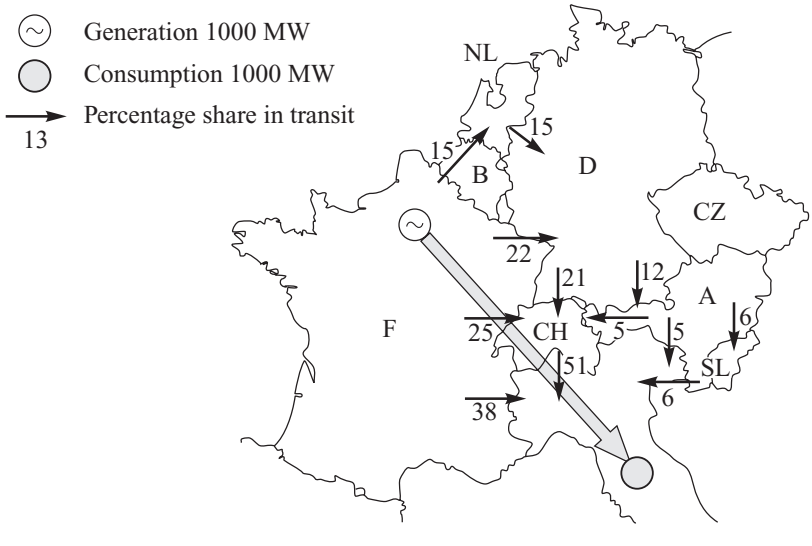

Figure 3.39 Percentage shares through different transit routes for a trade from northern France to Italy (Haubrich and Fritz, 1999). Reproduced by permission of H.-J. Haubrich

operation. For example, a significant change in actual wind generation was one of the contributing factors to a widespread disturbance leading to the shedding of 17 GW of load in a UCTE network in November 2006 (UCTE, 2007).

System operators can prevent loop flows from entering their systems by installing quadrature boosters in tie-lines. This solution has been implemented, or at least was being seriously considered, by small European countries strongly affected by loop flows, such as Belgium, Switzerland and Slovenia. Obviously such a hardware solution is quite expensive and a more cost-effective solution would be to notify all system operators in the interconnected network about all trades in the system and paying compensation for the utilization of transit networks. However, such a harmonization of arrangements is quite difficult to achieve in a multinational network due to political and institutional obstacles (Bialek, 2007).

3.6.2 Calculation of Power Flows

Basically a power flow solution predicts what the electrical state of the network will be when it is subject to a specified loading condition. The result of the power flow is the voltage magnitude and angle at each of the system nodes. These bus voltage magnitudes and angles are defined as the system *state variables* (or *independent variables*) as they allow all the other system quantities, such as the real and reactive power flows, current flows, voltage drops, power losses and so on, to be computed.

The starting point for any power flow study is the set of generation and load data with the electrical network being described by the nodal admittance matrix $\underline{\boldsymbol{Y}}$ of Equation (3.146). Usually the generation and load data are given in terms of the *scheduled* real and reactive power generation at the generator nodes and the *predicted* real and reactive power demand at the load nodes, rather than in terms of current injections. This means that the relationship between the data inputs (real and reactive power nodal injections) and the state variables (nodal voltage magnitudes and angles) is nonlinear, as indicated in Equations (3.150) or (3.156).

Generator nodes have a different specification to load nodes. For the load nodes, the real and reactive power demand can be predicted and both Equations (3.150) (or (3.156)) can be used. However, only real power generation can be specified at the generator nodes, which means that only the first of the equations in (3.150) or (3.156) is included. To understand this, refer to Figure 2.2. A power station has two main controllers, the turbine governor and the AVR. The turbine governor allows the real power output to be specified and kept constant. On the other hand, the AVR maintains the generator terminal voltage at a constant value by adjusting the generator excitation, subject to any operating limits. This means that the reactive power generation of a power station is controlled indirectly by specifying the voltage demanded at the station terminals. The voltage is usually set high (around 1.05–1.1 pu) in order to support the voltages at the load nodes. As the voltage magnitude is specified, there is no need for the power flow program to calculate it, and only the voltage angle needs to be found.

The input data for all the nodes in the system are summarized in Table 3.4. For the generation nodes, referred to as *voltage-controlled or PV nodes*, the required inputs are the net real power injection (scheduled generation minus predicted local demand) and the magnitude of the bus voltage, while the voltage angle is the unknown state variable. The unknown net reactive power injection will be determined once all the system state variables are calculated. For the load nodes, also referred to as *PQ nodes*, the inputs are in the form of the predicted real and reactive power demand (negative injections) with the unknown state variables being the bus voltage magnitude and angle. Usually one of the generator nodes is selected as the *slack node*. At this node the voltage angle and magnitude are specified and the unknown values of the real and reactive power injection (generation or demand) determined once the state variables at all the other nodes are calculated. Any power system imbalance will then appear as the required generation from the slack generator. Removing the row and column corresponding to the slack node from the admittance

Table 3.4 Node types in the power flow problem

Node type	Number of nodes	Quantities specified	Unknown state variables	Other unknown variables
Slack	Usually 1	$\delta = 0$, V	—	P, Q
PV (source)	NG	P, V	δ	Q
PQ (load)	$N - N$G $- 1$	P, Q	δ, V	—
Total	N	$2N$	$2N - N$G $- 2$	NG $+ 2$

matrix remedies the problem of the admittance matrix being singular for networks with no shunt branches.

The power flow problem described by Equations (3.150) or (3.156) is nonlinear and therefore must be solved iteratively. The first load flow computer programs used the *Gauss–Seidel method* because this required little computer memory. Nowadays, with increased computer speed and on-chip memory, the *Newton–Raphson method* is used almost exclusively. A detailed description of these algorithms is beyond the scope of this book but can be found in a number of textbooks on power system analysis, for example Gross (1986) and Grainger and Stevenson (1994). A detailed description of modelling FACTS devices in load flow programs can be found in Acha, Fuerte-Esquivel and Angeles-Camancho (2004).

Part II

Introduction to Power System Dynamics

4

Electromagnetic Phenomena

Chapter 1 explained how the different types of power system dynamics can be categorized according to their time scale. It also identified the fastest dynamics of interest to this book to be those associated with the electromagnetic interactions that occur within the generator immediately after a disturbance appears on the system. These dynamics lead to the generation of high currents and torques inside the generator and typically have a time scale of several milliseconds. Over this time period the inertia of the turbine and generator is sufficient to prevent any significant change in rotor speed so that the speed of the rotor can be assumed constant. Later chapters will consider longer time-scale electromechanical dynamics when the effect of rotor speed changes must be included.

To help understand how the fault currents and torques are produced this chapter will use basic physical laws to explain the electromagnetic interactions taking place within the generator. Although this approach requires some simplifications to be made, it does allow a physical, qualitative approach to be adopted. These explanations are then used to produce equations that quantify the currents and torques in a generator with a uniform air gap. Unfortunately complications arise if the air gap is non-uniform, for example in the salient-pole generator. However, the currents, and torques, in such generators are produced by exactly the same mechanism as in a generator with a uniform air gap, only their effects are a little more difficult to quantify, the details of which are best left to the more advanced analysis techniques presented in Chapter 11. Nevertheless, the way in which the current and torque expressions are modified in the salient-pole generator is discussed at the end of each section.

The chapter opens by considering the basic principles with regard to flux linkage and its application to short circuits in single-phase circuits. These principles are then used to study short-circuit effects in the synchronous generator where the interactions between the stator and rotor circuits must be included. Two types of fault are considered: firstly, a three-phase short circuit on the generator terminals and, secondly, a phase-to-phase short circuit. Fortunately, terminal three-phase short circuits are rare but, should one occur, the generator must be able to withstand the high currents and forces produced and remain intact. From a theoretical point of view, the analysis of such a fault allows a number of important terms and parameters to be introduced and quantified. A more common type of fault is the phase-to-phase fault. This type of fault introduces asymmetry into the problem and is considered later in the chapter. Finally the chapter analyses the currents and torques developed when a generator is synchronized to the grid.

4.1 Fundamentals

The currents and fluxes inside the generator after a fault can be analysed using the *law of constant flux linkages*. This law, based on the principle of *conservation of energy*, states that the magnetic flux

Power System Dynamics: Stability and Control, Second Edition Jan Machowski, Janusz W. Bialek and James R. Bumby
© 2008 John Wiley & Sons, Ltd

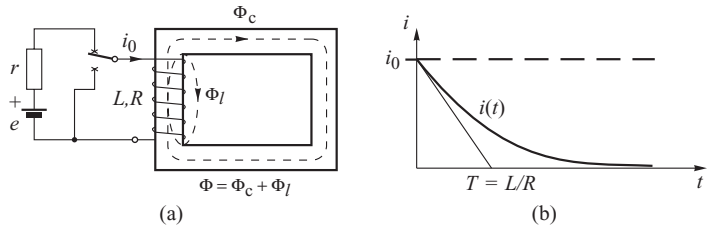

Figure 4.1 Continuity of the flux linking a coil after a change in the circuit configuration: (a) circuit diagram; (b) current as a function of time. Φ_l, leakage flux; Φ_c, core flux.

linking a closed winding cannot change instantaneously. Since the energy stored in the magnetic field is proportional to the flux linkage, this simply says that an instantaneous change in the stored energy is not possible.

The application of the law of constant flux linkages to a simple coil fed from a DC source is illustrated Figure 4.1a. At time $t = 0$ the switch disconnects the coil from the source and, at the same time, short-circuits the coil. Before the switching occurs the coil flux linkages are $\Psi_0 = N\Phi_0 = Li_0$, where L is the coil inductance, N the number of turns and i_0 the current. The law of constant flux linkages requires the coil flux linkage just before, and just after, the short circuit to be the same, that is $\Psi(t = 0^+) = \Psi(t = 0^-)$. If the coil resistance is zero the circuit is purely inductive and the current will remain constant at a value $i(t) = i_0$, as shown by the horizontal dashed line in Figure 4.1b. Normally the coil resistance is nonzero so that the magnetic energy stored in the circuit dissipates over a period of time and the current decays exponentially to zero with a time constant $T = L/R$. This is shown by the solid line in Figure 4.1b.

The law of constant flux linkage can now be used to analyse the way in which the generator responds to a short circuit. A natural first step is to consider the response of the simple RL circuit shown in Figure 4.2a as this circuit contains a number of features that are similar to the generator equivalent circuit described in Chapter 3. In this circuit the AC driving voltage is $e = E_m \sin(\omega t + \theta_0)$ and, as the circuit is assumed to be initially open circuit, $i(0^+) = i(0^-) = 0$. If the switch is now suddenly closed a short-circuit current $i(t)$ will flow which can be determined by solving the differential equation

$$E_m \sin(\omega t + \theta_0) = L\frac{di}{dt} + Ri, \tag{4.1}$$

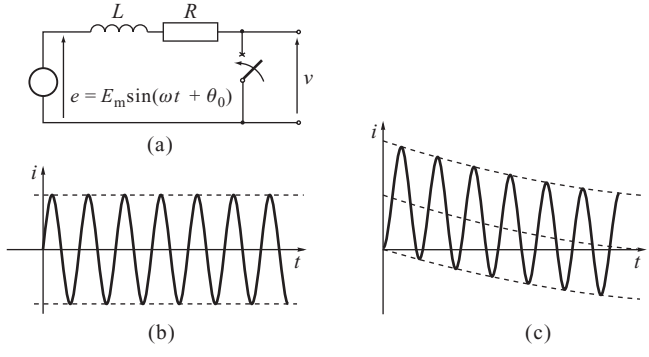

Figure 4.2 Single phase RL circuit: (a) equivalent circuit; (b) short-circuit currents with $(\theta_0 - \phi) = 0$; (c) short-circuit currents with $(\theta_0 - \phi) = -\pi/2$.

with the initial condition $i(0) = 0$. Solving this equation gives the current as

$$i(t) = \frac{E_m}{Z}\sin(\omega t + \theta_0 - \phi) - \frac{E_m}{Z}\sin(\theta_0 - \phi)e^{-Rt/L}, \tag{4.2}$$

where θ_0 defines the point in the AC cycle where the fault occurs, $\phi = \arctan(\omega L/R)$ is the phase angle and $Z = \sqrt{\omega^2 L^2 + R^2}$. The instant of the short circuit is taken as the time origin.

The first term in Equation (4.2) gives the forced response of the circuit. This alternating current is driven by the sinusoidal emf and will be the current remaining when the circuit settles down into its final steady-state condition. The second term constitutes the natural response of the circuit and is referred to as the *DC offset*. The AC component has a constant magnitude equal to E_m/Z while the initial magnitude of the DC offset depends on the point in the AC cycle where the fault occurs and decays with the time constant $T = L/R$. Figure 4.2b shows the current waveform when $(\theta_0 - \phi) = 0$ and there is no DC offset. Figure 4.2c shows the current waveform when $(\theta_0 - \phi) = -\pi/2$ and the initial DC offset is at its highest value.

The response of a synchronous generator to a short circuit is similar to that described above in the sense that it also consists of an AC component (the forced response) and a DC component (the natural response). However, Equation (4.2) must be modified to account for the three-phase nature of the generator and the effect of a varying impedance in the emf source.

4.2 Three-Phase Short Circuit on a Synchronous Generator

4.2.1 Three-Phase Short Circuit with the Generator on No Load and Winding Resistance Neglected

The cross-section of a basic generator in Figure 4.3 shows the relative position of all the windings. This diagram symbolizes both the round-rotor and salient-pole generator and, compared with the cross-section in Figure 3.13, shows the rotor to have one additional winding: the rotor d-axis damper winding denoted as D. At any point in time the position of the rotor is defined with reference to the axis of phase A by the angle γ. However, as a fault may occur when the rotor is at any position $\gamma = \gamma_0$, the time of the fault is taken as the time origin so that the rotor position at some time instant t after the fault is given by

$$\gamma = \gamma_0 + \omega t. \tag{4.3}$$

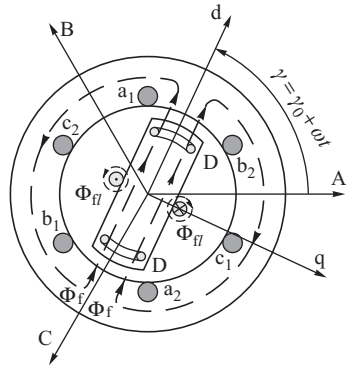

Figure 4.3 The generator and its windings.

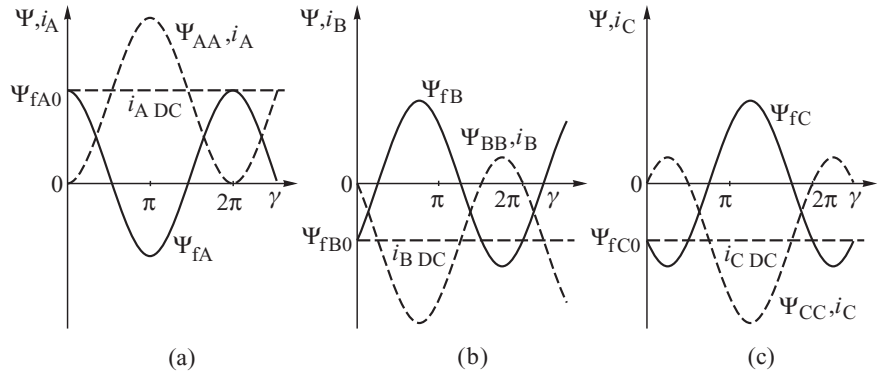

Figure 4.4 Application of the law of constant flux linkages to determine the fault currents due to a three-phase short circuit occurring at the instant $\gamma_0 = 0$: (a) phase A; (b) phase B; (c) phase C.

Before the fault occurs the generator is assumed to be running at no load with the three armature phase windings open-circuited when the only flux present in the generator is the excitation flux produced by the rotor field winding. This flux links with each phase of the armature winding producing the armature flux linkages shown in Figure 3.10a and given by Equations (3.35). When the fault occurs $\gamma = \gamma_0$ and the net flux linking each of the armature phase windings is

$$\Psi_{fA0} = \Psi_{fa}\cos\gamma_0, \quad \Psi_{fB0} = \Psi_{fa}\cos(\gamma_0 - 2\pi/3), \quad \Psi_{fC0} = \Psi_{fa}\cos(\gamma_0 - 4\pi/3), \tag{4.4}$$

where $\Psi_{fa} = N_\phi \Phi_{f0}$ is the amplitude of the excitation flux linkage of an armature phase winding before the fault occurs, Φ_{f0} is the prefault excitation flux per pole and $N_\phi = k_w N$. In this last equation N is the number of turns on each of the armature phase windings and k_w is the armature winding factor. An example of these phase flux linkages is shown by the horizontal dashed lines in Figure 4.4 which is drawn assuming that the fault occurs at $\gamma_0 = 0$.

If the resistance of the armature winding is neglected then, according to the law of constant flux linkage, the value of the flux linking each phase must remain constant after the fault at the value Ψ_{fA0}, Ψ_{fB0} and Ψ_{fC0} defined by the equations in (4.4). After the fault, the rotor continues to rotate and the linkages Ψ_{fA}, Ψ_{fB} and Ψ_{fC} continue to change sinusoidally as shown by the solid lines in Figure 4.4 and have an equivalent effect to the emf in Figure 4.2a. To keep the total flux linkages of each of the phase windings constant, additional currents i_A, i_B and i_C must be induced in the short-circuited phase windings to produce the flux linkages Ψ_{AA}, Ψ_{BB} and Ψ_{CC} shown by the sinusoidal dashed lines in Figure 4.4. The total flux linkage of each phase winding can now be obtained by adding the two components of flux linkage together to give

$$\begin{aligned} \Psi_A(t) &= \Psi_{AA} + \Psi_{fA} = \Psi_{fA0} = \text{constant} \\ \Psi_B(t) &= \Psi_{BB} + \Psi_{fB} = \Psi_{fB0} = \text{constant} \\ \Psi_C(t) &= \Psi_{CC} + \Psi_{fC} = \Psi_{fC0} = \text{constant}, \end{aligned} \tag{4.5}$$

which on rearranging gives the flux linkages Ψ_{AA}, Ψ_{BB} and Ψ_{CC} as

$$\Psi_{AA} = \Psi_{fA0} - \Psi_{fA}, \quad \Psi_{BB} = \Psi_{fB0} - \Psi_{fB}, \quad \Psi_{CC} = \Psi_{fC0} - \Psi_{fC}. \tag{4.6}$$

As the flux linkage is equal to the product of inductance and current, these flux linkages can now be used to obtain expressions for the phase current provided that the inductance value is known.[1]

[1] The inductance value required is not simply the winding self-inductance but an equivalent inductance that takes into account the way the winding is coupled with all the other windings in the generator. The importance of this coupling will be examined in Sections 4.2.3 and 4.2.4 when actual values for L_{eq} are discussed.

In the case of a generator with a uniform air gap the equivalent inductance of each of the phase windings L_{eq} is the same and does not depend on rotor position (see Section 3.3). In this case the short-circuit phase currents $i_A = \Psi_{AA}/L_{eq}$, $i_B = \Psi_{BB}/L_{eq}$ and $i_C = \Psi_{CC}/L_{eq}$ have the same shape as the flux linkages Ψ_{AA}, Ψ_{BB} and Ψ_{CC} and consist of both an AC and a DC component. The AC component currents can be expressed as

$$\begin{aligned} i_{A\,AC} &= -i_m(t)\cos(\omega t + \gamma_0), \quad i_{B\,AC} = -i_m(t)\cos(\omega t + \gamma_0 - 2\pi/3) \\ i_{C\,AC} &= -i_m(t)\cos(\omega t + \gamma_0 - 4\pi/3), \end{aligned} \tag{4.7}$$

and are proportional to the flux linkages Ψ_{fA}, Ψ_{fB} and $\Psi_{fC,}$ while the DC component currents can be expressed as

$$i_{A\,DC} = i_m(0)\cos\gamma_0, \quad i_{B\,DC} = i_m(0)\cos(\gamma_0 - 2\pi/3), \quad i_{C\,DC} = i_m(0)\cos(\gamma_0 - 4\pi/3), \tag{4.8}$$

and are proportional to Ψ_{fA0}, Ψ_{fB0} and Ψ_{fC0}. In order to generalize these two sets of equations the maximum value of the current in Equation (4.7) has been defined as $i_m(t)$ while in Equation (4.8) it is $i_m(0)$, the value of $i_m(t)$ at the instant of the fault. When the winding resistance is neglected, $i_m(t)$ is constant and equal to its initial value $i_m(0)$. The net current is obtained by adding the component currents to give

$$\begin{aligned} i_A &= -i_m(t)\cos(\omega t + \gamma_0) + i_m(0)\cos\gamma_0 \\ i_B &= -i_m(t)\cos(\omega t + \gamma_0 - 2\pi/3) + i_m(0)\cos(\gamma_0 - 2\pi/3) \\ i_C &= -i_m(t)\cos(\omega t + \gamma_0 - 4\pi/3) + i_m(0)\cos(\gamma_0 - 4\pi/3), \end{aligned} \tag{4.9}$$

where the DC offset depends on γ_0, the instant in the AC cycle when the fault occurs, and is different for each phase of the generator.

The combined effect of the AC and the DC components of the three armature phase currents is to produce an armature reaction mmf that drives an armature reaction flux across the air gap to link with the rotor windings and induce currents in them. Consider first the effect of the AC phase currents $i_{A\,AC}$, $i_{B\,AC}$ and $i_{C\,AC}$ as shown in the upper row of diagrams in Figure 4.5. These AC phase currents, Figure 4.5a, produce an AC armature reaction mmf $F_{a\,AC}$ that behaves in a similar way to the steady-state armature reaction mmf F_a discussed in Section 3.3. Recall that in the steady state F_a rotates at the same speed as the rotor (and the excitation mmf F_f), demagnetizes the machine and produces a torque proportional to the sine of the angle between F_a and F_f. During the short circuit the developed electrical torque and power are both zero so that the angle between $F_{a\,AC}$ and F_f is 180°; $F_{a\,AC}$ directly opposes F_f and the flux $\Phi_{a\,AC}$, produced by $F_{a\,AC}$, takes the path shown in Figure 4.5b. Consequently, the rotor flux linkages $\Psi_{a\,AC\,r}$ produced by $\Phi_{a\,AC}$ are constant and negative (with respect to the excitation linkages) as shown by the solid line in Figure 4.5c. Here the subscript 'r' has been added to emphasize that $\Psi_{a\,AC\,r}$ is the rotor flux linkage produced by the armature flux $\Phi_{a\,AC}$.

The lower row of diagrams in Figure 4.5 shows the combined effect of the DC phase currents $i_{A\,DC}$, $i_{B\,DC}$ and $i_{C\,DC}$. These currents, Figure 4.5a, produce a stationary DC mmf $F_{a\,DC}$ which drives the stationary armature flux $\Phi_{a\,DC}$ shown in Figure 4.5b. The space direction of $F_{a\,DC}$ can be obtained by adding the component mmfs due to $i_{A\,DC}$, $i_{B\,DC}$ and $i_{C\,DC}$ in a similar way as in Equation (3.40) when the resulting mmf $F_{a\,DC}$ is found to be always directed at an angle γ_0 with respect to the A-axis. As the rotor is also at angle γ_0 at the instant of the fault, $F_{a\,DC}$ is always aligned initially with the rotor d-axis and then counter-rotates with respect to it. This means that the rotor flux linkage $\Psi_{a\,DC\,r}$, produced by $\Phi_{a\,DC}$, is initially positive (magnetizes the machine) and then, as the rotor rotates, $\Psi_{a\,DC\,r}$ changes cosinusoidally as shown in Figure 4.5c.

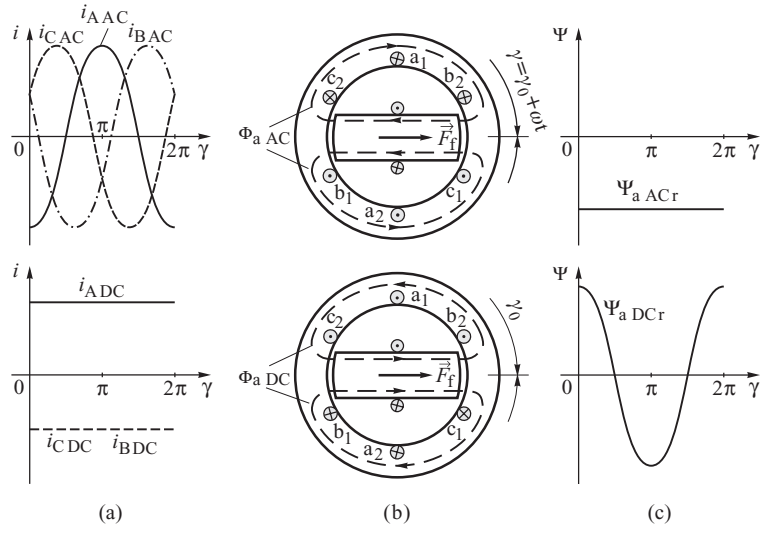

Figure 4.5 Effect of the AC component (upper row) and the DC component (lower row) of the armature currents: (a) AC and DC components of the currents; (b) path of the armature reaction flux (rotating for the AC component, stationary for the DC component); (c) linkages with the rotor windings. Position shown at the instant of fault $\gamma_0 = 0$.

As the rotor field and damper windings are closed, their total flux linkage must remain unchanged immediately after the fault. Consequently, additional currents must flow in these windings to compensate the armature flux $\Psi_{a\,r} = \Psi_{a\,AC\,r} + \Psi_{a\,DC\,r}$ that links with the rotor. Figure 4.6 shows the rotor linkages equal to $-\Psi_{a\,r}$ necessary for this and the field and damper currents which must flow to set up such linkages. Both currents contain DC and AC components. Consequently, the resulting rotor flux, as seen by the armature, can be assumed to be unchanged by the fault. These linkages were shown as Ψ_{fA}, Ψ_{fB} and Ψ_{fC} in Figure 4.4.

To summarize, a three-phase fault causes short-circuit armature currents to flow which have both an AC and a DC component. At the instant of the fault, both the AC and DC armature mmfs are directed along the rotor d-axis but then, as the rotor rotates, the AC armature mmf rotates with it inducing additional direct currents in the rotor, while the DC armature mmf is stationary inducing additional alternating currents in the rotor. *There is always a complementary pair of stator to rotor currents of the form* AC → DC *and* DC → AC. The value of the DC offset may be different for each stator phase and depends on the instant of the fault.

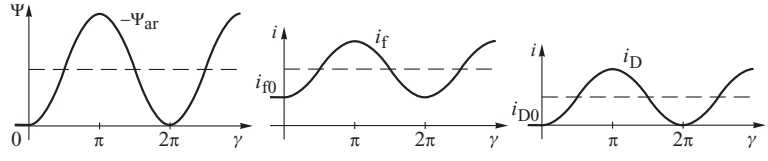

Figure 4.6 Application of the law of constant flux linkage to determine the currents flowing in the rotor windings : Ψ_r, induced flux linkages necessary in the rotor windings in order to compensate the armature reaction flux linkages; i_f, current in the field winding; i_D, current in the damper winding.

4.2.2 Including the Effect of Winding Resistance

A winding dissipates energy in its resistance at a rate proportional to the current squared. Consequently, the stored magnetic energy decays with time and the induced direct currents maintaining the flux linkages decay exponentially to zero at a rate determined by the circuit time constant $T = L/R$.

The DC component of the armature phase current decays with the *armature time constant* T_a determined by the equivalent inductance and resistance of the phase winding. To account for this decay the direct currents in Equations (4.8) must be modified to

$$\begin{aligned} i_{A\,DC} &= i_m(0)e^{-t/T_a}\cos\gamma_0, \quad i_{B\,DC} = i_m(0)e^{-t/T_a}\cos(\gamma_0 - 2\pi/3) \\ i_{C\,DC} &= i_m(0)e^{-t/T_a}\cos(\gamma_0 - 4\pi/3), \end{aligned} \tag{4.10}$$

when the total phase currents become

$$\begin{aligned} i_A &= -i_m(t)\cos(\omega t + \gamma_0) + i_m(0)e^{-t/T_a}\cos\gamma_0 \\ i_B &= -i_m(t)\cos(\omega t + \gamma_0 - 2\pi/3) + i_m(0)e^{-t/T_a}\cos(\gamma_0 - 2\pi/3) \\ i_C &= -i_m(t)\cos(\omega t + \gamma_0 - 4\pi/3) + i_m(0)e^{-t/T_a}\cos(\gamma_0 - 4\pi/3). \end{aligned} \tag{4.11}$$

These equations are identical in form to that obtained for the single-phase circuit in Equation (4.2) with $\gamma_0 = \theta_0$ and a phase angle $\phi = \pi/2$. However, in Equation (4.2) $i_m(t)$ is constant whereas for the synchronous generator it varies with time for reasons that will now be explained.

The currents $i_{A\,AC}$, $i_{B\,AC}$ and $i_{C\,AC}$ induce direct currents in the rotor windings. These direct currents decay with a time constant determined by the particular rotor circuit in which they flow. Consequently the DC component of the damper winding current decays with the damper winding time constant, called the d-*axis subtransient short-circuit time constant* T_d'', while the DC component of the field current decays with the field winding time constant, called the d-*axis transient short-circuit time constant* T_d'. Normally the resistance of the damper winding is much higher than the resistance of the field winding so that $T_d'' \ll T_d'$ and the DC component of the damper winding current decays much faster than the DC component of the field current. As the DC rotor currents induce AC stator currents, the magnitude of the AC component of the stator current $i_m(t)$ will decay to its steady-state value with these two time constants. Conversely, as the DC phase currents $i_{A\,DC}$, $i_{B\,DC}$ and $i_{C\,DC}$ induce alternating currents in the field and the damper windings, these AC rotor currents will also decay with the time constant T_a.

Table 4.1 summarizes the relationship between the relevant components of the stator and the rotor currents and their decay time constants.

Figure 4.7 shows a typical time variation of the generator currents resulting from a three-phase terminal short circuit. The diagrams constituting Figure 4.7 have been organized so that the first row shows the currents in phase A of the stator armature winding, the second row the field winding currents and the third row the damper winding currents. Only phase A of the armature winding is shown because the currents in phases B and C are similar but shifted by $\pm 2\pi/3$. The first column in Figure 4.7 shows the DC component of the armature current and the corresponding induced rotor currents, the second column the AC component of the armature current and the corresponding

Table 4.1 Pairs of coupled stator–rotor currents.

Three-phase stator winding	Rotor windings (field and damper)	Means of energy dissipation	Time constant
DC	AC	Resistance of the armature winding	T_a
AC	DC	Resistance of the damper winding	T_d''
		Resistance of the field winding	T_d'

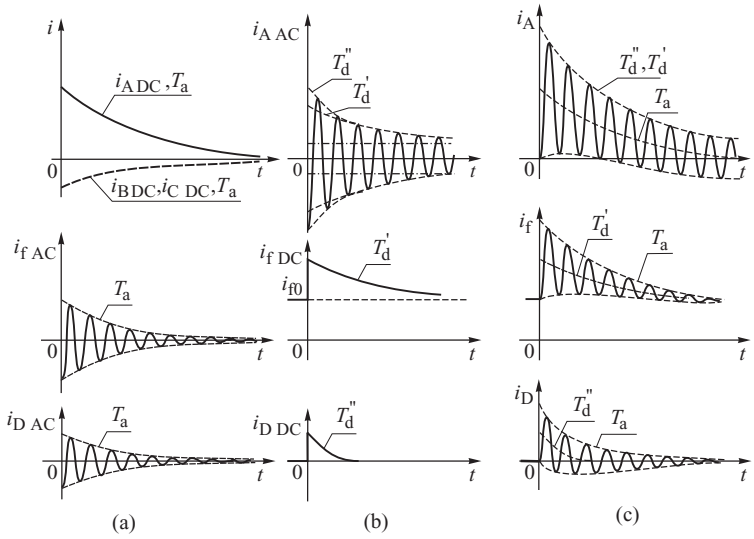

Figure 4.7 Short-circuit currents in the generator: (a) DC component of the phase current and the corresponding AC component of the field and damper winding current; (b) AC component of the current in phase A and the corresponding DC component of the field and damper winding current; (c) the resulting current in phase A, the field and the damper winding as the sum of the currents shown in (a) and (b).

induced rotor currents, and the third column the resultant currents in the armature, the field and the damper winding made up from their AC and DC components. The dashed lines indicate the exponential envelopes that correspond to the different time constants.

Note that the AC component of the armature current does not decay completely to zero but to a steady-state value. The field current decays to its prefault value i_{f0} while the damper winding current decays completely to zero, its prefault value.

Now it is possible to compare the generator short-circuit armature current shown in the top diagram of Figure 4.7c with the response of a short-circuited *RL* circuit shown in Figure 4.2c. Both currents have a DC component that depends on the instant the short circuit is applied and that decays with a time constant determined by the resistance and inductance of the winding. However, while the AC component shown in Figure 4.2c has a constant amplitude, the amplitude of the AC component of the armature current shown in Figure 4.7c is decaying with two time constants depending on the resistance and inductance of the damper and field windings. The changing amplitude of the alternating current suggests that the internal impedance of the generator is not constant, as in Figure 4.2, but is changing with time due to interactions between the armature, field and damper windings. This will be discussed further in the next section.

If $T_a > T_d''$ the fault current in phase A for $\gamma_0 = 0$ is positive for the first few cycles and does not cross zero until the DC offset decays. This is typical for large generators. If $T_d' > T_a$ the field current i_f will always oscillate above its steady-state value i_{f0}. If $T_d'' < T_a$, the damper current i_D may go negative.

4.2.3 Armature Flux Paths and the Equivalent Reactances

Section 3.3 explained how the effect of the steady-state AC armature flux on the generator performance could be accounted for in the equivalent circuit model by the voltage drop across the

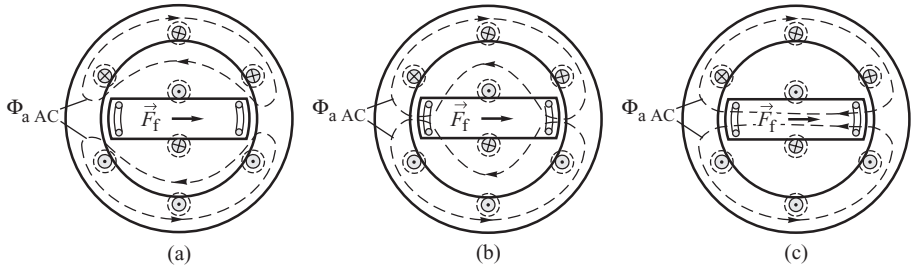

Figure 4.8 The path of the armature flux in: (a) the subtransient state (screening effect of the damper winding and the field winding); (b) the transient state (screening effect of the field winding only); (c) the steady state. In all three cases the rotor is shown to be in the same position but the actual rotor position corresponding to the three states will be separated by a number of rotations.

synchronous reactances X_d and X_q. A similar approach can be adopted during the fault period, but now the value of the armature reactance will be different as the additional currents induced in the rotor windings force the armature flux to take a different path to that in the steady state. As the additional rotor currents prevent the armature flux from entering the rotor windings, they have the effect of *screening the rotor* from these changes in armature flux.

Figure 4.8 shows three characteristic states that correspond to three different stages of rotor screening. Immediately after the fault, the current induced in both the rotor field and damper windings forces the armature reaction flux completely out of the rotor to keep the rotor flux linkages constant, Figure 4.8a, and the generator is said to be in the *subtransient state*. As energy is dissipated in the resistance of the rotor windings, the currents maintaining constant rotor flux linkages decay with time allowing flux to enter the windings. As the rotor damper winding resistance is the largest, the damper current is the first to decay, allowing the armature flux to enter the rotor pole face. However, it is still forced out of the field winding itself, Figure 4.8b, and the generator is said to be in the *transient state*. The field current then decays with time to its steady-state value allowing the armature reaction flux eventually to enter the whole rotor and assume the minimum reluctance path. This steady state is illustrated in Figure 4.8c and corresponds to the flux path shown in the top diagram of Figure 4.5b.

It is convenient to analyse the dynamics of the generator separately when it is in the subtransient, transient and steady states. This is accomplished by assigning a different equivalent circuit to the generator when it is in each of the above states, but in order to do this it is first necessary to consider the generator reactances in each of the characteristic states.

The inductance of a winding is defined as the ratio of the flux linkages to the current producing the flux. Thus, a low-reluctance path results in a large flux and a large inductance (or reactance) and vice versa. Normally a flux path will consist of a number of parts each of which has a different reluctance. In such circumstances it is convenient to assign a reactance to each part of the flux path when the equivalent reactance is made up of the individual path reactances. In combining the individual reactances it must be remembered that parallel flux paths correspond to a series connection of reactances while series paths correspond to a parallel connection of reactances. This is illustrated in Figure 4.9 for a simple iron-cored coil with an air gap in the iron circuit. Here the total coil flux Φ consists of the leakage flux Φ_l and the core flux Φ_c. The reactance of the leakage flux path is X_l, while the reactance of the core flux path has two components. The first component corresponds to the flux path across the air gap X_{ag} and the second component corresponds to the flux path through the iron core X_{Fe}. In the equivalent circuit X_l is connected in series with the parallel combination X_{ag} and X_{Fe}. As the reluctance of a flux path in iron is very small compared

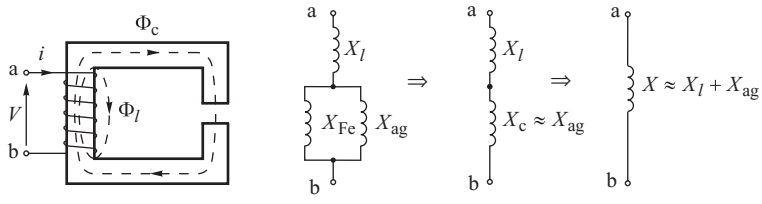

Figure 4.9 A coil with an air gap and its equivalent circuit diagram.

with that in air $X_{\text{Fe}} \gg X_{\text{ag}}$ and the total reactance of the winding is dominated by those parts of the path that are in air: the air gap and the flux leakage path. Consequently $X \approx X_{\text{ag}} + X_l$.

These principles are applied to the synchronous generator in Figure 4.10 for each of the three characteristic states. It also introduces a number of different reactances, each of which corresponds to a particular flux path:

X_l	corresponds to the path that the armature leakage flux takes around the stator windings and is referred to as the *armature leakage reactance*;
X_{a}	corresponds to the flux path across the air gap and is referred to as the *armature reaction reactance*;
X_{D}	corresponds to the flux path around the damper winding;
X_{f}	corresponds to the flux path around the field winding.

The reactances of the damper winding and the field winding are also proportional to the flux path around the winding. Thus X_{D} and X_{f} are proportional to the actual damper and field winding reactance respectively.

In Figure 4.10 the armature reactances in each of the characteristic states are combined to give the following equivalent reactances:

X''_{d}	direct-axis subtransient reactance
X'_{d}	direct-axis transient reactance
X_{d}	direct-axis synchronous reactance.

In the subtransient state the flux path is almost entirely in air and so the reluctance of this path is very high. In contrast, the flux path in the steady state is mainly through iron with the reluctance being dominated by the length of the air gap. Consequently, the reactances, in increasing magnitude,

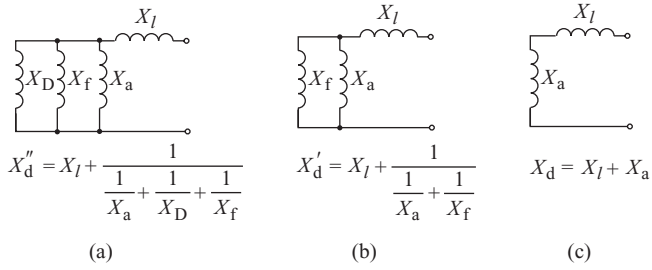

Figure 4.10 Equivalent reactance of a synchronous generator in the: (a) subtransient state; (b) transient state; (c) steady state.

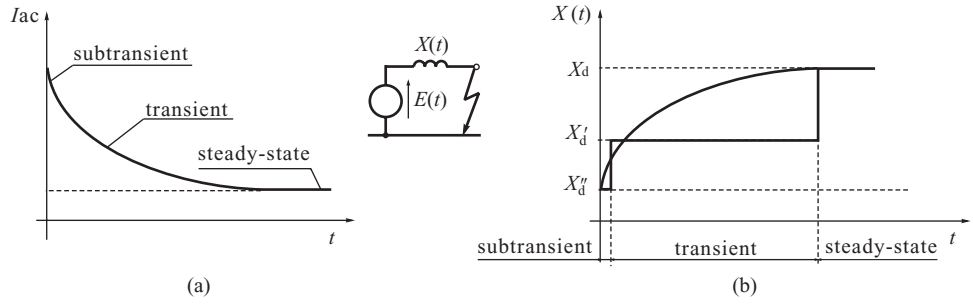

Figure 4.11 Three-step approximation of the generator model: (a) rms value of the AC component of the armature current; (b) generator reactances.

are $X''_d < X'_d < X_d$. In the case of large synchronous generators X'_d is about twice as large as X''_d, while X_d is about 10 times as large as X''_d.

As previously discussed, following a fault the generator becomes a dynamic source that has both a time-changing synchronous reactance $X(t)$ and an internal voltage $E(t)$. Dividing the generator response into the three characteristic states with associated constant reactances makes it easier to analyse the generator dynamics. Rather than considering one generator model with time-changing reactances and internal voltages, it is convenient to consider the three states separately using conventional AC circuit analysis. This is illustrated in Figure 4.11. The rms value of the AC component of the armature current $I_{AC}(t)$ is shown in Figure 4.11a. This AC component was previously shown in the top diagram of Figure 4.7b. The continuously changing synchronous reactance X, shown in Figure 4.11b, can be calculated by dividing the open-circuit emf E by the armature current $I_{AC}(t)$. In each of the three characteristic states, the generator will be represented by a constant emf behind a constant reactance X''_d, X'_d, X_d, respectively. Dividing the emf by the appropriate reactance will give the subtransient, transient and steady-state currents.

4.2.3.1 Quadrature-Axis Reactances

Figure 4.8 shows the path taken by the AC armature flux in the three characteristic states and is drawn assuming that the armature mmf is directed along the d-axis. This is true when the generator is on no load prior to the three-phase short circuit, but generally, for other types of disturbances or for a generator operating on load prior to a disturbance, the armature mmf will have both a d- and a q-component. In this more general case it is necessary to analyse the influence of the two armature mmf components separately using the two-reaction method introduced in Section 3.3.

If a generator is in the subtransient state, and the armature mmf is directed along the rotor d-axis, then the armature reaction flux will be forced out of the rotor by the currents induced in the field winding, the damper winding and the rotor core. This flux path corresponds to the direct-axis subtransient reactance X''_d. On the other hand, if the armature mmf is directed along the rotor q-axis, then the only currents forcing the armature reaction flux out of the rotor are the rotor core eddy currents and the currents in the q-axis damper winding. If a generator only has a d-axis damper winding, then the q-axis screening effect is much weaker than that for the d-axis, and the corresponding *quadrature axis subtransient reactance* X''_q is greater than X''_d. This difference between X''_q and X''_d is called *subtransient saliency*. For a generator with a damper winding in both the d-axis and the q-axis, the screening effect in both axes is similar, subtransient saliency is negligible and $X''_q \approx X''_d$.

When the generator is in the transient state, screening is provided by the field winding which is only in the d-axis. However, in the round-rotor generator some q-axis screening will be produced by eddy currents in the rotor iron with the effect that $X'_q > X'_d$. The actual value of X'_q is somewhere

between X'_d and X_q with typically $X'_q \approx 2X'_d$. In the salient-pole generator the laminated rotor construction prevents eddy currents flowing in the rotor body, there is no screening in the q-axis and $X'_q = X_q$. Because of the absence of a field winding in the q-axis, there is some degree of *transient saliency* in all types of generator.

Table 4.2 summarizes the different types of saliency and the reasons for it, while typical values for all the generator parameters are tabulated in Table 4.3.

In Table 4.3 the quadrature-axis subtransient short-circuit time constant T''_q and the transient short-circuit time constant T'_q are defined in the same way as for the direct-axis time constants T''_d, T'_d in Table 4.1. For the round-rotor generator, since there is no field winding in the q-axis, it is assumed that rotor body eddy currents contribute to the q-axis parameters.

Values of the short-circuit time constants T'_d, T'_q, T''_d, T''_q correspond to the armature winding when short-circuited. Some manufacturers may quote the time constants for the armature on open circuit as T'_{do}, T'_{qo}, T''_{do}, T''_{qo}. An approximate relationship between the open- and short-circuit time constants may be found from the equivalent circuits shown in Figure 4.10. If X_l is neglected then

$$X'_d \cong \frac{X_a X_f}{X_a + X_f}, \quad \frac{1}{X'_d} \cong \frac{1}{X_a} + \frac{1}{X_f} \tag{4.12}$$

and

$$X''_d \cong \frac{1}{\frac{1}{X_D} + \frac{1}{X'_d}}, \quad X_D \cong \frac{X'_d X''_d}{X'_d - X''_d}. \tag{4.13}$$

Table 4.2 Saliency in the three characteristic states of the synchronous generator.

			Saliency	
State	Generator type	Reactance	Yes/no	Reason
Subtransient	Any type but with a d-axis damper only	$X''_q > X''_d$	Yes	Weaker screening in the q-axis because of the lack of damper winding
	Any type but with both d- and q-axis damper windings	$X''_q \approx X''_d$	No	Similar screening in both axes
Transient	Round rotor	$X'_q > X'_d$	Yes	Strong screening in the d-axis due to the field winding but weak screening in the q-axis due to the rotor body currents
	Salient pole	$X'_q = X_q$	Yes	No screening in the q-axis because of the laminated rotor core
Steady state	Round rotor	$X_q \approx X_d$	No	Symmetrical air gap in both axes
	Salient pole	$X_q < X_d$	Yes	Larger air gap on the q-axis

Table 4.3 Typical parameter values for large generators. Reactances are per unit to the rated MVA and time constants are in seconds.

	Round rotor			Salient-pole rotor	
Parameter	200 MVA	600 MVA	1500 MVA	150 MVA	230 MVA
X_d	1.65	2.00	2.20	0.91	0.93
X_q	1.59	1.85	2.10	0.66	0.69
X'_d	0.23	0.39	0.44	0.3	0.3
X'_q	0.38	0.52	0.64	—	—
X''_d	0.17	0.28	0.28	0.24	0.25
X''_q	0.17	0.32	0.32	0.27	0.27
T'_d	0.83	0.85	1.21	1.10	3.30
T'_q	0.42	0.58	0.47	—	—
T''_d	0.023	0.028	0.030	0.05	0.02
T''_q	0.023	0.058	0.049	0.06	0.02

In order to determine the time constants T''_d, T''_{do} it is necessary to insert the resistance R_D into the branch with X_D in Figure 4.10a. This is illustrated in Figure 4.12. If X_l is neglected then the short circuit in Figure 4.12a bypasses all the shunt branches and the time constant is

$$T''_d = \frac{X_D}{\omega R_D}. \tag{4.14}$$

When the circuit is open circuit as in Figure 4.12b, the time constant is

$$T''_{do} = \frac{X_D + \frac{X_a X_f}{X_a + X_f}}{\omega R_D} \cong \frac{X_D + X'_d}{\omega R_D}. \tag{4.15}$$

Dividing Equation (4.14) by Equation (4.15), and substituting for X_D from Equation (4.13), gives $T''_d / T''_{do} \approx X''_d / X'_d$. Following a similar procedure for the remaining time constants in the d- and q-axes gives the relationships

$$T''_d \cong T''_{do} \frac{X'_d}{X_d}, \quad T''_q \cong T''_{qo} \frac{X''_q}{X'_q}, \quad T'_d \cong T'_{do} \frac{X'_d}{X_d}, \quad T'_q \cong T'_{qo} \frac{X'_q}{X_q}. \tag{4.16}$$

The open-circuit time constants are larger than the short-circuit ones.

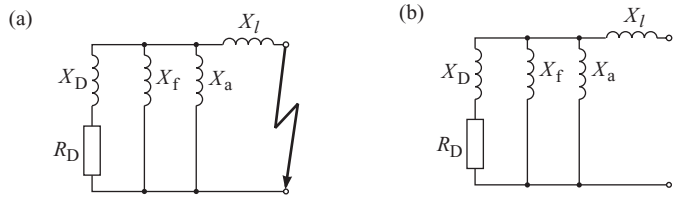

Figure 4.12 Equivalent circuits for determining the subtransient time constants: (a) short circuit; (b) open circuit.

4.2.4 Generator Electromotive Forces and Equivalent Circuits

Equivalent circuits were first used in Section 3.3 to analyse the steady-state behaviour of the generator and in this subsection their use is extended to cover all three characteristic states. As these equivalent circuits are valid only for AC circuit analysis purposes, they can only be used to analyse the AC component of the armature current and the DC component must be neglected. What follows is a physical justification for using such equivalent circuits to model the synchronous generator, with a full mathematical derivation being left until Chapter 11.

In the steady state the generator can be modelled by the equivalent circuit shown in Figure 3.17 where the generator is represented in both the d- and q-axes by constant internal emfs E_q and E_d acting behind the synchronous reactances X_d and X_q. The emf E_q is proportional to the excitation flux and, as the excitation flux is proportional to the field current, is also given the symbol E_f. As there is no excitation in the q-axis, the corresponding emf E_d is zero. Consequently the total internal emf is $\underline{E} = \underline{E}_q + \underline{E}_d = \underline{E}_q = \underline{E}_f$.

A similar representation can be used when the generator in the subtransient and transient states. However, as each of the three generator characteristic states is characterized by a different pair of reactances, there are now three different equivalent circuits, each valid at the beginning of a corresponding state, in which the generator is represented by a pair of constant internal emfs behind the appropriate reactances. It is important to realize that in each of the states, the internal emfs will be different and equal to that part of the rotor flux linkages that are assumed to remain constant in that particular characteristic state.

In the steady state the three emfs E, E_f and E_q are all equal, but during a disturbance they have a different interpretation and it is important to differentiate between them. E_q is proportional to the field current (which produces a d-axis mmf) and will vary in proportion to the changes in the field current. During a disturbance there are also currents induced in the q-axis rotor body so that E_d will no longer be zero but will vary in proportion to these rotor body currents. Consequently neither E_q nor E_d are constant during either the subtransient or transient state.

The emf E_f is defined as being proportional to the voltage V_f applied to the field winding and it is only in the steady state when the field current $i_f = i_{f0} = V_f / R_f$ that $E_f = E_q$ (R_f is the field winding resistance). In all other characteristic states $i_f \neq V_f / R_f$ and $E_f \neq E_q$. The importance of E_f is that it reflects the effect of excitation control.

4.2.4.1 Subtransient State

During the subtransient period the armature flux is forced into high-reluctance paths outside the rotor circuits by currents induced in the field and damper winding. This is shown in Figure 4.8a for the flux acting along the d-axis only, but in general the armature flux will have both d- and q-components. In this more general case the flux path is distorted not only by the d-axis field and damper currents but also by the q-axis damper current (if there is a q-axis damper winding) and q-axis rotor body currents. The reactances associated with the flux path are X''_d and X''_q. As the rotor flux linkages in both axes are assumed to remain constant during the subtransient state, the internal emf corresponding to these linkages may also be assumed to remain constant and the generator may be represented by a constant *subtransient internal emf* $\underline{E}'' = \underline{E}''_d + \underline{E}''_q$ acting behind the subtransient reactances X''_d and X''_q. The generator circuit equation is then

$$\underline{E}'' = \underline{V}_g + R\underline{I} + \mathrm{j}\underline{I}_d X''_d + \mathrm{j}\underline{I}_q X''_q, \tag{4.17}$$

where $\underline{I} = \underline{I}_d + \underline{I}_q$ is the armature current immediately after the fault. Its value can be calculated once $\underline{E}''$ is known. The emf E''_q is proportional to the rotor flux linkages along the d-axis, that is the sum of the field winding and the d-axis damper winding flux linkages. Similarly E''_d is proportional to q-axis rotor flux linkages, that is the sum of the q-axis rotor body and the q-axis damper winding flux linkages.

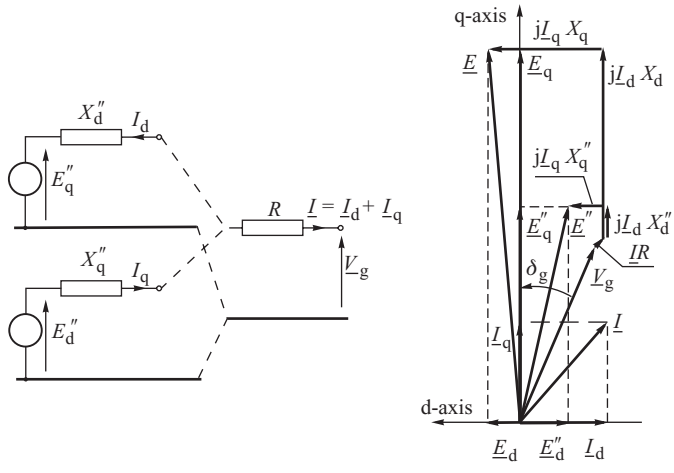

Figure 4.13 Equivalent circuit and phasor diagram of the generator in the subtransient state.

It is important to understand the difference between the steady-state and subtransient emfs. Consider first E_q and E''_q. E_q is proportional to the field current and therefore to the field winding self-flux linkages. In order to screen the field winding from the change in armature flux, the field current varies following the fault and E_q varies accordingly. The emf E''_q is proportional to the total rotor d-axis flux linkages (field and damper windings) and includes the linkages due to the armature flux. This total flux linkage must remain constant and equal to its prefault value following the fault. If the generator is on no load prior to the fault then the prefault armature current and flux are zero. In this case the total prefault rotor flux linkages are equal to the linkages due to the excitation flux only and the prefault values of E_q and E''_q are the same and equal to the terminal voltage. If, however, the generator is on load prior to the fault then the armature current is not zero and the total rotor flux linkages will include the effect of the prefault linkages due to the armature flux. In this case the prefault values of E_q and E''_q will not be the same. A similar argument is valid for the q-axis flux linkages and emfs. Thus the prefault value of E''_d is equal to zero only when the generator is on no load prior to the fault.

The emf $\underline{E} = \underline{E}_q + \underline{E}_d$ can be found by observing that

$$\begin{aligned}\underline{E} &= \underline{V}_g + R\underline{I} + j\underline{I}_d X_d + j\underline{I}_q X_q \\ &= \underline{V}_g + R\underline{I} + j\underline{I}_d \left(X_d - X''_d\right) + j\underline{I}_d X''_d + j\underline{I}_q \left(X_q - X''_q\right) + j\underline{I}_q X''_q \\ &= \underline{E}'' + j\underline{I}_d \left(X_d - X''_d\right) + j\underline{I}_q \left(X_q - X''_q\right).\end{aligned} \tag{4.18}$$

Figure 4.13 shows the equivalent circuit and the phasor diagram of the generator in the subtransient state. $\underline{E}$ is no longer along the q-axis and has both E_d and E_q components. Usually R is small, so the length of IR is small too. The length of IR has been exaggerated in Figure 4.13 to show clearly its influence.

4.2.4.2 Transient State

During the transient period the armature flux is forced into high-reluctance paths outside the field winding by currents induced in the field winding. This is shown in Figure 4.8b for the flux acting along the d-axis only, but in general the armature flux will have both d- and q-components. In this more general case the flux path is distorted not only by the d-axis field current, but also by the

q-axis rotor body currents. The reactances associated with the flux path are X'_d and X'_q. As the rotor flux linkages in both axes are assumed to remain constant during the transient state, the internal emf corresponding to these linkages may also be assumed to remain constant and equal to their prefault values. Thus the generator may be represented in the transient state by constant *transient internal emfs* E'_q and E'_d acting behind the transient reactances X'_d and X'_q. The circuit equation of the generator is then

$$\underline{E}' = \underline{E}'_q + \underline{E}'_d = \underline{V}_g + R\underline{I} + \mathrm{j}\underline{I}_d X'_d + \mathrm{j}\underline{I}_q X'_q, \tag{4.19}$$

where $\underline{I} = \underline{I}_d + \underline{I}_q$ is the armature current at the beginning of the transient period. Its value is different from that given by Equation (4.17) and can be calculated once $\underline{E}'$ is known. E'_q is proportional to the field winding flux linkages Ψ_f whilst E'_d is proportional to the flux linkage of the q-axis rotor body. Both components include the effect of the prefault armature current and are assumed to remain constant during the transient state. Following a similar argument as for the subtransient state, the prefault values of the emfs are $E'_{q0} = E_{q0} = V_g$ and $E'_{d0} = E_{d0} = 0$ only if prior to the fault the generator is on no load (zero armature reaction flux). If prior to the fault the generator is on load then E'_q and E'_d include the effect of the load current and $\underline{E}'_0 \neq \underline{E}''_0 \neq \underline{E}_0$.

Similar to the subtransient state the emf $\underline{E}$ can be found from

$$\underline{E} = \underline{V}_g + R\underline{I} + \mathrm{j}\underline{I}_d X_d + \mathrm{j}\underline{I}_q X_q = \underline{E}' + \mathrm{j}\underline{I}_d \left(X_d - X'_d\right) + \mathrm{j}\underline{I}_q \left(X_q - X'_q\right). \tag{4.20}$$

Figure 4.14 shows the equivalent circuit and the phasor diagram of the round-rotor generator in the transient state. The transient emf of such a generator has both d- and q-components. For the salient-pole generator with laminated rotor there is no screening in the q-axis and $X'_q = X_q$ so that $E'_d = 0$ and $E' = E'_q$.

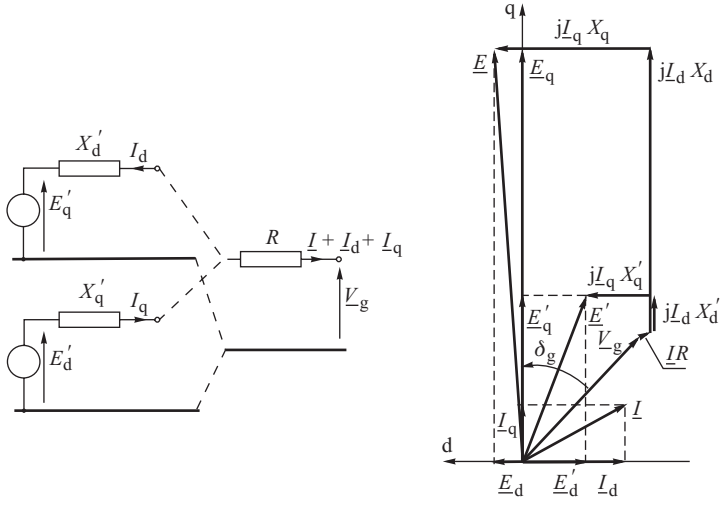

Figure 4.14 Equivalent circuit and phasor diagram of the round-rotor generator in the transient state. The length of *IR* has been exaggerated for clarity.

4.2.4.3 Establishing Initial emf Values

The previous discussion explained why the subtransient and transient emfs do not change during their respective periods (neglecting the influence of resistances) and are equal to their prefault values.

The simplest situation occurs when the generator is no load prior to the fault when the initial values of the transient and subtransient emfs are equal to the prefault steady-state emf E (and the generator prefault terminal voltage). When the generator is on load the influence of the prefault armature current $\underline{I}_0$ on the internal emfs must be taken into account. Note that the three equivalent circuits shown in Figures 3.17, 4.13 and 4.14 are valid for different states of the generator and therefore for different values of current $\underline{I}$. However, as the subtransient and transient emfs are equal to their prefault values, the three equivalent circuits must also be valid for the prefault current $\underline{I}_0$. Thus, according to Kirchhoff's law, the three equivalent circuits can be combined for the same current $\underline{I}_0$, as shown in Figure 4.15a.

By following a similar procedure to that described in Section 3.3 the initial values of $\underline{E}_0$, $\underline{E}'_0$ and $\underline{E}''_0$ can then be found from the phasor diagram, Figure 4.15b, assuming that $\underline{I}_0$ and its phase angle φ_{g0} are known. As excitation is only in the d-axis, E_0 acts along the q-axis while $\underline{E}''_0$ and $\underline{E}'_0$

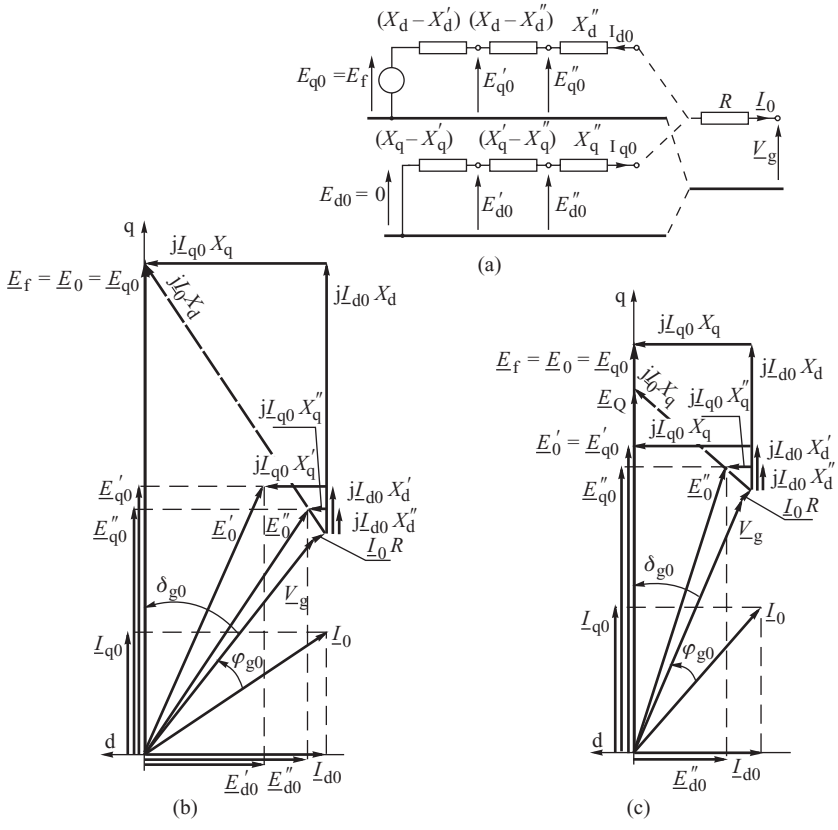

Figure 4.15 Finding the initial values of the emfs: (a) equivalent circuits; (b) phasor diagram of the round-rotor generator; (c) phasor diagram of the salient-pole generator. The length of IR has been exaggerated for clarity.

usually have nonzero direct and quadrature components. For the salient-pole generator, Figure 4.15c, $E_{d0} = 0$ and $\underline{E}'_0 = \underline{E}'_{q0}$. In the phasor diagram the value of the voltage drop across the generator resistance has been exaggerated for clarity but, in practice, the resistance is very small and can often be neglected. Once the initial values of the transient and subtransient emfs have been found, Equations (4.17) and (4.19) can be used to calculate the magnitude of the alternating current component at the start of the subtransient and transient periods respectively.

Example 4.1

A 200 MVA round-rotor generator with the parameters given in Table 4.3 is loaded with 1pu of real power and 0.5 pu of reactive power (lagging). The voltage at the generator terminals is 1.1 pu. Find the prefault values of the steady-state, transient and subtransient emfs. Assume $X_d = X_q = 1.6$ and neglect the armature resistance.

Assuming the generator voltage to be the reference, the load current is

$$\underline{I}_0 = \left(\frac{\underline{S}}{\underline{V}_g}\right)^* = \frac{P - jQ}{V_g} = \frac{1 - j0.5}{1.1} = 1.016\angle -26.6^\circ,$$

so that $\varphi_{g0} = 26.6^\circ$. The steady-state internal emf is

$$E_{q0} = \underline{V}_g + jX_d\underline{I}_0 = 1.1 + j1.6 \times 1.016\angle -26.6^\circ = 2.336\angle 38.5^\circ.$$

Thus $E_{q0} = 2.336$ and $\delta_{g0} = 38.5^\circ$. The d- and q-components of the current and voltage are

$$\begin{aligned}
I_{d0} &= -I_0 \sin(\varphi_{g0} + \delta_{g0}) = -1.016 \sin(26.6^\circ + 38.5^\circ) = -0.922 \\
I_{q0} &= I_0 \cos(\varphi_{g0} + \delta_{g0}) = 0.428 \\
V_{gd} &= -V_g \sin\delta_{g0} = -1.1 \sin 38.5^\circ = -0.685, \quad V_{gq} = V_g \cos\delta_{g0} = 0.861.
\end{aligned}$$

Now the d- and q-components of the transient and subtransient emfs can be calculated from the phasor diagram in Figure 4.15 as

$$\begin{aligned}
E'_{d0} &= V_{gd} + X'_q I_{q0} = -0.685 + 0.38 \times 0.428 = -0.522 \\
E'_{q0} &= V_{gq} - X'_d I_{d0} = 0.861 - 0.23 \times (-0.922) = 1.073 \\
E''_{d0} &= V_{gd} + X''_q I_{q0} = -0.612 \\
E''_{q0} &= V_{gq} - X''_d I_{d0} = 1.018.
\end{aligned}$$

Example 4.2

Solve a similar problem to that in Example 4.1 but for the 230 MVA salient-pole generator in Table 4.3.

The main problem with the salient-pole generator is in finding the direction of the q-axis. Equation (3.64) gives $\underline{E}_Q = \underline{V}_g + jX_q\underline{I}_0 = 1.1 + j0.69 \times 1.016\angle -26.6^\circ = 1.546\angle 23.9^\circ$. Thus $\delta_{g0} = 23.9^\circ$ and

$$\begin{aligned}
I_{d0} &= -1.016 \sin(26.6^\circ + 23.9^\circ) = -0.784, \quad I_{q0} = -1.016 \cos(26.6^\circ + 23.9^\circ) = 0.647 \\
V_{gd} &= -1.1 \sin 23.9^\circ = -0.446, \quad V_{gq} = 1.1 \cos 23.9^\circ = 1.006 \\
E_{q0} &= V_{gq} - I_{d0} X_d = 1.006 - (-0.784) \times 0.93 = 1.735 \\
E'_{d0} &= -0.446 + 0.69 \times 0.647 = 0, \quad E'_{q0} = 1.006 - 0.3 \times (-0.784) = 1.241, \\
E''_{d0} &= -0.446 + 0.27 \times 0.647 = -0.271, \quad E''_{q0} = 1.006 - 0.25 \times (-0.784) = 1.202.
\end{aligned}$$

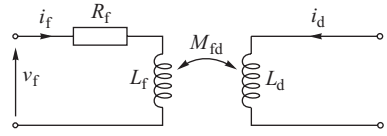

Figure 4.16 Coupling between the field winding and the d-axis armature coil.

4.2.4.4 Flux Decrement Effects

Although the subtransient and transient emfs remain constant immediately after a fault, their values change with time as the armature flux penetrates the rotor circuits. The time scale of these changes is such that changes during the subtransient period affect the short-circuit currents and torques, as will be discussed later in this chapter, while changes during the transient period can effect generator stability and are discussed at length in Chapters 5 and 6. Although a full mathematical treatment of these *flux decrement* effects must be left until Chapter 11, a basic understanding of the mechanisms behind them can be obtained by considering the simple d-axis coupled circuit shown in Figure 4.16. This circuit models the field winding and the d-axis armature coil, and the coupling that exists between them, and gives the field flux linkage as

$$\Psi_f = L_f i_f + M_{fd} i_d, \tag{4.21}$$

where L_f is the self-inductance of the field winding and M_{fd} is the mutual inductance between the two windings. Chapter 11 will show that $M_{fd} = \sqrt{3/2} M_f$.

According to the theorem of constant flux linkage, Ψ_f will remain constant immediately following any change in i_f or i_d and, since $E'_q \propto \Psi_f$, E'_q will also remain constant. However, as the field winding has a resistance greater than zero this will allow some of the magnetic stored energy to be dissipated and the winding flux linkage to change. This change in flux linkage is governed by the differential equation

$$\frac{d\Psi_f}{dt} = v_f - R_f i_f, \tag{4.22}$$

which, when rearranging and substituting Equation (4.21), gives

$$v_f = L_f \frac{di_f}{dt} + R_f i_f + M_{fd} \frac{di_d}{dt}. \tag{4.23}$$

At this point it is convenient to consider the changes Δi_f, Δi_d and Δv_f rather than absolute values when introducing the Laplace operator and writing Equation (4.23) in terms of these changes gives

$$\Delta v_f(s) = L_f s \Delta i_f(s) + R_f \Delta i_f(s) + M_{fd} s \Delta i_d(s). \tag{4.24}$$

This equation can then be written in transfer function form as

$$\Delta i_f(s) = \frac{1/R_f}{(1 + T'_{do} s)} \Delta v_f(s) - \frac{M_{fd}/R_f}{(1 + T'_{do} s)} s \Delta i_d(s), \tag{4.25}$$

where $T'_{do} = L_f / R_f$. Substituting Equation (4.25) into Equation (4.21) gives

$$\Delta \Psi_f(s) = \frac{L_f/R_f}{(1 + T'_{do} s)} \Delta v_f(s) + \frac{M_{fd}}{(1 + T'_{do} s)} \Delta i_d(s). \tag{4.26}$$

As $\Delta E'_q \propto \Delta \Psi_f$ and $\Delta E_f \propto \Delta v_f$, this equation can be written in terms of $\Delta E'_q$ and ΔE_f. Figure 4.14 shows that for a generator I_d flows into the winding while I flows out of the winding.

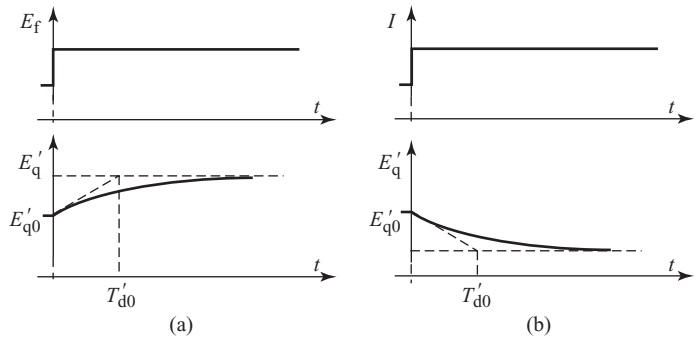

Figure 4.17 Changes in E_q' (a) to a step change in excitation ΔE_f and (b) to a step change in load ΔI.

Thus, assuming no change in the rotor angle, Δi_d can be replaced by a term proportional to $-\Delta I$ when a more rigorous analysis similar to the above but using the relationships established in Chapter 11 to evaluate the constants of proportionality would show that

$$\Delta E_q'(s) = \frac{1}{(1 + T_{do}'s)} \Delta E_f(s) - \frac{K}{(1 + T_{do}'s)} \Delta I(s), \tag{4.27}$$

where K is a constant. As can be seen, a change in the field winding flux linkage, and hence a change in E_q', can be produced by either a change in the excitation voltage or a change in the armature current. The rate at which these changes occur is determined by the transient time constant T_{do}' with the field winding filtering out high-frequency changes in ΔI and ΔE_f. Assuming for the moment that $\Delta I = 0$ and that a step change is made on E_f, then E_q' will change exponentially as shown in Figure 4.17a. Similarly, a step increase in the armature current I, such as occurs during a short circuit, would lead to an exponential reduction in E_q' as shown in Figure 4.17b.

In practice the armature will be connected to the system (a voltage source) by a transmission line of finite reactance when the actual time constants involved will depend on the impedance in the armature circuit. For a generator connected to an infinite busbar through a transmission link, Anderson and Fouad (1977) show that this modifies Equation (4.27) to

$$\Delta E_q'(s) = \frac{B}{(1 + BT_{do}'s)} \Delta E_f(s) - \frac{AB}{(1 + BT_{do}'s)} \Delta\delta(s), \tag{4.28}$$

where a change in the generator loading is now reflected by a change in the power angle $\Delta\delta$ (measured with respect to the system) and B is a constant that takes into account the effect of the impedance in the armature circuit. If both the generator armature resistance and the resistance of the transmission link are neglected then $B = (X_d' + X_s)/(X_d' + X_s) = x_d'/x_d$ and $A = [(1 - B)/B]\, V_s \sin\delta_0$. The importance of Equations (4.27) and (4.28) cannot be overemphasized as they show how changes in the excitation and generator loading alter E_q'.

4.2.5 Short-Circuit Currents with the Generator Initially on No Load

To consider the time variation of the fault current, assume the generator to be on no load prior to the fault. In this case the prefault values of the three internal emfs E, E' and E'' are all equal to the terminal voltage, that is $E'' = E' = E = E_f = V_g$, their d-components are all equal to zero, and only the q-axis variables need to be considered. This means that the separate d and q-axis diagrams shown in Figures 3.16, 4.13 and 4.14 can be replaced by the single d-axis equivalent circuit shown in

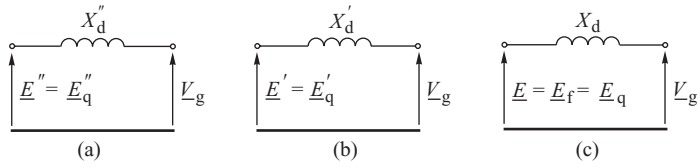

Figure 4.18 Equivalent circuit for a synchronous generator in (a) the subtransient state; (b) the transient state; (c) the steady state. The generator is assumed to be on no load prior to the fault.

Figure 4.18. The amplitude of the AC fault current component in each of the three characteristic states can be obtained directly from these equivalent circuits by short-circuiting the generator terminals, when

$$\text{for the subtransient state:} \qquad i''_m = \frac{E_{fm}}{X_d}, \tag{4.29}$$

$$\text{for the transient state:} \qquad i'_m = \frac{E_{fm}}{X'_d}, \tag{4.30}$$

$$\text{for the final steady state:} \qquad i^{\infty}_m = \frac{E_{fm}}{X_d}, \tag{4.31}$$

where $E_{fm} = \sqrt{2}E_f$.

As the AC component of the phase current, and its decay time constant, in all three characteristic states is known, it is now possible to derive formulae for the short-circuit currents as a function of time. Figure 4.19 shows the envelopes of the maximum value of the AC component of the short-circuit current corresponding to those shown in the top diagram of Figure 4.7b. The resultant envelope is defined by $i_m(t)$ and is obtained by adding the three components, each of which decays with a different time constant, to give

$$i_m(t) = \Delta i'' e^{-t/T''_d} + \Delta i' e^{-t/T'_d} + \Delta i, \tag{4.32}$$

where $\Delta i = i^{\infty}_m = E_{fm}/X_d$ is the maximum value of the AC component neglecting the screening effect of all the rotor windings (Equation 4.31); $\Delta i + \Delta i' = E_{fm}/X'_d$ is the maximum value of the AC component including the screening effect of the field winding but neglecting the screening effect of the damper winding (Equation 4.30); and $\Delta i + \Delta i' + \Delta i'' = E_{fm}/X''_d$ is the maximum value of

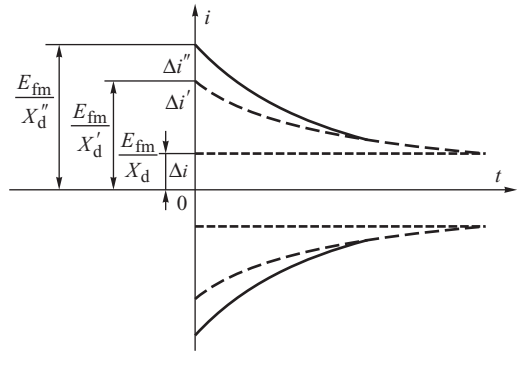

Figure 4.19 Envelopes of the three characteristic AC components of the short-circuit current.

the AC component when the screening effect of both the damper winding and the field winding are included (Equation 4.29).

Some simple algebra applied to Figure 4.19 then gives the equations for the three components of the short-circuit current as

$$\Delta i = E_{\mathrm{fm}} \frac{1}{X_{\mathrm{d}}}, \quad \Delta i' = E_{\mathrm{fm}} \left(\frac{1}{X'_{\mathrm{d}}} - \frac{1}{X_{\mathrm{d}}} \right), \quad \Delta i'' = E_{\mathrm{fm}} \left(\frac{1}{X''_{\mathrm{d}}} - \frac{1}{X'_{\mathrm{d}}} \right). \tag{4.33}$$

Substituting (4.33) into (4.32) gives the following expression for the envelope of the AC component of the fault current:

$$i_{\mathrm{m}}(t) = E_{\mathrm{fm}} \left[\left(\frac{1}{X''_{\mathrm{d}}} - \frac{1}{X'_{\mathrm{d}}} \right) \mathrm{e}^{-t/T''_{\mathrm{d}}} + \left(\frac{1}{X'_{\mathrm{d}}} - \frac{1}{X_{\mathrm{d}}} \right) \mathrm{e}^{-t/T'_{\mathrm{d}}} + \frac{1}{X_{\mathrm{d}}} \right]. \tag{4.34}$$

The initial value of Equation (4.34) at $t = 0$ is

$$i_{\mathrm{m}}(0) = \frac{E_{\mathrm{fm}}}{X''_{\mathrm{d}}}. \tag{4.35}$$

Substituting Equations (4.34) and (4.35) into (4.11) gives the expression for the short-circuit currents as

$$\begin{aligned} i_{\mathrm{A}} &= -\frac{E_{\mathrm{fm}}}{X''_{\mathrm{d}}} \left[g_3(t) \cos(\omega t + \gamma_0) - \mathrm{e}^{-t/T_{\mathrm{a}}} \cos \gamma_0 \right] \\ i_{\mathrm{B}} &= -\frac{E_{\mathrm{fm}}}{X''_{\mathrm{d}}} \left[g_3(t) \cos(\omega t + \gamma_0 - 2\pi/3) - \mathrm{e}^{-t/T_{\mathrm{a}}} \cos(\gamma_0 - 2\pi/3) \right] \\ i_{\mathrm{C}} &= -\frac{E_{\mathrm{fm}}}{X''_{\mathrm{d}}} \left[g_3(t) \cos(\omega t + \gamma_0 - 4\pi/3) - \mathrm{e}^{-t/T_{\mathrm{a}}} \cos(\gamma_0 - 4\pi/3) \right]. \end{aligned} \tag{4.36}$$

The function $g3(t)$ is defined as

$$g_3(t) = X''_{\mathrm{d}} \left[\left(\frac{1}{X''_{\mathrm{d}}} - \frac{1}{X'_{\mathrm{d}}} \right) \mathrm{e}^{-t/T''_{\mathrm{d}}} + \left(\frac{1}{X'_{\mathrm{d}}} - \frac{1}{X_{\mathrm{d}}} \right) \mathrm{e}^{-t/T'_{\mathrm{d}}} + \frac{1}{X_{\mathrm{d}}} \right], \tag{4.37}$$

and accounts for the decay of the AC component from the subtransient state to the transient state and then to the steady state. The subscript '3' relates to the three-phase short circuit.

The maximum instantaneous value of the current in each phase depends on the instant in the AC cycle when the fault occurs. For example, the current in phase A reaches its maximum value when the fault is applied at $\gamma_0 = 0$, that is when the excitation flux linking phase A, Ψ_{fA}, reaches its maximum value and the voltage E_{fA} is zero. Figure 4.7 showed currents flowing in a large generator after a three-phase fault assuming the armature time constant T_{a} to be much greater than the AC cycle time. With such a long armature time constant, the current i_{A} may reach a value almost equal to $2E_{\mathrm{fm}}/X''_{\mathrm{d}}$. On the other hand, when the fault occurs at $\gamma_0 = \pi/2$, the excitation flux linkage Ψ_{fA} is zero and the current i_{A} is minimal because it does not contain a DC component. However, the DC component will be evident in currents i_{B} and i_{C}.

4.2.5.1 Influence of the Rotor Subtransient Saliency

When saliency effects are included, the different reluctance on the d- and q-axes requires the effect of the armature mmf on the short-circuit current to be analysed using the two-reaction theory (Jones, 1967). However, an intuitive understanding of the effects of saliency can be obtained by considering the AC and DC armature mmf components separately.

Section 4.2.1 explained that the armature mmf due to the stator fault currents consists of a rotating component $F_{\mathrm{a\,AC}}$ directed along the d-axis and a stationary component $F_{\mathrm{a\,DC}}$ which is also

initially directed along the d-axis but then counter-rotates with respect to the rotor. As $F_{a\,AC}$ is always directed along the d-axis, it is associated with a reactance equal to X''_d and the AC term in Equation (4.23) remains unaffected by rotor saliency.

On the other hand, the stationary mmf component $F_{a\,DC}$ drives a flux across the air gap, the width of which appears to be continuously changing. This has two effects. Firstly, the maximum value of the DC component of the fault current, given by the second component in Equation (4.36), has to be modified by making it dependent on the mean of the subtransient reactances and equal to $E_{fm}\left(1/X''_d + 1/X''_q\right)/2$. Secondly, an additional double-frequency component of magnitude $E_{fm}\left(1/X''_d - 1/X''_q\right)/2$ is introduced into the fault current due to $F_{a\,DC}$ lying twice every cycle along the d-axis (q-axis). Both the DC and the double-frequency components decay with the same time constant equal to the mean of the d and q-axis time constants $T_a = (X''_d + X''_q)/(2\omega R)$ while their values depend on the instant of the fault.

The short-circuit current in phase A described by Equation (4.36) can now be adapted to include the modified DC component and the double-frequency AC component:

$$i_A = -\frac{E_{fm}}{X''_d}\left[g_3(t)\cos(\omega t + \gamma_0)\right] + \frac{E_{fm}}{2}e^{-t/T_a}\left[\left(\frac{1}{X''_d} + \frac{1}{X''_q}\right)\cos\gamma_0 + \left(\frac{1}{X''_d} - \frac{1}{X''_q}\right)\cos(2\omega t + \gamma_0)\right]. \tag{4.38}$$

At time $t = 0$ the second component in this equation is equal to $E_{fm}\cos\gamma_0/X''_d$ and corresponds to the DC component of the armature mmf always being in phase with the rotor d-axis when the fault is applied. In the case of a generator with damper windings in both axes, $X''_q \approx X''_d$ and Equation 4.38 reduces to (4.36).

4.2.6 Short-Circuit Currents in the Loaded Generator

When the generator is on load prior to the fault, the initial values of the emfs E''_{q0}, E'_{q0}, E''_{d0} and E'_{d0} are functions of the load current and, knowing the initial loading conditions, their values may be determined from the phasor diagram of Figure 4.15. These emfs now further modify Equation 4.38 to account for the prefault load current. Both d- and q-axis AC emfs and currents have now to be considered. The q-axis emfs will force the flow of d-axis alternating currents (changing as the cosine with time) while d-axis emfs will force the flow of q-axis alternating currents (changing as the sine with time). Denoting the angle between the q-axis and the terminal voltage V_g by δ_g, the following expression for the short-circuit current flowing in phase A is obtained:

$$\begin{aligned} i_A = &-\left[\left(\frac{E''_{qm0}}{X''_d} - \frac{E'_{qm0}}{X'_d}\right)e^{-t/T''_d} + \left(\frac{E'_{qm0}}{X'_d} - \frac{E_{qm0}}{X_d}\right)e^{-t/T'_d} + \frac{E_{qm0}}{X_d}\right]\cos(\omega t + \gamma_0) \\ &+ \left[\left(\frac{E''_{dm0}}{X''_q} - \frac{E'_{dm0}}{X'_q}\right)e^{-t/T''_q} + \frac{E'_{dm0}}{X'_q}e^{-t/T'_q}\right]\sin(\omega t + \gamma_0) \\ &+ \frac{V_{gm0}}{2}e^{-t/T_a}\left[\left(\frac{1}{X''_d} + \frac{1}{X''_q}\right)\cos(\gamma_0 + \delta_g) + \left(\frac{1}{X''_d} - \frac{1}{X''_q}\right)\cos(2\omega t + \gamma_0 + \delta_g)\right]. \end{aligned} \tag{4.39}$$

All the emfs, and the terminal voltage, include an additional subscript '0' to emphasize the fact that they are prefault quantities. The first two components represent the fundamental-frequency alternating currents due to the direct and quadrature components of the emfs. The last component consists of a DC term and a double-frequency term resulting from the subtransient saliency.

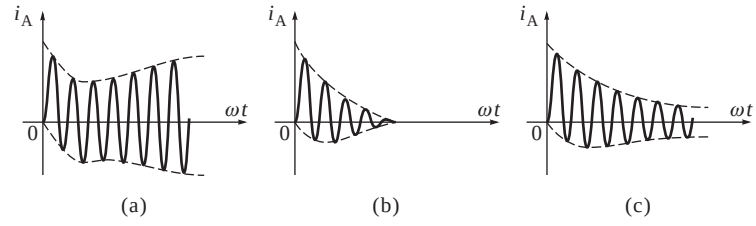

Figure 4.20 Influence of the AVR on the short-circuit current: (a) rotating exciter; (b) static exciter fed from the generator terminal voltage only; (c) static exciter fed from the generator terminal voltage and current.

4.2.6.1 Influence of the AVR

Depending on the type of exciter used, the action of the AVR can have a considerable effect on the shape of the short-circuit current. In the case of a rotating exciter, Figure 2.3a, the fault does not influence the generating capabilities of the excitation unit and the large voltage error, equal to the difference between the reference voltage and the actual value of the terminal voltage, quickly drives up the excitation voltage. This increases the value of the short-circuit current compared with its value without the AVR being active, as shown in Figure 4.20a. As E_q follows the field current, E_q will not now decay to E_{qo} but to a higher value corresponding to the new field current. Consequently E'_q will not decay to the same extent as when the AVR was inactive. If a static exciter is used, fed solely from the generator terminal voltage as in Figure 2.3e, the three-phase short-circuit reduces the excitation voltage to zero, the unit completely loses its excitation capabilities and all the emfs will decay to zero (Figure 4.20b). If the static exciter is fed by compounding both the generator voltage and current, as shown in Figure 2.3f, then excitation will not be lost during the short circuit as the exciter input voltage is augmented by the fault currents. The short-circuit current will not now vanish to zero but its shape will depend on the strength of the current component in the compounded excitation signal. An example of this is shown in Figure 4.20c.

4.2.7 Subtransient Torque

The torque creation mechanism was discussed in Section 3.2.2, Equation (3.71), with regards to a two-pole generator in the steady state. This mechanism is equally applicable here except that now the d-axis and q-axis damper flux Φ_D and Φ_Q must be added into Equation (3.71) to give

$$\tau = \tau_d - \tau_q = \frac{\pi}{2}(\Phi_f + \Phi_D + \Phi_{ad})F_{aq} - \frac{\pi}{2}(\Phi_Q + \Phi_{aq})F_{ad}. \tag{4.40}$$

In this equation the field flux, Φ_f, is made up from two components Φ_{f0} and $\Delta\Phi_f$ where Φ_{f0} is the flux due to the initial field current i_{f0} and $\Delta\Phi_f$ is the change in the flux due to the change in the field current. If resistance effects are neglected, then the rotor flux produced by the damper windings Φ_D and Φ_Q and the change in the field flux $\Delta\Phi_f$ completely cancels the armature reaction flux so that $\Phi_D + \Delta\Phi_f = -\Phi_{ad}$ and $\Phi_Q = -\Phi_{aq}$. Substituting these values into Equation (4.40) shows that the electromagnetic torque is produced solely by the interaction of the armature q-axis mmf with the original field flux Φ_{f0}. Denoting this torque as τ_ω gives

$$\tau_\omega(t) = \frac{\pi}{2}\Phi_{f0}F_{aq}. \tag{4.41}$$

As explained earlier, the AC component of the short-circuit armature mmf acts along the d-axis and does not contribute to the q-axis armature mmf. In contrast the DC component of armature

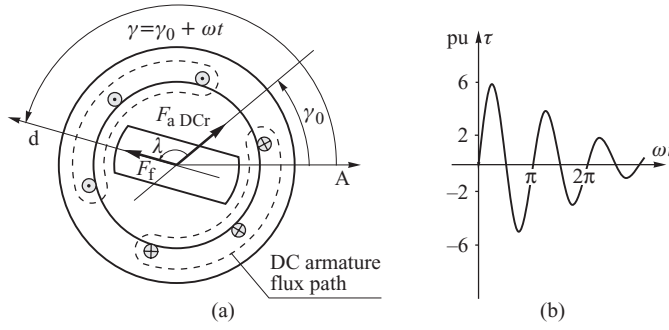

Figure 4.21 Subtransient electromagnetic torque following a three-phase fault: (a) torque creation mechanism; (b) example of torque variation with time.

flux is directed along the d-axis at the moment when the fault occurs, but then rotates relative to the rotor with the angle λ between the field and the armature mmfs changing as $\lambda = \omega t$. The amplitude of the DC armature mmf can be evaluated as $F_{\mathrm{a\,DC}} = 1.5 N_{\mathrm{a}} i_{\mathrm{m}}(0)$ by using a similar technique to that used to obtain Equation (3.42). The q-axis armature mmf with respect to the rotor is then given by

$$F_{\mathrm{aq}} = F_{\mathrm{a\,DC}} \sin\lambda = \frac{3}{2} N_{\mathrm{a}} i_{\mathrm{m}}(0) \sin\omega t. \tag{4.42}$$

As F_{aq} is solely dependant on the DC component of armature fault current, the torque is created by the initial field flux interacting with the DC component of the armature reaction mmf. This can be compared with two magnets, one rotating and the other stationary, as shown diagrammatically in Figure 4.21a. It is important to note that for the three-phase fault, the angle λ is independent of the time that the fault is applied and simply varies as ωt. The torque variation is obtained by substituting (4.42) into Equation (4.41) to give

$$\tau_{\omega}(t) = \frac{\pi}{2} \Phi_{\mathrm{f0}} N_{\mathrm{a}} \frac{3}{2} i_{\mathrm{m}}(0) \sin\omega t. \tag{4.43}$$

For the two-pole generator considered here $N_{\phi} = \pi N_{\mathrm{a}}/2$, Equation (3.39), when substituting for $E_{\mathrm{f}} = \omega N_{\phi} \Phi_{\mathrm{f0}}/\sqrt{2}$ from Equation (3.37) and for $i_{\mathrm{m}}(0)$ from Equation (4.35), finally gives the short-circuit torque as

$$\tau_{\omega}(t) = \frac{3}{\omega} \frac{E_{\mathrm{f}}^2}{X''_{\mathrm{d}}} \sin\omega t \quad \mathrm{N\,m}. \tag{4.44}$$

This equation shows that the short-circuit electromagnetic torque is independent of the fault instant but varies as $\sin\omega t$. During the first half-cycle the electromagnetic torque opposes the mechanical driving torque, while during the second half-cycle it assists the driving torque. The average value of the torque is zero. Equation (4.44) expresses the torque in SI units but, as explained in Appendix A.2, this can easily be changed to per unit by multiplying by $\omega/3$ to give the per-unit form $\tau_{\omega}(t) = E_{\mathrm{f}}^2 \sin\omega t \,/\, X''_{\mathrm{d}}$ and is valid for any generator regardless of pole number.

The effect of including winding resistance is twofold. Firstly, the DC phase currents that sustain the constant stator flux linkages $\Psi_{\mathrm{a\,DC}}$ decay with a time constant T_{a}. Secondly, the rotor currents sustaining the constant rotor linkages decay with time constants T''_{d} and T'_{d} allowing the armature reaction flux to penetrate the rotor. The net effect is that the torque τ_{ω} will decay to zero with the armature time constant T_{a} and the subtransient and transient time constants T''_{d} and T'_{d} which

modify Equation (4.44) to give

$$\tau_\omega(t) = \frac{3}{\omega}\frac{E_\mathrm{f}^2}{X''_\mathrm{d}} g_3(t) \mathrm{e}^{-t/T_\mathrm{a}} \sin \omega t \quad \mathrm{N\,m}, \tag{4.45}$$

where g_3(t) is defined by Equation (4.37). As the electromagnetic torque is equal to the product of two decaying functions, it vanishes very quickly (Figure 4.21b).

Strictly, the torque expression in Equation (4.45) should be modified to take into account the torque developed due to the power loss in the armature resistance. As this power loss is due to the flow of AC armature currents, which decay with the subtransient and transient time constants defined by the function $g_3(t)$ in Equation (4.37), the torque corresponding to the power loss in all three phases $\tau_\mathrm{R}(t)$ may be expressed as

$$\tau_\mathrm{R}(t) = \frac{3}{\omega}\left[\frac{E_\mathrm{f}}{X''_\mathrm{d}} g_3(t)\right]^2 R \quad \mathrm{N\,m}. \tag{4.46}$$

Similarly, the alternating currents induced in the rotor windings (damper and field) also cause a power loss. These currents decay with time constant T_a and the torque corresponding to the rotor losses may be approximately expressed as

$$\tau_\mathrm{r}(t) = \frac{3}{\omega}\left(\frac{i_\mathrm{m}(0)}{\sqrt{2}}\mathrm{e}^{-t/T_\mathrm{a}}\right)^2 r = \frac{3}{\omega}\left(\frac{E_\mathrm{f}}{X''_\mathrm{d}}\right)^2 r\mathrm{e}^{-2t/T_\mathrm{a}} \quad \mathrm{N\,m}, \tag{4.47}$$

where r is an equivalent resistance of all the rotor windings, referred to the stator (similarly as in a transformer). The torque τ_r is initially high but rapidly decays to zero.

As the armature resistance of a large generator is usually very small, the torque τ_R, corresponding to the stator losses, is several times smaller than the torque τ_r corresponding to the rotor losses. However, the former decays at a much slower rate.

The resultant torque acting on the rotor during the fault is equal to the sum of the three components τ_ω, τ_R, τ_r. None of these components depends on the fault instant γ_0. The function $g_3(t)$, given by Equation (4.37), does not decay to zero so that the component, τ_R, decays to a steady-state value corresponding to the losses that would be incurred by the steady-state short-circuit currents. If the generator is on load prior to the fault then the initial value of the torque would correspond to the prefault load torque rather than zero as shown in Figure 4.21.

Equation 4.38 suggests that there should also be an additional periodic torque component corresponding to the double-frequency currents caused by the rotor subtransient saliency. Assuming that the resistance of the armature windings is small, the double-frequency torque $\tau_{2\omega}$ may be expressed as

$$\tau_{2\omega}(t) = -\frac{3}{2}\frac{E_\mathrm{f}^2}{\omega}\left(\frac{1}{X''_\mathrm{d}} - \frac{1}{X''_\mathrm{q}}\right)\mathrm{e}^{-2t/T_\mathrm{a}} \sin 2\omega t \quad \mathrm{N\,m}. \tag{4.48}$$

Typically $X''_\mathrm{d} \approx X''_\mathrm{q}$ and the torque $\tau_{2\omega}$ only slightly distorts the single-frequency torque τ_ω. In some rare cases of high subtransient saliency the double-frequency component may produce a substantial increase in the maximum value of the AC torque.

4.3 Phase-to-Phase Short Circuit

The phase-to-phase fault will be analysed in a similar way as the three-phase fault with the generator initially considered to be on no load and with both winding resistance and subtransient saliency neglected. The effect of saliency and resistance on the short-circuit current will then be considered before finally developing expressions for the short-circuit torque. The short circuit will be assumed to occur across phases B and C of the stator winding.

4.3.1 Short-Circuit Current and Flux with Winding Resistance Neglected

Figure 4.22 shows the armature coils with a short circuit across phases B and C. The short circuit connects the armature coils such that the current flows in opposite directions in the two coils and $i_B = -i_C$. In the case of the three-phase fault, there were three closed armature circuits, one for each of the phase windings, and the flux linkage of each of these windings could be considered separately. In the case of the phase-to-phase short circuit there is only one closed circuit, the series connection of the two phase windings. When the fault occurs, the total energy stored in this closed circuit cannot change instantaneously and it is the net flux linkage $\Psi_B - \Psi_C$ of this closed circuit that must remain constant.

The flux linkages Ψ_B and Ψ_C of the two short-circuited windings consist of two components: the winding self-flux linkages Ψ_{BB} and Ψ_{CC} produced by the fault currents and the flux linkages produced by the excitation flux Ψ_{fB} and Ψ_{fC}. As the fault currents in the two short-circuited phases are equal and opposite, $\Psi_{BB} = -\Psi_{CC}$ and the net flux linkage $\Psi_B - \Psi_C$ can be expressed as

$$\Psi_B - \Psi_C = (\Psi_{BB} + \Psi_{fB}) - (\Psi_{CC} + \Psi_{fC}) = \Psi_{fB} - \Psi_{fC} - 2\Psi_{CC}. \tag{4.49}$$

With the generator on no load prior to the fault, $\Psi_{CC}(0^-) \propto i_C(0^-) = i_B(0^-) = 0$ and the only flux linking the windings is the excitation flux. Thus

$$\Psi_B(0^-) - \Psi_C(0^-) = \Psi_{fB0} - \Psi_{fC0}. \tag{4.50}$$

The law of constant flux linkage requires the net flux linkage $(\Psi_B - \Psi_C)$ just before and just after the fault to be equal so that

$$\Psi_{fB} - \Psi_{fC} - 2\Psi_{CC} = \Psi_{fB0} - \Psi_{fC0}. \tag{4.51}$$

Rearranging gives

$$\Psi_{CC} = \frac{1}{2}\left[(\Psi_{fB} - \Psi_{fC}) - (\Psi_{fB0} - \Psi_{fC0})\right]. \tag{4.52}$$

The variations of the flux linkages Ψ_{fB} and Ψ_{fC} are shown in Figure 4.4, with the initial values defined by Equations (4.4), so that

$$\begin{aligned} \Psi_{fB} &= \Psi_{fa}\cos(\gamma - 2\pi/3),\ \Psi_{fC} = \Psi_{fa}\cos(\gamma - 4\pi/3) \\ \Psi_{fB0} &= \Psi_{fa}\cos(\gamma_0 - 2\pi/3),\ \Psi_{fC0} = \Psi_{fa}\cos(\gamma_0 - 4\pi/3) \end{aligned} \tag{4.53}$$

which, when substituted into Equation (4.52), give

$$\Psi_{CC} = \frac{\sqrt{3}}{2}\Psi_{fa}(\sin\gamma - \sin\gamma_0). \tag{4.54}$$

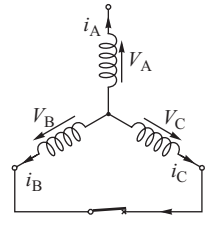

Figure 4.22 Phase-to-phase short circuit: $i_B = -i_C$; $V_{BC} = 0$; $i_A = 0$; $V_A \neq 0$.

Recall from Equation (3.37) that $E_{\mathrm{fm}} = \omega\Psi_{\mathrm{fa}}$ while immediately after the fault the subtransient current $i_{\mathrm{C}} = \Psi_{\mathrm{CC}}/L''_{\mathrm{d}}$. This allows a formula for the phase-to-phase short-circuit current to be written as

$$i_{\mathrm{C}} = -i_{\mathrm{B}} = \frac{\sqrt{3}}{2}\frac{E_{\mathrm{fm}}}{X''_{\mathrm{d}}}\left(\sin\gamma - \sin\gamma_0\right). \tag{4.55}$$

This short-circuit current consists of two components, an AC component

$$i_{\mathrm{C\,AC}} = -i_{\mathrm{B\,AC}} = \frac{\sqrt{3}E_{\mathrm{fm}}}{2X''_{\mathrm{d}}}\sin\gamma \tag{4.56}$$

whose magnitude is independent of the instant of the fault, and a DC component

$$i_{\mathrm{C\,DC}} = -i_{\mathrm{B\,DC}} = -\frac{\sqrt{3}E_{\mathrm{fm}}}{2X''_{\mathrm{d}}}\sin\gamma_0, \tag{4.57}$$

the value of which depends on the instant of the fault. If the fault occurs at $\gamma_0 = 0$, the voltage of phase A is zero, and the fault current is purely sinusoidal with no DC component present. If, on the other hand, the fault occurs at $\gamma_0 = -\pi/2$, the voltage in phase A is at its negative peak, and the DC component of the fault current will be at its maximum value.

The flux linkages for the case when $\gamma_0 = 0$ and for $\gamma_0 = -\pi/2$ are shown in Figure 4.23a and 4.23b respectively. When $\gamma_0 = 0$ the flux linkages Ψ_{fB0} and Ψ_{fC0} are identical, the net flux linkage $(\Psi_{\mathrm{fB0}} - \Psi_{\mathrm{fC0}})$ is zero and no DC component is required to maintain the flux linkages. The

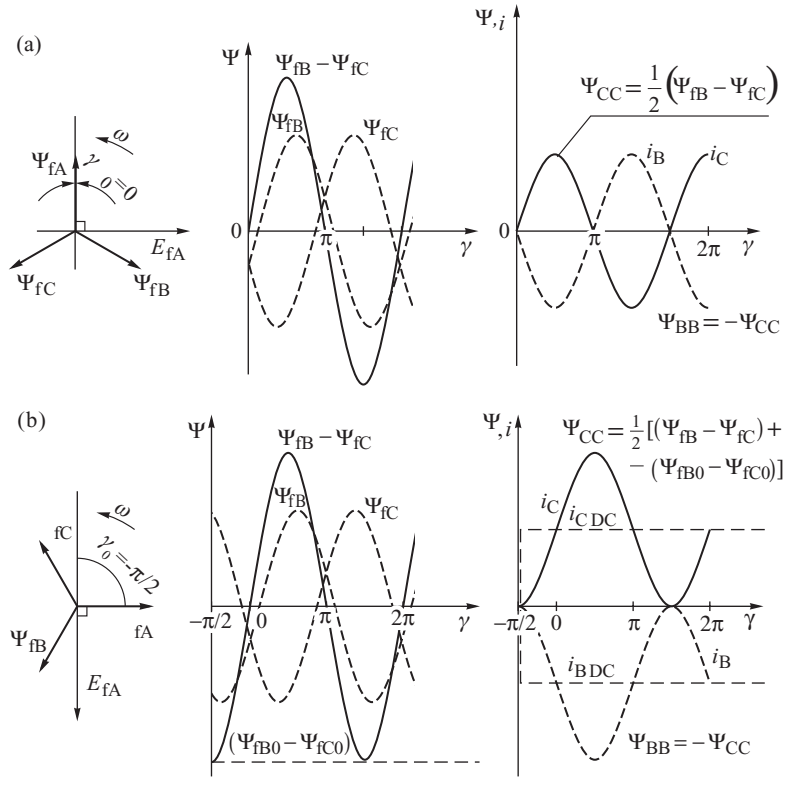

Figure 4.23 Application of the law of constant flux linkages to determine the phase-to-phase fault currents when the fault instant is: (a) $\gamma_0 = 0$; (b) $\gamma_0 = -\pi/2$.

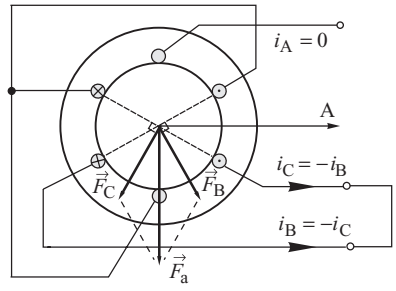

Figure 4.24 Phase-to-phase fault currents creating a stationary armature mmf $\vec{F}_B$ perpendicular to the axis of phase A. Generator windings are star connected.

flux linkages Ψ_{BB} and Ψ_{CC}, and hence i_B and i_C, simply vary sinusoidally with opposite sign (Figure 4.23a). However, when the fault occurs at $\gamma_0 = -\pi/2$ the voltage in phase A is a maximum and the flux linkages Ψ_{fB0} and Ψ_{fC0} now have the same magnitude but opposite sign. The net flux linkage is $\sqrt{3}\Psi_{fa}$ and a large DC circulating current $i_{C\,DC} = -i_{B\,DC}$ is necessary in order to maintain constant flux linkages (Figure 4.23b).

The resultant armature mmf $\vec{F}_a$ can be found by the vector addition of the individual mmfs $\vec{F}_B$ and $\vec{F}_C$ produced by the stator fault currents i_B and i_C. Taking phase A as a reference (real axis in the complex plane) gives

$$\begin{aligned}\vec{F}_a &= \vec{F}_B + \vec{F}_C = F_B e^{j2\pi/3} + F_C e^{j4\pi/3} = F_C(-e^{j2\pi/3} + e^{j4\pi/3}) \\ &= -j\sqrt{3}F_C = -j\sqrt{3}N_a i_C = j\sqrt{3}N_a \frac{\sqrt{3}}{2}\frac{E_{fm}}{X''_d}(\sin\gamma - \sin\gamma_0).\end{aligned} \tag{4.58}$$

The result of this phasor addition is shown in Figure 4.24 where the resultant armature mmf $\vec{F}_a$ is at all times perpendicular to the axis of phase A and proportional to the short-circuit current i_C. Consequently, $\vec{F}_a$ is stationary in space but pulsates at frequency ω. As the rotor position at any instant in time is determined by the angle γ measured with respect to the A-axis, this stationary armature mmf counter-rotates with respect to the rotor with the angle between the armature and the field mmf changing as $\lambda = \gamma + \pi/2$. This produces mmf components along the d- and q-axes

$$F_{ad} = F_a \cos\lambda = -\sqrt{3}F_C \sin\gamma, \quad F_{aq} = F_a \sin\lambda = \sqrt{3}F_C \cos\gamma, \tag{4.59}$$

which, when substituting for i_C from Equation (4.55), give

$$\begin{aligned}F_{ad} &= -\frac{3}{2}N_a \frac{E_{fm}}{X''_d}(\sin\gamma - \sin\gamma_0)\sin\gamma = -\frac{3}{4}N_a \frac{E_{fm}}{X''_d}(1 - 2\sin\gamma_0 \sin\gamma - \cos 2\gamma) \\ F_{aq} &= \frac{3}{2}N_a \frac{E_{fm}}{X''_d}(\sin\gamma - \sin\gamma_0)\cos\gamma.\end{aligned} \tag{4.60}$$

The d-axis armature mmf has three components: a DC component, an AC component of fundamental frequency and an AC component of double frequency. The magnitudes of both the DC component and the double-frequency component are independent of the instant of the fault while the value of the fundamental AC component depends on γ_0.

This variation in the d-axis armature mmf also explains the changes that occur in the rotor field current and the d-axis damper current following the fault. The d-axis armature mmf forces an armature flux across the air gap that produces flux linkages Ψ_{ar} with the rotor windings. These flux linkages are proportional to F_{ad} and are shown in Figure 4.25. As the flux linkage of the rotor circuits must remain constant following the fault, additional currents flow in both the field winding

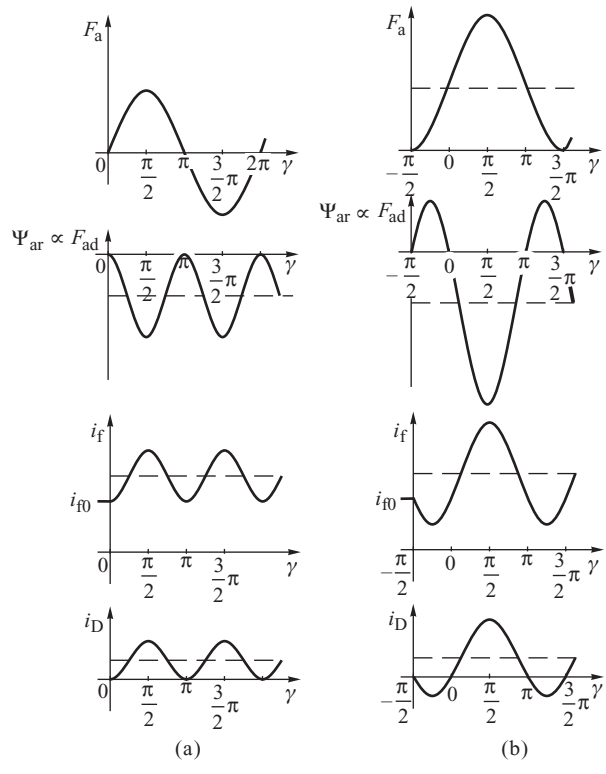

Figure 4.25 Illustration of the influence of the armature flux on the rotor currents when the fault occurs at: (a) $\gamma_0 = 0$; (b) $\gamma_0 = -\pi/2$.

and the d-axis damper winding to produce a flux linkage that is equal and opposite to that produced by the armature flux. These additional field and damper currents therefore have the same form as F_{ad} but are of opposite sign. The actual magnitude of the field current will depend on how well the field winding is screened by the d-axis damper winding. If perfect screening is obtained then the field current will remain constant with the armature flux being totally compensated by the d-axis damper current. If the fault occurs at $\gamma_0 = 0$ then the armature current and the resultant armature mmf do not contain a DC component (Figure 4.25a) and the flux linkages in the field and damper windings produced by the armature mmf simply pulsate at twice the system frequency. The induced rotor currents are then similar to those flowing during a three-phase fault, except they are now at twice the system frequency. If, on the other hand, the fault occurs at $\gamma_0 = -\pi/2$ (Figure 4.25b) then the armature mmf pulsates with a large DC component. The rotor flux linkages now contain both fundamental and double-frequency components and the induced rotor currents have a different shape than before in that both the field and the damper currents initially reduce their values as shown in Figure 4.25b.

The q-axis mmf F_{aq} will be compensated by damper currents in a similar manner to F_{ad} and its influence will be discussed when the torque is considered.

4.3.2 Influence of the Subtransient Saliency

The armature current Equation (4.55) is valid for a magnetically symmetrical rotor where the magnetic reluctance encountered by the armature flux is constant and does not depend on the rotor

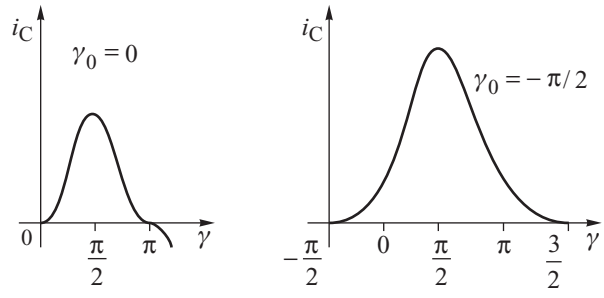

Figure 4.26 Phase-to-phase fault current waveforms strongly distorted due to subtransient saliency.

position. However, if the machine has substantial subtransient saliency then the reluctance of the d- and q-axes will be different and the solution must be obtained using two-reaction theory (Ching and Adkins, 1954; Kundur, 1994). The result of such an analysis shows that in Equation (4.55) X''_d is replaced by $(X''_d \sin^2\gamma + X''_q \cos^2\gamma)$ to give

$$i_C = -i_B = \frac{\sqrt{3}E_{fm}(\sin\gamma - \sin\gamma_0)}{2\left(X''_d \sin^2\gamma + X''_q \cos^2\gamma\right)} = \frac{\sqrt{3}E_{fm}(\sin\gamma - \sin\gamma_0)}{X''_d + X''_q - \left(X''_d - X''_q\right)\cos 2\gamma}. \tag{4.61}$$

Generators without a q-axis damper winding may have a large value of subtransient saliency which will distinctly distort the fault currents. Figure 4.26 shows these distorted currents for the same γ_0 as the sinusoidal waveforms shown previously in Figure 4.23 when X''_d was equal to X''_q.

The harmonic content of the distorted fault current can be quantified by expanding Equation (4.61) into a Fourier series[2]

$$\begin{aligned} i_C = -i_B = {} & \frac{\sqrt{3}E_{fm}}{X''_d + \sqrt{X''_d X''_q}}\left(\sin\gamma - b\sin 3\gamma + b^2\sin 5\gamma - b^3\sin 7\gamma + \ldots\right) \\ & - \frac{\sqrt{3}E_{fm}\sin\gamma_0}{\sqrt{X''_d X''_q}}\left(\frac{1}{2} - b\cos 2\gamma + b^2\cos 4\gamma - b^3\cos 6\gamma + \ldots\right), \end{aligned} \tag{4.62}$$

where the asymmetry coefficient, b, is

$$b = \frac{\sqrt{X''_q} - \sqrt{X''_d}}{\sqrt{X''_q} + \sqrt{X''_d}} = \frac{\sqrt{X''_d X''} - X''_d}{\sqrt{X''_d X''_q} + X''_d}. \tag{4.63}$$

[2] The Fourier series expansion of the two components in Equation (4.61) gives

$$\frac{\sin\gamma}{A+B-(A-B)\cos 2\gamma} = \frac{1}{A+\sqrt{AB}}(\sin\gamma - b\sin 3\gamma + b^2\sin 5\gamma - b^3\sin 7\gamma + \ldots)$$
$$\frac{1}{A+B-(A-B)\cos 2\gamma} = \frac{1}{\sqrt{AB}}\left(\tfrac{1}{2} - b\sin 2\gamma + b^2\cos 4\gamma - b^3\cos 6\gamma + \ldots\right)$$

where

$$b = \frac{\sqrt{B} - \sqrt{A}}{\sqrt{B} + \sqrt{A}}.$$

In the example shown in Figure 4.26 the generator possesses a high degree of subtransient saliency with $X''_q = 2X''_d$, giving an asymmetry coefficient $b \approx 0.17$, while the magnitude of the third, fifth and seventh harmonics are respectively 17, 3 and 0.5% of the fundamental.

Even-numbered harmonics appear only when the fault current contains a DC component, that is when $\sin\gamma_0 \neq 0$ and subtransient saliency is present. However, the odd-numbered harmonics appear whenever the generator possesses subtransient saliency, $b \neq 0$, regardless of the instant of the fault. The source of the odd-numbered harmonics is the negative-sequence component of the fault current as explained below.

4.3.2.1 Symmetrical Component Analysis of the Phase-to-Phase Fault

Symmetrical components allow any unsymmetrical set of three-phase currents to be expressed as the phasor sum of three symmetrical AC components: the positive-sequence component $\underline{\boldsymbol{i}}_1$, the negative-sequence component $\underline{\boldsymbol{i}}_2$ and the zero-sequence component $\underline{\boldsymbol{i}}_0$, the detailed derivation of which can be found in any standard textbook on power system analysis such as Grainger and Stevenson (1994).

The phase-to-phase fault currents shown in Figure 4.23a are given by $i_A = 0$ and $i_B = -i_C = i$. Applying the symmetrical component transformation gives

$$\begin{bmatrix} \underline{i}_0 \\ \underline{i}_1 \\ \underline{i}_2 \end{bmatrix} = \frac{1}{3}\begin{bmatrix} 1 & 1 & 1 \\ 1 & \underline{a} & \underline{a}^2 \\ 1 & \underline{a}^2 & \underline{a} \end{bmatrix}\begin{bmatrix} 0 \\ \underline{i} \\ -\underline{i} \end{bmatrix} = \frac{\underline{i}}{3}\begin{bmatrix} 0 \\ \underline{a} - \underline{a}^2 \\ \underline{a}^2 - \underline{a} \end{bmatrix} = \frac{\underline{i}}{\sqrt{3}}\begin{bmatrix} 0 \\ \mathrm{j} \\ -\mathrm{j} \end{bmatrix}, \tag{4.64}$$

where $\underline{a} = e^{j2\pi/3}$. The positive-sequence component, $\underline{i}_1$, leads the current in the B phase by $\pi/2$, while the negative-sequence components, $\underline{i}_2$, lags the current in the B phase by $\pi/2$. The zero-sequence component is equal to zero. The reverse transformation from the symmetric components to phase components gives the actual phase currents which can be conveniently written as the sum of two three-phase systems representing the positive-sequence and negative-sequence phase currents:

$$\begin{bmatrix} \underline{i}_A \\ \underline{i}_B \\ \underline{i}_C \end{bmatrix} = \begin{bmatrix} 1 & 1 & 1 \\ 1 & \underline{a}^2 & \underline{a} \\ 1 & \underline{a} & \underline{a}^2 \end{bmatrix}\begin{bmatrix} 0 \\ \underline{i}_1 \\ \underline{i}_2 \end{bmatrix} = \begin{bmatrix} \underline{i}_{A1} \\ \underline{i}_{B1} \\ \underline{i}_{C1} \end{bmatrix} + \begin{bmatrix} \underline{i}_{A2} \\ \underline{i}_{B2} \\ \underline{i}_{C2} \end{bmatrix}, \tag{4.65}$$

where $\underline{i}_{A1} = \underline{i}_1$, $\underline{i}_{B1} = \underline{a}^2\underline{i}_1$, $\underline{i}_{C1} = \underline{a}\,\underline{i}_1$, $\underline{i}_{A2} = \underline{i}_2$, $\underline{i}_{B2} = \underline{a}\,\underline{i}_2$ and $\underline{i}_{C2} = \underline{a}^2\underline{i}_2$.

Figure 4.27 shows the phase and symmetrical components of the phase-to-phase fault currents.

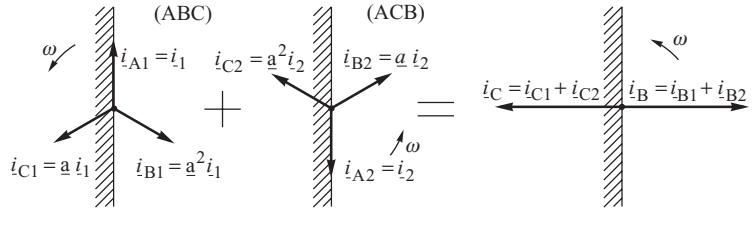

Figure 4.27 The phase-to-phase fault current transformed into its positive- and negative-sequence components rotating in opposite directions.

4.3.2.2 Phase-to-Phase Fault Current Harmonics Explained by Symmetrical Components

The phase-to-phase fault current defined by Equation (4.61) can be decomposed into two fundamental parts, an AC part containing terms in sin γ and a DC part containing terms in sin γ_0, each part of which may be analysed separately using symmetrical components.

The AC part of the fault current produces an armature mmf $F_{\mathrm{a\,AC}}$ which is stationary with respect to the stator but pulsates with time. By representing the AC component of the fault current by a positive-sequence and negative-sequence current, the effect of this pulsating mmf can be replicated by two counter-rotating mmf waves produced by the sequence currents. The positive-sequence currents ($\underline{i}_{\mathrm{A1}}, \underline{i}_{\mathrm{B1}}, \underline{i}_{\mathrm{C1}}$) produce an mmf $\vec{F}_{\mathrm{a\,AC1}}$ which rotates with the rotor and is stationary with respect to it. Changes in the flux linkages produced by this mmf are opposed by direct currents flowing in the rotor windings, just as in the generator with no subtransient saliency shown in Figure 4.25. The negative-sequence currents ($\underline{i}_{\mathrm{A2}}, \underline{i}_{\mathrm{B2}}, \underline{i}_{\mathrm{C2}}$) produce mmf $\vec{F}_{\mathrm{a\,AC2}}$ which rotates in the opposite direction to the rotor, and induces double-frequency currents in the rotor windings again as shown in Figure 4.25 for a generator with no subtransient saliency. In turn these double-frequency rotor currents produce a pulsating mmf which is stationary with respect to the rotor. This pulsating mmf can be represented by two mmf waves, one rotating with respect to the rotor with velocity (-2ω) and the other with velocity 2ω, with the relative magnitudes of these two mmf waves depending on the degree of subtransient saliency. As the rotor itself rotates with angular velocity ω, these two rotor mmf components rotate with respect to the stator with velocities $(-\omega)$ and 3ω and introduce a third-harmonic component into the fault current. Analysing the effect of this third harmonic on the rotor currents, and then the effect of the rotor currents on the armature, leads to an explanation for the presence of the fifth harmonic in the fault current. This analysis may be continuously repeated to account for all the odd-numbered harmonics in the armature fault current. For a generator with no subtransient saliency the magnitude of the rotor mmf wave that rotates at 3ω relative to the armature is zero and so no third- or higher order harmonics are present.

When $\sin\gamma_0 \neq 0$ a DC component of the fault current appears and produces a stationary armature mmf $\vec{F}_{\mathrm{a\,DC}}$ which counter-rotates with respect to the rotor. The rotor windings oppose this mmf by inducing fundamental-frequency alternating currents. These rotor currents produce a sinusoidally pulsating mmf which is stationary with respect to the rotor. As before, this mmf can be represented as two counter-rotating mmfs, but in this case with angular velocities ω and $(-\omega)$ with respect to the rotor. Again the relative magnitudes of these two mmfs depend on the degree of subtransient saliency present. As the rotational velocity of the rotor is ω, one of these mmfs is stationary with respect to the armature while the other rotates with velocity 2ω and induces a second-harmonic component into the fault current. Analysing the influence of this harmonic explains the presence of the fourth, and the other even-numbered, harmonics in the fault current when subtransient saliency is present. The phase-to-phase fault current may be then expressed as a sum of the harmonics

$$i_{\mathrm{C}} = -i_{\mathrm{B}} = i_{(\omega)} + \underbrace{i_{(3\omega)} + i_{(5\omega)} + \cdots}_{\substack{\text{induced by the negative-}\\ \text{sequence currents}}} + i_{\mathrm{DC}} + \underbrace{i_{(2\omega)} + i_{(4\omega)} + i_{(6\omega)} + \ldots}_{\substack{\text{induced by the direct currents}\\ \text{depending on the instant of fault}}}. \tag{4.66}$$

4.3.3 Positive- and Negative-Sequence Reactances

Equation (4.62) can now be used to determine the reactance with which the generator opposes the flow of the negative-sequence currents. Figure 4.28a shows the representation of the generator for the positive- and negative-sequence currents, while Figure 4.28b shows the connection of the sequence equivalent circuits required to represent the phase-to-phase fault (Grainger and Stevenson, 1994).

Applying Ohm's law to the circuit of Figure 4.28b gives

$$\underline{I}''_1 = -\underline{I}''_2 = \frac{\underline{E}''}{\mathrm{j}(X''_1 + X''_2)}, \tag{4.67}$$

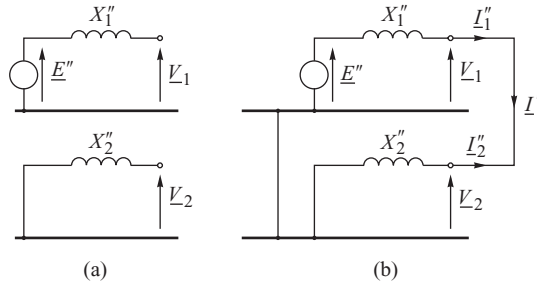

Figure 4.28 Equivalent circuits of the generator: (a) positive- and negative-sequence circuits; (b) connection of the circuits to account for the phase-to-phase fault.

where X_1'' is the positive-sequence subtransient reactance and X_2'' the negative-sequence subtransient reactance. Using the inverse symmetrical component transformation gives the phase currents

$$-\underline{I}_B = \underline{I}_C = \frac{\sqrt{3}\underline{E}''}{X_1'' + X_2''}. \tag{4.68}$$

The positive-sequence component of the fault current produces a rotating flux whose interaction with the rotor is similar to that produced by the AC component of the three-phase short-circuit current. As the generator opposes the flow of currents produced by this flux with the reactance X_d'', the reactance with which the generator opposes the flow of the positive-sequence currents is also equal to X_d'' and

$$X_1'' = X_d''. \tag{4.69}$$

Comparing Equation (4.68) with the first part of Equation (4.62) allows the negative-sequence reactance X_2'' to be evaluated as

$$X_2'' = \sqrt{X_d'' X_q''}, \tag{4.70}$$

and the generator opposes the flow of the negative-sequence currents with a reactance equal to the geometric average of the two subtransient reactances. Finally the second part of Equation (4.62) shows that the generator opposes the flow of the DC component of the fault current with a reactance that has the same value as the negative-sequence reactance, that is $\sqrt{X_d'' X_q''}$.

4.3.4 Influence of Winding Resistance

The winding resistance dissipates the magnetic energy stored in the winding and causes a decay in the DC component of the current flowing in that winding. As explained above, the generator opposes the flow of the DC component of the phase-to-phase fault current with the reactance $X_2'' = \sqrt{X_d'' X_q''}$. The resistance of the phase winding will then produce a decay in this DC component of the fault current with a time constant

$$T_\alpha = \frac{X_2''}{\omega R} = \frac{\sqrt{L_d'' L_q''}}{R}. \tag{4.71}$$

Equation (4.61) can now be modified by multiplying the $\sin\gamma_0$ term by the exponential function e^{-t/T_α}.

The decay of the AC component of the fault current can best be explained by considering its positive- and negative-sequence components as derived in the previous section. The positive-sequence component produces a rotating flux whose penetration into the rotor is opposed by DC rotor currents. The resistance of the rotor windings causes this component of the current to decay, first in the damper windings and then in the field winding, so that the armature reaction flux penetrates deeper and deeper into the rotor. As each of these flux conditions corresponds to the subtransient, transient and steady-state conditions, the generator effectively opposes the flow of the positive-sequence component of the fault current with the same reactances as for the three-phase fault:

$X_1'' = X_d''$	in the subtransient state
$X_1' = X_d'$	in the transient state
$X_1 = X_d$	in the steady state.

The armature mmf produced by the negative-sequence current rotates in the opposite direction to the rotor. The penetration of the flux produced by this mmf into the rotor is prevented by the flow of double-frequency rotor currents so that the same reactance opposes the flow of the negative-sequence fault currents in all three characteristic generator states. The value of this negative-sequence reactance is

$$X_2'' = X_2' = X_2 = \sqrt{X_d'' X_q''}. \tag{4.72}$$

As the positive- and negative-sequence reactances of the generator are connected in the same way for the transient state and the steady state as for the subtransient state, Figure 4.28, the AC phase-to-phase transient and steady-state fault currents are respectively $(X_d'' + X_2)/(X_d' + X_2)$ and $(X_d'' + X_2)/(X_d + X_2)$ times smaller than the subtransient fault currents. Equation (4.61) can be used to express the AC component of the fault current in the three characteristic states as

$$\begin{aligned} i''_{C\,AC}(t) &= \frac{\sqrt{3}E_{fm}\sin\gamma}{2\left(X_d''\sin^2\gamma + X_q''\cos^2\gamma\right)} \\ i'_{C\,AC}(t) &= i''_{C\,AC}(t)\frac{X_d'' + X_2}{X_d' + X_2}, \qquad i_{C\,AC}(t) = i''_{C\,AC}(t)\frac{X_d'' + X_2}{X_d + X_2}. \end{aligned} \tag{4.73}$$

As with the three-phase fault, the difference $\left(i''_{C\,AC} - i'_{C\,AC}\right)$ decays at a rate determined by the subtransient time constant, while the difference $\left(i'_{C\,AC} - i_{C\,AC}\right)$ decays with the transient time constant. Following similar arguments to those used to produce Equations (4.33) and (4.36), the following expression is obtained for the phase-to-phase fault current with the effect of winding resistance included:

$$i_C(t) = \frac{\sqrt{3}E_{fm}}{2\left(X_d''\sin^2\gamma + X_q''\cos^2\gamma\right)}\left[g_2(t)\sin\gamma - e^{-t/T_\alpha}\sin\gamma_0\right], \tag{4.74}$$

where the function

$$\begin{aligned} g_2(t) = (X_d'' + X_2)\Bigg[&\left(\frac{1}{X_d'' + X_2} - \frac{1}{X_d' + X_2}\right)e^{-t/T_\beta''} \\ &+ \left(\frac{1}{X_d' + X_2} - \frac{1}{X_d + X_2}\right)e^{-t/T_\beta'} + \frac{1}{X_d + X_2}\Bigg] \end{aligned} \tag{4.75}$$

is responsible for describing the decay of the AC component of the fault current (subscript 2 denotes the phase-to-phase fault).

As the reactances with which the generator opposes the flow of the phase-to-phase fault current are different to those opposing the flow of the three-phase fault current, the subtransient and

transient time constants must be changed in proportion to the ratio of the reactances

$$T''_\beta = T''_\mathrm{d}\left(\frac{X'_\mathrm{d}}{X''_\mathrm{d}}\right)\left(\frac{X''_\mathrm{d}+X_2}{X'_\mathrm{d}+X_2}\right), \quad T'_\beta = T'_\mathrm{d}\left(\frac{X_\mathrm{d}}{X'_\mathrm{d}}\right)\left(\frac{X'_\mathrm{d}+X_2}{X_\mathrm{d}+X_2}\right). \tag{4.76}$$

4.3.5 Subtransient Torque

As in the three-phase fault, the flux produced by the damper windings during the phase-to-phase fault is equal and opposite to the d- and q-axis armature flux and the electromagnetic torque is due solely to the interaction between the field flux and the quadrature component of the armature reaction mmf. Neglecting subtransient saliency and substituting Equation (4.60) into (4.41), similar to the three-phase fault, gives

$$\tau_\mathrm{AC} = \frac{\pi}{2}\Phi_\mathrm{f0}\frac{3}{2}N_\mathrm{a}\frac{E_\mathrm{fm}}{X''_\mathrm{d}}(\sin\gamma - \sin\gamma_0)\cos\gamma, \tag{4.77}$$

but as

$$E_\mathrm{f} = \frac{1}{\sqrt{2}}\omega\left(\frac{\pi}{2}N_\mathrm{a}\right)\Phi_\mathrm{f0}$$

the subtransient torque can be written as

$$\tau_\mathrm{AC} = \frac{3}{\omega}\frac{E_\mathrm{f}^2}{X''_\mathrm{d}}(\sin\gamma - \sin\gamma_0)\cos\gamma \quad \mathrm{N\,m}. \tag{4.78}$$

This equation neglects winding resistance, the effect of which is to cause the rotor currents to decay with time as determined by the function $g_2(t)$, while the decay of the stator currents is determined by the functions $g_2(t)$ and e^{-t/T_β}. Multiplying the corresponding components of Equation (4.78) by these functions gives

$$\begin{aligned}\tau_\mathrm{AC} &= \frac{3}{\omega}\frac{E_f^2}{X''_\mathrm{d}}\left[g_2(t)\sin\gamma - \mathrm{e}^{-t/T_\beta}\sin\gamma_0\right]g_2(t)\cos\gamma \\ &= \frac{3}{\omega}\frac{E_\mathrm{f}^2}{X''_\mathrm{d}}\left[\frac{1}{2}g_2^2(t)\sin 2\gamma - \sin\gamma_0\mathrm{e}^{-t/T_\beta}g_2(t)\cos\gamma\right] \quad \mathrm{N\,m}.\end{aligned} \tag{4.79}$$

Unlike the torque due to the three-phase fault, the electromagnetic torque produced during a phase-to-phase fault depends on the instant of the fault. The component of the torque that depends on γ_0 has a periodic variation at fundamental frequency and a maximum value when the fault occurs when the voltage in phase A reaches its negative maximum, that is when $\gamma_0 = -\pi/2$. In this situation the fundamental-frequency component is initially the highest and has a value twice the double-frequency component. As time progresses, the magnitude of the fundamental-frequency torque component reduces until, in the steady state, it vanishes completely, Figure 4.29, and the torque varies at double frequency.

Including the effect of subtransient saliency introduces considerable complications in the formulae. Firstly, the application of two-reaction theory leads to a term $X''_\mathrm{d}\sin^2\gamma + X''_\mathrm{q}\cos^2\gamma$ appearing in the denominator, similar to the expression for the current. Secondly, as in the case of the three-phase fault, an AC component at double frequency appears that is dependent on $\left(X''_\mathrm{q} - X''_\mathrm{d}\right)$. The torque is then expressed as

$$\begin{aligned}\tau_\mathrm{AC} = \frac{3}{\omega}\frac{E_\mathrm{f}^2}{X''_\mathrm{d}\sin^2\gamma + X''_\mathrm{q}\cos^2\gamma}\Big\{&\left[g_2(t)\sin\gamma - \mathrm{e}^{-t/T_\beta}\sin\gamma_0\right]g_2(t)\cos\omega t \\ &+\frac{1}{2}\frac{\left(X''_\mathrm{q} - X''_\mathrm{d}\right)\left[g_2(t)\sin\gamma - \mathrm{e}^{-t/T_\beta}\sin\gamma_0\right]^2\sin 2\gamma}{X''_\mathrm{d}\sin^2\gamma + X''_\mathrm{q}\cos^2\gamma}\Big\} \quad \mathrm{Nm}.\end{aligned} \tag{4.80}$$

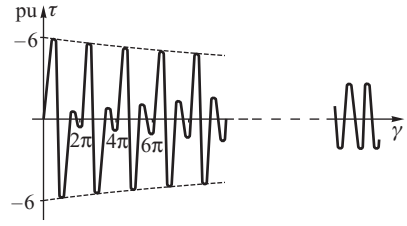

Figure 4.29 Example of the changes in the electromagnetic torque during phase-to-phase fault when $\gamma_0 = -\pi/2$.

When the difference $(X''_q - X''_d)$ is small, the torque given by Equation (4.80) is similar in both shape and maximum value to that obtained from Equation 4.79. If subtransient saliency is high then the second part of Equation (4.80) will distort the torque profile and may also increase the instantaneous value of the torque. Figure 4.30 shows the variation of the torque in a case of high subtransient saliency when $X''_q \approx 2X''_d$.

Equation (4.80) defines one part of the electromagnetic torque occurring during a phase-to-phase short circuit and, just as in the case of the three-phase fault, there will be other torque components due to the power losses in the armature phase windings and the rotor field and damper windings. However, these are usually small compared with the torque defined in Equation (4.80).

4.4 Synchronization

Synchronization is the name given to the process of connecting a generator, with its field winding excited, to the power system. Such a synchronization process is shown schematically in Figure 4.31a where the power system is replaced by an infinite busbar of voltage $\underline{V}_s$ behind an equivalent reactance X_s. It is assumed that just before the switch is closed the generator rotates at a speed ω close to synchronous speed ω_s and that the excitation produces a no-load terminal voltage E_f close to the system voltage V_s.

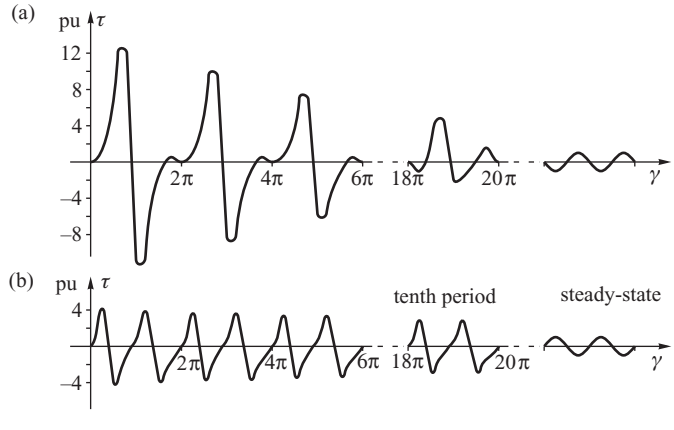

Figure 4.30 Example of torque variation during phase-to-phase fault in a case of high subtransient saliency of $X''_q \approx 2X''_d$ when the fault instant is: (a) $\gamma_0 = -\pi/2$; (b) $\gamma_0 = 0$.

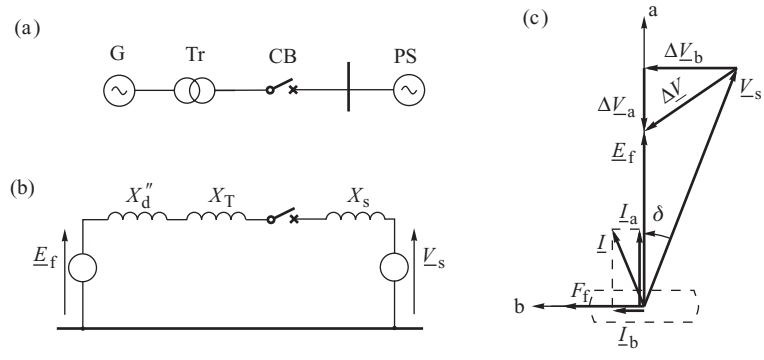

Figure 4.31 Synchronization: (a) schematic diagram; (b) equivalent circuit in the subtransient state; (c) phasor diagram. G, generator; Tr, transformer; bb, substation busbars; PS, power system, CB, circuit-breaker (synchronizing switch).

Ideal synchronization occurs when $\omega = \omega_s$, $\underline{E}_f = \underline{V}_s$ and $\delta = 0$ so that when the synchronizing switch is closed no circulating current will flow. Normally a generator is connected to a power system when these conditions are almost, but not exactly, satisfied, when closing the synchronizing switch will result in the flow of a circulating current that contains both an AC and a DC component. If the generator is assumed to have no local load prior to synchronization then it can be represented in the subtransient state by the excitation emf E_f behind the subtransient reactance X''_d. The circulating current can then be evaluated using Thévenin's theorem based on the voltage $\Delta\underline{V}$ across the synchronizing switch and the impedance as seen from the switch terminals. For simplicity armature resistance and rotor subtransient saliency will be neglected by assuming $R = 0$ and $X''_d = X''_q$.

4.4.1 Currents and Torques

The subtransient armature current can be found by resolving the voltage across the switch $\Delta\underline{V}$ into two orthogonal components directed along the axes a and b as shown in Figure 4.31c. It is important to stress that although the a- and b-axes are directed along the d- and q-axes, the resulting (a, b) voltage and current components have a different meaning to the (d, q) components. The (a, b) components are simply the components of the phase quantities resolved along two axes in the complex plane while the (d, q) voltage and current components are associated with fictitious, rotating, orthogonal armature windings as explained in Chapter 3. As the circuit is assumed to be purely reactive, the current must lag the forcing voltage by $\pi/2$. This means that the a-component voltage ΔV_a will force the flow of the b-component of current I_b and vice versa.

Applying Thévenin's theorem gives the maximum value of the b-axis current, i_{bm}, due to ΔV_a as

$$i_{bm} = \frac{\Delta V_{am}}{x''_d} = \frac{V_{sm}\cos\delta - E_{fm}}{x''_d}, \tag{4.81}$$

where $x''_d = X''_d + X_T + X_s$, $E_{fm} = \sqrt{2}E_f$ and $V_{sm} = \sqrt{2}V_s$. As the voltage component ΔV_a acts along the q-axis its effect in the Thévenin equivalent circuit, when looking from the terminals of the switch, is similar to that of the emf E_f during the three-phase short circuit on an unloaded generator. As a result, alternating and direct currents will be induced in the armature windings that are similar to those expressed by Equations (4.7) and (4.8) but with i_m replaced by i_{bm}.

As in the case of the three-phase fault, the AC component of the phase currents due to I_b produces an armature mmf which rotates with the rotor and is in phase with the excitation mmf

F_f (Figure 4.31c). Since there is no angular displacement between these two mmfs, they cannot produce an electromagnetic torque. On the other hand, the DC component of the phase currents produces a stationary mmf which counter-rotates with respect to the rotor. Consequently, the angular displacement between the field flux and the armature mmf varies with time producing a periodic torque given by Equation (4.43) as

$$\tau_I = -\frac{3}{2}\frac{1}{\omega}E_{fm}i_{bm}\sin\omega t = -\frac{3}{\omega}\frac{E_f}{x''_d}(V_s\cos\delta - E_f)\sin\omega t \quad \text{N m}. \tag{4.82}$$

Compared with Equation (4.43), the minus sign is due to the voltage $\Delta\underline{V}_a$ directly opposing E_f.

The b-axis voltage $\Delta\underline{V}_b$ produces the a-axis circulating current $\underline{I}_a$. The amplitude of this current is

$$i_{am} = \frac{\Delta V_{bm}}{x''_d} = \frac{V_{sm}\sin\delta}{x''_d}. \tag{4.83}$$

$\underline{I}_a$ produces an mmf which rotates with the rotor and is directed along its q-axis (Figure 4.31c). The interaction between this component of armature mmf and the excitation flux produces a constant driving torque given by

$$\tau_{II} = \frac{3}{2}\frac{1}{\omega}E_{fm}i_{am} = \frac{3}{\omega}\frac{E_fV_s}{x''_d}\sin\delta \quad \text{N m}. \tag{4.84}$$

The DC component of the phase current driven by $\Delta\underline{V}_b$ produces a stationary flux shifted by $\pi/2$ with respect to the stationary flux driven by ΔV_a, so that the resulting periodic torque is equal to

$$\tau_{III} = \frac{3}{2}\frac{1}{\omega}E_{fm}i_{am}\sin\left(\omega t - \frac{\pi}{2}\right) = -\frac{3}{\omega}\frac{E_fV_s}{x''_d}\sin\delta\cos\omega t \quad \text{N m}. \tag{4.85}$$

At this point it is worth noting that, although the circulating current resulting from synchronization has a similar shape to the three-phase fault current, the direct component can be larger, or smaller, than the three-phase fault current depending on the actual values of X_T, X_s and δ. In addition, the synchronization torque may be quite different from the three-phase fault torque due to the influence of the voltage component $\Delta\underline{V}_b$. Adding the three torque components in Equations (4.82), (4.84) and (4.85) gives

$$\tau = \tau_I + \tau_{II} + \tau_{III} = \frac{3}{\omega}\left[\frac{E_fV_s}{x''_d}\sin\delta(1-\cos\omega t) - \frac{E_f}{x''_d}(V_s\cos\delta - E_f)\sin\omega t\right] \quad \text{N m} \tag{4.86}$$

which can be rewritten by substituting $\cos\delta = 1 - \sin\delta\tan(\delta/2)$ as

$$\tau = \frac{3}{\omega}\left[\frac{E_fV_s}{x''_d}\sin\delta\left(1-\cos\omega t + \tan\frac{\delta}{2}\sin\omega t\right) + \frac{E_f(E_f - V_s)}{x''_d}\sin\omega t\right] \quad \text{N m}. \tag{4.87}$$

The maximum value of the torque produced on synchronization is highly dependent on the angle δ at which the switch is closed. When $E_f \approx V_s$, the second component in the above equation is zero and the torque is determined by the trigonometric expression

$$T_\delta(t) = \sin\delta\left(1 - \cos\omega t + \tan\frac{\delta}{2}\sin\omega t\right). \tag{4.88}$$

The variation of this expression with time for three different values of δ is shown in Figure 4.32a, while Figure 4.32b shows the maximum value of $T_\delta(t)$ as a function of δ. From these diagrams it

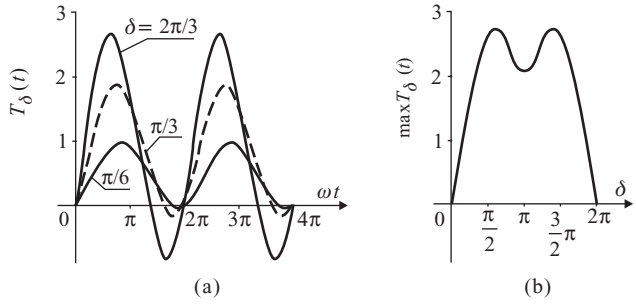

Figure 4.32 Expression (4.88): (a) as a function of time for various values of the synchronization angle δ; (b) its maximum value as a function of the synchronization angle δ.

can be seen that when δ is large, the maximum torque is large and occurs early in the cycle with the highest torque occurring when $\delta = 2\pi/3$.

If $E_f \neq V_s$ then according to Equation (4.87) the torque is increased by a periodic component depending on the difference $(E_f - V_s)$.

Example 4.3

The per-unit network data, referred to the generator unit, are: $X''_d = X''_q = 0.18$; $X_T = 0.11$; $X_s = 0.01$; $E_f = V_s = 1.1$. The per-unit subtransient torque produced on synchronization is obtained from Equation (4.87) by multiplying by $\omega/3$ to obtain $\tau = T_\delta(1.1)^2/(0.18 + 0.11 + 0.01) = 4T_\delta$. The torque may be evaluated by taking $T_\delta(t)$ from Figure 4.32b for various values of the synchronization angle δ. The results in the table show that the torque may exceed the rated torque:

Synchronization angle	$\pi/6$	$\pi/3$	$\pi/2$	$2\pi/3$	$5\pi/6$	π
Torque (pu)	4.08	7.48	9.64	10.4	9.64	8

The equations derived in this section are valid immediately after synchronization, that is during the subtransient period. As time progresses, magnetic energy will be dissipated in the winding resistances, the circulating current will decay and the generator will move from the subtransient state, through the transient state, until it eventually reaches the steady state. As the circulating current decays, so too do the corresponding torque components.

4.5 Short-Circuit in a Network and its Clearing

Section 4.2 discussed in some detail the effect of a three-phase short circuit across the generator terminals. Fortunately this type of fault does not occur very often and much more common are faults some distance from the generator elsewhere in the power system. Figure 4.33 shows a general case where the generator is connected to the power system via a transformer and two parallel lines.

When a three-phase-to-earth fault occurs at the beginning of one of the lines, point F2, then the fault can be treated as a generator short circuit but with some of the reactances and time constants modified to include the effect of the transformer. Firstly, the transformer reactance X_T must be added in series to the reactances X''_d, X'_d and X_d to form the resultant reactances

$$x''_d = X''_d + X_T, \quad x'_d = X'_d + X_T, \quad x_d = X_d + X_T. \tag{4.89}$$

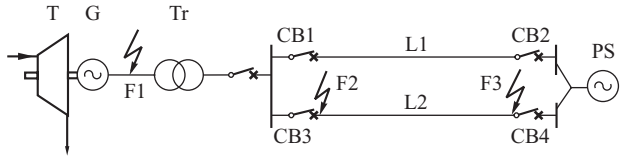

Figure 4.33 Schematic diagram of a fragment of a power system with examples of the short-circuit points F1, F2, F3. G, generator; Tr, transformer; bb, busbar; PS, power system (infinite busbar).

This has the effect of suppressing the magnitude of the currents given by Equations 4.29 to 4.31 and the electromagnetic torque containing both periodic and aperiodic components as given by Equations (4.45) to (4.48). Secondly, the transformer resistance R_T increases the rate at which the stored magnetic energy can be dissipated so that the DC component of the short-circuit current decays more rapidly. The time constants have to be modified, as in Equation (4.76), to

$$T''_{d(network)} = T''_d \left(\frac{X'_d}{X''_d}\right)\left(\frac{X''_d + X_T}{X'_d + X_T}\right), \quad T'_{d(network)} = T'_d \left(\frac{X_d}{X'_d}\right)\left(\frac{X'_d + X_T}{X_d + X_T}\right). \tag{4.90}$$

As a consequence of the increase in the time constants, the instantaneous value of the short-circuit current may pass through zero even on the first cycle.

The shapes of the currents and torques during the short circuit and following fault clearing are shown in Figure 4.34. During the short circuit, high currents flow in all three phases and the torque oscillates around near-zero average values. As the clearing time is usually small, the rotor angle, shown by the dashed line on the torque diagram, increases only slightly. When the fault is cleared, the changes in the torque and the currents are similar to those occurring during synchronization when the rotor angle first increases and then decreases, but the torque oscillates around an average value.

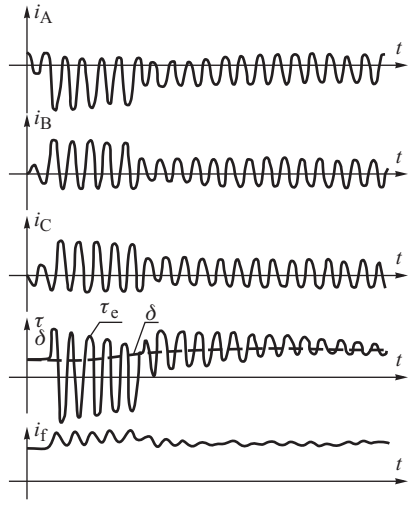

Figure 4.34 Three-phase fault and its clearing in the line connecting a generator to the system: i_A, i_B, i_C, phase currents; τ_e, electromagnetic torque; i_f, field current; δ, rotor angle. Adapted from Kulicke and Webs (1975). Reproduced by permission of VDE Verlag Gmbh

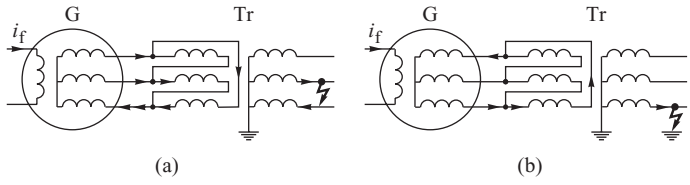

Figure 4.35 Transformation of the short-circuit current in the star–delta connection of the transformer: (a) phase-to-phase fault; (b) single-phase fault.

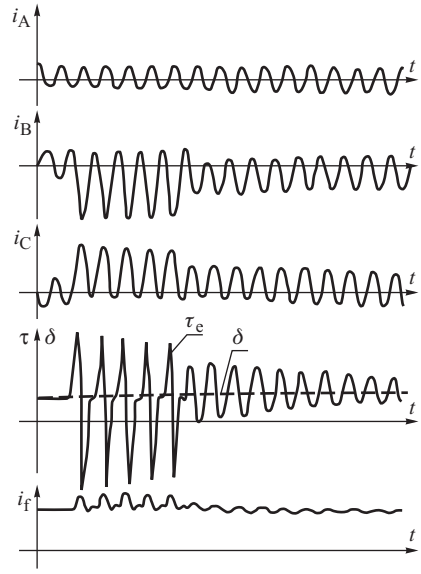

Figure 4.36 Phase-to-phase fault and its clearing in the line connecting a generator to the system: i_A, i_B, i_C, phase currents; τ_e, electromagnetic torque; i_f, field current; δ, rotor angle. Adapted from Kulicke and Webs (1975). Reproduced by permission of VDE Verlag Gmbh

In the case of an unsymmetrical fault in the network, the generator currents are distorted by the step-up transformer. This effect is illustrated in Figure 4.35 assuming the transformer to be star–delta connected when a phase-to-phase fault on the secondary of the transformer, Figure 4.35a, is seen as a three-phase unsymmetrical current on the primary. In the case of a single-phase-to-phase fault on the secondary, Figure 4.35b, this is seen on the primary side as a two-phase fault.

Figure 4.36 shows the time variation of the phase currents, air-gap torque and field current during, and after clearing, a short circuit between phases B and C in the line connecting the generator to a system. Such an unsymmetrical fault produces negative-sequence currents and consequently the electromagnetic torque contains a double-frequency component.

The dynamic behaviour of the generator during the short-circuit period and the importance of the clearing time are considered in more detail in Chapter 5.

5

Electromechanical Dynamics – Small Disturbances

In the previous chapter the currents and torques produced in a synchronous generator as the result of a system disturbance were discussed and, as the duration of the disturbance was very short, the generator rotational speed could be considered constant. In this chapter a longer time scale is considered during which the rotor speed will vary and interact with the electromagnetic changes to produce *electromechanical dynamic* effects. The time scale associated with these dynamics is sufficiently long for them to be influenced by the turbine and the generator control systems.

The aim of this chapter is both to provide an explanation of how, and why, mechanical movement of the generator rotor is influenced by electromagnetic effects and to examine how this movement varies depending on the operating state of the generator. During the course of this discussion some important stability concepts will be introduced together with their basic mathematical description and an explanation of the physical implications.

5.1 Swing Equation

Section 2.2 described the constructional features of a turbine and explained how a multi-stage turbine drives the generator rotor through a common drive shaft. A diagram of a multi-stage turbine consisting of high-pressure, intermediate-pressure and low-pressure stages is shown in Figure 5.1 where each turbine stage contributes a proportion of the total mechanical driving torque. The drive system can be modelled by a series of rotational masses, to represent the inertia of each turbine stage, connected together by springs, to represent the torsional stiffness of the drive shaft and coupling between the stages. Such a model can be used to compute the torsional natural frequencies of the drive system and can also be used in a detailed computer simulation to obtain information on the actual shaft torques that occur following a major fault or disturbance. This is discussed further in Section 6.7. One of the natural frequencies of the turbine/generator drive system will be at 0 Hz and represents free-body rotation where the turbine and generator inertias move together with no relative displacement of the individual rotor masses. When connected to the power system this free-body rotation will appear as a low-frequency oscillation of typically 1 to 2 Hz. It is this free-body rotation that is addressed in this section.

When considering free-body rotation the shaft can be assumed to be rigid when the total inertia of the rotor J is simply the sum of the individual inertias. Any unbalanced torque acting on the rotor will result in the acceleration or deceleration of the rotor as a complete unit according to

Power System Dynamics: Stability and Control, Second Edition Jan Machowski, Janusz W. Bialek and James R. Bumby
© 2008 John Wiley & Sons, Ltd

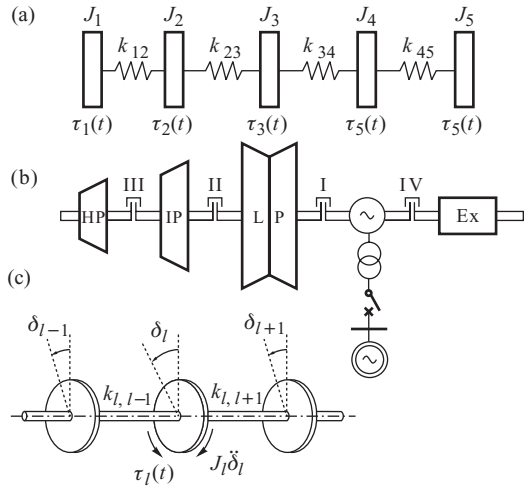

Figure 5.1 Generating unit as an oscillating system: (a) division of the rotor mass into individual sections; (b) schematic diagram; (c) torsional displacement. HP, IP, LP – high-pressure, intermediate-pressure and low-pressure section of the turbine; G, generator; Ex, rotating exciter; J, moment of inertia of individual sections; τ, external torque acting on a mass; k, stiffness of a shaft section; δ, angular displacement of a mass; I, II, III, IV – shaft couplers.

Newton's second law

$$J\frac{\mathrm{d}\omega_\mathrm{m}}{\mathrm{d}t} + D_\mathrm{d}\,\omega_\mathrm{m} = \tau_\mathrm{t} - \tau_\mathrm{e}, \tag{5.1}$$

where J is the total moment of inertia of the turbine and generator rotor (kg m^2), ω_m is the rotor shaft velocity (mechanical rad/s), τ_t is the torque produced by the turbine (N m), τ_e is the counteracting electromagnetic torque and D_d is the damping-torque coefficient (N m s) and accounts for the mechanical rotational loss due to windage and friction.

Although the turbine torque τ_t changes relatively slowly, due to the long thermal time constants associated with the boiler and turbine, the electromagnetic torque τ_e may change its value almost instantaneously. In the steady state the rotor angular speed is synchronous speed ω_sm while the turbine torque τ_t is equal to the sum of the electromagnetic torque τ_e and the damping (or rotational loss) torque $D_\mathrm{d}\omega_\mathrm{sm}$

$$\tau_\mathrm{t} = \tau_\mathrm{e} + D_\mathrm{d}\omega_\mathrm{sm} \quad \text{or} \quad \tau_\mathrm{m} = \tau_\mathrm{t} - D_\mathrm{d}\omega_\mathrm{sm} = \tau_\mathrm{e}, \tag{5.2}$$

where τ_m is the net mechanical shaft torque, that is the turbine torque less the rotational losses at $\omega_\mathrm{m} = \omega_\mathrm{sm}$. It is this torque that is converted into electromagnetic torque. If, due to some disturbance, $\tau_\mathrm{m} > \tau_\mathrm{e}$ then the rotor accelerates; if $\tau_\mathrm{m} < \tau_\mathrm{e}$ then it decelerates.

In Section 3.3 the rotor position with respect to a synchronously rotating reference axis was defined by the rotor, or power, angle δ. The rotor velocity can therefore be expressed as

$$\omega_\mathrm{m} = \omega_\mathrm{sm} + \Delta\omega_\mathrm{m} = \omega_\mathrm{sm} + \frac{\mathrm{d}\delta_\mathrm{m}}{\mathrm{d}t}, \tag{5.3}$$

where δ_m is the rotor angle expressed in mechanical radians and $\Delta\omega_\mathrm{m} = \mathrm{d}\delta_\mathrm{m}/\mathrm{d}t$ is the *speed deviation* in mechanical radians per second.

Substituting Equation (5.3) into (5.1) gives

$$J\frac{\mathrm{d}^2\delta_\mathrm{m}}{\mathrm{d}t^2} + D_\mathrm{d}\left(\omega_\mathrm{sm} + \frac{\mathrm{d}\delta_\mathrm{m}}{\mathrm{d}t}\right) = \tau_\mathrm{t} - \tau_\mathrm{e} \quad \text{or} \quad J\frac{\mathrm{d}^2\delta_\mathrm{m}}{\mathrm{d}t^2} + D_\mathrm{d}\frac{\mathrm{d}\delta_m}{\mathrm{d}t} = \tau_\mathrm{m} - \tau_\mathrm{e}. \tag{5.4}$$

Multiplying through by the rotor synchronous speed ω_sm gives

$$J\omega_\mathrm{sm}\frac{\mathrm{d}^2\delta_\mathrm{m}}{\mathrm{d}t^2} + \omega_\mathrm{sm}D_\mathrm{d}\frac{\mathrm{d}\delta_\mathrm{m}}{\mathrm{d}t} = \omega_\mathrm{sm}\tau_\mathrm{m} - \omega_\mathrm{sm}\tau_\mathrm{e}. \tag{5.5}$$

As power is the product of angular velocity and torque, the terms on the right hand side of this equation can be expressed in power to give

$$J\omega_\mathrm{sm}\frac{\mathrm{d}^2\delta_\mathrm{m}}{\mathrm{d}t^2} + \omega_\mathrm{sm}D_\mathrm{d}\frac{\mathrm{d}\delta_\mathrm{m}}{\mathrm{d}t} = \frac{\omega_\mathrm{sm}}{\omega_\mathrm{m}}P_\mathrm{m} - \frac{\omega_\mathrm{sm}}{\omega_\mathrm{m}}P_\mathrm{e}, \tag{5.6}$$

where P_m is the net shaft power input to the generator and P_e is the electrical air-gap power, both expressed in watts. During a disturbance the speed of a synchronous machine is normally quite close to synchronous speed so that $\omega_\mathrm{m} \approx \omega_\mathrm{sm}$ and Equation (5.6) becomes

$$J\omega_\mathrm{sm}\frac{\mathrm{d}^2\delta_\mathrm{m}}{\mathrm{d}t^2} + \omega_\mathrm{sm}D_\mathrm{d}\frac{\mathrm{d}\delta_\mathrm{m}}{\mathrm{d}t} = P_\mathrm{m} - P_\mathrm{e}. \tag{5.7}$$

The coefficient $J\omega_\mathrm{sm}$ is the *angular momentum* of the rotor at synchronous speed and, when given the symbol M_m, allows Equation (5.7) to be written as

$$M_\mathrm{m}\frac{\mathrm{d}^2\delta_\mathrm{m}}{\mathrm{d}t^2} = P_\mathrm{m} - P_\mathrm{e} - D_\mathrm{m}\frac{\mathrm{d}\delta_\mathrm{m}}{\mathrm{d}t}, \tag{5.8}$$

where $D_\mathrm{m} = \omega_\mathrm{sm}D_\mathrm{d}$ is the damping coefficient. Equation (5.8) is called the *swing equation* and is the fundamental equation governing the rotor dynamics.

It is common practice to express the angular momentum of the rotor in terms of a normalized *inertia constant* when all generators of a particular type will have similar 'inertia' values regardless of their rating. The inertia constant is given the symbol H defined as the stored kinetic energy in megajoules at synchronous speed divided by the machine rating S_n in megavolt-amperes so that

$$H = \frac{0.5J\omega_\mathrm{sm}^2}{S_\mathrm{n}} \quad \text{and} \quad M_\mathrm{m} = \frac{2HS_\mathrm{n}}{\omega_\mathrm{sm}}. \tag{5.9}$$

The units of H are seconds. In effect H simply quantifies the kinetic energy of the rotor at synchronous speed in terms of the number of seconds it would take the generator to provide an equivalent amount of electrical energy when operating at a power output equal to its MVA rating. In Continental Europe the symbol T_m is used for *mechanical time constant* where

$$T_\mathrm{m} = \frac{J\omega_\mathrm{sm}^2}{S_\mathrm{n}} = 2H \quad \text{and} \quad M_\mathrm{m} = \frac{T_\mathrm{m}S_\mathrm{n}}{\omega_\mathrm{sm}}. \tag{5.10}$$

Again the units are seconds but the physical interpretation is different. In this case, if the generator is at rest and a mechanical torque equal to $S_\mathrm{n}/\omega_\mathrm{sm}$ is suddenly applied to the turbine shaft, then the rotor will accelerate, its velocity will increase linearly and it will take T_m seconds to reach synchronous speed ω_sm.

Section 3.3 showed that the power angle and angular speed can be expressed in electrical radians and electrical radians per second respectively, rather than their mechanical equivalent, by substituting

$$\delta = \frac{\delta_{\mathrm{m}}}{p/2} \quad \text{and} \quad \omega_{\mathrm{s}} = \frac{\omega_{\mathrm{sm}}}{p/2}, \tag{5.11}$$

where p is the number of poles. Introducing the inertia constant and substituting Equations (5.11) into Equation (5.8) allows the swing equation to be written as

$$\frac{2HS_{\mathrm{n}}}{\omega_{\mathrm{s}}}\frac{\mathrm{d}^2\delta}{\mathrm{d}t^2} + D\frac{\mathrm{d}\delta}{\mathrm{d}t} = P_{\mathrm{m}} - P_{\mathrm{e}} \qquad \text{or} \qquad \frac{T_{\mathrm{m}}S_{\mathrm{n}}}{\omega_{\mathrm{s}}}\frac{\mathrm{d}^2\delta}{\mathrm{d}t^2} + D\frac{\mathrm{d}\delta}{\mathrm{d}t} = P_{\mathrm{m}} - P_{\mathrm{e}}, \tag{5.12}$$

where D, the damping coefficient, is $D = 2D_{\mathrm{m}}/p$. The equations in (5.12) can be rationalized by defining an *inertia coefficient* M and *damping power* P_{D} such that

$$M = \frac{2HS_{\mathrm{n}}}{\omega_{\mathrm{s}}} = \frac{T_{\mathrm{m}}S_{\mathrm{n}}}{\omega_{\mathrm{s}}}, \quad P_{\mathrm{D}} = D\frac{\mathrm{d}\delta}{\mathrm{d}t}, \tag{5.13}$$

when the swing equation takes the common form

$$M\frac{\mathrm{d}^2\delta}{\mathrm{d}t^2} = P_{\mathrm{m}} - P_{\mathrm{e}} - P_{\mathrm{D}} = P_{\mathrm{acc}}, \tag{5.14}$$

where P_{acc} is the net accelerating power. The time derivative of the rotor angle $\mathrm{d}\delta/\mathrm{d}t = \Delta\omega = \omega - \omega_{\mathrm{s}}$ is the *rotor speed deviation* in electrical radians per second. Often it is more convenient to replace the second-order differential equation (5.14) by two first-order equations:

$$\begin{aligned} M\frac{\mathrm{d}\Delta\omega}{\mathrm{d}t} &= P_{\mathrm{m}} - P_{\mathrm{e}} - P_{\mathrm{D}} = P_{\mathrm{acc}} \\ \frac{\mathrm{d}\delta}{\mathrm{d}t} &= \Delta\omega. \end{aligned} \tag{5.15}$$

It is also common power system practice to express the swing equation in a per-unit form. This simply means normalizing Equation (5.14) to a common MVA base. Assuming that this base is the MVA rating of the generator, then dividing both sides of Equation (5.14) by S_{n} does not modify the equation structure but all parameters are now normalized to the three-phase MVA base.

5.2 Damping Power

Damping of the rotor motion by mechanical losses is small and can be neglected for all practical considerations. The main source of damping in the synchronous generator is provided by the damper, or amortisseur, windings described in Section 2.2.1. The damper windings have a high resistance/reactance ratio and act in a similar way to the short-circuited squirrel-cage rotor windings in an induction motor. In the subtransient state these windings act as a perfect screen and the changes in the armature flux cannot penetrate them. In the transient state the air-gap flux, which rotates at the synchronous speed, penetrates the damper windings and induces an emf and current in them whenever the rotor speed ω is different from the synchronous speed ω_{s}. This induced current produces a damping torque which, according to Lenz's law, tries to restore the synchronous speed of the rotor. As this additional torque only appears when $\omega \neq \omega_{\mathrm{s}}$, it is proportional to $\Delta\omega = \mathrm{d}\delta/\mathrm{d}t$ and is referred to as the *asynchronous torque*.

Damper windings can be on both rotor axes, or on the d-axis only. In the round-rotor generator the solid-steel rotor body provides paths for eddy currents which have the same effect as damper windings. Machines with laminated salient poles require explicit damper windings for effective damping.

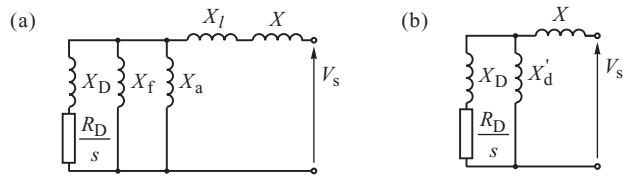

Figure 5.2 The equivalent circuit of the synchronous generator operating as an induction machine: (a) with leakage reactances included; (b) with leakage reactances neglected.

The rigorous derivation of an expression for damping power is long and complicated but an approximate equation for the generator–infinite busbar system can be derived if the following assumptions are made:

(i) the resistances of both the armature and the field winding are neglected;
(ii) damping is produced only by the damper windings;
(iii) the leakage reactance of the armature winding can be neglected;
(iv) excitation does not affect the damping torque.

With these assumptions an equation for damping power can be derived using the induction motor equivalent circuit shown in Figure 3.28.

Figure 4.10a showed that in the subtransient state the equivalent reactance of the generator, as seen from the network, consists of the armature winding leakage reactance X_l connected in series with the parallel-connected damper winding leakage reactance X_D, the field winding leakage reactance X_f and the armature reaction reactance X_a. Figure 5.2a shows a similar equivalent circuit of the generator–infinite busbar system with the generator operating as an induction machine. The reactance X represents the combined reactance of the step-up transformer and the network while V_s is the infinite busbar voltage. Due to assumption (iv) the field winding is closed but not excited. To take the speed deviation into account the equivalent resistance in the damper branch is divided by $s = \Delta\omega/\omega_s$ in the same way as for the induction machine. Initially rotor saliency is neglected.

Assumption (iii) allows the reactance X_l to be neglected when the subtransient and transient reactances are given approximately by the expressions in Equations (5.12) and (5.13):

$$X'_d \cong \frac{1}{\frac{1}{X_f} + \frac{1}{X_a}}, \quad X''_d \cong \frac{1}{\frac{1}{X_f} + \frac{1}{X_a} + \frac{1}{X_D}}. \tag{5.16}$$

The first of these equations allows the parallel connection of X_f and X_a in Figure 5.2a to be replaced by X'_d, as shown in Figure 5.2b.

Equation (5.16) also allows the damper winding leakage reactance to be approximately expressed as a function of the subtransient and transient reactances as

$$X_D \cong \frac{X'_d X''_d}{X'_d - X''_d}. \tag{5.17}$$

The subtransient short-circuit time constant $T''_d = X_D/\omega_s R_D$ can now be calculated as

$$T''_d = \frac{X_D}{\omega_s R_D} \cong \frac{X'_d X''_d}{\omega_s R_D \left(X'_d - X''_d\right)}, \tag{5.18}$$

allowing the damper winding resistance (R_D/s), as seen from the armature, to be written in the form

$$\frac{R_D}{s} = \frac{X'_d X''_d}{X'_d - X''_d} \frac{1}{T''_d \omega_s s} = \frac{X'_d X''_d}{X'_d - X''_d} \frac{1}{T''_d \Delta\omega}. \tag{5.19}$$

For small values of speed deviation the term R_D/s is large and the current flows mostly through X'_d, allowing the series connection of X and X'_d to be treated as a voltage divider. With this assumption the voltage drop across X'_d is equal to $V_s X'_d/(X + X'_d)$. Ohm's law applied to the damper equivalent branch then gives

$$I_D^2 \cong V_s^2 \left(\frac{X'_d}{X + X'_d}\right)^2 \frac{1}{(R_D/s)^2 + X_D^2}, \tag{5.20}$$

and the damping power as

$$P_D = I_D^2 \frac{R_D}{s} \cong V_s^2 \frac{(X'_d)^2}{(X + X'_d)^2} \frac{R_D/s}{\left(\frac{R_D}{s}\right)^2 + \frac{(X'_d X''_d)^2}{(X'_d - X''_d)^2}}. \tag{5.21}$$

Substituting R_D/s from Equation (5.19) gives

$$P_D \cong V_s^2 \frac{X'_d - X''_d}{(X + X'_d)^2} \frac{X'_d}{X''_d} \frac{T''_d \, \Delta\omega}{1 + (T''_d \, \Delta\omega)^2}. \tag{5.22}$$

When rotor saliency is taken into account a similar formula can be derived for the quadrature axis. The resultant damping power can be found by replacing the driving voltage V_s in both d and q equivalent circuits by the respective voltage components, $V_d = -V_s \sin\delta$ and $V_q = V_s \cos\delta$ to give

$$P_D = V_s^2 \left[\frac{X'_d - X''_d}{(X + X'_d)^2} \frac{X'_d}{X''_d} \frac{T''_d \Delta\omega}{1 + (T''_d \Delta\omega)^2} \sin^2\delta + \frac{X'_q - X''_q}{(X + X'_q)^2} \frac{X'_q}{X''_q} \frac{T''_q \Delta\omega}{1 + (T''_q \Delta\omega)^2} \cos^2\delta \right]. \tag{5.23}$$

The damper power depends on the rotor angle δ and fluctuates with the rotor speed deviation $\Delta\omega = \mathrm{d}\delta/\mathrm{d}t$. For small speed deviations the damping power is proportional to speed deviation, while for larger speed deviations it is a nonlinear function of speed deviation and resembles the power–slip characteristic of the induction motor (Figure 3.29).

For a small speed deviation $s = \Delta\omega/\omega_s \ll 1$ and the $(T''_d \, \Delta\omega)^2$ term in the denominator of Equation (5.23) can be neglected when Equation (5.23) simplifies to

$$P_D = V_s^2 \left[\frac{X'_d - X''_d}{(X + X'_d)^2} \frac{X'_d}{X''_d} T''_d \sin^2\delta + \frac{X'_q - X''_q}{(X + X'_q)^2} \frac{X'_q}{X''_q} T''_q \cos^2\delta \right] \Delta\omega. \tag{5.24}$$

This equation is identical to the expression derived by Dahl (1938) and quoted by Kimbark (1956). In both equations the time constants T''_d and T''_q are the subtransient short-circuit time constants.

When δ is large, damping is strongest in the d-axis, and when δ is small, the q-axis damper winding produce the stronger damping. Equation (5.24) can usefully be rewritten as

$$P_D = [D_d \sin^2\delta + D_q \cos^2\delta]\Delta\omega = D(\delta)\Delta\omega, \tag{5.25}$$

where $D(\delta) = D_d \sin^2\delta + D_q \cos^2\delta$ and D_d, D_q are damping coefficients in both axes. Figure 5.3 shows the variation of the damping coefficient D with δ as expressed by Equation (5.25). The function reaches extrema for $\delta = 0, \pi$ or $\delta = \pi/2, 3\pi/2$ with the corresponding extremal values of damping coefficient being equal to D_d and D_q respectively. The average value of the damping coefficient is $D_{av} = (D_d + D_q)/2$.

The network equivalent reactance X has a significant influence on the damping (asynchronous) power because its squared value appears in the denominator of Equations (5.23) and (5.24). In comparison, its influence on the synchronous power, Equation (3.150), is much less where it appears in the denominator and is not squared.

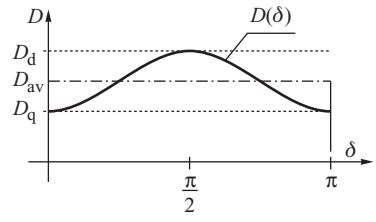

Figure 5.3 Damping coefficient as a function of rotor angle.

5.2.1 Damping Power at Large Speed Deviations

When analysing the damping power over a wide range of speed deviation values it is convenient to rewrite Equation (5.23) as

$$P_{\mathrm{D}} = P_{\mathrm{D(d)}} \sin^2 \delta + P_{\mathrm{D(q)}} \cos^2 \delta, \tag{5.26}$$

where $P_{\mathrm{D(d)}}$ and $P_{\mathrm{D(q)}}$ both depend on the speed deviation. Both components are proportional to nonlinear functions of the speed deviation of the form $\alpha/(1+\alpha^2)$, where $\alpha = T''_{\mathrm{d}}\,\Delta\omega$ for the first component and $\alpha = T''_{\mathrm{q}}\,\Delta\omega$ for the second component. This function reaches a maximum for $\alpha = 1$ so that each component of the damping power will normally reach a maximum critical value at a different *critical speed deviation* given by

$$s_{\mathrm{cr(d)}} = \frac{\Delta\omega_{\mathrm{cr(d)}}}{\omega_{\mathrm{s}}} = \frac{1}{T''_{\mathrm{d}}\,\omega_{\mathrm{s}}}, \quad s_{\mathrm{cr(q)}} = \frac{\Delta\omega_{\mathrm{cr(q)}}}{\omega_{\mathrm{s}}} = \frac{1}{T''_{\mathrm{q}}\,\omega_{\mathrm{s}}}, \tag{5.27}$$

with

$$P_{\mathrm{D(d)cr}} = \frac{V_{\mathrm{s}}^2}{2}\,\frac{X'_{\mathrm{d}} - X''_{\mathrm{d}}}{\left(X + X'_{\mathrm{d}}\right)^2}\,\frac{X'_{\mathrm{d}}}{X''_{\mathrm{d}}}, \quad P_{\mathrm{D(q)cr}} = \frac{V_{\mathrm{s}}^2}{2}\,\frac{X'_{\mathrm{d}} - X''_{\mathrm{d}}}{\left(X + X'_{\mathrm{d}}\right)^2}\,\frac{X'_{\mathrm{d}}}{X''_{\mathrm{d}}}. \tag{5.28}$$

Figure 5.4 shows the variation of both $P_{\mathrm{D(d)}}$ and $P_{\mathrm{D(q)}}$ as a function of the speed deviation. Both factors are equal to zero when $\Delta\omega = 0$ and increase their value as the speed deviation increases until the critical value is reached, after which they decrease. With changing δ the damping power P_{D} will assume values between $P_{\mathrm{D(d)}}$ and $P_{\mathrm{D(q)}}$ with the average value lying between the axes characteristics as shown by the bold line in Figure 5.4.

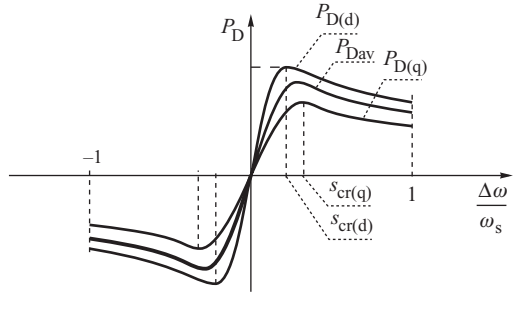

Figure 5.4 Average value of the damping power as a function of speed deviation.

5.3 Equilibrium Points

Section 5.1 showed how the accelerating power is dependent on the difference between the turbine power P_m and the electrical air-gap power P_e (minus the damping power P_D). The mechanical power is supplied by the turbine and its value is controlled by the turbine governor. The electrical air-gap power depends on the generator loading and varies depending on the generator parameters and the power angle. It also depends on the operating state of the generator, but in this section only the steady-state model of the generator–infinite busbar system will be considered. The infinite busbar voltage V_s, introduced in Section 3.3 and shown in Figure 3.24, will be assumed as the datum so that the rotor of the fictitious system's equivalent generator will provide a reference axis rotating at a constant speed. Expressions will be derived for P_e assuming that the combined generator and system resistance r is small and can be neglected. However, it is important to realize that the air-gap power is the power supplied to the system P_s plus the power loss in the equivalent resistance I^2r.

Section 3.3 showed that in the steady state the generator can be represented by a constant emf E_q behind the synchronous reactances X_d and X_q. If all the resistances and shunt admittances of the generator–infinite busbar system shown in Figure 3.24 are neglected then the air-gap power P_e is equal to the power delivered to the system P_{sEq} and is given by Equation (3.132):

$$P_e = P_{E_q} = \frac{E_q V_s}{x_d} \sin\delta + \frac{V_s^2}{2} \frac{x_d - x_q}{x_q x_d} \sin 2\delta, \tag{5.29}$$

where $x_d = X_d + X$, $x_q = X_q + X$ and $X = X_T + X_s$ is the combined reactance of the step-up transformer and the equivalent network. The suffix E_q indicates that the air-gap power is calculated with E_q assumed to be constant.

Section 3.3 showed that the angle δ is the angle between the $\underline{E}_q$ and $\underline{V}_s$ phasors (referred to as the power angle) and, at the same time, it is the spatial angle between the generator rotor and the fictitious system generator (referred to as the rotor angle). This is of vital importance as it allows the swing equation, Equation (5.14), describing the dynamics of the rotor, to be linked with Equation (5.29), describing the electrical state of the generator.

Equation (5.29) describes the steady-state, or static, power–angle characteristic of the generator. For constant E_q and V_s the characteristic becomes a function of the power/rotor angle δ only, that is $P_e = P_e(\delta)$, and Equation (5.14) can be rewritten as

$$M\frac{d^2\delta}{dt^2} = P_m - P_e(\delta) - D\frac{d\delta}{dt}, \tag{5.30}$$

in order to emphasize that P_e is a function of δ and that P_D is proportional to $d\delta/dt$.

When in equilibrium the generator operates at synchronous speed $\omega = \omega_s$ so that

$$\left.\frac{d\delta}{dt}\right|_{\delta=\hat{\delta}} = 0 \quad \text{and} \quad \left.\frac{d^2\delta}{dt^2}\right|_{\delta=\hat{\delta}} = 0, \tag{5.31}$$

where $\hat{\delta}$ is the rotor angle at the equilibrium point. Substituting the above conditions into Equation (5.30) shows that at equilibrium $P_m = P_e(\hat{\delta})$. To simplify considerations the round-rotor generator with $x_d = x_q$ is assumed when the expression for the air-gap power simplifies to

$$P_e(\delta) = P_{E_q}(\delta) = \frac{E_q V_s}{x_d} \sin\delta. \tag{5.32}$$

This characteristic is drawn in Figure 5.5. The maximum value of $P_{E_q}(\delta)$ is referred to as the *critical power* $P_{E_q\,cr}$, while the corresponding value of the rotor angle is referred to as the *critical angle* δ_{cr}. For the round-rotor generator described by Equation (5.32), $P_{E_q\,cr} = E_q V_s/x_d$ and $\delta_{cr} = \pi/2$.

As the mechanical power depends only on the flow of the working fluid through the turbine, and not on δ, the turbine mechanical power characteristic can be treated as a horizontal line

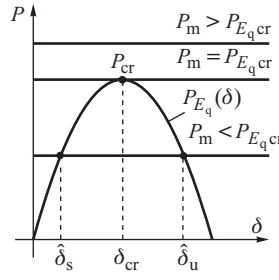

Figure 5.5 Equilibrium points for various values of mechanical power.

P_m = constant in the (δ, P) plane. The intersection between the horizontal P_m characteristic and the sine-like $P_e(\delta)$ characteristic gives the equilibrium points of the generator. Three situations, shown in Figure 5.5, are now possible:

1. $P_m > P_{E_q\,cr}$. Clearly no equilibrium points exist and the generator cannot operate at such a condition.
2. $P_m = P_{E_q\,cr}$. There is only one equilibrium point at δ_{cr}.
3. $P_m < P_{E_q\,cr}$. There are two equilibrium points at $\hat{\delta}_s$ and $\hat{\delta}_u$. This condition corresponds to normal operation and will be discussed in the next section.

5.4 Steady-State Stability of Unregulated System

Classically a system is said to be steady-state stable for a particular operating condition if, following any small disturbance, it reaches a steady-state operating point which is identical, or close to, the predisturbance condition. This is also known as *small-disturbance,* or *small-signal, stability*. A small disturbance is a disturbance for which the equations that describe the dynamics of the power system may be linearized for analytical purposes.

The dynamics of the generator, and its stability, are generally affected by automatic control of the generator and the turbine (Figure 2.2). To simplify considerations, analysis of the generator dynamics will be considered in two sections. In this section the *unregulated system* will be considered when the mechanical power and the excitation voltage are assumed to be constant. This corresponds to analysing the system *steady-state inherent* or *natural stability*. The influence of an AVR will be considered in Section 5.5.

5.4.1 Pull-Out Power

Section 4.4 showed that when a generator is about to be synchronized to the system it must rotate at synchronous speed and its terminal voltage must be equal to, and in phase with, the busbar voltage. When the synchronizing switch is closed the steady-state equilibrium point is reached at $\delta = 0$ and $P_m = 0$ and corresponds to the origin of the power–angle characteristic shown in Figure 5.5. If now the mechanical power P_m is slowly increased by a small amount, the electrical power P_e must follow the changes so that a new equilibrium point of $P_m = P_e$ is reached. In other words, the system is steady-state stable if an increase (decrease) in mechanical power causes a corresponding increase (decrease) in electrical power.

If the system reaction is opposite to this, that is an increase in mechanical power is accompanied by a decrease in electrical power, then no equilibrium point can be reached. These stability considerations are illustrated in Figure 5.6.

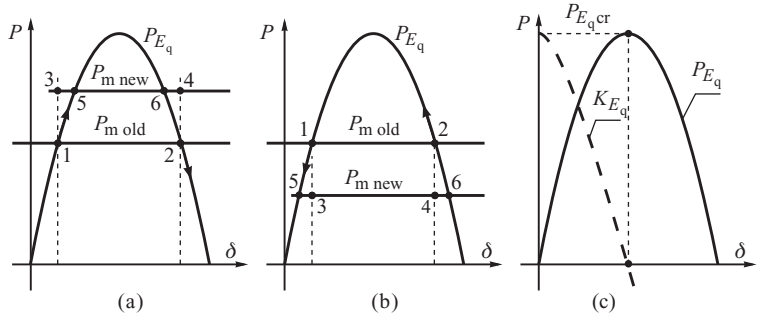

Figure 5.6 Illustration of the conditions for steady-state stability: (a) increase in mechanical power; (b) decrease in mechanical power; (c) the generator steady-state power and synchronizing power coefficient.

For a certain value of mechanical power, marked as 'old', there are two equilibrium points: 1 and 2. If mechanical power is increased to a 'new' value, Figure 5.6a, then this gives rise to a surplus of power at point 1. This surplus acceleration power is equal to segment 1–3 and will, according to Equation (5.14), accelerate the rotor and so increase the power angle and the electrical power. The resulting motion is shown by the arrow and is towards the new equilibrium point 5.

The opposite situation occurs at equilibrium point 2. Here the acceleration power, equal to segment 2–4, again accelerates the rotor and leads to an increase in the power angle but this now results in a reduction in the electrical power. The motion, as shown by the arrow, is away from the new equilibrium point 6.

A similar response is obtained if the mechanical power is reduced, Figure 5.6b. For equilibrium points on the left hand side of the power–angle characteristic the rotor motion is from point 1 towards the new equilibrium point 5. On the other hand, when starting from equilibrium point 2, on the right hand side of the characteristic, it is not possible to reach the new equilibrium point 6 as the rotor motion is in the opposite direction. Obviously an increase in the mechanical power to a value exceeding P_{cr} results in a loss of synchronism due to the lack of any equilibrium point.

From this discussion it is apparent that the generator–infinite busbar system with constant excitation emf E_f is steady-state stable only on the left hand side of the power–angle characteristic; that is, when the slope K_{E_q} of the characteristic is positive

$$K_{E_q} = \left.\frac{\partial P_{E_q}}{\partial \delta}\right|_{\delta=\hat{\delta}_s} > 0. \tag{5.33}$$

K_{E_q} is referred to as the *steady-state synchronizing power coefficient* and the critical power $P_{E_q\,cr}$ is often referred to as the *pull-out power* to emphasize the fact that a larger mechanical power will result in the unregulated generator losing synchronism with the rest of the system. Figure 5.6c shows the plot of $K_{E_q}(\delta)$ and $P_{E_q\,cr}$. The value of $P_{E_q\,cr}$ is also referred to as the *steady-state stability limit* and can be used to determine the *steady-state stability margin* as

$$c_{E_q} = \frac{P_{E_q\,cr} - P_m}{P_{E_q\,cr}}, \tag{5.34}$$

where P_m is the actual loading of the generator. The stability margin varies between $c_{E_q} = 1$ (when the generator is unloaded) and $c_{E_q} = 0$ (when the generator is critically loaded).

It should be emphasized that the pull-out power is determined by the steady-state characteristic $P_{E_q}(\delta)$ and the dynamic response of the generator to a disturbance is determined by the transient power–angle characteristic described in the next subsection.

5.4.2 Transient Power–Angle Characteristics

Chapter 4 explained how any disturbance acting on a generator will produce a sudden change in the armature currents and flux. This flux change induces additional currents in the rotor windings (field and damper) that expel the armature flux into high-reluctance paths around the rotor so as to screen the rotor and keep the rotor flux linkage constant. As the emf E_q is proportional to the field current, the additional induced field current will cause changes in E_q so that the assumption of constant E_q used to derive the static power–angle characteristic (5.32) is invalid in the analysis of postdisturbance rotor dynamics.

Chapter 4 also explained how the induced rotor currents decay with time as the armature flux penetrates first the damper windings (subtransient period) and then the field winding (transient period). Usually the frequency of rotor oscillations is about 1–2 Hz which corresponds to an electromechanical swing period of about 1–0.5s. This period can be usefully compared with the generator subtransient open-circuit time constants T''_{d0} and T''_{q0} which are in the region of few hundredths of a second. On the other hand, the d-axis transient time constant T'_{d0} is in the region of a few seconds while the q-axis time constant T'_{q0} is about a second (see Table 4.3 and Equations (4.16)). Consequently, on the time scale associated with rotor oscillations, it may be assumed that changes in the armature flux can penetrate the damper windings but that the field winding and the round-rotor body act as perfect screens maintaining constant flux linkages. This corresponds to assuming that the transient emfs E'_d and E'_q are constant. This assumption will modify the generator power–angle characteristic as described below.

5.4.2.1 Constant Flux Linkage Model

Assume that the generator is connected to the infinite busbar as shown in Figure 3.24 and that all the resistances and shunt impedances associated with the transformer and network can be neglected. The corresponding equivalent circuit and phasor diagram of the round-rotor and salient-pole generator in the transient state are then as shown in Figure 5.7. The fictitious rotor of the infinite busbar serves as the synchronously rotating reference axis. The reactances of the step-up transformer and the connecting network can be combined with that of the generator to give

$$x'_d = X'_d + X, \quad x'_q = X'_q + X, \tag{5.35}$$

where X'_d and X'_q are the d- and q-axis transient reactances of the generator, and $X = X_T + X_s$. The voltage equations can now be constructed using Figure 5.7b to give

$$E'_d = V_{sd} + x'_q I_q, \quad E'_q = V_{sq} - x'_d I_d, \tag{5.36}$$

where V_{sd} and V_{sq} are the d- and q-components of the infinite busbar voltage V_s given by $V_{sd} = -V_s \sin\delta$ and $V_{sq} = V_s \cos\delta$. As all resistances are neglected, the air-gap power is $P_e = V_{sd} I_d + V_{sq} I_q$. Substituting the values for V_{sd} and V_{sq} and the currents I_d and I_q calculated from Equations (5.36) gives

$$\begin{aligned} P_e = P_s &= V_{sd} I_d + V_{sq} I_q = -\frac{E'_q V_{sd}}{x'_d} + \frac{V_{sd} V_{sq}}{x'_d} + \frac{E'_d V_{sq}}{x'_q} - \frac{V_{sd} V_{sq}}{x'_q} \\ P_e &= P_{E'}(\delta) = \frac{E'_q V_s}{x'_d} \sin\delta + \frac{E'_d V_s}{x'_q} \cos\delta - \frac{V_s^2}{2} \frac{x'_q - x'_d}{x'_q x'_d} \sin 2\delta. \end{aligned} \tag{5.37}$$

Equation (5.37) defines the air-gap power as a function of δ and the d- and q-components of the transient emf and is valid for any generator (with or without transient saliency). The phasor

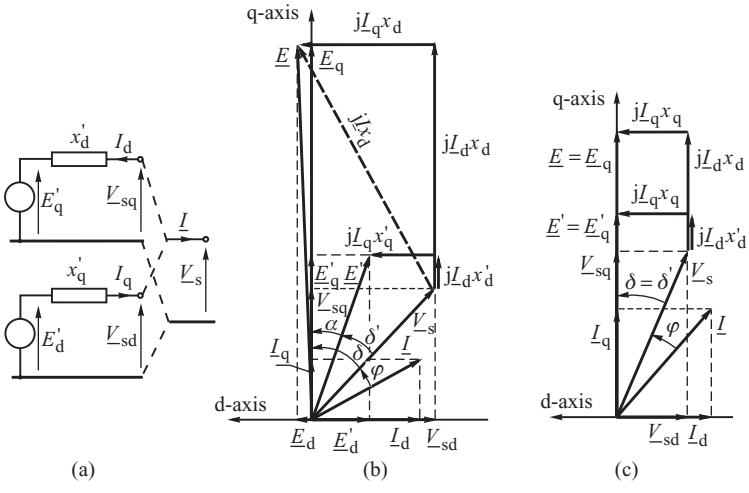

Figure 5.7 Generator–infinite busbar system in the transient state: (a) circuit diagram; (b) phasor diagram of the round-rotor generator; (c) phasor diagram of the salient-pole generator ($x'_q = x_q$).

diagram in Figure 5.7b shows that $E'_d = -E' \sin\alpha$, $E'_q = E' \cos\alpha$ and $\delta = \delta' + \alpha$. Substituting these relationships into Equation (5.37) gives, after some simple but tedious algebra,

$$P_e = P_{E'}(\delta') = \frac{E' V_s}{x'_d}\left[\sin\delta'\left(\cos^2\alpha + \frac{x'_d}{x'_q}\sin^2\alpha\right) + \frac{1}{2}\left(\frac{x'_q - x'_d}{x'_q}\right)\cos\delta'\sin 2\alpha\right] - \frac{V_s^2}{2}\frac{x'_q - x'_d}{x'_d x'_q}\sin 2(\delta' + \alpha). \tag{5.38}$$

Assuming constant rotor flux linkages, then the values of the emfs E'_d and E'_q are also constant, implying that both $E' =$ constant and $\alpha =$ constant. Equation (5.38) describes the generator power–angle characteristic $P_e(E', \delta')$ in terms of the transient emf and the transient power angle and is valid for any type of generator.

A generator with a laminated salient-pole rotor cannot produce effective screening in the q-axis with the effect that $x'_q = x_q$. Inspection of the phasor diagram in Figure 5.7c shows that in this case E' lies along the q-axis so that $\alpha = 0$ and $\delta' = \delta$. Consequently, in this special case, Equation (5.38) simplifies to

$$P_e = P_{E'_q}(\delta')\Big|_{x'_q = x_q} = \frac{E'_q V_s}{x'_d}\sin\delta' - \frac{V_s^2}{2}\frac{x_q - x'_d}{x_q x'_d}\sin 2\delta'. \tag{5.39}$$

5.4.2.2 Classical Model

The constant flux linkage model expressed by Equation (5.38) can be simplified by ignoring transient saliency, that is by assuming $x'_d \approx x'_q$. With this assumption Equation (5.38) simplifies to

$$P_e = P_{E'}(\delta')\big|_{x'_d \approx x'_q} \approx \frac{E' V_s}{x'_d}\sin\delta'. \tag{5.40}$$

The assumption of $x'_d = x'_q$ allows the separate d- and q-axis circuits shown in Figure 5.7b to be replaced by one simple equivalent circuit shown in Figure 5.8. In this *classical model* all the voltages, emfs and currents are phasors in the network reference frame rather than their components resolved along the d- and q-axes.

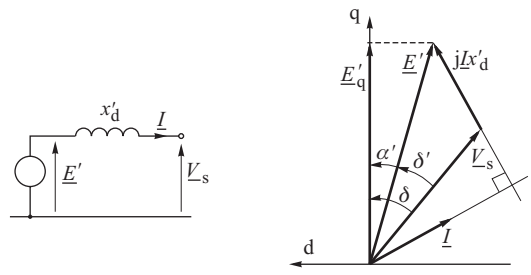

Figure 5.8 Classical model of the generator in the transient state: (a) circuit diagram; (b) phasor diagram.

Generally, as Table 4.3 shows, there is always some degree of transient saliency and $x'_d \neq x'_q$. However, it should be noted that the generator is connected to the infinite busbar through the reactance $X = X_T + X_s$ so that $x'_d = X'_d + X$ and $x'_q = X'_q + X$. The influence of X is such that, as its magnitude increases, the closer the term x'_d/x'_q approaches unity, the closer the term $\left(x'_q - x'_d\right)/x'_d x'_q$ approaches zero. Consequently, when the network reactance is large the classical model, and the constant flux linkage model defined by Equation (5.38), give very similar results even for a generator with a laminated salient-pole rotor.

It is important to note that δ' is the angle between $\underline{V}_s$ and $\underline{E}'$ and not the angle between $\underline{V}_s$ and the q-axis. However, during the transient period the emfs E'_d and E'_q are assumed to be constant (with respect to the rotor axes) and α is also constant with

$$\delta = \delta' + \alpha, \quad \frac{d\delta}{dt} = \frac{d\delta'}{dt} \quad \text{and} \quad \frac{d^2\delta}{dt^2} = \frac{d^2\delta'}{dt^2}. \tag{5.41}$$

This allows δ' to be used in the swing equation instead of δ when Equation (5.14) becomes

$$M\frac{d^2\delta'}{dt^2} = P_m - \frac{E'V_s}{x'_d}\sin\delta' - D\frac{d\delta'}{dt}. \tag{5.42}$$

An important advantage of the classical model is that the generator reactance may be treated in a similar way to the reactance of the transmission lines and other network elements. This has particular importance for multi-machine systems when combining the algebraic equations describing the generator and the network is not as easy as for the generator–infinite busbar system. Due to its simplicity, the classical model will be used extensively throughout this book to analyse and explain rotor dynamics.

5.4.2.3 Steady-State and Transient Characteristics on the Power–Angle Diagram

It is now important to understand how the dynamic characteristic of a generator is located with respect to the static characteristic on the power–angle diagram. For a given stable equilibrium point, when $P_e = P_m$, the balance of power must be held whichever characteristic is considered so that both the static and dynamic characteristics must intersect at the stable equilibrium point. Generally the angle α between δ_0 and δ'_0 is not equal to zero and the transient characteristic is shifted to the right. For salient-pole generators $\alpha = 0$, both characteristics originate at the same point, and the intersection between them at the equilibrium point is due to a distortion in the sine shape of the transient characteristic.

Example 5.1

The round-rotor generator considered in Example 4.1 is connected to the power system (infinite busbar) via a transformer with series reactance $X_T = 0.13$ pu and a transmission line with series reactance $X_L = 0.17$ pu. Find, and plot, the steady-state and the transient characteristics using both the constant flux linkage and the classical generator model. As in Example 4.1, the generator real power output is 1 pu, the reactive power output is 0.5 pu and the terminal voltage is 1.1 pu.

From Example 4.1, $I_0 = 1.016$, $\varphi_{g0} = 26.6^\circ$, $E_{q0} = 2.336$, $\delta_{g0} = 38.5^\circ$, $I_{d0} = -0.922$, $I_{q0} = 0.428$, $E'_q = E'_{q0} = 1.073$, $E'_d = E'_{d0} = 0.522$. Angle α can be found from $\alpha = \arctan(E'_0/E'_q) = 26^o$. The total reactances are $x_d = x_q = x_d + X_T + X_L = 1.9$, $x'_d = X'_d + X_T + X_L = 0.53$, $x'_q = X'_q + X_T + X_L = 0.68$.

Taking $\underline{V}_g$ as the reference, the phasor of the transient emf is $\underline{E'} = 1.193\angle 12.5^o$. It is now necessary to calculate the system voltage $\underline{V}_s$ and calculate the position of $\underline{E}_q$ and $\underline{E'}$ with respect to $\underline{V}_s$. The system voltage can be calculated from

$$\underline{V}_s = \underline{V}_g - j(X_T + X_L)\underline{I} = 1.1 - j0.3 \times 1.016\angle 26.6^\circ = 1.0\angle -15.8^\circ.$$

The angle δ_0 is therefore equal to $38.5 + 15.8 = 54.3^\circ$, δ'_0 is $12.5 + 15.8 = 28.3^\circ$ and φ_0 is $26.6 - 15.8 = 10.8^\circ$. The d- and q-components of the system voltage are

$V_{sd} = -1 \sin 54.3^\circ = -0.814$, $V_{sq} = 1 \cos 54.3^\circ = 0.584$.

The steady-state power-angle characteristic is

$$P_{E_q}(\delta) = \frac{E_d V_s}{x_d} \sin\delta = \frac{2.336 \times 1}{1.9} \sin\delta = 1.23 \sin\delta.$$

The transient characteristic (constant flux linkage model) can be calculated from Equation (5.37) as

$$P_{E'}(\delta) = \frac{1.07 \times 1}{0.53} \sin\delta + \frac{-0.5224 \times 1}{0.68} \cos\delta - \frac{1^2}{2} \frac{0.68 - 0.53}{0.68 \times 0.53} \sin 2\delta$$

$$= 2.02 \sin\delta - 0.768 \cos\delta - 0.208 \sin 2\delta.$$

The approximated transient characteristic for the classical model can be calculated assuming $x'_d = x'_q$. The transient emf can be calculated with respect to $\underline{V}_s$ as $\underline{E'} = V_s + jx'_d\underline{I}_0 = 1 + j\,0.53 \times 1.016\angle -10.8^\circ = 1.223\angle 25.7^\circ$. Thus $E' = 1.223$, $\delta'_0 = 25.7^\circ$ and $\alpha = \delta - \delta' = 54.3 - 25.7 = 28.6^\circ$. The approximated transient characteristic can now be calculated from Equation (5.40) as

$$P_{E'}(\delta') \approx \frac{1.223 \times 1}{0.53} \sin\delta' = 2.31 \sin\delta'.$$

This characteristic is shifted with respect to $P_{E_q}(\delta)$ by 28.6°. Figure 5.9a shows all three characteristics. It can be seen that the classical model gives a good approximation of the constant flux linkage model.

Example 5.2

Recalculate all the characteristics from Example 5.1 for the salient-pole generator considered previously in Example 4.2.

From Example 4.2, $I_0 = 1.016$, $\varphi_{g0} = 26.6^\circ$, $E_q = E_{q0} = 1.735$, $I_{d0} = -0.784$, $I_{q0} = 0.647$, $E'_q = E'_{q0} = 1.241$, $E'_d = 0$, $\delta_{g0} = 23.9^\circ$, $\alpha = 0$.

The total reactances are $x_d = X_d + X_T + X_L = 1.23$, $x_q = x'_q = X_q + X_T + X_L = 0.99$, $x'_d = X'_d + X_T + X_L = 0.6$.

Taking $\underline{V}_g$ as the reference, the phasor of the transient emf is $\underline{E'} = 1.241\angle 23.9^\circ$. The system voltage was calculated in Example 5.1 and is $\underline{V}_s = 1.0\angle 15.8^\circ$. Thus $\delta_0 = \delta'_0 = 23.9 + 15.8 = 39.7^\circ$ and $\delta_0 + \varphi_0 = 39.7 + 10.8 = 50.5^\circ$. The d- and q-components of the system voltage are $V_{sd} = -1 \sin 39.7^\circ = -0.64$, $V_{sq} = 1 \cos 39.7^\circ = 0.77$.

The steady-state power–angle characteristic is

$$P_{E_q}(\delta) = \frac{E_q V_s}{x_d} \sin\delta + \frac{V_s^2}{2} \frac{x_d - x_q}{x_d x_q} \sin 2\delta = \frac{1.735 \times 1}{1.23} \sin\delta + \frac{1}{2} \frac{1.23 - 0.99}{1.23 \times 0.99} \sin 2\delta$$

$$= 1.41 \sin\delta + 0.099 \sin 2\delta \cong 1.41 \sin\delta.$$

The transient characteristic (constant flux linkage model) can be calculated from Equation (5.39) as

$$P_{E'}(\delta) = \frac{1.241 \times 1}{0.6} \sin\delta - \frac{1^2}{2} \frac{0.99 - 0.6}{0.99 \times 0.6} \sin 2\delta = 2.07 \sin\delta - 0.322 \sin 2\delta$$

The approximated transient characteristic for the classical model can be calculated assuming $x'_d = x'_q$. The transient emf, calculated with respect to $\underline{V}_s$, is then $\underline{E'} = \underline{V}_s + \mathrm{j}x'_d \underline{I} = 1 + \mathrm{j}\, 0.6 \times 1.016\angle -10.8^\circ = 1.265\angle 28.3^\circ$. Thus $E' = 1.265$, $\delta' = 28.3^\circ$ and $\alpha = \delta - \delta' = 39.7 - 28.3 = 11.4^\circ$. The approximated transient characteristic can now be calculated from Equation (5.40) as

$$P_{E'}(\delta') \approx \frac{1.265 \times 1}{0.6} \sin\delta' = 2.108 \sin\delta'.$$

This characteristic is shifted with respect to $P_{E_q}(\delta)$ by $\alpha = 11.4^\circ$. Figure 5.9b shows all three characteristics. It can be seen that the classical model gives a good approximation of the constant flux linkage model.

Figure 5.9 shows that by neglecting transient saliency the classical model does not generally significantly distort the transient characteristics. As $x_d > x'_d$, the amplitude of the transient characteristic is greater than the amplitude of the steady-state characteristic. Consequently, the slope of

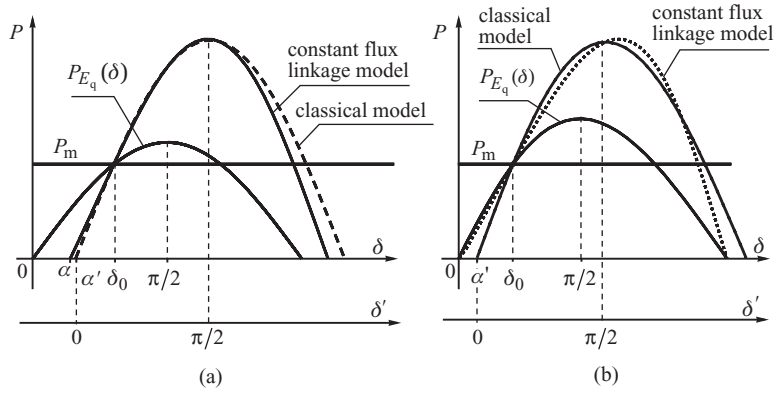

Figure 5.9 Steady-state and transient characteristics: (a) round-rotor generator ($\alpha > 0$); (b) laminated salient-pole machine ($\alpha = 0$).

the transient characteristic at the stable equilibrium point, referred to as the *transient synchronizing power coefficient*

$$K_{E'} = \left.\frac{\partial P_{E'}}{\partial \delta'}\right|_{\delta'=\hat{\delta}'_s}, \tag{5.43}$$

is steeper than the slope of the steady-state characteristic, K_{E_q}, defined in Equation (5.33). For the classical model $K_{E'} = E' V_s \cos \hat{\delta}'_s / x'_d$.

When the generator loading is changed, P_m changes and the stable equilibrium point is shifted to a new position on the steady-state characteristic $P_{E_q}(\delta)$, providing that P_m does not exceed the pull-out power. This increased load modifies the transient characteristic as illustrated in Figure 5.10a which shows three transient characteristics corresponding to three different mechanical powers P_{m1}, P_{m2}, P_{m3}. The generator excitation (and therefore the amplitude of the steady-state characteristic) is assumed to be unchanged. Each new steady-state equilibrium point corresponds to a different value of E' and a different transient characteristic $P_{E'}(\delta)$ crossing the equilibrium point. Note that increased loading results in a smaller transient emf E' so that the amplitude of the transient characteristic is reduced. This can be verified by inspecting the predisturbance d-axis phasor diagram, Figure 4.15, assuming E_f constant. This shows that an increase in the armature current I_0 results in a larger voltage drop across the reactances $(x_d - x'_d)$ and $(x_q - x'_q)$ and therefore a smaller $E'_0 = E'$ value. Figure 5.10b illustrates the same effect shown in Figure 5.10a but in a slightly different way as it shows the steady-state electrical power P_{E_q}, the steady-state synchronizing power coefficient K_{E_q} and the transient synchronizing power coefficient $K_{E'}$ as a function of the generation loading as expressed by the steady-state equilibrium angle $\hat{\delta}_s$. The case of the round-rotor generator is shown. An increase in the generator loading results in smaller steady-state and transient synchronizing power coefficients K_{E_q} and $K_{E'}$, but nevertheless $K_{E'}$ is always larger than K_{E_q}.

5.4.3 Rotor Swings and Equal Area Criterion

The generator models derived in the previous subsection can now be used to describe and analyse the rotor dynamics assuming that the generator is subjected to a sudden disturbance. Such a

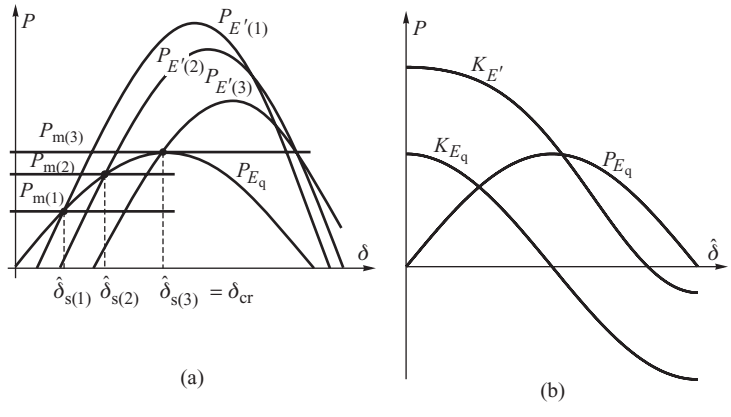

Figure 5.10 Effect of increased loading on the round-rotor generator: (a) the steady-state and transient characteristics for three different loads; (b) the steady-state electrical power and the steady-state and transient synchronizing power coefficients as a function of the steady-state equilibrium rotor angle.

disturbance will result in additional currents being induced in the rotor windings so as to maintain constant rotor flux linkages and therefore constant E'. As the synchronous emfs E_d and E_q follow the changes in the field winding current and the rotor body current respectively, they cannot be assumed to be constant and any rotor swings must therefore follow the transient power–angle curve $P_e = P_{E'}(\delta')$.

Disturbances in the generator–infinite busbar system may arise due to a change in the turbine mechanical power or a change in the equivalent system reactance. The effect of such practical disturbances will be considered in detail later, but here it suffices to consider the effect of disturbing the rotor angle δ from its equilibrium value $\hat{\delta}_s$ to a new value $(\hat{\delta}_s + \Delta\delta_0)$. Although such a disturbance is unlikely from a technical point of view, it does allow a number of important concepts to be introduced that are fundamental to understanding the effects of other, more practical types of disturbance. The initial disturbed conditions for the solution of the system differential equations are

$$\Delta\delta(t = 0^+) = \Delta\delta_0 \neq 0, \quad \Delta\omega(t = 0^+) = \Delta\omega_0 = 0. \tag{5.44}$$

The reaction of the system to this disturbance is illustrated in Figure 5.11 which shows both the steady-state and the transient power characteristics as a function of the rotor angle δ. As the disturbance cannot change the rotor flux linkage, the initial (disturbed) generator operating point will be at point 2 on the transient characteristic $P_{E'}(\delta)$ which crosses the predisturbance stable equilibrium point 1.

Any movement requires work to be done so that by increasing the rotor angle from $\hat{\delta}_s$ to $(\hat{\delta}_s + \Delta\delta_0)$ the disturbance performs work on the rotor. In rotational motion work is equal to the integral of the torque acting over the angular displacement and in this case the net torque is equal to the difference between the electrical (transient) torque and the mechanical torque. As power is equal to the product of torque and angular velocity, and assuming $\omega \approx \omega_s$, the work done by the disturbance is proportional to the integral of the net power acting over the angular displacement, that is

$$W_{1-2} = \int_{\hat{\delta}_s}^{\hat{\delta}_s + \Delta\delta_0} [P_{E'}(\delta) - P_m]\, d\delta = \text{area } 1 - 2 - 4. \tag{5.45}$$

Throughout this book the quantity W will be treated as energy (or work) although, strictly speaking, it should be divided by the synchronous speed ω_s. As the rotor speed deviation $\Delta\omega$ at point 2 is assumed to be zero (the speed is synchronous), the kinetic energy of the rotor is the same as that at

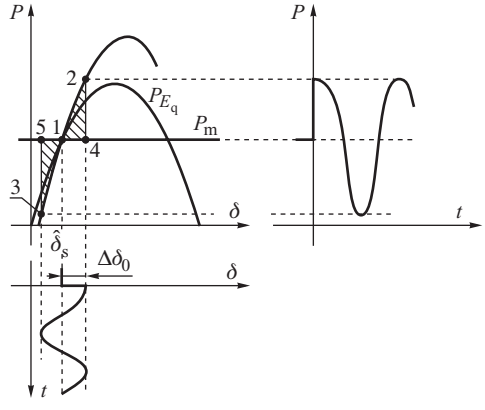

Figure 5.11 Rotor and power swings following a disturbance.

equilibrium point 1. This means that the work W_{1-2} done by the disturbance increases the system potential energy (with respect to equilibrium point 1) by

$$E_p = W_{1-2} = \text{area } 1\text{–}2\text{–}4. \tag{5.46}$$

This initial potential energy provides the impetus necessary to move the rotor back towards its equilibrium point 1. At the disturbed rotor position 2 the mechanical driving torque (and power) is less than the opposing electrical torque (and power), the resulting net deceleration power (equal to segment 4–2) starts to reduce the rotor speed (with respect to synchronous speed) and the rotor angle will decrease. At the equilibrium point 1 all the potential energy in Equation (5.46) will be converted into kinetic energy (relative to synchronous speed) and the deceleration work done is equal to

$$E_k = W_{1-2} = \text{area } 1\text{–}2\text{–}4 = \frac{1}{2} M\Delta\omega^2. \tag{5.47}$$

The kinetic energy will now push the rotor past the equilibrium point $\hat{\delta}_s$ so that it continues to move along curve 1–3. On this part of the characteristic the mechanical driving torque is greater than the opposing electrical torque and the rotor begins to accelerate. Acceleration will continue until the work performed by the acceleration torque (proportional to the integral of the accelerating power) becomes equal to the work performed previously by the deceleration torque. This happens at point 3 when

$$\text{area } 1\text{–}3\text{–}5 = \text{area } 1\text{–}2\text{–}4. \tag{5.48}$$

At this point the generator speed is again equal to synchronous speed but, as $P_m > P_{E'}$, the rotor will continue to accelerate, increasing its speed above synchronous, and will swing back towards $\hat{\delta}_s$. In the absence of any damping the rotor will continually oscillate between points 2 and 3, as described by the swing equation, Equation (5.30). The resulting swing curve is shown in the lower part of Figure 5.11 with the corresponding power swings being shown to the right.

Equation (5.48) defines the maximum deflection of the rotor in either direction on the basis of equalizing the work done during deceleration and acceleration. This concept will be used later in Chapter 6 to define the equal area criterion of stability.

5.4.4 Effect of Damper Windings

Equation (5.24) showed that for small deviations in rotor speed the damper windings produce a damping power $P_D = D\Delta\omega$ that is proportional to the rotor speed deviation. To help explain the effect of the damper windings on the system behaviour it is convenient to rewrite the swing equation, Equation (5.30), as

$$M\frac{d^2\delta}{dt^2} = P_m - [P_e(\delta) + P_D], \tag{5.49}$$

when the damping power is seen either to add to, or to subtract from, the electrical air-gap power $P_e(\delta)$ depending on the sign of the speed deviation. If $\Delta\omega < 0$ then P_D is negative, effectively opposing the air-gap power and shifting the resulting $(P_{E'} + P_D)$ characteristic downwards. If $\Delta\omega > 0$ then P_D is positive, effectively assisting the air-gap power and shifting the resultant characteristic upwards. The rotor will therefore move along a modified power–angle trajectory such as that shown in Figure 5.12. To help increase clarity, this diagram shows an enlarged part of the power–angle diagram in the vicinity of the equilibrium point.

As before, the rotor is initially disturbed from equilibrium point 1 to point 2. At point 2 the driving mechanical power is less than the opposing electrical power and the decelerating torque will

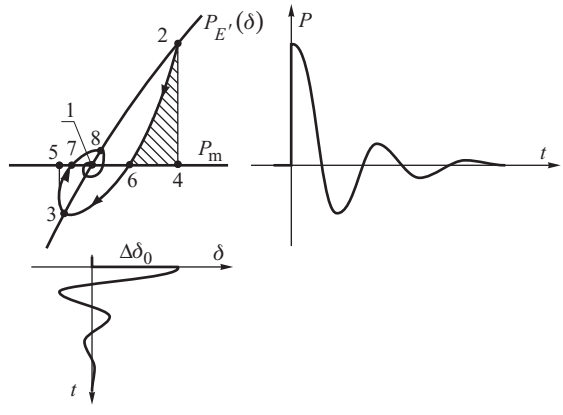

Figure 5.12 Rotor and power oscillations with damping included.

force the rotor back towards the equilibrium point. On deceleration the rotor speed drops and P_D becomes negative, decreasing the resulting decelerating torque. The rotor therefore moves along the line 2–6 when the work done by the decelerating torque is equal to the area 2–4–6. This is less than the area 2–4–1 in Figure 5.11 which represents the work that would have been done if no damping were present. At point 6 the rotor speed reaches a minimum and, as it continues to move along the curve 6–3, the accelerating torque counteracts further movement of the rotor and is assisted by the negative damping term. The rotor again reaches synchronous speed when the area 6–3–5 is equal to the area 2–4–6 which is achieved earlier than in the case without damping. The rotor then starts to swing back, still accelerating, so that the speed increases above synchronous speed. The damping term changes sign, becoming positive, and decreases the resulting accelerating torque. The rotor moves along the curve 3–7 and the work performed during the acceleration is equal to the small area 3–5–7. As a result the rotor reaches synchronous speed at point 8, much earlier than in the case without damping. The rotor oscillations are damped and the system quickly reaches equilibrium point 1.

5.4.5 Effect of Rotor Flux Linkage Variation

The discussion so far has assumed that the total flux linking the field winding and rotor body remains constant during rotor oscillations so that $E' = \text{constant}$. However, as the armature flux enters the rotor windings (Chapter 4) the rotor flux linkages change with time and the effect this has on the rotor swings must now be considered.

5.4.5.1 Linearized Form of the Generator Equations

For small-disturbance analysis, suitable for steady-state stability purposes, the equations describing the generator behaviour can be linearized in the vicinity of the predisturbance operating point. Assume that this operating point is defined by the transient rotor angle $\hat{\delta}'_s$ and the transient emf E'_0. An approximate expression for the change in power $\Delta P = P_e(\delta') - P_m$ with respect to the steady-state equilibrium point can be obtained as a function of the change in the transient rotor angle $\Delta\delta = \delta'(t) - \hat{\delta}'_s$ and a change in the transient emf $\Delta E' = E'(t) - E'_0$ as

$$\Delta P_e = \left.\frac{\partial P_e(\delta', E')}{\partial \delta'}\right|_{E'=E'_0} \Delta\delta' + \left.\frac{\partial P_e(\delta', E')}{\partial E'}\right|_{\delta'=\hat{\delta}'_s} \Delta E' = K_{E'}\Delta\delta + D_{\delta'}\Delta E', \tag{5.50}$$

where $P_e(\delta', E')$ is the air-gap power given by Equations (5.38), (5.39) or (5.40), $K_{E'} = \partial P_e/\partial\delta'$ is the transient synchronizing power coefficient and $D_{\delta'} = \partial P_e/\partial E'$ is a constant coefficient, all of which depend on the generator load. As the angle $\alpha = \delta - \delta'$ is assumed to be constant, $\Delta\delta' = \Delta\delta$. This allows the swing equation, Equation (5.30), to be linearized in the vicinity of the operating point as

$$M\frac{d^2\Delta\delta}{dt^2} + D\frac{d\Delta\delta}{dt} + K_{E'}\,\Delta\delta + D_{\delta'}\Delta E' = 0. \tag{5.51}$$

The transient emf can be resolved into two components E'_d and E'_q along the d and q rotor axes. Analysing the time changes of both components is complicated as the variations take place with different time constants. To simplify the discussion, the case of the salient-pole machine will be considered when $E'_d = 0$, $E' = E'_q$ and $E'_d = 0$, and only the flux linkages of the field winding need be considered.

Now assume that the salient-pole generator operates at a steady-state equilibrium point defined by $\delta = \hat{\delta}_s$ and $E'_q = E'_{q0}$. The incremental swing equation, Equation (5.51), is

$$M\frac{d^2\Delta\delta}{dt^2} + D\Delta\omega + K_{E'_q}\,\Delta\delta + D_{\delta'}\Delta E'_q = 0, \tag{5.52}$$

where $\Delta\omega = d\Delta\delta/dt$ and the values of the coefficients $K_{E'_q} = \partial P_e/\partial\delta'$ and $D_{\delta'} = \partial P_e/\partial E'_q$ can be obtained by differentiating the expression for the air-gap power of the salient-pole generator, Equation (5.39). Analysis of Equation (5.52) suggests that if the changes $\Delta E'_q$ are in phase with the rotor speed deviation $\Delta\omega$, then, just as with the damper winding, additional positive damping power will be introduced into the system.

Chapter 4 showed that the rate at which flux can penetrate the field winding is primarily determined by the field winding transient time constant T'_{d0}, although the generator and system reactances and the operating point will also have some influence. Assuming that the excitation emf E_f and the infinite busbar voltage V_s are constant, Equation (4.28) can be rewritten as

$$\Delta E'_q = -\frac{AB}{1 + BT'_{d0}s}\Delta\delta, \tag{5.53}$$

where A and B are constants that depend on the operating conditions (angle δ_0) and the generator and network reactances. If both the generator armature resistance and the network resistance are neglected then

$$A = \left(\frac{1-B}{B}\right) V_s \sin\delta_0 \quad \text{and} \quad B = (X'_d + X)/(X_d + X) = x'_d/x_d.$$

The time constant BT'_{d0} is often referred to as the *effective field winding time constant*.

If sinusoidal variations of $\Delta\delta$ are considered then the frequency response of Equation (5.53) can be obtained by setting $s = j\Omega$, where Ω is the frequency of the rotor swings (in rad/s) and $2\pi/\Omega$ is the swing period, as discussed later in this chapter (Equation (5.67)). This allows the phase of $\Delta E'_q$ to be compared with that of $\Delta\delta$. As T'_{d0} is typically much longer than the swing period and $T'_{d0} \gg 2\pi/\Omega$, it can be assumed that $BT'_{d0}\Omega > 1$ and

$$\Delta E'_q(j\Delta\omega) \cong -\frac{AB}{BT'_{d0}j\Omega}\Delta\delta(j\Omega) = j\frac{A}{T'_{d0}\Omega}\Delta\delta(j\Omega). \tag{5.54}$$

Thus, the changes $\Delta E'_q$ are seen to lead the changes $\Delta\delta$ by $\pi/2$, that is they are in phase with the rotor speed deviation $\Delta\omega = d\Delta\delta/dt$ thereby providing some additional positive damping torque.

Equation (5.54) also shows that the magnitude of the variation in $\Delta E'_q$ depends, via the coefficient $A = [(1 - B)/B]V_s \sin\delta_0$, on the power angle δ_0 at the linearization (operating) point. Thus the same

variation in δ will result in higher variations in $\Delta E'_q$ if the system is heavily loaded (higher value of δ_0) and the assumption of constant flux linkage ($E' = $ constant) is more accurate when the generator is lightly loaded (small δ_0) and the variations in $\Delta E'_q$ are small.

The effect of variations in the rotor flux linkages will be examined for two cases using the equal area method. In the first case the generator mechanical power $P_m < P_{E_q\,cr}$ while in the second case $P_m = P_{E_q\,cr}$. In both cases the effect of the damper winding will be neglected in the discussion in order to see more clearly the effect that the variation in rotor flux linkage has on the damping.

5.4.5.2 Equilibrium Point for $P_m < P_{E_q\,cr}$

Figure 5.13a shows how Figure 5.11 has to be modified to include the effect of the variation in rotor flux linkage. Again, only that part of the power–angle characteristic in the vicinity of the operating point is shown. As before, the disturbance causes the electrical power to move from point 1 to point 2 on the predisturbance transient $P_{E'_{q0}}(\delta)$ curve as the field winding acts initially like a perfect screen maintaining constant rotor flux linkages. As the rotor starts to decelerate, its speed drops so that the speed deviation $\Delta\omega$ becomes negative. The resistance of the field winding dissipates magnetic energy and the rotor linkages start to decay, reducing the value of transient emf E'_q as shown in Figure 5.13b. Consequently, the electrical power is less than would be the case with $E'_q = $ constant and the rotor motion is along the curve 2–6 rather than 2–1. The resulting deceleration area 2–4–6 is smaller than area 2–4–1 thereby reducing the kinetic energy that is responsible for providing the impetus for the backswing. As the rotor passes point 6 it starts to accelerate, the emf E'_q starts to recover and it reaches its predisturbance value when $\Delta\omega$ is zero at point 3 such that area 6–3–5 is equal to area 2–4–6. The rotor then continues to accelerate and swings back towards the equilibrium point. The speed deviation $\Delta\omega$ increases and E'_q continues to increase so modifying the dynamic characteristic which now lies above $P_{E'_{q0}}(\delta)$. This reduces the accelerating area and the kinetic energy, providing the impetus for the forward swing. The accelerating area is 3–5–7, the forward swing ends at point 8 and the whole cycle is repeated with a reduced amplitude of rotor swings.

Figure 5.13b shows that the E'_q variations are in phase with $\Delta\omega$ and lead the $\Delta\delta$ variations by $\pi/2$. Figure 5.13c illustrates the same effect using a phasor representation. All the increments of quantities shown in Figure 5.13c oscillate with the swing frequency Ω discussed later in this chapter (Equation (5.67)). Hence they can be shown on a phasor diagram in the same way as any sinusoidally changing quantities. Obviously the phasors shown rotate with the swing frequency Ω rather than 50 or 60 Hz as is the case for AC phasors. Strictly speaking, the phasors shown represent the phase and initial values of the quantities as their rms values decay with time. The synchronous

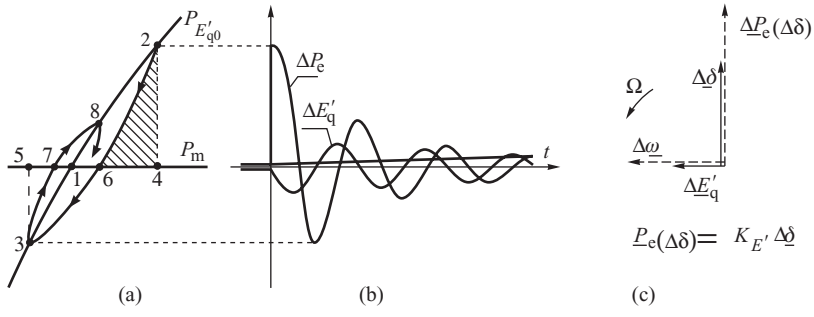

Figure 5.13 Including the effect of variation in rotor flux linkage: (a) trajectory of the operating point; (b) time variation of electrical power and transient emf oscillating with the swing frequency Ω; (c) rotating phasors of increments $\Delta\delta$, $\Delta E'_q$ and $\Delta\omega = d\delta/dt$.

power $\Delta \underline{P}_e$ is in phase with the rotor angle $\Delta \underline{\delta}$ while $\Delta \underline{E}'_q$ is in phase with the rotor speed deviation $\Delta \underline{\omega}$. Obviously $\Delta\omega$ is a derivative of $\Delta\delta$ and leads it by $\pi/2$. It should be emphasized that the changes in E'_q are very small, in the range of a small percentage.

Figure 5.13 shows that the field winding provides a similar damping action to the damper windings, but much weaker. The combined effect of the two damping mechanisms helps to return the rotor quickly to the equilibrium point. If the damping effect is large then the rotor motion may be aperiodic (without oscillations).

The constants A and B in Equations (5.53) and (5.54) were stated assuming that the effect of the network resistance could be neglected. A fuller analysis would show that A and B depend on the network resistance (Anderson and Fouad, 1977) and that at large values of this resistance A can change sign when, according to Equation (5.54), the term with $\Delta E'_q$ changes sign to negative (with respect to $\Delta\omega$) and negative damping is introduced to the system. This may happen when a generator operates in a medium-voltage distribution network (Venikov, 1978b) and such a case is illustrated in Figure 5.14. If $\Delta E'_q$ lags $\Delta\delta$ then during the backswing the rotor will move from point 2 along a characteristic, that is higher than the initial one, thereby performing deceleration work equal to the area 2–3–2′. This area is larger than if the rotor followed the initial characteristic 2–1 (cf. Figure 5.11. To balance this deceleration work the rotor must swing back to point 4 such that area 3–4–4′ is equal to area 2–3–2′. Consequently, the amplitude of the rotor swings increases and, if this negative damping is larger than the positive damping introduced by the damper windings, the generator may lose stability.

By analysing rotor swings similar to those shown in Figures 5.13 and 5.14 it can be shown that the positive damping due to the flux linkage variation described above can only take place when the slope of the transient characteristic is steeper than the slope of the steady-state characteristic, $K_{E'} > K_{E_q}$ (Machowski and Bernas, 1989). Consequently the steady-state stability condition defined in Equation (5.33) must be modified to take into account the rotor dynamics as

$$K_{E_q} = \frac{\partial P_{E_q}}{\partial \delta} > 0 \quad \text{and} \quad K_{E'} = \frac{\partial P_{E'}}{\partial \delta} > K_{E_q}. \tag{5.55}$$

Another type of disturbance, consisting of a small increase in the mechanical power to $(P_m + \Delta P_m)$, is shown in Figure 5.15. Again the characteristics are shown only in the vicinity of the equilibrium point. Initially the system operates at point 1, the intersection between the characteristics P_m, P_{E_q} and $P_{E'_{q0}}$. The increased mechanical loading produces a new, final equilibrium point ∞. The final value of the transient emf $E'_{q\infty}$ is smaller than the initial value E'_{q0} as indicated in Figure 5.10. Consequently E'_q must reduce as the rotor moves from point 1 towards point ∞. This means that the rotor oscillations will be similar to those shown in Figure 5.13, but occurring

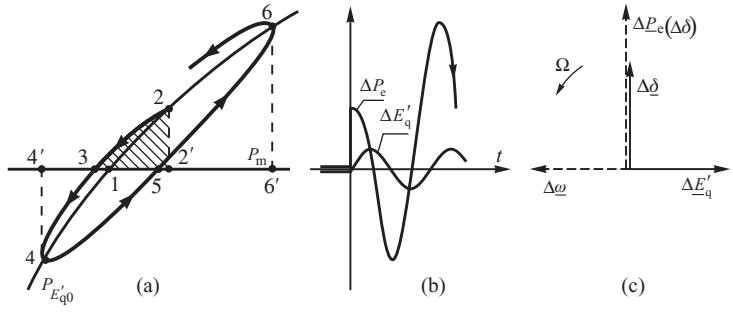

Figure 5.14 Negative damping: (a) trajectory of the operating point; (b) time variation of electrical power and transient emf; (c) relative position of phasors of oscillating increments.

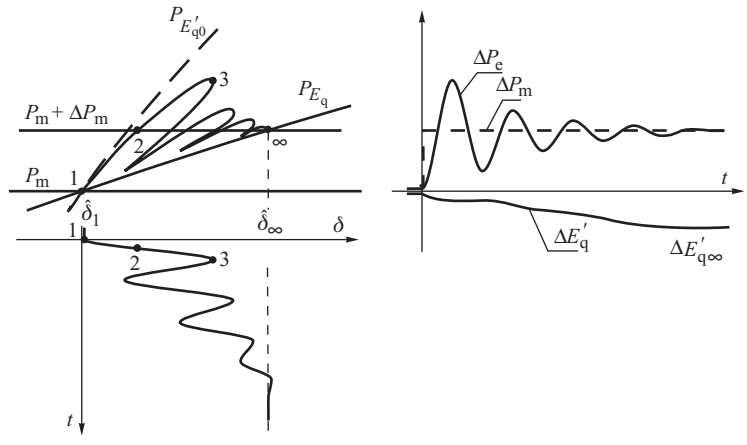

Figure 5.15 Rotor and power swings due to a disturbance in mechanical power.

along a series of dynamic characteristics of decreasing amplitude, all of them lying below the initial characteristic $P_{E'_{q0}}$. Small oscillations of E'_q around its average decaying value cause some damping similar to that shown in Figure 5.13. This damping again adds to the main damping coming from the damper windings.

5.4.5.3 Equilibrium Point at $P_m = P_{E_q\,cr}$

If $P_m = P_{E_q\,cr}$ then there is only one steady-state equilibrium point. As shown in Figure 5.10a, the transient characteristic $P_{E'_q}(\delta)$ crossing point (δ_{cr}, $P_{E_q\,cr}$) has a positive slope and a momentary disturbance in the angle δ will produce oscillations around the equilibrium point that are damped by the damper and field windings. Although this would suggest stable operation, the system is in practice unstable as will be explained below.

Any generator will be subjected to minor disturbances resulting from vibrations, slight changes in supplied power, switching in the network and so on. When the system operates at $P_m = P_{E_q\,cr}$ any such disturbance may cause a relative shift between the P_m and $P_{E_q}(\delta)$ characteristics. This is shown in Figure 5.16 where it is assumed that P_m is increased by ΔP_m such that the new mechanical ($P_m + \Delta P_m$) characteristic lies above $P_{E_q}(\delta)$. Initially, as the transient $P_{E'_q}(\delta)$ characteristic has a positive slope, the rotor starts to oscillate around ($P_m + \Delta P_m$) in a similar way to that shown in Figure 5.15. Gradually the armature flux penetrates the field winding, the emf E'_q decays and the rotor follows the $P_{E'_q}(\delta)$ characteristics of declining amplitude. Eventually the decay in E'_q is such that the $P_{E'_q}(\delta)$ curve lies below the new mechanical ($P_m + \Delta P_m$) characteristic and the generator loses synchronism. The behaviour of the generator during asynchronous operation will be described in Section 6.5.

The oscillatory loss of stability shown in Figure 5.16 takes place when the influence of the damper windings is neglected. In practice, damping at high loading can be significant when the loss of stability may occur in an aperiodic way for the reasons discussed in the next subsection.

5.4.6 Analysis of Rotor Swings Around the Equilibrium Point

In this subsection a quantitative analysis of rotor dynamics around the equilibrium point will be attempted. Assuming the constant flux linkage generator model with constant E', the incremental

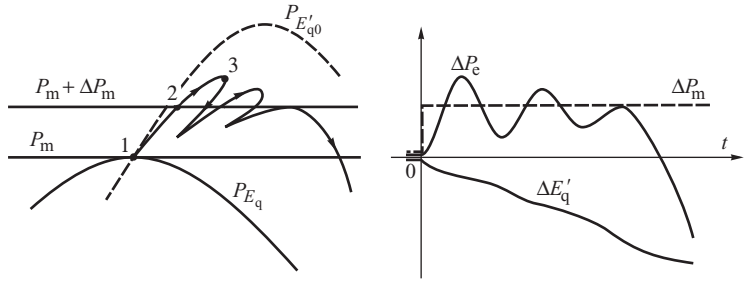

Figure 5.16 Rotor, power and transient emf oscillations after a small increase in P_m at the critical equilibrium point.

swing equation, Equation (5.51), becomes

$$M\frac{d^2\Delta\delta}{dt^2} + D\frac{d\Delta\delta}{dt} + K_{E'}\,\Delta\delta = 0, \tag{5.56}$$

with the initial disturbed conditions being

$$\Delta\delta(t = 0^+) = \Delta\delta_0 \neq 0 \quad \text{and} \quad \Delta\omega = \Delta\dot{\delta}(t = 0^+) = 0. \tag{5.57}$$

Equation (5.56) is a second-order linear differential equation. As shown in Appendix A.3 the solution of a linear differential equation of any order is of the form: $\Delta\delta(t) = e^{\lambda t}$. For the solution of that form one gets

$$\Delta\delta = e^{\lambda t}, \quad \frac{d\Delta\delta}{dt} = \lambda e^{\lambda t}, \quad \frac{d^2\Delta\delta}{dt^2} = \lambda^2 e^{\lambda t}. \tag{5.58}$$

Substituting this equation into Equation (5.56) and dividing by the nonzero term $e^{\lambda t}$ gives the following algebraic equation:

$$\lambda^2 + \frac{D}{M}\lambda + \frac{K_{E'}}{M} = 0. \tag{5.59}$$

This *characteristic equation* describes values of λ for which the assumed function $\Delta\delta = e^{\lambda t}$ constitutes the solution of the differential equation (5.56). The values of λ that solve the characteristic equation are referred to as the *roots* of the characteristic equation.

The characteristic equation (5.59) has two roots λ_1 and λ_2 given by

$$\lambda_{1,2} = -\frac{D}{2M} \pm \sqrt{\left(\frac{D}{2M}\right)^2 - \frac{K_{E'}}{M}}. \tag{5.60}$$

Three cases are now possible (see Appendix A.3):

(i) The roots are real and distinct and the solution is of the form $\Delta\delta\,(t) = A_1 e^{\lambda_1 t} + A_2 e^{\lambda_2 t}$, where A_1 and A_2 are the integration constants. This case is described in detail in Example A3.2 discussed in Appendix A.3. Substitution of the initial conditions defined in Equation (5.57) gives the aperiodic response

$$\Delta\delta(t) = \frac{\Delta\delta_0}{\lambda_2 - \lambda_1}\left[\lambda_2 e^{\lambda_1 t} - \lambda_1 e^{\lambda_2 t}\right], \tag{5.61}$$

where $-1/\lambda_1$ and $-1/\lambda_2$ are time constants.

(ii) The roots are real and equal, $\lambda_1 = \lambda_2 = \lambda$, and the solution is of the form $\Delta\delta(t) = e^{\lambda t}(A_1 + A_2 t)$. This case is described in detail in Example A.3.3 discussed in Appendix A.3. Substitution of the initial conditions in Equation (5.57) gives the aperiodic response

$$\Delta\delta(t) = \Delta\delta_0 e^{\lambda t}(1 - \lambda t), \tag{5.62}$$

where $-1/\lambda$ is the time constant.

(iii) The roots form a complex conjugate pair

$$\lambda_{1,2} = -\frac{D}{2M} \pm j\sqrt{\frac{K_{E'}}{M} - \left(\frac{D}{2M}\right)^2}. \tag{5.63}$$

Denoting

$$\alpha = -\frac{D}{2M}, \quad \Omega = \sqrt{\frac{K_{E'}}{M} - \left(\frac{D}{2M}\right)^2}, \tag{5.64}$$

one gets $\lambda_{1,2} = \alpha \pm j\Omega$ where Ω is the frequency of oscillations (in rad/s) while α is the damping coefficient. The coefficient

$$\zeta = \frac{-\alpha}{\sqrt{\alpha^2 + \Omega^2}}, \tag{5.65}$$

is referred to as the *damping ratio*. This notation allows Equation (5.56) to be rewritten as the standard second-order differential equation

$$\frac{d^2\Delta\delta}{dt^2} + 2\zeta\Omega_{nat}\frac{d\Delta\delta}{dt} + \Omega_{nat}^2\Delta\delta = 0, \tag{5.66}$$

with the roots

$$\lambda_{1,2} = -\zeta\Omega_{nat} \pm j\Omega, \tag{5.67}$$

where Ω_{nat} is the *undamped natural frequency* (in rad/s) of rotor swings for small oscillations, ζ is the damping ratio and $\Omega = \Omega_{nat}\sqrt{1 - \zeta^2}$ where Ω is now referred to as the *damped natural frequency* (in rad/s) of rotor swings. This case is described in detail in Example A3.4 and Example A3.5 discussed in Appendix A.3. Comparing Equation (5.66) with Equation (5.56) gives $\Omega_{nat} = \sqrt{K_{E'}/M}$ and $\zeta = D/2\sqrt{K_{E'}M}$. The solution for $\Delta\delta(t)$ is now given by

$$\Delta\delta(t) = \frac{\Delta\delta_0}{\sqrt{1 - \zeta^2}} e^{-\zeta\Omega_{nat}t}\cos[\Omega t - \phi], \tag{5.68}$$

where $\phi = \arcsin\zeta$.

The damping ratio ζ determines the amount of damping present in the system response expressing how quickly the amplitude of rotor swings decreases during subsequent periods. Let us express time as the multiplier of periods $t = 2\pi N/\omega_{nat}$ where N is the number of oscillation periods. Then Equation (5.68) gives

$$k_N = \frac{\Delta\delta(N)}{\Delta\delta_0} = \frac{e^{-2\pi N\zeta}}{\sqrt{1 - \zeta^2}}, \tag{5.69}$$

where $\Delta\delta(N)$ denotes the amplitude of oscillations after N periods. For a practical assessment of damping, it is convenient to analyse $N = 5$ periods. A plot of the function given by (5.69) for

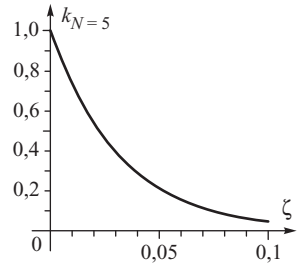

Figure 5.17 Amplitude $\Delta\delta/\Delta\delta_0$ as a function of the damping ratio ζ after $N = 5$ periods.

$N = 5$ is shown in Figure 5.17. For example, the amplitude decreases after $N = 5$ periods to 39% for $\zeta = 0.03$, to 21% for $\zeta = 0.05$ and to 4% for $\zeta = 0.10$.

In practice, damping of rotor swings is considered to be satisfactory if the damping ratio $\zeta = 0.05$.

As the values of the roots $\lambda_{1,2}$ depends on the actual values of $K_{E'}$, D and M, so too does the type of response. The inertia coefficient M is constant while both D and $K_{E'}$ depend on the generator loading. Figure 5.3 shows that the damping coefficient D increases with load and Figure 5.10b shows that the transient synchronizing power coefficient $K_{E'}$ decreases with load.

Equation (5.60) shows that if $K_{E'} > 0$ then, depending on the actual values of $K_{E'}$ and D, the roots of the characteristic equation can be either real or complex. For small initial values of power angle $\hat{\delta}_s$ the damping coefficient is small, while the transient synchronizing power coefficient $K_{E'}$ is large so that $(K_{E'}/M) > (D/2M)^2$ and the two roots form a complex conjugate pair. In this case the solution of the differential equation is given by Equation (5.68). The system response is oscillatory with the amplitude of rotor oscillations decaying with time as shown schematically in the inset near point A in Figure 5.18. The frequency of oscillations is Ω and is slightly smaller than the undamped natural frequency Ω_{nat}.

As the initial value of the power angle $\hat{\delta}_s$ increases, the synchronizing power coefficient $K_{E'}$ decreases while damping increases. Consequently Ω_{nat} decreases but the damping ratio ζ increases with the result that the rotor oscillations become slower and more heavily damped as shown in the inset near point B in Figure 5.18. At some point, when $(K_{E'}/M) = (D/2M)^2$, the damping ratio ζ is unity and the oscillations are said to be *critically damped*. In this case the roots are real and equal, $\lambda_1 = \lambda_2 = -\Omega_{nat}$, giving the aperiodic response expressed by Equation (5.62) and shown in the inset near point C in Figure 5.18.

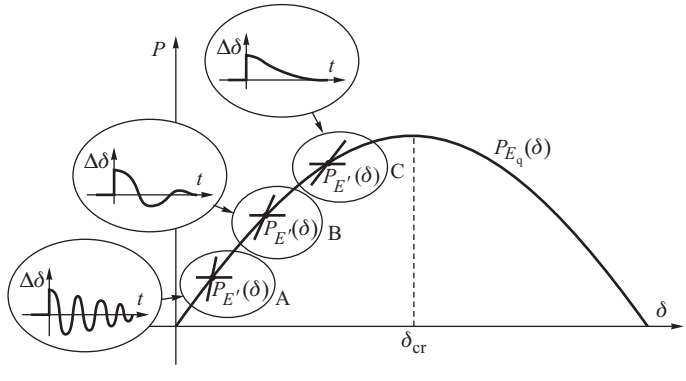

Figure 5.18 Examples of rotor swings for different stable equilibrium points.

As the initial power angle $\hat{\delta}_s$ is further increased, at some point it holds that $(K_{E'}/M) < (D/2M)^2$, the two roots are real and negative, and the rotor swings are expressed by Equation (5.61). In this case the damping ratio $\zeta > 1$, the rotor swings are overdamped, and the response is sluggish and vanishes aperiodically with time. Typically this condition may occur when the initial operating point is near the peak of the steady-state characteristic in Figure 5.18.

When the power angle $\hat{\delta}_s$ is equal to its critical value δ_{cr}, it is not possible to analyse the system dynamics using the constant flux linkage model ($E' = \text{constant}$) because the effect of flux decrement must be included. This was explained in Figure 5.16.

Chapter 12 will consider a similar problem but in a multi-machine system. The differential equations will then be represented in the matrix form $\dot{\mathbf{x}} = \mathbf{A}\mathbf{x}$, where $\boldsymbol{x}$ is the state vector and $\boldsymbol{A}$ is the state matrix. Using the matrix form, Equation (5.56) would become

$$\begin{bmatrix} \Delta\dot{\delta} \\ \hline \Delta\dot{\omega} \end{bmatrix} = \left[\begin{array}{c|c} 0 & 1 \\ \hline -\dfrac{K_{E'}}{M} & -\dfrac{D}{M} \end{array}\right] \begin{bmatrix} \Delta\delta \\ \hline \Delta\omega \end{bmatrix}. \tag{5.70}$$

The eigenvalues of this state matrix can be determined from solving

$$\det \left[\begin{array}{c|c} -\lambda & 1 \\ \hline -\dfrac{K_{E'}}{M} & -\lambda - \dfrac{D}{M} \end{array}\right] = \lambda^2 + \frac{D}{M}\lambda + \frac{K_{E'}}{M} = 0. \tag{5.71}$$

Clearly this equation is identical to Equation (5.59). Hence the roots of the characteristic equation (5.59) of the differential equation (5.56) are equal to the eigenvalues of the state matrix of the state equation 5.70.

5.4.7 *Mechanical Analogues of the Generator–Infinite Busbar System*

Further insight into the generator response to a small disturbance can be obtained by comparing the generator–infinite busbar system with the standard mass/spring/damper system shown in Figure 5.19a described by the equation

$$m\frac{\mathrm{d}^2\Delta x}{\mathrm{d}t^2} + c\frac{\mathrm{d}\Delta x}{\mathrm{d}t} + k\Delta x = 0. \tag{5.72}$$

Comparing this equation with Equation (5.56) suggests that the generator–infinite busbar system can be treated as an 'electromagnetic spring' where any increase in the spring extension Δx is

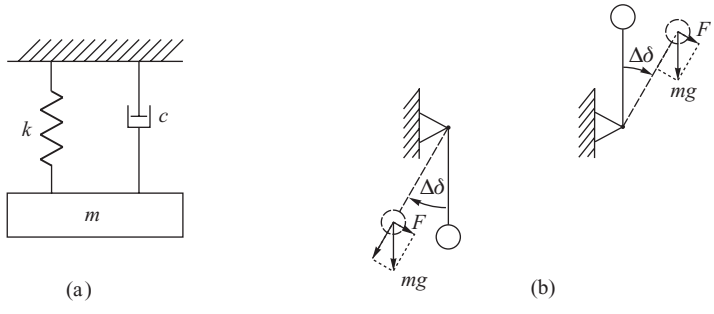

Figure 5.19 Mechanical analogues of the generator–infinite busbar system: (a) mass/spring/damper system; (b) a pendulum at stable and unstable equilibrium points.

equivalent to an increase in the rotor angle $\Delta\delta$. In this analogous system the mass m is equivalent to the inertia coefficient M, the spring damping coefficient c is equivalent to the generator damping coefficient D and the spring stiffness k is equivalent to the synchronizing power coefficient $K_{E'}$. This analogy allows the generator response, as expressed by Equations (5.61)–(5.68), to be directly related to the response of the standard mass/spring/damper system. Unlike the mechanical spring, the 'electromagnetic spring' is nonlinear because $K_{E'}$ depends strongly on the initial value of the power angle $\hat{\delta}_s$ (Figure 5.10b).

Another useful mechanical analogue is that of the pendulum of mass m and length l shown in Figure 5.19b. The pendulum has an upper and lower equilibrium point as shown where the weight of the ball is counterbalanced by the arm. When the pendulum is disturbed from its equilibrium position, a force equal to $F = -mg \sin\delta$ is developed and, neglecting damping, the motion of the pendulum is described by the differential equation

$$m\frac{d^2\delta}{dt^2} = -\frac{mg}{l}\sin\delta. \tag{5.73}$$

Near the lower (stable) equilibrium point the force F always acts towards the equilibrium point so that the pendulum oscillates around the equilibrium point. Near the upper (unstable) equilibrium point the force F pushes the pendulum away from the equilibrium point causing instability. The behaviour of the pendulum at these two equilibrium points can be directly compared with the behaviour of a generator at the stable and unstable equilibrium points shown in Figure 5.6.

The pendulum can also provide a useful analogue when analysing the generator dynamics. In this case Equation (5.73) has to be compared with the classical generator model in Equation (5.42). Again, both equation are of identical form.

5.5 Steady-State Stability of the Regulated System

The previous section considered the power–angle characteristics of a simple generator–infinite busbar system and the resulting steady-state, or small-signal, stability conditions when the excitation voltage (and therefore the excitation emf E_f) were assumed to be constant. This section considers steady-state stability when the action of an AVR is included. The influence of the AVR will be considered in three stages. Firstly, the modified steady-state power–angle characteristic will be derived. Secondly, the possibility of operation beyond the critical point (as defined by the pull-out power) will be discussed and finally the influence of the AVR on rotor swings will be analysed.

5.5.1 Steady-State Power–Angle Characteristic of Regulated Generator

The static $P_{E_q}(\delta)$ power–angle characteristic, Equation (5.29), was derived assuming that in steady state the excitation emf $E_f = E_q =$ constant. In practice every generator is equipped with an AVR which tries to maintain the voltage at the generator terminals constant (or at some point behind the terminals) by adjusting the value of the excitation voltage and, consequently, E_f. As the resulting formulae for the active and reactive power are more complicated than when $E_f =$ constant, the following discussion will be restricted to the case of a round-rotor generator ($x_d = x_q$) with resistance neglected ($r = 0$). For this case the steady-state equivalent circuit and phasor diagram are shown in Figure 5.20. The formulae for the active and reactive power will be derived by resolving the voltages and currents along the a- and b-axes, where the a-axis is located along the system voltage V_s.

The coordinates of $\underline{E}_q$ in the (a, b) reference frame are

$$E_{qa} = E_q \cos\delta, \quad E_{qb} = E_q \sin\delta. \tag{5.74}$$

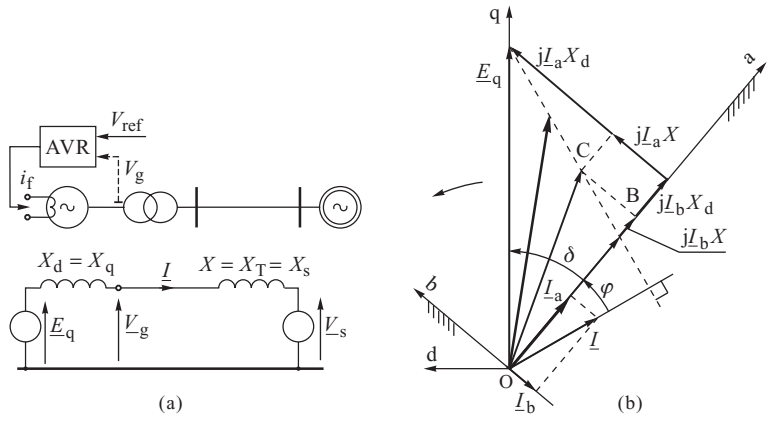

Figure 5.20 Generator operating on the infinite busbars: (a) schematic and equivalent circuit; (b) phasor diagram in the (d, q) and (a, b) reference frames.

Inspection of the phasor diagram gives

$$I_a = \frac{E_{qb}}{X_d + X}, \quad I_b = \frac{E_{qa} - V_s}{X_d + X}, \tag{5.75}$$

while the coordinates of the current are $I_a = I\cos\varphi$ and $I_b = -I\sin\varphi$. Pythagoras's theorem applied to the triangle OBC yields $(V_s + I_b X)^2 + (I_a X)^2 = V_g^2$, which, after taking into account Equation (5.75), gives

$$\left(E_{qa} + \frac{X_d}{X} V_s\right)^2 + E_{qb}^2 = \left[\frac{X_d + X}{X} V_g\right]^2. \tag{5.76}$$

This equation describes a circle of radius $\rho = (X_d/X + 1)\, V_g$ with centre lying on the a-axis at a distance $A = -X_d V_s/X$ from the origin. This means that with V_g = constant and V_s = constant, the tip of E_q moves on this circle. Figure 5.21 shows the circular locus centred on the origin made by the phasor V_g = constant, and another circular locus (shifted to the left) made by phasor E_q.

The circle defined by Equation (5.76) can be transformed into polar coordinates by substituting Equation (5.74) to give

$$E_q^2 + 2\frac{X_d}{X} E_q V_s \cos\delta + \left(\frac{X_d}{X} V_s\right)^2 = \left[\frac{X_d + X}{X} V_g\right]^2. \tag{5.77}$$

One of the roots of this equation is

$$E_q = \sqrt{\left(\frac{X_d + X}{X} V_g\right)^2 - \left(\frac{X_d}{X} V_s \sin\delta\right)^2} - \frac{X_d}{X} V_s \cos\delta, \tag{5.78}$$

which corresponds to the $E_f = E_q$ points that lie on the upper part of the circle. Substituting Equation (5.78) into the round-rotor power–angle equation, Equation (5.32), gives the generated

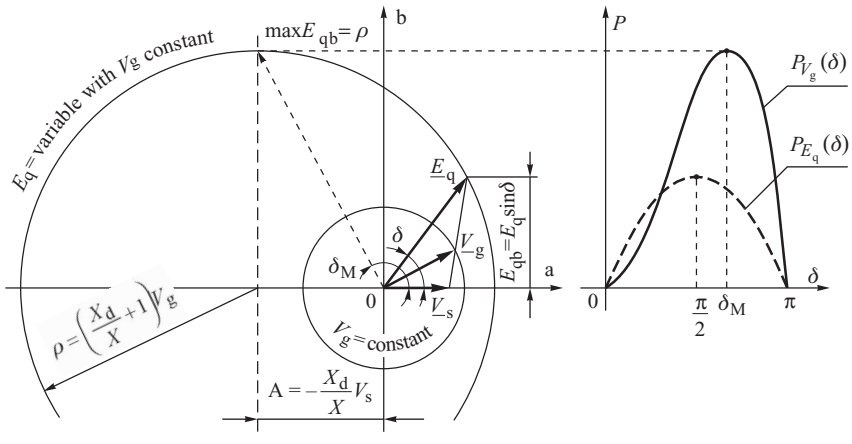

Figure 5.21 The circle diagrams and the power–angle characteristics for the round-rotor generator operating on the infinite busbars.

power as

$$P_{V_g}(\delta) = \frac{V_s}{X_d + X} \sin\delta \sqrt{\left(\frac{X_d + X}{X} V_g\right)^2 - \left(\frac{X_d}{X} V_s \sin\delta\right)^2} - \frac{1}{2} \frac{X_d}{X} \frac{V_s^2}{X_d + X} \sin 2\delta. \tag{5.79}$$

Equation (5.79) describes the power–angle characteristic $P_{V_g}(\delta)$ with $V_g = \text{constant}$ and is shown, together with $P_{E_q}(\delta)$, in Figure 5.21. Comparing the two shows that the AVR can significantly increase the amplitude of the steady-state power–angle characteristic.

The maximum value of the power given by Equation (5.79) can be easily found by examining Figure 5.21. Substituting the second of the equations in (5.74) into Equation (5.32) gives

$$P_{V_g}(\delta) = \frac{V_s}{X_d + X} E_{qb}, \tag{5.80}$$

indicating that the generator power is proportional to the projection of E_q on the b-axis. The function defined by Equation (5.80) reaches its maximum value when E_{qb} is a maximum. As can be seen from Figure 5.21, this occurs at the point on the E_q locus that corresponds to the centre of the circle. At this point E_q has the following coordinates:

$$E_{qb} = \rho = \left(\frac{X_d}{X} + 1\right) V_g \quad \text{at} \quad \delta_M = \arctan\left(\frac{\rho}{A}\right) = \arctan\left(-\frac{X_d + X}{X_d} \frac{V_g}{V_s}\right). \tag{5.81}$$

The angle δ_M at which $P_{V_g}(\delta)$ reaches maximum is always greater than $\pi/2$ irrespective of the voltages V_g and V_s. This is typical of systems with active AVRs. Substituting the first of the equations in (5.81) into (5.80) gives

$$P_{V_g M} = P_{V_g}(\delta)\big|_{\delta=\delta_M} = \frac{V_g V_s}{X}, \tag{5.82}$$

showing that the amplitude of the power–angle characteristic of the regulated system is independent of the generator reactance. It does, however, depend on the equivalent reactance of the transmission system. The steady-state synchronizing power coefficient of the regulated system is $K_{V_g} = \partial P_{V_g}(\delta)/\partial\delta$ and $K_{V_g} > 0$ when $\delta < \delta_M$.

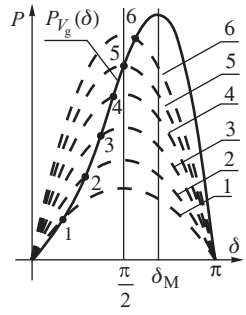

Figure 5.22 Creation of the $P_{V_g}(\delta)$ characteristic from a family of $P_{E_q}(\delta)$ characteristics.

5.5.1.1 Physical Interpretation

The sin 2δ component in Equation (5.79) has negative sign, making the maximum of the $P_{V_g}(\delta)$ characteristic shown in Figure 5.21 occur at $\delta_M > \pi/2$. For small rotor angles $\delta \ll \pi/2$ the characteristic is concave, while for $\delta > \pi/2$ the characteristic is very steep. The sin 2δ component has nothing to do with the reluctance power (as was the case with $P_{E_q}(\delta)$) because Equation (5.79) has been derived assuming $x_d = x_q$. The distortion of the characteristic is entirely due to the influence of the AVR.

Physically the shape of the $P_{V_g}(\delta)$ characteristic can be explained using Figure 5.22. Assume that initially the generator operates at point 1 corresponding to the characteristic $P_{E_{q1}} = P_{E_q}(\delta)\big|_{E_q = E_{q1}}$ shown by the dashed curve 1. An increase in the generator load causes an increase in the armature current, an increased voltage drop in the equivalent network reactance X, Figure 5.20, and therefore a decrease in the generator voltage V_g. The resulting voltage error forces the AVR to increase the excitation voltage so that E_q is increased to a value $E_{q2} > E_{q1}$ and a new operating point is established on a higher characteristic $P_{E_{q2}} = P_{E_q}(\delta)\big|_{E_q = E_{q2}}$ denoted by 2. Subsequent increases in load will cause the resulting $P_{V_g}(\delta)$ characteristic to cross at the points 2, 3, 4, 5 and 6 lying on consecutive $P_{E_q}(\delta)$ characteristics of increased amplitude. Note that starting from point 5 (for $\delta > \pi/2$) the synchronizing power coefficient $K_{E_q} = \partial P_{E_q}(\delta)/\partial\delta$ is negative while $K_{V_g} = \partial P_{V_g}(\delta)/\partial\delta$ is still positive.

5.5.1.2 Stability

If the AVR is very slow acting (i.e. it has a large time constant) then it may be assumed that following a small disturbance the AVR will not react during the transient state and the regulated and unregulated systems will behave in a similar manner. The stability limit then corresponds to point 5 when $\delta = \pi/2$ (for a round-rotor generator) and the stability condition is given by Equation (5.33). If the AVR is fast acting so that it is able to react during the transient state, then the stability limit can be moved beyond $\delta = \pi/2$ to a point lying below the top of the $P_{V_g}(\delta)$ curve. In this case stability depends on the parameters of the system and the AVR, and the system stability is referred to as *conditional stability*.

A fast-acting AVR may also reverse the situation when the stability limit is lowered (with respect to the unregulated system) to a point $\delta < \pi/2$, for example to point 4, or even 3, in Figure 5.22. In this situation the system may lose stability in an oscillatory manner because of the detrimental effect of the AVR. Such a situation, and the conditional stability condition, will be discussed later in this section.

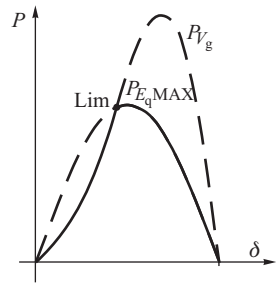

Figure 5.23 Example of the influence of the field current limiter on the steady-state power–angle characteristic.

5.5.1.3 Effect of the Field Current Limiter

Equation (5.79) was derived, and Figure 5.21 drawn, under the assumption that the AVR may change $E_q = E_f$ in order to keep the terminal voltage constant without any limit being placed on the maximum value of $E_q = E_f$. In practice the AVR is equipped with various limiters, described in Chapter 2, one of which limits the field current and hence E_f. This limiter operates with a long time delay. If the exciter reaches the maximum field current value during slow changes in operating conditions, then any further increase in the load will not increase the field current despite a drop in the terminal voltage V_g. Any further changes will take place at $E_q = E_{fMAX} = \text{constant}$ and the operating point will follow a $P_{E_q}(\delta)\big|_{E_q = E_{qMAX}}$ characteristic.

Whether or not the field current limiter will act before the top of the $P_{V_g}(\delta)$ characteristic is reached depends not only on the field current limit set, but also on the equivalent network reactance X. Equation (5.82) shows that the amplitude of the $P_{V_g}(\delta)$ characteristic depends on the reactance X. If X is large then the amplitude is small and the field current limit may not be reached. If X is small then the amplitude is very large and the field current limit is encountered before the peak of the characteristic is reached. Such a situation is illustrated in Figure 5.23. The limit is reached at point Lim. Below this point the steady-state characteristic is $P_{V_g}(\delta)$, while above this point the generator follows the $P_{E_q}(\delta)\big|_{E_q = E_{qMAX}}$ curve. The resulting characteristic is shown in bold.

From the stability point of view a more interesting case is when the field current limit is not reached. However, it is important to remember that the thermal field current limit may be reached before the stability limit.

5.5.2 Transient Power–Angle Characteristic of the Regulated Generator

If the AVR or the exciter has a large time constant then the regulation process is slow and the rotor swings follow the transient power–angle characteristic as discussed in Section 5.4. The transient characteristics of both the regulated and unregulated system are the same, the only difference being that the increased loading in the regulated system will cause an increase in the steady-state field current and therefore a higher value of E'_q and the amplitude of the $P_{E'}(\delta')$ characteristic. Moreover, the angle δ' will reach the critical value $\pi/2$ before δ reaches its critical value δ_M. This is illustrated in Figure 5.24 which is a repetition of a fragment of the phasor diagram in Figure 5.21.

For the critical angle $\delta = \delta_M$ the phasor of $\underline{V}_g$ lies on the vertical axis, Figure 5.24a, and $\delta' > \pi/2$ because the emf $\underline{E}'$ leads $\underline{V}_g$. This means that at the critical point δ_M the transient synchronizing power coefficient $K_{E'} = \partial P_{E'}/\partial\delta$ is negative. When $\delta' = \pi/2$, Figure 5.24b, the emf $\underline{E}'$ lies on the vertical axis and $\delta < \delta_M$. The question now arises: at which point on the $P_{V_g}(\delta)$ curve does the transient synchronizing power coefficient become zero?

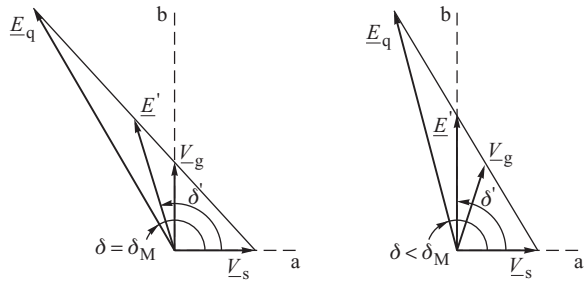

Figure 5.24 Phasor diagram of the regulated system with (a) $\delta = \delta_M$ and (b) $\delta' = \pi/2$.

This question is most easily answered if the classical generator model is used with transient saliency neglected. The following equation, similar to Equation (5.76), can be obtained for the transient emf when the phasor diagram of Figure 5.20b is used:

$$\left(E'_a + \frac{X'_d}{X} V_s\right)^2 + E'^2_b = \left[\frac{X'_d + X}{X} V_g\right]^2. \tag{5.83}$$

This equation describes a circle on which the tip of $\underline{E}'$ moves when the power angle and excitation are increased. This circle is similar to the circle shown in Figure 5.21 but has a radius and horizontal shift dependent on X'_d. Substituting $E'_a = E' \cos\delta'$ and $E'_b = E' \sin\delta'$ into Equation (5.83) gives

$$E'^2 + 2\frac{X'_d}{X} E' V_s \cos\delta' + \left(\frac{X'_d}{X} V_s\right)^2 = \left[\frac{X'_d + X}{X} V_g\right]^2. \tag{5.84}$$

Solving this equation with respect to E' yields

$$E' = \sqrt{\left(\frac{X'_d + X}{X} V_g\right)^2 - \left(\frac{X'_d}{X} V_s \sin\delta\right)^2} - \frac{X'_d}{X} V_s \cos\delta. \tag{5.85}$$

For $\delta' = \pi/2$ the second component in this equation is zero and the transient emf is

$$E'\big|_{\delta'=\pi/2} = \frac{V_g}{X}\sqrt{(X'_d + X)^2 - \left(X'_d \frac{V_s}{V_g}\right)^2}. \tag{5.86}$$

Substituting this value in Equation (5.40) and noting that $x'_d = X'_d + X$ gives

$$P_{V_g\,cr} = P_{V_g}(\delta')\big|_{\delta'=\pi/2} = \frac{V_s V_g}{X}\sqrt{1 - \left(\frac{X'_d}{X'_d + X}\right)^2 \left(\frac{V_s}{V_g}\right)^2}. \tag{5.87}$$

According to Equation (5.82), the factor $V_s V_g / X$ in this equation corresponds to the amplitude of the $P_{V_g}(\delta)$ curve. This means that the ratio of power at which $K_{E'} = 0$ to the power at which $K_{V_g} = 0$ corresponds to the square-root expression in Equation (5.87) and is equal to

$$\alpha = \frac{P_{V_g}(\delta' = \pi/2)}{P_{V_g}(\delta = \delta_M)} = \frac{P_{V_g\,cr}}{P_{V_g\,M}} = \sqrt{1 - \left(\frac{X'_d}{X'_d + X}\right)^2 \left(\frac{V_s}{V_g}\right)^2}. \tag{5.88}$$

This coefficient depends strongly on the equivalent network reactance X. If X is large then α is close to unity and the transient synchronizing power coefficient $K_{E'} = 0$. This takes place at a point close

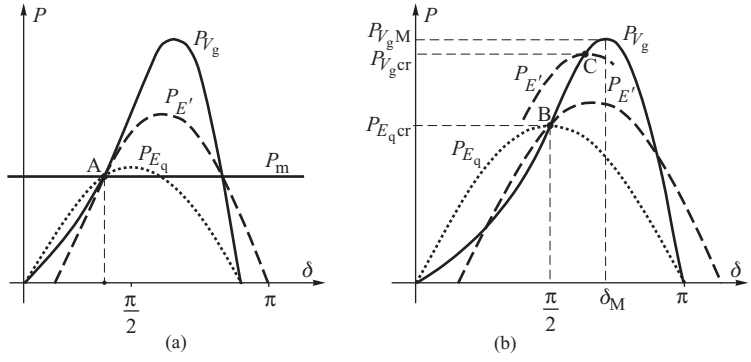

Figure 5.25 Power–angle characteristics of the regulated generator: (a) all synchronizing power coefficients are positive; (b) points above the limit of natural stability ($\delta = \pi/2$).

to the peak of $P_{V_g}(\delta)$ at which point $K_{V_g} = 0$. On the other hand, if X is small then $K_{E'}$ reaches zero at a point lying well below the peak of $P_{V_g}(\delta)$. This is illustrated in Figure 5.25.

Figure 5.25a shows the case when the power angle is small, all the characteristics have positive slope and all the synchronizing power coefficients are positive. Figure 5.25b shows two operating points. The lower point corresponds to the natural stability limit ($\delta = \pi/2$) when $K_{E_q} = 0$ but $K_{E'} > 0$. Further increasing the load (and the power angle) causes $K_{E_q} < 0$, while $K_{E'} > 0$ until the top point is reached where the $P_{E'}(\delta')$ curve, shown as a dashed line, intersects at its peak $P_{V_g}(\delta)$. Above this point $K_{E'}$ becomes negative despite $K_{V_g} > 0$. The ratio of both peaks is given by the coefficient α defined in Equation (5.88).

5.5.2.1 Stability

After a disturbance the rotor swings follow the transient power–angle characteristic $P_{E'}(\delta')$. The system is unstable above the point $P_{V_g\,cr}$ where $K_{E'} = \partial P_{E'}/\partial\delta < 0$ and no deceleration area is available. Therefore the necessary stability condition is

$$K_{E'} = \frac{\partial P_{E'}}{\partial \delta} > 0. \tag{5.89}$$

At the point $P_{V_g\,cr}$ any small increase in the mechanical power will cause asynchronous operation because the mechanical power is greater than the electrical power. Whether or not the generator can operate on the $P_{V_g}(\delta)$ characteristic below this point, that is when $P_m < P_{V_g\,cr}$, depends on the generator, network and AVR parameters. Two factors are decisive: (i) the influence that the regulator has on the variations in E'_q due to changes in the excitation flux linkage during rotor swings; and (ii) the influence that the regulator has on damping torques due to additional currents induced in the damper windings.

5.5.3 Effect of Rotor Flux Linkage Variation

The influence of changes in the excitation emf E_f on the transient emf E' is given by Equation (4.28). For the salient-pole machine when $E' = E'_q$ this equation can be rewritten as

$$\Delta E'_q = \Delta E'_{q\{\Delta\delta\}} + \Delta E'_{q(\Delta E_f)}, \tag{5.90}$$

where

$$\Delta E'_{q(\Delta\delta)} = -\frac{AB}{1+BT'_{d0}s}\Delta\delta, \quad \Delta E'_{q(\Delta E_f)} = +\frac{B}{1+BT'_{d0}s}\Delta E_f, \tag{5.91}$$

and $\Delta\delta = \Delta\delta'$. These two components are due to the rotor swings and voltage regulation, respectively. The influence of $\Delta E'_{q(\Delta\delta)}$ was described in Section 5.4.5 following Equation (5.53) where it was shown in Figure 5.13 that this component is in phase with the speed deviation $\Delta\omega$ and introduces an additional damping torque in Equation (5.52). A question arises as to what influence the voltage control component $\Delta E'_{q(\Delta E_f)}$ has on the problem. To answer this question it is necessary to determine the phase shift of $\Delta E'_{q(\Delta E_f)}$ with respect to $\Delta\omega$ (or $\Delta\delta$). This problem can be better understood with the help of Figure 5.26 which shows how a change in the rotor angle influences $\Delta E'_{q(\Delta E_f)}$.

The first block reflects the fact that (assuming constant infinite busbar voltage) a change in $\Delta\delta$ causes a voltage regulation error ΔV. The second block is the transfer function of the AVR and the exciter. Its effect is to convert the regulation error ΔV into a change in the excitation emf ΔE_f. The third block reflects the changes in $\Delta E'_q$ due to excitation changes and corresponds to Equation (5.91).

The first block in Figure 5.26 constitutes a proportional element, as an increase in the rotor angle by $\Delta\delta$ causes a decrease in the generator voltage by $\Delta V_g \cong \left(\partial V_g/\partial\delta\right)\Delta\delta$ so that the following voltage error is produced:

$$\Delta V = V_{ref} - V_g = -\frac{\partial V_g}{\partial\delta}\Delta\delta = K_{\Delta V/\Delta\delta}\Delta\delta \tag{5.92}$$

An expression for the proportionality coefficient $K_{\Delta V/\Delta\delta}$ can be obtained from Equation (5.84). Solving this equation with respect to V_g gives

$$V_g = \frac{\sqrt{E'^2 + 2\frac{X'_d}{X}E'V_s\cos\delta' + \left(\frac{X'_d}{X}V_s\right)^2}}{\frac{X'_d}{X}+1}. \tag{5.93}$$

Differentiation of this expression at the linearization point defined by δ'_0, E'_0, V_{g0} gives

$$K_{\Delta V/\Delta\delta} = -\frac{\partial V_g}{\partial\delta'} = \frac{X'_d X}{\left(X'_d + X\right)^2}\frac{E'_0}{V_{g0}}V_s\sin\delta'_0. \tag{5.94}$$

This coefficient is positive over a wide range of angle changes, which means that the voltage regulation error given by Equation (5.92) is always in phase with the angle changes $\Delta\delta$. The amplitude of ΔV depends on the generator load. For a small load (and δ'_0) the coefficient $K_{\Delta V/\Delta\delta}$ is small and the resulting voltage error is small. As the load is increased, changes in ΔV caused by the changes in $\Delta\delta$ become bigger.

The second block in Figure 5.26 introduces a phase shift between ΔE_f and ΔV dependent on the transfer functions of the AVR and exciter. In the case of a static exciter, Figure 2.3d–f with a proportional regulator, the phase shift is small and it may be assumed that ΔE_f is in phase with ΔV. In comparison a DC cascade exciter, or AC exciter with rectifier, Figure 2.3a–c, behaves like an

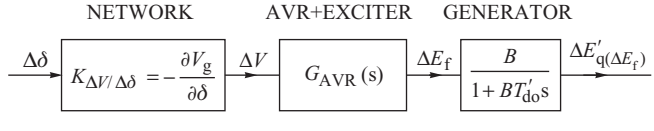

Figure 5.26 Components determining the phase shift between $\Delta\delta$ and $\Delta E'_{q(\Delta E_f)}$.

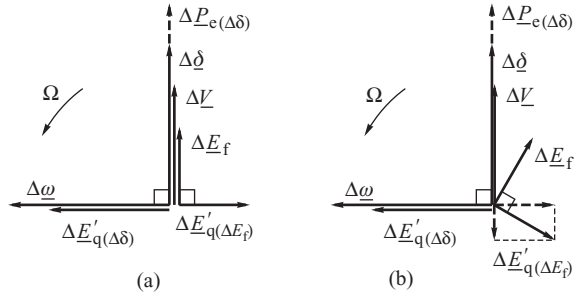

Figure 5.27 Phasors of increments rotating with the swing frequency Ω for: (a) the AVR proportional system; and (b) the AVR proportional system with inertia.

inertia element which introduces a phase shift of a few tens of degrees for a frequency of oscillation of about 1 Hz.

The generator block in Figure 5.26 introduces a phase shift which, as in Equation (5.54), is equal to $\pi/2$. However, the minus sign in Equations (5.53), (5.54) and the first of the equations in (5.91) will cause $\Delta E'_{q(\Delta\delta)}$ to lead the variations in $\Delta\delta$ by $\pi/2$, while the plus sign in the second of the equations in (5.91) will cause $\Delta E'_{q(\Delta E_f)}$ to lag the changes in $\Delta\delta$ by $\pi/2$.

A knowledge of all these phase shifts allows a phasor diagram similar to that shown in Figure 5.13c to be drawn but with both of the components of Equation (5.90) taken into account. This is shown in Figure 5.27 which contains two phasor diagrams of increments rotating with the swing frequency Ω (rad/s) drawn for two general types of AVR systems. In both diagrams the phasors of increments $\Delta\underline{\delta}$ and $\Delta\underline{V}$ are in phase, Equation (5.94). The component $\Delta\underline{E}'_{q(\Delta\delta)}$ leads $\Delta\underline{\delta}$ in the same was as in Figure 5.13c.

The phasor diagram shown in Figure 5.27a is valid for a proportional AVR system when $\Delta\underline{E}_f$ and $\Delta\underline{V}$ are almost in phase. The component $\Delta\underline{E}'_{q(\Delta E_f)}$ lags $\Delta\underline{E}_f$ by $\pi/2$ and directly opposes $\Delta\underline{E}'_{q(\Delta\delta)}$. This diagram clearly shows that voltage regulation, represented by $\Delta\underline{E}'_{q(\Delta E_f)}$, weakens the damping introduced by the field winding and represented by $\Delta\underline{E}'_{q(\Delta\delta)}$. If the magnitude of $\Delta\underline{E}'_{q(\Delta E_f)}$ is greater than that of $\Delta\underline{E}'_{q(\Delta\delta)}$ then the voltage regulation will introduce a net negative damping into the system. This negative damping is enhanced by:

- large generator load (large value of δ'_0) resulting in a large value of the coefficient $K_{\Delta V/\Delta\delta}$, Equation (5.94);
- large gain $|G_{AVR}(s)|$ in the AVR controller determining the magnitude of $\Delta\underline{E}_f$;
- large network reactance X determining the value of the coefficient $K_{\Delta V/\Delta\delta}$.[1]

Figure 5.27b shows an AVR system with cascaded DC exciter or an AC exciter with a rectifier when $\Delta\underline{E}_f$ lags $\Delta\underline{V}$ typically by a few tens of degrees. The phasor $\Delta\underline{E}'_{q(\Delta E_f)}$ lags $\Delta\underline{E}_f$ by $\pi/2$ giving rise to two components with respect to the direction of $\Delta\underline{\delta}$: (i) the quadrature component which introduces negative damping, as in Figure 5.27a; and (ii) the in-phase component which is in phase with $\Delta\underline{P}_e$ and does not influence damping. The effect of the latter component is to reduce the synchronizing power coefficient $K_{E'_q}$, Equation (5.52), and therefore change the frequency of oscillations.

The above analysis of the influence of an AVR system on the generator damping is of a qualitative nature only, with the aim of helping the understanding of these complicated phenomena. Detailed

[1] The maximum value of $K_{\Delta V/\Delta\delta}$ is obtained for $X = X'_d$. Usually in practice $X \ll X'_d$. Under that assumption, the higher the network reactance X, the higher the coefficient $K_{\Delta V/\Delta\delta}$.

quantitative analysis can be found in De Mello and Concordia (1969), later enhanced in Anderson and Fouad (1977), Yu (1983) and Kundur (1994).

5.5.4 Effect of AVR Action on the Damper Windings

Section 5.5.3 described how the AVR system can influence the damping torque due to the field winding, that is the last component in the swing equation, Equation (5.52). The second component in this equation, $P_D = D\Delta\omega$, corresponds to the damping power introduced by the damper windings. Assuming constant excitation voltage, that is $E_f =$ constant, the damping power is given by Equation (5.24). Recall that the mechanism by which this power is developed is similar to that on which operation of the induction machine is based. A change in the rotor angle δ results in the speed deviation $\Delta\omega$. According to Faraday's law, an emf is induced which is proportional to the speed deviation. The current driven by this emf interacts with the air-gap flux to produce a torque referred to as the *natural damping torque*. To simplify considerations, only the d-axis damper winding will be analysed.

Figure 5.28a shows a phasor diagram for the d-axis damper winding, similar to that shown in Figure 5.27. The emf induced in the winding $\underline{e}_{D(\Delta\omega)}$ is shown to be in phase with $\Delta\underline{\omega}$. The damper winding has a large resistance, which means that the current due to speed deviation, $\underline{i}_{D(\Delta\omega)}$, lags $\underline{e}_{D(\Delta\omega)}$ by an angle less than $\pi/2$. The component of this current which is in-phase with $\Delta\underline{\omega}$ gives rise to the natural damping torque. The quadrature component, which is in phase with $\Delta\underline{\delta}$, enhances the synchronizing power coefficient.

Now consider the influence of the AVR on the damper windings. The d-axis damper winding lies along the path of the excitation flux produced by the field winding, Figure 4.3. This means that the two windings are magnetically coupled and may be treated as a transformer, Figure 5.28b, supplied by $\Delta\underline{E}_f$ and loaded with the resistance R_D of the damper winding. Consequently, the additional current $\underline{i}_{D(\Delta E_f)}$ induced in the damper winding must lag $\Delta\underline{E}_f$. Figure 5.28c shows the position of phasors. The horizontal component of $\underline{i}_{D(\Delta E_f)}$ directly opposes the horizontal component of $\underline{i}_{D(\Delta\omega)}$. As the former is due to the AVR while the latter is due to speed deviation and is responsible for the natural damping, it may be concluded that voltage regulation weakens the natural damping. This weakening effect is referred to as *artificial damping*.

Artificial damping is stronger for larger $\underline{i}_{D(\Delta E_f)}$ currents. This current is, in turn, proportional to the variations in$\Delta\underline{E}_f$ and $\Delta\underline{V}$ caused by $\Delta\underline{\delta}$. Some of the factors influencing this effect were described in the previous subsection and are: generator load, reactance of the transmission network and gain of the voltage controller.

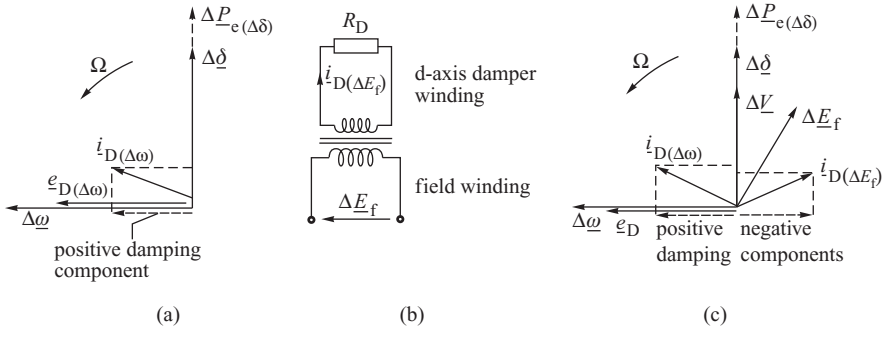

Figure 5.28 Phasor diagram of increments oscillating with the swing frequency Ω (in rad/s) for the damper windings: (a) natural damping only; (b) field and damper windings as a transformer; (c) natural and artificial damping.

5.5.5 Compensating the Negative Damping Components

The main conclusion from the previous two subsections is that a voltage controller, which reacts only to the voltage error, weakens the damping introduced by the damper and field windings. In the extreme case of a heavily loaded generator operating on a long transmission link, a large gain in the voltage controller gain may result in net negative damping leading to an oscillatory loss of stability. This detrimental effect of the AVR can be compensated using a supplementary control loop referred to as a *power system stabilizer* (PSS), discussed in more detail in Section 10.1. PSS is widely used in the United States, Canada and Western Europe. Another solution, preferred in the former Soviet Union, consists of voltage controllers with in-built feedback loops reacting to the time derivative of the voltage error and other quantities (Glebov, 1970).

6

Electromechanical Dynamics – Large Disturbances

The previous chapter explained how a power system responds to a small disturbance and determined the conditions necessary for the system to remain stable when subjected to such a disturbance. Much more dramatic from a stability point of view is the way in which a system responds to a large disturbance such as a short circuit or line tripping. When such a fault occurs, large currents and torques are produced and often action must be taken quickly if system stability is to be maintained. It is this problem of large-disturbance stability, and the effect such a disturbance has on the system behaviour, that is addressed in this chapter.

6.1 Transient Stability

Assume that before the fault occurs, the power system is operating at some stable steady-state condition. The power system transient stability problem is then defined as that of assessing whether or not the system will reach an acceptable steady-state operating point following the fault.

As the subtransient period is normally very short compared with the period of the rotor swings, the effect of the subtransient phenomena on the electromechanical dynamics can be neglected. This allows the classical model of the generator to be used to study the transient stability problem when the swing equation is expressed by Equation (5.15) and the air-gap power by Equation (5.40). During a major fault, such as a short circuit, the equivalent reactance x'_{d} appearing in Equation (5.40) will be subject to change so that the air-gap power $P_{\mathrm{e}} = P_{E'}$ will also change and the power balance within the system will be disturbed. This will result in energy transfers between the generators producing corresponding rotor oscillations. Usually there are three states accompanying a disturbance with three, generally different, values of x'_{d}: (i) the prefault state when the reactance $x'_{\mathrm{d}} = x'_{\mathrm{d\,PRE}}$; (ii) the fault state when $x'_{\mathrm{d}} = x'_{\mathrm{d\,F}}$; and (iii) the postfault state when $x'_{\mathrm{d}} = x'_{\mathrm{d\,POST}}$. This section will start by considering a fault that is cleared without any change in the network configuration being required. In this case $x'_{\mathrm{d\,POST}} = x'_{\mathrm{d\,PRE}}$.

6.1.1 Fault Cleared Without a Change in the Equivalent Network Impedance

Figure 6.1a shows an example of a fault which is cleared by tripping the faulty element but without changing the equivalent network impedance. It is assumed that only line L1 of a double-circuit connection is in use with line L2 energized but not connected at the system end. If a fault occurs on

Power System Dynamics: Stability and Control, Second Edition Jan Machowski, Janusz W. Bialek and James R. Bumby
© 2008 John Wiley & Sons, Ltd

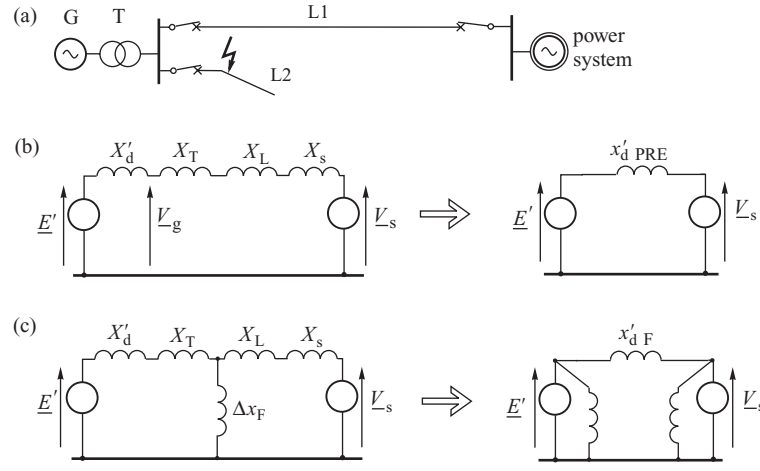

Figure 6.1 Example of a fault with the same pre- and postfault impedance: (a) schematic diagram; (b) equivalent circuit for the pre- and postfault state; (b) equivalent circuit during the fault.

the unconnected line L2, and is then cleared by opening the circuit-breaker at the generator end of the line, the prefault and postfault impedances between the generator and the system are the same.

6.1.1.1 Reactance Values During the Prefault, Fault and Postfault Periods

The equivalent circuit for the system is shown in Figure 6.1b. The generator is represented by the classical model with a constant transient emf E' behind the transient reactance X'_d while the system is represented by a constant voltage V_s behind the equivalent reactance X_s. The reactances of the transformer and line L1 are X_T and X_L respectively. The prefault equivalent reactance $x'_{d\,PRE}$ of the whole transmission link is

$$x'_{d\,PRE} = X'_d + X_T + X_L + X_s. \tag{6.1}$$

The use of symmetrical components allows any type of fault to be represented in the positive-sequence network by a fault shunt reactance Δx_F connected between the point of the fault and the neutral, as shown in Figure 6.1c (Gross, 1986). The value of the fault shunt depends on the type of fault and is given in Table 6.1 where X_1, X_2 and X_0 are respectively the positive-, negative- and zero-sequence Thévenin equivalent reactances as seen from the fault terminals.

Using the star–delta transformation, the fault network can be transformed as shown in Figure 6.1c so that the voltages E' and V_s are directly connected by the equivalent fault reactance

$$x'_{d\,F} = X'_d + X_T + X_L + X_s + \frac{(X'_d + X_T)(X_L + X_s)}{\Delta x_F}. \tag{6.2}$$

Table 6.1 Shunt reactances representing different types of fault

Fault type	Three phase (3ph)	Double phase to ground (2ph–g)	Phase to phase (2ph)	Single phase (1ph)
Δx_F	0	$\dfrac{X_2 X_0}{X_2 + X_0}$	X_2	$X_1 + X_2$

The value of this reactance is heavily dependent on the value of the fault shunt Δx_F given in Table 6.1. When the fault is cleared, by opening the circuit-breaker in line L2, the equivalent circuit is the same as that in the prefault period so that $x'_{d\,POST} = x'_{d\,PRE}$.

The circuit diagram of Figure 6.1c corresponds to the positive-sequence network so that when the reactance given in Equation (6.2) is used in the power–angle characteristic, Equation (5.40), only the torque and power due to the flow of positive-sequence currents is accounted for. The influence of negative- and zero-sequence fault currents and torques is neglected from further considerations in this chapter.

6.1.1.2 Three-Phase Fault

Figure 6.2 shows how the equal area criterion, described in Section 5.4.3, can be used to analyse the effect of a three-phase fault on the system stability. To simplify the discussion, damping will be neglected ($P_D = 0$) and the changes in the rotor speed will be assumed to be too small to activate the turbine governor system. In this case the mechanical power input P_m from the turbine can be assumed to be constant.

For a three-phase fault $\Delta x_F = 0$ and, according to Equation (6.2), $x'_{d\,F} = \infty$. Thus power transfer from the generator to the system is completely blocked by the fault with the fault current being purely inductive. During the fault the electrical power drops from its prefault value to zero as illustrated by line 1–2 in Figure 6.2 and remains at zero until the fault is cleared by opening the circuit-breaker. During this time the rotor acceleration ε can be obtained from the swing equation, Equation (5.15), by dividing both sides by M, substituting $P_e = 0$, $P_D = 0$ and writing in terms of δ' to give

$$\varepsilon = \frac{d^2\delta'}{dt^2} = \frac{P_m}{M} = \text{constant}. \tag{6.3}$$

Integrating Equation (6.3) twice with the initial conditions $\delta'(t = 0) = \delta'_0$ and $\Delta\omega(t = 0) = 0$ gives the power angle trajectory as

$$\delta' = \delta'_0 + \frac{\varepsilon t^2}{2} \quad \text{or} \quad \Delta\delta' = \delta' - \delta'_0 = \frac{\varepsilon t^2}{2}. \tag{6.4}$$

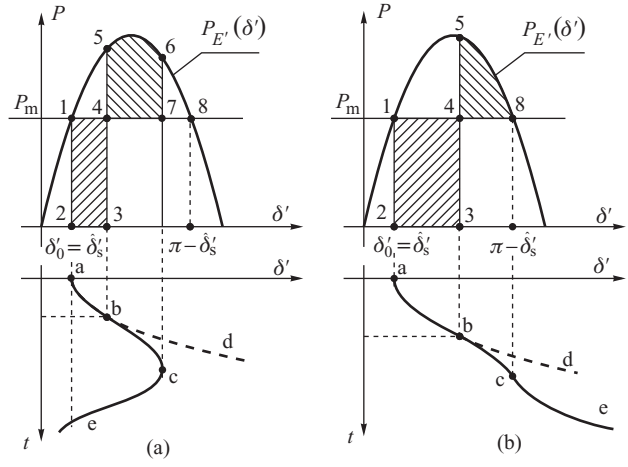

Figure 6.2 The acceleration and deceleration areas: (a) short clearing time; (b) long clearing time.

This corresponds to the parabola a–b–d in Figure 6.2a. Before the fault is cleared the rotor moves from point 2 to point 3 on the power–angle diagram and acquires a kinetic energy proportional to the shaded area 1–2–3–4.

When the fault is cleared at $t = t_1$ by opening the circuit-breaker, the rotor again follows the power–angle characteristic $P_{E'}(\delta')$ corresponding to the reactance given by Equation (6.1) so that the operating point jumps from point 3 to point 5. The rotor now experiences a deceleration torque, with magnitude proportional to the length of the line 4–5, and starts to decelerate. However, due to its momentum, the rotor continues to increase its angle until the work done during deceleration, area 4–5–6–7, equals the kinetic energy acquired during acceleration, area 1–2–3–4. The rotor again reaches synchronous speed at point 6 when

$$\text{area } 4\text{–}5\text{–}6\text{–}7 = \text{area } 1\text{–}2\text{–}3\text{–}4. \tag{6.5}$$

In the absence of damping the cycle repeats and the rotor swings back and forth around point 1 performing *synchronous swings*. The generator does not lose synchronism and the system is stable.

Figure 6.2b shows a similar situation but with a substantially longer fault clearing time $t = t_2$ when the kinetic energy acquired during acceleration, proportional to the area 1–2–3–4, is much larger than in Figure 6.2a. As a result the work performed during deceleration, proportional to the area 4–5–8, cannot absorb the kinetic energy acquired during acceleration and the speed deviation does not become equal to zero before the rotor reaches point 8. After passing point 8 the electrical power $P_{E'}(\delta')$ is less than the mechanical power P_m and the rotor experiences a net acceleration torque which further increases its angle. The rotor makes an *asynchronous rotation* and loses synchronism with the system. Further asynchronous operation is analysed in more detail in Section 6.5.

Two important points arise from this discussion. The first is that the generator loses stability if, during one of the swings, the operating point passes point 8 on the characteristic. This point corresponds to the transient rotor angle being equal to $(\pi - \hat{\delta}'_s)$, where $\hat{\delta}'_s$ is the stable equilibrium value of the transient rotor angle. Area 4–5–8 is therefore the *available deceleration area* with which to stop the swinging generator rotor. The corresponding transient stability condition states that the available deceleration area must be larger than the acceleration area forced by the fault. For the case shown in Figure 6.2a this criterion is

$$\text{area } 1\text{–}2\text{–}3\text{–}4 < \text{area } 4\text{–}5\text{–}8. \tag{6.6}$$

As the generator did not use the whole available decelerating area, the remaining area 6–7–8, divided by the available deceleration area, can be used to define the *transient stability margin*

$$K_{\text{area}} = \frac{\text{area } 6\text{–}7\text{–}8}{\text{area } 4\text{–}5\text{–}8}. \tag{6.7}$$

The second important observation is that fault clearing time is a major factor in determining the stability of the generator. This is borne out by Equation (6.4) where the accelerating area 1–2–3–4 is seen to be proportional to the clearing time squared. The longest clearing time for which the generator will remain in synchronism is referred to as the *critical clearing time*. The relative difference between the critical clearing time and the actual clearing time can be used to give another measure of the transient stability margin:

$$K_{\text{time}} = \frac{t_{\text{cr}} - t_{\text{f}}}{t_{\text{cr}}}, \tag{6.8}$$

where t_{cr} and t_{f} are the critical and actual clearing times.

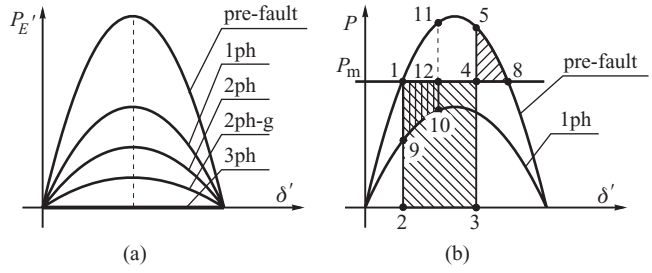

Figure 6.3 Effect of unbalanced faults: (a) comparison of power–angle characteristics; (b) acceleration and deceleration areas during a three-phase fault and a single-phase fault.

6.1.1.3 Unbalanced Faults

During an unbalanced fault at least one of the phases is unaffected, allowing some power to be transmitted to the system. The equivalent fault reactance $x'_{\mathrm{d\,F}}$ does not now increase to infinity, as for the three-phase fault, but to a finite value defined by Equation (6.2). The increase in the reactance is inversely proportional to Δx_{F} and depends on the type of fault, as shown in Table 6.1. This allows faults to be listed in order of decreasing severity as (i) a three-phase fault (3ph), (ii) a phase-to-phase-to-ground fault (2ph–g), (iii) a phase-to-phase fault (2ph) and (iv) a single-phase fault (1ph).

The corresponding power–angle characteristics during the fault are illustrated in Figure 6.3a.

The effect of an unbalanced fault on system stability is examined by considering the least severe single-phase fault. A fault clearing time is assumed that is slightly longer than the critical clearing time for the three-phase fault. The acceleration and the deceleration areas are shown in Figure 6.3b. In the case of the three-phase fault the acceleration area 1–2–3–4 is larger than the deceleration area 4–5–8 and the system is unstable, as in Figure 6.2a.

For the single-phase fault the power transfer is not completely blocked and the air-gap power drops from point 1 on the prefault characteristic to point 9 on the fault characteristic. The accelerating torque, corresponding to line 1–9, is smaller than that for the three-phase fault (line 1–2), the rotor accelerates less rapidly and, by the time that the fault is cleared, the rotor has reached point 10. At this point the rotor angle is smaller than in the case of the three-phase fault. The acceleration area 1–9–10–12 is now much smaller than the maximum available deceleration area 11–8–12 and the system is stable with a large stability margin. Obviously a longer clearing time would result in the generator losing stability, but the critical clearing time for the single-phase fault is significantly longer than that for the three-phase fault. Critical clearing times for other types of faults are of the same order as the Δx_{F} value given in Table 6.1.

6.1.1.4 Effect of the Prefault Load

Figure 6.4 shows a generator operating at load P_{m1} prior to a three-phase fault. The fault is cleared when the acceleration area 1–2–3–4 is smaller than the available deceleration area 4–5–8. The system is stable with stability margin 6–7–8. Increasing the prefault load by 50 % to $P_{\mathrm{m2}} = 1.5\,P_{\mathrm{m1}}$ increases the acceleration power $P_{\mathrm{acc}} = P_{\mathrm{m}} - P_{E'}(\delta') = P_{\mathrm{m}}$ by one and a half times so that, according to Equations (6.3) and (6.4), the change in the power angle $\Delta\delta'$ also increases by a factor of 1.5. Consequently, as each side of the accelerating area rectangle 1–2–3–4 has increased 1.5 times, the acceleration area 1–2–3–4 is now much larger than the available deceleration area 4–5–8 and the system is unstable.

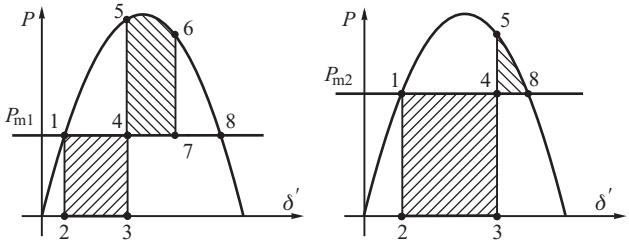

Figure 6.4 Acceleration and deceleration areas for two different prefault loads P_{m1} and $P_{m2} = 1.5P_{m1}$. The fault clearing time is the same for both cases.

The prefault load is an important factor with regard to determining the critical clearing time and generator stability. The higher the load, the lower the critical clearing time.

6.1.1.5 Influence of Fault Distance

So far it has been assumed that in Figure 6.1 the fault occurs close to the busbar. If the point of fault is further along the line, as shown in Figure 6.5a, then the impedance of the faulted line Δx_L is proportional to the fault distance and the per-unit length reactance of the line. The resulting equivalent circuit during the fault period is shown in Figure 6.5b. The equivalent series reactance $x'_{d\,F}$ can again be obtained from Equation (6.2) but with Δx_F replaced by $\Delta x = \Delta x_F + \Delta x_L$.

Figure 6.5c shows a family of power–angle characteristics for a three-phase fault ($\Delta x_F = 0$) occurring at increasing distances along the line. In comparison with the discussion on unbalanced faults it can be seen that the further the distance to the fault, the less severe the fault and the longer the critical clearing time.

In the case of unbalanced faults, $\Delta x_F \neq 0$ and the magnitude of the power–angle characteristic during the fault is further increased compared with the three-phase fault case. As a result the effect of the fault is less severe. In the case of a remote single-phase fault the disturbance to the generator may be very small.

6.1.2 Short-Circuit Cleared with/without Auto-Reclosing

The previous section described a particular situation where the network equivalent reactance does not change when the fault is cleared. In most situations the events surrounding the fault are more

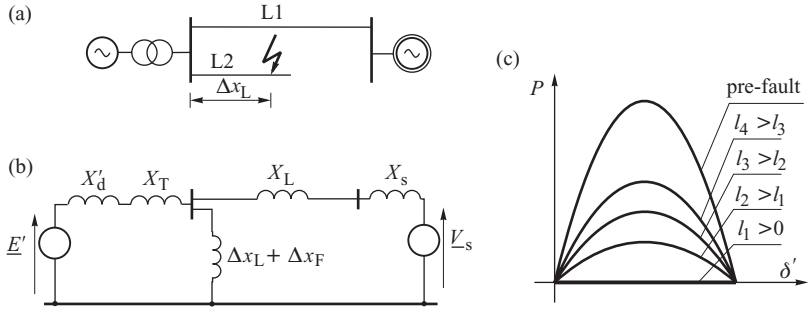

Figure 6.5 Influence of the fault distance: (a) schematic diagram; (b) equivalent circuit diagram; (c) power–angle characteristics before the fault and for various fault distances.

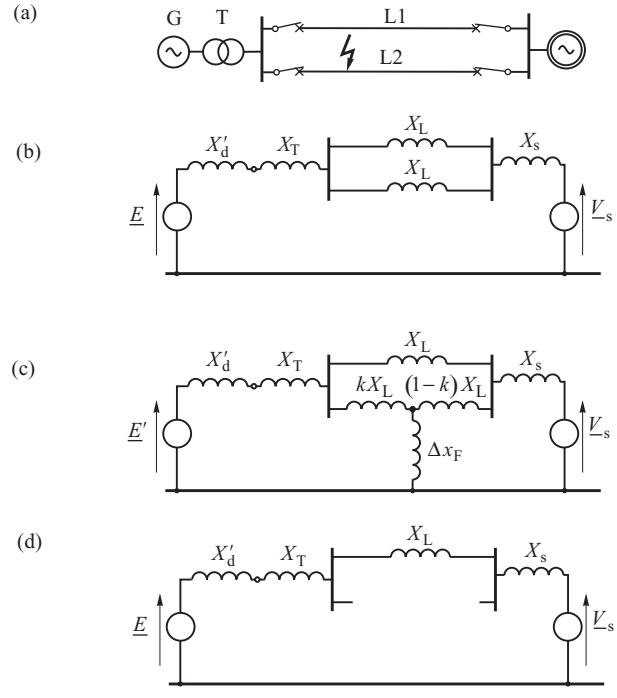

Figure 6.6 Auto-reclosing cycle: (a) schematic diagram; (b) equivalent circuit with both lines operating; (c) short circuit on one of the lines; (d) one line operating.

complex. Firstly, the fault itself would normally be on a loaded element, for example on line L2 when it was connected at both ends. Secondly, the fault will not usually clear itself and the faulted element must be switched out of circuit.

The majority of faults on transmission lines are intermittent so that, after clearing the fault by opening the necessary circuit-breakers, the faulty line can be switched on again after allowing sufficient time for the arc across the breaker points to extinguish. This process is known as *auto-reclosing*. The sequence events in a *successful auto-reclosing* cycle, shown in Figure 6.6, would be:

- both lines operate (before the fault) – Figure 6.6b;
- a short circuit – Figure 6.6c;
- the faulted line is tripped and only one line operates – Figure 6.6d;
- the faulted line is automatically reclosed and both lines again operate – Figure 6.6b.

In Figure 6.6 the fault is assumed to occur on line L2 at some distance k from the circuit-breaker. Each state is characterized by a different equivalent reactance x'_d in Equation (5.40) and a different power–angle characteristic corresponding to that reactance.

Figure 6.7 shows the effect of a three-phase fault with two fault clearing times, one producing a stable response and the other an unstable one. In both cases the accelerating power 1–2 accelerates the rotor from point 2 to point 3 during the fault. When line L2 is tripped, the operating point moves to point 5 and, because of the acquired kinetic energy, moves further along the characteristic. After a certain auto-reclose time required to extinguish the arc, the auto-recloser reconnects line L2 and

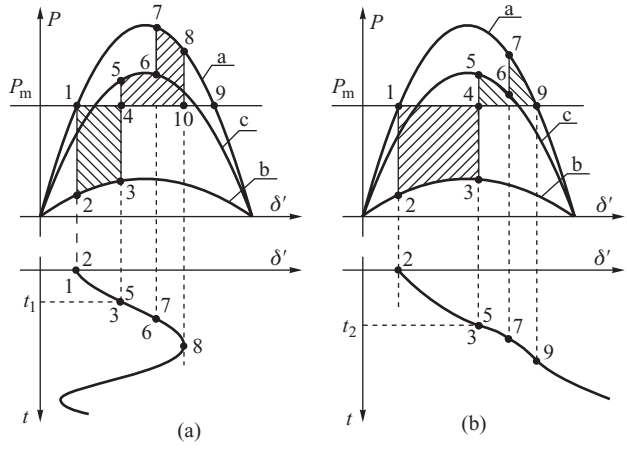

Figure 6.7 Acceleration and deceleration areas for successful auto-reclosing: (a) stable case; (b) unable case.

the system moves from point 6 to point 7. The power angle moves further along the characteristic a to point 8 when, in the stable case, the decelerating area 4–5–6–7–8–10 is equal to the accelerating area 1–2–3–4. The system is stable with a stability margin corresponding to the area 8–9–10. In the unstable case, Figure 6.7b, the increased clearing time enlarges the accelerating area 1–2–3–4 and the available decelerating area is too small to absorb this energy and stop the rotor. The generator rotor makes an asynchronous rotation and loses stability with the system.

In the case of a solid fault the reclosed line is again tripped and the cycle is referred to as *unsuccessful auto-reclosing*. Such a cycle poses a much greater threat to system stability than successful auto-reclosing. In the case of unsuccessful auto-reclosing the following sequence of events occurs:

- both lines operate (before the fault);
- a short circuit;
- the faulted line is tripped and one line operates;
- a short circuit (an attempt to auto-reclose onto the solidly faulted line);
- the faulted line is permanently tripped so that only one line remains in operation.

An illustration of unstable and stable unsuccessful auto-reclosing is shown in Figure 6.8. In the first case the rotor acquires kinetic energy during the short circuit proportional to the area 1–2–3–4. Then, during the break in the cycle, the rotor is decelerated and loses energy proportional to the area 4–5–6–7. An attempt to switch onto the solidly faulted line results in an increase of kinetic energy proportional to the area 7–8–9–11. When the faulted line is permanently tripped, the decelerating area left is 10–13–11. As the sum of the accelerating areas 1–2–3–4 and 7–8–9–11 is greater than the sum of the decelerating areas 4–5–6–7 and 10–13–11, the rotor passes point 13 and makes an asynchronous rotation.

If now the clearing time and the auto-reclosing time are reduced and, in addition, the prefault load on the generator is reduced from P_{m1} to P_{m2}, the system may remain stable as shown in Figure 6.8b. The sum of the accelerating areas 1–2–3–4 and 7–8–9–11 is now equal to the sum of the decelerating areas 4–5–6–7 and 10–11–12–14 and the system is stable with a stability margin corresponding to the area 12–14–13. Assuming that the oscillations are damped, then the new equilibrium point 1′ corresponds to the power characteristic with one line switched off.

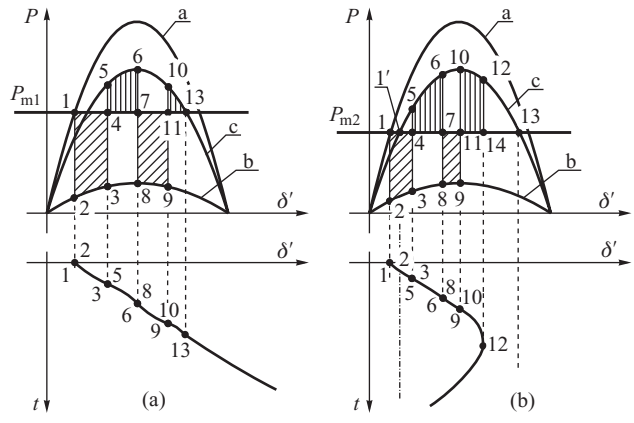

Figure 6.8 Acceleration and deceleration areas for unsuccessful auto-reclosing: (a) unstable case; (b) stable case.

6.1.3 Power Swings

The rotor oscillations accompanying a fault also produce oscillations in the generated power. The shape of power variations can be a source of useful, although approximate, information on the transient stability margin. Again consider the system shown in Figure 6.5a and assume that the fault on line L2 is cleared by tripping the circuit-breakers at each end of the line without auto-reclosing. If the stability margin 6–7–8, shown in Figure 6.9a, is small, the power angle oscillations will be large and may exceed a value of $\pi/2$. The corresponding power oscillations will increase until δ' passes over the peak of the power–angle characteristic, when they will start to decrease. During the rotor backswing the power will initially increase, as the rotor angle passes over the peak of the characteristic, before again decreasing. As a result the power waveform $P_e(t)$ exhibits characteristic 'humps' which disappear as the oscillations are damped out. If the transient stability margin 6–7–8 is large, as in Figure 6.9b, then the humps do not appear because the maximum value of the power angle oscillation is less than $\pi/2$ and the oscillations are only on one side of the power–angle characteristic.

It should be emphasized that power swings follow the transient power–angle characteristic $P_{E'}(\delta')$ rather than the static characteristic $P_{E_q}(\delta)$. This means that the value of power at which humps appear is usually much higher than the critical steady-state power $P_{E_{q\,cr}}$ (Figure 5.9).

6.1.4 Effect of Flux Decrement

The transient characteristic $P_{E'}(\delta')$ used to analyse transient stability is valid assuming that the flux linkage with the field winding is constant so that $E' =$ constant. In fact, as magnetic energy is dissipated in the field winding resistance, flux decrement effects will cause E' to decrease with time. If the fault clearing time is short then flux decrement effects can be neglected for transient stability considerations, but if the clearing time is long then the decay in E' may have a considerable effect. To understand this refer to Figure 6.2 which illustrates the case of $E' =$ constant. If now flux decrement effects are included, then following the fault, the amplitude of the $P_{E'}(\delta')$ characteristic will reduce leading to a decrease in the available deceleration area 4–5–8 and a deterioration in the transient stability. Consequently, the use of the classical model may lead to an optimistic assessment of the critical clearing time.

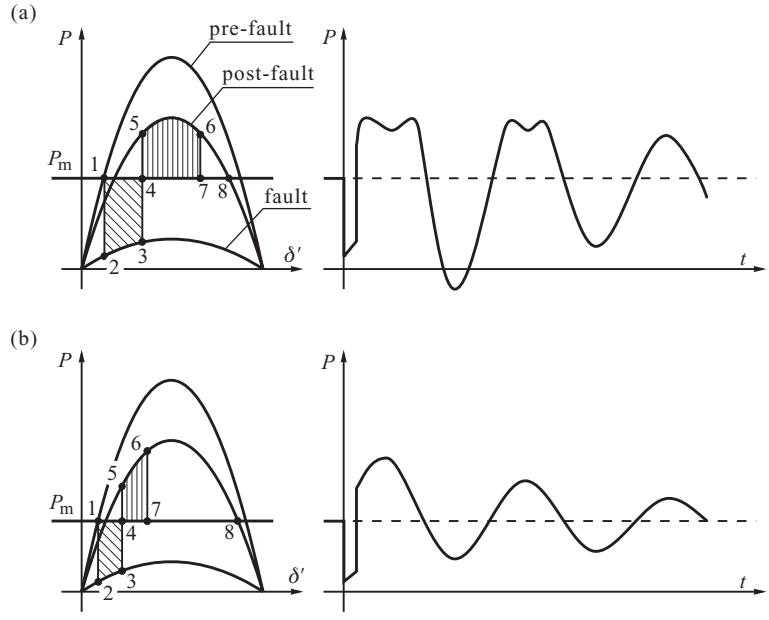

Figure 6.9 Power oscillations in the case of (a) a low stability margin and (b) a large stability margin.

6.1.5 Effect of the AVR

Section 5.5 explained how AVR action may reduce the damping of rotor swings following a small disturbance. In the case of large disturbances the influence of the AVR is similar. However, immediately after a fault occurs and is cleared, a strong-acting AVR may prevent a loss of synchronism. This can be explained as follows.

When a fault occurs, the generator terminal voltage drops and the large regulation error ΔV forces the AVR to increase the generator field current. However, the field current will not change immediately due to a delay depending on the gain and time constants of the AVR, and on the time constant of the generator field winding. To examine the effect of AVR action on transient stability the system shown in Figure 6.5a will be considered, assuming that a three-phase short circuit occurs some distance along line L2 so that $\Delta x_L \neq 0$ and $\Delta x_F = 0$.

When no AVR is present this system may lose stability as shown in Figure 6.10a. The effect of the AVR, shown in Figure 6.10b, is to increase the field current leading to an increase in the transient emf E' as explained in Section 4.2.4 and illustrated in Figure 4.17a. This increase in E' can be accounted for by drawing a family of power–angle characteristics $P_{E'}(\delta')$ for different values of E'. A fast-acting AVR and exciter can increase the excitation voltage up to its ceiling before the fault is cleared, although the change in the field current, and E', will lag behind this due to the time constant of the generator field winding. This increase in field current, and hence E', has two positive effects. Firstly, as E' increases, the accelerating power decreases and the accelerating area 1–2–3–4 is slightly reduced. Secondly, when the fault is cleared, the system will follow a higher power–angle characteristic resulting from the new E' so that a larger decelerating area is available. In this example the rotor reaches a maximum power angle at point 6, when the decelerating area 4–5–6–6′ equals the accelerating area 1–2–3–4, before starting to move back towards the equilibrium point.

Although a fast-acting AVR reduces the first rotor swing, it can increase the second and following swings depending on the system parameters, the dynamic properties of the AVR and the time

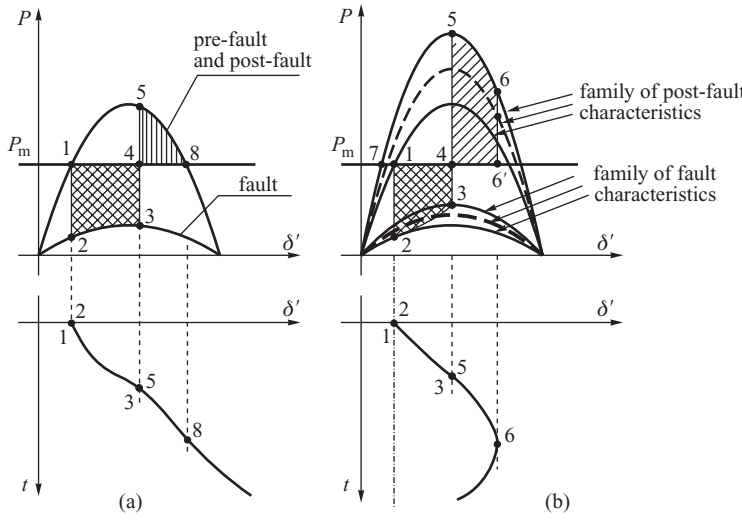

Figure 6.10 The acceleration area and the deceleration area when the influence of the voltage regulator is: (a) neglected; (b) included.

constant of the field winding. Consider the voltage regulation error $\Delta V = V_{\text{ref}} - V_{\text{g}}$, created when the fault is cleared. Equation (5.93) is now important as it shows how V_{g} depends on δ' and the ratio X'_{d}/X. An example of such dependence is shown in Figure 6.11.

The terminal voltage V_{g} reaches a minimum when $\delta' = \pi$. The actual value of this minimum depends on the ratio X'_{d}/X:

- $V_{\text{g}} = 0$ for $\delta' = \pi$ and $X'_{\text{d}}/X = E'/V_{\text{s}}$ (curve 1);
- $V_{\text{g}} = (E' - V_{\text{s}})/2$ for $\delta' = \pi$ and $X'_{\text{d}}/X = 1$ (curve 2).

As the generator reactance usually dominates other reactances in a transmission link, the case $X'_{\text{d}}/X = 1$ corresponds to a long transmission link. For a short transmission link $X'_{\text{d}}/X > 1$ and the minimum value of V_{g} is higher (curve 3).

Consider first the case of a long transmission link and assume that when the fault is cleared the angle δ' is large. On clearing the fault, the terminal voltage will recover from a small fault value to a somewhat small postfault value (curve 1 in Figure 6.11). Consequently, the AVR will

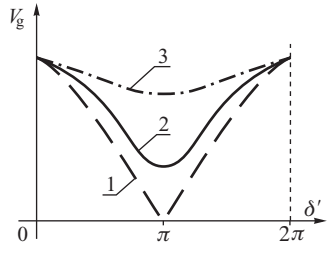

Figure 6.11 Generator terminal voltage as a function of δ': 1, for $X'_{\text{d}}/X = E'V_{\text{s}}$; 2, for $X'_{\text{d}}/X = 1$; 3, for $X'_{\text{d}}/X > 1$.

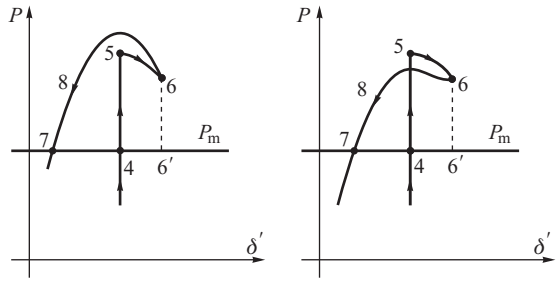

Figure 6.12 Rotor swing after the fault clearance in the case of: (a) a long transmission link and (b) a short transmission link.

continue to increase the excitation current in order to try and recover the terminal voltage. In this case the rotor backswing will occur on the highest possible transient characteristic $P_{E'}(\delta')$. This situation is illustrated in Figure 6.12a which shows the system trajectory following fault clearance. The AVR continues to increase the field current during the backswing, increasing the deceleration area 6–8–7–6′. This results in an increase in the amplitude of consecutive rotor swings such that, in this case, the AVR may have a detrimental effect on the generator transient stability.

Now consider the case of a short transmission link illustrated in Figure 6.12b. In this case the terminal voltage V_g recovers well when the fault is cleared, despite the large value of δ'. As a small increase in the transient emf E' will be forced by the increase in the excitation current during the fault period, the terminal voltage may recover to a value that is slightly higher than the reference value. Subsequently this high terminal voltage will force the AVR to reduce the field current during the rotor backswing, the amplitude of the transient power–angle characteristic will decrease and, as a result, the deceleration area 6–8–7–6′ will be reduced. This reduction in the deceleration area will lead to a reduction in the amplitude of subsequent rotor swings. In this case the AVR enhances the transient stability in both forward and backward swings.

Figure 6.12 is also closely related to the damping produced by the AVR when a small disturbance occurs. Section 5.5 concluded that the amount of negative damping produced by the AVR increases with the length of the line as this increases the proportionality coefficient $K_{\Delta V/\Delta\delta}$ between $\Delta\delta'$ and ΔV (Figure 5.26). The example shown in Figure 6.12a corresponds to the situation when this negative damping is greater than the system positive damping, while Figure 6.12b illustrates the reverse case.

As the influence of the AVR strongly depends on the postfault network reactance, the dynamic system response depends on the fault location and its clearance. This is illustrated in Figure 6.13. If fault F1 appears on line L1 and is cleared by tripping the faulted line, then the generator will operate in the postfault state via a long transmission link that consists of lines L2 and L3. Simulation results for this example are presented in Figure 6.14. Figure 6.14a shows the trajectory of the operating point while Figure 6.14b shows that the terminal voltage drops during the fault and does not recover

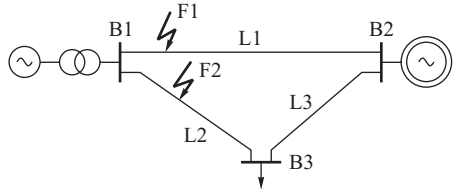

Figure 6.13 Example of a simple power system.

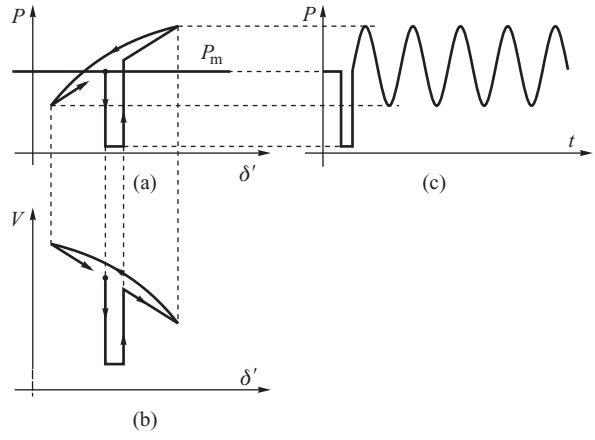

Figure 6.14 Simulation results for a fault on line L1 cleared by tripping the faulted line: (a) equal area method, (b) variation in the generator voltage, (c) power swings.

very well. This low value of terminal voltage forces the AVR to continue to increase the excitation current so that the rotor backswing occurs along the upper characteristic in Figure 6.14a. This repeats from cycle to cycle with the effect that the rotor swings are poorly damped (Figure 6.14c).

If the fault occurs on line L2 and is again cleared by tripping the faulted line, then the generator operates in the postfault period via a short transmission link that consists solely of line L1. Simulation results for this case are shown in Figure 6.15. Now, when the fault is cleared, the generator voltage recovers well and stays at a high level (Figure 6.15b). Consequently, the AVR decreases the excitation current and the rotor swings back along the lower power–angle characteristic in Figure 6.15a and the deceleration area is small. This repeats during each cycle of the rotor swings with the result that they are well damped (Figure 6.15c).

These examples show how the rotor oscillations may increase if the transmission link is long and the AVR keeps the excitation voltage at too high a value during the rotor backswing. Ideally the regulator should increase the excitation when the power angle δ' increases and lower it when δ' decreases, no matter what the value of the regulation error ΔV is. Section 10.1 will show how the

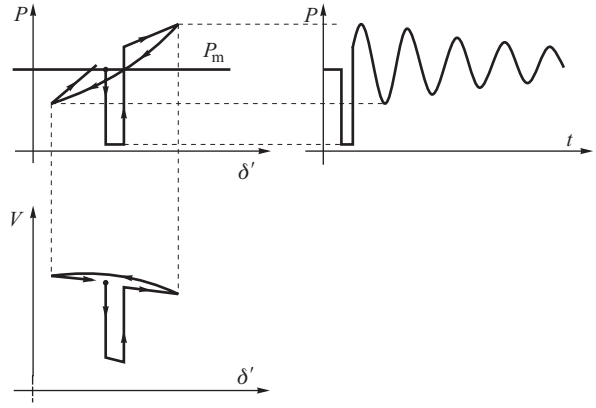

Figure 6.15 Simulation results for a fault on line L2 cleared by tripping the faulted line: (a) equal area method, (b) variation in the generator voltage, (c) power swings.

AVR can be provided with supplementary control loops to provide a regulation error that depends on the rotor speed deviation $\Delta\omega$ or the rate of change of real power. Such supplementary loops coordinate the regulation process with the rotor swings in order to ensure correct damping.

6.2 Swings in Multi-Machine Systems

Although the simplification of a multi-machine power system to a single generator–infinite busbar model enables many important conclusion to be made concerning the electromechanical dynamics and stability of the system, this simplification is only possible when the fault affects one generator and has little effect on other generators in the system. Contemporary power systems have a well-developed transmission network with power stations located relatively close to each other so that these conditions will not always be met. In these circumstances a fault near one of the power stations will also distort the power balance at neighbouring stations. The resulting electromechanical swings in the power system can be compared with the way that the masses swing in the mechanical system shown in Figure 6.16.

Section 5.2 showed that a single swinging rotor can be compared with a mass/spring/damper system. Hence a multi-machine system can be compared with a number of masses (representing the generators) suspended from a 'network' consisting of elastic strings (representing the transmission lines). In the steady state each of the strings is loaded below its breaking point (steady-state stability limit). If one of the strings is suddenly cut (representing a line tripping) the masses will experience coupled transient motion (swinging of the rotors) with fluctuations in the forces in the strings (line powers).

Such a sudden disturbance may result in the system reaching a new equilibrium state characterized by a new set of string forces (line powers) and string extensions (rotor angles) or, due to the transient forces involved, one string may break, so weakening network and producing a chain reaction of broken strings and eventual total system collapse.

Obviously this mechanical analogue of the power system has a number of limitations. Firstly, the string stiffnesses should be nonlinear so as to model correctly the nonlinear synchronizing power coefficients. Secondly, the string stiffness should be different in the steady state to the transient state to model correctly the different steady-state and transient state models of the generators.

In practice a disturbance may affect the stability of a power system in one of four ways:

1. The generator (or generators) nearest to the fault may lose synchronism without exhibiting any synchronous swings; other generators affected by the fault undergo a period of synchronous oscillations until they eventually return to synchronous operation.
2. The generator (or generators) nearest to the fault lose synchronism after exhibiting synchronous oscillations.

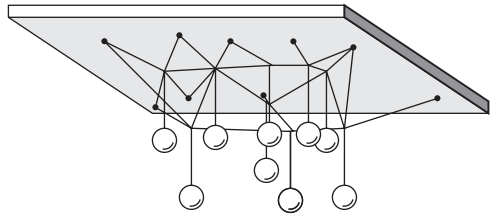

Figure 6.16 Mechanical analogue of swings in a multi-machine system. Based on Elgerd (1982).
Source: McGraw-Hill

3. The generator (or generators) nearest to the fault are the first to lose synchronism and are then followed by other generators in the system.
4. The generator (or generators) nearest to the fault exhibit synchronous swings without losing stability but one, or more, of the other generators remote from the fault lose synchronism with the system.

So far only the first case has been described because it may be represented by the generator–infinite busbar system. In the other three cases instability arises due to interaction with other generators located further from the fault. In the second case the generator initially has a chance to retain stability but, as the rotors of the other generators start to oscillate, conditions deteriorate and the generator loses synchronism. In the third case the generator nearest the fault is the first to lose synchronism; this has a major affect on the other generators in the system so that they may also lose synchronism. The fourth case is typical of the situation where some generators, located far from the point of fault, are weakly connected to the system. As the oscillations spread, the operating conditions of the weakly connected generators deteriorate so that they may lose stability. Another example of this fourth instability case is when the network configuration is changed following fault clearance. Although the tripped line may be just one of the lines that connects the nearest generator to the system, it could also be the main connection for a neighbouring power station. Example 6.1 illustrates all the above cases (Omahen, 1994).

Example 6.1

Figure 6.17 shows a schematic diagram of a power system that comprises three subsystems connected together at node 2. The capacity of generator 5 is large and can be considered as an infinite busbar. Figure 6.18a–d shows the power angles of all the generators, measured with respect to generator 5, for faults located at points a, b, c and d respectively. Each of these points corresponds to the four cases of instability. The faults are assumed to be cleared without auto-reclosing.

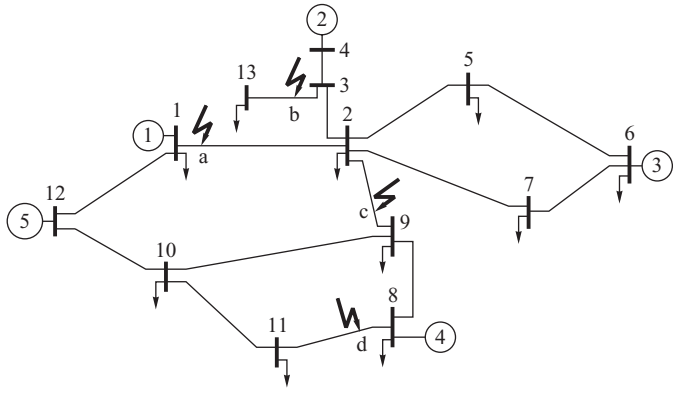

Figure 6.17 Schematic diagram of the test system.

When line 1–2 is faulted, case a, generator 1 quickly loses synchronism and the rotors of the other generators undergo a period of synchronous oscillation. When the fault is on line 3–13, case b, then, for a given clearing time, generator 2 could remain in synchronism just as if it were

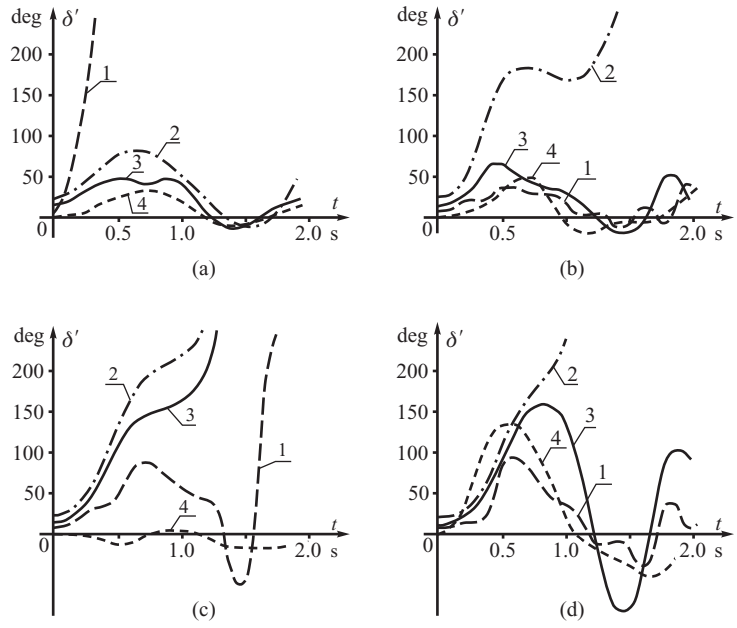

Figure 6.18 Rotor angle variations (measured with respect to generator rotor 5) for different fault locations. Based on Omahen (1994). Reproduced by permission of P. Omahen

operating on the infinite busbars. However, in this particular case the oscillations of the other generator rotors increase the relative difference in the power angles and the situation regarding generator 2 deteriorates and it loses stability on its second swing. When line 9–2 is faulted, case c, the weakly connected generators, 2 and 3, immediately lose stability while generator 1, which initially remains in synchronism with generator 5, loses synchronism some time later. When line 8–11 is faulted, case d, the power angles of all the generators considerably increase. After the fault is cleared, all the system loads take power from their neighbouring generators 1, 3, 4 and 5 but as generator 2 is far from these loads it loses stability.

6.3 Direct Method for Stability Assessment

Throughout this chapter use has been made of the equal area criterion to explain and assess system stability. This method will now be formalized using the *Lyapunov direct method* and an *energy-type Lyapunov function*. In this section the basic concepts on which the Lyapunov direct method is based will be described and applied to the simple generator–infinite busbar system. The Lyapunov direct method is also known as *Lyapunov's second method*.

Due to its potential in assessing power system stability, without the need to solve the system differential equations, the Lyapunov direct method has been the subject of much intensive research. However, the practical application of the direct method for real-time security assessment is still some time off due to modelling limitations and the unreliability of computational techniques. When applied to a multi-machine system, especially one operating close to its stability limits, the direct method is vulnerable to numerical problems and may give unreliable results. Interested readers looking for a detailed treatment of this topic are referred to Pai (1981, 1989), Fouad and Vittal (1992) and Pavella and Murthy (1994).

6.3.1 Mathematical Background

Dynamic systems are generally described by a set of nonlinear differential equations of the form

$$\dot{\boldsymbol{x}} = \boldsymbol{F}(\boldsymbol{x}), \tag{6.9}$$

where $\boldsymbol{x}$ is the vector of *state variables*. The Euclidean space determined by $\boldsymbol{x}$ is referred to as the *state space* whilst the point $\hat{\boldsymbol{x}}$, for which $\boldsymbol{F}(\hat{\boldsymbol{x}}) = \mathbf{0}$, is referred to as the *equilibrium point*. For an initial point $\boldsymbol{x_0} \neq \hat{\boldsymbol{x}}$, $\dot{\boldsymbol{x}}(t = 0) = \mathbf{0}$, Equation (6.9) has a solution $\mathbf{x}(t)$ in the state space and is referred to as the *system trajectory*. The system is said to be *asymptotically stable* if the trajectory returns to the equilibrium point as $t \to \infty$. If the trajectory remains in a vicinity of the equilibrium point as $t \to \infty$ then the system is said to be *stable*.

Lyapunov's stability theory, used in the direct method of stability assessment, is based on a scalar function $V(\boldsymbol{x})$ defined in the state space of the dynamic system. At a given point, the direction of the largest increase in the value of $V(\boldsymbol{x})$, is given by the gradient of the function grad $V(\boldsymbol{x}) = [\partial V/\partial x_i]$. The points $\tilde{\boldsymbol{x}}$ for which grad $V(\tilde{\boldsymbol{x}}) = \mathbf{0}$ are referred to as the *stationary points*. Each stationary point may correspond to a minimum, a maximum or a saddle point as illustrated in Figure 6.19. The stationary point $\tilde{\boldsymbol{x}}$ corresponds to a minimum, Figure 6.19a, if any small disturbance $\Delta\boldsymbol{x} \neq \mathbf{0}$ causes an increase in the function, that is $V(\tilde{\boldsymbol{x}} + \Delta\boldsymbol{x}) > V(\tilde{\boldsymbol{x}})$. Similarly a given stationary point $\tilde{\boldsymbol{x}}$ corresponds to a maximum, Figure 6.19b, if any small disturbance $\Delta\boldsymbol{x} \neq \mathbf{0}$ causes a decrease in the function, that is $V(\tilde{\boldsymbol{x}} + \Delta\boldsymbol{x}) < V(\tilde{\boldsymbol{x}})$. The mathematical condition for checking whether a function has a maximum or minimum at a stationary point can be derived by expanding $V(\boldsymbol{x})$ by a Taylor series to give

$$V(\tilde{\boldsymbol{x}} + \Delta\boldsymbol{x}) \cong V(\tilde{\boldsymbol{x}}) + \Delta\boldsymbol{x}^{\mathrm{T}}\,[\text{grad } V] + \frac{1}{2}\Delta\boldsymbol{x}^{\mathrm{T}}\boldsymbol{H}\Delta\boldsymbol{x} + \cdots \tag{6.10}$$

where $\boldsymbol{H} = \left[\partial^2 V/\partial x_i \partial x_j\right]$ is the *Hessian matrix*. At the stationary points, grad $V(\tilde{\boldsymbol{x}}) = \mathbf{0}$ and the increment in $V(\boldsymbol{x})$ caused by the disturbance can be found as

$$\Delta V = V(\tilde{\boldsymbol{x}} + \Delta\boldsymbol{x}) - V(\tilde{\boldsymbol{x}}) \cong \frac{1}{2}\Delta\boldsymbol{x}^{\mathrm{T}}\boldsymbol{H}\Delta\boldsymbol{x} = \sum_{i=1}^{N}\sum_{j=1}^{N} h_{ij}\Delta x_i \Delta x_j, \tag{6.11}$$

where h_{ij} is the (i, j) element of matrix $\boldsymbol{H}$. This equation shows that the increment in V is equal to the quadratic form of the state variables constructed using the Hessian matrix. Sylvester's theorem (Bellman, 1970) states that such a quadratic form has a minimum at a given stationary point if, and

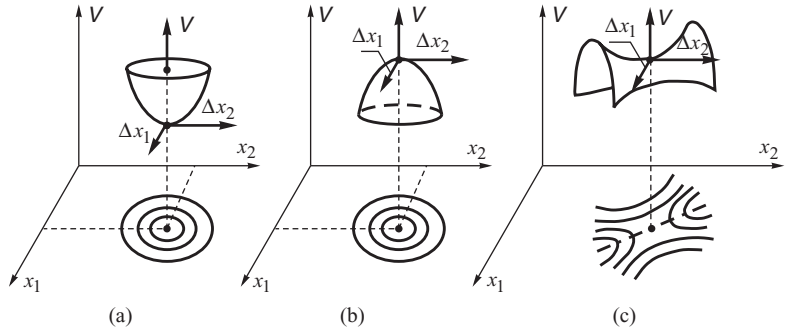

Figure 6.19 A scalar function of two variables with three types of stationary points: (a) minimum; (b) maximum; (c) saddle point.

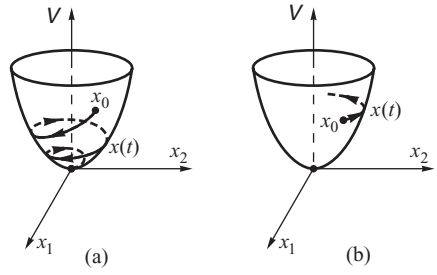

Figure 6.20 Illustration of Lyapunov's theorems on stability: (a) asymptotic stability; (b) instability.

only if, all leading principal minors of the matrix $\boldsymbol{H}$ are positive, Figure 6.19a. The matrix is then referred to as *positive definite*. If all leading principal minors of $\boldsymbol{H}$ are negative then the matrix is *negative definite* and the quadratic form has a maximum at a given stationary point, Figure 6.19b. If some leading principal minors are positive and some negative then the matrix is *non-definite* and the quadratic form has a saddle point at the stationary point, Figure 6.19c. The dot–dashed line at the bottom of Figure 6.19c shows a ridge line of the saddle going through the saddle point. As the gradient perpendicular to the ridge line is zero for each point on the ridge, function $V(\boldsymbol{x})$ reaches a local maximum in that direction for each point on the ridge. The function reaches a local minimum, in the direction along the ridge line, exactly at the saddle point.

As the scalar function $V(\boldsymbol{x})$ is defined in the state space, each point on the system trajectory $\boldsymbol{x}(t)$ corresponds to a value of $V(\boldsymbol{x}(t))$. The rate of change of $V(\boldsymbol{x})$ along the system trajectory (i.e. the derivative $\mathrm{d}V/\mathrm{d}t$) can be expressed as

$$\dot{V} = \frac{\mathrm{d}V}{\mathrm{d}t} = \frac{\partial V}{\partial x_1}\frac{\mathrm{d}x_1}{\mathrm{d}t} + \frac{\partial V}{\partial x_2}\frac{\mathrm{d}x_2}{\mathrm{d}t} + \cdots + \frac{\partial V}{\partial x_n}\frac{\mathrm{d}x_n}{\mathrm{d}t} = [\mathrm{grad}\, V(x)]^{\mathrm{T}}\,\dot{\boldsymbol{x}} = [\mathrm{grad}\, V(\boldsymbol{x})]^{\mathrm{T}}\,\boldsymbol{F}(\boldsymbol{x}). \qquad (6.12)$$

To introduce the direct (or second) Lyapunov method, assume that a positive definite scalar function $V(\boldsymbol{x})$ has a stationary point (minimum) at the equilibrium point $\tilde{\boldsymbol{x}} = \hat{\boldsymbol{x}}$. Any disturbance $\Delta\boldsymbol{x} \neq \boldsymbol{0}$ will move the system trajectory to an initial point $\boldsymbol{x}_0 \neq \hat{\boldsymbol{x}}$ as illustrated in Figure 6.20. If the system is asymptotically stable, as in Figure 6.20a, then the trajectory $\boldsymbol{x}(t)$ will tend towards the equilibrium point and $V(\boldsymbol{x})$ will decrease along the trajectory until $\boldsymbol{x}(t)$ settles at the minimum point $\tilde{\boldsymbol{x}} = \hat{\boldsymbol{x}}$. If the system is unstable, Figure 6.20b, then the trajectory will move away from the equilibrium point and $V(\boldsymbol{x})$ will increase along the trajectory. The essence of these considerations is summarized in Lyapunov's stability theorem:

> Let $\hat{\boldsymbol{x}}$ be an equilibrium point of a dynamic system $\dot{\boldsymbol{x}} = \boldsymbol{F}(\boldsymbol{x})$. Point $\hat{\boldsymbol{x}}$ is stable if there is a continuously differentiable positive definite function $V(\boldsymbol{x})$ such that $\dot{V}(\boldsymbol{x}) \leq 0$. Point $\hat{\boldsymbol{x}}$ is asymptotically stable if $\dot{V}(\boldsymbol{x}) < 0$.

One of the main attractions of Lyapunov's theorem is that it can be used to obtain an assessment of system stability without the need to solve the differential equation (6.9). The main problem is how to find a suitable positive definite Lyapunov function $V(\boldsymbol{x})$ for which the sign of the derivative $\dot{V}(\boldsymbol{x})$ can be determined without actually determining the system trajectory.

Generally the Lyapunov function $V(\boldsymbol{x})$ will be nonlinear and may have more than one stationary point. Figure 6.21 illustrates this using two functions of one variable: one which has three stationary points, Figure 6.21a, and one which has two stationary points, Figure 6.21b. Assume that in both cases the first of the stationary points corresponds to the equilibrium point $\tilde{\boldsymbol{x}}_1 = \hat{\boldsymbol{x}}$. The Lyapunov function determines the stability only if there is no other stationary point $\tilde{\boldsymbol{x}}_2$ between the initial

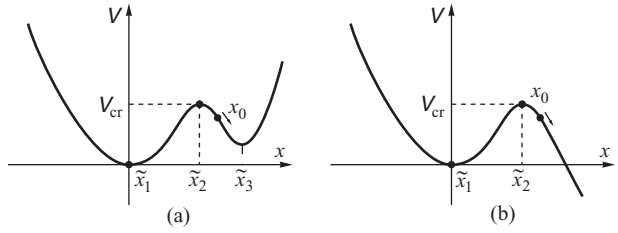

Figure 6.21 Examples of nonlinear functions with more than one stationary point.

point $\boldsymbol{x}_0 = \boldsymbol{x}(t = 0)$ and the equilibrium point $\tilde{\boldsymbol{x}}_1 = \hat{\boldsymbol{x}}$. If the initial point $\boldsymbol{x}_0$ is beyond the second stationary point $\tilde{\boldsymbol{x}}_2$ then the condition $\dot{V}(\boldsymbol{x}) < 0$ may mean that the system trajectory will tend towards another stationary point, Figure 6.21a, or run away, as in Figure 6.21b. The value of $V(\boldsymbol{x})$ at the nearest stationary point $\tilde{\boldsymbol{x}}_2 \neq \hat{\boldsymbol{x}}$ is referred to as the *critical value* of the Lyapunov function. These considerations lead to the following theorem:

> If there is a positive definite scalar function $V(\boldsymbol{x})$ in the vicinity of the equilibrium point $\hat{\boldsymbol{x}}$ of a dynamic system $\dot{\boldsymbol{x}} = \boldsymbol{F}(\boldsymbol{x})$ and the time derivative of this function is negative ($\dot{V}(\boldsymbol{x}) < 0$), then the system is asymptotically stable at $\hat{\boldsymbol{x}}$ for any initial conditions satisfying
>
> $$V(\boldsymbol{x}_0) < V_{cr}, \tag{6.13}$$
>
> where $V_{cr} = V(\tilde{\boldsymbol{x}} \neq \hat{\boldsymbol{x}})$ is the value of the Lyapunov function at the nearest stationary point.

It is important to realize that the stability conditions due to Lyapunov's theorems are only sufficient. Failure of the candidate Lyapunov function to satisfy the stability conditions does not mean that the equilibrium point is not stable. Moreover, for any given dynamic system there are usually many possible Lyapunov functions each of which gives a larger, or smaller, area of initial conditions that satisfies the stability theorems. This means that a particular Lyapunov function usually gives a pessimistic assessment of stability because it covers only a portion of the actual stability area. The function giving the largest area, and at the same time being closest to the actual stability area, is referred to as a *good Lyapunov function*. Usually good Lyapunov functions have a physical meaning.

6.3.2 Energy-Type Lyapunov Function

In Section 5.4, Equation (5.45) showed that the integral of the acceleration power is proportional to the work done by the acceleration torque. The proportionality constant ω_s was neglected and the integral of power was treated as 'work' or 'energy'. A similar approach will be adopted here.

6.3.2.1 Energy Function

Assume that the generator can be represented by the classical model defined by Equations (5.15) and (5.40) when the equation describing the generator–infinite busbar system is

$$M\frac{\mathrm{d}\Delta\omega}{\mathrm{d}t} = P_m - b\sin\delta' - D\frac{\mathrm{d}\delta'}{\mathrm{d}t}, \tag{6.14}$$

where $b = E'V_s/x'_d$ is the amplitude of the transient power–angle curve $P_{E'}(\delta')$ and $\Delta\omega = \mathrm{d}\delta'/\mathrm{d}t = \mathrm{d}\delta/\mathrm{d}t$ is the speed deviation. This equation has two equilibrium points:

$$(\hat{\delta}'_s; \Delta\hat{\omega} = 0) \quad \text{and} \quad (\hat{\delta}'_u = \pi - \hat{\delta}'_s; \Delta\hat{\omega} = 0). \tag{6.15}$$

Multiplying Equation (6.14) by $\Delta\omega$, neglecting the damping term and moving the right hand side to the left gives

$$M\Delta\omega\frac{\mathrm{d}\Delta\omega}{\mathrm{d}t} - (P_\mathrm{m} - b\sin\delta')\frac{\mathrm{d}\delta'}{\mathrm{d}t} = 0. \tag{6.16}$$

As the function on the left hand side of this equation is equal to zero, its integral must be constant. Integrating the function from the first of the equilibrium points defined in Equation (6.15) to any point on the system transient trajectory gives

$$V = \int_0^{\Delta\omega} (M\Delta\omega)\,\mathrm{d}\Delta\omega - \int_{\hat{\delta}'_\mathrm{s}}^{\delta'} (P_\mathrm{m} - b\sin\delta')\mathrm{d}\,\delta' = \text{constant}. \tag{6.17}$$

Evaluating the integrals gives the following form of the function:

$$V = \frac{1}{2}M\Delta\omega^2 - [P_\mathrm{m}(\delta' - \hat{\delta}'_\mathrm{s}) + b(\cos\delta' - \cos\hat{\delta}'_\mathrm{s})] = E_\mathrm{k} + E_\mathrm{p} = E, \tag{6.18}$$

where

$$E_\mathrm{k} = \frac{1}{2}M\Delta\omega^2, \quad E_\mathrm{p} = -[P_\mathrm{m}(\delta' - \hat{\delta}'_\mathrm{s}) + b(\cos\delta' - \cos\hat{\delta}'_\mathrm{s})]. \tag{6.19}$$

E_k is a measure of the system kinetic energy while E_p is a measure of potential energy, both taken with respect to the first equilibrium point ($\hat{\delta}'_\mathrm{s}$, $\Delta\hat{\omega} = 0$) and, for the remainder of this chapter, will be treated as energy. By neglecting damping, Equation (6.17) shows that the sum of potential and kinetic energy $V = E_\mathrm{k} + E_\mathrm{p}$ is constant.

It is now necessary to check whether the function V, defined by Equation (6.18), satisfies the definition of a Lyapunov function, that is whether: (i) it has stationary points at the equilibrium points defined in Equation (6.15); (ii) it is positive definite in the vicinity of one of the equilibrium points; and (iii) its derivative is not positive ($\dot{V} \leq 0$).

The first of the conditions can be checked by calculating the gradient of V. Differentiating Equation (6.18) gives

$$\text{grad}\,V = \begin{bmatrix} \dfrac{\partial V}{\partial\Delta\omega} \\ \dfrac{\partial V}{\partial\delta'} \end{bmatrix} = \begin{bmatrix} \dfrac{\partial E_\mathrm{k}}{\partial\Delta\omega} \\ \dfrac{\partial E_\mathrm{p}}{\partial\delta'} \end{bmatrix} = \begin{bmatrix} M\Delta\omega \\ -(P_\mathrm{m} - b\sin\delta') \end{bmatrix}. \tag{6.20}$$

This gradient is equal to zero at the stationary points where $\Delta\tilde{\omega} = 0$ and the electrical power is equal to mechanical power given by

$$\tilde{\delta}'_1 = \hat{\delta}'_\mathrm{s}, \quad \tilde{\delta}'_2 = \pi - \hat{\delta}'_\mathrm{s}. \tag{6.21}$$

Both these points are the equilibrium points of Equation (6.14).

The second condition can be checked by determining the Hessian matrix given by

$$\boldsymbol{H} = \begin{bmatrix} \dfrac{\partial^2 V}{\partial\Delta\omega^2} & \dfrac{\partial^2 V}{\partial\Delta\omega\,\partial\delta'} \\ \dfrac{\partial^2 V}{\partial\delta'\,\partial\Delta\omega} & \dfrac{\partial^2 V}{\partial\delta'^2} \end{bmatrix} = \begin{bmatrix} M & 0 \\ 0 & b\cos\delta' \end{bmatrix}. \tag{6.22}$$

Sylvester's theorem says that this matrix is positive definite when $M > 0$ (which is always true) and when $b \cos \delta' > 0$, which is true for $|\delta'| < \pi/2$ and holds for the first stationary point $\hat{\delta}'_1 = \hat{\delta}'_s$. Thus the function V is positive definite at the first equilibrium point $\hat{\delta}'_s$.

The third condition can be checked by determining $\dot{V} = \mathrm{d}V/\mathrm{d}t$ along the trajectory of Equation (6.14). As V represents the total system energy, its derivative $\dot{V} = \mathrm{d}V/\mathrm{d}t$ corresponds to the rate at which energy is dissipated by the damping. This can be proved by expressing the derivative of V as

$$\dot{V} = \frac{\mathrm{d}V}{\mathrm{d}t} = \frac{\mathrm{d}E_\mathrm{k}}{\mathrm{d}t} + \frac{\mathrm{d}E_\mathrm{p}}{\mathrm{d}t}. \tag{6.23}$$

The derivative of the kinetic energy can be calculated from Equation (6.18) as

$$\frac{\mathrm{d}E_\mathrm{k}}{\mathrm{d}t} = \frac{\partial E_\mathrm{k}}{\partial \Delta\omega}\frac{\mathrm{d}\Delta\omega}{\mathrm{d}t} = M\Delta\omega\frac{\mathrm{d}\Delta\omega}{\mathrm{d}t} = \left[M\frac{\mathrm{d}\Delta\omega}{\mathrm{d}t}\right]\Delta\omega. \tag{6.24}$$

The factor in the square brackets corresponds to left hand side of Equation (6.14). Replacing it by the right hand side gives

$$\frac{\mathrm{d}E_\mathrm{k}}{\mathrm{d}t} = \frac{\partial E_\mathrm{k}}{\partial \Delta\omega}\frac{\mathrm{d}\Delta\omega}{\mathrm{d}t} = +[P_\mathrm{m} - b\sin\delta']\Delta\omega - D\Delta\omega^2. \tag{6.25}$$

Differentiating the potential energy defined by Equation (6.18) gives

$$\frac{\mathrm{d}E_\mathrm{p}}{\mathrm{d}t} = \frac{\partial E_\mathrm{p}}{\partial \delta'}\frac{\mathrm{d}\delta'}{\mathrm{d}t} = -[P_\mathrm{m} - b\sin\delta']\Delta\omega. \tag{6.26}$$

Substituting Equations (6.25) and (6.26) into Equation (6.14) yields

$$\dot{V} = \frac{\mathrm{d}V}{\mathrm{d}t} = -D\Delta\omega^2, \tag{6.27}$$

which illustrates how the total system energy decays at a rate proportional to the damping coefficient ($D > 0$) and the square of the speed deviation ($\Delta\omega^2$). As $\dot{V} < 0$, the function $V(\delta', \Delta\omega)$ is a Lyapunov function and the first equilibrium point $\hat{\delta}'_s$ is asymptotically stable.

The second equilibrium point $\hat{\delta}'_u = \pi - \hat{\delta}'_s$ is unstable because the matrix $\boldsymbol{H}$, Equation (6.22), calculated at this point is not positive definite.

6.3.3 Transient Stability Area

The critical value of the Lyapunov function V introduced in Equation (6.13) corresponds to the value of V at the nearest stationary point which, for the system considered here, is equal to the second equilibrium point ($\pi - \hat{\delta}'_s$, $\Delta\hat{\omega} = 0$). Substituting these values into Equation (6.18) gives

$$V_\mathrm{cr} = 2b\cos\hat{\delta}'_s - P_\mathrm{m}(\pi - 2\hat{\delta}'_s). \tag{6.28}$$

According to Equation (6.13), the generator–infinite busbar system is stable for all initial conditions (δ'_0, $\Delta\omega_0$) satisfying the condition

$$V(\delta'_0, \Delta\omega_0) < V_\mathrm{cr}. \tag{6.29}$$

In this context the initial conditions are the values of the transient rotor angle and the rotor speed deviation at the instant of fault clearance when the generator starts to swing freely.

Careful examination of Equation (6.28) shows that the critical value of the Lyapunov function (total system energy) depends on the stable equilibrium point $\hat{\delta}'_s$ which, in turn, depends on the generator load P_m. At no load, when $\hat{\delta}'_s = 0$, the value of V_cr is greatest. Increasing the load on

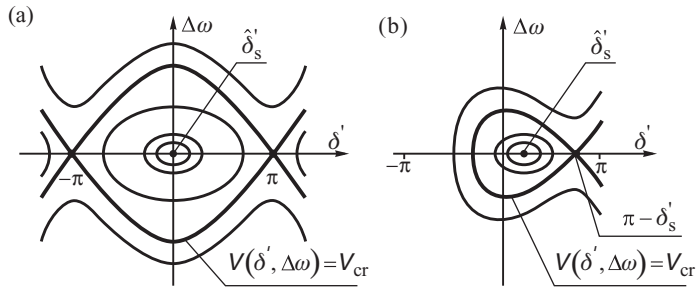

Figure 6.22 Equiscalar contours of the total system energy for the two equilibrium points: (a) $\hat{\delta}'_s = 0$; (b) $\hat{\delta}'_s < \pi/2$.

the generator, and hence $\hat{\delta}'_s$, reduces V_{cr} until, for $\hat{\delta}'_s = \pi/2$, its value is $V_{cr} = 0$. Figure 6.22 shows equiscalar contours $V(\delta', \Delta\omega) =$ constant on the phase plane $\Delta\omega$ vs δ'.

Figure 6.22a shows the case $\hat{\delta}'_s = 0$. For small values of $V(\delta', \Delta\omega) < V_{cr}$ the equiscalar contours $V(\delta', \Delta\omega) =$ constant are closed around the equilibrium point $\hat{\delta}'_s = 0$. The critical value $V(\delta', \Delta\omega) = V_{cr}$ corresponds to the closed contour shown in bold crossing the stationary points $\pm\pi$ equal to the unstable equilibrium points. As the equiscalar energy increases, the contours start to open up. The equilibrium point $\hat{\delta}'_s = 0$ is the point of minimum total energy while the stationary points $\pm\pi$ are the saddle points. Now assume that at the instant of fault clearance (i.e. at the initial point δ'_0, $\Delta\omega_0$) the system trajectory is inside the contour $V(\delta', \Delta\omega) < V_{cr}$. If damping is neglected then, according to Equation (6.27), the value of $V(\delta', \Delta\omega)$ remains constant and the trajectory will be a closed curve with $V(\delta', \Delta\omega) = V(\delta'_0, \Delta\omega_0) =$ constant. If damping is included, $D > 0$, then $V(\delta', \Delta\omega)$ will decrease with time and the trajectory will tend to spiral in towards the equilibrium point $\hat{\delta}'_s = 0$.

Figure 6.22b shows the case of $\hat{\delta}'_s > 0$ but less than $\pi/2$. In this case the curve $V(\delta', \Delta\omega) = V_{cr} =$ constant corresponds to a contour crossing the stationary point $(\pi - \hat{\delta}'_s)$ equal to the unstable equilibrium point. The area enclosed by this boundary contour is now much smaller than before.

If, at the instant of fault clearance, the transient stability condition (6.29) is satisfied then the calculated value of the total energy $V_0 = V(\delta'_0, \Delta\omega_0)$ can be used to calculate a *transient stability margin*

$$K_{\text{energy}} = \frac{V_{cr} - V_0}{V_{cr}}, \tag{6.30}$$

which describes the relative difference between the critical value of the total energy (transient stability boundary) and the energy released by the disturbance. K_{energy} determines the distance from the actual contour to the boundary contour of the transient stability area in terms of energy.

6.3.4 Equal Area Criterion

The equal area criterion was introduced in Equation (6.6) as a means of assessing transient stability and, like the Lyapunov stability condition in Equation (6.29), is also based on energy considerations. Both approaches can be shown to be equivalent by considering Figure 6.23 which shows the same three-phase fault as that illustrated in Figures 6.1 and 6.2a.

The first term of the energy-based Lyapunov function defined in Equation (6.18) corresponds to the kinetic energy

$$\frac{1}{2} M\Delta\omega^2 = \text{area 1–2–3–4} = \text{area A}. \tag{6.31}$$

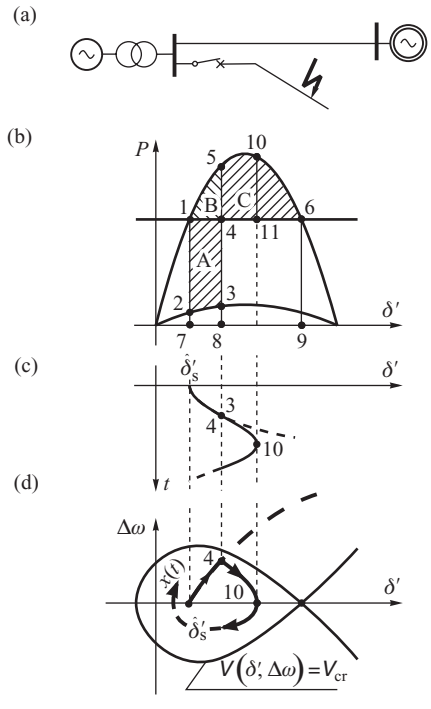

Figure 6.23 Equivalence between the Lyapunov direct method and the equal area criterion: (a) schematic diagram of the system; (b) transient power–angle characteristics with acceleration and deceleration areas; (c) angle variation; (d) stability area and trajectory of rotor motion.

The second component, equal to potential energy, can be expressed as

$$-\int_{\hat{\delta}'_s}^{\delta'} (P_m - b\sin\delta')\mathrm{d}\delta' = -[\text{area } 1\text{–}7\text{–}8\text{–}4 - \text{area } 1\text{–}7\text{–}8\text{–}5] = \text{area B}. \tag{6.32}$$

The Lyapunov function is equal to the sum of the two components:

$$V(\delta', \Delta\omega) = \text{area A} + \text{area B}. \tag{6.33}$$

The critical value of the Lyapunov function is equal to the value of the potential energy at the unstable equilibrium point, that is

$$V_{cr} = -\int_{\hat{\delta}'_s}^{\pi-\hat{\delta}'_s} (P_m - b\sin\delta')\mathrm{d}\delta' = \text{area } 1\text{–}7\text{–}9\text{–}6\text{–}5 - \text{area } 1\text{–}7\text{–}9\text{–}6 = \text{area B} + \text{area C}. \tag{6.34}$$

Thus, the stability condition $V(\delta'_0, \Delta\omega_0) < V_{cr}$ can be expressed as

$$\text{area A} + \text{area B} < \text{area B} + \text{area C} \quad \text{or} \quad \text{area A} < \text{area C}, \tag{6.35}$$

which is equivalent to the equal area criterion.

The equiscalar contour $V(\delta', \Delta\omega) = V_{cr}$ in the $(\delta', \Delta\omega)$ plane determines the stability area, Figure 6.23c. If, during the short circuit, the trajectory $\boldsymbol{x}(t)$ is contained within the area then, after clearing the fault, the trajectory will remain within the area and the system is stable. When $D > 0$ the trajectory tends towards the equilibrium point and the system is asymptotically stable. As the clearing time increases, the initial point approaches the critical contour and reaches it when the fault time is equal to the critical clearing time. If the clearing time is longer than this then area A > area C, the trajectory leaves the stability area and the system is unstable.

For the case considered here the transient stability margin defined in Equation (6.30) is equal to

$$K_{\text{energy}} = \frac{V_{cr} - V_0}{V_{cr}} = \frac{\text{area B} + \text{area C} - \text{area A}}{\text{area B} + \text{area C}} = \frac{\text{area 10–6–11}}{\text{area 1–5–6}} = K_{\text{area}}, \tag{6.36}$$

which is exactly the same as the transient stability margin defined by the equal area criterion in Equation (6.7). Consequently, for the generator–infinite busbar system, the equal area criterion is equivalent to the Lyapunov direct method based on an energy-type Lyapunov function.

6.3.5 *Lyapunov Direct Method for a Multi-Machine System*

In a simplified stability analysis each generator is modelled by employing the classical model, that is by using the swing equation and constant emf behind the transient reactance. The swing equations for all generators can be written as

$$\frac{\mathrm{d}\delta_i'}{\mathrm{d}t} = \Delta\omega_i, \tag{6.37a}$$

$$M_i \frac{\mathrm{d}\Delta\omega_i}{\mathrm{d}t} = P_{\mathrm{m}i} - P_i(\delta') - D_i \Delta\omega_i, \tag{6.37b}$$

where δ_i' and $\Delta\omega_i$ are the transient power angle and rotor speed deviation respectively, $P_{\mathrm{m}i}$ and $P_i(\boldsymbol{\delta}')$ are the mechanical and electrical power, $\boldsymbol{\delta}'$ is the vector of all transient power angles in the system, D_i is the damping coefficient and M_i is the inertia coefficient (Section 5.1), $i = 1, \ldots, N$.

Transient reactances of generators are included in the network model. All the network elements (lines and transformers) are modelled by their π equivalents. For the simplified power system transient stability analysis, the transmission network is modelled explicitly while power injected from/to the distribution network is modelled as a load. Each such load is replaced by a constant nodal shunt admittance. The load nodes are denoted as $\{\mathrm{L}\}$. Fictitious generator nodes behind generator transient reactances are denoted as $\{\mathrm{G}\}$.

The resulting network model of a multi-machine system is described by the nodal admittance equation (Section 3.6). That model is then reduced by eliminating the $\{\mathrm{L}\}$ nodes using the elimination method described in Section 12.2. Once the load nodes $\{\mathrm{L}\}$ have been eliminated, the reduced network contains only the fictitious generator nodes $\{\mathrm{G}\}$. The reduced network is described by the following nodal admittance equation:

$$\underline{\boldsymbol{I}}_{\mathrm{G}} = \underline{\boldsymbol{Y}}_{\mathrm{G}} \underline{\boldsymbol{E}}_{G}. \tag{6.38}$$

Expanding this equation for the ith generator gives

$$\underline{I}_i = \sum_{j=1}^{N} \underline{Y}_{ij} \underline{E}_j, \tag{6.39}$$

where $\underline{E}_j = E_j \mathrm{e}^{\mathrm{j}\delta_j'}$ and $\underline{Y}_{ij} = G_{ij} + \mathrm{j}B_{ij}$ are the elements of the reduced admittance matrix. It should be remembered that the off-diagonal elements of the nodal admittance matrix are taken with a minus sign and correspond to admittances of branches linking the nodes. Hence $\underline{y}_{ij} = -\underline{Y}_{ij}$ is the admittance of the equivalent branch linking nodes i, j. Such a branch linking fictitious generator

nodes i and j is referred to as the *transfer branch* while the corresponding admittance $\underline{y}_{ij}$ is referred to as the *transfer admittance*.

Equations expressing nodal injections (here also power generated) corresponding to the currents expressed by (6.39) are analogous to Equations (3.156) described in Section 3.6, that is

$$P_i = E_i^2 G_{ii} + \sum_{j \neq i}^{N} E_i E_j G_{ij} \cos(\delta_i' - \delta_j') + \sum_{j \neq i}^{N} E_i E_j B_{ij} \sin(\delta_i' - \delta_j'), \tag{6.40}$$

or

$$P_i = P_{0i} + \sum_{j=1}^{N} b_{ij} \sin \delta_{ij}', \tag{6.41}$$

where $b_{ij} = E_i E_j B_{ij}$ is the magnitude of the power–angle characteristic for the transfer equivalent branch and

$$P_{0i} = E_i^2 G_{ii} + \sum_{j \neq i}^{N} E_i E_j G_{ij} \cos(\delta_i' - \delta_j'). \tag{6.42}$$

Generally P_{0i} depends on power angles δ_i' and is not constant during the transient period when the rotors are swinging. Stability analysis of the multi-machine system by the Lyapunov direct method is straightforward assuming that $P_{0i} \cong P_{0i}(\hat{\boldsymbol{\delta}}') =$ constant, that is the power is constant and equal to its value at the stable equilibrium point, where

$$P_{0i}(\hat{\boldsymbol{\delta}}') = E_i^2 G_{ii} + \sum_{j \neq i}^{N} E_i E_j G_{ij} \cos(\hat{\delta}_i' - \hat{\delta}_j'). \tag{6.43}$$

That assumption in practice means that transmission losses in transfer branches are assumed to be constant and added to the equivalent loads connected at the fictitious generator nodes.

The simplified power system model resulting from Equations (6.37) and (6.41) can be summarized in the following set of state-space equations:

$$\frac{\mathrm{d}\delta_i'}{\mathrm{d}t} = \Delta\omega_i, \tag{6.44a}$$

$$M_i \frac{\mathrm{d}\Delta\omega_i}{\mathrm{d}t} = (P_{\mathrm{m}i} - P_{0i}) - \sum_{j=1}^{n} b_{ij} \sin \delta_{ij}' - D_i \Delta\omega_i. \tag{6.44b}$$

The third component on the right hand side of Equation (6.44b) dissipates energy. No energy is dissipated in the transmission network because power losses on transfer conductances have been added to the equivalent loads as constant values. Such a model is referred to as the *conservative model*.

Neglecting rotor damping, Equation (6.44b) can be written as

$$M_i \frac{\mathrm{d}\Delta\omega_i}{\mathrm{d}t} - (P_{\mathrm{m}i} - P_{0i}) + \sum_{j=1}^{N} b_{ij} \sin \delta_{ij}' = 0. \tag{6.45}$$

As the right hand side of this equation is equal to zero, integrating gives a constant value $V(\hat{\boldsymbol{\delta}}', \Delta\omega) = E_\mathrm{k} + E_\mathrm{p}$ equal to the system energy, where

$$E_\mathrm{k} = \sum_{i=1}^{N} \int_0^{\omega_i} M_i \Delta\omega_i \mathrm{d}\omega_i = \frac{1}{2} \sum_{i=1}^{N} M_i \Delta\omega_i^2, \tag{6.46}$$

$$E_\mathrm{p} = -\sum_{i=1}^{N} \int_{\hat{\delta}_i'}^{\delta_i'} (P_{\mathrm{m}i} - P_{0i}) \mathrm{d}\delta_i' + \sum_{i=1}^{N} \int_{\hat{\delta}_i'}^{\delta_i'} \left(\sum_{j=1}^{N} b_{ij} \sin \delta_{ij}' \right) \mathrm{d}\delta_i', \tag{6.47}$$

where $\hat{\delta}_i'$ is the power angle at the postfault stable equilibrium point, while E_k and E_p are the kinetic and potential energy of the power system conservative model. As damping has been neglected, the model does not dissipate energy and the total energy, equal to the sum of the kinetic and potential energy, is constant (the conservative model).

There is a double summation in (6.47) that corresponds to a summation of elements of the square matrix

$$\begin{array}{c} \\ i \\ j \\ \\ \end{array} \begin{array}{c} \begin{array}{cccc} & i & & j \end{array} \\ \begin{bmatrix} \ddots & \vdots & \vdots & \\ \cdots & 0 & b_{ij} \sin \delta_{ij}' & \cdots \\ \cdots & b_{ji} \sin \delta_{ji}' & 0 & \cdots \\ & \vdots & \vdots & \ddots \end{bmatrix} \end{array}. \tag{6.48}$$

The diagonal elements of the matrix are equal to zero because $\sin \delta_{ii}' = \sin(\delta_i' - \delta_i') = \sin 0 = 0$. The lower off-diagonal elements have the same value as the upper elements but with an inverted sign because $\sin \delta_{ij}' = -\sin \delta_{ji}'$. Hence

$$\int \sin \delta_{ij}' \, \mathrm{d}\delta_i' + \int \sin \delta_{ji}' \, \mathrm{d}\delta_j' = \int \sin \delta_{ij}' \, \mathrm{d}\delta_i' - \int \sin \delta_{ij}' \, \mathrm{d}\delta_j' = \int \sin \delta_{ij}' \, \mathrm{d}\delta_{ij}' = -\cos \delta_{ij}'. \tag{6.49}$$

Thus instead of integrating both the upper and lower off-diagonal elements of the matrix with respect to $\mathrm{d}\delta_i'$, it is enough to integrate only the upper elements with respect to $\mathrm{d}\delta_{ij}'$. Consequently, the second component on the right hand side of (6.47) can be written as

$$\sum_{i=1}^{N} \int_{\hat{\delta}_i'}^{\delta_i'} \left(\sum_{j=1}^{n} b_{ij} \sin \delta_{ij}' \right) \mathrm{d}\delta_i' = -\sum_{i=1}^{N-1} \sum_{j=i+1}^{N} b_{ij} [\cos \delta_{ij}' - \cos \hat{\delta}_{ij}']. \tag{6.50}$$

Let us now consider indices in the sums on the right hand side of (6.50). As only the upper off-diagonal elements are summed, the summation is for $j > i$. Moreover, the last row may be neglected since it contains no upper off-diagonal elements. Hence the summation is for $i \leq (N-1)$.

Finally, Equation (6.47) gives

$$E_\mathrm{p} = \sum_{i=1}^{N} (P_{\mathrm{m}i} - P_{0i}) (\delta_i' - \hat{\delta}_i') - \sum_{i=1}^{N-1} \sum_{j=i+1}^{N} b_{ij} [\cos \delta_{ij}' - \cos \hat{\delta}_{ij}']. \tag{6.51}$$

The total system energy is equal to the sum of the kinetic and potential energy:

$$V(\boldsymbol{\delta}', \Delta\boldsymbol{\omega}) = E_{\mathrm{k}} + E_{\mathrm{p}}. \tag{6.52}$$

The necessary condition for this function to be a Lyapunov function is that it is positive definite and with a minimum (Figure 6.20) at the stationary point $\hat{\boldsymbol{\delta}}'; \Delta\hat{\boldsymbol{\omega}} = \mathbf{0}$. That point is also the equilibrium point of differential equations (6.44a) and (6.44b). Following considerations similar to those related to Equations (6.10) and (6.11), the condition is satisfied if the Hessian matrix of function (6.52) is positive definite. Hence it is necessary to investigate the Hessian matrices of the kinetic and potential energy.

The Hessian matrix of the kinetic energy $\boldsymbol{H}_{\mathrm{k}} = [\partial E_{\mathrm{k}}^2/\partial\Delta\omega_i\partial\Delta\omega_j] = \mathrm{diag}\,[M_i]$ is a positive definite diagonal matrix. Therefore function V_{k} given by Equation (6.46) is positive definite.

The Hessian matrix of the potential energy $\boldsymbol{H}_{\mathrm{p}} = [\partial E_{\mathrm{p}}^2/\partial\delta'_{iN}\partial\delta'_{iN}]$ is a square matrix that consists of the generator's self- and mutual synchronizing powers:

$$H_{ii} = \sum_{j=1}^{N-1} b_{ij}\cos\delta'_{ij}, \quad H_{ij} = -b_{ij}\cos\delta'_{ij}. \tag{6.53}$$

It will be shown in Section 12.2.2 that this matrix is positive definite for any stable equilibrium point such that, for all generator pairs, $|\delta'_{ij}| < \pi/2$. Therefore, in the vicinity of the postfault equilibrium point, the potential energy V_{p} given by Equation (6.51) is positive definite.

Since the total system energy $V(\hat{\boldsymbol{\delta}}', \Delta\boldsymbol{\omega})$ is the sum of two positive definite functions, it is also positive definite. It can be treated as a Lyapunov function for the system model defined in Equations (6.44a) and (6.44b) providing the time derivative $\mathrm{d}V/\mathrm{d}t$ along the system trajectory is negative. The time derivative $\mathrm{d}V/\mathrm{d}t$ of the function in (6.52) along any system trajectory can be expressed as

$$\dot{V} = \frac{\mathrm{d}V}{\mathrm{d}t} = \frac{\mathrm{d}E_{\mathrm{k}}}{\mathrm{d}t} + \frac{\mathrm{d}E_{\mathrm{p}}}{\mathrm{d}t}, \tag{6.54}$$

where

$$\frac{\mathrm{d}E_{\mathrm{k}}}{\mathrm{d}t} = \sum_{i=1}^{N} \frac{\partial E_{\mathrm{k}}}{\partial\Delta\omega_i}\frac{\mathrm{d}\Delta\omega_i}{\mathrm{d}t}, \tag{6.55}$$

$$\frac{\mathrm{d}E_{\mathrm{p}}}{\mathrm{d}t} = \sum_{i=1}^{N} \frac{\partial E_{\mathrm{p}}}{\partial\delta'_i}\frac{\mathrm{d}\delta'_i}{\mathrm{d}t} = \sum_{i=1}^{N} \frac{\partial E_{\mathrm{p}}}{\partial\delta'_i}\Delta\omega_i. \tag{6.56}$$

Differentiating Equations (6.46) and (6.47) gives

$$\frac{\partial E_{\mathrm{k}}}{\partial\Delta\omega_i} = M_i\Delta\omega_i, \tag{6.57}$$

$$\frac{\partial E_{\mathrm{p}}}{\partial\delta'_i} = -(P_{\mathrm{m}i} - P_{0i}) - \sum_{j\neq i}^{N} b_{ij}\sin\delta'_{ij}. \tag{6.58}$$

Substituting Equation (6.57) into (6.55) gives

$$\frac{\mathrm{d}E_{\mathrm{k}}}{\mathrm{d}t} = \sum_{i=1}^{N} \frac{\partial E_{\mathrm{k}}}{\partial\Delta\omega_i}\frac{\mathrm{d}\Delta\omega_i}{\mathrm{d}t} = \sum_{i=1}^{N} \Delta\omega_i M_i\frac{\mathrm{d}\Delta\omega_i}{\mathrm{d}t}. \tag{6.59}$$

Finally, substituting Equation (6.44b) into (6.59) gives the time derivative of V_k as

$$\frac{dE_k}{dt} = \sum_{i=1}^{N} \Delta\omega_i (P_{mi} - P_{0i}) - \sum_{i=1}^{N} \Delta\omega_i \sum_{j=1}^{N} b_{ij} \sin \delta'_{ij} - \sum_{i=1}^{N} D_i \Delta\omega_i^2. \tag{6.60}$$

Similarly the time derivative of the potential energy is obtained by substituting the relevant components in Equation (6.56) by (6.58) to give

$$\frac{dE_p}{dt} = -\sum_{i=1}^{N} \Delta\omega_i (P_{mi} - P_{0i}) + \sum_{i=1}^{N} \Delta\omega_i \sum_{j \neq i}^{N} b_{ij} \sin \delta'_{ij}. \tag{6.61}$$

The derivative of the potential energy expressed by this equation and the first two components of (6.60) are the same but with opposite sign. This indicates that there is a continuous exchange of energy between the potential and kinetic energy terms. Adding the two equations as required by Equation (6.54) gives

$$\dot{V} = \frac{dV}{dt} = \frac{dE_k}{dt} + \frac{dE_p}{dt} = -\sum_{i=1}^{N} D_i \Delta\omega_i^2. \tag{6.62}$$

That concludes the proof that function $V(\boldsymbol{\delta}', \Delta\boldsymbol{\omega})$ given by (6.52) and (6.46), (6.51) is a Lyapunov function and may be used to investigate the transient stability of a power system. The function was originally proposed by Gless (1966). There are also other functions which could be used for transient stability analysis of a multi-machine power system but their detailed treatment is beyond the scope of this book.

Similar to the generator–infinite busbar system discussed in Section 6.3.3, the stability condition for a given postfault state in a multi-machine power system is given by

$$V(\boldsymbol{\delta}'_0, \Delta\boldsymbol{\omega}_0) < V_{cr}, \tag{6.63}$$

where V_{cr} is the critical value of a Lyapunov function and $\boldsymbol{\delta}'_0$ and $\Delta\boldsymbol{\omega}_0$ are the initial conditions at the postfault state.

The critical value of a given Lyapunov function for the generator–infinite busbar system is calculated at the unstable equilibrium point (6.28). The main difficulty with the multi-machine system is that the number of unstable equilibrium points is very large. If a system has N generators then there is $(N - 1)$ relative power angles and there may even be 2^{N-1} equilibrium points, that is one stable equilibrium point and $(2^{N-1} - 1)$ unstable equilibrium points. For example, if $N = 11$ then $2^{10} = 1024$, that is over a thousand equilibrium points. If $N = 21$ then $2^{20} = 1\,048\,576$, that is over a million equilibrium points.

Although 2^{N-1} is the maximum number of equilibrium points that may exist, the actual number of equilibrium points depends on the system load. Figure 5.5 showed that, for the generator–infinite busbar system (i.e. for $N = 2$), there are $2^{2-1} = 2^1 = 2$ equilibrium points when the load is small. As the load increases, the equilibrium points tend towards each other and, for the pull-out power (steady-state stability limit), they become a single unstable equilibrium point. As the load increases further, there are no equilibrium points. Similarly, in a multi-machine power system, there may be a maximum number of 2^{N-1} equilibrium points when the load is small. As the load increases, the pairs of neighbouring stable and unstable equilibrium points tend towards each other until they become single points at the steady-state stability limit. When the load increases even further, the system loses stability and the equilibrium points vanish.

The choice of a proper unstable equilibrium point determining V_{cr} is difficult. Choosing the lowest unstable equilibrium point in which $V(\boldsymbol{\delta}')$ is smallest requires searching a large number of points and usually leads to a very pessimistic transient stability assessment. A more realistic transient

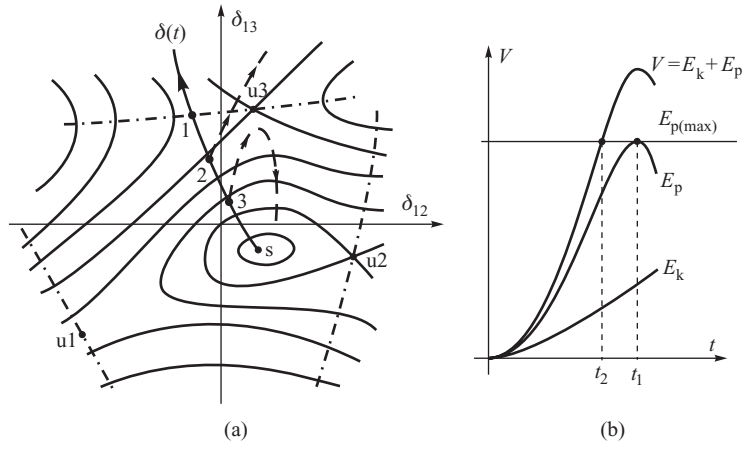

Figure 6.24 Illustration of potential boundary surface method.

stability assessment is obtained if V_{cr} is calculated assuming an unstable equilibrium point lying on the trajectory $\boldsymbol{\delta}'(t)$ enforced by a given disturbance. There are many methods of selecting such a point, each of them having their own advantages and disadvantages. Figure 6.24 illustrates the *potential boundary surface method* proposed by Athay, Podmore and Virmani (1979).

The solid lines in Figure 6.24a correspond to equiscalar lines of the potential energy for a three-machine system under certain loading conditions. The stable equilibrium point is denoted by the letters. There are three unstable equilibrium (saddle) points u1, u2, u3. Dot–dashed lines show the ridge lines of the saddles (see also Figure 6.19c). The ridge line of each saddle point corresponds to a different mode of losing the stability. The bold line shows the trajectory $\boldsymbol{\delta}'(t)$ following a sustained fault. The ridge line of saddle u3 is exceeded and that corresponds to generator 3 losing synchronism with respect to generators 1 and 2. If the trajectory exceeded the ridge line of saddle u2, it would mean that generator 2 had lost synchronism with respect to generators 1 and 2. If the trajectory exceeded the ridge line of saddle u1, it would mean that generator 1 had lost synchronism with respect to generators 2 and 3.

The potential energy increases on the way from the stable equilibrium point towards the ridge line of the saddle due to increased rotor angles. After the ridge line has been exceeded, the potential energy decreases. Figure 6.24b shows changes in the potential, kinetic and total energy corresponding to the trajectory $\boldsymbol{\delta}'(t)$ exceeding the ridge line of saddle u3 shown in Figure 6.24a. As the trajectory $\boldsymbol{\delta}'(t)$ corresponds to a sustained short circuit, the kinetic energy continues to increase during the fault because of rotor acceleration. The potential energy reaches its maximum at point 1 which corresponds to $E_{p(max)}$ in Figure 6.24b. The ridge line is usually flat in the vicinity of a saddle point. Hence it may be assumed that $E_p(u3) \cong E_{p(max)}$; that is, the potential energy at the saddle point u3 is equal to the maximum potential energy along the trajectory $\boldsymbol{\delta}'(t)$. Hence u3 is the sought unstable equilibrium point and it may be assumed that $V_{cr} = E_p(u3) \cong E_{p(max)}$. The system is stable for $V(\boldsymbol{\delta}'_0, \Delta\boldsymbol{\omega}_0) < E_{p(max)}$ which corresponds to the clearing time $t < t_2$ in Figure 6.24b. For clearing time $t = t_2$ the total energy (kinetic and potential) is slightly higher than the potential energy in u3 and the trajectory exceeds the ridge line of the saddle point u3. This is shown in Figure 6.24a by the dashed line from clearing point 2. For $t < t_2$ the total energy is too small to exceed the ridge line of the saddle point u3. The trajectory then changes direction and returns to the stable equilibrium point. This is shown in Figure 6.24a by the dashed line from clearing point 3. The conclusion is that the critical clearing time is slightly smaller than t_2.

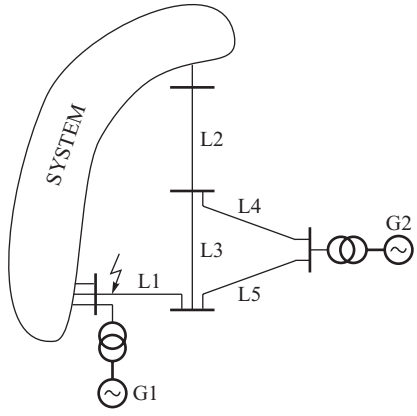

Figure 6.25 Example of a power system.

The potential boundary surface method is used to find the critical value of a Lyapunov function as the maximum value of potential energy along a trajectory following a sustained short circuit. The disadvantage of assuming a sustained fault is that the transient stability assessment may be misleading when the trajectory dramatically changes its direction after the fault is cleared. Consider, for example, a sustained fault in line L1 near generator G1 in Figure 6.25. The trajectory $\boldsymbol{\delta}'(t)$ tends towards the saddle point that corresponds to the loss of synchronism by generator G1. The rotor of G2 does not accelerate rapidly during the fault because the fault is remote and the generator is loaded by neighbouring loads. Generator G1 is strongly connected with the system so that the potential energy in the corresponding saddle point is high. Therefore the value of V_{cr} determined using the trajectory during the sustained fault is high and results in a large critical clearing time. Unfortunately this is not a correct transient stability assessment in the considered case. Right after the faulted line L1 is tripped, the swings of generator G1 are quickly damped. However, generator G2 loses synchronism because the tripped line L1 played a crucial role in the system. Once the line is tripped, G2 is connected to the system via a long transmission link L2, L3, L4, L5 and starts to lose synchronism. Trajectory $\boldsymbol{\delta}'(t)$ dramatically changes its direction and tends towards the saddle point corresponding to the loss of synchronism of generator G2. The potential energy at that point is small and the trajectory $\boldsymbol{\delta}'(t)$ will easily exceed the ridge line. This would correspond to the situation in Figure 6.24a when the trajectory starting at point 3 moves towards the ridge of saddle point u2 where the potential energy is small.

The critical value of a Lyapunov function that takes into account a dramatic change of trajectory direction can be determined using methods based on *coherency recognition* discussed in more detail in Chapter 14. A group of generators that have a similar dynamic response and rotor swings after a given disturbance are referred to as a *coherent group*. Finding groups of generators that are approximately coherent limits the number of unstable equilibrium points for which the ridge lines could be exceeded following a given disturbance. This could be explained using the example shown in Figure 6.25. Coherency recognition would show that generators G1 and G2 are not coherent with any other generator for the disturbance considered. Hence three possibilities of losing synchronism can be investigated: (1) generator G1 loses synchronism while G2 remains in synchronism with the rest of the system; (ii) generator G2 loses synchronism while G1 remains in synchronism with the rest of the system; (iii) generators G1 and G2 lose synchronism together. These three ways of losing synchronism correspond to three saddle points and their three ridge lines can be exceeded by the

trajectory $\delta'(t)$. The value of V_{cr} is determined from those three saddle points by choosing a point at which E_p is smallest. Such a choice, proposed by Machowski *et al.* (1986), gives a prudent transient stability assessment.

Application of the Lyapunov direct method for transient stability assessment has been discussed in a number of books, for example Pai (1981, 1989) or Pavella and Murthy (1994).

6.4 Synchronization

Section 4.4 described the electromagnetic dynamics occurring when a generator is synchronized to the system. This section expands this discussion to include the effect of the electromechanical dynamics that accompany synchronization and in determining those conditions necessary for resynchronization.

Consider the circuit shown in Figure 4.31. When the synchronizing switch is closed the resulting electromagnetic torque will attempt to pull the rotor into synchronization with the power system by either slowing down or accelerating the rotor until eventually the generator reaches its final equilibrium position defined by the steady-state rotor angle $\hat{\delta}_s = 0$ and the rotor speed $\omega = \omega_s$. To analyse these rotor dynamics, only the transient aperiodic component of the torque will be considered because the subtransient interval is normally too short to have any significant effect on the rotor swings. However, the subtransient torques are vital when determining shaft torque rating and fatigue strength as described in Section 4.2.7.

The generator is represented by the classical model, Equations (5.15) and (5.40). As the generator is on no load prior to synchronization, both $E' = E_f$ and $\delta = \delta'$ hold. Now consider the case illustrated in Figure 6.26 when all the synchronization conditions are satisfied apart from the phasors $\underline{V}_s$ and $\underline{E}_f$ being slightly out of phase, that is $P_m \approx 0$, $\omega_0 \approx \omega_s$ and $\delta'(t = 0^+) = \delta'_0 > 0$. When the synchronizing switch is closed the initial operating point lies at point 1 in Figure 6.26. The equilibrium point is defined by $P_m = P_e$ and $\hat{\delta}'_s = 0$, that is point 3. At the instant of synchronization $P_e(\delta') > 0$, the right hand side of the swing equation is negative, the rotor decelerates and the rotor

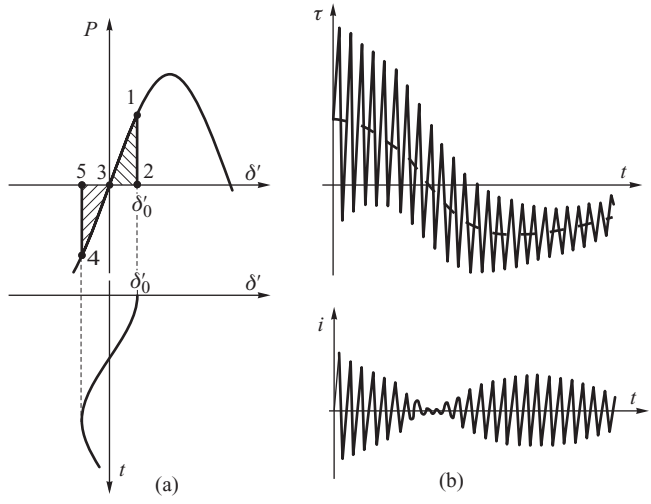

Figure 6.26 Synchronization when $\delta'_0 > 0$, $\omega_0 \approx \omega_s$: (a) power–angle characteristic and the swing curve; (b) time variation of the torque and current.

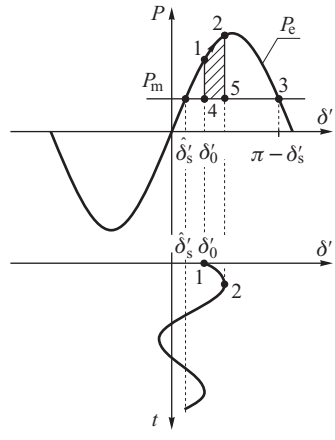

Figure 6.27 Equal area criterion applied to synchronization with $\omega_0 \neq \omega_s$ and $\delta'_0 > \delta'_s$.

angle δ' decreases. This causes the average value of the electrical torque and power to decrease with the energy used to decelerate the rotor being proportional to the shaded area 1–2–3. At the equilibrium point 3, rotor inertia effects ensure that the rotor angle continues to decrease towards negative δ' until it reaches point 4, where area 3–4–5 equals area 1–3–2. At point 4 the accelerating power is positive and the rotor swings back towards δ'_0. The oscillations continue until the damping torques cause the rotor to settle at its equilibrium angle $\hat{\delta}'_s = 0$.

Changes in δ' due to the swinging rotor produce corresponding oscillations in the torque and current as shown in Figure 6.26b. Initially, as δ' is large, the average value of the torque, shown by the dashed line, and the amplitude of the current are both large. As energy is dissipated in the windings, the generator changes from the subtransient state to the transient state and then to the steady state, and both the periodic components of the torque and the amplitude of the current vanish with time.

If at the instant of synchronization $\delta'_0 \neq 0$ and $\omega_0 \neq \omega_s$, then the changes in δ' may be much greater than those discussed above. Figure 6.27 shows a case when $\omega_0 > \omega_s$ and the rotor has an excess of kinetic energy. On closing the synchronizing switch, this excess kinetic energy will drive the rotor towards an increasing δ' along line 1–2 until the shaded area is equal to the excess kinetic energy. The rotor then swings back towards the equilibrium point $\hat{\delta}'_s$. The conditions necessary to achieve successful synchronization can be determined using the equal area criterion. At the instant of synchronization the rotor has an excess kinetic energy relative to the rotating reference frame (infinite busbar). This energy is equal to

$$E_k = \frac{1}{2} M \Delta\omega_0^2, \tag{6.64}$$

where M is the inertia coefficient and $\Delta\omega_0 = \dot{\delta}'(t = 0^+) = \omega_0 - \omega_s$.

The maximum deceleration work that can be done by the generator W_{max} is proportional to the area 4–1–2–3 in Figure 6.27:

$$W_{max} = \int_{\delta'_0}^{\pi - \hat{\delta}'_s} \left[\frac{E' V_s}{x'_d} \sin\delta' - P_m \right] d\delta' = \frac{E' V_s}{x'_d} (\cos\hat{\delta}'_s + \cos\delta'_0) - P_m[(\pi - \hat{\delta}'_s) - \delta'_0]. \tag{6.65}$$

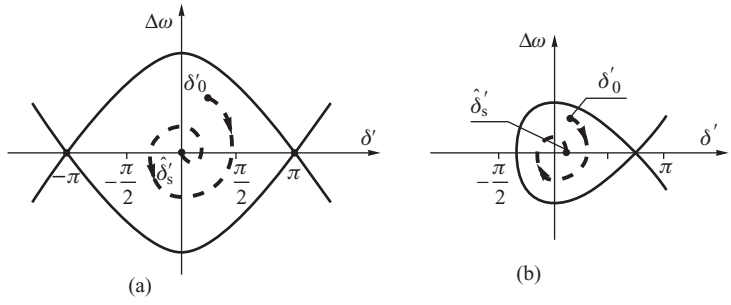

Figure 6.28 The trajectory of the operating point and the synchronization areas on the phase plane for: (a) $P_m = 0$; (b) $P_m = 0.5E'V_s/x'_d$.

The equal area criterion stipulates that the generator can be synchronized only if $E_k < W_{max}$. Using Equations (6.64) and (6.65), this gives

$$\Delta\omega_0^2 < \frac{2}{M}\left[\frac{E'V_s}{x'_d}(\cos\hat{\delta}'_s + \cos\delta'_0) - P_m(\pi - \hat{\delta}'_s - \delta'_0)\right]. \tag{6.66}$$

The maximum permissible value of $\Delta\omega_0$ depends on the synchronization angle δ'_0, the turbine power P_m and the parameters of the generator and transmission system as expressed by x'_d. Figure 6.28 shows two example areas on the phase plane diagram $(\Delta\omega, \delta)$ that satisfy the condition for successful synchronization as defined by Equation (6.66): one when $P_m = 0$ and the other when $P_m = 0.5E'V_s/x'_d$. The dashed lines show the trajectory of the operating point and the solid lines show the critical energy contours obtained from Equation (6.66) for the limiting conditions on δ'_0 and ω_0. Figure 6.28 shows that an increase in P_m has a detrimental effect on synchronization because the available decelerating area, defined by the area between P_m and P_e for $\delta'_0 < \delta' < \pi - \hat{\delta}'_s$, reduces as P_m increases. For $P_m > E'V_s/x'_d$ the system has no equilibrium point. Although it is unusual to synchronize a generator with the turbine developing large values of torque, similar conditions must be considered when synchronizing certain types of wind turbine (Westlake, Bumby and Spooner, 1996).

The condition defined by Equation (6.66) contains useful information regarding possible resynchronization after a fault is cleared by automatic reclosing action, Figures 6.7 and 6.8. In this case the value of the rotor angle and the speed deviation at the moment when the last switching occurs can be treated as the initial values δ_0 and $\Delta\omega_0$ in the synchronization process.

Section 6.3 showed that the equal area criterion is equivalent to the Lyapunov direct method when an energy-type Lyapunov function is used. The synchronization condition in Equation (6.66) can therefore be derived from the stability condition in Equation (6.29). The stability area shown in Figure 6.22 is the same as the synchronization area shown in Figure 6.28. When the synchronization condition in Equation (6.66) is not satisfied, and the point $(\delta_0, \Delta\omega_0)$ lies outside the synchronization area, then the generator will start to show *asynchronous operation*. This type of operation will be considered in the next section.

6.5 Asynchronous Operation and Resynchronization

The previous section explained how a generator may lose synchronism with the rest of the system when it makes asynchronous rotations at a slip frequency a few hertz above synchronous speed. With such high-speed changes the field winding time constant ensures that the net field winding flux linkage remains approximately constant so that the classical, constant flux linkage, generator model

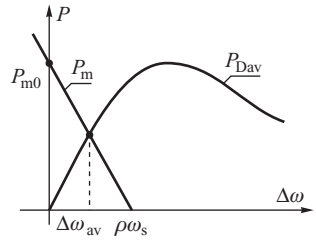

Figure 6.29 Static characteristics of the turbine power and damping power.

is valid with the synchronous power of the generator being given by $P_{E'}$, Equation (5.40). However, as $P_{E'}$ changes as $\sin\delta'$ and over one asynchronous rotation δ' goes through 360°, the average value of $P_{E'}$ over one rotation is zero. Furthermore, as the speed increases above synchronous the action of the turbine governing system comes into play, while the asynchronous damping torques, proportional to $\Delta\omega$, are also significant. Indeed, it is the interaction between the turbine–governor characteristic and the asynchronous damping torques that will determine the generator operating point.

As explained in Section 2.2.3, the turbine static characteristic $P_m(\Delta\omega)$ is a straight line of droop ρ which crosses the vertical power axis in Figure 6.29 at point P_{m0} and the horizontal speed deviation axis at point $\rho\omega_s$. The form of the average asynchronous, damping, power characteristic $P_{Dav}(\Delta\omega)$ was discussed in Section 5.2 and is also shown in Figure 6.29. As the average value of synchronous power $P_{E'}$ over each asynchronous rotation is zero, the intersection between the static turbine characteristic and the damping power characteristic will define the generator operating point during asynchronous operation.

6.5.1 Transition to Asynchronous Operation

In order to explain what happens when a generator loses synchronism with a system, consider the system shown in Figure 6.6. Now assume that a three-phase fault occurs on line L2 and is then cleared by tripping the faulted line (without auto-reclosing) after a time such that the acceleration area 1–2–3–4 shown in Figure 6.30a is larger than the available deceleration area 4–5–6. The dashed $P_{E'}(\delta')$ curve is valid for the prefault state while the solid $P(\delta')$ curve is valid for the postfault state. During the fault the rotor speed deviation increases, but when the fault is cleared it starts to fall. Synchronism is lost when the rotor passes point 6 and follows the lower part of the power–angle characteristic. The speed deviation quickly increases because of the large difference between the turbine power and the synchronous power, shown by the shaded area in Figure 6.30a. As the speed deviation increases, the turbine governing system starts to close the valves and the turbine mechanical power starts to decrease. Due to the long time constant of the turbine governing system, the dynamic turbine power $P_m(t)$ does not follow the static characteristic in Figure 6.30b but moves above it. With increased speed deviation the average damping power P_{Dav} increases, according to the characteristic shown in Figure 6.29. As P_{Dav} increases and P_m decreases, these two powers become equal at point B. Because of the delay introduced by the turbine time constants the mechanical power continues to decrease after passing point B and is now less than P_{Dav}. Consequently, the speed deviation starts to decrease and the turbine governor opens the valves to increase the turbine power until, at point C, the mechanical power and the asynchronous power are again equal. Again, because of the time delay in the turbine, the mechanical power continues to increase and is now greater than the asynchronous power. The speed deviation begins to increase, the governor valves close and the cycle repeats until eventually the system operates at point D corresponding to the intersection of the static turbine characteristic and the asynchronous power characteristic. This

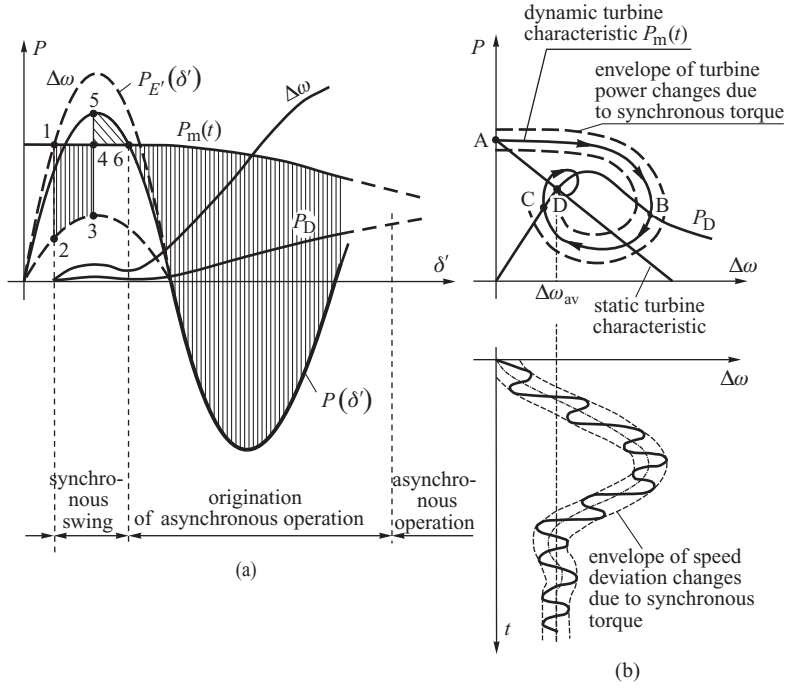

Figure 6.30 Transition to asynchronous operation: (a) development of high-speed deviation and high asynchronous power; (b) settling down of the asynchronous operating point. Based on Venikov (1978b).

point defines the average turbine speed deviation $\Delta\omega_{av}$ and power during asynchronous operation and is shown in Figure 6.29.

The effect of the synchronous power $P_{E'}$ is to produce speed deviation oscillations around the mean value as shown in the lower part of Figure 6.30b. The dashed lines in Figure 6.30b depict the envelopes of the power changes and the speed deviation changes due to the periodic acceleration and deceleration of the rotor caused by the synchronous power.

6.5.2 Asynchronous Operation

Assuming that the generator is allowed to settle at the asynchronous operating point, then typical variations in some of the electrical quantities are as shown in Figure 6.31. The voltage drop ΔV across the equivalent reactance x'_d can be calculated from the phasor diagram shown in Figure 5.8b. The cosine theorem gives

$$\Delta V^2 = (Ix'_d)^2 = (E')^2 + (V_s)^2 - 2E'V_s \cos\delta'. \tag{6.67}$$

Accordingly, the stator current is seen to change as the rotor angle changes, with its maximum value being when $\delta' = \pi$ and its minimum when $\delta' = 0$, while the generator terminal voltage, Equation (5.93), is obtained by adding the voltage drop across the system equivalent reactance to the infinite busbar voltage. Accounting for the variations in angle δ' shown in Figure 6.11 allows typical time variations of the current and voltage to be obtained as shown in Figure 6.31a.

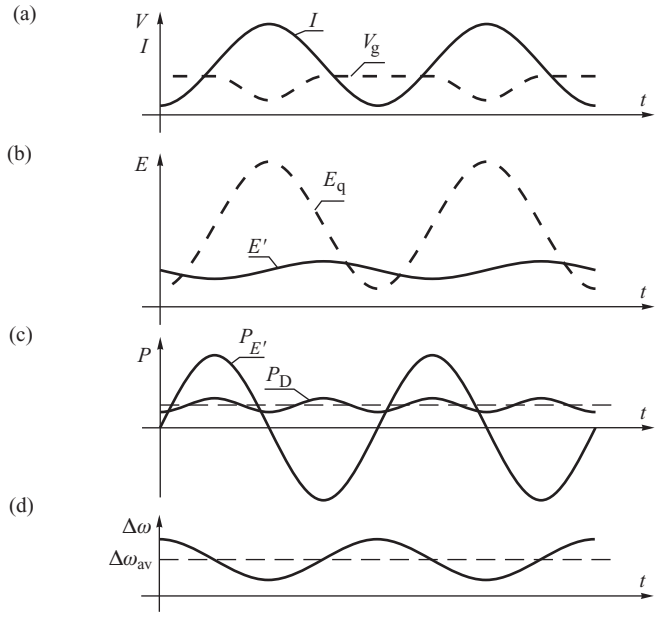

Figure 6.31 Changes in the electrical quantities of a generator operating at the asynchronous operating point: (a) current and terminal voltage; (b) internal emf and transient emf; (c) synchronous and asynchronous power; (d) speed deviation.

As the armature current changes, so too does the armature reaction flux linking the closed rotor circuits and, according to the law of constant flux linkage, currents must be induced in the rotor windings to maintain this flux linkage constant. Consequently, the field current will follow the armature current fluctuations thereby inducing large fluctuations in the internal emf E_q, and smaller variations in E', as shown in Figure 6.31b. As the transient emf E' is almost constant, the synchronous power $P_{E'}$ is given by Equation (5.40) and varies as $\sin\delta'$ (Figure 6.31c). The average value of the asynchronous damping power P_{Dav} is shown in Figure 6.31c and can be added to the synchronous power to obtain the resulting air-gap electrical power $P_e = P_{E'} + P_D$. This has the shape of a distorted sinusoid.

Figure 6.29 showed that the average speed deviation $\Delta\omega_{av}$ is determined by the intersection between the turbine characteristic $P_m(\Delta\omega)$ and the average asynchronous damping power characteristic $P_{Dav}(\Delta\omega)$. However, due to the sinusoidal changes in the synchronous power $P_{E'}$, the actual speed deviation will oscillate around $\Delta\omega_{av}$ in the way shown in Figure 6.31d.

6.5.3 Possibility of Resynchronization

In order to resynchronize with the system, the generator must fulfil the normal requirements for synchronization, that is its speed deviation and power angle must be small, condition (6.66). This subsection will investigate under what conditions these two requirements may be met.

Figure 6.30 was constructed assuming that the changes in the speed deviation produced by the synchronous power are small when compared with the average value $\Delta\omega_{av}$, while $\Delta\omega_{av}$ itself depends on the asynchronous power characteristic $P_{Dav}(\Delta\omega)$ shown in Figure 6.29. As the maximum value of $P_{Dav}(\Delta\omega)$ is inversely proportional to the square of the reactances $x'_d = X'_d + X$ and $x'_q = X'_q + X$, Equation (5.24), then if the equivalent reactance X is small, the intersection between

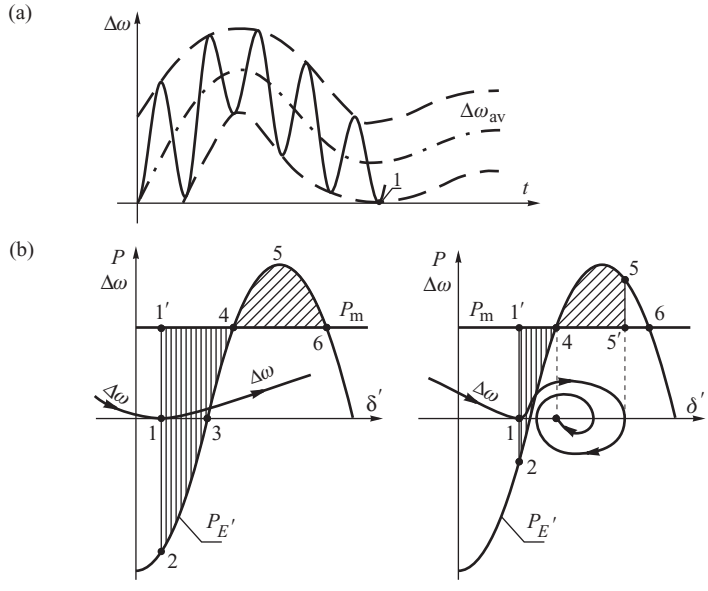

Figure 6.32 Resynchronization of a generator before the speed deviation reaches the average value $\Delta\omega_{av}$: (a) instantaneous value of the speed deviation approaches zero; (b) equal area criterion applied to check the condition for resynchronization. Based on Venikov (1978b).

the $P_{Dav}(\Delta\omega)$ characteristic and the $P_m(\Delta\omega)$ characteristic may occur at a small value of speed deviation. Moreover, a small value of X produces a large amplitude in the synchronous power $P_{E'}$ characteristic, Equation (5.40), so that large variations of $P_{E'}$ during asynchronous operation produce large variations of speed deviation around the average value $\Delta\omega_{av}$. Large speed deviation variations, combined with a small average value, may at some point in time result in the speed deviation approaching zero as shown in Figure 6.32a. As the speed deviation approaches zero, the rotor loses its excess kinetic energy, the asynchronous power is zero and the rotor behaviour is determined by the acceleration and deceleration work performed by the synchronous power $P_{E'}$. If the speed deviation reaches zero when $P_{E'}$ is sufficiently small then the generator may resynchronize with the system.

Figure 6.32b shows two cases. In the first case, the speed deviation becomes zero at point 1 when the synchronous power is large and negative. The synchronous power performs work proportional to area 1′–2–4 which is larger than the available deceleration area 4–5–6. Resynchronization is not possible and the rotor makes another asynchronous rotation. In the second case, the speed deviation reaches zero when the synchronous power is much smaller. The acceleration area 1′–2–4 is now much smaller than the available deceleration area 4–5–6 and, after reaching point 5, the decelerating power prevails and the rotor starts to swing back towards smaller values of the rotor angle. After a number of oscillations the rotor will settle at the synchronous equilibrium point 4. Resynchronization has been achieved but whether or not the generator remains stable depends on the subsequent action of the turbine governing system and the voltage regulator.

6.5.3.1 Influence of the Voltage Regulator

Figure 6.31 showed that during each asynchronous rotation the voltage at the generator terminals drops quite significantly before recovering to a higher value. This means that the regulator error

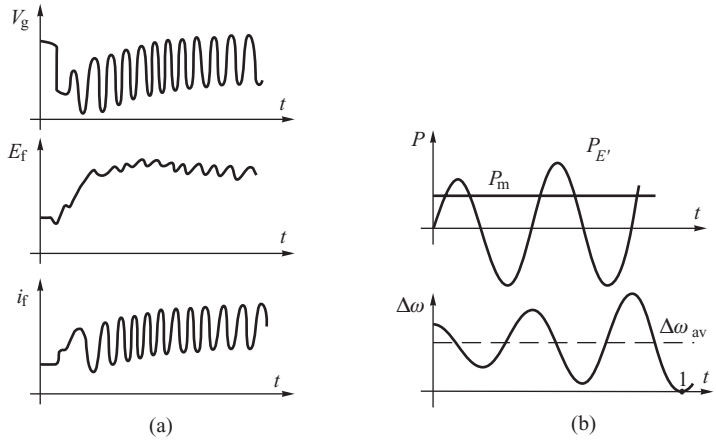

Figure 6.33 Effect of the AVR on resynchronization: (a) examples of the changes in the generator terminal voltage, excitation voltage and the field current during asynchronous operation following a fault; (b) increase in the amplitude of the synchronous power oscillations and the speed deviation oscillations as a result of voltage regulation.

will oscillate at the frequency of the speed deviation oscillations. Normally this frequency is too high for even a fast AVR to follow. Consequently, the AVR reacts, more or less, to the average value of the error signal, so maintaining a high value of excitation voltage as shown in Figure 6.33a. As the average voltage value is lower than the prefault value, the AVR increases the excitation voltage V_f almost to its ceiling value so that the amplitude of the $P_{E'}(\delta')$ characteristic increases.

It has already been explained that the larger the magnitude of the speed deviation oscillations around the average value, the greater the possibility that the speed deviation will reach zero value. By increasing the excitation voltage, the AVR increases the amplitude of the $P_{E'}(\delta')$ characteristic and so produces larger changes in the speed deviation. This increases the chance of the speed deviation reaching a zero value as shown in Figure 6.33b. Moreover, as the amplitude of the synchronous power increases, the available deceleration area in Figure 6.32b increases and the range of rotor angles which are acceptable for resynchronization also increases.

Obviously resynchronization will be followed by a period of large rotor swings which may be damped or aggravated by the action of the AVR for the reasons described in Section 6.1.5.

6.5.3.2 Other Possibilities of Resynchronization

Successful resynchronization depends on the action of the AVR and the turbine governing system. Turbine governors can be equipped with supplementary control loops which allow the turbine power to be quickly reduced after a fault in order to protect the generator from loss of synchronism and/or assist in resynchronization. This is referred to as fast valving and is discussed in detail in Section 10.2. If a generator is not equipped with such a governor, the operating staff may try to resynchronize the asynchronously rotating generator by manually reducing the turbine power to reduce the average speed deviation value. However, in order to avoid large power swings in the system, and possible damage to the generator, generators are usually tripped after a few asynchronous rotations.

6.6 Out-of-Step Protection Systems

Deep synchronous or asynchronous power swings are accompanied by large changes in voltages and currents which pose a serious threat to power system operation. They may cause maloperation

of some protection systems, especially distance protection and underimpedance protection (Section 2.5), which in turn may lead to cascaded outages and blackouts.

To avoid these consequences, power system protection is usually augmented by additional devices and functions making up the *out-of-step protection system*. The main elements of out-of-step protection are:

- special protection and supplementary control;
- power swing blocking (PSB) of distance and underimpedance protection;
- pole-slip protection (PSP) of synchronous generators;
- out-of-step tripping (OST) in transmission networks.

The task of *special protection* and *supplementary control* is to prevent loss of synchronism and the onset of asynchronous operation as well as rapid damping of power swings. These problems are treated in Chapter 10 which deals with stability enhancement methods.

If, despite special protection and supplementary control systems, there is an onset of asynchronous operation or deep synchronous power swings, then the apparent impedance measured by the distance or underimpedance protection can move away from the normal load area into the distance protection zone causing unnecessary tripping. The task of the PSB relays (or functions) is to detect that the changes in the measured impedance are due to power swings rather than short circuits. PSB should be used for distance protection of transmission lines and transformers and also for distance and underimpedance protection of synchronous generators and their step-up transformers.

OST tripping relays (or functions) may be installed either as part of the generator protection system or as part of the transmission network protection. When installed in the generator protection system, they isolate the generator in the event of asynchronous operation. The PSP relay (or function) operates after a set number of asynchronous cycles. OST relays (or functions) can also be used inside the transmission network in order to split the system at predetermined points should asynchronous power swings occur.

It is important for a power system operator to have a logical strategy of using PSB, PSP and OST. Examples have been discussed in the IEEE Report to the Power System Relaying Committee (1977). Generally speaking, protection of a power system against the consequences of power swings should consist of efficient blocking of impedance relays during synchronous and asynchronous swings using PSB relays (or functions). Efficient protection against long-lasting asynchronous operation should be achieved by using PSP relays (or functions) for generators and OST for the network.

6.6.1 Impedance Loci During Power Swings

The effect of power swings on the impedance loci can be studied using the simple equivalent circuit shown in Figure 6.34 in which two equivalent synchronous generators are linked via impedances $\underline{Z}'_a$ and $\underline{Z}'_b$. The voltage and current are measured at the relay point between these

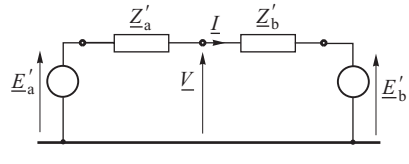

Figure 6.34 Equivalent circuit of the system with a relay point.

impedances to obtain the apparent impedance $\underline{Z}(t)$. The current and voltage at the relay point are given by

$$\underline{I} = \frac{\underline{E}'_{\mathrm{a}} - \underline{E}'_{\mathrm{b}}}{\underline{Z}'_{\mathrm{a}} + \underline{Z}'_{\mathrm{b}}}, \quad \underline{V} = \underline{E}'_{\mathrm{a}} - \underline{I}\underline{Z}'_{\mathrm{a}}, \tag{6.68}$$

where $\underline{E}'_{\mathrm{a}}$, $\underline{E}'_{\mathrm{b}}$ are the equivalent generator transient emfs and $\underline{Z}'_{\mathrm{a}}$, $\underline{Z}'_{\mathrm{b}}$ are the equivalent impedances that include the impedance of the transmission network and the generator transient reactances. If the magnitudes of the equivalent transient emfs are assumed to be constant then

$$\frac{\underline{E}'_{\mathrm{a}}}{\underline{E}'_{\mathrm{b}}} = \frac{\left|\underline{E}'_{\mathrm{a}}\right|}{\left|\underline{E}'_{\mathrm{b}}\right|} \mathrm{e}^{\mathrm{j}\delta'} = k\mathrm{e}^{\mathrm{j}\delta'}, \tag{6.69}$$

where $k = \left|\underline{E}'_{\mathrm{a}}\right| / \left|\underline{E}'_{\mathrm{b}}\right|$ = constant and the transient power angle δ' is the difference between the arguments of the emfs.

The apparent impedance measured by the relay is $\underline{Z}(t) = \underline{V}/\underline{I}$ which, when substituting for $\underline{V}$ and $\underline{I}$ from the equations in (6.68) and including (6.69), gives

$$\underline{Z}(t) = \frac{\underline{V}}{\underline{I}} = \frac{\underline{Z}'_{\mathrm{a}} + \underline{Z}'_{\mathrm{b}} k\mathrm{e}^{\mathrm{j}\delta'(t)}}{k\mathrm{e}^{\mathrm{j}\delta'(t)} - 1}. \tag{6.70}$$

Note that during power swings the power angle and the apparent impedance are both time dependent. Solving Equation (6.70) with respect to the power angle gives

$$k\mathrm{e}^{\mathrm{j}\delta'(t)} = \frac{\underline{Z}(t) - \left(-\underline{Z}'_{\mathrm{a}}\right)}{\underline{Z}(t) - \underline{Z}'_{\mathrm{b}}}. \tag{6.71}$$

With the exception of the coefficient k, all the variables in this equation are complex. Taking the absolute value of both sides of (6.71) and recognizing that $\left|\mathrm{e}^{\mathrm{j}\delta'}\right| = 1$ gives

$$\left|\frac{\underline{Z}(t) - \left(-\underline{Z}'_{\mathrm{a}}\right)}{\underline{Z}(t) - \underline{Z}'_{\mathrm{b}}}\right| = k = \text{constant} = \frac{\left|\underline{E}'_{\mathrm{a}}\right|}{\left|\underline{E}'_{\mathrm{b}}\right|}. \tag{6.72}$$

Equation (6.72) determines the locus in the complex plane of all points with the same value of k. This is illustrated in Figure 6.35. The impedances $(-\underline{Z}'_{\mathrm{a}})$ and $\underline{Z}'_{\mathrm{b}}$ determine the points A and B respectively while the apparent impedance $\underline{Z}(t)$ determines point C (Figure 6.35a). As $\left|\underline{Z}(t) - (-\underline{Z}'_{\mathrm{a}})\right| = \mathrm{AC}$ and $\left|\underline{Z}(t) - \underline{Z}'_{\mathrm{b}}\right| = \mathrm{BC}$, the ratio $k = \mathrm{AC}/\mathrm{BC} = \text{constant}$. As $\underline{Z}(t)$ varies, a locus of constant value k will be traced out by point C. The locus for a given value of k is a circle that surrounds either point A or point B. The diameter of this circle, and the location of its centre, depend on the value of k and the impedances $\underline{Z}'_{\mathrm{a}}$, $\underline{Z}'_{\mathrm{b}}$. The centre of each circle lies on the straight line that passes through points A and B and is shown dashed in Figure 6.35b. For $k = 1$ the diameter of the circle tends to infinity and the circle becomes a straight line that bisects AB. For $k < 1$, $\left|\underline{E}'_{\mathrm{a}}\right| < \left|\underline{E}'_{\mathrm{b}}\right|$, the circle lies in the lower part of the complex plane and encircles point A. For $k > 1$, $\left|\underline{E}'_{\mathrm{a}}\right| > \left|\underline{E}'_{\mathrm{b}}\right|$, the circle lies in the upper part of the complex plane and encircles point B.

Now consider the effect of a power swing on the trajectory of $\underline{Z}(t)$. For the prefault operating conditions the voltage V is close to the rated voltage and the current I is small when compared with the fault current. Consequently $\underline{Z}(t)$ is high and predominantly resistive (since normally the power factor is close to unity). A fault results in a significant drop in voltage and an increase in current so that $\underline{Z}(t)$ drops in value. Assuming that $k = \left|\underline{E}'_{\mathrm{a}}\right| / \left|\underline{E}'_{\mathrm{b}}\right| = \text{constant}$, then, when the fault is cleared, the value of Z rises again. Further changes in Z are solely due to the variation of the power angle δ' and must follow one of the circles shown in Figure 6.35.

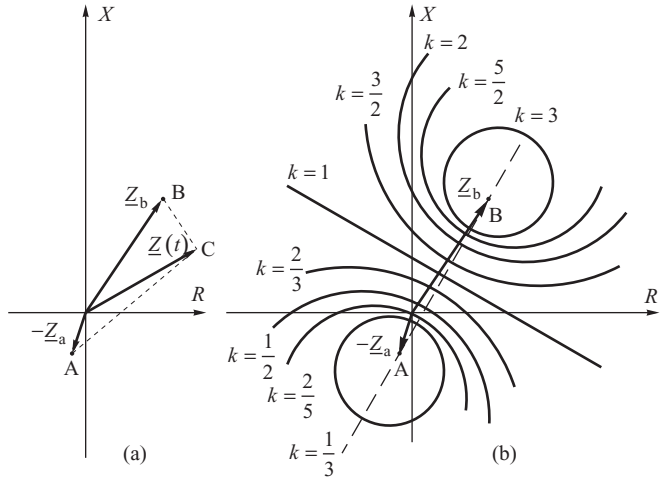

Figure 6.35 Graphical interpretation of Equation (6.72): (a) impedances on the complex plane: (b) circles determining the impedance loci.

Figure 6.36a illustrates the trajectory of $\underline{Z}(t)$ in the case of an asynchronous power swing, and Figure 6.36b in the case of a synchronous power swing, following a fault outside the relay protection zone. In both cases the trajectory starts from point O in the normal load area and, when the fault occurs, jumps to point F lying outside protection zones 1 and 2. During the short circuit the impedance trajectory moves to point C where the fault is cleared. On fault clearance the trajectory jumps to point P which does not quite lie on the same circle as point O because the emfs change their values slightly during the fault. Further changes in δ' will cause $\underline{Z}(t)$ to follow a circle of a constant ratio k or, more precisely, a family of closed circles corresponding to slightly varying emfs and hence ratios k.

When $\delta'(t)$ increases, $\underline{Z}(t)$ decreases and may encroach into the distance relay tripping zone. For the asynchronous power swing, shown in Figure 6.36a, the trajectory will trace a full circle as $\delta'(t)$ completes a full 360° cycle. For a synchronous power swing, shown in Figure 6.36b, the trajectory will reach point B1 on an impedance circle and then move back towards point B2 as $\delta'(t)$ decreases on the backswing. For constant $|\underline{E}'_a| / |\underline{E}'_b|$ the trajectory always lies on one circle. A change in the transient emfs due to AVR control will move the trajectory from circle to circle so that when power swings are damped, the trajectory tends towards a postfault equilibrium point in the load area.

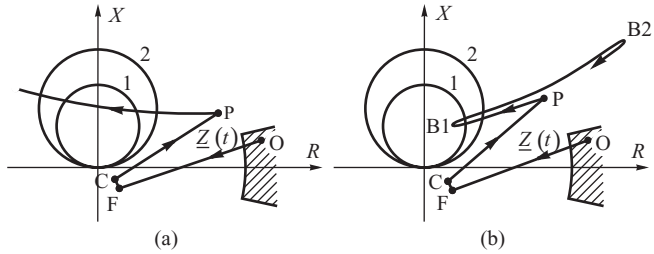

Figure 6.36 Example of the impedance trajectory for (a) asynchronous power swing and (b) synchronous power swing: 1, 2, tripping zones of the distance relay; load area is shaded.

6.6.2 *Power Swing Blocking*

A power swing can be detected by monitoring the speed at which the impedance locus $\underline{Z}(t)$ approaches the characteristic of the distance relay. If the fault is applied so that point F lies outside the relay protection zone (as in Figure 6.36) then the protection zones are approached by $\underline{Z}(t)$ with a finite speed. On the other hand, if the fault is applied so that point F lies inside one of the protection zones shown in Figure 6.36 then the impedance locus jumps from point O to a point inside the protection zone almost instantaneously.

Figure 6.37 illustrates the operation of a distance relay with an offset mho-type characteristic. The PSB relay (or function) has the same type of characteristic as the distance relay and surrounds the distance relay characteristic. A timer measures the time Δt taken for the trajectory to pass between the two characteristics. If the fault is inside the protection zone then the power swing relay and the fault detection relay will operate practically simultaneously and a blocking command is not generated. If the fault is outside the protection zone then, during a resulting power swing, the trajectory will take a finite time to move between the two relay characteristics and a blocking command is generated to hold up operation of the circuit-breaker for the time when the impedance locus stays inside the fault detection zone. To avoid blocking of relays during remote unbalanced faults and the dead time of single-phase auto-reclosing, the zero-sequence component of the current is monitored. If the zero-sequence component is present, the blocking command is not generated.

The above blocking principle is also used in distance relays with other types of characteristic such as quadrilateral, rhombus and oval. Obviously the power swing relay must have the same type of characteristic as the distance relay.

This method of detecting power swings was widely used in electromechanical relays. Modern digital protection is augmented by additional decision criteria. These criteria are checked by the power swing detection (PSD) function. Additional decision criteria in PSB functions of digital protection consist of monitoring other signals. When trajectories of the signals are smooth and have an expected shape, the blocking command is not generated. Decision criteria in PSD are used because measuring only the time when the measured impedance passes between the two zones is not a reliable method. There are instances when the relay does not operate when it should and vice versa.

One example of unnecessary activation of the blocking relay based on measuring the time of passing between zones $\underline{Z}(t)$ alone is a high-impedance developing fault. The changes of impedance value during the fault may be so slow that the relay activates and unnecessarily blocks the distance protection. That would be dangerous for both the short-circuited network element and the whole power system.

An example of an out-of-step relay, based on measuring the time of passing $\underline{Z}(t)$ alone, that does not operate, is shown in Figure 6.38. The trajectory of the impedance is shown for a case when the relay is placed at the beginning of line L2 while the short circuit occurs in line L1. At the instant

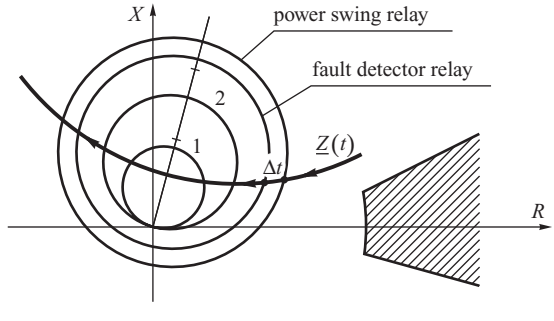

Figure 6.37 Power swing blocking and distance relay characteristics of the offset mho type.

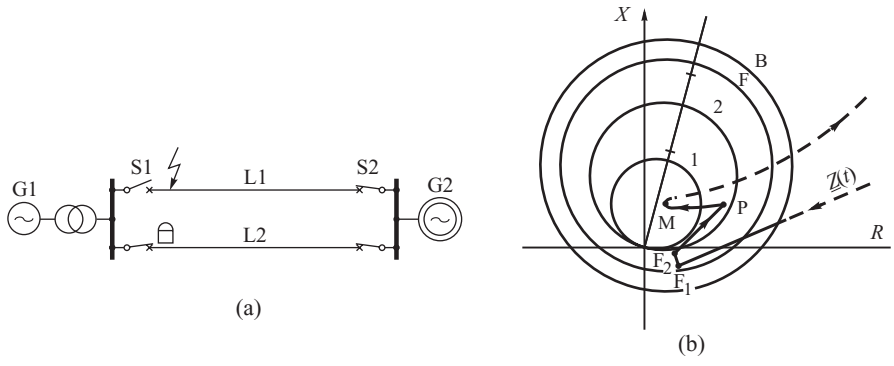

Figure 6.38 Example of the out-of step relay not operating: (a) block diagram of a simple system; (b) example of impedance changes during synchronous swings.

of the short circuit, the trajectory jumps to point F_1 in the fourth quadrant and moves during the short circuit towards point F_2. When the short circuit is cleared, the trajectory jumps to point P which lies inside the second tripping zone. Then the trajectory moves towards point M inside the first tripping zone. The protection activates with the tripping time of the first zone and the healthy line L2 is unnecessarily tripped. The out-of-step relay did not operate because, following the fault clearing, the trajectory did not move outside characteristic B. Hence there was no passing between characteristics B and F which is essential for operation of the relay. Thus augmenting the principle of operation by other decision criteria is clearly necessary.

A description of a number of reasons for unnecessary blocking of distance protection and its unwanted operation is given, for example, by Troskie and de Villiers (2004).

6.6.3 Pole-Slip Protection of Synchronous Generator

The purpose of this protection is to detect the loss of synchronism of a synchronous generator. The measurement points for the relay are the generator terminals as shown in Figure 6.39. The impedance $\underline{Z}_a$ to the left of the measurement point corresponds to the generator transient reactance $\underline{Z}_a \cong \mathrm{j}X'_d$. The impedance $\underline{Z}_b$ to the right of the measurement point consists of the step-up transformer impedance $\underline{Z}_T$ and the system equivalent impedance $\underline{Z}_S$. The whole transmission system can be divided into two zones. Zone 1 consists of the generator and the step-up transformer while zone 2 is the rest of the system. At completion of the first half of an asynchronous rotation, that is when $\delta' = 180^\circ$, the equivalent voltages oppose each other so that the voltage at a certain point of the transmission link must be equal to zero. That point is referred to as the *centre of power swing* or simply the *electrical centre*. Depending on how big the equivalent system impedance $\underline{Z}_S$ is for a given value of $\underline{Z}_a$ and $\underline{Z}_T$, the centre of power swing may be inside zone 1 or 2. In Figure 6.39, the centre is inside zone 1 and inside the impedance of the step-up transformer. Equation (6.70) shows that when $\delta' = 180^\circ$ the apparent impedance seen by the relay is proportional to the difference between the equivalent impedances, that is

$$\underline{Z}(\delta' = 180^\circ) = \frac{\underline{Z}_a - k\underline{Z}_b}{-k-1} = \frac{k\underline{Z}_b - \underline{Z}_a}{k+1}. \tag{6.73}$$

Because k is real, this equation shows that at $\delta' = 180^\circ$ the trajectory $\underline{Z}(t)$ intersects the line crossing points A and B in Figure 6.39. This means that an asynchronous rotation can be identified by a relay with an impedance characteristic that surrounds line AB based on $(-\underline{Z}_a)$ and $\underline{Z}_b$ respectively.

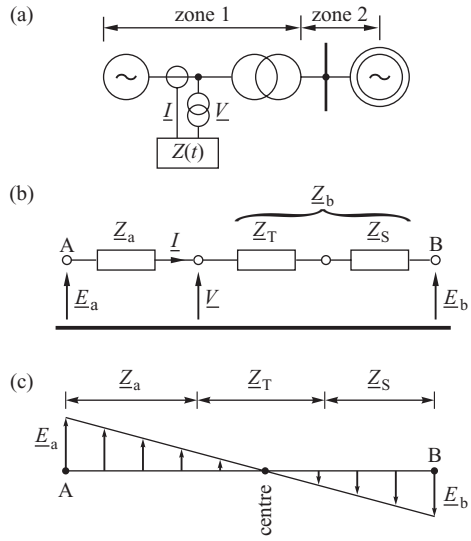

Figure 6.39 Pole-slip protection of synchronous generator: (a) block diagram; (b) equivalent circuit; (c) illustration of the centre of power swing.

Three such characteristics are shown in Figure 6.40. The first type (Figure 6.40a) has an offset mho characteristic 3 with the left and right parts cut off by two directional relays 1 and 2. The second type (Figure 6.40b) has a symmetrical lenticular characteristic and is obtained by using two impedance relays with offset mho characteristics shown by the dashed circles 1 and 2. The third type (Figure 6.40c) has an asymmetrical lenticular characteristic.

PSP usually has an additional impedance characteristic that divides $\underline{Z}(t)$ into two zones as shown by line 4 in Figure 6.40. The relay identifies an asynchronous rotation if the impedance locus passes completely through the relay characteristic. If the impedance locus $\underline{Z}(t)$ passes through the impedance characteristic below line 4, it means that the centre of power swing (Figure 6.39) is inside zone 1. In that case the generator should be disconnected right after the impedance $\underline{Z}(t)$ leaves the impedance characteristic, that is during the first asynchronous rotation. On the other hand, if the impedance locus $\underline{Z}(t)$ passes through the impedance characteristic above line 4, it means that the centre of power swings (Figure 6.39) is inside zone 2, that is inside the transmission network. In that

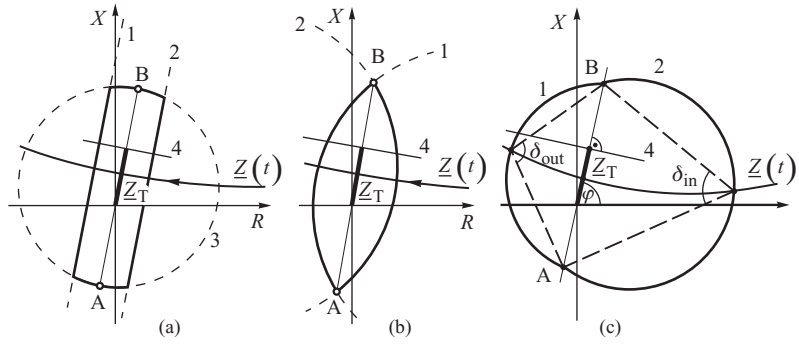

Figure 6.40 Three types of pole-slip protection characteristics: (a) offset mho type; (b) symmetrical lenticular type; (c) asymmetrical lenticular type.

case the generator may be disconnected after 2–4 asynchronous rotations. Such a delay is introduced in order to give a chance of operation for the OST relays installed in the transmission network and splitting the network into islands (as described in the next section). The delay is acceptable only if the generator can withhold a thermal and dynamic overload caused by a set number of asynchronous rotations. If there are no OST relays in the network, then there is no reason for the delay and the generator may be tripped after one asynchronous rotation independently of where the centre of power swing is.

The way that a generator is tripped depends on the configuration of the unit described in Section 2.2. For generating units containing a step-up transformer, the generator is tripped by opening its main circuit-breaker on the high-voltage side (Figure 2.2). The turbine is not disconnected but reduces its power output to the level necessary to supply the unit's auxiliary services. This makes it possible to resynchronize the generator quickly with the system.

6.6.4 Out-of-Step Tripping in a Network

It has already been mentioned that, during an asynchronous rotation, the impedance $\underline{Z}(t)$ measured by the distance protection of transmission lines close to the centre of power swing may encroach into the tripping zone of the distance protection. If PSB relays (or functions) are not used, a number of transmission lines may be tripped leading to a random network splitting into unbalanced zones. Generators in islands with a large surplus of generation will be disconnected by overfrequency protection while load shedding will be activated in islands with a large deficit of generation. These problems will be discussed in Chapter 9.

To prevent a random network splitting during asynchronous operation, it is necessary to use the earlier described PSB of distance protection in the network and PSP of generators. Additionally, OST relays (or functions) may be installed at locations selected for controlled network splitting in order to trip selected transmission lines once asynchronous operation has been detected. The lines are selected according to the following criteria:

1. The lines must be so close to the centre of power swings that the impedance loci encroach into the tripping zone of distance protection of those lines. Otherwise, the relays will not be able to issue tripping commands.
2. After the network has been split, the islands must have roughly balanced generation and demand. Otherwise, generators may be tripped or load shedding activated.
3. Islands have to be internally stable, that is further splitting should not occur.

Obviously it is not easy to find places in a meshed network that would satisfy all those conditions and at the same time ensure that the controlled network splitting would be satisfactory for all possible locations of short circuits leading to asynchronous operation. Hence controlled splitting in real systems is often restricted to tie-lines which naturally divide the network into strongly connected islands. An example of such structures is shown in Figure 6.41.

The network shown in Figure 6.41a has a longitudinal structure and consists of two weakly connected subsystems. Any disturbance leading to the loss of synchronism will lead to a natural split of the network into two subsystems operating asynchronously. Clearly the best place for placing OST is in the distance protection of the tie-lines. Once an asynchronous rotation has been identified, the relays will open circuit-breakers in the lines splitting the network into two subsystems.

The second network shown in Figure 6.41b consists of a number of internally well-meshed subsystems connected by relatively weak tie-lines. This situation is typical of an interconnected system. Weakness of connections may lead to asynchronous rotations in tie-lines following a disturbance. Relays installed in the tie-lines will separate the subsystems after a set number of asynchronous rotations. In both cases shown in Figure 6.41, automatic generation control (Chapter 9) supported by automatic load shedding should lead to balancing of generation and demand in each subsystem.

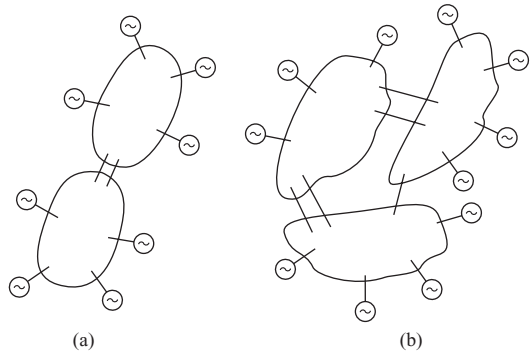

Figure 6.41 Network structures naturally amenable to splitting: (a) longitudinal system; (b) weakly connected subsystems.

Resynchronization must be preceded by matching frequencies in the subsystems and a check on synchronization.

It is important to appreciate that there is no natural way of splitting a tightly meshed network. Splitting such a network into islands usually leads to worsening stability conditions of generators operating inside separate islands and further splitting which may lead eventually to a total blackout. Hence it is not recommended to install OST relays (or functions) in tightly meshed transmission networks. Unfortunately some authors suggest that OST may be more widely used and that it is better to split the network into islands than trip generators. This view is valid only with respect to the weakly connected structures shown in Figure 6.41. In tightly meshed networks, keeping the network connected is most important and worth the sacrifice of tripping some generators. When the network is still connected, generators can be easily resynchronized and the power supply restored. On the other hand, when a tightly meshed large network has been split, reconnection is difficult and may take hours, requiring complicated action from system operators. Often some lines may be difficult to connect due to very large differences in voltages or angles in neighbouring subsystems.

Splitting a network into islands in predetermined places is achieved by the OST relay or, in newer digital solutions, the OST function added to distance relays. Figure 6.42 shows the impedance characteristic of such a function. To differentiate between power swings and short circuits, two polygon-shaped characteristics are used, the external and internal ones, denoted by 1 and 2 respectively in Figure 6.42. A short circuit is detected when the trajectory crosses one of the polygonal

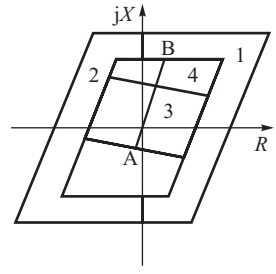

Figure 6.42 Characteristic of out-of-step tripping function.

areas in a time shorter than a set one. If the crossing time is longer than the set one, the impedance change is deemed to be due to power swings.

Detected power swings are deemed to be asynchronous if the impedance trajectory enters one side of the polygon, crosses line AB (corresponding to the angle $\delta' = 180^\circ$) and then leaves on the other side of the polygon. The protection divides the area of reach into close and remote ones, just as in PSP. This is achieved by two lines dividing the internal area into two areas denoted by 3 and 4, respectively. If the trajectory crosses area 3, the power swing is deemed to be close. If the trajectory crosses line 4, the swing is deemed to be remote. Each of the areas has its own counter of asynchronous rotations. Tripping of the lines is activated only when the number of identified cycles in a given area reaches a set value.

6.6.5 Example of a Blackout

There have been many papers and reports published describing actual power system disturbances when the lack, or maloperation, of PSB of distance protection caused unwanted line tripping. Most of the cases ended up with an alert state and a return to the normal state (see Section 1.5). There were cases, however, when a power system moved from a normal state to an emergency state or even *in extremis* ended up with a partial or total blackout. Troskie and de Villiers (2004) describe an interesting case of a blackout caused by out-of-step relaying that happened in ESCOM (South Africa).

On 14 September 2001 heavy snowfall in the Drakensberg area resulted in overhead line failures followed by a trip command from zone 3 of the distance protection. This caused a deep power swing in the network. There was no unified concept of using an out-of-step protection system. Some relays had blockades only for tripping zone 1 and others only for tripping zone 2 or 3. The lack of a unified concept and inefficient PSB functionality resulted in more lines tripping and finally a loss of the entire network. Detailed post-mortem analysis and simulation have shown the need to modify the out-of-step protection system and for more careful selection of the settings.

6.7 Torsional Oscillations in the Drive Shaft

In this section the effect that system faults can have on the torques in the shafts and couplings connecting each turbine stage, the turbine to the generator and the generator to the exciter is discussed. In the previous sections of this chapter these shafts and couplings, shown in Figure 5.1, were assumed to be very stiff when the total drive system moves as a rigid body and can be represented by a single inertia. In practice the drive shafts and couplings have a finite stiffness so that each turbine mass will be slightly displaced relative to the others. Consequently, any change in the external torque on any of the rotor components initiates a movement of the equivalent mass. The shaft connecting this element to its neighbours twists slightly and the resulting torsion transmits torque to the neighbouring element(s). This process is repeated down the shaft creating torsional oscillations in the shaft. These torsional oscillations are superimposed on the external torque which may either increase or reduce the torque in the shaft sections, depending on the direction of twist and the phase and frequency of the changes in the external torque, so that under certain conditions the shaft torques can become very large. Such large shaft torques can result in a reduction in the shaft fatigue life and possibly shaft failure. It is therefore important to understand the mechanisms leading to these high shaft torques and in what situations they might arise.

6.7.1 The Torsional Natural Frequencies of the Turbine–Generator Rotor

As the turbine–generator rotor can be considered as a number of discrete masses connected together by springs a lumped-mass model of the rotor can be developed in order to calculate the natural

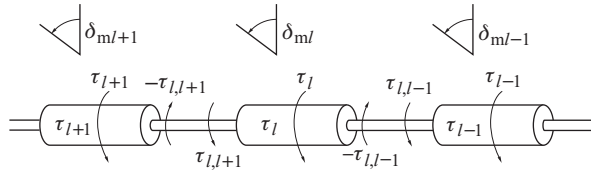

Figure 6.43 Torques acting on mass l; τ_l is the applied torque, $\tau_{l,l-1}$ and $\tau_{l,l+1}$ are the shaft torques, δ_{ml} the displacement of the mass and J_l the inertia.

frequencies of the rotor system. At each of these natural frequencies the rotor system will vibrate in a particular way defined by the *mode shape*.

Figure 6.43 shows the torques acting on each rotor mass when applying Newton's second law gives the equation of motion for the general mass l as

$$J_l \frac{\mathrm{d}^2\delta_{ml}}{\mathrm{d}t^2} = \tau_l + \tau_{l,l+1} - \tau_{l,l-1}, \tag{6.74}$$

where J_l is its moment of inertia, τ_l is the external applied torque to mass l and $\tau_{l,l+1}$ and $\tau_{l,l-1}$ are the torques in the two shafts $(l, l+1)$ and $(l, l-1)$. These shaft torques are respectively

$$\tau_{l,l+1}(t) = k_{l,l+1}\left(\delta_{ml+1} - \delta_{ml}\right) + D_{l,l+1}\left(\frac{\mathrm{d}\delta_{ml+1}}{\mathrm{d}t} - \frac{\mathrm{d}\delta_{ml}}{\mathrm{d}t}\right), \tag{6.75}$$

$$\tau_{l,l-1}(t) = k_{l,l-1}\left(\delta_{ml} - \delta_{ml-1}\right) + D_{l,l-1}\left(\frac{\mathrm{d}\delta_{ml}}{\mathrm{d}t} - \frac{\mathrm{d}\delta_{ml-1}}{\mathrm{d}t}\right), \tag{6.76}$$

where $k_{l,l-1}$ is the stiffness of the shaft section between masses l and $l-1$, δ_{ml} is the angle of the lth mass in mechanical radians and $D_{l,l-1}$ is the shaft damping coefficient. The shaft damping is due to the energy lost in the shaft as it oscillates and goes through a stress/strain hysteresis cycle. The above two equations can now be substituted into Equation (6.74) to give the equation of motion

$$\begin{aligned} J_l \frac{\mathrm{d}^2\delta_{ml}}{\mathrm{d}t^2} &= \tau_l(t) - k_{l,l-1}\left(\delta_{ml} - \delta_{ml-1}\right) - k_{l,l+1}\left(\delta_{ml} - \delta_{ml+1}\right) \\ &\quad - D_{l,l+1}\left(\frac{\mathrm{d}\delta_{ml}}{\mathrm{d}t} - \frac{\mathrm{d}\delta_{ml+1}}{\mathrm{d}t}\right) - D_{l,l-1}\left(\frac{\mathrm{d}\delta_{ml}}{\mathrm{d}t} - \frac{\mathrm{d}\delta_{ml-1}}{\mathrm{d}t}\right) - D_{l,l}\frac{\mathrm{d}\delta_{ml}}{\mathrm{d}t}. \end{aligned} \tag{6.77}$$

In this equation $D_{l,l}$ is an additional damping term used to represent the damping effect arising at each turbine stage due to the flow of steam through the turbine. Generally both the shaft damping and the steam damping mechanisms are small. Equation (6.77) is in SI units but a per-unit version can be obtained by following a similar procedure as in Section 5.1.[1]

Now consider a simple turbine–generator rotor consisting of three turbine stages and a generator as shown in Figure 6.44. A static exciter is assumed to act with this system so that no rotational

[1] In per-unit form J becomes $2H/\omega_s$ while τ and k are expressed in per units obtained by dividing the SI values by

$$T_{\text{base}} = \frac{S_{\text{base}}}{\omega_{sm}} = \frac{S_{\text{base}}}{\omega_s}\frac{p^2}{4} \quad \text{and} \quad k_{\text{base}} = T_{\text{base}}\frac{p}{2} = \frac{S_{\text{base}}}{\omega_s}\frac{p^2}{4}$$

respectively. δ_l is now expressed in electrical radians.

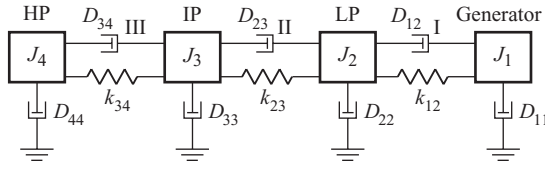

Figure 6.44 Four-mass turbine–generator rotor model.

mass is required to represent this component. Applying Equation (6.77) to each rotor mass in turn gives a set of four second-order differential equations

$$
\begin{aligned}
J_1\frac{\mathrm{d}\delta_{\mathrm{m1}}^2}{\mathrm{d}t^2} &= \tau_1 - k_{12}(\delta_{\mathrm{m1}} - \delta_{\mathrm{m2}}) - D_{12}\left(\frac{\mathrm{d}\delta_{\mathrm{m1}}}{\mathrm{d}t} - \frac{\mathrm{d}\delta_{\mathrm{m2}}}{\mathrm{d}t}\right) - D_{11}\frac{\mathrm{d}\delta_{\mathrm{m1}}}{\mathrm{d}t}\\
J_2\frac{\mathrm{d}\delta_{\mathrm{m2}}^2}{\mathrm{d}t^2} &= \tau_2 - k_{12}(\delta_{\mathrm{m2}} - \delta_{\mathrm{m1}}) - k_{23}(\delta_{\mathrm{m2}} - \delta_{\mathrm{m3}}) - D_{12}\left(\frac{\mathrm{d}\delta_{\mathrm{m2}}}{\mathrm{d}t} - \frac{\mathrm{d}\delta_{\mathrm{m1}}}{\mathrm{d}t}\right) - D_{23}\left(\frac{\mathrm{d}\delta_{\mathrm{m2}}}{\mathrm{d}t} - \frac{\mathrm{d}\delta_{\mathrm{m3}}}{\mathrm{d}t}\right)\\
&\quad - D_{22}\frac{\mathrm{d}\delta_{\mathrm{m2}}}{\mathrm{d}t}\\
J_3\frac{\mathrm{d}\delta_{\mathrm{m3}}^2}{\mathrm{d}t^2} &= \tau_3 - k_{23}(\delta_{\mathrm{m3}} - \delta_{\mathrm{m2}}) - k_{34}(\delta_{\mathrm{m3}} - \delta_{\mathrm{m4}}) - D_{23}\left(\frac{\mathrm{d}\delta_{\mathrm{m3}}}{\mathrm{d}t} - \frac{\mathrm{d}\delta_{\mathrm{m2}}}{\mathrm{d}t}\right) - D_{34}\left(\frac{\mathrm{d}\delta_{\mathrm{m3}}}{\mathrm{d}t} - \frac{\mathrm{d}\delta_{m4}}{\mathrm{d}t}\right)\\
&\quad - D_{33}\frac{\mathrm{d}\delta_{\mathrm{m3}}}{\mathrm{d}t}\\
J_4\frac{\mathrm{d}\delta_{\mathrm{m4}}^2}{\mathrm{d}t^2} &= \tau_4 - k_{34}(\delta_{\mathrm{m4}} - \delta_{m3}) - D_{34}\left(\frac{\mathrm{d}\delta_{\mathrm{m4}}}{\mathrm{d}t} - \frac{\mathrm{d}\delta_{\mathrm{m3}}}{\mathrm{d}t}\right) - D_{44}\frac{\mathrm{d}\delta_{\mathrm{m4}}}{\mathrm{d}t}.
\end{aligned}
\tag{6.78}
$$

This set of second-order equations is then written as a series of eight first-order equations by noting that for mass I,

$$
\frac{\mathrm{d}\delta_{\mathrm{m}i}}{\mathrm{d}t} = \omega_{\mathrm{m}i} - \omega_{\mathrm{sm}} = \Delta\omega_{\mathrm{m}i}, \quad \frac{\mathrm{d}^2\delta_{\mathrm{m}i}}{\mathrm{d}t^2} = \frac{\mathrm{d}\Delta\omega_{\mathrm{m}i}}{\mathrm{d}t}. \tag{6.79}
$$

Using this substitution, and taking mass l as an example, gives

$$
\begin{aligned}
J_1\frac{\mathrm{d}\Delta\omega_{\mathrm{m1}}}{\mathrm{d}t} &= \tau_1 - k_{12}(\delta_{\mathrm{m1}} - \delta_{\mathrm{m2}}) - D_{11}\Delta\omega_{\mathrm{m1}} - D_{12}(\Delta\omega_{\mathrm{m1}} - \Delta\omega_{\mathrm{m2}})\\
\frac{\mathrm{d}\delta_{\mathrm{m1}}}{\mathrm{d}t} &= \Delta\omega_{\mathrm{m1}}.
\end{aligned}
\tag{6.80}
$$

By considering small perturbations and defining a set of state variables $\boldsymbol{x}$ so that

$$
x_1 = \Delta\delta_{\mathrm{m1}}, x_2 = \Delta\delta_{\mathrm{m2}}, x_3 = \Delta\delta_{\mathrm{m3}}, x_4 = \Delta\delta_{\mathrm{m4}} \quad \text{and} \quad x_5 = \Delta\omega_{\mathrm{m1}}, x_6 = \Delta\omega_{\mathrm{m2}}, x_7 = \Delta\omega_{\mathrm{m3}},
$$
$$
x_8 = \Delta\omega_{\mathrm{m4}},
$$

substituting into Equations (6.80) gives a linearized matrix equation of the form

$$
\dot{\boldsymbol{x}} = \boldsymbol{A}\boldsymbol{x} + \boldsymbol{B}\boldsymbol{u}, \tag{6.81}
$$

where $\boldsymbol{A}$ is called the *plant* or *state matrix*, $\boldsymbol{B}$ the *driving matrix*, $\boldsymbol{x}$ a *vector of state variables* and $\boldsymbol{u}$ a *vector of inputs*, in this case the change in the external torque $\Delta\tau$ applied to each mass. A general

solution of the state equation (6.82) will be discussed in Chapter 12 and Appendix A.3. The plant matrix is given by

$$\boldsymbol{A} = \begin{bmatrix} \mathbf{0} & \mathbf{1} \\ \boldsymbol{K} & \boldsymbol{D} \end{bmatrix}, \tag{6.82}$$

where $\mathbf{0}$ is a null matrix, $\mathbf{1}$ the identity matrix, $\boldsymbol{K}$ the stiffness matrix and $\boldsymbol{D}$ the damping matrix. For the four-mass problem being considered these matrices are

$$\boldsymbol{K} = \begin{bmatrix} \dfrac{-k_{12}}{J_1} & \dfrac{k_{12}}{J_1} & & \\ \dfrac{k_{12}}{J_2} & \dfrac{-k_{12}-k_{23}}{J_2} & \dfrac{k_{23}}{J_2} & \\ & \dfrac{k_{23}}{J_3} & \dfrac{-k_{23}-k_{34}}{J_3} & \dfrac{k_{34}}{J_3} \\ & & \dfrac{k_{34}}{J_4} & \dfrac{-k_{34}}{J_4} \end{bmatrix}, \tag{6.83}$$

$$\boldsymbol{D} = \begin{bmatrix} \dfrac{-D_{12}-D_{11}}{J_1} & \dfrac{D_{12}}{J_1} & & \\ \dfrac{D_{12}}{J_2} & \dfrac{-D_{12}-D_{23}-D_{22}}{J_2} & \dfrac{D_{23}}{J_2} & \\ & \dfrac{D_{23}}{J_3} & \dfrac{-D_{23}-D_{34}-D_{33}}{J_3} & \dfrac{D_{34}}{J_3} \\ & & \dfrac{D_{34}}{J_4} & \dfrac{-D_{34}-D_{44}}{J_4} \end{bmatrix}, \tag{6.84}$$

while the driving matrix $\boldsymbol{B} = \begin{bmatrix} \mathbf{0} & \boldsymbol{J}^{-1} \end{bmatrix}^{\mathrm{T}}$, where $\boldsymbol{J}^{-1}$ is simply a (4×4) diagonal matrix with entries $1/J_1$, $1/J_2$, $1/J_3$ and $1/J_4$. The structure of all these matrices is very clear, allowing more inertia elements to be easily added if required.

The rotor natural frequencies are found from Equation (6.81) by assuming that there is no change in the applied torque when the input vector $\boldsymbol{u} = \mathbf{0}$ gives

$$\dot{\boldsymbol{x}} = \boldsymbol{A}\boldsymbol{x}. \tag{6.85}$$

Section 12.1 will show that the solution of this equation is of the form

$$x_k(t) = \sum_{i=1}^{n} w_{ki} \mathrm{e}^{\lambda_i t} \sum_{j=1}^{n} u_{ij} x_{j0}, \tag{6.86}$$

where λ_i is the eigenvalue of matrix $\boldsymbol{A}$, w_{ki} and u_{ij} are the elements of a matrix made up of eigenvectors of matrix $\boldsymbol{A}$, and x_{j0} is the initial condition of state variable $x_j(t)$.

The eigenvalues λ_i correspond to the rotor natural frequencies. As the damping is small the system will be underdamped and complex conjugate pairs of eigenvalues will be returned of the form

$$\lambda_{i,i+1} = -\zeta_i \Omega_{\mathrm{nat}i} \pm \mathrm{j}\Omega_i, \tag{6.87}$$

where ζ_i is the damping ratio associated with the particular oscillation mode, Ω_i is its damped natural frequency of oscillations (in rad/s) and $\Omega_{\mathrm{nat}\,i}$ is its undamped natural frequency (in rad/s).

The damped, and the undamped, natural frequencies are related by the standard expression $\Omega = \Omega_{\text{nat}}\sqrt{1-\zeta^2}$.

To obtain the mode shapes (see Section 12.1) all the damping coefficients are set to zero when the eigenvalues are purely imaginary and give the undamped natural frequencies. The eigenvector corresponding to each of these undamped natural frequencies is now real and defines how the different rotor masses will be displaced relative to each other if excited at this particular frequency. This is the mode shape and either the elements of the eigenvector associated with the speed deviation or the angle deviation can be used. It is also normal practice to normalize the eigenvectors so that the maximum displacement is set to unity.

The sensitivity of any particular shaft to a harmonic forcing torque on the generator can also be found via Equation (6.81) by defining an output equation

$$\boldsymbol{y} = \boldsymbol{C}\boldsymbol{x}, \tag{6.88}$$

where $\boldsymbol{y}$ is the output required, in this case the torque in a particular shaft or shafts, with the elements of the output matrix $\boldsymbol{C}$ following directly from Equations (6.75) or (6.76). If all the forcing torques are set to zero, except the generator torque which is assumed to be sinusoidal, the transfer function relating the shaft torque $\boldsymbol{y}$ to the input $\boldsymbol{u}$ can be found by substituting Equation (6.88) into (6.81) to give the standard transfer function matrix equation

$$\boldsymbol{G}(\mathrm{s}) = \boldsymbol{C}(\mathrm{s}\boldsymbol{1} - \boldsymbol{A})^{-1}\boldsymbol{B}, \tag{6.89}$$

where $\boldsymbol{B}$ now simply becomes [0 0 0 0 0 $1/J_1$ 0 0 0] and $G_{11}(\mathrm{s}) = y_1/u$, $G_{12}(\mathrm{s}) = y_2/u$ and so on. The inertia entry in $\boldsymbol{B}$ is that of the generator so that its position in the matrix will depend on which mass represents the generator.

The evaluation of the frequency response associated with Equation (6.89) is best achieved using some standard software package such as MATLAB (Hicklin and Grace, 1992) when the matrices $\boldsymbol{A}$, $\boldsymbol{B}$, $\boldsymbol{C}$ and $\boldsymbol{D}$ need only be defined and standard subroutines used to do the rest of the work.

Example 6.2

The shaft configuration for a 577 MVA, 3000 rpm thermal power plant is shown in Figure 6.45 with the parameters detailed in Table 6.2.

The plant matrix, Equation (6.82), is formed using the submatrices defined in Equations (6.83) and (6.84) and the eigenvectors and eigenvalues found using standard MATLAB routines. Figure 6.45 shows the undamped natural frequencies and mode shapes. As in standard practice, all the mode shapes have been normalized with the maximum deflection set to 1.0. Mode 0 represents free-body rotation and, when the generator is connected to the system, the frequency of this mode would increase and become the rotor frequency of oscillations. This can easily be shown by connecting the generator to the infinite system through an 'electromagnetic spring' of stiffness $K_{E'}$ where $K_{E'}$ is the transient synchronizing power coefficient. This concept was introduced in Section 5.4. As the value of $K_{E'}$ depends on the system loading condition, a figure of $K_{E'} = 2.0$ pu has been assumed. This 'electromagnetic spring' will replace the change in generator torque. As $\Delta\tau_2 = -K_{E'}\Delta\delta_2$, $K_{E'}$ must now be included in the stiffness matrix so that element $\boldsymbol{K}[2, 2]$ becomes $\boldsymbol{K}[2, 2] = -(k_{12} + k_{23} + K_{E'})/J_2$. The eigenvalues now give the rotor frequency of oscillations as 1.14 Hz but the rotor system continues to rotate as a rigid body as shown by the mode shape at the bottom of Figure 6.45.

Following the mode shapes through for each individual shaft indicates some degree of movement in the generator–exciter shaft at all the natural frequencies. In mode 1, at 5.6 Hz, the turbine and the generator components remain stationary and the exciter moves relative to them. Mode 4 shows a large amount of movement in the HP–LP_1 shaft while the LP_3–generator shaft displays movement in all modes except mode 1.

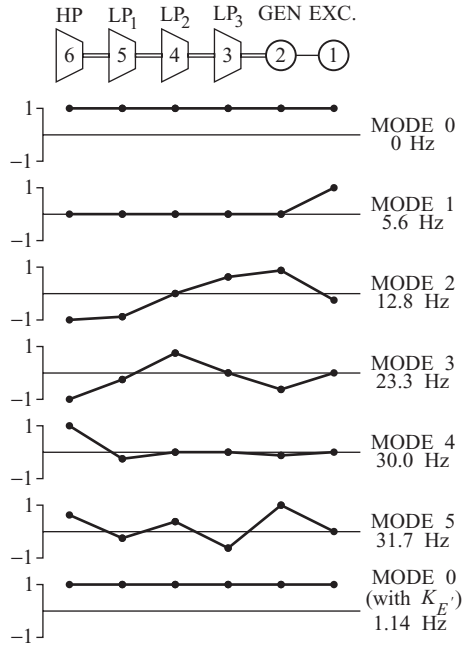

Figure 6.45 The 577 MVA, 3000 rpm, turbine–generator torsional natural frequencies and associated mode shapes.

Table 6.2 The 577 MVA, 3000 rpm, turbine–generator parameters (Ahlgren, Johansson and Gadhammar, 1978)

Node	H_i (s)	k_{ij} (pu torque/rad)	D_{ii} (pu torque/rad/s)	D_{ij} (pu torque/rad/s)
1	0.09	—	0.0	—
1–2	—	0.7	—	0.000 07
2	0.74	—	0.0	—
2–3	—	110	—	0.001
3	1.63	—	0.001	—
3–4	—	95	—	0.001
4	1.63	—	0.001	—
4–5	—	87	0	0.001
5	1.63	—	0.001	—
5–6	—	40	—	0.001
6	0.208	—	0.001	—

To study further the frequency sensitivity of the generator–exciter shaft and the LP_3–generator shaft, the frequency response of these two shafts to a sinusoidal generator torque is shown in Figure 6.46. To obtain this frequency response the $\boldsymbol{B}$ and $\boldsymbol{C}$ matrices are defined as

$$\boldsymbol{B} = \left[0, 0, 0, 0, 0, 0, 0, \frac{1}{J_2}, 0, 0, 0, 0\right]$$

$$\boldsymbol{C} = \begin{bmatrix} -k_{12} & k_{12} & 0 & 0 & 0 & 0 & -D_{12} & D_{12} & 0 & 0 & 0 & 0 \\ 0 & -k_{23} & k_{23} & 0 & 0 & 0 & 0 & -D_{23} & D_{23} & 0 & 0 & 0 \end{bmatrix}.$$

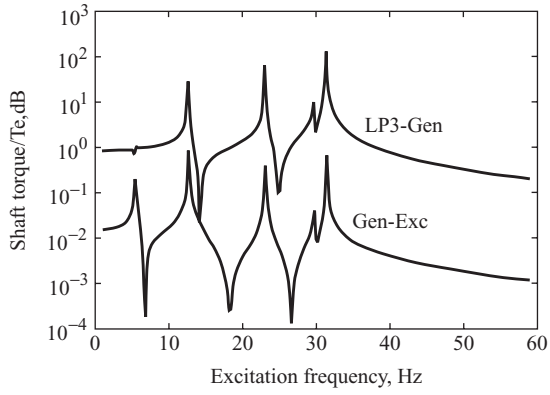

Figure 6.46 Frequency sensitivity of the LP3–generator and the generator–exciter drive shafts for the 577 MVA, 3000 rpm generator.

As expected the generator–exciter shaft is sensitive to all five modes but the torque is somewhat less than that in the LP_3–generator shaft which is particularly sensitive to frequencies around 31.7 Hz but is insensitive to the mode 1 type of oscillation. The distinct nature of these curves is due to the low degree of damping present in the system. Additional damping would reduce the peak values of these curves but unfortunately is not usually available, although a small amount of additional damping may be introduced by the electrical system.

Note that the natural frequencies are substantially removed from 50 and 100 Hz so that the periodic changes in external torque at fundamental or double frequency which occurs under fault conditions (Chapter 4) induce a relatively low value of shaft torque.

Such eigenvalue techniques can readily be extended to include details of the power system and are invaluable when conducting full system stability studies or when assessing the feasibility of new generator designs (Bumby, 1982; Bumby and Wilson, 1983; Westlake, Bumby and Spooner, 1996).

6.7.2 Effect of System Faults

When a system fault occurs, the highest shaft torque is usually in the main shaft connecting the generator and the turbine because the applied torque on these two rotor components is in opposing directions. The shaft between the last two turbine stages, the LP and the IP sections shown in Figure 5.1, can also experience high torques. Figure 6.47a–c shows typical changes in the shaft torque which may occur in the LP–generator shaft (denoted as I in Figure 5.1) when a generator is subjected to three different electromagnetic torques: a step change, a 50 Hz variation and a 100 Hz variation. The highest momentary values of shaft torque occur when the rotor is subject to an aperiodic external torque and are due to the oscillatory shaft torque being reinforced by the external torque on each backswing of the rotor masses. As a result the shaft torque oscillates around the average value of the external torque at a frequency determined by the different torsional natural frequencies. In this example a frequency response similar to that in Figure 6.46 showed the LP–generator shaft to be particularly sensitive to 12 and 24 Hz oscillations and these two frequencies can be observed to dominate the time response.

The above considerations lead to the conclusion that the highest shaft torque corresponds to an electromagnetic torque with a high aperiodic component which, as was shown in the previous sections, appears either after synchronization of a generator when the synchronizing angle is high, or after clearing a fault in the network. Figure 6.48 shows examples of the torque in the main

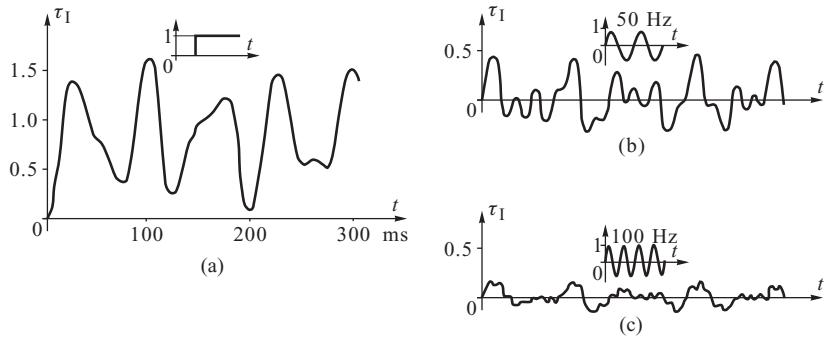

Figure 6.47 Examples of the changes in the torque in the main coupler due to: (a) aperiodic component of the electromagnetic torque; (b) fundamental-frequency component; (c) double-frequency component. Based on Bölderl, Kulig and Lambrecht (1975).

Source: VDE Verlag Gmbh

coupler I during a phase-to-phase short circuit on the generator terminals, after synchronization at a large angle and after clearing a three-phase short circuit in the network.

It is interesting to compare the last two cases. The average value of the shaft torque shown by the dashed line is the same in both cases, but the maximum value is much higher in case (c). This is a direct result of the shaft already being twisted when the fault is cleared, this twist being such that the aperiodic electromagnetic torque appearing on fault clearance reinforces the twist. The influence of the degree of shaft twist on the shaft torque, after the fault is cleared, is shown in Figure 6.49 where it can seen that, when the shaft torque has a negative value at the instant of clearing, the resulting shaft torque is substantially increased. This effect may be compounded by unsuccessful auto-reclosing.

The example shown in Figure 6.48a corresponded to a phase-to-phase short circuit on the generator terminals applied when the generator torque loading was high. However, the corresponding

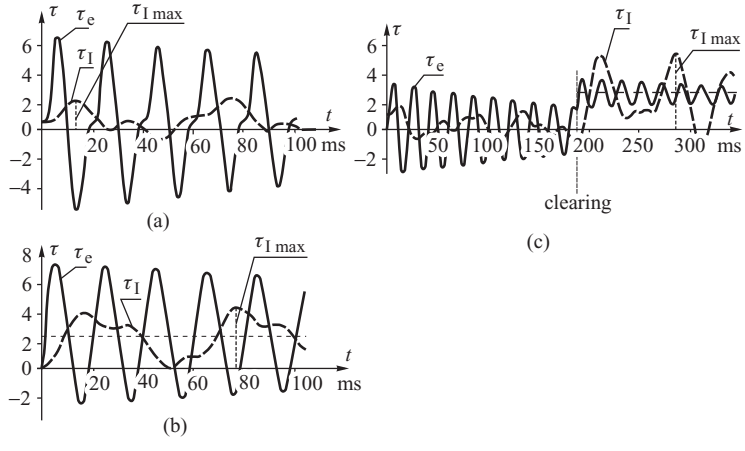

Figure 6.48 Torque acting on the main coupler for the case of: (a) phase-to-phase short circuit on the generator terminals; (b) synchronization when $\delta = 2\pi/3$; (c) fault in the network cleared after 0.187 s. Based on Läge and Lambrecht (1974).

Source: VDE Verlag Gmbh

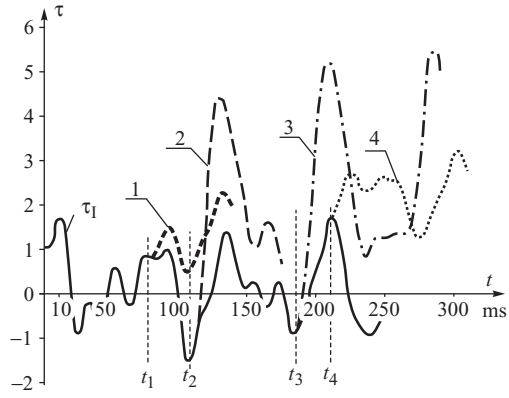

Figure 6.49 Influence of the initial shaft twist on the shaft torque when the fault is cleared after $1 : t_2 = 80$ ms, $2 : t_2 = 110$ ms, $3 : t_2 = 187$ ms, $4 : t_2 = 213$ ms. Based on Kulicke and Webs (1975).

Source: VDE Verlag Gmbh

torque in the main coupler is much smaller than that occurring after clearing a three-phase system fault, Figure 6.48c. This is characteristic of big machines, whereas in medium- and low-power machines the highest shaft torques generally accompany faults on the generator terminals. An approximate relationship between the maximum torque in the main coupler and the clearing time is shown in Figure 6.50. The greater susceptibility of large machines to short circuits in the network is primarily due to the lower per-unit impedance of the generator transformer associated with these large machines so that its influence in the transfer reactance is less than for smaller rated generators. Also the per-unit rotor inertia decreases as unit rating increases so that with large units even short clearing times may result in a relatively large angle increase and a high value of aperiodic torque when the fault is cleared.

6.7.3 Subsynchronous Resonance

Section 4.2 explained how, when a fault occurs in a power system, large currents are produced that consist of a DC offset and an AC term. The AC term depends on the type of fault and, in the case of a

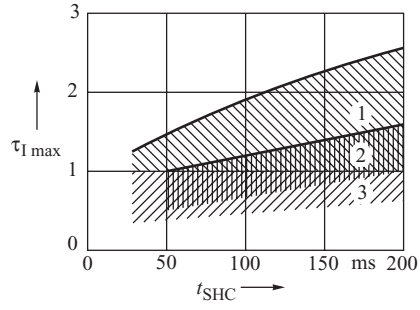

Figure 6.50 Approximate relationship between the maximum torque in the main coupler and the clearing time when the rating of the generator is: $1 : S \gg 500$ MVA; $2 : S < 500$ MVA; $3 : S < 300$ MVA. The value of τ_I is relative to the value of torque accompanying a phase-to-phase fault on the generator terminals. Based on Bölderl, Kulig and Lambrecht (1975).

Source: VDE Verlag Gmbh

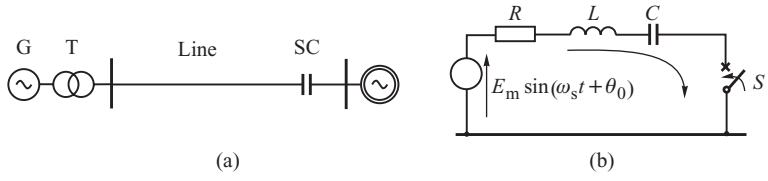

Figure 6.51 Series-compensated transmission line: (a) schematic diagram; (b) simple equivalent circuit to calculate the form of the current when shorting the line.

symmetrical fault, will consist of a positive-sequence component, while with unsymmetrical faults both positive-sequence and negative-sequence components will be present. Due to the relative speed of the rotor with respect to the stator, and the space distribution of the stator armature windings, these different current components produce rotor torques at f_s, 0 and $2f_s$ Hz respectively. Such observations assume that the transmission system is purely inductive and no capacitance compensation is present in the system. Such a system is often referred to as uncompensated.

If now the transmission line reactance is compensated by a series capacitor SC as shown in Figure 6.51a, then, depending on the relative magnitude of the total circuit resistance R, inductance L and capacitance C, the transient component of any current may now be an oscillation at a frequency f_d that decays slowly with time. This oscillation frequency is closely related to the undamped natural frequency of the line, $f_n = 1/2\pi\sqrt{LC}$ Hz. Such oscillations produce rotor currents and torques at a frequency $(f_s - f_n)$ which, if close to one of the rotor torsional natural frequencies, can produce very high shaft torques and ultimate shaft failure. The frequency $(f_s - f_n)$ is known as the *frequency complement* of the line natural frequency f_n as both these frequencies sum to f_s, the system frequency.

The way that such a damped oscillatory current is produced can be understood by considering the equivalent circuit in Figure 6.51b and calculating the current when the switch S is suddenly closed. The differential equation governing the flow of current is

$$L\frac{\mathrm{d}i}{\mathrm{d}t} + Ri + \frac{1}{C}\int i\,\mathrm{d}t = E_m \sin(\omega_s t + \theta_0). \tag{6.90}$$

Differentiating gives

$$\frac{\mathrm{d}^2 i}{\mathrm{d}t^2} + \frac{R}{L}\frac{\mathrm{d}i}{\mathrm{d}t} + \frac{1}{LC}i = \omega E_m \cos(\omega_s t + \theta_0), \tag{6.91}$$

the solution of which is of the form

$$i(t) = i_{trans}(t) + \frac{E_m}{Z}\sin(\omega_s t + \theta_0 + \psi), \tag{6.92}$$

where $Z = \sqrt{R^2 + (X_L - X_C)^2}$, $X_L = \omega_s L$, $X_C = 1/(\omega_s C)$, $\psi = \arctan[(X_C - X_L)/R]$. The left hand side of Equation (6.91) is of the standard second-order form (see Appendix A.3)

$$\frac{\mathrm{d}^2 x}{\mathrm{d}t^2} + 2\zeta\Omega_n\frac{\mathrm{d}x}{\mathrm{d}t} + \Omega_n^2 = 0, \tag{6.93}$$

the solution of which determines the form of transient current. Equation (6.93) will have a different type of solution depending on the value of the damping ratio ζ. Of particular interest is the underdamped solution obtained when $0 < \zeta < 1$, which is of the form

$$i_{trans}(t) = A\mathrm{e}^{-\zeta\,\Omega_n}\sin(\Omega t + \psi_2), \tag{6.94}$$

Table 6.3 Line natural frequency as a function of the degree of compensation

Degree of compensation X_C/X_L	Line natural frequency $f_n = \Omega_n/2\pi$ (Hz)	Frequency complement $(50 - f_n)$ (Hz)
0.1	15.8	34.2
0.2	22.4	27.6
0.3	27.4	22.6
0.4	31.6	18.4
0.5	35.4	14.6

where A and ψ_2 are constants and the damped natural frequency $\Omega = \Omega_n\sqrt{1-\zeta^2}$ (in rad/s). The undamped natural frequency Ω_n (in rad/s) and the damping ratio, ζ, can be found in terms of the circuit parameters by comparing Equation (6.93) with the left hand side of Equation (6.91) to give

$$\Omega_n = \sqrt{\frac{1}{LC}} = \omega_s\sqrt{\frac{X_C}{X_L}} \quad \text{and} \quad \zeta = \frac{R}{2}\sqrt{\frac{C}{L}}. \tag{6.95}$$

Substituting Equation (6.94) into (6.93) gives the total current for the underdamped condition as

$$i(t) = Ae^{-\zeta\Omega_n}\sin(\Omega t + \psi_2) + \frac{E_m}{Z}\sin(\omega_s t + \theta_0 + \psi). \tag{6.96}$$

With currents flowing in each armature phase at frequencies Ω and ω_s, torques are induced in the rotor at the sum and difference of these frequencies to produce rotor currents and torques at frequencies below (subsynchronous) and above (supersynchronous) system frequency given by $(\omega_s - \Omega)$ and $(\omega_s + \Omega)$ respectively. Of particular importance are the subsynchronous torques and the way in which they interact with the turbine and generator rotor. If any subsynchronous torques appear on the rotor at, or near to, any of the rotor torsional natural frequencies, additional energy can be fed into the mechanical vibrations producing a resonance effect in the mechanical system and large shaft torques. Such large shaft torques produce high shaft stresses, a reduction in shaft fatigue life and, possibly, shaft failure. To avoid such *subsynchronous resonance* effects it is important to ensure that no subsynchronous torques are present at, or near to, any of the shaft torsional natural frequencies. Typically these torsional natural frequencies will be in the range 10–40 Hz for a 3000 rpm, 50 Hz generator.

For the simple system shown in Figure 6.51a the subsynchronous frequencies can be estimated using $\Omega_n = \omega_s\sqrt{X_C/X_L}$, Equation (6.95), assuming that the degree of compensation employed is known. The results of such a calculation are shown in Table 6.3 for a 50 Hz system. Assuming the generator used in Example 6.2 to be operating in a simple system such as that shown in Figure 6.51 with ~30 % compensation, the results of Table 6.3 would suggest that subsynchronous resonance with the 23.3 Hz, mode 3, torsional natural frequency might be a problem.

A fuller analysis of subsynchronous resonance problems that includes all the system damping mechanisms would require the use of a full system eigenvalue study such as that conducted by Ahlgren, Johansson and Gadhammar (1978). This and other techniques can be used to study more practical, interconnected, power systems where a number of subsynchronous resonant frequencies may be present (Anderson, Agrawal and Van Ness, 1990).

7

Wind Power

The previous two chapters discussed the problems of steady-state stability (Chapter 5) and transient stability (Chapter 6) and were concerned mostly with system operation of synchronous generators driven by steam or hydro turbines. However, environmental pressures discussed in Chapter 2 have caused many countries to set ambitious targets of renewable generation often exceeding 20% of energy production. Currently wind energy is the dominant renewable energy source and wind generators usually use induction, rather than synchronous, machines. As a significant penetration of such generation will change the system dynamics, this chapter is devoted to a discussion of the induction generator and its influence on power system operation.

7.1 Wind Turbines

The power in the wind can be extracted using a wind turbine. Wind turbines can either rotate about a horizontal axis, *horizontal axis wind turbines* (HAWTs), or a vertical axis, *vertical axis wind turbines* (VAWTs). General practice is to use horizontal axis wind turbines with three blades. Although any number of blades can be used, if too many are used they tend to interfere with each other aerodynamically, while using only two blades tends to lead to large power pulsations as the blades pass by the tower; three blades reduce these power pulsations and are also generally deemed aesthetically more pleasing. Three-bladed HAWTs are therefore generally favoured. Modern wind turbines extract energy from the wind by using aerodynamic blades that produce a lift force along the length of the blade. This aerodynamic force integrated along the length of the blade produces the torque on the turbine shaft. The tip speed of the turbine is limited to typically 80–100 m/s so that as turbines get bigger their rotational speed reduces such that large multi-megawatt turbines rotate slowly at about 15–20 rpm.

Although a number of generator drive arrangements can be used, described later in this section, generally the wind turbine drives a generator through a gearbox that steps up the speed from about 20 rpm at the turbine shaft to 1500 rpm at the generator. The generator is then connected through a transformer to the main electricity supply. The generator and gearbox, along with other associated equipment, are placed at the top of the turbine tower in a *nacelle*. The layout of a typical turbine is shown in Figure 7.1. Besides the generation system other subsystems are required that will turn the turbine into the wind, the *yaw system*, and provide braking. On the turbine side of the gearbox, power is delivered at low speed and very high torque so that a large-diameter drive shaft is necessary. On the generator side the power is delivered at relatively high speed and low torque so that a thinner shaft can be used. Typically the generator will operate at 690 V and the transformer will be placed

Power System Dynamics: Stability and Control, Second Edition Jan Machowski, Janusz W. Bialek and James R. Bumby
© 2008 John Wiley & Sons, Ltd

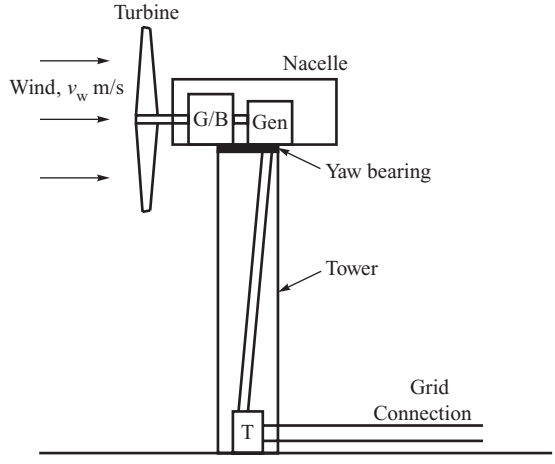

Figure 7.1 Typical arrangement for a wind turbine: G/B, gearbox; Gen, generator; T, transformer.

at the bottom of the tower or in a separate building close to the turbine. It is only in offshore wind turbines that the transformer will be located in the nacelle.

The power in the wind varies as the cube of wind speed, but unfortunately the wind turbine can only extract a fraction of this given by

$$P = \frac{1}{2}\rho A c_{\mathrm{p}} v_{\mathrm{w}}^3 \quad \mathrm{W}, \tag{7.1}$$

where ρ is the density of air, A the turbine swept area, v_w the wind speed and c_{p} the coefficient of performance of the turbine. If the turbine were to extract all the kinetic energy from the wind this would mean that the wind velocity behind the turbine was zero. This is not possible as the air flow must be continuous so that the theoretical maximum energy that can be extracted is with $c_{\mathrm{p}} = 0.599$ and is termed the *Betz limit*. In practice the coefficient of performance is less than this and also varies with the *tip speed ratio* λ as shown in Figure 7.2. The tip speed ratio λ is a non-dimensionless quantity defined as the ratio of the rotor tip speed to the wind speed v_w, that is

$$\lambda = \frac{\omega_{\mathrm{T}} r}{v_{\mathrm{w}}}, \tag{7.2}$$

where ω_{T} is the rotor rotational speed and r is the rotor radius.

The c_{p}/λ curve is unique to a particular design of wind turbine and to extract maximum power the turbine must be operated at the peak of this curve; referred to as *peak power tracking*. For any

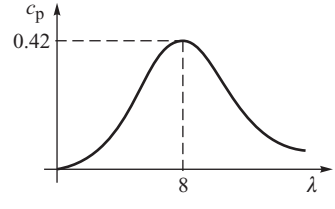

Figure 7.2 Typical c_{p}/λ curve for a wind turbine.

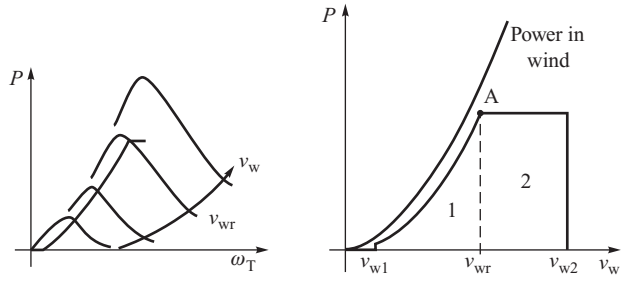

Figure 7.3 Turbine power (a) as a function of shaft speed (b) as a function of wind speed: v_{w1}, cut-in wind speed; v_{wr}, rated wind speed, v_{w2}, shutdown wind speed.

given wind speed, Equations (7.1) and (7.2) and the c_p/λ characteristic can be used to calculate the turbine power as a function of shaft speed as shown in Figure 7.3a.

For a given c_p the turbine power as a function of wind speed can be calculated from Equation (7.1) and is shown schematically in Figure 7.3b. At very low wind speeds the power is very small and the turbine will not operate until the wind speed is above the *cut-in speed*, typically about 3–4 m/s. Above this speed the turbine will produce increasing levels of power until rated wind speed is reached when the power is limited to its rated value. The power now remains constant until the wind speed reaches the *shutdown or furling wind speed*, typically 25 m/s, when the turbine is shut down and turned out of the wind to prevent damage. Turbines are designed to survive to winds of about 50 m/s, referred to as the *survival wind speed*.

As the power increases as the cube of wind speed, at high wind speeds the power can be very large and must be curtailed in some way to prevent damage to the turbine and power conversion equipment. Turbines are generally rated for a wind speed of 12.5 m/s and above this the power is limited in some way to the rated power to give the typical power output curve of Figure 7.3. At these high wind speeds the power content may be large but the number of hours that this occurs per year is small, so the energy content is small compared with the energy available in the mid-speed range. This effect is well represented in Figure 7.4 for a site with a *mean annual wind speed* (MAWS) of 7 m/s. This figure shows the number of hours per year that winds of a certain speed occur; it also shows the energy content associated with these winds in 1 m/s 'bins'. The data are for a turbine of 60 m diameter and show the total energy available at each wind speed and the energy extracted when the power output is limited to the rated value above rated wind speed.

The diameter and rotational speed of a wind turbine are readily calculated for a range of turbine ratings using Equations (7.1) and (7.2) as shown in Table 7.1. The rated wind speed is assumed to

Table 7.1 Diameter and operating speed of wind turbines in a 12.5 m/s wind

Power P (kWe)	Area A (m^2)	c_p	λ	Diameter $2r$ (m)	Rotational speed ω_T (rpm)
1	2.5	0.3	4.5	1.8	629
10	24.8	0.3	4.5	5.6	199
100	247.7	0.3	5	17.8	70
500	1 238.5	0.3	6	39.7	38
1000	2 477.1	0.3	6	56.2	27
2000	4 954.2	0.3	7	79.4	22
5000	12 385.5	0.3	8	125.6	16

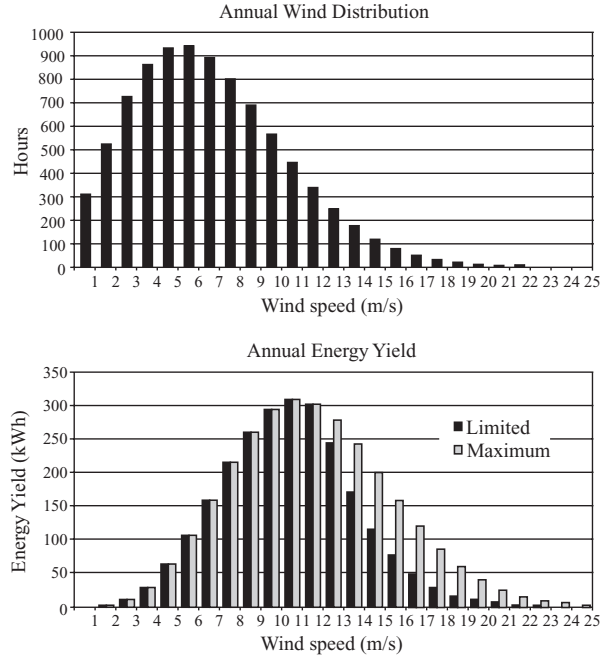

Figure 7.4 Annual energy production by a turbine of 60 m diameter in MAWS of 7 m/s.

be 12.5 m/s. Although a typical c_p value for a large wind turbine is about 0.42, the values used here have been reduced to account for losses in the electrical system so that the power output is electrical power output.

These turbines must be supported on a tower where the height of the nacelle is typically about the same as the blade diameter, but often the actual height of the tower used depends on location and is a manufacturing option.

The energy data in Figure 7.4 show how the energy capture is distributed through the range of wind speeds. Although the data on wind speed distribution are often measured, a good estimate of the distribution can be generated from knowledge of the MAWS at the site using the *Weibull distribution*

$$F(v) = \exp\left[-\left(\frac{v}{c}\right)^m\right]. \tag{7.3}$$

This equation gives the probability that the wind speed v_w is greater than v. In this equation m is the shape factor and c is the scaling factor and depends on the MAWS.

Shape factor varies with location, but for flat terrain in Western Europe a shape factor of two is generally used when the scaling factor can be linked to the MAWS. This special case of the Weibull distribution is sometimes called the *Rayleigh distribution* and the probability that the wind speed is greater than v becomes

$$F(v) = \exp\left[-\frac{\pi}{4}\left(\frac{v}{v_{\text{mean}}}\right)^2\right]. \tag{7.4}$$

This equation can be converted to the number of hours per year that the wind speed is greater than v as

$$\text{hours} = 8760 \times \exp\left[-\frac{\pi}{4}\left(\frac{v}{v_{\text{mean}}}\right)^2\right] = \frac{8760}{\exp\left[\frac{\pi}{4}\left(\frac{v}{v_{\text{mean}}}\right)^2\right]}. \tag{7.5}$$

The number of hours that the wind speed is in a (say) 1 m/s bin at v m/s is now easily found by calculating the number of hours at $v - 0.5$ and $v + 0.5$ and subtracting. Such an approach generates a curve similar to that in Figure 7.4. Of particular importance is the *capacity factor* c_f which is defined as the ratio of the actual energy produced *over a designated time* to the energy that would have been produced if the plant had operated continuously at maximum rating. The time period often used is one year (8760 h)

$$c_f = \frac{\text{actual annual energy production}}{\text{maximum plant rating} \times 8760}. \tag{7.6}$$

For a site with a MAWS of about 7 m/s the capacity factor is about 30 %, but if situated on a site where the MAWS is 5 m/s the capacity factor will drop to about 12 %.

The energy carried in the wind is transferred at discrete frequencies with three major energy peaks occurring at approximately 100 h, 12 h and 1 min, caused by the passing of large-scale weather systems, diurnal variations and atmospheric turbulence, respectively (Van der Hoven, 1957). The longer time variations are relatively predictable while the short-term fluctuations can have a significant effect on the turbine's aerodynamic performance and the power can, and does, fluctuate quite widely due to the turbulent nature of the wind. Although the power output of an individual turbine can vary on a second-by-second basis, the aggregation of the output of a number of turbines soon results in a smooth energy flow. Nevertheless, these fluctuations must be accommodated by the power system.

7.1.1 Generator Systems

A number of generator configurations are used in the conversion of wind energy and these are summarized in Figures 7.5–7.11. In all those diagrams $1:n$ denotes the gear ratio. Most drive systems for large wind turbines use a gearbox to step up the speed from 15 to 30 rpm at the turbine itself to typically 1200–1500 rpm at the generator for a 50 Hz system. Of the generator systems shown, the synchronous generator of Figure 7.5 runs at constant speed and the induction generator system of Figure 7.6 operates at a speed that is very nearly constant and may vary by 2–4 % from no load to full load. Because the change of speed of the induction generator is small, it is often referred to as a *fixed-speed generator*.

The other generator configurations in Figures 7.7–7.11 have different degrees of speed variation. As described earlier in Section 2.2.1, synchronous generators are normally used for power generation

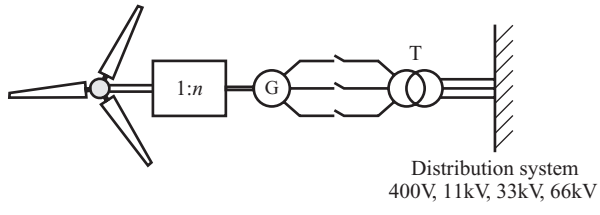

Figure 7.5 Synchronous generator.

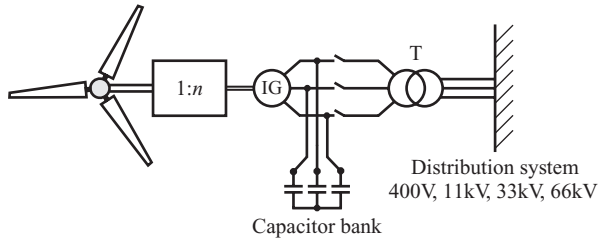

Figure 7.6 Squirrel-cage induction generator.

with conventional gas, steam or water turbines. For completeness Figure 7.5 shows the use of such a generator with a wind turbine but synchronous generators are not normally used for grid-connected wind turbines. The main reason for this is that as the generator runs at a constant speed, the coupling between the generator and the grid for this system is very stiff (see Section 5.4) with the result that all the transient torques produced in the turbine drive shaft due to wind turbulence produce significant mechanical stress on the gears reducing the system reliability. Generator systems with more compliance are therefore favoured. All the other systems shown have this compliance to varying degrees as the speed of the drive system can change when subject to transient torques. However, it is important to realize that synchronous generators may be used to advantage in some stand-alone turbine systems where the frequency of the system can change.

Traditionally the fixed-speed induction generator of Figure 7.6 has been used with the speed geared up to 1500 rpm in land-based turbines of up to about 750 kW. This arrangement is often referred to as the *Danish concept* with the power generated naturally changing as the wind speed changes (Section 7.2). When the turbine is subjected to a wind gust its speed can change slightly and transient torques are reduced compared with the stiff synchronous system. As this generator arrangement operates at a nominally fixed speed, energy capture cannot be maximized but improvements can be made by using an induction generator with a four-pole and six-pole stator winding. This allows the generator to be operated at two speeds, 1000 and 1500 rpm for a 50 Hz system, with a corresponding increase in energy captured. Figure 7.7 shows a modification of the fixed-speed induction machine where the squirrel-cage rotor of the fixed-speed machine has been replaced with a wound rotor. By controlling the resistance of the wound rotor, the speed range over which the turbine operates can be increased slightly, providing yet more compliance in the system (Section 7.4). All induction machines must be supplied with reactive power in order to produce the magnetizing flux in the machine. This reactive power must be supplied from the system and to try and reduce this demand, power factor correction capacitors are often fitted at the generator terminals. In operation the wind turbine system generates whatever power it can and has therefore

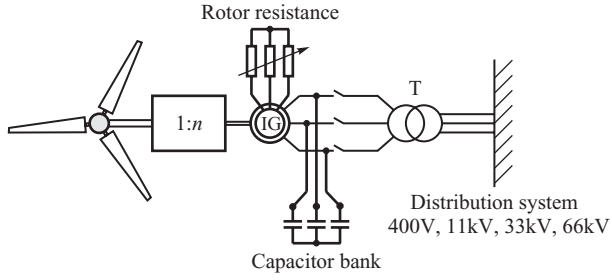

Figure 7.7 Wound-rotor induction generator.

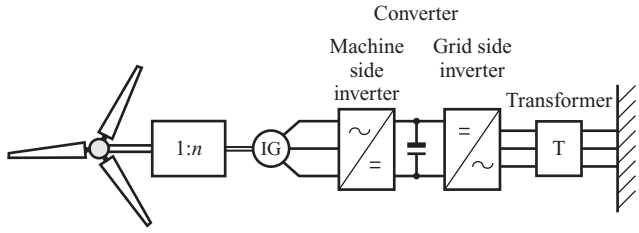

Figure 7.8 Squirrel-cage induction generator with fully rated converter.

traditionally been regarded as *negative load*. As turbine technology develops, network operators are requiring more control of the turbine so that the generator can contribute to a greater, or lesser, extent to voltage control (control of reactive power) and frequency control (control of real power).

By introducing power electronic control into the generator systems as in Figures 7.8–7.11 the speed range over which the generator operates can be increased, so increasing energy capture. As the speed may now change quite significantly as the turbine power changes, the system has a significant degree of compliance and transient torques are further reduced. In addition, the power electronic control allows the power factor at the generator terminals to be varied as required by the network operator. The induction generator with a *fully rated converter*, Figure 7.8, allows a great degree of control but the power electronic converter must be rated at the full MVA output of the turbine and carry the full output of the generator. Such fully rated converters are expensive and one way of reducing the cost is to use a *partially rated converter* and a *doubly fed induction generator* (DFIG). This generator arrangement is shown in Figure 7.9 and is currently the system favoured by many manufacturers for multi-megawatt turbine systems. The DFIG is an induction machine with a wound rotor and with the stator connected directly into the system at system frequency. The rotor is fed from a power converter at slip frequency and, as such, is usually rated at 25–30 % of the generator rating. A converter of this rating allows the speed to vary by a similar amount, that is ±25–30 %, with correct control of the converter allowing both the speed and output power factor of the generator to be controlled (Section 7.5). However, slip rings are necessary with this system to allow the power converter to feed the rotor circuit.

The final two systems in Figures 7.10 and 7.11 have some similar features in that both use fully rated converters and both use synchronous machines. As these generators are decoupled from the network by the converter, they do not suffer the problems of the directly connected synchronous generator of Figure 7.5. Both systems can be used with, or without, a gearbox and both can operate at variable speed. Because of the fully rated power converter, both have full control of the real and

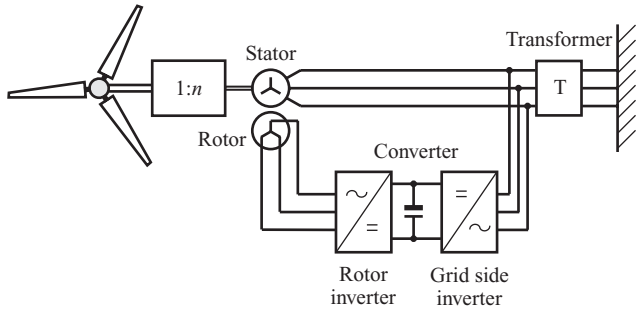

Figure 7.9 Doubly fed induction generator.

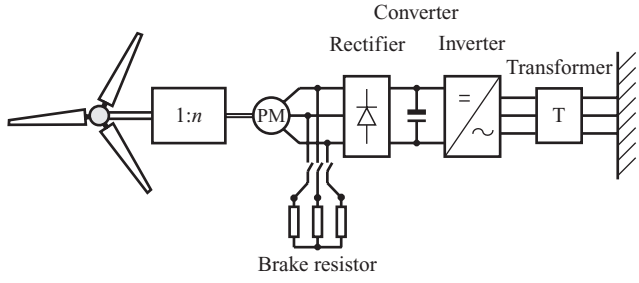

Figure 7.10 Permanent magnet generator with fully rated converter (gearbox optional).

reactive power they generate. Figure 7.10 shows a scheme using a permanent magnet generator where the magnetic field inside the generator is produced by permanent magnets on the rotor. Because there is no field winding in this generator, there is no associated I^2R loss so that this type of generator has a very high efficiency, well above 90 %. The output of the generator is first rectified before being inverted and connected into the network. Although passive rectifiers could be used, normally on large machines an *active rectifier* using IGBT technology is used to give full control over the power delivered to the DC link and also to improve the generator form factor and reduce generator losses and harmonic forces. One special feature of this arrangement is that the permanent magnets always ensure the magnetic field is active so that if the generator is turning it will always induce an emf in the armature windings. This feature can be taken advantage of because, if the generator windings are short-circuited (perhaps through a small resistance to limit the current), a large electromagnetic torque will be produced that will prevent the turbine rotating; that is, it can be used as a braking system.

The arrangement of Figure 7.11 shows a direct-drive synchronous machine. Removing the gearbox is seen to remove one source of failure in the system but requires a low-speed generator. Although a permanent magnet generator is sometimes used without a gearbox, an alternative is to use a wound field machine as shown in Figure 7.11. By using a wound field machine the strength of the magnetic field inside the generator can be controlled by adjusting the current in the field winding. This allows the magnitude of the induced emf to be controlled as the speed of the generator changes. A thyristor converter or an active IGBT rectifier can be used to rectify the variable frequency-generated AC power to DC power before being finally inverted to fixed-frequency AC power for connection to the network. The fully rated converter allows full control of the real and reactive power at the inverter terminals.

Figure 7.3 showed the need for some form of power control at high wind speeds that limits the turbine power output to the rated value so that the rotational speed of the turbine does not exceed its rated speed. In general two forms of power control are possible. The first is to design the turbine blades so that as the wind speed increases, the lift force on the turbine blade reduces and the turbine

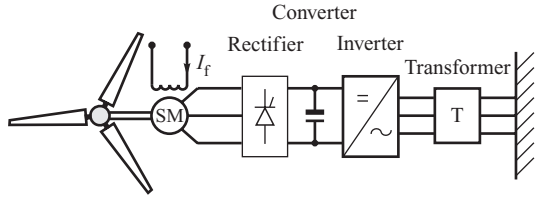

Figure 7.11 Wound field generator with fully rated converter.

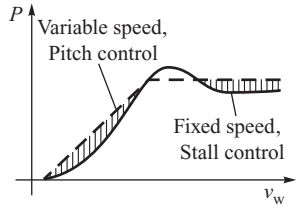

Figure 7.12 Typical power-out curves for a stall-controlled and active pitch-controlled turbine.

blade progressively goes into stall along its length. This is termed *passive stall control*. As stall is determined by *the relative angle at which the wind attacks the blade*, the *angle of attack*, such power control is normally used only on fixed-speed turbines. An alternative form of control is *active pitch control where the pitch of the blades is changed to reduce the power output*. This type of control requires an active control system that changes the pitch of the blades based on some feedback parameter such as rotational speed or output power and is similar in function to the conventional governing systems of Figure 2.12. A third possible control strategy is to pitch the blades in the opposite direction to the conventional pitch-controlled machine when the blades go into stall: this is sometimes termed *active stall*. Table 7.2 classifies the different generation systems of Figures 7.5–7.11 along with the type of power control in a similar way to Hansen, in Ackermann (2005).

The typical variations of power output for a fixed-speed wind turbine with stall control and for a variable speed turbine with pitch control are compared in Figure 7.12. As the rotational speed of a fixed-speed wind turbine does not change significantly, the tip speed ratio cannot be maintained constant as the wind speed varies, Equation (7.2), and the c_p value changes, Figure 7.2. Above rated conditions the blades are designed to stall progressively so that the change in c_p keeps the generated power sensibly constant. However, at lower wind speeds this means that the energy captured is reduced compared with operating at a fixed tip speed ratio and maximum value of c_p. To achieve maximum power output the tip speed ratio must be allowed to vary as wind speed varies so that c_p can be maintained at its peak value; this is called *peak power tracking*. Consequently, allowing the speed of the turbine to vary has a number of advantages over fixed-speed operation including allowing the turbine to operate at the peak of its c_p/λ curve and thereby maximizing energy capture. Also, above rated wind speed the actively controlled machines can maintain a more constant power output as shown in Figure 7.12. To try and improve energy capture, some fixed-speed turbines can operate at two speeds by using an induction generator with both a four-pole and six-pole winding.

Besides increasing the energy capture, allowing the speed of the wind turbine to vary as the wind speed changes also ensures a much softer coupling to the grid than for a fixed-speed turbine, particularly a directly coupled synchronous machine. This has important consequences because introducing compliance into the system by allowing the speed to vary reduces the stress loading on the drive shaft and in the gearbox, thereby increasing its reliability.

Table 7.2 Generator options

Speed range	Passive stall control	Pitch control
Fixed	Figure 7.6	Figure 7.6
Small	—	Figure 7.7
Limited (±30 %) – partially rated converter	—	Figure 7.9
Large – fully rated converter	—	Figures 7.8, 7.10 and 7.11

7.2 Induction Machine Equivalent Circuit

Induction machines are widely used in many applications due to their simple construction and ease of operation. They are mainly used as motors, so, from the power system point of view, they constitute loads. This was discussed in Section 3.5. However, induction machines are also often used as generators in wind farms. To consider how the induction machine can operate as a generator, it is necessary to consider its equivalent circuit in some detail. The induction machine consists of a three-phase stator winding and a rotor. This rotor can either have a squirrel-cage rotor where the rotor windings are simply connected to large shorting rings at either end of the rotor, or a fully wound rotor with the end of the windings brought out to slip rings. In the case of the wound-rotor machine, the winding is a three-phase winding connected in star with the end of each phase connected to one of three slip rings. These slip rings can then be shorted to form effectively a squirrel cage winding or connected into some other external circuit to help form the required machine characteristic. Some of the different connection options are described in this section.

The induction machine is essentially a transformer with a rotating secondary winding and can be represented by the equivalent circuit in Figure 7.13a. In this circuit $\underline{I}_1$ and $\underline{I}_r$ are the stator and rotor currents, respectively, and $\underline{V}$ is the terminal voltage. Current $\underline{I}_2$ is a fictitious current obtained after subtracting the magnetizing current $\underline{I}_m$ from the stator current $\underline{I}_1$. Current $\underline{I}_2$ flows through the equivalent primary winding of the transformer and is the rotor current $\underline{I}_r$ referred to the stator, or primary winding of the machine. Current $\underline{I}_1$ is seen to flow from the terminal voltage $\underline{V}$ towards the rotor, which is the convention used for motoring, rather than generating. Although the discussion in this section is concerned mainly with induction generators, rather than motors, the motoring convention of signs has been retained mainly because it is the convention that the reader is likely to be more used to.

In Figure 7.13a R_1 and X_1 are the resistance and leakage reactance of a stator phase winding while R_2 and L_2 are the rotor resistance and leakage inductance per phase. X_m is the *magnetizing reactance* and it is the current $\underline{I}_m$ flowing through this reactance that sets up the rotating magnetic field. Sometimes a resistance is connected in parallel with the magnetizing reactance to represent the stator *iron loss*: that is, the hysteresis loss and eddy-current loss in the stator core. However, the iron loss is generally small so that the equivalent iron loss resistance is very large compared with the magnetizing reactance and is therefore often omitted from the equivalent circuit. The three-phase stator winding produces a magnetic field that rotates at synchronous speed ω_{sm} and if the rotor is rotating at a speed ω_{rm} slightly different to this, an emf will be induced in the rotor at a frequency proportional to the difference between these speeds and inversely proportional to the pole number, the *slip frequency* f_{slip}. The slip speed is defined as the difference between these two speeds while the per-unit slip, or *slip*, is normalized to the synchronous speed, that is

$$s = \frac{(\omega_{sm} - \omega_{rm})}{\omega_{sm}} = \frac{(\omega_s - \omega_r)}{\omega_s}, \tag{7.7}$$

where $\omega_s = 2\pi f = \omega_{sm} p$ is the angular electrical synchronous frequency, $\omega_r = \omega_{rm} p$ is the rotor electrical angular frequency and p is the number of pole pairs.

In the equivalent circuit of Figure 7.13a the frequency of the currents in the primary winding is the grid frequency f while the current induced in the rotor is at slip frequency f_{slip}. The rotor current is given by

$$I_r = \frac{\frac{s}{n_T} E_1}{R_2 + j\omega_{slip} L_2}, \tag{7.8}$$

where E_1 is the air-gap emf, n_T the turns ratio between the rotor winding and the stator winding, and $\omega_{slip} = 2\pi f_{slip}$ is the slip angular electrical frequency. As the currents in the stator and rotor are at different frequencies, simplifying the equivalent circuit as it stands is not possible. However,

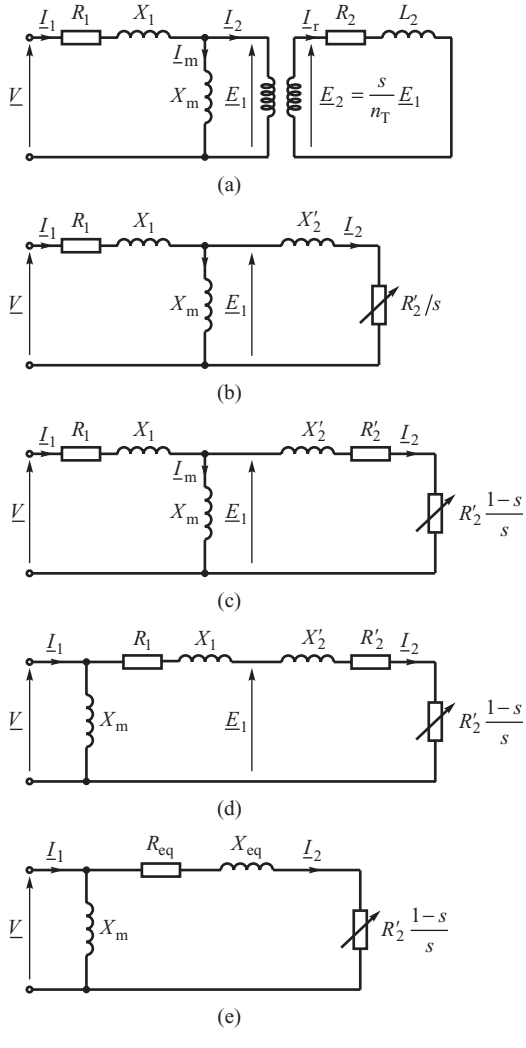

Figure 7.13 Development of the induction machine equivalent circuit (motoring positive).

if the top and bottom of Equation (7.8) are divided by the slip s, noting that the slip electrical frequency is the difference between the stator and rotor electrical frequencies, $\omega_{slip} = \omega_s - \omega_r = s\omega$, then referring to the primary stator winding by dividing by the turns ratio gives the rotor current I_2 referred to the stator as

$$\underline{I}_2 = \frac{\underline{E}_1}{\frac{R'_2}{s} + j\omega L'_2}. \tag{7.9}$$

In this equation R'_2 and L'_2 are the rotor resistance and leakage inductance referred to the stator. Equation (7.9) expresses the rotor current referred to the stator at the grid frequency so allowing the equivalent circuit to be simplified to that of Figure 7.13b. In Figure 7.13c the slip-dependent resistance element is conveniently separated into a fixed resistance R'_2 and a variable resistance

$R_2'(1-s)/s$ that respectively represent the rotor resistance and the mechanical power. This equivalent circuit, Figure 7.13c, is referred to as the *accurate equivalent circuit*. The final simplification is to recognize that the magnetizing current is small compared with the main rotor current and moves the stator resistance and leakage reactance to the rotor side of the magnetizing reactance as in Figure 7.13d to produce the *approximate equivalent circuit*. R_1 and R_2' along with X_1 and X_2' can be usefully combined into an equivalent resistance R_{eq} and equivalent reactance X_{eq} respectively to give the final approximate equivalent circuit of Figure 7.13e. Both the accurate and approximate equivalent circuits are necessary to understand fully the operation of the induction machine as a generator.

Because of its power system implications it is important to realize that the rotating magnetic field in the induction machine is always produced by drawing a magnetizing current $\underline{I}_m$ from the supply regardless of whether the machine acts a motor or generator. This magnetizing current is shown in Figure 7.13a and is represented by the magnetizing reactance X_m. As the magnetizing current must be drawn from the supply, the induction machine always absorbs reactive power and must be connected to a power system that can supply this reactive power if it is to function; only under exceptional circumstances can an induction machine be made to self-excite and this is not relevant to the subject of this book.

Analysis of the simplified circuit of Figure 7.13d gives

$$I_2 = \frac{V}{\sqrt{\left(R_1 + \frac{R_2'}{s}\right)^2 + \left(X_1 + X_2'\right)^2}}. \tag{7.10}$$

This equivalent circuit also defines the power flow through the machine and, if the losses in the stator resistance and the iron core are neglected, then the power supplied to the machine from the grid is the same as the power supplied to the rotor and is given by

$$P_s \approx P_{rot} = 3I_2^2 \frac{R_2'}{s} = \tau_m \omega_{sm}, \tag{7.11a}$$

while the power loss in the rotor resistance and the mechanical power delivered are

$$\Delta P_{rot} = 3I_2^2 R_2' = sP_s \tag{7.11b}$$

$$P_m = 3I_2^2 \frac{R_2(1-s)}{s} = P_s(1-s) = \tau_m \omega_{rm}. \tag{7.11c}$$

As the mechanical power output is equal to the product of the torque and the rotor angular speed ω_{rm}, and noting that slip s is given by Equation (7.7), the power supplied to the rotor can be written in terms of the torque and angular synchronous speed ω_{sm} as $P_s \approx P_{rot} = \tau_m \omega_{sm}$. This is noted in Equation (7.11a).

Equations (7.11a) allow the efficiency of the machine to be expressed as

$$\eta_{motor} = \frac{P_m}{P_s} = (1-s), \quad \eta_{gen} = \frac{P_s}{P_m} = \frac{1}{(1-s)}. \tag{7.12}$$

The shaft torque produced by the machine is obtained from Equation (7.11c) as

$$\tau_m = \frac{P_m}{\omega_{rm}} = \frac{P_m}{\omega_{sm}(1-s)} = \frac{3}{\omega_{sm}} \frac{V^2}{\left[\left(R_1 + \frac{R_2'}{s}\right)^2 + \left(X_1 + X_2'\right)^2\right]} \frac{R_2'}{s}. \tag{7.13}$$

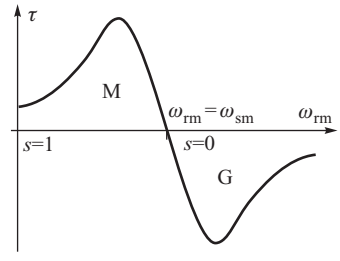

Figure 7.14 Torque–speed characteristics of an induction machine showing both motor and generator action (motoring positive).

The variation of torque with slip is shown in Figure 7.14 for both positive and negative slip. Positive slip is when the rotor speed is less than synchronous speed and corresponds to motor action, and has been discussed in Section 3.5, while negative slip is when the rotor speed is greater than synchronous speed and corresponds to generator action. Similarly, positive torque corresponds to motor action and negative torque to generator action. If the machine is driven at a speed greater than synchronous speed it will naturally generate electrical power into the grid. If the speed drops below synchronous speed then the machine will naturally motor.

The power flow described by Equations (7.11a) is shown diagrammatically in Figure 7.15 where P_g is the power from, or supplied to, the electricity grid. In this diagram the directions are shown as positive for motor action. If power is now supplied to the grid, that is generator action, P_m and P_s reverse direction and slip s becomes negative. As expected, the direction of the rotor loss ΔP_{rot} remains unchanged regardless of motor or generator action.

7.3 Induction Generator Coupled to the Grid

Section 5.4.7 explained how, when a synchronous generator is connected to the grid, it behaves in a similar way to a mechanical mass/spring/damper system where the effective spring stiffness is equivalent to the synchronizing power coefficient $K_{E'}$. This creates a very stiff coupling to the grid (Figure 7.16a) which, for a wind turbine system, can result in large stresses in the drive shaft and gearbox due to the way the system responds through the dynamic torques produced by wind turbulence. A coupling to the system that is much 'softer' and allows a degree of movement at the generator would help reduce these shock torques. Such a coupling is provided by an induction generator as described below.

If the slip is small the induction machine torque, given by Equation (7.13), can be approximated as

$$\tau_m = \frac{3}{\omega_{sm}} \frac{V^2}{\left[\left(R_1 + \frac{R'_2}{s}\right)^2 + \left(X_1 + X'_2\right)^2\right]} \frac{R'_2}{s} \approx \frac{3V^2}{\omega_{sm}} \frac{1}{R'_2} s = D_c \Delta\omega, \tag{7.14}$$

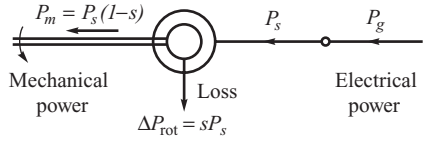

Figure 7.15 Power flow in an induction machine (motoring positive).

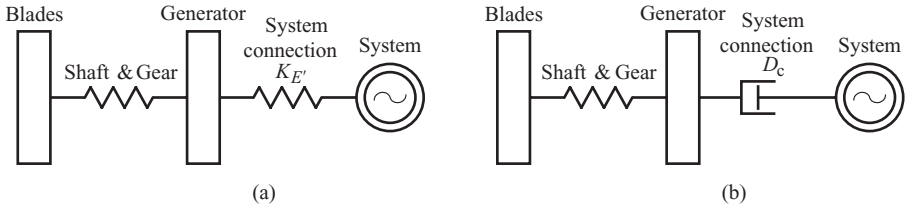

Figure 7.16 Effective system coupling of (a) synchronous and (b) induction generators.

where $\Delta\omega = \omega_s - \omega_r$ is the rotor speed deviation with respect to the synchronous speed and D_c is an equivalent 'damper constant'. Equation (7.14) shows that the induction machine torque is proportional to speed deviation, implying that the coupling of the induction machine to the grid is analogous to a mechanical damper as shown in Figure 7.16b. Such a coupling introduces a substantial degree of compliance, or 'give', into the system and is much softer than the stiff coupling associated with the synchronous generator. This has important advantages for some energy conversion systems, such as large wind turbines, because the additional compliance helps reduce the stress in the drive shaft due to the dynamic torques produced by wind gusting and wind turbulence. Equation (7.14) also shows that the 'damper constant' D_c determines the effective compliance and that this can be controlled by changing the rotor resistance.

Generally when an induction machine is connected to the grid, and used as a generator, it will be within the distribution network rather than the main transmission network. Used in this way, such generation is termed *embedded generation* and is typical of wind generators and other forms of renewable energy generation.

When assessing the performance of an induction generator embedded within the system, the system reactance X_s and resistance R_s impact on the operation of the induction generator and modify the equivalent circuit as shown in Figure 7.17 (Holdsworth, Jenkins and Strbac, 2001). The system impedance as seen by the induction generator is affected by a number of factors:

1. The 'strength' of the network. If the network is *strong* the reactance between the generator and the system will be small, leading to a large short-circuit level. The short-circuit level being defined at the *point of common connection* as V_s/X_s. On the other hand, a *weak s*ystem will have a large reactance and low short-circuit level.
2. For distribution networks, resistance affects are more apparent than at the transmission or subtransmission level with the X/R ratio changing from typically 10 for transmission networks to 2 for distribution networks.

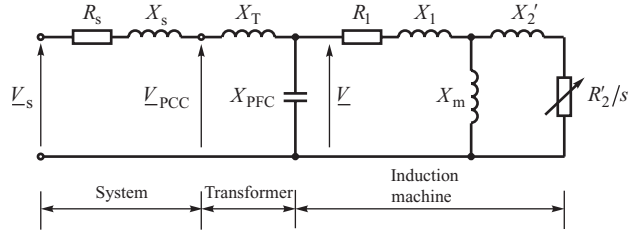

Figure 7.17 Induction machine equivalent circuit including system reactance and resistance (V_{PCC}, voltage at the point of common connection; X_{PFC}, power factor correction capacitance).

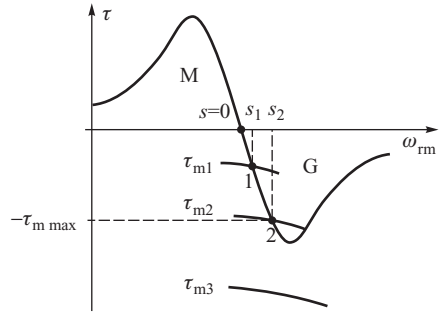

Figure 7.18 Steady-state stability of an induction generator (motoring positive).

Also impacting on the system behaviour is the need for power factor correction at the terminals of the induction generator. Whether motoring or generating, the power system must always supply the magnetizing current to the induction machine, therefore the induction machine always consumes reactive power and the system must supply this. The magnetizing current is represented by the magnetizing reactance in the equivalent circuits of Figure 7.13. The amount of reactive power varies depending on the loading condition, being a maximum at no load and reducing at full load.

The induction machine torque slip curve determines the steady-state stability of the generator. Figure 7.18 shows what happens if the applied mechanical driving torque increases. Initially the induction generator is operating at point 1 with a mechanical applied torque ($-\tau_{m1}$). The mechanical torque is now increased to τ_{m2}. As the applied mechanical torque is now greater than the electrical torque, the generator speeds up (slip increases) and operates at a slightly higher slip s_2 at point 2. If the applied torque is now increased to τ_{m3} the applied torque and the electrical torque curves do not intersect and there is no steady-state operating point so the system will be unstable. The peak of the torque/slip curve determines the *pull-out torque* and the system steady-state stability limit.

Equation (7.13) can be used to see the way in which system reactance modifies the torque/slip characteristic if the equivalent circuit is modified to a very approximate one as in Figure 7.13d with the network resistance R_s incorporated into R_1, the network reactance X_s and transformer reactance X_T incorporated into X_1, and the stator voltage becoming the system supply voltage V_s. However, accurate calculation must use the accurate equivalent circuit of Figure 7.13. Peak torque occurs when $d\tau_m/ds$ is a maximum and occurs when

$$s_{max} = \frac{R_2'}{\sqrt{R_1^2 + (X_1 + X_2')^2}} \approx \frac{R_2'}{X_1 + X_2'}, \tag{7.15}$$

giving the pull-out torque

$$\tau_{mmax} = \frac{3}{2\omega_{sm}} \frac{V_s^2}{\left[R_1 + \sqrt{R_1^2 + (X_1 + X_2')^2}\right]}. \tag{7.16}$$

This equation shows that the pull-out torque is independent of the rotor resistance, but as the system reactance increases, X_1 increases and the pull-out torque reduces, so reducing the generator steady-state stability. This will be most apparent on a weak system where system reactance is greatest, Figure 7.19a. Also the pull-out torque will reduce if the system voltage is reduced for any reason,

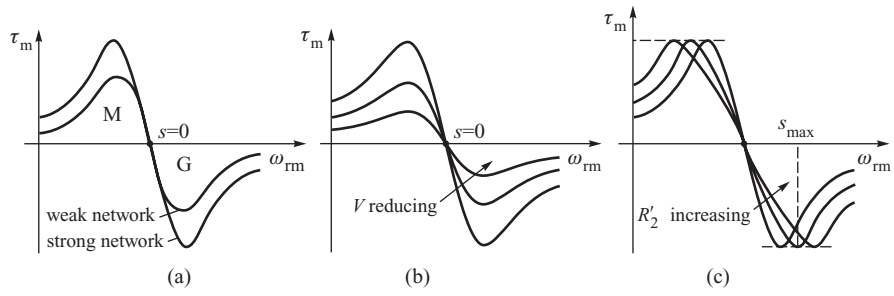

Figure 7.19 Effect of system reactance and voltage on pull-out torque: (a) system reactance; (b) system voltage; (c) rotor resistance (motoring positive).

Figure 7.19b, but the slip at which the pull-out torque occurs is not affected. In contrast Equation (7.15) shows that the slip at which the maximum torque occurs is determined by the rotor resistance; increasing the rotor resistance increases the maximum slip. This effect is shown in Figure 7.19c. Not only will increased rotor resistance make the system connection more compliant, as described by Equation (7.14), but also it increases the speed at which the pull-out torque occurs; this can have implications on the transient stability of induction machines (Section 7.9).

Typically the slip range that the induction generator will operate over will be 0.02 indicating a maximum speed change of 2 %, that is 30 rpm for a 1500 rpm generator. As this is a relatively small speed range, turbines using this type of induction generator are often referred to as *fixed-speed machines*.

7.4 Induction Generators with Slightly Increased Speed Range via External Rotor Resistance

In some instances it is required to increase the speed range over which the induction generator operates. For example, in the case of a wind turbine, allowing the speed to vary may increase the energy capture while allowing the speed to vary will also reduce the shock torques on the turbine and gearbox due to wind turbulence. Equation (7.15) shows that the maximum slip increases as the rotor resistance increases but the actual pull-out torque is not affected, Figure 7.19c. To achieve this a wound-rotor induction is normally used with the three-phase rotor winding connected to a variable resistor bank through slip rings, Figure 7.20, although the use of resistors rotating on the shaft is possible in order to avoid the use of slip rings. Such arrangements tend to increase the speed range by about 5–10 %.

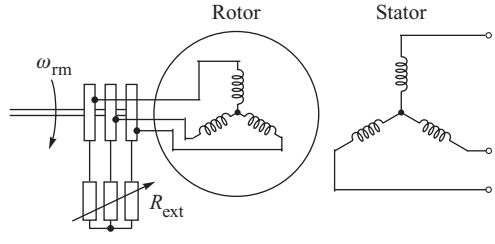

Figure 7.20 Induction generator with variable rotor resistance.

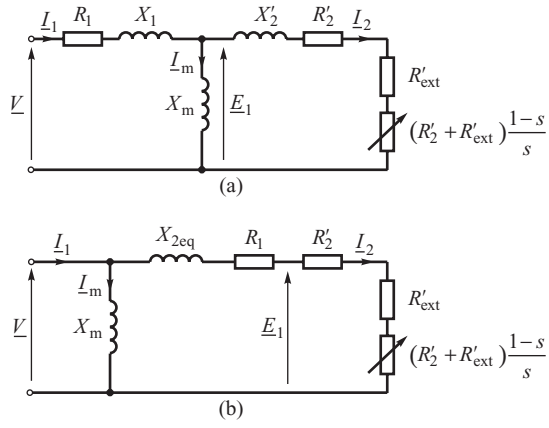

Figure 7.21 Equivalent circuit for induction machine with external rotor resistance: (a) accurate and (b) approximate equivalent circuits (motoring positive).

The equivalent circuit must now be modified as shown in Figure 7.21 with R'_{ext} being the external rotor resistance R_{ext} referred to the stator. Using the approximate equivalent circuit of Figure 7.21b, the current and torque expressions of Equations (7.10) and (7.13) now become

$$I_2 = \frac{V}{\sqrt{\left(R_1 + \frac{(R'_2+R'_{ext})}{s}\right)^2 + \left(X_1 + X'_2\right)^2}}, \tag{7.17}$$

$$\tau_m = \frac{P_m}{\omega_{rm}} = \frac{P_m}{\omega_{sm}(1-s)} = \frac{3}{\omega_{sm}} \frac{V^2}{\left[\left(R_1 + \frac{(R'_2+R'_{ext})}{s}\right)^2 + \left(X_1 + X'_2\right)^2\right]} \frac{\left(R'_2 + R'_{ext}\right)}{s}, \tag{7.18}$$

and Equations (7.11) change to

$$\text{Power supplied} \quad P_s \approx P_{rot} = 3I_2^2 \frac{(R'_2 + R'_{ext})}{s} = \tau_m \omega_{sm}, \tag{7.19a}$$

$$\text{Power loss in rotor} \quad \Delta P_{rot} = 3I_2^2(R'_2 + R'_{ext}) = sP_s, \tag{7.19b}$$

$$\text{Mechanical power} \quad P_m = 3I_2^2 \frac{(R'_2 + R'_{ext})(1-s)}{s} = P_s(1-s) = \tau_{sm}\omega_{rm}. \tag{7.19c}$$

Equations (7.17) and (7.19) show that if the ratio $(R'_2 + R'_{ext})/s$ is held constant then the current and the torque do not change. That is, if the effective total rotor resistance is doubled then the same torque and current will occur at twice the slip. Thus rated torque will always occur at rated current and only the slip (speed) will be different, the slip being scaled by the factor $(R'_2 + R'_{ext})/R'_2$ (O'Kelly, 1991).

The efficiency is again given by Equation (7.12) but as the slip is now greater than for a generator with no external rotor resistance the efficiency is less due to the additional loss in the external rotor resistors. However, in the case of a wind turbine generator the gain in energy capture achieved by allowing speed variation coupled with the more compliant grid coupling must be balanced against the loss in efficiency in the generator itself. The power flow is shown in Figure 7.22.

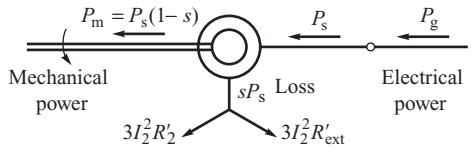

Figure 7.22 Power flow in an induction machine with additional external resistance (motoring positive).

7.5 Induction Generators with Significantly Increased Speed Range: DFIGs

Adding external resistance into the rotor circuit has been shown to allow a small increase in the speed range over which the induction machine can operate but at the cost of reduced efficiency due to the losses in the external rotor resistance. The beneficial features of an increased operating speed range can be retained (and expanded) if rather than dissipating the energy into external resistors, it is fed back into the power system using a power electronic converter such as that shown in Figure 7.23. This converter consists of two fully controlled IGBT bridge circuits: one, the machine-side inverter, connected to rotor slip rings; and the other, the grid-side inverter, connected to the grid. Together these two inverters produce a four-quadrant converter that can feed power at any frequency or voltage to or from the rotor. The machine-side inverter injects a voltage into the slip rings $\underline{V}_s$ at a slip frequency that is controlled in both magnitude and phase and allows both the torque and the power factor of the machine to be controlled over a large speed range. The grid-side inverter is typically controlled to maintain a constant DC link voltage. As the machine now has power 'feeds' to both the stator and rotor from the grid, this type of system is commonly referred to as a *doubly fed induction machine* (DFIM). This arrangement is commonly used as a generator with large wind turbines when it is known as a *doubly fed induction generator* (DFIG) and tends to increase the speed range by about 30 %.

The DFIM system shown in Figure 7.23 is very similar to the static Kramer and Scherbius schemes used in the past to control the speed of induction motors (O'Kelly, 1991). It differs from the static Kramer scheme in that it uses an IGBT inverter as the machine-side converter instead of a passive rectifier, thereby allowing the injected voltage to be fully controlled in both phase and magnitude. It also allows power flow in both directions to the rotor. In concept it is the same as the static Scherbius system but with the three-phase to three-phase cycloconverter of the Scherbius system replaced by the two fully controlled IGBT bridges.

As the voltage and current injected into the rotor are at slip frequency, the DFIM can be thought of as either an induction machine or a synchronous machine. When the machine operates at synchronous speed the slip frequency is zero, injected rotor current is at DC level and the machine

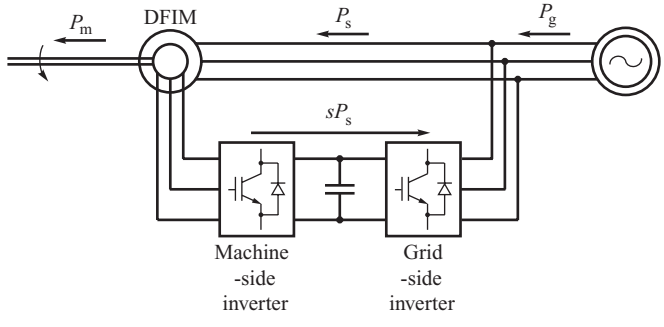

Figure 7.23 Doubly fed induction machine system.

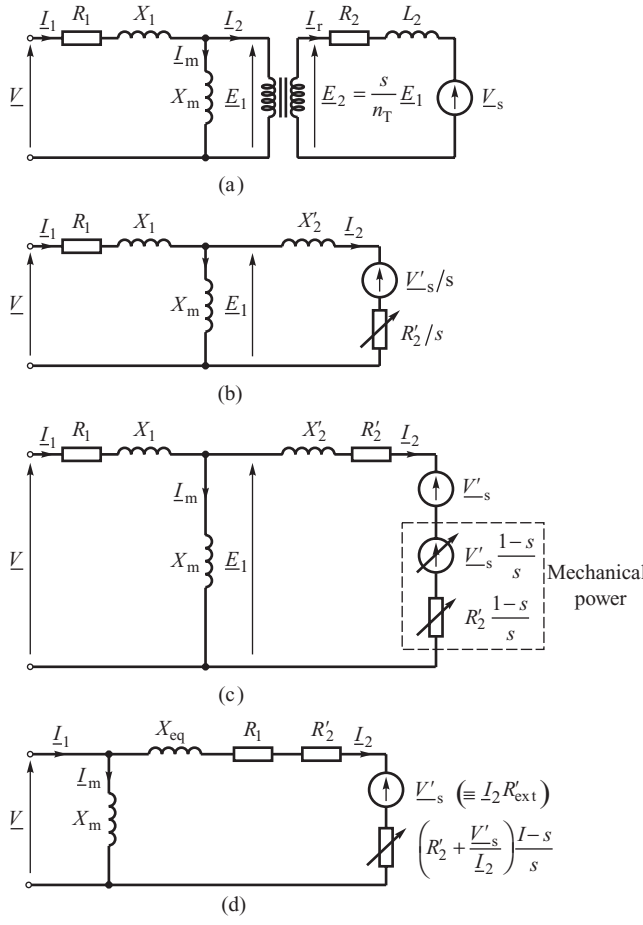

Figure 7.24 DFIM equivalent circuit: (a) stator and rotor; (b) and (c) rotor referred to stator – accurate equivalent circuit; (d) rotor referred to stator – approximate equivalent circuit (motoring positive).

behaves exactly as a synchronous machine. At other speeds the synchronous machine analogy can still be used but the injected rotor current is now at slip frequency. Analysing the machine as both an induction machine and a synchronous machine gives a valuable insight into its operation.

The equivalent circuit for the DFIM is shown in Figure 7.24a with $\underline{V}_s$ being the rotor injected voltage. Following the same procedure as in Section 7.2 for the standard squirrel-cage induction motor allows the rotor circuit, operating at slip frequency, to be referred to the stator at grid frequency to give the equivalent circuit of Figure 7.24b. The effect of the transfer is to have, as before, a rotor resistance that varies with slip but now also with an injected voltage that also varies with slip. These two components can be divided into a fixed value and a variable value as shown in Figure 7.24c. The fixed values reflect the actual rotor resistance R_2 and the actual injected voltage $\underline{V}_s$ while the variable terms represent the mechanical power. If required, the accurate equivalent circuit can again be modified to an approximate one by moving the magnetizing reactance in front of the stator components R_1 and X_1, Figure 7.24d.

7.5.1 Operation with the Injected Voltage in Phase with the Rotor Current

Assume that the injected voltage $\underline{V}_s$ is in phase with the rotor current. This is equivalent to adding an external resistance, equal to the ratio of the injected voltage to the rotor current, into the rotor circuit. Comparing the equivalent circuit in Figure 7.24c with that in Figure 7.21a, they are clearly the same if

$$V'_s = I_2 R'_{ext} \quad \text{or} \quad R'_{ext} = \frac{V'_2}{I_2}. \tag{7.20}$$

Substituting for R'_{ext} into Equations (7.17) and (7.18) allows the current and the torque to be written in terms of the injected voltage as

$$I_2 = \frac{V}{\sqrt{\left[R_1 + \left(R'_2 + \frac{V'_s}{I_2}\right)\frac{1}{s}\right]^2 + \left(X_1 + X'_2\right)^2}}, \tag{7.21}$$

and

$$\tau_m = \frac{P_m}{\omega_{rm}} = \frac{P_m}{\omega_{sm}(1-s)} = \frac{3}{\omega_{sm}} \frac{V^2}{\left\{\left[R_1 + \left(R'_2 + \frac{V'_s}{I_2}\right)\frac{1}{s}\right]^2 + \left(X_1 + X'_2\right)^2\right\}} \left(R'_2 + \frac{V'_s}{I_2}\right)\frac{1}{s}. \tag{7.22}$$

Rearranging Equation (7.21) with $X_{eq} = X_1 + X'_2$ gives slip as a function of current and injected voltage as

$$s = \frac{I_2 R'_2 + V'_s}{\sqrt{V^2 - [I_2 X_{eq}]^2} - I_2 R_1}. \tag{7.23}$$

The torque and current for a given slip can be calculated from Equations (7.21) and (7.22) but the equations are cumbersome and it easier to consider a range of values for I_2 and calculate the resulting torque and slip from Equations (7.22) and (7.23) respectively (O'Kelly, 1991). At no load $I_2 = 0$ and Equation (7.23) reduces to

$$s_0 = \frac{V'_s}{V}, \tag{7.24}$$

and the machine operates with a slip that depends on the magnitude and polarity of the injected voltage V_s:

- V_s positive, slip increases and the speed reduces: subsynchronous operation;
- V_s negative, slip becomes negative and the speed increases: supersynchronous operation.

Operation over a wide speed range both above and below synchronous speed is now possible by controlling the magnitude and polarity of the injected voltage.

The slip range over which the machine can operate depends on the magnitude of the injected voltage and that is controlled by the inverter. The greater the no-load slip, the greater the injected voltage. For example, if a speed range of ±30 % is required the injected voltage must be 30 % of the nominal supply value. It is this speed range that also determines the rating of the inverter system. The volt-amperes passing through the converter system is

$$\text{V A}_{inv} = 3V'_s I_2 = 3s_0 V I_2 \approx s_0 S_{rat}, \tag{7.25}$$

where S_{rat} is the volt-ampere rating of the machine.

So for a ±30 % speed range the rating of the converter must be 30 % of the machine rating. It is this range of speed control with a partially rated converter that makes this type of machine economically attractive as opposed to an induction generator or permanent magnet generator with all the machine output passing through an expensive, fully rated converter (Section 7.1).

Substituting for R'_{ext} from Equation (7.20) into the power flow equations (7.19) allows the power supplied by the machine to be written (neglecting the loss in armature resistance) as

$$P_{\text{s}} \approx P_{\text{rot}} = 3I_2^2 \frac{R'_2}{s} + 3\frac{V'_2}{s} I_2 = \tau_{\text{m}} \omega_{\text{sm}}. \tag{7.26}$$

Expanding and rewriting this expression gives

$$\begin{aligned} P_{\text{s}} \approx P_{\text{rot}} &= 3I_2^2 R_2 + 3V_{\text{s}} I_2 + 3I_2(V_{\text{s}} + I_2 R_2)\frac{(1-s)}{s} = \tau_{\text{m}} \omega_{\text{sm}} \\ &\equiv \text{rotor loss} + \text{injected power} + \text{mechanical power}. \end{aligned} \tag{7.27}$$

The first term in this expression is the power lost in the rotor resistance, the second the power that is extracted or injected into the rotor by the converter, and the third the mechanical power produced. Depending on the polarity of the injected voltage, power can be either:

- extracted from the rotor and fed back to the supply; or
- injected into the rotor from the supply.

In Equation (7.27) the first two terms are associated with the power lost or transferred in the rotor circuit while the third represents the mechanical power, that is

$$\text{Power transfer} \quad \Delta P_{\text{rot}} = 3I_2^2 R'_2 + 3V'_s I_2 = sP_{\text{s}}, \tag{7.28a}$$

$$\text{Mechanical power} \quad P_{\text{m}} = 3I_2(V'_{\text{s}} + I_2 R'_2)\frac{(1-s)}{s} = P_{\text{s}}(1-s) = \tau_{\text{m}} \omega_{\text{rm}}, \tag{7.28b}$$

with the stator and supply powers respectively being

$$\text{Stator power} \quad P_{\text{s}} \approx \tau_{\text{m}} \omega_{\text{sm}}, \tag{7.28c}$$

$$\text{Supply power} \quad P_{\text{g}} = P_{\text{s}} - \Delta P_{\text{rot}} = P_{\text{s}}(1-s). \tag{7.28d}$$

This power flow is shown in Figure 7.25 and, if the rotor resistance loss is assumed to be negligible, the regenerated power sP_{s} is added algebraically to the stator power to obtain the supply power. As loss in both the armature resistance and rotor resistance has been neglected, the power from or to the supply is the same as the mechanical power and the efficiency is a nominal 100 %; that is, it

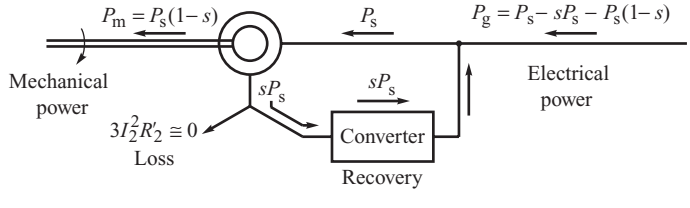

Figure 7.25 Power flow in a DFIM (motoring positive).

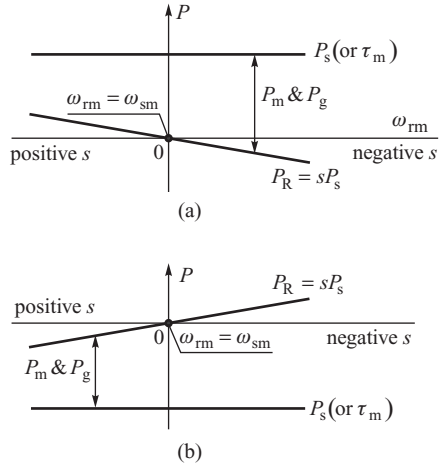

Figure 7.26 Power flow in a DFIM: (a) motoring; (b) generating.

is not slip dependent as occurs with external rotor resistance control, because now any additional 'loss' in the rotor circuit is fed back to the supply.

Assuming a constant stator power P_s (constant mechanical torque), Equations (7.28) explain how this type of machine can be controlled. Figure 7.26 sketches the power flow through the rotor for both motoring (a) and generating (b) over a slip range of about ±30 %.

The following observations can be made:

- Rotor speed above synchronous (supersynchronous operation) – slip negative:
  - acts as a motor if power is injected into the rotor from the supply;
  - acts as a generator if power is extracted from the rotor and fed back to the supply.
- Rotor speed below synchronous (subsynchronous operation) – slip positive:
  - acts as a motor if power is extracted from the rotor and fed back to the supply;
  - acts as a generator if power is injected into the rotor from the supply.
- For a constant slip the amount of power injected or extracted from the rotor determines the stator power and machine torque; increasing the amount of injected or extracted power increases the torque.

This is the basis for a control strategy that can be implemented in the two inverters of Figure 7.23 that supply the rotor circuit and will be examined further later in this section.

7.5.2 Operation with the Injected Voltage out of Phase with the Rotor Current

Equation (7.20) assumed that the voltage $\underline{V}_s$ was injected at slip frequency in phase with the rotor current. If, however, the voltage was injected at some arbitrary controlled phase angle to the rotor current then Equation (7.20) becomes

$$\frac{\underline{V}'_s}{\underline{I}_2} = R'_{ext} + j X'_{ext}, \tag{7.29}$$

and it appears as though the injected voltage is introducing a fictitious impedance $R'_{ext} + j X'_{ext}$. The effect of R'_{ext} has already been discussed, while the influence of X'_{ext} is to increase or decrease the effective rotor impedance depending on the sign and value of X'_{ext} (and will be determined by the

relative phase of the injected voltage). This will control the rotor and hence the machine power factor. So, by controlling the magnitude and phase of the injected voltage both the speed or torque and the power factor of the machine can potentially be controlled.

7.5.3 The DFIG as a Synchronous Generator

The previous discussion has considered the DFIM as an induction machine but it can usefully be considered as a synchronous machine. A synchronous machine rotates at synchronous speed and the current is fed into the rotor field circuit at DC level to produce the synchronously rotating field. In contrast, in the DFIG the speed can vary and the current is fed into the rotor at slip frequency in order to produce the synchronously rotating field.

Figure 7.23 shows that the rotor power converter comprises a grid-side and a machine-side inverter. A common control scheme is to operate both inverters using *pulse width modulation* (PWM) in a *current control mode* with the grid-side inverter being controlled to keep the DC link voltage constant. The machine-side inverter is then controlled to achieve the required torque loading and the required reactive power at the machine terminals. This is achieved by controlling the magnitude of the real and imaginary parts of the rotor current. To understand this control scheme the accurate equivalent circuit of Figure 7.24(c) is redrawn as in Figure 7.27 by noting that the current through the magnetizing reactance can be written in terms of the rotor $\underline{I}_2$ and stator $\underline{I}_1$ current as

$$\underline{I}_m = \underline{I}_2 - \underline{I}_1, \tag{7.30}$$

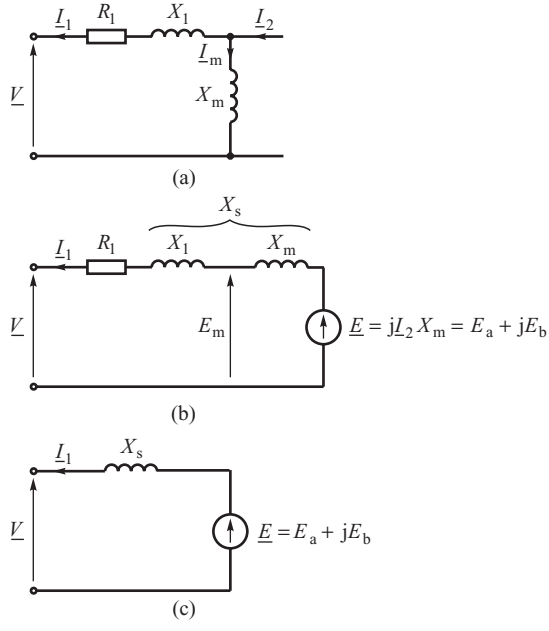

Figure 7.27 DFIG equivalent circuit as a synchronous machine: (a) stator and rotor current as induction machine; (b) rotor current as a voltage source; (c) equivalent circuit as a synchronous machine (generating positive).

when the voltage across the magnetizing reactance $\underline{E}_m$ can be written as

$$\underline{E}_m = j\underline{I}_m X_m = j\underline{I}_2 X_m - j\underline{I}_1 X_m = \underline{E} - j\underline{I}_1 X_m. \tag{7.31}$$

This allows the magnetizing reactance to be split between the rotor and stator currents and the equivalent circuit modified to that in Figure 7.27b with the synchronous reactance being the sum of the stator leakage reactance X_1 and the magnetizing reactance X_m (Section 4.2.3). If stator resistance is assumed negligible then the equivalent circuit simplifies to that of the standard synchronous generator shown in Figure 7.27c. Importantly now both the magnitude and phase of the induced emf relative to the stator voltage can be fully controlled by controlling the real and imaginary components of the induced emf $\underline{E}$. To conform with previous discussions on synchronous machines elsewhere in this book, generator action is taken as positive.

From Equation (7.31) the emf $\underline{E}$ induced by the rotor current is

$$\underline{E} = j\underline{I}_2 X_m. \tag{7.32}$$

The rotor current can be expressed in its real and imaginary components

$$\underline{I}_2 = I_{2a} + jI_{2b}, \tag{7.33}$$

so that

$$\underline{E} = E_a + jE_b = -X_m I_{2b} + jX_m I_{2a}, \tag{7.34}$$

and the induced emf $\underline{E}$ is controllable in both magnitude and phase by controlling the in-phase and out-of-phase components of the rotor current I_{2a} and I_{2b} respectively.

This is shown in the phasor diagrams of Figure 7.28. The first phasor diagram in Figure 7.28a shows how the real and imaginary rotor current components contribute to the emf $\underline{E}$. If the system voltage $\underline{V}$ is assumed to act along the real axis then Figure 7.28b shows a phasor diagram very similar to that for the standard synchronous generator, only now the current I_2 will fully control the

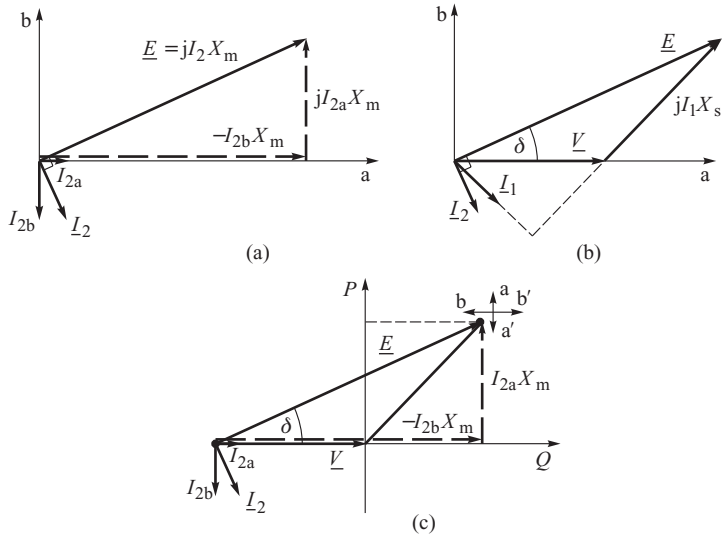

Figure 7.28 Phasor diagrams of DFIG as a synchronous machine. (a) showing how rotor current controls the induced emf; (b) phasor diagram; (c) operating chart.

magnitude and phase of $\underline{E}$. In contrast, in the standard synchronous machine, the emf is induced by a direct current in the rotor so that only the magnitude of the induced emf can be controlled; this allows the control of one output variable only, namely reactive power.

With the stator voltage acting along the real axis and defined as

$$\underline{V} = V_a + j0, \tag{7.35}$$

and neglecting stator resistance,

$$\underline{I}_s = \frac{\underline{E} - \underline{V}_s}{jX_s} = \frac{E_a + jE_b - V_a}{jX_s} = \frac{E_b}{X_s} - j\frac{(E_a - V_a)}{X_s}. \tag{7.36}$$

The stator power is then given by

$$\underline{S}_s = 3\underline{V}\underline{I}_s^* = P_s + jQ_s = 3\frac{V_a E_b}{X_s} + j3\frac{V_a(E_a - V_a)}{X_s}. \tag{7.37}$$

Substituting for E_a and E_b from Equation (7.34) gives the important expression

$$S_s = \left[3V_a\frac{X_m}{X_s}\right] I_{2a} + j\left[\frac{3V_a}{X_s}\right][-X_m I_{2b} - V_a]. \tag{7.38}$$

This equation allows the phasor diagram of Figure 7.28(b) to be redrawn as in Figure 7.28c to produce an operating chart similar to that for a synchronous machine (see Section 3.3.4) but note that the direction of the *P*- and *Q*-axes are now swapped compared with Figure 3.19. This operating chart clearly shows the control options with this type of generator:

- controlling the magnitude of I_{2a}, the component of rotor current in phase with the stator voltage, controls the real power (along aa′);
- controlling the magnitude of I_{2b}, the component of rotor current out of phase with the stator voltage, controls the reactive power (along bb′).

7.5.4 Control Strategy for a DFIG

The normal control strategy with this type of generator is to control both I_{2a} and I_{2b} independently in order to control both the generator torque (I_{2a}) and the reactive power (I_{2b}). Normally all calculations are done in a synchronous reference frame that uses the stator voltage space vector as the reference (as in Equation (7.35) and is termed a *vector controller*. In comparison many motor drive systems use the machine flux vector as the reference and are termed *field-orientated controllers* (Muller, Deicke and De Donker, 2002). In this stator voltage space vector reference frame I_a would become I_q and I_b would become I_d and so on.

When used with a wind turbine the power output required from the DFIG is defined as a function of rotational speed in order to maximize power output from the wind turbine system as described in Section 7.1. If the required power P_d (or torque) is known, and the required reactive power output Q_d is defined, the real and imaginary parts of Equation (7.38) define the demand values of the rotor current components I_{2ad} and I_{2bd} respectively, that is

$$I_{2ad} = \frac{P_d}{3V_a}\frac{X_s}{X_m} \quad \text{and} \quad I_{2bd} = -\left[\frac{Q_d}{3V_a} + \frac{V_a}{X_s}\right]\frac{X_s}{X_m}. \tag{7.39}$$

This control is implemented in the machine-side converter of Figure 7.23 while the grid-side converter is controlled to maintain the DC link voltage constant. Such a control scheme is shown in the schematic of Figure 7.29. This is a complex control structure using fast conversion algorithms

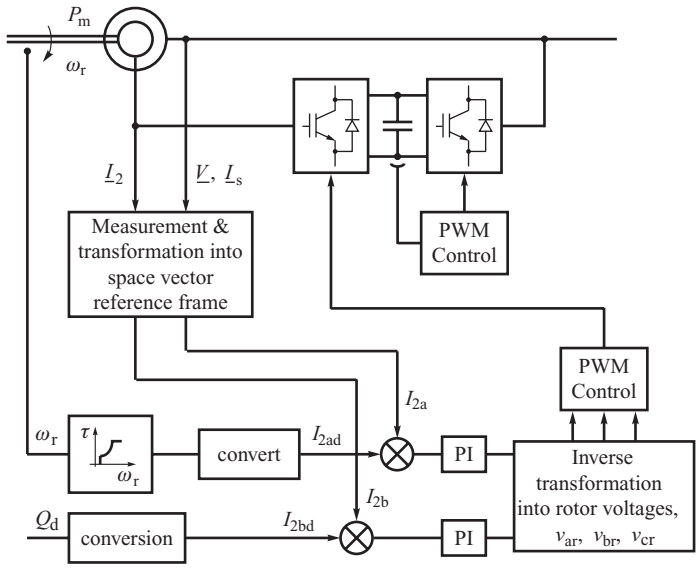

Figure 7.29 DFIG control implementation.

to convert from phase values to d and q space vector quantities. *Proportional plus integral* (PI) controllers determine the PWM variables that control the injected rotor currents to obtain the required reactive power and torque. Interested readers are referred to articles by Ekanayake, Holdsworth and Jenkins (2003a), Ekanayake *et al.* (2003b), Holdsworth *et al.* (2003), Muller, Deicke and De Donker (2002), Slootweg, Polinder and Kling (2001) and Xiang *et al.* (2006).

7.6 Fully Rated Converter Systems: Wide Speed Control

Instead of using a partially rated converter, fully rated converters can be used to control the real and reactive power injected into the system from either an induction generator or a synchronous generator as described in Section 7.1. The synchronous generator can have a wound field or can use permanent magnets to provide the rotating magnetic field. Such schemes are used with renewable energy systems and give the widest range of speed control but at the expense of a converter that must be rated to cope with the full power output of the generator. Such a power conversion scheme is shown schematically in Figure 7.30 and differs only in detail on the machine-side inverter for use with induction or synchronous machines. One attraction of the permanent magnet machine is its high efficiency since no magnetizing or field current is necessary to provide the magnetic field and it also allows new generator topologies to be devised to suit a specific application. As developments in power electronics progress, it is likely that the use of fully rated converter systems will replace the partially rated converters and DFIGs.

The fully rated converter system allows full control of real and reactive power. Although a number of control schemes are possible, the machine-side converter is normally operated to control the generator torque loading while the grid-side inverter is controlled to maintain constant voltage on the DC link and, at the same time, controlling the reactive power output in a similar way to a static compensator (Section 2.4.4).

Both converters will normally be current controlled to achieve their control objectives. However, it must be realized that the PWM converters can only adjust the phase and magnitude of the injected phase voltage. So, for example, the grid-side converter can only adjust the phase and magnitude of

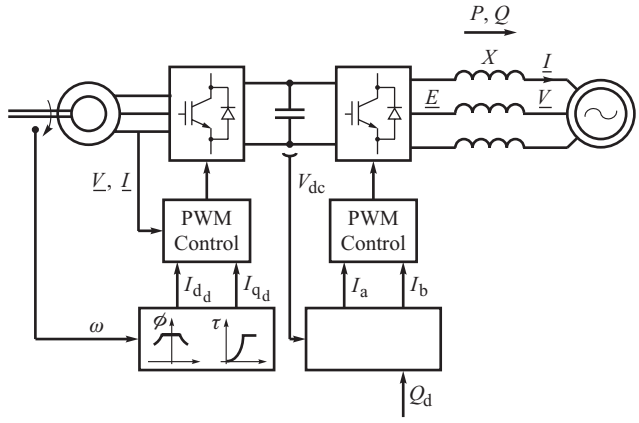

Figure 7.30 Fully rated converter system.

the injected voltage $\underline{E}$ relative to the system voltage $\underline{V}$. It is these two quantities of phase and magnitude that are adjusted via PI controllers to control the current to its set value, see also Figure 7.29.

7.6.1 Machine-Side Inverter

The machine-side inverter is normally controlled to give the required torque loading at any particular speed so as to maximize energy capture. This is achieved by controlling the quadrature-axis current I_q. To show this consider a permanent magnet machine when the voltage equations are given by Equations (3.65) but note that the induced emf E_f is related to the flux linkage per pole produced by the permanent magnets, that is

$$E_f = \omega\psi_{pm}. \tag{7.40}$$

With this change the voltage Equation (3.65) becomes

$$V_d = -RI_d - X_q I_q \quad \text{and} \quad V_q = \omega\psi_{pm} - RI_q + X_d I_d. \tag{7.41}$$

The terminal power is then given by Equation (3.82) as

$$P = V_d I_d + V_q I_q = I_d I_q (X_d - X_q) + \omega\psi_{pm} I_q - R\left(I_d^2 + I_q^2\right). \tag{7.42}$$

The first two terms in this expression define the shaft power and the third term the power lost in the armature resistance so that the machine torque is given by

$$\tau_m = \frac{I_d I_q (X_d - X_q)}{\omega_{rm}} + p\psi_{pm} I_q. \tag{7.43}$$

With permanent magnet machines the reactances X_d and X_q depend on how the magnets are mounted on the rotor; for surface-mounted magnets $X_d \approx X_q$ as the relative permeability of rare earth permanent magnet material is approximately 1. In this case Equation (7.43) reduces to

$$\tau_m = p\psi_{pm} I_q. \tag{7.44}$$

That is, the torque loading can be adjusted by controlling the quadrature-axis current I_q.

In the induction machine torque can be controlled in a very similar way but now the magnetizing flux must also be produced from the armature and it is important that the flux level in the machine

is maintained at the correct value all the time. Equation (3.37) shows how flux, emf and frequency are related and that to operate at speeds below rated the voltage must be reduced in proportion if the machine is not to be overfluxed (saturated). This means operating at constant volts per hertz at speeds below rated speed and at constant rated voltage, reduced flux, above rated speed. This is achieved by controlling the direct-axis current I_d.

7.6.2 Grid-Side Inverter

The grid-side inverter is normally controlled to transfer power so as to maintain a constant voltage on the DC link capacitor. If the charge on the capacitor increases, the control loop will increase the power transfer to reduce the voltage and vice versa. The grid-side converter also controls the reactive power delivered to the system. A vital part of this converter is the line reactor X shown in Figure 7.30.

Assume that the system voltage $\underline{V} = V_a + j0$ acts along the real axis, that the voltage injected by the converter is $\underline{E} = E_a + jE_b$ and that the current injected into the system is $\underline{I} = I_a + jI_b$. The phasor diagram for this system is shown in Figure 7.31. The current through the line reactance is given by

$$\underline{I} = I_a + jI_b = \frac{\underline{E} - \underline{V}}{jX} = \frac{E_b}{X} - j\frac{(E_a - V_a)}{X}, \tag{7.45}$$

that is

$$I_a = \frac{E_b}{X} \quad \text{and} \quad I_b = -\frac{(E_a - V_a)}{X}, \tag{7.46}$$

while the apparent power injected into the system is

$$\underline{S} = 3V_a\underline{I}^* = 3V_aI_a + 3jV_aI_b = 3\frac{V_aE_b}{X} + 3j\frac{V_a(E_a - V_a)}{X}. \tag{7.47}$$

From the phasor diagram the emf components E_a and E_b can be written in terms of the magnitude of the emf E and its phase δ as

$$E_a = E\cos\delta \quad \text{and} \quad E_b = E\sin\delta. \tag{7.48}$$

Substituting into Equation (7.47) gives

$$\underline{S} = 3\frac{V_aE\sin\delta}{X} + 3j\frac{V_a(E\cos\delta - V_a)}{X}. \tag{7.49}$$

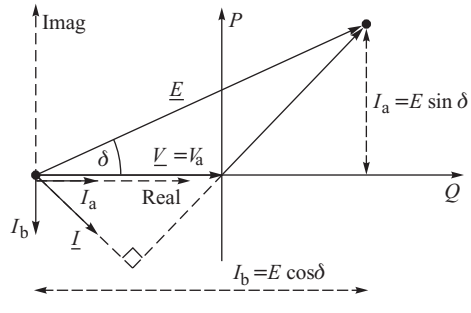

Figure 7.31 Phasor diagram describing the operation of the grid-side inverter.

Generally δ is small when Equation (7.49) becomes

$$\underline{S} \approx 3\frac{V_a E}{X}\delta + 3j\frac{V_a(E - V_a)}{X}, \tag{7.50}$$

demonstrating how real power can be controlled by the phase angle δ and reactive power by the magnitude of E. Although there is some cross-coupling between the terms, this can be taken into account in the control structure.

7.7 Peak Power Tracking of Variable Speed Wind Turbines

The discussion in the previous sections has explained how an induction machine can be used to generate electrical power and how, with the aid of power electronics, it can be operated over a large speed range. To optimize energy capture from the wind turbine, the electrical torque is generally controlled as a function of rotational speed while the speed of the generator will increase, or decrease, depending on the mechanical torque produced by the turbine. This change in speed is determined by the equation of motion, Equation (5.1). The rate at which the speed will change depends on the magnitude of the torque imbalance and the moment of inertia of the turbine and generator system including the effect of the gearbox.

For example, consider the situation shown in Figure 7.32 for a wind turbine where the generator is operating at point p_1 at rotational speed ω_1 producing power P_1. The wind speed is v_{w1}. At this point the mechanical power (and torque) produced by the turbine is balanced by the electrical power. The line ab is the operating line that the generator is controlled to follow for optimum loading, see Figure 7.3. If now the wind speed increases to v_{w2} the new optimum steady-state operating point is at p_2. Initially the speed and electrical power loading of the turbine do not change but the increase in wind speed leads to an increase in the mechanical shaft power ΔP and hence mechanical torque, point c. This increase in mechanical power accelerates the turbine system and the speed changes from ω_1 towards ω_2. As the speed changes, the electrical power also changes until the speed settles at the new equilibrium point p_2 when the electrical power again balances the mechanical power. It is important to realize that in practice the wind is turbulent and speed and power changes such as this will be continually taking place (Stannard and Bumby, 2007).

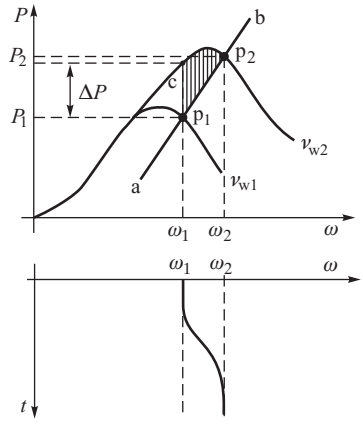

Figure 7.32 Speed changes in a wind turbine system (generating positive).

7.8 Connections of Wind Farms

Although the majority of wind turbines are situated on land, there is a growing demand for wind turbines to be placed offshore with some large wind farms now operational (Christiansen, 2003). The reasons for developing offshore sites are both technical and political with offshore turbines seen to pose fewer planning issues and offshore winds tending to be stronger and more consistent than those onshore. This does not mean that offshore sites are always better than those onshore, as some onshore sites have better wind regimes than sites offshore.

A common problem to all offshore energy conversion systems is the electrical cable connection to the onshore substation. This must be by a buried undersea cable and this then raises distance issues because all AC cables have high capacitance and the line charging current for long cable runs can be very high (Section 3.1). Some form of reactive power compensation may be required at the offshore end to help combat the large cable capacitance while a number of independent cable runs may be necessary in order to transmit the required power from an offshore wind farm. Because of the large cable capacitance AC cables are currently limited to a distance under the sea of about 100–150 km with the maximum rating of three-core submarine cables currently being about 200 MW at 145 kV (Kirby *et al.*, 2002), although larger ratings are under development. Generally the outputs of a number of turbines are collected together at an offshore substation for onward transmission to shore. Once the output of a number of turbines has been collected, an alternative to AC transmission to shore is to use DC transmission. New DC transmission technology uses IGBT voltage source converters at the sending end (and possibly also at the receiving end) allowing total control at the sending end. For higher powers, conventional DC technology using GTOs can be used. Interested readers are referred to Kirby *et al.* (2002).

Currently offshore wind farms are sufficiently close to shore that AC cables can be used, although a number of cables may be necessary to transmit the required power. One practical point to note is that the distance to shore also includes the shore-based cable run to the shore substation. In some situations this can be substantial.

The problems associated with transferring electrical power to shore from offshore wind farms is also faced by tidal stream generators and wave generators. Tidal stream generators tend to be relatively close to shore, although laying cables in the strong currents where these turbines are situated is not straightforward. Wave energy is in its infancy with the large amounts of resource available some way offshore. Harnessing this energy and transferring it to shore poses a significant challenge.

7.9 Fault Behaviour of Induction Generators

Section 7.7 described the steady-state behaviour of induction generators and how their power output might change when used with wind turbines and subjected to changes in wind speed. However, as with any generator, the wind turbine generator connected to the power system will be subjected to system faults and its behaviour during and after these faults is important with regard to system stability. This is examined here.

7.9.1 Fixed-Speed Induction Generators

Fixed-speed induction generators are normally regarded as ‘negative load’. That is, they generate power whenever they can and do not contribute to system voltage or frequency support. Section 7.2 explained how these generators always consume reactive power and how this increases as slip increases so that when a fault does occur and is subsequently cleared, these generators can have a detrimental effect on the recovery of system voltage. To avoid this it is normal practice to disconnect these generators from the system as soon as a drop in voltage is detected. The generators are then reconnected once the system is restored to normal operation.

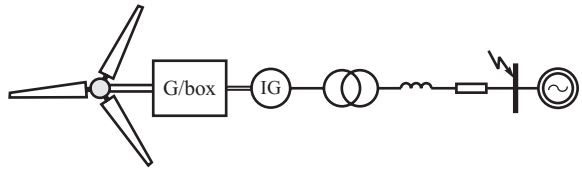

Figure 7.33 Example turbine and fixed-speed induction generator system: G/box, gearbox; IG, induction generator.

Notwithstanding this normal operation, it is instructive to examine the stability of an induction generator following a fault assuming that it remains connected to the system. Consider the system shown in Figure 7.33 where the turbine and induction generator are connected to the system through a transformer and a short line. The effective impedance of the line and transformer will impact on the generator torque–slip curve as described in Section 7.3. The sequence of events following a three-phase-to-earth fault is shown in Figure 7.34 by reference to the torque–slip curve of the generator. In Figure 7.34 the torque–slip curve has been inverted so that generator torque is now positive. The torque produced by the turbine as the rotor speed changes is shown by the line τ_m.

Initially the electrical generator torque and the mechanical turbine torque are balanced and the generator and turbine operate at a rotational speed ω_{r1} with a negative slip s_1. When the fault occurs at $t = t_0$ the electrical torque drops to zero, point 2, and the mechanical torque accelerates the rotor and the speed increases. The fault is cleared at time $t = t_1$ when the rotor speed has increased to ω_{r3} and the slip to s_3. At this point the system

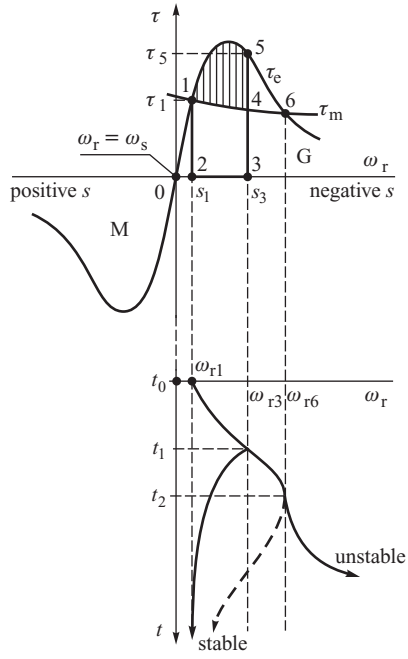

Figure 7.34 Transient stability of a fixed-speed induction generator turbine system (generating positive).

voltage is restored and the electrical torque increases from zero to τ_5. The electrical torque is now greater than the mechanical torque τ_4 and this acts like a braking torque reducing the speed of the rotor until once again the steady operating point 1 is reached. This system is stable.

If the fault were on for a longer period and not cleared until time $t = t_2$ the rotor speed would have increased to ω_{r6} so that when the electrical torque is restored the electrical torque and the mechanical torque are the same; this is the transient stability limit. If the fault were cleared at time $t < t_2$ the system would be stable, at $t > t_2$ the system would be unstable. This is shown in Figure 7.34.

Note that although a reasoning somewhat similar to that of the equal area criterion (see Chapter 5) was applied above, the equal area criterion could not be applied to Figure 7.34 because the integral of torque with speed is not energy but power. Moreover, re-establishing the flux requires time, so what the diagram does is to show the main effect with regard to stability and that is the relative magnitudes of the electrical and mechanical torques. Anything else would require detailed simulation.

A number of other factors described in Section 7.3 influence the above discussion. Firstly, when the fault is removed the torque–slip curve will take a finite time to re-establish itself because the flux inside the machine must be restored. This in turn will draw significant reactive power from the network. This reactive power draw can depress the system voltage, so reducing the peak of the torque–slip curve. It is for these reasons that detailed modelling of the induction machine as described in Section 11.4 is required. Finally the transient stability limit could be increased by changing the rotor resistance because this has the effect of moving the peak of the torque–slip curve further to the left (Section 7.3).

7.9.2 Variable-Speed Induction Generators

Large, variable speed induction generators such as the DFIG, described in Section 7.5, and the induction generator with a fully rated converter, Section 7.6, are both able to contribute to system voltage and frequency control by controlling their reactive power output and, to some extent, their real power output respectively. Such generators are required to 'ride through' a fault so that they can contribute to system stability once the fault is removed. To achieve this requires complex control of the power converters and interested readers are referred to Muller, Deicke and De Donker (2002), Slootweg, Polinder and Kling (2001), Ekanayake, Holdsworth and Jenkins (2003a), Holdsworth *et al.* (2003) and Xiang *et al.* (2006).

7.10 Influence of Wind Generators on Power System Stability

As discussed in Chapter 5, the synchronous generator is stiffly connected to the power system and exhibits an inherently oscillatory response to a disturbance because its power output is approximately proportional to the sine of the rotor angle. For small values of the rotor angle, power is proportional to the angle itself which produces spring-like oscillations – see Section 5.4.7 and also Figure 7.16a. On the other hand, Section 7.3 explained that squirrel-cage (fixed-speed) induction generators are coupled to the grid less stiffly than synchronous generators. Figure 7.16b shows that the torque of a fixed-speed induction generator is proportional to the speed deviation (slip) hence providing inherent damping of oscillations. This positive influence is counteracted by the vulnerability of fixed-speed induction generators to system faults – see Section 7.9.

Damping due to variable speed DFIGs depends very much on the particular control strategy employed. Section 7.5 explained that DFIGs have good control capabilities due to the possibility of controlling both the magnitude and phase of the injected voltage. This makes it possible to design a power system stabilizer that improves the damping of power swings without degrading the quality of voltage control provided (Hughes *et al.*, 2006). Fully rated converter systems effectively decouple the generator from the grid, so they offer a very good possibility of improving the damping of power swings. Hence the general conclusion is that a partial replacement of traditional thermal plants employing synchronous generators, which exhibit a relative poor natural damping, by renewable

generators, which exhibit a better damping, will improve the damping of electromechanical swings. This effect will be counterbalanced to some extent by the highly variable nature of renewable sources themselves, such as wind, marine or solar, but their variability may be effectively managed by either using energy storage or part loading one of the turbines in a farm and using its spare capacity to smooth power oscillations (Lubosny and Bialek, 2007).

The network effect of replacing large traditional generators by renewable ones will largely depend on the system in question. Recall that the stability of synchronous generators deteriorates if they are highly loaded, remote and operate with a low, or even leading, power factor. If renewable plants are connected closer to the loads, then the transmission networks will be less loaded, which will reduce reactive power consumption by the system and the voltages will rise. This effect can be compensated by reactive power devices, such as reactors or static VAR compensators, but this would require additional investment. If that is deemed uneconomical and the remaining synchronous generators are used for reactive power compensation, their operating points would move towards capacitive loading (leading power factor) so their dynamic properties might deteriorate. As the number of synchronous generators remaining in operation is reduced due to increased penetration of renewables, their overall compensation capabilities will also be reduced. Hence the overall effect might be a deterioration of the dynamic properties of the system (Wilson, Bialek and Lubosny, 2006).

On the other hand, if the renewable sources are located further away from the main load centres, as is the case for example in the United Kingdom, then power transfers over the transmission network will increase. Higher transfers will mean larger voltage angle differences between network nodes and deteriorated system dynamic properties (smaller stability margins).

Increased penetration of renewables might also affect frequency stability. Due to its construction, a wind plant has smaller inertia and speed so that kinetic energy stored in it is reduced by a factor of approximately 1.5 when compared with a traditional plant of the same rating. The reduction in stored kinetic energy will have an effect on system operation and security because the amplitude of frequency variations, discussed in Chapter 9, will increase.

8

Voltage Stability

Chapter 2 explained how an electrical power network is made up from many different elements, is divided into transmission, subtransmission and distribution levels, and is often organized in such a way that each level belongs to a different company. Because of its immense size, analysing a complete power system is not possible, even using supercomputers, and normally the system is divided into sensible parts some of which are modelled in detail and others more superficially. Obviously the system model used must represent the problem being studied so that when analysing distribution networks the transmission or subtransmission networks are treated as *sources* operating at a given voltage. On the other hand, when analysing the transmission or subtransmission networks, the distribution networks are treated (Section 3.5) as *sinks* of real and reactive power and referred to as *composite loads* or simply *loads*.

A distribution network is connected to the transmission network at the *grid supply point* where a change in voltage may cause complicated dynamic interactions inside the distribution network itself due to:

- voltage control action arising from transformer tap changing;
- control action associated with reactive power compensation and/or small embedded generators;
- a low supply voltage causing changes in the power demand as a result of induction motors stalling and/or the extinguishing of discharge lighting;
- operation of protective equipment by overcurrent or undervoltage relays, electromechanically held contactors and so on;
- reignition of discharge lighting and self-start induction motors when the supply voltage recovers.

In this chapter the effect that actions such as these can have on voltage stability is examined using the static characteristics of the composite loads introduced in Section 3.5. This simplified analysis will help to give an understanding of both the different mechanisms that may ultimately lead to voltage collapse and the techniques that may be used to assess the voltage stability of a particular system. These techniques can then be extended to the analysis of large systems using computer simulation methods (Taylor, 1994; Kundur, 1994; Van Cutsem and Vournas, 1998).

8.1 Network Feasibility

The system shown in Figure 8.1 is representative of the general power supply problem in that it shows a generator supplying some composite load. Generally there will be some limits on the power that can be supplied to the load and this will determine how stable the supply is. To analyse this

Power System Dynamics: Stability and Control, Second Edition Jan Machowski, Janusz W. Bialek and James R. Bumby
© 2008 John Wiley & Sons, Ltd

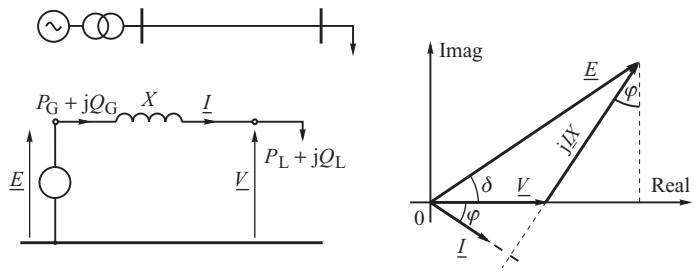

Figure 8.1 Equivalent circuit of the transmission link and its phasor diagram.

stability problem the composite load will be represented by its static voltage characteristics when the problem becomes that of determining the solutions to the power network equations, if they exist, and, if they do, determining what limits are placed on the solutions. This process is often referred to as determining the *network feasibility* or determining the *network loadability*.

The network feasibility problem can be explained by using the simple system shown in Figure 8.1. In this system the network is represented by an equivalent generator that can be modelled in the steady state by an equivalent voltage source E behind an equivalent reactance X_g. Under normal operating conditions the generator AVR will keep the terminal voltage constant when the equivalent voltage source has a value equal to the terminal voltage V_g and the equivalent reactance is zero. However, if the AVR is not operative, or the equivalent generator is operating near its excitation limit, then the field voltage will remain constant and the equivalent generator must be modelled by its synchronous emf E_f acting behind its synchronous reactance X_d. In general the resistance of the generator and transmission link is small and can be neglected, while the equivalent reactance X must combine the source reactance with that of the transformer and the transmission line. The real and reactive power absorbed by the load, $P_L(V)$ and $Q_L(V)$, can be calculated from the phasor diagram in Figure 8.1 by noting that $IX\cos\varphi = E\sin\delta$ and $IX\sin\varphi = E\cos\delta - V$. This gives

$$\begin{aligned} P_L(V) &= VI\cos\varphi = V\frac{IX\cos\varphi}{X} = \frac{EV}{X}\sin\delta \\ Q_L(V) &= VI\sin\varphi = V\frac{IX\sin\varphi}{X} = \frac{EV}{X}\cos\delta - \frac{V^2}{X}. \end{aligned} \tag{8.1}$$

The angle δ between the $\underline{E}$ and $\underline{V}$ phasors can be eliminated using the identity $\sin^2\delta + \cos^2\delta = 1$ to give

$$\left(\frac{EV}{X}\right)^2 = [P_L(V)]^2 + \left[Q_L(V) + \frac{V^2}{X}\right]^2. \tag{8.2}$$

This static power–voltage equation determines all the possible network solutions when the voltage characteristics $P_L(V)$ and $Q_L(V)$ are taken into account.

8.1.1 Ideally Stiff Load

For an ideally stiff load (Section 3.5) the power demand of the load is independent of voltage and is constant:

$$P_L(V) = P_n \quad \text{and} \quad Q_L(V) = Q_n, \tag{8.3}$$

where P_n and Q_n are the real and reactive power demand of the load at the rated voltage V_n. Equation (8.2) can now be rewritten as

$$\left(\frac{EV}{X}\right)^2 = P_n^2 + \left[Q_n + \frac{V^2}{X}\right]^2. \tag{8.4}$$

Substituting (8.4) into the equation $Q_n = P_n \tan\varphi$ gives

$$P_n^2 + P_n^2 \tan^2\varphi + 2P_n\frac{V^2}{X} = \left(\frac{EV}{X}\right)^2 - \left(\frac{V^2}{X}\right)^2. \tag{8.5}$$

After taking into account that $\tan\varphi = \sin\varphi/\cos\varphi$ and $\sin^2\varphi + \cos^2\varphi = 1$ and after some simple maths one gets

$$P_n^2 + 2P_n\frac{V^2}{X}\sin\varphi\cos\varphi = \frac{V^2}{X^2}(E^2 - V^2)\cos^2\varphi. \tag{8.6}$$

The left hand side of this equation is an incomplete square of a sum. Hence the equation can be transformed to

$$\left(P_n + \frac{V^2}{X}\sin\varphi\cos\varphi\right)^2 - \left(\frac{V^2}{X}\right)^2\sin^2\varphi\cos^2\varphi = \frac{V^2}{X^2}(E^2 - V^2)\cos^2\varphi$$

or

$$P_n + \frac{V^2}{X}\sin\varphi\cos\varphi = \frac{V}{X}\cos\varphi\sqrt{E^2 - V^2\cos^2\varphi}. \tag{8.7}$$

The voltage at the load bus can be expressed per unit as V/E. The above equation can be expressed as

$$P_n = -\frac{E^2}{X}\left(\frac{V}{E}\right)^2\sin\varphi\cos\varphi + \frac{E^2}{X}\frac{V}{E}\cos\varphi\sqrt{1 - \left(\frac{V}{E}\right)^2\cos^2\varphi}$$

or

$$p = -v^2\sin\varphi\cos\varphi + v\cos\varphi\sqrt{1 - v^2\cos^2\varphi}, \tag{8.8}$$

where

$$v = \frac{V}{E}, \quad p = \frac{P_n}{\frac{E^2}{X}}. \tag{8.9}$$

Equation (8.8) describes a family of curves with φ as a parameter. Figure 8.2 shows such a family of curves for four values of φ. Because of their characteristic shape, the curves are referred to as *nose curves*. For a lagging power factor (curves 1 and 2) the voltage decreases as the real load increases. For a low lagging power factor (curve 4) the voltage initially increases and then decreases.

It will be shown later in this chapter that in the considered generator–load system shown in Figure 8.1 the upper part of the nose curve (i.e. when the voltages are higher) is stable. The system is unstable in the lower part of the characteristic. It should be emphasized that a condition of the positive derivative $\mathrm{d}v/\mathrm{d}p > 0$ cannot be a criterion of stability as the curve $v(p)$ has a positive derivative in the upper part of the characteristic for a leading power factor (curve 4 in Figure 8.2). Nevertheless, the usefulness of the nose curve is high in practice as the difference between a current

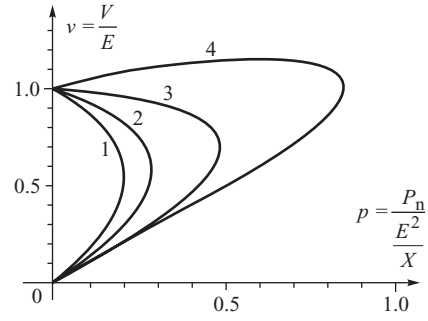

Figure 8.2 A family of nose curves with φ as a parameter: (1) $\varphi = 45^\circ$ lag; (2) $\varphi = 30^\circ$ lag; (3) $\varphi = 0$; (4) $\varphi = 30^\circ$ lead.

load and the maximum load determined by the peak of the characteristic is equal to the stability margin for a given power factor.

It should be noted that for $Q_n = 0$, that is for $\varphi = 0$, the peak of the nose curve occurs at $p = 0.5$, that is for $P_n = 0.5E^2/X = E^2/2X$.

Nose curves $V(P)$ illustrate the dependency of the voltage on real power of a composite load assuming that the power factor is a parameter. The curves $Q(P)$ discussed below are derived assuming that the voltage is a parameter.

For a given value of V, Equation (8.4) describes a circle in the (P_n, Q_n) plane as shown in Figure 8.3a. The centre of the circle lies on the Q_n-axis and is shifted vertically down from the origin by V^2/X. Increasing the voltage V produces a family of circles of increasing radius and downward shift, bounded by an envelope as shown in Figure 8.3b.

For each point inside the envelope, for example point A, there are two possible solutions to Equation (8.4) at voltage values V_1 and V_2, as defined by the two circles, whereas for any point B on the envelope there is only one value of V for which Equation (8.4) is satisfied. An equation for this envelope can therefore be obtained by determining those values of P_n and Q_n for which there is only one solution of Equation (8.4) with respect to V. Rearranging Equation (8.4) gives

$$\left(\frac{V^2}{X}\right)^2 + \left(2Q_n - \frac{E^2}{X}\right)\left(\frac{V^2}{X}\right) + \left(P_n^2 + Q_n^2\right) = 0. \tag{8.10}$$

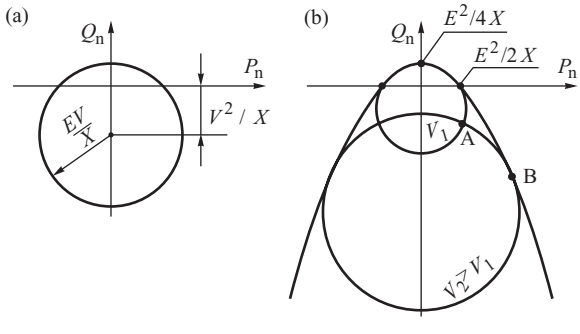

Figure 8.3 Circles determining the power that can be delivered to an ideally stiff load: (a) one circle for a given voltage V; (b) a family of circles and their envelope.

This is a quadratic equation in (V^2/X) and has only one solution when

$$\Delta = \left(2Q_{\mathrm{n}} - \frac{E^2}{X}\right)^2 - 4\left(P_{\mathrm{n}}^2 + Q_{\mathrm{n}}^2\right) = 0. \tag{8.11}$$

Solving for Q_{n} gives

$$Q_{\mathrm{n}} = \frac{E^2}{4X} - \frac{P_{\mathrm{n}}^2}{\frac{E^2}{X}}, \tag{8.12}$$

which is the equation of an inverted parabola that crosses the P_{n}-axis at $P_{\mathrm{n}} = E^2/2X$ and has its maximum at

$$P_{\mathrm{n}} = 0 \quad \text{and} \quad Q_{\mathrm{n\,MAX}} = \frac{E^2}{4X}. \tag{8.13}$$

A point with coordinates $P_{\mathrm{n}} = E^2/2X$ and $Q_{\mathrm{n}} = 0$ shown in Figure 8.3 corresponds to the peak of the nose curve in Figure 8.2 when $\varphi = 0$, that is when $Q_{\mathrm{n}} = 0$.

The parabola described by Equation (8.12) is important as it defines the shape of the envelope in Figure 8.3b that encloses all the possible solutions to the network equation (8.4). Each point $(P_{\mathrm{n}}, Q_{\mathrm{n}})$ inside the parabola satisfies two network solutions corresponding to two different values of the load voltage V while each point on the parabola satisfies one network solution corresponding to only one value of voltage. There are no network solutions outside the parabola. In other words, it is not possible to deliver power equal to P_{n} and Q_{n} corresponding to any point outside the parabola.

8.1.2 Influence of the Load Characteristics

For the more general case the power demand will depend on the voltage as described by the voltage characteristics $P_{\mathrm{L}}(V)$ and $Q_{\mathrm{L}}(V)$. The possible solutions to Equation (8.2) will not now be bounded by a simple parabola, as for $P_{\mathrm{L}}(V) = P_{\mathrm{n}}$, $Q_{\mathrm{L}}(V) = Q_{\mathrm{n}}$, but the shape of the solution area will vary depending on the actual voltage characteristics as shown in Figure 8.4. In general the less stiff the load, the more open the solution area. For the constant load discussed above, the solution area corresponds to a parabola, Figure 8.4a. If the reactive power characteristic is a square function of the voltage, $Q_{\mathrm{L}}(V) = (V/V_{\mathrm{n}})^2 Q_{\mathrm{n}}$, then the solution area opens up from the top, Figure 8.4b, so that for $P_{\mathrm{n}} = 0$ there is no limit on Q_{n}. If the real power characteristic is linear $P_{\mathrm{L}}(V) = (V/V_{\mathrm{n}})^2 P_{\mathrm{n}}$ as in Figure 8.4c, then the solution area is bounded by two parallel, vertical lines. If both real and reactive power characteristics are square functions of the voltage, $P_{\mathrm{L}}(V) = (V/V_{\mathrm{n}})^2 P_{\mathrm{n}}$ and $Q_{\mathrm{L}}(V) = (V/V_{\mathrm{n}})^2 Q_{\mathrm{n}}$, then there are no limits on the values of P_{n} and Q_{n} as shown in Figure 8.4d.

Consider again the characteristics of Figure 8.4d where there are no limits on the real and reactive power. This can be proved by expressing

$$P_{\mathrm{L}}(V) = P_{\mathrm{n}}\left(\frac{V}{V_{\mathrm{n}}}\right)^2 = \frac{P_{\mathrm{n}}}{V_{\mathrm{n}}^2} V^2 = G_{\mathrm{n}} V^2, \quad Q_{\mathrm{L}}(V) = Q_{\mathrm{n}}\left(\frac{V}{V_{\mathrm{n}}}\right)^2 = \frac{Q_{\mathrm{n}}}{V_{\mathrm{n}}^2} V^2 = B_{\mathrm{n}} V^2, \tag{8.14}$$

which shows that the load is represented by an equivalent admittance $\underline{Y}_{\mathrm{n}} = G_{\mathrm{n}} + \mathrm{j}B_{\mathrm{n}}$ shown in Figure 8.5. Varying the value of P_{n} and Q_{n} from zero to infinity corresponds to changing the equivalent admittance from zero (open circuit) to infinity (short circuit). As current will flow in the circuit of Figure 8.5 for any value of $\underline{Y}_{\mathrm{n}}$, so a solution of Equation (8.2) exists for any P_{n} and Q_{n}.

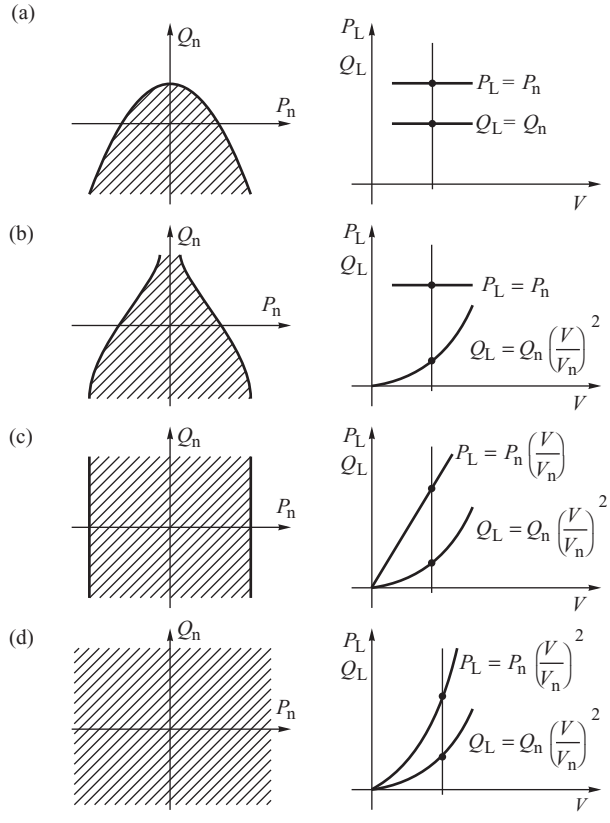

Figure 8.4 Dependence of the network solution area on the shape of the load characteristics.

This can be proved mathematically by substituting Equation (8.14) into Equation (8.2) when the following formula is obtained

$$V = \frac{E}{\sqrt{(G_n X)^2 + (B_n X + 1)^2}}, \tag{8.15}$$

confirming that for any G_n, B_n a network solution for V always exists.

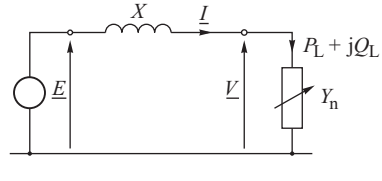

Figure 8.5 Transmission link loaded with an equivalent variable admittance.

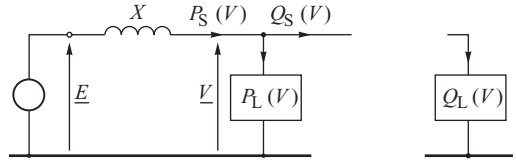

Figure 8.6 Equivalent circuit for determining the reactive power characteristic of the system.

8.2 Stability Criteria

For each point inside the envelope of network solutions, for example point A in Figure 8.3, there are two solutions with respect to the voltage V: one with a higher and one with a lower value of voltage. It is now necessary to examine which of these solutions corresponds to a stable equilibrium point. This problem of *voltage stability* is considered in this section when different, but equivalent, voltage stability criteria are derived.

8.2.1 The $\mathrm{d}\Delta Q/dV$ *Criterion*

This classic voltage stability criterion (Venikov, 1978b; Weedy, 1987) is based on the capability of the system to supply the load with reactive power for a given real power demand. To explain this criterion it is convenient to separate notionally the reactive power demand from the real power demand as shown in Figure 8.6. To distinguish between the power supplied by the source at the load node and the load demand itself, let $P_L(V)$ and $Q_L(V)$ be the load demand and $P_S(V)$ and $Q_S(V)$ be the powers supplied by the source to the load.

As the real power is always connected to the transmission link, then it holds that $P_L(V) = P_S(V)$. Similarly, during normal operation $Q_L(V) = Q_S(V)$ but, for the purposes of stability analysis, the link between $Q_L(V)$ and $Q_S(V)$ is notionally separated. $Q_S(V)$ is treated as the reactive power supplied by the source and is assumed not to be determined by the reactive power demand of the load. The real and reactive load powers are given by expressions similar to those in Equation (8.1):

$$P_L(V) = P_S(V) = \frac{EV}{X}\sin\delta \quad \text{and} \quad Q_S(V) = \frac{EV}{X}\cos\delta - \frac{V^2}{X}. \tag{8.16}$$

Eliminating the trigonometric functions using the identity $\sin^2\delta + \cos^2\delta = 1$ gives

$$\left(\frac{EV}{X}\right)^2 = P_L^2(V) + \left[Q_S(V) + \frac{V^2}{X}\right]^2, \tag{8.17}$$

and solving for $Q_S(V)$ gives

$$Q_S(V) = \sqrt{\left[\frac{EV}{X}\right]^2 - [P_L(V)]^2} - \frac{V^2}{X}. \tag{8.18}$$

This equation determines the reactive power–voltage characteristic and shows how much reactive power will be supplied by the source if the system is loaded only with the real power $P_L(V)$ and the load voltage is treated as a variable. For an ideally stiff real power load $P_L(V) = P_L = \text{constant}$ and Equation (8.18) takes the form of an inverted parabola as shown in Figure 8.7. The first term in Equation (8.18) depends on the equivalent system reactance X and the load real power P_L and has the effect of shifting the parabola downwards and towards the right as illustrated in

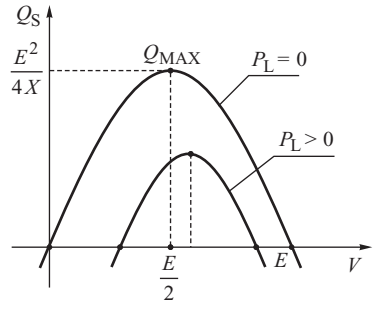

Figure 8.7 $Q_S(V)$ characteristic for $P_L = 0$ and $P_L > 0$.

Figure 8.7. For $P_L = 0$ the parabola crosses the horizontal axis at $V = E$ and $V = 0$ and has a maximum at $Q_{MAX} = E^2/4X$ and $V = E/2$. For $P_L > 0$ the maximum value of Q_S occurs at a voltage

$$V = \sqrt{[E/2]^2 + [P_L(V)X/E]^2}$$

which is greater than $E/2$.

If the reactive power of the notionally separated load is now reconnected to the system then both the $Q_S(V)$ and $Q_L(V)$ characteristics can be drawn on the same diagram as in Figure 8.8a. At equilibrium the supply must be equal to the demand, that is $Q_S(V) = Q_L(V)$, and is satisfied by the two equilibrium points V^s and V^u. This corresponds to the situation shown in Figure 8.3b where for one value of power demand, point A, there are two possible, but different, values of voltage $V_1 \neq V_2$.

The stability of both equilibrium points can be tested using the small-disturbance method. Recall from Section 3.1.2, Figure 3.4, that an excess of reactive power was shown to produce an increase in voltage while a deficit of reactive power resulted in a decrease in voltage. Now consider equilibrium points in Figure 8.8a and assume that there is a small negative voltage disturbance ΔV. This will result in the supplied reactive power $Q_S(V)$ being greater than the reactive power demand $Q_L(V)$. This excess of reactive power will tend to increase the voltage and therefore force the voltage to return to point s. If the disturbance produces an increase in voltage, the resulting deficit in reactive power will force the voltage to decrease and again return to point s. The conclusion is that equilibrium point s is stable.

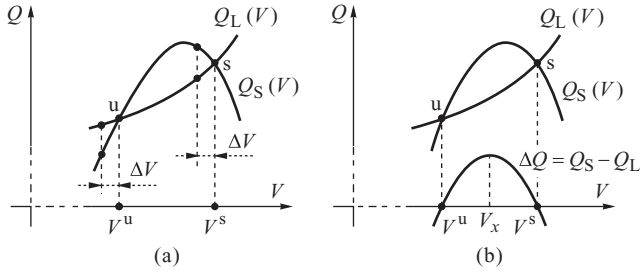

Figure 8.8 $Q_S(V)$ and $Q_L(V)$ characteristics: (a) two equilibrium points; (b) illustration of the classic stability criterion.

On the other hand, a disturbance in the vicinity of the second equilibrium point u which decreases the voltage will produce a deficit of reactive power with $Q_S(V) < Q_L(V)$ which will force a further decrease in voltage. As the disturbed system does not return to the equilibrium point, the equilibrium point u is unstable.

The classic voltage stability criterion is obtained by noting from Figure 8.8b that the derivative of the surplus of reactive power $\mathrm{d}(Q_S - Q_L)/\mathrm{d}V$ is of opposite sign at the two equilibrium points: it is negative at the stable point s and positive at the unstable point u. This is the essence of the classic $\mathrm{d}\Delta Q/\mathrm{d}V$ stability criterion:

$$\frac{\mathrm{d}(Q_S - Q_L)}{\mathrm{d}V} < 0 \quad \text{or} \quad \frac{\mathrm{d}Q_S}{\mathrm{d}V} < \frac{\mathrm{d}Q_L}{\mathrm{d}V}. \tag{8.19}$$

In the simple system shown in Figure 8.6 the supplied real and reactive powers, expressed by Equations (8.16), are functions of the two variables V and δ with increments given by

$$\begin{aligned} \Delta Q_S &= \frac{\partial Q_S}{\partial V}\Delta V + \frac{\partial Q_S}{\partial \delta}\Delta\delta \\ \Delta P_L = \Delta P_S &= \frac{\partial P_S}{\partial V}\Delta V + \frac{\partial P_S}{\partial \delta}\Delta\delta. \end{aligned} \tag{8.20}$$

Eliminating $\Delta\delta$ from these two equations, and dividing the result by ΔV, gives

$$\frac{\Delta Q_S}{\Delta V} = \frac{\partial Q_S}{\partial V} + \frac{\partial Q_S}{\partial \delta}\left(\frac{\partial P_S}{\partial \delta}\right)^{-1}\left[\frac{\Delta P_L}{\Delta V} - \frac{\partial P_S}{\partial V}\right], \tag{8.21}$$

or

$$\frac{\mathrm{d}Q_S}{\mathrm{d}V} \approx \frac{\partial Q_S}{\partial V} + \frac{\partial Q_S}{\partial \delta}\left(\frac{\partial P_S}{\partial \delta}\right)^{-1}\left[\frac{\mathrm{d}P_L}{\mathrm{d}V} - \frac{\partial P_S}{\partial V}\right], \tag{8.22}$$

where the partial derivatives are obtained from the equations in (8.16) as

$$\frac{\partial P_S}{\partial \delta} = \frac{EV}{X}\cos\delta, \quad \frac{\partial P_S}{\partial V} = \frac{E}{X}\sin\delta, \quad \frac{\partial Q_S}{\partial \delta} = -\frac{EV}{X}\sin\delta, \quad \frac{\partial Q_S}{\partial V} = \frac{E}{X}\cos\delta - 2\frac{V}{X}. \tag{8.23}$$

Substituting these partial derivatives into Equation (8.22) gives

$$\frac{\mathrm{d}Q_S}{\mathrm{d}V} \approx \frac{E}{X}\cos\delta - \frac{2V}{X} - \frac{EV}{X}\sin\delta\frac{X}{EV\cos\delta}\left[\frac{\mathrm{d}P_L}{\mathrm{d}V} - \frac{E}{X}\sin\delta\right] = \frac{E}{X\cos\delta} - \left(\frac{2V}{X} + \frac{\mathrm{d}P_L}{\mathrm{d}V}\tan\delta\right). \tag{8.24}$$

This allows the stability condition defined in Equation (8.19) to be expressed as

$$\frac{\mathrm{d}Q_L}{\mathrm{d}V} > \frac{E}{X\cos\delta} - \left(\frac{2V}{X} + \frac{\mathrm{d}P_L}{\mathrm{d}V}\tan\delta\right), \tag{8.25}$$

where the derivatives $\mathrm{d}Q_L/\mathrm{d}V$ and $\mathrm{d}P_L/\mathrm{d}V$ are calculated from the functions used to approximate the load characteristics.

Generally, for a multi-machine system, it is not possible to derive an analytical formula for the stability criterion. However, by using a load flow program it is possible to obtain the system supply characteristic $Q_S(V)$ by defining the load node under investigation as a PV node and executing the program several times for different values of the node voltage V. The resulting $Q_S(V)$ characteristic can then be compared with the load characteristic $Q_L(V)$ to check the stability condition.

8.2.2 The dE/dV Criterion

The system equivalent emf E can be expressed as a function of the load voltage by solving Equation (8.2) for E to give

$$E(V) = \sqrt{\left(V + \frac{Q_{\mathrm{L}}(V)X}{V}\right)^2 + \left(\frac{P_{\mathrm{L}}(V)X}{V}\right)^2}, \tag{8.26}$$

where $Q_{\mathrm{L}}(V)X/V$ is the in-phase and $P_{\mathrm{L}}(V)X/V$ the quadrature component of the voltage drop $\underline{I}X$ shown in Figure 8.1.

An example of an $E(V)$ characteristic is shown in Figure 8.9 with the load normally operating at a high voltage corresponding to the right hand side of the characteristic. As V is large, and much greater than both the in-phase and quadrature components of the voltage drop, then, according to Equation (8.26), a decrease in voltage will cause the emf $E(V)$ to fall. As V continues to decrease, the $Q_{\mathrm{L}}(V)X/V$ and $P_{\mathrm{L}}(V)X/V$ components become more important and below a certain value of V, they will cause $E(V)$ to rise. Consequently, each value of $E(V)$ may correspond to two possible solutions of the network equations with respect to V. As before, the stability of these solutions can be examined using the small-disturbance method.

First consider the system behaviour at point s lying on the right hand side of the characteristic $E(V)$ in Figure 8.9 and assume that the source emf E is maintained at a constant value. A decrease in the load voltage by ΔV will produce a reduction in the emf $E(V)$ that is less than the source emf E. As E is too large to maintain the lowered load, voltage V is forced to return to the initial equilibrium value. Similarly, a voltage increase by ΔV results in the source emf E being smaller than the emf required to maintain the increased load voltage V so that the source emf E again forces the voltage to return to its initial value.

Now consider a disturbance that produces a voltage decrease by ΔV from the equilibrium point u on the left hand side of the characteristic. This disturbance results in the source emf E being less than the emf $E(V)$ required to maintain the lowered voltage. As E is too small, the load voltage further declines and does not return to its initial value. The conclusion is that point u is unstable.

From these discussions it is apparent that the system is stable if the equilibrium point lies on the right hand side of the characteristic, that is when

$$\frac{\mathrm{d}E}{\mathrm{d}V} > 0. \tag{8.27}$$

Venikov (1978b) and Abe and Isono (1983) have both shown this condition to be equivalent to the classic stability condition defined in Equation (8.19).

Using the stability condition defined in Equation (8.27) to study the stability of a multi-node system is rather inconvenient when a load flow program is used. The derivative $\mathrm{d}E/\mathrm{d}V$ is based

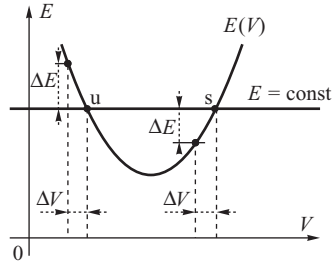

Figure 8.9 Illustration to the stability criterion $\mathrm{d}E/\mathrm{d}V > 0$.

on the equivalent circuit of Figure 8.1. In the load flow program, the load node should be of the PQ type (specified P_L and Q_L, unknown V and δ) which does not allow the voltage to be set. Consequently, the voltage increase necessary to obtain the derivative dE/dV has to be enforced from the generator nodes (PV type) for which the voltage can be set. As there is normally a large number of generator nodes in the system, a large number of load flows would have to be run to account for all the possible combinations of changes in the voltage settings.

8.2.3 The dQ_G/dQ_L Criterion

To understand this criterion it is necessary to analyse the behaviour of the reactive power generation $Q_G(V)$ as the load reactive demand $Q_L(V)$ varies. This approach is somewhat different to that taken in the two previous subsections in that $Q_G(V)$ now includes the reactive power demand of both the load, $Q_L(V)$, and the network, I^2X, whereas previously only the reactive power $Q_S(V)$ supplied by the source at the load node was considered.

The equation determining $Q_G(V)$ is similar to Equation (8.1) but with E and V interchanged, that is

$$Q_G(V) = \frac{E^2}{X} - \frac{EV}{X}\cos\delta, \tag{8.28}$$

where both V and δ depend on the demand $P_L(V)$ and $Q_L(V)$. Equation (8.1) allows the second component in this equation to be substituted to give

$$Q_G(V) = \frac{E^2}{X} - \frac{V^2}{X} - Q_L(V) \quad \text{or} \quad \frac{V^2}{X} = \frac{E^2}{X} - Q_L(V) - Q_G(V). \tag{8.29}$$

Substituting this expression into Equation (8.2) and performing some simple algebra gives

$$Q_G^2(V) - \frac{E^2}{X}Q_G(V) + P_L^2(V) + \frac{E^2}{X}Q_L(V) = 0, \tag{8.30}$$

or

$$Q_L(V) = -\frac{Q_G^2(V)}{\frac{E^2}{X}} + Q_G(\mathrm{V}) - \frac{P_L^2(V)}{\frac{E^2}{X}}. \tag{8.31}$$

For the case of the ideally stiff real power load with $P_L(V) = P_L = \text{constant}$, this equation describes a horizontal parabola in the (Q_G, Q_L) plane as shown in Figure 8.10a. The vertex of the parabola is at a constant Q_G value equal to $E^2/2X$ while the maximum value of Q_L depends on P_L and for $P_L = 0$ the maximum is at $E^2/4X$. Increasing P_L shifts the parabola to the left along the Q_L-axis but without any corresponding shift with respect to the Q_G-axis.

It is worth noting that the vertex of the parabola (the maximum value of Q_L for a given P_L) corresponds to a point on the envelope of the $Q_L(P_L)$ characteristics shown in Figure 8.3b and to the vertex of the $Q_S(V)$ characteristic in Figure 8.7. Obviously for $P_L = 0$ all three characteristics give the same maximum value $Q_{n\,MAX} = E^2/4X$ corresponding to Equation (8.13).

Figure 8.10b shows how the $Q_G(Q_L)$ characteristic can be used to analyse the system stability. Assuming that the reactive load demand Q_L is lower than its maximum value, there are always two equilibrium points, that is two values of reactive generation corresponding to a given demand. At the lower point s, a momentary disturbance ΔQ_L that increases the load reactive power demand results in an increase in the generated reactive power while a disturbance that reduces the demand results in a corresponding drop in the reactive power generation. As the generation follows the demand, the lower equilibrium point s is stable. The situation is reversed at the upper equilibrium point u. Here an increase in Q_L produces a reduction in Q_G while a reduction in Q_L produces

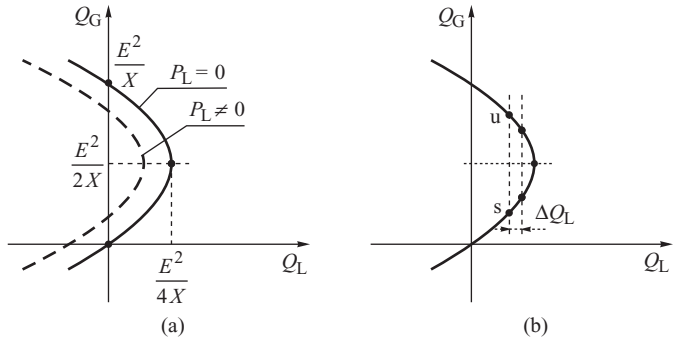

Figure 8.10 Generation and load characteristics: (a) Q_G (Q_L) with P_L as a parameter; (b) the small-disturbance method applied to the Q_G (Q_L) characteristic.

an increase in Q_G. As the changes in reactive generation are now in the opposite direction to the changes in demand, the upper equilibrium point u is unstable.

Consequently, the system is stable if a small change in reactive load demand produces a change in the generation which has the same sign or, in other words, the derivative $\mathrm{d}Q_G/\mathrm{d}Q_L$ is positive:

$$\frac{\mathrm{d}Q_G}{\mathrm{d}Q_L} > 0. \tag{8.32}$$

It is worth noting that at the maximum loading point at the nose of the $Q_G(Q_L)$ characteristic the derivative $\mathrm{d}Q_G/\mathrm{d}Q_L$ tends to infinity.

The characteristic defined by Equation (8.31), and shown in Figure 8.10, is a parabola only for the ideally stiff real power load, $P_L(V) = P_L = \text{constant}$. For a voltage-dependent load characteristic $P_L(V)$ will vary with voltage when it is not possible to obtain an explicit expression for $Q_L(Q_G)$ with $P_L(V)$ as a parameter. However, the $Q_L(Q_G)$ characteristic can be obtained iteratively by solving the network equations for given values of load demand, P_L and Q_L, and emf E at the generator node.

The main advantage of the $\mathrm{d}Q_G/\mathrm{d}Q_L$ criterion is the ease with which it can be used with a load flow program to analyse a multi-node system (Carpentier, Girard and Scano, 1984; Taylor, 1994). The generated reactive power Q_G is replaced by the sum of all the generated reactive powers at all the generator nodes, while the derivative is replaced by the quotient of the sum of all the generated reactive power increments over the increment of the reactive load demand at the examined load node, that is $\sum \Delta Q_{Gi} \big/ \Delta Q_L$.

8.3 Critical Load Demand and Voltage Collapse

Figure 8.4 showed how the network solution area depends on the shape of the load characteristic and Figure 8.8 illustrated the classical $\mathrm{d}\Delta Q/\mathrm{d}V$ stability criterion. Figure 8.11 extends this discussion and shows how the network equations may have two solutions, one solution or no solution at all depending on the relative position and shape of the $Q_L(V)$ and $Q_S(V)$ characteristics.

In Figure 8.11a there are two equilibrium points, corresponding to the intersection of the $Q_L(V)$ and $Q_S(V)$ characteristics, of which only point s is stable. For the special case of $Q_L(V) = \text{constant}$ and $P_L(V) = \text{constant}$ these two voltage values correspond to the voltages V_1 and V_2 designated by point A in Figure 8.3b, only one of which will be stable. For the more general case of $Q_L(V) \neq$ constant and $P_L(V) \neq$ constant shown in Figure 8.4b–d, then a point equivalent to A in Figure 8.3b will exist somewhere inside the envelope with two voltage solutions depicted by the general

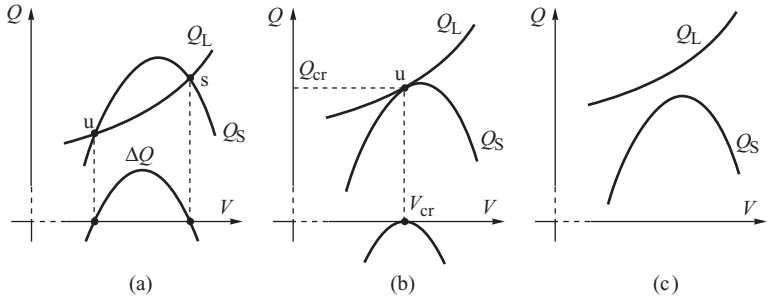

Figure 8.11 Relative position of the generation and load characteristics: (a) two equilibrium points; (b) a single critical equilibrium point; (c) no equilibrium points.

points u and s in Figure 8.11a. If the point lies on the envelope then there is only one equilibrium point and this corresponds to the one intersection point shown in Figure 8.11b. The power system is then in a *critical* state, the point is referred to as the *critical point* and its coordinates are the *critical power* and the *critical voltage*. Outside the network solution area in Figure 8.4 there are no equilibrium points and this corresponds to the $Q_L(V)$ and $Q_S(V)$ characteristics having no point of intersection as in Figure 8.11c where the $Q_L(V)$ characteristic lies above the $Q_S(V)$ characteristic. In general the area of network solution shown in Figure 8.4 is known as the *steady-state voltage stability area*.

Remember that Figure 8.11 has been drawn for the special case of the ideally stiff load with respect to real power, $P_L(V) = P_L = \text{constant}$, so that the critical power Q_{cr}, P_{cr} is defined by the coordinates (Q_{cr}, P_L) and only Q_{cr} and V_{cr} are marked on Figure 8.11b.

8.3.1 *Effects of Increasing Demand*

A slow increase in the system demand, such as that due to the normal daily load variations, can have two detrimental effects on the voltage stability. According to Equation (8.18) an increase in the real power lowers the $Q_S(V)$ characteristic as shown in Figure 8.7, while an increase in the reactive power raises the $Q_L(V)$ characteristic. As a consequence the stable equilibrium point s moves towards smaller values of voltage and the unstable equilibrium point u moves towards larger values of voltage. As the demand further increases, the equilibrium points move closer together until they finally merge at the critical equilibrium point shown in Figure 8.11b.

When a load operates at this critical point, then any small increase in the reactive power demand will produce a deficit in the reactive power, the reactive power demand will be greater than supply, and the voltage will reduce. As the voltage reduces, the deficit in reactive power increases and the voltage falls even further until it eventually falls to a very small value. This phenomenon is generally known as *voltage collapse* although in some countries the more graphic term of *voltage avalanche* is used. Two forms of voltage collapse are identified in the literature. When the voltage collapse is permanent some authors refer to it as a *total voltage collapse* (Taylor, 1994). On the other hand, the term *partial voltage collapse* is used when a large increase in demand causes the voltage to fall below some technically acceptable limit. As a partial voltage collapse does not correspond to system instability, it is perhaps better to consider the system as being in an emergency state since the system still operates, albeit at a reduced voltage.

An example of an actual voltage collapse is shown in Figure 8.12 (Nagao, 1975). In this figure curve 2 represents a typical morning period when the voltage drops slightly as the power demand increases but then recovers by a small percentage during the lunch break as the power demand reduces. At about 13:00, after the lunch break, the power demand again builds up and the voltage

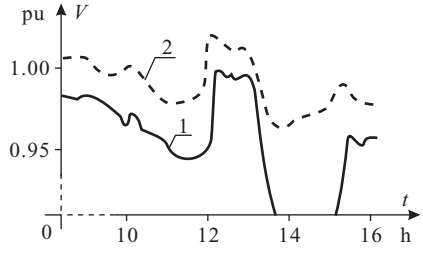

Figure 8.12 An example of the voltage collapse (Nagao, 1975): (1) voltage variations during the day of the voltage collapse; (2) voltage variations during the previous day.

drops. However, on one particular day, curve 1, the overall system load is greater, and the local voltage smaller, than normal so that as the load starts to increase after the lunch break, the voltage reaches its critical value and then collapses. The system operators then intervene and, after a long interruption, manually restore the normal operating conditions.

From the power system security point of view, knowledge of the critical power and voltage is very important as the operating voltage, and power, at the system nodes should be kept as far as possible from their critical values. Unfortunately the nonlinearity of the voltage characteristics makes it impossible to derive a general formula for the critical voltage that is valid for any type of active and reactive power variations even assuming a simple power system model. However, some simple iterative formula can be developed if the following three assumptions are made:

1. That when the load demand increases, the power factor is maintained constant by reactive power compensation in the consumer load so that

$$\frac{P_{\mathrm{n}}(t)}{P_0} = \frac{Q_{\mathrm{n}}(t)}{Q_0} = \xi, \tag{8.33}$$

   where $P_{\mathrm{n}}(t)$ and $Q_{\mathrm{n}}(t)$ are the nominal values of the load demand at the time instant t, P_0 and Q_0 are the initial values of the demand and ξ is the coefficient of demand increase.
2. That the power characteristic of an industrial composite load, with a large number of induction motors, can be approximated by the polynomials (Section 3.5.4)

$$\frac{Q_{\mathrm{L}}}{Q_{\mathrm{n}}} = a_2\left(\frac{V}{V_{\mathrm{n}}}\right)^2 - a_1\left(\frac{V}{V_{\mathrm{n}}}\right) + a_0, \quad \frac{P_{\mathrm{L}}}{P_{\mathrm{n}}} = b_1\left(\frac{V}{V_{\mathrm{n}}}\right), \tag{8.34}$$

   that is by a parabola and a straight line respectively.
3. That the load composition is constant thereby making the coefficients a_0, a_1, a_2 and b_1 constant.

Equation (8.33) allows the characteristics defined in Equation (8.34) to be converted to the following form:

$$Q_{\mathrm{L}} = \xi[\alpha_2 V^2 - \alpha_1 V + \alpha_0], \quad P_{\mathrm{L}} = \xi\beta_1 V, \tag{8.35}$$

where

$$\alpha_2 = \frac{Q_0}{V_{\mathrm{n}}^2}a_2, \quad \alpha_1 = \frac{Q_0}{V_{\mathrm{n}}}a_1, \quad \alpha_0 = Q_0 a_0 \quad \beta_1 = \frac{P_0}{V_{\mathrm{n}}}b_1.$$

Substituting the second of the equations in (8.35) into Equation (8.18) gives

$$Q_S(V) = V\sqrt{\left(\frac{E}{X}\right)^2 - \xi^2\beta_1^2} - \frac{V^2}{X}. \tag{8.36}$$

Figure 8.11b shows how, at the critical point, the supply characteristic and the demand power characteristic are tangential to each other, which allows the value of the critical voltage V_{cr} to be found by solving the following two equations:

$$Q_S(V_{cr}) = Q_L(V_{cr}), \tag{8.37}$$

$$\left.\frac{dQ_S}{dV}\right|_{V=V_{cr}} = \left.\frac{dQ_L}{dV}\right|_{V=V_{cr}}. \tag{8.38}$$

Substituting for Q_S and Q_L from Equations (8.35) and (8.36) gives

$$V_{cr}\sqrt{\left(\frac{E}{X}\right)^2 - \xi_{cr}^2\beta_1^2} - \frac{V_{cr}^2}{X} = \xi_{cr}\left(\alpha_2 V_{cr}^2 - \alpha_1 V_{cr} + \alpha_0\right), \tag{8.39}$$

$$\sqrt{\left(\frac{E}{X}\right)^2 - \xi_{cr}^2\beta_1^2} - 2\frac{V_{cr}}{X} = \xi_{cr}\left(2\alpha_2 V_{cr} - \alpha_1\right). \tag{8.40}$$

Equation (8.40) determines the critical voltage as a function of the system parameters and an unknown coefficient ξ_{cr} of the demand increase as

$$V_{cr} = \frac{\sqrt{\left(\frac{E}{\beta_1 X}\right)^2 - \xi_{cr}^2} + \frac{\alpha_1}{\beta_1}\xi_{cr}}{2\frac{\alpha_2}{\beta_1}\xi_{cr} + \frac{2}{\beta_1 X}}. \tag{8.41}$$

Multiplying Equation (8.40) by $(-V_{cr})$ and adding the result to Equation (8.39) gives

$$\frac{V_{cr}^2}{X} = \xi_{cr}\left[\alpha_0 - \alpha_2 V_{cr}^2\right], \tag{8.42}$$

from which finally

$$\xi_{cr} = \frac{1}{\frac{\alpha_0 X}{V_{cr}^2} - \alpha_2 X}. \tag{8.43}$$

Equations (8.41) and (8.43) can now be used in an iterative calculation to find the critical voltage V_{cr} and the critical demand increase ξ_{cr}.

Example 8.1

A composite load of rating $S_n = (150 + j100)$ MVA and $V_n = 110$ kV is supplied from the network by a 130 km, 220 kV transmission line with a reactance of 0.4 Ω/km via two parallel 160 MVA transformers, each with a reactance of 0.132 pu. Assume that the system can be replaced by a 251 kV voltage source with a reactance of 13 Ω and that the load characteristics in kV and MVA are $P_L = 0.682\xi V$ and $Q_L = \xi(0.0122V^2 - 4.318V + 460)$. Find the critical voltage and the critical coefficient of the load demand increase.

Simple calculation leads to the parameter values shown in Figure 8.13. Equations (8.41) and (8.43) then give

$$V_{\mathrm{cr}} = \frac{\sqrt{18.747 - \xi_{\mathrm{cr}}^2} + 6.331\xi_{\mathrm{cr}}}{0.035\,78\xi_{\mathrm{cr}} + 0.0345}, \qquad \xi_{\mathrm{cr}} = \frac{1}{\frac{39100}{V_{\mathrm{cr}}^2} - 1.037}. \tag{8.44}$$

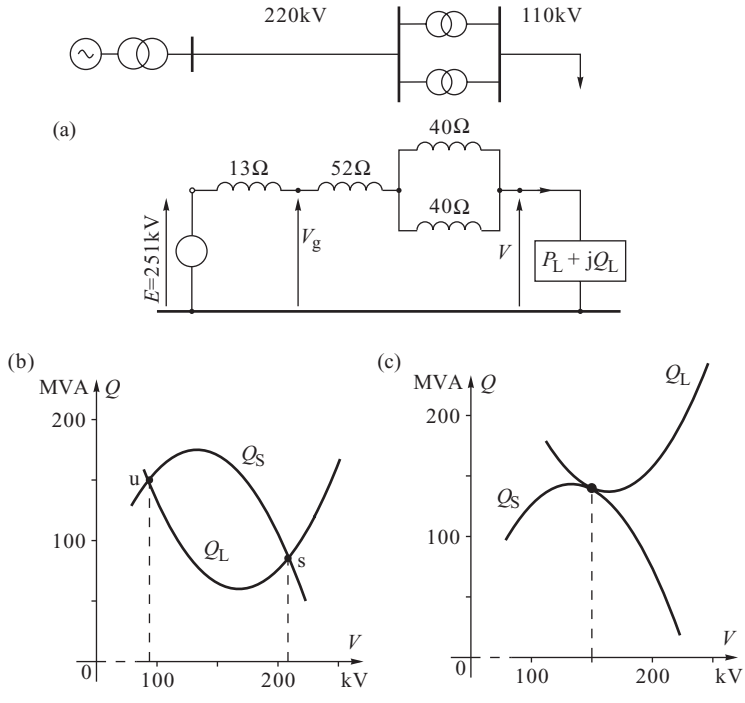

Figure 8.13 Illustration for Example 8.1: (a) equivalent circuit with parameters calculated at 220 kV; (b) initial characteristics; (c) characteristics at the critical state.

The initial substitution of $\xi_{\mathrm{cr}} = 1$ into the first of these equations gives $V_{\mathrm{cr}} = 151.69$. Substituting this value into the second equation gives $\xi_{\mathrm{cr}} = 1.51$. After five such iterations, the final solution of $\xi_{\mathrm{cr}} = 1.66$ and $V_{\mathrm{cr}} = 154.5\,\mathrm{kV}$ is obtained indicating that the system would lose stability if the demand increased 1.66 times. The primary voltage $V_{\mathrm{cr}} = 154.5\,\mathrm{kV}$ referred to the transformer secondary winding gives 77.25 kV, that is 70 % of the rated voltage of 110 kV. Figure 8.13b and c shows the system and the load characteristic in the initial and critical states. Initially the system operated at point s at a voltage of 208 or 104 kV at the transformer secondary, that is at 94.5 % of the rated voltage.

8.3.2 Effect of Network Outages

The relative position of the supply characteristic defined in Equation (8.18) depends on the equivalent system reactance. Large changes in this reactance, such as those caused by network outages, may lower the generation characteristic and cause voltage stability problems.

Example 8.2

A composite load of $S_n = (240 + j160)$ MVA and $V_n = 110$ kV is supplied from the network by a double-circuit transmission line of length 130 km and reactance 0.4 Ω/km via two parallel 160 MVA transformers each with a reactance of 0.132 pu. The power system may be represented by an emf of 251 kV acting behind an equivalent reactance of 13Ω. The load characteristics are: $P_L = 1.09V$ and $Q_L = 0.0195V^2 - 6.9V + 736$. Check the system stability after one of the lines is tripped.

Figure 8.14 shows the load characteristic and the generation characteristic before, Q'_S, and after, Q''_S, the line is tripped. Tripping the line causes a reduction in the load voltage to about 170 or 85 kV on the secondaries of the transformers, that is to about 77 % of the rated voltage. The system is on the verge of losing stability. Calculations similar to those in Example 8.1 show that a demand increase by 3.8 % will result in the system losing stability. Due to the unacceptably low voltage, the system is now in an emergency state with a high risk of instability.

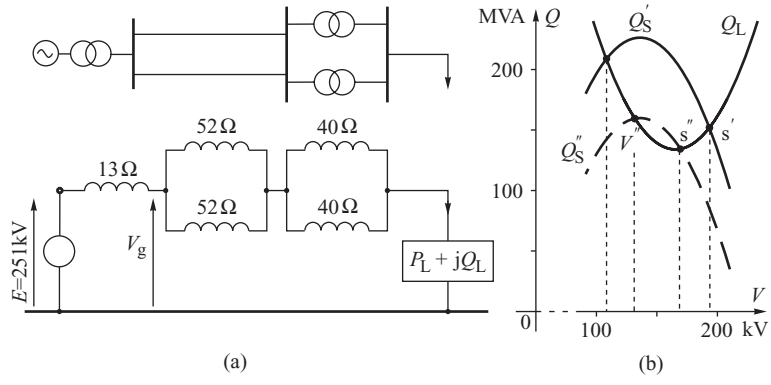

Figure 8.14 Illustration for Example 8.2: (a) equivalent circuit with parameters calculated at 220 kV; (b) voltage characteristics.

8.3.3 Influence of the Shape of the Load Characteristics

Figure 8.7 and Equation (8.18) demonstrate how an increase in the real power demand shifts the vertex of the reactive power supply characteristic downwards. This observation has important implications with regard to the voltage stability of systems where the real power varies with voltage. For example, if the real power demand reduces with reducing voltage then the stability of the system will be improved compared with when the real power characteristics is independent of voltage. This situation is examined further in Example 8.3.

Example 8.3

For the system in Example 8.2 determine the supply characteristics after one of the transmission lines is tripped assuming that the real power characteristics of the load (in MW) are as follows:

$$(1)\ P_L = 240 = \text{constant},\ (2)\ P_L = 16.18\sqrt{V},\ (3)\ P_L = 1.09V,\ (4)\ P_L = 0.004859V^2.$$

The four real power characteristics are shown graphically in Figure 8.15a with curve 1 representing an ideally stiff load. Curves 2, 3 and 4 represent voltage-sensitive loads. The corresponding reactive power supply characteristics can be easily determined using Equation (8.18) and are shown in Figure 8.15b. For the ideally stiff load, curve 1, the system has no equilibrium points

and line tripping results in immediate voltage collapse. The slightly less stiff load 2 is in the critical state and will also lose stability should the line trip. Load 3 is close to the critical state and will lose stability when the demand increases by 3.8 % (see Example 8.2) while load 4 is more voltage sensitive and operates with a greater safety margin. In this case stability will be lost if the demand increases by about 15 %.

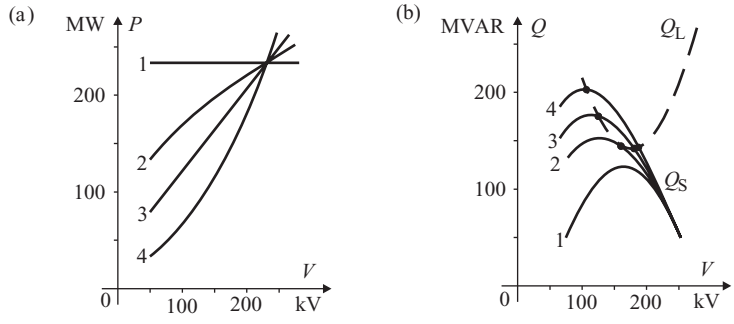

Figure 8.15 Real and reactive power characteristics for Example 8.3.

8.3.3.1 Absolutely Stable Loads

Figure 8.4 showed how the network solution area depends on the shape of the load characteristic with Figure 8.4d corresponding to a constant admittance load. The equivalent circuit for such a load was shown in Figure 8.5 and Section 8.1 explained how for a load with such a characteristic every equilibrium point for $V > 0$ is stable and the system cannot suffer voltage collapse. This can also be proved using the classical $\mathrm{d}Q/\mathrm{d}V$ criterion.

For a constant admittance load the $P_L(V)$ characteristic is given by Equation (8.14) which, when substituted into Equation (8.18), gives the reactive power supply characteristic as

$$Q_S = V\left[\sqrt{\left(\frac{E}{X}\right)^2 - (G_n V)^2} - \frac{V}{X}\right]. \tag{8.45}$$

The resulting characteristic is drawn in Figure 8.16 and shows that for any value of the load conductance G_n the supply characteristic always crosses the origin at $V = 0$. Again from Equation (8.14) the reactive power demand is given as $Q_L = B_n V^2$ so that the origin is always one of the equilibrium points for any value of the load susceptance B_n. As the load susceptance increases, the

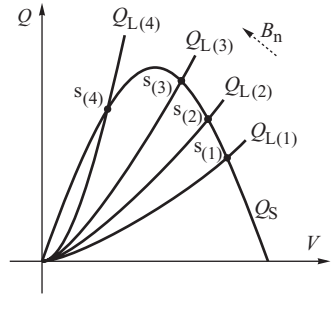

Figure 8.16 A family of reactive demand characteristics for a fixed-load conductance G_n and increased load susceptance B_n.

parabola defined by $Q_L = B_n V^2$ becomes steeper but the stability condition (8.19) is satisfied for all equilibrium points when $V > 0$. This is true even for the equilibrium point $S_{(4)}$ on the left hand side of the supply parabola. The constant admittance load is therefore absolutely stable because no value of Y_L can cause the voltage to collapse, although a large value of the load admittance Y_L will result in an inadmissible low operating voltage.

8.3.4 Influence of the Voltage Control

Section 8.1 showed that the reactance of the equivalent system generator, and therefore the point of constant voltage in the network model, depends on the voltage control capability of the generator. Provided that neither the excitation limits nor the stator current limit are exceeded, then the AVR will keep the generator terminal voltage constant and there is no need to add the generator synchronous reactance X_d to the network equivalent reactance X in Figure 8.1. However, if any of the generator current limits are met then the field voltage will be maintained constant and the generator must be modelled by and emf E_f behind X_d. The modelling reactance must now be increased to include the effect of X_d. Consequently, as the equivalent system reactance in the generator–line–load model depends significantly on the voltage control capability of the generator so too will the voltage stability.

Both the area of network feasibility, Section 8.1, and the characteristics used to analyse the voltage stability, Section 8.2, depend on the equivalent reactance of the system. This reactance occurs in two terms in Equation (8.18), the $-V^2/X$ term and the EV/X term, both of which determine the steepness of the parabola and the position of its vertex. If X is large then the supply characteristic parabola is shallow and its vertex is lowered as shown in Figure 8.7. This results in a reduction in the maximum reactive power and hence the critical power.

Example 8.4

For the system in Example 8.2 determine the supply characteristic when the system is operating with only one transmission line. Assume that the equivalent system generator is capable of keeping the voltage at the sending end of the line constant.

Before the line is tripped the load operated at 208 kV (referred to the primaries of the transformers). Figure 8.14 shows that the voltage drop across the source reactance gives the terminal voltage $V_g = 245$ kV. Assuming that the AVR keeps this voltage constant, the system can now be represented by a voltage $E = V_g = 245$ kV = constant with zero internal reactance. The reactance of one line, and two parallel transformers, give a total $X = 52 + 40/2 = 72\ \Omega$. Figure 8.17 shows that the supply characteristic is now much higher compared with when voltage control was neglected. Calculations similar to those in Example 8.1 show that the system would lose stability when the demand increases by about 12%. Neglecting voltage control gave the critical demand increase as 3.8%.

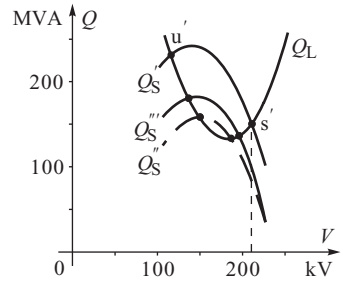

Figure 8.17 Generation and load characteristics analysed in Example 8.4. Q'_S, before tripping the line; Q''_S, after tripping with E = constant; Q'''_S, after tripping with V_g = constant.

It was assumed in the above example that the voltage regulator of the source supplying the load was able to keep the terminal voltage constant. This is an idealized situation. In practice, every source has a limited regulation range. For the synchronous generator, limitations of voltage regulators were discussed in Section 3.3.4. The characteristic of the generator as the source of reactive power was shown in Figure 3.22. That diagram shows that, after the limiting value of the field (rotor) current or the armature (stator) current is reached, the reactive power capability is quickly reduced as the voltage declines. The generator can no longer be treated as a constant voltage source but rather as a source with a large internal reactance equal to the synchronous reactance. For such a source, the generation characteristic Q_S is significantly lowered (curve Q_S'' in Figure 8.17) and voltage stability may be lost via voltage collapse.

8.4 Static Analysis

The analysis so far has concerned the simple generator–infinite busbar system. Voltage stability analysis of a more realistic representation of a multi-machine system supplying many composite loads via a meshed network is much more complicated.

For network planning purposes the critical load power can be calculated offline using a modified load flow computer program and the dQ/dV or dQ_G/dQ_L stability criterion (Van Cutsem, 1991; Ajjarapu and Christy, 1992; Taylor, 1994; Van Cutsem and Vournas, 1998). The procedure is similar to that described in Section 8.3 for the simple generator–line–load system and the idea is to bring the system to a critical state by increasing the power demand of a chosen load or a group of loads. The use of a load flow program allows a variety of effects such as generator voltage control, reactive power compensation, the distribution of real power among the generation units with active governors, the voltage characteristics of the loads, and so on, to be included.

Unfortunately the method is computationally time consuming and cannot be used for online applications, such as steady-state security assessment, which require a fast assessment of the voltage stability conditions and an estimation of how far a given operating point is from the critical state. The distance from the critical state is usually quantified by one of the so-called *voltage stability indices* (Kessel and Glavitsch, 1986; Tiranuchit and Thomas, 1987; Löf *et al.*, 1992 among others). A number of different indices are discussed by Taylor (1994).

8.4.1 Voltage Stability and Load Flow

Section 8.3 showed that when power demand increases to the critical value, there is only one solution of the network equation and it corresponds to the intersection of the demand characteristic $Q_L(V)$ with the system characteristic $Q_S(V)$. If the demand depends on voltage then its characteristic $Q_L(V)$ is bent at an angle corresponding to the coefficient k_{QV} referred to as the voltage sensitivity (Figure 3.26). In that case (Figures 8.11 and 8.13) the critical point is near the peak of the system characteristic $Q_S(V)$. On the other hand, the voltage characteristic of an ideally stiff load is a horizontal line, $Q_L(V) = Q_n = \text{constant}$, and the critical point corresponds exactly to the peak of the system characteristic $Q_S(V)$, that is the point at which $dQ_S/dV = 0$.

Real and reactive power of an ideally stiff load are correlated by the equation $Q_n = P_n \tan\varphi$. Hence, for a given $\tan\varphi$, real power reaches a maximum when reactive power reaches a maximum. This means that at the critical state when $dQ_S/dV = 0$ then also $dP_n/dV = 0$. This corresponds to the peak of the nose on the nose curve (Figure 8.2). Hence, when the demand approaches the critical value of the ideally stiff load, the following holds:

$$dP/dV \to 0 \quad \text{and} \quad dQ/dV \to 0, \tag{8.46}$$

that is the derivatives of real and reactive power calculated from the network equations tend to zero. This observation is the basis for determining the critical power demand using load flow programs.

8.4.1.1 Critical Power Demand

Section 3.6 explained that the network equations can be linearized at a given operating point using

$$\begin{bmatrix} \Delta \boldsymbol{P} \\ \hline \Delta \boldsymbol{Q} \end{bmatrix} = \begin{bmatrix} \boldsymbol{H} & \boldsymbol{M} \\ \hline \boldsymbol{N} & \boldsymbol{K} \end{bmatrix} \begin{bmatrix} \Delta \boldsymbol{\delta} \\ \hline \Delta \boldsymbol{V} \end{bmatrix} \quad \text{or} \quad \Delta \boldsymbol{y} = \boldsymbol{J} \Delta \boldsymbol{x}, \tag{8.47}$$

where $\boldsymbol{J}$ is the Jacobi matrix. In the critical state for nonzero voltage changes (i.e. for $\Delta \boldsymbol{x} \neq \boldsymbol{0}$) the power changes are equal to zero (i.e. $\Delta \boldsymbol{y} = \boldsymbol{0}$). Hence the equation $\boldsymbol{J} \Delta \boldsymbol{x} = \boldsymbol{0}$ is obtained and has a non-trivial solution $\Delta \boldsymbol{x} \neq \boldsymbol{0}$ if and only if $\det \boldsymbol{J} = 0$. Thus, when the demand is critical

$$\det \boldsymbol{J} = \det \begin{bmatrix} \boldsymbol{H} & \boldsymbol{M} \\ \hline \boldsymbol{N} & \boldsymbol{K} \end{bmatrix} = 0, \tag{8.48}$$

that is the determinant of the Jacobi matrix is zero and the matrix is singular. Such a point is referred to as the *bifurcation point*.

The critical state can be reached for different scenarios of power demand increase. Demand may be assumed to increase at a single load or in a given area or a subsystem. Starting from a base (typical) load flow, demand at chosen loads is increased stepwise and a new load flow is calculated. At each step, the determinant of the Jacobi matrix is calculated and its variation is monitored. If $\det \boldsymbol{J}$ approaches zero, it can be concluded that the system approaches the critical state. Obviously the closer it is to the critical state, the less convergent the iterative process of solving the network equations becomes. At the critical state the iterative process of solving the network equations based on the Newton method stops converging.

At each step, when consecutive load flows are determined, additional factors affecting voltage stability can be taken into account, such as the voltage characteristics of the loads, transformer tap ratio control, generator voltage control and its limits. This obviously requires that the load flow program is equipped with appropriate procedures. Nose curves can be determined at each step of increasing demand so that the simulation results can be shown graphically as in Figure 8.2.

Nose curves can be determined for individual composite loads or for load areas containing electrically close composite loads. The tip of a nose curve determines the critical real power demand. Obviously, when determining the real power nose curve, it is necessary to model in such a reasonable way that when real demand increases in each simulation step, reactive power increases too.

If, similar to (8.33), ξ denotes the coefficient of demand increase, then the critical value of this coefficient is given by $\xi_{\mathrm{cr}} = P_{\mathrm{n\,MAX}}/P_0$, where P_0 is power demand at given operating conditions while p_{nMAX} is the critical power demand corresponding to the tip of the determined nose curve. An example of the application of that methodology will be discussed in Section 8.5.2 (see Figure 8.20).

8.4.1.2 V–Q Sensitivity Analysis

In Figure 8.6 the system characteristic $Q_{\mathrm{S}}(V)$ was obtained assuming that the voltage at the load node is variable and that the source voltage and the real power of the load are constant parameters. Similar assumptions can be made when considering the network equation (8.47). The assumption that real powers are constant corresponds to $\Delta \boldsymbol{P} = \boldsymbol{0}$. Now, using the partial inversion described in Appendix A.2, Equation (8.47) gives

$$\Delta \boldsymbol{Q} = (\boldsymbol{K} - \boldsymbol{N}\boldsymbol{H}^{-1}\boldsymbol{M}) \Delta \boldsymbol{V}, \tag{8.49}$$

or

$$\Delta \boldsymbol{V} = \boldsymbol{W} \Delta \boldsymbol{Q}, \tag{8.50}$$

where

$$\boldsymbol{W} = (\boldsymbol{K} - \boldsymbol{N}\boldsymbol{H}^{-1}\boldsymbol{M})^{-1}. \tag{8.51}$$

Equation (8.50) describes the sensitivity of nodal voltages to the changes in reactive power in system nodes. It can be used to assess the influence of reactive power compensation at a given node, or changes in reactive power produced by a generator, on nodal voltages. This type of investigation is referred to as $V-Q$ *sensitivity analysis*. The diagonal elements of (8.51) determine the slope of the characteristic $Q_S(V)$ at a given linearization point of the network equations.

8.4.2 Voltage Stability Indices

The discussed coefficient $\xi_{cr} = P_{n\,MAX}/P_0$ may be treated as a measure of voltage stability margin from the point of view of demand increase. Voltage stability criteria discussed in Section 8.2 may also be used to determine voltage stability indices.

A voltage stability index based on the classical dQ/dV criterion can be constructed by observing that as the load demand gets closer to the critical value, both the equilibrium points shown in Figure 8.11 move towards each other until they become one unstable point. As shown in Figure 8.8b, there is always a point between the equilibrium points, of voltage V_x, such that

$$\left.\frac{d(Q_S - Q_L)}{dV}\right|_{V=V_x} = 0. \tag{8.52}$$

As the power demand of the composite load increases, the voltage V_x tends towards the critical voltage V_{cr}. A voltage proximity index can be therefore defined as (Venikov, 1978b)

$$k_V = \frac{V_s - V_x}{V_s}, \tag{8.53}$$

where V_x must satisfy Equation (8.52). In practice, calculating the proximity index defined by Equation (8.53) is quite cumbersome as it requires a fragment of the generation characteristic $Q_S(V)$ to be determined by means of a load flow program. An alternative proximity index that is easier to determine is the value of the derivative

$$k_{\Delta Q} = \frac{d(Q_S - Q_L)}{dV}\frac{V_s}{Q_s} \tag{8.54}$$

calculated near a given equilibrium point. As the load demand tends towards the critical value, the index (8.54) tends towards zero.

Yet another voltage proximity index can be derived directly from the dQ_G/dQ_L criterion as

$$k_Q = \frac{dQ_G}{dQ_L}. \tag{8.55}$$

When the network is lightly loaded the reactive power absorbed by the network is small so that the increment in the generation caused by the increment in the load demand is almost equal to the increment in the load demand itself and the index defined in Equation (8.55) is near unity. When the system approaches the critical state, the index tends to infinity (Figure 8.10). The value of this index can be calculated for a multi-node system using a load flow program.

Currently the problem of voltage stability is a rapidly developing research area with many new papers appearing either proposing new proximity indices and improved methods of calculation, or suggesting how proximity indices can be identified online using local measurements.

8.5 Dynamic Analysis

The voltage stability analysis presented so far in this chapter has assumed that the loads can be represented by their static voltage characteristics. Although this is useful to help understand the principles of voltage stability, and its relation to the network feasibility problem, the static load voltage characteristics can only approximate the real behaviour of the composite load for slow voltage variations. In practice the actual behaviour of both the composite load and the system is a tightly coupled dynamic process that is influenced by the load dynamics, especially induction motor dynamics, the automatic voltage and frequency control equipment, and by the operation of the protection systems. Any, or all, of these factors may speed up, slow down, or even prevent voltage collapse.

8.5.1 The Dynamics of Voltage Collapse

To complement the static considerations of the previous sections a few examples of some typical voltage collapse scenarios will now be briefly discussed (Taylor, 1994; Bourgin *et al.*, 1993).

8.5.1.1 Scenario 1: Load Build-Up

Section 8.3 explained how voltage collapse can result from a very large build-up of load, particularly during periods of heavy demand, so that the power demand exceeds the critical value as determined by the network parameters. In this scenario the main factors contributing to voltage collapse are:

1. The stiffness of the load characteristics continuing to demand high values of active and reactive power despite voltage dips in the load area. As Chapter 3 explained, induction motors are mainly responsible for producing a stiff load characteristic.
2. The control of tap-changing transformers in distribution and subtransmission networks maintaining constant voltage, and therefore high active and reactive power demand, when the supply voltage dips. High demand is undesirable in the emergency state.
3. The limited ability for reactive power control by the generators. Due to field and armature current limits, a high reactive power demand by the system loads may cause the generators to lose their ability to act as a constant voltage source. The generator then behaves like a voltage source behind the synchronous reactance and its terminal voltage reduces.

A voltage collapse due to load build-up may be caused by some, or all, of the above factors. The dynamics of the various voltage control devices (generators, compensators, transformers) may interact in such a way that the actual voltage collapse is different to that predicted by static considerations.

Voltage changes during voltage collapse were shown in Figure 8.12. The dynamics contain a long-term drift of voltage caused by a slow increase in the system load.

8.5.1.2 Scenario 2: Network Outages

As seen in previous sections of this chapter, the network parameters play a crucial role in determining the maximum power that can be delivered to the load areas. Tripping one of the lines in the power grid increases the equivalent reactance between the equivalent voltage source and the load thus increasing voltage drops in lines and therefore depressing network voltages. Reduced voltages and increased equivalent reactance reduce the critical power and increase the probability of voltage collapse. Generator tripping has a similar effect in that it not only increases the equivalent system reactance, but also reduces the systems capability to generate real and reactive power.

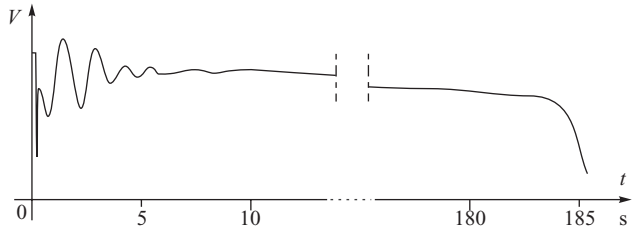

Figure 8.18 An example of voltage collapse initialized by network outage.

The dynamics of the various voltage control devices in the system can again influence the actual scenario.

Typical voltage changes during voltage collapse are shown in Figure 8.18. The dynamics contain about 10 seconds of transient oscillations caused by the outage and a drift of voltage caused by a slow increase in reactive power deficit in the system while taking into account the actions of various control devices and their limiters.

8.5.1.3 Scenario 3: Voltage Collapse and Asynchronous Operation

Voltage collapse at one, or a few, of the network nodes may cause the voltage to dip at neighbouring nodes leading to voltage collapse at these nodes. The voltage then dips at other nodes so propagating throughout the network and affecting the synchronous generators. If the affected generators are weakly connected with the system they may lose synchronism.

A voltage dip, accompanied by a reduction in the real power demand and an increase in the reactive power demand, has a similar effect on the synchronous generator as a short circuit in the network. An example of just such behaviour is shown in Figure 8.19 where the tripping of line L2 results in the generator and the load operating through one, quite long, line. The load is in the critical state and a small increase in the load demand results in voltage collapse and the generator losing synchronism with the rest of the system. The load voltage then undergoes periodic voltage variations characteristic of asynchronous operation. The asynchronously operating generator must now be tripped from the system, which further deteriorates the situation at the load node leading to an eventual total voltage collapse.

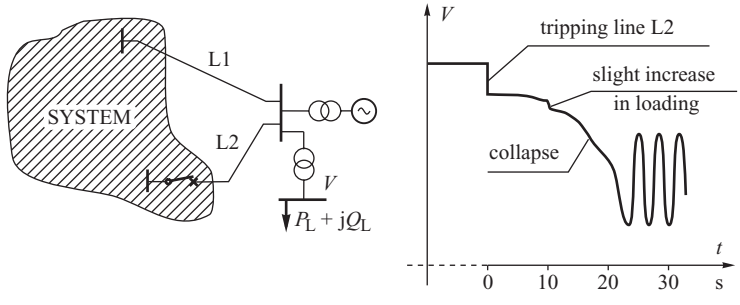

Figure 8.19 Loss of synchronism caused by the voltage collapse: (a) schematic diagram of the system; (b) voltage variations. Based on Venikov (1978b).

Source: VA Venikov

8.5.1.4 Scenario 4: Phenomena Inside the Composite Load

As already mentioned, the stiffness of the load characteristics is one of the dominant factors contributing to voltage collapse. However, the dynamic response of the composite load may result in the dynamic and static load characteristics being different. This difference is mainly attributed to induction motors and may result in a reduction in the system stability ultimately leading to voltage collapse. For example, a rapid, severe voltage dip, such as that which occurs during a slowly cleared short circuit, can cause a reduction in the motor torque and consequent motor stalling. As shown in Section 3.5, a stalled induction motor demands reactive power further reducing the voltage stability conditions. This may lead to other nearby motors stalling. In this scenario the voltage continues to fall until the protective equipment, or the electromechanically held contactors, trip the motors from the system thereby reducing the reactive power demand. The voltage will then start to recover but an uncontrolled restoration of the composite load by, for example, heavy induction motor self-starts, can again reduce the voltage and lead to a total voltage collapse.

8.5.2 Examples of Power System Blackouts

There have been a number of well-publicized blackouts in Europe and North America in the early years of this millennium. Although in each case the blackout was caused by a specific technical problem, the unprecedented concentration of blackouts has caused many observers to argue that there are underlying systemic reasons for such a large number of disturbances occurring at more or less the same time (Bialek, 2007). Increased liberalization of electricity supply industry in the 1990s has resulted in a significant increase in interarea (or cross-border) trades in interconnected networks of North America and Europe. This means that the interconnected systems are used for purposes they were not designed for. Interconnections grew by connecting self-sustained areas so that tie-lines tend to be relatively weak and require a careful monitoring of tie-line flows (this will be further discussed in Chapter 9). It should be emphasized that any transaction in a meshed network may affect all the network flows, sometimes quite far away from the direct contract path linking the source and the sink of a transaction. This is referred to as the loop flow effect (Section 3.7). Loop flows may be a problem because interarea transactions are often not properly accounted for when assessing system security by a TSO (Transmission System Operator) that does not know about all the transactions affecting its area. That effect is compounded by increased penetration of wind generation. Large changes of wind power due to changing weather patterns mean that actual network flows may be quite different from predicted ones. All this means that the traditional decentralized way of operating systems by TSOs, with each TSO looking after its own control area and with little real-time information exchange, resulted in inadequate and slow responses to contingencies. Bialek (2007) argues that a new mode of coordinated operation with real-time exchange of information for real-time security assessment and control is needed in order to maintain security of interconnected networks.

The remainder of this section is devoted to a description of blackouts related to voltage problems. The first blackout discussed in this section was a textbook case of a voltage collapse due to a combination of load growth and loss of power plants. In the other blackouts the voltage collapsed due to cascaded tripping of transmission lines.

8.5.2.1 Athens Blackout in 2004

The blackout affecting over 5 million people in southern Greece, including Athens, has been described by Vournas, Nikolaidis and Tassoulis (2006). It was well known that the Hellenic system was prone to voltage instability due to long transmission distance between the main generation in the north and west of Greece and the main load centre in Athens. Consequently, a number of system reinforcements, such as new transmission lines, autotransformers and capacitor banks, were ordered

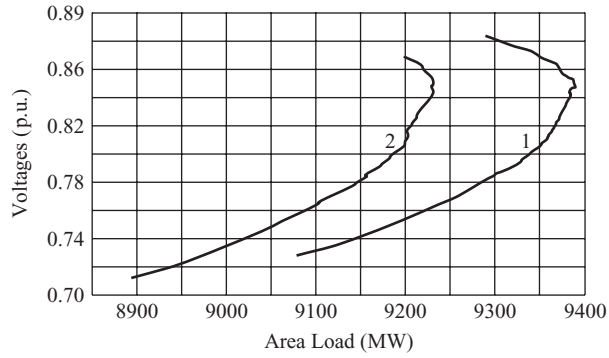

Figure 8.20 PV curves: (1) before Athens blackout; (2) after the second unit tripped (Vournas, Nikolaidis and Tassoulis 2006). Reproduced by permission of IEEE

in the run-up to the 2004 Olympic Games. The blackout happened when those reinforcements were not fully commissioned.

The disturbance started just after midday on a hot July day when the load was on the increase due to air-conditioning. A generating unit near Athens was lost and that brought the system to an emergency state. Load shedding was initiated but it had not been fully implemented when another unit at the same plant tripped. Curve 1 in Figure 8.20 shows the PV nose curve, simulated post-mortem, just before the second unit tripped. The load was 9320 MW, which is slightly less than the peak of the PV curve equal to about 9390 MW. Curve 2 in Figure 8.20 shows the simulated PV curve after the second unit tripped. Clearly the PV curve moved left with the critical load of about

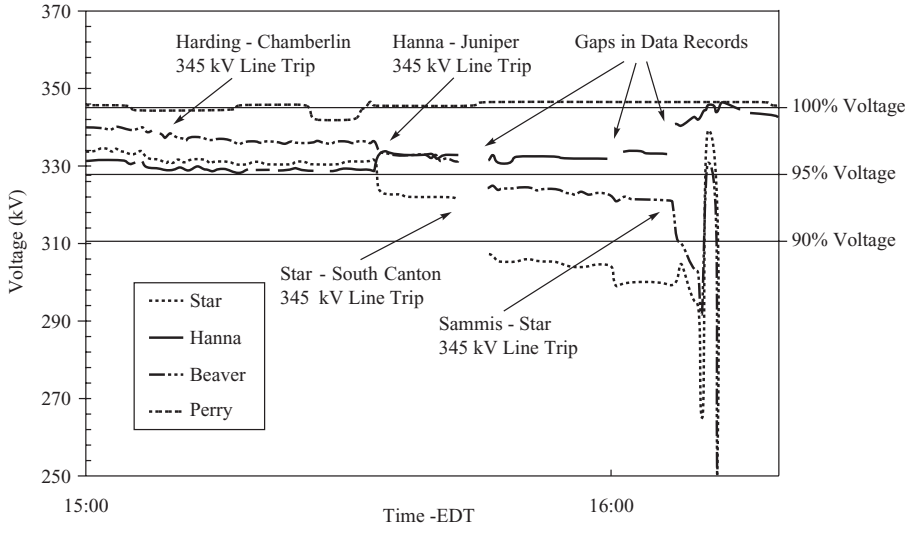

Figure 8.21 Cascaded line trips depressing voltages during US/Canada blackout (US–Canada Power System Outage Task Force, 2004).

Source: Final Report on the August 14, 2003 Blackout in the United States and Canada. US-Canada Power System Outage Task Force, 2004

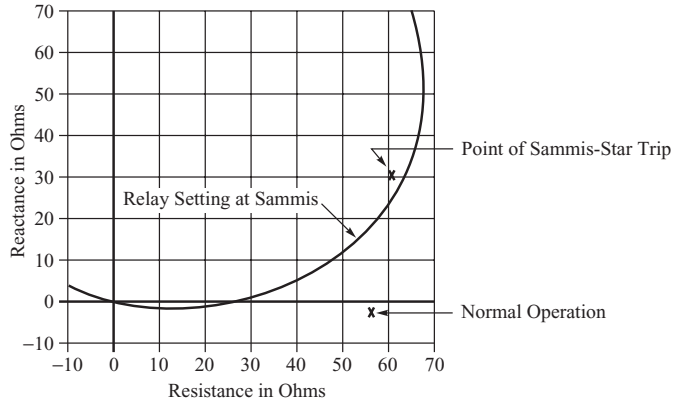

Figure 8.22 Normal operating point and the tripping point of Sammis–Star line during 2001 US/Canada blackout (US–Canada Power System Outage Task Force, 2004).

Source: Final Report on the August 14, 2003 Blackout in the United States and Canada. US-Canada Power System Outage Task Force, 2004

9230 MW, which was about 90 MW less than the actual load. With no equilibrium point, voltage collapse was inevitable. When voltages started to collapse, the undervoltage element of distance relays in the north–south 400 kV lines opened, separating the southern part of the Greek system from the northern part. The remaining generation in the southern part of Greece was tripped by undervoltage protection leading to a blackout.

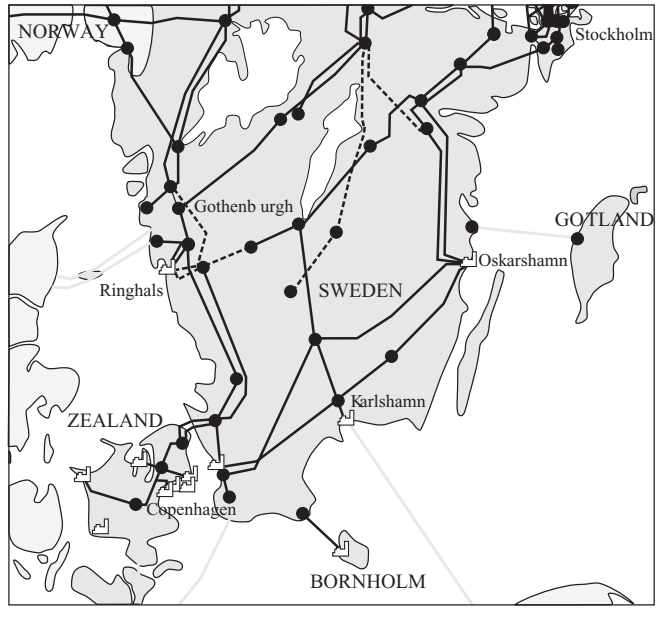

Figure 8.23 The grid 10 s after the substation fault. Tripped transmission lines are shown by dashed lines. Karlshamn Power Station was out of operation (Elkraft Systems, 2003).

Source: Elkraft Systems

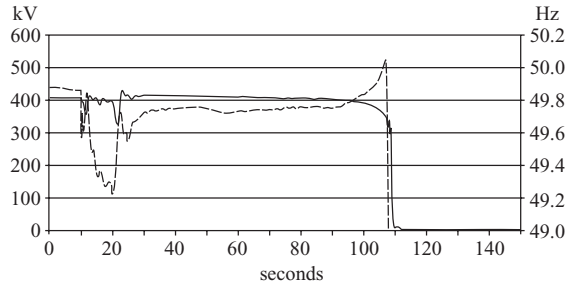

Figure 8.24 Voltage (solid line) and frequency (dashed line) measured at 400 kV connection between Sweden and Denmark (Elkraft Systems, 2003).

Source: Elkraft Systems

8.5.2.2 US/Canada Blackout in 2003

This widespread blackout affecting about 50 million customers in the United States/Canada has been described in the report by the US–Canada Power System Outage Task Force (2004). The direct cause of the disturbance was due to undetected cascaded tripping of transmission lines. Each line trip caused increased loading on the remaining lines and the resulting lowering of voltages, see Figure 8.21. Subsequent analysis has shown that the blackout was inevitable when a crucial Sammis–Star transmission line was unnecessarily tripped by zone 3 of the distance protection (see Section 2.5). The locus of a constant impedance determining a tripping threshold is a circle, see Figure 8.22. The normal point of operation is shown by a cross outside the circle. However, high currents and depressed voltages caused by earlier outages of other transmission lines caused a lowering of the measured value of the apparent impedance measured by the relay as shown by a cross inside the circle. The relay tripped the line causing rapid cascaded tripping of other lines and generators and resulting in the blacking out of a large part of the United States and Canada.

8.5.2.3 Scandinavian Blackout in 2003

This blackout affected 2.4 million customers in eastern Denmark and southern Sweden and has been described in the report by Elkraft Systems (2003). First a 1200 MW unit at Oskarshamn Power Station tripped due to problems with a valve in the feedwater circuit and 15 min later a double-busbar fault occurred at a substation in southern Sweden, which caused four 400 kV lines and two units (1800 MW) at Ringhals Nuclear Power Station to trip, see Figure 8.23. Such a heavy loss of generation and transmission caused heavy flows on the remaining transmission lines supplying southern Sweden. Consequently, voltages started to fall heavily in southern Sweden, where there was no generation left, but less so in eastern Denmark (Zealand) where local power plants were able to keep up voltages, see Figure 8.24. Overloading caused further tripping of a number of 130 and 220 kV transmission lines in southern Sweden and a consequent halving of voltage there. The combination of heavy flows and low voltages caused, as during the US/Canada blackout, tripping of zone 3 distance relays on a number of 400 kV lines in central and eastern Sweden so that these areas were no longer electrically connected. Finally, 90 s after the substation fault, the voltage fell to zero and a full blackout ensued.

8.5.3 Computer Simulation of Voltage Collapse

As mentioned above, voltage collapse is a dynamic process. The creation of a mathematical model of a large-scale power system while taking into account detailed models of structure and dynamics

of composite loads is practically impossible. It is, however, possible to create various task-oriented dynamic models devoted to the investigation of some scenarios of voltage collapse.

Voltage collapse caused by load build-up (scenario 1) is a long-term process. The slow drift of voltage may take many minutes or even hours, see Figure 8.12. Using dynamic simulation to investigate such a process is not required. It is much easier to investigate a number of snapshots as the disturbance progresses, using the static methods described in Section 8.4. The influence of all reactive power compensation devices, voltage regulators and limiters of relevant regulators should be taken into account.

Voltage collapse caused by network outages (scenario 2) and voltage collapse combined with asynchronous operation (scenario 3) can be simulated using computer programs devoted to short- and mid-term dynamic simulation. Such programs should include models of excitation and voltage control systems of synchronous generators, with their limiters, as well as models of all shunt and series FACTS devices and specialized reactive power compensation devices such as STATCOM. Composite loads should be modelled using their dynamic equivalent models.

The simulation of voltage collapse due to phenomena inside the composite load (scenario 3) requires the employment of specialized computer programs in which the transmission system is modelled using dynamic equivalents but the distribution network is modelled in detail. In particular, the on-load tap-changing transformers and their regulators should be modelled and dynamic models should be used for groups of induction motors.

Examples of such models used for short- and mid-term dynamic simulation are described in Chapter 11. Computer algorithms are described in Chapter 13.

8.6 Prevention of Voltage Collapse

Voltage collapse is a dangerous disturbance which may lead to a system blackout. Preventing voltage instability requires action from personnel responsible for power system security at every stage:

- at the network planning stage;
- at the system operational planning stage;
- at the system operation monitoring and control stage.

During the network planning stage, reliability criteria must be satisfied for all possible contingencies of at least $N - 1$ type. It should be ensured that for each contingency:

- maximum allowable voltage drops are not exceeded;
- stability margins for real and reactive power are large enough for each composite load and load area.

Satisfying these criteria can be ensured by an appropriate expansion of the network in response to the demand growth and by installing appropriate reactive power compensation and voltage regulation devices in the system.

During operational planning and real-time monitoring and control, a desired voltage profile should be continuously maintained and appropriate reactive power compensation devices activated. An adequate reserve of real and reactive power should be maintained at the generators. Reserve is the amount of power by which generators in operation can be additionally loaded without exceeding the reactive power capability curve shown in Figure 3.19 and described in Section 3.3.4. For the prevention of voltage collapse, the reserve of reactive power is more important. Such a reserve provided by synchronous generators is necessary to cover quickly a reactive power deficit when voltage collapse symptoms are detected.

The power capability curve (Figure 3.19) and the voltage characteristic (Figure 3.22) of a generating unit clearly show that a unit can support the system with additional reactive power if, at a given

operating point, the reactive power output is within the area determined by the power capability curve (curve G–F–E in Figure 3.19) and the unit operates within the voltage regulation range (curve A–B in Figure 3.22) and with an adequate margin (point B in Figure 3.22).

Apart from satisfying the reliability criteria during the operational planning and real-time monitoring and control stages, each system should be equipped with additional defence facilities in order to prevent a voltage collapse following extreme disturbances. The most commonly used methods include the following:

1. Using emergency back-up reactive power reserve not used during normal operation.
2. Automatic fast start-up of back-up generation (hydro and gas turbines) when a growing power imbalance appears.
3. Emergency increase of reactive power produced by generators in the areas of depressed voltages at the expense of reduction of real power outputs, if there is a possibility of increased imports to make up the resulting real power imbalance. This may be explained as follows. Covering reactive power imbalance in a given area is most easily done locally. If local generators operate at the limit of their power capability curves then any additional reactive power can be obtained only by reducing their real power output (Figure 3.22). This results in a real power imbalance which can be covered by increased imports (if possible).
4. Reduction of power demand in a given area by reducing voltages at load buses using on-load tap-changing transformers. When reactive power imbalance appears in a given area and it is not possible to increase reactive power generation, then real power demand may be reduced by reducing voltages at load buses. This makes use of the characteristics of a typical composite load (Figure 3.32) which show that the reactive power demand reduces with reduced voltages. The method can be executed using an auxiliary control loop in the controller of the on-load tap-changing transformer that controls the primary (supply) and secondary (load) side voltage. Normally, if the primary voltage is higher than a threshold value, then when the secondary voltage is dropping, the regulator changes the taps in order to increase the load voltage. However, if there is a deficit of reactive power in the transmission network and the primary voltage of the transformer supplying a distribution network is smaller than a threshold value, then when the secondary voltage drops, the regulator should act in the opposite direction. It should reduce voltage at the load bus and therefore reduce power demand. This could be referred to as the *reverse action* of the on-load tap-changing regulator. Reverse action of the regulator is justified only if a reduction in the voltage is accompanied by a reduction in reactive power demand. For some consumers operating at reduced voltages (Figure 3.32a) a further reduction of voltages may cause an increase in reactive power demand. If that happens, the reverse action of the regulator must be blocked so that the situation does not deteriorate further.
5. With deep voltage sags, when the described prevention methods are not sufficient, customers can be disconnected when a threshold voltage value is reached. This is referred to as *undervoltage load shedding*. Threshold values should be chosen such that the shedding is activated only in extreme situations caused, for example, by $N - 2$ or $N - 3$ contingencies.

Choosing the threshold values for the reverse action of the on-load tap-changing regulator or undervoltage load shedding is a delicate matter. Those values can be determined based on offline voltage stability analyses. In practice, when actual operating conditions are different from the assumed ones, the calculated threshold values can be too optimistic, with a resulting voltage collapse, or too pessimistic, with resulting unnecessary voltage reductions or load shedding. These disadvantages of simple algorithms based on threshold values require further research on new methods of voltage control in the vicinity of voltage collapse.

Two different approaches can be identified here. The first one is based on improving decision methods based on local signals. One example is the application of a very sophisticated method based on Hopf bifurcation theory and the Lyapunov exponents and entropy of the system (i.e. the

a-eberle CPR-D Collapse Prediction Relay). The second approach uses measurements from a large area, using WAMS or WAMPAC systems (described in Chapter 2 and CIGRE Report No. 316) in order to take a decision.

8.7 Self-Excitation of a Generator Operating on a Capacitive Load

Voltage instability may also arise due to *self-excitation*, that is a spontaneous rise in the voltage. The phenomenon is connected with the parametric resonance of *RLC* circuits and may appear when a generator supplies a capacitive load.

8.7.1 Parametric Resonance in RLC Circuits

Figure 8.25 shows an *RLC* series circuit that has been connected to a voltage source for sufficient time to fully charge the capacitor. The power source is then disconnected instantaneously allowing the capacitor to discharge through resistance R and inductance L. The resulting current is periodic. Its amplitude depends on whether the inductance is constant or periodic. When inductance L is constant, the resulting current will be periodic (curve 1) and decays with time as the energy is transferred back and forth from the capacitor to the coil with some of the energy being dissipated in the resistance.

Now assume that during this process an external action is applied to the coil so as to produce a periodic change in its inductance. This could be achieved by changing the length of the air gap in the core. It will also be assumed that the inductance increases when the current reaches a maximum and decreases when the current crosses zero. As the magnetic energy stored in the inductance is $Li^2/2$, the effect of the external force is to increase the stored magnetic energy by an amount that is proportional to the increase in the inductance. This energy is not transferred back to the external force when the inductance is decreased because the decrease in inductance takes place at zero current when all the energy has already been transferred to the capacitor. This increase in the stored energy results in an increase in the current when the energy is transferred back to the coil in the next period (curve 2). If the changes in L are large, then the increase of the energy in the circuit may be greater than the energy lost in the resistance and the current increases every period (curve 2). This increase in the current produces a cyclic increase in the voltage across the capacitor. This phenomenon, known as *parametric resonance*, may also occur when the inductance of the coil is changed sinusoidally as in the self-excitation of the synchronous generator described below.

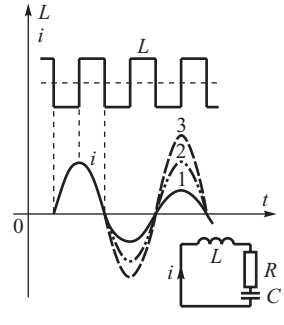

Figure 8.25 Current oscillations in *RLC* circuit depending on the changes in the inductance: (1) constant inductance; (2) small variations in the inductance; (3) large variations in the inductance.

8.7.2 *Self-Excitation of a Generator with Open-Circuited Field Winding*

Consider a salient-pole generator, shown in Figure 8.26, with open-circuited field winding and loaded by an *RC* series circuit. The arrangement is rather unusual for a synchronous generator but it will help to understand self-excitation.

For the salient-pole generator the air gap seen by the armature winding changes periodically (Figure 8.26a) so that the reactance of the generator fluctuates between X_d and X_q. The phasor diagram is shown in Figure 8.26b. If the generator has an open-circuited field winding then its synchronous electromotive force is very small, $E_q \cong 0$, and is due to the remnant magnetism. Hence the generator current is initially very small because it is driven by a small emf induced by remnant magnetism. Generator voltage V is delayed with respect to the current by angle φ and with respect to the q-axis by angle $\delta = \varphi - \beta$. Hence the real power can be expressed by

$$\begin{aligned} P &= VI\cos\varphi = VI\cos(\delta + \beta) \\ &= VI\cos\delta\cos\beta - VI\sin\delta\sin\beta = VI_q\cos\delta - VI_d\sin\delta. \end{aligned} \tag{8.56}$$

Inspection of the phasor diagram shown in Figure 8.26b yields

$$I_q X_q = V\sin\delta, \quad E_q + I_d X_d = V\cos\delta. \tag{8.57}$$

Now Equation (8.56) can be transformed to

$$P = \frac{E_q V}{X_d}\sin\delta + \frac{V^2}{2}\frac{X_d - X_q}{X_d X_q}\sin 2\delta. \tag{8.58}$$

This equation is analogous to Equation (3.126) derived in Section 3.3.6. Real power consists of two components, namely the synchronous power and the reluctance power. The former is due to the interaction between the stator and rotor magnetic fields, while the latter is due to magnetic asymmetry of the rotor and may be developed without any field excitation. In the considered case of the generator with open-circuited field winding, that is for $E_q \cong 0$, the synchronous power can

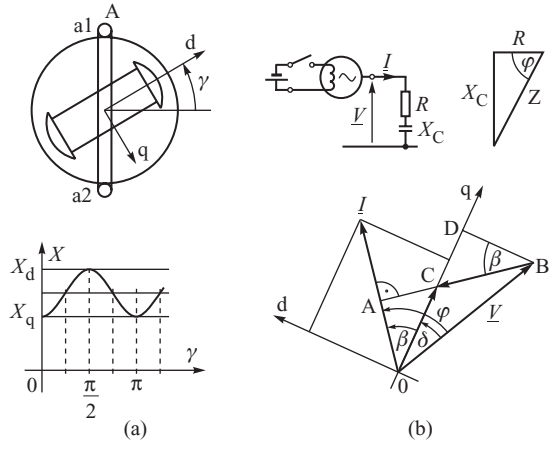

Figure 8.26 Salient-pole generator supplying a capacitive load: (a) periodic changes of the synchronous reactance; (b) block diagram and phasor diagram. For a generator with open-circuited field winding $\overline{OC} = E_q \cong 0$.

be neglected and (8.58) simplifies to

$$P \cong \frac{V^2}{2} \frac{X_\mathrm{d} - X_\mathrm{q}}{X_\mathrm{d} X_\mathrm{q}} \sin 2\delta, \tag{8.59}$$

which corresponds to the reluctance power only.

When the generator is loaded as in Figure 8.26, it may happen that real power $I^2 R$ consumed by the resistor R is smaller than the generated reluctance power so that a surplus of energy is created which causes the generator current to increase. This happens when

$$\frac{V^2}{2} \frac{X_\mathrm{d} - X_\mathrm{q}}{X_\mathrm{d} X_\mathrm{q}} \sin 2\delta > I^2 R, \tag{8.60}$$

or

$$\frac{V^2}{I^2} \frac{X_\mathrm{d} - X_\mathrm{q}}{X_\mathrm{d} X_\mathrm{q}} \sin\delta \cos\delta > R. \tag{8.61}$$

In the case considered $E_\mathrm{q} \cong 0$ so that applying (8.57) gives $\sin\delta = I_\mathrm{q} X_\mathrm{q} / V$ and $\cos\delta \cong I_\mathrm{d} X_\mathrm{d} / V$. Substituting these equations into (8.61) gives

$$(X_\mathrm{d} - X_\mathrm{q}) \frac{I_\mathrm{d}}{I} \frac{I_\mathrm{q}}{I} > R, \tag{8.62}$$

where $I_\mathrm{d} = I \sin\beta$ and $I_\mathrm{q} = I \cos\beta$. Consequently one gets

$$(X_\mathrm{d} - X_\mathrm{q}) \sin\beta \cos\beta > R. \tag{8.63}$$

Angle β of the current phase shift can be determined using the phasor diagram:

$$\tan\beta = \frac{\overline{\mathrm{AC}}}{\overline{\mathrm{OA}}} = \frac{\overline{\mathrm{AB}} - \overline{\mathrm{BC}}}{\overline{\mathrm{OA}}} = \frac{V \sin\varphi - I X_\mathrm{q}}{V \cos\varphi} = \frac{\frac{V}{I} \sin\varphi - X_\mathrm{q}}{\frac{V}{I} \cos\varphi} = \frac{Z \sin\varphi - X_\mathrm{q}}{Z \cos\varphi}. \tag{8.64}$$

The impedance triangle in Figure 8.26 gives $Z \sin\varphi = X_\mathrm{C}$ and $Z \cos\varphi = R$. Now Equation (8.64) yields

$$\tan\beta = \frac{X_\mathrm{C} - X_\mathrm{q}}{R}. \tag{8.65}$$

Noting that $\sin\beta \cos\beta = \tan\beta / (\tan^2\beta + 1)$, and substituting from the above equation for $\tan\beta$ into (8.63), gives the condition for self-excitation:

$$(X_\mathrm{C} - X_\mathrm{q})(X_\mathrm{C} - X_\mathrm{d}) + R^2 < 0. \tag{8.66}$$

This inequality is satisfied for all the points inside the circle in the impedance plane shown in Figure 8.27. Self-excitation arises for all the parameters inside that circle.

Physically self-excitation can be explained by recognizing that the self-inductance of each phase of the stator winding changes sinusoidally, due to the variable air-gap width, as the rotor rotates. These periodic changes produce parametric resonance, and the resulting increase in the current. If R and X_C are constant, self-excitation also results in an increase in the generator terminal voltage. Outside the circle shown in Figure 8.27, the energy supplied by the generator is too small to overcome the resistance loss and self-excitation cannot happen.

If the generator had a linear magnetization characteristic, then self-excitation would lead to an unlimited increase in the current and the terminal voltage of the generator. In reality both

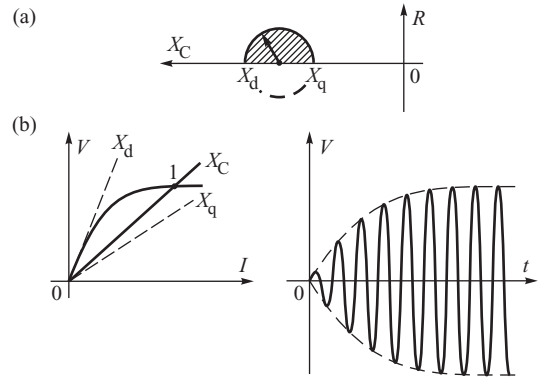

Figure 8.27 Synchronous self-excitation: (a) condition for self-excitation; (b) magnetization characteristic and voltage changes.

reactances X_d and X_q decrease as the current increases. Figure 8.27b shows four characteristics. The bold curve shows the generator voltage–current characteristic with saturation included. The dashed lines X_d and X_q show the idealized characteristics when the generator opposes the current with unsaturated reactances X_d and X_q, respectively. Line X_C corresponds to the capacitor voltage–current characteristic. As X_C is between X_d and X_q, condition (8.66) is satisfied and self-excitation occurs. However, as the voltage and the current increase, the armature saturates and both X_d and X_q start to decrease. The voltage rise stops at point 1 where the saturated reactance becomes equal to X_C. Beyond point 1 the reactance X_C is greater than the saturated reactance X_d and condition (8.66) is not satisfied. Any momentary increase of the voltage above this point results in the resistance loss exceeding the reluctance power, then the current drops and the system returns to point 1. As a result the generator voltage settles down to a level corresponding to point 1.

As the angle β between the current and q-axis (Figure 8.26) remains constant, self-excitation is referred to the as *synchronous self-excitation*. In practice, synchronous self-excitation is rare but may arise when a salient-pole generator, operating with a small field current, is connected to a lightly loaded long transmission line. In such a situation the terminal voltage will increase but at a slower rate than that shown in Figure 8.27.

8.7.3 Self-Excitation of a Generator with Closed Field Winding

Self-excitation can also occur when the excitation circuit is closed, but will be different in character to the synchronous self-excitation described above. If the resistance of the field winding is neglected, the field winding may be treated as a perfect magnetic screen and any change in the armature current will induce an additional field current which completely compensates the change in the armature flux linking with the rotor. This corresponds to the transient state of operation in which the generator opposes the armature current with transient reactance X'_d (see Chapter 4). There is no q-axis in the field winding so that $X'_q \neq X'_d$. This is referred to as the transient saliency (see Table 4.2 and 4.3). Real power generated per phase may be expressed by an equation similar to (8.59) as

$$P' = \frac{V^2}{2} \frac{X'_q - X'_d}{X'_d X'_q} \sin 2\delta, \tag{8.67}$$

and is referred to as the *dynamic reluctance power*. As before, parametric resonance will only occur if the dynamic reluctance power is greater than the real power I^2R consumed by the resistor R.

Similarly, as in Equations (8.60) and (8.66), the condition for dynamic self-excitation is satisfied when

$$(X_C - X'_q)(X_C - X'_d) + R^2 < 0. \tag{8.68}$$

The condition (8.68) is satisfied inside a circle based on X'_d and X'_q as shown in Figure 8.28. If magnetic saturation is neglected, then both the stator current and the field current, which opposes the changes in the stator field, will increase to infinity, as energy is continuously supplied in every cycle by the dynamic reluctance torque. Magnetic saturation limits the current increase but in a different way than when the excitation circuit was open.

Initially the relative position of the phasors is as shown in Figure 8.28a and the dynamic reluctance power causes a rapid increase in the armature current. This, according to the law of constant flux linkage, is accompanied by an increase in the field current, segment OA in Figure 8.28b. As the rotor iron saturates, the emf induced in the closed field winding decreases until the field current experiences no further increase. The resistance of the closed field circuit now plays a deciding role as the magnetic energy stored in the field winding starts to dissipate. This causes the field current to decay and allows the armature flux to enter the rotor iron resulting in an increase in the d-axis reactance. As a result the dynamic reluctance power decreases producing a corresponding decrease in the armature current – segment AB in Figure 8.28b. At the same time the stator field begins to slip behind the rotor field as the angle β changes, with the result that the machine operates as an induction generator with its armature current sustained by the asynchronous induction power. This continues until the resulting generator flux reaches a small shift with respect to the d-axis. The conditions sustaining the asynchronous operation now cease to exist and the armature current quickly vanishes – segment CO in Figure 8.28b. The whole cycle then repeats itself as denoted by letters O′A′B′C′O in Figure 8.28b. The described resonance is referred to as the *repulsive self-excitation* or *asynchronous self-excitation*.

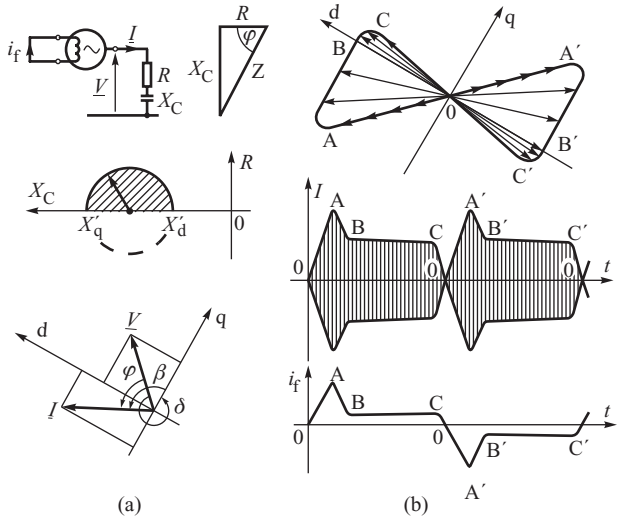

Figure 8.28 Repulsive self-excitation: (a) circuit diagram, area of self-excitation, phasor diagram; (b) changes in the phasor of the armature current, the envelope of the armature current, the field current.

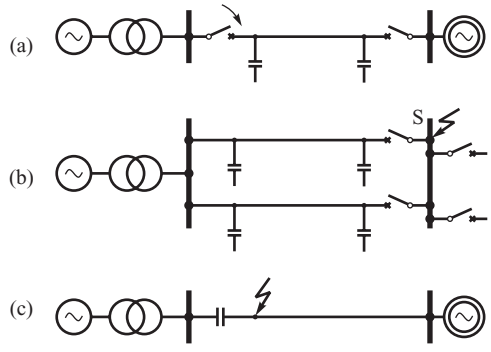

Figure 8.29 Possible cases of self-excitation: (a) connecting a generator to a no-load line; (b) a fault at a neighbouring substation; (c) a close fault in a line with series capacitive compensation.

8.7.4 Practical Possibility of Self-Excitation

From a technical point of view, the possibility of a generator meeting the conditions for either synchronous or asynchronous self-excitation is limited. Three possible situations are shown in Figure 8.29.

Figure 8.29a depicts a case when a disconnected long transmission line is first connected to the generating plant. This situation is similar to that shown in Figure 8.26 and may lead to synchronous self-excitation. To prevent this, a transmission line should be connected first to the rest of the network before connecting the generating plant.

Figure 8.29b shows a situation which may occur after a short circuit in a neighbouring substation. The fault on the substation busbars is cleared by opening the circuit-breakers so that the generator operates onto open-circuited lines. The sudden drop in real power load on the generator results in an increase in the angular speed and frequency of the generator. This increase in frequency produces a corresponding increase in the inductive reactances and a drop in the capacitive reactances. With such reactance changes the likelihood of the condition for self-excitation being met is increased.

Figure 8.29c shows the case of a nearby short circuit in a line with series capacitive compensation. A closed circuit is formed which has a high capacitance and a low reactance. This situation may also lead to subsynchronous resonance as described in Section 6.7.3 and in Anderson, Agrawal and Van Ness (1990).

9

Frequency Stability and Control

Previous chapters have described how the generators in a power system respond when there is a momentary disturbance in the power balance between the electrical power consumed in the system and the mechanical power delivered by the turbines. Such disturbances are caused by short circuits in the transmission network and are normally cleared without the need to reduce the generated or consumed power. However, if a large load is suddenly connected (or disconnected) to the system, or if a generating unit is suddenly disconnected by the protection equipment, there will be a long-term distortion in the power balance between that delivered by the turbines and that consumed by the loads. This imbalance is initially covered from the kinetic energy of rotating rotors of turbines, generators and motors and, as a result, the frequency in the system will change. This frequency change can be conveniently divided into a number of stages allowing the dynamics associated with each of these stages to be described separately. This helps illustrate how the different dynamics develop in the system. However, it is first necessary to describe the operation of the automatic generation control (AGC) as this is fundamental in determining the way in which the frequency will change in response to a change in load.

The general framework of frequency control described in this chapter was originally developed under the framework of traditional vertically integrated utilities which used to control generation, transmission and often distribution in their own service areas and where power interchanges between control areas were scheduled in advance and strictly adhered to. Chapter 2 described liberalization of the industry taking place in many countries in the world since the 1990s whereby utilities are no longer vertically integrated generation companies that compete against each other and the coordination necessary for reliable system operation, including frequency control, is undertaken by Transmission System Operators (TSOs). The framework of frequency control had to be adapted to the market environment in the sense that TSOs have to procure, and pay for, frequency support from individual power plants. The way those services are procured differs from country to country so the commercial arrangements will not be discussed in this book. However, the overall hierarchical control framework has been largely retained, with only some changes in the tertiary control level, as discussed later in this chapter.

The discussion will concentrate on frequency control in an interconnected power system, using the European UCTE as the example. It is worth adding that the framework of frequency control in an islanded system, such as in the United Kingdom, may be different. Also, the meaning of some of the terms may differ from country to country.

Power System Dynamics: Stability and Control, Second Edition Jan Machowski, Janusz W. Bialek and James R. Bumby
© 2008 John Wiley & Sons, Ltd

9.1 Automatic Generation Control

Section 2.1 explained how an electrical power system consists of many generating units and many loads while its total power demand varies continuously throughout the day in a more or less anticipated manner. The large, slow changes in demand are met centrally by deciding at regular intervals which generating units will be operating, shut down or in an intermediate hot reserve state. This process of *unit commitment* may be conducted once per day to give the daily operating schedule, while at shorter intervals, typically every 30 min, *economic dispatch* determines the actual power output required from each of the committed generators. Smaller, but faster, load changes are dealt with by AGC so as to:

- maintain frequency at the scheduled value (frequency control);
- maintain the net power interchanges with neighbouring control areas at their scheduled values (tie-line control);
- maintain power allocation among the units in accordance with area dispatching needs (energy market, security or emergency).

In some systems the role of AGC may be restricted to one or two of the above objectives. For example, tie-line power control is only used where a number of separate power systems are interconnected and operate under mutually beneficial contractual agreements.

9.1.1 Generation Characteristic

Section 2.2.3 discussed the operation of turbines and their governing systems. In the steady state the idealized power–speed characteristic of a single generating unit is given by Equation (2.3). As the rotational speed is proportional to frequency, Equation (2.3) may be rewritten for the ith generating unit as

$$\frac{\Delta f}{f_{\mathrm{n}}} = -\rho_i \frac{\Delta P_{\mathrm{m}i}}{P_{\mathrm{n}i}}, \quad \frac{\Delta P_{\mathrm{m}i}}{P_{\mathrm{n}i}} = -K_i \frac{\Delta f}{f_{\mathrm{n}}}. \tag{9.1}$$

In the steady state all the generating units operate synchronously at the same frequency when the overall change in the total power ΔP_{T} generated in the system can be calculated as the sum of changes at all generators:

$$\Delta P_{\mathrm{T}} = \sum_{i=1}^{N_{\mathrm{G}}} \Delta P_{\mathrm{m}i} = -\frac{\Delta f}{f_{\mathrm{n}}} \sum_{i=1}^{N_{\mathrm{G}}} K_i P_{\mathrm{n}i} = -\Delta f \sum_{i=1}^{N_{\mathrm{G}}} \frac{K_i P_{\mathrm{n}i}}{f_{\mathrm{n}}}, \tag{9.2}$$

where N_{G} is the number of generating units in the system. The subscript 'T' indicates that ΔP_{T} is the change in generated power as supplied by the turbines. Figure 9.1 illustrates how the characteristics of individual generating units can be added according to Equation (9.2) to obtain the equivalent

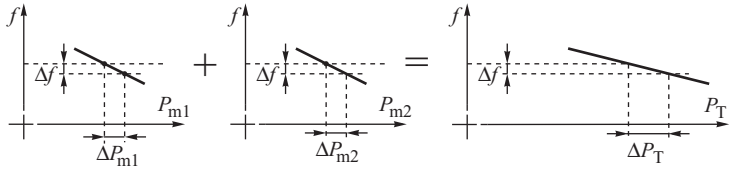

Figure 9.1 Generation characteristic as the sum of the speed–droop characteristics of all the generation units.

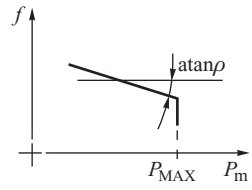

Figure 9.2 Speed–droop characteristic of a turbine with an upper limit.

generation characteristic. This characteristic defines the ability of the system to compensate for a power imbalance at the cost of a deviation in frequency. For a power system with a large number of generating units, the generation characteristic is almost horizontal such that even a relatively large power change only results in a very small frequency deviation. This is one of the benefits accruing from combining generating units into one large system.

To obtain the equivalent generation characteristic of Figure 9.1 it has been assumed that the speed–droop characteristics of the individual turbine generator units are linear over the full range of power and frequency variations. In practice the output power of each turbine is limited by its technical parameters. For example, coal-burn steam turbines have a lower power limit due to the need to maintain operational stability of the burners and an upper power limit that is set by thermal and mechanical considerations. In the remainder of this section only the upper limit will be considered, so the turbine characteristic will be as shown in Figure 9.2.

If a turbine is operating at its upper power limit then a decrease in the system frequency will not produce a corresponding increase in its power output. At the limit $\rho = \infty$ or $K = 0$ and the turbine does not contribute to the equivalent system characteristic. Consequently the generation characteristic of the system will be dependent on the number of units operating away from their limit at part load; that is, it will depend on the *spinning reserve*, where the spinning reserve is the difference between the sum of the power ratings of all the operating units and their actual load. The allocation of spinning reserve is an important factor in power system operation as it determines the shape of the generation characteristic. This is demonstrated in Figure 9.3 which shows a simple case of two generating units. In Figure 9.3a the spinning reserve is allocated proportionally to both units so that they both reach their upper power limits at the same frequency f_1. In this case the equivalent characteristic, obtained from Equation (9.2), is linear until the upper power limit for the whole system is reached. In Figure 9.3b the same amount of spinning reserve is available but is allocated solely to the second generator with the first unit operating at full load. The generation characteristic is now nonlinear and consists of two sections of different slope.

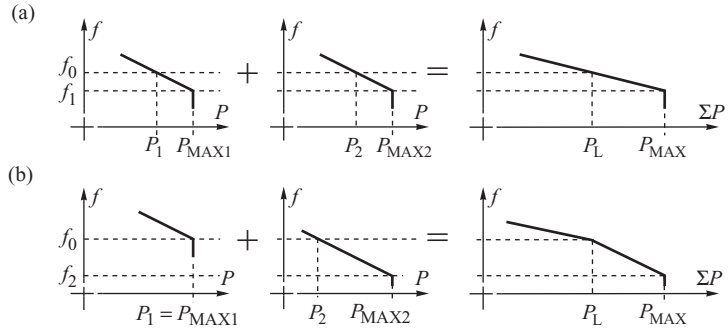

Figure 9.3 Influence of the turbine upper power limit and the spinning reserve allocation on the generation characteristic.

Similarly, the generation characteristic of an actual power system is nonlinear and consists of many short sections of increasing slope as more and more generating units reach their operating limits as the total load increases until, at maximum system load, there is no more spinning reserve available. The generation characteristic then becomes a vertical line. For small power and frequency disturbances it is convenient to approximate this nonlinear generation characteristic in the vicinity of the operation point by a linear characteristic with a local droop value. The total system generation is equal to the total system load P_{L} (including transmission losses)

$$\sum_{i=1}^{N_{\mathrm{G}}} P_{\mathrm{m}i} = P_{\mathrm{L}}, \tag{9.3}$$

where N_{G} is the number of generating units. Dividing Equation (9.2) by P_{L} gives

$$\frac{\Delta P_{\mathrm{T}}}{P_{\mathrm{L}}} = -K_{\mathrm{T}} \frac{\Delta f}{f_{\mathrm{n}}} \quad \text{or} \quad \frac{\Delta f}{f_{\mathrm{n}}} = -\rho_{\mathrm{T}} \frac{\Delta P_{\mathrm{T}}}{P_{\mathrm{L}}}, \tag{9.4}$$

where

$$K_{\mathrm{T}} = \frac{\sum_{i=1}^{N_{\mathrm{G}}} K_i P_{\mathrm{n}i}}{P_{\mathrm{L}}}, \quad \rho_{\mathrm{T}} = \frac{1}{K_{\mathrm{T}}}. \tag{9.5}$$

Equation (9.4) describes the linear approximation of the generation characteristic calculated for a given total system demand. Consequently, the coefficients in Equation (9.5) are calculated with respect to the total demand, not the sum of the power ratings, so that ρ_{T} is the local speed droop of the generation characteristic and depends on the spinning reserve and its allocation in the system as shown in Figure 9.3.

In the first case, shown in Figure 9.3a, it was assumed that the spinning reserve is allocated uniformly between both generators, that is both generators are underloaded by the same amount at the operating point (frequency f_0) and the maximum power of both generators is reached at the same point (frequency f_1). The sum of both characteristics is then a straight line up to the maximum power $P_{\mathrm{MAX}} = P_{\mathrm{MAX}1} + P_{\mathrm{MAX}2}$. In the second case, shown in Figure 9.3b, the total system reserve is the same but it is allocated to the second generator only. That generator is loaded up to its maximum at the operating point (frequency f_2). The resulting total generation characteristic is nonlinear and consists of two lines of different slope. The first line is formed by adding both inverse droops, $K_{\mathrm{T}1} \neq 0$ and $K_{\mathrm{T}2} \neq 0$, in Equation (9.5). The second line is formed noting that the first generator operates at maximum load and $K_{\mathrm{T}1} = 0$ so that only $K_{\mathrm{T}2} \neq 0$ appears in the sum in Equation (9.5). Hence the slope of that characteristic is higher.

The number of units operating in a real system is large. Some of them are loaded to the maximum but others are partly loaded, generally in a non-uniform way, to maintain a spinning reserve. Adding up all the individual characteristics would give a nonlinear resulting characteristic consisting of short segments with increasingly steeper slopes. That characteristic can be approximated by a curve shown in Figure 9.4. The higher the system load, the higher the droop until it becomes infinite $\rho_{\mathrm{T}} = \infty$, and its inverse $K_{\mathrm{T}} = 0$, when the maximum power P_{MAX} is reached. If the dependence of a power station's auxiliary requirements on frequency were neglected, that part of the characteristic would be vertical (shown as a dashed line in Figure 9.4). However, power stations tends to have a curled-back characteristic – see curve 4 in Figure 2.13. Similarly curled is the system characteristic shown in Figure 9.4.

For further considerations, the nonlinear generation characteristic shown in Figure 9.4 will be linearized at a given operating point, that is the linear approximation (9.4) will be assumed with the droop ρ_{T} given by (9.5).

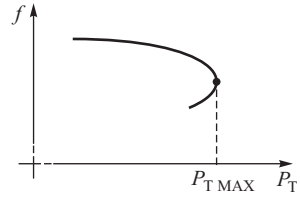

Figure 9.4 Static system generation characteristic.

9.1.2 Primary Control

When the total generation is equal to the total system demand (including losses) then the frequency is constant, the system is in equilibrium, and the generation characteristic is approximated by Equation (9.4). However, as discussed in Section 3.5, system loads are also frequency dependent and an expression similar to Equation (9.4) can be used to obtain a linear approximation of the frequency response characteristic of the total system load as

$$\frac{\Delta P_L}{P_L} = K_L \frac{\Delta f}{f_n}, \tag{9.6}$$

where K_L is the *frequency sensitivity coefficient of the power demand*. A similar coefficient k_{Pf} was defined in Equation (3.133) and referred to as the frequency sensitivity of a single composite load and should not be confused with K_L above, which relates to the total system demand. Tests conducted on actual systems indicate that the generation response characteristic is much more frequency dependent than the demand response characteristic. Typically K_L is between 0.5 and 3 (see Table 3.3) while $K_T \approx 20$ ($\rho = 0.05$). In Equations (9.4) and (9.6) the coefficients K_T and K_L have opposite sign so that an increase in frequency corresponds to a drop in generation and an increase in electrical load.

In the (P, f) plane the intersection of the generation and the load characteristic, Equations (9.4) and (9.6), defines the system equilibrium point. A change in the total power demand ΔP_L corresponds to a shift of the load characteristic in the way shown in Figure 9.5 so that the equilibrium point is moved from point 1 to point 2. The increase in the system load is compensated in two ways: firstly, by the turbines increasing the generation by ΔP_T; and secondly, by the system loads reducing the demand by ΔP_L from that required at point 3 to that required at point 2. Figure 9.5 shows that taking both increments into account gives

$$\Delta P_{demand} = \Delta P_T - \Delta P_L = -(K_T + K_L) P_L \frac{\Delta f}{f_n} = -K_f P_L \frac{\Delta f}{f_n}. \tag{9.7}$$

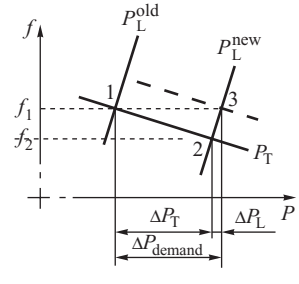

Figure 9.5 Equilibrium points for an increase in the power demand.

The new operating point of the system corresponds to a new demand and a new frequency. The new value of the system frequency f_2 is lower than the old one f_1. Equation (9.7) represents the frequency response of the system while the coefficient $K_f = K_T + K_L$ is referred to as the *stiffness*. It should be emphasized that $\Delta P_T \gg \Delta P_L$.

A reduction of the demand by ΔP_L is due to the frequency sensitivity of demand. An increase of generation by ΔP_T is due to turbine governors. The action of turbine governors due to frequency changes when reference values of regulators are kept constant is referred to as *primary frequency control*.

When the system demand increases, primary control is activated, obviously only if there are any units which are operating but are not fully loaded. Figure 9.3b shows that if any of the units operate at maximum output, a reduction in frequency cannot increase a unit's output. Only those units that are partly loaded and carry a spinning reserve can be loaded more.

In order to secure safe system operation and a possibility of activating the primary control, the system operator must have an adequate spinning reserve at its disposal. Spinning reserve to be utilized by the primary control should be uniformly distributed around the system, that is at power stations evenly located around the system. Then the reserve will come from a variety of locations and the risk of overloading some transmission corridors will be minimized. Locating the spinning reserve in one region may be dangerous from the point of view of security of the transmission network. If one or more power stations suffer outages, the missing power would come from just one region, some transmission corridors might get overloaded and the disturbance might spread.

An interconnected system requires coordination so the requirements regarding the primary control are normally the subject of agreements between partners cooperating in a given interconnected network. For the European UCTE system, the requirements are defined in document 'UCTE – Ground Rules – Supervision of the application of rules concerning primary and secondary control of frequency and active power in UCTE'.

For the purposes of primary frequency control, each subsystem in the UCTE system has to ensure a large enough spinning reserve proportional to a given subsystem's share in the overall UCTE energy production. This is referred to as the *solidarity principle*. It is required that the spinning reserve is uniformly located within each subsystem and the operating points of individual units providing the reserve are such that the whole reserve in the system is activated when the frequency deviation is not more than 200 mHz. The required time of activation of the reserve

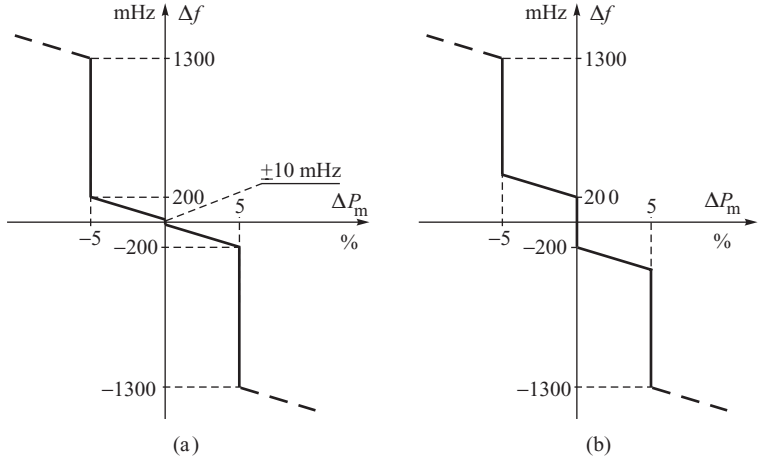

Figure 9.6 Example of speed – droop characteristics: (a) with small dead zones; (b) with large dead zones.

should not be longer than 15–23 s. To satisfy this condition, the units participating in the primary reserve should be able to regulate power quickly within ±5 % of their rated power. Turbine governors of those units have typically speed–droop characteristics with dead zones as in Figure 9.6a. The first dead zone has the width ±10 mHz which makes the unit operate with constant set power P_{ref} in the presence of small frequency error $|\Delta f| < 10$ mHz . When a frequency error $|\Delta f| > 10$ mHz appears, the unit operates in the primary control with a fast regulation range ±5 %. The whole range of the reserve is released when the frequency error is about ±200 mHz. These requirements mean the whole primary reserve is released in the system when the frequency error is not greater than 200 mHz. The droop can be calculated in the fast regulation range from (9.1). Substituting $\Delta f = (200 - 10)$ mHz $= 190$ mHz $= 0.190$ Hz , that is $\Delta f / f_{\text{n}} = 0.190/50 = 0.0038$ and $\Delta P_{\text{m}} / P_{\text{n}} = -0.05$, results in $\rho = 0.0038/0.05 = 0.076 = 7.6\ \%$. This is a typical value as, according to Section 2.2.3, the droop ρ is typically assumed to be between 4 and 9 %. For the range beyond fast regulation ±5 % the turbine governor maintains constant power until the frequency error reaches $|\Delta f| > 1300$ mHz $= 1.3$ Hz when the governor is switched from the power control regime to speed control.

Governors of units that do not participate in the primary frequency control have the first dead zone of the speed – droop characteristic set at ±200 mHz (Figure 9.6b). They form an additional primary reserve that activates only for large disturbances. This is necessary to defend the system against blackouts (details in Section 9.1.6).

9.1.3 Secondary Control

If the turbine–generators are equipped with governing systems, such as those described in Section 2.2.3, then, following a change in the total power demand, the system will not be able to return to the initial frequency on its own, without any additional action. According to Figure 9.5, in order to return to the initial frequency the generation characteristic must be shifted to the position shown by the dashed line. Such a shift can be enforced by changing the P_{ref} setting in the turbine governing system (the load reference set point in Figure 2.14). As shown in Figure 9.7, changes in the settings $P_{\text{ref(1)}}$, $P_{\text{ref(2)}}$ and $P_{\text{ref(3)}}$ enforce a corresponding shift of the characteristic to the positions $P_{\text{m(1)}}$, $P_{\text{m(2)}}$ and $P_{\text{m(3)}}$. To simplify, the first dead zone around P_{ref}, which was shown in Figure 9.6, has been neglected in Figure 9.7. Obviously no change of settings can force a turbine to exceed its maximum power rating P_{MAX}. Changing more settings P_{ref} of individual governors will move upwards the overall generation characteristic of the system. Eventually this will lead to the restoration of the rated frequency but now at the required increased value of power demand. Such control action on the governing systems of individual turbines is referred to as *secondary control*.

In an isolated power system, automatic secondary control may be implemented as a decentralized control function by adding a supplementary control loop to the turbine–governor system. This modifies the block diagram of the turbine governor, Figure 2.14, to that shown in Figure 9.8 where P_{ref} and P_{m} are expressed as a fraction of the rated power P_{n}. The supplementary control loop,

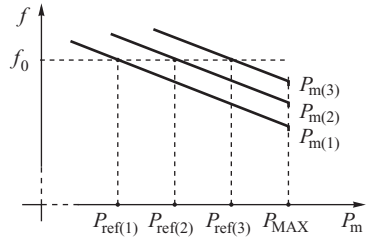

Figure 9.7 Turbine speed–droop characteristics for various settings of P_{ref}.

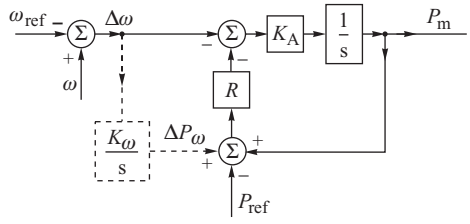

Figure 9.8 Supplementary control added to the turbine governing system.

shown by the dashed line, consists of an integrating element which adds a control signal ΔP_ω that is proportional to the integral of the speed (or frequency) error to the load reference point. This signal modifies the value of the setting in the P_{ref} circuit thereby shifting the speed–droop characteristic in the way shown in Figure 9.7.

Not all the generating units in a system that implements decentralized control need be equipped with supplementary loops and participate in secondary control. Usually medium-sized units are used for frequency regulation while large base load units are independent and set to operate at a prescribed generation level. In combined cycle gas and steam turbine power plants the supplementary control may affect only the gas turbine or both the steam and the gas turbines.

In an interconnected power system consisting of a number of different control areas, secondary control cannot be decentralized because the supplementary control loops have no information as to where the power imbalance occurs so that a change in the power demand in one area would result in regulator action in all the other areas. Such decentralized control action would cause undesirable changes in the power flows in the tie-lines linking the systems and the consequent violation of the contracts between the cooperating systems. To avoid this, centralized secondary control is used.

In interconnected power systems, AGC is implemented in such a way that each area, or subsystem, has its own central regulator. As shown in Figure 9.9, the power system is in equilibrium if, for each area, the total power generation P_T, the total power demand P_L and the net tie-line interchange power P_{tie} satisfy the condition

$$P_T - (P_L + P_{tie}) = 0. \tag{9.8}$$

The objective of each area regulator is to maintain frequency at the scheduled level (frequency control) and to maintain net tie-line interchanges from the given area at the scheduled values (tie-line control). If there is a large power balance disturbance in one subsystem (caused for example by the tripping of a generating unit), then regulators in each area should try to restore the frequency and net tie-line interchanges. This is achieved when the regulator in the area where the imbalance originated enforces an increase in generation equal to the power deficit. In other words, each area regulator should enforce an increased generation covering its own area power imbalance and maintain planned net tie-line interchanges. This is referred to as the *non-intervention rule*.

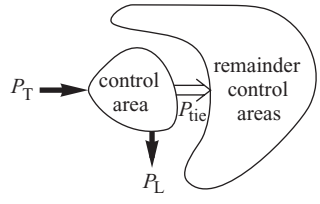

Figure 9.9 Power balance of a control area.

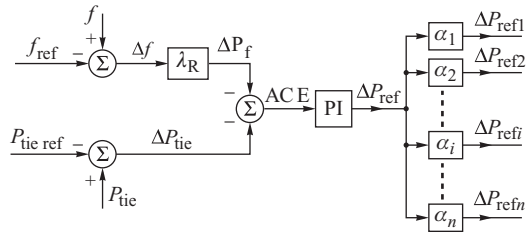

Figure 9.10 Functional diagram of a central regulator.

The regulation is executed by changing the power output of turbines in the area through varying P_{ref} in their governing systems. Figure 9.10 shows a functional diagram of the central regulator. Frequency is measured in the local low-voltage network and compared with the reference frequency to produce a signal that is proportional to the frequency deviation Δf. The information on power flows in the tie-lines is sent via telecommunication lines to the central regulator which compares it with the reference value in order to produce a signal proportional to the tie-line interchange error ΔP_{tie}. Before adding these two signals together, the frequency deviation is amplified by the factor λ_{R}, called the *frequency bias factor*, to obtain

$$\Delta P_{\text{f}} = \lambda_{\text{R}} \Delta f. \tag{9.9}$$

This represents a change in the generation power which must be forced upon the controlled area in order to compensate for the frequency deviation resulting from the power imbalance in this area.

The choice of the bias factor λ_{R} plays an important role in the non-intervention rule. According to this rule, each subsystem should cover its own power imbalance and try to maintain planned power interchanges. If the frequency drops following a generation deficit, then applying (9.7) gives $\Delta P_{\text{demand}} = -(K_{\text{f}} P_{\text{L}}/f_{\text{n}})\,\Delta f$. The central regulator should enforce an increased generation $\Delta P_{\text{f}} = \lambda_{\text{R}} \Delta f$ covering the deficit, that is $\Delta P_{\text{f}} = -\Delta P_{\text{demand}}$. Hence $\lambda_{\text{R}} \Delta f = (K_{\text{f}} P_{\text{L}}/f_{\text{n}})\,\Delta f$ or

$$\lambda_{\text{R}} = \frac{K_{\text{f}} P_{\text{L}}}{f_{\text{n}}} = K_{\text{f MW/Hz}}. \tag{9.10}$$

This equation indicates that the value of the bias λ_{R} can be assessed providing that the stiffness K_{f} of a given area and its total demand are known. $K_{\text{f MW/Hz}}$ denotes the frequency stiffness of the power system expressed in MW/Hz.

Clearly the non-intervention rule requires that the value of the bias set in the central regulator is equal to the area stiffness expressed in MW/Hz. In practice it is difficult to evaluate the exact value of the stiffness so that imprecise setting of the bias λ_{R} in the central regulator may have some undesirable effects on the regulation process. This will be discussed later in this chapter.

The signal ΔP_{f} is added to the net tie-line interchange error ΔP_{tie} so that the *area control error* (ACE) is created:

$$\text{ACE} = -\Delta P_{\text{tie}} - \lambda_{\text{R}} \Delta f. \tag{9.11}$$

Similarly, as in the decentralized regulator shown in Figure 9.8, the central regulator must have an integrating element in order to remove any error and this may be supplemented by a proportional element. For such a PI regulator the output signal is

$$\Delta P_{\text{ref}} = \beta_{\text{R}}(\text{ACE}) + \frac{1}{T_{\text{R}}} \int_0^t (\text{ACE})\,\text{d}t, \tag{9.12}$$

where β_R and T_R are the regulator parameters. Usually a regulator with a small, or even zero, participation of the proportional element is used, that is an integral element.

ACE corresponds to the power by which the total area power generation must be changed in order to maintain both the frequency and the tie-line flows at their scheduled values. The regulator output signal ΔP_{ref} is then multiplied by the *participation factors* $\alpha_1, \alpha_2, \ldots, \alpha_n$ which define the contribution of the individual generating units to the total generation control, Figure 9.10. The control signals $\Delta P_{ref1}, \Delta P_{ref2}, \ldots, \Delta P_{refn}$ obtained in this way are then transmitted to the power plants and delivered to the reference set points of the turbine governing systems (Figure 2.11). As with decentralized control, not all generating units need participate in generation control.

It is worth noting that regulation based on ACE defined by (9.11) does not always finish with the removal of both errors Δf and ΔP_{tie}. According to (9.11), zeroing of ACE can be generally achieved in two ways:

1. Zeroing of both errors, that is achieving $\Delta P_{tie} = 0$ and $\Delta f = 0$. This is a more desirable outcome. When the available regulation power in a given subsystem is large enough to cover its own power deficit, then the non-intervention rule enforces a return of the interchange power to a reference value and both frequency and power interchange errors are removed.
2. Achieving a compromise between the errors $\Delta P_{tie} + \lambda_R \Delta f = 0$ or $\Delta P_{tie} = -\lambda_R \Delta f$. When all the available regulation power in a given subsystem is not large enough to cover its own power imbalance, then the regulating units in that subsystem exhaust their capability before the errors are removed and the regulation ends with the violation of a reference value of power interchange. The missing power must be delivered from neighbouring networks. In that case the non-intervention rule will be violated and the following errors arise: $\Delta P_{tie\infty} = -\lambda_R \Delta f_\infty$, where $\Delta P_{W\infty}$ is power which the subsystem must additionally import to cover the power deficit.

Both cases will be illustrated in Section 9.2 using the results of computer simulation.

The exact determination of the actual stiffness $K_{fMW/Hz}$ in real time is a difficult task as the stiffness is continuously varying due to changes in the demand, its structure and the composition of power stations. Determination of $K_{fMW/Hz}$ in real time is the subject of on-going research. Generally, it would require a sophisticated dynamic identification methodology. In practice, the frequency bias factors λ_R are set in central regulators in the European UCTE system using a simplified methodology. In each year, the share of a given control area in the total energy production is determined. Then the value of $K_{fMW/Hz}$ is estimated for the whole interconnected system. This estimate of $K_{fMW/Hz}$ is divided between the control areas in proportion to their annual energy share and that value is set to be the frequency bias factor for each area.

For example, let $K_{fMW/Hz} = 20\,000$ MW/Hz be the estimate of stiffness of the whole interconnected system. Let the shares of the kth and jth control areas in the annual energy production be respectively $\alpha_k = 0.05$ and $\alpha_j = 0.20$. According to the approximate method, the frequency bias factors set in the central regulators are

$$\lambda_{Rk} = \alpha_k K_{f\,MW/Hz} = 0.05 \cdot 20\,000 = 1000 \text{ MW/Hz}$$
$$\lambda_{Rj} = \alpha_j K_{f\,MW/Hz} = 0.02 \cdot 20\,000 = 4000 \text{ MW/Hz}.$$

The described method is simple and results in an approximate fulfilment of the non-intervention rule.

Secondary frequency control is much slower than the primary one. As an example, given below is a description of requirements agreed by members of the European UCTE system.

Tie-line flow measurements have to be sent to the central regulator either cyclically or whenever the flow exceeds a certain value, with a delay not exceeding 1–5 s. Instructions to change the reference values are sent from the central regulator (Figure 9.10) to area regulators approximately

every 10 min. For the maximum speed of secondary control, activation of the whole range of secondary reserve must be done within 15 min.

Power stations contributing to secondary control, that is those controlled by the central regulator, must operate with a wide range of power regulation. This range depends on the type of the power station. For thermal plants, the typical range of power regulation operated within primary control (Figure 2.13) is from 40 % (technical minimum) to 100 % (maximum). Usually secondary control uses about ±5 % of the maximum power from within that range. The speed of regulation depends on the type of a unit. It is required that the speed of regulation is not less than:

- for gas or oil units: 8 % of rated power per minute;
- for coal and lignite units: 2–4 % of rated power per minute;
- for nuclear units: 1–5 % of rated power per minute;
- for hydro units: 30 % of rated power per minute.

The sum of regulation ranges, up and down, of all the generating units active in secondary control is referred to as the *bandwidth of secondary control*. The positive value of the bandwidth, that is from the maximum to the actual operating point, forms the *reserve of secondary control*. In the European UCTE system, the required value of the secondary reserve for each control area is in the range of 1 % of the power generated in the area. It is additionally required that the secondary reserve is equal at least to the size of the largest unit operating in the area. This requirement is due to the non-intervention rule if the largest unit is suddenly lost. If that happens, secondary control in the area must quickly, in no longer than 15 min, increase the power generated in the area by the value of the lost power.

The schedule of required values of power interchange $P_{\text{tie ref}}$ is sent to the central regulator based on a schedule for the whole interconnection. In order to prevent power swings between control areas due to rapid changes in the reference values, changes in the values of $P_{\text{tie ref}}$ are phased in as shown in Figure 9.11. The ramp of phasing in starts 5 min before, and finishes 5 min after, the set time of the change.

9.1.4 Tertiary Control

Tertiary control is additional to, and slower than, primary and secondary frequency control. The task of tertiary control depends on the organizational structure of a given power system and the role that power plants play in this structure.

Under the vertically integrated industry structure (see Chapter 2), the system operator sets the operating points of individual power plants based on the economic dispatch, or more generally optimal power flow (OPF), which minimizes the overall cost of operating plants subject to network constraints. Hence tertiary control sets the reference values of power in individual generating units to the values calculated by optimal dispatch in such a way that the overall demand is satisfied together with the schedule of power interchanges.

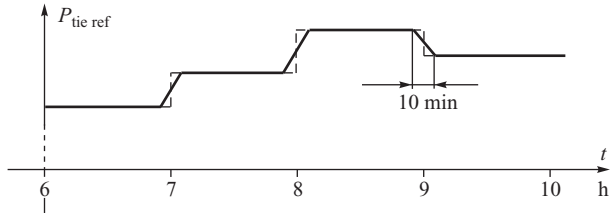

Figure 9.11 A schedule of changes in the required value of power interchange.

In many parts of the world, electricity supply systems have been liberalized and privately owned power plants are not directly controlled by the system operator. Economic dispatch is then executed via an energy market. Depending on the actual market structure in place, power plants either bid their prices to a centralized pool or arrange bilateral contracts directly with companies supplying power to individual customers. The main task of the system operator is then to adjust the supplied bids or contracts to make sure that the network constraints are satisfied and to procure the required amount of primary and secondary reserve from individual power plants. In such a market structure the task of tertiary control is to adjust, manually or automatically, the set points of individual turbine governors in order to ensure the following:

1. Adequate spinning reserve in the units participating in primary control.
2. Optimal dispatch of units participating in secondary control.
3. Restoration of the bandwidth of secondary control in a given cycle.

Tertiary control is supervisory with respect to the secondary control that corrects the loading of individual units within an area. Tertiary control is executed via the following:

1. Automatic change of the reference value of the generated power in individual units.
2. Automatic or manual connection or disconnection of units that are on the reserve of the tertiary control.

The reserve of the tertiary control is made up of those units that can be manually or automatically connected within 15 min of a request being made. The reserve should be utilized in such a way that the bandwidth of the secondary control is restored.

9.1.5 AGC as a Multi-Level Control

AGC is an excellent example of a multi-level control system whose overall structure is shown in Figure 9.12.

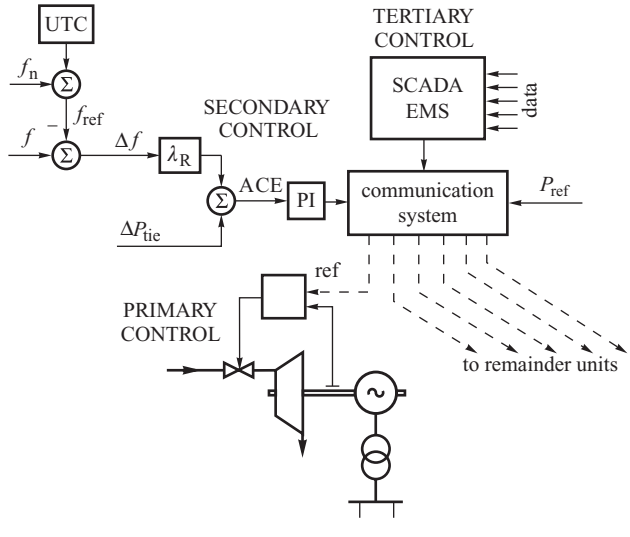

Figure 9.12 Levels of automatic generation control.

The turbine governing system with its load reference point is at the lowest primary control level and all the commands from the upper levels are executed at this level. Primary control is decentralized because it is installed in power plants situated at different geographical sites.

Frequency control and tie-line control constitute secondary control and force primary control to eliminate the frequency and net tie-line interchange deviations. In isolated systems secondary control is limited to frequency control and could be implemented locally without the need for coordination by the central regulator. In interconnected systems secondary control of frequency and tie-line flows is implemented using a central computer. Secondary control should be slower than primary control.

The task of tertiary control is to ensure an appropriate bandwidth of secondary control. Obviously tertiary control must be slower than both primary and secondary control. Hence it may be neglected when considering the dynamics of coordination between primary and secondary control.

Modern solutions execute the tasks of secondary and tertiary control using a function LFC (Load and Frequency Controller) in control algorithms of SCADA–EMS (Energy Management System) that supports the system operator. Apart from controlling frequency and power interchanges, SCADA–EMS contains a number of other optimization and security management functions. A detailed description is beyond the scope of this book but interested readers are referred to Wood and Wollenberg (1996).

The hierarchical structure shown in Figure 9.12 also contains a block UTC corresponding to control of the synchronous time, that is time measured by synchronous clocks based on the system frequency. Power system frequency varies continuously, so synchronous clocks tend to have an error proportional to the integral of the system frequency. This error is eliminated by occasionally changing the reference value of the frequency.

In the European UCTE system the nominal frequency is $f_n = 50$ Hz . The synchronous time deviation is calculated at the control centre in Laufenberg (Switzerland) using the UTC time standard. On certain days of each month, the centre broadcasts a value of frequency correction to be inserted in secondary control systems in order to eliminate the synchronous time deviation. If synchronous clocks are delayed then the frequency correction is set to 0.01 Hz, that is the set frequency is $f_{ref} = 50.01$ Hz . If synchronous clocks are ahead then the frequency correction is set to -0.01 Hz, that is the set frequency is $f_{ref} = 49.99$ Hz. Usually the system operates for a few tens of days with a correction of -0.01 Hz, for a few days with $+0.01$ Hz and then without any correction for the remainder of the year.

Usually control areas are grouped in large interconnected systems with the central regulator of one area (usually the largest) regulating power interchanges in the given area with respect to other areas. In such a structure the central controller of each area regulates its own power interchanges while the central controller of the main area additionally regulates power interchanges of the whole group.

9.1.6 Defence Plan Against Frequency Instability

The system of frequency and power control discussed above is adequate for typical disturbances of a real power balance consisting of the unplanned outage of a large generating unit. The largest disturbance which can be handled by the system is referred to as the *reference incident*. In the European UCTE system, the reference incident consists of losing units with a total power of 3000 MW. Larger incidences have to handled by each system operator using its own defence plan together with appropriate facilities that defend the power system from the disturbance spreading out. Examples of such a defence plan are shown in Tables 9.1 and 9.2.

The defence plan described in these tables should be treated as an example. It is based on a paper by Kuczyński, Paprocki and Strzelbicki (2005) and also includes updates resulting from experience gained from the wide area disturbance in UCTE interconnected power systems on 4 November 2006. The interested reader is advised to check the UCTE Master Plan document at www.ucte.org.

Table 9.1 Example of a defence plan against a frequency drop

f (Hz)	Δf (Hz)	Type of defence action
50.000	<0.200	Normal operation with primary control with small dead zones (Figure 9.6a) and secondary control of frequency and tie-line power: $\text{ACE} = -\Delta P_{\text{tie}} - \lambda_{\text{R}} \Delta f$
49.800	0.200	Central secondary controllers of subsystems are blocked. Generating units operate only with primary control and manual setting of reference power
		Primary control hidden in units operating with large dead zones ± 200 mHz (Figure 9.6b) is automatically activated
		Switching of pumped storage plants from the pump mode to the generation mode
		Starting of fast-start units (diesel and open-cycle gas units)
49.000 48.700	1.000 1.300	Underfrequency load shedding (first two stages)
48.700	1.300	Turbine governors (primary control) switch from power regulation according to droop characteristic to speed control (Figure 9.6)
48.500 48.300 48.100	1.500 1.700 1.900	Underfrequency load shedding (next three stages)
47.500	2.500	Generating units are allowed to trip by turbine protection. The units supply their own ancillary services and demand of their islands (if they survived). System operators start system restoration by reconnecting the islands and lost generating units

Table 9.2 Example of a defence plan against frequency rise.

f(Hz)	Δf(Hz)	Type of defence action
51.500	1.500	Generating units are allowed to trip by turbine protection. The units supply their own ancillary services
51.300	1.300	Turbine governors (primary control) switch from power regulation according to droop characteristic to speed control (Figure 9.6)
50.200	0.200	Switching of pumped storage plants from the generation mode to the pump mode
		Stopping of fast-start units (diesel and open-cycle gas units)
		Primary control hidden in units operating with large dead zones ±200 mHz (Figure 9.6b) is automatically activated
		Central secondary controllers of subsystems are blocked. Generating units operate only with primary control and manual setting of reference power
50.000	<0.200	Normal operation with primary control with small dead zones (Figure 9.6a) and secondary control of frequency and the tie-line power: $\text{ACE} = -\Delta P_{\text{tie}} - \lambda_{\text{R}} \Delta f$

9.1.7 *Quality Assessment of Frequency Control*

The quality assessment of frequency and power interchange control can be divided into two types:

1. Quality assessment of the control during normal system operation.
2. Quality assessment during large disturbances such as unplanned outages of a generating unit.

Quality assessment during normal system operation is executed using the standard deviation of the frequency error:

$$\sigma = \sqrt{\frac{1}{n}\sum_{i=1}^{n}(f - f_{\text{ref}})^2}, \tag{9.13}$$

where n is the number of measurements. The measurements are taken every 15 min in a month. Additionally, a percentage share of frequency deviations higher than 50 mHz is calculated together with the times of their appearance.

Quality assessment of frequency control following a large disturbance is shown in Figure 9.13. The bold line shows an example of frequency changes following an unplanned outage of a large generating unit. There was a frequency error of Δf_0 just before the disturbance. The disturbance happened during a correction to the synchronous time when $f_{\text{ref}} = 50.01$ Hz . Following the disturbance, the frequency dropped by a maximum of Δf_2. Frequency control restored the frequency to the reference value within the allowed error. The whole range of frequency variations was limited to within an area shown by the dashed lines and referred to as the *trumpet characteristic*. The trumpet characteristic is made up of two exponential curves defined by

$$\begin{aligned} H(t) &= f_{\text{ref}} \pm A\,\mathrm{e}^{-t/T} \quad \text{for} \quad t \le 900 \text{ s} \\ H(t) &= \pm 20 \text{ mHz} \quad \text{for} \quad t \ge 900 \text{ s}, \end{aligned} \tag{9.14}$$

where the $\pm$ signs correspond to the upper and lower parts of the characteristic and A is the initial width. The exponential characteristic finishes when $t = 900$ s , that is $t = 15$ min . Then the

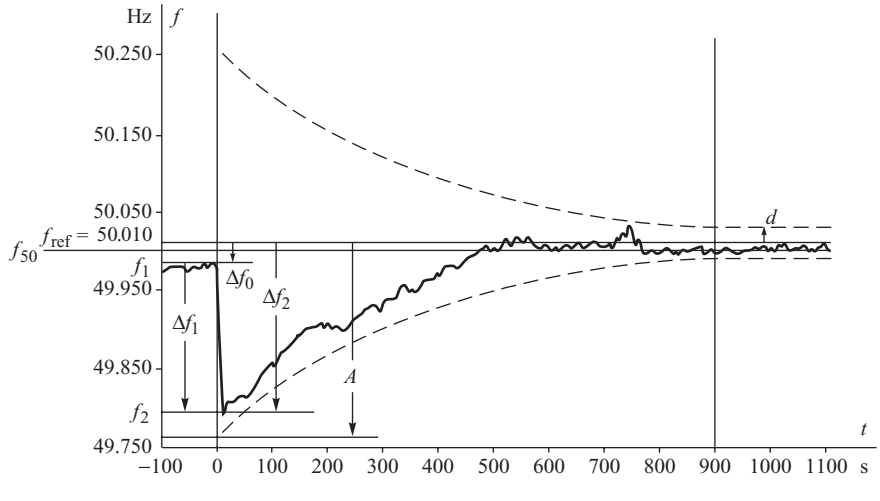

Figure 9.13 Illustration of the quality assessment of frequency control using a trumpet characteristic. Based on the document 'UCTE – Ground Rules – Supervision of the application of rules concerning primary and secondary control of frequency and active power in UCTE'. Reproduced by permission of UCTE.

characteristic consists of two horizontal lines limiting the frequency error to ±20 mHz corresponding to the required accuracy of frequency control during normal operation. The exponential curves must descend smoothly to the horizontal lines. For that to happen, the time constant of the exponential curves must be equal to

$$T = \frac{900}{\ln(A/d)}. \tag{9.15}$$

The initial width A depends on the disturbance size ΔP_0 according to

$$A = 1.2\left(\frac{|\Delta P_0|}{\lambda_R} + 0.030\right), \tag{9.16}$$

where λ_R is the frequency stiffness of the power system. As an example, if a unit of several hundred megawatts is tripped, the width of the trump characteristic, and therefore also the varying frequency error, is a few hundred millihertz.

If variations of frequency following a disturbance ΔP_0 are inside the trump characteristic then the frequency control is deemed to be satisfactory.

9.2 Stage I – Rotor Swings in the Generators

Having described the AGC, it is now possible to analyse the response of a power system to a power imbalance caused, for example, by the tripping of a generating unit. This response can be divided into four stages depending on the duration of the dynamics involved:

Stage I	Rotor swings in the generators (first few seconds)
Stage II	Frequency drop (a few seconds to several seconds)
Stage III	Primary control by the turbine governing systems (several seconds)
Stage IV	Secondary control by the central regulators (several seconds to a minute).

The dynamics associated with each of these four stages will be described separately in order to illustrate how they develop in the system. To begin the discussion the power system shown schematically in Figure 9.14a will be considered where a power station transmits its power to the system via two parallel transmission lines. The power station itself is assumed to consist of two identical generating units operating onto the same busbar. The disturbance considered will be the disconnection of one of the generating units. In Stage I of the disturbance the way in which the remaining generating unit contributes to the production of the lost power will be given special attention.

The sudden disconnection of one of the generators will initially produce large rotor swings in the remaining generating unit and much smaller rotor swings in the other generators within the system. For simplicity these small oscillations will be neglected to allow the rest of the system to be replaced by an infinite busbar. The time scale of the rotor swings is such that the generator transient model applies and the mechanical power supplied by the turbine remains constant. To simplify considerations, the classical model representation of the generator will be used, Equations (5.15) and (5.40). Figure 9.14b shows the equivalent predisturbance circuit diagram for the system. As both generators are identical they can be represented by the same transient emf $\underline{E}'$ behind an equivalent reactance that combines the generator transient reactance X'_d, the transformer reactance X_T and the system reactance X_s.

Figure 9.15 shows how the equal area criterion can be applied to this problem. In this diagram $P_-(\delta')$ and $P_+(\delta')$ are the transient power–angle characteristics, and P_{m-} and P_{m+} the mechanical powers, before and after the disturbance occurs. Initially the plant operates at point 1 and the equivalent power angle with respect to the infinite busbar is δ'_0. Disconnection of one of the generators has two effects. Firstly, the equivalent reactance of the system increases

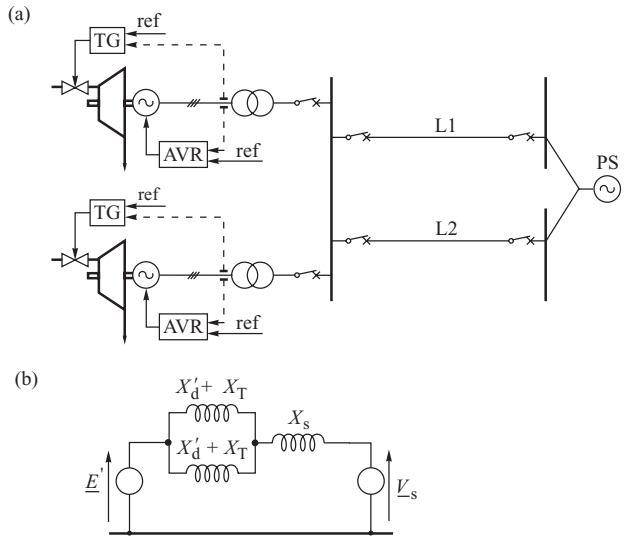

Figure 9.14 Parallel generating units operating onto an infinite busbar: (a) schematic diagram; (b) equivalent circuit.

so that the amplitude of the power–angle characteristic decreases. Consequently the pre- and postdisturbance power–angle characteristics are

$$P_-(\delta'_0) = \frac{E' V_s}{\frac{X'_d + X_T}{2} + X_s} \sin \delta'_0, \quad P_+(\delta'_0) = \frac{E' V_s}{X'_d + X_T + X_s} \sin \delta'_0. \tag{9.17}$$

Secondly, the mechanical power delivered to the system drops by an amount equal to the power of the lost unit, that is $P_{m+} = 0.5 P_{m-}$.

As the rotor angle of the remaining generator cannot change immediately after the disturbance occurs, the electrical power of the generator is greater than the mechanical power delivered by

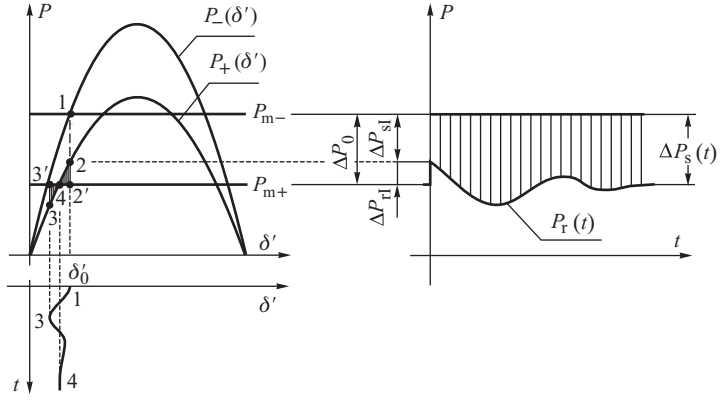

Figure 9.15 Application of the equal area criterion to determine the first stage of the dynamics. Duration of the phenomena – first few seconds.

its prime mover, point 2. The rotor is decelerated and loses kinetic energy corresponding to the area 2–2′–4. Due to its momentum the rotor continues to decrease its angle past point 4 until it stops at point 3 when the area 4–3–3′ equals the area 2–2′–4. The damping torques then damp out subsequent oscillations and the rotor tends towards its equilibrium point 4.

The amplitude of the rotor oscillations of any given generator will depend on the amount of lost generation it picks up immediately after the disturbance occurs. Using the notation of Figure 9.15 gives

$$\begin{aligned} \Delta P_0 &= P_{-}(\delta_0') - P_{\mathrm{m}+} = P_{\mathrm{m}-} - P_{\mathrm{m}+} \\ \Delta P_{\mathrm{rI}} &= P_{+}(\delta_0') - P_{\mathrm{m}+} \\ \Delta P_{\mathrm{sI}} &= \Delta P_0 - \Delta P_{\mathrm{rI}}, \end{aligned} \tag{9.18}$$

where ΔP_0 is the lost generating power and ΔP_{rI} and ΔP_{sI} are the contributions of the generating units remaining in operation and of the system, respectively, in meeting the power imbalance ΔP_0 at the very beginning of the disturbance. The subscript 'I' indicates that these equations apply to Stage I of the disturbance. Using the first of the equations in (9.18), a formula for ΔP_{rI} can be rewritten as

$$\Delta P_{\mathrm{rI}} = P_{+}(\delta_0') - P_{\mathrm{m}+} = \left[P_{+}(\delta_0') - P_{\mathrm{m}+}\right] \frac{1}{P_{-}(\delta_0') - P_{\mathrm{m}+}} \Delta P_0. \tag{9.19}$$

Substituting (9.17) into (9.19) and noting that $P_{\mathrm{m}+} = 0.5\,P_{\mathrm{m}-}$ gives

$$\Delta P_{\mathrm{rI}} = \frac{1}{1+\beta} \Delta P_0, \tag{9.20}$$

where $\beta = (X_{\mathrm{d}}' + X_{\mathrm{T}})/X_{\mathrm{s}}$. The amount that the system contributes in order to meet the lost generation can now be calculated as

$$\Delta P_{\mathrm{sI}} = \Delta P_0 - \Delta P_{\mathrm{rI}} = \frac{\beta}{\beta+1} \Delta P_0, \tag{9.21}$$

with the ratio of the contributions (9.20) and (9.21) being

$$\frac{\Delta P_{\mathrm{rI}}}{\Delta P_{\mathrm{sI}}} = \frac{1}{\beta} = \frac{X_{\mathrm{s}}}{X_{\mathrm{d}}' + X_{\mathrm{T}}}. \tag{9.22}$$

This equation shows that ΔP_{r}, the contribution of the unit remaining in operation in meeting the lost power, is proportional to the system equivalent reactance X_{s}. Both contributions ΔP_{r} and ΔP_{s} are depicted in Figure 9.15. Due to the fact that the inertia of the unit is much smaller than that of the power system, the generator quickly decelerates, loses kinetic energy, and both its rotor angle and generated power decrease (Figure 9.15b). As a consequence the power imbalance starts to increase and is met by the system which starts to increase its contribution ΔP_{s}. This power delivered by the system has been shaded in Figure 9.15 and, when added to the generator's share $P_{\mathrm{r}}(t)$, must equal the load existing before the disturbance. As can be seen from this figure, the proportion of lost generation picked up by the system changes with time so that the system contributes more and more as time progresses.

Although the formula in Equation (9.22) has been derived for two parallel generating units operating in the system, a similar expression can be derived for the general multi-machine case. This expression would lead to a conclusion that is similar to the two-machine case in that at the beginning of Stage I of the dynamics the share of any given generator in meeting the lost load will depend on its electrical distance from the disturbance (coefficient β). In the case of Figure 9.14 the imbalance appeared at the power plant busbar. Thus X_s is a measure of the electrical distance of the system from the disturbance and $(X_{\mathrm{d}}' + X_{\mathrm{T}})$ is a measure of the electrical distance of the unit remaining in operation.

9.3 Stage II – Frequency Drop

The situation shown in Figure 9.15 can only last for a few seconds before the power imbalance causes all the generators in the system to slow down and the system frequency to drop. Thus begins Stage II of the dynamics. During this stage the share of any one generator in meeting the power imbalance depends solely on its inertia and not on its electrical distance from the disturbance. Assuming that all the generators remain in synchronism, they will slow down at approximately the same rate after a few rotor swings in Stage I of the dynamics. This may be written as

$$\frac{\mathrm{d}\Delta\omega_1}{\mathrm{d}t} \approx \frac{\mathrm{d}\Delta\omega_2}{\mathrm{d}t} \approx \cdots \approx \frac{\mathrm{d}\Delta\omega_{N_\mathrm{G}}}{\mathrm{d}t} = \varepsilon, \tag{9.23}$$

where $\Delta\omega_i$ is the speed deviation of the ith generator, ε is the average acceleration and N_G is the number of generators.

According to the swing equation, Equation (5.14), the derivative of the speed deviation can be replaced by the ratio of the accelerating power ΔP_i of the ith unit over the inertia coefficient M_i. This modifies Equation (9.23) to

$$\frac{\Delta P_1}{M_1} \approx \frac{\Delta P_2}{M_2} \approx \cdots \approx \frac{\Delta P_n}{M_n} \approx \varepsilon. \tag{9.24}$$

If the change in the system load due to the frequency change is neglected, then the sum of the extra load taken by each generator must be equal to the power lost ΔP_0

$$\Delta P_0 = \sum_{i=1}^{N_\mathrm{G}} \Delta P_i. \tag{9.25}$$

Substituting the increment ΔP_i in this equation with $\Delta P_i = M_i\varepsilon$ gives

$$\Delta P_0 = \varepsilon \sum_{i=1}^{N_\mathrm{G}} M_i \quad \text{or} \quad \varepsilon = \frac{\Delta P_0}{\sum\limits_{i=1}^{N_\mathrm{G}} M_i} \quad \text{so that} \quad \Delta P_i = M_i\varepsilon = \frac{M_i}{\sum\limits_{k=1}^{N_\mathrm{G}} M_k}\Delta P_0. \tag{9.26}$$

This equation determines the contribution of the ith generator in meeting the lost power in Stage II of the dynamics when each generator contributes an amount of power proportional to its inertia. In practice the inertia constant H_i is similar for all the generators so that substituting for $M_i = 2H_iS_{\mathrm{n}i}/\omega_\mathrm{s}$ from Equation (5.13), then Equation (9.26) can be written as

$$\Delta P_i \approx \frac{S_{\mathrm{n}i}}{\sum\limits_{i=1}^{N_\mathrm{G}} S_{\mathrm{n}i}}\Delta P_0. \tag{9.27}$$

During Stage II the contribution of the generator remaining in operation and the rest of the power system in meeting the lost power can be expressed, using (9.26), as

$$\Delta P_{\mathrm{rII}} = \frac{M_\mathrm{r}}{M_\mathrm{r} + M_\mathrm{s}}\Delta P_0 \quad \text{and} \quad \Delta P_{\mathrm{sII}} = \frac{M_\mathrm{s}}{M_\mathrm{r} + M_\mathrm{s}}\Delta P_0. \tag{9.28}$$

Subscript II has been added here to emphasize that these equations are valid during Stage II. In a similar way as in Equation (9.22), the ratio of the contributions is

$$\frac{\Delta P_{\mathrm{rII}}}{\Delta P_{\mathrm{sII}}} = \frac{M_\mathrm{r}}{M_\mathrm{s}} \approx \frac{S_{\mathrm{nr}}}{S_{\mathrm{ns}}}, \tag{9.29}$$

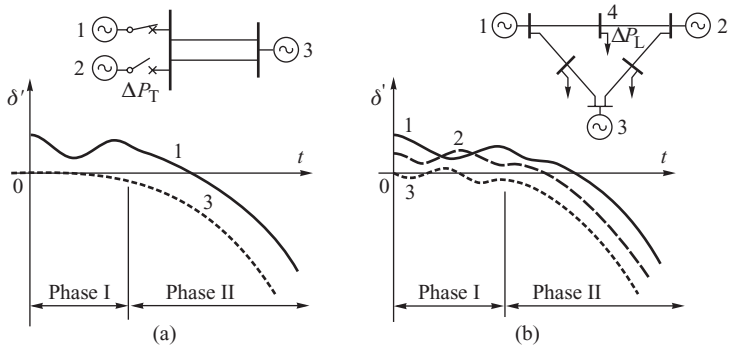

Figure 9.16 Examples of changes in the rotor angles in the case of a real power disturbance: (a) disconnection of generator 2; (b) sudden increase of the load at node 4. The duration of Stage II is a few to several seconds.

and is equal to the ratio of the inertia coefficients or, approximately, to the ratio of the rated powers. As $S_{ns} \gg S_{nr}$ (infinite busbar), the contribution by the generator remaining in operation in covering the lost power is very small. The assumption made when preparing Figure 9.15 was that $\Delta P_{rII} \approx \Delta P_0 S_{nr}/S_{ns} \approx 0$.

Figure 9.16a illustrates the case when the system has a finite equivalent inertia and the rotor angle of both the remaining generator and the system equivalent generator decreases as the frequency drops. The initial rotor angle oscillations are the same as those shown for the first stage of the dynamics in Figure 9.15. The angles then decrease together as the generators operate synchronously.

Figure 9.16b shows the case of a three-generator system where the load at node 4 suddenly increases. Generators 1 and 2 are close to the disturbance, so they participate more strongly in the first stage of the oscillations than does generator 3. During the second stage the power angles synchronously decrease and the system frequency drops.

9.4 Stage III – Primary Control

Stage III of the dynamics depends on how the generating units and the loads react to the drop in frequency. Section 2.2.3 explained how, as frequency (speed) drops, the turbine governor opens the main control valves to increase the flow of working fluid through the turbine and so increase the turbine mechanical power output. In the steady state, and during very slow changes of frequency, the increase in mechanical power for each generating unit is inversely proportional to the droop of the static turbine characteristic. Equations (9.4) and (9.6) can be rewritten as

$$\begin{aligned} P_T &= P_{T0} + \Delta P_T = P_{T0} - K_T \Delta f \frac{P_{T0}}{f_n} \\ P_L &= P_{L0} + \Delta P_L = P_{L0} + K_L \Delta f \frac{P_{L0}}{f_n}. \end{aligned} \tag{9.30}$$

The operating frequency of the system is determined by the point of intersection of these two characteristics.

Typical generation and load characteristics are shown in Figure 9.17 where the generation characteristic before the disturbance is denoted by P_{T-} and after by P_{T+}. If a generating unit is lost the system generation characteristic P_T moves to the left by the value of the lost power ΔP_0 and,

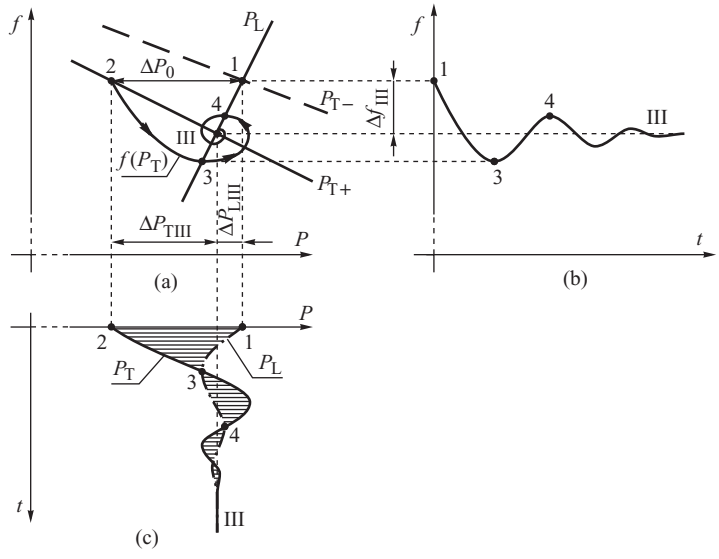

Figure 9.17 Stage III of the dynamics caused by an imbalance in real power: (a) the generation characteristic and the frequency response characteristic; (b) frequency changes; (c) power changes. The duration of Stage III is several seconds.

according to Equation (9.4), the slope of the characteristic increases slightly as a the value of K_T decreases.

Before the disturbance occurs, the system operates at point 1 corresponding to the intersection of the P_L and P_{T-} characteristics. After the generator is disconnected the frequency initially remains unchanged and the generation operating point is shifted to point 2. Then the generation tends to move towards point III which corresponds to the intersection of the P_L and P_{T+} characteristics but, because of the delay introduced by the time constants of the turbines and their governors, this point cannot be reached immediately. Initially the difference between the generated power, point 2, and the load power, point 1, is large and the frequency starts to drop as described in Stage I and Stage II of the dynamics. In Stage III the turbine reacts to the drop in frequency by increasing its power output but, because of the aforementioned time delays in the turbine regulator system, the trajectory of the turbine power $f(P_T)$ lies below the static generation characteristic P_{T+}. As the frequency drops, the generated power increases while the power taken by the load decreases. The difference between the load and the generation is zero at point 3. According to the swing equation, a zero value of deceleration power means

$$\frac{d\Delta\omega}{dt} = 2\pi \frac{d\Delta f}{dt} = 0, \tag{9.31}$$

and the frequency $f(t)$ reaches a local minimum, Figure 9.17b.

Because of the inherent inertia of the turbine regulation process, the mechanical power continues to increases after point 3 so that the generated power exceeds the load power and the frequency starts to rise. At point 4 the balance of power is again zero and corresponds to the local maximum in the frequency shown in Figure 9.17b. The oscillations continue until the steady-state value of the frequency f_{III} is reached at point III corresponding to the intersection of the P_L and P_{T+} static

characteristics. The value of f_{III} can be determined from Figure 9.17a

$$\Delta P_0 = \Delta P_{\mathrm{TIII}} - \Delta P_{\mathrm{LIII}} = -K_{\mathrm{T}} \frac{P_{\mathrm{L}}}{f_{\mathrm{n}}} \Delta f_{\mathrm{III}} - K_{\mathrm{L}} \frac{P_{\mathrm{L}}}{f_{\mathrm{n}}} \Delta f_{\mathrm{III}} = -P_{\mathrm{L}} (K_{\mathrm{T}} + K_{\mathrm{L}}) \frac{\Delta f_{\mathrm{III}}}{f_{\mathrm{n}}}, \tag{9.32}$$

with the frequency error f_{III} being

$$\frac{\Delta f_{\mathrm{III}}}{f_{\mathrm{n}}} = \frac{-1}{K_{\mathrm{T}} + K_{\mathrm{L}}} \frac{\Delta P_0}{P_{\mathrm{L}}} \quad \text{or} \quad \frac{\Delta f_{\mathrm{III}}}{f_{\mathrm{n}}} = \frac{-1}{K_{\mathrm{f}}} \frac{\Delta P_0}{P_{\mathrm{L}}}, \tag{9.33}$$

where the coefficient $K_{\mathrm{f}} = K_{\mathrm{T}} + K_{\mathrm{L}}$ is the system stiffness introduced in Equation (9.7). Figure 9.17c shows how the generated power and the load power change during this period. The difference between the two is shaded and corresponds to the power that decelerates ($P_{\mathrm{T}} < P_{\mathrm{L}}$) or accelerates ($P_{\mathrm{T}} > P_{\mathrm{L}}$) the rotor.

For the system shown in Figure 9.14 the contributions of the generator remaining in operation and that of the system in covering the lost generation in Stage III of the dynamics can be obtained from Equation (9.4) as

$$\Delta P_{\mathrm{rIII}} = -K_{\mathrm{Tr}} \frac{\Delta f_{\mathrm{III}}}{f_{\mathrm{n}}} P_{\mathrm{nr}}, \quad \Delta P_{\mathrm{sIII}} = -K_{\mathrm{Ts}} \frac{\Delta f_{\mathrm{III}}}{f_{\mathrm{n}}} P_{\mathrm{ns}}, \tag{9.34}$$

where the subscript III is added to emphasize that these equations are valid during Stage III of the dynamics. The ratio of contributions resulting from these equations is

$$\frac{\Delta P_{\mathrm{rIII}}}{\Delta P_{\mathrm{sIII}}} = \frac{K_{\mathrm{Tr}}}{K_{\mathrm{Ts}}} \frac{P_{\mathrm{nr}}}{P_{\mathrm{ns}}} \approx \frac{P_{\mathrm{nr}}}{P_{\mathrm{ns}}}. \tag{9.35}$$

The approximate equality in this equation is valid when the droop of all the turbine characteristics is approximately the same. In practice the ratios (9.35) and (9.29) are very similar. This physically corresponds to the fact that, during the transition period between the second and third stages, the generator is in synchronism with the system and there are no mutual oscillations between them.

9.4.1 The Importance of the Spinning Reserve

The discussion so far has assumed that, within the range of frequency variations, each of the generating units has a linear turbine characteristic and that the overall generation characteristic is also linear. In practice each generating unit must operate within the limits that are placed on its thermal and mechanical performance. To ensure that these limits are adhered to, its governing system is equipped with the necessary facilities to make certain that the unit does not exceed its maximum power limit or the limit placed on the speed at which it can take up power. These limits can have a substantial impact on how a unit behaves when the system frequency changes.

Figure 9.3 showed how the spinning reserve, and its allocation in the system, influences the shape of the generation characteristic. In order to help quantify the influence of spinning reserve, the following coefficients are defined:

$$r = \frac{\sum_{i=1}^{N_{\mathrm{G}}} P_{\mathrm{n}i} - P_{\mathrm{L}}}{P_{\mathrm{L}}}, \quad p = \frac{\sum_{i=1}^{R} P_{\mathrm{n}i}}{\sum_{i=1}^{N_{\mathrm{G}}} P_{\mathrm{n}i}}, \tag{9.36}$$

where $\sum_{i=1}^{N_{\mathrm{G}}} P_{\mathrm{n}i}$ is the sum of the power ratings of all the generating units connected to the system and $\sum_{i=1}^{R} P_{\mathrm{n}i}$ is the sum of the power ratings of all the units operating on the linear part of their characteristics; that is, loaded below their power limit. The coefficient r is the *spinning reserve*

coefficient and defines the relative difference between the maximum power capacity of the system and the actual load.

A simple expression for the local droop of the generation characteristic can be obtained by assuming that the droop of all the units which are not fully loaded are approximately identical, that is $\rho_i = \rho$ and $K_i = K = 1/\rho$. For the units operating at their limits, $\rho_i = \infty$ and $K_i = 0$. Under these conditions

$$\begin{aligned}\Delta P_{\mathrm{T}} &= -\sum_{i=1}^{N_{\mathrm{G}}} K_i P_{\mathrm{n}i} \frac{\Delta f}{f_{\mathrm{n}}} = -\sum_{i=1}^{R} K_i P_{\mathrm{n}i} \frac{\Delta f}{f_{\mathrm{n}}} \cong -K \sum_{i=1}^{R} P_{\mathrm{n}i} \frac{\Delta f}{f_{\mathrm{n}}} \\ &= -Kp \sum_{i=1}^{N_{\mathrm{G}}} P_{\mathrm{n}i} \frac{\Delta f}{f_{\mathrm{n}}} = -Kp\,(r+1)\,P_{\mathrm{L}} \frac{\Delta f}{f_{\mathrm{n}}}.\end{aligned} \tag{9.37}$$

Dividing by P_{L} gives

$$\frac{\Delta P_{\mathrm{T}}}{P_{\mathrm{L}}} = -K_{\mathrm{T}} \frac{\Delta f}{f_{\mathrm{n}}}, \tag{9.38}$$

where

$$K_{\mathrm{T}} = p\,(r+1)\,K \quad \text{and} \quad \rho_{\mathrm{T}} = \frac{\rho}{p\,(r+1)}. \tag{9.39}$$

Equation (9.38) is similar to Equation (9.4) and describes the linear approximation of the nonlinear generation characteristic for a given load. The local droop ρ_{T} increases as the spinning reserve decreases. At the limit, when the load P_{L} is equal to the system generating capacity, both the coefficients r and p are zero and $\rho_{\mathrm{T}} = \infty$. This corresponds to all the generating units being fully loaded.

The influence of the spinning reserve on the frequency drop in Stage III of the dynamics can now be determined. For the linear approximation to the generator characteristic given in Equation (9.38) the drop in frequency can be determined from Equation (9.33) as

$$\frac{\Delta f_{\mathrm{III}}}{f_{\mathrm{n}}} = \frac{-1}{p\,(r+1)\,K + K_{\mathrm{L}}} \frac{\Delta P_0}{P_{\mathrm{L}}}, \tag{9.40}$$

indicating that the smaller the spinning reserve coefficient r, the bigger the drop in frequency due to the loss of power ΔP_0. With a large spinning reserve the static characteristic $P_{\mathrm{T}(1)}$ shown in Figure 9.18 has a shallow slope and the drop in frequency is small. On the other hand, when the spinning reserve is small, the $P_{\mathrm{T}(2)}$ characteristic is steep, and the frequency drop is increased for the same power disturbance ΔP_0. In the extreme case when no spinning reserve is available, the

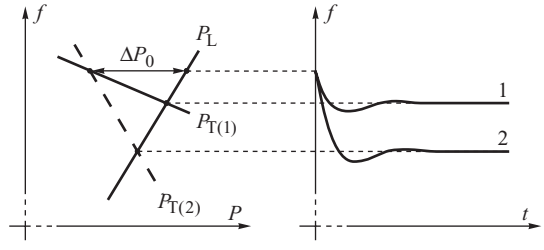

Figure 9.18 The influence of spinning reserve on the frequency drop due to a power imbalance: 1, large spinning reserve; 2, small spinning reserve.

generating units would be unable to increase their generation and the whole power imbalance ΔP_0 could only be covered by the frequency effect of the loads. As the frequency sensitivity K_L of the loads is generally small, the frequency drop would be very high.

Equation (9.37) defines the way in which each of the generating units contributes to the power imbalance at the end of Stage III with Equation (9.38) quantifying the net effect of the primary turbine control in meeting the lost load.

Example 9.1

Consider a 50 Hz system with a total load $P_L = 10\,000$ MW in which $p = 60\,\%$ of the units give $r = 15\,\%$ of the spinning reserve. The remaining 40 % of the units are fully loaded. The average droop of the units with spinning reserve is $\rho = 7\,\%$ and the frequency sensitivity coefficient of the loads is $K_L = 1$. If the system suddenly loses a large generating unit of $\Delta P_0 = 500$ MW, calculate the frequency drop and the amount of power contributed by the primary control.

From Equation (9.39) $K_T = 0.6(1 + 0.15)1/0.07 = 9.687$ and, according to Equation (9.33), primary control will give the frequency drop in Stage III as

$$\Delta f_{III} = \frac{-1}{9.867 + 1} \times \left[\frac{500}{10\,000}\right] \times 50 \approx 0.23 \text{ Hz},$$

where the turbine governor primary control contributes

$$\Delta P_{T\,III} = 9.867 \times \frac{0.23}{50} \times 10\,000 = 454 \text{ MW},$$

with the remaining deficit of

$$\Delta P_{L\,III} = 1 \times \frac{0.23}{50} \times 10\,000 = 46 \text{ MW},$$

being covered by the frequency effect of the loads. If there were no spinning reserve, the deficit would be covered entirely by the frequency effect of the loads giving a frequency drop of

$$\Delta f_{III} = \frac{-1}{0 + 1} \times \left[\frac{500}{10\,000}\right] \times 50 = 2.5 \text{ Hz},$$

which is about 10 times greater than in the case with (only) 15 % spinning reserve.

9.4.2 Frequency Collapse

Spinning reserve is much more important than is suggested by the approximate formula in Equation (9.40). In practice the power output of the turbine is frequency dependent so that if the frequency is much lower than the nominal frequency the turbine power will be less than that given by Equation (9.38) and the frequency may drop further and further until the system suffers a *frequency collapse*.

The hidden assumption made in the generation characteristics of Figure 9.18 is that when a unit is fully loaded the mechanical driving power delivered by the turbine does not depend on the frequency deviation. This assumption is only true for small frequency deviations while a larger frequency drop reduces mechanical power due to a deterioration in the performance of boiler feed pumps, see Section 2.2.3. In this case the static generation characteristic takes the form shown in Figure 9.13. Adding the power–frequency characteristics of individual generating units now gives the system generation characteristic P_T shown in Figure 9.19.

On the upper part of the generation characteristic the local droop at each point is positive and depends on the system load according to the formulae given in (9.39). The lower part of the characteristic corresponds to the decrease in the power output due to the deterioration in the

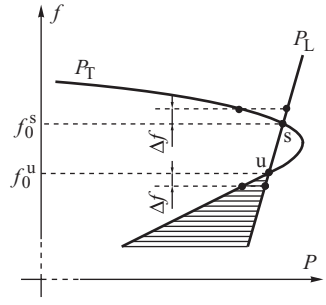

Figure 9.19 The static generation and load characteristics of the power system and the equilibrium points: s, locally stable equilibrium point; u, locally unstable equilibrium point.

performance of the boiler feed pumps. For a given load frequency characteristic P_L the inflexion in the generation characteristic produces two equilibrium points. At the upper point s any small disturbance that produces an increase in the frequency $\Delta f > 0$ will result in the load power exceeding the generation power; the generators are decelerated and the system returns to the equilibrium point s. Similarly, any small disturbance that causes a decrease in frequency will result in the generation power exceeding the load power, the rotors accelerate, the frequency increases and the system again returns to the equilibrium point. Point s is therefore *locally stable* because for any small disturbance within the vicinity of this point the system returns to point s. The region in which this condition holds is referred to as the *area of attraction*.

In contrast the lower point u is *locally unstable* because any disturbance within the vicinity of this point will result in the system moving away from the equilibrium point. The region in which this happens is referred to as the *area of repulsion*. For example, if a disturbance reduces the frequency $\Delta f < 0$ then the system moves into the shaded area below point u, the generated power is reduced so that the system load is greater than the system generation, the rotors decelerate and the frequency drops further.

With these qualifications of turbine performance in mind, assume that the system operates with a low spinning reserve at point 1 on Figure 9.20. A loss ΔP_0 in generation now occurs and the operating point moves from point 1 to point 2. The excess load over generation is large and produces an initial rapid drop in frequency. As the difference between the load and generation reduces, the rate at which the frequency drops slows down and the system generation trajectory $f(P_T)$ approaches the equilibrium point u. When the trajectory $f(P_T)$ enters the area of repulsion of point u it is forced away and the system suffers a frequency collapse.

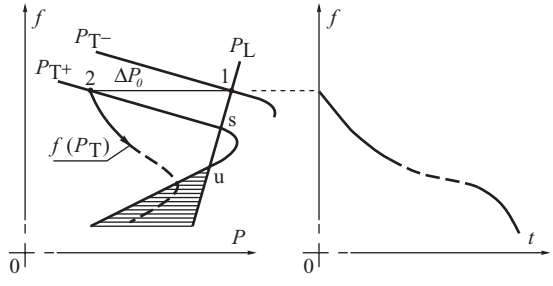

Figure 9.20 An example of frequency collapse.

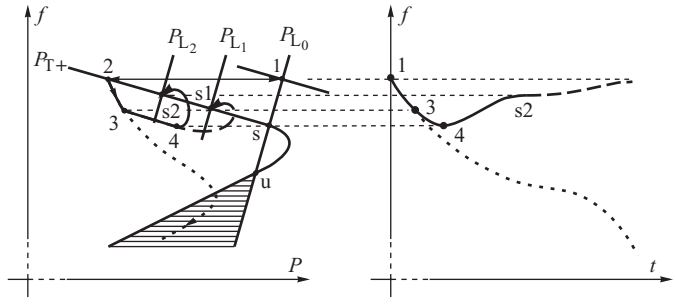

Figure 9.21 Two-stage load shedding to protect against frequency collapse.

The frequency collapse illustrated in Figure 9.20 occurred following the *sudden* appearance of the power imbalance ΔP_0. Had the system generation characteristic changed slowly from P_{T+} to P_{T-} by gradually reducing the generation, then it would have met the locally stable points and stayed there. Obviously if the power imbalance ΔP_0 is greater than the spinning reserve then the postdisturbance demand characteristic P_L lies to the right of the nose of the generation characteristic P_{T+} and the frequency would collapse regardless of how sudden the power change was.

9.4.3 Underfrequency Load Shedding

Many systems can be protected from frequency collapse by importing large blocks of power from neighbouring systems to make up for the lost generation. However, in an islanded system, or in an interconnected system with a shortage of tie-line capacity, this will not be possible and the only way to prevent a frequency collapse following a large disturbance is to employ *automatic load shedding*.

Automatic load shedding is implemented using underfrequency relays. These relays detect the onset of decay in the system frequency and shed appropriate amounts of system load until the generation and load are once again in balance and the power system can return to its normal operating frequency. Load shedding relays are normally installed in distribution and subtransmission substations as it is from here that the feeder loads can be controlled.

As load shedding is a somewhat drastic control measure, it is usually implemented in stages with each stage triggered at a different frequency level to allow the least important loads to be shed first. Figure 9.21 shows the effect of load shedding when a power imbalance ΔP_0 appears on a system with a low spinning reserve. Without load shedding the system would suffer a frequency collapse as shown by the dotted line. The first stage of load shedding is activated at point 3 and limits the load to a value corresponding to characteristic P_{L_1}. The rate of frequency drop is now much slower as the difference between the load and generation is smaller. At point 4 the second stage of load shedding is triggered, further reducing the load to a value corresponding to characteristic P_{L_2}. Generation is now higher than the load, the frequency increases, and the system trajectory tends towards point s2 where the P_{L_2} and P_{T+} characteristics intersect.

Besides protecting against frequency collapse, load shedding may also be used to prevent deep drops in system frequency.

9.5 Stage IV – Secondary Control

In Stage IV of the dynamics, the drop in system frequency and the deviation in the tie-line power flows activate the central AGC, the basic operation of which has been described in Section 9.1.

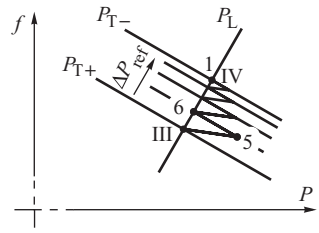

Figure 9.22 Stepped shifting of the generation characteristic by a slow-acting central regulator.

9.5.1 Islanded Systems

In an islanded system there are no tie-line connections to neighbouring systems so that the central regulator controls only the system frequency. As the frequency drops, the central regulator transmits control signals to the participating generating units to force them to increase their power output. This lifts the system generation characteristic in the (f, P) plane.

Figure 9.22 illustrates the action of a very slow-acting central regulator which transmits its first control signal at the end of Stage III corresponding to point III. This first control signal shifts the generation characteristic upwards a small amount so that at a given frequency, point 5, there is an excess of generation over load. The generators start to accelerate and the frequency increases until point 6 is reached. The central regulator now sends a further signal to increase power output and the generation characteristic is shifted further up. After a few such steps point IV is reached at which the frequency returns to its reference value and the central regulator ceases operating.

Although the zigzag line in Figure 9.22 is only a rough approximation to the actual trajectory, it illustrates the interaction between the secondary control action of the central regulator, which shifts the generation characteristic upwards, and the primary control action of the turbine governing systems, which moves the operating point along the static generation characteristic. In a real power system the inertia within the power regulation process ensures smooth changes in the power around the zigzag line to produce the type of response shown in Figure 9.23. Stages I, II and III of the frequency change are as described in the previous sections and, at the end of Stage III, the trajectory tends to wrap itself around the temporary equilibrium point III, Figure 9.23a, but does not settle at this point. The AGC of Stage IV now comes into operation and the trajectory tends towards the new equilibrium point IV. Although the difference between the frequency at points III and IV is small, the central regulator acts slowly so that correction of the frequency drop during Stage IV of the dynamics may take a long time as shown by the broken curves in Figure 9.23b and c.

If the central frequency control acts faster than as shown in Figure 9.23, it will come into operation before the end of Stage III. The trajectory $f(P_T)$ does not now wrap around point III and the frequency starts to increase earlier as shown by curve 2 in Figure 9.24.

The way in which the frequency is returned to its nominal value depends on the dynamics of the central regulator shown in Figure 9.10 and defined by Equation (9.12). The regulator dynamics consist of proportional and integral action, both of which increase the regulator output signal ΔP_{ref} as the frequency drops. The amount of integral action is determined by the integral time constant T_R while the proportional action is dependent on the coefficient β_R. Careful selection of these two coefficients ensures that the frequency returns smoothly to its reference value as shown in Figure 9.24. Particularly problematic is a small integral time constant, because the smaller is this time constant, the faster the regulation signal increases. This can be compensated to some extent by the coefficient β_R which will start to decrease the signal ΔP_{ref} as soon as the frequency starts to rise. In the extreme case of small values of β_R and T_R the response is underdamped and the reference frequency value will be reached in an oscillatory way.

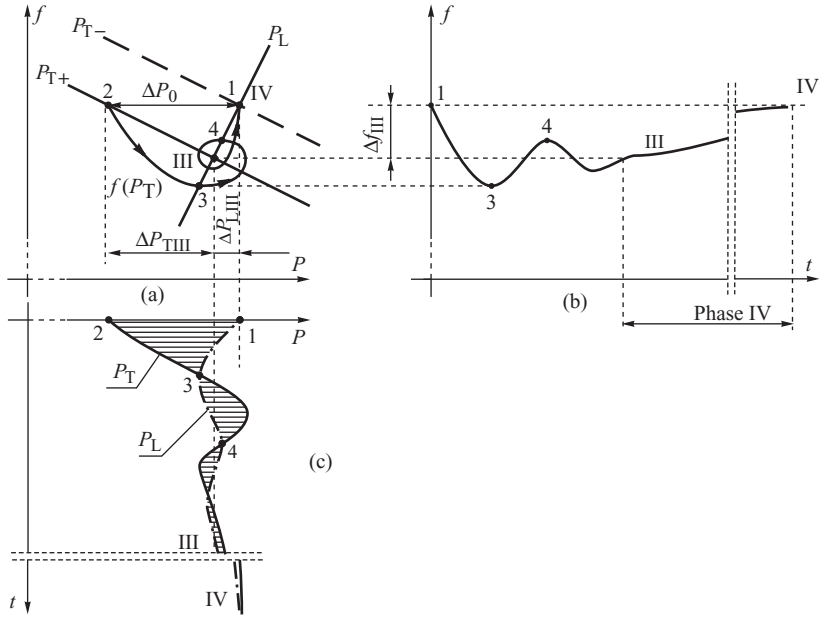

Figure 9.23 Stages III and IV of the frequency variations produced by a disturbance in the balance of real power: (a) generation and load characteristics and the system trajectory; (b) changes in frequency; (c) changes in power. The time duration of Stage IV is several seconds to a minute.

Section 9.1 explained how not all the generating units necessarily participate in AGC. This means that only a part of the spinning reserve can be activated by the central regulator during secondary control. That part of the spinning reserve that belongs to the generators participating in secondary control is referred to as the *available regulation power*.

If the available regulation power is less than the lost power, then Stage IV of the dynamics will terminate when all the available regulation power has been used. This corresponds to the system trajectory settling at an equilibrium point somewhere between points III and IV on Figure 9.23 at a frequency that is lower than the reference value. The system operators may now verbally instruct other generating stations not on central control to increase their power output to help remove the frequency offset. In the case of a large power deficit, further action would consist of connecting new generating units from the cold reserve which, when connected, will release the capacity controlled by the central regulator. The frequency changes associated with this process are very slow and are not considered here.

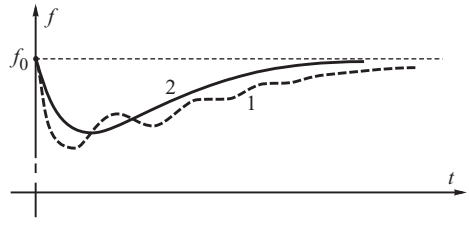

Figure 9.24 Examples of changes in frequency: 1, with a slow central regulator; 2, with a fast central regulator.

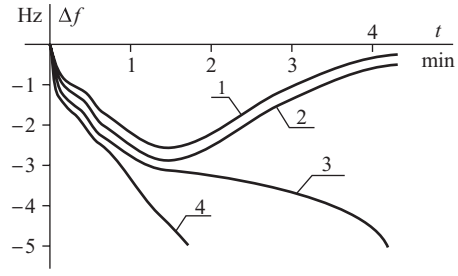

Figure 9.25 An example of the frequency variations when $\Delta P_0 = 10\,\%\Delta P_L$. Curve 1 corresponds to $r = 16\,\%$; 2 corresponds to $r = 14\,\%$; 3 corresponds to $r = 12\,\%$; and 4 corresponds to $r = 8\,\%$.

Equation (9.35) defines the contribution of each of the generating units in covering the power imbalance at the end of Stage III. In Stage IV the increase in generation is enforced by the central regulator and the contribution of each unit, and the ratio $\Delta P_{rIV}/\Delta P_{sIV}$, will depend on whether or not the particular generating unit participates in central control.

Provided that the spinning reserve and the available regulation power are large enough, then in many cases they can prevent the system suffering a frequency collapse. Figure 9.25 shows an example of how the frequency variations depend on the value of the spinning reserve coefficient. The disturbance consists of losing generation ΔP_0 equivalent to 10 % of the total load power P_L. In the first two cases $r \geq 14\,\%$ and the frequency returns to its reference value thanks to the operation of primary and secondary control. The third case corresponds to the frequency collapse shown in Figure 9.20. In the fourth case there is no intersection point between the generation and the load characteristic and the frequency quickly collapses.

9.5.1.1 The Energy Balance over the Four Stages

When a power system loses a generating unit it loses a source of both electrical and mechanical energy. By the end of the power system dynamic response, this lost energy has been recovered as illustrated in Figure 9.26. The upper bold curve shows the variations of the mechanical power provided by the system while the lower bold curve shows the variations of electrical power of the loads due to frequency variations. All these variations are similar to those shown in Figure 9.23c. Initially the energy shortfall is produced by converting the kinetic energy of the rotating masses of the generating units and the loads to electrical energy, area 1 and area 2. This reduction in kinetic

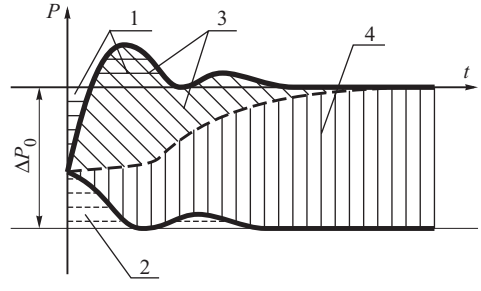

Figure 9.26 Share of the individual components in covering the power imbalance: 1, rotating masses of the generating units; 2, rotating masses of the loads; 3, primary control; 4, secondary control. Based on Welfonder (1980). Reproduced by permission of E. Welfoner.

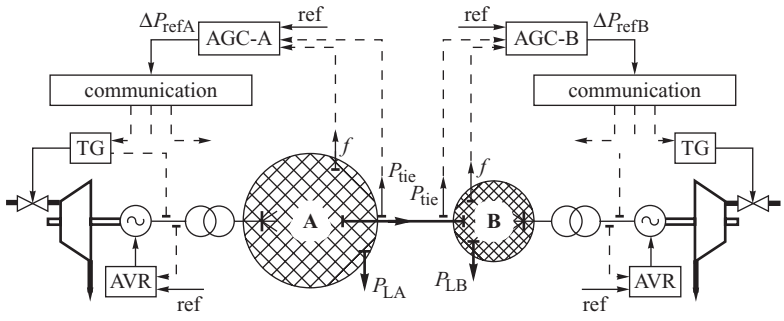

Figure 9.27 The functional diagram of an interconnected system consisting of two subsystems: a big system A and a small system B.

energy causes a drop in frequency which activates the turbine governor primary control so that the mechanical energy supplied to the system is increased but at a lower frequency, area 3. This energy is used partially to generate the required energy shortfall, and partially to return the kinetic energy borrowed from the rotating masses. Secondary control then further increases the mechanical energy, area 4, which is used to generate the required additional electrical energy and to increase the kinetic energy of the rotating masses so restoring the system frequency.

9.5.2 Interconnected Systems and Tie-Line Oscillations

This discussion will be limited to the interconnected system shown in Figure 9.27 consisting of two subsystems of disproportionate size, system A and system B, referred to as the big system and the small system respectively. The tie-line interchange power P_{tie} will be assumed to flow from the big system to the small system and an imbalance of power ΔP_0 assumed to arise in the small system. During the first three stages of the dynamics the influence of the central regulators in both system A and system B may be neglected.

Both systems are replaced by an equivalent generator, as in Figure 9.14b, to obtain the equivalent circuit of Figure 9.28a. In this circuit the reactance X combines the reactances of the tie-line connecting the two systems, the equivalent network reactance of both systems and the transient reactances of all the generators. As one of the subsystems is large compared with the other, the generator–infinite busbar model and the equal area criterion can be used to analyse Stage I of the dynamics.

The power–angle characteristic $P_{\text{B}}(\delta')$ of the small system is a sinusoid, corresponding to a power transfer between the systems, shifted by a constant value corresponding to the power demand in the small system P_{LB}. It is assumed that system B imports power from A so that $P_{\text{TB}} < P_{\text{LB}}$ and its power angle is negative with respect to system A. Before the disturbance occurs, the system operates at point 1 corresponding to the intersection of the $P_{\text{B}}(\delta')$ characteristic and the horizontal line representing the mechanical power $P_{\text{TB}-}$. The small system now loses generation equal to ΔP_0 and the power generated in this system drops to $P_{\text{TB}+}$. The electrical power exceeds the mechanical power and the rotors of the generators in system B slow down. The equivalent system rotor moves from point 1 to point 2 and then to point 3 in Figure 9.28b. Along this motion the electrical power generated in system B decreases and, as a result, additional power starts to flow from system A, Figure 9.28d. The maximum change in the value of the instantaneous power in the tie-lines increases to almost double the value of the lost power, the difference between points 1 and 3. Oscillations in the power begin during which kinetic energy in both systems is used to cover the lost generation. The angular velocities of the generator rotors drop and the system enters Stage II of the dynamics.

Stage I of the dynamics is dangerous from a stability point of view in that if the area 1–1′–2 is greater than the area 2–3–4 then the system loses stability and the small system will operate

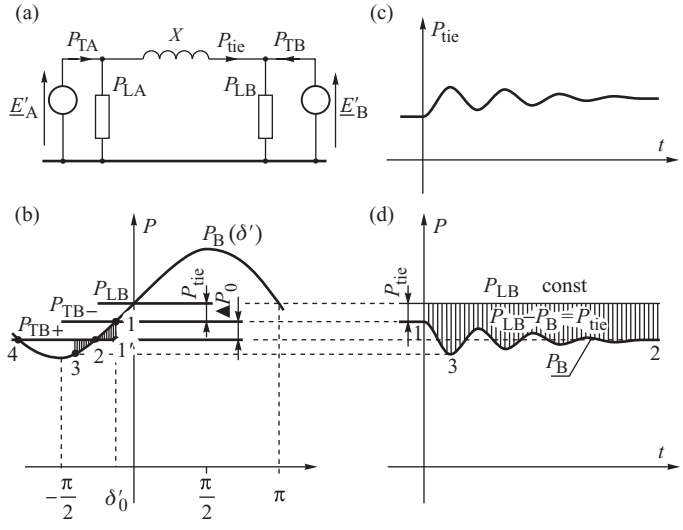

Figure 9.28 Application of the equal area criterion to determine the tie-line power during the first stage of the dynamics: (a) equivalent circuit; (b) the power–angle characteristic taking into account equivalent loads; (c) changes in the tie-line power; (d) changes in the generated power. The time duration of the phenomena is a few seconds.

asynchronously with respect to the big system with $\omega_B < \omega_A$. Such a situation may occur when the tie-line capacity is small and the disturbance in power balance large. During asynchronous operation large oscillations in the power tie-line power will occur with the difference between the maximum and the minimum value being twice the amplitude of the sinusoid shown in Figure 9.28b. As the possibility of resynchronizing the systems is small, they would usually be disconnected to avoid damaging equipment in either system.

In Stage II the power imbalance is covered in proportion to the inertia coefficients of the equivalent systems as determined by Equations (9.28), that is

$$\Delta P_{AII} = \frac{M_A}{M_A + M_B}\Delta P_0 \quad \text{and} \quad \Delta P_{BII} = \frac{M_B}{M_A + M_B}\Delta P_0, \tag{9.41}$$

where $M_A = \sum_{i=1}^{N_{GA}} M_i$ and $M_B = \sum_{i=1}^{N_{GB}} M_i$ are the sums of the inertia coefficients of the rotating masses in each system. Equations (9.41) suggest that the big system A will almost entirely cover the power imbalance since $M_A \gg M_B$, so in Stage II of the frequency variations $\Delta P_{tieII} \approx \Delta P_0$ and the tie-lines will be additionally loaded with a value of the power lost in system B.

At the end of Stage III the frequency drops by a value Δf_{III} that can be calculated from the system stiffness K_f defined in Equation (9.33). ΔP_0 is given by

$$\Delta P_0 = (\Delta P_{TAIII} - \Delta P_{LAIII}) + (\Delta P_{TBIII} - \Delta P_{LBIII}), \tag{9.42}$$

and, when substituting the values for K_{TA}, K_{LA}, K_{TB} and K_{LB} obtained from Equations (9.39) and (9.6), a similar formula to that in Equation (9.33) for the frequency drop in Stage III is obtained:

$$\frac{\Delta f_{III}}{f_n} = \frac{-1}{K_{fA}P_{LA} + K_{fB}P_{LB}}\Delta P_0, \tag{9.43}$$

where $K_{fA} = K_{TA} + K_{LA}$ and $K_{fB} = K_{TB} + K_{LB}$ are the stiffnesses of the big and the small system respectively. The increase in the tie-line interchange can be determined from a power balance on

one of the systems, in this case the big system A, when

$$\begin{aligned}\Delta P_{\text{tieIII}} &= \Delta P_{\text{TAIII}} - \Delta P_{\text{LAIII}} = -(K_{\text{TA}} + K_{\text{LA}})\, P_{\text{LA}} \frac{\Delta f_{\text{III}}}{f_{\text{n}}} \\ &= -K_{\text{fA}} P_{\text{LA}} \frac{\Delta f_{\text{III}}}{f_{\text{n}}} = \frac{K_{\text{fA}} P_{\text{LA}}}{K_{\text{fA}} P_{\text{LA}} + K_{\text{fB}} P_{\text{LB}}} \Delta P_0.\end{aligned} \tag{9.44}$$

Under the assumption that $P_{\text{LA}} \gg P_{\text{LB}}$ this formula simplifies to $\Delta P_{\text{tieIII}} \approx \Delta P_0$ when, during Stage III, the tie-line power interchange is increased by the value of the lost power, as during Stage II. Such an increase in the power flow may result in system instability when the interconnected systems split into two asynchronously operating subsystems. Also, with such a large power transfer the thermal limit on the line may be exceeded when the overcurrent relays trip the line, again leading to asynchronous operation of both systems.

Assuming that the tie-line remains intact, the increase in the tie-line interchange power, combined with the drop of frequency, will force the central regulators in both systems to intervene. The ACE at the end of Stage III can be calculated from Equation (9.11) using the formulae given in Equations (9.43) and (9.44) as

$$\text{ACE}_{\text{A}} = -\Delta P_{\text{tieIII}} - \lambda_{\text{RA}} \Delta f_{\text{III}} \quad \text{and} \quad \text{ACE}_{\text{B}} = +\Delta P_{\text{tieIII}} - \lambda_{\text{RB}} \Delta f_{\text{III}}. \tag{9.45}$$

As explained in Section 9.1 (Equation (9.10)), the ideal regulator bias settings are

$$\lambda_{\text{RA}} = K_{\text{fA}} \frac{P_{\text{LA}}}{f_{\text{n}}} \quad \text{and} \quad \lambda_{\text{RB}} = K_{\text{fB}} \frac{P_{\text{LB}}}{f_{\text{n}}}, \tag{9.46}$$

but this is difficult to achieve in practice as the values of the stiffnesses K_{fA} and K_{fB} can only be estimated. Consequently, assuming that K_{RA} and K_{RB} are estimates of K_{fA} and K_{fB} respectively, then the bias settings are

$$\lambda_{\text{RA}} = K_{\text{RA}} \frac{P_{\text{LA}}}{f_{\text{n}}} \quad \text{and} \quad \lambda_{\text{RB}} = K_{\text{RB}} \frac{P_{\text{LB}}}{f_{\text{n}}}, \tag{9.47}$$

and Equations (9.45) become

$$\text{ACE}_{\text{A}} = -\Delta P_{\text{tieIII}} - \lambda_{\text{RA}} \Delta f_{\text{III}} = \frac{-K_{\text{fA}} P_{\text{LA}} + K_{\text{RA}} P_{\text{LA}}}{K_{\text{fA}} P_{\text{LA}} + K_{\text{fB}} P_{\text{LB}}} \Delta P_0, \tag{9.48}$$

$$\text{ACE}_{\text{B}} = +\Delta P_{\text{tieIII}} - \lambda_{\text{RB}} \Delta f_{\text{III}} = \frac{K_{\text{fA}} P_{\text{LA}} + K_{\text{RB}} P_{\text{LB}}}{K_{\text{fA}} P_{\text{LA}} + K_{\text{fB}} P_{\text{LB}}} \Delta P_0. \tag{9.49}$$

9.5.2.1 Ideal Settings of the Regulators

Assume that the stiffnesses K_{fA} and K_{fB} of both systems are known and that the central regulator bias settings λ_{RA} and λ_{RB} are selected such that

$$K_{\text{RA}} = K_{\text{fA}}, \quad K_{\text{RB}} = K_{\text{fB}}. \tag{9.50}$$

In this case, Equations (9.48) and (9.49) give

$$\text{ACE}_{\text{A}} = 0 \quad \text{and} \quad \text{ACE}_{\text{B}} = \Delta P_0, \tag{9.51}$$

and the central regulator of the big system, system A, will not demand an increase in the power generation in its area. Only the small system will increase its generation in order to cover its own power imbalance. If the available regulation power in the small system is high enough to cover the lost generation then the big system will not intervene at all and, as the generation in the small system is increased, the tie-line power interchange will drop to its scheduled value.

The value of the system stiffness $K_f = K_T + K_L$ is never constant because it depends on the composition of the system load and generation and on the spinning reserve. Consequently, the condition defined by Equation (9.50) is almost never satisfied and the central regulator of the bigger system will take part in the secondary control to an amount defined by Equation (9.48).

Example 9.2

An interconnected system consists of two subsystems of different size. The data of the subsystems are: f_n= 50 Hz, P_{LA}=37 500 MW, $K_{TA} = 8$ (ρ_{TA}= 0.125), $K_{LA} \approx 0$, $K_{RA} = K_{TA}$, $P_{LB} = 4000$ MW, $K_{TB} = 10$ ($\rho_{TB} = 0.1$), $K_{LB} \approx 0$, $K_{RB} = K_{TB}$.

Two large generating units are suddenly lost in the smaller system producing a power deficit of $\Delta P_0 = 1300$ MW, that is 32.5 % of the total generation in this subsystem. The resulting frequency and power variations for both subsystems, assuming no limits on the power generation (linear generation characteristics), are shown in Figure 9.29.

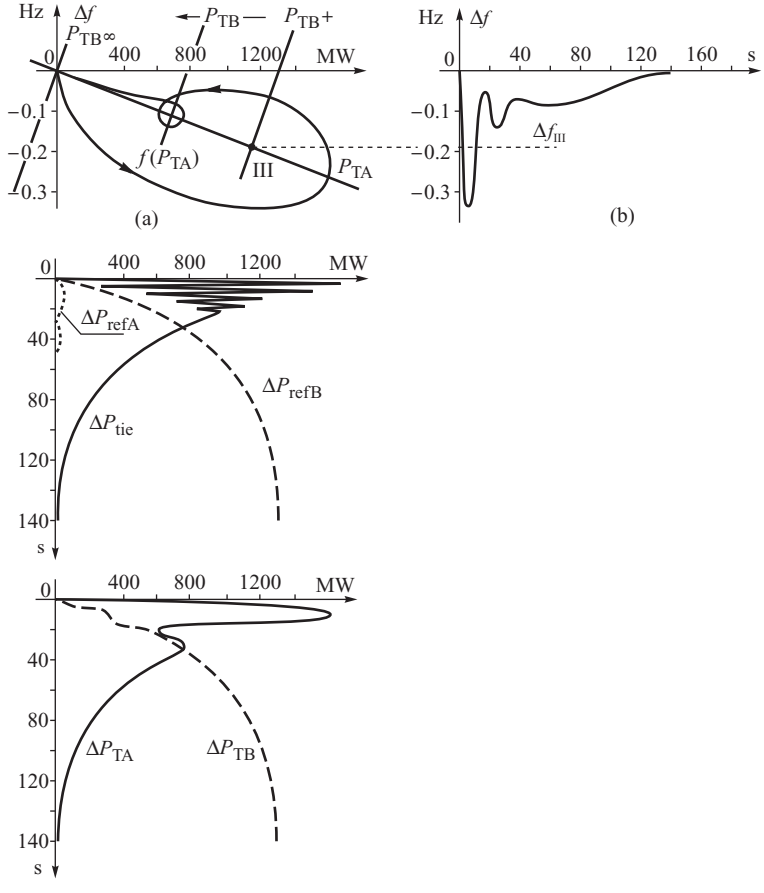

Figure 9.29 Illustration for Example 9.2: (a) the static characteristics of both systems and the trajectory $f(P_{TA})$; (b) frequency variations; (c) tie-line power interchange oscillations and the change of power demanded by the central regulators of both subsystems; (d) change in the mechanical power supplied by the turbines.

The characteristic P_{TA} has a small slope corresponding to $K_{TA}P_{LA}/f_n = 6000$ MW/Hz. The slope of the characteristic of the smaller system is much higher and corresponds to $K_{TB}P_{LB}/f_n = 800$ MW/Hz. The characteristic P_{TB+} is inverted and shifted by $\Delta P_0 = 1300$ MW, so that intersection of the characteristics P_{TB+} and P_{TA} determines the frequency deviation Δf_{III} at point III. The central regulator of the small system acts fast enough for the P_{TB} characteristic to move so that point III is not reached. Further action due to the integral term in the regulator shifts the characteristic P_{TB} slowly to the position $P_{TB\infty}$ corresponding to nominal frequency.

It is worth noting the small frequency oscillations characteristic of the third stage of the dynamics. Because of the fast-acting central regulator, these oscillations take place above the value Δf_{III}, Figure 9.29b. The tie-line power flow initially increases very quickly in Stage I of the dynamics, and then oscillates around the scheduled value increased by the value of the lost generation. The period of oscillations is around 3 s. Then, as the central regulator in the small system enforces an increase in the generation, the tie-line flow slowly decreases to its scheduled value.

The central PI regulator quite quickly creates the output signal ΔP_{refB} as shown in Figure 9.29c. The generating units respond to this increased power demand by increasing the generation by ΔP_{TB}, Figure 9.29d. Because of the primary turbine control, the mechanical power of the big system P_{TA} initially increases to cover the power imbalance and then quickly drops to the instantaneous equilibrium point corresponding to the end of Stage III. After that P_{TA} slowly decreases as the generation P_{TB}, forced by secondary control, increases. At the same time the frequency increases so that the frequency error of the central regulator of the big system becomes negligibly small and the regulator becomes inactive.

9.5.2.2 Non-Ideal Settings of the Central Regulator

If $K_{RA} > K_{fA}$, then the signal $\lambda_{RA}\Delta f$ is initially larger than the signal ΔP_{tie} and the regulator tries to increase the generation in system A. Although the increased generation speeds up the rate at which the frequency increases, it slows down the rate at which the tie-line error ΔP_{tie} decreases and in some cases can lead to a temporary increase in this error. Consequently, the signal ΔP_{tie} becomes greater than the signal $\lambda_{RA}\Delta f$ and the central regulator starts to reduce the generation in system A, so essentially withdrawing this subsystem from secondary control.

If $K_{RA} < K_{fA}$, then the signal ΔP_{tie} is initially higher than the signal $\lambda_{RA}\Delta f$ and the regulator of the big system tries to reduce its generation despite the fact that the frequency is smaller than nominal. This drop in generation is not desirable from the frequency regulation point of view but does reduce the tie-line flows. When $\lambda_{RA}\Delta f$ becomes larger than ΔP_{tie} the regulator will start to increase the recently reduced generation so as to re-establish the required power in system A.

In both the above cases the inaccuracy of the frequency bias setting causes unnecessary intervention of the bigger system in covering the generation loss in the smaller system. In the above example a large amount of regulation power was available so that use of the non-ideal regulator settings was not dangerous. However, should the amount of regulation power available be insufficient to cover the lost power then the consequence of non-ideal regulator settings becomes more significant as described below.

9.5.2.3 Insufficient Available Regulation Power

When the available regulation power ΔP_{regB} in the small system is less than the generation loss ΔP_0 then system B is unable to cover the power loss on its own and the big system A must intervene to cover part of the lost power. Initially the dynamics are identical to the case in which the regulation power in the small system was unlimited. The difference between the two cases appears when the small system has used up all its available regulation power. Further changes can only take place via regulation of the big system. Its central regulator is now subject to two error signals of opposite

sign (Figure 9.12). The signal $\lambda_{RA}\Delta f$ generated by the frequency error demands an increase in the generation while the signal ΔP_{tie} generated by the tie-line power deviation demands a decrease in the generation. The regulation process terminates when the signals balance each other and the total error signal is zero. Denoting the final steady-state values of the error signals as Δf_∞ and $\Delta P_{tie\infty}$, the regulation equation is

$$\mathrm{ACE_A} = -\Delta P_{tie\,\infty} - K_{RA} P_{LA} \frac{\Delta f_\infty}{f_n} = 0. \tag{9.52}$$

On the other hand, the tie-line power interchange must satisfy the overall power balance of the small system

$$\Delta P_0 - \Delta P_{regB} = \Delta P_{tie\,\infty} - (K_{TB} + K_{LB})\, P_{LB} \frac{\Delta f_\infty}{f_n}. \tag{9.53}$$

Physically this means that the power imbalance in the small system B may be covered partly by an increase in the power imported from the big system A, partly by a change in internal generation and partly by a decreased demand resulting from the frequency drop in the whole interconnected system. Solving Equations (9.52) and (9.53) gives

$$\Delta P_{tie\infty} = \frac{K_{RA} P_{LA}}{K_{RA} P_{LA} + K_{fB} P_{LB}} \left(\Delta P_0 - \Delta P_{regB}\right), \tag{9.54}$$

$$\frac{\Delta f_\infty}{f_n} = -\frac{1}{K_{RA} P_{LA} + K_{fB} P_{LB}} \left(\Delta P_0 - \Delta P_{regB}\right). \tag{9.55}$$

Under the assumption that $P_{LA} \gg P_{LB}$ Equations (9.54) and (9.55) may be simplified to

$$\Delta P_{tie\,\infty} \cong \left(\Delta P_0 - \Delta P_{regB}\right), \tag{9.56}$$

$$\frac{\Delta f_\infty}{f_n} \cong -\frac{1}{K_{RA} P_{LA}} (\Delta P_0 - \Delta P_{regB}). \tag{9.57}$$

Additional validity is given to this simplification if the small system is fully loaded ($\Delta P_{regB} = 0$ and $K_{TB} = 0$) when the stiffness $K_{fB} = K_{TB} + K_{LB}$ has a small value corresponding to the frequency sensitivity of the loads K_{LB}. In this situation the whole power imbalance is covered by the tie-line interchange.

The frequency deviation Δf_∞ is inversely proportional to the coefficient $\lambda_{RA} = K_{RA} P_{LA}/f_n$ set at the central regulator. If the available regulation power is not large enough then too low a setting of the central regulator produces a steady-state frequency error. If $K_{RA} = K_{fA}$ then the final value of the frequency will correspond to the frequency level at which the available regulation power of the small system has run out. If $K_{RA} > K_{fA}$ then the regulator of the big system will increase its generation, decreasing the frequency error and allowing the tie-line interchange error to increase. If $K_{RA} < K_{fA}$, then the regulator of the big system will decrease its generation, increasing the frequency error, and the tie-line interchange error will not be allowed to increase. This can be illustrated by the following example.

Example 9.3

The available regulating power of the small subsystem considered in Example 9.2 is $\Delta P_{regB} = 500$ MW. The settings of the central regulators are $K_{RA} = 5.55 < K_{TA}$ and $K_{RB} = 12.5 > K_{TB}$. Neglecting the frequency sensitivity of the load, Equations (9.56) and (9.57) give: $\Delta P_{tie\infty} = 800$ MW and $\Delta f_\infty = -0.16$ Hz. The power and frequency variations are illustrated in Figure 9.30. During the first 20 s of the disturbance the trajectory is the same as the one shown in

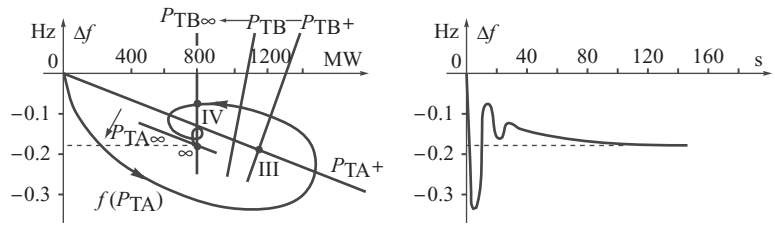

Figure 9.30 Illustration for Example 9.3.

Figure 9.29, but now the characteristic P_{TB} eventually settles at $P_{TB\infty}$. Trajectory $f(P_{TA})$ begins to wrap around the instantaneous equilibrium point IV, but the big system regulator decreases its generation shifting the characteristic from position P_{TA+} to position $P_{TA\infty}$. The dynamics end up at point ∞ where the frequency of the interconnected system is lower, by about $\Delta f_\infty = -0.16$ Hz, than the required value. A small portion of the trajectory $f(P_{TA})$, between point IV and ∞, corresponds to a slow reduction of frequency over several tens of seconds. The variations in the tie-line power interchange are similar to those shown in Figure 9.29, but settle down at a level corresponding to point ∞, that is $\Delta P_{tie\infty} = 800$ MW (the generation lost was $\Delta P_0 = 1300$ MW).

If the tie-line power interchange determined by Equation (9.54) is greater than the maximal thermal capacity of the tie-line, then the line will be tripped and the systems separated. The imbalance of power in the small system will cause a further drop in frequency which, in the absence of automatic load shedding, may lead to frequency collapse in that subsystem.

9.6 FACTS Devices in Tie-Lines

Series FACTS devices, described in Section 2.4.4, may be installed in tie-lines linking control areas in an interconnected power system. Their main function is execution of steady-state control functions described in Section 3.6. During the transient state caused by a sudden disturbance of a power balance in one of the subsystems, series FACTS devices installed in the tie-lines may affect the values of tie-line power interchanges P_{tie} and therefore also the value of the ACE given by (9.11) and the dynamics of secondary control executed by the central regulator shown in Figure 9.10. Hence a proper control algorithm and proper parameter selection have to be implemented at the regulator of the series FACTS device so that the control does not deteriorate the frequency and tie-line power interchange regulation process. This problem will be discussed in detail using as an example a thyristor-controlled phase angle regulator (TCPAR) which, from the power system point of view, acts as a fast phase shifting transformer.

A schematic diagram of a TCPAR regulator is shown in Figure 9.31. An integral-type regulator with negative feedback is placed in the main control path. The task of the regulator is to regulate real power flow in the line in which the FACTS device is installed. The reference value is supplied from the supervisory control system. A supplementary control loop devoted to damping of power swings and improving power stability is shown in the lower part of the diagram.

From the point of view of power system dynamics, an important problem for a series FACTS device installed in a tie-line is the control algorithm executing the supplementary control loop ensuring damping of interarea power swings in such a way that the frequency control executed by the central LFC regulator is not disturbed. The control algorithm described in this section is based on Nogal (2008).

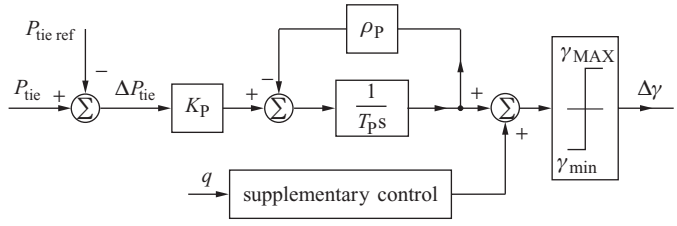

Figure 9.31 Power flow controller installed in a tie-line of an interconnected power system.

9.6.1 Incremental Model of a Multi-Machine System

Figure 9.32 illustrates the stages of developing a model of a phase shifting transformer installed in a tie-line. A booster voltage, which is in quadrature to the supply voltage, is injected in the transmission line using a booster transformer:

$$\Delta V_{\text{P}} = \gamma V_{\text{a}}, \tag{9.58}$$

where γ is the controlled variable. The booster transformer reactance has been added to the equivalent line reactance. To simplify considerations, the line and transformer resistances have been neglected.

The following relationships can be derived using the phasor diagram of Figure 9.32:

$$\sin\theta = \frac{\Delta V_{\text{P}}}{V_{\text{c}}} = \frac{\gamma V_{\text{a}}}{V_{\text{c}}}; \quad \cos\theta = \frac{V_{\text{a}}}{V_{\text{c}}}; \quad \delta_{\text{cb}} = \delta_{\text{ab}} + \theta. \tag{9.59}$$

According to Equation (3.15), real power flowing through a transmission line is given by

$$P_{\text{ab}} = P_{\text{cb}} = \frac{V_{\text{c}} V_{\text{b}}}{X} \sin\delta_{\text{cb}}. \tag{9.60}$$

Substituting (9.59) gives

$$\begin{aligned} P_{\text{ab}} &= \frac{V_{\text{c}} V_{\text{b}}}{X} \sin(\delta_{\text{ab}} + \theta) = \frac{V_{\text{c}} V_{\text{b}}}{X} (\sin\delta_{\text{ab}} \cos\theta + \cos\delta_{\text{ab}} \sin\theta) \\ &= \frac{V_{\text{a}} V_{\text{b}}}{X} \sin\delta_{\text{ab}} + \gamma \frac{V_{\text{a}} V_{\text{b}}}{X} \cos\delta_{\text{ab}}. \end{aligned} \tag{9.61}$$

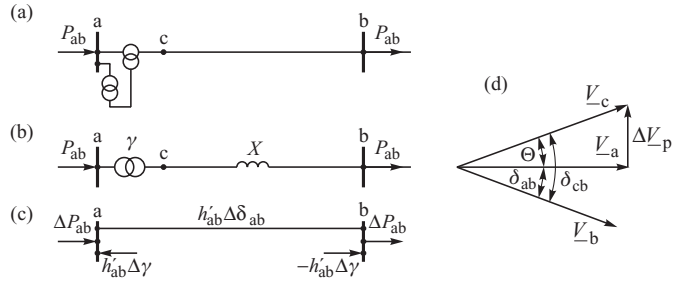

Figure 9.32 Stages of developing an incremental model of a transmission line with a phase shifting transformer: (a) one-line diagram; (b) admittance model with ideal transformation ratio; (c) incremental model; (d) phasor diagram.

This equation can also be written as

$$P_{ab} = b_{ab}\ \sin\delta_{ab} - b_{ab}\ \cos\delta_{ab}\gamma(t), \tag{9.62}$$

where $b_{ab} = V_a V_b / X$ is the amplitude of the power–angle characteristic of the transmission line.

The values of variables at a given operating point are $(\hat{P}_{ab}, \hat{\delta}, \hat{\gamma})$. Using these values, Equation (9.62) gives

$$\hat{P}_{ab} = b_{ab}\ \sin\hat{\delta}_{ab} - b_{ab}\ \cos\hat{\delta}_{ab}\ \hat{\gamma}. \tag{9.63}$$

The tie-line flow in (9.62) depends on both the power angle δ_{ab} and the quadrature transformation ratio $\gamma(t)$. Taking that into account and differentiating (9.62) in the vicinity of the operating point gives

$$\Delta P_{ab} = \left.\frac{\partial P_{ab}}{\partial \delta_{ab}}\right|_{\delta_{ab}=\hat{\delta}_{ab}} \Delta\delta_{ab} + \left.\frac{\partial P_{ab}}{\partial \gamma}\right|_{\gamma=\hat{\gamma}} \Delta\gamma. \tag{9.64}$$

Hence, taking into account (9.62),

$$\Delta P_{ab} = \left(b_{ab}\ \cos\ \hat{\delta}_{ab} + \hat{\gamma}\ b_{ab}\sin\hat{\delta}_{ab}\right)\Delta\delta - \left(b_{ab}\ \cos\ \hat{\delta}_{ab}\right)\Delta\gamma. \tag{9.65}$$

The coefficients $b_{ab}\cos\hat{\delta}_{ab}$ and $b_{ab}\sin\hat{\delta}_{ab}$ in this equation are the same as those in (9.63). Component $b_{ab}\sin\hat{\delta}_{ab}$ can be eliminated from (9.65) using (9.63) in the following way. Equation (9.63) gives

$$b_{ab}\sin\hat{\delta}_{ab} = \hat{P}_{ab} + \hat{\gamma} b_{ab}\ \cos\ \hat{\delta}_{ab}, \tag{9.66}$$

or

$$\hat{\gamma} b_{ab}\sin\hat{\delta}_{ab} = \hat{\gamma}\,\hat{P}_{ab} + \hat{\gamma}^2 b_{ab}\ \cos\ \hat{\delta}_{ab}. \tag{9.67}$$

Substituting this equation into (9.65) gives

$$\Delta P_{ab} = \left[\left(1+\hat{\gamma}^2\right)\left(b_{ab}\ \cos\ \hat{\delta}_{ab}\right) + \hat{\gamma}\,\hat{P}_w\right]\Delta\delta_{ab} - \left(b_{ab}\ \cos\ \hat{\delta}_{ab}\right)\Delta\gamma. \tag{9.68}$$

The following notation is now introduced:

$$h_{ab} = \left.\frac{\partial P_{ab}}{\partial \delta_{ab}}\right|_{\delta_{ab}=\hat{\delta}_{ab},\ \hat{\gamma}=0} = b_{ab}\ \cos\ \hat{\delta}_{ab}, \tag{9.69}$$

$$h'_{ab} = \left(1+\hat{\gamma}^2\right)\left(b_{ab}\ \cos\ \hat{\delta}_{ab}\right) + \hat{\gamma}\,\hat{P}_{ab} = \left(1+\hat{\gamma}^2\right)h_{ab} + \hat{\gamma}\,\hat{P}_{ab}. \tag{9.70}$$

The variable h_{ab} given by (9.69) corresponds to the mutual synchronizing power for the line ab calculated neglecting the booster transformer. On the other hand, h'_{ab} given by (9.70) corresponds to the synchronizing power when the booster transformer has been taken into account. Using that notation, Equation (9.68) takes the form

$$\Delta P_{ab} = h'_{ab}\ \Delta\delta_{ab} - h_{ab}\ \Delta\gamma. \tag{9.71}$$

Equation (9.71) describes the incremental model of the transmission line shown in Figure 9.32c. There is an equivalent transmission line between nodes 'a' and 'b'. A change in the flow in that line corresponds to a change in the voltage angles at both nodes. Nodal power injections correspond to flow changes due to regulation of the quadrature transformation ratio $\gamma(t)$. The power injections

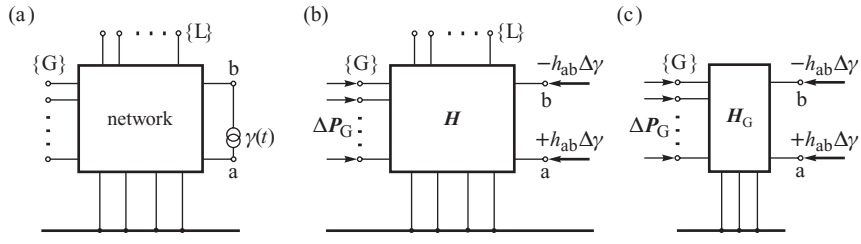

Figure 9.33 Stages of developing the incremental model: (a) admittance model with a phase shifting transformer; (b) incremental model; (c) incremental model after elimination of nodes {L}.

in nodes 'a' and 'b' are $+h_{ab}\ \Delta\gamma$ and $-h_{ab}\ \Delta\gamma$, respectively. To understand this, note that (9.71) holds for node 'a' while the same equation for node 'b' is

$$h'_{ab}\ \Delta\delta_{ab} = \Delta P_{ab} + h_{ab}\ \Delta\gamma. \tag{9.72}$$

It will be shown later that the derived incremental model of a branch with a phase shifting transformer is convenient for network analysis, especially for large networks, because it models changes in the quadrature transformation ratio by changes in power injections without changing the parameters of the branches.

Equation (3.157) derived in Section 3.6 modelled the effect of small changes of nodal voltages in a network. In analysing system frequency regulation, one can assume that changes in voltage magnitudes can be neglected and only changes in voltage angles are considered. Then Equation (3.157) takes the form

$$\Delta \boldsymbol{P} \cong \boldsymbol{H}\Delta\boldsymbol{\delta}, \tag{9.73}$$

where $\Delta\boldsymbol{P}$ and $\Delta\boldsymbol{\delta}$ are the vectors of changes in real power injections and voltage angles, respectively. Matrix $\boldsymbol{H}$ is the Jacobi matrix and consists of the partial derivatives $H_{ij} = \partial P_i/\partial\delta_j$. Equation (9.73) describes the *incremental model* of a network. Including a phase shifting transformer in incremental model of a network is illustrated in Figure 9.33. There are the following node types:

- {G} – generator nodes behind transient generator reactances;
- (L} – load nodes;
- a,b – terminal nodes of a line with a phase shifting transformer (as in Figure 9.32).

The line with the phase shifting transformer, Figure 9.33, is modelled using a transformation ratio and a branch. In the incremental model shown in Figure 9.33 this line is modelled in the same way as shown in Figure 9.32. Matrix $\boldsymbol{H}$ describing that network includes branch h'_{ab} from the incremental line model with the phase shifting transformer. There are real power injections in nodes 'a' and 'b', similar to Figure 9.32c, corresponding to flow changes due to transformation ratio regulation $\gamma(t)$.

Now Equation (9.73) describing the model shown in Figure 9.33b can be expanded as

$$\begin{matrix}\{\mathrm{G}\}\\ \mathrm{a}\\ \mathrm{b}\\ \{\mathrm{L}\}\end{matrix}\begin{bmatrix}\Delta\boldsymbol{P}_{\mathrm{G}}\\ \hline +h_{ab}\Delta\gamma\\ \hline -h_{ab}\Delta\gamma\\ \hline \boldsymbol{0}\end{bmatrix} \cong \begin{bmatrix}\\ \boldsymbol{H}\\ \\ \end{bmatrix}\begin{bmatrix}\Delta\boldsymbol{\delta}_{\mathrm{G}}\\ \hline \Delta\delta_{\mathrm{a}}\\ \hline \Delta\delta_{\mathrm{b}}\\ \hline \Delta\boldsymbol{\delta}_{\mathrm{L}}\end{bmatrix}. \tag{9.74}$$

Substitution $\Delta \boldsymbol{P}_{\mathrm{L}} = 0$ has been made on the left hand side of (9.74) because loads at $\{\mathrm{L}\}$ nodes are modelled as constant powers. Eliminating variables related to load nodes $\{\mathrm{L}\}$ in (9.74) by using the partial inversion method shown in Appendix A.2 makes it possible to transform Equation (9.74) to the following form:

$$\begin{matrix}\{\mathrm{G}\}\\ \mathrm{a}\\ \mathrm{b}\end{matrix}\left[\begin{array}{c}\Delta \boldsymbol{P}_{\mathrm{G}}\\ \hdashline +h_{\mathrm{ab}}\Delta\gamma\\ \hdashline -h_{\mathrm{ab}}\Delta\gamma\end{array}\right] \cong \left[\begin{array}{c:c:c}\boldsymbol{H}_{\mathrm{GG}} & \boldsymbol{H}_{\mathrm{Ga}} & \boldsymbol{H}_{\mathrm{Gb}}\\ \hdashline \boldsymbol{H}_{\mathrm{aG}} & H_{\mathrm{aa}} & H_{\mathrm{ab}}\\ \hdashline \boldsymbol{H}_{\mathrm{bG}} & H_{\mathrm{ba}} & H_{\mathrm{bb}}\end{array}\right]\left[\begin{array}{c}\Delta\boldsymbol{\delta}_{\mathrm{G}}\\ \hdashline \Delta\delta_{\mathrm{a}}\\ \hdashline \Delta\delta_{\mathrm{b}}\end{array}\right]. \tag{9.75}$$

This equation can be further transformed by partial inversion to the following equations:

$$\Delta \boldsymbol{P}_{\mathrm{G}} \cong \boldsymbol{H}_{\mathrm{G}}\Delta\boldsymbol{\delta}_{\mathrm{G}} + \left[\begin{array}{c:c}\boldsymbol{K}_{\mathrm{Ga}} & \boldsymbol{K}_{\mathrm{Gb}}\end{array}\right]\left[\begin{array}{c}+h_{\mathrm{ab}}\ \ \Delta\gamma\\ \hdashline -h_{\mathrm{ab}}\ \ \Delta\gamma\end{array}\right], \tag{9.76}$$

$$\left[\begin{array}{c}\Delta\delta_{\mathrm{a}}\\ \hdashline \Delta\delta_{\mathrm{b}}\end{array}\right] \cong -\left[\begin{array}{c}\boldsymbol{K}_{\mathrm{aG}}\\ \hdashline \boldsymbol{K}_{\mathrm{bG}}\end{array}\right]\Delta\boldsymbol{\delta}_{\mathrm{G}} + \left[\begin{array}{c:c}H_{\mathrm{aa}} & H_{\mathrm{ab}}\\ \hdashline H_{\mathrm{ba}} & H_{\mathrm{ba}}\end{array}\right]^{-1}\left[\begin{array}{c}+h_{\mathrm{ab}}\ \ \Delta\gamma\\ \hdashline -h_{\mathrm{ab}}\ \ \Delta\gamma\end{array}\right], \tag{9.77}$$

where

$$\boldsymbol{H}_{\mathrm{G}} = \boldsymbol{H}_{\mathrm{GG}} - \left[\begin{array}{c:c}\boldsymbol{H}_{\mathrm{Ga}} & \boldsymbol{H}_{\mathrm{Gb}}\end{array}\right]\left[\begin{array}{c:c}H_{\mathrm{aa}} & H_{\mathrm{ab}}\\ \hdashline H_{\mathrm{ba}} & H_{\mathrm{ba}}\end{array}\right]^{-1}\left[\begin{array}{c}\boldsymbol{H}_{\mathrm{aG}}\\ \hdashline \boldsymbol{H}_{\mathrm{bG}}\end{array}\right], \tag{9.78}$$

$$\left[\begin{array}{c:c}\boldsymbol{K}_{\mathrm{Ga}} & \boldsymbol{K}_{\mathrm{Gb}}\end{array}\right] = \left[\begin{array}{c:c}\boldsymbol{H}_{\mathrm{Ga}} & \boldsymbol{H}_{\mathrm{Gb}}\end{array}\right]\left[\begin{array}{c:c}H_{\mathrm{aa}} & H_{\mathrm{ab}}\\ \hdashline H_{\mathrm{ba}} & H_{\mathrm{ba}}\end{array}\right]^{-1} \tag{9.79}$$

$$\left[\begin{array}{c}\boldsymbol{K}_{\mathrm{aG}}\\ \hdashline \boldsymbol{K}_{\mathrm{bG}}\end{array}\right] = \left[\begin{array}{c:c}H_{\mathrm{aa}} & H_{\mathrm{ab}}\\ \hdashline H_{\mathrm{ba}} & H_{\mathrm{ba}}\end{array}\right]^{-1}\left[\begin{array}{c}\boldsymbol{H}_{\mathrm{aG}}\\ \hdashline \boldsymbol{H}_{\mathrm{bG}}\end{array}\right]. \tag{9.80}$$

Equations (9.76) and (9.77) describe the incremental model shown in Figure 9.33c. The former describes how a change in the transformation ratio of a phase shifting transformer affects power changes in all power system generators. The latter describes the influence of changes in the transformation ratio on the voltage angle changes in the terminal nodes of the line with the phase shifting transformer.

Equation (9.76) can be transformed to

$$\Delta \boldsymbol{P}_{\mathrm{G}} \cong \boldsymbol{H}_{\mathrm{G}}\ \Delta\boldsymbol{\delta}_{\mathrm{G}} + \Delta\boldsymbol{K}_{\mathrm{ab}}\ h_{\mathrm{ab}}\ \Delta\gamma, \tag{9.81}$$

where

$$\Delta\boldsymbol{K}_{\mathrm{ab}} = \boldsymbol{K}_{\mathrm{Ga}} - \boldsymbol{K}_{\mathrm{Gb}}. \tag{9.82}$$

Hence a power change in the ith generator can be expressed as

$$\Delta P_i \cong \sum_{j\in\{\mathrm{G}\}} H_{ij}\ \Delta\delta_j + \Delta K_i\ h_{\mathrm{ab}}\ \Delta\gamma, \tag{9.83}$$

where $\Delta K_i = K_{i\mathrm{a}} - K_{i\mathrm{b}}$. Thus, if $K_{i\mathrm{a}} \cong K_{i\mathrm{b}}$ then changes in $\Delta\gamma$ cannot influence power changes in the ith generator. In other words, that generator cannot be controlled using that phase shifting transformer. Coefficients $K_{i\mathrm{a}}$, $K_{i\mathrm{b}}$ can be treated as measures of the distance from nodes 'a' and 'b' to the ith generator. This means that if nodes 'a' and 'b' are at the same distance from the ith generator then the device cannot influence the generator. This can be checked using Figure 9.33c,

since power injections in nodes 'a' and 'b' have opposite signs. Hence if the distances are the same, then the influences on that generator cancel each other out.

The swing equation describing increments of rotor angles, Equation (5.15) in Section 5.1, is

$$\begin{aligned} \frac{\mathrm{d}\Delta\delta_i}{\mathrm{d}t} &= \Delta\omega_i \\ M_i \frac{\mathrm{d}\Delta\omega_i}{\mathrm{d}t} &= -\Delta P_i - D_i\ \Delta\omega_i, \end{aligned} \tag{9.84}$$

for $i \in \{\mathrm{G}\}$. As the network equations were derived in matrix form, it is convenient to write the above equation in matrix form too:

$$\begin{aligned} \Delta\dot{\boldsymbol{\delta}}_{\mathrm{G}} &= \Delta\boldsymbol{\omega}_{\mathrm{G}} \\ \boldsymbol{M}\Delta\dot{\boldsymbol{\omega}}_{\mathrm{G}} &= -\Delta\boldsymbol{P}_{\mathrm{G}} - \boldsymbol{D}\,\Delta\boldsymbol{\omega}_{\mathrm{G}}, \end{aligned} \tag{9.85}$$

where $\boldsymbol{M}$ and $\boldsymbol{D}$ are diagonal matrices of the inertia and damping coefficients, and $\Delta\boldsymbol{\delta}_{\mathrm{G}}$, $\Delta\boldsymbol{\omega}_{\mathrm{G}}$ and $\Delta\boldsymbol{P}_{\mathrm{G}}$ are column matrices of changes in rotor angles, rotor speed deviations and real power generations respectively.

Substituting (9.81) into the second equation of (9.85) gives the following state equation:

$$\boldsymbol{M}\,\Delta\dot{\boldsymbol{\omega}}_{\mathrm{G}} = -\boldsymbol{H}_{\mathrm{G}}\,\Delta\boldsymbol{\delta}_{\mathrm{G}} - \boldsymbol{D}\,\Delta\boldsymbol{\omega}_{\mathrm{G}} - \Delta\boldsymbol{K}_{\mathrm{ab}}\,h_{\mathrm{ab}}\,\Delta\gamma(t). \tag{9.86}$$

Here $\Delta\gamma(t)$ is the control function corresponding to the transformation ratio change of the phase shifting transformer. Function $\Delta\gamma(t)$ affects rotor motions in proportional to the coefficients $\Delta K_i h_{\mathrm{ab}} = (K_{i\mathrm{a}} - K_{i\mathrm{b}})h_{\mathrm{ab}}$.

The main question is how $\Delta\gamma(t)$ should be changed so that control of a given phase shifting transformer improves damping of oscillations. The control algorithm of $\Delta\gamma(t)$ will be derived using the Lyapunov direct method.

9.6.2 State-Variable Control Based on Lyapunov Method

In Section 6.3, the total system energy $V(\delta, \omega) = E_{\mathrm{k}} + E_{\mathrm{p}}$ was used as the Lyapunov function in the nonlinear system model (with line conductances neglected). In the considered linear model (9.86) the total system energy can be expressed as the sum of rotor speed and angle increments. This corresponds to expanding $V(\delta, \omega) = E_{\mathrm{k}} + E_{\mathrm{p}}$ in a Taylor series in the vicinity of an operating point, as in (6.11). This equation shows that $V(\boldsymbol{x})$ can be approximated in the vicinity of an operating point using a quadratic form based on the Hessian matrix of function $V(\boldsymbol{x})$.

For the potential energy E_{p} given by (6.47), the Hessian matrix corresponds to the gradient of real power generations and therefore also the Jacobi matrix used in the above incremental model:

$$\left[\frac{\partial^2 E_{\mathrm{p}}}{\partial\delta_i\partial\delta_j}\right] = \left[\frac{\partial P_i}{\partial\delta_j}\right] = \boldsymbol{H}_{\mathrm{G}}. \tag{9.87}$$

Equations (6.11) and (9.85) lead to

$$\Delta E_{\mathrm{p}} = \frac{1}{2}\Delta\boldsymbol{\delta}_{\mathrm{G}}^{\mathrm{T}}\boldsymbol{H}_{\mathrm{G}}\Delta\boldsymbol{\delta}_{\mathrm{G}} \tag{9.88}$$

It will be shown in Chapter 12 that if the network conductances are neglected, matrix $\boldsymbol{H}_{\mathrm{G}}$ is positive definite at an operating point (stable equilibrium point). Hence the quadratic form (9.88) is also positive definite.

Using (6.11), the kinetic energy E_{k} given by (6.46) can be expressed as

$$\Delta E_{\mathrm{k}} = \frac{1}{2}\Delta\boldsymbol{\omega}_{\mathrm{G}}^{\mathrm{T}}\boldsymbol{M}\,\Delta\boldsymbol{\omega}_{\mathrm{G}}. \tag{9.89}$$

This is a quadratic form made up of the vector of speed changes and a diagonal matrix of inertia coefficients. Matrix $\boldsymbol{M}$ is positive definite so the above quadratic form is also positive definite.

The total energy increment $\Delta V(\delta, \omega) = \Delta E_{\mathrm{k}} + \Delta E_{\mathrm{p}}$ is given by

$$\Delta V = \Delta E_{\mathrm{k}} + \Delta E_{\mathrm{p}} = \frac{1}{2}\Delta\boldsymbol{\omega}_{\mathrm{G}}^{\mathrm{T}}\,\boldsymbol{M}\,\Delta\boldsymbol{\omega}_{\mathrm{G}} + \frac{1}{2}\,\Delta\boldsymbol{\delta}_{\mathrm{G}}^{\mathrm{T}}\,\boldsymbol{H}_{\mathrm{G}}\Delta\boldsymbol{\delta}_{\mathrm{G}} \tag{9.90}$$

This function is positive definite as the sum of positive definite functions and therefore can be used as a Lyapunov function provided its time derivative at the operating point is negative definite.

Differentiating (9.88) and (9.89) gives

$$\Delta\dot{E}_{\mathrm{p}} = \frac{1}{2}\Delta\boldsymbol{\omega}_{\mathrm{G}}^{\mathrm{T}}\,\boldsymbol{H}_{\mathrm{G}}\Delta\boldsymbol{\delta}_{\mathrm{G}} + \frac{1}{2}\Delta\boldsymbol{\delta}_{\mathrm{G}}^{\mathrm{T}}\,\boldsymbol{H}_{\mathrm{G}}\Delta\boldsymbol{\omega}_{\mathrm{G}} \tag{9.91}$$

$$\Delta\dot{E}_{\mathrm{k}} = \frac{1}{2}\Delta\dot{\boldsymbol{\omega}}_{\mathrm{G}}^{\mathrm{T}}\boldsymbol{M}\Delta\boldsymbol{\omega}_{\mathrm{G}} + \frac{1}{2}\Delta\boldsymbol{\omega}_{\mathrm{G}}^{\mathrm{T}}\boldsymbol{M}\Delta\dot{\boldsymbol{\omega}}_{\mathrm{G}}. \tag{9.92}$$

Now, it is useful to transpose Equation (9.86):

$$\Delta\dot{\boldsymbol{\omega}}_{\mathrm{G}}^{\mathrm{T}}\,\mathbf{M} = -\Delta\delta_{\mathrm{G}}^{\mathrm{T}}\mathbf{H}_{\mathrm{G}} - \Delta\omega_{\mathrm{G}}^{\mathrm{T}}\mathbf{D} - \Delta\mathbf{K}_{\mathrm{ab}}^{\mathrm{T}}\,h_{\mathrm{ab}}\,\Delta\gamma(t). \tag{9.93}$$

Substituting the right hand side of (9.93) for $\Delta\dot{\boldsymbol{\omega}}_{\mathrm{G}}^{\mathrm{T}}\,\boldsymbol{M}$ in the first component of (9.92) gives

$$\begin{aligned}\Delta\dot{E}_{\mathrm{k}} = &-\frac{1}{2}\Delta\boldsymbol{\delta}_{\mathrm{G}}^{\mathrm{T}}\,\boldsymbol{H}_{\mathrm{G}}\,\Delta\boldsymbol{\omega}_{\mathrm{G}} - \frac{1}{2}\Delta\boldsymbol{\omega}_{\mathrm{G}}^{\mathrm{T}}\,\boldsymbol{H}_{\mathrm{G}}\,\Delta\boldsymbol{\delta}_{\mathrm{G}} - \Delta\boldsymbol{\omega}_{\mathrm{G}}^{\mathrm{T}}\,\boldsymbol{D}\,\Delta\boldsymbol{\omega}_{\mathrm{G}} \\ &-\frac{1}{2}\left(\Delta\boldsymbol{K}_{\mathrm{ab}}^{\mathrm{T}}\Delta\boldsymbol{\omega}_{\mathrm{G}} + \Delta\boldsymbol{\omega}_{\mathrm{G}}^{\mathrm{T}}\Delta\boldsymbol{K}_{\mathrm{ab}}\right)h_{\mathrm{ab}}\,\Delta\gamma(t).\end{aligned} \tag{9.94}$$

It can be easily checked that both expressions in the last component of (9.94) are identical scalars as

$$\Delta\boldsymbol{K}_{\mathrm{ab}}^{\mathrm{T}}\,\Delta\boldsymbol{\omega}_{\mathrm{G}} = \Delta\omega_{\mathrm{G}}^{\mathrm{T}}\,\Delta\boldsymbol{K}_{\mathrm{ab}} = \sum_{i\in\{\mathrm{G}\}}\Delta K_i\,\Delta\omega_i. \tag{9.95}$$

Hence Equation (9.94) can be rewritten as

$$\Delta\dot{E}_{\mathrm{k}} = -\frac{1}{2}\Delta\boldsymbol{\delta}_{\mathrm{G}}^{\mathrm{T}}\boldsymbol{H}_{\mathrm{G}}\Delta\boldsymbol{\omega}_{\mathrm{G}} - \frac{1}{2}\Delta\boldsymbol{\omega}_{\mathrm{G}}^{\mathrm{T}}\boldsymbol{H}_{\mathrm{G}}\Delta\boldsymbol{\delta}_{\mathrm{G}} - \Delta\boldsymbol{\omega}_{\mathrm{G}}^{\mathrm{T}}\boldsymbol{D}\Delta\boldsymbol{\omega}_{\mathrm{G}} - \Delta\boldsymbol{K}_{\mathrm{ab}}^{\mathrm{T}}\Delta\boldsymbol{\omega}_{\mathrm{G}}h_{\mathrm{ab}}\Delta\gamma(t). \tag{9.96}$$

Adding both sides of (9.96) and (9.91) gives

$$\Delta\dot{V} = \Delta\dot{E}_{\mathrm{k}} + \Delta\dot{E}_{\mathrm{p}} = -\Delta\boldsymbol{\omega}_{\mathrm{G}}^{\mathrm{T}}\boldsymbol{D}\Delta\boldsymbol{\omega}_{\mathrm{G}} - \Delta\boldsymbol{K}_{\mathrm{ab}}^{\mathrm{T}}\Delta\boldsymbol{\omega}_{\mathrm{G}}h_{\mathrm{ab}}\Delta\gamma(t). \tag{9.97}$$

In a particular case when there is no control, that is when $\Delta\gamma(t) = 0$, the equation in (9.97) gives

$$\Delta\dot{V} = \Delta\dot{E}_{\mathrm{k}} + \Delta\dot{E}_{\mathrm{p}} = -\Delta\boldsymbol{\omega}_{\mathrm{G}}^{\mathrm{T}}\boldsymbol{D}\Delta\boldsymbol{\omega}_{\mathrm{G}}. \tag{9.98}$$

As matrix $\boldsymbol{D}$ is positive definite, the function above is negative definite. Hence function (9.90) can be treated as the Lyapunov function for the system described by (9.86).

In order for the considered system to be stable when $\Delta\gamma(t) \neq 0$ changes, the second component in (9.97) should always be positive:

$$\Delta\boldsymbol{K}_{\mathrm{ab}}^{\mathrm{T}}\,\Delta\boldsymbol{\omega}_{\mathrm{G}}\,h_{\mathrm{ab}}\,\Delta\gamma(t) \geq 0. \tag{9.99}$$

This can be ensured using the following control law:

$$\Delta\gamma(t) = \kappa h_{\mathrm{ab}}\,\Delta\boldsymbol{K}_{\mathrm{ab}}^{\mathrm{T}}\,\Delta\boldsymbol{\omega}_{\mathrm{G}}. \tag{9.100}$$

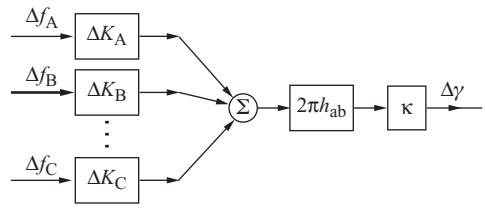

Figure 9.34 Block diagram of the stabilizing control loop of a power flow controller installed in a tie-line of an interconnected power system.

With this control law the derivative (9.97) of the Lyapunov function is given by

$$\Delta\dot{V} = -\Delta\boldsymbol{\omega}_G^T \boldsymbol{D}\Delta\boldsymbol{\omega}_G - \kappa\left(h_{ab}\Delta\boldsymbol{K}_{ab}^T\Delta\boldsymbol{\omega}_G\right)^2 \leq 0, \tag{9.101}$$

where κ is the control gain. Taking into account (9.95), the control law (9.100) can be written as

$$\Delta\gamma(t) = \kappa h_{ab}\sum_{i\in\{G\}}\Delta K_i\ \Delta\omega_i \tag{9.102}$$

where $\Delta K_i = K_{ia} - K_{ib}$ This control law is valid for any location of the phase shifting transformer. For the particular case when the phase shifting transformer is located in a tie-line, the control law can be simplified as described below.

The generator set $\{G\}$ in an interconnected system can be divided into a number of subsets corresponding to subsystems. Let us consider three subsystems as in Figure 9.34, that is $\{G\} = \{G_A\} + \{G_B\} + \{G_C\}$. Now the summation in Equation (9.102) can be divided into three sums:

$$\Delta\gamma(t) = \kappa h_{ab}\left[\sum_{i\in\{G_A\}}\Delta K_i\ \Delta\omega_i + \sum_{i\in\{G_B\}}\Delta K_i\ \Delta\omega_i + \sum_{i\in\{G_C\}}\Delta K_i\ \Delta\omega_i\right]. \tag{9.103}$$

Following a disturbance in one of the subsystems, there are *local swings* of generator rotors inside each subsystem and *interarea swings* of subsystems with respect to each other. The frequency of local swings is about 1 Hz while the frequency of interarea swings is much lower, usually about 0.25 Hz. Hence, when investigating the interarea swings, the local swings can be approximately neglected. Therefore it can be assumed that

$$\begin{aligned}
&\Delta\omega_1 \cong \cdots = \Delta\omega_i \cong \cdots \cong \Delta\omega_{n_A} \cong 2\pi\Delta f_A \quad \text{for} \quad i \in \{G_A\}\\
&\Delta\omega_1 \cong \cdots = \Delta\omega_i \cong \cdots \cong \Delta\omega_{n_B} \cong 2\pi\Delta f_B \quad \text{for} \quad i \in \{G_B\}\\
&\Delta\omega_1 \cong \cdots = \Delta\omega_i \cong \cdots \cong \Delta\omega_{n_C} \cong 2\pi\Delta f_C \quad \text{for} \quad i \in \{G_C\}.
\end{aligned} \tag{9.104}$$

Now Equation (9.103) can be expressed as

$$\Delta\gamma(t) = \kappa 2\pi h_{ab}\left[\Delta f_A\sum_{i\in\{G_A\}}\Delta K_i + \Delta f_B\sum_{i\in\{G_B\}}\Delta K_i + \Delta f_C\sum_{i\in\{G_C\}}\Delta K_i\right], \tag{9.105}$$

or, after summing the coefficients,

$$\Delta\gamma(t) = \kappa 2\pi h_{ab}\left(\Delta K_A\ \Delta f_A + \Delta K_B\ \Delta f_B + \Delta K_C\ \Delta f_C\right), \tag{9.106}$$

where

$$\Delta K_{\mathrm{A}} = \sum_{i\in\{\mathrm{G_A}\}} \Delta K_i, \quad \Delta K_{\mathrm{B}} = \sum_{i\in\{\mathrm{G_B}\}} \Delta K_i, \quad \Delta K_{\mathrm{C}} = \sum_{i\in\{\mathrm{G_C}\}} \Delta K_i. \tag{9.107}$$

Equation (9.106) shows that the control of a phase shifting transformer should employ the signals of frequency deviations weighted by coefficients (9.107).

A block diagram of the supplementary control loop based on (9.106) is shown in Figure 9.34. The way in which the supplementary control loop is added to the overall regulator was shown earlier in Figure 9.31.

The input signals to the supplementary control are frequency deviations Δf in each subsystem. These signals should be transmitted to the regulator using telecommunication links or WAMS discussed in Section 2.6. For the frequency of interarea swings of about 0.25 Hz, the period of oscillation is about 4 s and the speed of signal transmission to the regulator does not have to be high. It is enough if the signals are transmitted every 0.1 s, which is not a tall order for modern telecom systems.

The coefficients h_{ab}, ΔK_{A} , ΔK_{B} , ΔK_{C} in (9.106) have to be calculated by an appropriate SCADA/EMS function using current state estimation results and the system configuration. Obviously those calculations do not have to be repeated frequently. Modifications have to be done only after system configuration changes or after a significant change of power system loading.

When deriving Equation (9.106), for simplicity only one phase shifting transformer was assumed. Similar considerations can be taken for any number of phase shifting transformers installed in any number of tie-lines. For each transformer, identical control laws are obtained but obviously with different coefficients calculated for the respective tie-lines.

9.6.3 Example of Simulation Results

Neglecting local swings within the subsystems of an interconnected system, Equations (9.104), a simplified system model can be created using the incremental network model. This model, described by Rasolomampionona (2007), can take into account frequency and tie-line control and include models of phase shifting transformers installed in tie-lines. An example of the influence of phase shifting transformer regulation will be described below using simulation results.

Figure 9.35 shows a test system with parameters. All three tie-lines contain TCPAR-type devices controlled by the regulators shown in Figure 9.34. The stabilizing controllers use frequency deviations as their input signals.

Figure 9.36 shows the simulation results for a power balance disturbance $\Delta P_0 = 200$ MW consisting of an outage of a generating unit in system A. A thick line shows the responses when a TCPAR device was active and a thin line the responses when the device was not active. Frequency changes in the subsystems are shown in Figure 9.36a. When TCPAR devices are not active, frequency responses are affected by interarea oscillations (the thin line). Active TCPAR devices quickly damp out the interarea oscillations and the remaining slow frequency changes are due to the frequency and tie-line flow control (the thick line). The maximum frequency deviation in subsystems B and C is reduced due to the action of the TCPAR.

Tie-line flow changes are shown in Figure 9.36b. When TCPAR devices are not acting, changes due to frequency and tie-line flow control are superimposed on interarea swings (the thin line). Acting TCPAR devices quickly damp out the interarea swings. The remaining tie-line deviations tend to zero with time, which shows that the non-intervention rule is fulfilled. Fulfilment of the rule is also visible in Figure 9.36b showing generation changes. Following the power balance disturbance in subsystem A, subsystems B and C support A for a short time by means of a power injection. As the frequency returns to its reference value and subsystem A increases its generation, generation

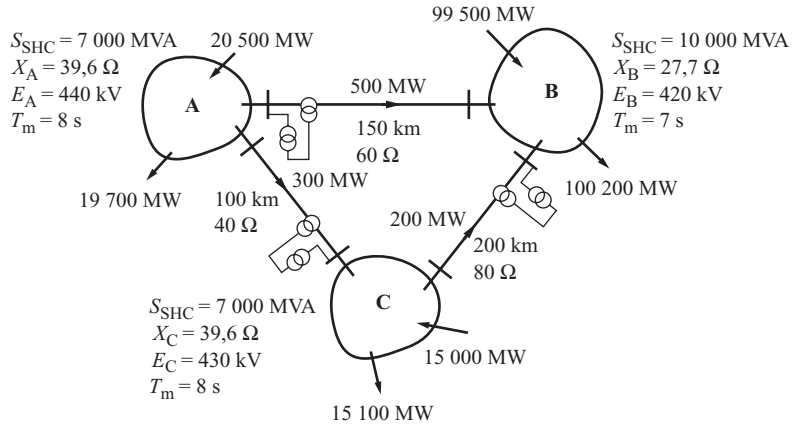

Figure 9.35 A test system.

in B and C returns to its initial value. The diagram also shows interarea oscillations in generation (especially in subsystem C) when the TCPAR device was not active.

9.6.4 Coordination Between AGC and Series FACTS Devices in Tie-Lines

The power flow controller shown in Figure 9.31 can be treated as a multi-level controller consisting of three control paths:

level 1: supplementary control loop with frequency deviations Δf_A , Δf_B , Δf_C as the input signals (Figure 9.34);
level 2: main control path with real power P_{tie} as the input signal;
level 3: supervisory control at SCADA/EMS level setting $P_{tie\ ref}$.

The actions of these three control loops are superimposed on top of each other and, through changes in $\gamma(t)$, influence tie-line flows and therefore also operation of AGC in individual subsystems of an interconnected power system. In order for both FACTS and AGC controls to be effective and beneficial for the power system, there must be appropriate coordination. This coordination has to be achieved by adjusting the speed of operation of the three control paths of the FACTS devices to the speed of operation of the three levels of AGC (primary, secondary, tertiary). The three control loops of AGC (Figure 9.12) differ widely in their speed of operation. The three control levels of the FACTS device installed in the tie-line of an interconnected power system must also exhibit a similarly differing speed of operation.

Referring to the description of four stages of power system dynamics due to AGC after a large power imbalance (Sections 9.2–9.5) and the description of operation of a TCPAR-type FACTS device (Section 9.6.4), the following conclusions can be drawn about time coordination of individual control levels.

Supplementary loop control (level 1) should respond quickly, according to the control law (9.106), to frequency changes due to interarea swings. Hence the speed of reaction of that control level must be the fastest, similar to that of primary control performed by AGC (prime mover control).

Control executed in the main path (level 2) cannot be fast and must be slower than secondary control performed by AGC (frequency and tie-line flow control). This can be explained in the

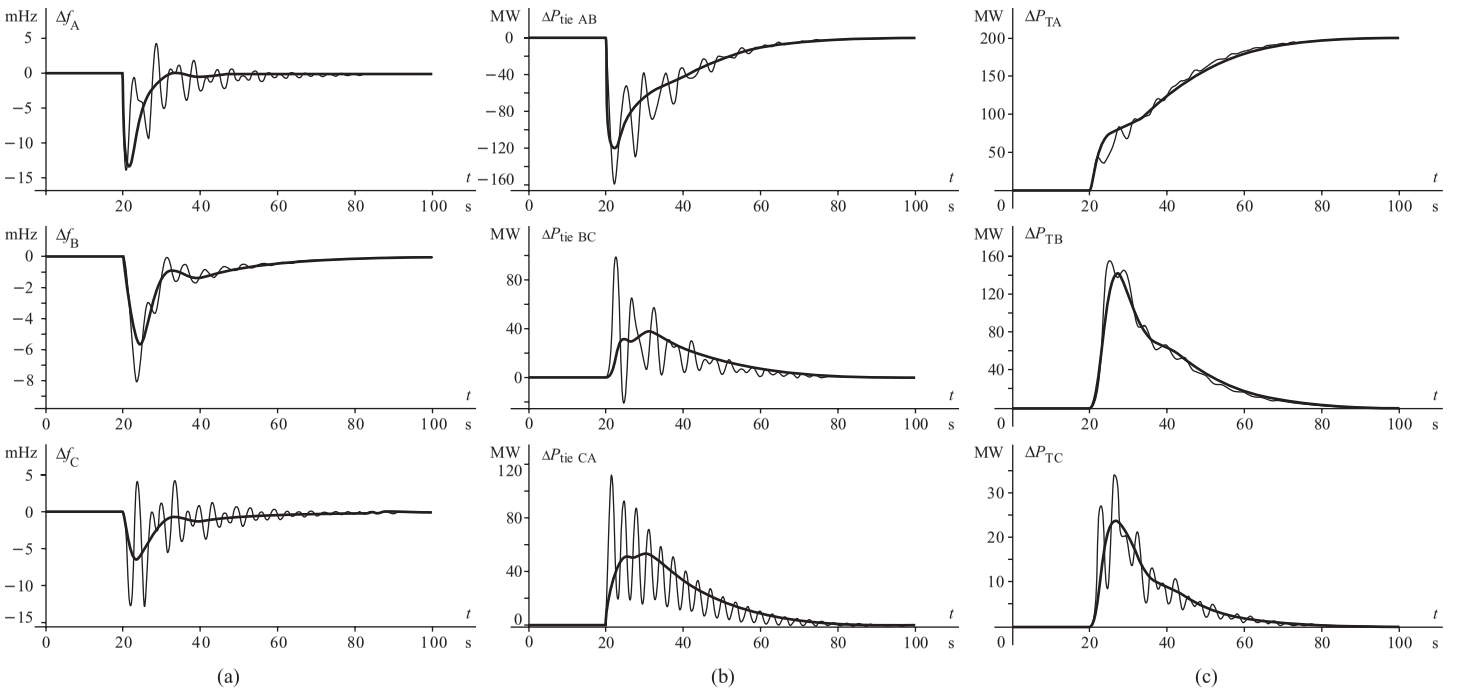

Figure 9.36 Simulation results following a power balance disturbance in subsystem A: (a) local frequency changes; (b) tie-line flow changes; (c) generation changes.

following way. Following a real power imbalance in a given subsystem, a power injection, lasting several tens of seconds, may flow to that subsystem from the other subsystems (Figure 9.36b). This power injection causes P_{tie} to be different from $P_{\text{tie ref}}$ and a control error appears in that control path. If the controller reacted too quickly, then the FACTS device could affect the power injection which would adversely affect the frequency control of the secondary level of AGC. The maximum frequency deviation would increase and the quality of regulation would decrease (Figure 9.13). To prevent this, the discussed control level should act with a long time constant. Figure 9.31 shows that the main control path contains an integrator with a feedback loop. The transfer function of the element is $G(\text{s}) = 1/(\rho_{\text{P}} + T_{\text{P}}\text{s})$, which means that the speed of operation of the element is determined by the time constant $T_{\text{P}}/\rho_{\text{P}}$ If this time constant is several times higher than the duration time of power injection then the discussed control level should not adversely affect secondary control executed by AGC.

The supervisory control (level 3) setting $P_{\text{tie ref}}$ executed by SCADA/EMS must be the slowest. Especially important for the dynamic performance is the case shown in Figure 9.36d when insufficient regulation power in the subsystem where the power imbalance occurred must result in a permanent deviation in exchanged power. The FACTS device controlled by the regulator shown in Figure 9.31 will try to regulate P_{tie} to a value $P_{\text{tie ref}}$ It may turn out that such regulation is not beneficial for the system and result in, for example, overloading of other transmission lines. Regulation at that level must be centrally executed by SCADA/EMS based on the analysis of the whole network.

10

Stability Enhancement

The stability of a power system is understood as its ability to return to the equilibrium state after being subjected to a physical disturbance. Important variables at power system equilibrium are rotor (power) angles, nodal voltages and frequency. Hence power system stability can be divided into: (i) rotor (power) angle stability, (ii) voltage stability and (iii) frequency stability. These terms were introduced in Chapter 1 when discussing Figure 1.5. Prevention of voltage instability (voltage collapse) was discussed in Section 8.6. A defence plan against frequency instability was discussed in Section 9.1.6. This chapter will deal with the possibilities of counteracting rotor (power) angle instability.

The rotor (power) angle stability of a power system can be enhanced, and its dynamic response improved, by correct system design and operation. For example, the following features help to improve stability:

- the use of protective equipment and circuit-breakers that ensure the fastest possible fault clearing;
- the use of single-pole circuit-breakers so that during single-phase faults only the faulted phase is cleared and the unfaulted phases remain intact;
- the use of a system configuration that is suitable for the particular operating conditions (e.g. avoiding long, heavily loaded transmission links);
- ensuring an appropriate reserve in transmission capability;
- avoiding operation of the system at low frequency and/or voltage;
- avoiding weakening the network by the simultaneous outage of a large number of lines and transformers.

In practice, financial considerations determine the extent to which any of these features can be implemented and there must always be a compromise between operating a system near to its stability limit and operating a system with an excessive reserve of generation and transmission. The risk of losing stability can be reduced by using additional elements inserted into the system to help smooth the system dynamic response. This is commonly referred to as *stability enhancement* and is the subject of this chapter.

10.1 Power System Stabilizers

A power system stabilizer (PSS) is a device which provides additional supplementary control loops to the automatic voltage regulator (AVR) system and/or the turbine-governing system of a generating unit. A PSS is also one of the most cost-effective methods of enhancing power system stability.

Power System Dynamics: Stability and Control, Second Edition Jan Machowski, Janusz W. Bialek and James R. Bumby
© 2008 John Wiley & Sons, Ltd

10.1.1 PSS Applied to the Excitation System

Adding supplementary control loops to the generator AVR is one of the most common ways of enhancing both small-signal (steady-state) stability and large-signal (transient) stability. Adding such additional control loops must be done with great care; Section 5.5 explained how an AVR (without supplementary control loops) can weaken the damping provided by the damper and field windings. This reduction in the damping torque is primarily due to the voltage regulation effects inducing additional currents in the rotor circuits that oppose the currents induced by the rotor speed deviation $\Delta\omega$. This phase relationship was illustrated in Figure 5.27 for the field winding (and in Figure 5.28 for the d-axis damper winding) and gives an immediate insight into what is required from the PSS.

The main idea of power system stabilization is to recognize that in the steady state, that is when the speed deviation is zero or nearly zero, the voltage controller should be driven by the voltage error ΔV only. However, in the transient state the generator speed is not constant, the rotor swings and ΔV undergoes oscillations caused by the change in rotor angle. The task of the PSS is to add an additional signal which compensates for the ΔV oscillations and provides a damping component that is in phase with $\Delta\omega$. This is illustrated in Figure 10.1a where the signal V_{PSS} is added to the main voltage error signal ΔV. In the steady state V_{PSS} must be equal to zero so that it does not distort the voltage regulation process. Figure 10.1b shows the phasor diagram of the signals in the transient state. As in Section 5.5.3, it is assumed that each signal varies sinusoidally with the frequency of rotor swings and may therefore be represented by a phasor. The phasor $\underline{V}_{\mathrm{PSS}}$ directly opposes $\Delta\underline{V}$ and is larger than it. The net voltage error phasor $\Delta\underline{V}_{\Sigma}$ now leads the speed deviation phasor $\Delta\underline{\omega}$ instead of lagging it as in Figure 5.27b. As explained in Section 5.5.3, the phasor of the incremental excitation emf $\Delta\underline{E}_{\mathrm{f}}$ lags $\Delta\underline{V}_{\Sigma}$ by an angle introduced by the AVR and the exciter so that the quadrature component (with respect to $\Delta\underline{\delta}$) of the phasor $\Delta\underline{E}'_{\mathrm{q}(\Delta E_{\mathrm{f}})}$ due to the excitation control is now in phase with $\Delta\underline{\omega}$. This, together with $\Delta\underline{E}'_{\mathrm{q}(\Delta\delta)}$, introduces a large damping torque into the system. However, if the magnitude of $\underline{V}_{\mathrm{PSS}}$ is less than that of $\Delta\underline{V}$ then only partial compensation of the negative damping component introduced by the AVR is achieved.

The general structure of the PSS is shown in Figure 10.2 where the PSS signal V_{PSS} can be provided from a number of different input signals measured at the generator terminals. The measured quantity (or quantities) is passed through low- and high-pass filters. The filtered signal is then passed through a lead and/or lag element in order to obtain the required phase shift and, finally, the signal is amplified and passed to a limiter. When designing the phase compensation it is necessary to take into account the phase shift of the input signal itself and that introduced by the low- and high- pass

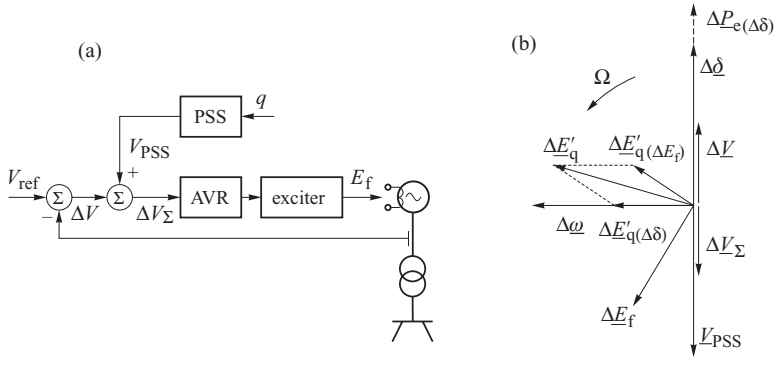

Figure 10.1 Supplementary control loop for the AVR system: (a) block diagram; (b) phasor diagram.

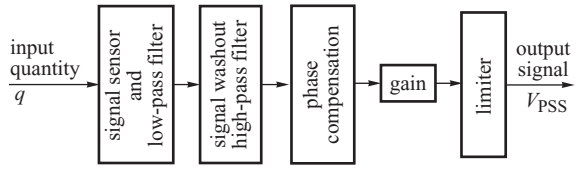

Figure 10.2 The major elements of a PSS.

filters. Sometimes the filters are designed in such a way that they give a net zero phase shift for the frequency of rotor oscillations (Huwer, 1992). The mathematical model of the PSS will be described in more detail in Section 11.2.

Typically the measured quantities used as input signals to the PSS are the rotor speed deviation, the generator active power or the frequency of the generator terminal voltage. There are a number of possible ways of constructing a PSS depending on the signal chosen.

10.1.1.1 PSS Based on $\Delta\omega$

The oldest types of PSSs use a measurement of the speed deviation of the generator shaft. Obviously this signal must be processed in order to filter out all the measurement noise. The main problem with this method, when applied to turbogenerators with long shafts prone to torsional oscillations, relates to selecting a measurement position on the shaft that properly represents the speed deviation of the rotor magnetic poles. For long shafts it is necessary to measure the speed deviation at a number of points along the shaft and use this information to calculate the average speed deviation. Moreover, the stabilizer gain is constrained by the influence that the PSS has on the torsional oscillations. These problems are described by Watson and Coultes (1973) and Kundur, Lee and Zein El-Din (1981).

10.1.1.2 PSS Based on $\Delta\omega$ and P_e

The need to measure the speed deviation at a number of points along the shaft can be avoided by calculating the average speed deviation from measured electrical quantities. The method calculates the equivalent speed deviation $\Delta\omega_{eq}$ indirectly from the integral of the accelerating power:

$$\Delta\omega_{eq} = \frac{1}{M}\int (\Delta P_m - \Delta P_e)\,dt, \tag{10.1}$$

and ΔP_e is calculated from measurements of the generated real power P_e. The integral of the change in the mechanical power ΔP_m can be obtained from

$$\int \Delta P_m\,dt = M\Delta\omega_{measured} + \int \Delta P_e\,dt, \tag{10.2}$$

where $\omega_{measured}$ is based on the end-of-shaft speed sensing system. Because the mechanical power changes are relatively slow, the derived integral of the mechanical power can be passed through a low-pass filter to remove the torsional frequencies from the speed measurement. The resulting PSS contains two input signals, $\Delta\omega_{measured}$ and ΔP_e, which are used to calculate $\Delta\omega_{eq}$. The final V_{PSS} signal is designed to lead $\Delta\omega_{eq}$. The block diagram of the system is shown in Figure 10.3 (Kundur, 1994) where $G(s)$ is the transfer function of the torsional filter. This type of PSS with two input signals allows a large gain to be used so that good damping of power swings is obtained (Lee, Beaulieu and Service, 1981).

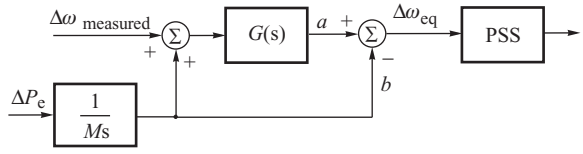

Figure 10.3 Block diagram of a PSS using speed deviation and real power as input signals.

10.1.1.3 PSS Based on P_e

A simplified form of the PSS shown in Figure 10.3 can be obtained by neglecting the shaft speed measurement and only measuring the generator real power P_e. With this arrangement only one input signal is required but can only be used when the mechanical power can be assumed to be constant. If the mechanical power does change, for example due to secondary frequency control, this solution produces transient oscillations in the voltage and reactive power that are unnecessarily forced by the PSS because it sees the change in the mechanical power as a power swing.

10.1.1.4 PSS Based on f_{V_g} and $f_{E'}$

The measurement of shaft speed can be replaced by a measurement of the generator terminal voltage frequency f_{V_g} (Larsen and Swan, 1981). A disadvantage of this solution is that the terminal voltage waveform can contain noise produced by large industrial loads such as arc furnaces. The accuracy of this measured speed signal can be improved by adding the voltage drop across the transient reactance to the generator voltage to obtain the transient emf E' and its frequency $f_{E'}$. The PSS now receives two signals, the generator current and voltage. Similar to the case of the PSS utilizing the measured shaft speed deviation, the PSS gain is limited by the effect of shaft torsional oscillations. The advantage of this solution compared with other types of stabilizers is that it improves the damping of interarea oscillations in interconnected power systems.

10.1.1.5 PSS Design

Designing and applying the PSS is not simple and requires a thorough analysis of the regulator structure and its parameters. A badly designed PSS can become the source of a variety of undesired oscillations. It should be remembered that the phasor diagrams in Figures 5.27, 5.28 and 10.1 are valid only for a simple generator–infinite busbar system with all the resistances and local loads neglected. A more detailed analysis shows that the phase shift between $\Delta \underline{E}_f$ and $\Delta \underline{E}'_{q(\Delta E_f)}$ is not exactly $\pi/2$ and depends on the loading and system parameters (De Mello and Concordia, 1969). This requires a more precise matching of the phase compensation to the actual loading and system parameters.

The parameters of a PSS are usually optimized with respect to the damping of small-disturbance power swings. However, a properly designed PSS also improves the damping under large-disturbance conditions. In order to enhance the first-swing transient stability, an additional control loop can be added to the PSS that acts in a similar way as the *forced excitation* in old electromechanical AVR systems. Such forced excitation was executed by short-circuiting resistors in the excitation winding in order to increase E_f to its ceiling value for about 0.5 s. The resistors were then reinserted and E_f decreased. A similar solution is used in so-called *discontinuous excitation control* systems. In the solution described by Kundur (1994) an additional element is switched in by a relay which supplies, in parallel with the PSS, a signal to force the excitation to an increased value. This element is switched off when the sign of the speed deviation changes (i.e. the rotor decelerates).

In the former Soviet Union a separate supplementary PSS control loop was not used in the AVR but instead a multi-variable AVR with internal feedback loops performing the stabilizing function (Glebov, 1970).

10.1.2 PSS Applied to the Turbine Governor

Since all the generators in the power system are linked by the transmission network, voltage control on one of the generators influences the dynamic response of all the other generators. Consequently, a PSS that improves the damping of one generator does not necessarily improve the damping of the other generators. Therefore a local design may not provide the global optimal solution and a coordinated synthesis procedure is desirable. This coordination increases the design computation and is usually valid only for typical network configurations and loading conditions. When a severe fault occurs, the postfault network configuration, and load, may be significantly different from the prefault conditions and poorly damped swings may result. Because of these factors, interest has focused on utilizing the turbine governor for the damping of local and interarea oscillations.

Including a PSS signal in the turbine governing systems with the aim of improving damping is not new. Moussa and Yu (1972) describe some solutions regarding hydro turbines. The principle of providing an additional damping torque from the turbine governor is similar to that used when adding a PSS loop to the excitation system. The time constants in the turbine governor introduce a phase shift between the oscillations in the speed deviation $\Delta\omega$ and the turbine mechanical power. As the input signal to the supplementary PSS control loop is equal to $\Delta\omega$, the PSS transfer function must be chosen in such a way that at the frequency of rotor oscillations it compensates the phase shift introduced by the turbine governor. Consequently the PSS will force changes in the mechanical power ΔP_m that are in phase with $\Delta\omega$ and, according to the swing equation, Equation (5.15), provide positive damping.

The main advantage of applying a PSS loop to the turbine governor lies in the fact that the turbine governor dynamics are weakly coupled with those of the rest of the system. Consequently the parameters of the PSS do not depend on the network parameters. Wang *et al.* (1993) show interesting simulation results for systems equipped with a PSS applied to the governors of steam turbines. Although this type of PSS is not currently used in practice, such solutions should not be ruled out in the future.

10.2 Fast Valving

Chapter 6 explained how a large disturbance near to a generator (e.g. a sudden short circuit) will produce a sudden drop in the generator output power followed by rapid acceleration of the generator rotor. The natural action to counteract this drop in electrical power would be to reduce rapidly the mechanical input power, thereby limiting the acceleration torque. The effect of such action can be explained by considering Figure 10.4 which shows the equal area criterion applied to the system shown in Figure 6.6 when a fault appears on line L2 and is cleared without auto-reclosure. If it is assumed that the accelerating area 1–2–3–4 in Figure 10.4a is greater than the maximum possible decelerating area 4–5–7 then, when the line is tripped, the rotor will make an asynchronous rotation and the system will lose stability. Now assume that the mechanical power P_m is reduced immediately after the disturbance occurs. The technical possibilities of providing such a fast power reduction will be discussed later. Figure 10.4b shows that reduction of P_m during the forward swing reduces the accelerating area 1–2–3–4 and increases the decelerating area to area 4–5–6–6′. The system remains stable with the stability margin being proportional to area 6–7–6′. The maximum improvement in stability is obtained when the reduction in P_m takes place as early, and as fast, as possible.

Figure 10.4c shows the situation to be somewhat different during the backswing. With the mechanical input power reduced, the system returns towards a rotor angle δ' that is smaller than the initial value and performs deceleration work equal to the integral of the difference between the

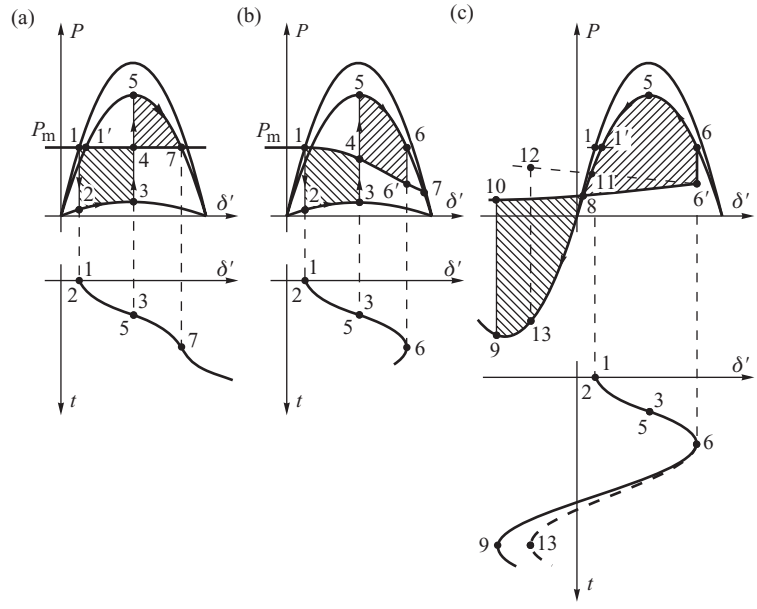

Figure 10.4 Equal area criterion with: (a) constant mechanical power; (b) fast reduction of the mechanical power during the forward swing; (c) influence of the mechanical power on the backswing.

electrical and mechanical power. In this phase a further decrease in the mechanical power, shown by the solid line 6′–8–10, has a detrimental effect on the system dynamics because the deceleration work 6′–6–5–8 performed during the backswing can only be balanced by a large accelerating area 8–9–10 giving a large rotor deflection towards negative δ'. The backswing is increased by the drop in P_m. The dashed line in Figure 10.4c shows how the amplitude of the backswing could be reduced by increasing P_m during the backswing. This would result in a smaller decelerating area 6′–6–5–11 which is then balanced by the smaller accelerating area 11–13–12.

After a disturbance, the system shown in Figure 10.4c recovers to the prefault value of the mechanical power. In systems operating near to their steady-state stability limit it may happen that the fault clearance increases the system equivalent reactance to a value that would correspond to steady-state instability; that is, when the mechanical power is greater than the amplitude of the postfault characteristic. In order to ensure steady-state stability in such situations it is necessary to reduce the final, postfault value of the mechanical power. This is illustrated in Figure 10.5a where, on fault clearance, the postfault power–angle characteristic lies below the dashed line $P_{m0} = \text{constant}$ and the system would lose stability even if the fault were cleared instantaneously. To prevent such an instability, the final, postfault value of mechanical power must be reduced to $P_{m\infty}$ as illustrated in Figure 10.5b.

Fast changes in the mechanical power as shown in Figures 10.4 and 10.5 require a very fast response from the turbine. The examples shown above indicate that the decrease in the turbine power should take place within the first third of the swing period, that is during the first few tenths of a second following a disturbance. Restoring the power to the required postfault value should take about half of the swing period, that is less than a second. Such fast control is not possible with hydro turbines due to the large change in pressure, and huge torques, necessary to move the control gates. However, a steam turbine can be used for stability enhancement because it can be made to respond almost as quickly as required. The control action required within the turbine to produce

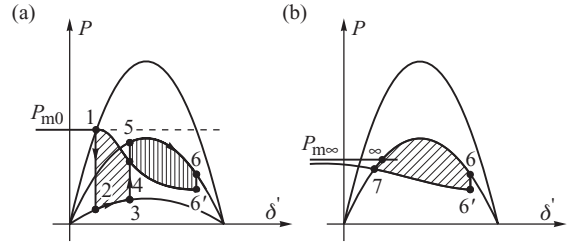

P_{m0}, $P_{m\infty}$ - pre-fault (initial) and post-fault (final) mechanical power

Figure 10.5 Equal area criterion with fast changes of mechanical power in a system operating near its steady-state stability limit: (a) forward swing; (b) backswing.

this rapid response is referred to as *fast valving*. When the mechanical power is restored to a final value that is equal to the prefault value, the fast valving is said to be *momentary fast valving*. When the final value of mechanical power is smaller than the prefault value, the fast valving is said to be *sustained fast valving*. Power variations corresponding to both these cases are shown in Figure 10.6.

Steam turbine fast valving cannot be achieved using the standard closed-loop turbine governor shown in Figure 2.12 because a change in the valve setting only occurs after a speed error appears at the controller input. Due to the large inertia of the turbine–generator rotor the speed can only change slowly so that the response of the closed-loop arrangement, with speed as the control variable, is too slow. As control action is required immediately when the fault is detected, open-loop control systems are normally used.

In a modern steam turbine fast valving is executed using the existing control valves. Consider, for example, the single reheat unit shown in Figure 2.7. Here rapid closure of the main governor control valves will not produce a large reduction in the turbine power because the high-pressure stage produces only about 30% of the power. The reheater stores a large volume of steam and, even with the main governor valve closed, the turbine still supplies about 70% of power through the intermediate- and low-pressure stages. A large, rapid reduction of power can only be obtained by closing the intercept control valves because it is these which control the steam flow to the intermediate- and low-pressure parts of the turbine.

Momentary fast valving, shown in Figure 10.7a, is achieved by rapid closing of the intercept control valves, holding them closed for a short time and then reopening them in order to restore the power to its initial, prefault value. During the short time when the intercept valves are shut, the steam flows from the boiler through the high-pressure turbine and is accumulated in the reheater.

Sustained fast valving can be provided by a rapid closing of the intercept valves, Figure 10.7b, followed by slow partial closing of the main governor valve. After a short period the intercept valves

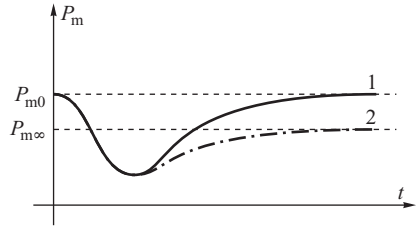

Figure 10.6 Mechanical power variations in the case of: 1, momentary fast valving; 2, sustained fast valving.

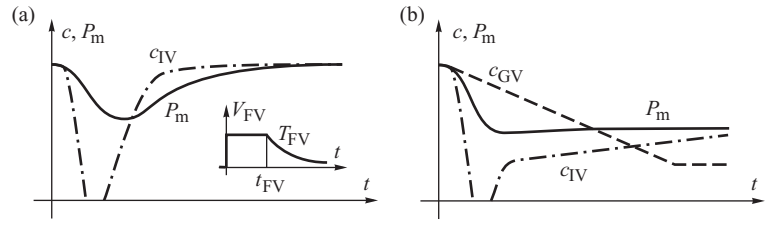

Figure 10.7 Variations in the valve position and output power of a single-reheat steam turbine due to: (a) momentary fast valving; (b) sustained fast valving. c_{GV}, position of the main governor control valve; c_{IV}, position of the intercept control valve.

are again reopened. This guarantees a rapid initial reduction in the mechanical power followed by its restoration to a value smaller than the initial one.

Fast valving of modern turbines equipped with the electro-hydraulic governing systems shown in Figure 2.12b can be achieved by feeding a fast-valving signal $V_{FV}(t)$ directly to the coil of the electro-hydraulic converter. The signal is produced by an additional controller FV operating in open-loop mode. In the case of momentary fast valving the signal $V_{FV}(t)$ consists of two parts as shown in Figure 10.7a. The first part is a rectangular pulse necessary for rapid closing of the valves. The height of the rectangular signal determines the magnitude of the voltage applied to the converter coil and, if large enough, the servomotor will close the valve in about 0.1–0.4 s. The width of the rectangular pulse t_{FV} determines the duration of the power reduction. The second part of the signal is a pulse that decays with a time constant T_{FV}, where T_{FV} is selected so that the speed at which the valves are reopened does not exceed a preset maximum value. This limit on the speed of valve reopening is mainly set by the strength of the rotor blades so that when reopening the valves a 100 % change in the valve position cannot normally be completed in less than about 1 s.

Generally the fast-valving controller FV operates with a predetermined set of control parameters that are prepared offline, by performing a large number of power system simulations, that take into account:

- the prefault network configuration;
- the prefault loading condition;
- the location of the fault, that is in which line it occurs;
- the distance and the type of fault measured by, for example, the accelerating power or voltage drop;
- if the fault clearance is with, or without, auto-reclosure.

A control signal is then prepared offline for a large number of possible fault scenarios. When a fault occurs, the controller is fed real-time information on all the above factors so that it can pick a control strategy from its predetermined set of signals that most closely matches the actual fault condition.

In practice the reduction, and restoration, of power shown in Figure 10.7 tends to be slower than that required from the stability enhancement point of view described in Figure 10.4. If the control valves are reopened too late the backswing will increase and may lead to *second-swing instability*. When a generator is equipped with a fast AVR and a PSS, the situation can be improved as illustrated in Figure 10.8. Fast power reduction takes place within the first few tenths of a second after the fault so that the rotor does not lose stability but swings over the peak of the power–angle characteristic as indicated by the two humps in the first power swing (cf. Figure 6.9a). Restoration of the turbine power takes a few seconds, which is too slow and so causes two deep rotor backswings that reach the

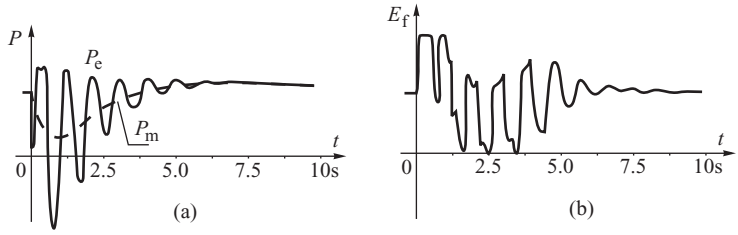

Figure 10.8 Influence of fast valving and PSS on the transient state: (a) mechanical and electrical power variations; (b) excitation voltage variations. Based on Brown *et al.* (1970).

Source: © IEEE 1970

motoring range of operation (negative electrical power). The depth of these backswings is reduced by rapid control of the excitation voltage enforced by the AVR equipped with PSS. The average value of E_f is decreased and the average value of P_e follows the mechanical power P_m.

Although the cost of implementing fast valving is usually small, the adverse effect on the turbine and boiler may be serious. Generally fast valving is only used in difficult situations where the AVR and PSS cannot, on their own, prevent instability.

10.3 Braking Resistors

One of the possibilities of affecting the rotor motion following a disturbance is by connecting a *braking resistor* (BR) at the generator or substation terminals. Such an action amounts to *electrical braking* of the accelerating rotor.

The BR may be switched on using a mechanical circuit-breaker, which is discussed in this section, or it may be controlled using FACTS devices, which will be discussed in Section 10.5.

The influence of connecting a BR in the generator–infinite busbar system is illustrated in Figure 10.9. To simplify considerations, a short circuit in a radial network was assumed similar to Figure 6.1. The system is unstable without the BR and with the assumed fault duration and prefault system loading. This was shown previously in Figure 6.2b and is repeated here in Figure 10.9b.

Using considerations similar to those accompanying Figure 6.1 but for a shunt resistor, it can be shown that inserting BR causes an increase in the amplitude of the power–angle characteristic $P(\delta')$ and a shift to the left of the intersection point of that characteristic with the δ'-axis. In Figure 10.9, the power–angle characteristic with the BR inserted is shown using a dashed line.

A signal to insert the BR is obtained from the protection of the transmission line. This protection gives a signal to trip the short-circuited line and to close the circuit-breaker of the BR. In the characteristic shown in Figure 10.9c, the BR is inserted at the instant when the faulted line is tripped. After disconnecting the line and inserting the BR, the electrical power corresponds to point 5. At that point, the generator power is greater than when the BR was absent (Figure 10.9b). The rotor swings to point 6 where the area 4–5–6–6′ is equal to area 1–2–3–4. The system is now stable with a stability margin corresponding to the area 6′–6–8.

Keeping the BR connected during the rotor backswing is not appropriate as the rotor would do a large amount of deceleration work and would swing deeply in the direction of motor operation of the generator. To avoid this, the BR should be disconnected when the rotor speed deviation changes its sign from positive to negative. In the discussed case (Figure 10.9c) this happens at point 6. After the BR has been disconnected, the system moves to point 9 on the characteristic without the BR and then returns towards the equilibrium point doing deceleration work corresponding to the area 9–1–6′.

During the second rotor swing, when the speed deviation becomes positive again, the BR can be inserted again. This type of control is of bang–bang type and consists of inserting the BR when

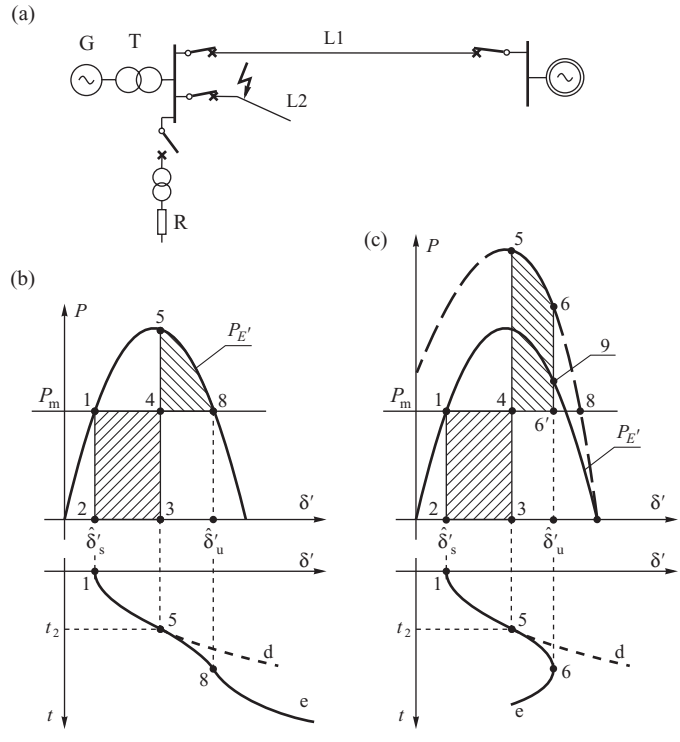

Figure 10.9 Influence of braking resistor: (a) circuit diagram; (b) situation without braking resistor; (c) situation with braking resistor.

the speed deviation is positive and disconnecting it when the speed deviation is negative. To avoid excessive wear of the circuit-breaker, a maximum of two or three BR insertions are usually made following a fault. When the measurement of rotor speed deviation is not available, a simpler control is used consisting of a single BR insertion for a predetermined period of about 0.3–0.5 s (Kundur, 1994).

BRs operate only for a short period of time so they can be made cheaply and volume-efficiently using cast-iron wire strung on towers. They can withstand strong heating up to several hundred degrees centigrade. The mass of the BR is relatively small at about 150 kg per 100 MW of power consumption.

BRs are a relatively cheap and efficient means of preventing loss of synchronism. They are used in hydro-electric power plants where, due to heavy control gates, fast valving discussed in Section 10.2 cannot be used.

10.4 Generator Tripping

Tripping one or more generators from a group of generators that are operating in parallel on a common busbar is perhaps the simplest, and most effective, means of rapidly changing the torque balance on the generator rotors. Historically, generator tripping was confined to hydro power stations where fast valving could not be used, but now many power companies have extended its use to both fossil fuel and nuclear power generating units in order to try and prevent system instability after severe disturbances.

When a generator is tripped it will normally go through a standard shutdown and start-up cycle which can take several hours. To avoid this long procedure the generator is usually disconnected from the network but still used to supply the station auxiliary demand. This allows the generator to be resynchronized to the system and brought back to full or partial load in several minutes.

The main disadvantage of generator tripping is that it creates a long-term power imbalance characterized by variations in frequency and power interchange between interconnected systems as shown in Chapter 9. Moreover, generator tripping results in a sudden increase in the electromagnetic torque acting on a generator rotor which can lead to a reduction in the shaft fatigue life. Although unlikely, if two or more units are tripped at exactly the same time, then the shaft loading on the remaining generators can become very severe indeed.

Generator tripping falls into two different categories. *Preventive tripping* is when tripping is coordinated with fault clearing to ensure that the generators remaining in operation maintain synchronism. *Restitutive tripping* is when one, or more, generators are tripped from a group of generators that have already lost synchronism. The objective here is to make resynchronization of the remaining generators easier.

10.4.1 Preventive Tripping

Preventive generator tripping is illustrated in Figure 10.10. In this example both generators are assumed to be identical and, since they are connected in parallel, may be treated as one equivalent generator. This means that the equivalent generator will have a reactance half that of each individual generator but an input power twice that of an individual generator. The prefault, fault and postfault power–angle characteristics are denoted as I, II and III, respectively. In the case without tripping, Figure 10.10b, the acceleration area 1–2–3–4 is larger than the available deceleration area 4–5–6. The system is unstable and both generators lose synchronism. In the second

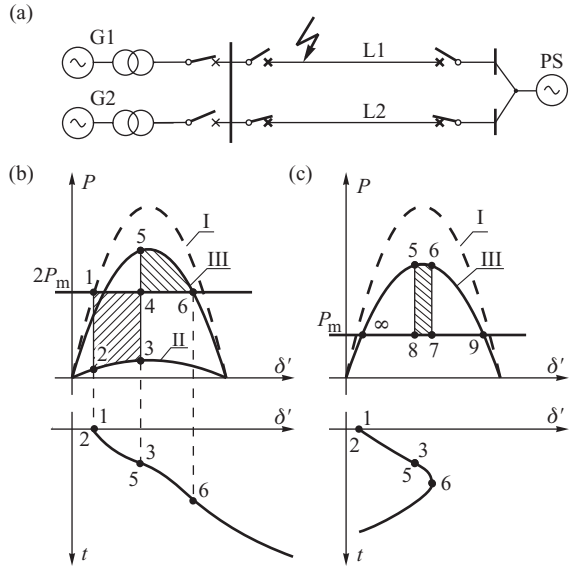

Figure 10.10 Illustration of generator tripping: (a) schematic diagram of the system; (b) acceleration and deceleration area when no generator is tripped; (b) deceleration area when one of the generators is tripped.

case, Figure 10.10c, one of the generators is assumed to be tripped at the same instant as the fault is cleared. The postfault characteristic III now has a smaller amplitude than in Figure 10.10b as the tripping of one of the generators increases the system equivalent reactance. However, the mechanical power of one generator is half that of the equivalent generator so that the acceleration area corresponding to one generator is half the acceleration area 1–2–3–4 shown in Figure 10.10b. The rotor now reaches synchronous speed (speed deviation equal to zero) at point 6 when area 8–5–6–7 is half of area 1–2–3–4. The system remains stable with a stability margin equal to the area 6–9–7. The new stable equilibrium point ∞ corresponds to the intersection between the electrical characteristic III and the mechanical power P_m, and will be reached after a number of deep rotor swings. In this example the synchronism of one generator has been saved at the cost of tripping the other.

As the objective of generator tripping is to maintain the stability of a number of generators operating in parallel on the same busbar, tripping one generator may be insufficient and *multi-tripping* may be necessary. The number of generators that must be tripped depends on a number of factors including the prefault loading conditions, fault type and location, and the fault clearing time. The control system that executes the tripping must be able to take into account all of these factors in order to prevent asynchronous operation while minimizing the number of generators tripped.

Broadly, there are two types of control system that can be used to achieve the above objective. The first is similar to that used to select the fast-valving control signal described in the previous section. Central to such a control scheme is the logic predetermined offline on the basis of a detailed stability analysis of the system. Just as in the fast-valving control scheme, the control system obtains real-time information about the fault and from this information selects the number of generators to be tripped. As the predetermined logic cannot always accurately assess the actual fault condition an overpessimistic assessment may be made resulting in more generators than necessary being tripped. This is the main drawback of preventive generator tripping.

The second type of control system is more sophisticated and is based on real-time simulation by fast microcomputer systems (Kumano *et al.*, 1994). Briefly this system consists of a number of microcomputers connected by a fast telecommunications network. Each microcomputer obtains real-time measurements from the power plant and information about the disturbance. The microcomputers then simulate the dynamic process faster than real time in order to predict instability and compute the minimum number of generators that must be tripped to maintain stability.

10.4.2 Restitutive Tripping

As explained above, preventive tripping systems can be too pessimistic and trip too many generators while the more sophisticated control schemes using faster than real-time simulation are very new and expensive. An alternative solution is to use restitutive tripping and utilize signals from the out-of-step relays described in Section 6.6.3. When a group of generators operating in parallel on the same busbars loses synchronism, one of the generators is tripped to make resynchronization of the remaining generators easier. However, if, after a set number of asynchronous rotations, resynchronization is unsuccessful another generator in the group is tripped and the process repeated until resynchronization is successful.

The main disadvantage of restitutive tripping is in allowing momentary asynchronous operation. The main advantage, when compared with preventive tripping, is that it never disconnects more generators than necessary.

Careful study of Figure 6.30a shows that the optimum instant for restitutive tripping is when the rotor angle passes through the unstable equilibrium point when the large acceleration area (shaded) behind point 6 is reduced by a sudden change in P_m. The unstable equilibrium point is close to $\pi/2$ so that when the system trajectory passes through it, the apparent impedance measured by the out-of-step relay crosses the lenticular or offset mho characteristic of the relay shown in Figure 6.40.

The signal from the relay can therefore be used to trigger the generator tripping. The circuit-breakers have a certain operating time so that the generator is tripped after a short delay. In order to avoid this delay, and provide for earlier tripping, the relay can be extended with the measurement of the derivative of the apparent resistance $\mathrm{d}R/\mathrm{d}t$ (Taylor *et al.*, 1983; Taylor, 1986).

10.5 Shunt FACTS Devices

Power swings can also be damped by changing the parameters in the transmission network that links the generator with the system. Such a parameter change can be accomplished by using additional network elements, such as shunt capacitors and reactors switched on and off at appropriate moments. Optimal system performance can be achieved by correct control of the switching instants and has been the subject of a large number of publications. Rather than describing such control schemes here, the aim in this section is to explain how a proper switching strategy can force damping of power swings and what control signals can be used to execute the switching sequence. The following explanations are based on publications by Machowski and Nelles (1992a, 1992b, 1993, 1994) and Machowski and Bialek (2008).

10.5.1 Power–Angle Characteristic

Figure 10.11 shows the situation where a shunt element is connected at a point along a transmission link. The generator is represented by $E_\mathrm{g} = E' = \text{constant}$ behind the transient reactance and by the swing equation (the classical model). The shunt element is modelled by admittance $\underline{Y}_\mathrm{sh} = G_\mathrm{sh} + \mathrm{j}B_\mathrm{sh}$. Depending on the type of shunt element used, the admittance is calculated from the current or power of the shunt element and the actual value of V_sh. For example, for SMES or BESS, the admittance is calculated from $\underline{Y}_\mathrm{sh} = G_\mathrm{sh} + \mathrm{j}B_\mathrm{sh} = \underline{S}^*_\mathrm{sh}/V^2_\mathrm{sh}$. Similarly, as was the case with Equation (2.9), the following constraint has to be satisfied:

$$[G_\mathrm{sh}(t)]^2 + [B_\mathrm{sh}(t)]^2 \le |Y_\mathrm{max}|^2 \quad \text{where} \quad |\underline{Y}_\mathrm{max}| = \frac{|\underline{S}_\mathrm{max}|}{|\underline{V}_\mathrm{sh}|^2}. \tag{10.3}$$

Obviously for SVC or STATCOM the real power is zero and $G_\mathrm{sh}(t) = 0$. For the BR the reactive power is zero and $B_\mathrm{sh}(t) = 0$. To emphasize that the admittance is not constant, the following notation was assumed: $\underline{Y}_\mathrm{sh}(t) = G_\mathrm{sh}(t) + \mathrm{j}B_\mathrm{sh}(t)$.

The reactance to the left of the shunt element (including the reactance of the generator) is denoted as X_g. The reactance to the right of the shunt element (including the reactance of the system) is denoted as X_s.

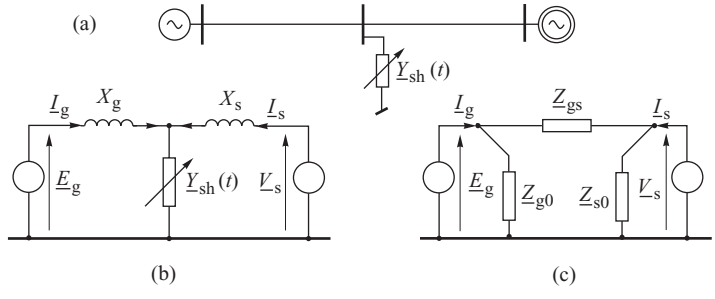

Figure 10.11 Generator–infinite busbar system with the shunt element and its equivalent circuits.

Using the star–delta transformation a π-equivalent is obtained which contains a resistance in its equivalent series branch if the shunt element, $\underline{Y}_{\rm sh} = G_{\rm sh} + {\rm j}B_{\rm sh}$, contains a non-zero conductance. The resulting values of the π-equivalent circuit are

$$\begin{aligned} \underline{Z}_{\rm gs} &= \left(X_{\rm g} + X_{\rm s}\right)\left[-X_{\rm SHC}G_{\rm sh} + {\rm j}(1 - X_{\rm SHC}B_{\rm sh})\right] \\ \tan\mu_{\rm gs} &= \frac{{\rm Re}\underline{Z}_{\rm gs}}{{\rm Im}\underline{Z}_{\rm gs}} = -\frac{X_{\rm SHC}G_{\rm sh}}{1 - X_{\rm SHC}B_{\rm sh}} \\ \underline{Y}_{\rm g0} &= \frac{1}{\underline{Z}_{\rm g0}} = \frac{1}{X_{\rm g}}\frac{X_{\rm SHC}G_{\rm sh} + {\rm j}X_{\rm SHC}B_{\rm sh}}{(1 - X_{\rm SHC}B_{\rm sh}) + {\rm j}X_{\rm SHC}G_{\rm sh}}, \end{aligned} \tag{10.4}$$

where $X_{\rm SHC} = X_{\rm g}X_{\rm s}/\left(X_{\rm g} + X_{\rm s}\right)$ is the short-circuit reactance of the system as seen from the node where the shunt element is installed. Normally the short-circuit power $S_{\rm SHC} = V_{\rm n}^2/X_{\rm SHC}$ tends to be between a few thousand and up to about 20 000 MVA while the rated power of the shunt element $P_{\rm n\,sh} = G_{\rm sh}V_{\rm n}^2$ and $Q_{\rm n\,sh} = B_{\rm sh}V_{\rm n}^2$ tends to be less than 100 MVA. Therefore, as $P_{\rm n\,sh}$ and $Q_{\rm n\,sh}$ are at least 10 times less than $S_{\rm SHC}$, it can be safely assumed that

$$X_{\rm SHC}G_{\rm sh} \ll 1, \quad X_{\rm SHC}B_{\rm sh} \ll 1. \tag{10.5}$$

Now consider the real number α such that for $\alpha \ll 1$ it can be assumed, with good accuracy, that

$$\frac{1}{1-\alpha} \cong 1 + \alpha \quad \text{and} \quad \frac{1}{1+\alpha} \cong 1 - \alpha. \tag{10.6}$$

Equations (10.5), and the identity in Equation (10.6), now allow the equations in (10.4) to be simplified to give

$$\underline{Y}_{\rm gs} = G_{\rm gs} + {\rm j}B_{\rm gs} = \frac{1}{\underline{Z}_{\rm gs}} \cong \frac{1}{X_{\rm g} + X_{\rm s}}\left[-X_{\rm SHC}G_{\rm sh} - {\rm j}\left(1 + X_{\rm SHC}B_{\rm sh}\right)\right], \tag{10.7}$$

$$Y_{\rm gs} \cong \frac{1}{X_{\rm g} + X_{\rm s}}\left(1 + X_{\rm SHC}B_{\rm sh}\right), \tag{10.8}$$

$$\tan\mu_{\rm gs} \cong -X_{\rm SHC}G_{\rm sh}\left(1 + X_{\rm SHC}B_{\rm sh}\right) = -X_{\rm SHC}G_{\rm sh}, \tag{10.9}$$

$$\underline{Y}_{\rm g0} = G_{\rm g0} + {\rm j}B_{\rm g0} \cong \frac{1}{X_{\rm g}}\left(X_{\rm SHC}G_{\rm sh} + {\rm j}X_{\rm SHC}B_{\rm sh}\right), \tag{10.10}$$

$$G_{\rm gg} = G_{\rm g0} + G_{\rm gs} \cong \frac{1}{X_{\rm g} + X_{\rm s}}\frac{X_{\rm s}}{X_{\rm g}}X_{\rm SHC}G_{\rm sh}. \tag{10.11}$$

Diligent readers may find the plus sign in Equation (10.7) rather surprising but it is correct and arises from the use of the small-value approximations in Equation (10.6). These derived parameters now allow a formula for the generator real power to be determined using the general formula given in Equation (3.150)[1] adapted to the π-equivalent circuit of Figure 10.11c to give

$$P(\delta') = G_{\rm g0}E_{\rm g}^2 + Y_{\rm gs}E_{\rm g}V_{\rm s}\sin(\delta' - \mu_{\rm gs}), \tag{10.12}$$

[1] Equation (3.150) used the angle $\theta = \arg(\underline{Y})$ but it is more convenient to use here the angle $\mu = \pi/2 - \theta$.

where $E_g = E' =$ constant and δ' is the transient rotor angle measured with respect to the infinite busbar. The sine function can be expressed as

$$\sin(\delta' - \mu_{gs}) = \sin\delta' \cos\mu_{gs} - \cos\delta' \sin\mu_{gs} = \cos\mu_{gs}\left(\sin\delta' - \tan\mu_{gs}\cos\delta'\right). \tag{10.13}$$

According to Equations (10.5) and (10.9), the angle μ_{gs} is small and $\cos\mu_{gs} \approx 1$. Making this approximation, and substituting Equation (10.9) into (10.13), gives

$$\sin(\delta' - \mu_{gs}) \cong \sin\delta' - X_{SHC} G_{sh} \cos\delta'. \tag{10.14}$$

This equation, and the expressions in Equations (10.8) and (10.10), can now be substituted into Equation (10.12) to give

$$P(\delta') \cong b\sin\delta' + b\,(\xi + \cos\delta')\, X_{SHC} G_{sh} + (b\sin\delta')\, X_{SHC} B_{sh}, \tag{10.15}$$

where $b = E_g V_s/(X_g + X_s)$ and $\xi = (E_g/V_s)/(X_s/X_g)$. Careful examination of this equation shows that the coefficient b is the amplitude of the power–angle characteristic *without* the shunt element, while the coefficient ξ depends on the location of the shunt element along the transmission link. With the shunt element disconnected, the characteristic defined by Equation (10.15) is the transient power–angle characteristic defined in Equation (5.40).

Figure 10.12 shows the influence of both G_{sh} and B_{sh} on the transient power–angle characteristic. Inserting a purely resistive shunt element, $G_{sh} \neq 0$, $B_{sh} = 0$, shifts the characteristic to the left, or the right, by the angle μ_{GS} depending on the sign of G_{sh}, Figure 10.12a. This shift by the angle μ_{GS}, and controlled by G_{sh}, is clearly demonstrated in Equation (10.12). Figure 10.12b shows how inserting a pure reactive shunt element, $G_{sh} = 0$, $B_{sh} \neq 0$, increases the amplitude of the characteristic by $X_{SHC} B_{sh}$.

Further examination of Figure 10.12 shows that the main influence of G_{sh} is at small values of δ' before the peak of the characteristic is reached. For large values of δ', beyond the peak, the influence of the conductance is negligible. In contrast the influence of B_{sh} is mostly at large values of δ', near the peak of the characteristic.

10.5.2 State-Variable Control

Since the shunt element influences the shape of the power–angle characteristic, it can be used to damp rotor swings either by switching it on and off at appropriate moments (bang–bang control) or by suitable continuous control action (provided continuous control of the shunt element is

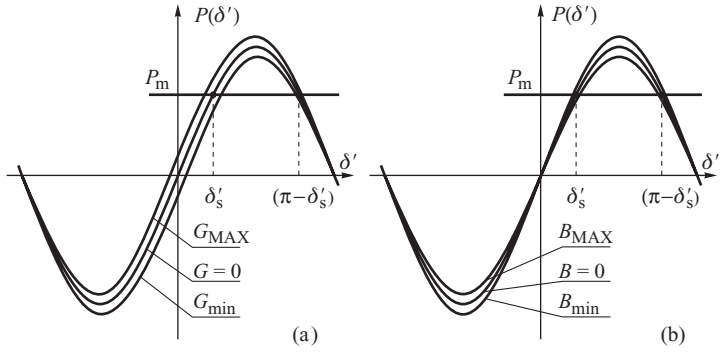

Figure 10.12 Influence of the shunt element on the power–angle characteristic: (a) pure conductance G_{sh}; (b) pure susceptance B_{sh}.

possible). The method used to control the shunt element is called the *control strategy*. Control using the system state variables is referred to as *state-variable control*.

The system state equations can be obtained by substituting the generator real power given by Equation (10.15) into the swing equation, Equation (5.15), to give

$$\begin{aligned} \frac{\mathrm{d}\delta'}{\mathrm{d}t} &= \Delta\omega \\ M\frac{\mathrm{d}\Delta\omega}{\mathrm{d}t} &= (P_\mathrm{m} - b\sin\delta') - D\frac{\mathrm{d}\delta'}{\mathrm{d}t} \\ &\quad - b\,(\xi + \cos\delta')\,X_\mathrm{SHC}G_\mathrm{sh}(t) - (b\sin\delta')\,X_\mathrm{SHC}B_\mathrm{sh}(t). \end{aligned} \tag{10.16}$$

The last two terms in the second equation depend on the conductance and susceptance of the controlled shunt element. Both these parameters are shown as functions of time to emphasize that they are the time-varying control variables.

10.5.2.1 Energy Dissipation

In order to derive the required control strategy, the energy approach described in Section 6.3 will be used. When a disturbance occurs in a power system, part of the kinetic energy stored in the rotating masses of generators and loads is released and undergoes oscillatory conversions from kinetic to potential energy and then back again during subsequent rotor swings. The oscillations continue until the damping torques dissipate all the released energy and the system trajectory returns to the equilibrium point. The goal is to control $G_\mathrm{sh}(t)$ and $B_\mathrm{sh}(t)$ in such a way as to maximize the speed of energy dissipation. This can be accomplished by maximizing the value of the derivative of the total system energy with time along the trajectory of the differential equations (10.16).

The total system energy $V = E_\mathrm{k} + E_\mathrm{p}$ for the generator–infinite busbar system is determined by Equation (6.18). The speed of energy changes is

$$\frac{\mathrm{d}V}{\mathrm{d}t} = \frac{\partial V}{\partial\delta'}\frac{\mathrm{d}\delta'}{\mathrm{d}t} + \frac{\partial V}{\partial\Delta\omega}\frac{\mathrm{d}\Delta\omega}{\mathrm{d}t}. \tag{10.17}$$

The partial derivatives $\partial V/\partial\delta'$ and $\partial V/\partial\Delta\omega$ can be calculated by differentiating the total energy given by Equation (6.18). The ordinary time derivatives $\mathrm{d}\delta'/\mathrm{d}t$ and $\mathrm{d}\Delta\omega/\mathrm{d}t$ can now be substituted for using Equation (10.16) to give

$$\frac{\mathrm{d}V}{\mathrm{d}t} = -\left[D\Delta\omega^2 + \Delta\omega b(\xi + \cos\delta')X_\mathrm{SHC}G_\mathrm{sh}(t) + \Delta\omega(b\sin\delta')X_\mathrm{SHC}B_\mathrm{sh}(t)\right]. \tag{10.18}$$

The first term in this equation corresponds to the energy dissipated by the natural damping torques (coefficient D) while the next two terms are contributed by the shunt element. Proper control of this element can contribute to a faster dissipation of energy. This will happen if $G_\mathrm{sh}(t)$ and $B_\mathrm{sh}(t)$ are varied so that the signs of the two last terms in (10.18) are always positive. This requires the signs of $G_\mathrm{sh}(t)$ and $B_\mathrm{sh}(t)$ to vary depending on the sign of the two state variables $\Delta\omega$ and δ'. This can be realized using either bang–bang control or continuous control.

10.5.2.2 Continuous Control

The aim of the control is firstly to ensure that the last two terms in Equation (10.18) are of positive sign and, secondly, to maximize their sum. This can be achieved by enforcing the following values

on the control variables:

$$\begin{aligned} G_{\mathrm{sh}}(t) &= K\ \Delta\omega\,[b(\xi + \cos\delta')]\ X_{\mathrm{SHC}} \\ B_{\mathrm{sh}}(t) &= K\ \Delta\omega\,[b\sin\delta']\ X_{\mathrm{SHC}}, \end{aligned} \tag{10.19}$$

where K is the gain of the controller. Substituting this equation into Equation (10.18) gives

$$\frac{\mathrm{d}V}{\mathrm{d}t} = -D\Delta\omega^2 - D_{\mathrm{sh}}\Delta\omega^2, \tag{10.20}$$

where

$$D_{\mathrm{sh}} = K\left\{[b(\xi + \cos\delta')]^2 + (b\sin\delta')^2\right\} X_{\mathrm{SHC}}^2, \tag{10.21}$$

is the equivalent damping coefficient introduced by the shunt element control. For the control strategy in Equation (10.19), the swing equation then becomes

$$\begin{aligned} \frac{\mathrm{d}\delta'}{\mathrm{d}t} &= \Delta\omega \\ M\frac{\mathrm{d}\Delta\omega}{\mathrm{d}t} &= (P_{\mathrm{m}} - b\sin\delta') - D\frac{\mathrm{d}\delta'}{\mathrm{d}t} - D_{\mathrm{sh}}\frac{\mathrm{d}\delta'}{\mathrm{d}t}. \end{aligned} \tag{10.22}$$

In the first of the two equations in (10.19) the expression $(\xi + \cos\delta')$ is positive over a large range of δ' $(-\pi/2 < \delta' < \pi/2)$ so that the sign of $G_{\mathrm{sh}}(t)$ will change at the same time as the rotor speed deviation $\Delta\omega$. On the other hand, the sign of $B_{\mathrm{sh}}(t)$ depends on both $\Delta\omega$ and $\sin\delta'$ and changes sign whenever the angle crosses through zero.

Figure 10.13 shows the changes in the sign of $G_{\mathrm{sh}}(t)$ and $B_{\mathrm{sh}}(t)$ that must occur along the system trajectory in order to produce positive damping. Whenever the trajectory crosses the horizontal axis, $\Delta\omega$ changes its sign and this will be accompanied by a change in sign of both $G_{\mathrm{sh}}(t)$ and $B_{\mathrm{sh}}(t)$. These points of sign changes have been denoted by small squares on the trajectory. Whenever the trajectory crosses the vertical axis, δ' changes its sign and this is accompanied by a sign change of $B_{\mathrm{sh}}(t)$ only. These points of sign changes have been denoted by the small solid circles on the trajectory.

In Figure 10.13 the characteristic states of the shunt element have been illustrated schematically in each quadrant in the phase plane. Negative susceptance is denoted by a coil symbol while positive susceptance is denoted by a capacitor symbol. Positive conductance is denoted by a resistance symbol while negative resistance (i.e. a source of real power) is denoted by an arrow. This obviously corresponds to the general case when the power of the shunt element can be adjusted in all four quadrants of the complex power plane.

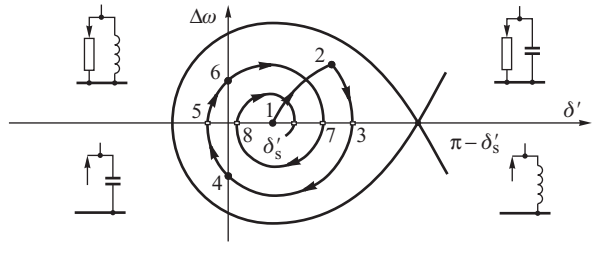

Figure 10.13 Stability area and the system trajectory.

10.5.2.3 Bang–Bang Control

The term bang–bang control refers to a control mode in which the element is switched on and off at appropriate moments. This type of control can be used with a shunt element whose parameters cannot be smoothly controlled. The switching then takes place at instants when the system trajectory crosses one of the phase axes shown in Figure 10.13 and passes into the next quadrant.

Equation (10.19) leads to the following bang–bang control strategies:

$$G_{\mathrm{sh}}(t) = \begin{cases} G_{\mathrm{MAX}} & \text{for} \quad [b(\xi + \cos\delta')\Delta\omega] \geq +\varepsilon \\ 0 & \text{for} + \varepsilon > [b(\xi + \cos\delta')\Delta\omega] > -\varepsilon \\ G_{\mathrm{min}} & \text{for} \quad [b(\xi + \cos\delta')\Delta\omega] \leq -\varepsilon \end{cases} \tag{10.23}$$

$$B_{\mathrm{sh}}(t) = \begin{cases} B_{\mathrm{MAX}} & \text{for} \quad [\Delta\omega(b\sin\delta')] \geq +\varepsilon \\ 0 & \text{for} + \varepsilon < [\Delta\omega(b\sin\delta')] > -\varepsilon \\ B_{\mathrm{min}} & \text{for} \quad [\Delta\omega(b\sin\delta')] \leq -\varepsilon \end{cases} \tag{10.24}$$

where G_{MAX} and B_{MAX} are the maximum, and G_{min} and B_{min} the minimum, values of the switching element. If the element cannot assume a negative value then the minimum value will be zero. The small positive number determines the dead zone ($\pm\varepsilon$) where the control variables are set to zero. The dead zone is necessary in order to avoid unstable operation of the controller for small signals.

As $(\xi + \cos\delta') > 0$ for a wide range of δ', the strategy for controlling the conductance $G_{\mathrm{sh}}(t)$ can be simplified to

$$G_{\mathrm{sh}}(t) = \begin{cases} G_{\mathrm{MAX}} & \text{for} \quad \Delta\omega \geq +\varepsilon \\ 0 & \text{for} + \varepsilon > \Delta\omega > -\varepsilon \\ G_{\mathrm{min}} & \text{for} \quad \Delta\omega \leq -\varepsilon \end{cases} \tag{10.25}$$

and the conductance switching is triggered by a change in sign of the speed deviation.

10.5.2.4 Interpretation of Shunt Element Control Using the Equal Area Criterion

As the energy approach is directly related to the equal area criterion (Section 6.3.4) the control strategies derived above can be usefully interpreted using the equal area criterion.

Figure 10.14 shows how the bang–bang control strategy enlarges the available deceleration area and reduces the acceleration area during every rotor forward swing, while during the backward swing the control reduces the deceleration area and enlarges the available acceleration area. The initial prefault state is point 1. The fault reduces the electrical real power to a value corresponding to point 2 and the rotor accelerates. The rotor angle increases until the fault is cleared at point 3 giving the first acceleration area 1–2–3–4. After clearing the fault, $\Delta\omega$ and δ' are positive so that G_{MAX} and B_{MAX} are switched in and the electrical power follows the higher $P(\delta')$ curve. As the maximum available decelerating area is 4–5–6–7, the generator remains stable with a stability margin proportional to area 6–7–8. At point 6 the speed deviation changes sign, the shunt admittance values switch to G_{min} and B_{min}, and the electrical power follows the lower $P(\delta')$ curve. This reduces the deceleration area during the backward swing and enlarges the available acceleration area so that the amplitude of the backward swing is reduced. The cycle then repeats and helps damp consecutive rotor swings.

10.5.3 Control Based on Local Measurements

The control strategy given by Equation (10.19) is based on the state variables δ' and $\Delta\omega$. As these quantities are not normally available at the shunt element busbar, the practical implementation of the control must be based on other signals that can be measured locally. How exactly such a local

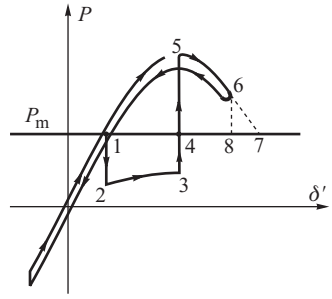

Figure 10.14 Interpretation of the control strategy using the equal area criterion.

control emulates the state-variable control depends on the choice of the measured quantities and the structure of the controller.

10.5.3.1 Dynamic Properties of Local Measurements

Let q_G and q_B be some quantities used as input signals to the shunt element controller. In the control strategy given by Equation (10.19) the shunt admittance depends on the rotor speed deviation $\Delta\omega$. If the magnitude of the transient emf is assumed constant (classical model), the derivative with respect to time of any electric quantity q_G can be expressed as

$$\frac{dq_G}{dt} = \frac{\partial q_G}{\partial \delta'}\Delta\omega + \alpha_{GG}\frac{dG_{sh}}{dt} + \alpha_{GB}\frac{dB_{sh}}{dt}, \tag{10.26}$$

where the coefficients

$$\alpha_{GG} = \frac{\partial q_G}{\partial G_{sh}}, \quad \alpha_{GB} = \frac{\partial q_G}{\partial B_{sh}}, \tag{10.27}$$

determine the sensitivity of q_G to a change in the control variables $G_{sh}(t)$ and $B_{sh}(t)$. Equation (10.26) gives

$$\Delta\omega\frac{\partial q_G}{\partial \delta'} = \frac{dq_G}{dt} - \alpha_{GG}\frac{dG_{sh}}{dt} - \alpha_{GB}\frac{dB_{sh}}{dt}. \tag{10.28}$$

If the sensitivity coefficients α_{GG} and α_{GB} are known, the right hand side of Equation (10.28) can be computed in real time and used to determine a signal proportional to the rotor speed deviation necessary for the control of $G_{sh}(t)$. Comparing the right hand side of the first of the equations in (10.19) with the left hand side of Equation (10.28) shows that the signal obtained from Equation (10.28) is the same as the state-variable control signal if

$$\frac{\partial q_G}{\partial \delta'} = \left[b\left(\xi + \cos\delta'\right)\right] X_{SHC}. \tag{10.29}$$

Substitution of the right hand side of the first equation in (10.19) by Equation (10.28) gives the following control principle:

$$G_{sh}(t) = K\left[\frac{dq_G}{dt} - \alpha_{GG}\frac{dG_{sh}}{dt} - \alpha_{GB}\frac{dB_{sh}}{dt}\right]. \tag{10.30}$$

This means that if a measured quantity q_G satisfies the condition in Equation (10.29) then the modulation controller need simply differentiate q_G with respect to time and subtract from the result values proportional to the rate of change of the controlled variables $B_{sh}(t)$ and $G_{sh}(t)$.

The control principle for the shunt susceptance can be obtained in a similar way as

$$B_{\mathrm{sh}}(t) = K\left[\frac{\mathrm{d}q_{\mathrm{B}}}{\mathrm{d}t} - \alpha_{\mathrm{BG}}\frac{\mathrm{d}G_{\mathrm{sh}}}{\mathrm{d}t} - \alpha_{\mathrm{BB}}\frac{\mathrm{d}B_{\mathrm{sh}}}{\mathrm{d}t}\right], \tag{10.31}$$

where the coefficients

$$\alpha_{\mathrm{BG}} = \frac{\partial q_{\mathrm{B}}}{\partial G_{\mathrm{sh}}}, \quad \alpha_{\mathrm{BB}} = \frac{\partial q_{\mathrm{B}}}{\partial B_{\mathrm{sh}}}, \tag{10.32}$$

determine the sensitivity of q_{B} to changes in the control variables $B_{\mathrm{sh}}(t)$ and $G_{\mathrm{sh}}(t)$. Comparison with the second of the equations in (10.19) shows that the input quantity q_{B} should satisfy the following condition:

$$\frac{\partial q_{\mathrm{B}}}{\partial \delta'} = \left[b\sin\delta'\right] X_{\mathrm{SHC}}. \tag{10.33}$$

It now remains to determine what locally measurable quantities q_{B} and q_{G} will satisfy the conditions defined in Equations (10.29) and (10.33).

10.5.3.2 Voltage-Based Quantities

The current flowing from the network to the shunt element in Figure 10.11 is given by

$$\underline{I}_{\mathrm{sh}} = \underline{V}_{\mathrm{sh}}\underline{Y}_{\mathrm{sh}} = \frac{\underline{E}_{\mathrm{g}} - \underline{V}_{\mathrm{sh}}}{\mathrm{j}X_{\mathrm{g}}} + \frac{\underline{V}_{\mathrm{s}} - \underline{V}_{\mathrm{sh}}}{\mathrm{j}X_{\mathrm{s}}}, \tag{10.34}$$

where $\underline{Y}_{\mathrm{sh}} = G_{\mathrm{sh}}(t) + \mathrm{j}B_{\mathrm{sh}}(t)$ and X_{g} and X_{s} are the equivalent reactances denoted in Figure 10.11. Multiplying the current by the short-circuit reactance X_{SHC} and moving $\underline{V}_{\mathrm{sh}}$ to the left hand side gives

$$\underline{V}_{\mathrm{sh}}\left\{\left[X_{\mathrm{SHC}}G_{\mathrm{sh}}(t)\right] + \mathrm{j}\left[1 - X_{\mathrm{SHC}}B_{\mathrm{sh}}(t)\right]\right\} = \frac{\underline{E}_{\mathrm{g}}X_{\mathrm{s}} + \underline{V}_{\mathrm{s}}X_{\mathrm{g}}}{\mathrm{j}\left(X_{\mathrm{g}} + X_{\mathrm{s}}\right)}. \tag{10.35}$$

Substituting for the complex voltages

$$\underline{E}_{\mathrm{g}} = E_{\mathrm{g}}\left(\cos\delta' + \mathrm{j}\,\sin\delta'\right) \quad \text{and} \quad \underline{V}_{\mathrm{s}} = V_{\mathrm{s}}, \tag{10.36}$$

and multiplying the resulting equation by its conjugate gives, after a little algebra,

$$V_{\mathrm{sh}}^2 = \frac{bX_{\mathrm{SHC}}\left(\xi + \frac{1}{\xi} + 2\cos\delta'\right)}{\left[X_{\mathrm{SHC}}G_{\mathrm{sh}}(t)\right]^2 + \left[1 - X_{\mathrm{SHC}}B_{\mathrm{sh}}(t)\right]^2}, \tag{10.37}$$

where ξ is the coefficient defined in Equation (10.15). When deriving Equation (10.37), it is also possible to find the phase angle θ of the shunt element voltage measured with respect to the infinite bus:

$$\tan\theta = \frac{\left(\frac{1}{\xi} + \cos\delta'\right)X_{\mathrm{SHC}}G_{\mathrm{sh}}(t) + \sin\delta'\left[1 - X_{\mathrm{SHC}}B_{\mathrm{sh}}(t)\right]}{\sin\delta' X_{\mathrm{SHC}}G_{\mathrm{sh}}(t) + \left(\frac{1}{\xi} + \cos\delta'\right)\left[1 - X_{\mathrm{SHC}}B_{\mathrm{sh}}(t)\right]}. \tag{10.38}$$

The inequalities in Equation (10.5) allow Equations (10.37) and (10.38) to be simplified to

$$V_{\mathrm{sh}}^2 \cong b\left(\xi + \frac{1}{\xi} + 2\cos\delta'\right)X_{\mathrm{SHC}}; \quad \tan\theta \cong \frac{\sin\delta'}{\frac{1}{\xi} + \cos\delta'}. \tag{10.39}$$

Using the first of Equations (10.39), and after differentiating with respect to δ', gives

$$\frac{\partial V_{\text{sh}}^2}{\partial \delta'} = -2\left[b \sin \delta'\right] X_{\text{SHC}}. \tag{10.40}$$

Calculation of the derivative $\partial\theta/\partial\delta'$ is slightly more difficult. The second of Equations (10.39) may be written as $f(\theta, \delta') = 0$. Hence θ is an implicit function of δ'. The derivative of that function can be calculated from

$$\frac{\partial \theta}{\partial \delta'} = -\frac{\frac{\partial f}{\partial \delta'}}{\frac{\partial f}{\partial \theta}}. \tag{10.41}$$

Using this equation gives

$$\frac{\partial \theta}{\partial \delta'} = \frac{\xi + \cos \delta'}{\xi + \frac{1}{\xi} + 2\cos \delta'}. \tag{10.42}$$

The expression in the denominator of Equation (10.42) is the same as the expression in brackets in the first of the equations in (10.39). Substitution gives

$$V_{\text{sh}}^2 \frac{\partial \theta}{\partial \delta'} = \left[b\left(\xi + \cos \delta'\right)\right] X_{\text{SHC}}. \tag{10.43}$$

Equations (10.40) and (10.43) show that local measurements of the squared magnitude of the shunt element voltage and its phase angle can give good signals for controlling the shunt element. Comparing Equations (10.40) and (10.33) shows that the signal V_{sh}^2 satisfies the condition in Equation (10.33) for the control strategy of the shunt susceptance. Similarly, comparing Equations (10.43) and (10.29) shows that θ satisfies the condition in (10.29) for the required control of the shunt conductance provided that the derivative is multiplied by V_{sh}^2.

A sensitivity analysis of the effect of changes in V_{sh}^2 and θ on the changes in the controlled variables $B_{\text{sh}}(t)$ and $G_{\text{sh}}(t)$ can be conducted by evaluating the derivatives in Equations (10.27) and (10.32) using Equations (10.37) and (10.38). This involves a lot of simple, but arduous, algebraic and trigonometric transformations which finally lead to the following simplified formulae:

$$\begin{aligned} \alpha_{\text{GG}} &= \frac{\partial q_{\text{G}}}{\partial G_{\text{sh}}} \cong -X_{\text{SHC}}, \quad & \alpha_{\text{GB}} &= \frac{\partial q_{\text{G}}}{\partial B_{\text{sh}}} \cong 0 \\ \alpha_{\text{BG}} &= \frac{\partial q_{\text{B}}}{\partial G_{\text{sh}}} \cong 0, & \alpha_{\text{BB}} &= \frac{\partial q_{\text{B}}}{\partial B_{\text{sh}}} \cong -V_{\text{sh}}^2 X_{\text{SHC}}. \end{aligned} \tag{10.44}$$

Zero values of α_{GB} and α_{BG} signify that changes in the shunt susceptance/conductance have a negligibly small effect on the given quantity.

10.5.3.3 Control Schemes

Substituting Equations (10.44) into Equations (10.30) and (10.31) and taking the squared voltage magnitude and the voltage phase angle as control signals yields

$$G_{\text{sh}}(t) = K V_{\text{sh}}^2 \left[\frac{\mathrm{d}\theta}{\mathrm{d}t} + X_{\text{SHC}} \frac{\mathrm{d}G_{\text{sh}}}{\mathrm{d}t}\right], \tag{45a}$$

$$B_{\text{sh}}(t) = K \left[-\frac{1}{2}\frac{\mathrm{d}\left(V_{\text{sh}}^2\right)}{\mathrm{d}t} + X_{\text{SHC}} V_{\text{sh}}^2 \frac{\mathrm{d}B_{\text{sh}}}{\mathrm{d}t}\right]. \tag{45b}$$

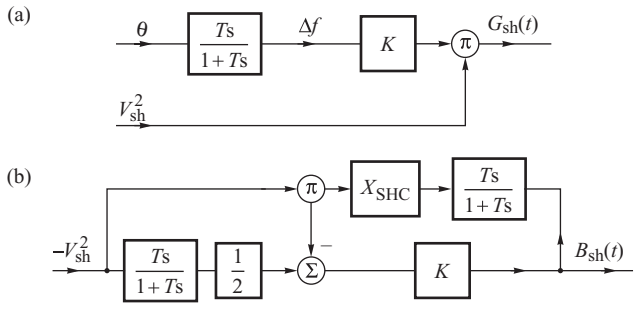

Figure 10.15 Modulation controller employing the frequency–voltage control scheme for: (a) $G_{sh}(t)$; (b) $B_{sh}(t)$.

The rotor angle δ' and the voltage phase angle θ are measured with respect to the infinite busbar voltage or the synchronous reference frame. As the derivative of θ with time is equal to the deviation of the local frequency, that is $d\theta/dt = 2\pi\Delta f$, control (10.45) is referred to as *frequency- and voltage-based control*.

Figure 10.15 shows the block diagram of the appropriate control circuits. Differentiation has been replaced by a real differentiating element with a small time constant T. The shunt susceptance controller is nonlinear because the output signal in the main feedback loop is multiplied by the main input signal. The shunt conductance controller is linear but its effective gain is modulated by the squared voltage magnitude which is also the main input signal for the shunt susceptance controller. The short-circuit reactance X_{SHC} plays only a corrective role and its value may be set with a large error. For practical applications its value can be assessed offline and set as a constant parameter.

It is worth noting that the time derivative of the voltage angle $d\theta/dt$ is equal to the deviation of the local frequency Δf. Thus the proposed shunt element controller is a frequency- and voltage-orientated controller. The input signals for the control system may be measured using digital techniques described by Phadke, Thorap and Adamiak (1983) or Kamwa and Grondin (1992).

10.5.4 Examples of Controllable Shunt Elements

Continuous state-variable control, and its practical implementation based on locally measurable quantities, is possible assuming that both $G_{sh}(t)$ and $B_{sh}(t)$ can be changed smoothly over a range of negative and positive values. Some of the different types of shunt elements that can be thyristor controlled have been described in Section 2.4.4 where the ability to change $G_{sh}(t)$ and $B_{sh}(t)$ was seen to depend on the particular device in question. When using a particular shunt element, any such limitation must be taken into account in the control structure by inserting appropriate limiters into the control circuits shown in Figure 10.15.

10.5.4.1 Supplementary Control of SVC and STATCOM

SVC based on conventional thyristors (Figure 2.27) is equipped with a voltage regulator (Figure 2.28) giving the static characteristic (Figure 2.29) with a small droop in the regulation area. In the steady state such regulation is very effective in forcing the steady-state voltage error to zero. In the transient state the regulator is incapable of providing enough damping because the voltage error does not carry proper information about the system dynamic response. A more robust control can be obtained when the voltage regulator is equipped with the supplementary control loop as shown in Figure 10.16. This additional supplementary loop can be used to force a control signal for $B_{sh}(t)$

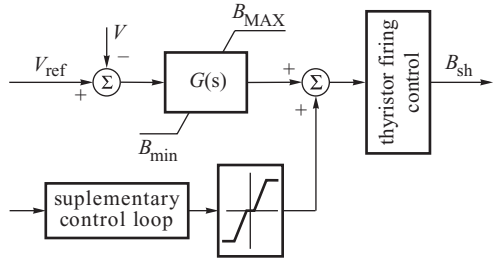

Figure 10.16 Voltage regulator of the SVC with supplementary control loop.

to enhance damping of power swings. This control loop acts much faster than the main voltage controller. The controller in the supplementary control loop will be based on Equations (10.45) and is shown in Figure 10.15b.

In a similar way the supplementary control loop may be also equipped with the voltage regulator of STATCOM (Figure 2.30).

10.5.4.2 Control of BR

Application of BRs switched by a mechanical circuit-breaker was described in Section 10.3. Another, more expensive possibility is to switch or control the BR using thyristors as described in Section 2.4.4.

Thyristor-switched BRs (Figure 2.33) may be equipped with a bang–bang controller to implement the strategy defined in Equation (10.25) with $G_{min} = 0$. Alternatively, the resistors may be equipped with a continuous controller to implement the strategy defined in Equation (10.23) with $G_{min} = 0$. If the rotor speed deviation signal $\Delta\omega$ is not available, it may be replaced by the local frequency deviation $2\pi\,\Delta f = \mathrm{d}\theta/\mathrm{d}t$, as in the shunt controller shown in Figure 10.15a. Obviously an output limiter and a dead zone would have to be added before the output in the block diagram, as in Figure 10.16. In the steady state the BRs are switched off and the modulation controller (Figure 10.15a) is their only control circuit.

10.5.4.3 STATCOM + BR as a More Effective Device

The influence of an active and reactive shunt element on real power of a generator was shown in Figure 10.12. When power angle δ' is small, the influence of a shunt reactive element is quite small. Consequently, when the generator operates at a small power angle, little damping of the power swings using STATCOM alone can be obtained. This can be improved by adding to STATCOM a thyristor-controlled BR. Such a resistor may be included in the DC circuit of STATCOM in the same way as a battery is included with BESS (Figure 2.32). STATCOM would then act alone during the steady-state operation providing a return on investment from the voltage control and reactive compensation. The additional BR would support STATCOM in the transient state by providing additional damping of power swings.

10.5.4.4 Modulation of Energy Storage SMES or BESS

The schematic diagram of energy storage systems BESS or SMES utilizing voltage source converters was shown in Figure 2.32. The voltage source converter is controlled using a power conditioning system (PCS). The PCS allows BESS or SMES to generate power, for a short time, from any quadrant of the complex power plane assuming that the apparent power (or equivalent admittance)

satisfies the limits described by Equation (2.9). The frequency- and voltage-based controller shown in Figure 10.15 can be used as the modulation controller of an SMES system by forcing the required values of the real and reactive power to be proportional to signals $G_{\text{sh}}(t)$ and $B_{\text{sh}}(t)$. If the values of these signals are too large then they can be proportionally reduced to satisfy the limits.

10.5.5 Generalization to Multi-Machine Systems

The control strategy given by Equations (10.19) and (10.45) was derived for the generator–infinite busbar system. These equations can be generalized to a multi-machine system regardless of where the shunt element is located within the system. A detailed proof can be found in Machowski and Bialek (2008). Here only the general framework of the proof and the final equations will be shown.

10.5.5.1 Mathematical Model

All the lines and transformers belonging to the modelled network are represented by π-equivalent circuits. Power flowing from the transmission to the distribution network is treated as a load and replaced by a constant admittance included in the network model. All nodes of the network model can be divided into three types:

$\{G\}$ – internal generator nodes (behind the transient reactances);
k – a chosen node where the considered shunt FACTS device is installed;
$\{L\}$ – remaining network nodes.

Similar to Figure 10.11, the shunt FACTS device is included in the network model as the varying shunt admittance $\underline{Y}_{\text{sh}}(t) = G_{\text{sh}}(t) + \text{j}B_{\text{sh}}(t)$. In the first step of the proof, all the load nodes $\{L\}$ are eliminated from the network model using the network transformation method described in Section 14.2. Consequently, an equivalent network is obtained that is shown schematically in Figure 10.17. The equivalent network connects all generator nodes $\{G\}$ with node k in which the considered shunt FACTS device is installed.

As in Figure 10.11, conductances G_{ij} of the equivalent network are neglected and only susceptances B_{ij} are included in the equivalent network model. To retain the balance of power between generation and demand, fictitious loads responsible for real power losses on the conductances G_{ij} of the equivalent network are added in $\{G\}$ nodes. This is obviously a simplified method of treating conductances and real power losses.

After long and tedious algebraic transformations the following equation for real power at a generator node is obtained:

$$P_i = P_{0i}^0 + \sum_{j=1}^{n} b_{ij} \sin \delta_{ij} + \left[\sum_{j=1}^{n} \beta_{ik}\beta_{kj} \cos \delta_{ij} \right] G_{\text{sh}}(t) + \left[\sum_{j=1}^{n} \beta_{ik}\beta_{kj} \sin \delta_{ij} \right] B_{\text{sh}}(t), \qquad (10.46)$$

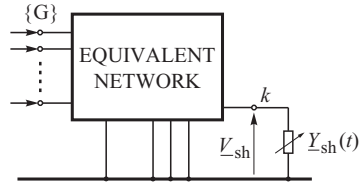

Figure 10.17 Schematic illustration of equivalent network.

where P_{0i}^0 is real power of the equivalent load at a generator node and $b_{ij} = \left|\underline{E}_i\right| \left|\underline{E}_j\right| B_{ij}$ is the magnitude of the power–angle characteristic for an equivalent branch connecting a given pair of internal generator nodes $\{i, j\}$. Coefficients β_{ik}, β_{jk} constitute electrical measures of the distance between node k and internal generator nodes $\{i, j\}$, respectively. These coefficients are given by

$$\beta_{ik} = X_{\mathrm{SHC}} B_{ik} \left|\underline{E}_i\right|, \quad \beta_{jk} = X_{\mathrm{SHC}} B_{jk} \left|\underline{E}_j\right|, \tag{10.47}$$

where B_{ik}, B_{jk} are susceptances of the equivalent branches connecting a given pair of internal generator nodes $\{i, j\}$ with node k, and X_{SHC} is the short-circuit reactance of the system seen from node k in which the shunt FACTS device is installed. Equation (10.46) is important in the sense that it shows that a shunt FACTS device introduces two components proportional to $G_{\mathrm{sh}}(t)$ and $B_{\mathrm{sh}}(t)$, respectively, into the equation expressing real power of a generator. Note the similarity of Equations (10.15) and (10.46).

10.5.5.2 Control Strategy

Using Equation (10.46), the swing equations can be formed for all generators, as in Equation (10.16):

$$\begin{aligned}
\frac{\mathrm{d}\delta_i}{\mathrm{d}t} &= \Delta\omega \\
\frac{\mathrm{d}\Delta\omega_i}{\mathrm{d}t} &= \frac{1}{M_i}\left[P_{\mathrm{m}i} - P_{0i}^0\right] - \frac{1}{M_i}\sum_{j=1}^{n} b_{ij}\sin\delta_{ij} - \frac{D_i}{M_i}\Delta\omega_i \\
&\quad - \frac{1}{M_i}\left[\sum_{j=1}^{n}\beta_{ik}\beta_{kj}\cos\delta_{ij}\right] G_{\mathrm{sh}}(t) - \frac{1}{M_i}\left[\sum_{j=1}^{n}\beta_{ik}\beta_{kj}\sin\delta_{ij}\right] B_{\mathrm{sh}}(t),
\end{aligned} \tag{10.48}$$

where rotor angles δ_i and speed deviations $\Delta\omega_i$ are the state variables of the system. Equations (10.48) form the nonlinear state-space model describing a dynamic response of the system when changes in the equivalent admittance of the shunt FACTS device are considered.

As a Lyapunov function, the total system energy equal to the sum of the kinetic and potential energy may be used:

$$V(\delta, \omega) = E_{\mathrm{k}} + E_{\mathrm{p}}, \tag{10.49}$$

where E_{k} and E_{p} are given by Equations (6.46) and (6.47). Using Equations (6.55) and (6.56) and the state-space equations (10.48), it can be shown that time derivatives of the kinetic and potential energy are given by

$$\begin{aligned}
\frac{\mathrm{d}E_{\mathrm{k}}}{\mathrm{d}t} &= \sum_{i=1}^{n}\Delta\omega_i\left[P_{\mathrm{m}i} - P_{0i}^0\right] - \sum_{i=1}^{n}\Delta\omega_i\sum_{j=1}^{n} b_{ij}\sin\delta_{ij} - \sum_{i=1}^{n} D_i\Delta\omega_i^2 \\
&\quad - \left[\sum_{i=1}^{n}\Delta\omega_i\sum_{j=1}^{n}\beta_{ik}\beta_{kj}\cos\delta_{ij}\right] G_{\mathrm{sh}}(t) - \left[\sum_{i=1}^{n}\Delta\omega_i\sum_{j=1}^{n}\beta_{ik}\beta_{kj}\sin\delta_{ij}\right] B_{\mathrm{sh}}(t),
\end{aligned} \tag{10.50}$$

$$\frac{\mathrm{d}E_{\mathrm{p}}}{\mathrm{d}t} = -\sum_{i=1}^{n}\Delta\omega_i\left(P_{mi} - P_{0i}^0\right) + \sum_{i=1}^{n}\Delta\omega_i\sum_{j\neq i}^{n} b_{ij}\sin\delta_{ij}. \tag{10.51}$$

Note that the first two components of (10.50) are equal to (10.51) but with opposite signs. This means that there is a continuous exchange of energy in the transient state between the potential

and kinetic energy terms. Moreover, as shown in Equation (10.50), the shunt FACTS element has a direct influence on the rate of change of the kinetic energy.

Adding (10.50) and (10.51) gives

$$\dot{V} = \frac{\mathrm{d}V}{\mathrm{d}t} = \frac{\mathrm{d}E_{\mathrm{k}}}{\mathrm{d}t} + \frac{\mathrm{d}E_{\mathrm{p}}}{\mathrm{d}t} = -\sum_{i=1}^{n} D_i \Delta\omega_i^2 + \dot{V}(\mathrm{sh}), \tag{10.52}$$

where

$$\dot{V}(\mathrm{sh}) = -\left[\sum_{i=1}^{n} \Delta\omega_i \beta_{ik} \sum_{j=1}^{n} \beta_{kj} \cos\delta_{ij}\right] G_{\mathrm{sh}}(t) - \left[\sum_{i=1}^{n} \Delta\omega_i \sum_{j=1}^{n} \beta_{ik}\beta_{kj} \sin\delta_{ij}\right] B_{\mathrm{sh}}(t). \tag{10.53}$$

The first component of (10.52) is due to natural damping of generator swings and is always negative for $D_i > 0$. The second component of (10.52) represents damping introduced by the supplementary control of the shunt FACTS device.

The shunt FACTS device contributes to the system damping if $\dot{V}(\mathrm{sh})$ is negative. Inspection of (10.53) shows that it is possible to make $\dot{V}(\mathrm{sh})$ always negative by making the values of $G_{\mathrm{sh}}(t)$ and $B_{\mathrm{sh}}(t)$ always have the same sign as the relevant values in the square brackets in (10.53). Hence the stabilizing control based on the measurement of the state variables should follow the following control strategies:

$$G_{\mathrm{sh}}(t) = K \cdot \sum_{i=1}^{n} \Delta\omega_i \beta_{ik} \sum_{j=1}^{n} \beta_{kj} \cos\delta_{ij}, \tag{10.54}$$

$$B_{\mathrm{sh}}(t) = K \cdot \sum_{i=1}^{n} \Delta\omega_i \beta_{ik} \sum_{j=1}^{n} \beta_{kj} \sin\delta_{ij}, \tag{10.55}$$

where K is the control gain.

State-variable control based on the above strategies can be treated as multi-loop control with the speed deviations of generators as the input signals and dynamic gains dependent on power angles. This can be shown by expressing Equations (10.54) and (10.55) as

$$G_{\mathrm{sh}}(t) = K \cdot \sum_{i=1}^{n} \Delta\omega_i \beta_{ik} g_i(\boldsymbol{\delta}), \tag{10.56}$$

$$B_{\mathrm{sh}}(t) = K \cdot \sum_{i=1}^{n} \Delta\omega_i \beta_{ik} b_i(\boldsymbol{\delta}), \tag{10.57}$$

where

$$g_i(\boldsymbol{\delta}) = \sum_{j=1}^{n} \beta_{kj} \cos\delta_{ij} \quad \text{and} \quad b_i(\boldsymbol{\delta}) = \sum_{j=1}^{n} \beta_{kj} \sin\delta_{ij}, \tag{10.58}$$

are dynamic gains dependent on the current values of the power angles $\boldsymbol{\delta} = [\delta_1, \delta_2, \ldots, \delta_n]$ and distance measures β_{ik}, β_{jk} are given by Equations (10.47). A block diagram of such multi-loop control of $G_{\mathrm{sh}}(t)$ is shown in Figure 10.18. For $B_{\mathrm{sh}}(t)$ control, the block diagram is identical but $g_i(\boldsymbol{\delta})$ is replaced by $b_i(\boldsymbol{\delta})$.

Application of dynamic gains $g_i(\boldsymbol{\delta})$ and $b_i(\boldsymbol{\delta})$ significantly influences the dynamic properties of the control process in two ways:

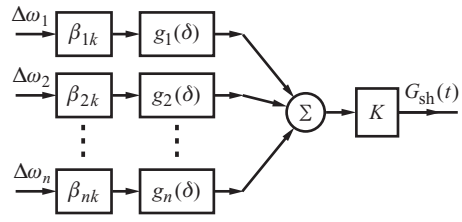

Figure 10.18 Schematic illustration of the multi-loop control of $G_{sh}(t)$.

1. Remote generators (small β_{ik}) have little influence on the output signal. The output signal is influenced mostly by generators close to the node k where the shunt device is installed (big β_{ik}). Such dependence of gains on distance measures is justified because shunt FACTS devices have little influence on power produced by remote generators. Hence there would be no point in making control of the device dependent on the state variables of remote generators.
2. Current values of power angles change dynamic gains. In the case of $G_{sh}(t)$, dynamic gains $g_i(\boldsymbol{\delta})$ decrease as the power angles increase (cosine function). In the case of $B_{sh}(t)$, dynamic gains $b_i(\boldsymbol{\delta})$ increase as the power angles increase (sine function). Such dynamic changes of gains are justified because the influence of reactive elements $B_{sh}(t)$ on generated power is significant only when the power angle is high (Figure 10.12b). On the other hand, the influence of active elements $G_{sh}(t)$ is reduced when the power angle increases (Figure 10.12a).

The control algorithm satisfying the above properties 1 and 2 is therefore intelligent in the sense that it does not act when the control does not bring the required effects in the system dynamic response. Obviously the effectiveness of the proposed controller in damping a particular mode of oscillation will depend on its location in the system. This would be revealed by observability and controllability analysis but such analysis is beyond the scope of this book.

The double summation in (10.55) corresponds to the sum of elements of a square matrix with elements equal to $\Delta\omega_i\beta_{ik}\beta_{kj}\sin\delta_{ij}$. The diagonal elements of the matrix are zero because $\sin\delta_{ii} = \sin 0 = 0$ while the sign of the elements in the upper triangle of the matrix is opposite to that in the lower triangle because $\sin\delta_{ij} = -\sin\delta_{ji}$. Hence

$$\sum_{i=1}^{n}\Delta\omega_i\sum_{j=1}^{n}\beta_{ik}\beta_{kj}\sin\delta_{ij} = \sum_{i=1}^{n}\sum_{j>i}^{n}\Delta\omega_{ij}\beta_{ik}\beta_{kj}\sin\delta_{ij}, \tag{10.59}$$

where $\Delta\omega_{ij} = \Delta\omega_i - \Delta\omega_j$. Equation (10.59) allows the control strategy (10.57) to be expressed as

$$B_{sh}(t) = K\cdot\sum_{i=1}^{n}\sum_{j>i}^{n}\beta_{ik}\beta_{kj}\Delta\omega_{ij}\sin\delta_{ij}, \tag{10.60}$$

which means that $B_{sh}(t)$ depends on the relative speed deviations $\Delta\omega_{ij}$. This property is very important for the response of the supplementary control when disturbances lead to changes in the system frequency. In that case all rotors of all the generators change their speed coherently and the signal produced by (10.60) or (10.57) is equal to zero, $B_{sh}(t) = 0$. This makes sense because reactive shunt elements cannot influence the frequency.

In the case of $G_{sh}(t)$ control, it is not possible to transform the strategy (10.54) in such a way that a relationship similar to (10.59) is obtained because $\cos\delta_{ij} = \cos\delta_{ji}$. Hence the value of $G_{sh}(t)$ is determined by individual $\Delta\omega_i$ rather than relative values $\Delta\omega_{ij}$. This makes sense because, when

there is a surplus of energy in the system, frequency increases and all the loops in Figure 10.18 produce a positive signal. The controlled SMES or BR will then absorb energy reducing the surplus. On the other hand, when there is an energy deficit in the system, the frequency decreases and all the loops shown in Figure 10.18 produce a negative signal. The SMES will then inject real power into the system thereby reducing the energy deficit.

It is also worth noticing that the coordinates of the postfault equilibrium point δ_i^s, which were present in the energy-type Lyapunov function, are not present in the control strategies described by (10.54) and (10.55). This means that it is not necessary to calculate the coordinates of δ_i^s following a disturbance. Control strategies described by (10.54) and (10.55) utilize only the values of angles δ_i in the transient state.

10.5.5.3 Wide Area Control System WAMPAC

Each loop of the supplementary stabilizing control contains a coefficient β_{ik} corresponding to the measures of the distance between a given ith generator and a given node k where the shunt FACTS device is installed. When the distance is long, the distance measure β_{ik} is small and it may be approximately assumed that $\beta_{ik} \cong 0$ so that the corresponding loop can be neglected. Hence, in practice, the proposed multi-loop controller will contain only a few loops corresponding to generators in a small area surrounding the shunt FACTS device. Hence, from the point of view of the state-variable stabilizing control of shunt FACTS devices, it is not necessary to measure phasors $\underline{E}_i = E_i e^{j\delta_i}$ in the whole power system. It is sufficient to measure phasors only in a small area around the shunt FACTS device. Such control may be referred to as *area control*.

Control strategies (10.56) and (10.57) simplified to area control could be utilized in a WAMPAC-type (Section 2.6) control system making use of phasor measurements. A possible structure of such a system is shown in Figure 10.19. The main steady-state control loop (the upper part of Figure 10.19) is based on measuring a locally observable signal to be controlled by a FACTS device. For example, in the case of STATCOM, it is the voltage at a given node of the system. The supplementary stabilizing loop (the lower part of Figure 10.19) utilizes state variables as input signals and, from the point of view of the whole system, it is a state-variable control. The main problem for such a closed-loop control is the speed of data transmission. Current modern flexible communication platforms (Figure 2.45) cannot transmit data fast enough in order to damp power swings. However, it may be expected that the speed of data transmission will increase in the near future so that practical implementation of a WAMPAC system similar to that shown in Figure 10.19 will be possible.

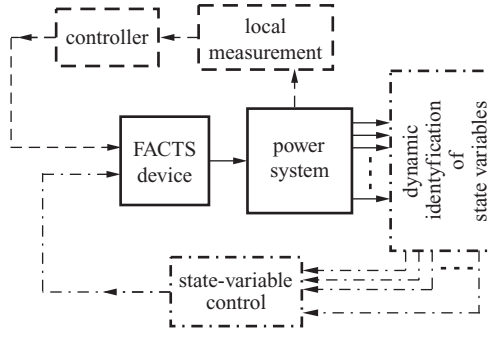

Figure 10.19 Schematic illustration of the local control and state-variable stabilizing control.

10.5.5.4 Emulation of State-Variable Control by Local Control

As the speed of data transmission is not fast enough to implement the WAMPAC shown in Figure 10.19, it is necessary to look for controllers using local measurements and which are able to emulate the control strategy (10.54) and (10.55). How exactly such local control will emulate optimal control depends on the choice of local signals used and the structure of the regulator. A detailed analysis of the choice of signals can be found in EPRI (1999). Here an analysis will be presented based on Machowski and Nelles (1994). Equations derived in their paper show that the controller of Figure 10.15 implementing Equation (10.45) is also valid for the multi-machine system regardless of where the shunt FACTS device is located within the system.

For the multi-machine system, an equation similar to (10.26) can be written as

$$\frac{\mathrm{d}q_{\mathrm{G}}}{\mathrm{d}t} = \sum_{i=1}^{n} \Delta\omega_i \frac{\partial q_{\mathrm{G}}}{\partial \delta_i} + \alpha_{\mathrm{GG}} \frac{\mathrm{d}G_{\mathrm{sh}}}{\mathrm{d}t} + \alpha_{\mathrm{GB}} \frac{\mathrm{d}B_{\mathrm{sh}}}{\mathrm{d}t}, \tag{10.61}$$

where α_{GG}, α_{GB} are sensitivity factors determined by Equations (10.27). Equation (10.61) can be transformed to give

$$\sum_{i=1}^{n} \Delta\omega_i \frac{\partial q_{\mathrm{G}}}{\partial \delta_i} = \frac{\mathrm{d}q_{\mathrm{G}}}{\mathrm{d}t} - \alpha_{\mathrm{GG}} \frac{\mathrm{d}G_{\mathrm{sh}}}{\mathrm{d}t} - \alpha_{\mathrm{GB}} \frac{\mathrm{d}B_{\mathrm{sh}}}{\mathrm{d}t}. \tag{10.62}$$

The left hand side of Equation (10.62) depends on $\Delta\omega_i$. It is exactly the same as in the theoretically optimal strategy determined by Equation (10.54) if the following condition is satisfied:

$$\frac{\partial q_{\mathrm{G}}}{\partial \delta_i} = \sum_{j=1}^{n} \beta_{ik}\beta_{kj} \cos \delta_{ij}. \tag{10.63}$$

Substituting the partial derivative on the left hand side of Equation (10.62) by the right hand side of Equation (10.63) and inserting the result into Equation (10.54) gives the local control (10.30).

In the control strategy given by Equation (10.60) the shunt susceptance depends on the relative speed deviations $\Delta\omega_{ij}$. The time derivative of q_{B}, expressed in terms of the relative speed deviations, is given by

$$\frac{\mathrm{d}q_{\mathrm{B}}}{\mathrm{d}t} = \sum_{i=1}^{n} \sum_{j>i}^{\mathrm{n}} \Delta\omega_{ij} \frac{\partial q_{\mathrm{B}}}{\partial \delta_{ij}} + \alpha_{\mathrm{BG}} \frac{\mathrm{d}G_{\mathrm{sh}}}{\mathrm{d}t} + \alpha_{\mathrm{BB}} \frac{\mathrm{d}B_{\mathrm{sh}}}{\mathrm{d}t}, \tag{10.64}$$

where α_{GG}, α_{GB} are sensitivity factors determined by Equations (10.32). Rearranging Equation (10.64) gives

$$\sum_{i=1}^{n} \sum_{j>i}^{\mathrm{n}} \Delta\omega_{ij} \frac{\partial q_{\mathrm{B}}}{\partial \delta_{ij}} = \frac{\mathrm{d}q_{\mathrm{B}}}{\mathrm{d}t} - \alpha_{\mathrm{BG}} \frac{\mathrm{d}G_{\mathrm{sh}}}{\mathrm{d}t} - \alpha_{\mathrm{BB}} \frac{\mathrm{d}B_{\mathrm{sh}}}{\mathrm{d}t}. \tag{10.65}$$

The left hand side of this equation depends on $\Delta\omega_{ij}$. It is exactly the same as in the theoretically optimal strategy given by Equation (10.60) if the following condition is satisfied:

$$\frac{\partial q_{\mathrm{B}}}{\partial \delta_{ij}} = \beta_{ik}\beta_{kj} \sin \delta_{ij}. \tag{10.66}$$

Substituting the partial derivative on the left hand side of Equation (10.65) by the right hand side of Equation (10.66), and inserting the result into Equation (10.60), gives the local control (10.31).

The conditions defined by Equations (10.63) and (10.66) are the basic conditions under which the local control defined by Equations (10.30) and (10.31) can emulate the theoretical optimal control

defined by Equations (10.54) and (10.60). An additional condition is that for the given input variables the sensitivity factors defined by Equations (10.27) and (10.32) must be either known or negligible.

In the considered model shown in Figure 10.17, when the network conductances are neglected it can be shown that the magnitude and angle of voltage $\underline{V}_k$ at node k are given by

$$\underline{V}_k \cong \varphi(\text{sh})\varphi(\boldsymbol{\delta}), \tag{10.67}$$

where

$$\varphi(\text{sh}) = (1 + X_{\text{SHC}} B_{\text{sh}}) - \text{j} X_{\text{SHC}} G_{\text{sh}}, \tag{10.68}$$

$$\varphi(\delta) = -\sum_{j=1}^{n} \beta_{kj} \left[\cos \delta_j + \text{j} \sin \delta_j\right]. \tag{10.69}$$

Both functions $\varphi(\text{sh})$ and $\varphi(\boldsymbol{\delta})$ are complex.

Using (10.5) for a simplified analysis of voltage $\underline{V}_k$, it may be assumed that both components $X_{\text{SHC}} B_{\text{sh}}$ and $X_{\text{SHC}} G_{\text{sh}}$ in Equation (10.68) are negligible. Consequently, the following simplifications are obtained which are important for further considerations:

$$\varphi(\text{sh}) \cong 1 \quad \text{and} \quad \underline{V}_k \cong \varphi(\boldsymbol{\delta}). \tag{10.70}$$

Using the simplifications above, Equations (10.67) and (10.69) give

$$\underline{V}_k \cong \varphi(\delta) = -\sum_{j=1}^{n} \beta_{kj} \left[\cos \delta_j + \text{j} \sin \delta_j\right]. \tag{10.71}$$

Symbol θ denotes the phase angle of voltage $\underline{V}_k$ measured with respect to the reference frame common for all nodes of the network model. Thus Equation (10.71) gives

$$\left|\underline{V}_k\right| \cos\theta = -\sum_{j=1}^{n} \beta_{kj} \cos \delta_j \quad \text{and} \quad \left|\underline{V}_k\right| \sin\theta = -\sum_{j=1}^{n} \beta_{kj} \sin \delta_j. \tag{10.72}$$

Hence

$$\tan\theta \cong \frac{\sum_{j=1}^{n} \beta_{kj} \sin \delta_j}{\sum_{j=1}^{n} \beta_{kj} \cos \delta_j}, \tag{10.73}$$

$$\left|\underline{V}_k\right|^2 = \left[\sum_{j=1}^{n} \beta_{kj} \sin \delta_j\right]^2 + \left[\sum_{j=1}^{n} \beta_{kj} \cos \delta_j\right]^2. \tag{10.74}$$

Similar to the second of Equations (10.39), Equation (10.73) allows θ to be treated as an implicit function of δ, that is $f(\theta, \boldsymbol{\delta}) = 0$. Using Equations (10.41), (10.73) and (10.74) gives

$$\begin{aligned} \left|\underline{V}_k\right|^2 \frac{\partial \theta}{\partial \delta_i} &= \beta_{ki} \cos \delta_i \sum_{j=1}^{n} \beta_{kj} \cos \delta_j + \beta_{ki} \sin \delta_i \sum_{j=1}^{n} \beta_{kj} \sin \delta_j \\ &= \sum_{j=1}^{n} \beta_{ki} \beta_{kj} \left[\cos \delta_i \cos \delta_j + \sin \delta_i \sin \delta_j\right] = \sum_{j=1}^{n} \beta_{ki} \beta_{kj} \cos \delta_{ij}. \end{aligned} \tag{10.75}$$

Comparison of Equations (10.75) and (10.63) leads to

$$\left|\underline{V}_k\right|^2 \frac{\partial\theta}{\partial\delta_i} = \sum_{j=1}^{n} \beta_{ik}\beta_{kj}\cos\delta_{ij} = \frac{\partial q_{\mathrm{G}}}{\partial\delta_i}. \tag{10.76}$$

The conclusion from this equation is that the time derivative of the voltage phase angle θ multiplied by the voltage squared $\left|\underline{V}_k\right|^2$ satisfies the conditions of a good input signal for local control of $G_{\mathrm{sh}}(t)$.

When the sensitivity of θ with respect to $G_{\mathrm{sh}}(t)$ and $B_{\mathrm{sh}}(t)$ is considered it is necessary to take into account Equation (10.67) with φ(sh) given by Equation (10.68). Calculating the derivative of the implicit function and further simplifying the result gives

$$\left|\underline{V}_k\right|^2 \frac{\partial\theta}{\partial G_{\mathrm{sh}}} = -\left|\underline{V}_k\right|^2 X_{\mathrm{SHC}} \quad \text{and} \quad \left|\underline{V}_k\right|^2 \frac{\partial\theta}{\partial B_{\mathrm{sh}}} \cong 0. \tag{10.77}$$

This means that the phase angle θ of the voltage $\underline{V}_k$ is mainly sensitive to the changes of $G_{\mathrm{sh}}(t)$ and its sensitivity factor can be assessed on the basis of the expected value of the short-circuit reactance X_{SHC}.

Substituting the relevant sensitivity factors in Equation (10.30) by Equations (10.77) and (10.76) gives the same control scheme as (10.45a).

The signal depending on the magnitude of the squared voltage can be expressed, using Equations (10.67)–(10.69), as

$$q_{\mathrm{B}} = -\frac{1}{2}\left|\underline{V}_k\right|^2 = -\frac{1}{2}\underline{V}_k^*\underline{V}_k = -\frac{1}{2}\left|\varphi(\mathrm{sh})\right|^2 \left|\varphi(\delta)\right|^2, \tag{10.78}$$

where

$$\left|\varphi(\mathrm{sh})\right|^2 = \left[1 + X_{\mathrm{SHC}} B_{\mathrm{sh}}(t)\right]^2 + \left[X_{\mathrm{SHC}} G_{\mathrm{sh}}(t)\right]^2, \tag{10.79}$$

$$\left|\varphi(\delta)\right|^2 = \sum_{i=1}^{n}\sum_{j=1}^{n} \beta_{ik}\beta_{kj}\cos\delta_{ij} = \sum_{i=1}^{n} \beta_{ik}^2 + 2\sum_{i=1}^{n}\sum_{j>1}^{n} \beta_{ik}\beta_{kj}\cos\delta_{ij}. \tag{10.80}$$

In order to calculate the sensitivity of signal (10.78) with respect to power angles, it may be assumed as in (10.70) that $\varphi(\mathrm{sh}) \cong 1$. Then Equations (10.78) and (10.80) give

$$\frac{\partial q_{\mathrm{B}}}{\partial\delta_{ij}} = -\frac{1}{2}\frac{\partial\left|\underline{V}_k\right|^2}{\partial\delta_{ij}} \cong -\frac{1}{2}\frac{\partial\left|\varphi(\delta)\right|^2}{\partial\delta_{ij}} = \beta_{ik}\beta_{kj}\sin\delta_{ij}. \tag{10.81}$$

Equations (10.81) and (10.66) are the same, showing that the signal given by Equation (10.78) satisfies the condition of a good input signal for control of the shunt susceptance $B_{\mathrm{sh}}(t)$.

Sensitivity factors α_{GG}, α_{GB} determined by Equations (10.32) can be easily found assuming that $\underline{V}_k \cong \varphi(\boldsymbol{\delta})$. Under this assumption, differentiation of Equation (10.78) gives

$$\frac{\partial q_{\mathrm{B}}}{\partial G_{\mathrm{sh}}} \cong -\left|\underline{V}_k\right|^2 X_{\mathrm{SHC}}\left[X_{\mathrm{SHC}} G_{\mathrm{sh}}(t)\right] \cong 0, \tag{82a}$$

$$\frac{\partial q_{\mathrm{B}}}{\partial B_{\mathrm{sh}}} \cong -\left|\underline{V}_k\right|^2 X_{\mathrm{SHC}}\left[1 + X_{\mathrm{SHC}} B_{\mathrm{sh}}(t)\right] \cong -\left|\underline{V}_k\right|^2 X_{\mathrm{SHC}}. \tag{82b}$$

This means that the magnitude of the squared voltage is sensitive mainly to the changes of $B_{\mathrm{sh}}(t)$. Its sensitivity factor can be assessed on the basis of the expected value of the short-circuit reactance and the measured voltage magnitude.

Substituting the relevant sensitivity factors in Equation (10.31) by Equations (10.82) and (10.81), and the local signal by (10.78), gives the same control formula as (10.45b).

10.5.6 Example of Simulation Results

Simulation results of the considered controller of a shunt FACTS device based on local measurements can be found in publications by Machowski and Nelles (1992a, 1992b, 1993, 1994). Here only the simulations of the state-variable stabilizing control using the WAMPAC-type structure shown in Figure 10.19 will be presented. The time delay introduced by the telecommunication system of WAMPAC has been modelled using a first-order block with a time constant of 30 ms. Currently typical delays recorded in WAMPAC systems are about 100 ms. Such a big delay would significantly worsen the control process.

Simulations have been executed for the CIGRE test system (Figure 10.20). Generator G4 in this system has very high inertia constituting effectively the infinite busbar and providing a reference. The considered test system experiences transient stability problems mainly for generators G7 and G6, especially as a result of a short circuit in line L7 without reclosing. Such a case has been chosen to illustrate the robustness of the proposed control algorithm.

Table 10.1 shows the values of distance measures β_{ik} for nodes B6, B7, B8 and all internal generator nodes behind transient reactances of the generator. Symbols 'on' and 'off' in column L7 in Table 10.1 correspond to appropriate 'on' and 'off' states of line L7. The results show that only generators G4, G6 and G7 are important for shunt FACTS devices installed at each of the three chosen nodes B6, B7 and B8. For the remaining generators, the distance measures are an order of magnitude smaller and it may be safely assumed that $\beta_{ik} \cong 0$. Consequently, control of shunt FACTS devices in nodes B6, B7 and B8 can be based only on state variables ω_i, δ_i for generators G4, G6 and G7. A corresponding multi-loop supplementary controller (Figure 10.18) will then contain only three loops with $[\omega_4, \omega_6, \omega_7]$ as input signals.

Figure 10.21 shows the simulation results when one SMES (rated 40 MVA) at bus B8 was controlled using state-variable stabilizing control limited to the closest generators G4, G6 and G7 (local area control). The two lower graphs illustrate the changes in the values of $G_{\mathrm{sh\,B8}}$ and $B_{\mathrm{sh\,B8}}$

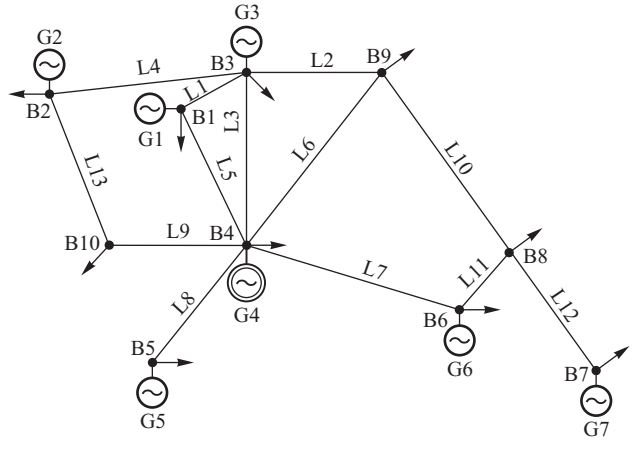

Figure 10.20 Schematic diagram of the CIGRE test system.

Table 10.1 Distance measures β_{ik} for $S_{\text{base}} = 100$ MVA.

—	L7	G1	G2	G3	G4	G5	G6	G7
B6	On	0.024	0.006	0.034	0.406	0.008	0.538	0.134
	Off	0.023	0.005	0.038	0.147	0.003	0.762	0.188
B7	On	0.024	0.006	0.037	0.283	0.005	0.279	0.552
	Off	0.015	0.003	0.025	0.094	0.002	0.121	0.482
B8	On	0.034	0.008	0.053	0.397	0.008	0.387	0.229
	Off	0.034	0.008	0.056	0.214	0.004	0.547	0.268

which correspond to real and reactive power of the SMES. The apparent power absorbed from the network or injected into the network is limited as shown by Equation (10.3). Consequently, the control algorithm uses more active power (conductance $G_{\text{sh B8}}$) than reactive power (susceptance $B_{\text{sh B8}}$). The two upper graphs show the changes in the values of rotor angles of generators G6 and G7. For comparison dashed lines show the case without SMES.

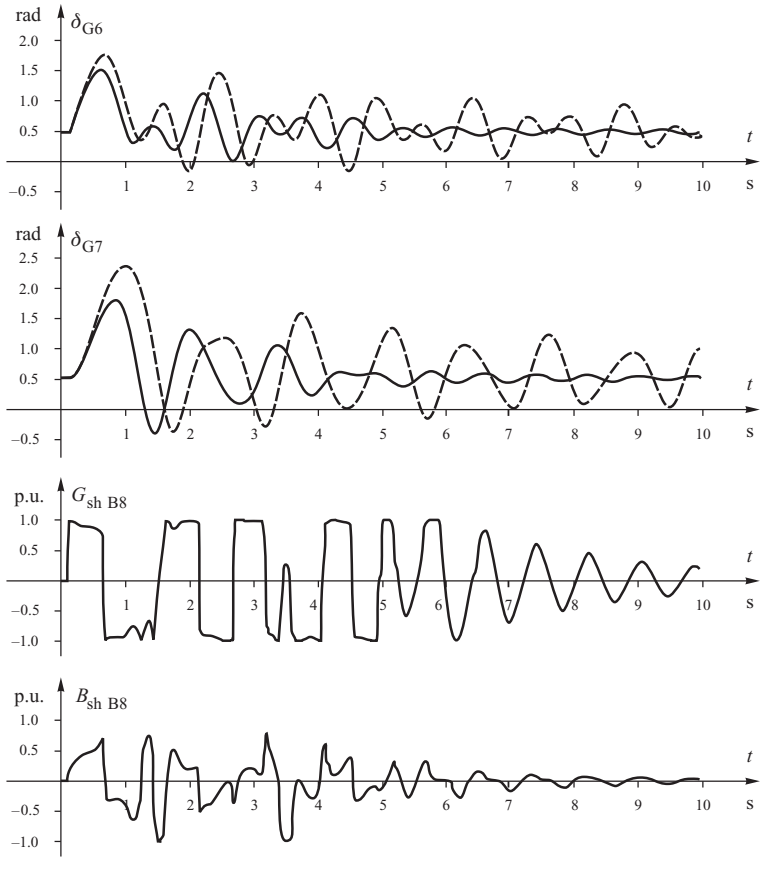

Figure 10.21 Simulation results for one SMES installed at bus B8.

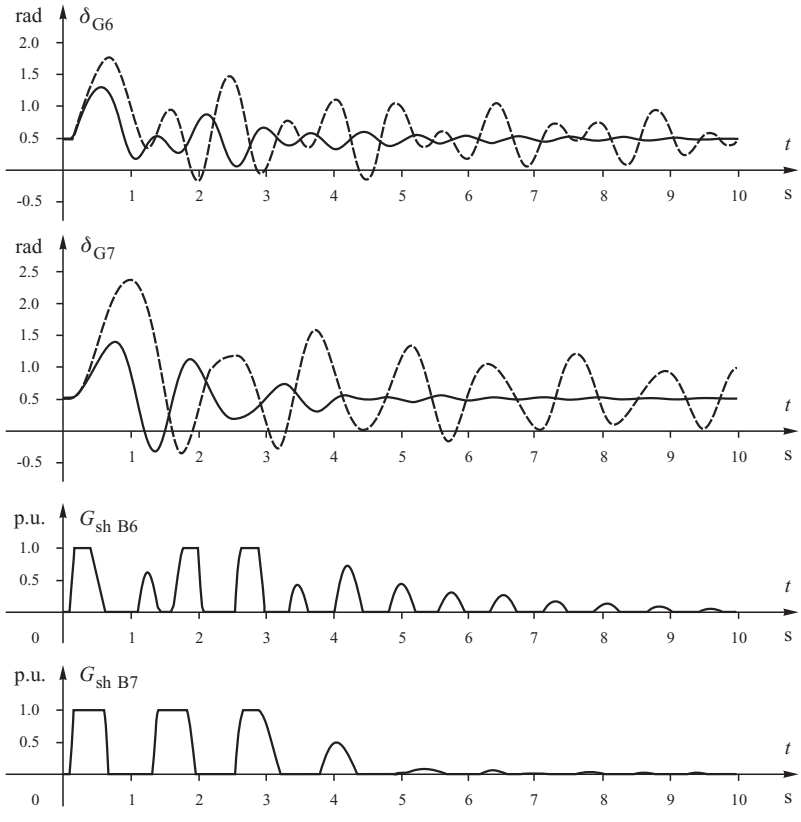

Figure 10.22 Simulation results for two BRs installed at bus B6 and bus B7.

Very good damping can be obtained by using thyristor-controlled BRs connected at generator busbars. Simulation results for such a case are shown in Figure 10.22 when two BRs (each rated 40 MW) are installed at bus B6 and bus B7. In this case rotor swings are damped very quickly.

10.6 Series Compensators

Section 3.1.2 showed how the power transfer capability of a long transmission line depends on its inductive reactance and how this reactance can be offset by inserting a series capacitor. Besides being useful in the steady state, such a reduction in the line reactance is also useful in the transient state as it increases the amplitude of the transient power–angle characteristic thereby increasing the available deceleration area. By proper control of a switched series capacitor this change in amplitude can be used to provide additional damping of power swings. In particular the conventional series capacitor, equipped with a zinc oxide protective scheme (Figure 2.24) and thyristor-switched series capacitor (Figure 2.34a), can be used in a bang–bang control mode as it can be almost instantaneously bypassed and reinserted at appropriate moments. The thyristor-controlled series capacitor (Figure 2.34b) and the static synchronous series compensator (Figure 2.35) allow the equivalent reactance to be smoothly controlled so that they can be used in a continuous control mode.

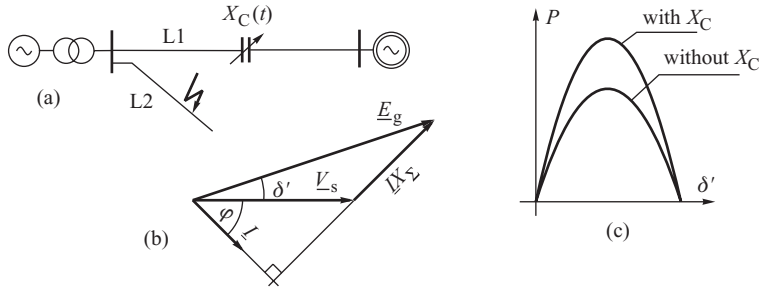

Figure 10.23 System with a shunt capacitor: (a) network diagram; (b) phasor diagram; (c) power–angle characteristic with and without series compensation.

10.6.1 State-Variable Control

Consider the simple generator–infinite busbar system shown in Figure 10.23a. Line L2 is assumed to be open-circuited before a fault occurs. The fault results in tripping the line after some clearing time. The generator is represented by the classical model, that is constant transient emf E' behind the transient reactance X'_d. Neglecting the resistance and shunt capacitance, the generated real power is

$$P(\delta') = \frac{E' V_s}{X_\Sigma} \sin \delta', \tag{10.83}$$

where V_s is the infinite busbar voltage, δ' is the transient power angle between V_s and E' and

$$X_\Sigma = \left(X'_d + X_T + X_{L1} + X_s\right) - X_C(t) = X - X_C(t) \tag{10.84}$$

is the equivalent reactance of the transmission link where X_T is the reactance of the transformer, X_{L1} is the reactance of the line, X_s is the equivalent reactance of the infinite busbar, and X is the equivalent reactance of the transmission link without the compensator. A positive value of $X_C(t)$ corresponds to a capacitance while a negative $X_C(t)$ corresponds to an inductance.

A change in the compensator reactance $X_C(t)$ causes a change in X_Σ and therefore a change in the amplitude of the power–angle characteristic. Figure 10.23c shows the power–angle characteristics corresponding to the maximum and minimum values of X_Σ.

To simplify considerations further, it is worth separating the system reactance into components with and without the series compensator. This can be done in the following way:

$$\frac{1}{X_\Sigma} = \frac{1}{X - X_C(t)} = \frac{1}{X} + \frac{1}{X_\Sigma}\frac{X_C}{X} \tag{10.85}$$

so that Equation (10.83) takes the following form:

$$P(\delta') = \frac{E' V_s}{X} \sin \delta' + \frac{E' V_s}{X_\Sigma}\frac{X_C(t)}{X} \sin \delta' = b \sin \delta' + b_\Sigma \frac{X_C(t)}{X} \sin \delta', \tag{10.86}$$

where $b_\Sigma = E' V_s / X_\Sigma$ and $b = E' V_s / X$ are the amplitudes of the power–angle characteristic with and without the series compensator, respectively. The first component in Equation (10.86) defines power which would flow in the system if the series compensator was not used, that is for $X_C(t) = 0$. The second component is responsible for a change in the power flow due to the variation in the compensator reactance. As series compensation is normally less than 100 % of the line reactance, it can be assumed that X_Σ is always positive, which is important for further considerations.

Taking into account Equation (10.86), the swing equation of the system can now be written as

$$\begin{aligned} \frac{\mathrm{d}\delta'}{\mathrm{d}t} &= \Delta\omega \\ M\frac{\mathrm{d}\Delta\omega}{\mathrm{d}t} &= P_\mathrm{m} - b\sin\delta' - D\frac{\mathrm{d}\delta'}{\mathrm{d}t} - (b_\Sigma \sin\delta')\frac{X_\mathrm{C}(t)}{X}, \end{aligned} \tag{10.87}$$

where $\Delta\omega$ is the speed deviation, M is the inertia coefficient, P_m is the mechanical power input from the prime mover and D is the damping coefficient. The equilibrium point of this equation has coordinates $(\hat{\delta}', \Delta\hat{\omega} = 0)$. The control variable is $X_\mathrm{C}(t)$.

The system described by Equation (10.87) is nonlinear. A standard approach to derive the optimal state-variable control of such a system would be to linearize the system around its operating point. Here, as before in this book, the optimal state-variable control will be derived from the nonlinear model using the Lyapunov direct method.

The Lyapunov function for the system is equal to the sum of the potential and kinetic energy $V = E_\mathrm{k} + E_\mathrm{p}$, where

$$\begin{aligned} E_\mathrm{k} &= \tfrac{1}{2}M\Delta\omega^2 \\ E_\mathrm{p} &= -\left[P_\mathrm{m}\left(\delta' - \hat{\delta}'\right) + b\left(\cos\delta' - \cos\hat{\delta}'\right)\right]. \end{aligned} \tag{10.88}$$

At the equilibrium point $(\hat{\delta}', \Delta\hat{\omega} = 0)$ the total energy given by Equation (10.88) is zero. A fault releases some energy, that is it causes an increase in the total energy expressed by Equation (10.88), which results initially in acceleration of the rotor and an increase in δ' and $\Delta\omega$. The goal of a control strategy is to enforce such changes in the equivalent reactance of the transmission link so that the system is brought back as fast as possible to the equilibrium point $(\hat{\delta}', \Delta\hat{\omega} = 0)$ where $V = 0$. This is equivalent to a fast dissipation of the energy released by the fault and quick damping of rotor swings. The control strategy must therefore maximize the value of the derivative $\dot{V} = \mathrm{d}V/\mathrm{d}t$ calculated along the trajectory of the differential equation (10.87).

It can be easily proved that, for functions given by Equation (10.88), the following hold:

$$\frac{\mathrm{d}E_\mathrm{k}}{\mathrm{d}t} = \frac{\partial E_\mathrm{k}}{\partial\omega}\frac{\mathrm{d}\Delta\omega}{\mathrm{d}t} = M\frac{\mathrm{d}\Delta\omega}{\mathrm{d}t}\Delta\omega, \tag{10.89}$$

$$\frac{\mathrm{d}E_\mathrm{p}}{\mathrm{d}t} = \frac{\partial E_\mathrm{p}}{\partial\delta'}\frac{\mathrm{d}\delta'}{\mathrm{d}t} = \frac{\partial E_\mathrm{p}}{\partial\delta'}\Delta\omega = -\left[P_\mathrm{m} - b\sin\delta'\right]\Delta\omega. \tag{10.90}$$

Substituting the left hand side of the second of Equations (10.87) into the right hand side of Equation (10.89) gives

$$\frac{\mathrm{d}E_\mathrm{k}}{\mathrm{d}t} = +\left[P_\mathrm{m} - b\sin\delta'\right]\Delta\omega - D\Delta\omega^2 - (b_\Sigma\sin\delta')\frac{X_\mathrm{C}(t)}{X}\Delta\omega. \tag{10.91}$$

Adding Equations (10.90) and (10.91) gives a time derivative of the Lyapunov function:

$$\dot{V} = \frac{\mathrm{d}V}{\mathrm{d}t} = \frac{\mathrm{d}E_\mathrm{k}}{\mathrm{d}t} + \frac{\mathrm{d}E_\mathrm{p}}{\mathrm{d}t} = -D\Delta\omega^2 - (b_\Sigma\sin\delta')\frac{X_\mathrm{C}(t)}{X}\Delta\omega. \tag{10.92}$$

The system is stable if this derivative is negative. Moreover, the speed with which the system returns to the equilibrium point is proportional to $\dot{V}$, that is the greater the negative value of $\dot{V}$, the faster the dissipation of energy released by the fault and the faster the damping of the swings.

The second component of Equation (10.92) depends on the control variable $X_\mathrm{C}(t)$ and the state variables $(\delta', \Delta\omega)$. This component will be negative if the control strategy of the series compensator

is such that

$$X_C(t) = K X (\sin \delta') \Delta\omega, \tag{10.93}$$

where K is the gain of the regulator. Recall that $X =$ constant is the link reactance without the compensator. Substituting Equation (10.93) into (10.92) gives

$$\frac{dV}{dt} = \frac{dE_k}{dt} + \frac{dE_p}{dt} = -D\Delta\omega^2 - K b_\Sigma (\sin \delta')^2 \Delta\omega^2, \tag{10.94}$$

which means that assuming the control strategy given by Equation (10.93), the derivative $\dot{V}$ is always negative. At any moment during the transient state such control will improve the damping. This can be additionally shown by substituting $X_C(t)$ from Equation (10.93) into the swing equation, Equation (10.87). The swing equation will then take the form

$$\begin{aligned} \frac{d\delta'}{dt} &= \Delta\omega \\ M\frac{d\Delta\omega}{dt} &= P_m - b \sin \delta' - D\frac{d\delta'}{dt} - D_{ser}\frac{d\delta'}{dt}, \end{aligned} \tag{10.95}$$

where

$$D_{ser} = K b_\Sigma (\sin \delta')^2 \geq 0 \tag{10.96}$$

is a positive damping coefficient due to control of the series compensator.

10.6.2 Interpretation Using the Equal Area Criterion

The influence of the control given by Equation (10.93) on the transient stability can be simply explained by assuming that the FACTS device is a thyristor-switched series capacitor (Figure 2.47a). In that case the control given by Equation (10.93) can be implemented only as bang–bang control:

$$X_C(t) = \begin{cases} X_{CMAX} & \text{for} \quad (\sin \delta') \Delta\omega \geq +\varepsilon \\ 0 & \text{for} \quad (\sin \delta') \Delta\omega < +\varepsilon, \end{cases} \tag{10.97}$$

where ε determines the dead zone.

Consider again the simple generator–infinite busbar system of Figure 10.23 with the fault occurring on line L2. Figure 10.24 shows the power–angle curves with $X_C = 0$, the lower characteristic, and with $X_C = X_{CMAX}$, the upper characteristic. The fault causes the generator power to drop so that kinetic energy proportional to area 1–2–3–4 is released. At the instant of fault clearance the expression $(\Delta\omega \sin \delta')$ is positive so that the signal $X_C(t)$ is set to its maximal value $X_C = X_{CMAX}$ and the whole capacitor is inserted. The available declaration area is 4–5–6–10. The rotor reaches speed deviation $\Delta\omega = 0$ at point 6 when area 4–5–6–7 becomes equal to area 1–2–3–4 and then starts to swing back. The expression $(\Delta\omega \sin \delta')$ becomes negative and the control strategy in Equation (10.93) causes the capacitor to be bypassed $X_C(t) = 0$. The rotor follows the lower $P(\delta')$ characteristic. The power jumps from point 6 to point 8 and the rotor swings back along path 8–9 performing deceleration work proportional to area 8–9–7. This backswing deceleration area is now much smaller than area 6–7–1, the deceleration area available when $X_C = X_{CMAX}$. When the rotor starts to swing forward, the speed deviation changes sign, $X_C(t)$ is increased and the acceleration area is reduced. The complete switching cycle is then repeated but with rotor swings of reduced amplitude. Thus the control principle is established. During the forward swing the acceleration area

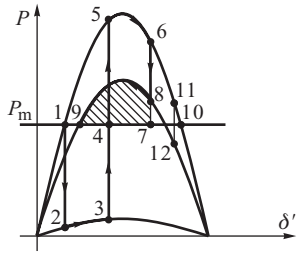

Figure 10.24 Interpretation of series capacitor control using the equal area criterion.

should be minimized and the available deceleration area maximized, while during the backward swing the deceleration area should be minimized and the available acceleration area maximized.

In some circumstances bang–bang control with a small dead zone can lead to large power angle swings and instability. To explain this, again consider Figure 10.24 and assume that the rotor reaches point 11 during its forward swing. Sudden bypassing of the capacitor causes the system trajectory to jump to point 12 from which the rotor would be further accelerated causing a subsequent asynchronous operation. This would not happen with continuous control because both the control signal and $X_C(t)$ change smoothly. Such control can be implemented using the thyristor-controlled series capacitor (Figure 2.34b) or the static synchronous series compensator (Figure 2.35). The next section will describe a state-variable stabilizing control of the series compensator, based on Equation (10.93), which can be emulated using local measurements.

10.6.3 Control Strategy Based on the Squared Current

The control strategy (10.93) utilizes state variables (δ', $\Delta\omega$) which are not readily available at the point of installation of the series compensator. Therefore it is convenient to emulate this optimal strategy using another strategy based on locally available measurements. Similar considerations were used in Section 10.5.3 but with regard to the shunt compensation.

For the case considered, the cosine theorem applied to the voltage triangle from Figure 10.23b gives

$$(I X_\Sigma)^2 = (E')^2 + V_s^2 - 2E' V_s \cos\delta' \tag{10.98}$$

so that

$$I^2 = \frac{1}{X_\Sigma^2}\left[(E')^2 + V_s^2 - 2E' V_s \cos\delta'\right]. \tag{10.99}$$

Assuming constant values of E' and V_s, the signal given by Equation (10.99) depends on X_Σ and δ'. Hence the speed of the signal changes can be expressed as

$$\frac{\mathrm{d}\left(I^2\right)}{\mathrm{d}t} = \frac{\partial\left(I^2\right)}{\partial\delta'}\frac{\mathrm{d}\delta'}{\mathrm{d}t} + \frac{\partial\left(I^2\right)}{\partial X_\Sigma}\frac{\mathrm{d}X_\Sigma}{\mathrm{d}t}, \tag{10.100}$$

and the partial derivatives are given by

$$\frac{\partial\left(I^2\right)}{\partial\delta'} = \frac{2}{X_\Sigma^2}E' V_s \sin\delta' \quad \text{and} \quad \frac{\partial\left(I^2\right)}{\partial X_\Sigma} = -\frac{2}{X_\Sigma}I^2. \tag{10.101}$$

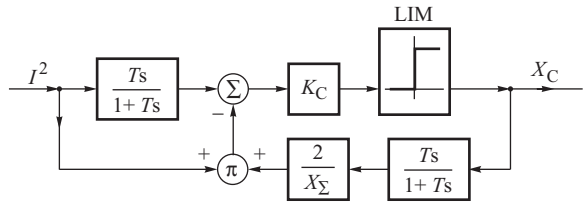

Figure 10.25 Supplementary control of $X_C(t)$.

As $X_\Sigma = X - X_C(t)$ and $X =$ constatnt, it holds that $dX_\Sigma/dt = -dX_C/dt$. Substituting the expressions given by Equation (10.101) into (10.100) gives

$$\frac{d\left(I^2\right)}{dt} = \frac{2}{X_\Sigma^2} E' V_s (\sin\delta') \Delta\omega + \frac{2}{X_\Sigma} I^2 \frac{dX_C}{dt}, \tag{10.102}$$

which, after reordering the terms, gives

$$(\sin\delta') \Delta\omega = \frac{X_\Sigma^2}{2E' V_s} \left[\frac{d\left(I^2\right)}{dt} - \frac{2}{X_\Sigma} I^2 \frac{dX_C}{dt} \right]. \tag{10.103}$$

Substituting Equation (10.103) into Equation (10.93) gives

$$X_C(t) = K_C \left[\frac{d\left(I^2\right)}{dt} - \frac{2}{X_\Sigma} I^2 \frac{dX_C}{dt} \right], \tag{10.104}$$

where K_C is the equivalent gain of the controller.

Figure 10.25 shows the block diagram of a controller executing the control strategy (10.104). Derivation is executed by a real differentiator with a small time constant T. The limiter at the output of the controller limits the output signal to that applicable for a particular type of series compensator. The controller is nonlinear because it contains a product of the input signal and the derivative of the output signal. Sensitivity of the squared current I^2 to the changes in the control variable $X_C(t)$ is compensated by using a feedback loop with a gain inversely proportional to X_Σ. This feedback plays a secondary role when compared with the main feedback loop. Consequently, the gain in the corrective loop can be determined approximately using an estimate of the equivalent reactance X_Σ.

If the series compensator is equipped with a steady-state power flow controller then the considered controller can be attached as a supplementary control loop for damping of power swings.

10.6.4 Control Based on Other Local Measurements

It was shown above that control based on the squared current allows the optimal control strategy to be executed. Some authors suggest that other locally measured signals such as real power or the current magnitude (but not squared) can be used as input signals for the regulator. A question then arises as to what the differences are between the controllers using these three input signals in the case of large disturbances involving large changes of the power angle.

When the sensitivity of the given signal $q(t)$ to the changes in X_Σ is neglected, then as in Equation (10.100) the control signal can be expressed as

$$\frac{dq}{dt} \cong \frac{\partial q}{\partial \delta'} \frac{d\delta'}{dt} = \frac{\partial q}{\partial \delta'} \Delta\omega. \tag{10.105}$$

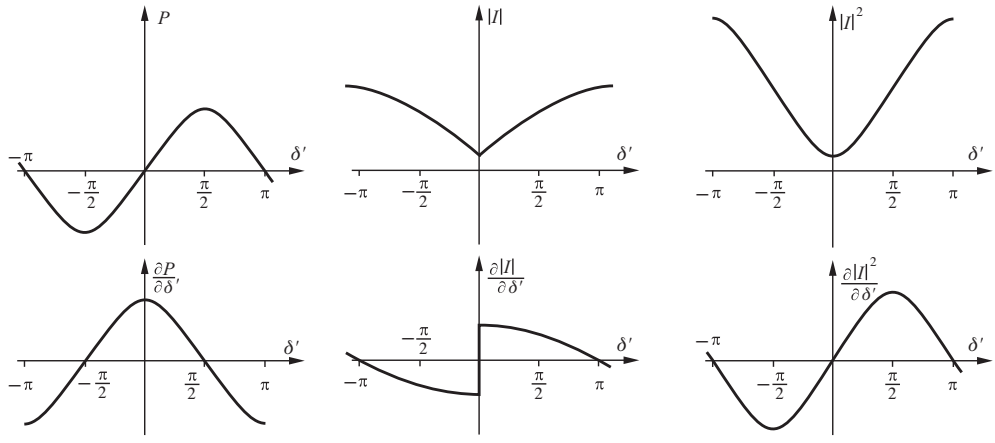

Figure 10.26 Electrical quantities and their partial derivatives: (a) real power; (b) squared current magnitude; (c) current magnitude.

For a given speed deviation $\Delta\omega$, the value of the control signal $\mathrm{d}q/\mathrm{d}t$ is determined by the value of the partial derivative $\partial q/\partial\delta'$. A comparison with Equation (10.93) shows that the partial derivative $\partial q/\partial\delta'$ should ideally be of a sine type, that is it should be positive for $\delta' > 0$ and negative for $\delta' < 0$. Figure 10.26 shows the partial derivative $\partial q/\partial\delta'$ for the real power P, current I and squared current magnitude I^2.

The partial derivative of the real power, $\partial P/\partial\delta'$, is largest at $\delta' = 0$ and then it decreases taking negative values for $\delta' > \pi/2$. The derivative of the current magnitude is large and discontinuous, changing its sign around $\delta' = 0$. The derivative of the squared current magnitude has a sine shape, that is it is zero at $\delta' = 0$ and it reaches a maximum at $\delta' = \pi/2$. This leads to conclusions described in Sections 10.6.4.1 to 10.6.4.3.

10.6.4.1 Controller Based on Real Power

In the vicinity of $\delta' = 0$, when the control is not effective because it does not influence damping in a significant way, the produced control signal is unnecessarily large. When the power angle increases and the control action starts to influence damping, the control signal decreases. Around $\delta' = \pi/2$, when the control is the most effective, the control signal is zero. For $\delta' > \pi/2$ the control signal changes sign and becomes negative, causing negative damping which harms the system. Similarly, negative damping occurs for $\delta' < -\pi/2$, that is for a large power angle during backswing. Obviously at any operating point when $-\pi/2 < \delta' < \pi/2$ a small disturbance will produce a correct control signal and positive damping. Hence the linearized analysis of the controller in the vicinity of the operating point does not expose the disadvantages of using real power as an input signal for the regulator.

10.6.4.2 Controller Based on Current

The produced control signal has the correct sign over the whole range of power angle changes. However, the controller produces an unnecessarily large signal in the vicinity of $\delta' = 0$, when the control is ineffective. Moreover, when crossing the value $\delta' = 0$, the control signal is discontinuous.

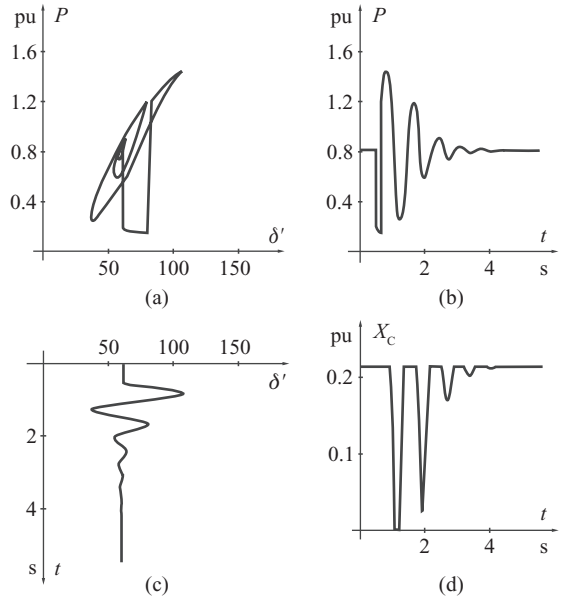

Figure 10.27 Simulation results for the generator–infinite busbar system.

10.6.4.3 Controller Based on Squared Current

The control signal has the correct sign and shape over the whole range of power angle changes. In the vicinity of $\delta' = 0$, when the control is ineffective, the signal is small but increases with angle, reaching a maximum at $\delta' = \pi/2$, when the control is the most effective. Also, note that the control signal is continuous.

10.6.5 Simulation Results

The proposed controller has been tested using a variety of systems. Due to the lack of space, the simulation results for the simple generator–infinite busbar system only will be presented. A short circuit was assumed at the end of the line, beyond the series compensator. The considered case was stable. Without the series compensator the resulting power swings vanished after about 10 s. The regulation process when the series compensator was used is shown in Figure 10.27.

Figure 10.27a shows the system trajectory in the (P, δ) plane. One can see a sudden change in the value of real power following the fault and then its clearance. The system trajectory during the backswing lies below the trajectory corresponding to the forward swing. Good damping of power swings may be observed as the oscillations vanish after about 3 s (Figure 10.27b and c). After the disturbance the first two changes in $X_C(t)$ are large (Figure 10.27d) and as the swings disappear the controller enforces smaller changes in $X_C(t)$.

10.7 Unified Power Flow Controller

As discussed in Section 2.4.4, series FACTS devices also include, apart from the controlled series capacitor, the phase angle regulator (TCPAR, Figure 2.37) and the unified power flow controller UPFC (Figure 2.38). The UPFC can control three signals: (i) the quadrature component of the booster voltage; (ii) the direct component of the booster voltage; and (iii) the reactive shunt current.

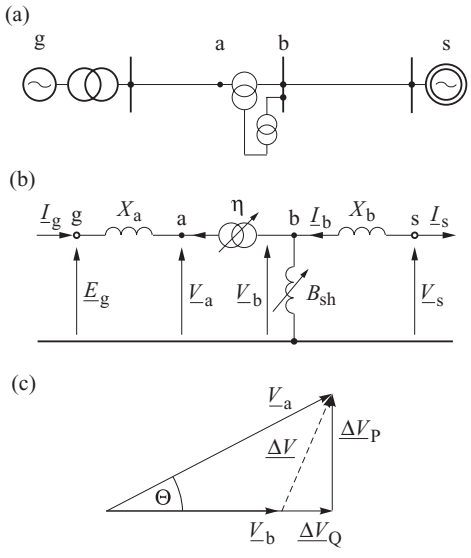

Figure 10.28 Generator–infinite busbar system to investigate UPFC control: (a) block diagram; (b) equivalent network; (c) phasor diagram.

The TCPAR can control only the first signal, that is the quadrature component of the booster voltage. Hence this section will discuss the more general case, that is supplementary stabilizing control of the UPFC.

10.7.1 Power–Angle Characteristic

To simplify considerations, the generator–infinite busbar system will be discussed as shown in Figure 10.28. The generator is represented by the classical model. The shunt part of the UPFC is modelled by a variable susceptance $B_{sh}(t)$. The series part, inserting the booster voltage, is modelled by a complex transformation ratio defined as

$$\eta = \frac{\underline{V}_a}{\underline{V}_b} = |\eta|\, e^{j\theta} \quad \text{and} \quad \frac{\underline{I}_b}{\underline{I}_a} = \eta^* = |\eta|\, e^{-j\theta}. \tag{10.106}$$

Booster transformer reactance is added, on the generator side, to the equivalent reactance of the network.

The phasor diagram shown in Figure 10.28c breaks down the booster voltage into its direct ΔV_Q and quadrature ΔV_P components. These components can be expressed as a fraction of the busbar voltage

$$\Delta V_P = \gamma V_b \quad \text{and} \quad \Delta V_Q = \beta V_b, \tag{10.107}$$

where β and γ are the output variables of the supplementary control of the UPFC. To emphasize the time dependency, the variables will be denoted as $\beta(t)$ and $\gamma(t)$. The voltage triangle in Figure 10.28c gives

$$\sin\theta = \frac{\Delta V_P}{V_a} = \frac{\gamma V_b}{V_a} = \frac{\gamma}{|\eta|}, \tag{10.108}$$

$$\cos\theta = \frac{V_b + \Delta V_Q}{V_a} = \frac{V_b + \beta V_b}{V_a} = \frac{1+\beta}{|\eta|}, \tag{10.109}$$

$$(1+\beta)^2 + \gamma^2 = |\eta|^2 \quad \text{or} \quad |\eta| = \sqrt{(1+\beta)^2 + \gamma^2}. \tag{10.110}$$

Derivation of a formula for the generator power that includes all three control variables $B_{sh}(t) \neq 0$, $\gamma(t) \neq 0$ and $\beta(t) \neq 0$ takes over three pages of algebraic transformations even for the simple generator–infinite busbar system. To illustrate the problem, only a simplified case of neglected shunt compensation, that is $B_{sh}(t) = 0$, will be discussed here.

When the shunt susceptance $B_{sh}(t)$ is neglected, the equivalent system reactance as seen by the generator is equal to $X_\Sigma = X_a + |\eta|^2 X_b$, where the second component corresponds to reactance X_b transformed by the transformation ratio to the generator side. The angle between the generator emf and the infinite busbar voltage is δ'. The angle between the voltages on both sides of the booster transformer is θ, see (10.106). This means that the phase angle of the voltage drop on reactance X_Σ is $(\delta' - \theta)$. The infinite busbar voltage transformed to the generator side is $V_s|\eta|$. Hence, taking into account the general equation (1.8), one can write

$$P = \frac{E_g V_s |\eta|}{X_\Sigma} \sin(\delta' - \theta) = \frac{E_g V_s}{X_\Sigma} |\eta| \left(\sin\delta' \cos\theta - \cos\delta' \sin\theta\right). \tag{10.111}$$

Substituting (10.108) and (10.109) into (10.111) gives

$$P = b_\Sigma \sin\delta' - b_\Sigma \cos\delta' \gamma(t) + b_\Sigma \sin\delta' \beta(t), \tag{10.112}$$

where $b_\Sigma = E_g V_s / X_\Sigma$ is the amplitude of the power–angle characteristic when the transformation ratio given by Equation (10.110) is included. When the booster voltage is absent, that is when $\gamma(t) = 0$ and $\beta(t) = 0$, the characteristic corresponds to the first component of (10.112). The second and third components correspond to the direct and quadrature components of the booster voltage (10.107), respectively.

The influence of the booster voltages on the power–angle characteristic is illustrated in Figure 10.29. The quadrature component enforces a non-zero value of the angle θ and, according to (10.111), causes a shift in the power–angle characteristic to the left if $\gamma > 0$, or to the right if $\gamma < 0$. The direct component changes the amplitude of the characteristic, increasing it when $\beta > 0$ and reducing it when $\beta < 0$.

Figure 10.12b showed that the shunt compensation $B_{sh}(t)$ of reactive power also affects the amplitude of the power–angle characteristic. Hence the shunt element $B_{sh}(t)$ neglected in (10.111)

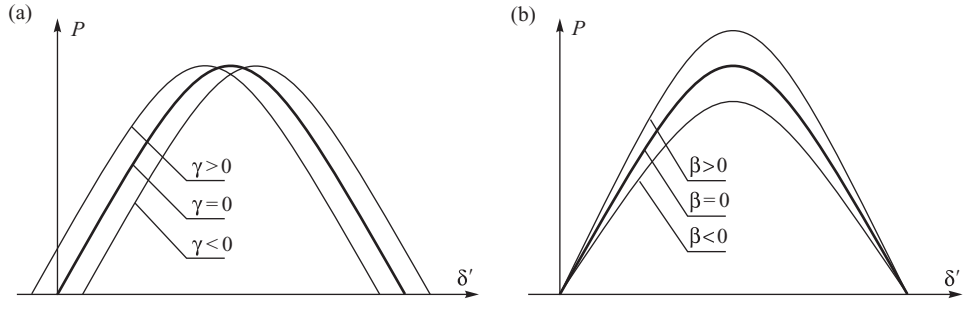

Figure 10.29 Influence of the booster voltages on the power–angle characteristic: (a) influence of the quadrature component; (b) influence of the direct component.

will also have an influence on the amplitude of the characteristic just like the direct component of the booster voltage.

Januszewski (2001) has derived a similar equation to (10.112) but including simultaneous control of all three quantities:

$$\begin{aligned} P \cong\ & b_\Sigma \sin\delta' \\ & - b_\Sigma \sin\delta' \, X_{\mathrm{SHC}} B_{\mathrm{sh}}(t) \\ & + b_\Sigma \sin\delta' \,(1 - X_{\mathrm{SHC}} B_{\mathrm{sh}})\, \beta(t) - b_\Sigma \cos\delta' \,(1 - X_{\mathrm{SHC}} B_{\mathrm{sh}})\, \gamma(t). \end{aligned} \tag{10.113}$$

It is worth remembering that, as in Equation (10.5), $X_{\mathrm{SHC}} B_{\mathrm{sh}} \ll 1$ holds. This means that expression $(1 - X_{\mathrm{SHC}} B_{\mathrm{sh}})$ is positive and $(1 - X_{\mathrm{SHC}} B_{\mathrm{sh}}) \cong 1$.

10.7.2 State-Variable Control

Taking into account Equation (10.113), the swing equation of the system can now be written as

$$\begin{aligned} M\frac{\mathrm{d}\Delta\omega}{\mathrm{d}t} = & P_{\mathrm{m}} - b_\Sigma \sin\delta' - D\frac{\mathrm{d}\delta'}{\mathrm{d}t} \\ & + b_\Sigma X_{\mathrm{SHC}} B_{\mathrm{sh}} \sin\delta' - (1 - X_{\mathrm{SHC}} B_{\mathrm{sh}}) \left[\beta b_\Sigma \sin\delta' - \gamma b_\Sigma \cos\delta'\right], \end{aligned} \tag{10.114}$$

where $\Delta\omega$, δ' are the state variables and $X_{\mathrm{C}}(t)$ is the controlled variable. The control law will be derived, similar to the shunt devices, using the Lyapunov direct method.

The total system energy $V = E_{\mathrm{k}} + E_{\mathrm{p}}$ is chosen as the Lyapunov function, as for the shunt devices and the series capacitor:

$$V = \frac{1}{2} M\Delta\omega^2 - \left[P_{\mathrm{m}}\left(\delta' - \hat{\delta}'\right) + b_\Sigma\left(\cos\delta' - \cos\hat{\delta}'\right)\right]. \tag{10.115}$$

Calculating the partial derivative along the system trajectory of Equation (10.114) gives

$$\begin{aligned} \dot{V} = & \frac{\mathrm{d}E_{\mathrm{k}}}{\mathrm{d}t} + \frac{\mathrm{d}E_{\mathrm{p}}}{\mathrm{d}t} \\ = & - D\Delta\omega^2 + \Delta\omega\,(b_\Sigma \sin\delta')\, X_{\mathrm{SHC}} B_{\mathrm{sh}}(t) \\ & + \Delta\omega\,(1 - X_{\mathrm{SHC}} B_{\mathrm{sh}})\,(b_\Sigma \cos\delta')\,\gamma(t) - \Delta\omega\,(1 - X_{\mathrm{SHC}} B_{\mathrm{sh}})\,(b_\Sigma \sin\delta')\,\beta(t). \end{aligned} \tag{10.116}$$

Taking into account that $(1 - X_{\mathrm{SHC}} B_{\mathrm{sh}}) > 0$, it can be concluded that controlling each of the three quantities will introduce a negative term in the derivative (10.116) if the control is according to the following three equations:

$$\beta(t) = + K_\beta \left[b_\Sigma \sin\delta'\right] \Delta\omega, \tag{10.117}$$

$$\gamma(t) = - K_\gamma \left[b_\Sigma \cos\delta'\right] \Delta\omega, \tag{10.118}$$

$$B_{\mathrm{sh}}(t) = - K_{\mathrm{B}} \left[b_\Sigma \sin\delta'\right] \Delta\omega, \tag{10.119}$$

where K_β, K_γ, K_B are the control gains. With that control, the system energy will change according to

$$\dot{V} = -D\Delta\omega^2 - \left[K_\beta (\sin\delta')^2 + K_\gamma (\cos\delta')^2\right] b_\Sigma^2 \Delta\omega^2 + K_B X_{SHC} (\sin\delta')^2 b_\Sigma^2 \Delta\omega^2. \quad (10.120)$$

For $K_\beta = K_\gamma = K_\eta$, controlling both booster voltage components gives a constant damping independent of the power angle, because the expression in the square brackets in (10.120) is equal to K_η, and Equation (10.120) becomes

$$\dot{V} = -D\Delta\omega^2 - K_\eta b_\Sigma^2 \Delta\omega^2 + K_B X_{SHC} (\sin\delta')^2 b_\Sigma^2 \Delta\omega^2. \quad (10.121)$$

Control using the direct booster voltage component (signal β) and controlling the shunt compensation (signal B_{sh}) is executed in the same way as controlling the shunt reactive power compensator, Equation (10.45). Control action is proportional to the speed deviation $\Delta\omega$ and the sine of the power angle $\sin\delta'$. When the power angle is positive and when $\Delta\omega > 0$, Figure 10.29b, the control chooses values $\beta > 0$ such that the amplitude of the power–angle characteristic is increased and therefore the available deceleration area is increased. During the backswing when $\Delta\omega < 0$, the control chooses such values $\beta < 0$ that the amplitude of the characteristic is reduced, Figure 10.29b, causing a reduction in the deceleration work during the backswing and a reduction of the maximum rotor displacement.

Control of the quadrature voltage component (signal $\gamma(t)$) is proportional to the speed deviation $\Delta\omega$ and cosine of the power angle $\cos\delta'$. The influence of such control is illustrated in Figure 10.30. During the short circuit, the rotor gains energy corresponding to the acceleration area 1–2–3–4. At the same time, the control system applies control $\gamma > 0$ such that the power–angle characteristic is moved to the left. As a result, electrical power at point 5 is higher than it would otherwise have been (the middle bold line). Power then changes along line 5–6 on the characteristic; that is, shifted to the left. At the peak of the characteristic $\cos\delta'$ tends to zero and signal $\gamma(t)$ tends to zero too. Hence power changes along the middle characteristic corresponding to the lack of control. Then $\cos\delta'$ changes sign, the signal $\gamma(t)$ changes sign too and power changes according to the characteristic shifted to the right. The available deceleration area is 4–5–6–7–8. In the case considered, this area is bigger than the area 1–2–3–4 and the system is stable. The rotor does not move beyond point 8 because, immediately after moving past point 7, the speed deviation decreases significantly so that the signal $\gamma(t)$ decreases too. Hence the movement is no longer along line 7–8 but along the middle characteristic. After reaching $\Delta\omega = 0$ the rotor starts the backswing and the control signal $\gamma(t) > 0$ appears as long as $\cos\delta' < 0$. The backswing is along the characteristic shifted to the left. Based on that description a trajectory of the rotor motion could be constructed, similar to that shown in Figure 10.14 for the braking resistor.

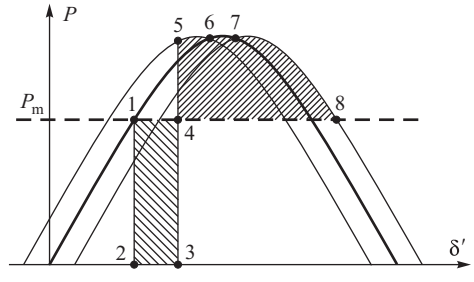

Figure 10.30 Influence of the control strategy in the generator–infinite busbar system.

Control based on Equations (10.117)–(10.119) is state-variable control and requires measurements of both the speed deviation and the rotor angle, which are difficult to measure in a multimachine system. Hence, similar to the case for the shunt FACTS devices and the series capacitor, Equations (10.117)–(10.119) have to be replaced by equations making it possible to control the UPFC using local measurements.

10.7.3 Control Based on Local Measurements

In order to obtain a signal proportional to the speed deviation, a locally available signal $q(t)$ should be used. As in Equations (10.61) and (10.64) discussed earlier, one can write

$$\dot{q} = \frac{\mathrm{d}q}{\mathrm{d}t} = \frac{\partial q}{\partial \delta'}\frac{\mathrm{d}\delta'}{\mathrm{d}t} + \frac{\partial q}{\partial \beta}\frac{\mathrm{d}\beta}{\mathrm{d}t} + \frac{\partial q}{\partial \gamma}\frac{\mathrm{d}\gamma}{\mathrm{d}t} + \frac{\partial q}{\partial B_{\mathrm{sh}}}\frac{\mathrm{d}B_{\mathrm{sh}}}{\mathrm{d}t}. \tag{10.122}$$

In this equation only the first component is proportional to the speed deviation and can be used for state-variable control. The other components should have as small an influence as possible on the value of the derivative. The equation can be rewritten as follows:

$$\dot{q} = \frac{\mathrm{d}q}{\mathrm{d}t} = \frac{\partial q}{\partial \delta'}\Delta\omega + \varepsilon(t), \tag{10.123}$$

where $\Delta\omega = \mathrm{d}\delta'/\mathrm{d}t$ and $\varepsilon(t)$ are functions of variables β, γ, B_{sh}. If a local measurement $q(t)$ is to emulate well state-variable control, two conditions must be satisfied:

1. For the control of $\beta(t)$ and $B_{\mathrm{sh}}(t)$, partial derivatives $\partial q/\partial\delta'$ should be proportional to $\sin\delta'$. For the control of $\gamma(t)$, the partial derivative $\partial q/\partial\delta'$ should be proportional to $\cos\delta'$.
2. The first component, proportional to the speed deviation, should dominate on the right hand side of Equation (10.123). The second component should be negligible, that is a given signal should not be sensitive to the changes in β, γ, B_{sh}.

Januszewski (2001) showed that the above conditions are reasonably well satisfied for the reactive power Q and real power P measured in a line where a booster transformer is connected (Figure 10.28). Hence state-variable control defined by Equations (10.117)–(10.119) can be approximately replaced by a control that uses local measurements and is defined by

$$\gamma\,(t) \cong +\,K_{\gamma}\frac{\mathrm{d}P}{\mathrm{d}t}, \tag{10.124}$$

$$\beta\,(t) \cong +\,K_{\beta}\frac{\mathrm{d}Q}{\mathrm{d}t}, \tag{10.125}$$

$$B_{\mathrm{sh}}\,(t) \cong -\,K_{\mathrm{B}}\frac{\mathrm{d}Q}{\mathrm{d}t}, \tag{10.126}$$

where K_{γ}, K_{β}, K_{B} are appropriately chosen control gains.

According to Equations (10.120) and (10.121), booster voltage control through control of $\gamma(t)$, $\beta(t)$ gives a strong damping independent of the actual value of the power angle. Compared with that, damping introduced by the regulation of shunt compensation $B_{\mathrm{sh}}(t)$ is quite weak. Hence the UPFC could be used only to control its nodal voltage without introducing shunt compensation supplementary control.

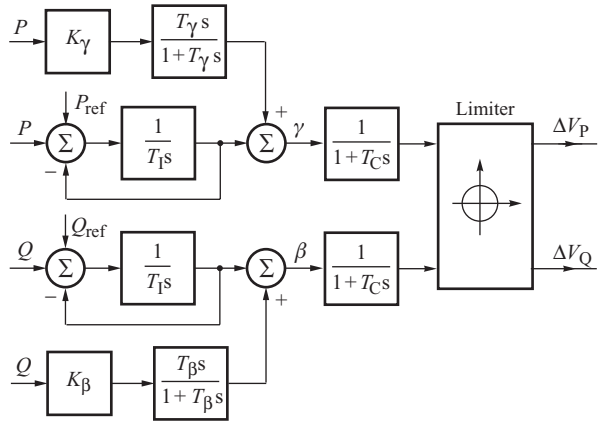

Figure 10.31 Block diagram of the booster voltage controller.

The series controller may have the structure shown in Figure 10.31. Control of the booster voltage components is achieved by using an integral regulator with a feedback loop and a PSS acting according to Equations (10.124) and (10.125). There is an output limiter common for both components of the booster voltage limiting its value ΔV where (see Figure 10.28c)

$$(\Delta V)^2 = (\Delta V_P)^2 + (\Delta V_Q)^2. \tag{10.127}$$

This limit is shown schematically in Figure 10.31 as a circle.

10.7.4 Examples of Simulation Results

Stability enhancement using supplementary UPFC control will now be illustrated using the simple test system shown in Figure 10.32. A UPFC device has been installed to control the flow of power in a transmission link consisting of lines L4 and L5 that is parallel to a link consisting of lines L3 and L2. The UPFC has the structure shown in Figure 10.31. It was assumed that there was a short

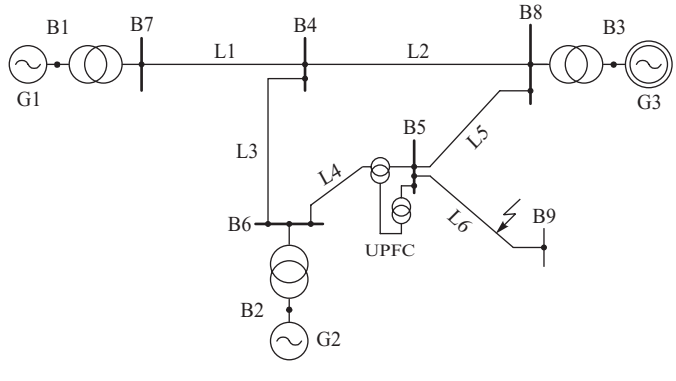

Figure 10.32 Three-machine test system.

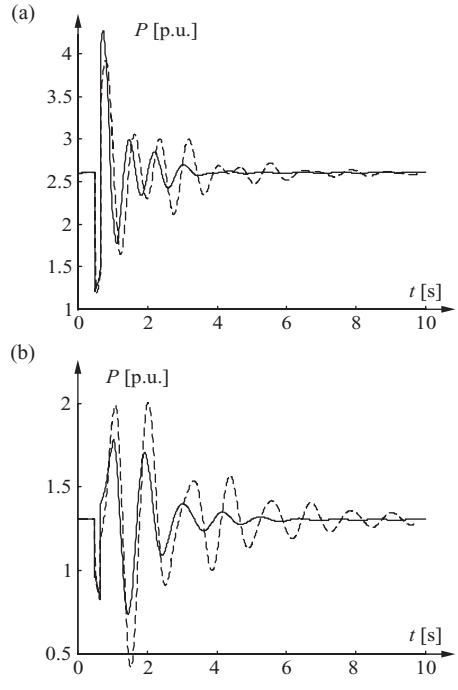

Figure 10.33 Examples of simulation results: (a) real power of generator G1; (b) real power of generator G2.

circuit in line L6 and the fault was cleared by tripping the line. The resulting simulation results are shown in Figure 10.33.

The fault caused swinging of both generators. Because of their different parameters, the frequencies of rotor swings are also quite different, which makes damping difficult. However, Figure 10.33 shows that the swings are quickly damped and a new steady state is achieved after a few seconds.

Part III

Advanced Topics in Power System Dynamics

11

Advanced Power System Modelling

In Chapter 4 the dynamic interactions taking place inside a generator following a disturbance were explained by considering the changes in the armature and rotor mmf and flux linkage. Although this type of approach allows the mechanisms by which the currents and torques are produced to be explained, it is difficult to quantify the behaviour of the generator under all operating conditions. In this chapter a more general mathematical approach is adopted that can be used to quantify the changes in the currents and the torque but is slightly more removed from the physics. To produce this *mathematical model* the generator will be represented by a number of electrical circuits, each with its own inductance and resistance and with mutual coupling between the circuits. By making some judicious assumptions with regard to the dominant changes taking place inside the generator during a particular type of disturbance, this detailed mathematical model can be simplified to produce a series of generator models. These simplified models can then be used in the appropriate situation.

To utilize fully these mathematical models of the generator it is also necessary to produce mathematical models of the turbine and its governor, as well as the AVR. These aspects are covered in the second part of the chapter. The chapter ends by considering suitable models of power system loads and FACTS devices.

11.1 Synchronous Generator

In order to examine what happens inside a synchronous machine when it is subjected to an abrupt change in operating conditions, Section 4.2 described the behaviour of the generator following a sudden short circuit on the machine terminals. The effect of the fault is to cause the current in, and the flux linking, the different windings to change in such a way that three characteristic states can be identified. These characteristic states are termed the subtransient state, the transient state and the steady state. In each of these three characteristic states the generator may be represented by an emf behind a reactance, the value of which is linked to the reluctance of the armature reaction flux path as explained in Section 4.2.4. In reality the transition from one state to another takes place smoothly so that the values of the fictitious internal emfs also change smoothly with time. In previous chapters these smooth changes were neglected and the emfs assumed to be constant in each of the characteristic states. In this chapter the flux changes occurring within the synchronous machine will be analysed more rigorously with the resulting algebraic and differential equations constituting an advanced, dynamic, mathematical model of the synchronous generator.

Power System Dynamics: Stability and Control, Second Edition Jan Machowski, Janusz W. Bialek and James R. Bumby
© 2008 John Wiley & Sons, Ltd

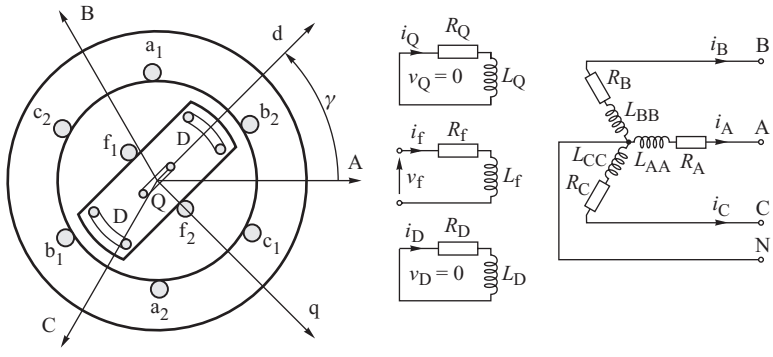

Figure 11.1 The windings in the synchronous generator and their axes.

11.1.1 Assumptions

A schematic cross-section of a generator is shown in Figure 11.1. The generator is assumed to have a three-phase stator armature winding (A, B, C), a rotor field winding (F) and two rotor damper windings – one in the d-axis (D) and one in the q-axis (Q). Figure 11.1 also shows the relative position of the windings, and their axes, with the centre of phase A taken as the reference. The notation is the same as that used in Figure 4.3 and follows the normal IEEE convention (IEEE Committee Report, 1969). In developing the mathematical model the following assumptions are made:

1. The three-phase stator winding is symmetrical.
2. The capacitance of all the windings can be neglected.
3. Each of the distributed windings may be represented by a concentrated winding.
4. The change in the inductance of the stator windings due to rotor position is sinusoidal and does not contain higher harmonics.
5. Hysteresis loss is negligible but the influence of eddy currents can be included in the model of the damper windings.
6. In the transient and subtransient states the rotor speed is near synchronous speed ($\omega \approx \omega_s$).
7. The magnetic circuits are linear (not saturated) and the inductance values do not depend on the current.

11.1.2 The Flux Linkage Equations in the Stator Reference Frame

All the generator windings are magnetically coupled so that the flux in each winding depends on the currents in all the other windings. This is represented by the following matrix equation:

$$\left[\begin{array}{c}\Psi_A\\ \Psi_B\\ \Psi_C\\ \hline \Psi_f\\ \Psi_D\\ \Psi_Q\end{array}\right] = \left[\begin{array}{ccc:ccc} L_{AA} & L_{AB} & L_{AC} & L_{Af} & L_{AD} & L_{AQ}\\ L_{BA} & L_{BB} & L_{BC} & L_{Bf} & L_{BD} & L_{BQ}\\ L_{CA} & L_{CB} & L_{CC} & L_{Cf} & L_{CD} & L_{CQ}\\ \hdashline L_{fA} & L_{fB} & L_{fC} & L_{ff} & L_{fD} & L_{fQ}\\ L_{DA} & L_{DB} & L_{DC} & L_{Df} & L_{DD} & L_{DQ}\\ L_{QA} & L_{QB} & L_{QC} & L_{Qf} & L_{QD} & L_{QQ}\end{array}\right] \left[\begin{array}{c} i_A\\ i_B\\ i_C\\ \hline i_f\\ i_D\\ i_Q\end{array}\right],$$

or

$$\left[\begin{array}{c}\Psi_{ABC}\\ \hline \Psi_{fDQ}\end{array}\right] = \left[\begin{array}{c:c} \boldsymbol{L}_S & \boldsymbol{L}_{SR}\\ \hline \boldsymbol{L}_{SR}^T & \boldsymbol{L}_R\end{array}\right] \left[\begin{array}{c} \boldsymbol{i}_{ABC}\\ \hline \boldsymbol{i}_{fDQ}\end{array}\right], \tag{11.1}$$

where $\boldsymbol{L}_S$ is a submatrix of the stator self- and mutual inductances, $\boldsymbol{L}_R$ is a submatrix of the rotor self- and mutual inductances and $\boldsymbol{L}_{SR}$ is a submatrix of the rotor to stator mutual inductances. Most of these inductances are subject to periodic changes due to both the saliency and rotation of the rotor. Consistent with the assumptions outlined above, the higher harmonics of these inductance changes will be neglected and the inductances represented by a constant component and a single periodic component.

In the case of the two-pole machine shown in Figure 11.1 the self-inductance of each stator phase winding will reach a maximum value whenever the rotor d-axis aligns with the axis of the phase winding because, with the rotor in this position, the reluctance of the flux path is a minimum. This minimum reluctance condition occurs twice during each rotation of the rotor so that the stator self-inductances are of the form

$$L_{AA} = L_S + \Delta L_S \cos 2\gamma, \quad L_{BB} = L_S + \Delta L_S \cos\left(2\gamma - \frac{2}{3}\pi\right), \quad L_{CC} = L_S + \Delta L_S \cos\left(2\gamma + \frac{2}{3}\pi\right). \tag{11.2}$$

Both L_S and ΔL_S are constant and $L_S > \Delta L_S$.

As each of the stator windings is shifted in space relative to the others by 120° the mutual inductance between each of the stator windings is negative. The magnitude of the inductance is a maximum when the rotor d-axis is midway between the axes of two of the windings. Referring to Figure 11.1 gives

$$\begin{aligned} L_{AB} &= L_{BA} = -M_S - \Delta L_S \cos 2\left(\gamma + \frac{1}{6}\pi\right) \\ L_{BC} &= L_{CB} = -M_S - \Delta L_S \cos 2\left(\gamma - \frac{1}{2}\pi\right) \\ L_{CA} &= L_{AC} = -M_S - \Delta L_S \cos 2\left(\gamma + \frac{5}{6}\pi\right), \end{aligned} \tag{11.3}$$

where $M_s > \Delta L_s$.

The mutual inductances between the stator and rotor windings change with rotor position and have a positive maximum value when the axes of a stator winding and the rotor winding align and have the same positive flux direction. When the flux directions are in opposition the value of the inductance is a negative minimum and when the axes are perpendicular the inductance is zero. Referring again to Figure 11.1 gives

$$\begin{aligned} L_{Af} &= L_{fA} = M_f \cos\gamma \\ L_{AD} &= L_{DA} = M_D \cos\gamma \\ L_{AQ} &= L_{QA} = M_Q \sin\gamma \end{aligned}$$

$$\begin{aligned} L_{Bf} &= L_{fB} = M_f \cos\left(\gamma - \frac{2}{3}\pi\right), & L_{Cf} &= L_{fC} = M_f \cos\left(\gamma + \frac{2}{3}\pi\right) \\ L_{BD} &= L_{DB} = M_D \cos\left(\gamma - \frac{2}{3}\pi\right), & L_{CD} &= L_{DC} = M_D \cos\left(\gamma + \frac{2}{3}\pi\right) \\ L_{BQ} &= L_{QB} = M_Q \sin\left(\gamma - \frac{2}{3}\pi\right), & L_{CQ} &= L_{QC} = M_Q \sin\left(\gamma + \frac{2}{3}\pi\right). \end{aligned} \tag{11.4}$$

The self- and mutual inductances of the rotor windings are constant and do not depend on rotor position. As the d- and q-axis windings are perpendicular to each other, their mutual inductances

are zero

$$L_{\mathrm{fQ}} = L_{\mathrm{Qf}} = 0 \quad \text{and} \quad L_{\mathrm{DQ}} = L_{\mathrm{QD}} = 0. \tag{11.5}$$

Most of the elements forming the inductance matrix $\boldsymbol{L}$ in the flux linkage equation (11.1) depend on rotor position and are therefore functions of time.

11.1.3 The Flux Linkage Equations in the Rotor Reference Frame

At any instant in time the position of the rotor relative to the stator reference axis is defined by the angle γ shown in Figure 11.1. Each phasor, whether voltage, current or flux linkage, in the stator reference frame (A, B, C) can be transformed into the (d, q) reference frame by projecting one reference frame onto the other using trigonometric functions of the angle γ. Using the notation of Figure 11.1, the current vectors are

$$\begin{aligned} i_{\mathrm{d}} &= \beta_{\mathrm{d}} \left[i_{\mathrm{A}} \cos\gamma + i_{\mathrm{B}} \cos\left(\gamma - \frac{2}{3}\pi\right) + i_{\mathrm{C}} \cos\left(\gamma + \frac{2}{3}\pi\right) \right] \\ i_{\mathrm{q}} &= \beta_{\mathrm{q}} \left[i_{\mathrm{A}} \sin\gamma + i_{\mathrm{B}} \sin\left(\gamma - \frac{2}{3}\pi\right) + i_{\mathrm{C}} \sin\left(\gamma + \frac{2}{3}\pi\right) \right], \end{aligned} \tag{11.6}$$

where β_{d} and β_{q} are arbitrary non-zero coefficients introduced due to the change of reference frame. Equation (11.6) describes a unique transformation from the stator (A, B, C) to the rotor (d, q) reference axis. The reverse transformation from (d, q) to (A, B, C) is not unique as the two equations in Equation (11.6) have three unknowns i_{A}, i_{B}, i_{C}. A unique transformation may be achieved by supplementing the (d, q) coordinates by an additional coordinate. It is convenient to assume this additional coordinate to be the zero-sequence coordinate defined in the same way as in the method of symmetrical components

$$i_0 = \beta_0 \left(i_{\mathrm{A}} + i_{\mathrm{B}} + i_{\mathrm{C}} \right), \tag{11.7}$$

where β_0 is again an arbitrary coefficient introduced due to the change in reference frame. Combining Equations (11.6) and (11.7) gives the following matrix equation:

$$\begin{bmatrix} i_0 \\ \hline i_{\mathrm{d}} \\ \hline i_{\mathrm{q}} \end{bmatrix} = \left[\begin{array}{c|c|c} \beta_0 & \beta_0 & \beta_0 \\ \hline \beta_{\mathrm{d}} \cos\gamma & \beta_{\mathrm{d}} \cos\left(\gamma - \frac{2}{3}\pi\right) & \beta_{\mathrm{d}} \cos\left(\gamma + \frac{2}{3}\pi\right) \\ \hline \beta_{\mathrm{q}} \sin\gamma & \beta_{\mathrm{q}} \sin\left(\gamma - \frac{2}{3}\pi\right) & \beta_{\mathrm{q}} \sin\left(\gamma + \frac{2}{3}\pi\right) \end{array}\right] \begin{bmatrix} i_{\mathrm{A}} \\ \hline i_{\mathrm{B}} \\ \hline i_{\mathrm{C}} \end{bmatrix} \quad \text{or} \quad \boldsymbol{i}_{0\mathrm{dq}} = \boldsymbol{W} \boldsymbol{i}_{\mathrm{ABC}}. \tag{11.8}$$

The coefficients β_0, β_{d} and β_{q} are non-zero. Matrix $\boldsymbol{W}$ is non-singular and the inverse transformation is uniquely determined by

$$\boldsymbol{i}_{\mathrm{ABC}} = \boldsymbol{W}^{-1} \boldsymbol{i}_{0\mathrm{dq}}. \tag{11.9}$$

A similar transformation can be defined for the phasors of stator voltage and flux linkage.

The rotor currents, voltages and flux linkages are already in the (d, q) reference frame and no transformation is necessary, allowing the transformation of all the winding currents to be written as

$$\begin{bmatrix} \boldsymbol{i}_{0\mathrm{dq}} \\ \boldsymbol{i}_{\mathrm{fDQ}} \end{bmatrix} = \begin{bmatrix} \boldsymbol{W} & \boldsymbol{0} \\ \boldsymbol{0} & \boldsymbol{1} \end{bmatrix} \begin{bmatrix} \boldsymbol{i}_{\mathrm{ABC}} \\ \boldsymbol{i}_{\mathrm{fDQ}} \end{bmatrix}. \tag{11.10}$$

In this equation $\boldsymbol{i}_{\mathrm{fDQ}}$ is a column vector of the currents i_{f}, i_{D} and i_{Q}, and $\mathbf{1}$ is a diagonal unit matrix. A similar transformation can be defined for the rotor voltages and flux linkages. The inverse transformation of Equation (11.10) is

$$\begin{bmatrix} \boldsymbol{i}_{\mathrm{ABC}} \\ \boldsymbol{i}_{\mathrm{fDQ}} \end{bmatrix} = \begin{bmatrix} \boldsymbol{W}^{-1} & \mathbf{0} \\ \mathbf{0} & \mathbf{1} \end{bmatrix} \begin{bmatrix} \boldsymbol{i}_{\mathrm{0dq}} \\ \boldsymbol{i}_{\mathrm{fDQ}} \end{bmatrix}. \tag{11.11}$$

Substituting this inverse transformation, along with a similar transformation for the fluxes, into the flux linkage equation (11.1) gives

$$\begin{bmatrix} \boldsymbol{\Psi}_{\mathrm{0dq}} \\ \boldsymbol{\Psi}_{\mathrm{fDQ}} \end{bmatrix} = \begin{bmatrix} \boldsymbol{W} & \mathbf{0} \\ \mathbf{0} & \mathbf{1} \end{bmatrix} \begin{bmatrix} \boldsymbol{L}_{\mathrm{S}} & \boldsymbol{L}_{\mathrm{SR}} \\ \boldsymbol{L}_{\mathrm{SR}}^{\mathrm{T}} & \boldsymbol{L}_{\mathrm{W}} \end{bmatrix} \begin{bmatrix} \boldsymbol{W}^{-1} & \mathbf{0} \\ \mathbf{0} & \mathbf{1} \end{bmatrix} \begin{bmatrix} \boldsymbol{i}_{\mathrm{0dq}} \\ \boldsymbol{i}_{\mathrm{fDQ}} \end{bmatrix}, \tag{11.12}$$

which, after multiplying the three square matrices by each other, yields

$$\left[\begin{array}{c} \boldsymbol{\Psi}_{\mathrm{0dq}} \\ \hline \boldsymbol{\Psi}_{\mathrm{fDQ}} \end{array}\right] = \left[\begin{array}{c|c} \boldsymbol{W}\boldsymbol{L}_{\mathrm{S}}\boldsymbol{W}^{-1} & \boldsymbol{W}\boldsymbol{L}_{\mathrm{SR}} \\ \hline \boldsymbol{L}_{\mathrm{SR}}^{\mathrm{T}}\boldsymbol{W}^{-1} & \boldsymbol{L}_{\mathrm{W}} \end{array}\right] \left[\begin{array}{c} \boldsymbol{i}_{\mathrm{0dq}} \\ \hline \boldsymbol{i}_{\mathrm{fDQ}} \end{array}\right]. \tag{11.13}$$

The coefficients introduced due to the change in the reference frame are now chosen as $\beta_0 = 1/\sqrt{3}$ and $\beta_{\mathrm{d}} = \beta_{\mathrm{q}} = \sqrt{2/3}$ to give the following transformation matrix:

$$\boldsymbol{W} = \sqrt{\frac{2}{3}} \left[\begin{array}{c|c|c} \dfrac{1}{\sqrt{2}} & \dfrac{1}{\sqrt{2}} & \dfrac{1}{\sqrt{2}} \\ \hline \cos\gamma & \cos\left(\gamma - \dfrac{2}{3}\pi\right) & \cos\left(\gamma + \dfrac{2}{3}\pi\right) \\ \hline \sin\gamma & \sin\left(\gamma - \dfrac{2}{3}\pi\right) & \sin\left(\gamma + \dfrac{2}{3}\pi\right) \end{array}\right]. \tag{11.14}$$

With this choice of transformation coefficients $\boldsymbol{W}^{-1} = \boldsymbol{W}^{\mathrm{T}}$ where $\boldsymbol{W}^{-1}$ and $\boldsymbol{W}^{\mathrm{T}}$ are respectively the inverse and the transpose of $\boldsymbol{W}$. For a matrix that satisfies the condition $\boldsymbol{W}^{-1} = \boldsymbol{W}^{\mathrm{T}}$, then $\boldsymbol{W}\boldsymbol{W}^{\mathrm{T}} = \mathbf{1}$ and the matrix is said to be *orthogonal*. As will be seen later, such an orthogonal transformation is necessary to ensure that the power calculated in both the (A, B, C) and (d, q) reference frames is identical and the transformation is said to be *power invariant*. The transformation matrix $\boldsymbol{W}$ transforms the submatrix of self- and mutual inductances of the stator windings $\boldsymbol{L}_{\mathrm{S}}$ into

$$\boldsymbol{W}\boldsymbol{L}_{\mathrm{S}}\boldsymbol{W}^{-1} = \boldsymbol{W} \begin{bmatrix} L_{\mathrm{AA}} & L_{\mathrm{AB}} & L_{\mathrm{AC}} \\ L_{\mathrm{BA}} & L_{\mathrm{BB}} & L_{\mathrm{BC}} \\ L_{\mathrm{CA}} & L_{\mathrm{CB}} & L_{\mathrm{CC}} \end{bmatrix} \boldsymbol{W}^{-1} = \begin{bmatrix} L_0 & & \\ & L_{\mathrm{d}} & \\ & & L_{\mathrm{q}} \end{bmatrix}. \tag{11.15}$$

This is a diagonal matrix in which $L_0 = L_{\mathrm{S}} - 2M_{\mathrm{S}}$, $L_{\mathrm{d}} = L_{\mathrm{S}} + M_{\mathrm{S}} + 3\Delta L_{\mathrm{S}}/2$ and $L_{\mathrm{q}} = L_{\mathrm{S}} + M_{\mathrm{S}} - 3\Delta L_{\mathrm{S}}/2$. Similarly the submatrix of the mutual inductances between the stator and the rotor windings is transformed into

$$\boldsymbol{W}\boldsymbol{L}_{\mathrm{SR}} = \boldsymbol{W} \begin{bmatrix} L_{\mathrm{Af}} & L_{\mathrm{AB}} & L_{\mathrm{AQ}} \\ L_{\mathrm{Bf}} & L_{\mathrm{BD}} & L_{\mathrm{BQ}} \\ L_{\mathrm{Cf}} & L_{\mathrm{CD}} & L_{\mathrm{CQ}} \end{bmatrix} = \begin{bmatrix} kM_{\mathrm{f}} & kM_{\mathrm{D}} & \\ & & kM_{\mathrm{Q}} \end{bmatrix},$$

where $k = \sqrt{3/2}$. The submatrix of the mutual inductances between the rotor and the stator windings is transformed into the same form, because $\boldsymbol{W}^{-1} = \boldsymbol{W}^{\mathrm{T}}$ and

$$\boldsymbol{L}_{\mathrm{SR}}^{\mathrm{T}}\boldsymbol{W}^{-1} = \boldsymbol{L}_{\mathrm{SR}}^{\mathrm{T}}\boldsymbol{W}^{\mathrm{T}} = (\boldsymbol{W}\boldsymbol{L}_{\mathrm{SR}})^{\mathrm{T}}.$$

The matrix of the self- and mutual inductances of the rotor windings is not changed. As a result of these transformations Equation (11.13) becomes

$$\begin{bmatrix} \Psi_0 \\ \Psi_d \\ \Psi_q \\ \Psi_f \\ \Psi_D \\ \Psi_Q \end{bmatrix} = \begin{bmatrix} L_0 & & & & & \\ & L_d & & kM_f & kM_D & \\ & & L_q & & & kM_Q \\ & kM_f & & L_f & L_{fD} & \\ & kM_D & & L_{fD} & L_D & \\ & & kM_Q & & & L_Q \end{bmatrix} \begin{bmatrix} i_0 \\ i_d \\ i_q \\ i_f \\ i_D \\ i_Q \end{bmatrix}. \tag{11.16}$$

An important feature of this equation is that the matrix of inductances is symmetrical. This is due to the correct choice of the transformation coefficients β_0, β_d and β_q ensuring orthogonality of the transformation matrix, $\boldsymbol{W}$.

The transformation of all the generator windings into the rotor reference frame is referred to as the 0dq *transformation* or *Park's transformation*. The original transformation matrix proposed by Park (Concordia, 1951) was not orthogonal and consequently the resulting matrix of equivalent inductances was not symmetrical. Concordia corrected this but customarily the transformation is still referred to as Park's, or the modified Park's transformation. All the elements of the inductance matrix in Equation (11.16) are constant and independent of time. This is the main advantage of Park's transformation.

After reordering the variables Equation (11.16) can be written as three independent sets of equations

$$\Psi_0 = L_0 i_0, \tag{11.17}$$

$$\begin{bmatrix} \Psi_d \\ \Psi_f \\ \Psi_D \end{bmatrix} = \begin{bmatrix} L_d & kM_f & kM_D \\ kM_f & L_f & L_{fD} \\ kM_D & L_{fD} & L_D \end{bmatrix} \begin{bmatrix} i_d \\ i_f \\ i_D \end{bmatrix}, \tag{11.18}$$

$$\begin{bmatrix} \Psi_q \\ \Psi_Q \end{bmatrix} = \begin{bmatrix} L_q & kM_Q \\ kM_Q & L_Q \end{bmatrix} \begin{bmatrix} i_q \\ i_Q \end{bmatrix}. \tag{11.19}$$

These equations describe three sets of magnetically coupled windings as shown in Figure 11.2. Each set of windings is independent of the others in that there is no magnetic coupling between the different winding sets. Figure 11.2 reflects this by showing the three winding sets perpendicular to each other. The first set of windings, represented by Equation (11.18), consists of three windings in

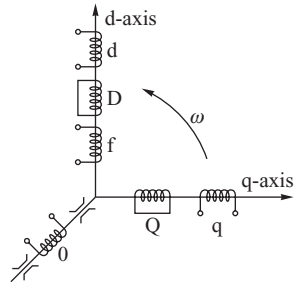

Figure 11.2 Three sets of fictitious perpendicular windings representing the synchronous generator.

the d-axis. Two of these, f and D, correspond to the real field and damper windings of the rotor. The third winding, denoted as d, is fictitious and represents the effect of the three-phase stator winding in the d-axis of the rotor. This fictitious d-axis winding rotates with the rotor.

The second set of windings, represented by Equation (11.19), consists of two windings. The first one, denoted by Q, corresponds to the real damper winding in the rotor q-axis, while the second, denoted by q, is a fictitious winding representing the effect of the three-phase stator winding in the q-axis. Obviously both windings rotate with the rotor.

Equation (11.17) represents the third winding set which consists of a single winding which is magnetically separate from both of the other two sets. This winding is shown in Figure 11.2 to be perpendicular to the both the d- and q-axes and to be along the axis of rotation of the equivalent rotor. This winding can be omitted if the three-phase stator winding is connected in star with the neutral point isolated, that is not earthed. With this winding connection the sum of the stator phase currents must be zero and, as $i_0 = (i_A + i_B + i_C)/\sqrt{3} = 0$, the current flowing in this third winding is also zero.

A physical interpretation of the d- and q-axes coils can be obtained by considering Equation (11.16). This equation defines the flux linkages within the generator but with the actual three-phase stator armature winding replaced by one winding in the d-axis and another in the q-axis. As shown in Chapter 3, currents in the three-phase stator armature winding produce a rotating armature reaction flux which enters the rotor at an angle that depends on the armature loading condition. In the rotor (d, q) reference frame this rotating flux is simply represented by two DC flux components, one acting along the d-axis and the other along the q-axis. These (d, q) component fluxes are produced by the currents flowing in the two fictitious (d, q) armature windings. In light of this, selecting the transformation coefficients $\beta_d = \beta_q = \sqrt{2/3}$ has important implications with regard to the number of turns on the fictitious d and q armature windings. For balanced three-phase currents in the armature, Equation (3.42) showed that the value of the armature mmf rotating with the rotor was equal to $3/2 N_a I_m$ where N_a is the effective number of turns in series per phase and $I_m = \sqrt{2} I_g$. However, as will be shown in Equation (11.82), the same balanced three-phase current gives the maximum values of i_d and i_q as $\sqrt{3/2} I_m$. Consequently, if i_d and i_q are to produce the same mmf as the actual three-phase armature winding the d and q armature windings must each have $\sqrt{3/2}$ more turns than an actual armature phase winding. This effect is reflected by the factor $k = \sqrt{3/2}$ which appears in the mutual inductance between the d-axis armature winding and both d-axis rotor windings. The same factor is present in the mutual inductance between the q-axis armature winding and the q-axis damper winding.

Other values of transformation coefficient can be used to produce an orthogonal transformation. In particular, a transformation coefficient of 2/3 is favoured by a number of authors, for example Adkins (1957). The reason for this is discussed by Harris, Lawrenson and Stephenson (1970) who compare different transformation systems. In their discussion these authors argue that a transformation coefficient of 2/3 is more closely related to flux conditions in the generator than a transformation coefficient of $\sqrt{2/3}$. With a current transformation coefficient of 2/3 both the d- and q-axis armature coils have the same number of turns as an individual phase winding. However, in order to maintain a power-invariant transformation, the transformation coefficient used for voltages is different from that used for currents unless a per-unit system is used. In such a system it is necessary to have a different value of base current in the phase windings to the d, q windings; the (d, q) base current differs by a factor of 3/2 to the (A, B, C) base current.

11.1.3.1 Power in the (0dq) Reference Frame

The three-phase power output of the generator is equal to the scalar product of the stator voltages and currents

$$p_g = v_A i_A + v_B i_B + v_C i_C = \boldsymbol{v}_{ABC}^T \boldsymbol{i}_{ABC}. \tag{11.20}$$

The orthogonal transformation from the (A, B, C) to the (0, d, q) reference frame ensures that the transformation is power invariant so that the power is also given by

$$p_g = v_0 i_0 + v_d i_d + v_q i_q = \boldsymbol{v}_{0dq}^T \boldsymbol{i}_{0dq}. \tag{11.21}$$

Equation (11.21) can be verified by substituting the voltage and current transformations $\boldsymbol{v}_{ABC} = \boldsymbol{W}^{-1}\boldsymbol{v}_{0dq}$ and $\boldsymbol{i}_{ABC} = \boldsymbol{W}^{-1}\boldsymbol{i}_{0dq}$ into Equation (11.20) to give

$$\begin{aligned} p_g &= \boldsymbol{v}_{ABC}^T \boldsymbol{i}_{ABC} = \left(\boldsymbol{W}^{-1}\boldsymbol{v}_{0dq}\right)^T \boldsymbol{W}^{-1}\boldsymbol{i}_{0dq} = \boldsymbol{v}_{0dq}^T (\boldsymbol{W}^{-1})^T \boldsymbol{W}^{-1}\boldsymbol{i}_{0dq} \\ &= \boldsymbol{v}_{0dq}^T (\boldsymbol{W}^T)^T \boldsymbol{W}^{-1}\boldsymbol{i}_{0dq} = \boldsymbol{v}_{0dq}^T \boldsymbol{W}\boldsymbol{W}^{-1}\boldsymbol{i}_{0dq} = \boldsymbol{v}_{0dq}^T \boldsymbol{i}_{0dq} \end{aligned}$$

and noting that, as the matrix $\boldsymbol{W}$ is orthogonal, $\boldsymbol{W}^{-1} = \boldsymbol{W}^T$.

11.1.4 Voltage Equations

The winding circuits shown in Figure 11.1 can be divided into two characteristic types. The first type, consisting of the stator windings (A, B, C) and the damper windings (D, Q), are circuits in which the emf induced in the winding drives the current in the winding. The application of Kirchhoff's voltage law to such a circuit is shown in Figure 11.3a. The second type of circuit is represented by the rotor field winding f in which the current is supplied by an external voltage source. In this case an emf is induced in the winding which opposes the current. The equivalent circuit for this circuit is shown in Figure 11.3b. The convention for the direction of the voltages is the same as that used in Figure 11.1.

Using this convention, the voltage equation in the (A, B, C) reference frame follows as

$$\begin{bmatrix} v_A \\ v_B \\ v_C \\ -v_f \\ 0 \\ 0 \end{bmatrix} = -\begin{bmatrix} R_A & & & & & \\ & R_B & & & & \\ & & R_C & & & \\ & & & R_f & & \\ & & & & R_D & \\ & & & & & R_Q \end{bmatrix} \begin{bmatrix} i_A \\ i_B \\ i_C \\ i_f \\ i_D \\ i_Q \end{bmatrix} - \frac{d}{dt}\begin{bmatrix} \Psi_A \\ \Psi_B \\ \Psi_C \\ \Psi_f \\ \Psi_D \\ \Psi_Q \end{bmatrix}, \tag{11.22}$$

or, when written in compact matrix form,

$$\begin{bmatrix} \boldsymbol{v}_{ABC} \\ \boldsymbol{v}_{fDQ} \end{bmatrix} = -\begin{bmatrix} \boldsymbol{R}_{ABC} & \\ & \boldsymbol{R}_{fDQ} \end{bmatrix} \begin{bmatrix} \boldsymbol{i}_{ABC} \\ \boldsymbol{i}_{fDQ} \end{bmatrix} - \frac{d}{dt}\begin{bmatrix} \boldsymbol{\Psi}_{ABC} \\ \boldsymbol{\Psi}_{fDQ} \end{bmatrix}, \tag{11.23}$$

where $\boldsymbol{R}_{ABC}$ and $\boldsymbol{R}_{fDQ}$ are diagonal resistance matrices. These equations can be transformed into the rotating reference frame using the transformation equation (11.11) for currents, voltages and

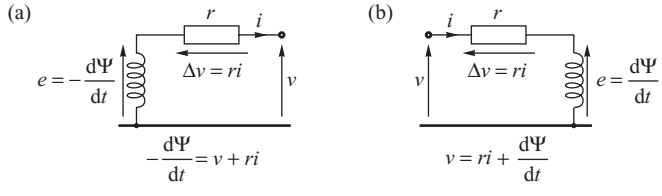

Figure 11.3 Kirchhoff's voltage law applied to the two types of circuits: (a) generator circuit; (b) motor circuit.

flux linkages. After some algebra this gives

$$\begin{bmatrix} \boldsymbol{W}^{-1} & \\ & \mathbf{1} \end{bmatrix} \begin{bmatrix} \boldsymbol{v}_{0dq} \\ \boldsymbol{v}_{fDQ} \end{bmatrix} = - \begin{bmatrix} \boldsymbol{R}_{ABC} & \\ & \boldsymbol{R}_{fDQ} \end{bmatrix} \begin{bmatrix} \boldsymbol{W}^{-1} & \\ & \mathbf{1} \end{bmatrix} \begin{bmatrix} \boldsymbol{i}_{0dq} \\ \boldsymbol{i}_{fDQ} \end{bmatrix} - \frac{\mathrm{d}}{\mathrm{d}t} \begin{bmatrix} \boldsymbol{W}^{-1} & \\ & \mathbf{1} \end{bmatrix} \begin{bmatrix} \boldsymbol{\Psi}_{0dq} \\ \boldsymbol{\Psi}_{fDQ} \end{bmatrix},$$

which, when left-multiplied by the transformation matrix $\boldsymbol{W}$, becomes

$$\begin{bmatrix} \boldsymbol{v}_{0dq} \\ \boldsymbol{v}_{fDQ} \end{bmatrix} = - \begin{bmatrix} \boldsymbol{W} & \\ & \mathbf{1} \end{bmatrix} \begin{bmatrix} \boldsymbol{R}_{ABC} & \\ & \boldsymbol{R}_{fDQ} \end{bmatrix} \begin{bmatrix} \boldsymbol{W}^{-1} & \\ & \mathbf{1} \end{bmatrix} \begin{bmatrix} \boldsymbol{i}_{0dq} \\ \boldsymbol{i}_{fDQ} \end{bmatrix} - \begin{bmatrix} \boldsymbol{W} & \\ & \mathbf{1} \end{bmatrix} \frac{\mathrm{d}}{\mathrm{d}t} \left\{ \begin{bmatrix} \boldsymbol{W}^{-1} & \\ & \mathbf{1} \end{bmatrix} \begin{bmatrix} \boldsymbol{\Psi}_{0dq} \\ \boldsymbol{\Psi}_{fDQ} \end{bmatrix} \right\}. \tag{11.24}$$

If the resistance of each of the stator phases is identical, $R_A = R_B = R_C = R$, and the product of the first three matrices on the right is a diagonal matrix, then

$$\boldsymbol{W} \boldsymbol{R}_{ABC} \boldsymbol{W}^{-1} = \boldsymbol{R}_{ABC}. \tag{11.25}$$

According to Equation (11.14), the transformation matrix $\boldsymbol{W}$ is a function of time and the derivative of the last term on the right in Equation (11.24) must be calculated as the derivative of a product of two functions

$$\frac{\mathrm{d}}{\mathrm{d}t}(\boldsymbol{W}^{-1} \boldsymbol{\Psi}_{0dq}) = \dot{\boldsymbol{W}}^{-1} \boldsymbol{\Psi}_{0dq} + \boldsymbol{W}^{-1} \dot{\boldsymbol{\Psi}}_{0dq}$$

where the dot on the top of a symbol denotes a derivative with respect to time. Multiplication by the transformation matrix gives

$$\boldsymbol{W} \frac{\mathrm{d}}{\mathrm{d}t}(\boldsymbol{W}^{-1} \boldsymbol{\Psi}_{0dq}) = (\boldsymbol{W} \dot{\boldsymbol{W}}^{-1}) \boldsymbol{\Psi}_{0dq} + \dot{\boldsymbol{\Psi}}_{0dq} = -(\dot{\boldsymbol{W}} \boldsymbol{W}^{-1}) \boldsymbol{\Psi}_{0dq} + \dot{\boldsymbol{\Psi}}_{0dq}, \tag{11.26}$$

as the derivative of the product $\boldsymbol{W}\boldsymbol{W}^{-1} = \mathbf{1}$ is $\dot{\boldsymbol{W}}\boldsymbol{W}^{-1} + \boldsymbol{W}\dot{\boldsymbol{W}}^{-1} = \mathbf{0}$ and $\dot{\boldsymbol{W}}\boldsymbol{W}^{-1} = -\boldsymbol{W}\dot{\boldsymbol{W}}^{-1}$. Calculating $\dot{\boldsymbol{W}}$ as $\dot{\boldsymbol{W}} = \mathrm{d}\boldsymbol{W}/\mathrm{d}t$ and multiplying by $\boldsymbol{W}^{-1} = \boldsymbol{W}^{T}$ gives $\dot{\boldsymbol{W}}\boldsymbol{W}^{-1}$ as

$$\boldsymbol{\Omega} = \dot{\boldsymbol{W}} \boldsymbol{W}^{-1} = \omega \begin{bmatrix} 0 & 0 & 0 \\ 0 & 0 & -1 \\ 0 & 1 & 0 \end{bmatrix}. \tag{11.27}$$

This matrix is referred to as the *rotation matrix* as it introduces terms into the voltage equations which are dependent on the speed of rotation.

The voltage equations in the (d, q) reference frame can be obtained after substituting the formulae (11.25)–(11.27) into Equation (11.24) to give

$$\begin{bmatrix} \boldsymbol{v}_{0dq} \\ \boldsymbol{v}_{fDQ} \end{bmatrix} = - \begin{bmatrix} \boldsymbol{R}_{ABC} & \\ & \boldsymbol{R}_{fDQ} \end{bmatrix} \begin{bmatrix} \boldsymbol{i}_{0dq} \\ \boldsymbol{i}_{fDQ} \end{bmatrix} - \begin{bmatrix} \dot{\boldsymbol{\Psi}}_{0dq} \\ \dot{\boldsymbol{\Psi}}_{fDQ} \end{bmatrix} + \begin{bmatrix} \boldsymbol{\Omega} & \\ & \mathbf{0} \end{bmatrix} \begin{bmatrix} \boldsymbol{\Psi}_{0dq} \\ \boldsymbol{\Psi}_{fDQ} \end{bmatrix}. \tag{11.28}$$

This equation, without the term $\boldsymbol{\Omega}\boldsymbol{\Psi}_{0dq}$, describes Kirchhoff's voltage law for the equivalent generator circuits shown in Figure 11.2. The rotational term represents the emfs induced in the stator windings due to the rotation of the magnetic field. These *rotational emfs* are represented as

$$\boldsymbol{\Omega}\boldsymbol{\Psi}_{0dq} = \omega \begin{bmatrix} 0 & 0 & 0 \\ 0 & 0 & -1 \\ 0 & 1 & 0 \end{bmatrix} \begin{bmatrix} \Psi_0 \\ \Psi_d \\ \Psi_q \end{bmatrix} = \begin{bmatrix} 0 \\ -\omega\Psi_q \\ +\omega\Psi_d \end{bmatrix}. \tag{11.29}$$

Importantly this equation shows that the d-axis rotational emf is induced by the q-axis flux, while the q-axis rotational emf is induced by the d-axis flux. The plus and minus signs are a result of the assumed direction, and rotation, of the rotor axes and the fact that an induced emf must lag the flux which produces it by 90°.

The armature emfs proportional to the rate of change of the flux, that is the $\dot{\boldsymbol{\Psi}}$ terms, are referred to as the *transformer emfs* and are due to changing currents in coils on the same axis as the one being considered. They would be present even if the machine was stationary.

Equation (11.28) may be expanded to give

$$\left.\begin{aligned} v_0 &= -Ri_0 - \dot{\Psi}_0 \\ v_\mathrm{d} &= -Ri_\mathrm{d} - \dot{\Psi}_\mathrm{d} - \omega\Psi_\mathrm{q} \\ v_\mathrm{q} &= -Ri_\mathrm{q} - \dot{\Psi}_\mathrm{q} + \omega\Psi_\mathrm{d} \end{aligned}\right\} \text{stator,} \tag{11.30}$$

$$\left.\begin{aligned} v_\mathrm{f} &= R_\mathrm{f} i_\mathrm{f} + \dot{\Psi}_\mathrm{f} \\ 0 &= R_\mathrm{D} i_\mathrm{D} + \dot{\Psi}_\mathrm{D} \\ 0 &= R_\mathrm{Q} i_\mathrm{Q} + \dot{\Psi}_\mathrm{Q} \end{aligned}\right\} \text{rotor.} \tag{11.31}$$

If balanced operation only is considered then there are no zero-sequence currents and the first of the stator equations, corresponding to the zero sequence, can be omitted.[1] Generally, changes in the generator speed are small ($\omega \approx \omega_\mathrm{s}$) while the transformer emfs ($\dot{\Psi}_\mathrm{d}$ and $\dot{\Psi}_\mathrm{q}$) are also small when compared with the rotation emfs ($-\omega\Psi_\mathrm{q}$ and $+\omega\Psi_\mathrm{d}$), whose values are close to the corresponding components of the generator voltage. Neglecting the transformer emfs allows the differential equations (11.30) describing the stator voltage to be replaced by the following two algebraic equations:

$$\begin{bmatrix} v_\mathrm{d} \\ v_\mathrm{q} \end{bmatrix} \approx -\begin{bmatrix} R & 0 \\ 0 & R \end{bmatrix}\begin{bmatrix} i_\mathrm{d} \\ i_\mathrm{q} \end{bmatrix} + \omega\begin{bmatrix} -\Psi_\mathrm{q} \\ +\Psi_\mathrm{d} \end{bmatrix}. \tag{11.32}$$

The differential voltage equations of the rotor windings (11.31) remain unchanged and can be rewritten as

$$\begin{bmatrix} \dot{\Psi}_\mathrm{f} \\ \dot{\Psi}_\mathrm{D} \\ \dot{\Psi}_\mathrm{Q} \end{bmatrix} = -\begin{bmatrix} R_\mathrm{f} & 0 & 0 \\ 0 & R_\mathrm{D} & 0 \\ 0 & 0 & R_\mathrm{Q} \end{bmatrix}\begin{bmatrix} i_\mathrm{f} \\ i_\mathrm{D} \\ i_\mathrm{Q} \end{bmatrix} + \begin{bmatrix} v_\mathrm{f} \\ 0 \\ 0 \end{bmatrix}. \tag{11.33}$$

The differential equations (11.32) and (11.33) together with the algebraic flux linkage equations (11.18) and (11.19) constitute the full model of the synchronous generator with the transformer emfs neglected.

To be used for power system studies the generator equations must be interfaced to the equations describing the power system transmission network. If the armature transformer emfs are included in the model then the implication of having two differential equations to describe the armature voltage is that the power system transmission network equations themselves must be differential equations. For all but the simplest systems this introduces significant complexity into the system equations, requires a large amount of computation time, implies a parameter accuracy that is often unrealistic and is usually not necessary when studying electromechanical dynamics, other than shaft torques. By neglecting the transformer emfs the armature differential equations are replaced by two algebraic equations which permits the power system to be modelled by a set of algebraic equations as described in Chapter 3, Equation (3.146). This significantly simplifies the generator to power system interface.

For many power system studies it is possible, and highly desirable, to rephrase and simplify the full set of generator equations, Equations (11.32), (11.33), (11.18) and (11.19), so that they are in a more acceptable form and easier to interface to the power system network equations. Before examining how these changes can be made it is necessary to relate these circuit equations to the

[1] As the zero-axis voltage and flux equations are decoupled from the other two axes, these equations can be solved separately for the unbalanced operation.

flux conditions inside the generator when it is in the steady state, transient state or the subtransient state. These flux conditions and characteristic states were extensively described and discussed in Chapter 4.

11.1.5 Generator Reactances in Terms of Circuit Quantities

The d-axis consists of three *RL* coupled circuits, one each for the d-axis armature coil, the field coil and the d-axis damper as shown in Figure 11.4a. Only two coils are on the q-axis, one each for the q-axis armature winding and the q-axis damper, Figure 11.4b. When viewed from the terminals of the armature, the effective impedance of the armature coil to any current change will depend on the parameters of the different circuits, their mutual coupling and whether or not the circuits are open or closed.

11.1.5.1 Steady State

When in the steady state the armature flux has penetrated through all the rotor circuits, the field and damper winding currents are constant and the armature current simply sees the synchronous inductance L_d in the direct axis and L_q in the quadrature axis.

11.1.5.2 Transient State

In the transient state the armature flux has penetrated the damper circuits and the field winding screens the rotor body from the armature flux. The damper circuits are no longer effective and can be removed from the model, while the screening behaviour of the field winding is modelled by short-circuiting the field winding and setting its resistance to zero, Figure 11.5a. This effectively represents the current changes that would occur in the field winding in order to maintain the flux linkage of this winding constant, the definition of the transient state. The circuit equations for the d-axis can be written as

$$\begin{aligned} v_d &= Ri_d + L_d\frac{di_d}{dt} + kM_f\frac{d\Delta i_f}{dt} \\ \Delta v_f &= 0 = L_f\frac{d\Delta i_f}{dt} + kM_f\frac{di_d}{dt}. \end{aligned} \tag{11.34}$$

At this point it is convenient to use Laplace transform techniques to simplify these simultaneous differential equations. As the initial conditions are all zero, then d/dt can be replaced by the Laplace

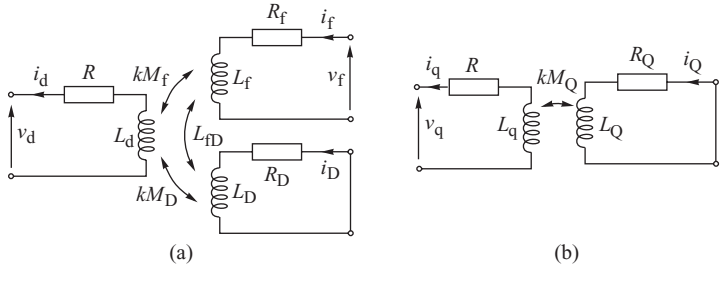

Figure 11.4 The d- and q-axis coupled circuits: (a) d-axis: (b) q-axis.

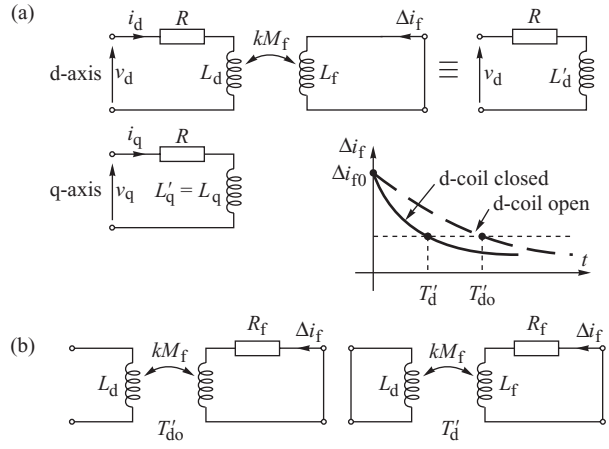

Figure 11.5 The d- and q-axis coupled circuits in the transient state: (a) for determining transient inductance; (b) for determining the field winding time constants.

operator and the differential equations written in matrix form as

$$\begin{bmatrix} v_\mathrm{d} \\ 0 \end{bmatrix} = \begin{bmatrix} R + \mathrm{s}L_\mathrm{d} & \mathrm{s}kM_\mathrm{f} \\ \mathrm{s}kM_\mathrm{f} & \mathrm{s}L_\mathrm{f} \end{bmatrix} \begin{bmatrix} i_\mathrm{d} \\ \Delta i_\mathrm{f} \end{bmatrix}. \tag{11.35}$$

This equation[2] can be solved for v_d by eliminating Δi_f and writing

$$v_\mathrm{d} = (R + \mathrm{s}L'_\mathrm{d})i_\mathrm{d}, \tag{11.36}$$

where the d-axis transient inductance

$$L'_\mathrm{d} = L_\mathrm{d} - \frac{k^2 M_\mathrm{f}^2}{L_\mathrm{f}}, \quad X'_\mathrm{d} = \omega L'_\mathrm{d}. \tag{11.37}$$

As there is no field winding in the quadrature axis

$$L'_\mathrm{q} = L_\mathrm{q}, \quad X'_\mathrm{q} = \omega L'_\mathrm{q} = X_\mathrm{q}. \tag{11.38}$$

However, in many cases it is convenient to represent the rotor body of a turbogenerator by an additional q-axis rotor coil when an equation for L'_q, similar to that for L'_d with appropriate parameter changes, will result. This important point will arise again later when generator models are considered.

It is also useful to define the decay time constant of the induced field current. This time constant will depend on whether the d-axis armature coil is open circuit or short circuit, Figure 11.5b. The circuit situation is very similar to that used to establish the relationship for the transient inductance, but now viewed from the field winding, so that the same equation can be used for the effective

[2] The general matrix equation

$$\begin{bmatrix} \boldsymbol{v}_1 \\ \boldsymbol{0} \end{bmatrix} = \begin{bmatrix} \boldsymbol{z}_{11} & \boldsymbol{z}_{12} \\ \boldsymbol{z}_{21} & \boldsymbol{z}_{22} \end{bmatrix} \begin{bmatrix} \boldsymbol{i}_1 \\ \boldsymbol{i}_2 \end{bmatrix}$$

has the solution $\boldsymbol{v}_1 = \boldsymbol{z}_\mathrm{eq}\boldsymbol{i}_1$ where $\boldsymbol{z}_\mathrm{eq} = [\boldsymbol{z}_{11} - \boldsymbol{z}_{12}\boldsymbol{z}_{22}^{-1}\boldsymbol{z}_{21}]$.

field winding inductance, with appropriate symbol changes. When the direct-axis armature circuit is open circuit the d-*axis transient open-circuit time constant* T'_{do} is obtained as

$$T'_{do} = \frac{L_f}{R_f}, \tag{11.39}$$

and, when the armature circuit is short circuit, the time constant becomes the d-*axis transient short-circuit time constant* T'_d

$$T'_d = \left(L_f - \frac{k^2 M_f^2}{L_d}\right) \frac{1}{R_f} = T'_{do} \frac{L'_d}{L_d}. \tag{11.40}$$

As there is no quadrature-axis field circuit there are no q-axis transient time constants.

11.1.5.3 Subtransient State

In the subtransient state the armature flux is deflected around the damper winding screening the field winding from the armature flux. The circuit configurations that reflect this flux condition are shown in Figure 11.6a. All the rotor circuits are now represented by short-circuited coils with zero resistance.

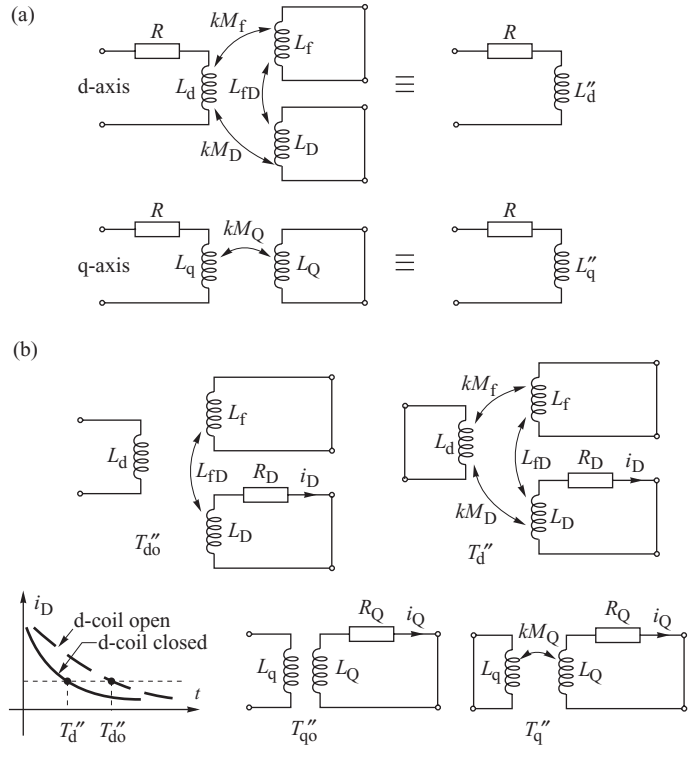

Figure 11.6 The d- and q-axis coupled circuits in the subtransient state: (a) for determining subtransient inductance; (b) for determining the damper winding time constants.

In the d-axis the matrix equation for the coupled circuits becomes

$$\begin{bmatrix} v_\mathrm{d} \\ 0 \\ 0 \end{bmatrix} = \begin{bmatrix} R + \mathrm{s}L_\mathrm{d} & \mathrm{s}kM_\mathrm{f} & \mathrm{s}kM_\mathrm{D} \\ \mathrm{s}kM_\mathrm{f} & \mathrm{s}L_\mathrm{f} & \mathrm{s}L_\mathrm{fD} \\ \mathrm{s}kM_\mathrm{D} & \mathrm{s}L_\mathrm{fD} & L_\mathrm{D} \end{bmatrix} \begin{bmatrix} i_\mathrm{d} \\ \Delta i_\mathrm{f} \\ i_\mathrm{D} \end{bmatrix}, \tag{11.41}$$

with

$$v_\mathrm{d} = (R + \mathrm{s}L''_\mathrm{d}) i_\mathrm{d}. \tag{11.42}$$

Eliminating the second two rows and columns using the same matrix procedure as before gives

$$L''_\mathrm{d} = L_\mathrm{d} - \left[\frac{k^2 M_\mathrm{f}^2 L_\mathrm{D} + k^2 M_\mathrm{D}^2 L_\mathrm{f} - 2kM_\mathrm{f} kM_\mathrm{D} L_\mathrm{fD}}{L_\mathrm{D} L_\mathrm{f} - L_\mathrm{fD}^2} \right] \quad \text{and} \quad X''_\mathrm{d} = \omega L''_\mathrm{d}, \tag{11.43}$$

while in the quadrature axis an equation similar to Equation (11.37) for the d-axis transient reactance gives

$$L''_\mathrm{q} = L_\mathrm{q} - \frac{k^2 M_\mathrm{Q}^2}{L_\mathrm{Q}}, \quad X''_\mathrm{q} = \omega L''_\mathrm{q}. \tag{11.44}$$

Similarly as for the transient state, direct-axis time constants can be established for the decay of current in the damper winding using the equivalent circuits of Figure 11.6b as

$$\begin{aligned} T''_\mathrm{do} &= \left(L_\mathrm{D} - \frac{L_\mathrm{fD}^2}{L_\mathrm{f}} \right) \frac{1}{R_\mathrm{D}} \\ T''_\mathrm{d} &= \left[L_\mathrm{D} - \left(\frac{L_\mathrm{fD}^2 L_\mathrm{d} + k^2 M_\mathrm{D}^2 L_\mathrm{f} - 2L_\mathrm{fD} kM_\mathrm{D} kM_\mathrm{f}}{L_\mathrm{d} L_\mathrm{f} - k^2 M_\mathrm{f}^2} \right) \right] \frac{1}{R_\mathrm{D}} = T''_\mathrm{do} \frac{L''_\mathrm{d}}{L'_\mathrm{d}}, \end{aligned} \tag{11.45}$$

where T''_do is the d-axis subtransient open-circuit time constant and T''_d the d-axis subtransient short-circuit time constant.

If there are no rotor body screening effects in the q-axis then the equivalent quadrature-axis time constants are

$$T''_\mathrm{qo} = \frac{L_\mathrm{Q}}{R_\mathrm{Q}}, \quad T''_\mathrm{q} = \left(L_\mathrm{Q} - \frac{k^2 M_\mathrm{Q}^2}{L_\mathrm{q}} \right) \frac{1}{R_\mathrm{Q}} = T''_\mathrm{qo} \frac{L''_\mathrm{q}}{L'_\mathrm{q}}. \tag{11.46}$$

Recall that similar relations between open- and short-circuit time constants were derived in a less precise way in Chapter 4, Equation (4.16).

11.1.6 Synchronous Generator Equations

Having established how the parameters of the coupled circuits are related to the generator reactances and time constants, the set of equations that constitute the full generator model, with the armature transformer emfs neglected, can now be examined more closely with a view to establishing more meaningful expressions.

11.1.6.1 Steady-State Operation

In the steady state the field winding current is constant and the damper winding currents $i_\mathrm{D} = i_\mathrm{Q} = 0$ so that the armature flux linkages Ψ_d and Ψ_q in Equations (11.18) and (11.19) become

$$\Psi_\mathrm{d} = L_\mathrm{d} i_\mathrm{d} + kM_\mathrm{f} i_\mathrm{f}, \quad \Psi_\mathrm{q} = L_\mathrm{q} i_\mathrm{q}. \tag{11.47}$$

Substituting for these flux linkages into the armature voltage Equations (11.32) gives

$$v_{\mathrm{d}} = -Ri_{\mathrm{d}} - X_{\mathrm{q}}i_{\mathrm{q}}, \quad v_{\mathrm{q}} = -Ri_{\mathrm{q}} + X_{\mathrm{d}}i_{\mathrm{d}} + e_{\mathrm{q}}, \tag{11.48}$$

where $e_{\mathrm{q}} = \omega k M_{\mathrm{f}} i_{\mathrm{f}}$ is the open-circuit armature voltage induced by the field current i_{f}. When on open circuit the armature current is zero and the field current can be related to the self-flux linkage $\Psi_{\mathrm{f}(i_{\mathrm{d}}=0)}$ from the flux equation (11.18) to give

$$e_{\mathrm{q}} = \omega k M_{\mathrm{f}} i_{\mathrm{f}} = \omega \frac{k M_{\mathrm{f}}}{L_{\mathrm{f}}} \Psi_{\mathrm{f}(i_{\mathrm{d}}=0)}. \tag{11.49}$$

11.1.6.2 Transient Operation

When the generator is in the transient state the armature flux has penetrated the damper coils and the damper currents have decayed to a relatively small value. This allows the circuits representing the damper windings to be removed from the equation set so that the flux equations become

$$\begin{bmatrix} \Psi_{\mathrm{d}} \\ \Psi_{\mathrm{f}} \end{bmatrix} = \begin{bmatrix} L_{\mathrm{d}} & kM_{\mathrm{f}} \\ kM_{\mathrm{f}} & L_{\mathrm{f}} \end{bmatrix} \begin{bmatrix} i_{\mathrm{d}} \\ i_{\mathrm{f}} \end{bmatrix}, \quad \Psi_{\mathrm{q}} = L_{\mathrm{q}} i_{\mathrm{q}}, \tag{11.50}$$

while

$$\dot{\Psi}_{\mathrm{f}} = v_{\mathrm{f}} - R_{\mathrm{f}} i_{\mathrm{f}}, \tag{11.51}$$

$$\begin{aligned} v_{\mathrm{d}} &= -Ri_{\mathrm{d}} - \omega\Psi_{\mathrm{q}} \\ v_{\mathrm{q}} &= -Ri_{\mathrm{q}} + \omega\Psi_{\mathrm{d}}. \end{aligned} \tag{11.52}$$

These equations can be considered in two parts. Firstly, the way in which the armature voltage equations (11.52) are influenced by the presence of the field winding and, secondly, how the differential equation (11.51) determines the way in which the armature flux penetrates the field winding. Consider first the armature voltage equations and in particular the voltage on the quadrature axis.

The flux linkage equation allows Ψ_{d} to be written in terms of i_{d} and Ψ_{f} so that, when substituted into the quadrature-axis voltage equation, this gives

$$v_{\mathrm{q}} = -Ri_{\mathrm{q}} + \omega \left[i_{\mathrm{d}} \left(L_{\mathrm{d}} - \frac{k^2 M_{\mathrm{f}}^2}{L_{\mathrm{f}}} \right) + \frac{kM_{\mathrm{f}}}{L_{\mathrm{f}}} \Psi_{\mathrm{f}} \right]. \tag{11.53}$$

This equation is readily simplified by noting that the coefficient of the first term in the square brackets is L'_{d} while the second term represents a voltage proportional to the field flux linkage Ψ_{f}. This voltage is given the symbol e'_{q} and is called the *quadrature-axis transient emf* where

$$e'_{\mathrm{q}} = \omega \left(\frac{kM_{\mathrm{f}}}{L_{\mathrm{f}}} \right) \Psi_{\mathrm{f}}. \tag{11.54}$$

This emf can be usefully compared with the q-axis steady-state emf

$$e_{\mathrm{q}} = \omega \frac{kM_{\mathrm{f}}}{L_{\mathrm{f}}} \Psi_{\mathrm{f}(i_{\mathrm{d}}=0)}.$$

Here $\Psi_{\mathrm{f}(i_{\mathrm{d}}=0)}$ is the field winding self-flux linkages in the steady state and e_{q} the emf that the corresponding field current would induce in the armature. This emf is equal to the armature open-circuit voltage. In contrast, in the transient state Ψ_{f} is the field flux linkages that include the effect of armature reaction. The voltage e'_{q} is the equivalent armature emf that would be induced by a field current proportional to these flux linkages. As these field flux linkages must remain constant

in the short period after the disturbance, Ψ_f only changes its value slowly. Making the substitutions for the transient inductance and transient emf, and assuming that $\omega \approx \omega_s$, gives

$$v_q = -Ri_q + X'_d i_d + e'_q. \tag{11.55}$$

As there is no field winding on the quadrature axis $X'_q = X_q$ and

$$v_d = -Ri_d - X'_q i_q. \tag{11.56}$$

Although Equation (11.56) is correct for the rotor model assumed, many generators, and in particular turbogenerators, have a solid-steel rotor body which acts as a screen in the q-axis. It is convenient to represent this by an additional q-axis, short-circuited coil, given the symbol g, when the q-axis flux equation becomes

$$\begin{bmatrix} \Psi_q \\ \Psi_g \end{bmatrix} = \begin{bmatrix} L_q & kM_g \\ kM_g & L_g \end{bmatrix} \begin{bmatrix} i_q \\ i_g \end{bmatrix}, \tag{11.57}$$

with the change of flux linking this coil defined by the additional differential equation

$$\dot{\Psi}_g = v_g - R_g i_g = -R_g i_g \quad (v_g = 0). \tag{11.58}$$

The similarity with the d-axis rotor coils is immediately apparent and the voltage in the d-axis armature coil becomes

$$v_d = -Ri_d - X'_q i_q + e'_d, \tag{11.59}$$

where $X'_q \neq X_q$ and

$$e'_d = -\omega \left(\frac{kM_g}{L_g} \right) \Psi_g \tag{11.60}$$

The flux linking the field winding Ψ_f does not remain constant during the entire period but changes slowly as the armature flux penetrates through the winding. This change in the field flux linkage is determined from the differential equation (11.51). Although this equation, along with Equation (11.54) for e'_q, can be used directly to evaluate how e'_q changes with time, it is usually more convenient to rephrase the flux linkage differential equation so that it can be more easily related to the armature. This modification can be accomplished by substituting into the differential equation (11.51) for i_f obtained from the flux linkage equation (11.50) to give

$$v_f = \dot{\Psi}_f + \frac{R_f}{L_f} \Psi_f - R_f \frac{kM_f}{L_f} i_d. \tag{11.61}$$

Differentiating Equation (11.54) gives

$$\dot{e}'_q = \omega \frac{kM_f}{L_f} \dot{\Psi}_f, \tag{11.62}$$

which, when rearranged and substituted into Equation (11.61), gives after some simplification

$$e_f = \dot{e}'_q T'_{do} + e'_q - (X_d - X'_d) i_d, \tag{11.63}$$

where e_f is the field voltage v_f referred to the armature given by

$$e_f = \omega k M_f v_f / R_f, \tag{11.64}$$

and e_f is also the output voltage of the exciter referred to the armature. Rearranging Equation (11.63) gives

$$\dot{e}'_q = \frac{e_f - e'_q + i_d(X_d - X'_d)}{T'_{do}}. \tag{11.65}$$

This analysis can be repeated for the quadrature axis when, assuming an additional rotor coil to represent the rotor body,

$$\dot{e}'_d = \frac{-i_q(X_q - X'_q) - e'_d}{T'_{qo}}, \quad X'_q \neq X_q. \tag{11.66}$$

If no additional coil is present $X'_q = X_q$ and $e'_d = 0$.

11.1.6.3 Subtransient Operation

During the subtransient period the rotor damper coils screens both the field winding and the rotor body from changes in the armature flux. The field flux linkages Ψ_f remain constant during this period while the damper winding flux linkages are constant immediately after the fault or disturbance but then decay with time as the generator moves towards the transient state. These changes can be quantified using a similar procedure as for the transient period. Now the full equation set for the flux linkages, Equations (11.18) and (11.19), and the flux decay equation (11.33) apply.

The armature voltage equations (11.32) are now modified due to their coupling with the rotor circuits in both the d- and q-axes. The d-axis flux linkage equations allow the armature flux Ψ_d to be written in terms of i_d, Ψ_D and Ψ_f as

$$\Psi_d = L''_d i_d + (k_1 \Psi_f + k_2 \Psi_D), \tag{11.67}$$

where

$$k_1 = \frac{k M_f L_D - k M_D L_{fD}}{L_f L_D - L_{fD}^2}, \quad k_2 = \frac{k M_D L_f - k M_f L_{fD}}{L_f L_D - L_{fD}^2}, \tag{11.68}$$

which, when substituted into the armature voltage equation (11.32), gives

$$v_q = -R i_q + X''_d i_d + e''_q, \tag{11.69}$$

where

$$e''_q = \omega(k_1 \Psi_f + k_2 \Psi_D), \tag{11.70}$$

and represents an armature voltage proportional to the d-axis rotor flux linkages. These flux linkages remain constant immediately after the fault and only change as Ψ_D changes.

A similar analysis for the quadrature-axis armature voltage yields

$$v_d = -R i_d - X''_q i_q + e''_d. \tag{11.71}$$

The way in which the subtransient voltage decays can be found using a similar approach as for the transient period. The differential equation governing the decay of the flux through the d-axis damper is given in Equation (11.33) as

$$\dot{\Psi}_D = -R_D i_D. \tag{11.72}$$

From the d-axis flux linkage equations (11.18) i_D can be written in terms of i_d, Ψ_D and Ψ_f when

$$\dot{\Psi}_D = k_2 i_d + \frac{1}{T''_{do}} \frac{L_{fD}}{L_f} \Psi_f - \frac{1}{T''_{do}} \Psi_D. \tag{11.73}$$

Differentiating e''_q, Equation (11.70) gives

$$\dot{e}''_q = \omega k_2 \dot{\Psi}_D, \tag{11.74}$$

as the field flux linkages Ψ_f are constant during the subtransient period. The relationships for e''_q and $\dot{e}''_q$ can now be substituted into Equation (11.73) to give, after some simplification,

$$\dot{e}''_q = \frac{e'_q + (X'_d - X''_d) i_d - e''_q}{T''_{do}}. \tag{11.75}$$

A similar analysis for the q-axis armature coil gives

$$\dot{e}''_d = \frac{e'_d - (X'_q - X''_q) i_q - e''_d}{T''_{qo}}. \tag{11.76}$$

11.1.6.4 The Generator (d, q) Reference Frame and the System (a, b) Reference Frame

All the generator equations so far developed have been expressed in the (d, q) reference frame, whereas the network equations developed in Chapter 3 are expressed in phase quantities in the system (a, b) reference frame. It is now necessary to examine how the two reference frames can be linked together. This is most conveniently done by considering the steady-state operation of the generator when the instantaneous phase voltages and currents constitute a balanced set given by

$$\begin{aligned} v_A &= \sqrt{2} V_g \sin(\omega t), & i_A &= \sqrt{2} I_g \sin(\omega t + \phi) \\ v_B &= \sqrt{2} V_g \sin(\omega t - 2\pi/3), & i_B &= \sqrt{2} I_g \sin(\omega t - 2\pi/3 + \phi) \\ v_C &= \sqrt{2} V_g \sin(\omega t - 4\pi/3), & i_C &= \sqrt{2} I_g \sin(\omega t - 4\pi/3 + \phi). \end{aligned} \tag{11.77}$$

At time $t = 0$ the terminal voltage of phase A is zero and the angle between the axis of phase A and the rotor d-axis is the rotor angle δ_g. As the rotational speed of the generator is $\delta\omega t$, the position of the rotor, relative to the axis of phase A, at any instant in time is given by $\gamma = \omega t + \delta_g$. Applying the transformation of Equation (11.8) to the phase voltages in Equation (11.77) then gives

$$v_d = -\sqrt{3} V_g \sin \delta_g, \quad v_q = \sqrt{3} V_g \cos \delta_g. \tag{11.78}$$

The phasor diagram in Figure 11.7 is similar to that in Figure 3.30 and shows how the rms terminal phase voltage V_g can be resolved into two orthogonal components, V_d and V_q, along the d- and q-axes where

$$V_q = V_g \cos \delta_g, \quad V_d = -V_g \sin \delta_g \quad \text{and} \quad \underline{V}_g = V_q + \mathrm{j} V_d. \tag{11.79}$$

Substituting Equation (11.79) into (11.78) allows the instantaneous generator voltages v_d and v_q to be related to the orthogonal rms terminal voltage components V_d and V_d by the relationship

$$v_d = \sqrt{3} V_d, \quad v_q = \sqrt{3} V_q. \tag{11.80}$$

This same process can also be applied to the currents to give

$$I_q = I_g \cos(\delta_g + \phi), \quad I_d = -I_g \sin(\delta_g + \phi), \tag{11.81}$$

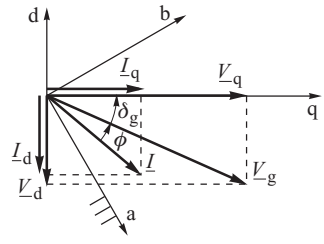

Figure 11.7 Phasor diagram in the (d, q) reference frame showing how the terminal voltage and current can be resolved into two components in quadrature. Also shown is the relative position of the system (a, b) reference frame.

with the instantaneous currents being

$$i_d = -\sqrt{3} I_g \sin(\delta_g + \phi) = \sqrt{3} I_d, \quad i_q = \sqrt{3} I_g \cos(\delta_g + \phi) = \sqrt{3} I_q. \tag{11.82}$$

The identities in Equations (11.80) and (11.82) show that the instantaneous (d, q) currents and voltages are DC variables that are proportional to the orthogonal components of the rms phase currents and voltages. Consequently, the instantaneous voltages and currents in the steady-state armature voltage equations (11.48) can be replaced by the orthogonal components of the phase currents and voltages to give

$$\begin{aligned} V_d &= -RI_d - X_q I_q \\ V_q &= -RI_q + X_d I_d + E_q, \end{aligned} \tag{11.83}$$

which can be expressed in matrix form as

$$\begin{bmatrix} V_d \\ V_q \end{bmatrix} = \begin{bmatrix} 0 \\ E_q \end{bmatrix} - \begin{bmatrix} R & X_q \\ -X_d & R \end{bmatrix} \begin{bmatrix} I_d \\ I_q \end{bmatrix}, \tag{11.84}$$

and

$$E_q = \omega M_f i_f / \sqrt{2}. \tag{11.85}$$

The meaning of E_q is now much clearer as it is the rms voltage that would be induced in each of the armature phases by the field current i_f when the generator is on open circuit. Equation (11.83) is identical to Equation (3.65) derived in Chapter 3 and the equivalent circuit and phasor diagram corresponding to this equation were shown in Figure 3.17 and Figure 3.24.

This concept can now be extended to the generator in the transient and subtransient states by recognizing that by neglecting the transformer emf terms in the armature voltage equations, the effect of asymmetric armature currents (DC offset) has been omitted so that the armature currents are always AC quantities of varying magnitude. The effect of the transformation of Equation (11.8) is therefore to produce (d, q) currents that are solely DC quantities; they have no AC component. The DC (d, q) currents and voltages, (i_d, i_q, v_d, v_q), are related to the armature rms values (I_g, V_g) by the identities in Equations (11.80) and (11.82). This allows the generator to be represented in the (d, q) reference frame by slowly changing DC quantities in all three characteristic states. All the emf equations and armature voltage equations developed in the previous section maintain the same form except that the instantaneous values i_d, i_q, e_d, e_q and so on are replaced by orthogonal phase values I_d, I_q, E_d, E_q and so on. This then allows equivalent circuits and phasor diagrams similar to those developed in Section 4.2 to be used to model the generator in the different operating states.

As the network equations are all expressed in the system (a, b) reference frame, the current and voltage equations for each generator must be transformed from its own (d, q) reference frame to the system reference. The two reference frames are linked through the terminal voltage which appears explicitly in the generator equations, (d, q) reference frame, and the system equations (a, b) reference frame. Although Figure 11.7 correctly shows the relationship between the generator (d, q) and the system (a, b) reference frames, the necessary transformation is more clearly seen by reference to Figure 3.36. A phasor $\underline{E}$ can be defined in either the (d, q) or (a, b) reference frame with the two related by the $\boldsymbol{T}$ transformation defined by Equations (3.166) and (3.167).

11.1.6.5 Power, Torque and the Swing Equation

To complete the set of equations necessary to describe the generator, expressions are required for the three-phase terminal electrical power and the air-gap power. With transformer emfs neglected, the terminal power can be obtained by substituting for v_d, v_q, i_d, i_q from Equations (11.80) and (11.82) into the instantaneous terminal power Equation (11.21) to obtain

$$P_g = 3(V_d I_d + V_q I_q) \quad \text{W}. \tag{11.86}$$

This equation is consistent with the normal three-phase power output expression $V_d I_d + V_q I_q = VI\cos\phi$ and the generator terminal power is, as would be expected, three times the phase power.

The air-gap power is obtained from the terminal power, Equation (11.86), by adding the resistance loss

$$P_e = 3\left[V_d I_d + V_q I_q + \left(I_d^2 + I_q^2\right) R\right] \quad \text{W}. \tag{11.87}$$

As $P = \omega\tau$ the air-gap torque is given by

$$\tau = \frac{3}{\omega}\left[V_d I_d + V_q I_q + \left(I_d^2 + I_q^2\right) R\right] \quad \text{Nm}. \tag{11.88}$$

The final equation required to complete the equation set is the swing equation derived in Chapter 5, Equation (5.15), as

$$\frac{d\Delta\omega}{dt} = \frac{1}{M}(P_m - P_e - D\Delta\omega), \quad \Delta\omega = \omega - \omega_s = \frac{d\delta}{dt}, \tag{11.89}$$

where P_e is the air-gap electrical power, P_m is the mechanical turbine power, D is the damping power coefficient, ω is the generator rotational speed, ω_s is the synchronous speed and $\Delta\omega$ is the speed deviation.

11.1.6.6 Per-Unit Notation

It is standard practice in power system analysis to normalize all quantities to a common MVA base and, in the per-unit system used here (see Appendix A.1), this is taken as the generator rated MVA/phase $S_{1\phi}$. A base voltage V_b is also defined equal to the rated generator phase voltage. This allows the base current and the base impedance to be defined as

$$I_b = \frac{S_{1\phi}}{V_b}, \quad Z_b = \frac{V_b}{I_b}. \tag{11.90}$$

Every parameter and equation can now be normalized by dividing by the appropriate base value as described in the Appendix. Of particular importance is the impact that normalization has on power and torque as these are normalized to the total three-phase rated generator output $S_{3\phi}$. As shown in the Appendix, when currents, voltages and flux linkages are all expressed in per unit

notation the three-phase power expressions (11.86) and (11.87) normalized to the three-phase MVA base become

$$\begin{aligned} P_{\mathrm{g}} &= (V_{\mathrm{d}} I_{\mathrm{d}} + V_{\mathrm{q}} I_{\mathrm{q}}) \\ P_{\mathrm{e}} &= \left[V_{\mathrm{d}} I_{\mathrm{d}} + V_{\mathrm{q}} I_{\mathrm{q}} + \left(I_{\mathrm{d}}^2 + I_{\mathrm{q}}^2 \right) R \right] \end{aligned} \quad \text{per unit}, \tag{11.91}$$

while the per-unit notation adopted requires $\tau_{\mathrm{pu}} = P_{\mathrm{pu}}$ so that Equation (11.88) becomes

$$\tau = \frac{\omega_{\mathrm{s}}}{\omega} \left[V_{\mathrm{d}} I_{\mathrm{d}} + V_{\mathrm{q}} I_{\mathrm{q}} + \left(I_{\mathrm{d}}^2 + I_{\mathrm{q}}^2 \right) R \right] \quad \text{per unit.} \tag{11.92}$$

A full explanation of the per-unit system is given in the Appendix. In general all voltage, current and flux linkage equations retain the same form whether or not they are expressed in SI or in per-unit notation. It is only the power and torque equations that change their form with the introduction of a 1/3 factor into the power expressions and a $\omega_{\mathrm{s}}/3$ factor into the torque expressions. The introduction of the 1/3 factor into the total power expression carries the implication that the total generator power output, normalized to the $S_{3\phi}$ base, is the same as the power output per phase, normalized to $S_{1\phi}$, where $S_{1\phi} = S_{3\phi}/3$.

One of the advantages of referring all the rotor quantities to the armature winding, as in Section 11.1.5, is that only base quantities for the armature circuit need be considered. If the rotor equations had not been referred to the armature then additional base quantities for the rotor circuits would be necessary. Such a per-unit system based on the concept of *equal mutual flux linkages* (Anderson and Fouad, 1977) is described in the Appendix and ensures that all the equations developed earlier in this chapter retain exactly the same form whether in per unit or SI. This per-unit system also has the effect that the per-unit value of all the mutual inductances on one axis are equal and, in per-unit notation, are given the symbol L_{ad} on the d-axis and L_{aq} on the q-axis, that is

$$kM_{\mathrm{f}} = kM_{\mathrm{D}} = L_{\mathrm{fD}} \equiv L_{\mathrm{ad}}, \quad kM_{\mathrm{Q}} \equiv L_{\mathrm{aq}}. \tag{11.93}$$

The self-inductances are also expressed as being equal to the sum of a magnetizing inductance and a leakage component so that

$$\begin{aligned} L_{\mathrm{d}} &= L_{\mathrm{md}} + l_l, \quad L_{\mathrm{f}} = L_{\mathrm{mf}} + l_{\mathrm{f}}, \quad L_{\mathrm{D}} = L_{\mathrm{mD}} + l_{\mathrm{D}} \\ L_{\mathrm{q}} &= L_{\mathrm{mq}} + l_l, \quad L_{\mathrm{Q}} = L_{\mathrm{mQ}} + l_{\mathrm{Q}} \end{aligned} \tag{11.94}$$

and, in per-unit notation,

$$L_{\mathrm{md}} = L_{\mathrm{mf}} = L_{\mathrm{mD}} \equiv L_{\mathrm{ad}}, \quad L_{\mathrm{mq}} = L_{\mathrm{mQ}} \equiv L_{\mathrm{aq}}. \tag{11.95}$$

It is common to use these substitutions when expressing all the reactance and time constant expressions and so on derived in Section 11.1.4 in per-unit notation.

11.1.7 Synchronous Generator Models

The equations derived in the previous subsection can now be used to model the behaviour of a synchronous generator. A number of different models will be developed where the generator is modelled by either its subtransient or transient emfs acting behind appropriate reactances. The way that the armature flux gradually penetrates into the rotor during a fault and affects these emfs is quantified by the differential equations (11.75), (11.76), (11.65) and (11.66). These differential equations are gathered here and expressed in orthogonal phase quantities as

$$T''_{\mathrm{do}} \dot{E}''_{\mathrm{q}} = E'_{\mathrm{q}} - E''_{\mathrm{q}} + I_{\mathrm{d}}(X'_{\mathrm{d}} - X''_{\mathrm{d}}), \tag{11.96}$$

$$T''_{\mathrm{qo}} \dot{E}''_{\mathrm{d}} = E'_{\mathrm{d}} - E''_{\mathrm{d}} - I_{\mathrm{q}}(X'_{\mathrm{q}} - X''_{\mathrm{q}}), \tag{11.97}$$

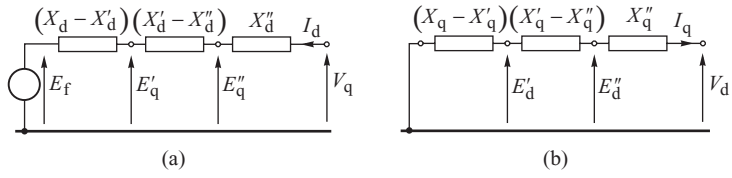

Figure 11.8 Generator equivalent circuits with resistances neglected: (a) d-axis; (b) q-axis.

$$T'_{do}\dot{E}'_q = E_f - E'_q + I_d(X_d - X'_d), \tag{11.98}$$

$$T'_{qo}\dot{E}'_d = -E'_d - I_q(X_q - X'_q). \tag{11.99}$$

It is worth noting the similar structure of these equations. On the left hand side is the time derivative of the emf multiplied by the relevant time constant and the right hand side relates to the equivalent d- or q-axis armature circuit, with resistance neglected, shown in Figure 11.8. These armature circuits were initially introduced in Chapter 4, Figure 4.15. The first component on the right hand side in the equations constitutes a driving voltage while the final component constitutes a voltage drop in the relevant reactance.

The right hand side of Equation (11.96) constitutes Kirchhoff's voltage law for the middle part of the circuit shown in Figure 11.8a, that is for the driving voltage E'_q, the voltage drop $I_d(X'_d - X''_d)$ and the emf E''_q. Similarly, the right hand side of Equation (11.97) constitutes Kirchhoff's voltage law for the middle part of Figure 11.8b while Equation (11.98) corresponds to the left part of Figure 11.8a with the driving voltage E_f, the voltage drop $I_d(X_d - X'_d)$ and the emf E'_q. In Equation (11.99), corresponding to the left hand part of Figure 11.8b, there is no driving voltage due to the lack of excitation in the q-axis.

Equations (11.96)–(11.99) allow five different generator models of decreasing complexity and accuracy to be developed. Each model is given a model number that indicates the number of differential equations required in the model. The larger the number, the greater the model complexity and the greater the time required to solve the differential equations. The model number is then followed by a number of terms enclosed in brackets which define the differential equations used by the model. In developing the generator models it is assumed that all quantities are expressed in per-unit notation.

11.1.7.1 Sixth-Order Model – ($\dot{\delta}$, $\dot{\omega}$, $\dot{E}''_d$, $\dot{E}''_q$, $\dot{E}'_d$, $\dot{E}'_q$)

In this model the generator is represented by the subtransient emfs E''_q and E''_d behind the subtransient reactances X''_d and X''_q as defined by the modified armature voltage equations (11.69) and (11.71)

$$\begin{bmatrix} V_d \\ V_q \end{bmatrix} = \begin{bmatrix} E''_d \\ E''_q \end{bmatrix} - \begin{bmatrix} R & X''_q \\ -X''_d & R \end{bmatrix} \begin{bmatrix} I_d \\ I_q \end{bmatrix}. \tag{11.100}$$

This equation corresponds to Equation (4.17) derived in Chapter 4. The corresponding equivalent circuit and phasor diagram are shown in Figure 4.12.

The differential equations (11.96)–(11.99) describe the change in these emfs as the flux linking the rotor circuits decays. To these must be added Equations (11.89) in order to include the speed deviation and angle change of the rotor. As the differential equations (11.96) and (11.97) include the influence of the damper windings, the damping coefficient in the swing equation need only

quantify the mechanical damping due to windage and friction and, as this is usually small, it may be neglected ($D \approx 0$).

Under these assumptions, the full set of six differential equations describing the generator is

$$\begin{aligned} M\Delta\dot{\omega} &= P_{\mathrm{m}} - P_{\mathrm{e}} \\ \dot{\delta} &= \Delta\omega \\ T'_{\mathrm{do}}\dot{E}'_{\mathrm{q}} &= E_{\mathrm{f}} - E'_{\mathrm{q}} + I_{\mathrm{d}}(X_{\mathrm{d}} - X'_{\mathrm{d}}) \\ T'_{\mathrm{qo}}\dot{E}'_{\mathrm{d}} &= -E'_{\mathrm{d}} - I_{\mathrm{q}}(X_{\mathrm{q}} - X'_{\mathrm{q}}) \\ T''_{\mathrm{do}}\dot{E}''_{\mathrm{q}} &= E'_{\mathrm{q}} - E''_{\mathrm{q}} + I_{\mathrm{d}}(X'_{\mathrm{d}} - X''_{\mathrm{d}}) \\ T''_{\mathrm{qo}}\dot{E}''_{\mathrm{d}} &= E'_{\mathrm{d}} - E''_{\mathrm{d}} - I_{\mathrm{q}}(X'_{\mathrm{q}} - X''_{\mathrm{q}}). \end{aligned} \tag{11.101}$$

Changes in the mechanical power P_{m} in the first equation should be calculated from differential equations describing the models of turbines and their governing systems discussed in Section 11.3. Changes in emf E_{f} in the third equation should be calculated from the differential equations describing the models of excitation systems discussed in Section 11.2.

The air-gap power of the generator can be calculated using Equation (11.91) which, after substituting for the armature voltages from Equation (11.100), gives

$$P_{\mathrm{e}} = (E''_{\mathrm{d}} I_{\mathrm{d}} + E''_{\mathrm{q}} I_{\mathrm{q}}) + (X''_{\mathrm{d}} - X''_{\mathrm{q}}) I_{\mathrm{d}} I_{\mathrm{q}}. \tag{11.102}$$

The second term in this power equation defines the subtransient saliency power discussed in Chapter 4.

11.1.7.2 Fifth-Order Model – ($\dot{\delta}$, $\dot{\omega}$, $\dot{E}''_{\mathrm{d}}$, $\dot{E}''_{\mathrm{q}}$, $\dot{E}'_{\mathrm{q}}$)

In this model the screening effect of the rotor body eddy currents in the q-axis is neglected so that $X'_{\mathrm{q}} = X_{\mathrm{q}}$ and $E'_{\mathrm{d}} = 0$. This model reverts to the classical fifth-order model with armature transformer emfs neglected. Equation (11.99) from the equation set of the sixth-order model is eliminated to give a set of five differential equations:

$$\begin{aligned} M\Delta\dot{\omega} &= P_{\mathrm{m}} - P_{\mathrm{e}} \\ \dot{\delta} &= \Delta\omega \\ T'_{\mathrm{do}}\dot{E}'_{\mathrm{q}} &= E_{\mathrm{f}} - E'_{\mathrm{q}} + I_{\mathrm{d}}(X_{\mathrm{d}} - X'_{\mathrm{d}}) \\ T''_{\mathrm{do}}\dot{E}''_{\mathrm{q}} &= E'_{\mathrm{q}} - E''_{\mathrm{q}} + I_{\mathrm{d}}(X'_{\mathrm{d}} - X''_{\mathrm{d}}) \\ T''_{\mathrm{qo}}\dot{E}''_{\mathrm{d}} &= E'_{\mathrm{d}} - E''_{\mathrm{d}} - I_{\mathrm{q}}(X'_{\mathrm{q}} - X''_{\mathrm{q}}). \end{aligned} \tag{11.103}$$

Changes in mechanical power P_{m} and emf E_{f} should be calculated as in the sixth-order model.

11.1.7.3 Fourth-Order Model – ($\dot{\delta}$, $\dot{\omega}$, $\dot{E}'_{\mathrm{d}}$, $\dot{E}'_{\mathrm{q}}$)

In this model the effect of the damper windings in the sixth-order model are neglected and Equations (11.96) and (11.97) are removed from the equation set. The generator is now represented by the transient emfs E'_{q} and E'_{d} behind the transient reactances X'_{d} and X'_{q} as defined by the equation

$$\begin{bmatrix} V_{\mathrm{d}} \\ V_{\mathrm{q}} \end{bmatrix} = \begin{bmatrix} E'_{\mathrm{d}} \\ E'_{\mathrm{q}} \end{bmatrix} - \begin{bmatrix} R & X'_{\mathrm{q}} \\ -X'_{\mathrm{d}} & R \end{bmatrix} \begin{bmatrix} I_{\mathrm{d}} \\ I_{\mathrm{q}} \end{bmatrix}. \tag{11.104}$$

This equation is identical to Equation (4.19) derived in Chapter 4. The corresponding equivalent circuit and phasor diagram were shown in Figure 4.14.

The changes in the emfs E'_q and E'_d are determined from differential equations (11.98) and (11.99) while the electrical air-gap power is

$$P_e = E'_q I_q + E'_d I_d + (X'_d - X'_q) I_d I_q, \tag{11.105}$$

with the second part of the equation defining the transient saliency power.

As the damper windings are ignored, the air-gap power calculated by this equation neglects the asynchronous torque produced by the damper windings. Consequently, the damping coefficient in the swing equation should be increased by an amount corresponding to the average asynchronous torque, or power, calculated using the simplified formulae in Equation (5.25).

Under these assumptions, the model is described by the following four differential equations:

$$\begin{aligned} M\Delta\dot{\omega} &= P_m - P_e - D\Delta\omega \\ \dot{\delta} &= \Delta\omega \\ T'_{do}\dot{E}'_q &= E_f - E'_q + I_d(X_d - X'_d) \\ T''_{qo}\dot{E}'_d &= -E'_d - I_q(X_q - X'_q). \end{aligned} \tag{11.106}$$

Changes in mechanical power P_m and emf E_f should be calculated as in the sixth-order model.

This simplified model of the synchronous generator is widely considered to be sufficiently accurate to analyse electromechanical dynamics (Stott, 1979). Experience has shown that including the second differential equation to account for rotor body effects in the q-axis improves the accuracy of the model. The main disadvantage of this model is that the equivalent damping coefficient, appearing in the swing equation, can only be calculated approximately.

11.1.7.4 Third-Order Model – ($\dot{\delta}$, $\dot{\omega}$, $\dot{E}'_q$)

This model is similar to the fourth-order model except that the d-axis transient emf E'_d is assumed to remain constant allowing Equation (11.97) to be removed from the equation set. The generator is described only by Equations (11.98) and (11.89) with real power again given by Equation (11.105). Besides neglecting the effect of the damper windings by assuming E'_d to be constant, this model also neglects the damping produced by the rotor body eddy currents, even if an additional coil is used to represent the rotor body. If there is no winding in the quadrature axis to represent the rotor body then $E'_d = 0$, $X'_q = X_q$ and Equation (11.105) reduces to

$$P = E'_q I_q + (X'_d - X_q) I_d I_q. \tag{11.107}$$

As in the fourth-order model, damper winding effects are neglected and so their effect must be included by increasing the value of the damping coefficient in the swing equation. The model is described by the following three differential equations:

$$\begin{aligned} M\Delta\dot{\omega} &= P_m - P_e - D\Delta\omega \\ \dot{\delta} &= \Delta\omega \\ T'_{do}\dot{E}'_q &= E_f - E'_q + I_d(X_d - X'_d). \end{aligned} \tag{11.108}$$

Changes in mechanical power P_m and emf E_f should be calculated as in the sixth-order model.

11.1.7.5 Second-Order Model – the Classical Model ($\dot{\delta}$, $\dot{\omega}$)

The classical synchronous generator model, widely used in all the previous chapters for a simplified analysis of power system dynamics, assumes that neither the d-axis armature current I_d nor the internal emf E_f representing the excitation voltage change very much during the transient state. In

this model the generator is represented by a constant emf E' behind the transient reactance X'_{d} and the swing equations

$$\begin{aligned} M\Delta\dot{\omega} &= P_{\mathrm{m}} - P_{\mathrm{e}} - D\Delta\omega \\ \dot{\delta} &= \Delta\omega. \end{aligned} \tag{11.109}$$

The justification of the classical model is that the time constant T'_{do}, appearing in Equation (11.98), is relatively long, the order of a few seconds, so that E'_{q} does not change much providing that changes in E_{f} and I_{d} are small. This means that $E'_{\mathrm{q}} \approx$ constant and, because it has already been assumed that $E'_{\mathrm{d}} \approx$ constant, both the magnitude of the transient emf E' and its position α with respect to the rotor may be assumed to be constant. If rotor transient saliency is neglected, $X'_{\mathrm{q}} = X'_{\mathrm{d}}$ and the two equivalent circuits in Figure 4.13a may be replaced by the one equivalent circuit shown in Figure 5.8 for a generator connected to an infinite busbar. As

$$\underline{I} = \underline{I}_{\mathrm{q}} + \mathrm{j}\underline{I}_{\mathrm{d}}, \quad \underline{V} = \underline{V}_{\mathrm{q}} + \mathrm{j}\underline{V}_{\mathrm{d}}, \quad \underline{E}' = \underline{E}'_{q} + \mathrm{j}\underline{E}'_{\mathrm{d}} \tag{11.110}$$

the two algebraic equations describing the armature voltage in Equations (11.104) can now be replaced by one equation

$$\underline{V} = (\underline{E}'_{\mathrm{q}} + \mathrm{j}\underline{E}'_{\mathrm{d}}) - \mathrm{jX}'_{\mathrm{d}}(\underline{I}_{\mathrm{q}} + \mathrm{j}\underline{I}_{\mathrm{d}}) = \underline{E}' - \mathrm{j}X'_{\mathrm{d}}\underline{I} \tag{11.111}$$

The assumption of small changes in the direct component of the generator current, and in the internal emf, means that only generators located a long way from the point of disturbance should be represented by the classical model.

11.1.7.6 Summary

The number of reactances and time constants representing the generator depends on the number of equivalent windings used in a particular model. The five-winding model has two equivalent rotor windings and time constants (T''_{do}, T'_{do}) on the d-axis and three armature reactances (X''_{d}, X'_{d}, X_{d}). In the q-axis there is one equivalent rotor winding, with a time constant (T''_{qo}), and two armature reactances (X''_{q}, X_{q}). Although generators with rotors constructed from ferromagnetic, electrically insulated sheets of steel are well characterized by these parameters, this is not the case for generators whose rotors are made from solid steel. In such generators the rotor eddy currents play a significant role in the q-axis damping. This damping may be modelled approximately by introducing an additional q-axis winding as in the sixth-order model. This expands the model by an additional reactance $X'_{\mathrm{q}} \neq X'_{\mathrm{d}}$ and a time constant T'_{qo} to represent the flux decay through this circuit. If these parameters are not specified by the manufacturer it is typical to assume that $X'_{\mathrm{q}} = 2X''_{\mathrm{q}}$ and $T'_{\mathrm{q}} = 10T''_{\mathrm{q}}$. Due to the screening effect of the field winding, the influence of the eddy currents in the d-axis is small and there is no need to introduce an additional winding to account for this. For slower changing disturbances, and to enable faster solution in complex systems, the generator model can be simplified by omitting the damper windings from the electrical equations, the fourth- and third-order models, and representing their damping effect by an increased damping coefficient in the swing equation. The simplest second-order model is the model traditionally used in quantitative power system analysis. It is simple, but very approximate, and only really suitable for representing generators well away from the fault. It can also be useful for evaluating generator behaviour during the first rotor swing.

In developing all the generator models it has been assumed that $\omega \approx \omega_{\mathrm{s}}$ and that the transformer emfs in the armature voltage equations can be neglected. Speed changes can be accounted for in all the models by introducing a factor $\omega/\omega_{\mathrm{s}}$ in front of every reactance. Accounting for the armature transformer emfs is significantly more difficult and is only justified if detailed modelling

of the electromagnetic transients immediately after the fault is required, for example in computing short-circuit currents.

11.1.8 Saturation Effects

The generator equations derived in the previous subsection ignored the effect of magnetic saturation in the stator and rotor iron and the effect this would have on the generator parameters and the operating conditions. Saturation effects are highly nonlinear and depend on the generator loading conditions so that trying to account for them accurately in the generator model is nigh on impossible. What is required is a relatively simple saturation model that produces acceptable results, is linked to the physical process and uses easily obtainable data.

At this stage it is interesting to consider the flux paths in Figures 4.8 that are associated with the different generator reactances. As it is only the iron paths that saturate, one might expect those generator reactances where the flux path is mainly in air, that is X'_d, X'_q, X''_d, X''_q, to be less susceptible to saturation effects than X_d and X_q where a substantial part of the flux path is through iron (at least for the round-rotor generator). This concept of parameter sensitivity will be investigated later in this section, but first it is necessary to investigate the general effects of saturation itself. This is more easily accomplished and understood if all generator parameters are expressed in per-unit notation.

11.1.8.1 Saturation Characteristic

For any magnetic circuit that comprises an iron path and an air path the mmf and flux will be related by the general curve shown in Figure 11.9a. When the iron path is unsaturated the relationship between the mmf and the flux is linear and is represented by the *air-gap line*, 0A. In this situation the reluctance of the magnetic circuit is dominated by the reluctance of the air gap. As the mmf is increased, the iron saturates and the mmf/flux relationship ceases to be linear and follows the *saturation curve* 0B. Consequently, for some flux linkage Ψ_T the mmf required to produce this flux can be considered to have two components, the air-gap mmf F_a and the iron mmf F_i, so that the total mmf is given by

$$F_T = F_a + F_i. \tag{11.112}$$

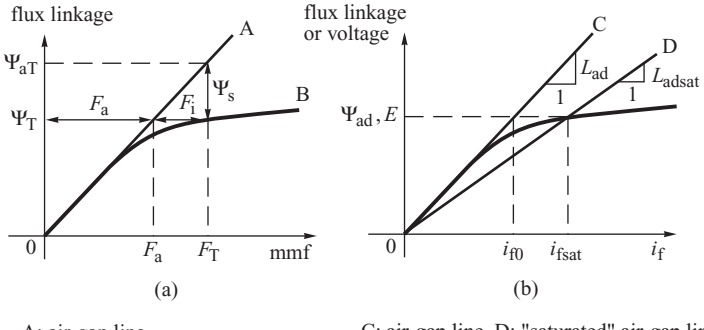

Figure 11.9 Saturation: (a) typical saturation curve for a magnetic circuit whose flux path is in iron and air; (b) generator open-circuit saturation characteristic. C, air-gap line; D, 'saturated' air-gap line.

A *saturation factor S* can now be defined as

$$S = \frac{\text{air-gap mmf}}{\text{air-gap mmf} + \text{iron mmf}} = \frac{F_a}{F_a + F_i} = \frac{F_a}{F_T}, \tag{11.113}$$

and, by similar triangles,

$$S = \frac{F_a}{F_a + F_i} = \frac{\Psi_T}{\Psi_T + \Psi_s}. \tag{11.114}$$

Having defined a saturation factor, it is now necessary to provide a simple method of finding its value for any generator loading condition and then be able to take this into account when computing the generator parameters. To achieve these objectives it is usually assumed that:

1. The open-circuit generator saturation curve can be used under load conditions. On no load the mmf in the d-axis is due to the field current, i_f, while on load it is due to $(i_f + i_D + i_d)$. As Kundur (1994) points out, this is usually the only saturation data available.
2. As the leakage flux path is mainly in air, the leakage inductances are assumed to be independent of saturation. This implies that it is only the mutual inductances L_{ad} and L_{aq} that are affected by saturation (and of course the self-inductance $L_d = L_{ad} + l_l$, $L_f = L_{ad} + l_f$, etc., as explained in Equation (11.94) and Section A.4).
3. Saturation on the d-axis and that on the q-axis are independent of each other.

11.1.8.2 Calculation of the Saturation Factor

When the generator is on no load, Equation (11.85) shows that the voltage induced in one of the armature phases V_{g0} is

$$V_{g0} = E = E_q = \frac{1}{\sqrt{2}}\omega_s M_f i_{f0} = \frac{1}{\sqrt{3}}\omega_s k M_f i_{f0} = \left[\frac{1}{\sqrt{3}}\omega_s\right] L_{ad} i_{f0} = \left[\frac{1}{\sqrt{3}}\omega_s\right] \Psi_{ad}, \tag{11.115}$$

because $\Psi_{ad} = L_{ad} i_{f0}$ and is the mutual flux linkage defined in Equation (A.34) in the Appendix. This equation can now be related to the open-circuit characteristic in Figure 11.9b where the slope of the air-gap line is proportional to L_{ad}. It should also be recognized that as the flux linkage and the voltage are related by Equation (11.115), the vertical axis can be interpreted in *either* voltage *or* flux linkage.

If at some open-circuit voltage E the required flux linkage is Ψ_{ad} then if there is no saturation of the iron paths, the field current required to set up this flux linkage would be i_{f0}; however, if saturation is present then the required field current would be i_{fsat}. From the definition of saturation factor in Equation (11.114)

$$i_{fsat} = \frac{i_{f0}}{S}, \tag{11.116}$$

while

$$L_{ad} = \frac{\Psi_{ad}}{i_{f0}} \quad \text{and} \quad L_{adsat} = \frac{\Psi_{ad}}{i_{fsat}}. \tag{11.117}$$

Substituting Equation (11.116) into (11.117) gives

$$L_{adsat} = S L_{ad}, \tag{11.118}$$

where L_{adsat} is the slope of the 'saturated' air-gap line in Figure 11.9b. Consequently, if Ψ_{ad} is known then the saturation factor S can be calculated from Equation (11.114) by recognizing that Ψ_{ad} and

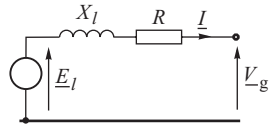

Figure 11.10 Equivalent circuit to calculate the armature voltage behind leakage reactance.

Ψ_T are equivalent. The saturated value of L_{ad} is then found from Equation (11.118) and used to account for saturation in all the generator parameter equations developed in Section 11.1.4.

The flux linkage, Ψ_{ad}, can be calculated provided that the armature voltage proportional to these flux linkages is known. As shown in Figure 11.10, this voltage is the voltage behind the armature leakage reactance X_l and, since X_l is not affected by saturation,

$$\underline{E}_l = \underline{V}_g + (R + \mathrm{j}X_l)\underline{I}, \tag{11.119}$$

so that provided $\underline{V}_g$ and $\underline{I}$ are known, E_l and Ψ_{ad} can be computed for any loading condition. In some instances the voltage E_p behind the Potier reactance X_p is used instead of E_l (Arrillaga and Arnold, 1990).

The final piece of the jigsaw is to have some method of conveniently storing the saturation curve in computer memory so as to facilitate the calculation of the saturation factor. A number of methods are available with perhaps the simplest being to fit the saturation curve by the function

$$I_f = V + C_n V^n, \tag{11.120}$$

where n is 7 or 9 and C_n is a constant for the particular curve (Hammons and Winning, 1971; Arrillaga and Arnold, 1990). Alternatively a polynomial can be used.

A slightly different approach is to use a two-stage exponential process (Anderson and Fouad, 1977; Anderson, Agrawal and Van Ness, 1990; Kundur, 1994) where

$$\begin{aligned} &\Psi_{ad} < 0.8, \quad \Psi_s = 0 \\ &\Psi_{ad} \geq 0.8, \quad \Psi_s = A_{sat} e^{B_{sat}(\Psi_{ad} - 0.8)}, \end{aligned} \tag{11.121}$$

where A_{sat} and B_{sat} are constants that are easily calculated by taking two points from the known saturation curve. When using this method there is usually a slight discontinuity at $\Psi_{ad} = 0.8$ but it is usually of no consequence (Anderson and Fouad, 1977).

The procedure for accounting for saturation in the generator equations can now be summarized as:

Step 1: Knowing $\underline{V}_g$ and $\underline{I}$, use Equation (11.119) to calculate E_l.
Step 2: Divide E_l by $\omega_s/\sqrt{3}$ to obtain Ψ_{ad}.
Step 3: Use Equation (11.121) to compute Ψ_s.
Step 4: Use Equation (11.114) to calculate the saturation factor S.
Step 5: Modify L_{ad} to account for saturation using Equation (11.118).
Step 6: Modify all the generator parameters that are a function of L_{ad}.

The procedure described above defines saturation in the d-axis and, although a similar procedure can be used in the q-axis, it is usual to assume:

- for round-rotor generators the saturation factor is the same in both axes when $S_d = S_q$;
- for salient-pole generators, since the q-axis reluctance is dominated by air paths, L_{aq} does not vary as much with saturation as L_{ad} and $S_q = 1$ is assumed under all loading conditions.

Although the saturation factor can be varied during a dynamic simulation, it is quite common to calculate it at the beginning of the simulation and assume that it remains constant during the simulation period. This ensures that the initial conditions are calculated correctly. If the saturation factor is varied during a dynamic simulation then it will be necessary to iterate steps 1 to 6 at each integration step in order to find a solution for L_{adsat}. This is because $\underline{V}_{\text{g}}$ and $\underline{I}$ depend on the degree of saturation while the saturation factor itself is dependent on $\underline{V}_{\text{g}}$ and $\underline{I}$. Other variations of this method of accounting for saturation can be found in Arrillaga and Arnold (1990) and Pavella and Murthy (1994).

11.1.8.3 Sensitivity of Parameters to Saturation

It was explained at the beginning of this section how generator reactances associated with flux paths mainly in air are less susceptible to saturation effects than are those associated with flux paths in iron. Such parameter sensitivity can be quantified by assessing the sensitivity of the particular parameter to variations in L_{ad} (or L_{aq}). For example, assume that the general parameter X is a function of L_{ad} so that for a small change in X

$$X = X_0 + \Delta X, \tag{11.122}$$

where ΔX, the change in X, is given by

$$\Delta X = \left.\frac{\partial X}{\partial L_{\text{ad}}}\right|_0 \Delta L_{\text{ad}}, \tag{11.123}$$

and the suffix 0 indicates an initial value.

In the context of the present discussion, Table 11.1 summarizes the per-unit d-axis steady-state and transient parameters defined in Section 11.1.4 with the sensitivity parameter determined using Equation (11.122). For example, the synchronous inductance $L_{\text{d}} = L_{\text{ad}} + l_l$. Therefore

$$\Delta L_{\text{d}} = \left.\frac{\partial L_{\text{d}}}{\partial L_{\text{ad}}}\right|_0 \Delta L_{\text{ad}}$$

but as

$$\left.\frac{\partial L_{\text{d}}}{\partial L_{\text{ad}}}\right|_0 = 1$$

Table 11.1 Sensitivity of d-axis parameters to saturation (based on Anderson, Agrawal and Van Ness, 1990)

Parameter	Equation	Equation number	Δ parameter	Typical sensitivity to a 10 % change in mutual flux linkage (%)
L_{d}	$L_{\text{ad}} + l_l$	(11.94)	ΔL_{ad}	21
L'_{d}	$L_{\text{d}} - \dfrac{L_{\text{ad}}^2}{L_{\text{f}}}$	(11.37)	$\left[\dfrac{l_{\text{f}}}{L_{\text{f0}}}\right]^2 \Delta L_{\text{ad}}$	1.5
T'_{d0}	$\dfrac{L_{\text{f}}}{R_{\text{f}}}$	(11.39)	$\dfrac{1}{R_{\text{f}}} \Delta L_{\text{ad}}$	20
E_{f}	$\omega_{\text{s}} L_{\text{ad}} \dfrac{v_{\text{f}}}{R_{\text{f}}}$	(11.64)	$\left[\dfrac{\omega_{\text{s}} v_{\text{f}}}{R_{\text{f}}}\right] \Delta L_{\text{ad}}$	21

then $\Delta L_{\mathrm{d}} = \Delta L_{\mathrm{ad}}$. Similarly, for the d-axis transient inductance

$$L'_{\mathrm{d}} = L_{\mathrm{d}} - \frac{L_{\mathrm{ad}}^2}{L_{\mathrm{f}}} = L_{\mathrm{ad}} + l_l - \frac{L_{\mathrm{ad}}^2}{L_{\mathrm{f}}}, \tag{11.124}$$

and differentiating gives

$$\Delta L'_{\mathrm{d}} = \Delta L_{\mathrm{ad}} - \left[\frac{2L_{\mathrm{ad0}}\Delta L_{\mathrm{ad}}}{L_{\mathrm{f0}}} - \frac{L_{\mathrm{ad0}}^2 \Delta L_{\mathrm{f}}}{L_{\mathrm{f0}}^2}\right], \tag{11.125}$$

but $L_{\mathrm{f}} = L_{\mathrm{ad}} + l_l$ so that $\Delta L_{\mathrm{f}} = \Delta L_{\mathrm{ad}}$ and

$$\Delta L'_{\mathrm{d}} = \Delta L_{\mathrm{ad}} - \left[\frac{2L_{\mathrm{ad0}}\Delta L_{\mathrm{ad}}}{L_{\mathrm{f0}}} - \frac{L_{\mathrm{ad0}}^2 \Delta L_{\mathrm{ad}}}{L_{\mathrm{f0}}^2}\right]. \tag{11.126}$$

Rearranging and writing $L_{\mathrm{f0}} = L_{\mathrm{ad0}} + l_{\mathrm{f}}$ gives

$$\Delta L'_{\mathrm{d}} = \left[\frac{l_{\mathrm{f}}}{L_{\mathrm{f0}}}\right]^2 \Delta L_{\mathrm{ad}}. \tag{11.127}$$

Anderson, Agrawal and Van Ness (1990) calculated typical values for these sensitivity parameters assuming a 10 % change in the mutual flux linkage Ψ_{ad}, the values of which are shown in Table 11.1. As expected, the synchronous inductance is particularly sensitive to saturation but the transient inductance, associated with flux paths mainly in air, shows little change. Indeed, if the analysis is extended to include subtransient inductance the change in this parameter is negligible.

11.2 Excitation Systems

In Chapter 2 the different types of excitation system and AVR used to supply, and control, the field current to the generator were described and the complete exciter and AVR subsystem shown in block diagram form in Figure 2.4. Generally the exciter is equipped with both an AVR and a manual regulator. In some cases a back-up AVR will also be provided. It is the AVR that is of particular interest here. As the power system industry uses a wide range of exciters and AVRs, with the details varying from one manufacturer to another, the aim of this section is to develop generic models of some of the most common types of excitation system. With careful parameter selection these models can then be used to represent different exciter systems from different manufacturers. A comprehensive study of excitation system models can be found in the IEEE Committee Reports on excitation systems (IEEE Committee Report, 1968, 1973a, 1973b, 1973c, 1981, 1992) and the interested reader should consult these excellent sources.

Ultimately the exciter and the AVR model must be interfaced with the generator model developed in Section 11.1.6. This interface is through the variable E_{f}, which represents the generator main field voltage v_{f} referred to the generator armature winding; v_{f} is also the exciter output voltage v_{ex}. Initially exciter subsystem models will be developed in terms of the currents and voltages at the field winding but will finally be referred to the armature and the values converted to per-unit notation. This is equivalent to expressing the exciter variables in a per-unit system where one per-unit exciter output voltage corresponds to the field voltage required to produce one per-unit armature voltage on the air-gap line, the per-unit system used in the armature. This exciter per-unit system is commonly used by manufacturers.

11.2.1 Transducer and Comparator Model

Figure 11.11 shows the block diagram of the transducer and comparator together with the load compensation element. The first block in this model corresponds to the load compensation element,

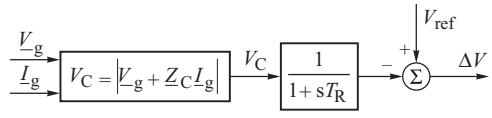

Figure 11.11 Block diagram of the transducer and comparator.

shown previously in Figure 2.5, which corrects the generator terminal voltage according to the value of the compensation impedance. The second block represents the delay introduced by the signal transducers. Normally the equivalent time constant of the transducers is small so that this block is often neglected. The third element represents the comparator at which the corrected generator voltage is added algebraically to the reference voltage V_{ref}.

11.2.2 Exciters and Regulators

Section 2.2.2 discussed different types of exciters. Modern excitation systems usually employ either a brushless AC exciter or a static exciter with either an analogue or digital AVR, although digital AVRs are becoming more common. However many older generators are fitted with DC excitation systems and consequently the models developed in this section are typical of the excitation systems in use today.

11.2.2.1 DC Exciters

Two different DC exciters are shown in Figure 11.12, the first being separately excited and the second self-excited. In order to develop a mathematical model of these two exciters, consider first the separately excited case in Figure 11.12a. A change in the exciter field current i_{exf} can be described by the following equation:

$$v_R = R_{exf} i_{exf} + L_{exf} \frac{di_{exf}}{dt}, \tag{11.128}$$

where L_{exf} depends on saturation and is an incremental inductance. The relationship between the exciter field current i_{exf} and the emf e_{ex} induced in the exciter armature is nonlinear because of magnetic saturation in the exciter core, while the exciter output voltage v_{ex} depends on both the saturation characteristic and the armature loading. Both of these effects can be included in the modelling process by using the constant resistance load saturation curve shown in Figure 11.13.

The first step in the modelling process is to observe that the slope of the air-gap line in Figure 11.13 is tangential to the linear part of the no-load saturation curve and can be represented by a resistance with the value $R = v_A / i_C$. The exciter field current that corresponds to the nonlinear

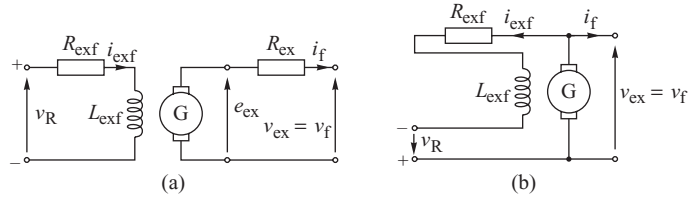

Figure 11.12 Equivalent circuit diagrams of DC exciters: (a) separately excited; (b) self-excited.

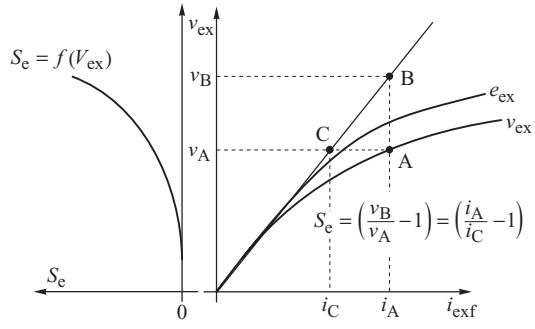

Figure 11.13 Illustration to define the saturation coefficient: e_{ex} is the no-load saturation curve, v_{ex} the constant resistance load saturation curve. The saturation characteristic is shown only around its saturation knee and has been exaggerated for clarity.

part of the constant resistance load characteristic can then be expressed using similar triangles as

$$i_A = i_C \frac{v_B}{v_A} = i_C(1 + S_e) = \frac{v_A}{R}(1 + S_e), \tag{11.129}$$

where S_e is a saturation coefficient defined in Figure 11.13 with reference to the constant resistance load saturation curve. This means that any point on the constant resistance load saturation characteristic is defined by

$$i_{exf} = \frac{v_{ex}}{R}(1 + S_e). \tag{11.130}$$

Substituting (11.130) into Equation (11.128) and writing

$$L_{exf} \frac{\mathrm{d}i_{exf}}{\mathrm{d}t} = L_{exf} \left[\frac{\mathrm{d}i_{exf}}{\mathrm{d}v_{ex}}\right]_{v_{ex0}} \frac{\mathrm{d}v_{ex}}{\mathrm{d}t}$$

gives

$$v_R = \frac{R_{exf}}{R}(1 + S_e)v_{ex} + L_{exf} \left[\frac{\mathrm{d}i_{exf}}{\mathrm{d}v_{ex}}\right]_{v_{ex0}} \frac{\mathrm{d}v_{ex}}{\mathrm{d}t}, \tag{11.131}$$

where the derivative in square brackets is simply the slope of the saturation characteristic at the initial operating point.

To enable the exciter to be easily interfaced with the generator model, the exciter base quantities are defined with the base exciter voltage E_{exb} being that voltage which gives rated open-circuit generator voltage $V_{go/c}$ on the generator air-gap line. This means that E_{exb} and the generator voltage are related by

$$V_{go/c} = \frac{1}{\sqrt{2}} \frac{\omega M_f}{R_f} E_{exb}.$$

The base exciter resistance is defined as $R_b = R$ with base current $I_{exfb} = E_{exb}/R_b$. Equation (11.131) can now be expressed in per-unit notation by dividing through by E_{exb}. It is also convenient to normalize the saturation curve to the base quantities E_{exb} and I_{exfb} when

$$L_{exf} \left[\frac{\mathrm{d}i_{exf}}{\mathrm{d}v_{ex}}\right]_{v_{ex0}} = \frac{L_{exf}}{R} \left[\frac{\mathrm{d}I_{exf}}{\mathrm{d}V_{ex}}\right]_{V_{ex0}}$$

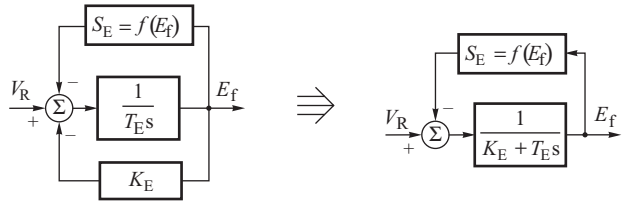

Figure 11.14 Block diagram of the regulated DC exciter.

and Equation (11.131) becomes

$$V_R = \frac{R_{exf}}{R}(1 + S_e)V_{ex} + \frac{L_{exf}}{R}\left[\frac{dI_{exf}}{dV_{ex}}\right]_{V_{ex0}} \frac{dV_{ex}}{dt}. \tag{11.132}$$

Noting that $E_f = V_{ex}$ and writing

$$\frac{L_{exf}}{R}\left[\frac{dI_{exf}}{dV_{ex}}\right]_{V_{ex0}} = T_E$$

gives Equation (11.132) in normalized form as

$$V_R = (K_E + S_E)E_f + T_E\frac{dE_f}{dt}, \tag{11.133}$$

where $K_E = R_{exf}/R$ and $S_E = (R_{exf}/R)S_e$. This equation is shown in block diagram form in Figure 11.14 and comprises an integrating element, with integration time T_E, and two negative feedback loops with gains K_E and S_E respectively.[3] The negative feedback loop with gain S_E models the saturation in the exciter iron. As the saturation increases so does the value S_E, the magnitude of the negative feedback signal increases, and the influence of the regulator on the exciter voltage, E_f, is reduced. A DC exciter that is separately excited usually operates with $R_f < R$ so that $K_E =$ 0.8–0.95. Often, approximated values of $K_E = 1$ and $S_E = S_e$ are assumed in the exciter model. The constant, T_E, is under 1 second and is often taken to be $T_E \approx 0.5$ s.

If the exciter is self-excited as shown in Figure 11.12b then the voltage v_R is the difference between the exciter internal emf and the excitation voltage, v_{ex}. Including this in Equation (11.128) would give a differential equation that is identical to (11.133) except that $K_E = (R_{exf}/R - 1)$. Consequently, the exciter block diagram in Figure 11.14 is also valid for self-excited exciters. Typically R_{exf} is slightly less than R so that K_E assumes a small negative value in the range -0.05 to -0.2.

The block diagram of the main part of the excitation system can now be formulated by combining the block diagram of the exciter with that of the regulator and the stabilizing feedback signal as shown in Figure 11.15. The regulator is represented by a first-order transfer function with a time constant T_A and gain K_A. Typical values of these parameters are $T_A = 0.05$–0.2 s and $K_A =$ 20–400. The high regulator gain is necessary to ensure small voltage regulation of the order of 0.5 %. Unfortunately, although this high gain ensures low steady-state error, when coupled with the length of the time constants the transient performance of the exciter is unsatisfactory. To achieve acceptable transient performance the system must be stabilized in some way that reduces the transient (high-frequency) gain. This is achieved by a feedback stabilization signal represented

[3] The constant T_E is sometimes called the exciter time constant. It is not a time constant. As shown in Figure 10.14, the time constant would depend on K_E and S_E. If saturation is neglected then the effective exciter time constant would be T_E/K_E.

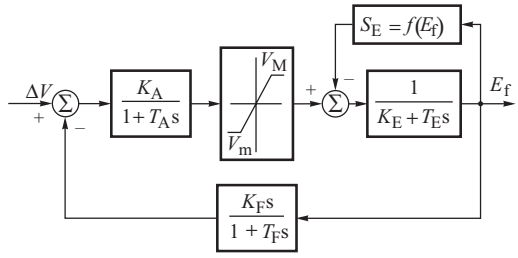

Figure 11.15 Block diagram of the excitation system with a DC exciter. Based on IEEE Committee Report (1968).

Source: © IEEE 1968

by the first-order differentiating element with gain K_F and time constant T_F. Typical values of the parameters in this element are $T_F = 0.35 - 1$s and $K_F = 0.01 - 0.1$.

Although the saturation function $S_E = f(E_f)$ can be approximated by any nonlinear function, an exponential function of the form $S_E = A_{ex}e^{B_{ex}E_f}$ is commonly used. As this function must model the saturation characteristic over a wide range of exciter operating conditions, the parameters A_{ex} and B_{ex} of the exponential function are determined by considering the heavily saturated region of the characteristic corresponding to high excitation voltage and high exciter field current. For example, Anderson *et al.* (1990) recommend that points on the characteristic corresponding to 100 and 75 % of the maximum excitation voltage be used.

It is important to note that the limits on E_f are linked to the regulator limit and the saturation function such that the maximum value E_{fM} is obtained from

$$V_M - (K_E E_{fM} + S_{EM}) = 0. \tag{11.134}$$

11.2.2.2 AC Rotating Exciters

These exciters usually use a three-phase bridge rectifier consisting of six diode modules as shown in Figure 11.16a. The rectifier is fed from a three-phase AC voltage source of emf V_E and reactance X_E. As with any rectifier system, the output voltage depends on the commutation characteristics of the rectifier as determined by the degree of commutation overlap. As the effect of commutation overlap depends on the current through the rectifiers and the commutating reactance X_E, three

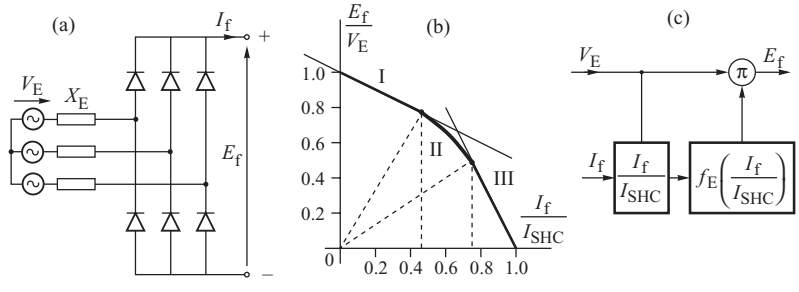

Figure 11.16 Three-phase uncontrolled bridge rectifier: (a) equivalent circuit; (b) voltage–current characteristic; (c) block diagram. V_E, X_E are the emf and the reactance of the voltage source, E_f, I_f are the internal emf and the field current, and I_{SHC} is the rectifier short-circuit current. Based on IEEE Committee Report (1981).

Source: © IEEE 1968

main operating states can be identified as a function of field current as shown in Figure 11.16b. These three states, denoted as I, II, III on the characteristic, depend on the commutation behaviour of the rectifier and allow the voltage at the rectifier terminals to be determined for a given field current I_f and voltage source emf V_E (Witzke, Kresser and Dillard, 1953; IEEE Committee Report, 1981).

State I refers to the case where commutation in one branch of the bridge finishes before commutation in another branch starts. During this state the relationship between the rectifier terminal voltage and the field current is linear and is described by

$$\frac{E_f}{V_E} = 1 - \frac{1}{\sqrt{3}} \frac{I_f}{I_{SHC}}, \tag{11.135}$$

where $I_{SHC} = \sqrt{2}\, V_E / X_E$ is the rectifier short-circuit current conveniently chosen here to be one per unit. This relationship is valid for field currents $I_f < 2I_{SHC}/\sqrt{3}$.

As the field current increases, commutation overlap also increases and the rectifier reaches state II when each diode can only conduct current when the counter-connected diode of the same phase has finished its conduction. In this state the relationship between the rectifier voltage and the field current is nonlinear and corresponds to a circle with radius $\sqrt{3}/2$ as described by the equation

$$\left(\frac{E_f}{V_E}\right)^2 + \left(\frac{I_f}{I_{SHC}}\right)^2 = \left(\frac{\sqrt{3}}{2}\right)^2. \tag{11.136}$$

This relationship is valid for current

$$\frac{2}{\sqrt{3}} I_{SHC} \le I_f \le \frac{2}{4} I_{SHC}$$

As the field current increases further, the rectifier reaches state III where commutation overlap is such that four diodes all conduct at the same time, two in each of the upper and lower arms. In this state the relationship between the rectifier voltage and the field current is linear and is described by the equation

$$\frac{E_f}{V_E} = \sqrt{3}\left(1 - \frac{I_f}{I_{SHC}}\right). \tag{11.137}$$

This relationship is valid for currents $3I_{SHC}/4 \le I_f \le I_{SHC}$.

The block diagram that models the rectifier is shown in Figure 11.16c with all values in per-unit form. In this diagram the first block on the left calculates the value of the field current relative to the short-circuit current I_{SHC}. The second block calculates the value of the function $f_E(I_f/I_{SHC})$ before passing it to the multiplying element to find the voltage at the terminals of the rectifier.

Figure 2.3b and c shows how the rectifier can be fed from either an inductor generator or an inside-out AC generator with the latter being most common as it eliminates the need for slip rings. Although the alternator can be modelled using one of the generator models described in Section 11.1, it is usually sufficiently accurate to simplify the alternator model to be similar to that used to represent the DC exciter. This simplification allows the complete excitation system to be modelled as shown in Figure 11.17.

As for the DC exciter, the alternator is modelled by an integrating element with three feedback loops. The feedback loops with gain K_E and S_E play the same role as in the DC excitation system. However, the effect of the alternator resistance is now included in the voltage–current characteristics of the rectifier when S_E is determined from the no-load saturation characteristic rather than the load saturation line as used for the DC exciter. As the armature current in the AC exciter is proportional to the current in the main generator field winding, the third feedback loop, with gain K_D, uses this

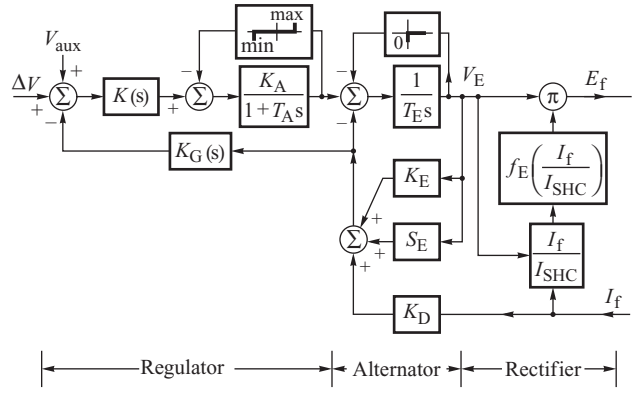

Figure 11.17 Block diagram of the excitation system with AC alternator and the uncontrolled rectifier.

current to model the demagnetizing effect of the armature reaction in the AC exciter. As the output voltage of a diode rectifier cannot drop below zero, this is modelled by the negative feedback loop containing the signal limiter. If the excitation voltage drops below zero a large negative signal is fed back to the summing point that prevents a further drop in the voltage, thereby keeping it at zero.

The system is stabilized by the feedback loop with transfer function $K_G(s) = K_F s/(1 + T_F s)$. In this case the stabilizing loop is supplied by a signal that is proportional to the exciter field current. Alternatively the system could be stabilized by supplying this block directly from the output of the voltage regulator or from the excitation voltage E_f. In this diagram the feedback stabilization is supplemented by an additional block with the transfer function $K(s)$ in the forward path preceding the regulator block. Both $K_G(s)$ and $K(s)$ depend on the specific excitation system and can be implemented by either analogue or digital techniques. Normally $K(s)$ will have a PI or PID type of structure and is often represented by the transfer function $(1 + T_C s)/(1 + T_B s)$. A major simplification to the model can be made by neglecting the variable effect of the field current on the rectifier voltage. In this case the model reduces to one that is very similar to that shown in Figure 11.15 for the DC exciter.

11.2.2.3 Static Exciters

In static excitation systems the source of the direct current is a controlled three-phase bridge rectifier consisting of six thyristor modules as shown in Figure 11.18. The output characteristic of the rectifier depends on both the thyristor firing angle α and the system commutation characteristic. In the limiting case $\alpha = 0$ and the output characteristic is similar to that of the uncontrolled rectifier shown in Figure 11.16b. One very important characteristic of the controlled rectifier is the ability to provide a negative exciter output voltage so providing the exciter with *exciter buck* capability. Although the exciter output voltage may go negative, the current cannot and must always flow in the same direction. As the firing angle increases, the output voltage of the controlled rectifier decreases proportionally to cos α (Lander, 1987) to give the family of characteristics shown in Figure 11.18.

The firing angle is set by the voltage regulator. The cosinusoidal dependency of the firing angle and the rectifier output voltage can be negated by introducing an inverted cosine function at the regulator output so as to produce a linear relationship. As the slight delays caused by discretization of the firing sequence in each phase are much smaller than the power system time constants, the rectifier can be regarded as a current source with no time delay.

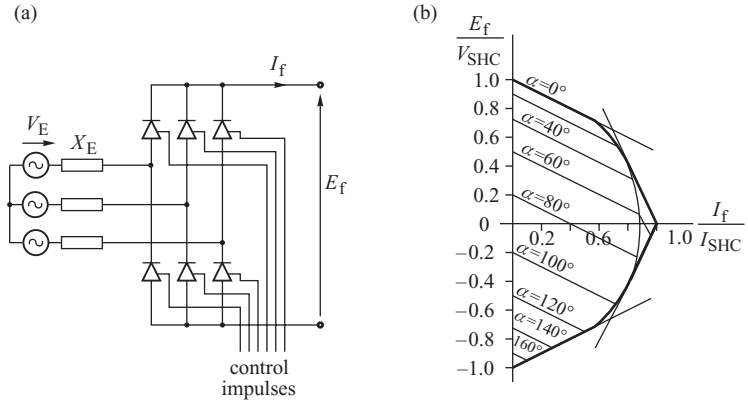

Figure 11.18 Three-phase controlled bridge rectifier: (a) circuit diagram; (b) voltage–current characteristic. α is the firing angle of the thyristors.

The complete excitation system can then be modelled by the block diagram shown in Figure 11.19. In this figure the regulator and the stabilization element are shown in the upper part of the diagram while the static characteristic of the rectifier is shown in the bottom part of the diagram. The rectifier supply voltage V_E is proportional to both the generator armature voltage and armature current as determined by the constants K_v and K_i. The values of these constants depend on how the rectifier is fed (Figure 2.3d–f). When $K_i = 0$ and $K_v = 1$ the system has no load compensation and corresponds to the rectifier being supplied directly from the terminals of the generator.

The way in which the main generator field current effects the rectifier output voltage is modelled in the same way as the uncontrolled rectifier. The regulator, together with the firing circuits, are modelled by a first-order transfer function with gain K_A and time constant T_A. If the systems does not contain cosinusoidal compensation of the voltage–firing angle dependency the gain K_A

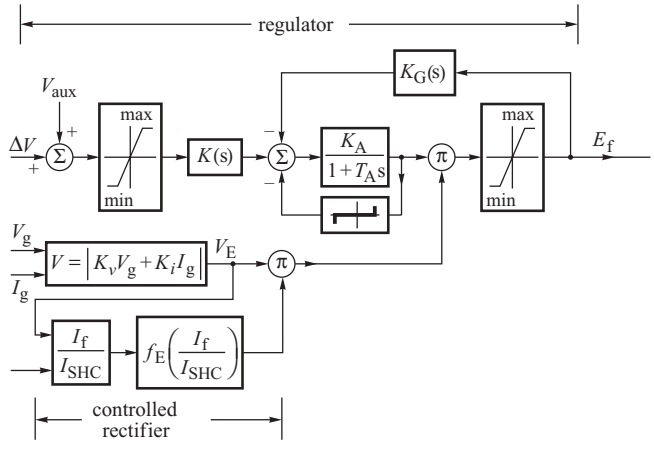

Figure 11.19 Block diagram of the excitation system with a static exciter. Based on IEEE Committee Report (1968).

Source: © IEEE 1968

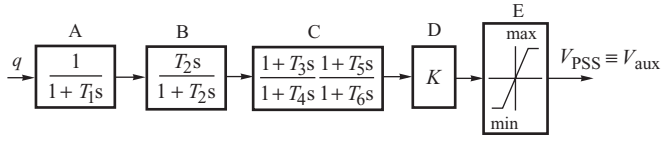

Figure 11.20 Block diagram of the power system stabilizer. A, signal sensor; B, high-pass filter; C, lead compensation element; D, amplifier gain; E, limiter.

will not be constant and should be modelled as a cosine function of the regulator signal. The system is stabilized by the transfer function $K(s)$ in the forward path and by feedback of the exciter output voltage through the block $K_G(s)$. For example, the transfer function $K(s) = K_1(1 + T_C s)/(1 + T_B s)$ and a constant gain $K_G(s) = K_G$ may be used. Although $K(s)$ and $K_G(s)$ can be implemented using digital or analogue methods, digital AVRs are becoming common as they allow more sophisticated functions to be built into the AVR while only software changes are needed between different generators. The exciter output voltage E_f is given by the product of the supply voltage and the regulator output signal which represents the firing angle. If the influence of the generator field current on the rectifier output voltage is neglected then the exciter block diagram may be simplified to that consisting of the transfer function of the regulator and its stabilization element.

11.2.3 Power System Stabilizer (PSS)

Section 9.1 explained how a PSS can help to damp generator rotor oscillations by providing an additional input signal that produces a torque component that is in phase with the rotor speed deviation. The general structure of a PSS was shown Figure 10.2 where the main elements are: the signal sensor, a low-pass filter, a high-pass filter, at least one lead compensation element, an amplifier and a limiter. A block diagram of the PSS model corresponding to the functional diagram of Figure 10.2 is shown in Figure 11.20. The input signal q can be rotor speed, real power, frequency or some other signal as described in Section 10.1. The output signal is shown in Figure 11.20 as V_{PSS} and is passed to the AVR as the auxiliary signal V_{aux}. The parameters within the PSS are carefully selected for each PSS depending on its input signals and location in the system.

11.3 Turbines and Turbine Governors

Chapter 2 explained how turbines, of one form or another, are used almost exclusively to provide the mechanical input power to the generator. It also explained how the basic governing systems on these turbines work. In this section models of the turbine and its governor will be developed so that the input power into the generator model can be regulated in the same way as in the actual system. The turbine models developed are simplified models designed solely to be used for power system analysis rather than for detailed mechanical modelling of the turbine itself. Models of both the mechanical–hydraulic and the electro-hydraulic governor will be developed. As with the AVR, modern generators tend to be fitted with sophisticated digital governors that allow a high degree of functionality. As the structure of these vary between manufacturers, the models developed here are typical of the turbines and governors currently in use. Although the turbine control system allows for both start-up of the turbine and for its control when in operation, it is the latter that is of interest here. A comprehensive discussion on the modelling of both steam and water turbines and their governors can be found in IEEE Committee Reports (1973a, 1973b, 1973c, 1991, 1992, 1994).

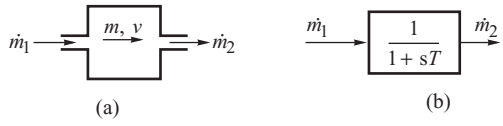

Figure 11.21 Model of the steam flow through a steam vessel: (a) vessel of capacity V; (b) block diagram.

11.3.1 Steam Turbines

Steam turbines are used extensively throughout the world to provide mechanical power to the generator. The mathematical model of the turbine will be derived using a simple model of steam flow through a steam vessel shown in Figure 11.21.

The vessel introduces a time delay into the system as changes in the steam flow at the input take a finite time to appear at the output. This time delay can be quantified by considering a steam vessel of volume V as shown in Figure 11.21a. In this diagram m is the mass of steam in the vessel, p the steam pressure and $\dot{m}_1$ and $\dot{m}_2$ the steam mass flowrates at the input and output. The mass of the steam in the vessel is constant when $\dot{m}_1 = \dot{m}_2$. When the steam input flowrate changes due to a change in the valve position then the mass of steam in the vessel will change at a rate proportional to the difference between the input flowrate and the output flowrate, that is $\mathrm{d}m/\mathrm{d}t = (\dot{m}_1 - \dot{m}_2)$. If the steam temperature is constant then the change of mass in the vessel must result in a pressure change when this equation can be written as

$$\dot{m}_1 - \dot{m}_2 = \frac{\mathrm{d}m}{\mathrm{d}t} = \frac{\partial m}{\partial p}\frac{\mathrm{d}p}{\mathrm{d}t} = V\frac{\partial}{\partial p}\left(\frac{1}{v}\right)\frac{\mathrm{d}p}{\mathrm{d}t}, \tag{11.138}$$

where v is the steam specific volume at a given pressure (volume divided by mass). Assuming that the outflow of steam is proportional to the pressure in the vessel

$$\dot{m}_2 = \dot{m}_0\frac{p}{p_0} \quad \text{or} \quad \frac{\mathrm{d}p}{\mathrm{d}t} = \frac{p_0}{\dot{m}_0}\frac{\mathrm{d}\dot{m}_2}{\mathrm{d}t}, \tag{11.139}$$

where $\dot{m}_0 = \dot{m}_1(t = 0) = \dot{m}_2(t = 0)$ and $p_0 = p(t = 0)$. Substituting (11.139) into (11.138) gives

$$\dot{m}_1 - \dot{m}_2 = T\frac{\mathrm{d}\dot{m}_2}{\mathrm{d}t}, \tag{11.140}$$

where

$$T = V\frac{p_0}{\dot{m}_0}\frac{\partial}{\partial p}\left(\frac{1}{v}\right)$$

is a time constant corresponding to the inertia of the mass of steam in the vessel. Applying Laplace transforms and writing in transfer function form gives

$$\frac{\dot{m}_2(\mathrm{s})}{\dot{m}_1(\mathrm{s})} = \frac{1}{(1 + T\mathrm{s})}, \tag{11.141}$$

which corresponds to the inertia block in Figure 11.21b.

Figure 11.22 shows how the above equation can be used to model the tandem compound single-reheat turbine described in Section 2.2.3. A schematic diagram of this arrangement, Figure 11.22a, shows how the steam passes through the governor control valves and the inlet piping to the HP steam chest (A). On leaving the steam chest it passes through the HP turbine before entering the reheat stage between the HP and IP steam turbines. After being reheated the steam passes through

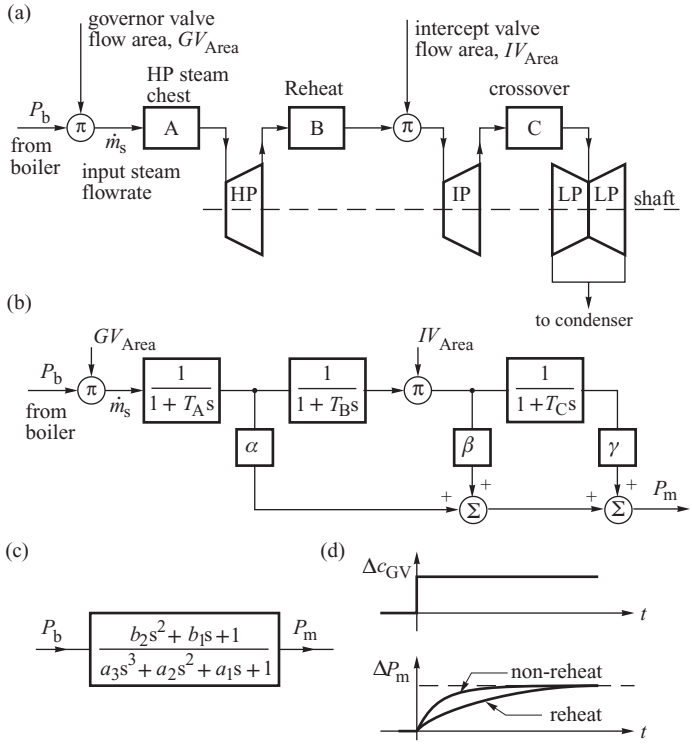

Figure 11.22 Tandem compound single-reheat turbine: (a) schematic diagram; (b) block diagram; (c) transformed block diagram; (d) response of the linear turbine model to a step change in valve position. Symbols P_i, P_m are the power of the inlet steam and of the turbine.

the intercept valves to the IP turbine and then through the crossover piping to the LP turbine. The mathematical model of such a system is shown in Figure 11.22b and can be divided into two parts. Firstly, as the power extracted by a turbine is proportional to the steam mass flowrate $\dot{m}_s$, each turbine stage can be modelled by a constant α, β, γ which correspond to the portion of the total turbine power developed in the different turbine stage with $\alpha + \beta + \gamma = 1$. Typically, for the single-reheat turbine shown here, $\alpha \approx 0.3$, $\beta \approx 0.4$ and $\gamma \approx 0.3$ defined on the turbine megawatt output base. If the generator MVA base is used then these values must be modified in the ratio of the two bases.

The second part of the turbine model concerns the storage of the steam chests and associated piping and corresponds to Figure 11.21b. Typical values of the parameters are: $T_A = 0.1$ to 0.4 s, $T_B = 4$ to 11 s, $T_C = 0.3$ to 0.5 s, $\alpha = 0.3$, $\beta = 0.4$, $\gamma = 0.3$.

Assuming that there is no control of the intercept valves, the block diagram of Figure 11.22b can be simplified to that shown in Figure 11.22c by combining the three inertia blocks to give an equivalent third-order block with the combined parameters

$$a_1 = T_A + T_B + T_C, \quad a_2 = T_A T_B + T_A T_C + T_B T_C, \quad a_3 = T_A T_B T_C$$
$$b_1 = \alpha(T_B + T_C) + \beta T_C, \quad b_2 = \alpha T_B T_C.$$

As turbine power is proportional to the steam mass flowrate, the input flowrate is changed in this diagram to input power to simplify the diagram further. As the reheat time constant T_B is several

times higher than either T_A or T_C, the turbine model can be further simplified by assuming $T_A \approx 0$ or even $T_A \approx T_C \approx 0$, reducing the turbine model to a second- and first-order block respectively.

A steam turbine without reheat can be modelled by a first-order block with time constant $T_A = 0.2$ to 0.5 s and with $\alpha = 1$, $\beta = \gamma = 0$, $T_B = T_C = 0$.

A comparison of the time response of a turbine with and without reheat with an incremental step increase in the opening of the governor valve Δc_{GV} is shown in Figure 11.22d. When the valve opening increases so does the valve flow area GV_{Area} so that for a constant boiler pressure the steam flowrate also increases. However, steam storage effects introduce a delay before the increased steam flowrate can reach the turbine blades and increase the output power. This effect is particular noticeable for a turbine with reheat when the rise time may be as long as 10 seconds as shown in Figure 11.22d. As this delay between activating the valve and the power changing can be excessively long in reheat turbines, coordinated control of both the governor and the interceptor valves is necessary as explained in the next section.

11.3.1.1 Governing System for Steam Turbines

Chapter 2 explained that the reheat turbine shown in Figure 11.22a is fitted with two sets of control valves and two sets of emergency stop valves. Normally turbine control is accomplished by regulating the position of the governor valves and the intercept valves while the emergency stop valves are kept fully open and only used in an emergency to stop the turbine. As both sets of stop valves are normally kept fully open, they can be neglected for modelling purposes.

Although the way in which control of the governor valves and the intercept valves is coordinated depends on the purpose of the control action, the type of governor and the manufacturer concerned, the generic features of the governor can be included in a general model capable of representing both the mechanical–hydraulic and the electro-hydraulic governor. This model allows for overspeed control and load/frequency control as described in Chapter 9. The fast-valving features described in Chapter 10 can be readily added if necessary.

In order to develop this governor model the functional diagram of the mechanical–hydraulic governor shown in Figure 11.23a will be used. This diagram shows the main elements of a mechanical–hydraulic governor as the speed transducer, regulator, speed relay, servomotor and the steam control valves. Compared with Figure 2.12 an additional element, the speed relay, is shown that develops an output proportional to the load reference signal less any contribution due to speed deviation. This additional element is required because on some larger generators the force required to adjust the position of the main steam valves is very large and an additional spring-loaded servomotor, the speed relay, is required between the speeder linkage and the main servomotor. On some smaller machines the spring-loaded servomotor of the speed relay is used to adjust the position of the control valves rather than the servomotor arrangement shown in Figure 2.12.

The elements in this functional diagram are modelled as shown in the block diagram of Figure 11.23b. The regulator is modelled by a gain $K = 1/\rho$, where ρ is the droop of the regulator static characteristic, while the speed relay is modelled by a first-order lag with time constant T_2. The effect of the load reference has been modelled as the required opening of the main governor control valves c_{0GV}. The main servomotor, which alters the position of the control valves, is modelled by an integrator with direct feedback of valve position along with two limiters. The first limiter is necessary to protect the turbine from rapid opening or closing of the steam valves. The second limiter limits the valve position between fully open and fully closed, or to some set position if a load limiter is present. The final, nonlinear block models the valve characteristics, effectively converting the valve position to normalized flow area. The nonlinearity of the valve characteristic may be compensated in the governor by a linearizing cam located between the speed relay and the servomotor. These two mutually compensating nonlinearities are often neglected in the model. The

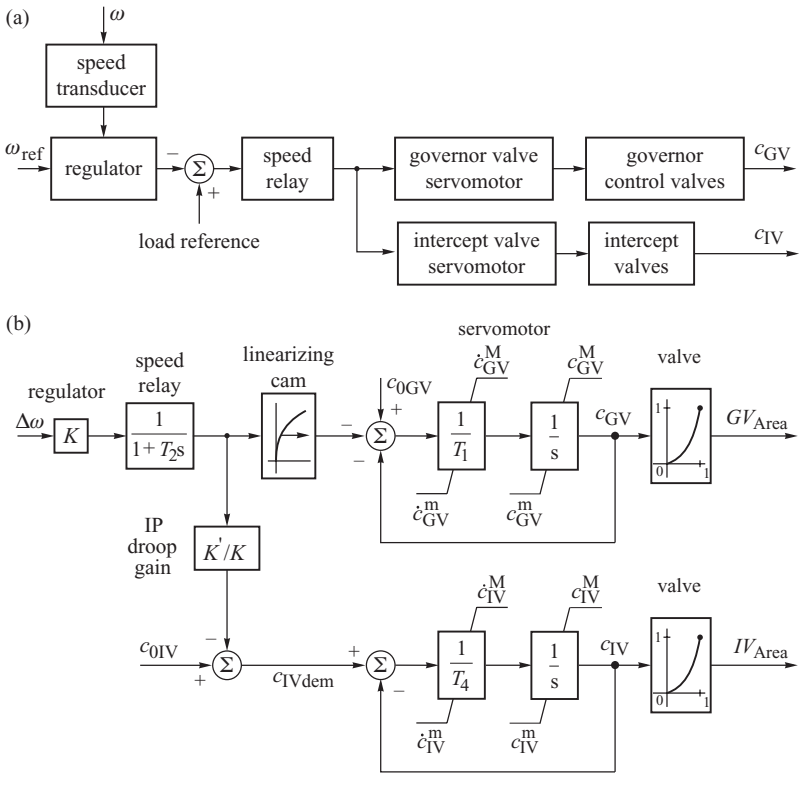

Figure 11.23 Mechanical–hydraulic steam turbine governor of the steam turbine: (a) functional diagram; (b) block diagram; (c) simplified block diagram. Symbols: c, main steam valve position; GV, governor valves; IV, intercept valves.

output of the model is the normalized valve flow area and appears as the main input to the turbine model in Figure 11.22b.

One way in which the intercept valves can be controlled to limit overspeed is also shown in Figure 11.23b. In this example the position of the intercept valves is controlled to follow a demand position signal c_{IVdem} generated according to the equation

$$c_{\mathrm{IVdem}} = c_{0\mathrm{IV}} - K'\Delta\omega, \tag{11.142}$$

where K' is the IP gain and is the inverse of the IP droop; $K' > K$.

To examine in further detail how this control loop works, assume that $K = 25$ (main droop 4%) and that $K' = 50$ (IP droop 2%) and that it is necessary to keep the intercept valves fully open until the overspeed is 4%. At this speed the main governor valves will just have fully closed. The reference signal $c_{0\mathrm{IV}}$ is set to 3. With $0.04 > \Delta\omega > 0$ then the demand $c_{\mathrm{IVdem}} \geq 1$ and the intercept valves are kept fully open. When $\Delta\omega = 0.04$ the intercept valves start to close and are fully closed when $\Delta\omega = 0.06$.

In some cases an auxiliary governor is used that acts in parallel with the normal regulator. This auxiliary governor only comes into operation when large speed deviations are registered and has the effect of increasing the regulator gain K. In this way the regulator output is increased to close quickly both the interceptor valves and the governor control valves.

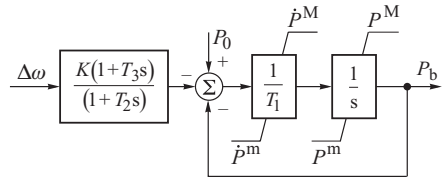

Figure 11.24 Simplified governor model.

The governor model can also be used to model the electro-hydraulic governor because the main power components are similar, except that now the mechanical components have been replaced by electronic circuits. Such changes provide a greater degree of flexibility and functionality than can be achieved in the traditional mechanical–hydraulic governor. A further advance is the digital–hydraulic governor where the control functions are implemented in software, so providing even greater flexibility. From a modelling point of view this increased flexibility means that the actual governor control used is manufacturer dependent, particularly with regard to the more advanced features such as fast valving. Nevertheless, the governor model developed in Figure 11.23b with the speed relay replaced by the general transfer function $(1 + T_3s)/(1 + T_2s)$ to provide any phase compensation forms a good basis for modelling an electro-hydraulic governor. If a particular control logic is to be implemented then it is relatively straightforward to modify Figure 11.23b accordingly.

When analysing electromechanical dynamics in a time interval of around 10 s the boiler pressure can be assumed to be constant and can be equated to the initial power P_0 so that $P_b = P_m(t = 0) = P_0 =$ constant. With this assumption the governor block diagram can be simplified to that shown in Figure 11.24 by multiplying the limits, and the initial conditions, in the servomotor model by P_0. In this model the regulator and the speed relay transfer functions have been replaced by a general control block $K\,(1 + T_3s)\,/\,(1 + T_2s)$ to enable this model to be used for both mechanical–hydraulic and electromechanical governors. The additional time constant now allows both types of governor to be modelled by correct choice of values. Intercept valve control is not shown on this diagram as it assumes that they are kept fully open but could be added if required. Other forms of electro-hydraulic and mechanical–hydraulic governors are described in IEEE Committee Reports (1973b, 1991) and Kundur (1994).

11.3.1.2 Boiler Control

In the modelling process the boiler output is linked to the turbine via the boiler pressure parameter P_b. It is not the purpose here to describe boiler models but a brief discussion of boiler/turbine interaction is necessary because throughout this book it has been assumed that P_b effectively remains constant. Traditionally, conventional turbine control operated in a 'boiler follows turbine' mode where all load changes are carried out by control of the turbine valves with the boiler controls operating to maintain constant steam conditions, that is pressure and flow. Although this control mode allows rapid turbine response and good frequency control by utilizing the stored energy in the boiler, the changes in the boiler pressure and other variables can be quite large. To prevent this an alternative 'turbine follows boiler' control mode can be used when all load changes are made via the boiler controls. The turbine valves are controlled to regulate the boiler pressure. As the speed of response of the turbine valves is very fast, almost perfect pressure control can be achieved. However, load changes are now very slow with time constants of 1–2 min, depending on the type of boiler and the fuel, since now no use is made of the stored energy in the boiler. As a compromise, 'integrated boiler and turbine' control may be used to achieve both a quick turbine response and limiting of the changes in the boiler variables.

11.3.2 Hydraulic Turbines

If water flows from a high level to a low level through a hydraulic turbine the potential energy of the water stored in a high reservoir is converted into mechanical work on the turbine shaft as described in Section 2.2.3. The turbine may be either an impulse turbine or a reaction turbine and, although the way in which they operate hydraulically differs, the work done by both types is entirely due to the conversion of kinetic energy. In impulse turbines, such as the Pelton wheel, all the available energy in the water is converted into kinetic energy as the water passes through the nozzle. The water forms a free jet as it leaves the nozzle and strikes the runner where the kinetic energy is converted into mechanical work. In the reaction turbine, such as the Francis turbine, only a part of the energy in the water is converted into kinetic energy as the water passes through the adjustable wicket gates, with the remaining conversion taking place inside the runner itself. All passages are filled with water including the draft tube. In both turbines the power is controlled by regulating the flow into the turbine by wicket gates on the reaction turbine and by a needle, or spear, on the impulse turbine. What is required is a mathematical description of how the turbine power changes as the position of the regulating device is changed.

Figure 11.25a shows a schematic diagram of a turbine installation where water flows down the penstock and through the turbine before exiting into the tailwater. The penstock is modelled by assuming that the flow is incompressible when the rate of change of flow in the penstock is obtained by equating the rate of change of momentum of the water in the penstock to the net force on the water in the penstock when

$$\rho L \frac{\mathrm{d}Q}{\mathrm{d}t} = F_{\mathrm{net}}, \tag{11.143}$$

where Q is the volumetric flowrate, L the penstock length and ρ the mass density of water.

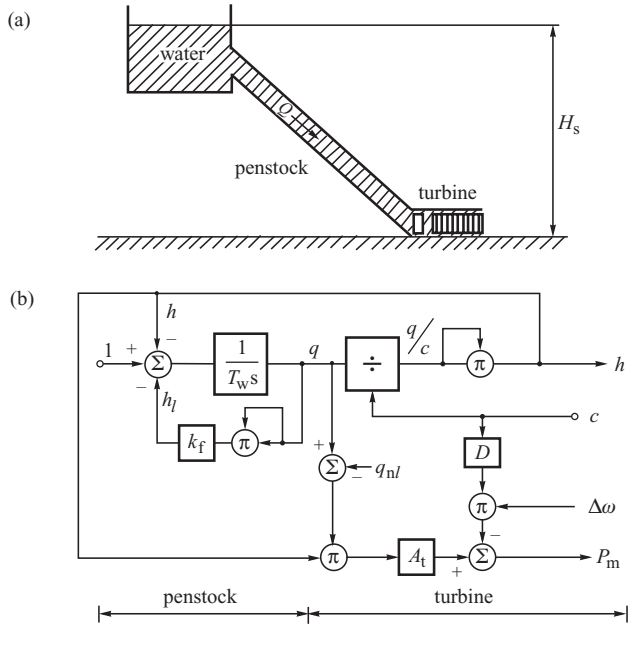

Figure 11.25 Hydraulic turbine: (a) schematic diagram; (b) nonlinear model. Based on IEEE Committee Report (1968).

Source: © IEEE 1968

The net force on the water can be obtained by considering the pressure head at the conduit. On entry to the penstock the force on the water is simply proportional to the static head H_s, while at the wicket gate it is proportional to the head H across the turbine. Due to friction effects in the conduit, there is also a friction force on the water represented by the head loss H_l so that the net force on the water in the penstock is

$$F_{\text{net}} = (H_s - H_l - H)A\rho g, \tag{11.144}$$

where A is the penstock cross-sectional area and g the acceleration due to gravity. Substituting the net force into Equation (11.143) gives

$$\rho L \frac{\mathrm{d}Q}{\mathrm{d}t} = (H_s - H_l - H)A\rho g. \tag{11.145}$$

It is usual to normalize this equation to a convenient base. Although this base system is arbitrary, the base head h_{base} is taken as the static head *above* the turbine, in this case H_s, while the base flowrate q_{base} is taken as the flowrate through the turbine with the gates fully open and the head at the turbine equal to h_{base} (IEEE Committee Report, 1992). Dividing both sides of Equation (11.145) by $h_{\text{base}}q_{\text{base}}$ gives

$$\frac{\mathrm{d}q}{\mathrm{d}t} = \frac{1}{T_w}(1 - h_l - h), \tag{11.146}$$

where $q = Q/q_{\text{base}}$ and $h = H/h_{\text{base}}$ are the normalized flowrates and pressure heads respectively and $T_w = Lq_{\text{base}}/Agh_{\text{base}}$ is the *water starting time*. Theoretically T_w is defined as the time taken for the flowrate in the penstock to change by a value equal to q_{base} when the head term in brackets changes by a value equal to h_{base}. The head loss h_l is proportional to the flowrate squared and depends on the conduit dimensions and friction factor. It suffices here to assume that $h_l = k_f q^2$ and can often be neglected. This equation defines the penstock model and is shown in block diagram form in the left hand part of Figure 11.25b.

In modelling the turbine itself both its hydraulic characteristics and mechanical power output must be modelled. Firstly, the pressure head across the turbine is related to the flowrate by assuming that the turbine can be represented by the valve characteristic

$$Q = kc\sqrt{H}, \tag{11.147}$$

where c is the gate position between 0 and 1 and k is a constant. With the gate fully open $c = 1$ and this equation can be normalized by dividing both sides by $q_{\text{base}} = k\sqrt{h_{\text{base}}}$ to give, in per-unit form,

$$q = c\sqrt{h}. \tag{11.148}$$

Secondly, the power developed by the turbine is proportional to the product of the flowrate and the head and depends on the efficiency. To account for the turbine not being 100% efficient the no-load flow q_{nl} is subtracted from the actual flow to give, in normalized parameters,

$$P_m = h(q - q_{nl}). \tag{11.149}$$

Unfortunately this expression is in a different per-unit system to that used for the generator whose parameters are normalized to the generator MVA base so that Equation (11.149) is written as

$$P_m = A_t h(q - q_{nl}), \tag{11.150}$$

where the factor A_t is introduced to account for the difference in the bases. The value of the factor A_t can be obtained by considering the operation of the turbine at rated load when

$$P_m = A_t h_r (q_r - q_{nl}) = \frac{\text{turbine power (MW)}}{\text{generator MVA rating}}, \tag{11.151}$$

and the suffix 'r' indicates the value of the parameters at rated load. Rearranging Equation (11.151) gives

$$A_t = \frac{\text{turbine power (MW)}}{\text{generator MVA rating}} \frac{1}{h_r (q_r - q_{nl})}. \tag{11.152}$$

A damping effect is also present that is dependent on gate opening so that at any load condition the turbine power can be expressed by

$$P_m = A_t h (q - q_{nl}) - Dc\ \Delta\omega, \tag{11.153}$$

where D is the damping coefficient. Equations (11.148) and (11.153) constitute the turbine nonlinear model shown on the right of Figure 11.25b where the wicket gate position is the control variable.

11.3.2.1 Linear Turbine Model

The classical model of the water turbine (IEEE Committee Report, 1973a, 1973b, 1973c) uses a linearized version of the nonlinear model. Such a model is valid for small changes of mechanical power and can be obtained by linearizing Equations (11.146), (11.148) and (11.150) about an initial operating point to give

$$\frac{d\Delta q}{dt} = -\frac{\Delta h}{T_w}, \quad \Delta q = \frac{\partial q}{\partial c}\Delta c + \frac{\partial q}{\partial h}\Delta h, \quad \Delta P_m = \frac{\partial P_m}{\partial h}\Delta h + \frac{\partial P_m}{\partial q}\Delta q. \tag{11.154}$$

Introducing the Laplace operator s and eliminating Δh and Δq from the equations gives

$$\frac{\Delta P_m}{\Delta c} = \frac{\left[\dfrac{\partial q}{\partial c}\dfrac{\partial P_m}{\partial q} - sT_w \dfrac{\partial P_m}{\partial h}\dfrac{\partial q}{\partial c}\right]}{1 + sT_w \dfrac{\partial q}{\partial h}}, \tag{11.155}$$

where the partial derivatives are

$$\begin{aligned} \frac{\partial q}{\partial h} &= \frac{1}{2}\frac{c_0}{\sqrt{h_0}}, & \frac{\partial q}{\partial c} &= \sqrt{h_0} \\ \frac{\partial P_m}{\partial q} &= A_t h_0, & \frac{\partial P_m}{\partial h} &= A_t (q_0 - q_{nl}) \approx A_t (q_0) \end{aligned} \tag{11.156}$$

and the suffix 0 indicates an initial value. Substituting into Equation (11.155) and noting that $q_0 = c_0\sqrt{h_0}$ gives

$$\frac{\Delta P_m}{\Delta c} = A_t h_0^{3/2} \frac{1 - sT'_w}{1 + s\frac{T'_w}{2}}, \tag{11.157}$$

where

$$T'_w = T_w \frac{q_0}{h_0} = \frac{L}{Ag}\frac{Q_0}{H_0}.$$

Typically T'_w is between 0.5 and 5 s.

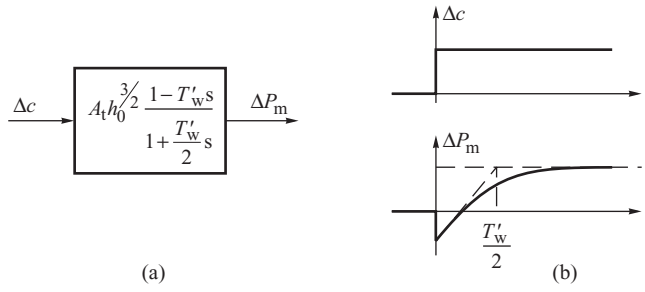

Figure 11.26 Hydraulic turbine: (a) linear model; (b) response of the linear turbine model to a step change in gate position.

This is the classic definition of water starting time but is dependent on the values of the head and flowrate at the linearization point. It therefore varies with load. If required, the constant A_t can be absorbed into the gate position when it effectively converts the gate opening to per unit turbine power on the generator MVA base. The block diagram of this linear turbine model is shown in Figure 11.26a.

Equation (11.157) describes an interesting and important characteristic of water turbines. For example, suppose that the position of the gate is suddenly closed slightly so as to reduce the turbine power output. The flowrate in the penstock cannot change instantaneously so the velocity of the flow through the turbine will initially increase. This increase in water velocity will produce an initial increase in the turbine power until, after a short delay, the flowrate in the penstock has time to reduce when the power will also reduce. This effect is reflected in Equation (11.157) by the minus sign in the numerator. This characteristic is shown in Figure 11.26b where a step increase in the gate position Δc initially produces a rapid drop in power output. As the flowrate in the penstock increases, the power output increases.

Although the linearized model (11.157) has been successfully used in both steady-state and transient stability studies, IEEE Committee Report (1992) recommends the use of the nonlinear turbine model in power system studies because its implementation using computers is no more difficult than the approximate linear transfer function. Other, more detailed models are discussed in IEEE Committee Reports (1973a, 1973b, 1973c, 1992).

11.3.2.2 Governing System for Hydraulic Turbines

Governing systems for hydraulic turbines differ from those used in steam turbines in two main ways. Firstly, a very high force is required to move the control gate as it must overcome both high water pressure and high friction forces and, secondly, the peculiar response of the hydraulic turbine to changes in valve position must be adequately compensated. To provide the necessary force to move the gate two servomotors are used as shown in the functional diagram in Figure 11.27a. In a similar way as in the steam turbine, the speed regulator acts through a system of levers on the *pilot valve* which controls the flow of hydraulic fluid into the *pilot servomotor*. The pilot servomotor then acts on the *relay valve* of the very high-power *main servomotor* which controls the gate position. Just like the servomotor on the steam turbine, negative feedback of the position of both the servomotors is necessary to achieve the required movement. To compensate for the peculiar response of the water turbine to changes in the gate position it is necessary to slow down the initial gate movement to allow the water flow in the penstock to catch up. This is achieved by the *transient droop* element which reduces the gain of the governor for fast changes in valve position and, in mechanical–hydraulic

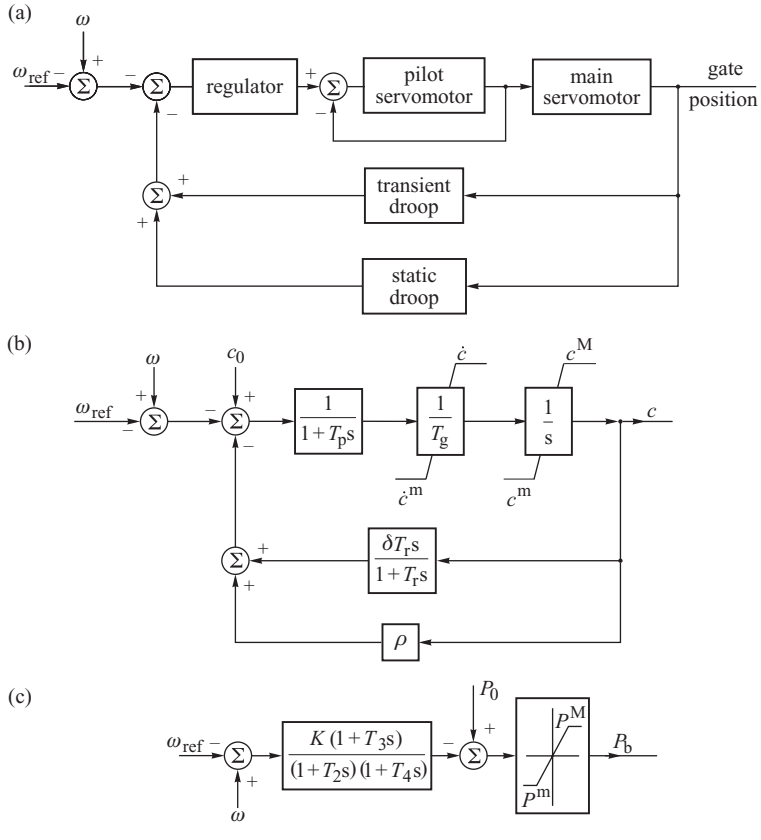

Figure 11.27 Block diagram of hydraulic turbine governing system: (a) functional diagram; (b) full diagram; (c) simplified diagram.

governor systems, is achieved by feeding back the position of the gate via a system of levers that includes a dashpot system. Similar to the steam turbine governor shown in Figure 2.11, direct feedback of the gate position through a series of levers controls the static droop.

The block diagram model of the governor, including the transient droop, is shown in Figure 11.27b. The main servomotor is modelled by an integrating element, with integration time T_g, and two limiters. The first limiter limits the gate position between fully open and fully closed, while the second, the rate limiter, limits the rate at which the gate can be moved. This is necessary because, if the gate is closed too rapidly, the resulting high pressure could damage the penstock. The pilot servomotor with its position feedback is modelled by a first-order lag with a time constant T_p. The system has two main feedback loops. The proportional feedback loop provides the static droop characteristic equal to ρ while the feedback loop with the differentiating element corrects the transient droop to a value δ. Typical values of the parameters recommended by Ramey and Skooglund (1970) are: $T_p = 0.04$ s, $T_g = 0.2$ s, $T_r = 5T'_w$, $\delta = 2.5T'_w/T_m$ and $\rho = 0.03$ to 0.06, where T'_w is the water starting time and T_m is the mechanical time constant of the unit.

Table 11.2 Typical values of parameters of turbine governing systems

	Parameters				
Type of turbine	ρ	T_1 (s)	T_2 (s)	T_3 (s)	T_4 (s)
Steam	0.02–0.07	0.1	0.2–0.3	0	—
Hydraulic	0.02–0.04	—	0.5	5	50

If the nonlinearities introduced by the limiters are, for the moment, neglected the system may be described by the third-order transfer function

$$\frac{\Delta c}{\Delta \omega} = \frac{\dfrac{(1 + T_r s)}{\rho}}{\dfrac{T_p T_r T_g}{\rho} s^3 + \dfrac{(T_p + T_r) T_g}{\rho} s^2 + \dfrac{T_g + T_r(\rho + \delta)}{\rho} s + 1}. \tag{11.158}$$

As the time constant T_p is several times smaller than the time constants T_g and T_r, it may be neglected to give the second-order transfer function

$$\frac{\Delta c}{\Delta \omega} = \frac{(1 + T_3 s)K}{(1 + T_2 s)(1 + T_4 s)}, \tag{11.159}$$

where $K = 1/\rho$, $T_2 \approx T_r T_g/[T_g + T_r(\rho + \delta)]$, $T_3 = T_r$ and $T_4 = [T_g + T_r(\rho + \delta)]/\rho$. Usually $T_4 \gg T_2$ when $T_4 + T_2 \approx T_4$.

If the gate limiters are now added to the transfer function the simplified governor block diagram shown in Figure 11.27c is obtained and is similar to the simplified system used to represent the steam turbine governor.

Typical parameter values for use in the simplified block diagram of the steam and hydraulic turbine governors are tabulated in Table 11.2.

11.3.3 Wind Turbines

Modelling the behaviour of wind turbines follows a similar approach to that for a conventional steam or water turbine except that now more detailed modelling of the energy resource is often required to take account of its variable nature.

11.3.3.1 Wind Energy Systems

Figures 7.5–7.11 in Section 7.1 described the general structure of wind turbine generation systems. Although the general structure of all these system options is similar, they differ in the type of electrical generator that is used and the way that it is controlled. However, all the systems can be broken down into a number of subsystems each of which can be modelled individually. Slootweg *et al.* (2003) suggests a convenient set of subsystems as follows:

1. A wind speed model representative of the site that takes account of turbulence, wind gusts and so on.
2. A rotor model that converts the power in the wind into mechanical power at the turbine low-speed drive shaft.
3. A transmission model that accounts for the effect of the gearbox, if present.
4. A model of the generator and, if necessary, its associated power electronic converter.

5. A power or speed controller to control the power output of the generator, particularly at wind speeds below rated speed, if required.
6. A voltage or reactive power controller, if required.
7. A pitch controller to control the power output of the turbine, particularly at wind speed above rated, if required.
8. A protection system for limiting converter current, isolating the turbine if voltage or frequency exceeds specified values. This system may also be required to shut the turbine down.

Not all these subsystems are required in all turbine and generator systems. However, items 1, 2, 4 and 8 will always be required while the other subsystems will depend on the type of generator and speed control system used. For example, the fixed-speed induction generator with stall control (Figure 7.6) will not require items 5 or 7 while the variable speed turbines utilizing pitch control will require all the subsystems to a greater or lesser extent.

11.3.3.2 Wind Speed

The wind is not steady. It is time variable and subject to variable amounts of turbulence depending on location. The wind speed can be modelled either by using a suitable spectral density method to predict turbulence or by directly recorded wind speed data. In either case the wind speed produced will be a *point wind speed*. Spectral models use a suitable transfer function to produce a time-domain turbulence variation of wind speed that can be added to a steady wind speed to obtain the net point wind speed (Leithead, Delasalle and Reardon, 1991; Leithead, 1992; Stannard and Bumby, 2007). In deriving this wind speed account can be taken of the nature of the terrain and the height above ground level. This wind speed may be valid over a time period of tens of seconds but for longer periods the model may need to be augmented by wind gusts and a steady increase in the mean wind speed (Slootweg *et al.*, 2003).

Because of the size of the wind turbine, the point wind speed will vary across the diameter of the turbine and the effective wind speed that the turbine reacts to will be different from the point wind speed. Leithead (1992) identifies four major effects of rotational sampling, wind shear, tower shadow and disc averaging. *Rotational sampling* accounts for the averaging of the torque over a rotational period while *tower shadow* takes account of the effect of blades passing in front of the tower (or behind if a downwind turbine) losing lift and hence torque. For a three-bladed wind turbine this tends to produce torque pulsations at three times the rotational speed. *Disc averaging* accounts for the fact that the turbulence will not be constant over the turbine swept area so impacting on the local point wind speed. Similarly *wind shear* recognizes that the diameter of the turbine is such that the effect of height above ground level cannot be assumed constant in the wind speed calculation. These effects should be included in computing the effective wind speed used in the turbine rotor model. Wind speed modelling is a sophisticated subject and interested readers are referred to the references above and also Wasynczuk, Man and Sullivan (1981) and Anderson and Bose (1983).

11.3.3.3 Turbine Rotor Model

The power from the turbine rotor can be calculated using Equation (7.1) but here it is modified slightly to make clear that the coefficient of performance depends on both the tip speed ratio and the pitch angle β of the blades

$$P = \frac{1}{2}\rho A c_{\mathrm{p}}(\lambda, \beta) v_{\mathrm{w}}^3. \tag{11.160}$$

Generally as the pitch angle is decreased the performance coefficient c_{p} reduces as shown in Figure 11.28.

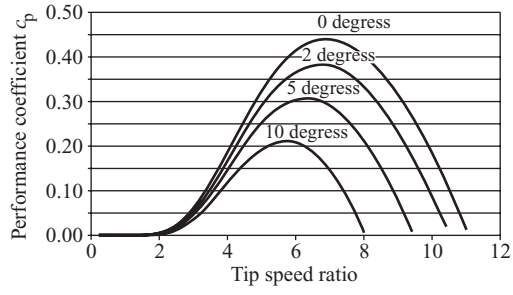

Figure 11.28 Turbine performance coefficient showing the effect of pitch angle.

The tip speed ratio depends on the turbine rotational speed and the wind speed and is given by Equation (7.2) as

$$\lambda = \frac{\omega_T r}{v_w}, \tag{11.161}$$

where the rotational speed of the turbine is ω_T and the wind speed v_w. The turbine rotor radius r is constant. To compute the tip speed ratio both the wind speed and the rotational speed of the turbine must be known. Knowing the tip speed ratio, the current value of c_p can be computed either from a look-up table that models the curves in Figure 11.28 or by using an appropriate curve fit to these curves. For example, Slootweg *et al.* (2003) use the approximation

$$c_p(\lambda, \beta) = 0.73\left(\frac{151}{\lambda_i} - 0.58\beta - 0.002\beta^{2.14} - 13.2\right) e^{-18.4/\lambda_i}, \tag{11.162a}$$

with

$$\lambda_i = \frac{1}{\dfrac{1}{\lambda - 0.02\beta} - \dfrac{0.003}{\beta^3 + 1}}. \tag{11.162b}$$

The variation of c_p with tip speed ratio produced by these curves is shown in Figure 11.28.

With the performance coefficient determined the turbine power can be calculated for the instantaneous effective wind speed using Equation (11.160). The turbine torque τ_T is then obtained from

$$\tau_T = \frac{P}{\omega_T}. \tag{11.163}$$

With this torque known, the turbine speed can be determined from the equation of motion.

11.3.3.4 Pitch Control System

The speed and torque control of a variable speed turbine is a sophisticated control process designed to maximize the power output of the turbine and prevent turbine overspeed. In its simplest form, at wind speeds below rated, controlling the generator electromagnetic torque as an optimized function of rotor speed will maximize energy capture and control the turbine speed. However, at high wind speed when the generator is operating at rated output the electromechanical torque cannot be increased further without overloading the generator and the speed and power output of the turbine must be controlled by pitching the turbine blades. A simple model of the pitch controller and the pitch actuator is shown in Figure 11.29. The pitch actuator is normally modelled by a first-order

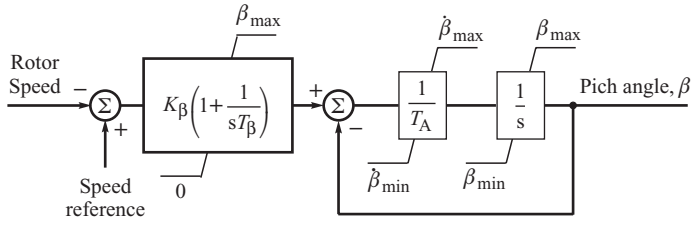

Figure 11.29 Pitch angle controller.

system with a time constant T_A but, as the pitch actuator is a relatively slow-moving hydraulic system, it is necessary to impose rate limits on the movement. Typically this may be of the order of 3° per second. The pitch controller used is normally a PI controller. Pitch control may only become operative at high wind speeds.

11.3.3.5 Shaft and Gear System

A schematic of the turbine shaft and gear system is shown in Figure 11.30 and assumes that the gearbox has a transmission ratio n so that the speed of the high-speed shaft of the generator ω_{mg} is related to the speed of the low-speed shaft of the turbine ω_{mT} by

$$\omega_{mg} = n\omega_{mT}. \tag{11.164}$$

For a perfect gearbox with no losses the power input and output are equal so that the torque on the high-speed shaft is related to the torque on the low-speed shaft by

$$\tau'_{tr} = \frac{\tau_{tr}}{n}. \tag{11.165}$$

Two equations of motion, one for the low-speed shaft and one for the high-speed shaft, describe the torque transmission in Figure 11.30:

$$J_T \frac{d\omega_{mT}}{dt} = \tau_T - \tau_{tr}, \tag{11.166}$$

$$J_g \frac{d\omega_{mg}}{dt} = \tau'_{tr} - \tau_g. \tag{11.167}$$

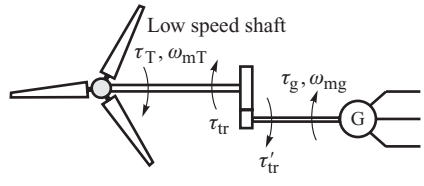

Figure 11.30 Turbine shaft and gear system.

Combining Equations (11.166) and (11.167) and referring all torques and speeds to the high-speed shaft gives the combined torque equation of motion referred to the high-speed shaft in SI units as

$$J\frac{\mathrm{d}\omega_{\mathrm{mg}}}{\mathrm{d}t} = \frac{\tau_{\mathrm{T}}}{n} - \tau_{\mathrm{g}}, \tag{11.168}$$

where

$$J = \left(J_{\mathrm{g}} + \frac{J_{\mathrm{T}}}{n^2}\right)$$

is the combined inertia of the turbine and generator referred to the high-speed shaft. If necessary τ_{tr} can allow for a finite shaft stiffness and shaft damping if required (Estanqueiro, 2007).

The above equation can readily be expressed in per-unit notation as described in Section 5.1 and Section 11.4 as

$$M\frac{\mathrm{d}\omega}{\mathrm{d}t} = \tau_{\mathrm{t}} - \tau_{\mathrm{g}}, \tag{11.169}$$

where $M = 2H/\omega_{\mathrm{s}}$.

If no gearbox is present the gear ratio $n = 1$.

11.3.3.6 Generator Model

The range of generators used in wind turbine systems are described in Section 7.1 with the 'fixed-speed' induction generator and doubly fed induction generator being most common. The fixed-speed induction generator can be modelled by the induction motor model described in detail in Section 11.4. This model is equally valid for generator action, the only difference being that the operational speed will now be greater than synchronous speed with the machine operating at negative slip. If required, the necessary sign changes can be made so that generator torque is positive.

In order to model the doubly fed induction generator, models of the generator, the power converter and its control system must be developed. Detailed models of these components that include the effect of the rotation emfs (see Section 11.1.3) are described in detail by Ekanayake, Holdsworth and Jenkins (2003) and Holdsworth *et al.* (2003). However, as discussed in Section 11.1.3, including the rotational emfs requires the power system network equations also to be modelled by differential equations rather than algebraic equations. Consequently, the detailed model is useful for single-machine, infinite-busbar simulations but not so useful for studies incorporating parallel generators and more complex networks. For this type of work a reduced order model is required, similar to that used for the fixed-speed induction generator in Section 11.4. Such a model is derived by Erlich *et al.* (2007).

11.4 Dynamic Load Models

Section 3.5 explained how power system loads, at the transmission and subtransmission levels, can be represented by a static load characteristic which describes how the real and reactive power at a busbar change with both voltage and frequency. Although this is an adequate method of representing modest changes of voltage and/or frequency for a composite load, there are cases when it is necessary to account for the dynamics of the load components themselves.

Typically, motors consume 60 to 70% of the total power system energy and their dynamics are important for studies of interarea oscillations, voltage stability and long-term stability. In this section the dynamic model of an induction motor will be presented. The dynamic model of the synchronous motor is not discussed as it is identical to that of the synchronous generator presented

in Section 11.1, except for a sign change on the armature current necessary to reflect the motoring action.

The induction motor can be modelled in the same way as the synchronous generator but with three important differences. Firstly, as there is no field winding in the induction motor, the cage rotor is modelled by two coils in quadrature (as for the damper windings in the synchronous machine) while the armature is modelled in the normal way by a d- and a q-axis armature coil. Secondly, as the induction motor does not rotate at synchronous speed, both the stator armature coils and the two rotor coils are transformed into a reference frame that rotates at synchronous speed. This means that the two rotor equations now include a rotational emf term proportional to the rotor slip speed $s\omega_s$ and are of the form

$$\begin{aligned} v_{dR} = 0 &= R_R i_{dR} + \dot{\Psi}_{dR} - s\omega_s \Psi_{qR} \\ v_{qR} = 0 &= R_R i_{qR} + \dot{\Psi}_{qR} + s\omega_s \Psi_{dR}, \end{aligned} \tag{11.170}$$

where the suffix 'R' signifies rotor quantities and the slip $s = (\omega_s - \omega)/\omega_s$.

The two rotational voltages are proportional to the rotor slip speed and to the flux linkage of the other rotor coil. During a disturbance the flux linkages Ψ_{qR} and Ψ_{dR} cannot change instantaneously and, just as in Equations (11.54) and (11.60), can be equated to d- and q-axis armature emfs E'_d and E'_q. If Equation (11.170) is further compared with (11.51) the rotational voltages $s\omega_s\Psi_{qR}$ and $s\omega_s\Psi_{dR}$ can be seen to play a similar role as the excitation voltage E_f and will therefore appear in the corresponding flux decay equations.

The third important difference is that positive current is now defined for motoring action, requiring a sign change in the appropriate equations.

With these points in mind Figure 11.31 shows how the induction motor can be modelled by a transient emf E' behind a transient impedance X' in the same way as in the fourth-order model of the synchronous generator (Section 11.1.6). However, as the reactance is unaffected by rotor position, and the model is in the synchronously rotating reference frame, the necessary equations are more conveniently expressed in the network (a, b) coordinates (Arrillaga and Arnold, 1990) as

$$\begin{bmatrix} V_b \\ V_a \end{bmatrix} = \begin{bmatrix} E'_b \\ E'_a \end{bmatrix} + \begin{bmatrix} R_S & X' \\ -X' & R_S \end{bmatrix} \begin{bmatrix} I_b \\ I_a \end{bmatrix}, \tag{11.171}$$

with the change in the emfs E'_b and E'_a given by

$$\begin{aligned} \dot{E}'_b &= -s\omega_s E'_a - \frac{E'_b - (X - X')I_a}{T'_0} \\ \dot{E}'_a &= s\omega_s E'_b - \frac{E'_a + (X - X')I_b}{T'_0}, \end{aligned} \tag{11.172}$$

where $s = (\omega_s - \omega)/\omega_s$ is the rotor slip, $X' = X_S + X_\mu X_R/(X_\mu + X_R)$ is the transient reactance and is equal to the blocked-rotor (short-circuit) reactance, $X = X_S + X_\mu$ is the motor no-load (open-circuit) reactance and $T'_0 = (X_R + X_\mu)/(\omega_s R_R)$ is the transient open-circuit time constant. The other reactances take the meaning explained in the induction motor's steady-state equivalent

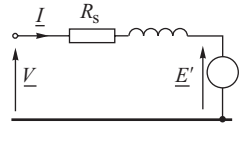

Figure 11.31 Transient state representation of induction motor.

circuit in Figure 3.28. The stator current can be calculated from Equation (11.171). Alternatively Equations (11.171) and (11.172) can be written directly in phasor notation as

$$\begin{aligned} \underline{V} &= \underline{E}' + \mathrm{j}X'\underline{I} + \underline{I}R_\mathrm{s} \\ \dot{\underline{E}}' &= -s\omega_\mathrm{s}\,\mathrm{j}\underline{E}' - \frac{[\underline{E}' - \mathrm{j}\underline{I}(X - X')]}{T_0'}. \end{aligned} \tag{11.173}$$

To evaluate the slip $s = (\omega_\mathrm{s} - \omega)/\omega_\mathrm{s}$ it is necessary to calculate the rotor speed ω from the equation of motion

$$J\frac{\mathrm{d}\omega}{\mathrm{d}t} = \tau_\mathrm{e} - \tau_\mathrm{m}, \tag{11.174}$$

where J is the inertia of the motor and load, τ_m is the mechanical load torque and τ_e is the electromagnetic torque that can be converted into useful work.

Taking into account that the slip is $s = (\omega_\mathrm{s} - \omega)/\omega_\mathrm{s}$ and using the notation shown in the equivalent circuit of Figure 3.28, the induction motor air-gap power can be expressed as

$$P_\mathrm{ag} = I^2\frac{R}{s} = I^2 R\frac{\omega_\mathrm{s}}{\omega_\mathrm{s} - \omega}, \tag{11.175}$$

while the electromagnetic power P_e is given by

$$P_\mathrm{e} = I^2 R\frac{(1-s)}{s} = P_\mathrm{ag}(1-s) = P_\mathrm{ag}\frac{\omega}{\omega_\mathrm{s}}. \tag{11.176}$$

The electromagnetic torque may now be expressed using the last two equations as

$$\tau_\mathrm{e} = \frac{P_\mathrm{e}}{\omega} = \frac{P_\mathrm{ag}}{\omega_\mathrm{s}}, \tag{11.177}$$

where for the considered model (Figure 11.28)

$$P_\mathrm{ag} = \mathrm{Re}(\underline{E}'\underline{I}^*) = E_\mathrm{b}' I_\mathrm{b} + E_\mathrm{a}' I_\mathrm{a}. \tag{11.178}$$

Normally τ_m will vary with speed and is commonly represented by a quadratic equation of the form

$$\tau_\mathrm{m} = \tau_{\mathrm{m}0}(A\omega^2 + B\omega + C), \tag{11.179}$$

where $\tau_{\mathrm{m}0}$ is the rated load torque, $A\omega_0^2 + B\omega_0 + C = 1$ and ω_0 is the rated speed. For example, a simple pump load, the torque of which is proportional to speed squared, can be represented by setting $B = C = 0$.

The above analysis is derived for single-cage induction motors but can be readily extended to double-cage and deep-bar rotors by using slip-dependent rotor parameters $X_\mathrm{R}(s)$ and $R_\mathrm{R}(s)$ in the calculation of X' and T_0' as explained by Arrillaga and Arnold (1990). However, in many cases it is sufficient to model the induction motor by its steady-state equivalent circuit when the electrical torque is obtained from the static torque–speed characteristic and the slip calculated via Equation (11.174). The format of the induction motor dynamic model is similar to that of the synchronous generator, so its inclusion in a simulation program is relatively straightforward.

With the increased penetration of renewable generation often connected at the distribution level, it may become necessary to include dynamic models of distribution networks when assessing the system stability. As that would increase the size of the problem quite considerably, dynamic equivalents of the full distribution network model could be used – see Chapter 14. Often the actual configuration and models of generators connected may not be known and then the equivalent would

be derived from measurements of certain electrical quantities taken inside the distribution network and/or at the border nodes – see, for example, Feng, Lubosny and Bialek (2007).

11.5 FACTS Devices

In power system stability analysis it necessary to include dynamic models of those elements whose control is fast enough to influence electromechanical dynamics. FACTS elements belong to that category and were described in Section 2.5. CIGRE (Technical Brochure No. 145) published a detailed report on modelling FACTS devices. Here only some simple models will be discussed.

11.5.1 Shunt FACTS Devices

Figure 11.32 shows a dynamic model of the SVC based on conventional thyristors. The model is developed from the simplified model shown in Figure 2.28. The first and second blocks of the dynamic model represent the regulator. Time constants T_1, T_2 of the correction block are chosen based on stability analysis of the power system. That choice is heavily influenced by the type of optional power system stabilizer (PSS) whose task is to stabilize control of the compensator (see Section 10.5). The gain of the regulator is $K \approx 10$–100. Such a gain corresponds to the droop of the regulator static characteristic (Figure 2.29) of about 1−10 %. The time constant of the regulator is $T_R \approx 20$–150 ms. The third block represents the thyristor firing circuits. The time constants are in the range $T_d \approx 1$ ms and $T_b \approx 10$–50 ms. At the bottom of the diagram there is a differentiating block used in the SVC to stabilize the circuit using the compensator current I_{SVC}.

In the discussed SVC model the most important role is played by the models of the voltage regulator and the PSS. From the point of view of electromechanical dynamics, thyristors and their firing circuits are proportional elements.

The dynamic model of STATCOM is shown in Figure 11.33 and includes the regulator's transfer function and the feedback loop ρ enforcing a required droop of the compensator static characteristic (Figure 2.31). The converter is modelled by a first-order block with time constant $T_C = 10$–30 ms. The output signal is the compensator current. In the steady state when $t \to \infty$ or $s \to 0$ the model results in the static characteristic shown in Figure 2.31 with droop ρ.

11.5.2 Series FACTS Devices

The most general series FACTS device is the UPFC described in Section 2.4. Hence here only the dynamic model of the UPFC will be discussed. Descriptions of models of other series FACTS devices can be found in CIGRE (Technical Brochure No. 145).

Figure 2.38 shows that the UPFC has two voltage-sourced converters and each of them is equipped with its own PWM controller with two control parameters: m_1, ψ_1 for CONV 1 and

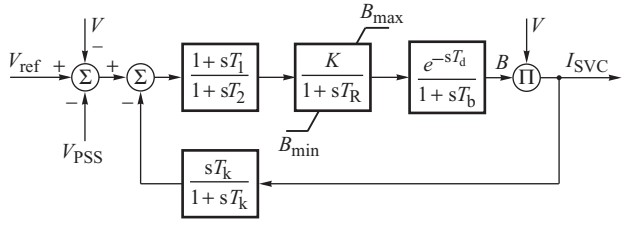

Figure 11.32 Simplified dynamic model of the SVC.

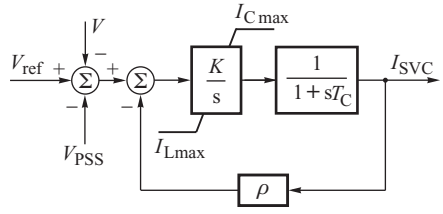

Figure 11.33 Simplified dynamic model of STATCOM.

m_2, ψ_2 for CONV 2. These four parameters are selected by the UPFC regulator controlling the following three important quantities:

1. Direct component Re($\underline{\Delta V}$) of the booster voltage.
2. Quadrature component Im($\underline{\Delta V}$) of the booster voltage.
3. Reactive component of the shunt current Im($\underline{I}_{shunt}$).

From the point of view of electromechanical dynamics, thyristors and their firing circuits are proportional elements and may be neglected. Hence the dynamic model of the UPFC consists of its regulator model including technical constraints and is shown in Figure 11.34. The input variables in the series part of the regulator (Figure 11.34a) are the transmitted real and reactive power. The output variables are the direct and quadrature components of the booster voltage. The reference values at the input of the regulator are divided by the actual voltage values in order to obtain the required current components. The actual values of the components are subtracted from the reference ones in order to create control errors. The regulator is of integral type with negative feedback. The time constants of the integral block $T_P = T_Q$ are chosen depending on the speed with which power flow has to be regulated and on the type of PSS used. Converters are modelled

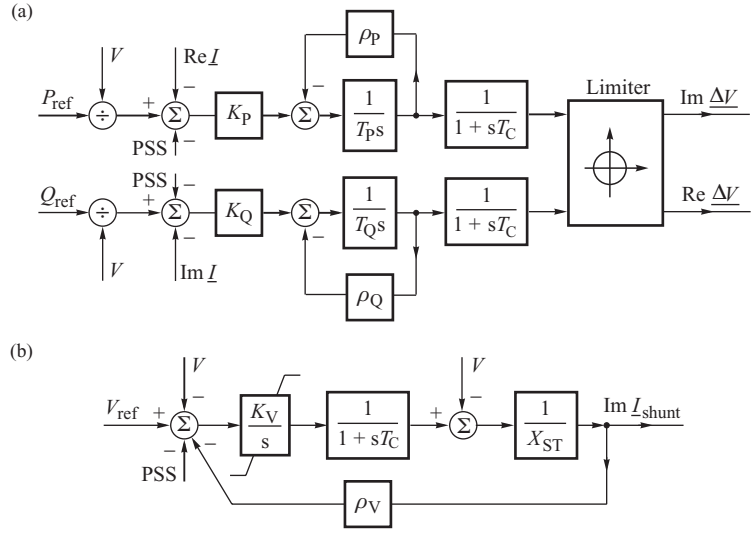

Figure 11.34 Simplified dynamic model of the UPFC with regulators: (a) series part; (b) shunt part.

by first-order blocks with time constants in the range of $T_C = 10$–30 ms. There is a limiter on the output of the regulator that proportionally reduces the components of the booster voltage when its magnitude exceeds the allowed value.

The input signal of the regulator's shunt part (Figure 11.34b) is the busbar voltage while the output signal is the reactive component of the shunt current. The regulator is of integral type with constraints. The converter is modelled by a first-order block. The output of the block produces the converter voltage, that is the voltage on the lower side of the excitation (supply) transformer. From that value the voltage on the upper side of the excitation transformer is subtracted in order to obtain the reactive part of the UPFC shunt current. Similar to STATCOM, there is also a negative feedback loop responsible for a required droop of the static characteristic. There is also an additional signal PSS entering the summation point of regulation loops. This signal is due to an additional optional block responsible for damping of power swings in the system – see Section 10.7.

12

Steady-State Stability of Multi-Machine System

The steady-state, or small-signal, stability of a power system is the ability of the system to maintain synchronism when subjected to a small disturbance. In Chapter 5 the steady-state stability of the generator–infinite busbar system was discussed and the system was seen to be steady-state stable about an equilibrium point if, following a small disturbance, the system remained within a small region surrounding the equilibrium point. In such cases the system is said to be locally stable. Furthermore, if, as time progresses, the system returns to the equilibrium point, then it is also said to be asymptotically stable. These concepts, and those introduced in Chapter 5, will be expanded in this chapter to assess the steady-state stability of a multi-machine power system in which the generators are described by the mathematical models introduced in Chapter 11.

12.1 Mathematical Background

Section 5.4.6 analysed the classical model of a synchronous generator connected to the infinite busbar and showed that rotor swings around the synchronous speed can be described by a second-order differential equation (the swing equation). Depending on the values of the roots of the characteristic equation (5.59), the swings can be aperiodic or oscillatory. A power system consists of many generators and each of the generators is more accurately described by a higher order model discussed in Section 11.1.6. Consequently a real power system will be described by a high number of nonlinear differential equations. This chapter will analyse the steady-state stability of such a large dynamic system using *eigenvalue analysis*. The main aim of eigenvalue analysis is to simplify analysis of a large dynamic system by representing the system response to a disturbance as a linear combination of uncoupled aperiodic and oscillatory responses, similar to those analysed in Section 5.4.6 and referred to as the *modes*.

12.1.1 Eigenvalues and Eigenvectors

A number λ is referred to as an *eigenvalue* of matrix $\boldsymbol{A}$ if there is a nonzero column vector $\boldsymbol{w}$ satisfying

$$\boldsymbol{A}\boldsymbol{w} = \boldsymbol{w}\lambda. \tag{12.1}$$

Power System Dynamics: Stability and Control, Second Edition Jan Machowski, Janusz W. Bialek and James R. Bumby
© 2008 John Wiley & Sons, Ltd

Each such vector $\boldsymbol{w}$ is referred to as the *right eigenvector* associated with eigenvalue λ. Equation (12.1) shows that eigenvectors are not unique as they can be rescaled by multiplying or dividing the elements by a nonzero number. If $\boldsymbol{w}_i$ is an eigenvector then any other vector $c\boldsymbol{w}_i$ is also an eigenvector, where $c \neq 0$ is a nonzero number. This property makes it possible to multiply or divide eigenvectors by any number. In practice eigenvalues are normalized by dividing their values by the vector length

$$\|\boldsymbol{w}\| = \sqrt{\boldsymbol{w}^{\mathrm{T}^*}\boldsymbol{w}} = \sqrt{|w_1|^2 + \cdots + |w_n|^2}. \tag{12.2}$$

Equation (12.1) can be rewritten as

$$(\boldsymbol{A} - \lambda\ \mathbf{1})\ \boldsymbol{w} = \mathbf{0}, \tag{12.3}$$

where $\mathbf{1}$ is a diagonal identity matrix while $\mathbf{0}$ is a column vector of zeros. Equation (12.3) has a non-trivial solution $\boldsymbol{w} \neq \mathbf{0}$ if and only if

$$\det(\boldsymbol{A} - \lambda\ \mathbf{1}) = 0. \tag{12.4}$$

Equation (12.4) is called the *characteristic equation*. It can be written in a polynomial form

$$\det(\boldsymbol{A} - \lambda\ \mathbf{1}) = \varphi(\lambda) = (-1)^n(\lambda^n + c_{n-1}\lambda^{n-1} + \cdots + c_1\lambda + c_0), \tag{12.5}$$

where n is the rank of $\boldsymbol{A}$, c_{n-1} is the sum of the main minors of the first degree, c_{n-2} is the sum of the main minors of the second degree and so on, and finally c_0 is the main minor of the highest degree, that is the determinant of matrix $\boldsymbol{A}$. Polynomial (12.5) is of the nth order and therefore has n roots $\lambda_1,\ \lambda_2, \ldots,\ \lambda_n$ which are at the same time the eigenvalues of matrix $\boldsymbol{A}$.

Numerical methods for determining the eigenvalues and eigenvectors of a matrix can be found in Press *et al.* (1992) or other textbooks on numerical methods and they will not be dealt with in this book. Instead, attention will be concentrated on the application of eigenvalues and eigenvectors to the stability analysis of power systems.

Knowing eigenvalue λ_i of matrix $\boldsymbol{A}$, it is easy to find its associated eigenvector $\boldsymbol{w}_i$ using the following equation:

$$\boldsymbol{w}_i = \mathrm{col}\ (\boldsymbol{A} - \lambda_i\ \mathbf{1})^{\mathrm{D}}, \tag{12.6}$$

where col denotes selection of any non-zero column from a square matrix and upper index D denotes an adjacent matrix. The correctness of Equation (12.6) can be proved using the definition of the adjacent matrix. For any matrix $\boldsymbol{B}$ it holds that $\boldsymbol{B}\boldsymbol{B}^{\mathrm{D}} = \det \mathbf{B} \cdot \mathbf{1}$. This property is true also for matrix $\boldsymbol{B} = (\boldsymbol{A} - \lambda_i\ \mathbf{1})$, which can be written as $(\boldsymbol{A} - \lambda_i\ \mathbf{1})(\boldsymbol{A} - \lambda_i\ \mathbf{1})^{\mathrm{D}} = \det(\boldsymbol{A} - \lambda_i\ \mathbf{1}) \cdot \mathbf{1}$. Hence, taking into account (12.4), one gets $(\boldsymbol{A} - \lambda_i\ \mathbf{1})(\boldsymbol{A} - \lambda_i\ 1)^{\mathrm{D}} = 0 \cdot \mathbf{1}$. This equation shows that multiplying matrix $(\boldsymbol{A} - \lambda_i\ \mathbf{1})$ by any column of matrix $(\boldsymbol{A} - \lambda_i\ \mathbf{1})^{\mathrm{D}}$ gives $0 \cdot \mathbf{1} = \mathbf{0}$, where $\mathbf{0}$ is a column vector of zeros. This shows that if $\boldsymbol{a} \neq \mathbf{0}$ is a non-zero column of $(\boldsymbol{A} - \lambda_i\ \mathbf{1})^{\mathrm{D}}$, then $(\boldsymbol{A} - \lambda_i\ \mathbf{1})\boldsymbol{a} = \mathbf{0}$, or $\boldsymbol{A}\boldsymbol{a} = \lambda_i\ \boldsymbol{a}$. This shows, according to Equation (12.1), that $\boldsymbol{a} = \boldsymbol{w}_i$ is a right eigenvector associated with λ_i. In other words, any non-zero column of $(\boldsymbol{A} - \lambda_i\ \mathbf{1})^{\mathrm{D}}$ is an eigenvector of $\boldsymbol{A}$ associated with λ_i.

This methodology can be used to determine eigenvectors for all eigenvalues if the eigenvalues are distinct, that is $\lambda_1 \neq \lambda_2 \neq \cdots \neq \lambda_n$. However, if λ_i is a multiple eigenvalue repeated k times then the described methodology can be used to determine only one eigenvector associated with such a multiple eigenvalue. The other $(k - 1)$ linearly independent eigenvectors associated with λ_i have to be determined in a different way. This will not be discussed here; the reader can find details in many textbooks, for example Ogata (1967).

A square complex matrix $\boldsymbol{A}$ is Hermitian if $\boldsymbol{A}^{\mathrm{T}^*} = \boldsymbol{A}$, that is the transposed conjugate matrix $\boldsymbol{A}^{\mathrm{T}^*}$ is equal to $\boldsymbol{A}$. Obviously a real symmetrical matrix $\boldsymbol{A} = \boldsymbol{A}^{\mathrm{T}}$ satisfies the definition of a Hermitian matrix as for a real matrix $\boldsymbol{A}^* = \boldsymbol{A}$.

Now it will be shown that eigenvalues of a Hermitian matrix are always real. The proof will be indirect by assuming that there is a complex eigenvalue $\lambda = \alpha + \mathrm{j}\Omega$. Then Equation (12.1) gives

$$\boldsymbol{A}\boldsymbol{w} = \boldsymbol{w}(\alpha + \mathrm{j}\Omega). \tag{12.7}$$

Left-multiplying this equation by $\boldsymbol{w}^{\mathrm{T}^*}$ gives

$$\boldsymbol{w}^{\mathrm{T}^*}\boldsymbol{A}\boldsymbol{w} = (\alpha + \mathrm{j}\Omega)\boldsymbol{w}^{\mathrm{T}^*}\boldsymbol{w}. \tag{12.8}$$

Transposing and conjugating (12.8) gives $\boldsymbol{w}^{\mathrm{T}^*}\boldsymbol{A}^{\mathrm{T}^*} = (\alpha - \mathrm{j}\Omega)\boldsymbol{w}^{\mathrm{T}^*}$. As $\boldsymbol{A}^{\mathrm{T}^*} = \boldsymbol{A}$, one can write

$$\boldsymbol{w}^{\mathrm{T}^*}\boldsymbol{A} = (\alpha - \mathrm{j}\Omega)\boldsymbol{w}^{\mathrm{T}^*}. \tag{12.9}$$

Right-multiplying this by $\boldsymbol{w}$ gives

$$\boldsymbol{w}^{\mathrm{T}^*}\boldsymbol{A}\boldsymbol{w} = (\alpha - \mathrm{j}\Omega)\boldsymbol{w}^{\mathrm{T}^*}\boldsymbol{w}. \tag{12.10}$$

Comparing (12.8) and (12.10) results in

$$(\alpha + \mathrm{j}\Omega)\boldsymbol{w}^{\mathrm{T}^*}\boldsymbol{w} = (\alpha - \mathrm{j}\Omega)\boldsymbol{w}^{\mathrm{T}^*}\boldsymbol{w}. \tag{12.11}$$

Obviously $\boldsymbol{w}^{\mathrm{T}^*}\boldsymbol{w} \neq 0$ is real and positive as the sum of products of complex conjugate numbers. Hence Equation (12.11) results in $(\alpha + \mathrm{j}\Omega) = (\alpha - \mathrm{j}\Omega)$, or $\alpha + \mathrm{j}\Omega - \alpha + \mathrm{j}\Omega = 0$. Obviously the imaginary part must be zero, $\mathrm{j}2\Omega = 0$, which proves that the eigenvalues of a Hermitian matrix are real.

Example 12.1

Using Equation (12.6), find right eigenvalues of the following symmetrical matrix:

$$\boldsymbol{A} = \left[\begin{array}{c|c|c} 5 & 0 & 0 \\ \hline 0 & 2 & -\sqrt{2} \\ \hline 0 & -\sqrt{2} & 3 \end{array}\right]. \tag{12.12}$$

The characteristic equation is

$$\det(\boldsymbol{A} - \lambda 1) = \left[\begin{array}{c|c|c} 5-\lambda & 0 & 0 \\ \hline 0 & 2-\lambda & -\sqrt{2} \\ \hline 0 & -\sqrt{2} & 3-\lambda \end{array}\right] = (5-\lambda)[(2-\lambda)(3-\lambda) - 2] = (5-\lambda)(\lambda^2 - 5\lambda + 4)] = 0.$$

Hence $(5 - \lambda)(\lambda - 4)(\lambda - 1) = 0$, which means that: $\lambda_1 = 5$; $\lambda_2 = 4$; $\lambda_3 = 1$.

For $\lambda_1 = 5$ one gets

$$(\boldsymbol{A} - \lambda_1 \mathbf{1}) = \begin{bmatrix} 0 & 0 & 0 \\ 0 & -3 & -\sqrt{2} \\ 0 & -\sqrt{2} & -2 \end{bmatrix}, \quad (\boldsymbol{A} - \lambda_1 \mathbf{1})^{\mathrm{T}} = \begin{bmatrix} 0 & 0 & 0 \\ 0 & -3 & -\sqrt{2} \\ 0 & -\sqrt{2} & -2 \end{bmatrix},$$

$$(\boldsymbol{A} - \lambda_1 \mathbf{1})^{\mathrm{D}} = \begin{bmatrix} 4 & 0 & 0 \\ 0 & 0 & 0 \\ 0 & 0 & 0 \end{bmatrix}$$

$$(\boldsymbol{A} - \lambda_2 \mathbf{1}) = \begin{bmatrix} 1 & 0 & 0 \\ 0 & -2 & -\sqrt{2} \\ 0 & -\sqrt{2} & -1 \end{bmatrix}, \quad (\boldsymbol{A} - \lambda_2 \mathbf{1})^{\mathrm{T}} = \begin{bmatrix} 1 & 0 & 0 \\ 0 & -2 & -\sqrt{2} \\ 0 & -\sqrt{2} & -1 \end{bmatrix},$$

$$(\boldsymbol{A} - \lambda_2 \mathbf{1})^{\mathrm{D}} = \begin{bmatrix} 0 & 0 & 0 \\ 0 & -1 & \sqrt{2} \\ 0 & \sqrt{2} & -2 \end{bmatrix}$$

$$(\boldsymbol{A} - \lambda_3 \mathbf{1}) = \begin{bmatrix} 4 & 0 & 0 \\ 0 & 1 & -\sqrt{2} \\ 0 & -\sqrt{2} & 2 \end{bmatrix}, \quad (\boldsymbol{A} - \lambda_3 \mathbf{1})^{\mathrm{T}} = \begin{bmatrix} 4 & 0 & 0 \\ 0 & 1 & -\sqrt{2} \\ 0 & -\sqrt{2} & 2 \end{bmatrix},$$

$$(\boldsymbol{A} - \lambda_3 \mathbf{1})^{\mathrm{D}} = \begin{bmatrix} 0 & 0 & 0 \\ 0 & 8 & 4\sqrt{2} \\ 0 & 4\sqrt{2} & 4 \end{bmatrix}.$$

For λ_1, only one column is different from zero. This column can therefore be taken as an eigenvector, divided by, for example, four. For λ_2, the second and third columns are non-zero. As an eigenvector, for example, third column can be chosen divided by four. Similarly for λ_3. Consequently, the following eigenvectors are obtained:

$$\boldsymbol{w}_1 = \begin{bmatrix} 1 \\ 0 \\ 0 \end{bmatrix}, \quad \boldsymbol{w}_2 = \begin{bmatrix} 0 \\ -1 \\ \sqrt{2} \end{bmatrix}, \quad \boldsymbol{w}_3 = \begin{bmatrix} 0 \\ \sqrt{2} \\ 1 \end{bmatrix}; \quad \text{hence} \quad \boldsymbol{W} = \begin{bmatrix} 1 & 0 & 0 \\ 0 & -1 & \sqrt{2} \\ 0 & \sqrt{2} & 1 \end{bmatrix}. \tag{12.13}$$

The eigenvectors in all examples in this chapter are not normalized in order to make manual calculations easy by maintaining round numbers.

A real unsymmetric matrix $\boldsymbol{A} \neq \boldsymbol{A}^{\mathrm{T}}$ may have real eigenvalues (Example 12.1) or complex eigenvalues or a mix of real and complex eigenvalues. Regarding complex eigenvalues, the following property holds:

> If matrix $\boldsymbol{A} \neq \boldsymbol{A}^{\mathrm{T}}$ has a complex eigenvalue λ_i then the complex conjugate number λ_i^* is also an eigenvalue of that matrix. Moreover, the eigenvector associated with λ_i^* is equal to the conjugate eigenvector associated with λ_i.

In other words, complex eigenvalues and eigenvectors appear in complex conjugate pairs:

$$\lambda_i, \ \boldsymbol{w}_i \quad \text{and} \quad \lambda_i^*, \boldsymbol{w}_i^*. \tag{12.14}$$

Proof of this important property is simple and results from Equation (12.1) while taking into account that for a real matrix $\boldsymbol{A}^* = \boldsymbol{A}$. Conjugating $\boldsymbol{A}\boldsymbol{w}_i = \boldsymbol{w}_i\lambda_i$ (without transposing) gives $\boldsymbol{A}\boldsymbol{w}_i^* = \boldsymbol{w}_i^*\lambda_i^*$. Hence λ_i^*, $\boldsymbol{w}_i^*$ satisfy the definition of an eigenvalue and eigenvector of matrix $\boldsymbol{A}$.

Obviously a pair of complex conjugate eigenvalues constitutes two distinct eigenvalues $\lambda_i^* \neq \lambda_i$ and therefore their associated eigenvectors are linearly independent, that is $\boldsymbol{w}_i^* \neq c\boldsymbol{w}_i$ for any $c \neq 0$.

Example 12.2

Calculate the eigenvalues and eigenvectors of the matrix

$$\boldsymbol{A} = \begin{bmatrix} -6 & 0 & 0 \\ 0 & -1 & 5 \\ 0 & -5 & -1 \end{bmatrix} \quad \det(\boldsymbol{A} - \lambda\,\mathbf{1}) = \begin{bmatrix} -6-\lambda & 0 & 0 \\ 0 & -1-\lambda & 5 \\ 0 & -5 & -1-\lambda \end{bmatrix}. \tag{12.15}$$

As there are two zero elements in the first row, expansion of the determinant is easy:

$$\det(\boldsymbol{A} - \lambda\,\mathbf{1}) = (-6-\lambda)\,[(1+\lambda)(1+\lambda) + 5 \cdot 5] = -(6+\lambda)[\lambda^2 + 2\lambda + 26] = 0.$$

Consider the second-degree polynomial in the square brackets. The determinant of that polynomial is negative giving a pair of complex conjugate roots:

$$\det(\boldsymbol{A} - \lambda\,\mathbf{1}) = -(6+\lambda)[\lambda - (-1-\mathrm{j}5)][\lambda - (-1+\mathrm{j}5)] = 0. \tag{12.16}$$

Hence matrix $\boldsymbol{A}$ will have the following eigenvalues:

$$\lambda_1 = -6, \quad \lambda_2 = (-1-\mathrm{j}5), \quad \lambda_3 = (-1+\mathrm{j}5) = \lambda_2^*. \tag{12.17}$$

Eigenvectors can be calculated from Equation (12.6), using the adjacent matrix similarly as in Example 12.1:

$$(\boldsymbol{A} - \lambda_1\,\mathbf{1}) = \begin{bmatrix} 0 & 0 & 0 \\ 0 & 5 & 5 \\ 0 & -5 & 5 \end{bmatrix}, \quad (\boldsymbol{A} - \lambda_1\,\mathbf{1})^{\mathrm{T}} = \begin{bmatrix} 0 & 0 & 0 \\ 0 & 5 & -5 \\ 0 & 5 & 5 \end{bmatrix}, \quad (\boldsymbol{A} - \lambda_1\,\mathbf{1})^{\mathrm{D}} = \begin{bmatrix} 50 & 0 & 0 \\ 0 & 0 & 0 \\ 0 & 0 & 0 \end{bmatrix}$$

$$(\boldsymbol{A}-\lambda_2\,\mathbf{1}) = \left[\begin{array}{c|c|c} -5+\mathrm{j}5 & 0 & 0 \\ \hline 0 & \mathrm{j}5 & 5 \\ \hline 0 & -5 & \mathrm{j}5 \end{array}\right], \quad (\boldsymbol{A}-\lambda_2\,\mathbf{1})^{\mathrm{T}} = \left[\begin{array}{c|c|c} -5+\mathrm{j}5 & 0 & 0 \\ \hline 0 & \mathrm{j}5 & -5 \\ \hline 0 & 5 & \mathrm{j}5 \end{array}\right],$$

$$(\boldsymbol{A}-\lambda_2\,\mathbf{1})^{\mathrm{D}} = \left[\begin{array}{c|c|c} 0 & 0 & 0 \\ \hline 0 & -25-\mathrm{j}25 & 25-\mathrm{j}25 \\ \hline 0 & -25+\mathrm{j}25 & -25-\mathrm{j}25 \end{array}\right]$$

$$(\boldsymbol{A}-\lambda_3\,\mathbf{1}) = \left[\begin{array}{c|c|c} -5-\mathrm{j}5 & 0 & 0 \\ \hline 0 & -\mathrm{j}5 & 5 \\ \hline 0 & -5 & -\mathrm{j}5 \end{array}\right], \quad (\boldsymbol{A}-\lambda_3\,\mathbf{1})^{\mathrm{T}} = \left[\begin{array}{c|c|c} -5-\mathrm{j}5 & 0 & 0 \\ \hline 0 & -\mathrm{j}5 & -5 \\ \hline 0 & 5 & -\mathrm{j}5 \end{array}\right],$$

$$(\boldsymbol{A}-\lambda_3\,\mathbf{1})^{\mathrm{D}} = \left[\begin{array}{c|c|c} 0 & 0 & 0 \\ \hline 0 & -25+\mathrm{j}25 & 25+\mathrm{j}25 \\ \hline 0 & -25-\mathrm{j}25 & -25+\mathrm{j}25 \end{array}\right].$$

For λ_1, only the first column is non-zero and dividing it by 50 gives eigenvector $\boldsymbol{w}_1$. For λ_2, the second and third columns are non-zero. The second column, divided by 25, may be assumed to be eigenvector $\boldsymbol{w}_2$. Similarly for λ_3, the second and third columns are non-zero. To be consistent, the second column, divided by 25, may be assumed to be eigenvector $\boldsymbol{w}_3$, giving

$$\boldsymbol{w}_1 = \left[\begin{array}{c} 1 \\ \hline 0 \\ \hline 0 \end{array}\right], \quad \boldsymbol{w}_2 = \left[\begin{array}{c} 0 \\ \hline -1-\mathrm{j}1 \\ \hline -1+\mathrm{j}1 \end{array}\right], \quad \boldsymbol{w}_3 = \left[\begin{array}{c} 0 \\ \hline -1+\mathrm{j}1 \\ \hline -1-\mathrm{j}1 \end{array}\right] = \boldsymbol{w}_2^*. \tag{12.18}$$

Hence $\lambda_3 = \lambda_2^*$ resulted in $\boldsymbol{w}_3 = \boldsymbol{w}_2^*$.

Example 12.2 confirmed that complex eigenvalues and eigenvectors form complex conjugate pairs as in Equation (12.14). This property is important for further considerations.

12.1.2 Diagonalization of a Square Real Matrix

Let λ_i and $\boldsymbol{w}_i$ be an eigenvalue and a right eigenvector of matrix $\boldsymbol{A}$. Then for every pair of eigenvalues and eigenvectors, $\boldsymbol{A}\boldsymbol{w}_i = \boldsymbol{w}_i\lambda_i$ holds and

$$\boldsymbol{A}[\boldsymbol{w}_1,\ \boldsymbol{w}_2, \ldots,\ \boldsymbol{w}_n] = [\boldsymbol{w}_1,\ \boldsymbol{w}_2\ , \ldots,\ \boldsymbol{w}_n] \begin{bmatrix} \lambda_1 & 0 & \cdots & 0 \\ 0 & \lambda_2 & \cdots & 0 \\ \vdots & \vdots & \ddots & \vdots \\ 0 & 0 & \cdots & \lambda_n \end{bmatrix} \quad \text{or} \quad \boldsymbol{A}\boldsymbol{W} = \boldsymbol{W}\boldsymbol{\Lambda}, \tag{12.19}$$

where $\boldsymbol{W} = [\boldsymbol{w}_1,\ \boldsymbol{w}_2, \ldots,\ \boldsymbol{w}_n]$ is a square matrix whose columns are the right eigenvectors of matrix $\boldsymbol{A}$ and $\boldsymbol{\Lambda} = \operatorname{diag} \lambda_i$ is a diagonal matrix of the corresponding eigenvalues.

If all the eigenvalues λ_i are distinct, $\lambda_1 \neq \lambda_2 \neq \cdots \neq \lambda_n$, then the corresponding eigenvectors are linearly independent. The proof of this property is conducted indirectly by assuming that the eigenvectors are linearly dependent and showing that the false assumption leads to a contradiction. Details can be found in many textbooks, for example Ogata (1967).

If vectors $\boldsymbol{w}_1,\ \boldsymbol{w}_2, \ldots,\ \boldsymbol{w}_n$ are linearly independent then matrix $\boldsymbol{W}$ made up from those vectors is non-singular and the inverse $\boldsymbol{U} = \boldsymbol{W}^{-1}$ exists. The following notation will be used:

$$\boldsymbol{U} = \boldsymbol{W}^{-1} = [\boldsymbol{w}_1,\ \boldsymbol{w}_2, \ldots,\ \boldsymbol{w}_n]^{-1} = \begin{bmatrix} \boldsymbol{u}_1 \\ \boldsymbol{u}_2 \\ \vdots \\ \boldsymbol{u}_n \end{bmatrix}, \tag{12.20}$$

where $\boldsymbol{u}_i$ are the rows of matrix $\boldsymbol{U} = \boldsymbol{W}^{-1}$. Pre-multiplying both sides of Equation (12.19) by $\boldsymbol{W}^{-1}$ gives

$$\boldsymbol{\Lambda} = \operatorname{diag} \lambda_i = \boldsymbol{W}^{-1}\boldsymbol{A}\boldsymbol{W} = \boldsymbol{U}\boldsymbol{A}\boldsymbol{W}. \tag{12.21}$$

Right-multiplying this equation by $\boldsymbol{W}^{-1} = \boldsymbol{U}$ gives $\boldsymbol{U}\boldsymbol{A} = \boldsymbol{\Lambda}\boldsymbol{U}$, that is

$$\begin{bmatrix} \boldsymbol{u}_1 \\ \boldsymbol{u}_2 \\ \vdots \\ \boldsymbol{u}_n \end{bmatrix} \boldsymbol{A} = \begin{bmatrix} \lambda_1 & 0 & \cdots & 0 \\ 0 & \lambda_2 & \cdots & 0 \\ \vdots & \vdots & \ddots & \vdots \\ 0 & 0 & \cdots & \lambda_n \end{bmatrix} \begin{bmatrix} \boldsymbol{u}_1 \\ \boldsymbol{u}_2 \\ \vdots \\ \boldsymbol{u}_n \end{bmatrix}. \tag{12.22}$$

Hence for each eigenvalue λ_i, $\boldsymbol{u}_i \boldsymbol{A} = \lambda_i \boldsymbol{u}_i$ holds. Neglecting the indices gives

$$\boldsymbol{u}\,\boldsymbol{A} = \boldsymbol{u}\lambda. \tag{12.23}$$

This equation is similar to Equation (12.1) but now with the row vector $\boldsymbol{u}$ on the left hand side of matrix $\boldsymbol{A}$. Hence the row vector $\boldsymbol{u}$ is referred to as the *left eigenvector* of matrix $\boldsymbol{A}$ associated with eigenvalue λ.

It should be noted that transposing matrices in Equation (12.23) gives

$$\boldsymbol{A}^{\mathrm{T}}\boldsymbol{u}^{\mathrm{T}} = \lambda\ \boldsymbol{u}^{\mathrm{T}}. \tag{12.24}$$

This equation shows that the column vector $\boldsymbol{u}^{\mathrm{T}}$ is the right eigenvector of matrix $\boldsymbol{A}^{\mathrm{T}}$. This means that the left eigenvector of matrix $\boldsymbol{A}$ has the same values as the right eigenvector of matrix $\boldsymbol{A}^{\mathrm{T}}$. Hence the left eigenvector of matrix $\boldsymbol{A}$ is defined by some authors as the right eigenvector of matrix $\boldsymbol{A}^{\mathrm{T}}$.

Example 12.3

Consider the matrix $\boldsymbol{A}$ given below. Its eigenvalues are $\lambda_1 = 3$, $\lambda_2 = 2$ and $\lambda_3 = 1$. Application of Equation (12.6) results in the following eigenvectors:

$$\boldsymbol{A} = \left[\begin{array}{c|c|c} 2 & -1 & 2 \\ \hline 0 & -1 & 4 \\ \hline 0 & -2 & 5 \end{array}\right], \quad \boldsymbol{\Lambda} = \left[\begin{array}{c|c|c} \lambda_1 & & \\ \hline & \lambda_2 & \\ \hline & & \lambda_3 \end{array}\right] = \left[\begin{array}{c|c|c} 3 & & \\ \hline & 2 & \\ \hline & & 1 \end{array}\right], \quad \boldsymbol{W} = \left[\begin{array}{c|c|c} 1 & 1 & 0 \\ \hline 1 & 0 & 2 \\ \hline 1 & 0 & 1 \end{array}\right]. \tag{12.25}$$

Checking the definition of right eigenvectors $\boldsymbol{AW} = \boldsymbol{W\Lambda}$ corresponding to Equation (12.1),

$$\boldsymbol{AW} = \begin{bmatrix} 2 & -1 & 2 \\ 0 & -1 & 4 \\ 0 & -2 & 5 \end{bmatrix} \cdot \begin{bmatrix} 1 & 1 & 0 \\ 1 & 0 & 2 \\ 1 & 0 & 1 \end{bmatrix} = \begin{bmatrix} 3 & 2 & 0 \\ 3 & 0 & 2 \\ 3 & 0 & 1 \end{bmatrix} = \begin{bmatrix} 1 & 1 & 0 \\ 1 & 0 & 2 \\ 1 & 0 & 1 \end{bmatrix} \cdot \begin{bmatrix} 3 & & \\ & 2 & \\ & & 1 \end{bmatrix} = \boldsymbol{W\Lambda}. \tag{12.26}$$

Inverting matrix $\boldsymbol{W}$ gives

$$\boldsymbol{U} = \boldsymbol{W}^{-1} = \begin{bmatrix} 0 & -1 & 2 \\ 1 & 1 & -2 \\ 0 & 1 & -1 \end{bmatrix} \quad \text{or} \quad \begin{aligned} \boldsymbol{u}_1 &= [0 \;\; -1 \;\; 2] \\ \boldsymbol{u}_2 &= [1 \;\; 1 \;\; -2]. \\ \boldsymbol{u}_3 &= [0 \;\; 1 \;\; -1] \end{aligned} \tag{12.27}$$

Checking the definition of left eigenvectors $\boldsymbol{UA} = \boldsymbol{\Lambda U}$ in Equation (12.22),

$$\boldsymbol{UA} = \begin{bmatrix} 0 & -1 & 2 \\ 1 & 1 & -2 \\ 0 & 1 & -1 \end{bmatrix} \cdot \begin{bmatrix} 2 & -1 & 2 \\ 0 & -1 & 4 \\ 0 & -2 & 5 \end{bmatrix} = \begin{bmatrix} 0 & -3 & 6 \\ 2 & 2 & -4 \\ 0 & 1 & -1 \end{bmatrix} = \begin{bmatrix} 3 & & \\ & 2 & \\ & & 1 \end{bmatrix} \cdot \begin{bmatrix} 0 & -1 & 2 \\ 1 & 1 & -2 \\ 0 & 1 & -1 \end{bmatrix}$$

$$= \boldsymbol{\Lambda U}. \tag{12.28}$$

Transposing matrix $\boldsymbol{A}$ gives

$$\boldsymbol{A}^{\mathrm{T}} = \begin{bmatrix} 2 & 0 & 0 \\ -1 & -1 & -2 \\ 2 & 4 & 5 \end{bmatrix}. \tag{12.29}$$

Checking that vectors $\boldsymbol{u}_1^{\mathrm{T}}$, $\boldsymbol{u}_2^{\mathrm{T}}$, $\boldsymbol{u}_3^{\mathrm{T}}$ are indeed right eigenvectors of $\boldsymbol{A}^{\mathrm{T}}$, that is that equation $\boldsymbol{A}^{\mathrm{T}}\boldsymbol{U}^{\mathrm{T}} = \boldsymbol{U}^{\mathrm{T}}\boldsymbol{\Lambda}$ is satisfied (corresponding to Equation (12.24)),

$$\boldsymbol{A}^{\mathrm{T}}\boldsymbol{U}^{\mathrm{T}} = \begin{bmatrix} 2 & 0 & 0 \\ -1 & -1 & -2 \\ 2 & 4 & 5 \end{bmatrix} \cdot \begin{bmatrix} 0 & 1 & 0 \\ -1 & 1 & 1 \\ 2 & -2 & -1 \end{bmatrix} = \begin{bmatrix} 0 & 2 & 0 \\ -3 & 2 & 1 \\ 6 & -4 & -1 \end{bmatrix} = \begin{bmatrix} 0 & 1 & 0 \\ -1 & 1 & 1 \\ 2 & -2 & -1 \end{bmatrix}$$

$$\cdot \begin{bmatrix} 3 & & \\ & 2 & \\ & & 1 \end{bmatrix} = \boldsymbol{U}^{\mathrm{T}}\boldsymbol{\Lambda}. \tag{12.30}$$

The following practical note should be borne in mind when calculating eigenvectors. Some professional programs, such as MATLAB, calculate eigenvalues and the corresponding right eigenvectors.

In order to calculate left eigenvectors, manuals recommend that similar calculations are performed for the transposed matrix, that is the left eigenvectors of $\boldsymbol{A}$ should be calculated as right eigenvectors of $\boldsymbol{A}^{\mathrm{T}}$. This recommendation may be confusing because the eigenvalues of $\boldsymbol{A}^{\mathrm{T}}$ and the corresponding eigenvectors are usually ordered differently than those obtained for matrix $\boldsymbol{A}$. Consequently, the corresponding pairs of right and left eigenvectors $(\boldsymbol{w}_i; \boldsymbol{u}_i)$ have to be selected manually based on the identification of identical eigenvalues λ_i. Therefore it is simpler to calculate left eigenvectors by inverting the matrix $\boldsymbol{W}^{-1} = \boldsymbol{U}$. Then the pairs $(\boldsymbol{w}_i; \boldsymbol{u}_i)$ can be selected as the columns of $\boldsymbol{W}$ and rows of $\boldsymbol{U}$, respectively.

According to Equation (12.20), the square matrix $\boldsymbol{U}$ made up of left eigenvectors corresponds to the inverse matrix of $\boldsymbol{W}$ made up of right eigenvectors. Obviously the product of both matrixes is the identity matrix $\boldsymbol{UW} = \mathbf{1}$, that is

$$\boldsymbol{UW} = \begin{bmatrix} \boldsymbol{u}_1 \\ \boldsymbol{u}_2 \\ \vdots \\ \boldsymbol{u}_n \end{bmatrix} [\boldsymbol{w}_1,\ \boldsymbol{w}_2, \ldots,\ \boldsymbol{w}_n] = \begin{bmatrix} \boldsymbol{u}_1\boldsymbol{w}_1 & 0 & \cdots & 0 \\ 0 & \boldsymbol{u}_2\boldsymbol{w}_2 & \cdots & 0 \\ \vdots & \vdots & \ddots & \vdots \\ 0 & 0 & \cdots & \boldsymbol{u}_n\boldsymbol{w}_n \end{bmatrix} = \begin{bmatrix} 1 & & & \\ & 1 & & \\ & & \ddots & \\ & & & 1 \end{bmatrix} = 1. \tag{12.31}$$

Hence the following equations are true for left and right eigenvectors:

$$\boldsymbol{u}_i\boldsymbol{w}_i = 1 \quad \text{and} \quad \boldsymbol{u}_i\boldsymbol{w}_j = 0 \quad \text{for} \quad j \neq i. \tag{12.32}$$

Note that if λ_i is complex then this equation also holds, that is $\boldsymbol{u}_i^*\boldsymbol{w}_i^* = 1$. In that case matrices $\boldsymbol{U}$ and $\boldsymbol{W}$ have the following structure:

$$\boldsymbol{U} = \left[\begin{array}{c} \vdots \\ \hline \boldsymbol{u} \\ \hline \boldsymbol{u}^* \\ \hline \vdots \end{array}\right], \quad \boldsymbol{W} = [\ldots \mid \boldsymbol{w} \mid \boldsymbol{w}^* \mid \ldots]. \tag{12.33}$$

Equations (12.32) and (12.33) are important when considering the solution of differential equations covered in Section 12.1.5.

Example 12.4

Calculate the matrix of left eigenvectors $\boldsymbol{U} = \boldsymbol{W}^{-1}$ of matrix $\boldsymbol{A}$ from Example 12.2 and use Equation (12.21) to diagonalize the matrix $\boldsymbol{\Lambda} = \boldsymbol{UAW}$. Matrix $\boldsymbol{W}$ was calculated in Example 12.2:

$$\boldsymbol{A} = \left[\begin{array}{c|c|c} -6 & 0 & 0 \\ \hline 0 & 1 & 5 \\ \hline 0 & -5 & 1 \end{array}\right], \quad \boldsymbol{W} = \left[\begin{array}{c|c|c} 1 & 0 & 0 \\ \hline 0 & -1-\mathrm{j}1 & -1+\mathrm{j}1 \\ \hline 0 & -1+\mathrm{j}1 & -1-\mathrm{j}1 \end{array}\right]. \tag{12.34}$$

Simple calculations lead to

$$\boldsymbol{U} = \boldsymbol{W}^{-1} = \frac{1}{4}\left[\begin{array}{c|c|c} 4 & 0 & 0 \\ \hline 0 & -1+\mathrm{j}1 & -1-\mathrm{j}1 \\ \hline 0 & -1-\mathrm{j}1 & -1+\mathrm{j}1 \end{array}\right] = \left[\begin{array}{c} \boldsymbol{u}_1 \\ \hline \boldsymbol{u}_2 \\ \hline \boldsymbol{u}_3 \end{array}\right] = \left[\begin{array}{c} \boldsymbol{u}_1 \\ \hline \boldsymbol{u}_2 \\ \hline \boldsymbol{u}_2^* \end{array}\right]. \tag{12.35}$$

$$\boldsymbol{u}_1 = \frac{1}{4}[4 \,|\, 0 \,|\, 0], \quad \boldsymbol{u}_2 = \frac{1}{4}[0 \,|\, -1+\mathrm{j}1 \,|\, -1-\mathrm{j}1], \quad \boldsymbol{u}_3 = \frac{1}{4}[0 \,|\, -1-\mathrm{j}1 \,|\, -1+\mathrm{j}1] = \boldsymbol{u}_2^*.$$

It is easy to check that $\boldsymbol{u}_3 = \boldsymbol{u}_2^*$ is a pair of complex conjugate row vectors, which confirms the validity of Equation (12.33). Multiplying matrices (12.34) gives

$$\boldsymbol{AW} = \left[\begin{array}{c|c|c} -6 & 0 & 0 \\ \hline 0 & 1 & 5 \\ \hline 0 & -5 & 1 \end{array}\right]\left[\begin{array}{c|c|c} 1 & 0 & 0 \\ \hline 0 & -1-\mathrm{j}1 & -1+\mathrm{j}1 \\ \hline 0 & -1+\mathrm{j}1 & -1-\mathrm{j}1 \end{array}\right] = \left[\begin{array}{c|c|c} -6 & 0 & 0 \\ \hline 0 & -4+\mathrm{j}6 & -4-\mathrm{j}6 \\ \hline 0 & +6+\mathrm{j}4 & +6-\mathrm{j}4 \end{array}\right]. \tag{12.36}$$

$$\boldsymbol{UAW} = \frac{1}{4}\left[\begin{array}{c|c|c} 4 & 0 & 0 \\ \hline 0 & -1+\mathrm{j}1 & -1-\mathrm{j}1 \\ \hline 0 & -1-\mathrm{j}1 & -1+\mathrm{j}1 \end{array}\right]\left[\begin{array}{c|c|c} -6 & 0 & 0 \\ \hline 0 & -4+\mathrm{j}6 & -4-\mathrm{j}6 \\ \hline 0 & +6+\mathrm{j}4 & +6-\mathrm{j}4 \end{array}\right] = \left[\begin{array}{c|c|c} -6 & 0 & 0 \\ \hline 0 & -1-\mathrm{j}5 & 0 \\ \hline 0 & 0 & -1+\mathrm{j}5 \end{array}\right]. \tag{12.37}$$

The obtained diagonal matrix contains previously calculated eigenvalues of matrix $\boldsymbol{A}$ (Example 12.2, Equation (12.17)).

Diagonalization of a square matrix $\boldsymbol{A}$ using matrices $\boldsymbol{W}$ and $\boldsymbol{U}$ made up of right and left eigenvectors is important for the next section that considers the solution of matrix differential equations.

12.1.3 Solution of Matrix Differential Equations

The solution of scalar differential homogeneous equations is discussed in Appendix A3. It is shown that the fundamental solution of ordinary linear differential equations consists of exponential functions $\mathrm{e}^{\lambda t}$, where numbers λ must be chosen so that the Wronskian matrix of solutions is different from zero. In the case of a first-order differential homogeneous equation $\dot{x} - ax = 0$ or $\dot{x} = ax$ the fundamental system of solutions consists of only one exponential function e^{at}. The particular solution is of the form $x(t) = \mathrm{e}^{at}x_0$, where $x_0 = x(t_0)$ is the initial condition. In this section the matrix form of a linear differential homogeneous equation is considered:

$$\dot{\boldsymbol{x}} = \boldsymbol{A}\boldsymbol{x}, \tag{12.38}$$

where $\boldsymbol{A}$ is a square real matrix referred to as the *state matrix*. Equation (12.38) is referred to as the *state equation*, vector $\boldsymbol{x}$ is the vector of the *state variables* or in short the *state vector*.

Matrix equation (12.38) has a solution in the same form as the scalar equation

$$\boldsymbol{x}(t) = \mathrm{e}^{\boldsymbol{A}t}\boldsymbol{x}_0, \tag{12.39}$$

where $\boldsymbol{x}(t)$ and $\boldsymbol{x}_0$ are column matrices while $e^{\boldsymbol{A}t}$ is a square matrix which can be proved by expanding $e^{\boldsymbol{A}t}$ as a Taylor series:

$$e^{\boldsymbol{A}t} = 1 + \boldsymbol{A}t + \frac{(\boldsymbol{A}t)^2}{2!} + \frac{(\boldsymbol{A}t)^3}{3!} + \cdots \tag{12.40}$$

The Taylor expansion also proves that for a real matrix $\boldsymbol{A}$, matrix $e^{\boldsymbol{A}t}$ is also real and the solution given by (12.39) is also real.

A number of different methods of calculation of $e^{\boldsymbol{A}t}$ are given in textbooks, see, for example, Ogata (1967) or Strang (1976). In power system analysis practice the calculation of $e^{\boldsymbol{A}t}$ is replaced by diagonalization of $\boldsymbol{A}$ and calculation of $e^{\boldsymbol{A}t}$, where $\boldsymbol{\Lambda} = \text{diag}\ \lambda_i$ is a diagonal matrix – see (12.21).

In order to utilize matrix diagonalization for the solution of the state equation (12.38), the state vector $\boldsymbol{x}$ can be transformed into a new state vector $\boldsymbol{z}$ using the linear transformation

$$\boldsymbol{x} = \boldsymbol{W}\boldsymbol{z}, \tag{12.41}$$

where $\boldsymbol{W}$ is a square matrix consisting of right eigenvectors of matrix $\boldsymbol{A}$. Note that vector $\boldsymbol{z}$ is generally complex. Using the inverse matrix $\boldsymbol{U} = \boldsymbol{W}^{-1}$ the following inverse transformation can be defined:

$$\boldsymbol{z} = \boldsymbol{W}^{-1}\boldsymbol{x} = \boldsymbol{U}\boldsymbol{x}. \tag{12.42}$$

Substituting Equations (12.41) into Equation (12.38) gives $\boldsymbol{W}\dot{\boldsymbol{z}} = \boldsymbol{A}\boldsymbol{W}\boldsymbol{z}$, or $\dot{\boldsymbol{z}} = \boldsymbol{W}^{-1}\boldsymbol{A}\boldsymbol{W}\boldsymbol{z}$, which after taking into account Equation (12.21) gives

$$\dot{\boldsymbol{z}} = \boldsymbol{\Lambda}\boldsymbol{z}. \tag{12.43}$$

Equation (12.43) is the *modal form* of the state equation (12.38). Matrix $\boldsymbol{\Lambda}$ given by Equation (12.21) is the modal form of the state matrix, matrix $\boldsymbol{W}$ is the *modal matrix* and variables $\boldsymbol{z}(t)$ are the *modal variables*.[1]

Because matrix $\boldsymbol{\Lambda}$ is diagonal the matrix equation (12.43) describes a set of uncoupled scalar differential equations

$$\dot{z}_i = \lambda_i z_i \quad \text{for} \quad i = 1, 2, \ldots, n. \tag{12.44}$$

Each of the equations is of first order and its solution is of the form

$$z_i(t) = e^{\lambda_i t} z_{i0} \quad \text{for} \quad i = 1, 2, \ldots, n, \tag{12.45}$$

where z_{i0} is the initial condition of the modal variable. The set of these scalar solutions can be expressed as the following column vector:

$$\boldsymbol{z}(t) = e^{\boldsymbol{\Lambda}t}\boldsymbol{z}_0, \tag{12.46}$$

where

$$e^{\boldsymbol{\Lambda}t} = \begin{bmatrix} e^{\lambda_1 t} & 0 & \cdots & 0 \\ 0 & e^{\lambda_2 t} & \cdots & 0 \\ \vdots & \vdots & \ddots & \vdots \\ 0 & 0 & \cdots & e^{\lambda_n t} \end{bmatrix} = \text{diag}\,[e^{\lambda_i t}]. \tag{12.47}$$

[1] Note that $\boldsymbol{z}(t)$ are complex variables while $\boldsymbol{x}(t)$ are real. Many authors refer to $\boldsymbol{z}(t)$ as simply the *modes*. In this book $\boldsymbol{z}(t)$ are referred to as the *modal variables* analogously to $\boldsymbol{x}(t)$ as the *state variables*. It will be shown later in this section that a state variable can be expressed as a linear combination of uncorrelated real variables of the form $e^{\alpha_i t} \cdot \cos(\Omega_i t) + \phi_{ki})$ or $e^{\alpha_i t}$ which will be referred to as the *modes* in this book.

Equations (12.41) and (12.46) give

$$\boldsymbol{x} = \boldsymbol{W}\mathrm{e}^{\boldsymbol{\Lambda} t}\boldsymbol{z}_0, \tag{12.48}$$

where $\boldsymbol{z}_0 = \boldsymbol{z}(t_0)$ is a column of initial conditions for the modal variables $\boldsymbol{z}(t)$. These initial conditions can be found using Equation (12.42) as

$$\boldsymbol{z}_0 = \boldsymbol{U}\boldsymbol{x}_0. \tag{12.49}$$

Substituting (12.49) into (12.48) gives

$$\boldsymbol{x} = \boldsymbol{W}\mathrm{e}^{\boldsymbol{\Lambda} t}\boldsymbol{U}\boldsymbol{x}_0. \tag{12.50}$$

Obviously the solution given by (12.50) is equivalent to the solution given by (12.39) as:

$$\mathrm{e}^{\boldsymbol{A}t} = \boldsymbol{W}\mathrm{e}^{\boldsymbol{\Lambda} t}\boldsymbol{U}. \tag{12.51}$$

The correctness of Equation (12.51) can be proved by using the Taylor series expansion (12.40) and Equation (12.19). The proof can be found in Strang (1976).

It should be noted that generally matrix $\boldsymbol{A}$ may be unsymmetric, giving complex eigenvalues λ_i (see Example 12.2). In that case the modal variables $z_i(t)$ given by Equation (12.45) are complex. The solution of complex differential equations (12.44) in the complex domain is discussed in Section A3.6 of the Appendix. It is shown that for complex λ_i the trajectories of solutions $z_i(t)$ form logarithmic spirals in the complex plane. The spirals are converging for $\alpha_i = \mathrm{Re}\lambda_i < 0$ and diverging for $\alpha_i = \mathrm{Re}\lambda_i > 0$. For $\alpha_i = \mathrm{Re}\lambda_i = 0$ the solution $z_i(t)$ represents a circle in the complex plane. The spiral rotates anticlockwise when $\Omega_i = \mathrm{Im}\lambda_i > 0$ and clockwise when $\Omega_i = \mathrm{Im}\lambda_i < 0$.

In the case of matrix equations (see Equation (12.14)) there is always a pair of complex conjugate eigenvalues $\lambda_j = \lambda_i^*$. This pair results in two solutions $z_i(t)$ and $z_j(t)$ forming counter-rotating spirals in the complex plane (see Appendix A3). Obviously the imaginary parts of the spirals cancel each other out (because they have opposite signs) so that the real solution will be equal to the double real part, that is

$$z_i(t) + z_j(t) = z_i(t) + z_i^*(t) = 2\,\mathrm{Re}\,z_i(t)$$

This cancelling of the imaginary parts of the solution will now be proved formally for the discussed matrix state equation (12.38) and its modal form (12.43).

When the eigenvalues are complex, matrix $\mathrm{e}^{\boldsymbol{A}t}$ is complex too. From the definition of eigenvectors it can be concluded that complex eigenvalues correspond to complex eigenvectors (see Example 12.4). Hence matrices $\boldsymbol{W}$ and $\boldsymbol{U}$ may be generally complex. In Equation (12.50) there is a product of three complex matrices $\boldsymbol{W}\mathrm{e}^{\boldsymbol{\Lambda} t}\boldsymbol{U}$ and one real matrix $\boldsymbol{x}_0$. On the other hand, it is clear from Equation (12.39) that the solution $\boldsymbol{x}(t)$, and therefore also the product $\boldsymbol{W}\mathrm{e}^{\boldsymbol{\Lambda} t}\boldsymbol{U}\boldsymbol{x}_0$, must be real. Hence there is a question about how the product of complex matrices produces a real result. The answer comes from a previous observation that complex eigenvalues and eigenvectors must always form conjugate pairs λ, λ^* and the associated matrices of left and right eigenvectors have the structure shown in Equation (12.33).

Let the ith and jth eigenvalues be a complex conjugate pair

$$\lambda_j = \lambda_i^*, \quad \boldsymbol{w}_j = \boldsymbol{w}_i^*, \quad \boldsymbol{u}_j = \boldsymbol{u}_i^*. \tag{12.52}$$

Then the column of initial conditions of modal variables $\boldsymbol{z}(t)$ has the following structure:

$$\boldsymbol{z}_0 = \begin{bmatrix} \vdots \\ \hline z_{i0} \\ \hline z_{j0} \\ \hline \vdots \end{bmatrix} = \boldsymbol{U}\boldsymbol{x}_0 = \begin{bmatrix} \vdots \\ \hline \boldsymbol{u}_i \\ \hline \boldsymbol{u}_i^* \\ \hline \vdots \end{bmatrix} \cdot \boldsymbol{x}_0 = \begin{bmatrix} \vdots \\ \hline \boldsymbol{u}_i \boldsymbol{x}_0 \\ \hline \boldsymbol{u}_i^* \boldsymbol{x}_0 \\ \hline \vdots \end{bmatrix} = \begin{bmatrix} \vdots \\ \hline z_{i0} \\ \hline z_{i0}^* \\ \hline \vdots \end{bmatrix}, \tag{12.53}$$

that is, for the considered pair, $z_{j0} = z_{i0}^*$ and the two elements of the column $\boldsymbol{z}_0$ are a complex conjugate pair. The product $\boldsymbol{W}\mathrm{e}^{\boldsymbol{\Lambda} t}$ is a square matrix that in this case has the following structure:

$$\boldsymbol{W}\mathrm{e}^{\boldsymbol{\Lambda} t} = [\ldots \vdots \boldsymbol{w}_i \vdots \boldsymbol{w}_i^* \vdots \ldots] \cdot \begin{bmatrix} \ddots & \vdots & \vdots & \cdots \\ \cdots & \mathrm{e}^{\lambda_i t} & 0 & \cdots \\ \cdots & 0 & \mathrm{e}^{\lambda_i^* t} & \cdots \\ \cdots & \vdots & \vdots & \ddots \end{bmatrix} = [\ldots \vdots \boldsymbol{w}_i \mathrm{e}^{\lambda_i t} \vdots \boldsymbol{w}_i^* \mathrm{e}^{\lambda_i^* t} \vdots \ldots], \tag{12.54}$$

that is the matrix has two columns which are complex conjugates. Taking into account the matrix structure expressed by Equations (12.53) and (12.54), Equation (12.48) gives

$$\boldsymbol{x}(t) = \begin{bmatrix} x_1(t) \\ \hline \vdots \\ \hline x_k(t) \\ \hline \vdots \\ \hline x_n(t) \end{bmatrix} = \boldsymbol{W}\mathrm{e}^{\boldsymbol{\Lambda} t}\boldsymbol{z}_0 = \begin{bmatrix} \ldots & w_{1i}\mathrm{e}^{\lambda_i t} & w_{1i}^*\mathrm{e}^{\lambda_i^* t} & \cdots \\ \hline & \vdots & \vdots & \\ \hline \cdots & w_{ki}\mathrm{e}^{\lambda_i t} & w_{ki}^*\mathrm{e}^{\lambda_i^* t} & \cdots \\ \hline & \vdots & \vdots & \\ \hline \cdots & w_{ni}\mathrm{e}^{\lambda_i t} & w_{ni}^*\mathrm{e}^{\lambda_i^* t} & \cdots \end{bmatrix} \cdot \begin{bmatrix} \vdots \\ \hline z_{i0} \\ \hline z_{i0}^* \\ \hline \vdots \end{bmatrix}. \tag{12.55}$$

This structure shows that the solution for the state variable for any k is

$$x_k(t) = \cdots + w_{ki} z_{i0} \mathrm{e}^{\lambda_i t} + w_{ki}^* z_{i0}^* \mathrm{e}^{\lambda_i^* t} + \cdots \tag{12.56}$$

or

$$x_k(t) = \cdots + c_{ki} \mathrm{e}^{\lambda_i t} + c_{ki}^* \mathrm{e}^{\lambda_i^* t} + \cdots \tag{12.57}$$

where $c_{ki} = w_{ki} z_{i0}$ is a complex number depending on the eigenvector and the initial condition. Denoting $\lambda_i = \alpha_i + \mathrm{j}\Omega_i$ gives

$$c_{ki}\mathrm{e}^{\lambda_i t} + c_{ki}^*\mathrm{e}^{\lambda_i^* t} = c_{ki}\mathrm{e}^{\alpha_i t}(\cos\ \Omega_i t + \mathrm{j}\ \sin\ \Omega_i t) + c_{ki}^*\mathrm{e}^{\alpha_i t}(\cos\ \Omega_i t - \mathrm{j}\ \sin\ \Omega_i t).$$

Rearranging the right hand side gives

$$c_{ki}\mathrm{e}^{\lambda_i t} + c_{ki}^*\mathrm{e}^{\lambda_i^* t} = \mathrm{e}^{\alpha_i t}[(c_{ki} + c_{ki}^*)\cos\ \Omega_i t + \mathrm{j}(c_{ki} - c_{ki}^*)\sin\ \Omega_i t]. \tag{12.58}$$

Note that

$$a_i = (c_i + c_i^*) = 2\,\mathrm{Re}\,c_i \quad \text{and} \quad b_i = \mathrm{j}(c_i - c_i^*) = -2\,\mathrm{Im}\,c_i, \tag{12.59}$$

are real numbers equal to the real part and double imaginary part of the integration constant $c_{ki} = w_{ki} z_{i0}$. Hence Equation (12.58) takes the form

$$c_{ki} e^{\lambda_i t} + c_{ki}^* e^{\lambda_i^* t} = e^{\alpha_i t} [a_{ki} \cos \Omega_i t - b_{ki} \sin \Omega_i t]. \tag{12.60}$$

Note that the difference between the cosine and sine functions in the square brackets can be replaced by a cosine function (see also Figure A.2 in the Appendix):

$$c_{ki} e^{\lambda_i t} + c_{ki}^* e^{\lambda_i^* t} = e^{\alpha_i t} \cdot \sqrt{a_{ki}^2 + b_{ki}^2} \left[\frac{a_{ki}}{\sqrt{a_{ki}^2 + b_{ki}^2}} \cdot \cos \Omega_i t - \frac{b_{ki}}{\sqrt{a_{ki}^2 + b_{ki}^2}} \cdot \sin \Omega_i t \right]. \tag{12.61}$$

In the same way as in Appendix A3 it can be assumed that

$$\cos \phi_{ki} = \frac{a_{ki}}{\sqrt{a_{ki}^2 + b_{ki}^2}} = \frac{\operatorname{Re} c_i}{\sqrt{(\operatorname{Re} c_i)^2 + (\operatorname{Im} c_i)^2}} = \frac{\operatorname{Re} c_i}{|c_i|}, \tag{12.62}$$

$$\sin \phi_{ki} = \frac{b_{ki}}{\sqrt{a_{ki}^2 + b_{ki}^2}} = \frac{\operatorname{Im} c_i}{\sqrt{(\operatorname{Re} c_i)^2 + (\operatorname{Im} c_i)^2}} = \frac{\operatorname{Im} c_i}{|c_i|}, \tag{12.63}$$

$$\phi_{ki} = \arcsin (\operatorname{Im} c_i / |c_i|), \tag{12.64}$$

$$|c_{ki}| = \sqrt{(\operatorname{Re} c_i)^2 + (\operatorname{Im} c_i)^2} \quad \text{and} \quad \sqrt{a_{ki}^2 + b_{ki}^2} = 2 \cdot \sqrt{(\operatorname{Re} c_i)^2 + (\operatorname{Im} c_i)^2} = 2 \cdot |c_i|. \tag{12.65}$$

With this notation Equation (12.61) gives

$$c_{ki} e^{\lambda_i t} + c_{ki}^* e^{\lambda_i^* t} = 2 \cdot |c_{ki}| \, e^{\alpha_i t} \cdot \cos(\Omega_i t + \phi_{ki}). \tag{12.66}$$

Finally, substituting (12.66) into (12.57) gives

$$x_k(t) = \cdots + 2 \cdot |c_{ki}| \, e^{\alpha_i t} \cdot \cos(\Omega_i t + \phi_{ki}) + \cdots. \tag{12.67}$$

This means that in the solution for the state variable $x_k(t)$, a pair of complex eigenvalues λ_i, λ_i^* corresponds to an oscillatory term $e^{\alpha_i t} \cdot \cos(\Omega_i t + \phi_{ki})$ where $\alpha_i = \operatorname{Re}\lambda_i$ and $\Omega_i = \operatorname{Im}\lambda_i$ are the real and imaginary parts of the eigenvalue. This term is referred to as the *oscillatory mode* and it corresponds to a solution of a second-order underdamped differential equation analysed in the Appendix, Example A3.4.

The above considerations were concerned with complex eigenvalues. The case of real eigenvalues can be obtained from the derived equations by substituting $\Omega_i = \operatorname{Im}\lambda_i = 0$ and $\phi_{ki} = \arcsin(\operatorname{Im} c_i / |c_i|) = 0$. The only difference is that the resulting term will not be multiplied by 2 as real eigenvalues are considered individually, not in pairs. This gives for a real eigenvalue $\lambda_i = \alpha_i$

$$x_k(t) = \cdots + c_{ki} e^{\alpha_i t} + \cdots. \tag{12.68}$$

The term $e^{\alpha_i t}$ is referred to as the *aperiodic mode* and it corresponds to a solution of a first-order differential equation analysed in Appendix A3. Taking into account in (12.55) both the real and imaginary parts of eigenvalues after multiplying both matrices for each variable, the following solution is obtained:

$$x_k(t) = \sum_{\lambda_i \in \text{real}} c_{ki} \cdot e^{\alpha_i t} + \sum_{\lambda_i \in \text{complex}} 2 \, |c_{ki}| \cdot e^{\alpha_i t} \cdot \cos(\Omega_i t + \phi_{ki}). \tag{12.69}$$

Analysis of Equation (12.69) leads to the following conclusions which are important for the analysis of power system dynamics:

1. Real eigenvalues $\lambda_i = \alpha_i$ introduce to the response of $x_k(t)$ aperiodic modes that are proportional to $e^{\alpha_i t}$. If $\alpha_i < 0$ then the corresponding aperiodic mode is stable and $(-1/\alpha_i)$ is the time constant of the exponential decay of the mode. If $\alpha_i > 0$ then the corresponding aperiodic mode is unstable and exponentially increasing.
2. Each conjugate pair of complex eigenvalues $\lambda_i = \alpha_i \pm j\Omega_i$ introduces to the response of $x_k(t)$ oscillatory modes proportional to $e^{\alpha_i t} \cdot \cos(\Omega_i t + \phi_{ki})$. If $\alpha_i < 0$ then the corresponding oscillatory mode is stable. If $\alpha_i > 0$ then the corresponding oscillatory mode is unstable. The term Ω_i is the frequency of oscillation (in rad/s) of the oscillatory mode. The angle ϕ_{ki} is the phase angle of the oscillatory mode and its value depends on the initial conditions.
3. The solution $x_k(t)$ of a differential equation is a linear combination of the modes and the coefficients of proportionality in that combination depend on the initial conditions. As an oscillatory mode corresponds to a response of a second-order underdamped system while an aperiodic mode corresponds to a response of a first-order system, effectively a small-signal response of a dynamic system of high order is represented as a linear combination of responses of decoupled second- and first-order systems.
4. A dynamic system described by Equation (12.38) is unstable if any of the modes are unstable.

The definition and the types of modes are given in Table 12.1.

For an oscillatory mode, analogously to Equation (5.65), the following definition of the *damping ratio* may be introduced:

$$\zeta_i = \frac{-\alpha_i}{\sqrt{\alpha_i^2 + \Omega_i^2}}. \tag{12.70}$$

In practice, as discussed in Section 5.4.6, damping is considered to be satisfactory if the damping ratio $\zeta \geq 0.05$.

Table 12.1 Illustration of the definition and types of modes

	Eigenvalue λ_i	
	Real	Complex pair
Notation	$\lambda_i = \alpha_i$	$\lambda_i = \alpha_i + j\Omega_i,\ \lambda_i^* = \alpha_i - j\Omega_i$
Mode definition	$e^{\alpha_i t}$	$e^{\alpha_i t} \cos \Omega_i t$
Mode type	Aperiodic	Oscillatory
Corresponding to	Response of a first-order system	Response of a second-order underdamped system
$\alpha_i < 0$		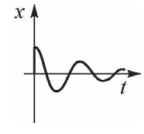
$\alpha_i > 0$	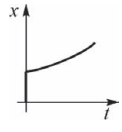	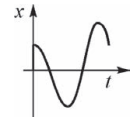

Note that $c_{ki} = w_{ki} z_{i0}$ in Equation (12.69) depends on the initial conditions z_{i0} of a given modal variable $z_i(t)$. If this modal variable has zero initial conditions then obviously $c_{ki} = 0$ and the mode has no influence on the value of $x_k(t)$. A mode or a modal variable $z_i(t)$ is said to be *excited* if $c_{ki} \neq 0$. Equation (12.69) shows that the trajectory of $x_k(t)$ is influenced only by the excited modes or excited modal variables. Those modes or modal variables that have the largest values of c_{ki} are said to be *dominant modes* or *dominant modal variables*.

The analysis in Section 5.4.6 of the second-order classical model of a synchronous generator connected to an infinite busbar showed that rotor swings around the synchronous speed can be aperiodic or oscillatory, depending on the roots of the characteristic equation. These roots are equal to the eigenvalues of the state matrix – see Equations (5.70) and (5.71) – and the swings are characterized by the frequency Ω and the damping ratio ζ. This section showed that the response of a multi-machine power system, or of a generator described by a higher order differential equation, can be expressed as a linear combination of uncoupled aperiodic and oscillatory responses, depending on whether the eigenvalues are real or complex. In other words, rotor swings in a multi-machine power system can be expressed as a linear combination of uncoupled swings of different frequencies Ω_i and damping ratios ζ_i, similar to those analysed in Section 5.4.6. This finding simplifies significantly the analysis of multi-machine power systems.

Example 12.5

Find the solution of the differential equation $\dot{\boldsymbol{x}} = \boldsymbol{A}\boldsymbol{x}$ for matrix $\boldsymbol{A}$ from Example 12.2. The eigenvalues are $\lambda_1 = -6, \lambda_2 = (-1 - \mathrm{j}5)$ and the corresponding matrices $\boldsymbol{W}$ and $\boldsymbol{U}$ were calculated in Example 12.2 and Example 12.4, respectively:

$$\boldsymbol{A} = \left[\begin{array}{c|c|c} -6 & 0 & 0 \\ \hline 0 & 1 & 5 \\ \hline 0 & -5 & 1 \end{array}\right], \quad \boldsymbol{W} = \left[\begin{array}{c|c|c} 1 & 0 & 0 \\ \hline 0 & -1-\mathrm{j}1 & -1+\mathrm{j}1 \\ \hline 0 & -1+\mathrm{j}1 & -1-\mathrm{j}1 \end{array}\right], \quad \boldsymbol{U} = \frac{1}{4}\left[\begin{array}{c|c|c} 4 & 0 & 0 \\ \hline 0 & -1+\mathrm{j}1 & -1-\mathrm{j}1 \\ \hline 0 & -1-\mathrm{j}1 & -1+\mathrm{j}1 \end{array}\right]. \tag{12.71}$$

The initial conditions are $x_{10} = x_1(t_0) \neq 0$, $x_{20} = x_2(t_0) \neq 0$. To simplify complex number manipulations, multiplication of matrices in Equation (12.50) will be executed in such a way that first the product $(\boldsymbol{W}\mathrm{e}^{\boldsymbol{\Lambda}t})$ will be calculated, then $(\boldsymbol{W}\mathrm{e}^{\boldsymbol{\Lambda}t})\boldsymbol{U}$ and finally the solution $\boldsymbol{x}(t) = (\boldsymbol{W}\mathrm{e}^{\boldsymbol{\Lambda}t}\boldsymbol{U})\boldsymbol{x}_0$:

$$\boldsymbol{W}\mathrm{e}^{\boldsymbol{\Lambda}t} = \left[\begin{array}{c|c|c} 1 & 0 & 0 \\ \hline 0 & -1-\mathrm{j}1 & -1+\mathrm{j}1 \\ \hline 0 & -1+\mathrm{j}1 & -1-\mathrm{j}1 \end{array}\right] \left[\begin{array}{ccc} \mathrm{e}^{\lambda_1 t} & & \\ & \mathrm{e}^{\lambda_2 t} & \\ & & \mathrm{e}^{\lambda_2^* t} \end{array}\right] = \left[\begin{array}{c|c|c} \mathrm{e}^{\lambda_1 t} & 0 & 0 \\ \hline 0 & (-1-\mathrm{j})\cdot\mathrm{e}^{\lambda_2 t} & (-1+\mathrm{j})\cdot\mathrm{e}^{\lambda_2^* t} \\ \hline 0 & (-1+\mathrm{j})\cdot\mathrm{e}^{\lambda_2 t} & (-1-\mathrm{j})\cdot\mathrm{e}^{\lambda_2^* t} \end{array}\right] \tag{12.72}$$

$$\boldsymbol{W}\mathrm{e}^{\boldsymbol{\Lambda}t}\boldsymbol{U} = \frac{1}{4}\left[\begin{array}{c|c|c} \mathrm{e}^{\lambda_1 t} & 0 & 0 \\ \hline 0 & (-1-\mathrm{j})\cdot\mathrm{e}^{\lambda_2 t} & (-1+\mathrm{j})\cdot\mathrm{e}^{\lambda_2^* t} \\ \hline 0 & (-1+\mathrm{j})\cdot\mathrm{e}^{\lambda_2 t} & (-1-\mathrm{j})\cdot\mathrm{e}^{\lambda_2^* t} \end{array}\right] \left[\begin{array}{c|c|c} 4 & 0 & 0 \\ \hline 0 & -1+\mathrm{j}1 & -1-\mathrm{j}1 \\ \hline 0 & -1-\mathrm{j}1 & -1+\mathrm{j}1 \end{array}\right].$$

Patiently multiplying the matrices and ordering the terms gives

$$\boldsymbol{W}\mathrm{e}^{\boldsymbol{\Lambda} t}\boldsymbol{U} = \frac{1}{4}\left[\begin{array}{c|c|c} 4\cdot \mathrm{e}^{\lambda_1 t} & 0 & 0 \\ \hline 0 & 2\cdot(\mathrm{e}^{\lambda_2 t}+\mathrm{e}^{\lambda_2^* t}) & 2\mathrm{j}\cdot(\mathrm{e}^{\lambda_2 t}-\mathrm{e}^{\lambda_2^* t}) \\ \hline 0 & 2\mathrm{j}\cdot(-\mathrm{e}^{\lambda_2 t}+\mathrm{e}^{\lambda_2^* t}) & 2\cdot(\mathrm{e}^{\lambda_2 t}+\mathrm{e}^{\lambda_2^* t}) \end{array}\right]. \tag{12.73}$$

Substituting into this equation $\lambda_1 = \alpha_1$, $\lambda_2 = (\alpha_2 + \mathrm{j}\Omega_2)$, $\lambda_3 = \lambda_2^* = (\alpha_2 - \mathrm{j}\Omega_2)$ gives the following matrix:

$$\boldsymbol{W}\mathrm{e}^{\boldsymbol{\Lambda} t}\boldsymbol{U} = \left[\begin{array}{c|c|c} \mathrm{e}^{\alpha_1 t} & 0 & 0 \\ \hline 0 & \mathrm{e}^{\alpha_2 t}\cos\Omega_2 t & -\mathrm{e}^{\alpha_2 t}\sin\Omega_2 t \\ \hline 0 & +\mathrm{e}^{\alpha_2 t}\sin\Omega_2 t & \mathrm{e}^{\alpha_2 t}\cos\Omega_2 t \end{array}\right]. \tag{12.74}$$

Substituting this matrix into Equation (12.50) gives

$$\boldsymbol{x}(t) = \boldsymbol{W}\mathrm{e}^{\boldsymbol{\Lambda} t}\boldsymbol{U}\boldsymbol{x}_0 = \begin{bmatrix} x_1(t) \\ x_2(t) \\ x_3(t) \end{bmatrix} = \left[\begin{array}{c|c|c} \mathrm{e}^{\alpha_1 t} & 0 & 0 \\ \hline 0 & \mathrm{e}^{\alpha_2 t}\cos\Omega_2 t & -\mathrm{e}^{\alpha_2 t}\sin\Omega_2 t \\ \hline 0 & +\mathrm{e}^{\alpha_2 t}\sin\Omega_2 t & \mathrm{e}^{\alpha_2 t}\cos\Omega_2 t \end{array}\right] \begin{bmatrix} x_{10} \\ x_{20} \\ x_{30} \end{bmatrix}, \tag{12.75}$$

or

$$\begin{aligned} x_1(t) &= x_{10}\cdot \mathrm{e}^{\alpha_1 t} \\ x_2(t) &= \mathrm{e}^{\alpha_2 t}\cdot[x_{20}\cos\Omega_2 t - x_{30}\sin\Omega_2 t] \\ x_3(t) &= \mathrm{e}^{\alpha_2 t}\cdot[x_{30}\cos\Omega_2 t + x_{20}\sin\Omega_2 t]. \end{aligned} \tag{12.76}$$

Obviously the solutions $x_2(t)$ and $x_3(t)$ corresponding to complex eigenvalues can be expressed in a form containing an oscillatory mode $\mathrm{e}^{\alpha_2 t}\cos\Omega_2 t$ with a phase angle ϕ_2. To do this the following notation is introduced (see also Figure A2 in the Appendix):

$$\sin\phi_2 = \frac{x_{30}}{\sqrt{x_{20}^2 + x_{30}^2}}, \quad \cos\phi_2 = \frac{x_{20}}{\sqrt{x_{20}^2 + x_{30}^2}}, \quad \phi_2 = \arcsin\left(x_{30}/\sqrt{x_{20}^2 + x_{30}^2}\right). \tag{12.77}$$

Now the solutions can be expressed as

$$\begin{aligned} x_2(t) &= \mathrm{e}^{\alpha_2 t}\cdot\sqrt{x_{20}^2 + x_{30}^2}\cdot(\cos\phi_2\cdot\cos\Omega_2 t - \sin\phi_2\cdot\sin\Omega_2 t) \\ x_3(t) &= \mathrm{e}^{\alpha_2 t}\cdot\sqrt{x_{20}^2 + x_{30}^2}\cdot(\sin\phi_2\cdot\cos\Omega_2 t + \cos\phi_2\cdot\sin\Omega_2 t), \end{aligned}$$

and finally

$$\begin{aligned} x_1(t) &= x_{10}\cdot \mathrm{e}^{\alpha_1 t} \\ x_2(t) &= \sqrt{x_{20}^2 + x_{30}^2}\cdot \mathrm{e}^{\alpha_2 t}\cdot\cos(\Omega_2 t + \phi_2) \\ x_3(t) &= \sqrt{x_{20}^2 + x_{30}^2}\cdot \mathrm{e}^{\alpha_2 t}\cdot\sin(\Omega_2 t + \phi_2). \end{aligned} \tag{12.78}$$

Substituting the numbers $\alpha_1 = -6$, $\alpha_2 = -1$, $\Omega_2 = 5$ gives

$$\begin{aligned} x_1(t) &= x_{10} \cdot \mathrm{e}^{-6t} \\ x_2(t) &= \sqrt{x_{20}^2 + x_{30}^2} \cdot \mathrm{e}^{-t} \cdot \cos(5t + \phi_2) \\ x_3(t) &= \sqrt{x_{20}^2 + x_{30}^2} \cdot \mathrm{e}^{-t} \cdot \sin(5t + \phi_2), \end{aligned} \tag{12.79}$$

where ϕ_2 is given by Equation (12.77) and depends on the initial conditions. As oscillatory responses $x_3(t)$ and $x_2(t)$ are proportional to cosine and sine functions, they are shifted in phase by $\pi/2$.

Initial conditions $x_{10} = x_{20} = x_{30} = 1$ give the phase angle of the mode equal to $\phi_2 = 45^\circ = \pi/4$ and the following time responses

$$x_1(t) = \mathrm{e}^{-6t}, \quad x_2(t) = \sqrt{2} \cdot \mathrm{e}^{-t} \cdot \cos\left(5t + \frac{\pi}{4}\right), \quad x_3(t) = \sqrt{2} \cdot \mathrm{e}^{-t} \cdot \sin\left(5t + \frac{\pi}{4}\right)$$

shown in Figure 12.1.

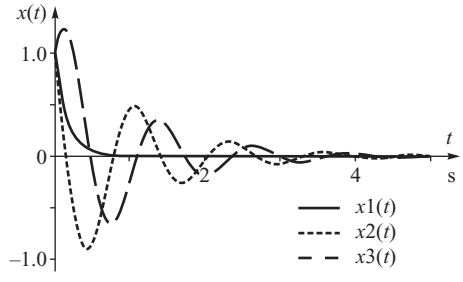

Figure 12.1 Illustration for the solution of Example 12.5.

The example shows that the overall system response can be represented as a linear combination of aperiodic and oscillatory modes. The real eigenvalue $\lambda_1 = -6$ produces the aperiodic mode e^{-6t} decaying with a time constant of $1/6 = 0.17$ s. The complex conjugate pair of eigenvalues $\lambda_{2,3} = (-1 \pm \mathrm{j}5)$ produces the oscillatory mode $\mathrm{e}^{-t} \cdot \cos(5t + \phi_2)$ oscillating at frequency 5rad/s and exponentially decaying with a time constant of 1 s. The system is stable because the real parts of all the eigenvalues are negative, that is the exponential functions are decaying. In this particular case the aperiodic mode shows itself only in the response of $x_1(t)$ while the oscillatory mode shows itself only in the responses of $x_2(t)$ and $x_3(t)$ because the first row of matrix $\boldsymbol{A}$ (corresponding to $x_1(t)$) contains only one diagonal element. In other words, the first row of $\boldsymbol{A}$ is decoupled from the other rows.

The considerations so far have assumed that all the eigenvalues of matrix $\boldsymbol{A}$ are distinct, $\lambda_1 \neq \lambda_2 \neq \cdots \neq \lambda_n$. If matrix $\boldsymbol{A}$ has multiple eigenvalues then the situation is more complicated. Nevertheless, it can be shown (Willems, 1970) that:

> The linear equation $\dot{\boldsymbol{x}} = \boldsymbol{A}\boldsymbol{x}$ is stable if, and only if, all the eigenvalues of matrix $\boldsymbol{A}$ have non-positive real parts, $\mathrm{Re}(\lambda_i) \leq 0$. The system is asymptotically stable if, and only if, all the eigenvalues of matrix $\boldsymbol{A}$ have negative real parts, $\mathrm{Re}(\lambda_i) < 0$.

The stability of a linear equation does not depend on the initial conditions but only on the eigenvalues of the state matrix $\boldsymbol{A}$.

12.1.4 Modal and Sensitivity Analysis

Equation (12.42) shows that each modal variable $z_i(t)$ can be expressed as a linear combination of the state variables, that is

$$z_i(t) = \sum_{j=1}^{n} u_{ij} x_j(t), \tag{12.80}$$

where u_{ij} is the (i, j) element of matrix $\boldsymbol{U}$ consisting of left eigenvectors. Expanding the sum in Equation (12.80) gives

$$z_i(t) = u_{i1}x_1(t) + u_{i2}x_2(t) + \cdots + u_{ij}x_j(t) + \cdots + u_{in}x_n(t). \tag{12.81}$$

This equation shows that the left eigenvectors carry information about the controllability of individual modal variable by individual state variables. If the eigenvectors are normalized then u_{ij} determines the magnitude and phase of the share of a given variable $x_j(t)$ in the activity of a given mode $z_i(t)$. Controlling $x_j(t)$ influences a given modal variable $z_i(t)$ only if element u_{ij} is large. If u_{ij} is small, then controlling $x_j(t)$ cannot influence modal variable $z_i(t)$.

Equation (12.41) shows that each state variable can be expressed as a linear combination of modal variables

$$x_k(t) = \sum_{i=1}^{n} w_{ki} z_i(t), \tag{12.82}$$

where w_{ki} is the (k, i) element of matrix $\boldsymbol{W}$ consisting of right eigenvectors. Expanding the sum in Equation (12.82) gives

$$x_k(t) = w_{k1}z_1(t) + w_{k2}z_2(t) + \cdots + w_{kj}z_j(t) + \cdots + w_{kn}z_n(t). \tag{12.83}$$

This equation shows that the right eigenvectors carry information about the observability of individual modal variables in individual state variables. If the eigenvectors are normalized then w_{kj} determines the magnitude and phase of the share of modal variable $z_j(t)$ in the activity of state variable $x_k(t)$. This is referred to as the *mode shape*. Note that the mode shape represents an inherent feature of a linear dynamic system and does not depend on where and how a disturbance is applied. The mode shape plays an important role in power system stability analysis, especially for determining the influence of individual oscillatory modes on swings of rotors of individual generators.

Example 12.6

For a certain large interconnected system, it has been calculated that the damping ratio of one of the oscillatory modes is unsatisfactory, $\zeta < 0.05$. This mode corresponds to a complex conjugate pair of eigenvalues $\lambda_i = -0.451 + \mathrm{j}2.198$ and $\lambda_j = \lambda_i^* = -0.451 - \mathrm{j}2.198$. The frequency of the mode is $2.198/2\pi \cong 0.35$ Hz while the damping ratio is $\zeta = 0.045/\sqrt{0.045^2 + 2.198^2} \cong 0.02$. The important elements of the right eigenvector associated with λ_i and the corresponding mode shapes are shown in Figure 12.2.

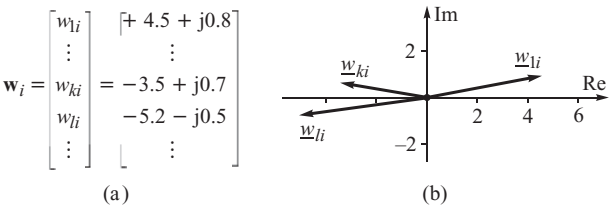

Figure 12.2 Example of mode shapes: (a) right eigenvector associated with the considered eigenvalue; (b) mode shapes in the complex plane.

The state variables corresponding to the considered mode shapes are the rotor angles of three generators: $x_1(t) = \Delta\delta_1(t)$, $x_k(t) = \Delta\delta_k(t)$, $x_l(t) = \Delta\delta_l(t)$. For these variables one gets, according to (12.83),

$$\begin{aligned} \Delta\delta_1(t) &= \cdots + w_{1i} z_i(t) + \cdots \\ \Delta\delta_k(t) &= \cdots + w_{ki} z_i(t) + \cdots \\ \Delta\delta_l(t) &= \cdots + w_{li} z_i(t) + \cdots . \end{aligned} \tag{12.84}$$

Figure 12.2 shows the mode shapes in the complex plane. Note that the mode shapes $\underline{w}_{ki}$, $\underline{w}_{li}$ are almost directly in the opposite direction with respect to the mode shape $\underline{w}_{1i}$. The interpretation of this is that if a disturbance excites a mode corresponding to the pair of complex eigenvalues $\lambda_i = \lambda_j^*$ then the rotor of generator 1 will swing at a frequency of 0.35 Hz against the rotors of generators k, l which are coherent with respect to each other at that particular frequency. Generator l swings almost directly against generator 1 (the phase difference is 186°) while the 0.35 Hz swings of generator k are shifted by 159° with respect to generator 1. Obviously these conclusions may not be true for other modes, that is other frequencies of modal oscillations making up the overall rotor swings.

Interesting examples of the application of mode shapes to analyse power swings in UCTE interconnected power systems can be found in Breulmann *et al.* (2000). The article describes how a number of poorly damped modes have been discovered and how they were grouped, using mode shapes, into coherent groups of generators swinging against each other.

Knowledge of matrices $\boldsymbol{W}$ and $\boldsymbol{U}$ allows the sensitivity of a particular modal variable $z_i(t)$ to the changes in a particular system parameter to be determined. This is especially important when choosing the parameter values of any control device installed in the system. Such a *sensitivity analysis* is accomplished in the following way.

Let λ_i be an eigenvalue of matrix $\boldsymbol{A}$ and $\boldsymbol{w}_i$ and $\boldsymbol{u}_i$ be the right and left eigenvectors associated with this eigenvalue. Equation (12.23) shows that $\boldsymbol{u}_i \boldsymbol{A} = \lambda_i \boldsymbol{u}_i$. Right-multiplying by $\boldsymbol{w}_i$ gives $\boldsymbol{u}_i \boldsymbol{A}\boldsymbol{w}_i = \lambda_i \boldsymbol{u}_i \boldsymbol{w}_i$. Substituting $\boldsymbol{u}_i \boldsymbol{w}_i = 1$ into the right hand side of that equation (see Equation (12.32)) gives

$$\lambda_i = \boldsymbol{u}_i \boldsymbol{A} \boldsymbol{w}_i . \tag{12.85}$$

Now let β be a system parameter. Equation (12.85) shows that

$$\frac{\partial \lambda_i}{\partial \beta} = \boldsymbol{u}_i \frac{\partial \boldsymbol{A}}{\partial \beta} \boldsymbol{w}_i . \tag{12.86}$$

If the derivative $\partial \boldsymbol{A}/\partial\beta$ in Equation (12.86) is known, then it is possible to determine whether or not a given parameter improves the system stability by observing if the eigenvalues acquire a larger real part, that is move to the left in the complex plane, when the value of a parameter changes.

A particular case of sensitivity analysis is the investigation of the influence of the diagonal elements of a state matrix on the eigenvalues. Assuming $\beta = A_{kk}$ gives

$$\boldsymbol{A} = \begin{bmatrix} A_{11} & \cdots & A_{1k} & \cdots \\ \vdots & \ddots & \vdots & \\ A_{k1} & \cdots & A_{kk} & \\ \vdots & & \vdots & \ddots \end{bmatrix} \quad \text{and} \quad \frac{\partial \boldsymbol{A}}{\partial \beta} = \frac{\partial \boldsymbol{A}}{\partial A_{kk}} = \begin{bmatrix} 0 & \cdots & 0 & \cdots \\ \vdots & \ddots & \vdots & \\ 0 & \cdots & 1 & \\ \vdots & & \vdots & \ddots \end{bmatrix} \tag{12.87}$$

$$\frac{\partial \lambda_i}{\partial A_{kk}} = \boldsymbol{u}_i \frac{\partial \boldsymbol{A}}{\partial A_{kk}} \boldsymbol{w}_i = \begin{bmatrix} u_{i1} & \cdots & u_{ik} & \cdots \end{bmatrix} \begin{bmatrix} 0 & \cdots & 0 & \cdots \\ \vdots & \ddots & \vdots & \\ 0 & \cdots & 1 & \\ \vdots & & \vdots & \ddots \end{bmatrix} \begin{bmatrix} w_{1i} \\ \vdots \\ w_{ki} \\ \vdots \end{bmatrix}. \tag{12.88}$$

Multiplying the matrices on the right hand side of Equation (12.88) gives

$$\frac{\partial \lambda_i}{\partial A_{kk}} = u_{ik} w_{ki} = p_{ki}. \tag{12.89}$$

Coefficients $p_{ki} = u_{ik} w_{ki}$ are referred to as the *participation factors*. Each participation factor is a product of the kth element of the ith left and right eigenvectors. It quantifies the sensitivity of the ith eigenvalue to the kth diagonal element of the state matrix. Element w_{ki} contains information about the observability of the ith modal variable in the kth state variable, while u_{ik} contains information about the controllability of the ith modal variable using the kth state variable. Hence the product $p_{ki} = u_{ik} w_{ki}$ contains information about the observability and controllability. Consequently, the participation factor $p_{ki} = u_{ik} w_{ki}$ is a good measure of correlation between the ith modal variable and the kth state variable. Participation factors can be used to determine the siting of devices, enhancing system stability. Generally a damping controller or a stabilizer is preferably sited where the modal variables associated with a given eigenvalue are both well observable and well controllable.

The method of calculation of participation factors for the ith eigenvalue and all diagonal elements $A_{11}, \ldots, A_{kk}, \ldots, A_{nn}$ of the state matrix $\boldsymbol{A}$ is illustrated below in Equation (12.90) in which for convenience transposition of the left eigenvalue was used:

$$\boldsymbol{u}_i^{\mathrm{T}} = \begin{bmatrix} u_{i1} \\ \vdots \\ u_{ik} \\ \vdots \\ u_{in} \end{bmatrix}, \quad \boldsymbol{w}_i = \begin{bmatrix} w_{1i} \\ \vdots \\ w_{ki} \\ \vdots \\ w_{ni} \end{bmatrix}; \quad \text{hence} \quad \begin{bmatrix} u_{i1} \\ \vdots \\ u_{ik} \\ \vdots \\ u_{in} \end{bmatrix} \begin{matrix} \rightarrow \\ \rightarrow \\ \\ \rightarrow \end{matrix} \begin{bmatrix} w_{1i} \\ \vdots \\ w_{ki} \\ \vdots \\ w_{ni} \end{bmatrix} \begin{matrix} \Rightarrow \\ \Rightarrow \\ \\ \Rightarrow \end{matrix} \begin{bmatrix} u_{i1} w_{1i} \\ \vdots \\ u_{ik} w_{ki} \\ \vdots \\ u_{in} w_{ni} \end{bmatrix} = \begin{bmatrix} p_{1i} \\ \vdots \\ p_{ki} \\ \vdots \\ p_{ni} \end{bmatrix} = \boldsymbol{p}_i. \tag{12.90}$$

Elements of column vector $\boldsymbol{p}_i$ contain participation factors quantifying to what extent individual diagonal elements $A_{11}, \ldots, A_{kk}, \ldots, A_{nn}$ of the state matrix may influence eigenvalue λ_i. If, for example, p_{ki} is large, it means that a diagonal element A_{kk} of the state matrix has s large influence on λ_i.

Example 12.7

Consider again the system used previously in Example 12.2, Example 12.4 and Example 12.5 characterized by

$$\boldsymbol{A} = \left[\begin{array}{c:c:c} -6 & 0 & 0 \\ \hdashline 0 & -1 & 5 \\ \hdashline 0 & -5 & -1 \end{array}\right]; \quad \lambda_1 = -6, \quad \lambda_2 = (-1 - \mathrm{j}5), \quad \lambda_3 = (-1 + \mathrm{j}5) = \lambda_2^*. \tag{12.91}$$

The concluding remark in Example 12.5 stated that, due to the block diagonal structure of matrix $\boldsymbol{A}$, the aperiodic mode corresponding to λ_1 was linked only with the first row of $\boldsymbol{A}$ while the oscillatory mode corresponding to $\lambda_2 = \lambda_3^*$ was linked only to the second and third rows of $\boldsymbol{A}$. This conclusion will now be confirmed formally by calculating participation factors.

Right eigenvalues $\boldsymbol{w}_1, \boldsymbol{w}_2, \boldsymbol{w}_3$ were calculated in Example 12.2. Left eigenvalues $\boldsymbol{u}_1, \boldsymbol{u}_2, \boldsymbol{u}_3$ were calculated in Example 12.4. For convenience, left-transposed eigenvectors are used, $\boldsymbol{u}_1^{\mathrm{T}}, \boldsymbol{u}_2^{\mathrm{T}}, \boldsymbol{u}_3^{\mathrm{T}}$. For the first pair, that is for λ_1, one gets

$$\boldsymbol{u}_1^{\mathrm{T}} = \frac{1}{4}\begin{bmatrix} 4 \\ 0 \\ 0 \end{bmatrix}, \quad \boldsymbol{w}_1 = \left[\begin{array}{c} 1 \\ \hdashline 0 \\ \hdashline 0 \end{array}\right] \quad \text{or} \quad \frac{1}{4}\begin{bmatrix} 4 \\ 0 \\ 0 \end{bmatrix} \begin{matrix} \rightarrow \\ \rightarrow \\ \rightarrow \end{matrix} \left[\begin{array}{c} 1 \\ \hdashline 0 \\ \hdashline 0 \end{array}\right] \begin{matrix} \Rightarrow \\ \Rightarrow \\ \Rightarrow \end{matrix} \left[\begin{array}{c} 1 \\ \hdashline 0 \\ \hdashline 0 \end{array}\right] = \boldsymbol{p}_1. \tag{12.92}$$

This confirms that that the first eigenvalue may be influenced only by changing element A_{11} of matrix $\boldsymbol{A}$. Elements A_{22} and A_{33} have no influence on λ_1 and the corresponding aperiodic mode.

For the second pair, that is for λ_2, one gets

$$\boldsymbol{u}_2^{\mathrm{T}} = \frac{1}{4}\begin{bmatrix} 0 \\ -1+\mathrm{j} \\ -1-\mathrm{j} \end{bmatrix}, \quad \boldsymbol{w}_2 = \left[\begin{array}{c} 0 \\ \hdashline -1-\mathrm{j} \\ \hdashline -1+\mathrm{j} \end{array}\right] \quad \text{or} \quad \frac{1}{4}\begin{bmatrix} 0 \\ -1+\mathrm{j} \\ -1-\mathrm{j} \end{bmatrix} \begin{matrix} \rightarrow \\ \rightarrow \\ \rightarrow \end{matrix} \left[\begin{array}{c} 0 \\ \hdashline -1-\mathrm{j} \\ \hdashline -1+\mathrm{j} \end{array}\right] \begin{matrix} \Rightarrow \\ \Rightarrow \\ \Rightarrow \end{matrix} \left[\begin{array}{c} 0 \\ \hdashline 2 \\ \hdashline 2 \end{array}\right] \frac{1}{4} = \boldsymbol{p}_2. \tag{12.93}$$

For the third pair, that is for $\lambda_3 = \lambda_2^*$, one gets

$$\boldsymbol{u}_3^{\mathrm{T}} = \frac{1}{4}\begin{bmatrix} 0 \\ -1-\mathrm{j} \\ -1+\mathrm{j} \end{bmatrix}, \quad \boldsymbol{w}_3 = \left[\begin{array}{c} 0 \\ \hdashline -1+\mathrm{j} \\ \hdashline -1-\mathrm{j} \end{array}\right] \quad \text{or} \quad \frac{1}{4}\begin{bmatrix} 0 \\ -1-\mathrm{j} \\ -1+\mathrm{j} \end{bmatrix} \begin{matrix} \rightarrow \\ \rightarrow \\ \rightarrow \end{matrix} \left[\begin{array}{c} 0 \\ \hdashline -1+\mathrm{j} \\ \hdashline -1-\mathrm{j} \end{array}\right] \begin{matrix} \Rightarrow \\ \Rightarrow \\ \Rightarrow \end{matrix} \left[\begin{array}{c} 0 \\ \hdashline 2 \\ \hdashline 2 \end{array}\right] \frac{1}{4} = \boldsymbol{p}_3. \tag{12.94}$$

This confirms that eigenvalues λ_2 and $\lambda_3 = \lambda_2^*$ may be equally influenced by changing elements A_{22} and A_{33} of $\boldsymbol{A}$. Element A_{11} has no influence on λ_2 and $\lambda_3 = \lambda_2^*$.

12.1.5 Modal Form of the State Equation with Inputs

The state equation (12.38) is homogeneous; that is, it is of the form $\dot{\boldsymbol{x}} - \boldsymbol{A}\boldsymbol{x} = 0$. Sometimes it is necessary to consider a non-homogeneous equation of the form $\dot{\boldsymbol{x}} - \boldsymbol{A}\boldsymbol{x} = \boldsymbol{B}\boldsymbol{u}$. This equation is

usually written as

$$\dot{\boldsymbol{x}} = \boldsymbol{A}\boldsymbol{x} + \boldsymbol{B}\boldsymbol{u} \tag{12.95}$$

where $\boldsymbol{B}$ is a rectangular matrix and $\boldsymbol{u}$ is a column vector containing system inputs.

Equation (12.95) can also be analysed using modal analysis. Substituting Equations (12.41) into Equation (12.95) gives $\boldsymbol{W}\dot{\boldsymbol{z}} = \boldsymbol{A}\boldsymbol{W}\boldsymbol{z} + \boldsymbol{B}\boldsymbol{u}$, or $\dot{\boldsymbol{z}} = \boldsymbol{W}^{-1}\boldsymbol{A}\boldsymbol{W}\boldsymbol{z} + \boldsymbol{W}^{-1}\boldsymbol{B}\boldsymbol{u}$. After taking into account Equations (12.20) and (12.21), this gives

$$\dot{\boldsymbol{z}} = \boldsymbol{\Lambda}\boldsymbol{z} + \boldsymbol{b}\boldsymbol{u}. \tag{12.96}$$

where $\boldsymbol{b} = \boldsymbol{W}^{-1}\boldsymbol{B} = \boldsymbol{U}\boldsymbol{B}$. Equation (12.96) represents the modal form of the state equation (12.95). This equation may be used to study the influence of inputs $\boldsymbol{u}$ on the excitation of modal variables $\boldsymbol{z}(t)$. Equation (12.96) may be written as

$$\begin{bmatrix} \dot{z}_1 \\ \vdots \\ \dot{z}_i \\ \vdots \\ \dot{z}_n \end{bmatrix} = \begin{bmatrix} \lambda_1 & & & & \\ & \ddots & & & \\ & & \lambda_i & & \\ & & & \ddots & \\ & & & & \lambda_n \end{bmatrix} \begin{bmatrix} z_1 \\ \vdots \\ z_i \\ \vdots \\ z_n \end{bmatrix} + \begin{bmatrix} \boldsymbol{b}_1 \\ \vdots \\ \boldsymbol{b}_i \\ \vdots \\ \boldsymbol{b}_n \end{bmatrix} \boldsymbol{u}, \tag{12.97}$$

or $\dot{z}_i = \lambda_i z_i + \boldsymbol{b}_i \boldsymbol{u}$. It shows that the excitation of a given modal variable by input $\boldsymbol{u}$ is decided by row vector $\boldsymbol{b}_i$. It may happen that a certain structure of matrix $\boldsymbol{B}$ results in some modal variables not being excited. An example of this will be given in Section 14.6.3.

12.1.6 Nonlinear System

Generally a nonlinear dynamic system can be described by the differential matrix equation

$$\dot{\boldsymbol{x}} = \boldsymbol{F}(\boldsymbol{x}), \tag{12.98}$$

where $\boldsymbol{x}$ is the vector of the $\boldsymbol{n}$ state variables. The equilibrium points $\hat{x}$ are those points where the system is at rest, that is where all the state variables are constant and their values do not change with time, so that $\boldsymbol{F}(\hat{x}) = \boldsymbol{0}$. Expanding function $\boldsymbol{F}(\boldsymbol{x})$ in the vicinity of $\hat{\boldsymbol{x}}$ in a Taylor series, and neglecting the nonlinear part of the expansion, gives the *linear approximation* of the nonlinear equation (12.98) as

$$\Delta\dot{\boldsymbol{x}} = \boldsymbol{A}\Delta\boldsymbol{x}, \tag{12.99}$$

where $\Delta\boldsymbol{x} = \boldsymbol{x} - \hat{\boldsymbol{x}}$ and $\boldsymbol{A} = \partial\boldsymbol{F}/\partial\boldsymbol{x}$ is the Jacobi matrix calculated at the point $\hat{\boldsymbol{x}}$. Equation (12.99) is known as the state equation.

Lyapunov's first method now defines the stability of the nonlinear system based on its linear approximation as follows:

> A nonlinear system is steady-state stable in the vicinity of the equilibrium point $\hat{x}$ if its linear approximation is asymptotically stable. If the linear approximation is unstable, then the nonlinear system is also unstable. If the linear approximation is stable, but not asymptotically stable, then it is not possible to assess the system stability based on its linear approximation.

This theorem, together with Lyapunov's first theorem, leads to the conclusion that if the nonlinear equation $\dot{\boldsymbol{x}} = \boldsymbol{F}(\boldsymbol{x})$ can be approximated by the linear equation $\Delta\dot{\boldsymbol{x}} = \boldsymbol{A}\Delta\boldsymbol{x}$ then the nonlinear system is asymptotically stable if all the eigenvalues of the state matrix $\boldsymbol{A}$ are negative ($\mathrm{Re}(\lambda_i) < 0$).

If any of the eigenvalues have a positive real part then the system is unstable. If any of the eigenvalues are zero then no conclusion can be reached with regard to the system stability and some other method, such as Lyapunov's second method, must be used.

12.2 Steady-State Stability of Unregulated System

The *inherent steady-state stability* of a power system is concerned with analysing the response of generators when the system is subjected to a small disturbance and when the effect of the voltage regulators is neglected. This form of stability was first discussed in Section 5.4 for the generator–infinite busbar system where the steady-state stability limit (critical power) was determined (Figure 5.5) by the steady-state model of the generator; that is constant emfs $E_\mathrm{f} = E_\mathrm{q}$ and $E_\mathrm{d} = 0$ behind the synchronous reactances X_d and X_q in conjunction with the swing equation, Equation (5.15). The same assumption is valid in this chapter when each ith generator is replaced by emf E_i behind reactance X_i. In the considered case of an unregulated system it is further assumed that

$$\underline{E}_i = \underline{E}_{\mathrm{q}i} \quad \text{and} \quad X_i = X_{\mathrm{d}i} = X_{\mathrm{q}i}. \tag{12.100}$$

Nodes behind the generator reactances form the generator nodes set {G}. The system model is shown schematically in Figure 12.3a. {L} is the set of load nodes that are eliminated, which leads to an equivalent transfer network, shown in Figure 12.3b. In the equivalent network, the generator nodes {G} are directly connected with each other.

Assuming small power angle variations, the swing equation, Equation (5.15), can be written in the following way for each ith generator:

$$\begin{aligned} \frac{\mathrm{d}\Delta\delta_i}{\mathrm{d}t} &= \Delta\omega_i \\ \frac{\mathrm{d}\Delta\omega_i}{\mathrm{d}t} &= -\frac{\Delta P_i}{M_i} - \frac{D_i}{M_i}\Delta\omega_i \end{aligned} \qquad \text{for} \quad i = 1, 2, \ldots, n, \tag{12.101}$$

where ΔP_i is the change in the generator real power determined using the incremental network equations (3.157). Equations (3.157) and (12.101) constitute the basic linearized system model suitable for assessing small-signal stability. However, the final form of the state equation will depend on additional assumptions regarding the value of the damping coefficients and the load model used.

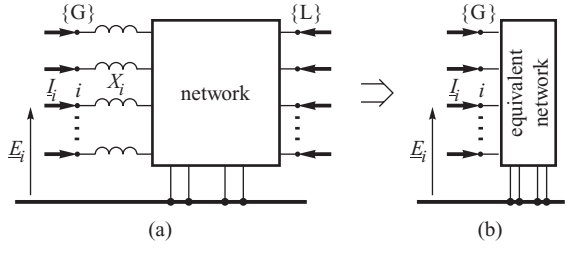

Figure 12.3 Network model for the steady-state stability analysis: (a) before elimination of load nodes; (b) after elimination. {G} is the set of generator nodes behind the synchronous reactances, {L} is the set of load nodes including generator terminals.

12.2.1 State-Space Equation

Computations are considerably simplified if all the system loads are modelled as constant impedance loads. Further simplifications can be introduced by neglecting steady-state saliency so that for all the generators $X_d = X_q$. The next step is to eliminate all the load nodes, including the generator terminal nodes, in the network model of Figure 12.3 using the method described in Section 12.2. The only retained nodes are the fictitious generator nodes behind the synchronous reactances. The equivalent transfer network directly links all the generator nodes. For this network, Equations (3.154) and (3.157) can be used with the voltages V_i replaced by the synchronous emfs E_i. As $\Delta E_i = 0$, Equation (3.157) can be simplified to

$$\Delta \boldsymbol{P} = \boldsymbol{H}\Delta\boldsymbol{\delta}, \tag{12.102}$$

where, according to Equation (3.160), the elements of the Jacobi matrix are

$$\begin{aligned} H_{ij} &= \frac{\partial P_i}{\partial \delta_j} = E_i E_j(-B_{ij}\cos\delta_{ij} + G_{ij}\sin\delta_{ij}) \\ H_{ii} &= \frac{\partial P_i}{\partial \delta_i} = \sum_{j=1}^{n} E_i E_j(B_{ij}\cos\delta_{ij} - G_{ij}\sin\delta_{ij}). \end{aligned} \tag{12.103}$$

The matrix $\boldsymbol{H}$ is singular because the sum of the elements in each of its rows is zero:

$$\sum_{j=1}^{n} H_{ij} = H_{ii} + \sum_{j\neq i}^{n} H_{ij} = 0. \tag{12.104}$$

At this stage it is tempting to define the increments in the power angles as the state variables but, as a loss of synchronism does not correspond to a simultaneous increase in all the power angles, this is not a valid choice. Rather, as a loss of synchronism is determined by the relative angles $\Delta\delta_{in}$ calculated with respect to a *reference generator*, it is the increments in these relative angles that must be used as the state variables. This is illustrated in Figure 12.4.

The power change in all the generators must now be related to the relative angles $\Delta\delta_{in}$. Assuming that the last generator, numbered n, acts as the reference, Equation (12.104) gives

$$H_{in} = -\sum_{j\neq n}^{n} H_{ij}. \tag{12.105}$$

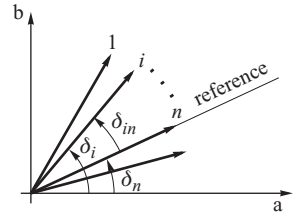

Figure 12.4 The emfs in the complex plane. Finding the relative angles $\delta_{in} = \delta_i - \delta_n$ where n is the reference generator and (a, b) are the rectangular coordinates of network equations.

The power change in any of the generators, Equation (12.102), can be expressed as

$$\begin{aligned}\Delta P_i &= \sum_{j=1}^{n} H_{ij}\Delta\delta_i = \sum_{j\neq n} H_{ij}\Delta\delta_j + H_{in}\Delta\delta_n = \sum_{j\neq n} H_{ij}\Delta\delta_j - \sum_{j\neq n} H_{ij}\Delta\delta_n \\ &= \sum_{j\neq n} H_{ij}(\Delta\delta_j - \Delta\delta_n) = \sum_{j\neq n} H_{ij}\Delta\delta_{jn}.\end{aligned} \tag{12.106}$$

Equation (12.102) can now be expressed as a function of the relative angles by removing the last column of $\boldsymbol{H}$, that is

$$\begin{bmatrix}\Delta P_1\\ \Delta P_2\\ \vdots\\ \Delta P_n\end{bmatrix} = \begin{bmatrix}H_{11} & H_{12} & \cdots & H_{1,n-1}\\ H_{21} & H_{22} & \cdots & H_{2,n-1}\\ \vdots & \vdots & \ddots & \vdots\\ H_{21} & H_{n2} & \cdots & H_{n,n-1}\end{bmatrix}\begin{bmatrix}\Delta\delta_{1n}\\ \Delta\delta_{2n}\\ \vdots\\ \Delta\delta_{n-1,n}\end{bmatrix} \quad \text{or} \quad \Delta\boldsymbol{P} = \boldsymbol{H}_n\Delta\boldsymbol{\delta}_n, \tag{12.107}$$

where the matrix $\boldsymbol{H}_n$ is rectangular and is of dimension $n \times (n-1)$ while the vector $\Delta\delta_n$ contains $(n-1)$ relative rotor angles calculated with respect to the nth reference generator.

Substituting Equation (12.107) into the differential equation (12.101) gives

$$\begin{bmatrix}\Delta\dot{\delta}_{1n}\\ \Delta\dot{\delta}_{2n}\\ \vdots\\ \Delta\dot{\delta}_{n-1,n}\\ \hline \Delta\dot{\omega}_1\\ \Delta\dot{\omega}_2\\ \vdots\\ \Delta\dot{\omega}_{n-1}\\ \hline \Delta\dot{\omega}_n\end{bmatrix} = \left[\begin{array}{cccc:cccc:c} 0 & 0 & \cdots & 0 & 1 & 0 & \cdots & 0 & -1\\ 0 & 0 & \cdots & 0 & 0 & 1 & \cdots & 0 & -1\\ \vdots & \vdots & \ddots & \vdots & \vdots & \vdots & \ddots & \vdots & \vdots\\ 0 & 0 & \cdots & 0 & 0 & 0 & \cdots & 1 & -1\\ \hline -\frac{H_{11}}{M_1} & -\frac{H_{12}}{M_1} & \cdots & -\frac{H_{1,n-1}}{M_1} & -\frac{D_1}{M_1} & 0 & \cdots & 0 & 0\\ -\frac{H_{21}}{M_2} & -\frac{H_{22}}{M_2} & \cdots & -\frac{H_{2,n-1}}{M_2} & 0 & -\frac{D_2}{M_2} & \cdots & 0 & 0\\ \vdots & \vdots & \ddots & \vdots & \vdots & \vdots & \ddots & \vdots & \vdots\\ -\frac{H_{n-1,1}}{M_{n-1}} & -\frac{H_{n-1,n-1}}{M_{n-1}} & \cdots & -\frac{H_{n-1,n-1}}{M_{n-1}} & 0 & 0 & \cdots & -\frac{D_{n-1}}{M_{n-1}} & 0\\ \hline -\frac{H_{n1}}{M_n} & -\frac{H_{n2}}{M_n} & \cdots & -\frac{H_{n,n-1}}{M_n} & 0 & 0 & \cdots & 0 & -\frac{D_n}{M_n}\end{array}\right]\begin{bmatrix}\Delta\delta_{1n}\\ \Delta\delta_{2n}\\ \vdots\\ \Delta\delta_{n-1,n}\\ \hline \Delta\omega_1\\ \Delta\omega_2\\ \vdots\\ \Delta\omega_{n-1}\\ \hline \Delta\omega_n\end{bmatrix}. \tag{12.108}$$

Equation (12.108) can be expressed more compactly as

$$\begin{bmatrix}\boldsymbol{\Delta\dot{\delta}}_n\\ \hline \boldsymbol{\Delta\dot{\omega}}\end{bmatrix} = \left[\begin{array}{c:c} \mathbf{0} & \mathbf{1}_{-1}\\ \hline -\boldsymbol{M}^{-1}\boldsymbol{H}_n & -\boldsymbol{M}^{-1}\boldsymbol{D}\end{array}\right]\begin{bmatrix}\boldsymbol{\Delta\delta}_n\\ \hline \boldsymbol{\Delta\omega}\end{bmatrix} \quad \text{or} \quad \boldsymbol{\Delta\dot{x}} = \boldsymbol{A}\boldsymbol{\Delta x}, \tag{12.109}$$

where $\mathbf{1}_{-1}$ denotes a diagonal unit matrix extended by a column whose elements are equal to (-1). In this equation the state vector has $(2n-1)$ elements consisting of $(n-1)$ angle changes and n speed deviations. The matrix $\boldsymbol{A}$ has a rank equal to $(2n-1)$.

For the generator–infinite busbar system Equation (12.108) takes the form

$$\begin{bmatrix} \Delta\dot{\delta} \\ \hline \Delta\dot{\omega} \end{bmatrix} = \left[\begin{array}{c|c} 0 & 1 \\ \hline -\dfrac{H}{M} & -\dfrac{D}{M} \end{array}\right] \begin{bmatrix} \Delta\delta \\ \hline \Delta\omega \end{bmatrix}. \tag{12.110}$$

The characteristic equation of this matrix is

$$\lambda^2 + \frac{D}{M}\lambda + \frac{H}{M} = 0 \tag{12.111}$$

and results in two eigenvalues. This equation is identical to the characteristic equation (5.59) but with $H = K_{E_q}$ used instead of the transient synchronizing power coefficient $K_{E'}$. This is a consequence of using Equation (12.108) or (12.110) to assess the steady-state stability, not the frequency of rotor oscillations. If the classical transient model were used with the generator represented by the transient reactance X'_d then Equation (12.108) or (12.110) could be used to determine the frequency of oscillations but not for assessing the steady-state stability. As shown in Section 5.4, Figure 5.16, the steady-state stability limit is determined by the steady-state characteristic obtained when the generator is represented by the emf E_q behind the synchronous reactance X_d.

12.2.2 Simplified Steady-State Stability Conditions

Equation (12.108) is valid when the network conductances are included and for any value of the damping coefficients. Checking the steady-state stability condition requires the calculation of eigenvalues of matrix $\boldsymbol{A}$, which is time consuming. This can be significantly simplified if network conductances are neglected and uniform weak damping of swings of all generators is assumed.

Damping of rotor swing in a system is *uniform* if

$$\frac{D_1}{M_1} = \frac{D_2}{M_2} = \cdots = \frac{D_n}{M_n} = d. \tag{12.112}$$

With uniform damping the swing equation for any machine, and for the reference machine, can be written as

$$\frac{\mathrm{d}\Delta\omega_i}{\mathrm{d}t} = -\frac{\Delta P_i}{M_i} - d\Delta\omega_i, \quad \frac{\mathrm{d}\Delta\omega_n}{\mathrm{d}t} = -\frac{\Delta P_n}{M_n} - d\Delta\omega_n. \tag{12.113}$$

Subtracting the last equation from the first gives

$$\frac{\mathrm{d}\Delta\omega_{in}}{\mathrm{d}t} = -\left(\frac{\Delta P_i}{M_i} - \frac{\Delta P_n}{M_n}\right) - d\Delta\omega_{in} \quad \text{or} \quad i = 1,\ 2, \ldots, (n-1), \tag{12.114}$$

where $\Delta\omega_{in} = \Delta\omega_i - \Delta\omega_n = \mathrm{d}\delta_{in}/\mathrm{d}t$ and is the rotor speed deviation of the ith generator relative to the reference machine. Substituting the power changes calculated from Equation (12.107) into Equation (12.114) gives

$$\begin{bmatrix} \boldsymbol{\Delta\dot{\delta}}_{n-1} \\ \hline \boldsymbol{\Delta\dot{\omega}}_{n-1} \end{bmatrix} = \left[\begin{array}{c|c} \boldsymbol{0} & \boldsymbol{1} \\ \hline \boldsymbol{a} & -\boldsymbol{d} \end{array}\right] \begin{bmatrix} \boldsymbol{\Delta\delta}_{n-1} \\ \hline \boldsymbol{\Delta\omega}_{n-1} \end{bmatrix} \quad \text{or} \quad \boldsymbol{\Delta\dot{x}} = \boldsymbol{A\Delta x}, \tag{12.115}$$

where $\mathbf{1}$ is the unit matrix, $\Delta\boldsymbol{\delta}_{n-1}$ and $\Delta\boldsymbol{\omega}_{n-1}$ are the vectors of the $(n-1)$ relative changes in the power angles and speed deviations, and $\boldsymbol{d}$ is a diagonal matrix in which all the diagonal elements

are identical and equal to d given by Equation (12.112). The matrix $\boldsymbol{a}$ is equal to

$$\boldsymbol{a} = -\begin{bmatrix} \dfrac{H_{11}}{M_1} - \dfrac{H_{n1}}{M_n} & \dfrac{H_{12}}{M_1} - \dfrac{H_{n2}}{M_n} & \cdots & \dfrac{H_{1,n-1}}{M_1} - \dfrac{H_{n,n-1}}{M_n} \\ \dfrac{H_{21}}{M_2} - \dfrac{H_{n1}}{M_n} & \dfrac{H_{22}}{M_2} - \dfrac{H_{n2}}{M_n} & \cdots & \dfrac{H_{2,n-1}}{M_2} - \dfrac{H_{n,n-1}}{M_n} \\ \vdots & \vdots & \ddots & \vdots \\ \dfrac{H_{n-1,1}}{M_{n-1}} - \dfrac{H_{n1}}{M_n} & \dfrac{H_{n-1,2}}{M_{n-1}} - \dfrac{H_{n2}}{M_n} & \cdots & \dfrac{H_{n-1,n-1}}{M_{n-1}} - \dfrac{H_{n,n-1}}{M_n} \end{bmatrix}. \tag{12.116}$$

Comparing the matrix $\boldsymbol{a}$ with the square state matrix in Equation (12.108) shows that the matrix $\boldsymbol{a}$ is created by subtracting the last row in Equation (12.108) from all the upper rows corresponding to the elements H_{ij}. The state vector in Equation (12.115) has $(2n-2)$ elements, including $(n-1)$ relative angles $\Delta\delta_{in}$ and $(n-1)$ relative speed deviations $\Delta\omega_{in}$. The problem of finding the eigenvalues of the state matrix in Equation (12.115) can now be simplified to that of determining the eigenvalues of the matrix $\boldsymbol{a}$ which, with rank $(n-1)$, is half the size. This can be explained as follows.

Let λ_i and w_i be the eigenvalues and eigenvectors of the matrix $\boldsymbol{A}$ in Equation (12.115). The definition of the eigenvalues and eigenvectors gives

$$\begin{bmatrix} \mathbf{0} & \vdots & \mathbf{1} \\ \cdots & \vdots & \cdots \\ \boldsymbol{a} & \vdots & -\boldsymbol{d} \end{bmatrix} \begin{bmatrix} \boldsymbol{w'}_i \\ \text{----} \\ \boldsymbol{w''}_i \end{bmatrix} = \lambda_i \begin{bmatrix} \boldsymbol{w'}_i \\ \text{----} \\ \boldsymbol{w''}_i \end{bmatrix}, \tag{12.117}$$

or, after multiplying, $\boldsymbol{w}''_i = \lambda_i \boldsymbol{w}'_i$ and $(\boldsymbol{a}\boldsymbol{w}'_i - \boldsymbol{d}\boldsymbol{w}''_i) = \lambda_i \boldsymbol{w}''_i$. Substituting $\boldsymbol{w}''_i$ calculated from the first equation into the second gives $\boldsymbol{a}\boldsymbol{w}'_i = (\lambda_i^2 + d\lambda_i)\boldsymbol{w}'_i$ or $\boldsymbol{a}\boldsymbol{w}'_i = \mu_i \boldsymbol{w}'_i$ where $\mu_i = \lambda_i^2 + d\lambda_i$. Hence

$$\lambda_i^2 + d\lambda_i - \mu_i = 0. \tag{12.118}$$

Obviously μ_i and $\boldsymbol{w}'_i$ also satisfy the definition of eigenvalues and eigenvectors of matrix $\boldsymbol{a}$. The eigenvalue λ_i can be found by solving Equation (12.118) to give

$$\lambda_i = -\frac{d}{2} \pm \sqrt{\frac{d^2}{4} + \mu_i}. \tag{12.119}$$

Thus, knowing the eigenvalues μ_i of matrix $\boldsymbol{a}$ it is possible to determine the eigenvalues λ_i. With this information it is possible to evaluate the system stability knowing the eigenvalues μ_i and the damping coefficient d. Obviously, determining the eigenvalues μ_i of matrix $\boldsymbol{a}$ of rank $(n-1)$ is less computationally intensive than determining the eigenvalues λ_i of matrix $\boldsymbol{A}$ which has a rank $(2n-2)$. Thus the assumption of uniform damping, if valid, considerably simplifies stability calculations.

Equation (12.118) shows that if the damping coefficient is zero, $d \cong 0$, then $\lambda_i = \pm\sqrt{\mu_i}$, that is the eigenvalues of the state matrix $\boldsymbol{A}$ are the square root values of the eigenvalues of matrix $\boldsymbol{a}$. Hence if an eigenvalue μ_i is complex (Figure 12.5a) then one of the eigenvalues λ_i lies on the right hand side of the complex plane and the system is unstable. On the other hand, if an eigenvalue μ_i is real and negative (Figure 12.5b) then the corresponding eigenvalues λ_i lie on the imaginary axis. In this case any small positive damping will move the eigenvalues to the left hand plane and the system will be stable (Figure 12.5c).

When damping is weak, the steady-state stability condition is that eigenvalues μ_i of matrix $\boldsymbol{a}$ should be real and negative:

$$\mu_i \in \text{Real} \quad \text{and} \quad \mu_i < 0 \quad \text{for} \quad i = 1,\ 2, \ldots,\ n-1. \tag{12.120}$$

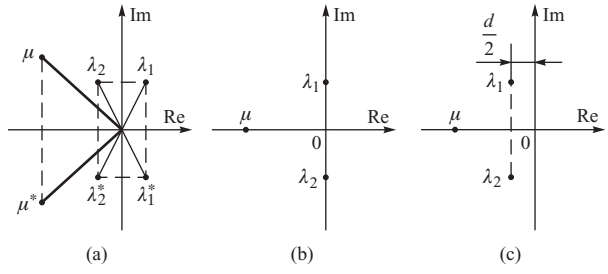

Figure 12.5 Eigenvalues μ and λ when: (a) μ is complex; (b) μ is real and negative; (c) μ is real and negative and there is positive damping.

Further simplification can be obtained by neglecting network conductances. Equation (12.103) shows that if $G_{ij} \cong 0$ then $H_{ij} \cong H_{ji}$, that is the matrix of synchronizing powers is symmetric $\boldsymbol{H}^{\mathrm{T}} = \boldsymbol{H}$.

When matrix $\boldsymbol{H}$ is symmetric, Equation (12.104) is valid for rows and also valid for columns of the matrix. Similar to (12.105) one gets

$$H_{nj} = -\sum_{i \neq n}^{n} H_{ij}. \tag{12.121}$$

Under this assumption matrix (12.116) can be written in a product form

$$\boldsymbol{a} = -\boldsymbol{m}\ \boldsymbol{H}_{n-1}, \tag{12.122}$$

where

$$\boldsymbol{m} = \begin{bmatrix} \frac{1}{M_1} + \frac{1}{M_n} & \frac{1}{M_n} & \cdots & \frac{1}{M_n} \\ \frac{1}{M_n} & \frac{1}{M_2} + \frac{1}{M_n} & \cdots & \frac{1}{M_n} \\ \vdots & \vdots & \ddots & \vdots \\ \frac{1}{M_n} & \frac{1}{M_n} & \cdots & \frac{1}{M_{n-1}} + \frac{1}{M_n} \end{bmatrix} \tag{12.123}$$

$$\boldsymbol{H}_{n-1} = \begin{bmatrix} H_{11} & H_{12} & \cdots & H_{1,n-1} \\ H_{21} & H_{22} & \cdots & H_{2,n-1} \\ \vdots & \vdots & \ddots & \vdots \\ H_{n-1,1} & H_{n-1,2} & \cdots & H_{n-1,n-1} \end{bmatrix}. \tag{12.124}$$

According to the definition of the right eigenvector and eigenvalue, $\boldsymbol{a}\boldsymbol{w}_i = \mu_i \boldsymbol{w}_i$ holds. Substituting for $\boldsymbol{a}$ on the right hand side of Equation (12.122) gives $\boldsymbol{m}\boldsymbol{H}_{n-1}\boldsymbol{w}_i = -\mu_i \boldsymbol{w}_i$, that is

$$\boldsymbol{H}_{n-1}\boldsymbol{w}_i = -\mu_i \boldsymbol{m}^{-1}\boldsymbol{w}_i \tag{12.125}$$

and

$$\boldsymbol{w}_i^{*\mathrm{T}}\,\boldsymbol{H}_{n-1}^{*\mathrm{T}} = -\mu_i^* \boldsymbol{w}_i^{*\mathrm{T}} (\boldsymbol{m}^{-1})^{*\mathrm{T}}. \tag{12.126}$$

Now Equation (12.125) should be left-multiplied by $\boldsymbol{w}_i^{*\mathrm{T}}$ and Equation (12.126) right-multiplied by $\boldsymbol{w}_i$. This gives

$$\boldsymbol{w}_i^{*\mathrm{T}} \boldsymbol{H}_{n-1} \boldsymbol{w}_i = -\mu_i \boldsymbol{w}_i^{*\mathrm{T}} \boldsymbol{m}^{-1} \boldsymbol{w}_i \tag{12.127}$$

$$\boldsymbol{w}_i^{*\mathrm{T}} \boldsymbol{H}_{n-1}^{*\mathrm{T}} \boldsymbol{w}_i = -\mu_i^* \boldsymbol{w}_i^{*\mathrm{T}} (\boldsymbol{m}^{-1})^{*\mathrm{T}} \boldsymbol{w}_i. \tag{12.128}$$

Under the discussed assumptions matrix $\boldsymbol{H}_{n-1}$ is real and symmetric and therefore $\boldsymbol{H}_{n-1} = \boldsymbol{H}_{n-1}^{*\mathrm{T}}$ holds. Similarly for the matrix in Equation (12.123), $\boldsymbol{m}^{-1} = (\boldsymbol{m}^{-1})^{*\mathrm{T}}$ holds. Now comparing Equations (12.127) and (12.128) gives $\mu_i^* = \mu_i$. This means that under the considered assumptions (neglecting conductances) the eigenvalues μ_i of matrix $\boldsymbol{a}$ are real $\mu_i \in \mathrm{Real}$. Hence the first of conditions (12.120) is satisfied and there is no need to check it. Checking the second of conditions (12.120), that is $\mu_i < 0$, can be simplified by the following observations.

It is easy to check that matrix $\boldsymbol{m}$ is positive definite, hence $\boldsymbol{w}_i^{*\mathrm{T}} \boldsymbol{m}^{-1} \boldsymbol{w}_i > 0$. Equation (12.127) shows that if $\mu_i < 0$ then $\boldsymbol{w}_i^{*\mathrm{T}} \boldsymbol{H}_{n-1} \boldsymbol{w}_i > 0$. This means that instead of checking if the eigenvalues μ_i are negative, it is enough to check if matrix $\boldsymbol{H}_{n-1}$ is positive definite. If conductances are neglected, the steady-state stability condition is that the matrix of synchronizing powers $\boldsymbol{H}_{n-1}$ is positive definite. According to Sylvester's theorem, this condition is satisfied if the main minors are positive, that is

$$H_{11} > 0, \quad \begin{vmatrix} H_{11} & H_{12} \\ H_{21} & H_{22} \end{vmatrix} > 0, \quad \begin{vmatrix} H_{11} & H_{12} & H_{13} \\ H_{21} & H_{22} & H_{23} \\ H_{31} & H_{32} & H_{33} \end{vmatrix} > 0, \quad \text{etc.} \tag{12.129}$$

Condition (12.129) is a generalization of condition (5.33) in Section 5.4.1 obtained for the generator–infinite busbar system when condition (12.129) simplifies to $H_{11} > 0$, that is $H = (\partial P / \partial \delta) > 0$.

It can be shown that when the conductances are neglected, the sufficient condition for matrix $\boldsymbol{H}_{n-1}$ to be positive definite is

$$\left|\delta_i - \delta_j\right| < \frac{\pi}{2} \quad \text{for} \quad i, j = 1, 2, \ldots, n \tag{12.130}$$

This means that the angle between the emfs of any pair of generators must be less than $\pi/2$. Proof of this will be undertaken in the following way. Matrix $\boldsymbol{H}_{n-1}$ can be expressed as

$$\boldsymbol{H}_{n-1} = \boldsymbol{C}^{\mathrm{T}} (\mathrm{diag} H_{ij})\, \boldsymbol{C} \tag{12.131}$$

where $\boldsymbol{C}$ is the incidence matrix of generator nodes and the branches linking them. Each such branch corresponds to a parameter

$$H_{ij} = \partial P_i / \partial \delta_j = -E_i E_j B_{ij} \cos \delta_{ij}, \tag{12.132}$$

corresponding to the synchronizing power. According to the Cauchy–Binet theorem (Seshu and Reed, 1961), the determinant of matrix (12.131) can be expressed as

$$\det \boldsymbol{H}_{n-1} = \sum_{\text{trees}} \left(\prod_{\text{branches}} (-H_{ij}) \right), \tag{12.133}$$

that is as the sum of negative values of synchronizing powers over all the possible branches of the graph. The sufficient condition for the sum to be positive is that each component is positive. The sufficient condition for each component to be positive is $(-H_{ij}) = E_i E_j B_{ij} \cos \delta_{ij} > 0$, or $\cos \delta_{ij} > 0$, as for the inductive branches $B_{ij} > 0$. Condition $\cos \delta_{ij} > 0$ is satisfied if condition (12.130) is satisfied. Similar considerations can be applied for matrices $\boldsymbol{H}_{n-2}$, $\boldsymbol{H}_{n-3}$ and so on, that is the main minors of matrix $\boldsymbol{H}_{n-1}$.

The stability conditions (12.120), (12.129) and (12.130) are all based on a variety of assumptions. Condition (12.120) is the most accurate because it includes network conductances which are neglected in condition (12.129). Condition (12.130) holds when the network conductances are neglected. Compared with (12.120), conditions (12.129) and (12.130) give an approximate assessment of steady-state stability. This will be illustrated using an example.

Example 12.8

Consider a three-machine system in which elimination of the load nodes has resulted in the following admittances (in per-unit notation) of the branches linking the generator nodes: $y_{12} = (0.3 + \mathrm{j}1.0)$, $y_{13} = (2.5 + \mathrm{j}7.0)$ and $y_{23} = (1.5 + \mathrm{j}4.0)$. The inertia coefficients of the generators are $M_1 = 10$, $M_2 = 2$ and $M_3 = 1$. The third generator was assumed to be the reference machine; hence the angles δ_{13} and δ_{23} are the state variables. The steady-state stability area is shown in Figure 12.6 in the $(\delta_{23}, \delta_{13})$ plane for each of the stability conditions (12.120), (12.129) and (12.130).

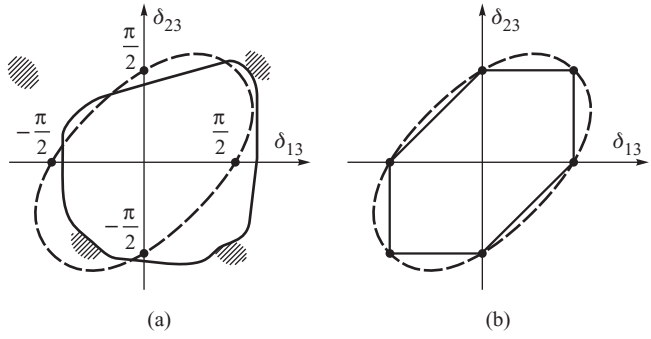

Figure 12.6 Examples of steady-state stability areas in the three-machine system: (a) the area with conductances included (solid line) and conductances neglected (dashed line); (b) the area with conductances neglected (dashed line) and the area due to the necessary condition (dashed line).

The solid line in Figure 12.6a corresponds to the case when the network conductances have been included and condition (12.120) used. When the line is exceeded, the system loses stability in an aperiodic way, that is real positive eigenvalues λ will appear. Oscillatory instability corresponds to the small dashed areas when complex eigenvalues λ have positive real parts. When the network conductances are neglected, condition (12.129) corresponds to the area restricted by the dashed line in Figure 12.6a. The area corresponding to condition (12.129) is repeated in Figure 12.6b and compared with the area corresponding to the necessary condition (12.130). Clearly both areas are quite close to each other.

12.2.3 Including the Voltage Characteristics of the Loads

The linear equation in (12.108) was derived in two stages. First the load nodes in the network admittance model were eliminated, Figure 12.3a, and then the power equations of the equivalent transfer matrix were linearized. By reversing the order of these steps the voltage characteristics of the loads can be included in the model. To accomplish this it is first necessary to linearize the original

network model and replace the power increments of the loads by the increments resulting from the voltage characteristics before eliminating the load nodes in the linearized network equation.

As the voltage magnitude at all the generator nodes {G} is constant (steady-state representation), all the increments $\Delta E_i = 0$ for $i \in \{\mathrm{G}\}$. In this case the incremental network equation (3.157) has the following form for the original network model (Figure 12.3a):

$$\begin{bmatrix} \Delta \boldsymbol{P}_{\mathrm{G}} \\ \hdashline \Delta \boldsymbol{P}_{\mathrm{L}} \\ \Delta \boldsymbol{Q}_{\mathrm{L}} \end{bmatrix} = \left[\begin{array}{c:c:c} \boldsymbol{H}_{\mathrm{GG}} & \boldsymbol{H}_{\mathrm{GL}} & \boldsymbol{M}_{\mathrm{GL}} \\ \hdashline \boldsymbol{H}_{\mathrm{LG}} & \boldsymbol{H}_{\mathrm{LL}} & \boldsymbol{M}_{\mathrm{LL}} \\ \hdashline \boldsymbol{N}_{\mathrm{LG}} & \boldsymbol{N}_{\mathrm{LL}} & \boldsymbol{K}_{\mathrm{LL}} \end{array}\right] \begin{bmatrix} \Delta \delta_{\mathrm{G}} \\ \hdashline \Delta \delta_{\mathrm{L}} \\ \Delta \boldsymbol{V}_{\mathrm{L}} \end{bmatrix}, \tag{12.134}$$

where the submatrices, forming the square matrix, are the partial derivatives of the power with respect to the nodal voltage angles and magnitudes. The indices show which set of nodes, {G} or {L}, a particular submatrix refers to.

In Section 3.5, the voltage sensitivities of the loads k_{PV} and k_{QV} were introduced so that for a small change in the voltage at each of the load nodes $j \in \{\mathrm{L}\}$, both $\Delta P_j = k_{\mathrm{PV}j} \Delta V_j$ and $\Delta Q_j = k_{\mathrm{QV}j} \Delta V_j$ hold. These can be written for the whole set {L} as

$$\Delta \boldsymbol{P}_{\mathrm{L}} = -\boldsymbol{k}_{\mathrm{P}} \Delta \boldsymbol{V}_{\mathrm{L}}, \quad \Delta \boldsymbol{Q}_{\mathrm{L}} = -\boldsymbol{k}_{\mathrm{Q}} \Delta \boldsymbol{V}_{\mathrm{L}}, \tag{12.135}$$

where $\boldsymbol{k}_{\mathrm{P}} = \mathrm{diag}(k_{\mathrm{PV}i})$ and $\boldsymbol{k}_{\mathrm{Q}} = \mathrm{diag}(k_{\mathrm{QV}i})$ are diagonal matrices of the voltage sensitivities. The minus sign is present because loads in the network equations represent negative injections, that is outflow from the node.

Substituting Equation (12.135) into Equation (12.134) gives after some algebra

$$\begin{bmatrix} \Delta \boldsymbol{P}_{\mathrm{G}} \\ \hdashline \boldsymbol{0} \\ \hdashline \boldsymbol{0} \end{bmatrix} = \left[\begin{array}{c:c:c} \boldsymbol{H}_{\mathrm{GG}} & \boldsymbol{H}_{\mathrm{GL}} & \boldsymbol{M}_{\mathrm{GL}} \\ \hdashline \boldsymbol{H}_{\mathrm{LG}} & \boldsymbol{H}_{\mathrm{LL}} & \boldsymbol{M}_{\mathrm{LL}} + \boldsymbol{k}_{\mathrm{P}} \\ \hdashline \boldsymbol{N}_{\mathrm{LG}} & \boldsymbol{N}_{\mathrm{LL}} & \boldsymbol{K}_{\mathrm{LL}} + \boldsymbol{k}_{\mathrm{Q}} \end{array}\right] \begin{bmatrix} \Delta \boldsymbol{\delta}_{\mathrm{G}} \\ \hdashline \Delta \boldsymbol{\delta}_{\mathrm{L}} \\ \hdashline \Delta \boldsymbol{V}_{\mathrm{L}} \end{bmatrix}. \tag{12.136}$$

Partial inversion of this equation allows the submatrices $\Delta \boldsymbol{\delta}_{\mathrm{L}}, \Delta \boldsymbol{V}_{\mathrm{L}}$ to be eliminated to obtain an equation of the same form as Equation (12.102) where

$$\boldsymbol{H} = \boldsymbol{H}_{\mathrm{GG}} - \left[\begin{array}{c:c} \boldsymbol{H}_{\mathrm{GL}} & \boldsymbol{M}_{\mathrm{GL}} \end{array}\right] \left[\begin{array}{c:c} \boldsymbol{H}_{\mathrm{LL}} & \boldsymbol{M}_{\mathrm{LL}} + \boldsymbol{k}_{\mathrm{P}} \\ \hdashline \boldsymbol{N}_{\mathrm{LL}} & \boldsymbol{K}_{\mathrm{LL}} + \boldsymbol{k}_{\mathrm{Q}} \end{array}\right]^{-1} \begin{bmatrix} \boldsymbol{H}_{\mathrm{LG}} \\ \hdashline \boldsymbol{N}_{\mathrm{LG}} \end{bmatrix}. \tag{12.137}$$

The remaining calculations follow the same pattern as described in the previous section with Equations (12.108) and (12.117) being equally valid but now with the elements H_{ij} calculated from the matrix defined in Equation (12.137).

12.2.4 Transfer Capability of the Network

System operators often want to know the *transfer capability*, that is the maximum power that can be exported from a given power plant to the system or from one subsystem to another. Calculation of the transfer capability can be done using a modified load flow program in which impedances of the generating units are also taken into account while the fictitious nodes behind those nodes are treated as the generator (PV) nodes. The calculations are done step by step. The power demand for a given set of nodes is increased in each step, and load flow together with steady-state stability conditions are determined. The power at which the steady-stability condition is reached is considered to represent the transfer capability.

The previous section showed that system stability can be checked using the simple necessary condition (12.130) or (12.129). When checking condition (12.129) one can calculate only the determinant of the Jacobi matrix. This is because, when the operating point is moved towards the stability limit, the first to reach zero is the main minor, that is the determinant of the Jacobi matrix. Some professional load flow programs based on the Newton method calculate the value of the determinant of the Jacobi matrix and hence may be used to determine the stability limit.

12.3 Steady-State Stability of the Regulated System

In Section 5.5 the steady-state stability of the regulated generator–infinite busbar system was discussed. In the present section this analysis will be extended to multi-machine systems.

In order to assess the steady-state stability of a regulated power system, detailed models of the generators, the exciters, the turbine governors and the power system stabilizers must be used. This leads to a large number of state variables being required to describe each generating unit. As a complete description of the full linearized system model would therefore be complicated, and take up a lot of space, the approach adopted here is to describe the overall methodology of creating the system model using relatively simple component models. The creation of more extensive system models would then follow similar lines.

12.3.1 Generator and Network

To simplify considerations the fifth-order generator model described in Section 11.1.6 will be used. For this model it is convenient to attach the generator subtransient reactance to the network model. The procedure is similar to that shown in Figure 12.3 with the only difference being that for the purpose of assessing the inherent steady-state stability the generator was represented by the synchronous reactances and synchronous emf $E_\mathrm{q} = \text{constant}$. As variations in the subtransient emfs now have to be considered, the generator reactances attached to the network are the subtransient (not steady-state) reactances and hence (similar to Equation (12.100)) can be written

$$\underline{E}_i = \underline{E}'' \quad \text{and} \quad X_i = X''_{\mathrm{d}\,i} = X''_{\mathrm{q}\,i} \tag{12.138}$$

After all the load nodes, including the generator terminal nodes, have been eliminated, the generator currents can be expressed in terms of the subtransient emfs. Working in rectangular coordinates, the currents can be expressed in the same way as in Equation (3.153) to give

$$I_{\mathrm{a}i} = \sum_{j=1}^{n} \left(G_{ij} E''_{\mathrm{a}j} - B_{ij} E''_{\mathrm{b}j} \right), \quad I_{\mathrm{b}i} = \sum_{j=1}^{n} \left(G_{ij} E''_{\mathrm{b}j} + B_{ij} E''_{\mathrm{a}j} \right). \tag{12.139}$$

The emfs E''_d and E''_q in the individual generator (d, q) coordinate system can be transformed to the (a, b) coordinate system using Equation (3.166) to give

$$E''_{\mathrm{a}j} = -E''_{\mathrm{d}j} \sin\delta_j + E''_{\mathrm{q}j} \cos\delta_j, \quad E''_{\mathrm{b}j} = E''_{\mathrm{d}j} \cos\delta_j + E''_{\mathrm{q}j} \sin\delta_j, \tag{12.140}$$

while the reverse transformation in Equation (3.167) can be used for the generator currents

$$I_{\mathrm{d}i} = -I_{\mathrm{a}i} \sin\delta_i + I_{\mathrm{b}i} \cos\delta_i, \quad I_{\mathrm{q}i} = I_{\mathrm{a}i} \cos\delta_i + I_{\mathrm{b}i} \sin\delta_i. \tag{12.141}$$

It should be noted that the rotor angle δ is the angle of the rotor q-axis measured with respect to the reference frame and not the phase angle of the subtransient emf $\underline{E}''$.

Substituting Equations (12.139) and (12.140) into Equation (12.141) gives after some simple but arduous algebra

$$\begin{aligned} I_{\mathrm{d}i} &= \sum_{j=1}^{n} [(B_{ij}\cos\delta_{ij} - G_{ij}\sin\delta_{ij})E''_{\mathrm{q}j} + (B_{ij}\sin\delta_{ij} + G_{ij}\cos\delta_{ij})E''_{\mathrm{d}j}] \\ I_{\mathrm{q}i} &= \sum_{j=1}^{n} [(B_{ij}\sin\delta_{ij} + G_{ij}\cos\delta_{ij})E''_{\mathrm{q}j} - (B_{ij}\cos\delta_{ij} - G_{ij}\sin\delta_{ij})E''_{\mathrm{d}j}]. \end{aligned} \tag{12.142}$$

These are the transfer network equations in the (d, q) coordinates of the individual generators.

Similar to the power increment in Equation (12.106), Equation (12.142) allows the current increments to be expressed in terms of the increments in the relative angles $\Delta\delta_{jn}$ and the increments of the component emfs as

$$\begin{bmatrix} \Delta \boldsymbol{I}_{\mathrm{q}} \\ \hline \Delta \boldsymbol{I}_{\mathrm{d}} \end{bmatrix} = \left[\begin{array}{c|c|c} \dfrac{\partial \boldsymbol{I}_{\mathrm{q}}}{\partial \boldsymbol{\delta}_{n-1}} & \dfrac{\partial \boldsymbol{I}_{\mathrm{q}}}{\partial \boldsymbol{E}''_{\mathrm{q}}} & \dfrac{\partial \boldsymbol{I}_{\mathrm{q}}}{\partial \boldsymbol{E}''_{\mathrm{d}}} \\ \hline \dfrac{\partial \boldsymbol{I}_{\mathrm{d}}}{\partial \boldsymbol{\delta}_{n-1}} & \dfrac{\partial \boldsymbol{I}_{\mathrm{d}}}{\partial \boldsymbol{E}''_{\mathrm{q}}} & \dfrac{\partial \boldsymbol{I}_{\mathrm{d}}}{\partial \boldsymbol{E}''_{\mathrm{d}}} \end{array}\right] \begin{bmatrix} \Delta \boldsymbol{\delta}_{n-1} \\ \hline \Delta \boldsymbol{E}''_{\mathrm{q}} \\ \hline \Delta \boldsymbol{E}''_{\mathrm{d}} \end{bmatrix}, \tag{12.143}$$

where $\Delta \boldsymbol{I}_{\mathrm{q}}$, $\Delta \boldsymbol{I}_{\mathrm{d}}$, $\Delta \boldsymbol{\delta}_{n-1}$, $\Delta \boldsymbol{E}''_{\mathrm{q}}$ and $\Delta \boldsymbol{E}''_{\mathrm{d}}$ are the appropriate generator increment vectors. The elements of the Jacobi matrix can be found by differentiating the right hand side of the equations in (12.142) and will not be considered further here. However. it should be remembered that vector $\Delta\boldsymbol{\delta}_{n-1}$ is of size $(n-1)$ so that the submatrices $\partial \boldsymbol{I}_{\mathrm{q}}/\partial\boldsymbol{\delta}_{n-1}$ and $\partial \boldsymbol{I}_{\mathrm{d}}/\partial\boldsymbol{\delta}_{n-1}$ are rectangular with dimensions $n \times (n-1)$.

If transient saliency is neglected $X''_{\mathrm{q}} \approx X''_{\mathrm{d}}$ then Equation (11.102) simplifies to $P_i = E''_{\mathrm{q}i} I_{\mathrm{q}i} + E''_{\mathrm{d}i} I_{\mathrm{d}i}$ which, after substituting for $I_{\mathrm{d}i}$ and $I_{\mathrm{q}i}$ from Equation (12.142), yields

$$\begin{aligned} P_i = E''_{\mathrm{d}i} \sum_{j=1}^{n}](B_{ij}\cos\delta_{ij} - G_{ij}\sin\delta_{ij})E''_{\mathrm{q}j} + (B_{ij}\sin\delta_{ij} + G_{ij}\cos\delta_{ij})E''_{\mathrm{d}j}] \\ + E''_{\mathrm{q}i} \sum_{j=1}^{n} [(B_{ij}\sin\delta_{ij} + G_{ij}\cos\delta_{ij})E''_{\mathrm{q}j} - (B_{ij}\cos\delta_{ij} - G_{ij}\sin\delta_{ij})E''_{\mathrm{d}i}]. \end{aligned} \tag{12.144}$$

Linearizing and expressing this equation in matrix form gives

$$[\Delta \boldsymbol{P}] = \left[\begin{array}{c|c|c} \dfrac{\partial \boldsymbol{P}}{\partial \boldsymbol{\delta}_{n-1}} & \dfrac{\partial \boldsymbol{P}}{\partial \boldsymbol{E}''_{\mathrm{q}}} & \dfrac{\partial \boldsymbol{P}}{\partial \boldsymbol{E}''_{\mathrm{d}}} \end{array}\right] \begin{bmatrix} \Delta \boldsymbol{\delta}_{n-1} \\ \hline \Delta \boldsymbol{E}''_{\mathrm{q}} \\ \hline \Delta \boldsymbol{E}''_{\mathrm{d}} \end{bmatrix}, \tag{12.145}$$

where $\Delta \boldsymbol{P}$ is the vector of the power increments in all the generators and $\partial \boldsymbol{P}/\partial\boldsymbol{\delta}_{n-1}$ is a rectangular Jacobi matrix of dimension $n \times (n-1)$. The Jacobi submatrices are calculated by differentiating the right hand side of the equations in (12.144).

The terminal voltage equation (11.100) can be treated in a similar way. Substituting Equation (12.142) into Equation (11.100) gives

$$\begin{aligned} V_{\mathrm{q}i} &= E''_{\mathrm{q}i} + X''_{\mathrm{d}i} \sum_{j=1}^{n} [(B_{ij}\cos\delta_{ij} - G_{ij}\sin\delta_{ij})E''_{\mathrm{q}j} + (B_{ij}\sin\delta_{ij} + G_{ij}\cos\delta_{ij})E''_{\mathrm{d}j}] \\ V_{\mathrm{d}i} &= E''_{\mathrm{d}i} - X''_{\mathrm{q}i} \sum_{j=1}^{n} [(B_{ij}\sin\delta_{ij} + G_{ij}\cos\delta_{ij})E''_{\mathrm{q}j} - (B_{ij}\cos\delta_{ij} - G_{ij}\sin\delta_{ij})E''_{\mathrm{d}j}]. \end{aligned} \tag{12.146}$$

The quantity of interest with regard to voltage regulator action is the voltage magnitude $V_i = \sqrt{V_{qi}^2 + V_{di}^2}$ so that

$$[\Delta \boldsymbol{V}] = \left[\frac{\partial \boldsymbol{V}}{\partial \boldsymbol{\delta}_{n-1}} \;\vdots\; \frac{\partial \boldsymbol{V}}{\partial \boldsymbol{E}''_{q}} \;\vdots\; \frac{\partial \boldsymbol{V}}{\partial \boldsymbol{E}''_{d}} \right] \begin{bmatrix} \Delta \boldsymbol{\delta}_{n-1} \\ \text{-----} \\ \Delta \boldsymbol{E}''_{q} \\ \text{-----} \\ \Delta \boldsymbol{E}''_{d} \end{bmatrix}, \tag{12.147}$$

where $\Delta \boldsymbol{V}$ is the vector of the magnitude increments in the terminal voltages of all the generators. The Jacobi submatrices can be calculated by taking the partial derivative of the voltage magnitude with respect to a variable α as

$$\frac{\partial V_i}{\partial \alpha} = \frac{1}{V_i} \left(V_{qi} \frac{\partial V_{qi}}{\partial \alpha} + V_{di} \frac{\partial V_{di}}{\partial \alpha} \right), \tag{12.148}$$

where α signifies E''_{qi}, E''_{qj}, E''_{di}, E''_{dj}, δ_i or δ_j. The derivatives $\partial V_{qi}/\partial \alpha$ and $\partial V_{di}/\partial \alpha$ are obtained by differentiating the right hand sides of the equations in (12.146).

The linearized generator differential equations can now be obtained from Equations (10.96), (10.97), (10.98) and (10.89) as

$$\begin{aligned} \Delta \dot{\delta}_{n-1} &= 1_{-1} \Delta \boldsymbol{\omega} \\ \boldsymbol{M} \Delta \dot{\omega} &= -\Delta \boldsymbol{P} - \boldsymbol{D} \Delta \boldsymbol{\omega} \\ \boldsymbol{T}'_{d0} \Delta \dot{E}'_{q} &= -\Delta \boldsymbol{E}'_{q} + \Delta \boldsymbol{X}'_{d} \Delta \boldsymbol{I}_{d} + \Delta \boldsymbol{E}_{f} \\ \boldsymbol{T}''_{d0} \Delta \dot{E}''_{q} &= -\Delta \boldsymbol{E}'_{q} - \Delta \boldsymbol{E}''_{q} + \Delta \boldsymbol{X}''_{d} \Delta \boldsymbol{I}_{d} \\ \boldsymbol{T}''_{q0} \Delta \dot{E}''_{d} &= -\Delta \boldsymbol{E}''_{d} - \Delta \boldsymbol{X}''_{q} \Delta \boldsymbol{I}_{q}, \end{aligned} \tag{12.149}$$

where $\Delta \boldsymbol{E}'_{q}$, $\Delta \boldsymbol{E}''_{q}$, $\Delta \boldsymbol{E}''_{d}$, $\Delta \boldsymbol{I}_{q}$, $\Delta \boldsymbol{T}_{d}$, $\Delta \boldsymbol{P}$ and $\Delta \omega$ are the generator increment vectors of size n while $\Delta \boldsymbol{\delta}_{n-1}$ is the increment vector of the relative angles of size $(n-1)$. The matrices $\boldsymbol{T}'_{q0}$, $\boldsymbol{T}'_{d0}$, $\boldsymbol{M}$ and $\boldsymbol{D}$ are the respective diagonal matrices of the generator time constants, inertia coefficients and damping coefficients. Matrices ΔX are diagonal and contain the following elements:

$$\begin{aligned} \Delta \boldsymbol{X}'_{d} &= \text{diag} \left(X_{di} - X'_{di} \right) \\ \Delta \boldsymbol{X}''_{d} &= \text{diag} \left(X'_{di} - X''_{di} \right) \\ \Delta \boldsymbol{X}''_{q} &= \text{diag} \left(X'_{qi} - X''_{qi} \right). \end{aligned} \tag{12.150}$$

Substituting Equations (12.143), (12.145) and (12.147) into Equation (12.149) gives the state equation (12.49). The four submatrices in the upper left corner of the state matrix have the same structure as the state matrix used in Equation (12.110) to assess the steady-state inherent stability. The changes in E_f, appearing in the last component of Equation (12.151), are due to the action of the generator exciters and AVR systems.

12.3.2 Including Excitation System Model and Voltage Control

Models were derived in Section 11.2 for the different types of excitation systems. For steady-state stability purposes nonlinearity effects do not play a major role and may be neglected, allowing the excitation systems to be represented by a high-order transfer function. To show how the linearized

$$
\begin{bmatrix} \Delta\dot{\boldsymbol{\delta}}_{n-1} \\ \cdots\cdots \\ \Delta\dot{\boldsymbol{\omega}} \\ \cdots\cdots \\ \Delta\dot{\boldsymbol{E}}'_{\mathrm{q}} \\ \cdots\cdots \\ \Delta\dot{\boldsymbol{E}}''_{\mathrm{q}} \\ \cdots\cdots \\ \Delta\dot{\boldsymbol{E}}''_{\mathrm{d}} \end{bmatrix} = \left[\begin{array}{c|c|c|c|c} \mathbf{0} & \mathbf{1}_{-1} & \mathbf{0} & \mathbf{0} & \mathbf{0} \\ -\boldsymbol{M}^{-1}\dfrac{\partial \boldsymbol{P}}{\partial \boldsymbol{\delta}_{n-1}} & -\boldsymbol{M}^{-1}\boldsymbol{D} & \mathbf{0} & -\boldsymbol{M}^{-1}\dfrac{\partial \boldsymbol{P}}{\partial \boldsymbol{E}''_{\mathrm{q}}} & -\boldsymbol{M}^{-1}\dfrac{\partial \boldsymbol{P}}{\partial \boldsymbol{E}''_{\mathrm{d}}} \\ \hline (\boldsymbol{T}'_{\mathrm{do}})^{-1}\Delta\boldsymbol{X}'_{\mathrm{d}}\dfrac{\partial \boldsymbol{I}_{\mathrm{d}}}{\partial \boldsymbol{\delta}_{n-1}} & \mathbf{0} & -(\boldsymbol{T}'_{\mathrm{do}})^{-1} & (\boldsymbol{T}'_{\mathrm{do}})^{-1}\Delta\boldsymbol{X}'_{\mathrm{d}}\dfrac{\partial \boldsymbol{I}_{\mathrm{d}}}{\partial \boldsymbol{E}''_{\mathrm{q}}} & (\boldsymbol{T}'_{\mathrm{do}})^{-1}\Delta\boldsymbol{X}'_{\mathrm{d}}\dfrac{\partial \boldsymbol{I}_{\mathrm{d}}}{\partial \boldsymbol{E}''_{\mathrm{d}}} \\ \hline (\boldsymbol{T}''_{\mathrm{do}})^{-1}\Delta\boldsymbol{X}''_{\mathrm{d}}\dfrac{\partial \boldsymbol{I}_{\mathrm{d}}}{\partial \boldsymbol{\delta}_{n-1}} & \mathbf{0} & -(\boldsymbol{T}''_{\mathrm{do}})^{-1} & (\boldsymbol{T}''_{\mathrm{do}})^{-1}\left(\Delta\boldsymbol{X}''_{\mathrm{d}}\dfrac{\partial \boldsymbol{I}_{\mathrm{d}}}{\partial \boldsymbol{E}''_{\mathrm{q}}} - 1\right) & (\boldsymbol{T}''_{\mathrm{do}})^{-1}\Delta\boldsymbol{X}''_{\mathrm{d}}\dfrac{\partial \boldsymbol{I}_{\mathrm{d}}}{\partial \boldsymbol{E}''_{\mathrm{d}}} \\ \hline -(\boldsymbol{T}''_{\mathrm{qo}})^{-1}\Delta\boldsymbol{X}''_{\mathrm{q}}\dfrac{\partial \boldsymbol{I}_{\mathrm{q}}}{\partial \boldsymbol{\delta}_{n-1}} & \mathbf{0} & \mathbf{0} & -(\boldsymbol{T}''_{\mathrm{qo}})^{-1}\Delta\boldsymbol{X}''_{\mathrm{q}}\dfrac{\partial \boldsymbol{I}_{\mathrm{q}}}{\partial \boldsymbol{E}''_{\mathrm{q}}} & -(\boldsymbol{T}''_{\mathrm{qo}})^{-1}\left(\Delta\boldsymbol{X}''_{\mathrm{q}}\dfrac{\partial \boldsymbol{I}_{\mathrm{q}}}{\partial \boldsymbol{E}''_{\mathrm{d}}} + 1\right) \end{array}\right] \begin{bmatrix} \Delta\boldsymbol{\delta}_{n-1} \\ \cdots\cdots \\ \Delta\boldsymbol{\omega} \\ \cdots\cdots \\ \Delta\boldsymbol{E}'_{\mathrm{q}} \\ \cdots\cdots \\ \Delta\boldsymbol{E}''_{\mathrm{q}} \\ \cdots\cdots \\ \Delta\boldsymbol{E}''_{\mathrm{d}} \end{bmatrix} + \begin{bmatrix} \mathbf{0} \\ \cdots\cdots \\ \mathbf{0} \\ \cdots\cdots \\ (\boldsymbol{T}'_{\mathrm{do}})^{-1}\Delta\boldsymbol{E}_{\mathrm{f}} \\ \cdots\cdots \\ \mathbf{0} \\ \cdots\cdots \\ \mathbf{0} \end{bmatrix} . \tag{12.151}
$$

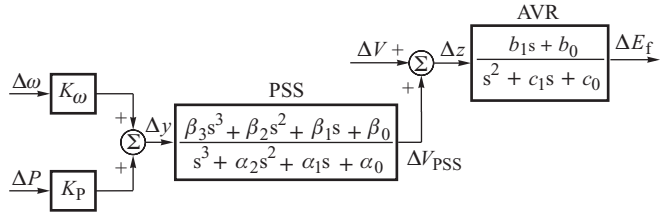

Figure 12.7 Simplified block diagram of the exciter with AVR and PSS.

equations of the excitation system can be included in the complete linearized system model, a second-order transfer function will be used to represent the exciter and the AVR while a third-order transfer function will be used to represent the PSS. The block diagram corresponding to such an excitation system is shown in Figure 12.7. In this system the PSS will react to a signal proportional to rotor speed deviation, when $K_{\mathrm{P}} = 0$, or to a signal proportional to the generator real power, when $K_{\omega} = 0$.

The differential equation describing the excitation system can be obtained from the transfer function in Figure 12.7 by introducing two auxiliary variables, x_1 and x_2, to give

$$\begin{aligned} \dot{x}_{2i} &= \Delta z_i - c_{1i} x_{2i} - c_{0i} x_{1i} \qquad (12.152) \\ \dot{x}_{1i} &= x_{2i}, \\ \Delta E_{\mathrm{f}i} &= b_{1i} x_{2i} + b_{0i} x_{1i}, \qquad (12.153) \end{aligned}$$

where i is the generator number. Expressing this equation in matrix form, and substituting Equation (12.147), gives

$$\begin{bmatrix} \dot{\boldsymbol{x}}_1 \\ \cdots \\ \dot{\boldsymbol{x}}_2 \end{bmatrix} = \left[\begin{array}{c:c} \mathbf{0} & \mathbf{1} \\ \cdots & \cdots \\ -\boldsymbol{c}_0 & -\boldsymbol{c}_1 \end{array}\right] \begin{bmatrix} \boldsymbol{x}_1 \\ \cdots \\ \boldsymbol{x}_2 \end{bmatrix} + \left[\begin{array}{c:c:c} \mathbf{0} & \mathbf{0} & \mathbf{0} \\ \cdots & \cdots & \cdots \\ -\dfrac{\partial \boldsymbol{V}}{\partial \boldsymbol{\delta}_{n-1}} & -\dfrac{\partial \boldsymbol{V}}{\partial \boldsymbol{E}''_{\mathrm{q}}} & -\dfrac{\partial \boldsymbol{V}}{\partial \boldsymbol{E}''_{\mathrm{d}}} \end{array}\right] \begin{bmatrix} \Delta\boldsymbol{\delta}_{n-1} \\ \cdots \\ \Delta\boldsymbol{E}''_{\mathrm{q}} \\ \cdots \\ \Delta\boldsymbol{E}''_{\mathrm{d}} \end{bmatrix} + \begin{bmatrix} \mathbf{0} \\ \cdots \\ -\Delta\boldsymbol{V}_{\mathrm{PSS}} \end{bmatrix} \qquad (12.154)$$

$$[\Delta\boldsymbol{E}_{\mathrm{f}}] = \left[\begin{array}{c:c} \boldsymbol{b}_0 & \boldsymbol{b}_1 \end{array}\right] \begin{bmatrix} \boldsymbol{x}_1 \\ \cdots \\ \boldsymbol{x}_2 \end{bmatrix},$$

where $\boldsymbol{c}_0$, $\boldsymbol{c}_1$, $\boldsymbol{b}_0$, $\boldsymbol{b}_1$ are diagonal submatrices of the coefficients in the excitation system transfer functions.

The vector $\Delta \boldsymbol{V}_{\mathrm{PSS}}$ can be obtained from the stabilizer equations which, because the stabilizer transfer function is third order, can be constructed using three auxiliary variables $\boldsymbol{x}_3$, $\boldsymbol{x}_4$ and $\boldsymbol{x}_5$. This results in

$$\begin{aligned} \dot{x}_{5i} &= \Delta y_i - \alpha_{2i} x_{5i} - \alpha_{1i} x_{4i} - \alpha_{0o} x_{3i} \\ \dot{x}_{4i} &= x_{5i} \qquad (12.155) \\ \Delta V_{\mathrm{PSS}} &= \beta_{3i} \Delta y_i - (\alpha_{2i}\beta_{3i} - \beta_{2i})\, x_{5i} - (\alpha_{1i}\beta_{3i} - \beta_{1i})\, x_{4i} - \beta_{3i} x_{3i}, \end{aligned}$$

where $\Delta y_i = K_{\omega i}\Delta\omega_i + K_{\mathrm{P}i}\Delta P_i$ is the input signal and i is the generator number. Representing the equations in matrix form and taking into account Equation (12.145) gives

$$\begin{bmatrix} \dot{\boldsymbol{x}}_3 \\ \cdots \\ \dot{\boldsymbol{x}}_4 \\ \cdots \\ \dot{\boldsymbol{x}}_5 \end{bmatrix} = \left[\begin{array}{c:c:c} \mathbf{0} & \mathbf{1} & \mathbf{0} \\ \hdashline \mathbf{0} & \mathbf{0} & \mathbf{1} \\ \hdashline -\boldsymbol{\alpha}_0 & -\boldsymbol{\alpha}_1 & -\boldsymbol{\alpha}_2 \end{array}\right] \begin{bmatrix} \boldsymbol{x}_3 \\ \cdots \\ \boldsymbol{x}_4 \\ \cdots \\ \boldsymbol{x}_5 \end{bmatrix} + \left[\begin{array}{c:c:c:c} \mathbf{0} & \mathbf{0} & \mathbf{0} & \mathbf{0} \\ \hdashline \mathbf{0} & \mathbf{0} & \mathbf{0} & \mathbf{0} \\ \hdashline -\boldsymbol{K}_{\mathrm{P}}\dfrac{\partial \boldsymbol{P}}{\partial \boldsymbol{\delta}_{n-1}} & -\boldsymbol{K}_{\omega} & -\boldsymbol{K}_{\mathrm{P}}\dfrac{\partial \boldsymbol{P}}{\partial E''_{\mathrm{q}}} & -\boldsymbol{K}_{\mathrm{P}}\dfrac{\partial \boldsymbol{P}}{\partial E''_{\mathrm{d}}} \end{array}\right] \begin{bmatrix} \Delta\boldsymbol{\delta}_{n-1} \\ \cdots \\ \Delta\boldsymbol{\omega} \\ \cdots \\ \Delta\boldsymbol{E}''_{\mathrm{q}} \\ \cdots \\ \Delta\boldsymbol{E}''_{\mathrm{d}} \end{bmatrix}$$

$$[\Delta \boldsymbol{V}_{\mathrm{PSS}}] = \left[\begin{array}{c:c:c:c:c:c} \boldsymbol{K}_{\mathrm{P}}\boldsymbol{\beta}_3\dfrac{\partial \boldsymbol{P}}{\partial \boldsymbol{\delta}_{n-1}} & \boldsymbol{K}_{\omega}\boldsymbol{\beta}_3 & \boldsymbol{K}_{\mathrm{P}}\boldsymbol{\beta}_3\dfrac{\partial \boldsymbol{P}}{\partial E''_{\mathrm{q}}} & \boldsymbol{K}_{\mathrm{P}}\boldsymbol{\beta}_3\dfrac{\partial \boldsymbol{P}}{\partial E''_{\mathrm{d}}} & -\boldsymbol{\beta}_3 & \boldsymbol{\beta}_1 - \boldsymbol{\alpha}_1\boldsymbol{\beta}_3 & \boldsymbol{\beta}_2 - \boldsymbol{\alpha}_2\boldsymbol{\beta}_3 \end{array}\right] \begin{bmatrix} \Delta\boldsymbol{\delta}_{n-1} \\ \cdots \\ \Delta\boldsymbol{\omega} \\ \cdots \\ \Delta\boldsymbol{E}''_{\mathrm{q}} \\ \cdots \\ \Delta\boldsymbol{E}''_{\mathrm{d}} \\ \cdots \\ \boldsymbol{x}_3 \\ \cdots \\ \boldsymbol{x}_4 \\ \cdots \\ \boldsymbol{x}_5 \end{bmatrix}, \tag{12.156}$$

where α_0, α_1, α_2, β_0, β_1, β_2, β_2, $\boldsymbol{K}_{\mathrm{P}}$ and K_{ω} are diagonal matrices of the stabilizer coefficients.

12.3.3 Linear State Equation of the System

As the linear equations in (12.151), (12.154) and (12.156) have common state variables they can be combined to form one large state equation that includes the effect of all the generators (fifth-order model), exciters, AVRs and PSSs. This results in the matrix equation (12.157). The solid line in the upper left corner separates the submatrix corresponding to the swing equation. The dashed line separates the submatrix corresponding to the generator equations without voltage control. The lower side of the state matrix below the dashed line corresponds to the voltage control and PSS.

So far the turbine power has been assumed to be constant. If this is not the case then additional equations that describe the turbine and its governor must be added to the state equation, further increasing its size. The size of the state equation will be increased yet further if the effect of control devices, such as SVC or other FACTS devices, is included. Provided a suitable model is known, then including the effect of such elements is straightforward and follows similar lines as for the exciter and AVR and for this reason is not considered further in this book.

As the state matrix in Equation (12.157) is sparse it is advantageous to use sparse matrix techniques when calculating the eigenvalues and eigenvectors even if a small system is under investigation. In the case of a large interconnected system, when all the control devices influencing the steady-state stability and damping are included, then the dimension of the state matrix may be very large indeed and well outside the range of conventional eigenvalue analysis methods. In such cases special solution techniques, which evaluate a selected subset of the eigenvalues associated with the complete system response, are necessary (Kundur, 1994).

12.3.4 Examples

A number of interesting examples of the application of modal analysis to large interconnected power systems can be found in Wang (1997) and Breulmann *et al.* (2000). Below are two examples based on data from a paper by Rasolomampionona (2000).

$$
\begin{bmatrix}
\Delta\dot{\delta}_{n-1} \\
\cdots\cdots \\
\Delta\dot{\omega} \\
\hline
\Delta\dot{E}'_{\mathrm{q}} \\
\cdots\cdots \\
\Delta\dot{E}''_{\mathrm{q}} \\
\Delta\dot{E}''_{\mathrm{d}} \\
\hline
\dot{x}_1 \\
\cdots\cdots \\
\dot{x}_2 \\
\cdots\cdots \\
\dot{x}_3 \\
\cdots\cdots \\
\dot{x}_4 \\
\cdots\cdots \\
\dot{x}_5
\end{bmatrix}
=
\begin{bmatrix}
\mathbf{0} & \cdots & \mathbf{1}_{-1} & \cdots & \mathbf{0} & \cdots & \mathbf{0} & \cdots & \mathbf{0} & \cdots & \mathbf{0} & \cdots & \mathbf{0} & \cdots & \mathbf{0} & \cdots \\
-\boldsymbol{M}^{-1}\dfrac{\partial \boldsymbol{P}}{\partial \delta_{n-1}} & \cdots & -\boldsymbol{M}^{-1}\boldsymbol{D} & \cdots & -\boldsymbol{M}^{-1}\dfrac{\partial \boldsymbol{P}}{\partial E''_{\mathrm{q}}} & \cdots & -\boldsymbol{M}^{-1}\dfrac{\partial \boldsymbol{P}}{\partial E''_{\mathrm{d}}} & \cdots & \boldsymbol{0} & \cdots & \boldsymbol{0} & \cdots & \boldsymbol{0} & \cdots & \boldsymbol{0} & \cdots \\
\hline
(T'_{\mathrm{do}})^{-1}\Delta X'_{\mathrm{d}}\dfrac{\partial I_{\mathrm{d}}}{\partial \delta_{n-1}} & \cdots & \mathbf{0} & \cdots & -(T'_{\mathrm{do}})^{-1} & \cdots & (T'_{\mathrm{do}})^{-1}\Delta X'_{\mathrm{d}}\dfrac{\partial I_{\mathrm{d}}}{\partial E''_{\mathrm{d}}} & \cdots & (T'_{\mathrm{do}})^{-1}\boldsymbol{b}_0 & \cdots & (T'_{\mathrm{do}})^{-1}\boldsymbol{b}_1 & \cdots & \mathbf{0} & \cdots & \mathbf{0} & \cdots \\
\cdots\cdots & \cdots & \cdots\cdots & \cdots & \cdots\cdots & \cdots & \cdots\cdots & \cdots & \cdots\cdots & \cdots & \cdots\cdots & \cdots & \cdots\cdots & \cdots & \cdots\cdots & \cdots \\
(T''_{\mathrm{do}})^{-1}\Delta X''_{\mathrm{d}}\dfrac{\partial I_{\mathrm{d}}}{\partial \delta_{n-1}} & \cdots & \mathbf{0} & \cdots & -(T''_{\mathrm{do}})^{-1} & \cdots & (T''_{\mathrm{do}})^{-1}\left(\Delta X''_{\mathrm{d}}\dfrac{\partial I_{\mathrm{d}}}{\partial E''_{\mathrm{q}}} - 1\right) & \cdots & (T''_{\mathrm{do}})^{-1}\Delta X''_{\mathrm{d}}\dfrac{\partial I_{\mathrm{d}}}{\partial E''_{\mathrm{d}}} & \cdots & \mathbf{0} & \cdots & \mathbf{0} & \cdots & \mathbf{0} & \cdots \\
\Delta\dot{E}'_{\mathrm{q}} & \cdots & \cdots\cdots & \cdots & \cdots\cdots & \cdots & \cdots\cdots & \cdots & \cdots\cdots & \cdots & \cdots\cdots & \cdots & \cdots\cdots & \cdots & \cdots\cdots & \cdots \\
\Delta\dot{E}''_{\mathrm{q}} & \cdots & \cdots\cdots & \cdots & \cdots\cdots & \cdots & \cdots\cdots & \cdots & \cdots\cdots & \cdots & \cdots\cdots & \cdots & \cdots\cdots & \cdots & \cdots\cdots & \cdots \\
\Delta\dot{E}''_{\mathrm{d}} & \cdots & \cdots\cdots & \cdots & \cdots\cdots & \cdots & \cdots\cdots & \cdots & \cdots\cdots & \cdots & \cdots\cdots & \cdots & \cdots\cdots & \cdots & \cdots\cdots & \cdots \\
\hline
-(T''_{\mathrm{qo}})^{-1}\Delta X''_{\mathrm{q}}\dfrac{\partial I_{\mathrm{q}}}{\partial \delta_{n-1}} & \cdots & \mathbf{0} & \cdots & -(T''_{\mathrm{qo}})^{-1}\Delta X''_{\mathrm{q}}\dfrac{\partial I_{\mathrm{q}}}{\partial E''_{\mathrm{q}}} & \cdots & -(T''_{\mathrm{qo}})^{-1}\left(\Delta X''_{\mathrm{q}}\dfrac{\partial I_{\mathrm{q}}}{\partial E''_{\mathrm{d}}} + 1\right) & \cdots & \mathbf{0} & \cdots & \mathbf{0} & \cdots & \mathbf{0} & \cdots & \mathbf{0} & \cdots \\
\hline
\mathbf{0} & \cdots & \mathbf{0} & \cdots & \mathbf{0} & \cdots & \mathbf{0} & \cdots & \mathbf{0} & \cdots & \mathbf{0} & \cdots & \mathbf{0} & \cdots & \mathbf{0} & \cdots \\
\cdots\cdots & \cdots & \cdots\cdots & \cdots & \cdots\cdots & \cdots & \cdots\cdots & \cdots & \cdots\cdots & \cdots & \cdots\cdots & \cdots & \cdots\cdots & \cdots & \cdots\cdots & \cdots \\
\boldsymbol{K}_{\mathrm{P}}\boldsymbol{\beta}_3\dfrac{\partial \boldsymbol{P}}{\partial \delta_{n-1}} - \dfrac{\partial V}{\partial \delta_{n-1}} & \cdots & \boldsymbol{K}_{\omega}\boldsymbol{\beta}_3 & \cdots & \boldsymbol{K}_{\mathrm{P}}\boldsymbol{\beta}_3\dfrac{\partial \boldsymbol{P}}{\partial E''_{\mathrm{q}}} - \dfrac{\partial V}{\partial E''_{\mathrm{q}}} & \cdots & \boldsymbol{K}_{\mathrm{P}}\boldsymbol{\beta}_3\dfrac{\partial \boldsymbol{P}}{\partial E''_{\mathrm{d}}} - \dfrac{\partial V}{\partial E''_{\mathrm{d}}} & \cdots & -\boldsymbol{c}_0 & \cdots & -\boldsymbol{c}_1 & \cdots & -\boldsymbol{\beta}_3 & \cdots & \boldsymbol{\beta}_2 - \boldsymbol{a}_2\boldsymbol{\beta}_3 & \cdots \\
\cdots\cdots & \cdots & \cdots\cdots & \cdots & \cdots\cdots & \cdots & \cdots\cdots & \cdots & \cdots\cdots & \cdots & \cdots\cdots & \cdots & \cdots\cdots & \cdots & \cdots\cdots & \cdots \\
\mathbf{0} & \cdots & \mathbf{0} & \cdots & \mathbf{0} & \cdots & \mathbf{0} & \cdots & \mathbf{0} & \cdots & \mathbf{0} & \cdots & \mathbf{0} & \cdots & \mathbf{0} & \cdots \\
\cdots\cdots & \cdots & \cdots\cdots & \cdots & \cdots\cdots & \cdots & \cdots\cdots & \cdots & \cdots\cdots & \cdots & \cdots\cdots & \cdots & \cdots\cdots & \cdots & \cdots\cdots & \cdots \\
\mathbf{0} & \cdots & \mathbf{0} & \cdots & \mathbf{0} & \cdots & \mathbf{0} & \cdots & \mathbf{0} & \cdots & \mathbf{0} & \cdots & \mathbf{0} & \cdots & \mathbf{0} & \cdots \\
\cdots\cdots & \cdots & \cdots\cdots & \cdots & \cdots\cdots & \cdots & \cdots\cdots & \cdots & \cdots\cdots & \cdots & \cdots\cdots & \cdots & \cdots\cdots & \cdots & \cdots\cdots & \cdots \\
\boldsymbol{K}_{\mathrm{P}}\dfrac{\partial \boldsymbol{P}}{\partial \delta_{n-1}} & \cdots & \boldsymbol{K}_{\omega} & \cdots & \boldsymbol{K}_{\mathrm{P}}\dfrac{\partial \boldsymbol{P}}{\partial E''_{\mathrm{q}}} & \cdots & \boldsymbol{K}_{\mathrm{P}}\dfrac{\partial \boldsymbol{P}}{\partial E''_{\mathrm{d}}} & \cdots & \mathbf{0} & \cdots & \mathbf{0} & \cdots & -\mathbf{a}_0 & \cdots & -\mathbf{a}_1 & \cdots & -\mathbf{a}_2 & \cdots
\end{bmatrix}
\begin{bmatrix}
\Delta\delta_{n-1} \\
\cdots\cdots \\
\Delta\omega \\
\hline
\Delta E'_{\mathrm{q}} \\
\cdots\cdots \\
\Delta E''_{\mathrm{q}} \\
\Delta E''_{\mathrm{d}} \\
\hline
x_1 \\
\cdots\cdots \\
x_2 \\
\cdots\cdots \\
x_3 \\
\cdots\cdots \\
x_4 \\
\cdots\cdots \\
x_5
\end{bmatrix}
\tag{12.157}
$$

Example 12.9

Consider the generator–infinite busbar system shown in Figure 6.13 when line L1 has an outage due to maintenance. Since this will weaken the connection of the generator with the system, it is necessary to check the steady-state stability. The lines remaining in operation are of the length 250 km (line L2) and 80 km (line L3). The lines operate at the rated voltage of 220 kV and their reactance is $x = 0.4\ \Omega/\text{km}$. There is a load of $(350 + \text{j}150)$ MVA at node B3. The generator operates with a step-up transformer of reactance $X_\text{T} = 0.14$. The generator is salient-pole (hydro) one with the following parameters: $S_\text{n} = 426$ MVA, $X''_\text{d} \cong X''_\text{d} = 0.160$, $X'_\text{d} = 0.21$, $X_\text{d} = 1.57$, $X'_\text{q} \cong X_\text{q} = 0.85$, $T'_\text{do} = 6.63$, $T''_\text{do} = 0.051$, $T''_\text{qo} = 1.2$, $T_\text{m} = 10$. The transfer function of the voltage control and excitation system is

$$\frac{\Delta E_\text{f}(\text{s})}{\Delta V(\text{s})} = K_\text{A}\frac{2\text{s}+1}{0.3\,\text{s}^2 + 10\text{s} + 1} = K_\text{A}\frac{6.66\text{s}+3.33}{\text{s}^2 + 33.3\text{s} + 3.33} = \frac{b_1\text{s} + b_0}{\text{s}^2 + c_1\text{s} + c_0}, \tag{12.158}$$

where (according to Figure 12.7) $b_0 = 3.33K_\text{A}$, $b_1 = 6.66K_\text{A}$ and $c_0 = 3.33$, $c_1 = 33.3$.

It is necessary to compute eigenvalues and the associated eigenvectors and, on the basis of the participation factors, determine which diagonal elements of the state matrix and which state variables are strongly related to which eigenvalues. Assume a small regulator gain $K_\text{A} = 30$.

Substituting the data into (12.157), the following state equation of the fifth-order generator model together with voltage control and excitation system is obtained:

$$\begin{bmatrix} \Delta\dot{\delta} \\ \Delta\dot{\omega} \\ \Delta\dot{E}'_\text{q} \\ \Delta\dot{E}''_\text{q} \\ \Delta\dot{E}''_\text{d} \\ \dot{x}_1 \\ \dot{x}_2 \end{bmatrix} = \begin{bmatrix} 0 & 1 & 0 & 0 & 0 & 0 & 0 \\ -20.316 & 0 & 0 & -25.048 & -1.411 & 0 & 0 \\ -0.061 & 0 & -0.773 & -0.083 & 0.018 & 15.06 & 30.12 \\ -0.213 & 0 & 7.050 & -5.026 & 0.063 & 0 & 0 \\ -2.654 & 0 & 0 & -1.463 & -12.958 & 0 & 0 \\ 0 & 0 & 0 & 0 & 0 & 0 & 1 \\ -0.008 & 0 & 0 & -0.565 & 0.971 & -3.33 & -33.33 \end{bmatrix} \begin{bmatrix} \Delta\delta \\ \Delta\omega \\ \Delta E'_\text{q} \\ \Delta E''_\text{q} \\ \Delta E''_\text{d} \\ x_1 \\ x_2 \end{bmatrix}. \tag{12.159}$$

The 2×2 submatrix in the upper left corner corresponds to the swing equation. It relates to the state matrix in Equation (12.115) corresponding to the inherent stability and the second-order generator model. The matrix has two imaginary eigenvalues $\lambda_{1,2} = \pm\text{j}4.507$ which correspond to the frequency of oscillations of about 0.72 Hz. The upper left 5×5 submatrix corresponds to the swing equation together with the equations describing the excitation system and the damping circuits in both axes. It relates to the state equation (12.151). The state matrix in Equation (12.159) has the following eigenvalues:

$$\lambda_{1,2} = -0.177 \pm \text{j}4.535, \quad \lambda_3 = -1.239, \quad \lambda_4 = -3.681, \quad \lambda_5 = -13.036,$$
$$\lambda_6 = -0.342, \quad \lambda_7 = -33.334.$$

Equation (12.90) was used to determine the complex values of participation factors for all eigenvalues. The matrix of participation factors $\boldsymbol{p}$ below contains the magnitudes $|p_{ki}|$:

$$\boldsymbol{x} = \begin{bmatrix} \Delta\dot{\delta} \\ \Delta\dot{\omega} \\ \Delta\dot{E}'_{\mathrm{q}} \\ \Delta\dot{E}''_{\mathrm{q}} \\ \Delta\dot{E}''_{\mathrm{d}} \\ \dot{x}_1 \\ \dot{x}_2 \end{bmatrix}, \quad \mathrm{diag}\ \boldsymbol{A} = \begin{bmatrix} A_{11} \\ A_{22} \\ A_{33} \\ A_{44} \\ A_{55} \\ A_{66} \\ A_{77} \end{bmatrix}, \quad \boldsymbol{p} = \begin{array}{c} \begin{matrix} \lambda_1 & \lambda_2 & \lambda_3 & \lambda_4 & \lambda_5 & \lambda_6 & \lambda_7 \end{matrix} \\ \left[\begin{array}{ccccccc} \mathbf{0.5} & \mathbf{0.5} & 0.05 & 0.06 & & & \\ \mathbf{0.5} & \mathbf{0.5} & 0.05 & 0.06 & & & \\ 0.04 & 0.04 & \mathbf{1.80} & \mathbf{0.54} & & 0.33 & \\ 0.03 & 0.03 & \mathbf{0.29} & \mathbf{1.33} & 0.01 & 0.03 & \\ & & 0.03 & 0.02 & \mathbf{1.0} & & \\ & & \mathbf{0.41} & 0.05 & & \mathbf{1.36} & \\ & & 0.03 & 0.05 & & & \mathbf{1.0} \end{array}\right] \end{array}. \tag{12.160}$$

The dominant values of $|p_{ki}|$ are shown in bold. Values less than 0.01 are neglected. The majority of eigenvalues are connected with a few diagonal elements of the state matrix and therefore with a few state variables. However, by considering only the dominant values of $|p_{ki}|$, it is possible to link individual eigenvalues approximately with some state variables. The simplest relationship is for λ_7 which has only one dominant participation factor associated with A_{77} and x_2, that is with the voltage controller. Eigenvalue λ_5 is associated with A_{55} and emf E''_{d} which corresponds to the damping circuit in the q-axis. Eigenvalue λ_4 is mainly associated with A_{44} and emf E''_{q} which corresponds to the damping circuit in the d-axis. The same λ_4 is also, but less strongly, associated with A_{33} and emf E'_{q} which corresponds to the excitation circuit. Eigenvalue λ_6 is mainly associated with A_{66} and emf x_1 which corresponds to the voltage controller, and to a lesser extent with A_{33} and emf E'_{q} which corresponds to the excitation circuit. The complex conjugate pair of eigenvalues $\lambda_{1,2}$ is equally associated with A_{11} and A_{22}, that is with $\Delta\delta$ and $\Delta\omega$, which correspond to the swing equation. A summary of these associations and the physical meaning of all the eigenvalues is shown in Table 12.2.

Table 12.2 Physical meaning and values of modes in Example 12.9

Equation	Physical meaning of the mode	Notation	Eigenvalue
$\Delta\dot{\delta}_{n-1},\ \Delta\dot{\omega}$	Rotor swings	$\lambda_{1,2}$	$-0.177 \pm \mathrm{j}4.535$
$\Delta\dot{E}'_{\mathrm{q}}$	Excitation circuit	λ_3	-0.342
$\Delta\dot{E}''_{\mathrm{q}}$	Damping circuit in the d-axis and excitation circuit	λ_4	-3.681
$\Delta\dot{E}''_{\mathrm{d}}$	Damping circuit in the q-axis	λ_5	-13.036
$\dot{x}_1$	Voltage controller and excitation circuit	λ_6	-3.681
$\dot{x}_2$	Voltage controller	λ_7	-33.334

Example 12.10

Consider the generator–infinite busbar system described in Example 12.9. It is necessary to check the steady-state stability conditions and determine the influence of the regulator gain K_{A} on the position of the eigenvalues.

Taking into account the voltage control and excitation system introduces two additional eigenvalues shown in Table 12.3. All the eigenvalues lie in the left half-plane so the system is stable over a wide range of the regulator gain values K_A. For small values of the gain, the eigenvalues λ_3, λ_4 are still real. As the gain increases, the values come close to each other until they become complex values $\lambda_{3,4}$. Increased damping causes an increase in the imaginary part. This means that as the gain increases, electromagnetic phenomena in the excitation winding start to be oscillatory. The higher the gain, the higher the frequency of oscillations. As the gain increases, the eigenvalues $\lambda_{1,2}$ move left. Figure 12.8 shows the loci of eigenvalues $\lambda_{1,2}$ and $\lambda_{3,4}$ as the gain increases.

Table 12.3 Physical meaning and values of modes in Example 12.10

Regulator gain	Rotor swings	Excitation circuit	d-axis damping	q-axis damping	Voltage control and excitation system	
K_A	$\lambda_{1,2}$	λ_3	λ_4	λ_5	λ_6	λ_7
0	$-0.111 \pm j4.432$	-0.784	-4.828	-12.931	0	0
50	$-0.193 \pm j4.555$	-1.602	-2.585	-12.983	-0.352	-33.468
60	$-0.215 \pm j4.584$	$-2.403 \pm j\,0.1531$		-19.056	-0.376	-33.498
80	$-0.257 \pm j4.637$	$-2.301 \pm j1.1519$		-18.976	-0.403	-33.548
150	$-0.459 \pm j4.866$	$-1.918 \pm j2.379$		-18.968	-0.448	-33.732
200	$-0.644 \pm j5.090$	$-1.619 \pm j2.837$		-11.871	-0.462	-33.861
250	$-0.828 \pm j5.395$	$-1.331 \pm j3.097$		-19.419	-0.469	-33.988
325	$-1.083 \pm j5.976$	$-1.082 \pm j3.264$		-19.563	-0.477	-34.185

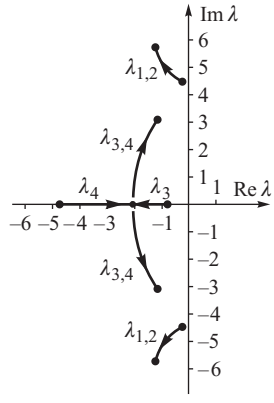

Figure 12.8 Eigenvalue loci when the regulator gain K_A increases.

Increasing the regulator gain improves the damping of swing modes $\lambda_{1,2}$ but deteriorates the damping of modes $\lambda_{3,4}$ connected with oscillations in the rotor circuits. When $K_A = 325$ the real parts of $\lambda_{1,2}$ and $\lambda_{3,4}$ are the same (Table 12.3). It is reasonable to assume that rotor circuit oscillations should not be less well damped than the rotor oscillations. Assuming that the rotor circuit oscillations should be better damped than the rotor oscillation, the gain is $K_A = 250$. With this gain $\lambda_{1,2} = -0.828 \pm j5.395$ and the damping ratio is $\zeta = 0.828/\sqrt{0.828^2 + 5.395^2} \cong 0.15 = 15\ \%$. This value is quite high because usually satisfactory damping corresponds to $\zeta \geq 5\ \%$.

Example 12.11

Consider the same generator–infinite busbar system as before by assuming that the transfer function of the voltage control and excitation system is

$$\frac{\Delta E_f(\mathrm{s})}{\Delta V(\mathrm{s})} = \frac{K_A}{\mathrm{s}} \frac{(2\mathrm{s}+1)}{(0.2\,\mathrm{s}+1)}. \tag{12.161}$$

This is an integrating regulator with a corrective circuit of the lead type. It should be emphasized that such a transfer function is not recommended for a voltage regulator. It was selected just to demonstrate how eigenvalue analysis can expose the bad influence of a particular regulator on damping of rotor swings.

Using the same model as before, eigenvalues have been calculated for a range of values of the regulator gain K_A:

$$\begin{aligned}
K_\mathrm{A} = 0: &\quad \lambda_{1,2} = -0.111 \pm \mathrm{j}4.432, \quad \lambda_3 = -0.784, \quad \lambda_4 = -4.821\\
K_\mathrm{A} = 10: &\quad \lambda_{1,2} = -0.085 \pm \mathrm{j}4.638, \quad \lambda_{3,4} = -1.442 \pm \mathrm{j}1.588\\
K_\mathrm{A} = 20: &\quad \lambda_{1,2} = -0.018 \pm \mathrm{j}4.941, \quad \lambda_{3,4} = -0.977 \pm \mathrm{j}2.426.
\end{aligned}$$

For $K_\mathrm{A} = 0$ the eigenvalues correspond to the regulator being deactivated and therefore inherent damping of swings. Increased gain reduces the negative real parts of $\lambda_{1,2}$ and therefore deteriorates damping. For $K_\mathrm{A} = 20$ the eigenvalues $\lambda_{1,2}$ lie close to the imaginary axis and damping is weak. When $K_\mathrm{A} > 20$ the eigenvalues $\lambda_{1,2}$ move to the right half-plane and the system becomes oscillatory unstable.

It should, however, be remembered that in order to achieve good voltage regulation (Chapter 2) the regulator gain should be high, usually higher than $K_\mathrm{A} = 20$. Such a high gain is unacceptable from the point of view of damping. Hence the discussed regulator must be equipped with a supplementary control loop such as a PSS. For example, a PSS with real power input signal could be used.

Assume that the transfer function of the PSS is

$$\frac{\Delta V_{\mathrm{PSS}}(\mathrm{s})}{\Delta P(\mathrm{s})} = K_\mathrm{P} \frac{0.05\,\mathrm{s}}{1+0.05\mathrm{s}} \frac{1+0.15\,\mathrm{s}}{1+0.05\mathrm{s}} \frac{1+0.15\,\mathrm{s}}{1+3\mathrm{s}}. \tag{12.162}$$

Now it is necessary to check if the PSS improves damping and to select gain K_P assuming that voltage regulation requires the regulator gain $K_\mathrm{A} = 20$.

The eigenvalue loci of the influence of the PSS gain K_P are shown in Figure 12.9. For $K_\mathrm{P} = 0$ the eigenvalues $\lambda_{1,2}$ are close to the imaginary axis. Increasing K_P causes a shift to the left, that

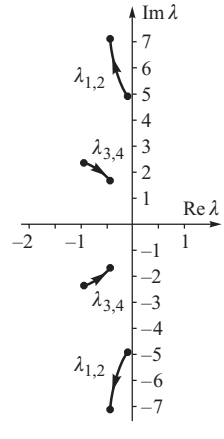

Figure 12.9 Eigenvalue loci when the gain K_P of PSS increases.

is improved damping. At the same time the eigenvalues $\lambda_{3,4}$ corresponding to the rotor circuits move to the right, therefore deteriorating damping. For $K_P = 3$ one gets $\lambda_{1,2} = -0.441 \pm j7.214$ and $\lambda_{3,4} = -0.441 \pm j1.730$, that is the same real parts. Further increase of K_P causes too high a deterioration of oscillations in the rotor circuits.

For $K_P = 3$ the eigenvalues are $\lambda_{1,2} = -0.441 \pm j7.214$ and the damping ratio is $\zeta = 0.441/\sqrt{0.441^2 + 7.214^2} \cong 0.06 = 6\,\%$. Such damping is satisfactory, as it is higher than 5 %, but much weaker than with the previously discussed regulator with transfer function (12.159). Both examples show the importance of choosing the right value for the transfer function of the voltage regulator.

13

Power System Dynamic Simulation

Simulation of power system behaviour, which is the subject of this chapter, is a highly useful tool for planning, for the analysis of stability and for operator training. The individual models of the generator, AVR, turbine–governor and the system loads are given by the differential and algebraic equations developed in Chapter 11 and the network is modelled by the algebraic equations developed in Chapter 3. Together these equations form a complete mathematical model of the system, which can be solved numerically to simulate the system behaviour.

To develop a power system dynamic simulation the equations used to model the different elements are collected together to form a set of differential equations

$$\dot{\boldsymbol{x}} = \boldsymbol{f}(\boldsymbol{x}, \boldsymbol{y}) \tag{13.1}$$

that describe the system dynamics, primarily contributed by the generating units and the dynamic loads, and a set of algebraic equations

$$\boldsymbol{0} = \boldsymbol{g}(\boldsymbol{x}, \boldsymbol{y}) \tag{13.2}$$

that describe the network, the static loads and the algebraic equations of the generator. The solution of these two sets of equations defines the electromechanical state of the power system at any instant in time. A disturbance in the network usually requires a change to both the network configuration and the boundary conditions. These are modelled by changing the coefficients in the functions appearing on the right hand side of Equations (13.1) and (13.2). The computer program for the power system dynamic simulation program must then solve the differential and algebraic equations over a period of time for a given sequence of network disturbances.

Equations (13.1) and (13.2) can be solved using either a partitioned solution or a simultaneous solution. The partitioned solution is sometimes referred to as the *alternating solution* and the simultaneous solution as the *combined solution*. In the partitioned solution the differential equations are solved using a standard explicit numerical integration method with the algebraic equations (13.2) being solved separately at each time step. The simultaneous solution uses implicit integration methods to convert the differential equations (13.1) into a set of algebraic equations which are then combined with the algebraic network equations (13.2) to be solved as one set of simultaneous algebraic equations. The effectiveness of these two solutions depends both on the generator model used and on the method of numerical integration.

Power System Dynamics: Stability and Control, Second Edition Jan Machowski, Janusz W. Bialek and James R. Bumby
© 2008 John Wiley & Sons, Ltd

In order to select the most appropriate integration method it is necessary to understand the time scale of the dynamics included in the model of the generating unit. As explained in Chapter 12, the solution of any set of linear differential equations is in the form of a linear combination of exponential functions each of which describes the individual system modes. These modes are themselves defined by the system eigenvalues which are linked to the time scale of the different dynamics in the model. When the eigenvalues have a range of values that are widely distributed in the complex plane, the solution will consist of the sum of fast-changing dynamics, corresponding to large eigenvalues, and slow-changing dynamics, corresponding to small eigenvalues. In this instance the system of differential equations is referred to as a *stiff system*. A nonlinear system is referred to as stiff if its linear approximation is stiff. Among the power system electromechanical models developed in Chapter 11, all the models that include both the subtransient equations, with their very small time constants, and the relatively slow rotor dynamics constitute stiff models. The model stiffness is further aggravated if the AVR equations, with their small time constants, and the turbine equations, with their long time constants, are included in the model. Consequently, if the power system model includes AVR systems and high-order generator models then the solution method should use integration methods well suited to stiff systems. In contrast, the classical power system model does not constitute a stiff set of differential equations because it only includes slow rotor dynamics. Transient stability programs using this model can use simpler integration formulae.

13.1 Numerical Integration Methods

The analytical solution of nonlinear differential equations is not generally possible and a numerical solution consisting of a series of values $(x_1, x_2, \ldots, x_k, \ldots)$ that satisfies the equation $\dot{x} = f(x, t)$ at the time instants $(t_1, t_2, \ldots, t_k, \ldots)$ must be found. This requires the use of *numerical integration formulae* that calculate the value x_{k+1} knowing all the previous values $(\ldots, x_{k-2}, x_{k-1}, x_k)$. These formulae fall into two general categories: the single-step *Runge–Kutta methods* and the multi-step *predictor–corrector methods*. Both are used in power system simulation programs and the interested reader is referred to Chua and Lin (1975) or Press *et al.* (1992) where these methods, and in particular the Runge–Kutta methods, are discussed in detail along with examples of the necessary computer code. In this section discussion is mainly concentrated on implicit integration methods because they can be effectively used in both the partitioned solution and the simultaneous solution of stiff differential equations. Such equations are generally used to describe power system behaviour. The standard Runge–Kutta methods are restricted to the partitioned solution of non-stiff systems.

When numerically solving differential equations each calculated value of the solution will differ from the accurate solution by an amount called the *local error*. This error comprises a *round-off error* that depends on the computational accuracy of the particular computer used, and the *method error* that depends on the type, order and step length of the integration method used. As the local error propagates to subsequent steps, the total error at any one step consists of the local error made at that step plus the local errors transmitted from previous steps. The way in which the error propagates to subsequent steps determines the practical usefulness of a method. If the error does not increase from step to step then the formula is *numerically stable*, otherwise the formulae is *numerically unstable*. In the latter case the cumulative effect of the errors may cause the solution x_k to be drastically different from the accurate solution.

For the differential equation $\dot{x} = f(x, t)$ the value of x_{k+1} can be found by either integrating the function $f(x, t)$ along its time path between t_k and t_{k+1} or integrating $x(t)$ along its path from x_k to x_{k+1}. Each method will result in a different set of formulae known as the *Adams formulae* and the *Gear formulae* respectively.

The Adams formulae used in predictor–corrector schemes are obtained by approximating the function $f(x, t)$ by a power series $w(t)$ in the time interval over which the function $f(x, t)$ must be

integrated. This gives

$$x_{k+1} = x_k + \int_{t_k}^{t_{k+1}} f(x, t)\mathrm{d}t \approx x_k + \int_{t_k}^{t_{k+1}} w(t)\mathrm{d}t, \tag{13.3}$$

where the power series $w(t)$ is based on r values of $f(x, t)$. The coefficients in this power series depend on the values of $f(x, t)$ at the individual points so that the integration formula becomes

$$x_{k+1} = x_k + h\left(\sum_{j=1}^{r} b_j f_{k+1-j} + b_0 f_{k+1}\right), \tag{13.4}$$

where the function $f_i = f(x(t_i))$ is the value of the function at a given point t_i in time and h is the integration step length. The number of points r used in the power series is referred to as the *order* of the formula.

If $b_0 = 0$ then the resulting formulae are referred to as the *explicit* or *Adams–Bashforth formulae*. In these formulae the approximating polynomial $w(t)$ is calculated using the known values $(\ldots, f_{k-2}, f_{k-1}, f_k)$ and used to extrapolate the function $f(x, t)$ in the new interval from t_k to t_{k+1}. If $b_0 \neq 0$, then the resulting formulae are referred to as the *implicit* or *Adams–Moulton formulae*. In these formulae the approximating polynomial $w(t)$ is calculated using the known values $(\ldots, f_{k-2}, f_{k-1}, f_k)$ and the unknown value of f_{k+1} in order to interpolate function $f(x, t)$ in the interval from t_k to t_{k+1}. Table 13.1 contains Adams–Bashforth and Adams–Moulton formulae up to third order.

The first-order formulae in the Adams family are the *Euler formulae* and they can have either an explicit or implicit form. The second-order interpolation formula is the *trapezoidal rule* when the polynomial $w(t)$ corresponds to the area of a trapezium below a line linking the points f_k and f_{k+1}.

The error in the Adams formulae depends on the order and is the integral of the error between the function $f(x, t)$ and the polynomial approximation $w(t)$. This error may be expressed as

$$\varepsilon_{k+1} = \varepsilon_0 h^{r+1} x_k^{r+1}(\tau), \tag{13.5}$$

where $x_k^{(r+1)}(\tau)$ is the $(r + 1)$ th derivative at a point τ lying in the interval from t_{k-r} to t_{k+1}, while ε_0 is a constant. Table 13.1 shows that for $r > 1$ the size of the error introduced by the implicit formulae is much smaller than that introduced by the explicit formulae.

Table 13.1 Examples of Adams–Bashforth and Adams–Moulton formulae

Type	Order	Formula	ε_0
Adams–Bashforth (explicit) formulae	1	$x_{k+1} = x_k + hf_k$	1/2
	2	$x_{k+1} = x_k + \frac{h}{2}(3f_k - f_{k-1})$	5/12
	3	$x_{k+1} = x_k + \frac{h}{12}(23f_k - 16f_{k-1} + 5f_{k-2})$	9/24
Adams–Moulton (implicit) formulae	1	$x_{k+1} = x_k + hf_{k+1}$	–1/2
	2	$x_{k+1} = x_k + \frac{h}{2}(f_{k+1} + f_k)$	–1/12
	3	$x_{k+1} = x_k + \frac{h}{12}(5f_{k+1} + 8f_k - f_{k-1})$	–1/24

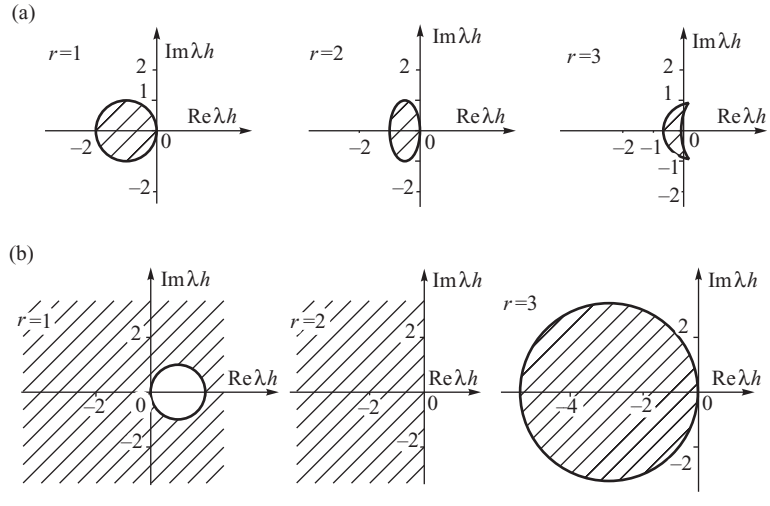

Figure 13.1 Areas of numerical stability for the Adams formulae: (a) explicit; (b) implicit.

An additional advantage of the implicit formulae is their better numerical stability. Figure 13.1 shows the area of numerical stability in the complex (λ, h) plane where h is the integration step length and λ is the largest system eigenvalue. The integration process is numerically stable if the integration step length is small enough so that for all the system eigenvalues λ_i the product $h\lambda_i$ lies inside the stability area. The figure shows that the stability area of the explicit formulae is much smaller than that of their implicit counterparts. The first- and second-order implicit formulae are stable over the whole left half-plane and are therefore numerically *absolutely stable*. This stability issue is particularly important for stiff systems where large eigenvalues force the use of a small integration step h. The low-order implicit formulae are numerically stable over a large part of the complex plane and potentially allow the use of a longer integration step. When using these formulae, the length of the integration step is limited only by the accuracy required in the calculation and the error as determined by Equation (13.5).

A disadvantage of the implicit formulae is that the value of x_{k+1} cannot be calculated directly. When $b \neq 0$ Equation (13.4) can be expressed as

$$x_{k+1} = \beta_k + hb_0 f(x_{k+1}), \tag{13.6}$$

where

$$\beta_k = x_k + \sum_{j=1}^{r} b_j f_{k+1-j}.$$

The unknown value of x_{k+1} now lies on both sides of the equation, which means that, if the function $f(x)$ is nonlinear, it must be found iteratively.

The simplest method of solving (13.6), referred to as *functional iteration*, consists of a series of substitutions according to the following iterative formula:

$$x_{k+1}^{(l+1)} = \beta_k + hb_0 f\left(x_{k+1}^{(l)}\right), \tag{13.7}$$

where the upper indices in brackets denote the iteration number. If the first value $x_{k+1}^{(0)}$ used in the iteration is calculated using an explicit Adams formula, then the whole procedure is known as the *prediction–correction method*. The explicit formula is used as a predictor, while the implicit formula is the corrector. The iterative process (13.7) converges if

$$hb_0 L < 1, \tag{13.8}$$

where L is the *Lipschitz constant*, $L = \sqrt{\alpha_{\mathrm{M}}}$, and α_{M} is the maximum eigenvalue of the matrix product $\left(\boldsymbol{A}^{\mathrm{T}}\boldsymbol{A}\right)$, where $\boldsymbol{A} = \partial f/\partial x$ is the Jacobi matrix calculated at point $\hat{x}_{k+1}$ being a solution of Equation (13.6). The smaller the value of the product $(hb_0 L)$, the faster the convergence.

Because of the presence of large eigenvalues in stiff systems the convergence condition of Equation (13.8) may force a limitation on the integration step length that is more restrictive than that required either by the required accuracy or by numerical stability. In such a case Equation (13.6) may be solved using *Newton's method* instead of by functional iteration. For any equation $F(x) = 0$ Newton's formula is

$$x^{(l+1)} = x^{(l)} - \left[\frac{\partial F}{\partial x}\right]_{(l)}^{-1} F\left(x^{(l)}\right), \tag{13.9}$$

where the upper index in brackets denotes the iteration number. Applying (13.9) to the implicit formula of Equation (13.6) gives

$$x_{k+1}^{(l+1)} = x_{k+1}^{(l)} - \left[1 - hb_0 A_{k+1}^{(l)}\right]^{-1}\left[x_{k+1}^{(l)} - \beta_k - hb_0 f\left(x_{k+1}^{(l)}\right)\right], \tag{13.10}$$

where $A_{k+1}^{(l)}$ is the Jacobi matrix calculated for the lth iteration. Newton's method allows the integration step length to be increased to a much higher value than that defined by (13.8) but, because the matrix is inverted at each step, the complexity of the method is much greater than functional iteration. However, if the integration step length is sufficiently large then the added complexity of Newton's method may be justified.

In developing the Adams formulae the function $f(x, t)$ was approximated by the power series $w(t)$ in order to find x_{k+1}. An alternative approach is to approximate $x(t)$, rather than the function $f(x, t)$, by the power series $x(t)$. In this case $w(t) \approx x(t)$ and the coefficients in the approximating polynomial $w(t)$ are functions of consecutive values of $(\ldots, x_{k-2}, x_{k-1}, \ldots)$. Taking the time derivative gives $\dot{x} = \dot{w}(t)$, or $\dot{w}(t) = f(x, t)$. When $w(t)$ is used as the extrapolation formula this leads to the following explicit integration formula:

$$x_{k+1} = \sum_{j=0}^{r} a_j x_{k-j} + b_0 h f_k. \tag{13.11}$$

If $w(t)$ is used as the interpolation formula the following implicit integration formula is obtained:

$$x_{k+1} = \sum_{j=0}^{r} a_j x_{k-j} + b_0 h f_{k+1}. \tag{13.12}$$

These formulae, known as the Gear formulae, are shown in Table 13.2 (Variant I) up to third order. The first order formula is the Euler formula while the second-order formula is referred to as the *intermediate point formula*.

The solution of Equation (13.12) may be obtained using either functional iteration or Newton's method, just as for the Adams formulae. If Equation (13.12) is solved by functional iteration then Equation (13.11) is used as the predictor and Equation (13.12) as the corrector.

Table 13.2 Examples of Gear formulae

Type	Order	Formula	ε_0
Explicit Variant I	1	$x_{k+1} = x_k + hf_k$	
	2	$x_{k+1} = x_{k-1} + 2hf_k$	
	3	$x_{k+1} = -\frac{3}{2}x_k + 3x_{k-1} - \frac{1}{2}x_{k-2} + 3f_k h$	
Explicit Variant II	1	$x_{k+1} = 2x_k - x_{k-1}$	
	2	$x_{k+1} = 3x_k - 3x_{k-1} + x_{k-2}$	
	3	$x_{k+1} = 4x_k - 6x_{k-1} + 4x_{k-2} - x_{k-3}$	
Implicit	1	$x_{k+1} = x_k + hf_{k+1}$	–1/2
	2	$x_{k+1} = \frac{4}{3}x_k - \frac{1}{3}x_{k-1} + \frac{2}{3}hf_{k+1}$	–2/9
	3	$x_{k+1} = \frac{18}{11}x_k - \frac{9}{11}x_{k-1} + \frac{2}{11}x_{k-2} + \frac{6}{12}hf_{k+1}$	–3/22

The main advantage of the Gear formulae over the Adams formulae is that they have a larger area of numerical stability as shown in Figure 13.2. They are therefore better suited to stiff systems. If a large integration step length is used on a stiff system the predictor in (13.11) may not give a good approximation and instead $x(t)$ may be extrapolated directly using the values $(\ldots, x_{k-2}, x_{k-1}, x_k)$. The Lagrange extrapolation equations then give

$$x_{k+1} = a_0 x_k + \sum_{j=1}^{r} a_j x_{k-1}. \tag{13.13}$$

Values of the coefficients for these formulae up to third order are given in Table 13.2 (Variant II).

When a set of differential equations is nonlinear the Jacobi matrix and its eigenvalues are not constant and the criteria that limit the integration step length constantly change with time. For example, the numerical stability depends on the eigenvalues and the step length, the convergence properties on the Lipschitz constant and the step length, while the local error is determined by the derivative $x^{(r+1)}(\tau)$ and the step length so that the correct choice of integration step length is of fundamental importance.

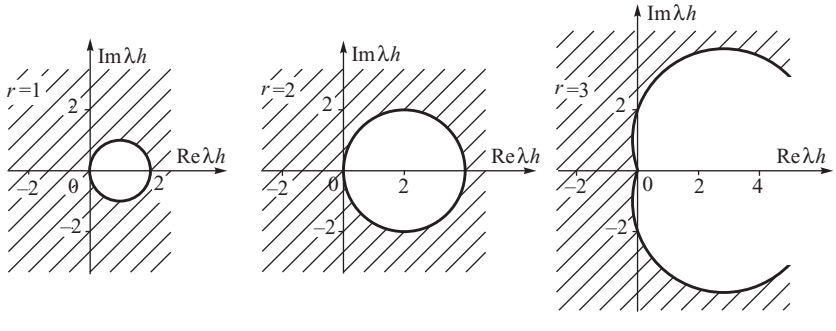

Figure 13.2 Areas of numerical stability of the Gear formulae.

To combat these problems there are two extreme ways in which the difference formulae can be used. The first is to use a low-order formula, which is absolutely stable numerically, together with a constant integration step length that is limited to a value that will guarantee good convergence of the iterative corrector and limited local errors for the whole of the simulation period. Alternatively the order of the formulae can be automatically varied during the simulation process so that the integration step length can be maximized without compromising either the accuracy or the convergence properties.

Because higher order formulae have a low area of numerical stability, the highest order formula that is normally used in practice is the sixth. Simple programs use second- or third-order formulae in order to avoid problems with numerical stability. It is also possible to use a constant order, variable step procedure. Automatic changes in either the integration step length or the order of the formula used require additional calculation. In addition, a change in the integration step length is not easy because if the step length is changed then the coefficients in most of the formulae also change since they depend on the distance between the interpolation nodes. Problems with the use of variable order, constant step formulae are alleviated if the equations are written in *canonical form*, details of which can be found in Chua and Lin (1975).

13.2 The Partitioned Solution

In each step of the numerical integration procedure the partitioned solution alternates between the solutions of the differential equations (13.1) and the algebraic equations (13.2). In order to match the values of the variables $\boldsymbol{y}(t)$ to the values of the variables $\boldsymbol{x}(t)$ it is necessary to solve the algebraic equations before numerically integrating the differential equations. A general solution algorithm for the partitioned solution, using a predictor–corrector numerical integration method, is shown in Figure 13.3. In this algorithm the algebraic equations are solved at three stages. The first solution is at stage 3, and occurs whenever there is a change in the network configuration. This change in the network configuration alters the coefficients in the algebraic equations so that for a given set of state variables $\boldsymbol{x}_k$ the value of the dependent variables $\boldsymbol{y}_k$ change. The second solution of the algebraic equations takes place at stage 5, after predicting the new values of the variables $\boldsymbol{x}_{k+1}$. The third, and final solution, is at stage 7 after correcting $\boldsymbol{x}_{k+1}$ in stage 6. The solution at stage 7 is repeated for each integration step as many times as there are corrections of $\boldsymbol{x}_{k+1}$.

In the algorithm shown in Figure 13.3 the solution of the algebraic equations takes a significant proportion of the total computation time. It is therefore important to consider the methods available for effectively realizing the solution. In the following discussion the network equations will be solved assuming the network to be represented as shown in Figure 13.4.

In the considered network model (Figure 13.4) each generator is represented by an additional generator node i' and a fictitious emf $\underline{E}_i^{\mathrm{f}}$ behind a fictitious reactance X_i^{f} with $\underline{I}_i$ being the injected generator current. If rotor saliency is neglected then, depending on the generator model used, the fictitious emf and the fictitious reactance will correspond to the transient or subtransient values (Section 11.1.6). If, on the other hand, rotor saliency is included then both the reactance and the emf will have some fictitious value.

Each load is represented (Figure 13.4) by an equivalent admittance $\underline{y}_l$ and a correction nodal current $\Delta\underline{I}_l$. Figure 13.5 illustrates the way $\Delta\underline{I}_l$ is calculated. The loads are modelled (see Section 3.5.4) using nonlinear voltage characteristics $P_l(V_l)$ and $Q_l(V_l)$ denoted by solid lines in the diagram. Dashed lines denote parabolas corresponding to, respectively, real and reactive power consumed by admittance $\underline{y}_l = g_l + \mathrm{j}b_l$ inserted in the network model. Differences between the required load characteristic and the admittance characteristic are made up by correction powers ΔP_l and ΔQ_l, respectively, which are denoted by vertical lines in Figure 13.5. When the load voltage is $\underline{V}_l$, correction power $\Delta\underline{S}_l = \Delta P_l + \mathrm{j}\Delta Q_l$ corresponds to a correction current $\Delta\underline{I}_l = \Delta\underline{S}_l^*/\underline{V}_l$. Note that the voltage is a complex number as nodal voltage is a phasor in the common network reference frame (Figure 13.4).

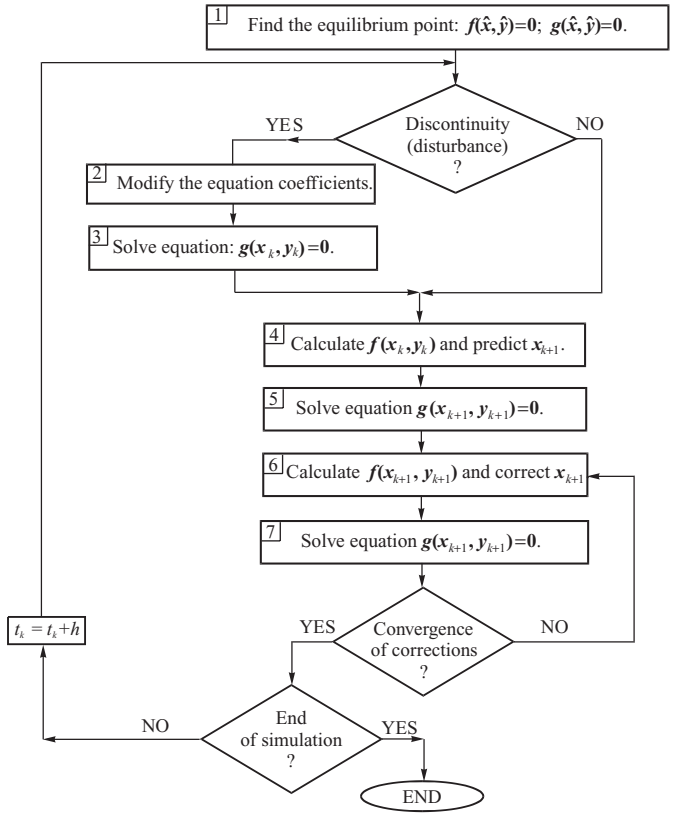

Figure 13.3 Simplified algorithm of the partitioned solution using the predictor–corrector method.

Under the above assumptions the network is described by the following nodal equation using complex numbers:

$$\begin{bmatrix} \underline{\boldsymbol{I}}_{\mathrm{G}} \\ \Delta\underline{\boldsymbol{I}}_{\mathrm{L}} \end{bmatrix} = \begin{bmatrix} \underline{\boldsymbol{Y}}_{\mathrm{GG}} & \underline{\boldsymbol{Y}}_{\mathrm{GL}} \\ \underline{\boldsymbol{Y}}_{\mathrm{LG}} & \underline{\boldsymbol{Y}}_{\mathrm{LL}} \end{bmatrix} \begin{bmatrix} \underline{\boldsymbol{E}}_{\mathrm{G}} \\ \underline{\boldsymbol{V}}_{\mathrm{L}} \end{bmatrix}, \tag{13.14}$$

where $\{\mathrm{G}\}$ is the set of fictitious generator nodes, $\{\mathrm{L}\}$ is the set of all the other nodes (called the load nodes) that includes the generator terminal nodes, $\underline{\boldsymbol{I}}_{\mathrm{G}}$ is a vector of the generator currents, $\Delta\underline{\boldsymbol{I}}_{\mathrm{L}}$ a vector of the load corrective currents, $\underline{\boldsymbol{E}}_{\mathrm{G}}$ a vector of the fictitious emfs and $\underline{\boldsymbol{V}}_{\mathrm{L}}$ a vector of the

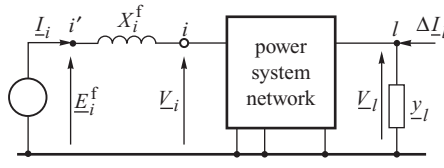

Figure 13.4 Network model with each generator replaced by a Thévenin voltage source: i', a generator node; l, a load node.

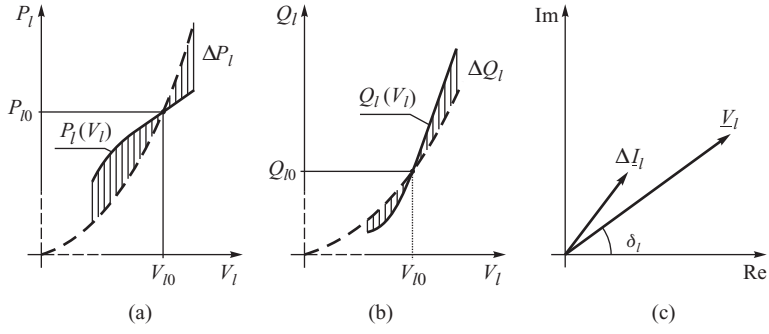

Figure 13.5 Modelling of nonlinear voltage characteristic of a load: (a) correction real power; (b) correction reactive power; (c) phasors of the nodal voltage and nodal correction current.

voltages at the load nodes. The matrix $\underline{\boldsymbol{Y}}_{\mathrm{GG}}$ is a diagonal matrix of generator admittance $\underline{y}_i = 1/\mathrm{j}X_i^{\mathrm{f}}$. $\underline{\boldsymbol{Y}}_{\mathrm{GL}}$ is a rectangular matrix comprising a diagonal submatrix with elements equal to $-\underline{y}_i$ and all other elements equal to zero. $\underline{\boldsymbol{Y}}_{\mathrm{LG}}$ is the transpose of $\underline{\boldsymbol{Y}}_{\mathrm{GL}}$. The matrix $\underline{\boldsymbol{Y}}_{\mathrm{LL}}$ is a modified version of the nodal admittance matrix, introduced in Chapter 3, whose diagonal terms now include the load and generator admittances at the rows corresponding to the relevant load nodes and generator terminal nodes, respectively. If each load is represented by a constant admittance then the correction currents $\Delta \underline{\boldsymbol{I}}_{\mathrm{L}} = \underline{\mathbf{0}}$.

13.2.1 Partial Matrix Inversion

Appendix A.2 contains the derivation of partial matrix inversion which may be applied to Equation (13.14). This equation can be expanded as

$$\underline{\boldsymbol{I}}_{\mathrm{G}} = \underline{\boldsymbol{Y}}_{\mathrm{GG}}\underline{\boldsymbol{E}}_{\mathrm{G}} + \underline{\boldsymbol{Y}}_{\mathrm{GL}}\underline{\boldsymbol{V}}_{\mathrm{L}}, \tag{13.15}$$

$$\Delta \underline{\boldsymbol{I}}_{\mathrm{L}} = \underline{\boldsymbol{Y}}_{\mathrm{LG}}\underline{\boldsymbol{E}}_{\mathrm{G}} + \underline{\boldsymbol{Y}}_{\mathrm{LL}}\underline{\boldsymbol{V}}_{\mathrm{L}}. \tag{13.16}$$

Rearranging Equation (13.16),

$$\underline{\boldsymbol{V}}_{\mathrm{L}} = -\underline{\boldsymbol{Y}}_{\mathrm{LL}}^{-1}\underline{\boldsymbol{Y}}_{\mathrm{LG}}\underline{\boldsymbol{E}}_{\mathrm{G}} + \underline{\boldsymbol{Y}}_{\mathrm{LL}}^{-1}\Delta \underline{\boldsymbol{I}}_{\mathrm{L}}, \tag{13.17}$$

and substituting into Equation (13.15) gives

$$\underline{\boldsymbol{I}}_{\mathrm{G}} = (\underline{\boldsymbol{Y}}_{\mathrm{GG}} - \underline{\boldsymbol{Y}}_{\mathrm{GL}}\underline{\boldsymbol{Y}}_{\mathrm{LL}}^{-1}\underline{\boldsymbol{Y}}_{\mathrm{LG}})\underline{\boldsymbol{E}}_{\mathrm{G}} + \underline{\boldsymbol{Y}}_{\mathrm{GL}}\underline{\boldsymbol{Y}}_{\mathrm{LL}}^{-1}\Delta \underline{\boldsymbol{I}}_{\mathrm{L}}. \tag{13.18}$$

These last two equations (13.17) and (13.18) can be rewritten in matrix form as

$$\begin{bmatrix} \underline{\boldsymbol{I}}_{\mathrm{G}} \\ \underline{\boldsymbol{V}}_{\mathrm{L}} \end{bmatrix} = \begin{bmatrix} \underline{\boldsymbol{Y}}_{\mathrm{G}} & \underline{\boldsymbol{K}}_{\mathrm{I}} \\ \underline{\boldsymbol{K}}_{\mathrm{V}} & \underline{\boldsymbol{Z}}_{\mathrm{LL}} \end{bmatrix} \begin{bmatrix} \underline{\boldsymbol{E}}_{\mathrm{G}} \\ \Delta \underline{\boldsymbol{I}}_{\mathrm{L}} \end{bmatrix}, \tag{13.19}$$

where $\underline{\boldsymbol{Y}}_{\mathrm{G}} = \underline{\boldsymbol{Y}}_{\mathrm{GG}} - \underline{\boldsymbol{Y}}_{\mathrm{GL}}\underline{\boldsymbol{Y}}_{\mathrm{LL}}^{-1}\underline{\boldsymbol{Y}}_{\mathrm{LG}}$, $\underline{\boldsymbol{K}}_{\mathrm{I}} = \underline{\boldsymbol{Y}}_{\mathrm{GL}}\underline{\boldsymbol{Y}}_{\mathrm{LL}}^{-1}$, $\underline{\boldsymbol{K}}_{\mathrm{V}} = -\underline{\boldsymbol{Y}}_{\mathrm{LL}}^{-1}\underline{\boldsymbol{Y}}_{\mathrm{LG}}$ and $\underline{\boldsymbol{Z}}_{\mathrm{LL}} = \underline{\boldsymbol{Y}}_{\mathrm{LL}}^{-1}$. The square matrix in Equation (13.19) is called the *partial inversion matrix* and refers to the fact that only the submatrix $\underline{\boldsymbol{Y}}_{\mathrm{LL}}$ is explicitly inverted to obtain $\underline{\boldsymbol{Z}}_{\mathrm{LL}} = \underline{\boldsymbol{Y}}_{\mathrm{LL}}^{-1}$.

If rotor saliency is neglected then the fictitious emfs $\underline{E}_i^{\mathrm{f}}$ in the network model are equal to the generator emfs and are calculated during the numerical integration of the differential equations. If, in addition, each load is represented by a constant admittance then the correction currents $\Delta \underline{\boldsymbol{I}}_{\mathrm{L}}$ are

equal to zero and the generator currents and the load voltages can be calculated directly from

$$\begin{aligned} \underline{\boldsymbol{I}}_{\mathrm{G}} &= \underline{\boldsymbol{Y}}_{\mathrm{G}} \underline{\boldsymbol{E}}_{\mathrm{G}} \\ \underline{\boldsymbol{V}}_{\mathrm{L}} &= \underline{\boldsymbol{K}}_{\mathrm{V}} \underline{\boldsymbol{E}}_{\mathrm{G}}, \end{aligned} \tag{13.20}$$

without the need for an iterative solution. However, if the loads are nonlinear the correction currents are non-zero and depend on the load voltage according to the function $\Delta \underline{\boldsymbol{I}}_{\mathrm{L}}(\underline{\boldsymbol{V}}_{\mathrm{L}})$. As the unknown load voltages now appear on both sides of Equation (13.19), they must be calculated iteratively. The lower equation in (13.19) can be used to formulate the iterative formula

$$\underline{\boldsymbol{V}}_{\mathrm{L}}^{(l+1)} = \underline{\boldsymbol{K}}_{\mathrm{V}} \underline{\boldsymbol{E}}_{\mathrm{G}} + \underline{\boldsymbol{Z}}_{\mathrm{LL}} \Delta \underline{\boldsymbol{I}}_{\mathrm{L}} \left(\underline{\boldsymbol{V}}_{\mathrm{L}}^{(l)} \right), \tag{13.21}$$

where the upper index in brackets denotes the iteration number. When the iteration process is complete, the voltage $\underline{\boldsymbol{V}}_{\mathrm{L}} = \underline{\boldsymbol{V}}_{\mathrm{L}}^{(l+1)}$ and the generator currents may be calculated from the upper equation in (13.19) as

$$\underline{\boldsymbol{I}}_{\mathrm{G}} = \underline{\boldsymbol{Y}}_{\mathrm{G}} \underline{\boldsymbol{E}}_{\mathrm{G}} + \underline{\boldsymbol{K}}_{\mathrm{I}} \Delta \underline{\boldsymbol{I}}_{\mathrm{L}}, \tag{13.22}$$

where $\Delta \underline{\boldsymbol{I}}_{\mathrm{L}}$ are the correction currents corresponding to the calculated values of the voltages.

If rotor saliency is included then the fictitious emfs representing the generators in the network equations must also be calculated iteratively together with the generator currents. To explain how this is done the generator fourth-order transient model ($\dot{E}'_{\mathrm{d}}$, $\dot{E}_{\mathrm{q}}$, $\dot{\delta}$, $\dot{\omega}$) will be used, but the technique can equally well be applied to the sixth-order subtransient model ($\dot{E}''_{\mathrm{d}}$, $\dot{E}''_{\mathrm{q}}$, $\dot{E}'_{\mathrm{d}}$, $\dot{E}'_{\mathrm{q}}$, $\dot{\delta}$, $\dot{\omega}$) or the fifth-order subtransient model ($\dot{E}''_{\mathrm{d}}$, $\dot{E}''_{\mathrm{q}}$, $\dot{E}'_{\mathrm{q}}$, $\dot{\delta}$, $\dot{\omega}$) defined in Section 11.1.6.

Figure 13.6 shows three circuit diagrams. The first two diagrams correspond to the generator in the transient state, while the third diagram corresponds to the fictitious Thévenin source used in the network model to replace the generator. The emf of the fictitious generator voltage source $\underline{E}^{\mathrm{f}}$ must satisfy the equation $\underline{E}^{\mathrm{f}} = \underline{V} + \mathrm{j} X^{\mathrm{f}} \underline{I}$, or $\left(E_{\mathrm{a}}^{\mathrm{f}} + \mathrm{j} E_{\mathrm{b}}^{\mathrm{f}}\right) = (V_{\mathrm{a}} + \mathrm{j} V_{\mathrm{b}}) + \mathrm{j} X^{\mathrm{f}} (I_{\mathrm{a}} + \mathrm{j} I_{\mathrm{b}})$, which expressed in matrix form is

$$\begin{bmatrix} E_{\mathrm{a}}^{\mathrm{f}} \\ E_{\mathrm{b}}^{\mathrm{f}} \end{bmatrix} = \begin{bmatrix} V_{\mathrm{a}} \\ V_{\mathrm{b}} \end{bmatrix} - \begin{bmatrix} 0 & -X^{\mathrm{f}} \\ X^{\mathrm{f}} & 0 \end{bmatrix} \begin{bmatrix} I_{\mathrm{a}} \\ I_{\mathrm{b}} \end{bmatrix} \quad \text{or} \quad \boldsymbol{E}_{\mathrm{ab}}^{\mathrm{f}} = \boldsymbol{V}_{\mathrm{ab}} - \boldsymbol{Z}_{\mathrm{ab}}^{\mathrm{f}} \boldsymbol{I}_{\mathrm{ab}}. \tag{13.23}$$

This equation can be transformed from the system (a, b) reference frame to the individual generator (d, q) reference frame using the $\boldsymbol{T}$ transformation defined in Equation (3.166) to give

$$\begin{bmatrix} E_{\mathrm{d}}^{\mathrm{f}} \\ E_{\mathrm{q}}^{\mathrm{f}} \end{bmatrix} = \begin{bmatrix} V_{\mathrm{d}} \\ V_{\mathrm{q}} \end{bmatrix} - \begin{bmatrix} 0 & -X^{\mathrm{f}} \\ X^{\mathrm{f}} & 0 \end{bmatrix} \begin{bmatrix} I_{\mathrm{d}} \\ I_{\mathrm{q}} \end{bmatrix} \quad \text{or} \quad \boldsymbol{E}_{\mathrm{dq}}^{\mathrm{f}} = \boldsymbol{V}_{\mathrm{dq}} - \boldsymbol{Z}_{\mathrm{dq}}^{\mathrm{f}} \boldsymbol{I}_{\mathrm{dq}}, \tag{13.24}$$

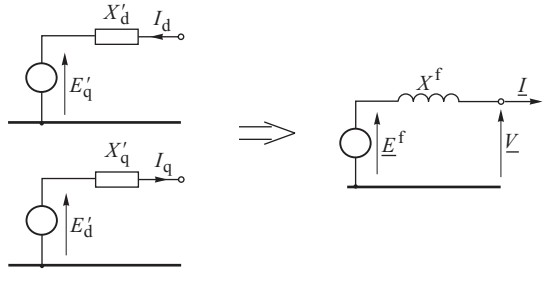

Figure 13.6 Replacing the equivalent d-axis and q-axis circuit of the generator by one equivalent circuit with fictitious reactance X^{f} and fictitious emf $\underline{E}^{\mathrm{f}}$.

where $\boldsymbol{Z}_{\mathrm{dq}}^{\mathrm{f}} = \boldsymbol{T}^{-1}\boldsymbol{Z}_{\mathrm{ab}}^{\mathrm{f}}\boldsymbol{T} = \boldsymbol{Z}_{\mathrm{ab}}^{\mathrm{f}}$ and $\boldsymbol{T}^{-1} = \boldsymbol{T}$. On the other hand, the armature voltage equation for the fourth-order model of the generator ($\dot{E}'_{\mathrm{d}}$, $\dot{E}'_{\mathrm{q}}$, $\dot{\delta}$, $\dot{\omega}$) is given by Equation (11.104) as

$$\begin{bmatrix} V_{\mathrm{d}} \\ V_{\mathrm{q}} \end{bmatrix} = \begin{bmatrix} E'_{\mathrm{d}} \\ E'_{\mathrm{q}} \end{bmatrix} - \begin{bmatrix} 0 & X'_{\mathrm{q}} \\ -X'_{\mathrm{d}} & 0 \end{bmatrix} \begin{bmatrix} I_{\mathrm{d}} \\ I_{\mathrm{q}} \end{bmatrix} \quad \text{or} \quad \boldsymbol{V}_{\mathrm{dq}} = \boldsymbol{E}'_{\mathrm{dq}} - \boldsymbol{Z}_{\mathrm{dq}}\boldsymbol{I}_{\mathrm{dq}}, \tag{13.25}$$

which, when substituted into (13.24), gives

$$\begin{bmatrix} E_{\mathrm{d}}^{\mathrm{f}} \\ E_{\mathrm{q}}^{\mathrm{f}} \end{bmatrix} = \begin{bmatrix} E'_{\mathrm{d}} \\ E'_{\mathrm{q}} \end{bmatrix} - \begin{bmatrix} 0 & -\Delta X_{\mathrm{q}} \\ \Delta X_{\mathrm{d}} & 0 \end{bmatrix} \begin{bmatrix} I_{\mathrm{d}} \\ I_{\mathrm{q}} \end{bmatrix} \quad \text{or} \quad \boldsymbol{E}_{\mathrm{dq}}^{\mathrm{f}} = \boldsymbol{E}'_{\mathrm{dq}} - \Delta\boldsymbol{Z}\boldsymbol{I}_{\mathrm{dq}}, \tag{13.26}$$

where $\Delta X_{\mathrm{q}} = X'_{\mathrm{q}} - X^{\mathrm{f}}$ and $\Delta X_{\mathrm{d}} = X'_{\mathrm{d}} - X^{\mathrm{f}}$. This equation determines the emf of the fictitious voltage source in terms of the generator current.

Equation (13.26) can be solved iteratively together with the network equations (13.19). To show how this is done Equation (13.26) is rewritten as

$$\begin{bmatrix} E_{\mathrm{d}}^{\mathrm{f}(l+1)} \\ E_{\mathrm{q}}^{\mathrm{f}(l+1)} \end{bmatrix} = \begin{bmatrix} E'_{\mathrm{d}} \\ E'_{\mathrm{q}} \end{bmatrix} - \begin{bmatrix} 0 & -\Delta X_{\mathrm{q}} \\ \Delta X_{\mathrm{d}} & 0 \end{bmatrix} \begin{bmatrix} I_{\mathrm{d}}^{(l)} \\ I_{\mathrm{q}}^{(l)} \end{bmatrix} \quad \text{or} \quad \boldsymbol{E}_{\mathrm{dq}}^{\mathrm{f}(l+1)} = \boldsymbol{E}'_{\mathrm{dq}} - \Delta\boldsymbol{Z}\boldsymbol{I}_{\mathrm{dq}}^{(l)}, \tag{13.27}$$

where l is the iteration number. The iterative solution algorithm is then:

1. Estimate the values of $E_{\mathrm{d}}^{\mathrm{f}}$, $E_{\mathrm{q}}^{\mathrm{f}}$ for every generator and transform them to the system reference frame (a, b) in order to obtain $\underline{E}^{\mathrm{f}} = E_{\mathrm{a}}^{\mathrm{f}} + \mathrm{j}E_{\mathrm{b}}^{\mathrm{f}}$.
2. Solve the network equations (13.19). Calculate the current $\underline{I} = I_{\mathrm{a}} + \mathrm{j}I_{\mathrm{b}}$ for every generator and transform I_{a}, I_{b} to the generator (d, q) reference frame in order to obtain I_{d}, I_{q}.
3. Use Equation (13.27) to correct the values of $E_{\mathrm{d}}^{\mathrm{f}}$, $E_{\mathrm{q}}^{\mathrm{f}}$.
4. Compare the result with the pervious iteration; if they differ, transform the new values of $E_{\mathrm{d}}^{\mathrm{f}}$, $E_{\mathrm{q}}^{\mathrm{f}}$ to the system reference frame (a, b) and repeat step 2 until the voltages converge.

The number of iterations necessary to solve the generator equations and the network equations depends on the value of the reactance chosen for the fictitious Thévenin source. Let $\hat{E}_{\mathrm{d}}^{\mathrm{f}}$, $\hat{E}_{\mathrm{q}}^{\mathrm{f}}$ and $\hat{I}_{\mathrm{d}}$, $\hat{I}_{\mathrm{q}}$ be the solutions to the equations. According to Equation (13.27), the solution must satisfy

$$\begin{bmatrix} \hat{E}_{\mathrm{d}}^{\mathrm{f}} \\ \hat{E}_{\mathrm{q}}^{\mathrm{f}} \end{bmatrix} = \begin{bmatrix} E'_{\mathrm{d}} \\ E'_{\mathrm{q}} \end{bmatrix} - \begin{bmatrix} 0 & -\Delta X_{\mathrm{q}} \\ \Delta X_{\mathrm{d}} & 0 \end{bmatrix} \begin{bmatrix} \hat{I}_{\mathrm{d}} \\ \hat{I}_{\mathrm{q}} \end{bmatrix} \quad \text{or} \quad \hat{\boldsymbol{E}}_{\mathrm{dq}}^{\mathrm{f}} = \boldsymbol{E}'_{\mathrm{dq}} - \Delta\boldsymbol{Z}\hat{\boldsymbol{I}}_{\mathrm{dq}}. \tag{13.28}$$

Subtracting Equation (13.27) from (13.28) gives

$$\left(\boldsymbol{E}_{\mathrm{dq}}^{\mathrm{f}(l+1)} - \hat{\boldsymbol{E}}_{\mathrm{dq}}^{\mathrm{f}}\right) = \Delta\boldsymbol{Z}\left(\boldsymbol{I}_{\mathrm{dq}}^{(l)} - \hat{I}_{\mathrm{dq}}\right). \tag{13.29}$$

This equation is important because it means that for a given error $\Delta\boldsymbol{I}_{\mathrm{dq}}^{(l)} = (\boldsymbol{I}_{\mathrm{dq}}^{(l)} - \hat{I}_{\mathrm{dq}})$ in the current estimation, then the smaller the elements $\Delta X_{\mathrm{q}} = X'_{\mathrm{q}} - X^{\mathrm{f}}$ and $\Delta X_{\mathrm{d}} = X'_{\mathrm{d}} - X^{\mathrm{f}}$ in the matrix $\Delta\boldsymbol{Z}$, the closer the next estimation of the fictitious emf to the final solution. Consequently, the iterative process will converge quickly if the equivalent generator reactance is chosen to have a value equal to an average value of X'_{d} and X'_{q} when the fictitious emf $\underline{E}^{\mathrm{f}}$ then has a value close to the generator transient emf $\underline{E}'$. Generally one of the following 'average' reactance values is used for the fictitious reactance:

$$X^{\mathrm{f}} = \frac{1}{2}\left(X'_{\mathrm{d}} + X'_{\mathrm{q}}\right), \quad X^{\mathrm{f}} = 2\frac{X'_{\mathrm{d}}X'_{\mathrm{q}}}{X'_{\mathrm{d}} + X'_{\mathrm{q}}}, \quad X^{\mathrm{f}} = \sqrt{X'_{\mathrm{d}}X'_{\mathrm{q}}}. \tag{13.30}$$

The use of one of these values guarantees a small number of iterations in the solution of Equation (13.27). If X'_d is close to X'_q then one or two iterations will suffice. If transient saliency is neglected then $X'_d = X'_q = X^f$ and $\hat{E}^f_{dq} = E'_{dq}$ and the solution is obtained without any iterations. When $X'_d \neq X'_q$, then the number of iterations depends on the initial choice of the fictitious emfs. If the value of X^f is chosen according to one of the formulae in (13.30) then the magnitude, and the angle, of the fictitious emf are close to the magnitude and the angle of the generator transient emf. In order to achieve a good estimate for the final value, the fictitious emfs should be changed at each integration step in proportion to the generator emfs.

When rotor saliency and load nonlinearity are included, the algorithm will involve both of the iterative processes described above. A simplified algorithm is shown in Figure 13.7.

A disadvantage of the partial matrix inversion technique used in Equation (13.19) to solve the network equation is that all the submatrices $\underline{\boldsymbol{Y}}_G$, $\underline{\boldsymbol{K}}_I$, $\underline{\boldsymbol{K}}_V$ and $\underline{\boldsymbol{Z}}_{LL}$ are dense and therefore have a large computer memory requirement while also requiring a large number of arithmetic operations to calculate the currents and the voltages. If the number of loads for which the voltage must be computed is small, in comparison with the total number of nodes, then the partial matrix inversion technique is worth using because then only part of the submatrices $\underline{\boldsymbol{K}}_I$, $\underline{\boldsymbol{K}}_V$ and $\underline{\boldsymbol{Z}}_{LL}$ need be stored and the number of arithmetic operations is also reduced. If the voltage must be computed for the

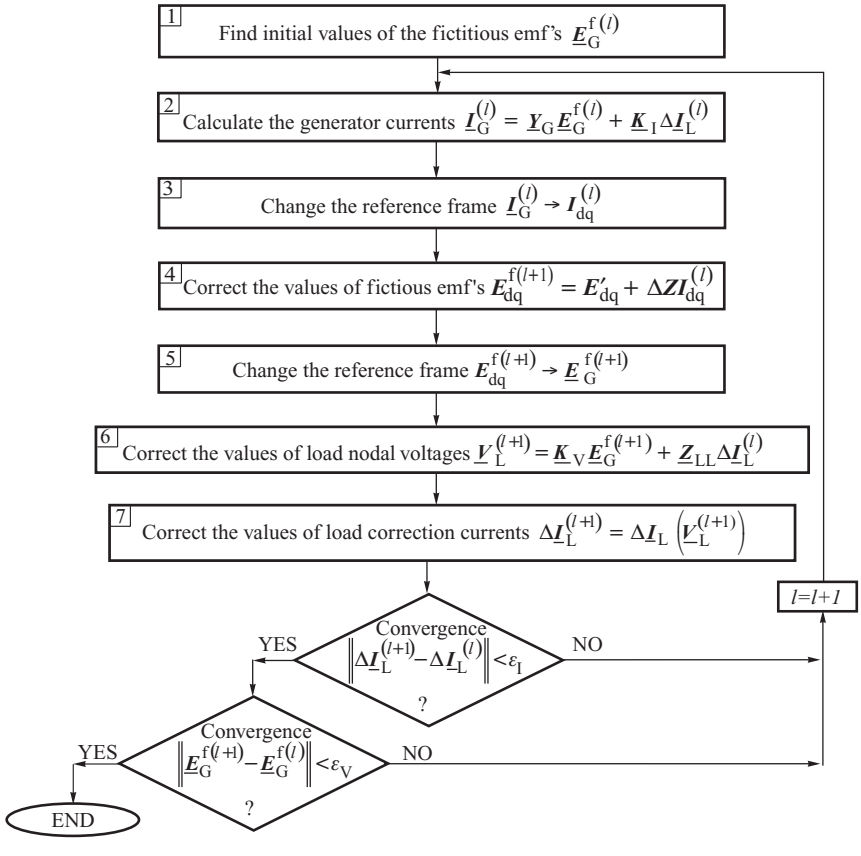
1
Find initial values of the fictitious emf's $\underline{E}_G^{f(l)}$
2
Calculate the generator currents $\underline{I}_G^{(l)} = \underline{Y}_G \underline{E}_G^{f(l)} + \underline{K}_I \Delta \underline{I}_L^{(l)}$
3
Change the reference frame $\underline{I}_G^{(l)} \rightarrow I_{dq}^{(l)}$
4
Correct the values of fictious emf's $E_{dq}^{f(l+1)} = E'_{dq} + \Delta Z I_{dq}^{(l)}$
5
Change the reference frame $E_{dq}^{f(l+1)} \rightarrow \underline{E}_G^{f(l+1)}$
6
Correct the values of load nodal voltages $\underline{V}_L^{(l+1)} = \underline{K}_V \underline{E}_G^{f(l+1)} + \underline{Z}_{LL} \Delta \underline{I}_L^{(l)}$
7
Correct the values of load correction currents $\Delta \underline{I}_L^{(l+1)} = \Delta \underline{I}_L \left(\underline{V}_L^{(l+1)} \right)$
Convergence $\left\| \Delta \underline{I}_L^{(l+1)} - \Delta \underline{I}_L^{(l)} \right\| < \varepsilon_I$?
YES
NO
Convergence $\left\| \underline{E}_G^{f(l+1)} - \underline{E}_G^{f(l)} \right\| < \varepsilon_V$?
YES
NO
END
l=l+1

Figure 13.7 A simplified flowchart for the solution of the network equations using partial matrix inversion with both load nonlinearity and rotor saliency included.

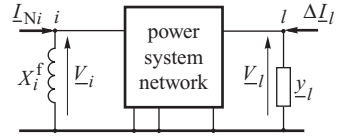

Figure 13.8 Network model with each generator replaced by a Norton source.

majority of the load nodes then the partial matrix inversion method is not recommended since the matrix factorization technique described in the next section is more efficient.

13.2.2 Matrix Factorization

The lower equation in (13.14) gives

$$\underline{\boldsymbol{Y}}_{\mathrm{LL}}\underline{\boldsymbol{V}}_{\mathrm{L}} = (\Delta\underline{\boldsymbol{I}}_{\mathrm{L}} + \underline{\boldsymbol{I}}_{\mathrm{N}}), \tag{13.31}$$

where $\underline{\boldsymbol{I}}_{\mathrm{N}} = -\underline{\boldsymbol{Y}}_{\mathrm{LG}}\underline{\boldsymbol{E}}_{\mathrm{G}}$ is a vector of the currents having non-zero elements only at the nodes where the generators are connected to the system. Equation (13.31) corresponds to the network shown in Figure 13.8.

Using *triangular factorization* (Press *et al.*, 1992) the square matrix $\underline{\boldsymbol{Y}}_{\mathrm{LL}}$ can be replaced by the product of an upper, or right, triangular matrix $\underline{\boldsymbol{R}}_{\mathrm{LL}}$ and a lower, or left, triangular matrix $\underline{\boldsymbol{L}}_{\mathrm{LL}}$ to give

$$\underline{\boldsymbol{Y}}_{\mathrm{LL}} = \underline{\boldsymbol{L}}_{\mathrm{LL}}\underline{\boldsymbol{R}}_{\mathrm{LL}}. \tag{13.32}$$

Equation (13.31) can then be rewritten as two equations

$$\underline{\boldsymbol{L}}_{\mathrm{LL}}\underline{\boldsymbol{b}}_{\mathrm{L}} = (\Delta\underline{\boldsymbol{I}}_{\mathrm{L}} + \underline{\boldsymbol{I}}_{\mathrm{N}}), \quad \underline{\boldsymbol{R}}_{\mathrm{LL}}\underline{\boldsymbol{V}}_{\mathrm{L}} = \underline{\boldsymbol{b}}_{\mathrm{L}}, \tag{13.33}$$

where $\underline{\boldsymbol{b}}_{\mathrm{L}}$ is an unknown vector.

Assuming that the loads are represented by constant admittances, then, for a given set of generator emfs $\underline{\boldsymbol{E}}_{\mathrm{G}}$, Equations (13.33) can be solved non-iteratively. As the vector $\underline{\boldsymbol{I}}_{\mathrm{N}} = -\underline{\boldsymbol{Y}}_{\mathrm{LG}}\underline{\boldsymbol{E}}_{\mathrm{G}}$ and the lower triangular matrix $\underline{\boldsymbol{L}}_{\mathrm{LL}}$ are both known and $\Delta\underline{\boldsymbol{I}}_{\mathrm{L}} = \underline{\boldsymbol{0}}$, the unknown vector $\underline{\boldsymbol{b}}_{\mathrm{L}}$ can be found using a series of *forward substitutions* starting from the upper left hand corner of $\underline{\boldsymbol{L}}_{\mathrm{LL}}$. After calculating $\underline{\boldsymbol{b}}_{\mathrm{L}}$ the values of $\underline{\boldsymbol{V}}_{\mathrm{L}}$ can be found by a series of *back substitutions* starting from the lower right hand corner of the upper triangular matrix $\underline{\boldsymbol{R}}_{\mathrm{LL}}$. The advantage of this method is that if the matrix $\underline{\boldsymbol{Y}}_{\mathrm{LL}}$ is sparse then both the factor submatrices $\underline{\boldsymbol{R}}_{\mathrm{LL}}$ and $\underline{\boldsymbol{L}}_{\mathrm{LL}}$ are also sparse, thus allowing sparse matrix techniques to be used to save on computer memory and the number of arithmetic operations needed to effect a solution (Tewerson, 1973; Brameller, Allan and Hamam, 1976; Pissanetzky, 1984; Duff, Erisman and Reid, 1986).

If nonlinearity of the loads is included, Equations (13.33) must be solved iteratively since the correction currents $\Delta\underline{\boldsymbol{I}}_{\mathrm{L}}$ depend on the voltages. The iteration formulae are

$$\underline{\boldsymbol{L}}_{\mathrm{LL}}\underline{\boldsymbol{b}}_{\mathrm{L}}^{(l+1)} = \left(\Delta\underline{\boldsymbol{I}}_{\mathrm{L}}^{(l)} + \underline{\boldsymbol{I}}_{\mathrm{N}}\right), \quad \underline{\boldsymbol{R}}_{\mathrm{LL}}\underline{\boldsymbol{V}}_{\mathrm{L}}^{(l+1)} = \underline{\boldsymbol{b}}_{\mathrm{L}}^{(l+1)}, \tag{13.34}$$

where $\Delta\underline{\boldsymbol{I}}_{\mathrm{L}}^{(l)} = \Delta\underline{\boldsymbol{I}}_{\mathrm{L}}\left(\underline{\boldsymbol{V}}_{\mathrm{L}}^{(l)}\right)$ is a vector of the load correction currents. The upper index l denotes the iteration number.

If rotor saliency is included then the generator Norton current $\underline{\boldsymbol{I}}_{\mathrm{N}}$ must also be calculated iteratively, in a similar way to the equivalent emfs in Equation (13.27). These iterations can be

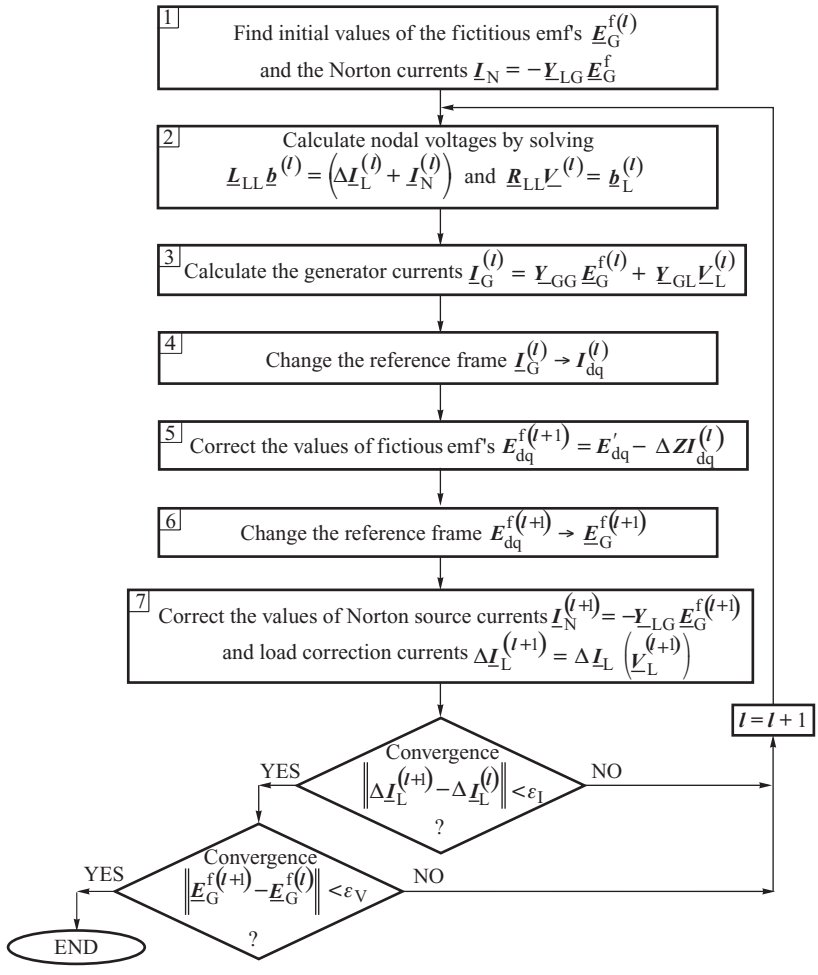

Figure 13.9 Simplified network solution flowchart using triangular factorization with load nonlinearity and rotor saliency included.

executed together with the iterations necessary to calculate the voltages and the correction currents at the load nodes. A simplified algorithm of the method is shown in Figure 13.9.

13.2.3 Newton's Method

Newton's method was introduced in Chapter 3 as a way to solve the network power–voltage equations. In system simulation Newton's method is also used but must now solve a set of current–voltage equations so that the solution algorithm is different from that used in the steady-state load flow. A particularly attractive feature of Newton's method is that if the network nodal current–voltage equations are solved in rectangular coordinates, in the system (a, b) reference frame, then rotor saliency can be conveniently included in the solution. To account for saliency the generator equations are added to the network nodal admittance equation expressed in real numbers as in Equation (3.154).

Assuming that the generators are represented by the fourth-order transient model ($\dot{E}'_{\mathrm{d}}$, $\dot{E}'_{\mathrm{q}}$, $\dot{\delta}$, $\dot{\omega}$), the generator armature voltage equations (11.104) can be written as

$$\begin{bmatrix} E'_{\mathrm{d}} - V_{\mathrm{d}} \\ E'_{\mathrm{q}} - V_{\mathrm{q}} \end{bmatrix} = \begin{bmatrix} 0 & -X'_{\mathrm{q}} \\ X'_{\mathrm{d}} & 0 \end{bmatrix} \begin{bmatrix} I_{\mathrm{d}} \\ I_{\mathrm{q}} \end{bmatrix}, \tag{13.35}$$

which, when inverted, give

$$\begin{bmatrix} I_{\mathrm{d}} \\ I_{\mathrm{q}} \end{bmatrix} = \frac{1}{X'_{\mathrm{d}} X'_{\mathrm{q}}} \begin{bmatrix} 0 & X'_{\mathrm{q}} \\ -X'_{\mathrm{d}} & 0 \end{bmatrix} \begin{bmatrix} E'_{\mathrm{d}} - V_{\mathrm{d}} \\ E'_{\mathrm{q}} - V_{\mathrm{q}} \end{bmatrix} \quad \text{or} \quad \boldsymbol{I}_{\mathrm{dq}} = \boldsymbol{Y}_{\mathrm{dq}} \left(\boldsymbol{E}'_{\mathrm{dq}} - \boldsymbol{V}_{\mathrm{dq}} \right). \tag{13.36}$$

These voltages and currents are in the generator (d, q) reference frame and are transformed into the system (a, b) reference frame using the transformation matrix $\boldsymbol{T}$ in Equation (3.166) to give

$$\begin{bmatrix} I_{\mathrm{a}} \\ I_{\mathrm{b}} \end{bmatrix} = \left(\boldsymbol{T}^{-1} \boldsymbol{Y}_{\mathrm{dq}} \boldsymbol{T} \right) \begin{bmatrix} E'_{\mathrm{a}} - V_{\mathrm{a}} \\ E'_{\mathrm{b}} - V_{\mathrm{b}} \end{bmatrix} \quad \text{or} \quad \boldsymbol{I}_{\mathrm{ab}} = \boldsymbol{Y}_{\mathrm{ab}} \left(\boldsymbol{E}'_{\mathrm{ab}} - \boldsymbol{V}_{\mathrm{ab}} \right), \tag{13.37}$$

where

$$\begin{aligned} \boldsymbol{Y}_{\mathrm{ab}} = \boldsymbol{T}^{-1} \boldsymbol{Y}_{\mathrm{dq}} \boldsymbol{T} &= \frac{1}{X'_{\mathrm{d}} X'_{\mathrm{q}}} \begin{bmatrix} -\sin\delta & \cos\delta \\ \cos\delta & \sin\delta \end{bmatrix} \begin{bmatrix} 0 & X'_{\mathrm{q}} \\ -X'_{\mathrm{d}} & 0 \end{bmatrix} \begin{bmatrix} -\sin\delta & \cos\delta \\ \cos\delta & \sin\delta \end{bmatrix} \\ &= \frac{1}{X'_{\mathrm{d}} X'_{\mathrm{q}}} \begin{bmatrix} \frac{1}{2}\left(X'_{\mathrm{d}} - X'_{\mathrm{q}}\right) \sin 2\delta & -X'_{\mathrm{q}} \sin^2\delta - X'_{\mathrm{d}} \cos^2\delta \\ X'_{\mathrm{q}} \cos^2\delta + X'_{\mathrm{d}} \sin^2\delta & -\frac{1}{2}\left(X'_{\mathrm{d}} - X'_{\mathrm{q}}\right) \sin 2\delta \end{bmatrix} = \begin{bmatrix} g_{\mathrm{a}} & -b_{\mathrm{ab}} \\ b_{\mathrm{ba}} & g_{\mathrm{b}} \end{bmatrix} \end{aligned} \tag{13.38}$$

is a submatrix similar in form to $\boldsymbol{Y}_{ij}$ in Equation (3.154). In the nodal admittance technique the submatrix $\boldsymbol{Y}_{\mathrm{ab}}$ describes a generator with transient saliency. Generally, because $g_{\mathrm{a}} \neq g_{\mathrm{b}}$ and $b_{\mathrm{ab}} \neq b_{\mathrm{ba}}$, there is no one equivalent branch with admittance $\underline{Y}_{\mathrm{ab}}$ so that an equivalent circuit for the salient-pole machine cannot be drawn. In such a case Equation (13.37) cannot be written in complex form as $\underline{I} = \underline{Y}_{\mathrm{ab}}(\underline{E}' - \underline{V})$ since the equivalent admittance $\underline{Y}_{\mathrm{ab}}$ does not exist. If transient saliency is neglected, $X'_{\mathrm{d}} = X'_{\mathrm{q}}$, then the submatrix $\boldsymbol{Y}_{\mathrm{ab}}$ is skew symmetric as $g_{\mathrm{a}} = g_{\mathrm{b}} = 0$ and $b_{\mathrm{ab}} = b_{\mathrm{ba}} = 1/X'_{\mathrm{d}}$ and an equivalent branch with admittance $\underline{Y}_{\mathrm{ab}} = 0 + \mathrm{j}b_{\mathrm{ab}} = \mathrm{j}(1/X'_{\mathrm{d}})$ now exists to represent the generator as shown in Figure 13.4 for the Thévenin source or in Figure 13.8 for the Norton source with, in both cases, $X_i^{\mathrm{f}} = X'_{\mathrm{d}}$.

Because of saliency the generator current–voltage equation can only be written using real numbers in the (a, b) coordinate system. Complex notation cannot be used. In order to include Equation (13.37) with the network equation (13.14) or (13.31), the latter must also be written using real numbers in the same way as Equation (3.155). Then each generator will be represented by a submatrix as in Equation (13.38), which is added to the respective elements of the real submatrices $\boldsymbol{Y}_{\mathrm{GG}}$, $\boldsymbol{Y}_{\mathrm{GL}}$, $\boldsymbol{Y}_{\mathrm{LG}}$ and $\boldsymbol{Y}_{\mathrm{LL}}$. In the case of the Norton source, Equation (13.31) can be rewritten as

$$\boldsymbol{Y}_{\mathrm{LL}}(\delta)\, \boldsymbol{V}_{\mathrm{L}} = \Delta \boldsymbol{I}_{\mathrm{L}}(\boldsymbol{V}_{\mathrm{L}}) + \boldsymbol{I}_{\mathrm{N}}, \tag{13.39}$$

where the real matrix $\boldsymbol{Y}_{\mathrm{LL}}(\delta)$ is shown as a function of δ to emphasize that the diagonal elements of this matrix that refer to the generator depend on the power angle in the way defined by the submatrix (13.38). The elements of these submatrices change with time as the generator rotor angles change. The Norton source currents $\boldsymbol{I}_{\mathrm{N}}$ are given by

$$\boldsymbol{I}_{\mathrm{N}} = -\boldsymbol{Y}_{\mathrm{LG}}(\delta) \boldsymbol{E}_{\mathrm{G}}, \tag{13.40}$$

where matrix $\boldsymbol{Y}_{\mathrm{LG}}(\delta)$ consists of the submatrices (13.38) and $\boldsymbol{E}_{\mathrm{G}}$ is a vector comprising the individual generator emfs $\boldsymbol{E}'_{\mathrm{ab}}$. All variables are in the (a, b) system coordinates.

To solve Equation (13.39) it can be rewritten in the standard Newton form as

$$\boldsymbol{F}(\boldsymbol{V}_{\mathrm{L}}) = [\boldsymbol{Y}_{\mathrm{LG}}(\delta)\boldsymbol{E}_{\mathrm{G}} - \Delta\boldsymbol{I}_{\mathrm{L}}(\boldsymbol{V}_{\mathrm{L}})] + \boldsymbol{Y}_{\mathrm{LL}}(\delta)\,\boldsymbol{V}_{\mathrm{L}} = 0. \tag{13.41}$$

Using Newton's iterative formula gives

$$\boldsymbol{V}_{\mathrm{L}}^{(l+1)} = \boldsymbol{V}_{\mathrm{L}}^{(l)} - \left[\frac{\partial \boldsymbol{F}}{\partial \boldsymbol{V}_{\mathrm{L}}}\right]_l^{-1} \boldsymbol{F}\left(\boldsymbol{V}_{\mathrm{L}}^{l}\right), \tag{13.42}$$

where the Jacobi matrix

$$\left[\frac{\partial \boldsymbol{F}}{\partial \boldsymbol{V}_{\mathrm{L}}}\right] = \boldsymbol{Y}_{\mathrm{LL}}(\delta) - \left[\frac{\partial \Delta \boldsymbol{I}_{\mathrm{L}}}{\partial \boldsymbol{V}_{\mathrm{L}}}\right] \tag{13.43}$$

is equal to the nodal admittance matrix minus the matrix of the derivatives of the correction currents with respect to the voltages. This correction matrix is diagonal and its elements are of the form

$$\left[\frac{\partial \Delta I_i}{\partial V_i}\right] = \begin{bmatrix} \dfrac{\partial \Delta I_{\mathrm{a}i}}{\partial V_{\mathrm{a}i}} & \dfrac{\partial \Delta I_{\mathrm{a}i}}{\partial V_{\mathrm{b}i}} \\ \dfrac{\partial \Delta I_{\mathrm{b}i}}{\partial V_{\mathrm{a}i}} & \dfrac{\partial \Delta I_{\mathrm{b}i}}{\partial V_{\mathrm{b}i}} \end{bmatrix}. \tag{13.44}$$

The way in which the derivatives in Equation (13.44) are calculated needs some explanation. In rectangular coordinates the relationship between the correction powers and the correction currents can be expressed as

$$\begin{bmatrix} \Delta P_i \\ \Delta Q_i \end{bmatrix} = \begin{bmatrix} V_{\mathrm{a}i} & V_{\mathrm{b}i} \\ V_{\mathrm{b}i} & -V_{\mathrm{a}i} \end{bmatrix} \begin{bmatrix} \Delta I_{\mathrm{a}i} \\ \Delta I_{\mathrm{b}i} \end{bmatrix} \quad \text{or} \quad \begin{bmatrix} \Delta I_{\mathrm{a}i} \\ \Delta I_{\mathrm{b}i} \end{bmatrix} = \frac{1}{|V_i|^2} \begin{bmatrix} V_{\mathrm{a}i} & V_{\mathrm{b}i} \\ V_{\mathrm{b}i} & -V_{\mathrm{a}i} \end{bmatrix} \begin{bmatrix} \Delta P_i \\ \Delta Q_i \end{bmatrix}. \tag{13.45}$$

Making the substitution

$$\Delta p_i = \frac{\Delta P_i}{|V_i|^2}, \quad \Delta q_i = \frac{\Delta Q_i}{|V_i|^2} \tag{13.46}$$

allows Equation (13.45) to be rewritten as

$$\begin{bmatrix} \Delta I_{\mathrm{a}i} \\ \Delta I_{\mathrm{b}i} \end{bmatrix} = \begin{bmatrix} V_{\mathrm{a}i} & V_{\mathrm{b}i} \\ V_{\mathrm{b}i} & -V_{\mathrm{a}i} \end{bmatrix} \begin{bmatrix} \Delta p_i \\ \Delta q_i \end{bmatrix}. \tag{13.47}$$

Differentiating Equation (13.47) gives

$$\begin{aligned}
\frac{\partial \Delta I_{\mathrm{a}i}}{\partial V_{\mathrm{a}i}} &= V_{\mathrm{a}i}\frac{\partial \Delta p_i}{\partial V_{\mathrm{a}i}} + \Delta p_i + V_{\mathrm{b}i}\frac{\partial \Delta q_i}{\partial V_{\mathrm{a}i}} \\
\frac{\partial \Delta I_{\mathrm{a}i}}{\partial V_{\mathrm{b}i}} &= V_{\mathrm{b}i}\frac{\partial \Delta q_i}{\partial V_{\mathrm{b}i}} + \Delta q_i + V_{\mathrm{a}i}\frac{\partial \Delta p_i}{\partial V_{\mathrm{b}i}} \\
\frac{\partial \Delta I_{\mathrm{b}i}}{\partial V_{\mathrm{a}i}} &= -V_{\mathrm{a}i}\frac{\partial \Delta q_i}{\partial V_{\mathrm{a}i}} - \Delta q_i + V_{\mathrm{b}i}\frac{\partial \Delta p_i}{\partial V_{\mathrm{a}i}} \\
\frac{\partial \Delta I_{\mathrm{b}i}}{\partial V_{\mathrm{b}i}} &= V_{\mathrm{b}i}\frac{\partial \Delta p_i}{\partial V_{\mathrm{a}i}} + \Delta p_i - V_{\mathrm{a}i}\frac{\partial \Delta q_i}{\partial V_{\mathrm{b}i}},
\end{aligned}$$

which, when substituted into Equation (13.44) and the matrix rearranged, leads to

$$\begin{aligned}\begin{bmatrix}\dfrac{\partial \Delta I_i}{\partial V_i}\end{bmatrix} &= \begin{bmatrix} V_{ai} & V_{bi} \\ V_{bi} & -V_{ai}\end{bmatrix}\begin{bmatrix}\dfrac{\partial \Delta p_i}{\partial V_{ai}} & \dfrac{\partial \Delta p_i}{\partial V_{bi}} \\ \dfrac{\partial \Delta q_i}{\partial V_{ai}} & \dfrac{\partial \Delta q_i}{\partial V_{bi}}\end{bmatrix} + \begin{bmatrix}\Delta p_i & \Delta q_i \\ -\Delta q_i & \Delta p_i\end{bmatrix} \\ &= \frac{1}{|V_i|}\begin{bmatrix} V_{ai} & V_{bi} \\ -V_{bi} & -V_{ai}\end{bmatrix}\begin{bmatrix}\dfrac{\partial \Delta p_i}{\partial |V_i|} & \dfrac{\partial \Delta p_i}{\partial |V_i|} \\ \dfrac{\partial \Delta q_i}{\partial |V_i|} & \dfrac{\partial \Delta q_i}{\partial |V_i|}\end{bmatrix}\begin{bmatrix} V_{ai} & 0 \\ 0 & V_{bi}\end{bmatrix} + \begin{bmatrix}\Delta p_i & \Delta q_i \\ -\Delta q_i & \Delta p_i\end{bmatrix}.\end{aligned} \tag{13.48}$$

If the derivatives in the second matrix are expressed in the form

$$\frac{\partial \Delta p_i}{\partial V_{ai}} = \frac{\partial \Delta p_i}{\partial |V_i|}\frac{\partial |V_i|}{\partial V_{ai}} = \frac{\partial \Delta p_i}{\partial |V_i|}\frac{\partial}{\partial V_{ai}}\sqrt{V_{ai}^2 + V_{bi}^2} = \frac{1}{|V_i|}\frac{\partial \Delta p_i}{\partial |V_i|}V_{ai},$$

then the partial derivatives $\partial \Delta p_i / \partial |V_i|$ and $\partial \Delta q_i / \partial |V_i|$ can be computed from the static load characteristics $P(V)$ and $Q(V)$.

The solution algorithm consists of the iterative equation (13.42), the Jacobi matrix equation (13.43) and the correction currents (13.48). The algorithm may be simplified by using the *dishonest Newton method*, where the Jacobi matrix is calculated only once at the beginning of each integration step using the initial values of the correction currents. This simplification should not be used during those integration steps when a network disturbance is being simulated because the change in the correction currents may be large.

If rotor saliency, and the load correction currents, are neglected, Equation (13.42) of the Newton method is identical to the second equation of (13.20) in the partial matrix inversion method. This can be shown by substituting $\Delta \boldsymbol{I}_{\mathrm{L}} = 0$, $\boldsymbol{Y}_{\mathrm{LL}}(\delta) = \boldsymbol{Y}_{\mathrm{LL}} = \text{constant}$ and $\boldsymbol{V}_{\mathrm{L}}^{(l+1)} = \boldsymbol{V}_{\mathrm{L}}^{l}$ into Equations (13.42) and (13.41).

13.2.4 Ways of Avoiding Iterations and Multiple Network Solutions

The basic algorithm of the partitioned solution shown in Figure 13.1 attempts to match the values of the variables $\boldsymbol{y}(t)$, for given values of $\boldsymbol{x}(t)$, by solving the linear algebraic equation (13.2). This solution is repeated after each prediction and each correction of $\boldsymbol{x}(t)$. One way to speed up the algorithm is to replace the solution of the algebraic equation by an extrapolation of the value of $\boldsymbol{y}(t)$ at some appropriate stage in the solution. As the extrapolated values of $\boldsymbol{y}(t)$ are only approximate, an error is introduced into the right hand side of Equation (13.1), called the *interface error*, which influences the accuracy of $\boldsymbol{x}(t)$.

There are three ways of introducing extrapolation into the algorithm:

- the algebraic equations are solved after each prediction, with extrapolated values being used after each correction;
- the algebraic equations are solved after each prediction and after the last correction;
- the algebraic equations are solved after each correction with the prediction of $\boldsymbol{y}(t)$ and $\boldsymbol{x}(t)$ being done together, by extrapolation.

The first method is not recommended as it may introduce large interface errors which force the integration step length to shorten. The second and third methods are much better, with the third method being preferred because, with this method, interface errors generated at the prediction stage are eliminated during correction. In this case extrapolation eliminates one solution of the

algebraic equations in each integration step. Obviously this method is beneficial only if the number of corrections required is small and the corrector converges quickly.

In most cases the variables in $\boldsymbol{y}(t)$ are extrapolated individually and independently of each other. Simple extrapolation formulae are normally employed that use the past values of the variable obtained from the previous two or three steps. Typical of these formulae are those listed as Variant II in Table 13.2 as

$$x_{k+1} = 2x_k - x_{k-1} \quad \text{or} \quad x_{k+1} = 3x_k - 3x_{k-1} + x_{k-2},$$

though Adibi, Hirsch and Jordan (1974) suggest updating the complex load voltages using

$$\underline{V}_{k+1} = \frac{\underline{V}_k^2}{\underline{V}_{k-1}} \quad \text{or} \quad \underline{V}_{k+1} = \frac{\underline{V}_k^3 \underline{V}_{k-2}}{\underline{V}_{k-1}^2}. \tag{13.49}$$

After extrapolating the voltages at all the load nodes using Equation (13.49) the generator currents are computed from the nodal equation (13.14) using the generator emfs obtained from the numerical integration. Extrapolation procedures can also be used to obtain the values of other variables such as generator real power, voltage error and so on (Stott, 1979). Generally high-order extrapolation formulae are not used to update $\boldsymbol{y}(t)$ as the improvement in the accuracy is small compared with the simple formulae. In addition, complications occur following network disturbances because, at the instant of the discontinuity, all the previous old values of the variable are invalid and extrapolation must start at the step where the disturbance occurs. Sometimes no previous values are used in the extrapolation process but a linearized equation is formed that links the increments in $\boldsymbol{y}(t)$ with the increments in $\boldsymbol{x}(t)$ (Stott, 1979).

Besides reducing the number of times that the algebraic equations need to be solved at each integration step, it is also possible to avoid iterations in the network solution. These iterations result from nonlinear load characteristics and from saliency in the generator rotors. The number of iterations necessary to account for generator saliency can be reduced by using either the sixth- or the fifth-order subtransient models rather than the fourth- or third-order transient models. Table 4.3 shows that transient saliency, $X'_{\mathrm{q}} \neq X'_{\mathrm{d}}$, is usually much larger than subtransient saliency, $X''_{\mathrm{q}} \neq X''_{\mathrm{d}}$, so that the iteration process for the subtransient model converges faster, and with fewer iterations, than that for the transient model. Unfortunately the reduction in computing time due to the faster convergence is partially offset by the shorter integration time step required by the subtransient model to account for the smaller time constants. As subtransient saliency effects are normally quite small, Dandeno and Kundur (1973) suggest that in order to produce a fast non-iterative solution the subtransient model with subtransient saliency effects neglected should be used. By adopting this approach a solution is obtained that is more accurate than that produced by the transient model where the damper windings are neglected. In this non-iterative algorithm the iterations required to account for load nonlinearity are performed only at discontinuities, that is only at the time of the disturbance. Except at disturbances, the change of the voltage at the load nodes is smooth and slow so that the correction currents can be approximately calculated at each integration step by basing them on the voltages in the previous step, that is

$$\Delta \boldsymbol{I}_{\mathrm{L}(k+1)} = \Delta \boldsymbol{I}_{\mathrm{L}} \left(\boldsymbol{V}_{\mathrm{L}(k)} \right). \tag{13.50}$$

With these assumptions the network equations can be solved non-iteratively, apart from the instants of discontinuity, using either partial matrix inversion or matrix factorization. At discontinuities, changes in the voltages may be large and it is necessary to execute a few iterations in order to calculate accurately the correction currents. Adibi, Hirsch and Jordan (1974) noted that small errors resulting from (13.50) can be partially eliminated by extrapolating the voltages at the load nodes thereby improving the estimated correction currents.

Based on these assumptions, the solution algorithm in Figure 13.3 can be modified. When solving the algebraic equations at the discontinuity, stage 3, Equations (13.21) or (13.34) can be used to introduce the iterations necessary to model the nonlinear loads. Solution of the algebraic equations at stage 5, after the prediction, can be replaced by extrapolation of the algebraic variables $\boldsymbol{y}(t)$, while the solution at stage 7, after correction, can be executed using Equations (13.20) or (13.33) to solve the network equations non-iteratively.

13.3 The Simultaneous Solution Methods

The concept of the simultaneous solution methods is to use implicit integration formulae to change the differential equations (13.1) into algebraic form and then to solve these algebraic equations simultaneously with the algebraic network equations in (13.2).

Any implicit integration formula can be written in the general form

$$x_{k+1} = \beta_k + hb_0 f(x_{k+1}), \tag{13.51}$$

where h is the integration step length, b_0 is a coefficient that depends on the actual integration method, $f(x_{k+1})$ is the right hand side of the differential equations (13.1) calculated at the value x_{k+1} and

$$\beta_k = x_k + \sum_j b_j f_{k+1-j} \tag{13.52}$$

is a coefficient depending on all the previous steps. Using the formula in Equation (13.51), Equations (13.1) and (13.2) can be rewritten as

$$\begin{aligned} \boldsymbol{F}_1\left(\boldsymbol{x}_{k+1}, \boldsymbol{y}_{k+1}\right) &= \boldsymbol{f}\left(\boldsymbol{x}_{k+1}, \boldsymbol{y}_{k+1}\right) - \tfrac{1}{hb_0}\boldsymbol{x}_{k+1} - \boldsymbol{\beta}_k = \boldsymbol{0} \\ \boldsymbol{F}_2\left(\boldsymbol{x}_{k+1}, \boldsymbol{y}_{k+1}\right) &= \boldsymbol{g}\left(\boldsymbol{x}_{k+1}, \boldsymbol{y}_{k+1}\right) = \boldsymbol{0}, \end{aligned} \tag{13.53}$$

where $\boldsymbol{\beta}_k$ is a column vector containing the values β_k.

Newton's method gives the iteration formula as

$$\begin{bmatrix} \boldsymbol{x}_{k+1}^{(l+1)} \\ \boldsymbol{y}_{k+1}^{(l+1)} \end{bmatrix} = \begin{bmatrix} \boldsymbol{x}_{k+1}^{(l)} \\ \boldsymbol{y}_{k+1}^{(l)} \end{bmatrix} - \left[\begin{array}{c|c} \boldsymbol{f}_x - \frac{1}{hb_0}\boldsymbol{1} & \boldsymbol{f}_y \\ \hline \boldsymbol{g}_x & \boldsymbol{g}_y \end{array}\right]^{-1} \begin{bmatrix} \boldsymbol{F}_1\left(\boldsymbol{x}_{k+1}^{(l)}, \boldsymbol{y}_{k+1}^{(l)}\right) \\ \boldsymbol{F}_2\left(\boldsymbol{x}_{k+1}^{(l)}, \boldsymbol{y}_{k+1}^{(l)}\right) \end{bmatrix}, \tag{13.54}$$

where $\boldsymbol{1}$ is the unit diagonal matrix and $\boldsymbol{f}_x = \partial \boldsymbol{f}/\partial \boldsymbol{x}$, $\boldsymbol{f}_y = \partial \boldsymbol{f}/\partial \boldsymbol{y}$, $\boldsymbol{g}_x = \partial \boldsymbol{g}/\partial \boldsymbol{x}$, $\boldsymbol{g}_y = \partial \boldsymbol{g}/\partial \boldsymbol{y}$ are the Jacobi submatrices. The Jacobi matrix in Equation (13.54) is sparse, so computer programs that simulate large systems do not generally explicitly invert this matrix. Instead Equation (13.54) is solved using triangular factorization and forward and back substitution. The network equations are expressed in rectangular form in the system (a, b) reference frame so that rotor saliency can be included without any difficulty. The nonlinear load correction currents are modified during each iteration. The effectiveness of the method depends both on the choice of variables to be iterated in the Newton method and on skilful use of sparse matrix techniques. A significant role is also played by appropriate grouping of the variables allowing block matrices to be used.

Vorley (1974) presents one of the variants of this method where Equations (13.1) and (13.2) are arranged in such a way that the differential and algebraic equations of the generator are grouped

together to produce an equation of the form

$$\left[\begin{array}{ccc:ccc} 1 & \dots & 0 & & & \\ \vdots & \ddots & \vdots & & & \\ 0 & \dots & 1 & & & \\ \hdashline & & & 0 & \dots & 0 \\ & & & \vdots & \ddots & \vdots \\ & & & 0 & \dots & 0 \end{array}\right] \left[\begin{array}{c} \dot{x}_1 \\ \vdots \\ \dot{x}_r \\ \hdashline \dot{x}_{r+1} \\ \vdots \\ \dot{x}_m \end{array}\right] = \left[\begin{array}{c} f_1 \\ \vdots \\ f_r \\ \hdashline f_{r+1} \\ \vdots \\ f_m \end{array}\right] \quad \text{or} \quad \boldsymbol{c}_i \dot{\boldsymbol{x}}_i = \boldsymbol{f}_i(\boldsymbol{x}_i, \boldsymbol{V}), \tag{13.55}$$

where $(x_1, \dots, x_r)$ are the variables of the differential equations describing the ith generating unit and $(x_{r+1}, \dots, x_m)$ are the variables of the algebraic equations describing this unit. As matrix $\boldsymbol{c}_i$ is singular, this equation is singular. The whole system is described by

$$\begin{aligned} \boldsymbol{C}\dot{\boldsymbol{x}} &= \boldsymbol{F}(\boldsymbol{x}, \boldsymbol{V}) \\ \boldsymbol{0} &= \boldsymbol{G}(\boldsymbol{x}, \boldsymbol{V}), \end{aligned} \tag{13.56}$$

where the first of the equations consists of Equations (13.55) corresponding to individual generating units and the second, describing the network, is the equation of nodal voltages. Using the implicit integration formulae and Newton's equation (as in (13.54)) gives

$$\left[\begin{array}{c} \boldsymbol{x}_{k+1}^{(l+1)} \\ \boldsymbol{V}_{k+1}^{(l+1)} \end{array}\right] = \left[\begin{array}{c} \boldsymbol{x}_{k+1}^{(l)} \\ \boldsymbol{V}_{k+1}^{(l)} \end{array}\right] - \left[\begin{array}{c:c} \boldsymbol{F}_x - \frac{1}{hb_0}\boldsymbol{C} & \boldsymbol{F}_v \\ \hdashline \boldsymbol{G}_x & \boldsymbol{G}_v \end{array}\right]^{-1} \left[\begin{array}{c} \boldsymbol{F}\left(\boldsymbol{x}_{k+1}^{(l)}, \boldsymbol{V}_{k+1}^{(l)}\right) - \frac{1}{hb_0}\boldsymbol{C}\left(\boldsymbol{x}_{k+1}^{(l)} - \beta_k\right) \\ \boldsymbol{G}\left(\boldsymbol{x}_{k+1}^{(l)}, \boldsymbol{V}_{k+1}^{(l)}\right) \end{array}\right], \tag{13.57}$$

where $\boldsymbol{F}_x = \partial \boldsymbol{f}/\partial \boldsymbol{x}$, $\boldsymbol{F}_v = \partial \boldsymbol{f}/\partial \boldsymbol{V}$, $\boldsymbol{G}_x = \partial \boldsymbol{G}/\partial \boldsymbol{x}$ and $\boldsymbol{G}_v = \partial \boldsymbol{G}/\partial \boldsymbol{V}$ are the submatrices of the Jacobi matrix.

The Jacobi matrices of the individual generating units have a block structure which simplifies the factorization. To speed up calculations the dishonest Newton method is used where the iterations at each integration step are executed for a constant matrix calculated from predicted values. It is also possible to simplify the method further by modifying the Jacobi matrix only after network disturbances and after a certain number of integration steps. The number of iterations necessary for convergence can be used as an indicator for when to modify the Jacobi matrix, with this matrix being updated if the number of iteration exceeds a preset value, for example three.

Variable integration step length and variable order interpolation formulae are also used. As the differential and algebraic equations are solved together, there is no interfacing problem, and the use of Newton's method ensures no convergence problems, even when a long integration step length is used with a stiff system. At the start of each integration step, extrapolated initial values are used in the iterations.

Descriptions of other examples of the simultaneous solution method can be found in (Adibi, Hirsch and Jordan, 1974; Harkopf, 1978; Stott, 1979; Rafian, Sterling and Irving, 1987).

13.4 Comparison Between the Methods

The simultaneous solution methods allow rotor saliency and nonlinear loads to be readily included and are especially attractive for simulations that cover a long time period. Newton's method, together with implicit integration formulae, allow the integration step length to be increased when the changes in the variables are not very steep. The dishonest Newton method can be used to speed up the calculations. Interfacing problems between the algebraic and differential equations do not exist.

In contrast, the partitioned solution methods are attractive for simulations that cover a shorter time interval. They are more flexible, easier to organize and allow a number of simplifications to be introduced that speed up the solution. However, unless care is taken, these simplifications may cause large interfacing errors. The majority of dynamic simulation programs described in the literature are based on partitioned solution methods.

The main characteristics of the partitioned solution methods relate to the way in which the network equations are solved. Partial matrix inversion is only attractive for simplified systems because the submatrices of the partially inverted nodal matrix are dense. If the nodal matrix is large these submatrices take up a lot of computer memory. Additionally, because of the large number of non-zero elements in these submatrices, the number of arithmetic operations needed to solve the network equations is also large. The speed of solution can be improved by assuming that the loads are linear (constant admittances) and by calculating the voltages at only a small number of load nodes thereby limiting the size of the relevant inverted submatrices. This method becomes particularly attractive when model reduction is employed based on the aggregation of coherent generators as discussed in Chapter 14. In this case, when the algorithm is reorganized, the transfer matrix that is used to predict groups of coherent generators (after certain transformations corresponding to aggregation) can also be used to solve the equations of the reduced network.

If nonlinear loads are included, or the voltage change at a certain number of loads is required, then triangular factorization is superior to partial inversion because the factor matrices remain sparse after factorization. For a typical power network the factor matrices only contain about 50 % more elements than the original admittance matrix and the number of arithmetic operations required to solve the network is not very high. If additional modifications that limit the number of iterations due to rotor saliency and nonlinear loads are included, then triangular factorization becomes by far the fastest solution method.

The properties of the computer algorithms that use Newton's method are similar to those for the simultaneous solution method. Compared with triangular factorization, Newton's method requires a larger computer memory and more arithmetic calculations per integration step. However, due to good convergence, Newton's method can use a longer integration step than the factorization method, which partially compensates for the greater number of computations per step. The use of the dishonest Newton method speeds up the calculations quite considerably. Moreover, rotor saliency and nonlinear loads can be included more easily than is the case with triangular factorization.

It is worth adding that fairly recently, with the ever-increasing power of computers, there has been a tendency to develop *real-time simulators* to train operators for dispatch and security monitoring and which can also be used as the core of an online dynamic security assessment system. To make these simulators operate in real time, it is often required to split the program into independent tasks to be executed in parallel (Chai and Bose, 1993; Bialek, 1996).

14

Power System Model Reduction – Equivalents

Because contemporary power systems are so large, power system analysis programs do not usually model the complete system in detail. This problem of modelling a large system arises for a number of reasons including:

- Practical limitations on the size of computer memory.
- The excessive computing time required by large power systems, particularly when running dynamic simulation and stability programs.
- Parts of the system far away from a disturbance have little effect on the system dynamics and it is therefore unnecessary to model them with great accuracy.
- Often parts of large interconnected systems belong to different utilities, each having its own control centre which treats the other parts of the system as external subsystems.
- In some countries private utilities compete with each other and are reluctant to disclose detailed information about their business. This means that vital data regarding the whole system may not be available.
- Even assuming that full system data are available, maintaining the relevant databases would be very difficult and expensive.

To avoid all these problems, only a part of the system, called the *internal subsystem*, is modelled in detail. The remainder of the system, called the *external subsystem*, is represented by simple models referred to as the *equivalent system* or simply as the *equivalent*.

14.1 Types of Equivalents

The methods by which the equivalent of an external subsystem can be produced can be broadly divided into two groups depending on whether or not they require any knowledge of the configuration and parameters of the external subsystem itself. Methods that do not require any knowledge of the external subsystem are used for online security assessment and will not be considered further here, but details of these methods can be found in Dopazo *et al.* (1977), Contaxis and Debs (1977) and Feng, Lubosny and Bialek (2007). Typically these methods use the measurement of certain electrical quantities taken inside the internal subsystem and at the border nodes and tie-lines to form the equivalent. Methods that do require knowledge of the subsystem are called *model*

Power System Dynamics: Stability and Control, Second Edition Jan Machowski, Janusz W. Bialek and James R. Bumby
© 2008 John Wiley & Sons, Ltd

reduction methods. These methods are used for offline system analysis and are the subject of this chapter.

Model reduction methods can be further divided into the following three groups:

- *Physical reduction*, which consists of choosing appropriate models for the system elements (generators, loads, etc.) depending on how influential an individual element is in determining the system response to a particular disturbance. Generally elements electrically close to the disturbance are modelled more accurately while elements further away are modelled more simply.
- *Topological reduction*, which consists of eliminating and/or aggregating selected nodes in order to reduce the size of the equivalent network and the number of generating units modelled.
- *Modal reduction* techniques which use linearized models of the external subsystem that eliminate, or neglect, the unexcited modes.

The equivalent model obtained using modal reduction is in the form of a reduced set of linear differential equations (Undrill and Turner, 1971). This requires extending the standard power system software to take into account the special form of the equivalent. As standardization of the software is difficult to achieve with modal reduction, this type of equivalent is rarely used in practice.

Topological reduction, used together with physical reduction, gives an equivalent model that comprises standard system elements such as equivalent generating units, equivalent lines, equivalent nodes and so on. Consequently, topological equivalents are easy to attach to the internal subsystem model and allow the whole system to be analysed using standard software.

If the topological reduction is performed using one of the methods described in this chapter then the reduced model obtained will generally be a good representation of both the system static performance and the system dynamic performance for the first few seconds following a disturbance. The reduced model can therefore be used for load flow analysis and transient stability analysis when disturbances occur in the internal subsystem.

The division of the whole system into external and internal components is illustrated in Figure 14.1. A reduced model of the external subsystem is created assuming that the disturbance occurs only inside the internal subsystem. The *border nodes* between the internal and external subsystems are sometimes referred to as the *boundary nodes* or *tearing nodes*. Topological reduction consists of transforming a large external network that consists of load nodes and/or generation nodes into a smaller network by eliminating and/or aggregating the nodes. Eliminated nodes are removed completely from the network while every group of aggregated nodes is replaced by one equivalent node.

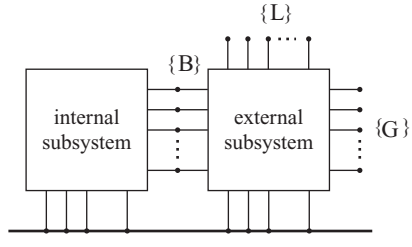

Figure 14.1 Internal and external subsystems: {B}, boundary nodes; {L}, load nodes; {G}, generator nodes of the external subsystem.

14.2 Network Transformation

Topological reduction is achieved by transforming a large network into a smaller equivalent network by either elimination or aggregation of nodes.

14.2.1 Elimination of Nodes

Figure 14.2 illustrates that when nodes are eliminated from the network model, set {E}, they must be removed in such a way that the currents and nodal voltages at the retained nodes, set {R}, are unchanged.

Before any nodes are eliminated the network is described by the following nodal equation (see Section 3.5):

$$\begin{bmatrix} \underline{\boldsymbol{I}}_{\mathrm{R}} \\ \underline{\boldsymbol{I}}_{\mathrm{E}} \end{bmatrix} = \begin{bmatrix} \underline{\boldsymbol{Y}}_{\mathrm{RR}} & \underline{\boldsymbol{Y}}_{\mathrm{RE}} \\ \underline{\boldsymbol{Y}}_{\mathrm{ER}} & \underline{\boldsymbol{Y}}_{\mathrm{EE}} \end{bmatrix} \begin{bmatrix} \underline{\boldsymbol{V}}_{\mathrm{R}} \\ \underline{\boldsymbol{V}}_{\mathrm{E}} \end{bmatrix}, \tag{14.1}$$

where the subscripts refer to the eliminated {E} and retained {R} sets of nodes. The eliminated voltages and currents can be swapped using simple matrix algebra to give

$$\begin{bmatrix} \underline{\boldsymbol{I}}_{\mathrm{R}} \\ \underline{\boldsymbol{V}}_{\mathrm{E}} \end{bmatrix} = \begin{bmatrix} \underline{\boldsymbol{Y}}_{\mathrm{R}} & \underline{\boldsymbol{K}}_{\mathrm{I}} \\ \underline{\boldsymbol{K}}_{\mathrm{V}} & \underline{\boldsymbol{Y}}_{\mathrm{EE}}^{-1} \end{bmatrix} \begin{bmatrix} \underline{\boldsymbol{V}}_{\mathrm{R}} \\ \underline{\boldsymbol{I}}_{\mathrm{E}} \end{bmatrix}, \tag{14.2}$$

where

$$\underline{\boldsymbol{Y}}_{\mathrm{R}} = \underline{\boldsymbol{Y}}_{\mathrm{RR}} - \underline{\boldsymbol{Y}}_{\mathrm{RE}}\underline{\boldsymbol{Y}}_{\mathrm{EE}}^{-1}\underline{\boldsymbol{Y}}_{\mathrm{ER}}, \quad \underline{\boldsymbol{K}}_{\mathrm{I}} = \underline{\boldsymbol{Y}}_{\mathrm{RE}}\underline{\boldsymbol{Y}}_{\mathrm{EE}}^{-1}, \quad \underline{\boldsymbol{K}}_{\mathrm{V}} = -\underline{\boldsymbol{Y}}_{\mathrm{EE}}^{-1}\underline{\boldsymbol{Y}}_{\mathrm{ER}}. \tag{14.3}$$

The square matrix in Equation (14.2) is the *partial inversion of the admittance matrix* and is described in detail in Appendix A2. The nodal currents in the set {R} are

$$\underline{\boldsymbol{I}}_{\mathrm{R}} = \underline{\boldsymbol{Y}}_{\mathrm{R}}\underline{\boldsymbol{V}}_{\mathrm{R}} + \Delta\underline{\boldsymbol{I}}_{\mathrm{R}}, \tag{14.4}$$

where

$$\Delta\underline{\boldsymbol{I}}_{\mathrm{R}} = \underline{\boldsymbol{K}}_{\mathrm{I}}\underline{\boldsymbol{I}}_{\mathrm{E}}.$$

Equation (14.4) describes the relationship between the currents and voltages of the retained nodes in the reduced network. As any electrical network is uniquely described by its admittance matrix, the matrix $\underline{\boldsymbol{Y}}_{\mathrm{R}}$ corresponds to a reduced equivalent network that consists of the retained nodes and equivalent branches linking them. This network is often referred to as the *transfer network* and the matrix describing it as the *transfer admittance matrix*. Matrix $\underline{\boldsymbol{K}}_{\mathrm{I}}$ passes the nodal currents from the eliminated nodes to the retained nodes and is referred to as the *distribution matrix*. Each equivalent current is a combination of the eliminated currents.

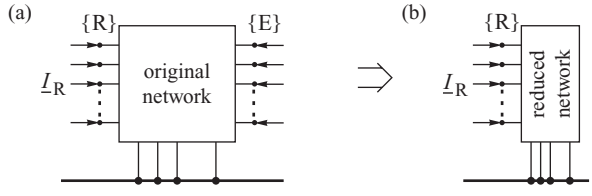

Figure 14.2 Elimination of nodes: (a) network before elimination; (b) network after elimination. {E}, set of eliminated nodes; {R}, set of retained nodes.

Another form of Equation (14.4) can be obtained by replacing the nodal power injection at each eliminated node by a constant shunt admittance $\underline{Y}_{Ei} = \underline{S}_i^* / V_i^2$ added, with an appropriate sign, to the diagonal elements of the submatrix $\underline{\boldsymbol{Y}}_{EE}$ (and to the network diagram as a shunt connection). The nodal injections at the eliminated nodes then become zero ($\underline{\boldsymbol{I}}_E = \underline{\boldsymbol{0}}$) and the reduced model does not contain any equivalent currents ($\Delta \underline{\boldsymbol{I}}_R = \underline{\boldsymbol{0}}$). This is quite convenient but has a drawback. The equivalent shunt branches have large conductance values, corresponding to the real power injections, which become part of the equivalent branches in the reduced model. Consequently, the branches of the equivalent network may have a poor X/R ratio causing convergence problems for some load flow computer programs.

Different authors give different names to the elimination of the network nodes using Equations (14.2) and (14.4). Edelmann (1974) refers to it as Gauss–Rutishauser elimination while Brown (1975) and Grainger and Stevenson (1994) call the reduced circuit a Ward equivalent.

14.2.1.1 Sparse Matrix Techniques

Equation (14.4) formally describes the elimination algorithm. In practice sparse matrix techniques are used and the nodes are processed one at a time in order to minimize the complexity and memory requirements of the elimination process (Tewerson, 1973; Brameller, Allan and Hamam, 1976). This is equivalent to Gaussian elimination of a corresponding row and column from the admittance matrix.

Consider one elimination step, namely that of eliminating node k of set $\{E\}$. Matrix $\underline{\boldsymbol{Y}}_{EE} = \underline{Y}_{kk}$ is a scalar, $\underline{\boldsymbol{Y}}_{RE}$ is a column and $\underline{\boldsymbol{Y}}_{ER}$ is a row. The second component of matrix $\underline{\boldsymbol{Y}}_R$ becomes

$$\underline{\boldsymbol{Y}}_{RE}\underline{\boldsymbol{Y}}_{EE}^{-1}\underline{\boldsymbol{Y}}_{ER} = \frac{1}{\underline{Y}_{kk}} \begin{bmatrix} \underline{Y}_{1k} \\ \vdots \\ \underline{Y}_{ik} \\ \vdots \\ \underline{Y}_{nk} \end{bmatrix} \begin{bmatrix} \underline{Y}_{k1} & \cdots & \underline{Y}_{kj} & \cdots & \underline{Y}_{kn} \end{bmatrix} = \frac{1}{\underline{Y}_{kk}} \begin{bmatrix} & \vdots & \\ \cdots & \underline{Y}_{ik}\underline{Y}_{kj} & \cdots \\ & \vdots & \\ & j & \end{bmatrix} i, \qquad (14.5)$$

where n is the number of nodes in set $\{R\}$. Assume now that $\underline{Y}_{ij}^{old}$ is an element of matrix $\underline{\boldsymbol{Y}}_{RR}$ while $\underline{Y}_{ij}^{new}$ is an element of matrix $\underline{\boldsymbol{Y}}_R$. Equations (14.3) and (14.5) show that elimination of node k modifies each element of the 'new' matrix $\underline{\boldsymbol{Y}}_R$ to

$$\underline{Y}_{ij}^{new} = \underline{Y}_{ij}^{old} - \frac{\underline{Y}_{ik}\underline{Y}_{kj}}{\underline{Y}_{kk}} \quad \text{for} \quad i \neq k,\ j \neq k. \qquad (14.6)$$

If node i is directly connected to the eliminated node k then it is called its *neighbour* and the corresponding mutual admittance is $\underline{Y}_{ik} \neq 0$. The mutual admittances $\underline{Y}_{ik}$ of a node i which is not a neighbour of node k are all zero. Equation (14.6) shows that:

- if nodes i and j are not neighbours of node k then elimination of k does not modify the admittance $\underline{Y}_{ij}$;
- elimination of node k modifies the admittance between all its neighbours, which creates additional connections between the neighbours replacing the original connections of node k;
- self-admittances of all the neighbours of node k are also modified according to Equation (14.6) when $i = j$.

Both situations are illustrated in Figure 14.3. Nodes $\{1, 2, 3\}$ are the neighbours of node k so that its elimination creates additional connections between the nodes. Nodes $\{4, 5\}$ are not neighbours of node k and their connections do not change.

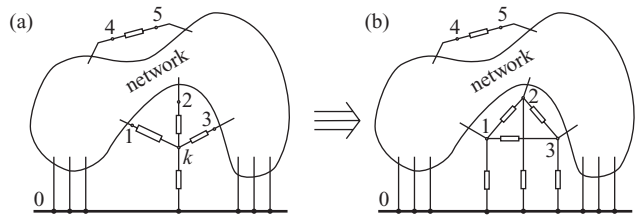

Figure 14.3 Elimination of a single node: (a) situation before elimination; (b) situation after elimination.

When using sparse matrix techniques, the order in which the rows/columns of a matrix (or nodes of the network) are processed is important from the point of view of preserving the sparsity of the resultant matrix and minimizing the number of algebraic manipulations required. Although it is not possible to devise a general optimal elimination ordering strategy, simple heuristic schemes usually work well (Tinney and Walker, 1967; Brameller, Allan and Hamam, 1976). Typically these node elimination schemes adopt one of the following procedures at each elimination step:

- eliminate the node which has the least number of neighbours, or
- eliminate the node which introduces the least number of new connections.

It is worth noting that elimination defined by Equation (14.6) is a generalization of the star–delta transformation. In that particular case three branches are connected to the eliminated node (Figure 14.4). Note that an off-diagonal element of the admittance matrix is equal to the branch admittance with a reversed sign, while the diagonal element is equal to the sum of branches connected to the node. Taking into account that admittance is the reciprocal of impedance, Equation (14.6) for the delta connection (Figure 14.4b) gives

$$\underline{y}_{AB} = \frac{\underline{y}_A \underline{y}_B}{\underline{y}_A + \underline{y}_B + \underline{y}_C}. \tag{14.7}$$

Changing to impedances,

$$\underline{Z}_{AB} = \frac{\underline{y}_A + \underline{y}_B + \underline{y}_C}{\underline{y}_A \underline{y}_B} = \underline{Z}_A \underline{Z}_B \left(\frac{1}{\underline{Z}_A} + \frac{1}{\underline{Z}_B} + \frac{1}{\underline{Z}_C} \right). \tag{14.8}$$

And finally

$$\underline{Z}_{AB} = \underline{Z}_A + \underline{Z}_B + \frac{\underline{Z}_A \underline{Z}_B}{\underline{Z}_C}. \tag{14.9}$$

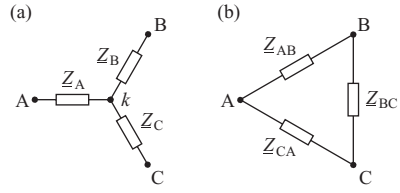

Figure 14.4 Replacing the star connection by the delta connection: (a) the star connection, (b) the equivalent delta connection.

A similar procedure can be applied to the remaining branches $\underline{Z}_{AC}$ and $\underline{Z}_{BC}$. Equation (14.9) is the well-known formula for the star–delta transformation.

14.2.2 Aggregation of Nodes Using Dimo's Method

This method is illustrated in Figure 14.5 and consists of replacing a group of nodes {A} by an equivalent node a. As before, {R} is the set of retained nodes.

In the first step of the transformation (Dimo, 1971), some fictitious branches are added to the aggregated nodes, set {A}. Each branch admittance is chosen in such a way as to make the terminal voltage of all the added branches equal. The terminal equipotential nodes can then be connected together to form a fictitious auxiliary node f. The admittance of each of the fictitious branches can be chosen freely provided that they all give the same terminal voltage. Usually these admittances are made to correspond to the nodal injections (at a given voltage) in the aggregated nodes

$$\underline{Y}_{fi} = \frac{\underline{S}_i^*}{V_i^2} \quad \text{for} \quad i \in \{A\}, \tag{14.10}$$

and then the voltage at the fictitious node f is zero. As it is inconvenient to have an equivalent node operating at zero voltage, an extra fictitious branch with negative admittance is usually added to node f. This branch raises the voltage at its terminal node a to the value close to the rated network voltage. A typical choice of the negative admittance is

$$\underline{Y}_{fa} = -\frac{\underline{S}_a^*}{V_a^2} \quad \text{where} \quad \underline{S}_a = \sum_{i\in\{A\}} \underline{S}_i. \tag{14.11}$$

This makes the voltage $\underline{V}_a$ at the equivalent node equal to the weighted average of the voltages at the aggregated nodes:

$$\underline{V}_a = \frac{\underline{S}_a}{\underline{I}_a^*} = \frac{\sum\limits_{i\in\{A\}} \underline{S}_i}{\sum\limits_{i\in\{A\}} \left(\frac{\underline{S}_i}{\underline{V}_i}\right)^*}. \tag{14.12}$$

The auxiliary node f is eliminated together with the nodes belonging to set {A} giving an equivalent network, referred to as the *radial equivalent independent* (*REI*) circuit, connecting the equivalent node a with the retained nodes {R}. As well as the REI circuit, the elimination process also creates additional connections between the retained nodes.

If the operating conditions are different from the ones for which the reduction was performed, then the obtained equivalent will only imitate the external network accurately if the admittances of the fictitious branches, Equation (14.10), can be assumed to remain constant. For load nodes this is equivalent to assuming that the loads can be modelled as constant admittances and is only valid for loads with a power–voltage characteristic of the form $\underline{S}_i = V_i^2 \underline{Y}_{fi}^*$, $\underline{Y}_{fi}$ = constant. The generation

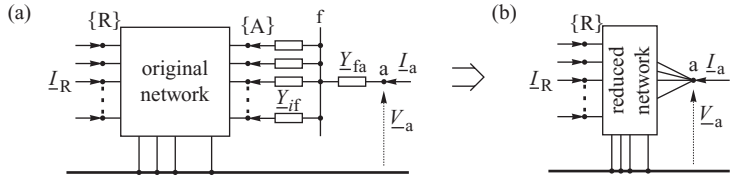

Figure 14.5 Node aggregation using Dimo's method: (a) network with fictitious branches; (b) network after elimination of the nodes and fictitious branches.

nodes operate at a constant voltage and the condition $\underline{Y}_{fi} = \underline{S}_i^* / V_i^2 = \text{constant}$ is only satisfied by those generators where the real and reactive power output can be assumed to be constant.

Dimo's method produces a large number of fictitious branches due to the elimination of node f and nodes {A}. As aggregation introduces a branch with negative admittance, Equation (14.11), the branches in the final network model may have negative admittances. Moreover, large nodal injections in the aggregated nodes produce large resistance values in the equivalent branches, Equation (14.10). Negative branch admittances combined with large resistances may cause convergence problems for some load flow programs.

14.2.3 Aggregation of Nodes Using Zhukov's Method

This method of aggregation was first formulated by Zhukov (1964). The matrix formulation described below was developed by Bernas (1971) but in view of Zhukov's early publication is referred to here as *Zhukov's aggregation*.

Aggregation consists of replacing a set of nodes {A} by a single equivalent node a as shown in Figure 14.6. {R} denotes the set of retained nodes. Aggregation must satisfy the following conditions:

1. It does not change the currents and voltages, $\underline{\boldsymbol{I}}_R$ and $\underline{\boldsymbol{V}}_R$, at the retained nodes.
2. The real and reactive power injection at the equivalent node must be equal to the sum of injections at the aggregated nodes, $\underline{S}_a = \sum_{i\in\{A\}} \underline{S}_i$.

The transformation of the network can then be described by

$$\begin{bmatrix} \underline{\boldsymbol{I}}_R \\ \underline{\boldsymbol{I}}_A \end{bmatrix} = \begin{bmatrix} \underline{\boldsymbol{Y}}_{RR} & \underline{\boldsymbol{Y}}_{RA} \\ \underline{\boldsymbol{Y}}_{AR} & \underline{\boldsymbol{Y}}_{AA} \end{bmatrix} \begin{bmatrix} \underline{\boldsymbol{V}}_R \\ \underline{\boldsymbol{V}}_A \end{bmatrix} \Rightarrow \begin{bmatrix} \underline{\boldsymbol{I}}_R \\ \underline{I}_a \end{bmatrix} = \begin{bmatrix} \underline{\boldsymbol{Y}}_{RR} & \underline{\boldsymbol{Y}}_{Ra} \\ \underline{\boldsymbol{Y}}_{aR} & \underline{Y}_{aa} \end{bmatrix} \begin{bmatrix} \underline{\boldsymbol{V}}_R \\ \underline{V}_a \end{bmatrix}, \tag{14.13}$$

where the subscripts refer to the appropriate sets. As a is a single node, $\underline{\boldsymbol{Y}}_{Ra}$ is a column, $\underline{\boldsymbol{Y}}_{aR}$ is a row and $\underline{Y}_{aa}$ is a scalar.

The first condition is satisfied when

$$\underline{\boldsymbol{Y}}_{RR}\underline{\boldsymbol{V}}_R + \underline{\boldsymbol{Y}}_{RA}\underline{\boldsymbol{V}}_A = \underline{\boldsymbol{Y}}_{RR}\underline{\boldsymbol{V}}_R + \underline{\boldsymbol{Y}}_{Ra}\underline{V}_a \quad \text{or} \quad \underline{\boldsymbol{Y}}_{RA}\underline{\boldsymbol{V}}_A = \underline{\boldsymbol{Y}}_{Ra}\underline{V}_a. \tag{14.14}$$

If this condition is to be satisfied for any vector $\underline{\boldsymbol{V}}_A$, the following must hold:

$$\underline{\boldsymbol{Y}}_{Ra} = \underline{\boldsymbol{Y}}_{RA}\underline{\boldsymbol{\vartheta}}, \tag{14.15}$$

where

$$\underline{\boldsymbol{\vartheta}} = \underline{V}_a^{-1}\underline{\boldsymbol{V}}_A = \begin{bmatrix} \underline{\boldsymbol{\vartheta}}_1 \\ \underline{\boldsymbol{\vartheta}}_2 \\ \vdots \end{bmatrix} \tag{14.16}$$

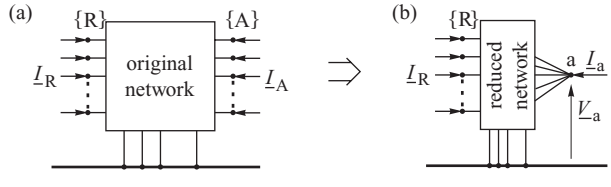

Figure 14.6 Node aggregation using Zhukov's method: (a) network before aggregation; (b) network after aggregation.

is the vector of voltage transformation ratios between the aggregated nodes and the equivalent node.

The second assumption is satisfied when

$$\underline{V}_{\mathrm{a}}\underline{I}_{\mathrm{a}}^{*} = \underline{\boldsymbol{V}}_{\mathrm{A}}^{\mathrm{T}}\underline{\boldsymbol{I}}_{\mathrm{A}}^{*}, \tag{14.17}$$

where the left hand side expresses the injection at the equivalent node and the right hand side expresses the sum of all the aggregated injections. Substituting into Equation (14.17) for $\underline{I}_{\mathrm{a}}$ and $\underline{\boldsymbol{I}}_{\mathrm{A}}$ calculated from Equation (14.13) gives

$$\underline{V}_{\mathrm{a}}\underline{\boldsymbol{Y}}_{\mathrm{aR}}^{*}\underline{\boldsymbol{V}}_{\mathrm{R}}^{*} + \underline{V}_{\mathrm{a}}\underline{Y}_{\mathrm{aa}}^{*}\underline{V}_{\mathrm{a}}^{*} = \underline{\boldsymbol{V}}_{\mathrm{A}}^{\mathrm{T}}\underline{\boldsymbol{Y}}_{\mathrm{AR}}^{*}\underline{\boldsymbol{V}}_{\mathrm{R}}^{*} + \underline{\boldsymbol{V}}_{\mathrm{A}}^{\mathrm{T}}\underline{\boldsymbol{Y}}_{\mathrm{AA}}^{*}\underline{\boldsymbol{V}}_{\mathrm{A}}^{*}. \tag{14.18}$$

If this equation is to be satisfied for any vector of $\underline{\boldsymbol{V}}_{\mathrm{A}}$, the following two conditions must hold:

$$\underline{\boldsymbol{Y}}_{\mathrm{aR}} = \underline{\boldsymbol{\vartheta}}^{*\mathrm{T}}\underline{\boldsymbol{Y}}_{\mathrm{AR}}, \tag{14.19}$$

$$\underline{\boldsymbol{Y}}_{\mathrm{aa}} = \underline{\boldsymbol{\vartheta}}^{*\mathrm{T}}\underline{\boldsymbol{Y}}_{\mathrm{AA}}\underline{\boldsymbol{\vartheta}}. \tag{14.20}$$

Substituting Equations (14.15), (14.19) and (14.20) into the second of Equations (14.13) finally gives

$$\begin{bmatrix} \underline{\boldsymbol{I}}_{\mathrm{R}} \\ \underline{I}_{\mathrm{a}} \end{bmatrix} = \left[\begin{array}{c:c} \underline{\boldsymbol{Y}}_{\mathrm{RR}} & \underline{\boldsymbol{Y}}_{\mathrm{RA}}\underline{\boldsymbol{\vartheta}} \\ \hdashline \underline{\boldsymbol{\vartheta}}^{*\mathrm{T}}\underline{\boldsymbol{Y}}_{\mathrm{AR}} & \underline{\boldsymbol{\vartheta}}^{*\mathrm{T}}\underline{\boldsymbol{Y}}_{\mathrm{AA}}\underline{\boldsymbol{\vartheta}} \end{array}\right] \begin{bmatrix} \underline{\boldsymbol{V}}_{\mathrm{R}} \\ \underline{V}_{\mathrm{a}} \end{bmatrix}. \tag{14.21}$$

Equations (14.15), (14.19) and (14.20) describe the admittances of the equivalent network. The admittances of the equivalent branches linking the equivalent node with the retained nodes depend on the vector of transformation ratios $\underline{\vartheta}$, and hence on the voltage angle at the equivalent node. As it is convenient to have equivalent branches of low resistances, the voltage angle δ_{a} at the equivalent node is assumed to be equal to the weighted average of voltage angles at the aggregated nodes

$$\delta_{\mathrm{a}} = \frac{\sum\limits_{i\in\{\mathrm{A}\}} S_i\delta_i}{\sum\limits_{i\in\{\mathrm{A}\}} S_i} \quad \text{or} \quad \delta'_{\mathrm{a}} = \frac{\sum\limits_{i\in\{\mathrm{A}\}} M_i\delta'_i}{\sum\limits_{i\in\{\mathrm{A}\}} M_i}, \tag{14.22}$$

where S_i is the apparent power injection at the aggregated node i and $M_i = T_{\mathrm{m}i}S_{\mathrm{n}i}/\omega_{\mathrm{s}}$ is the inertia coefficient of the unit installed at the ith aggregated node. The first formula can be used for forming the equivalent to be used for steady-state analysis and the second formula can be applied for aggregation of a group of generators represented by the classical transient stability model (constant transient emfs E'_i).

When compared with Dimo's method, the advantage of Zhukov's method is that it does not introduce fictitious branches between the retained nodes $\{\mathrm{R}\}$. This is because submatrix $\underline{\boldsymbol{Y}}_{\mathrm{RR}}$ is unchanged by aggregation. It does, however, introduce fictitious shunt branches at the retained nodes. To understand this, examine the ith diagonal element of $\underline{\boldsymbol{Y}}_{\mathrm{RR}}$ which is equal to the sum of admittances of all the series and shunt branches connected to i:

$$\underline{Y}_{ii} = \underline{y}_{i0} + \sum_{j\in\{\mathrm{R}\}} \underline{y}_{ij} + \sum_{k\in\{\mathrm{A}\}} \underline{y}_{ik} \quad \text{for} \quad i \in \{\mathrm{R}\}, \tag{14.23}$$

where $\underline{y}_{i0}$ is the sum of admittances of all shunt branches connected to i and $\underline{y}_{ij}$ is the admittance of a branch linking nodes i and j. During aggregation, all the branches of admittance $\underline{y}_{ik}$ that link node $i \in \{\mathrm{R}\}$ with the aggregated nodes $k \in \{\mathrm{A}\}$ are replaced by a single branch with admittance $\underline{y}_{i\mathrm{a}}$ generally not equal to $\sum_{k\in\{\mathrm{A}\}} \underline{y}_{ik}$. As $\underline{Y}_{ii}$ and $\sum_{j\in\{\mathrm{R}\}} \underline{y}_{ik}$ must remain unchanged, replacing

$\sum_{k\in\{A\}} \underline{y}_{ik}$ by $\underline{y}_{ia}$ must be compensated by a change in the value $\underline{y}_{i0}$. The interpretation of this in network terms is that Zhukov's aggregation introduces some equivalent shunt admittances at the retained nodes {R}.

14.2.3.1 Symmetry of the Equivalent Admittance Matrix

If the vector $\underline{\boldsymbol{\vartheta}}$ is complex then Zhukov's equivalent admittance matrix is not generally symmetric ($\underline{\boldsymbol{Y}}_{aR} \neq \underline{\boldsymbol{Y}}_{Ra}^{T}$). This means that if $\underline{Y}_{ia} \neq \underline{Y}_{ai}$ for $i \in \{R\}$ then the value of the admittances in the equivalent branches obtained after aggregation are direction dependent. From a computational point of view, asymmetry of the admittance matrix is inconvenient and Figure 14.7 shows how this asymmetry can be removed by inserting a correction current $\underline{I}_c$ at the equivalent node a. The nodal equation of the system then takes the form

$$\begin{bmatrix} \underline{\boldsymbol{I}}_R \\ \underline{I}_a \end{bmatrix} = \begin{bmatrix} \underline{\boldsymbol{Y}}_{RR} & \underline{\boldsymbol{Y}}_{Ra} \\ \underline{\boldsymbol{Y}}_{Ra}^{T} & \underline{Y}_{aa} + \dfrac{\underline{I}_c}{\underline{V}_a} \end{bmatrix} \begin{bmatrix} \underline{\boldsymbol{V}}_R \\ \underline{V}_a \end{bmatrix}, \tag{14.24}$$

where $\underline{I}_c = [(\underline{\boldsymbol{\vartheta}}^* - \underline{\boldsymbol{\vartheta}})^T \underline{\boldsymbol{Y}}_{AR}]\underline{\boldsymbol{V}}_R$ is the correction current. This current is not constant because it depends on the voltages in set {R}. The correction current is small (negligible when compared with $\underline{I}_a$) when the difference $(\underline{\boldsymbol{\vartheta}}^* - \underline{\boldsymbol{\vartheta}})$ is small, that is when the imaginary parts of the transformation ratios are small. This condition is usually satisfied because the angle of the equivalent voltage, Equation (14.22), is averaged over the aggregated nodes. Consequently, variations of the correction current can be neglected and a constant current replaced by a constant admittance ($\underline{I}_c/\underline{V}_a$) added to the self-admittance of the equivalent node a. This has been shown using the dotted line in Figure 14.7.

14.2.4 Coherency

The admittances in the equivalent Zhukov network depend on the transformation ratios $\underline{\vartheta}_i = \underline{V}_i/\underline{V}_a$ between the aggregated nodes $i \in \{A\}$ and the equivalent node a. This means that an equivalent network obtained for an initial (prefault) state is only valid for other states (transient or steady state) if the transformation ratios (see Figure 14.15) can be assumed to remain constant for all nodes $i \in \{A\}$ in a given group:

$$\frac{\underline{V}_i(t)}{\underline{V}_a(t)} = \frac{\hat{\underline{V}}_i}{\hat{\underline{V}}_a} = \underline{\vartheta}_i = \text{constant} \quad \text{for} \quad i \in \{A\}, \tag{14.25}$$

where the circumflex denotes the initial state (stable equilibrium point) for which the reduced model has been constructed. For any two nodes $i, j \in \{A\}$ this condition is equivalent to

$$\frac{\underline{V}_i(t)}{\underline{V}_j(t)} = \frac{V_i(t)}{V_j(t)} e^{j[\delta_i(t)-\delta_j(t)]} = \frac{\hat{V}_i}{\hat{V}_j} e^{j[\hat{\delta}_i-\hat{\delta}_j]} = \text{constant} \quad \text{for} \quad i, j \in \{A\}. \tag{14.26}$$

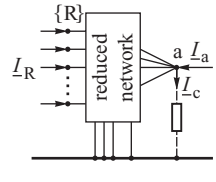

Figure 14.7 Symmetry of the equivalent network.

Nodes satisfying this condition are referred to as *electrically coherent nodes* or simply *coherent nodes*. If the voltage magnitude of the aggregated node can be assumed to be constant (as for PV nodes in the steady-state power flow problem) the above coherency condition (14.26) simplifies to

$$\delta_i(t) - \delta_j(t) = \hat{\delta}_{ij} \quad \text{for} \quad i, j \in \{\text{A}\}, \tag{14.27}$$

where $\hat{\delta}_{ij} = \hat{\delta}_i - \hat{\delta}_j$ are the initial values.

Practical experience with power system simulation shows that load nodes are almost never electrically coherent. Only the load nodes very far away from a disturbance maintain constant voltage magnitude and angle. On the other hand, it is usually possible to find groups of coherent generation nodes because some groups of generators in the system have a natural tendency to swing together. This means that Zhukov's method is well suited for aggregation of groups of electrically coherent generation nodes.

For the generators modelled by the classical generator model (Figure 5.8) the nodal voltage at the generator nodes is equal to the transient emf $\underline{E}'_i$, the magnitude of which is assumed to be constant $E'_i = \text{constant}$, and the angle corresponds to the rotor angle $\delta'_i(t)$. For these generator nodes the coherency condition (14.26) simplifies to

$$\delta'_i(t) - \delta'_j(t) = \hat{\delta}'_{ij} \quad \text{for} \quad i, j \in \{\text{A}\}, \tag{14.28}$$

where $\hat{\delta}'_{ij} = \hat{\delta}'_i - \hat{\delta}'_j$ are the initial values. The coherency defined by Equation (14.28) is valid also for generator rotors and is therefore referred to as the *electromechanical coherency*.

An example of rotor swings for three generators is shown in Figure 14.8. Generators i, j are electromechanically coherent because the difference between their rotor angles is almost constant despite both angles undergoing quite deep oscillations. Generator k is not coherent with the other two because its rotor angle variations are different.

Condition (14.28) may also be written as $[\delta'_i(t) - \hat{\delta}'_i] - [\delta'_j(t) - \hat{\delta}'_j] = 0$ or $[\Delta\delta'_i(t) - \Delta\delta'_j(t)] = 0$. For practical considerations it may be assumed that coherency is only approximate with accuracy $\varepsilon_{\Delta\delta}$, which corresponds to the condition

$$\left|\Delta\delta'_i(t) - \Delta\delta'_j(t)\right| < \varepsilon_{\Delta\delta} \quad \text{for} \quad i, j \in \{\text{A}\} \quad \text{and} \quad t \le t_{\text{c}}, \tag{14.29}$$

where $\varepsilon_{\Delta\delta}$ is a small positive number and t_{c} is the duration time of coherency.

The generators are said to be *exactly coherent generators* if

$$\varepsilon_{\Delta\delta} = 0 \quad \text{and} \quad t_{\text{c}} = \infty. \tag{14.30}$$

Exactly coherent generators rarely occur in practice, but the definition is useful for theoretical considerations.

It should be noted that swings of coherent generators can be treated as a constrained motion as illustrated in Figure 14.9 where generators i and j are electromechanically coherent. In the plane with

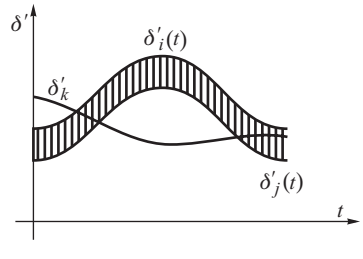

Figure 14.8 Example of variation of rotor angles for three generators.

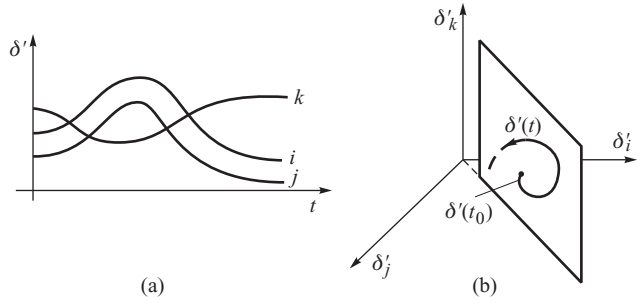

Figure 14.9 Illustration of exact coherency: (a) rotor swings; (b) trajectory in the rotor angle space.

coordinates $\delta'_i(t)$, $\delta'_j(t)$, the trajectory of these two coherent generators is given by $\delta'_i(t) = \delta'_j(t) + \hat{\delta}'_{ij}$ resulting from the coherency condition (14.28). Obviously $\delta'_i(t)$ as a function of $\delta'_j(t)$ is a straight line. Generator k is not coherent with generators i, j (Figure 14.9a). Consequently, the trajectory $\delta'(t)$ in the space with coordinates $\delta'_i(t)$, $\delta'_j(t)$, $\delta'_k(t)$ lies in the plane crossing the previously mentioned straight line (Figure 14.9b).

When there are more coherent generators, the trajectory lies on the intersection line of the planes. The intersection line may be described using the following equation:

$$\boldsymbol{\varphi}(\boldsymbol{\delta}') = \mathbf{0}, \tag{14.31}$$

where $\boldsymbol{\varphi}(\boldsymbol{\delta}')$ is a vector function consisting of the following functions:

$$\varphi_j(\boldsymbol{\delta}) = \delta'_1(t) - \delta'_j(t) - \hat{\delta}'_{1j} = 0 \quad \text{for} \quad j \in \{\mathrm{A}\} \quad \text{and} \quad j > 1, \tag{14.32}$$

where $\delta'_{1j0} = \delta'_{10} - \delta'_{j0}$. For every generator belonging to a coherent group $\{\mathrm{A}\}$, the above equation can be treated as a constraint for the rotor motion.

14.3 Aggregation of Generating Units

The elimination and aggregation of nodes considered so far will produce a reduced network model for use in steady-state analysis. If the reduced model is to be used for dynamic analysis then equivalent generating units must be added to the equivalent nodes.

From a mechanical point of view, the rotors of electromechanically coherent generators can be treated as if they rotated on one common rigid shaft, Figure 14.10. A group $\{\mathrm{A}\}$ containing n such generators can be replaced by one equivalent generator with inertia coefficient M_a and mechanical power input P_ma given by

$$M_\mathrm{a} = \sum_{i \in \{\mathrm{A}\}} M_i, \quad P_\mathrm{ma} = \sum_{i \in \{\mathrm{A}\}} P_{\mathrm{m}i}, \tag{14.33}$$

where $M_i = T_{\mathrm{m}i} S_{\mathrm{n}i} / \omega_\mathrm{s}$ is the inertia coefficient and $P_{\mathrm{m}i}$ is the mechanical power input of the ith aggregated generator. This is consistent with Zhukov's aggregation, which sets the power injection at the equivalent node equal to the sum of power injections to all the aggregated nodes, Equation (14.17).

The equivalent model of a group of electromechanically coherent generation units is therefore created by Zhukov's aggregation of the generation nodes and by replacing the aggregated generators by one equivalent generator with inertia coefficient and mechanical power given by Equation (14.33). The equivalent generator is represented by the classical model with constant equivalent transient emf and by the swing equation.

If more detailed models are used then parameters of the equivalent unit can be found by matching the frequency response characteristics of the equivalent unit to the characteristics of the aggregated units. Details can be found in Garmond and Podmore (1978) and Cai and Wu (1986).

14.4 Equivalent Model of External Subsystem

The described method of creating a dynamic equivalent model is based on the following assumptions:

1. The system is divided as in Figure 14.1 into internal and external parts.
2. In the internal part, detailed generator and load models are used as described in Chapter 11.
3. In the external part, the loads are replaced by constant admittances while the generators are modelled using the classical model (the rotor swing equation and a constant transient emf behind a transient reactance).

Under these assumptions the creation of the dynamic equivalent model is significantly simplified and consists of three steps:

1. Elimination of the load nodes in the external subsystem.
2. Identification of coherent groups of generators in the external subsystem.
3. Aggregation of the coherent groups.

All three steps are briefly described in the following subsections.

All the load nodes in the external subsystem can be eliminated using the method described in Section 14.2.1. The resulting external equivalent network is referred to as the *PV equivalent network* because, with the exception of the border nodes, it contains only generation nodes (the terminology used with respect to load flow calculations in Section 3.7 referred to such nodes as PV nodes). The power demand of the external system is then distributed among the border nodes and generation nodes. All the generation nodes, and the border nodes, are connected by the equivalent network, which is much more dense than the original.

For some power system analysis problems it may be more convenient not to eliminate the load nodes altogether, but to replace a few of them by equivalent load nodes using Dimo's aggregation method. These equivalent nodes can then be used to change the power demand of the external subsystem if a change in tie-line flows is required.

Coherency recognition is the most difficult step in creating a dynamic equivalent model of the external subsystem. Coherency criteria and coherency recognition algorithms are described in next section.

When all the groups of coherent generators in the external subsystems have been recognized, the next step is to use Zhukov's method to aggregate the nodes in these groups. Equivalent generating

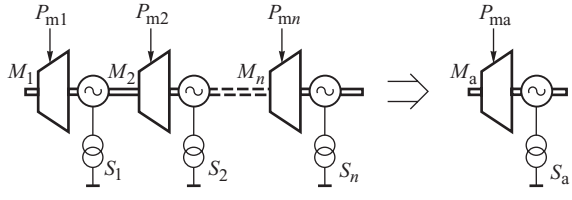

Figure 14.10 Mechanical aggregation of coherent rotors.

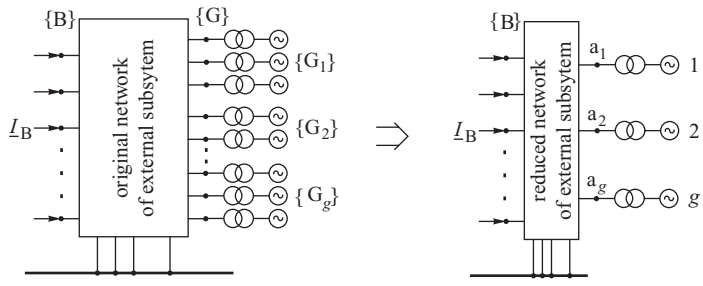

Figure 14.11 Model reduction of the external system.

units with parameters calculated as described in Section 14.3 are connected to the equivalent nodes obtained by Zhukov's method.

Figure 14.11 illustrates the whole process of forming an equivalent model of the external subsystem. The original model of the subsystem contains a large number of load nodes and a large number of generation nodes $\{G\} = \{G_1\} + \{G_2\} + \cdots + \{G_g\}$. The load nodes are either completely eliminated or aggregated into a few equivalent nodes using Dimo's method. The generator nodes are divided into groups of approximately coherent nodes $\{G_1\}, \{G_2\}, \ldots, \{G_g\}$ and each of the groups is replaced by one equivalent node with an equivalent generating unit.

14.5 Coherency Recognition

The topological network equivalent obtained by aggregation of generation nodes will only give valid results if, following a disturbance inside the internal subsystem, the generators within each aggregated group are coherent. The problem is therefore how to assess generator coherency without first completing a detailed dynamic simulation of the complete system for a particular disturbance. Fortunately methods are available that will assess generator coherency without the need for such detailed simulation and this is referred to as coherency recognition. The simplest solution to this problem is to assume that all the generators installed at the aggregated nodes can be modelled by the classical generator model and electromechanical coherency must be recognized.

Several methods of coherency recognition have been reported in the literature. The approach described here is based on coherency criteria derived by Machowski *et al.* (1988).

Coherency criteria for nonlinear dynamic system models have been mathematically derived by Machowski (1985) using the theory of motion with prescribed trajectory due to Olas (1975). The methodology was based on an observation that electromechanical coherency is a case of the constrained motion (Figure 14.9) with constraints given by Equation (14.32). As the proof is rather complicated, the idea of coherency recognition will be described here using a single disturbance when the voltage angle at one of the nodes $k \in \{B\}$ is changed.

Providing that all the load nodes of the external subsystem have been eliminated, any disturbance inside the internal subsystem influences the generators in the external subsystem through equivalent branches of the transfer network. According to Equation (3.156), if the mutual conductances G_{ij} in the transfer admittance matrix are neglected, the real power produced by generator $i \in \{G\}$ in the external subsystem (Figure 14.11) can be expressed as

$$P_i = (E_i')^2 G_{ii} + \sum_{k\in\{B\}} E_i' V_k B_{ik} \sin\delta_{ik}' + \sum_{l\in\{G\}} E_i' E_l' B_{il} \sin\delta_{il}', \tag{14.34}$$

where E'_i for $i \in \{G\}$ is the generator transient emf, V_k for $k \in \{B\}$ is the voltage at the border node, $\delta'_{ik} = \delta'_i - \delta_k$, $\delta'_{il} = \delta'_i - \delta'_l$ and G_{ii}, B_{ik} and B_{il} are the appropriate elements of the transfer admittance matrix.

Assuming that the disturbance is caused by a change in the voltage angle of the border node k from the initial value $\hat{\delta}_k$ to a value $\delta_k = \hat{\delta}_k + \Delta\delta_k$, and assuming that the voltages at the other nodes are constant, this change in angle will cause a change in the power generation at node $i \in \{G\}$ equal to

$$\Delta P_i(\Delta\delta_k) = b_{ik}[\sin(\hat{\delta}'_{ik} + \Delta\delta_k) - \sin\hat{\delta}'_{ik}], \tag{14.35}$$

where $b_{ik} = E'_i V_k B_{ik}$ is the maximum power transfer in the equivalent branch linking a generator node $i \in \{G\}$ with a border node $k \in \{B\}$. As $\Delta\delta_k$ is small, it holds that $\cos\Delta\delta_k \approx 1$ and $\sin\Delta\delta_k \approx \Delta\delta_k$. Expanding the sine term in Equation (14.35) gives

$$\Delta P_i(\Delta\delta_k) \approx H_{ik}\Delta\delta_k, \tag{14.36}$$

where $H_{ik} = b_{ik}\cos\delta_{ik0}$ is the synchronizing power between a given generator $i \in \{G\}$ and a given border node $k \in \{B\}$. The considered disturbance causes the rotor acceleration

$$\varepsilon_i = \frac{\Delta P_i(\Delta\delta_k)}{M_i} = \frac{H_{ik}}{M_i}\Delta\delta_k \quad \text{for} \quad k \in \{B\}, \tag{14.37}$$

where M_i is the inertia coefficient. A similar expression for acceleration can be written for another generator in the external subsystem as

$$\varepsilon_j = \frac{\Delta P_j(\Delta\delta_k)}{M_j} = \frac{H_{jk}}{M_j}\Delta\delta_k \quad \text{for} \quad k \in \{B\}. \tag{14.38}$$

Generators $i, j \in \{G\}$ are *electromechanically exactly coherent generators* (see Equation (14.30)) if their rotor accelerations ε_i and ε_j caused by the disturbance are the same, that is when

$$\frac{H_{ik}}{M_i} = \frac{H_{jk}}{M_j} \quad \text{for} \quad i, j \in \{A\}, \quad k \in \{B\}. \tag{14.39}$$

Equation (14.39) constitutes the exact coherency condition during the postfault state and means that the synchronizing powers divided by the inertia constants must be identical.

It will be shown in Section 14.6 that exact coherency has an elegant and interesting modal interpretation and that the exact coherency condition (14.39) may be derived using modal analysis.

Equation (14.39) is the condition for exact coherency. In real power systems (apart from the trivial case of identical generating units operating in parallel on the same busbar) the exact coherency practically does not appear. This is not a significant problem as simulation of the internal system gives results of satisfactory accuracy if the external subsystem can be replaced by an approximate equivalent created by the aggregation of generators that are only approximately coherent. For practical purposes the equality (14.39) can be replaced by the following inequality:

$$\frac{\max\limits_{i\in\{G\}}\dfrac{H_{ik}}{M_i} - \min\limits_{j\in\{G\}}\dfrac{H_{jk}}{M_j}}{d_{\{G\}}} \le \rho_h \quad \text{for} \quad i, j \in \{G\}, \quad k \in \{B\}, \tag{14.40}$$

where ρ_h is a small number determining the admissible error and $d_{\{G\}}$ is a density measure of the considered group $\{A\}$. The density measure for a pair of generators i, j is defined using the following parameter:

$$d_{ij} = \min_{i,j\in\{G\}}\left(\frac{H_{ij}}{M_i};\quad \frac{H_{ji}}{M_j}\right), \tag{14.41}$$

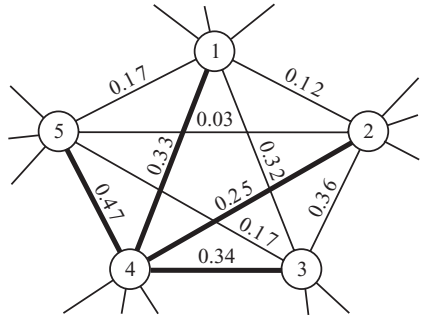

Figure 14.12 Illustration of the definition of the density measure.

which relates to the direct connection of this pair and appropriate inertia coefficients. For the group of generators {G} this parameter can be used to define the following density measure:

$$d_{\{G\}} = \min_{i,j\in\{T\}} d_{ij}, \tag{14.42}$$

where {T} is a tree made up of the equivalent branches with the highest values of $d_{\{i,j\}}$. Such a definition is justified by the fact that, inside the group, the nodes with weak direct connections can be strongly connected via other nodes. This is illustrated in Figure 14.12. For example, nodes 5 and 2 are directly very weakly connected by a branch of parameters $d_{\{2,5\}} = 0.03$. However, these nodes are strongly connected via nodes 3 and 4. In Figure 14.12 the tree {T} is denoted using bold lines. The weakest branch of this tree is the branch connecting nodes 1 and 4. Hence in the discussed example the density measure of the group $\{G\} = \{1, 2, 3, 4, 5\}$ is equal to $d_{\{G\}} = d_{14} = 0.33$.

Justification of the density measure (14.42) results from the following observations of simulations of power system dynamic response. Each strongly connected group of generators has a natural tendency to maintain synchronism. The synchronism may be disturbed only by disturbances close to that group. For remote disturbances the further away is the disturbance, the less the synchronism is disturbed and the more the group motion is close to exact coherency.

Inequality (14.40) was derived based on condition (14.39) for exact coherency when the above observations were taken into account. Hence inequality (14.40) is referred to as the *coherency criterion* while Equation (14.39) constitutes the coherency condition.

Another important observation in the simulation of power system dynamic response concerns the influence of the coherency error of a group of generators aggregated in the external subsystem on the simulation accuracy of the internal subsystem. The more the group of aggregated generators is remote from the internal subsystem, the smaller is the influence of the coherency error on the simulation accuracy of dynamic response in internal subsystems. This observation makes it possible to make ρ_h in criterion (14.40) dependent on the distance of group {A} from the border nodes:

$$\rho_h = \rho_{h0} + \Delta\rho_h \frac{d_{\{G\}}}{\max\limits_{k\in\{B\};i\in\{G\}} d_{ik}}, \tag{14.43}$$

where ρ_{h0} and $\Delta\rho_h$ are small positive numbers ($\rho_{h0} = 0.2$–0.5 and $\Delta\rho_h = 0.1$–0.3). For the border nodes {B} the coefficient of inertia is zero and according to Equation (14.41), $d_{ik} = h_{ik}/M_i$ holds for $k \in \{B\}$ and $i \in \{G\}$.

The coherency recognition algorithm based on criterion (14.40) works as follows:

1. Determine the transfer admittance matrix for the border nodes {B} and all the generation nodes in the external subsystem.

2. Mark all the generators of the external subsystem as eligible generators for grouping.
3. Order all the equivalent branches in ascending order according to the values of the distance measure d_{ij}. Create an ordered list of those branches containing, for each branch, the value of d_{ij} and numbers of the terminal nodes i and j.
4. Take from the list created in step 3 the data of the next equivalent branch. Memorize its terminal nodes i and j and density measure d_{ij}. If there are no branches left, stop the algorithm.
5. If the generator i or j is not eligible for grouping then return to step 4.
6. If the criterion (14.40) is not satisfied for pair $\{i, j\}$, then return to step 4. Otherwise, create group $\{\mathrm{G}\}$ consisting of two generators $\{i, j\}$.
7. Search all the eligible generators for a new generator x which satisfies criterion (14.40) for the extended group substituting $\{\mathrm{G}, x\}$ and gives a minimum value for the left hand side of (14.40). If such a generator cannot be found, store group $\{\mathrm{G}\}$ as a new group and return to step 4. Otherwise, go to step 8.
8. Mark generator x as not eligible and add it to group $\{\mathrm{G}\}$. Return to step 7.

The algorithm is very fast and gives good results in practice. Test results of the above coherency recognition algorithm for test systems and real, large interconnected power systems can be found in Machowski (1985), Machowski, Gubina and Omahen (1986) and Machowski *et al.* (1986, 1988). Due to lack of space here only one example will be presented.

Example 14.1

The diagram of a 25-machine test system is shown in Figure 14.13. In order to show in such a small system the influence of the disturbance distance on the grouping of generators, it was assumed that the internal subsystem is very small, it is on the verge of the test system and it contains two power plants with generators 7 and 18 (bottom right corner of the diagram). The remaining part of the test system was treated as the external subsystem.

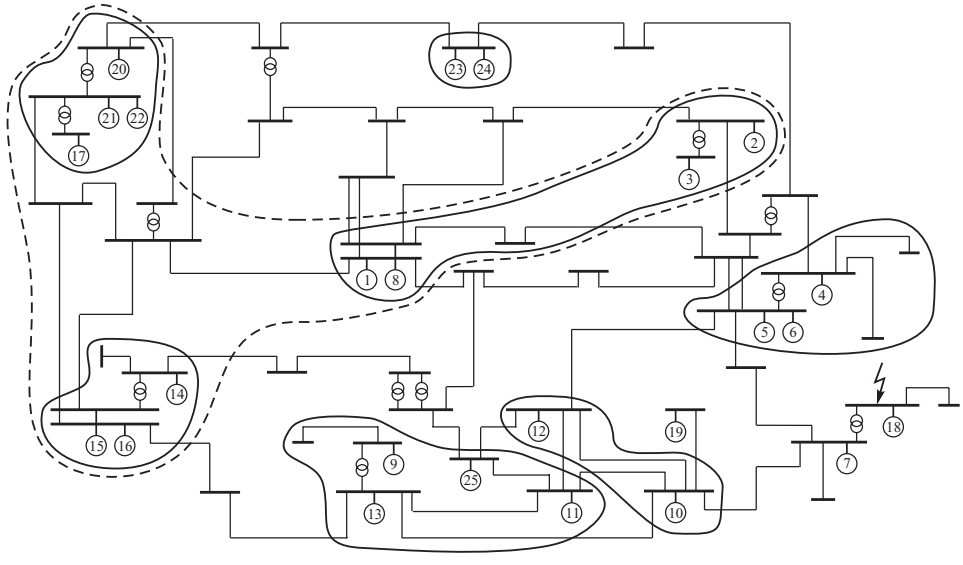

Figure 14.13 Test system and recognized coherent groups.

For the parameter values $\rho_{h0} = 0.3$ and $\Delta\rho_h = 0$ a number of groups were obtained that are shown by solid lines in Figure 14.13. The groups are: {4, 5, 6}, {10, 12}, {9, 11, 13, 25}, {14, 15, 16}, {1, 2, 3, 8}, {17, 20, 21, 22}, {23, 24}. Altogether 22 generators were replaced by 7 equivalent generators. Generator 19 close to the internal subsystem did not enter any of the groups.

After introducing a dependence of the parameter ρ_h on the distance to the disturbance and assuming $\Delta\rho_h = 0.2$, three groups were obtained close to the internal system. The first three groups were identical to the previous case: {4, 5, 6}, {10, 12}, {9, 11, 13, 25}. Three further groups were joined together to form one large group: {14, 15, 16, 1, 2, 3, 8, 17, 20, 21, 22} encircled by a dashed line in Figure 14.13. Group {23, 24} was not included in any other group. Altogether 22 generators were replaced by 5 equivalent generators.

Figure 14.14 shows the simulation results for the original system consisting of 25 generators and the reduced models. The assumed disturbance was an intermittent short circuit on the busbars of power plant 18. The solid line corresponds to the rotor swing of generator 18 for the original (unreduced) system model. The dotted line corresponds to the group obtained using $\Delta\rho_h = 0$. The dashed line corresponds to the group obtained using $\Delta\rho_h = 0.2$, that is when larger coherency tolerance was assumed for remote generators. In the transient state of about 1.5 s the rotor swings obtained for the reduced model were quite close to the swings for the original (unreduced) model.

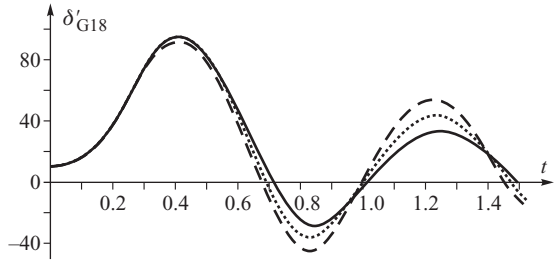

Figure 14.14 Simulation results for original and reduced system model.

14.6 Properties of Coherency-Based Equivalents

Coherency-based equivalents using Zhukov's aggregation exhibit many interesting static and dynamic properties which will be discussed in this section.

14.6.1 Electrical Interpretation of Zhukov's Aggregation

De Mello, Podmore and Stanton (1975) proposed an aggregation method whereby all the nodes to be aggregated are connected together through ideal transformers with transformation ratios that give a common secondary voltage $\underline{V}_a$. This is illustrated in Figure 14.15. Now it will be shown that such an aggregation method is, from the mathematical point of view, equivalent to Zhukov's aggregation.

Let $\underline{\boldsymbol{\tau}}$ be a diagonal matrix containing transformation ratios of all the ideal transformers used to aggregate the nodes by using De Mello's method:

$$\underline{\boldsymbol{\tau}} = \begin{bmatrix} \underline{\vartheta}_1 & & \\ & \underline{\vartheta}_2 & \\ & & \ddots \end{bmatrix}. \tag{14.44}$$

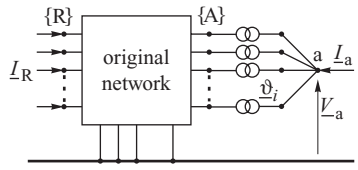

Figure 14.15 Electrical interpretation of Zhukov's aggregation.

Note that there is the following relationship between the above diagonal matrix and vector (14.16) defined in the Zhukov's aggregation:

$$\underline{\boldsymbol{\vartheta}} = \begin{bmatrix} \underline{\boldsymbol{\vartheta}}_1 \\ \underline{\boldsymbol{\vartheta}}_2 \\ \vdots \end{bmatrix} = \begin{bmatrix} \underline{\vartheta}_1 & & \\ & \underline{\vartheta}_2 & \\ & & \ddots \end{bmatrix} \begin{bmatrix} 1 \\ 1 \\ \vdots \end{bmatrix} = \underline{\boldsymbol{\tau}}\, \mathbf{1}_A, \tag{14.45}$$

where $\mathbf{1}_A$ is a column vector with all elements equal to one.

The network shown in Figure 14.15, but without the ideal transformers, is defined by the following nodal admittance equation:

$$\begin{bmatrix} \underline{\boldsymbol{I}}_R \\ \underline{\boldsymbol{I}}'_A \end{bmatrix} = \begin{bmatrix} \underline{\boldsymbol{Y}}_{RR} & \underline{\boldsymbol{Y}}_{RA} \\ \underline{\boldsymbol{Y}}_{AR} & \underline{\boldsymbol{Y}}_{AA} \end{bmatrix} \begin{bmatrix} \underline{\boldsymbol{V}}_R \\ \underline{\boldsymbol{V}}'_A \end{bmatrix}, \tag{14.46}$$

where the prime denotes variables on the primary side of the ideal transformers. For the ideal transformers

$$\underline{\boldsymbol{I}}''_A = \underline{\boldsymbol{\tau}}^* \underline{\boldsymbol{I}}'_A, \quad \underline{\boldsymbol{V}}'_A = \boldsymbol{\tau}\, \underline{\boldsymbol{V}}_a, \quad \underline{\boldsymbol{V}}_a = \mathbf{1}_A \underline{V}_a, \tag{14.47}$$

where $\underline{\boldsymbol{V}}_a$ is a vector column with all the elements identical and equal to $\underline{V}_a$. For the equivalent node

$$\underline{I}_a = \mathbf{1}_A^T \underline{\boldsymbol{I}}''_A, \tag{14.48}$$

which is the mathematical expression of the fact that the sum of secondary currents in the ideal transformers is equal to the nodal current at the equivalent node (Figure 14.15).

Equation (14.46) can be written as

$$\underline{\boldsymbol{I}}_R = \underline{\boldsymbol{Y}}_{RR} \underline{\boldsymbol{V}}_R + \underline{\boldsymbol{Y}}_{RA} \underline{\boldsymbol{V}}'_A, \tag{14.49a}$$

$$\underline{\boldsymbol{I}}'_A = \underline{\boldsymbol{Y}}_{AR} \underline{\boldsymbol{V}}_R + \underline{\boldsymbol{Y}}_{AA} \underline{\boldsymbol{V}}'_A. \tag{14.49b}$$

Vector $\underline{\boldsymbol{V}}'_A$ in these equations can be, according to Equation (14.47), replaced by $\underline{\boldsymbol{\tau}\, \boldsymbol{V}}_a$. Taking this into account and left-multiplying Equation (14.49b) by $\underline{\boldsymbol{\tau}}^*$ gives

$$\underline{\boldsymbol{I}}_R = \underline{\boldsymbol{Y}}_{RR} \underline{\boldsymbol{V}}_R + \underline{\boldsymbol{Y}}_{RA} \underline{\boldsymbol{\tau}\, \boldsymbol{V}}_a, \tag{14.50a}$$

$$\underline{\boldsymbol{\tau}}^* \underline{\boldsymbol{I}}'_A = \underline{\boldsymbol{\tau}}^* \underline{\boldsymbol{Y}}_{AR} \underline{\boldsymbol{V}}_R + \underline{\boldsymbol{\tau}}^* \underline{\boldsymbol{Y}}_{AA} \underline{\boldsymbol{\tau}\, \boldsymbol{V}}_a. \tag{14.50b}$$

Now, according to Equation (14.47), $\underline{\boldsymbol{\tau}}^* \underline{\boldsymbol{I}}'_A$ may be replaced by $\underline{\boldsymbol{I}}''_A$ and $\underline{\boldsymbol{V}}_a$ by $\mathbf{1}_A \underline{V}_a$. Equations (14.50) will then take the form

$$\underline{\boldsymbol{I}}_R = \underline{\boldsymbol{Y}}_{RR} \underline{\boldsymbol{V}}_R + \underline{\boldsymbol{Y}}_{RA} \underline{\boldsymbol{\tau}} \mathbf{1}_A \underline{V}_a, \tag{14.51a}$$

$$\underline{\boldsymbol{I}}''_A = \underline{\boldsymbol{\tau}}^* \underline{\boldsymbol{Y}}_{AR} \underline{\boldsymbol{V}}_R + \underline{\boldsymbol{\tau}}^* \underline{\boldsymbol{Y}}_{AA} \underline{\boldsymbol{\tau}} \mathbf{1}_A \underline{V}_a. \tag{14.51b}$$

Equation (14.49b) is left-multiplied by $\mathbf{1}_{\mathrm{A}}^{\mathrm{T}}$ which, after taking into account (14.46), gives

$$\underline{I}_{\mathrm{a}} = \mathbf{1}_{\mathrm{A}}^{\mathrm{T}}\underline{\boldsymbol{\tau}}^{*}\underline{\boldsymbol{Y}}_{\mathrm{AR}}\underline{\boldsymbol{V}}_{\mathrm{R}} + \mathbf{1}_{\mathrm{A}}^{\mathrm{T}}\underline{\boldsymbol{\tau}}^{*}\underline{\boldsymbol{Y}}_{\mathrm{AA}}\underline{\boldsymbol{\tau}}\mathbf{1}_{\mathrm{A}}\underline{V}_{\mathrm{a}}. \tag{14.51c}$$

Taking into account (14.45), it is possible to write Equations (14.51a) and (14.51c) as

$$\underline{\boldsymbol{I}}_{\mathrm{R}} = \underline{\boldsymbol{Y}}_{\mathrm{RR}}\underline{\boldsymbol{V}}_{\mathrm{R}} + \underline{\boldsymbol{Y}}_{\mathrm{RA}}\underline{\boldsymbol{\vartheta}}\,\underline{V}_{\mathrm{a}}, \tag{14.52a}$$

$$\underline{I}_{\mathrm{a}} = \underline{\boldsymbol{\vartheta}}^{*\mathrm{T}}\underline{\boldsymbol{Y}}_{\mathrm{AR}}\underline{\boldsymbol{V}}_{\mathrm{R}} + \underline{\boldsymbol{\vartheta}}^{*\mathrm{T}}\underline{\boldsymbol{Y}}_{\mathrm{AA}}\underline{\boldsymbol{\vartheta}}\,\underline{V}_{\mathrm{a}}, \tag{14.52b}$$

or in matrix form

$$\begin{bmatrix} \underline{\boldsymbol{I}}_{\mathrm{R}} \\ \underline{I}_{\mathrm{a}} \end{bmatrix} = \left[\begin{array}{c|c} \underline{\boldsymbol{Y}}_{\mathrm{RR}} & \underline{\boldsymbol{Y}}_{\mathrm{RA}}\underline{\boldsymbol{\vartheta}} \\ \hline \underline{\boldsymbol{\vartheta}}^{*\mathrm{T}}\underline{\boldsymbol{Y}}_{\mathrm{AR}} & \underline{\boldsymbol{\vartheta}}^{*\mathrm{T}}\underline{\boldsymbol{Y}}_{\mathrm{AA}}\underline{\boldsymbol{\vartheta}} \end{array}\right] \begin{bmatrix} \underline{\boldsymbol{V}}_{\mathrm{R}} \\ \underline{V}_{\mathrm{a}} \end{bmatrix}. \tag{14.53}$$

Note that Equation (14.53) is identical to Equation (14.21) obtained for Zhukov's aggregation. This means that the methods proposed by De Mello, Podmore and Stanton (1975) and by Zhukov (1964) are equivalent. The advantage of De Mello's approach is that it gives an electrical interpretation of mathematical transformations.

14.6.2 Incremental Equivalent Model

For the system shown in Figure 14.6 in which nodes {R} and {A} have been emphasized, the incremental equation (12.99) takes the following form:

$$\begin{bmatrix} \Delta\boldsymbol{P}_{\mathrm{R}} \\ \Delta\boldsymbol{P}_{\mathrm{A}} \end{bmatrix} = \begin{bmatrix} \boldsymbol{H}_{\mathrm{RR}} & \boldsymbol{H}_{\mathrm{RA}} \\ \boldsymbol{H}_{\mathrm{AR}} & \boldsymbol{H}_{\mathrm{AA}} \end{bmatrix} \begin{bmatrix} \Delta\boldsymbol{\delta}'_{\mathrm{R}} \\ \Delta\boldsymbol{\delta}'_{\mathrm{A}} \end{bmatrix}, \tag{14.54}$$

where elements in matrix $\boldsymbol{H} = [\partial\boldsymbol{P}/\partial\boldsymbol{\delta}']$ are the synchronizing powers.

In the case of exact coherency (Section 14.2.4) the increments of rotor angles are identical and can be written as

$$\Delta\delta'_i(t) = \Delta\delta'_j(t) = \Delta\delta'_{\mathrm{a}}(t) \quad \text{for} \quad i, j \in \{\mathrm{A}\}, \tag{14.55}$$

where $\Delta\delta_{\mathrm{a}}(t)$ is a common change of angles for the node group {A}. Equation (14.55) can be expressed in matrix form as

$$\Delta\boldsymbol{\delta}'_{\mathrm{A}} = \mathbf{1}_{\mathrm{A}} \cdot \Delta\delta'_{\mathrm{a}}(t), \tag{14.56}$$

where $\mathbf{1}_{\mathrm{A}}$ is a vector of unity elements of the size of group {A}.

When a group of generators is replaced by one equivalent generating node (Figure 14.6) it is assumed that $\underline{S}_{\mathrm{a}} = \sum_{i\in\{\mathrm{A}\}} \underline{S}_i$ which also means $P_{\mathrm{a}} = \sum_{i\in\{\mathrm{A}\}} P_i$. In the case of the incremental model

$$\Delta P_{\mathrm{a}} = \sum_{i\in\{\mathrm{A}\}} \Delta P_i, \tag{14.57}$$

which means that a change of power in the equivalent node is equal to the sum of changes of power in the replaced nodes.

Equation (14.57) can be written in matrix form as

$$\Delta P_{\mathrm{a}} = \mathbf{1}_{\mathrm{A}}^{\mathrm{T}} \cdot \Delta \boldsymbol{P}_{\mathrm{A}}. \tag{14.58}$$

Equation (14.58) gives

$$\Delta \boldsymbol{P}_{\mathrm{R}} = \boldsymbol{H}_{\mathrm{RR}} \Delta \boldsymbol{\delta}_{\mathrm{R}} + \boldsymbol{H}_{\mathrm{RA}} \Delta \boldsymbol{\delta}'_{\mathrm{A}}, \tag{14.59a}$$

$$\Delta \boldsymbol{P}_{\mathrm{A}} = \boldsymbol{H}_{\mathrm{AR}} \Delta \boldsymbol{\delta}_{\mathrm{R}} + \boldsymbol{H}_{\mathrm{AA}} \Delta \boldsymbol{\delta}'_{\mathrm{A}}. \tag{14.59b}$$

Substituting into Equations (14.59) the value from Equation (14.56) gives

$$\Delta \boldsymbol{P}_{\mathrm{R}} = \boldsymbol{H}_{\mathrm{RR}} \Delta \boldsymbol{\delta}_{\mathrm{R}} + \boldsymbol{H}_{\mathrm{RA}} \mathbf{1}_{\mathrm{A}} \cdot \Delta \delta'_{\mathrm{a}}, \tag{14.60a}$$

$$\Delta \boldsymbol{P}_{\mathrm{A}} = \boldsymbol{H}_{\mathrm{AR}} \Delta \boldsymbol{\delta}_{\mathrm{R}} + \boldsymbol{H}_{\mathrm{AA}} \mathbf{1}_{\mathrm{A}} \cdot \Delta \delta'_{\mathrm{a}}. \tag{14.60b}$$

Left-multiplying (14.60b) by $\mathbf{1}_{\mathrm{A}}^{\mathrm{T}}$ and taking into account (14.58) gives

$$\Delta P_{\mathrm{a}} = \mathbf{1}_{\mathrm{A}}^{\mathrm{T}} \boldsymbol{H}_{\mathrm{AR}} \Delta \boldsymbol{\delta}_{\mathrm{R}} + \mathbf{1}_{\mathrm{A}}^{\mathrm{T}} \boldsymbol{H}_{\mathrm{AA}} \mathbf{1}_{\mathrm{A}} \cdot \Delta \delta'_{\mathrm{a}}. \tag{14.61}$$

Equations (14.60a) and (14.61) may be merged in matrix form as

$$\begin{bmatrix} \Delta \boldsymbol{P}_{\mathrm{R}} \\ \Delta P_{\mathrm{a}} \end{bmatrix} = \begin{bmatrix} \boldsymbol{H}_{\mathrm{RR}} & \boldsymbol{H}_{\mathrm{RA}} \mathbf{1}_{\mathrm{A}} \\ \mathbf{1}_{\mathrm{A}}^{\mathrm{T}} \boldsymbol{H}_{\mathrm{AR}} & \mathbf{1}_{\mathrm{A}}^{\mathrm{T}} \boldsymbol{H}_{\mathrm{AA}} \mathbf{1}_{\mathrm{A}} \end{bmatrix} \begin{bmatrix} \Delta \boldsymbol{\delta}_{\mathrm{R}} \\ \Delta \delta'_{\mathrm{a}} \end{bmatrix}, \tag{14.62}$$

or

$$\begin{bmatrix} \Delta \boldsymbol{P}_{\mathrm{R}} \\ \Delta P_{\mathrm{a}} \end{bmatrix} = \begin{bmatrix} \boldsymbol{H}_{\mathrm{RR}} & \boldsymbol{H}_{\mathrm{Ra}} \\ \boldsymbol{H}_{\mathrm{aR}} & H_{\mathrm{aa}} \end{bmatrix} \begin{bmatrix} \Delta \boldsymbol{\delta}_{\mathrm{R}} \\ \Delta \delta'_{\mathrm{a}} \end{bmatrix}, \tag{14.63}$$

where

$$\boldsymbol{H}_{\mathrm{aR}} = \mathbf{1}_{\mathrm{A}}^{\mathrm{T}} \boldsymbol{H}_{\mathrm{AR}}, \quad \boldsymbol{H}_{\mathrm{Ra}} = \boldsymbol{H}_{\mathrm{RA}} \mathbf{1}_{\mathrm{A}}, \quad H_{\mathrm{aa}} = \mathbf{1}_{\mathrm{A}}^{\mathrm{T}} \boldsymbol{H}_{\mathrm{AA}} \mathbf{1}_{\mathrm{A}} \tag{14.64}$$

and $\boldsymbol{H}_{\mathrm{aR}}$ is a row vector, $\boldsymbol{H}_{\mathrm{Ra}}$ is a column vector, while H_{aa} is a scalar.

Note that $\boldsymbol{H}_{\mathrm{aR}}$ is created from $\boldsymbol{H}_{\mathrm{AR}}$ by adding up its rows and $\boldsymbol{H}_{\mathrm{Ra}}$ is created from $\boldsymbol{H}_{\mathrm{RA}}$ by adding up its columns. Element H_{aa} is created by adding up all the elements of $\boldsymbol{H}_{\mathrm{AA}}$. This means that aggregation of generators in the incremental model in effect adds up all the synchronizing powers.

The described aggregation method corresponding to Equation (14.62) was proposed by Di Caprio and Marconato (1975).

Now it will be shown that the linearized reduced model proposed by Di Caprio and Marconato corresponds to the linearized form of the reduced model obtained by Zhukov's aggregation. The operations of linearization and aggregation are commutative, which is illustrated in Figure 14.16.

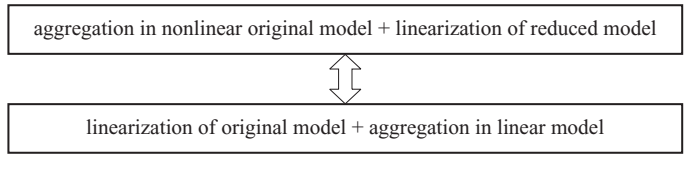
aggregation in nonlinear original model + linearization of reduced model
linearization of original model + aggregation in linear model

Figure 14.16 Illustration of the fact that aggregation and linearization are commutative.

A simple proof of this can be conducted in the complex-number domain by calculating the derivatives $\underline{J}_{ij} = \partial \underline{S}_i / \partial \delta_j$ directly from the apparent power $\underline{S}_i$ instead of real power $P_i = \mathrm{Re}_i$. Obviously $\underline{S}_i = P_i + \mathrm{j}Q_i$ and hence $H_{ij} = \partial P_i / \partial \delta'_j = \mathrm{Re}\underline{J}_{ij}$. Thus the proof conducted for $\underline{\boldsymbol{J}} = \left[\partial \underline{\boldsymbol{S}} / \partial \boldsymbol{\delta}'\right]$ is at the same time valid also for $\boldsymbol{H} = [\partial \boldsymbol{P} / \partial \boldsymbol{\delta}']$. Calculation of the derivative in the complex-number domain makes it possible to avoid complicated transformations of trigonometric functions which appear in the equations for real power.

14.6.2.1 Aggregation in the Linear Model

In the original model before aggregation (Figure 14.6) the apparent power for node $i \in \{\mathrm{R}\}$ can be expressed as

$$\underline{S}_i = \underline{V}_i \sum_{j \in \{\mathrm{R}\}} \underline{Y}^*_{ij} \underline{V}^*_j + \underline{V}_i \sum_{k \in \{\mathrm{A}\}} \underline{Y}^*_{ik} \underline{E}^*_k, \tag{14.65}$$

where

$$\underline{V}_i = V_i \mathrm{e}^{\mathrm{j}\delta_i}, \quad \underline{V}^*_j = V_j \mathrm{e}^{-\mathrm{j}\delta_j}, \quad \underline{E}^*_k = E_a \mathrm{e}^{-\mathrm{j}\delta'_k}. \tag{14.66}$$

Differentiating gives

$$\underline{J}_{ij} = \frac{\partial \underline{S}_i}{\partial \delta_j} = -\mathrm{j}\underline{V}_i \underline{Y}^*_{ij} \underline{V}^*_j \quad \text{and} \quad \underline{J}_{ik} = \frac{\partial \underline{S}_i}{\partial \delta'_k} = -\mathrm{j}\underline{V}_i \underline{Y}^*_{ik} \underline{E}^*_k. \tag{14.67}$$

Similarly one gets for $l \in \{\mathrm{A}\}$

$$\underline{S}_l = \underline{E}_l \sum_{j \in \{\mathrm{R}\}} \underline{Y}^*_{lj} \underline{V}^*_j + \underline{E}_l \sum_{k \in \{\mathrm{A}\}} \underline{Y}^*_{lk} \underline{E}^*_k, \tag{14.68}$$

where

$$\underline{E}_l = E_i \mathrm{e}^{\mathrm{j}\delta'_l}, \quad \underline{V}^*_j = V_j \mathrm{e}^{-\mathrm{j}\delta_j}, \quad \underline{E}^*_k = E_k \mathrm{e}^{-\mathrm{j}\delta'_k}. \tag{14.69}$$

After calculating the derivatives one gets

$$\underline{J}_{lj} = \frac{\partial \underline{S}_l}{\partial \delta_j} = -\mathrm{j}\underline{E}_l \underline{Y}^*_{lj} \underline{V}^*_j \quad \text{and} \quad \underline{J}_{lk} = \frac{\partial \underline{S}_l}{\partial \delta'_k} = -\mathrm{j}\underline{E}_l \underline{Y}^*_{lk} \underline{E}^*_k. \tag{14.70}$$

After aggregation of group $\{\mathrm{A}\}$ using the method of Di Caprio and Marconato, that is by adding the synchronizing powers, one gets

$$\underline{J}_{i\mathrm{a}} = \sum_{k \in \{\mathrm{A}\}} \underline{J}_{ik} = -\mathrm{j}\underline{V}_i \sum_{k \in \{\mathrm{A}\}} \underline{Y}^*_{ik} \underline{E}^*_k, \tag{14.71a}$$

$$\underline{J}_{\mathrm{a}j} = \sum_{l \in \{\mathrm{A}\}} \underline{J}_{lj} = -\mathrm{j}\underline{V}^*_j \sum_{l \in \{\mathrm{A}\}} \underline{Y}^*_{lj} \underline{E}_l. \tag{14.71b}$$

Elements $\underline{J}_{ij}$ for $i, j \in \{\mathrm{R}\}$ do not change during aggregation of group $\{\mathrm{A}\}$.

14.6.2.2 Linearization of the Reduced Nonlinear Model

In the reduced model obtained after aggregation by Zhukov's method (Figure 14.6), the apparent power for node $i \in \{\mathrm{R}\}$ can be expressed as

$$\underline{S}_i = \underline{V}_i \sum_{j\in\{\mathrm{R}\}} \underline{Y}^*_{ij}\underline{V}^*_j + \underline{V}_i \underline{Y}^*_{i\mathrm{a}}\underline{E}^*_{\mathrm{a}}, \tag{14.72}$$

where

$$\underline{V}_i = V_i \mathrm{e}^{\mathrm{j}\delta_i}, \quad \underline{V}^*_j = V_j \mathrm{e}^{-\mathrm{j}\delta_j}, \quad \underline{E}^*_{\mathrm{a}} = E_{\mathrm{a}} \mathrm{e}^{-\mathrm{j}\delta'_{\mathrm{a}}}. \tag{14.73}$$

Differentiation gives

$$\underline{J}_{ij} = \frac{\partial \underline{S}_i}{\partial \delta_j} = -\mathrm{j}\underline{V}_i \underline{Y}^*_{ij}\underline{V}^*_j, \quad \underline{J}_{i\mathrm{a}} = \frac{\partial \underline{S}_i}{\partial \delta'_{\mathrm{a}}} = -\mathrm{j}\underline{V}_i \underline{Y}^*_{i\mathrm{a}}\underline{E}^*_{\mathrm{a}}. \tag{14.74}$$

Utilizing Equation (14.15) one can write

$$\underline{Y}_{i\mathrm{a}} = \sum_{k\in\{\mathrm{A}\}} \underline{Y}_{ik} \frac{\underline{E}_k}{\underline{E}_{\mathrm{a}}},$$

and after substituting in the second of Equations (14.74) one finally gets

$$\underline{J}_{i\mathrm{a}} = \frac{\partial \underline{S}_i}{\partial \delta'_{\mathrm{a}}} = -\mathrm{j}\underline{V}_i \sum_{k\in\{\mathrm{A}\}} \underline{Y}^*_{ik} \frac{\underline{E}^*_k}{\underline{E}^*_{\mathrm{a}}} \underline{E}^*_{\mathrm{a}} = -\mathrm{j}\underline{V}_i \sum_{k\in\{\mathrm{A}\}} \underline{Y}^*_{ik}\underline{E}^*_k. \tag{14.75}$$

The apparent power in the equivalent node (Figure 14.6) is given by

$$\underline{S}_{\mathrm{a}} = \underline{E}_{\mathrm{a}} \sum_{j\in\{\mathrm{R}\}} \underline{Y}^*_{\mathrm{a}j}\underline{V}^*_j + \underline{E}_{\mathrm{a}}\underline{Y}^*_{\mathrm{aa}}\underline{E}^*_{\mathrm{a}}. \tag{14.76}$$

Differentiation gives

$$\underline{J}_{\mathrm{a}j} = \frac{\partial \underline{S}_{\mathrm{a}}}{\partial \delta_j} = -\mathrm{j}\underline{E}_{\mathrm{a}} \underline{Y}^*_{\mathrm{a}j}\underline{V}^*_j. \tag{14.77}$$

Utilizing Equation (14.19) one can write

$$\underline{Y}_{\mathrm{a}j} = \sum_{l\in\{\mathrm{A}\}} \frac{\underline{E}^*_l}{\underline{E}^*_{\mathrm{a}}} \underline{Y}_{lj},$$

and after substituting into Equation (14.77) one finally gets

$$\underline{J}_{\mathrm{a}j} = \frac{\partial \underline{S}_{\mathrm{a}}}{\partial \delta_j} = -\mathrm{j}\underline{V}^*_j \underline{E}_{\mathrm{a}} \sum_{l\in\{\mathrm{A}\}} \frac{\underline{E}_l}{\underline{E}_{\mathrm{a}}} \underline{Y}^*_{lj} = -\,\mathrm{j}\underline{V}^*_j \sum_{l\in\{\mathrm{A}\}} \underline{Y}^*_{lj}\underline{E}_l. \tag{14.78}$$

Comparing (14.71a) with (14.75) and (14.71b) with (14.78) clearly shows that the values obtained through aggregation in the linear model, and by linearization in the reduced model, are the same. Equivalence of the synchronizing power $\underline{J}_{\mathrm{aa}} = \partial \underline{S}_{\mathrm{a}}/\partial \delta'_{\mathrm{a}}$ in both cases is due to the self-synchronizing power being equal to the sum of mutual synchronizing powers taken with the opposite sign – see Equations (3.164) and (3.165) in Section 3.5. This concludes the proof that aggregation and linearization are commutative.

14.6.3 Modal Interpretation of Exact Coherency

In Chapter 12 power swings in the linearized power system model were analysed using modal analysis. Each mode (corresponding to an eigenvalue of the state matrix) has a frequency of oscillation and a damping ratio. Now it will be shown that exact coherency can also be analysed using modal analysis. Also, a proof of the exact coherency condition given by (14.39) will be conducted.

Partial inversion (Appendix A.2) of Equation (14.54) gives

$$\Delta \boldsymbol{P}_{\mathrm{A}} = \boldsymbol{H}_{\mathrm{A}} \Delta \boldsymbol{\delta}'_{\mathrm{A}} + \boldsymbol{R}_{\mathrm{A}} \Delta \boldsymbol{P}_{\mathrm{R}}, \tag{14.79}$$

where

$$\boldsymbol{H}_{\mathrm{A}} = \boldsymbol{H}_{\mathrm{AA}} - \boldsymbol{H}_{\mathrm{AR}} \boldsymbol{H}_{\mathrm{RR}}^{-1} \boldsymbol{H}_{\mathrm{RA}}, \tag{14.80}$$

$$\boldsymbol{R}_{\mathrm{A}} = \boldsymbol{H}_{\mathrm{AR}} \boldsymbol{H}_{\mathrm{RR}}^{-1}. \tag{14.81}$$

The matrix equation for the motion of rotors in group {A} can be written in a similar way to Equation (11.23), while for further considerations it is more convenient to express the equations as

$$M_{\mathrm{A}} \Delta \ddot{\delta}'_{\mathrm{A}} = -\boldsymbol{H}_{\mathrm{A}} \Delta \delta'_{\mathrm{A}} - \boldsymbol{R}_{\mathrm{A}} \Delta \boldsymbol{P}_{\mathrm{R}} - \mathbf{D}_{\mathrm{A}} \Delta \dot{\boldsymbol{\delta}}'_{\mathrm{A}}, \tag{14.82}$$

where $\boldsymbol{M}_{\mathrm{A}}$ and $\boldsymbol{D}_{\mathrm{A}}$ are diagonal matrices containing inertia and damping coefficients. Neglecting damping, the equation can be written as

$$\Delta \ddot{\boldsymbol{\delta}}'_{\mathrm{A}} = -\boldsymbol{M}_{\mathrm{A}}^{-1} \boldsymbol{H}_{\mathrm{A}} \Delta \boldsymbol{\delta}'_{\mathrm{A}} - \boldsymbol{M}_{\mathrm{A}}^{-1} \boldsymbol{R}_{\mathrm{A}} \Delta \boldsymbol{P}_{\mathrm{R}}. \tag{14.83}$$

This is the state equation of group {A} in which changes of power $\Delta \boldsymbol{P}_{\mathrm{R}}$ in nodes {R} are treated as inputs. This is a second-order equation (discussed in Section 12.2) which can be replaced by a first-order matrix equation

$$\begin{bmatrix} \Delta \dot{\boldsymbol{\delta}}'_{\mathrm{A}} \\ \hline \Delta \dot{\boldsymbol{\omega}}_{\mathrm{A}} \end{bmatrix} = \left[\begin{array}{c|c} \mathbf{0} & 1 \\ \hline -\boldsymbol{M}_{\mathrm{A}}^{-1} \boldsymbol{H}_{\mathrm{A}} & \mathbf{0} \end{array}\right] \begin{bmatrix} \Delta \boldsymbol{\delta}'_{\mathrm{A}} \\ \hline \Delta \boldsymbol{\omega}_{\mathrm{A}} \end{bmatrix} - \begin{bmatrix} \mathbf{0}_{\mathrm{A}} \\ \hline \boldsymbol{M}_{\mathrm{A}}^{-1} \boldsymbol{R}_{\mathrm{A}} \Delta \boldsymbol{P}_{\mathrm{R}} \end{bmatrix}, \tag{14.84}$$

where $\mathbf{0}_{\mathrm{A}}$ is a zero column vector and $\Delta \boldsymbol{\omega}_{\mathrm{A}} = \Delta \boldsymbol{\delta}'_{\mathrm{A}}$. Equation (14.84) has the form of Equation (12.95) described in Section 12.1.5. Now changes of $\Delta \boldsymbol{\delta}'_{\mathrm{A}}$ enforced by changes of $\Delta \boldsymbol{P}_{\mathrm{R}}$ will be considered using modal analysis.

Let μ_i be an eigenvalue of the state matrix $\boldsymbol{a} = -\boldsymbol{M}_{\mathrm{A}}^{-1} \boldsymbol{H}_{\mathrm{A}}$ from Equation (14.83) and let $\boldsymbol{w}_i$ and $\boldsymbol{u}_i$ be respectively the right and left eigenvectors of this matrix. It was shown in Section 12.2.2 that a system is stable when all the eigenvalues μ_i are real and negative. The eigenvalues λ_i of the state matrix in Equation (14.84) are equal to $\lambda_i = \sqrt{\mu_i}$ and, as $\mu_i < 0$, they are imaginary numbers (see Figure 12.5). To simplify considerations, eigenvalues μ_i of the state matrix in Equation (14.83) will be analysed rather than λ_i.

From Section 12.1.1

$$\boldsymbol{W} = \begin{bmatrix} \boldsymbol{w}_1 & \boldsymbol{w}_2 & \cdots & \boldsymbol{w}_N \end{bmatrix} \quad \text{and} \quad \boldsymbol{U} = \boldsymbol{W}^{-1} = \begin{bmatrix} \boldsymbol{u}_1 \\ \boldsymbol{u}_2 \\ \vdots \\ \boldsymbol{u}_N \end{bmatrix}, \tag{14.85}$$

where $\boldsymbol{W}$ and $\boldsymbol{U}$ are square matrices consisting of right and left eigenvectors.

Equation (3.164) proved in Section 3.6 showed that the sum of elements in each row of matrix $\boldsymbol{H} = [\partial \boldsymbol{P}/\partial \boldsymbol{\delta}']$ is equal to zero. Let $\mathbf{1}_\mathrm{A}$, $\mathbf{1}_\mathrm{R}$ and $\mathbf{0}_\mathrm{A}$, $\mathbf{0}_\mathrm{R}$ be column vectors with all elements equal to zero or one, respectively. Then Equation (14.54) can be transformed, using (3.164), to

$$\begin{bmatrix} \mathbf{0}_\mathrm{R} \\ \mathbf{0}_\mathrm{A} \end{bmatrix} = \begin{bmatrix} \boldsymbol{H}_{\mathrm{RR}} & \boldsymbol{H}_{\mathrm{RA}} \\ \boldsymbol{H}_{\mathrm{AR}} & \boldsymbol{H}_{\mathrm{AA}} \end{bmatrix} \begin{bmatrix} \mathbf{1}_\mathrm{R} \\ \mathbf{1}_\mathrm{A} \end{bmatrix}. \tag{14.86}$$

That is, for $\Delta\boldsymbol{\delta}'_\mathrm{A} = \mathbf{1}_\mathrm{A}$ and $\Delta\boldsymbol{\delta}_\mathrm{R} = \mathbf{1}_\mathrm{R}$ one gets $\Delta\boldsymbol{P}_\mathrm{A} = \mathbf{0}_\mathrm{A}$ and $\Delta\boldsymbol{P}_\mathrm{R} = \mathbf{0}_\mathrm{R}$. Substituting these equations into (14.79) gives $\boldsymbol{H}_\mathrm{A}\mathbf{1}_\mathrm{A} = \mathbf{1}_\mathrm{A}$. This means that partial inversion given by (14.80) maintains property (3.164) that the sum of elements in each row is equal to zero. Left-multiplying the last equation by $\boldsymbol{M}_\mathrm{A}^{-1}$ gives

$$\boldsymbol{a} \cdot \mathbf{1}_\mathrm{A} = -\boldsymbol{M}_\mathrm{A}^{-1}\boldsymbol{H}_\mathrm{A} \cdot \mathbf{1}_\mathrm{A} = \mathbf{0}_\mathrm{A} = 0 \cdot \mathbf{1}_\mathrm{A}, \tag{14.87}$$

that is $\boldsymbol{a} \cdot \mathbf{1}_\mathrm{A} = 0 \cdot \mathbf{1}_\mathrm{A}$. This equation is the same as Equation (12.1) defining the eigenvalue and the right eigenvector. Hence finally

$$\mu_1 = 0 \quad \text{and} \quad \boldsymbol{w}_1 = \mathbf{1}_\mathrm{A}. \tag{14.88}$$

This leads to an important conclusion that one of the eigenvalues of the state matrix $\boldsymbol{a} = -\boldsymbol{M}_\mathrm{A}^{-1}\boldsymbol{H}_\mathrm{A}$ in Equation (14.83) is equal to zero and the corresponding right eigenvector consists of ones.

As $\boldsymbol{U}\boldsymbol{W} = \mathbf{1}$ is a diagonal identity matrix, the following hold for the right and left eigenvectors defined by (14.85): $\boldsymbol{u}_1\boldsymbol{w}_1 = 1$; $\boldsymbol{u}_2\boldsymbol{w}_1 = 0$; …; $\boldsymbol{u}_n\boldsymbol{w}_1 = 0$. Substituting $\boldsymbol{w}_1 = \mathbf{1}_\mathrm{A}$ gives

$$\begin{aligned} &\boldsymbol{u}_1\mathbf{1}_\mathrm{A} = 1 \\ &\boldsymbol{u}_2\mathbf{1}_\mathrm{A} = 0 \\ &\vdots \\ &\boldsymbol{u}_n\mathbf{1}_\mathrm{A} = 0. \end{aligned} \tag{14.89}$$

These relationships are crucial for further considerations.

As in Equation (12.41), new variables $\boldsymbol{z}$ are introduced, referred to as the modal variables, which are related to the state variables $\Delta\boldsymbol{\delta}'_\mathrm{A}$ by

$$\Delta\boldsymbol{\delta}'_\mathrm{A} = \boldsymbol{W}\boldsymbol{z} \quad \text{and} \quad \boldsymbol{z} = \boldsymbol{U}\Delta\boldsymbol{\delta}'_\mathrm{A}. \tag{14.90}$$

Expanding the second equation gives

$$\begin{bmatrix} z_1 \\ z_2 \\ \vdots \\ z_n \end{bmatrix} = \begin{bmatrix} \boldsymbol{u}_1 \\ \boldsymbol{u}_2 \\ \vdots \\ \boldsymbol{u}_n \end{bmatrix} \cdot \Delta\boldsymbol{\delta}'_\mathrm{A} = \begin{bmatrix} \boldsymbol{u}_1\Delta\boldsymbol{\delta}'_\mathrm{A} \\ \boldsymbol{u}_2\Delta\boldsymbol{\delta}'_\mathrm{A} \\ \vdots \\ \boldsymbol{u}_n\Delta\boldsymbol{\delta}'_\mathrm{A} \end{bmatrix}. \tag{14.91}$$

The generators from group (A) are assumed to be exactly coherent, that is they satisfy (14.28) and (14.56). Substituting $\Delta\boldsymbol{\delta}'_\mathrm{A}$ for the right hand side of Equation (14.56) and taking into account (14.89) leads to

$$\begin{bmatrix} z_1 \\ z_2 \\ \vdots \\ z_n \end{bmatrix} = \begin{bmatrix} \boldsymbol{u}_1\mathbf{1}_\mathrm{A} \\ \boldsymbol{u}_2\mathbf{1}_\mathrm{A} \\ \vdots \\ \boldsymbol{u}_n\mathbf{1}_\mathrm{A} \end{bmatrix} \cdot \Delta\delta'_\mathrm{a} = \begin{bmatrix} 1 \\ 0 \\ \vdots \\ 0 \end{bmatrix} \cdot \Delta\delta'_\mathrm{a} = \begin{bmatrix} \Delta\delta'_\mathrm{a} \\ 0 \\ \vdots \\ 0 \end{bmatrix}. \tag{14.92}$$

This means that if group {A} is exactly coherent then among its n modal variables there is only one modal variable $z_1(t)$ excited. This modal variable is responsible for the swinging of the whole group

against the rest of the system. The remaining modal variables $z_2(t), \ldots, z_n(t)$ corresponding to the swings inside the group are not excited, that is $z_2(t) = \cdots = z_n(t) = 0$. These considerations lead to the following conclusion:

> In modal analysis, the exact electromechanical coherency of generators belonging to the external subsystem corresponds to a situation where modal variables representing the swinging of generator rotors inside the coherent group are not excited by disturbances in the internal subsystem. Disturbances in the internal subsystem excite only that modal variable that represents the swinging of the whole coherent group with respect to the rest of the system.

Now it will be investigated what the structure of matrix $\boldsymbol{M}_{\mathrm{A}}^{-1}\boldsymbol{R}_{\mathrm{A}}$ in Equation (14.84) must be so that disturbances in the internal subsystem represented by $\Delta\boldsymbol{P}_{\mathrm{R}}$ cannot excite modal variables $z_2(t), \ldots, z_n(t)$. Section 12.1.6 outlined the general conditions for a particular modal variable not to be excited and this theory will be applied now. Substituting (14.90) into (14.83) gives

$$\ddot{\boldsymbol{z}} = \Lambda \boldsymbol{z} - \boldsymbol{r} \cdot \Delta\boldsymbol{P}_{\mathrm{R}}, \tag{14.93}$$

where

$$\boldsymbol{r} = \boldsymbol{W}^{-1}\boldsymbol{M}_{\mathrm{A}}^{-1}\boldsymbol{R}_{\mathrm{A}}. \tag{14.94}$$

Substituting (14.81) for $\boldsymbol{R}_{\mathrm{A}}$ gives

$$\boldsymbol{r} = \boldsymbol{W}^{-1}\boldsymbol{M}_{\mathrm{A}}^{-1}\boldsymbol{H}_{\mathrm{AR}}\boldsymbol{H}_{\mathrm{RR}}^{-1}, \tag{14.95}$$

and

$$\boldsymbol{W}\boldsymbol{r}\boldsymbol{H}_{\mathrm{RR}} = \boldsymbol{M}_{\mathrm{A}}^{-1}\boldsymbol{H}_{\mathrm{AR}}. \tag{14.96}$$

Equation (14.93) shows that excitation of modal variables enforced by $\Delta\boldsymbol{P}_{\mathrm{R}}$ is decided by matrix $\boldsymbol{r}$ given by (14.94). Hence investigation of the structure of matrix $\boldsymbol{r}$ should lead to the derivation of a condition for only one modal variable to be excited, that is the condition for exact coherency. To simplify considerations further, Equation (14.93) can be rewritten as

$$\begin{bmatrix} \ddot{z}_1 \\ \ddot{z}_2 \\ \vdots \\ \ddot{z}_n \end{bmatrix} = \begin{bmatrix} \lambda_1 & & & \\ & \lambda_2 & & \\ & & \ddots & \\ & & & \lambda_n \end{bmatrix} \begin{bmatrix} z_1 \\ z_2 \\ \vdots \\ z_n \end{bmatrix} - \begin{bmatrix} \boldsymbol{r}_1 \\ \boldsymbol{r}_2 \\ \vdots \\ \boldsymbol{r}_n \end{bmatrix} \cdot \Delta\boldsymbol{P}_{\mathrm{R}}. \tag{14.97}$$

Equation (14.97) shows that any input $\Delta\boldsymbol{P}_{\mathrm{R}}$ will excite only one modal variable $z_1(t)$ if matrix $\boldsymbol{r}$ has the following structure:

$$\boldsymbol{r} = \begin{bmatrix} \boldsymbol{r}_1 \\ \boldsymbol{r}_2 \\ \vdots \\ \boldsymbol{r}_n \end{bmatrix} = \begin{bmatrix} \boldsymbol{r}_1 \\ \boldsymbol{0} \\ \vdots \\ \boldsymbol{0} \end{bmatrix}, \tag{14.98}$$

that is it will have only one row (the first) non-zero. The first column of $\boldsymbol{W}$ consists of ones – see (14.88). Now taking into account (14.98) leads to

$$\boldsymbol{W}\boldsymbol{r} = \begin{bmatrix} \mathbf{1}_{\mathrm{A}} & \boldsymbol{w}_2 & \cdots & \boldsymbol{w}_n \end{bmatrix} \cdot \begin{bmatrix} \boldsymbol{r}_1 \\ \mathbf{0} \\ \vdots \\ \mathbf{0} \end{bmatrix} = \begin{bmatrix} \boldsymbol{r}_1 \\ \boldsymbol{r}_1 \\ \vdots \\ \boldsymbol{r}_1 \end{bmatrix}, \tag{14.99}$$

which means that a matrix equal to the product $\boldsymbol{W}\boldsymbol{r}$ has all its rows identical. Then the left hand side of Equation (14.96) will be

$$\boldsymbol{W}\boldsymbol{r}\,\boldsymbol{H}_{\mathrm{RR}} = \begin{bmatrix} \boldsymbol{r}_1 \\ \boldsymbol{r}_1 \\ \vdots \\ \boldsymbol{r}_1 \end{bmatrix} \cdot \boldsymbol{H}_{\mathrm{RR}} = \begin{bmatrix} \boldsymbol{h}_1 \\ \boldsymbol{h}_1 \\ \vdots \\ \boldsymbol{h}_1 \end{bmatrix}, \tag{14.100}$$

that is it will also be a matrix of identical rows. Substituting (14.100) into (14.96) leads to

$$\boldsymbol{M}_{\mathrm{A}}^{-1}\boldsymbol{H}_{\mathrm{AR}} = \begin{bmatrix} \boldsymbol{h}_1 \\ \boldsymbol{h}_1 \\ \vdots \\ \boldsymbol{h}_1 \end{bmatrix}, \tag{14.101}$$

that is a matrix equal to the product $\boldsymbol{M}_{\mathrm{A}}^{-1}\boldsymbol{H}_{\mathrm{AR}}$ also has all its rows identical. Hence all the elements in its column k are identical, which may be written as

$$\frac{H_{ik}}{M_i} = \frac{H_{jk}}{M_j} \quad \text{for} \quad i, j \in \{\mathrm{A}\}, \quad k \in \{\mathrm{R}\}. \tag{14.102}$$

This means that the necessary and sufficient condition for exciting only one modal variable $z_1(t)$ by any disturbance $\Delta\boldsymbol{P}_{\mathrm{R}}$ in Equation (14.97), and therefore for group $\{\mathrm{A}\}$ to be exactly coherent, is that condition (14.102) is satisfied. Remember that the excited modal variable $z_1(t)$ corresponds to swings of group $\{\mathrm{A}\}$ with respect to the rest of the system and the modes $z_2(t) = \cdots = z_n(t) = 0$ correspond to the internal swinging modes inside group $\{\mathrm{A}\}$ that are not excited.

Clearly Equations (14.102) and (14.39) are identical. The conclusion is that modal analysis confirms the considerations in Section 14.5.

14.6.4 Eigenvalues and Eigenvectors of the Equivalent Model

The analysis in the previous subsection was undertaken under an assumption that, in the state equation (14.83), changes of power in the remaining part of the system constitute a disturbance. Such a model was used to investigate internal group swings and external swings between the group and the rest of the system. The model could not be used to asses the influence of aggregation of nodes in group $\{\mathrm{A}\}$ on the modes corresponding to oscillations in the rest of the system. That task will require the creation of the incremental model of the whole system and an investigation of how aggregation of group $\{\mathrm{A}\}$ influences eigenvalues and eigenvectors in the whole system. This difficult task will be simplified by reducing the system model using aggregation which will be shown as a projection of the state space on a subspace.

Let $\boldsymbol{x}$ be the state vector of a dynamic system described by the state equation

$$\dot{\boldsymbol{x}} = \boldsymbol{A}\boldsymbol{x}. \tag{14.103}$$

System reduction will be undertaken by projecting vector $\boldsymbol{x}$ onto a smaller vector

$$\boldsymbol{x}_{\mathrm{e}} = \boldsymbol{C}\boldsymbol{x}, \tag{14.104}$$

where $\boldsymbol{C}$ is a rectangular matrix defining this projection and further referred to as the *projection matrix*. The lower index comes from the word 'equivalent'. The reduced model is described by

$$\dot{\boldsymbol{x}}_{\mathrm{e}} = \boldsymbol{a}\boldsymbol{x}_{\mathrm{e}}, \tag{14.105}$$

where $\boldsymbol{a}$ is a square matrix that will now be expressed using matrices $\boldsymbol{A}$ and $\boldsymbol{C}$.

Equation (14.105) describes a reduced dynamic system obtained by the reduction of the state vector using transformation (14.104).

Differentiating both sides of Equation (14.104) gives $\dot{\boldsymbol{x}}_{\mathrm{e}} = \boldsymbol{C}\dot{\boldsymbol{x}}$. Substitution of $\dot{\boldsymbol{x}}_{\mathrm{e}}$ by the right hand side of Equation (14.105) leads to $\boldsymbol{a}\boldsymbol{x}_{\mathrm{e}} = \boldsymbol{C}\boldsymbol{A}\boldsymbol{x}$. Substitution of $\boldsymbol{x}_{\mathrm{e}}$ by the right hand side of (14.104) gives $\boldsymbol{a}\boldsymbol{C}\boldsymbol{x} = \boldsymbol{C}\boldsymbol{A}\boldsymbol{x}$ which finally leads to

$$\boldsymbol{a}\boldsymbol{C} = \boldsymbol{C}\boldsymbol{A}. \tag{14.106}$$

Right-multiplying by $\boldsymbol{C}^{\mathrm{T}}$ gives $\boldsymbol{a}\boldsymbol{C}\boldsymbol{C}^{\mathrm{T}} = \boldsymbol{C}\boldsymbol{A}\boldsymbol{C}^{\mathrm{T}}$ leading to

$$\boldsymbol{a} = \boldsymbol{C}\boldsymbol{A}\boldsymbol{C}^{\mathrm{T}}(\boldsymbol{C}\boldsymbol{C}^{\mathrm{T}})^{-1}, \tag{14.107}$$

where matrix $\boldsymbol{C}\boldsymbol{C}^{\mathrm{T}}$ is a square matrix with rank equal to the number of state variables in the reduced model.

The relationship given by (14.106) is very important because it will make it possible to show that the reduced model (14.105) obtained from reducing the state vector using transformation (14.104) partially retains eigenvalues and eigenvectors of the original (unreduced) system (14.103).

Let λ_i be an eigenvalue of the state matrix $\boldsymbol{A}$ in Equation (14.103) and let $\boldsymbol{w}_i$ be a right eigenvector of that matrix. Then according to the definition of eigenvectors, $\boldsymbol{A}\boldsymbol{w}_i = \lambda_i \boldsymbol{w}_i$. Left-multiplying by $\boldsymbol{C}$ gives $\boldsymbol{C}\boldsymbol{A}\boldsymbol{w}_i = \lambda_i \boldsymbol{C}\boldsymbol{w}_i$. Substitution of $\boldsymbol{C}\boldsymbol{A}$ by the left hand side of (14.106) results in $\boldsymbol{a}\boldsymbol{C}\boldsymbol{w}_i = \lambda_i \boldsymbol{C}\boldsymbol{w}_i$ or

$$\boldsymbol{a}\boldsymbol{w}_{\mathrm{e}i} = \lambda_i \boldsymbol{w}_{\mathrm{e}i}, \tag{14.108}$$

where

$$\boldsymbol{w}_{\mathrm{e}i} = \boldsymbol{C}\boldsymbol{w}_i. \tag{14.109}$$

Equation (14.108) shows that for each $\boldsymbol{w}_{\mathrm{e}i} \neq \boldsymbol{0}$ the number λ_i is an eigenvalue of matrix $\boldsymbol{a}$ and $\boldsymbol{w}_{\mathrm{e}i}$ is the corresponding right eigenvector. Obviously λ_i is also an eigenvalue of $\boldsymbol{A}$. Equation (14.109) shows that vector $\boldsymbol{w}_{\mathrm{e}i}$ is created by the reduction of vector $\boldsymbol{w}_i$. This means that by satisfying the condition

$$\boldsymbol{w}_{\mathrm{e}i} = \boldsymbol{C}\boldsymbol{w}_i \neq \boldsymbol{0}, \tag{14.110}$$

the reduced dynamic system (14.105) obtained by reducing the state vector using (14.104) partially retains eigenvalues and eigenvectors of the original (unreduced) system (14.103). Note that the relationship between eigenvector $\boldsymbol{w}_{\mathrm{e}i}$ of the reduced model and eigenvector $\boldsymbol{w}_i$ of the original (unreduced) model is the same as that between the state vector $\boldsymbol{x}_{\mathrm{e}}$ and the state vector $\boldsymbol{x}$. This means that $\boldsymbol{w}_{\mathrm{e}i}$ corresponds to the projection of $\boldsymbol{w}_i$ obtained using the projection matrix $\boldsymbol{C}$.

Obviously condition (14.110) is not satisfied for every matrix $\boldsymbol{C}$ and the reduced model does not maintain all eigenvalues and eigenvectors of the original (unreduced) model.

In the case of the incremental model of a power system, Machowski (1985) showed that the projection matrix should be of the following form:

$$\boldsymbol{C} = \left[\begin{array}{ccc:c} 1 & & & \\ & \ddots & & \mathbf{0} \\ & & 1 & \\ \hdashline & \mathbf{0} & & \frac{1}{n}\ \frac{1}{n}\ \cdots\ \frac{1}{n} \end{array}\right] = \left[\begin{array}{c:c} \mathbf{1} & \mathbf{0} \\ \hdashline \mathbf{0} & \frac{1}{n}\mathbf{1}_{\mathrm{A}}^{\mathrm{T}} \end{array}\right], \tag{14.111}$$

where $\mathbf{1}_{\mathrm{A}}$ is a vector of ones and n is the number of generators in group $\{\mathrm{A}\}$.

The discussed reduction using the projection matrix may be applied to Equation (14.84) or (14.83). This will be shown for the latter since: (i) the state matrix in (14.83) is simpler than in (14.84); (ii) there is an exact relationship $\lambda_i = \sqrt{\mu_i}$ between the eigenvalues of both matrices.

When applying the projection matrix (14.111), vector $\Delta\boldsymbol{\delta}'$ in Equation (14.62) is transformed in the following way:

$$\boldsymbol{C}\left[\begin{array}{c} \Delta\boldsymbol{\delta}'_{\mathrm{R}} \\ \Delta\boldsymbol{\delta}'_{\mathrm{A}} \end{array}\right] = \left[\begin{array}{c} \Delta\boldsymbol{\delta}'_{\mathrm{R}} \\ \Delta\delta'_{\mathrm{a}} \end{array}\right], \tag{14.112}$$

where

$$\Delta\delta'_{\mathrm{a}} = \frac{1}{n}\sum_{j\in\{\mathrm{A}\}} \Delta\delta'_j. \tag{14.113}$$

Equation (14.113) shows that, when using the discussed reduction method, the rotor of the equivalent generator moves on average with respect to all the rotors of aggregated generators. Obviously, for exactly coherent generators this movement is the same for all the generators in group $\{\mathrm{A}\}$ and its average value is equal simply to the value for each generator in the group.

For matrix $\boldsymbol{C}$ in the structure (14.111) it can be shown that

$$\boldsymbol{C}^{\mathrm{T}}(\boldsymbol{C}\boldsymbol{C}^{\mathrm{T}})^{-1} = \left[\begin{array}{ccc:c} 1 & & & \\ & \ddots & & \mathbf{0}_{\mathrm{A}} \\ & & 1 & \\ \hdashline & & & 1 \\ & & & 1 \\ & \mathbf{0}_{\mathrm{RA}} & & \vdots \\ & & & 1 \end{array}\right] = \left[\begin{array}{c:c} \mathbf{1} & \mathbf{0}_{\mathrm{A}} \\ \hdashline \mathbf{0}_{\mathrm{RA}} & \mathbf{1}_{\mathrm{A}} \end{array}\right] = \boldsymbol{B}^{\mathrm{T}}. \tag{14.114}$$

Thus the state matrix of the reduced model given by Equation (14.107) takes the simple form

$$\boldsymbol{a} = \boldsymbol{C}\boldsymbol{A}\boldsymbol{B}^{\mathrm{T}}. \tag{14.115}$$

The matrix equation of motion, with damping neglected, for the original model (Figure 14.6a) containing generators in groups $\{\mathrm{A}\}$ and $\{\mathrm{R}\}$ can be written similarly to Equation (11.23):

$$\left[\begin{array}{c} \Delta\ddot{\boldsymbol{\delta}}'_{\mathrm{R}} \\ \hdashline \Delta\ddot{\boldsymbol{\delta}}'_{\mathrm{A}} \end{array}\right] = -\left[\begin{array}{c:c} \boldsymbol{M}_{\mathrm{R}}^{-1}\boldsymbol{H}_{\mathrm{RR}} & \boldsymbol{M}_{\mathrm{R}}^{-1}\boldsymbol{H}_{\mathrm{RA}} \\ \hdashline \boldsymbol{M}_{\mathrm{A}}^{-1}\boldsymbol{H}_{\mathrm{AR}} & \boldsymbol{M}_{\mathrm{A}}^{-1}\boldsymbol{H}_{\mathrm{AA}} \end{array}\right]\left[\begin{array}{c} \Delta\boldsymbol{\delta}'_{\mathrm{R}} \\ \hdashline \Delta\boldsymbol{\delta}'_{\mathrm{A}} \end{array}\right]. \tag{14.116}$$

After applying reduction using matrix $\boldsymbol{C}$ in the form (14.111), the state vector is reduced to the form (14.112) while Equation (14.116) reduces to

$$\begin{bmatrix} \Delta\ddot{\boldsymbol{\delta}}'_{\mathrm{R}} \\ \hline \Delta\ddot{\delta}'_{\mathrm{a}} \end{bmatrix} = -\left[\begin{array}{c|c} \boldsymbol{M}_{\mathrm{R}}^{-1}\boldsymbol{H}_{\mathrm{RR}} & \boldsymbol{M}_{\mathrm{R}}^{-1}\boldsymbol{H}_{\mathrm{RA}}\mathbf{1}_{\mathrm{A}} \\ \hline \dfrac{1}{n}\mathbf{1}_{\mathrm{A}}^{\mathrm{T}}\boldsymbol{M}_{\mathrm{A}}^{-1}\boldsymbol{H}_{\mathrm{AR}} & \dfrac{1}{n}1_{\mathrm{A}}^{\mathrm{T}}\boldsymbol{M}_{\mathrm{A}}^{-1}\boldsymbol{H}_{\mathrm{AA}}\mathbf{1}_{\mathrm{A}} \end{array}\right] \begin{bmatrix} \Delta\boldsymbol{\delta}'_{\mathrm{R}} \\ \hline \Delta\delta'_{\mathrm{a}} \end{bmatrix}, \tag{14.117}$$

where the state matrix has been calculated according to (14.115). As shown previously, the reduced model given by (14.117) partially retains eigenvalues and eigenvectors of the original (unreduced) model of (14.116).

It is easy to see some similarity between the described reduced model (14.117) and the reduced model obtained using the Di Caprio and Marconato aggregation described in Section 14.6.2. In both cases there is a summation of matrix elements corresponding to multiplication by $\mathbf{1}_{\mathrm{A}}$ and $\mathbf{1}_{\mathrm{A}}^{\mathrm{T}}$. Using Equation (14.62) obtained from the Di Caprio and Marconato aggregation. it is possible, as in (14.117), to write the following state equation:

$$\begin{bmatrix} \Delta\ddot{\boldsymbol{\delta}}'_{\mathrm{R}} \\ \hline \Delta\ddot{\delta}'_{\mathrm{a}} \end{bmatrix} = -\left[\begin{array}{c|c} \boldsymbol{M}_{\mathrm{R}}^{-1}\boldsymbol{H}_{\mathrm{RR}} & \boldsymbol{M}_{\mathrm{R}}^{-1}\boldsymbol{H}_{\mathrm{RA}}\mathbf{1}_{\mathrm{A}} \\ \hline M_{\mathrm{a}}^{-1}\mathbf{1}_{\mathrm{A}}^{\mathrm{T}}\boldsymbol{H}_{\mathrm{AR}} & M_{\mathrm{a}}^{-1}\mathbf{1}_{\mathrm{A}}^{\mathrm{T}}\boldsymbol{H}_{\mathrm{AA}}\mathbf{1}_{\mathrm{A}} \end{array}\right] \begin{bmatrix} \Delta\boldsymbol{\delta}'_{\mathrm{R}} \\ \hline \Delta\delta'_{\mathrm{a}} \end{bmatrix}, \tag{14.118}$$

where, according to (14.33), the inertia coefficients of the equivalent machine are $M_{\mathrm{a}} = \sum_{i\in\{\mathrm{A}\}} M_i$.

It is also easy to see, when comparing Equations (14.117) and (14.118), that they differ in the bottom row corresponding to the equivalent generator. The difference lies in the different order of factors, which is important for the result as the multiplication of matrices is generally not commutative. A detailed analysis leads to the conclusion that the elements in the bottom row of Equation (14.117) are given by

$$a_{\mathrm{a}k} = -\frac{1}{n}\sum_{i\in\{\mathrm{A}\}}\frac{H_{ik}}{M_i}, \tag{14.119}$$

and those in Equation (14.118) are given by

$$a_{\mathrm{a}k} = -\frac{\sum\limits_{i\in\{\mathrm{A}\}} H_{ik}}{\sum\limits_{i\in\{\mathrm{A}\}} M_i}. \tag{14.120}$$

This is obvious because generally both elements given by Equations (14.119) and (14.120) are not the same. In the particular case when Equation (14.39) is satisfied, that is when the group is exactly coherent, the following holds:

$$\frac{H_{ik}}{M_i} = h_k \quad \text{for} \quad i, j \in \{\mathrm{A}\}, \quad k \in \{\mathrm{B}\}. \tag{14.121}$$

Hence $H_{ik} = h_k M_i$. Substituting this into (14.120) gives

$$a_{\mathrm{a}k} = -\frac{\sum\limits_{i\in\{\mathrm{A}\}} h_k M_i}{\sum\limits_{i\in\{\mathrm{A}\}} M_i} = -\frac{h_k \sum\limits_{i\in\{\mathrm{A}\}} M_i}{\sum\limits_{i\in\{\mathrm{A}\}} M_i} = -h_k. \tag{14.122}$$

The same value of $a_{\mathrm{a}k} = -h_k$ can be obtained by substituting (14.121) into (14.119). This shows that when the exact coherency condition (14.39) is satisfied, the matrices in (14.117) and (14.118) are the same.

Example 14.2

To illustrate how the reduced model partially retains eigenvalues and eigenvectors, a simple three-machine system will be studied in which two generators satisfy the exact coherency condition given by (14.121). The state matrix given by Equation (14.116) is

$$\left[\begin{array}{c|cc} -6 & 3 & 3 \\ \hline 2 & -4 & 2 \\ 2 & 3 & -5 \end{array}\right].$$

The eigenvalues and eigenvectors are

$$\begin{aligned} \mu_1 &= 0 \quad \text{and} \quad \boldsymbol{w}_1 = \begin{bmatrix} 1 & 1 & 1 \end{bmatrix}^{\mathrm{T}} \\ \mu_2 &= -8 \quad \text{and} \quad \boldsymbol{w}_2 = \begin{bmatrix} -3 & 1 & 1 \end{bmatrix}^{\mathrm{T}} \\ \mu_3 &= -7 \quad \text{and} \quad \boldsymbol{w}_3 = \begin{bmatrix} 3 & -4 & 3 \end{bmatrix}^{\mathrm{T}}. \end{aligned}$$

The state matrix reduces using Equation (14.117) to

$$\left[\begin{array}{c|c} -6 & 6 \\ \hline 2 & -2 \end{array}\right].$$

The eigenvalues and eigenvectors of this state matrix are

$$\begin{aligned} \mu_1 &= 0 \quad \text{and} \quad \boldsymbol{w}_{e1} = \begin{bmatrix} 1 & 1 \end{bmatrix}^{\mathrm{T}} \\ \mu_2 &= -8 \quad \text{and} \quad \boldsymbol{w}_{e2} = \begin{bmatrix} -3 & 1 \end{bmatrix}^{\mathrm{T}}. \end{aligned}$$

The reduced system also retained, apart from the zero eigenvalue, the eigenvalue $\mu_2 = -8$ and the associated right eigenvector $\boldsymbol{w}_{e2} = \begin{bmatrix} -3 & 1 \end{bmatrix}^{\mathrm{T}}$ which is a part of the original eigenvector $\boldsymbol{w}_2 = \begin{bmatrix} -3 & 1 & 1 \end{bmatrix}^{\mathrm{T}}$. Equation (14.110) is satisfied as

$$\boldsymbol{C}\boldsymbol{w}_2 = \left[\begin{array}{c|c|c} 1 & 0 & 0 \\ \hline 0 & \frac{1}{2} & \frac{1}{2} \end{array}\right] \begin{bmatrix} -3 \\ 1 \\ 1 \end{bmatrix} = \begin{bmatrix} -3 \\ 1 \end{bmatrix} = \boldsymbol{w}_{e2}.$$

This illustrates that the reduced model partially retains eigenvalues and eigenvectors of the original (unreduced) model.

To summarize the observations contained in this chapter:

1. The operations of aggregation and linearization are commutative (proof in Section 14.6.2).
2. The reduced linear model (14.62) obtained using the method of Di Caprio and Marconato corresponds to the linearized form of the reduced model obtained by Zhukov's aggregation (proof in Section 14.6.2).
3. When the exact coherency condition given by Equation (14.39) is satisfied, the reduced linear model (14.118) is equivalent to the reduced model (14.117) obtained using transformation (14.111) and the projection matrix (14.111).
4. The reduced model (14.117) partially retains the eigenvalues of the original (unreduced) model.

These observations clearly show that, when the exact coherency condition (14.39) is satisfied, the reduced model obtained by Zhukov's aggregation (Section 14.2.3) also partially retains the eigenvalues of the original (unreduced) model. This is a very important property of the coherency-based dynamic equivalent model obtained by Zhukov's aggregation.

In practice, exact coherency rarely occurs in real power systems apart from identical generators operating on the same busbar. Reduced dynamic models are created by aggregation of generators for which the coherency definition is satisfied within accuracy $\varepsilon_{\Delta\delta}$ as in condition (14.29). Obviously any inaccuracy of coherency means that all the dynamic properties of the original (unreduced) model will be maintained only to some degree by the equivalent (reduced) model. Hence it may be expected that also eigenvalues and eigenvectors of the equivalent (reduced) model will be only approximately equal to eigenvalues and eigenvectors of the original (unreduced) model. It is important here that the equivalent (reduced) model maintains as precisely as possible those modal variables that are strongly excited by disturbances in the internal subsystem and which therefore have the strongest influence on power swings in the internal subsystem. These modal variables will be referred to as *dominant modal variables* (see also Section 12.1.6). Modal analysis (Section 12.1) shows that matrices $\boldsymbol{U}$ and $\boldsymbol{W}$ built from right and left eigenvectors decide which modal variables are most strongly excited and influence power swings. The example below will show that a coherency-based equivalent model quite accurately retains the dominant modes.

Example 14.3

Figure 14.17 shows a 15-machine test system. Plant 7 was assumed to constitute the internal system. For this internal system, the algorithm described in Section 14.5 was used to identify coherent groups which are encircled in Figure 14.17 using solid lines.

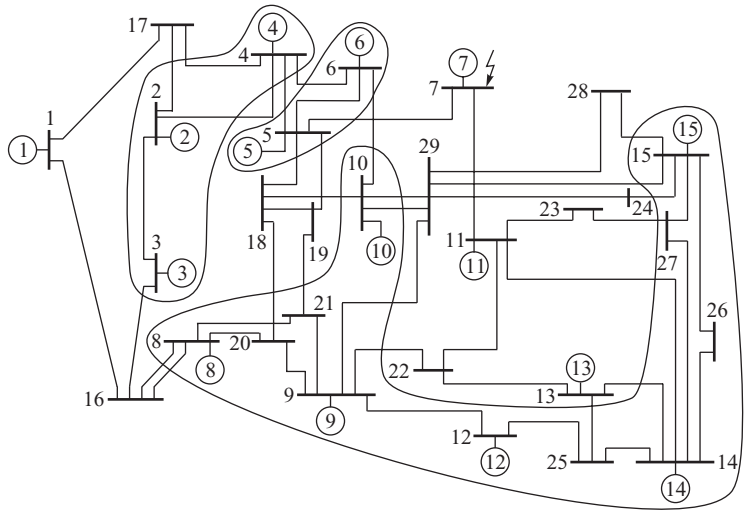

Figure 14.17 Test system and recognized coherent groups.

The dominant modes have been identified assuming that the initial disturbance is a rotor angle change of generator 7, that is $\Delta\boldsymbol{\delta}' = \left[\, 0 \cdots 0 |\ \Delta\delta_7' |\ 0 \cdots 0 \,\right]^{\mathrm{T}}$. With this disturbance, the equation $\boldsymbol{z} = \boldsymbol{U} \cdot \Delta\boldsymbol{\delta}'$ results in $\boldsymbol{z} = \boldsymbol{u}_{\circ 7} \cdot \Delta\delta_7'$ where $\boldsymbol{u}_{\circ 7}$ denotes the seventh column of matrix $\boldsymbol{U}$. For the assumed data (Machowski *et al.*, 1986; Machowski, Gubina and Omahen, 1986), the following results were obtained:

- for the original (unreduced) model

$$\boldsymbol{u}_{\circ 7} = 10^{-3} \cdot \left[\, \mathbf{-184} \,\vdots\, 0 \,\vdots\, \underline{\mathbf{914}} \,\vdots\, -11 \,\vdots\, \mathbf{160} \,\vdots\, -3 \,\vdots\, -56 \,\vdots\, -9 \,\vdots\, -71 \,\vdots\, -18 \,\vdots\, -64 \,\vdots\, -1 \,\vdots\, -90 \,\vdots\, 0 \,\vdots\, 20 \,\right]^{\mathrm{T}};$$

- for the equivalent (reduced) model

$$\boldsymbol{u}_{\circ 7} = 10^{-3} \cdot \left[-\mathbf{154} \,\vdots\, 29 \,\vdots\, \underline{\mathbf{915}} \,\vdots\, -47 \,\vdots\, \mathbf{124} \,\vdots\, -2 \,\vdots\, 0 \right]^{\mathrm{T}}.$$

The largest values correspond to the third modal variable z_3 and are shown in bold and underlined. Note that they are almost the same for the original and the equivalent model, which means that excitation of the third modal variable in both systems is the same. Also strongly exited are the first modal variable z_1 and the fifth z_5. That excitation is nevertheless several times weaker than excitation of the third modal variable z_3. The remaining values are much smaller, so it may be assumed that the remaining modes are either weakly excited or not excited at all. The excited modal variables are associated with the following eigenvalues:

original model :	equivalent model :
$\mu_1 = -11.977$	$\mu_1 = -13.817$
$\mu_3 = -42.743$	$\mu_3 = -44.170$
$\mu_5 = -72.499$	$\mu_5 = -119.390.$

Clearly the third eigenvalue corresponding to the most excited modal variable is almost the same for both the equivalent and original models. The first eigenvalue has similar values for both models while the fifth is quite different. However, it should be remembered that the first and fifth modal variables are weakly excited and do not have to be accurately modelled.

Matrix $\boldsymbol{W}$ decides how individual modal variables influence power swings in the internal subsystem. The equation $\boldsymbol{z}\Delta\boldsymbol{\delta}' = \boldsymbol{W}\boldsymbol{z}$ results in $\Delta\delta_7' = \boldsymbol{w}_{7\circ}\boldsymbol{z}$ where $\boldsymbol{w}_{7\circ}$ denotes the seventh row of $\boldsymbol{W}$. For the assumed data the following results were obtained:

- for the original (unreduced) model

$$\boldsymbol{w}_{7\circ} = 10^{-1} \cdot \left[-\mathbf{34} \,\vdots\, -26 \,\vdots\, \underline{\mathbf{98}} \,\vdots\, -10 \,\vdots\, 21 \,\vdots\, 0 \,\vdots\, -50 \,\vdots\, -10 \,\vdots\, -80 \,\vdots\, -20 \,\vdots\, -40 \,\vdots\, 0 \,\vdots\, 0 \,\vdots\, 0 \,\vdots\, -20 \right];$$

- for the equivalent (reduced) model

$$\boldsymbol{w}_{7\circ} = 10^{-1} \cdot \left[-\mathbf{52} \,\vdots\, 6 \,\vdots\, \underline{\mathbf{99}} \,\vdots\, -12 \,\vdots\, \mathbf{60} \,\vdots\, 0 \,\vdots\, 7 \right].$$

The largest values again correspond to the third modal variable z_3 and they are almost the same for both models. This means that the influence of the third modal variable on power swings in the internal system is the same in both models. The values for the first modal variable z_1 and the fifth z_5 are quite different, but those modal variables are weakly excited. Nevertheless, model reduction by aggregation causes some differences between power swings simulated in both models – see the simulation results shown previously in Figure 14.14 for a different test system.

By making use of $\boldsymbol{u}_{\circ 7}$ (seventh column of $\boldsymbol{U}$) and $\boldsymbol{w}_{7\circ}$ (seventh row of $\boldsymbol{W}$) it is possible to calculate participation factors defined in Section 11.1. According to Equation (12.90), it is necessary to multiply elements of matrix column $\boldsymbol{u}_{\circ 7}$ by elements of matrix row $\boldsymbol{w}_{7\circ}$. For example, the first participation factor for the original (unreduced) model is: $10^{-4} \cdot 184 \cdot 34 \cong 63 \cdot 10^{-2}$. The calculated participation factors can be expressed in the following way:

- for the original (unreduced) model

$$10^{-2} \cdot \left[\mathbf{63} \,\vdots\, 0 \,\vdots\, \underline{\mathbf{896}} \,\vdots\, 1 \,\vdots\, \mathbf{34} \,\vdots\, 0 \,\vdots\, 28 \,\vdots\, 1 \,\vdots\, 57 \,\vdots\, 4 \,\vdots\, 26 \,\vdots\, 0 \,\vdots\, 0 \,\vdots\, 0 \,\vdots\, -4 \right];$$

- for the equivalent (reduced) model

$$10^{-2} \cdot \left[\mathbf{80} \,\vdots\, 2 \,\vdots\, \underline{\mathbf{906}} \,\vdots\, 6 \,\vdots\, \mathbf{74} \,\vdots\, 0 \,\vdots\, 0 \right].$$

Based on the values of participation factors, it can be concluded that there is a strong relationship between the investigated variable $\Delta\delta'_7$ in the internal subsystem and the third modal variable z_3. The relationships between $\Delta\delta'_7$ and the first modal variable z_1 and the fifth z_5 are an order of magnitude weaker.

When analysing Example 14.3 it should be remembered that the calculated eigenvalues μ_i are the eigenvalues of a matrix in the second-order equation, respectively (14.116) and (14.117). These values are real and negative. The corresponding eigenvalues λ_i of first-order equations of the type (14.84) are complex numbers $\lambda_i = \sqrt{\mu_i}$.

14.6.5 Equilibrium Points of the Equivalent Model

The coherency-based equivalent model obtained by Zhukov's aggregation is constructed for a stable equilibrium point which is at the same time the steady-state operating point of the system. Consequently, the equivalent model must partially retain the coordinates of the stable equilibrium. This can be illustrated in the following way when denoting the nodes as in Figure 14.6. Let r be the number of generators in group $\{\mathrm{R}\}$ and N be the total number of system generators, that is in both groups $\{\mathrm{R}\}$ and $\{\mathrm{A}\}$. Then the coordinates of the stable equilibrium point of the original (unreduced) model and the equivalent (reduced) model can be written as

$$\hat{\boldsymbol{\delta}}' = \left[\, \hat{\delta}'_1 \quad \cdots \quad \hat{\delta}'_r \;\vdots\; \hat{\delta}'_{r+1} \quad \cdots \quad \hat{\delta}'_N \,\right]^{\mathrm{T}}, \tag{14.123}$$

$$\hat{\boldsymbol{\delta}}'_{\mathrm{e}} = \left[\, \hat{\delta}'_1 \quad \cdots \quad \hat{\delta}'_r \;\vdots\; \hat{\delta}'_{\mathrm{a}} \,\right]^{\mathrm{T}}, \tag{14.124}$$

where $\hat{\delta}'_{\mathrm{a}}$ is the power angle of the equivalent generator given by Equation (14.22). Now the question arises whether, and which, unstable equilibrium points are retained by the reduced (equivalent) model. This question is especially important from the point of view of the Lyapunov direct method. It was shown in Section 6.3.5 (Figure 6.24) that when transient stability is lost, each unstable equilibrium point corresponds to the system splitting in a certain way into groups of asynchronously operating generators. From that point of view the reduced (equivalent) model is a good model if it partially retains those unstable equilibrium points which are important for disturbances in the internal subsystem (Figure 14.1).

The coordinates of an unstable equilibrium point of the original (unreduced) model and the equivalent (reduced) model will be denoted as follows:

$$\tilde{\boldsymbol{\delta}}' = \left[\, \tilde{\delta}'_1 \quad \cdots \quad \tilde{\delta}'_r \;\vdots\; \tilde{\delta}'_{r+1} \quad \cdots \quad \tilde{\delta}'_N \,\right]^{\mathrm{T}}, \tag{14.125}$$

$$\tilde{\boldsymbol{\delta}}'_{\mathrm{e}} = \left[\, \tilde{\delta}'_{\mathrm{e}1} \quad \cdots \quad \tilde{\delta}'_{\mathrm{e}r} \;\vdots\; \tilde{\delta}'_{\mathrm{a}} \,\right]^{\mathrm{T}}. \tag{14.126}$$

The equivalent model will be said to partially retain the unstable equilibrium point of the original model if

$$\tilde{\delta}'_{\mathrm{e}k} = \tilde{\delta}'_k \quad \text{for} \quad k \in \{\mathrm{R}\}. \tag{14.127}$$

The electrical interpretation of Zhukov's aggregation shown in Figure 14.15 will reveal which particular unstable equilibrium points satisfy Equation (14.127). Aggregation will not distort the coordinates of an unstable equilibrium point if at that point the ratio of the voltages is equal to the transformation ratio used for aggregation, that is the ratio of voltages at the stable equilibrium point. As in Equation (14.16), the condition may be written as

$$\underline{\tilde{V}}_{\mathrm{a}}^{-1}\,\underline{\tilde{V}}_{\mathrm{A}} = \underline{\vartheta} = \underline{\hat{V}}_{\mathrm{a}}^{-1}\,\underline{\hat{V}}_{\mathrm{A}}. \tag{14.128}$$

For the classical generator model (constant magnitudes of emfs) the condition simplifies to

$$\tilde{\delta}'_i - \tilde{\delta}'_{\mathrm{a}} = \hat{\delta}'_i - \hat{\delta}'_{\mathrm{a}} \quad \text{for} \quad i \in \{\mathrm{A}\}, \tag{14.129}$$

or $\tilde{\delta}'_i - \hat{\delta}'_i = \tilde{\delta}'_{\mathrm{a}} - \hat{\delta}'_{\mathrm{a}}$. This equation must be satisfied for each $i \in \{\mathrm{A}\}$ and therefore for each $i, j \in \{\mathrm{A}\}$. Hence $\tilde{\delta}'_i - \hat{\delta}'_i = \tilde{\delta}'_j - \hat{\delta}'_j = \tilde{\delta}'_{\mathrm{a}} - \hat{\delta}'_{\mathrm{a}}$ must be satisfied, or

$$\tilde{\delta}'_i - \hat{\delta}'_i = \tilde{\delta}'_j - \hat{\delta}'_j \quad i, j \in \{\mathrm{A}\}. \tag{14.130}$$

This means that for each generator belonging to a given group $i, j \in \{\mathrm{A}\}$, the distance between an unstable equilibrium point and the stable equilibrium point must be the same. Such unstable equilibrium points can be called *partially equidistant points* with respect to a given group of variables belonging to group $\{\mathrm{A}\}$.

The equivalent model obtained using Zhukov's aggregation partially retains each unstable equilibrium point equidistant with respect to a given group of variables belonging to group $\{\mathrm{A}\}$. Aggregation destroys only those unstable equilibrium points that are not partially equidistant. This property will be illustrated using an example that is intuitively simple to understand.

Example 14.4

Figure 14.18 shows an example of two parallel generators 1 and 2 operating on an infinite busbar represented by a generator of large capacity 3. For each external short circuit in the transmission line 4–3, the two parallel generators are exactly coherent. Oscillations between the generators may appear only in the case of an internal short circuit inside the power plants at nodes 5 or 6. The lower part of Figure 14.18a shows the equivalent diagram after elimination of load nodes. The parameters have symbols following the notation in Equation (6.41). Figure 14.18b shows equiscalar lines of potential energy similar to Figure 6.24.

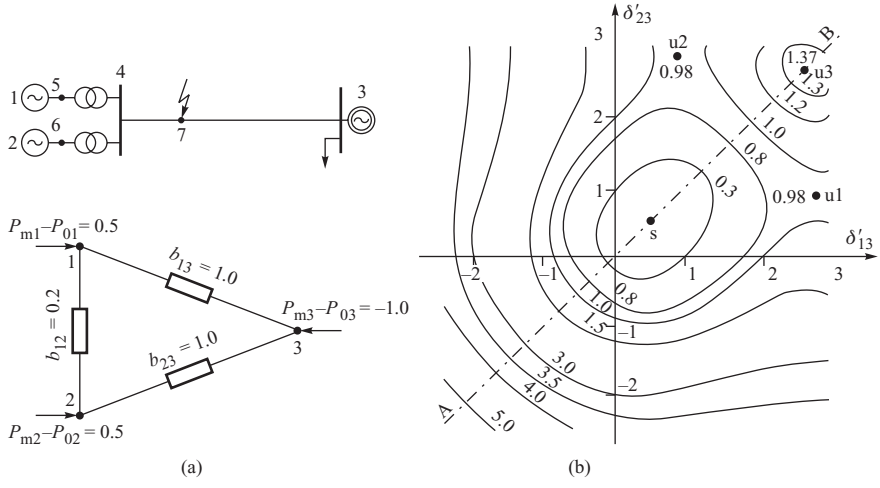

Figure 14.18 Illustration to the definition of the partially equidistant equilibrium point: (a) network diagrams; (b) equiscalar lines of potential energy.

There are three unstable equilibrium points: u1, u2, u3. The saddle point u1 corresponds to the loss of synchronism of generator 1 with respect to generators 2 and 3. This may happen when a short circuit appears at node 5. The saddle point u2 corresponds to a loss of synchronism of generator 2 with respect to generators 1 and 3. This may happen when there is a short circuit at

node 6. Point u3 is of the maximum type. It corresponds to a loss of synchronism of generators 1 and 2 with respect to generator 3. This may happen when there is a short circuit in line 4–3 at, for example at point 7. For point u3, condition (14.130) is satisfied as $\tilde{\delta}'_{13} - \hat{\delta}'_{13} = \tilde{\delta}'_{23} - \hat{\delta}'_{23}$. Point u3 is at the same time partially equidistant. Note that when the exact coherency condition is satisfied, trajectory $\boldsymbol{\delta}'(t)$ lies on the straight line AB crossing the origin, point s and point u3. The line is defined by

$$\delta'_{13}(t) - \delta'_{23}(t) = \hat{\delta}'_{13} - \hat{\delta}'_{23} = \hat{\delta}'_{12} = \text{constant},$$

similar to Equation (14.31). Aggregation of generators 1 and 2 reduces the three-machine system to a two-machine system and destroys the unstable equilibrium points u1, u2. After aggregation the unstable equilibrium point u3 is retained. A plot of potential energy for the reduced model (two-machine model) corresponds to a cross-section of the diagram in Figure 14.18 along line AB. This plot has the same shape as shown previously in Figure 6.21b.

The next important issue for the Lyapunov direct method is the question whether or not the dynamic equivalent (reduced) model retains the values of the Lyapunov function during the transient state and at unstable equilibrium points of the original (unreduced) model. For the Lyapunov function $V(\delta', \Delta\omega) = E_\mathrm{k} + E_\mathrm{p}$ given by Equation (6.52) the answer to this question is positive, which will now be proved.

For kinetic energy E_k the proof is trivial. It is enough to separate Equation (6.46) into two sums:

$$E_\mathrm{k} = \frac{1}{2}\sum_{i=1}^{N} M_i \Delta\omega_i^2 = \frac{1}{2}\sum_{i\in\{\mathrm{R}\}} M_i \Delta\omega_i^2 + \frac{1}{2}\sum_{i\in\{\mathrm{A}\}} M_i \Delta\omega_i^2 = \frac{1}{2}\sum_{i\in\{\mathrm{R}\}} M_i \Delta\omega_i^2 + \frac{1}{2} M_\mathrm{a} \Delta\omega_\mathrm{a}^2,$$

where for $i \in \{\mathrm{A}\}$ the definition of exact coherency gives $\Delta\omega_1 = \cdots = \Delta\omega_n = \Delta\omega_\mathrm{a}$ and, according to Equation (14.33), $M_\mathrm{a} = \sum_{i\in\{\mathrm{A}\}} M_i$. This concludes the proof.

For potential energy given by Equation (6.51) the proof is also simple but long. Here only an outline will be given:

1. The sum of components $(P_{\mathrm{m}i} - P_{0i})(\delta'_i - \hat{\delta}'_i)$ should be broken down (similarly as for kinetic energy) into two sums: one for $i \in \{\mathrm{R}\}$ and one for $i \in \{\mathrm{A}\}$. Then it should be noted that when the exact coherency condition is satisfied for $i \in \{\mathrm{A}\}$, then $(\delta'_i - \hat{\delta}'_i) = (\delta'_\mathrm{a} - \hat{\delta}'_\mathrm{a})$ while, according to the principles of aggregation, $\sum_{i\in(\mathrm{A})} (P_{\mathrm{m}i} - P_{0i}) = (P_{\mathrm{ma}} - P_{0\mathrm{a}})$.
2. The double sum of components $b_{ij}(\cos\delta'_{ij} - \cos\hat{\delta}'_{ij})$ in Equation (6.51) should be broken down into three sums: (i) for $i, j \in \{\mathrm{R}\}$; (ii) for $i \in \{\mathrm{R}\}$, $j \in \{\mathrm{A}\}$; and (iii) for $i, j \in \{\mathrm{A}\}$. Then it should be noted that components $b_{ij}\cos\delta'_{ij}$ and $b_{ij}\cos\hat{\delta}'_{ij}$ correspond to synchronizing powers. It was shown in Section 14.6.2 that for the equivalent (reduced) model, synchronizing powers are equal to the sum of synchronizing powers of aggregated generators. Hence the corresponding sums of components give the same values as for the equivalent (reduced) model.

Conclusions from the above points 1 and 2 conclude the proof for potential energy. This will now be illustrated using the results of calculations conducted for a test system.

Example 14.5

Consider again the test system shown in Figure 14.17. In this example the internal subsystem is assumed to consist of power plant 11 located in the middle of the test network. Treating the test system as the original (unreduced) model, the gradient method was used to calculate the coordinates of the stable equilibrium point and the unstable equilibrium point corresponding to the loss of synchronism of generator 11. The coordinates of those points are shown in Table

14.1 in columns under the heading 'Original'. For the assumed internal subsystem, the coherency recognition algorithm has identified two groups: {2, 3, 4} and {5, 6, 8, 9, 10, 12, 13, 14, 15}. The groups have been aggregated using Zhukov's method. For the equivalent (reduced) model obtained, the stable equilibrium point and unstable equilibrium point corresponding to the loss of synchronism of generator 11 have been calculated. The coordinates of these points are shown in Table 14.1 in columns under the heading 'Reduced'. The results show that for generators {1, 7, 11}, the coordinates for both the stable and unstable equilibrium points have been well retained. The lower rows of Table 14.1 show the values of the Lyapunov function calculated for the unstable equilibrium point of the original (unreduced) and equivalent (reduced) model. Clearly the values are quite close, similar to the values of the critical clearing time for a short circuit in busbar 11.

Table 14.1 Results for a fault at bus 11

		Coordinates of equilibrium points			
		Stable		Unstable	
Generator no.	Group no.	Original	Reduced	Original	Reduced
1	—	0.00	0.00	0.00	0.00
7	—	23.36	23.40	50.76	49.65
11	—	14.22	14.30	**183.80**	**181.81**
2	1	20.54	19.65	26.42	24.50
3		19.84		25.10	
4		10.56		19.02	
5	2	13.25	18.24	28.22	34.68
6		12.48		27.02	
8		15.39		26.58	
9		12.73		28.28	
10		11.15		26.59	
12		14.23		33.02	
13		14.14		34.44	
14		31.08		52.63	
15		25.55		44.67	
Value of Lyapunov function				11.05	10.95
Critical clearing time				0.322	0.325

Similar results have been obtained for the same and other test systems when choosing different internal subsystems. More examples can be found in the publications by Machowski (1985) and Machowski *et al.* (1986, 1988).

Appendix

A.1 Per-Unit System

Perhaps the one area in power system analysis that causes more confusion than any other is that of per-unit systems. This confusion is further compounded when a synchronous machine is included in the system. However, the per-unit system is well established and has a number of attractions. For example, by normalizing the generator equations derived in Chapter 11, the parameters of generators of the same type, but different ratings, will fall within the same range thereby providing the engineer with an intuitive understanding of the generator's performance. Such a normalized set of parameters can also lead to computational efficiencies.

In the following subsections the per-unit system used in this book is described. Firstly, the base system used in the stator armature is described followed by a brief discussion on power invariance in both SI and per-unit forms. The per-unit system is then examined in more detail in order to derive base values for the different rotor circuits before finally explaining how the generator and the network per-unit systems fit together.

A.1.1 Stator Base Quantities

The principal armature base values used are:

Base voltage V_b = generator line to neutral rms terminal voltage, $V_{L-N,}$ (this will normally be the rated voltage).
Base power S_b = the generator MVA rating/phase, $S_{1\phi}$
Base time $t_b = 1$ s.

These principal base values lead to the following derived base values:

Base current $$I_b = \frac{S_b}{V_b} = \frac{S_{1\phi}}{V_b} \quad \text{A.}$$

Base impedance $$Z_b = \frac{V_b}{I_b} \quad \Omega.$$

Base inductance $$L_b = \frac{V_b t_b}{I_b} \quad \text{H.}$$

Base flux linkage $\Psi_b = L_b I_b = V_b t_b \equiv V_b$ Vs.
Base electrical angle $\theta_b = 1$ electrical radian.
Base electrical speed $\omega_b = 1$ electrical radian/s.
Base mechanical angle $\theta_{mb} = 1$ mechanical radian.

Power System Dynamics: Stability and Control, Second Edition Jan Machowski, Janusz W. Bialek and James R. Bumby
© 2008 John Wiley & Sons, Ltd

Base mechanical speed $\omega_{mb} = 1$ mechanical radian/s.
Base machine power $S_{3\phi} = 3S_{1\phi}$ VA.
Base torque $\tau_b = \dfrac{S_{3\phi}}{\omega_{sm}}$ Nm.

To use these base values, any particular current, voltage and so on in SI is simply divided by the corresponding base value to obtain the per-unit value (or vice versa):

$$\text{per-unit value} = \frac{\text{actual value}}{\text{base value}}. \tag{A.1}$$

It is important to note that with the voltage and current ABC/dq transformation equations introduced in Chapter 11 the same base values are used for the armature coils in both the A, B, C and the d, q reference frames. This is not the case with other values of transformation coefficient (Harris, Lawrenson and Stephenson, 1970). As explained in Chapter 11, the ABC/dq transformation is power invariant such that

$$v_a i_a + v_b i_b + v_c i_c = v_d i_d + v_q i_q. \tag{A.2}$$

With the base values defined above, the transformations are power invariant in both SI and per-unit notation.

The following points should be noted:

1. With a base time of 1 s all time constants are expressed in seconds.
2. A per-unit reactance is related to a per-unit inductance by $X_{pu} = \omega L_{pu}$ so that the normal relationship between inductance and reactance is maintained. The per-unit inductance is *not equal* to the per-unit reactance.
3. The definition of base torque is such that at synchronous speed per-unit torque is equal to per-unit power, for example a turbine torque of 0.8 pu corresponds to a turbine power of 0.8 pu. In general

$$P = \tau\ \omega_m \quad \text{(SI)}. \tag{A.3}$$

Dividing by $S_{3\phi}$,

$$\frac{P}{S_{3\phi}} = \frac{\tau\omega_m}{S_{3\phi}} = \frac{\tau\omega_m}{\tau_b\omega_{sm}}, \quad P_{pu} = \tau_{pu}\frac{\omega_m}{\omega_{sm}}, \tag{A.4}$$

but as $\omega_m = \omega/p$ and $\omega_{sm} = \omega_s/p$

$$P_{pu} = \tau_{pu}\frac{\omega_m}{\omega_{sm}} = \tau_{pu}\frac{\omega}{\omega_s} \tag{A.5}$$

at synchronous speed $\omega = \omega_s$ and

$$P_{pu} = \tau_{pu}. \tag{A.6}$$

4. Under balanced operation the power output of a single phase, normalized to $S_{1\phi}$, is numerically the same per unit as the generator power output normalized to $S_{3\phi}$. Under balanced operation

$$P_{1\phi} = V_{rms} I_{rms} \cos\phi, \quad P_{3\phi} = 3 V_{rms} I_{rms} \cos\phi. \tag{A.7}$$

Dividing by $S_{1\phi}$ and $S_{3\phi}$ respectively gives

$$P_{pu} = V_{pu} I_{pu} \cos\phi. \tag{A.8}$$

This is an extremely useful identity, particularly when balanced operation is being studied by means of a phasor diagram.

5. Because of the per-unit notation adopted, most of the equations developed in this book are the same whether the quantities are expressed in SI or in per-unit notation. The two important exceptions to this are generator power and torque, both of which must be normalized to the generator MVA base rather than the phase MVA base. Consequently

$$P_{\text{pu}} = \frac{P_{\text{SI}}}{S_{3\phi}} = \frac{1}{3}\left[\frac{P_{\text{SI}}}{V_{\text{b}} I_{\text{b}}}\right], \tag{A.9}$$

while

$$\tau_{\text{pu}} = \frac{\tau_{\text{SI}}}{\tau_{\text{b}}} = \tau_{\text{SI}} \frac{\omega_{\text{s}}}{S_{3\phi}} = \frac{\omega_{\text{s}}}{3}\left[\frac{\tau_{\text{SI}}}{V_{\text{b}} I_{\text{b}}}\right]. \tag{A.10}$$

The implication of these two equations is that generator power or torque equations derived in SI can be simply converted to per-unit form by multiplying by $1/3$ and $\omega_{\text{s}}/3$, respectively. See, for example, the torque expressions in Chapter 4.

6. Full load power (and torque) should not be confused with 1 pu power (and torque). They are not the same. In general

$$\text{Full load power} = S_{3\phi} \cos\phi_{\text{rated}}$$
$$\text{Full load torque} = \tau_{\text{b}} \cos\phi_{\text{rated}}.$$

Mechanical engineers like to refer to a shaft rated, for example, as four times full load torque. This does not mean four times τ_{b} – they are different by $\cos\phi_{\text{rated}}$.

7. Because of the base values used, the relationship between v_{d}, v_{q} and V_{d}, V_{q} and i_{d}, i_{q} and I_{d}, I_{q} derived in Chapter 11 are valid in both SI and per-unit form, that is

$$v_{\text{dpu}} = \sqrt{3}\, V_{\text{dpu}}, \quad i_{\text{dpu}} = \sqrt{3}\, I_{\text{dpu}}, \tag{A.11}$$
$$v_{\text{qpu}} = \sqrt{3} V_{\text{qpu}}, \quad i_{\text{qpu}} = \sqrt{3}\, I_{\text{qpu}}. \tag{A.12}$$

A.1.2 Power Invariance

A check on power invariance in SI is useful. Under balanced conditions, and using the current and voltage identities of Equations (11.80) and (11.82),

$$\begin{aligned} P_{3\phi} &= v_{\text{d}} i_{\text{d}} + v_{\text{q}} i_{\text{q}} = 3\left(V_{\text{d}} I_{\text{d}} + V_{\text{q}} I_{\text{q}}\right) \\ &= 3 V_{\text{g}} I_{\text{g}} \left[\sin\delta_0 \sin(\delta_0 + \phi) + \cos\delta_0 \cos(\delta_0 + \phi)\right] \\ &= 3 V_{\text{g}} I_{\text{g}} \cos\phi \text{W}, \end{aligned} \tag{A.13}$$

showing that power invariance is maintained.

As $P_{3\phi} = 3 V_{\text{g}} I_{\text{g}} \cos\phi$, dividing both sides by $S_{3\phi}$ gives the generator power in per-unit form

$$\frac{P_{3\phi}}{S_{3\phi}} = \frac{v_{\text{d}} i_{\text{d}} + v_{\text{q}} i_{\text{q}}}{3 V_{\text{b}} I_{\text{b}}} = \frac{3(V_{\text{d}} I_{\text{d}} + V_{\text{q}} I_{\text{q}})}{3 V_{\text{b}} I_{\text{b}}} = \frac{3 V_{\text{g}} I_{\text{g}} \cos\phi}{3 V_{\text{b}} I_{\text{b}}} = V_{\text{g pu}} I_{\text{g pu}} \cos\phi, \tag{A.14}$$

$$P_{\text{pu}} = \frac{1}{3}(v_{\text{dpu}} i_{\text{dpu}} + v_{\text{qpu}} i_{\text{qpu}}) = (V_{\text{dpu}} I_{\text{dpu}} + V_{\text{qpu}} I_{\text{qpu}}) = V_{\text{g pu}} I_{\text{g pu}} \cos\phi, \tag{A.15}$$

and power invariance is also maintained in the per-unit system.

A.1.3 Rotor Base Quantities

Although a number of per-unit systems are possible (Harris, Lawrenson and Stephenson, 1970) the system considered here is that of *equal mutual flux linkages* as expounded by Anderson and Fouad (1977) and also explained in depth by Pavella and Murthy (1994). In this system the base field current, or base d-axis damper current, is defined so that each will produce the same fundamental air-gap flux wave as that produced by the base armature current acting in the fictitious d-axis armature coil. As will be seen as a consequence of this choice of per-unit system, all the per-unit mutual inductances on a particular axis are equal.

It is convenient at this stage to separate each individual winding self-inductance into a magnetizing inductance and a leakage inductance so that

$$\begin{aligned} L_{\mathrm{d}} &= L_{\mathrm{md}} + l_l & L_{\mathrm{q}} &= L_{\mathrm{mq}} + l_l \\ L_{\mathrm{D}} &= L_{\mathrm{mD}} + l_{\mathrm{D}} & L_{\mathrm{Q}} &= L_{\mathrm{mQ}} + l_{\mathrm{Q}}, \\ L_{\mathrm{f}} &= L_{\mathrm{mf}} + l_{\mathrm{f}} \end{aligned} \tag{A.16}$$

where l represents the winding leakage inductance. The per-unit system requires the mutual flux linkage in each winding to be equal, that is

$$\begin{aligned} &\text{d-coil:} && L_{\mathrm{md}} I_{\mathrm{b}} = k M_{\mathrm{f}} I_{\mathrm{fb}} = k M_{\mathrm{D}} I_{\mathrm{Db}} \\ &\text{f-coil:} && k M_{\mathrm{f}} I_{\mathrm{b}} = L_{\mathrm{mf}} I_{\mathrm{fb}} = L_{\mathrm{fD}} I_{\mathrm{Db}} \\ &\text{D-coil:} && k M_{\mathrm{D}} I_{\mathrm{b}} = L_{\mathrm{fD}} I_{\mathrm{fb}} = L_{\mathrm{mD}} I_{\mathrm{Db}} \\ &\text{q-coil:} && L_{\mathrm{mq}} I_{\mathrm{b}} = k M_{\mathrm{Q}} I_{\mathrm{Qb}} \\ &\text{Q-coil:} && k M_{\mathrm{Q}} I_{\mathrm{b}} = L_{\mathrm{mQ}} I_{\mathrm{Qb}}. \end{aligned} \tag{A.17}$$

Multiplying each of these winding mutual flux linkages by the coil base current gives the fundamental constraint between the base currents as

$$\begin{aligned} &L_{\mathrm{md}} I_{\mathrm{b}}^2 = L_{\mathrm{mf}} I_{\mathrm{fb}}^2 = L_{\mathrm{mD}} I_{\mathrm{Db}}^2 = k M_{\mathrm{f}} I_{\mathrm{fb}} I_{\mathrm{b}} = k M_{\mathrm{D}} I_{\mathrm{Db}} I_{\mathrm{b}} = L_{\mathrm{fD}} I_{\mathrm{fb}} I_{\mathrm{Db}} \\ &L_{\mathrm{mq}} I_{\mathrm{b}}^2 = L_{\mathrm{mQ}} I_{\mathrm{Qb}}^2 = k M_{\mathrm{Q}} I_{\mathrm{b}} I_{\mathrm{Qb}}. \end{aligned} \tag{A.18}$$

As the MVA base for each winding must be the same and equal to $S_{\mathrm{b}} = V_{\mathrm{b}} I_{\mathrm{b}}$, this gives

$$\begin{aligned} \frac{V_{\mathrm{fb}}}{V_{\mathrm{b}}} &= \frac{I_{\mathrm{b}}}{I_{\mathrm{fb}}} = \sqrt{\frac{L_{\mathrm{mf}}}{L_{\mathrm{md}}}} = \frac{k M_{\mathrm{f}}}{L_{\mathrm{md}}} = \frac{L_{\mathrm{mf}}}{k M_{\mathrm{f}}} = \frac{L_{\mathrm{fD}}}{k M_{\mathrm{D}}} \equiv k_{\mathrm{f}} \\ \frac{V_{\mathrm{Db}}}{V_{\mathrm{b}}} &= \frac{I_{\mathrm{b}}}{I_{\mathrm{Db}}} = \sqrt{\frac{L_{\mathrm{mD}}}{L_{\mathrm{md}}}} = \frac{k M_{\mathrm{D}}}{L_{\mathrm{md}}} = \frac{L_{\mathrm{mD}}}{k M_{\mathrm{D}}} = \frac{L_{\mathrm{fD}}}{k M_{\mathrm{f}}} \equiv k_{\mathrm{D}} \\ \frac{V_{\mathrm{Qb}}}{V_{\mathrm{b}}} &= \frac{I_{\mathrm{b}}}{I_{\mathrm{Qb}}} = \sqrt{\frac{L_{\mathrm{mQ}}}{L_{\mathrm{mq}}}} = \frac{k M_{\mathrm{Q}}}{L_{\mathrm{mq}}} = \frac{L_{\mathrm{mQ}}}{k M_{\mathrm{Q}}} \equiv k_{\mathrm{Q}}. \end{aligned} \tag{A.19}$$

Since Equation (A.19) defines the base currents and voltages in all the windings as a function of the stator base quantities V_{b} and I_{b},

$$Z_{\mathrm{fb}} = \frac{V_{\mathrm{fb}}}{I_{\mathrm{fb}}} = k_{\mathrm{f}}^2 Z_{\mathrm{b}} \quad \Omega, \quad Z_{\mathrm{Db}} = \frac{V_{\mathrm{Db}}}{I_{\mathrm{Db}}} = k_{\mathrm{D}}^2 Z_{\mathrm{b}} \quad \Omega, \quad Z_{\mathrm{Qb}} = \frac{V_{\mathrm{Qb}}}{I_{\mathrm{Qb}}} = k_{\mathrm{Q}}^2 Z_{\mathrm{b}} \quad \Omega \tag{A.20}$$

and

$$L_{\mathrm{fb}} = \frac{V_{\mathrm{fb}} t_{\mathrm{b}}}{I_{\mathrm{fb}}} = k_{\mathrm{f}}^2 L_{\mathrm{b}} \quad \mathrm{H}, \quad L_{\mathrm{Db}} = \frac{V_{\mathrm{Db}} t_{\mathrm{b}}}{I_{\mathrm{Db}}} = k_{\mathrm{D}}^2 L_{\mathrm{b}} \quad \mathrm{H}, \quad L_{\mathrm{Qb}} = k_{\mathrm{Q}}^2 L_{\mathrm{b}} \quad \mathrm{H}, \tag{A.21}$$

while the base mutual inductances are

$$\begin{aligned} M_{\mathrm{fb}} &= \frac{V_{\mathrm{fb}} t_{\mathrm{b}}}{I_{\mathrm{b}}} = \frac{V_{\mathrm{b}} t_{\mathrm{b}}}{I_{\mathrm{fb}}} = k_{\mathrm{f}} L_{\mathrm{b}} \quad \mathrm{H}, \quad M_{\mathrm{Db}} = k_{\mathrm{D}} L_{\mathrm{b}} \quad \mathrm{H} \\ M_{\mathrm{Qb}} &= k_{\mathrm{Q}} L_{\mathrm{b}} \quad \mathrm{H}, \quad L_{\mathrm{fDb}} = k_{\mathrm{f}} k_{\mathrm{D}} L_{\mathrm{b}} \quad \mathrm{H}. \end{aligned} \tag{A.22}$$

With the base values now defined, Equations (11.18), (11.19) and (10.30), (10.31) can now be normalized and expressed in per-unit form. As an example consider the normalization of the field flux linkage Ψ_{f} in Equation (11.18) where

$$\Psi_{\mathrm{f}} = kM_{\mathrm{f}} i_{\mathrm{d}} + L_{\mathrm{f}} i_{\mathrm{f}} + L_{\mathrm{fD}} i_{\mathrm{D}}. \tag{A.23}$$

Divide by $\Psi_{\mathrm{fb}} = L_{\mathrm{fb}} I_{\mathrm{fb}}$ to give

$$\Psi_{\mathrm{fpu}} = \frac{kM_{\mathrm{f}}}{L_{\mathrm{fb}}} \frac{i_{\mathrm{d}}}{I_{\mathrm{fb}}} + \frac{L_{\mathrm{f}}}{L_{\mathrm{fb}}} \frac{i_{\mathrm{f}}}{I_{\mathrm{fb}}} + \frac{L_{\mathrm{fD}}}{L_{\mathrm{fb}}} \frac{i_{\mathrm{D}}}{I_{\mathrm{fb}}}. \tag{A.24}$$

Substituting for I_{fb} and L_{fb} from Equations (A.19) and (A.20) gives

$$\Psi_{\mathrm{fpu}} = \left[\frac{kM_{\mathrm{f}}}{k_{\mathrm{f}} L_{\mathrm{b}}}\right]\left[\frac{i_{\mathrm{d}}}{I_{\mathrm{b}}}\right] + \left[\frac{L_{\mathrm{f}}}{L_{\mathrm{fb}}}\right]\left[\frac{i_{\mathrm{f}}}{I_{\mathrm{fb}}}\right] + \left[\frac{L_{\mathrm{fD}}}{k_{\mathrm{f}} k_{\mathrm{D}} L_{\mathrm{b}}}\right]\left[\frac{i_{\mathrm{D}}}{I_{\mathrm{Db}}}\right] \tag{A.25}$$

and

$$\Psi_{\mathrm{fpu}} = kM_{\mathrm{fpu}} i_{\mathrm{dpu}} + L_{\mathrm{fpu}} i_{\mathrm{fpu}} + L_{\mathrm{fDpu}} i_{\mathrm{Dpu}}. \tag{A.26}$$

This normalized equation is of exactly the same form as the equation in SI and this is true for all other equations in Section 11.1.4. In other words, all the voltage, current and flux equations in Section 11.1.4 are of same form whether in per-unit or SI form.

One further interesting feature of the per-unit system is that the per-unit values of all the mutual inductances on one axis are equal: that is, L_{md}, L_{mf}, L_{mD}, kM_{f}, kM_{D} and L_{fD} are all equal. For example,

$$\begin{aligned} kM_{\mathrm{fpu}} &= \frac{kM_{\mathrm{f}}}{M_{\mathrm{fb}}} = \frac{kM_{\mathrm{f}}}{k_{\mathrm{f}} L_{\mathrm{b}}} = \frac{k_{\mathrm{f}} L_{\mathrm{md}}}{k_{\mathrm{f}} L_{\mathrm{b}}} = L_{\mathrm{mdpu}} \\ L_{\mathrm{fDpu}} &= \frac{L_{\mathrm{fD}}}{L_{\mathrm{fDb}}} = \frac{L_{\mathrm{fD}}}{k_{\mathrm{f}} k_{\mathrm{D}} L_{\mathrm{b}}} = \frac{L_{\mathrm{fD}}}{\frac{kM_{\mathrm{f}}}{L_{\mathrm{md}}} \frac{L_{\mathrm{fD}}}{kM_{\mathrm{f}}} L_{\mathrm{b}}} = \frac{L_{\mathrm{md}}}{L_{\mathrm{b}}} = L_{\mathrm{mdpu}}. \end{aligned} \tag{A.27}$$

It is common practice to replace all these per-unit mutual values by a per-unit mutual inductance L_{ad} so that

$$L_{\mathrm{ad}} \equiv L_{\mathrm{md}} = L_{\mathrm{mf}} = L_{\mathrm{mD}} = kM_{\mathrm{f}} = kM_{\mathrm{D}} = L_{\mathrm{fD}}, \tag{A.28}$$

and, in the q-axis,

$$L_{\mathrm{aq}} \equiv L_{\mathrm{mq}} = L_{\mathrm{mQ}} = kM_{\mathrm{Q}}. \tag{A.29}$$

All the equations in Section 11.1.4 can now be written in per-unit form in terms of the mutual inductances L_{ad} and L_{aq}. For example, Equation (11.43) for the d-axis subtransient inductance would become

$$L''_{\mathrm{d}} = L_{\mathrm{d}} - \left[\frac{L_{\mathrm{ad}}^2 L_{\mathrm{D}} + L_{\mathrm{ad}}^2 L_{\mathrm{f}} - 2L_{\mathrm{ad}}^3}{L_{\mathrm{D}} L_{\mathrm{f}} - L_{\mathrm{ad}}^2}\right], \tag{A.30}$$

where $L_{\mathrm{d}} = L_{\mathrm{ad}} + l_l, L_{\mathrm{D}} = L_{\mathrm{ad}} + l_{\mathrm{D}}$ and $L_{\mathrm{f}} = L_{\mathrm{ad}} + l_{\mathrm{f}}$.

With this knowledge it is constructive to examine the per-unit flux linking each winding. Using Equation (11.18), and dropping the pu symbol for simplicity, the flux linkage of the d-axis coil is

$$\Psi_{\mathrm{d}} = L_{\mathrm{d}} i_{\mathrm{d}} + k M_{\mathrm{f}} i_{\mathrm{f}} + k M_{\mathrm{D}} i_{\mathrm{D}}. \tag{A.31}$$

Substituting for L_{ad} and introducing the winding leakage inductance gives

$$\Psi_{\mathrm{d}} = L_{\mathrm{ad}}(i_{\mathrm{d}} + i_{\mathrm{f}} + i_{\mathrm{D}}) + l_l i_{\mathrm{d}}, \tag{A.32}$$

and similarly for the field and d-axis damper coil

$$\begin{aligned} \Psi_{\mathrm{f}} &= L_{\mathrm{ad}}(i_{\mathrm{d}} + i_{\mathrm{f}} + i_{\mathrm{D}}) + l_{\mathrm{f}} i_{\mathrm{f}} \\ \Psi_{\mathrm{D}} &= L_{\mathrm{ad}}(i_{\mathrm{d}} + i_{\mathrm{f}} + i_{\mathrm{D}}) + l_{\mathrm{D}} i_{\mathrm{D}}. \end{aligned} \tag{A.33}$$

Thus if the per-unit leakage flux linkage of a particular winding is subtracted from the total flux linkage then the remaining mutual flux linkage in all the windings on each axis is equal. This mutual flux linkage is often given the symbol Ψ_{ad} and, for the q-axis, Ψ_{aq} where

$$\begin{aligned} \Psi_{\mathrm{ad}} &= L_{\mathrm{ad}}(i_{\mathrm{d}} + i_{\mathrm{f}} + i_{\mathrm{D}}) \\ \Psi_{\mathrm{aq}} &= L_{\mathrm{aq}}(i_{\mathrm{q}} + i_{\mathrm{Q}}). \end{aligned} \tag{A.34}$$

A.1.4 Power System Base Quantities

It is customary in three-phase power system analysis to use rated line-to-line voltage as the base voltage and an arbitrary three-phase voltage-ampere base, typically 10 MVA, 100 MVA and so on. Such a base system would, at first sight, seem to be totally inconsistent with the generator armature base defined in Section A.1.1. In fact the two are entirely consistent.

For the power system

$$\begin{aligned} V_{\mathrm{L-L,b}} &= V_{\mathrm{L-L}} = \sqrt{3} V_{\mathrm{L-N}} && \mathrm{V} \\ S_{\mathrm{b}} &= S_{3\phi} && \mathrm{V\,A} \\ I_{\mathrm{b}} &= \frac{S_{3\phi}}{\sqrt{3} V_{\mathrm{L-L,b}}} && \mathrm{A} \\ Z_{\mathrm{b}} &= \frac{V_{\mathrm{L-L,b}}}{\sqrt{3} I_{\mathrm{b}}} = \frac{V_{\mathrm{L-L,b}}^2}{S_{3\phi}} && \Omega. \end{aligned} \tag{A.35}$$

Ignoring any transformer effects and assuming that the system MVA base $S_{3\phi}$ is equal to the generator MVA rating, then $V_{\mathrm{L-N}} = V_{\mathrm{b}}$, where V_{b} is the generator base voltage, and

$$\begin{aligned} Z_{\mathrm{b}} &= \frac{V_{\mathrm{L-L,b}}^2}{S_{3\phi}} = \frac{3 V_{\mathrm{L-N}}^2}{S_{3\phi}} = \frac{V_{\mathrm{b}}^2}{S_{1\phi}} \\ I_{\mathrm{b}} &= \frac{S_{3\phi}}{\sqrt{3} V_{\mathrm{L-L,b}}} = \frac{S_{1\phi}}{V_{\mathrm{b}}}, \end{aligned} \tag{A.36}$$

showing that the power system base and the generator base are totally consistent.

However, there is one complication and this is that $S_{3\phi}$ for the system is chosen arbitrarily while $S_{1\phi}$ for the generator is the rated MVA per phase. In fact for all the equipment making up the power

system, the per-unit impedance values will be defined with respect to the individual MVA ratings. Consequently, in the system analysis it will be necessary either:

- to convert all the generator parameters to be on the system base; or
- to have a base conversion between the individual generator equations and the system equations in the computer software. This is easily achieved and has the advantage that the generator per-unit values not only retain their familiarity, but also are exactly as provided by the equipment manufacturer.

Both methods are used and converting per-unit values from one system (base 1) to another (base 2) is readily achieved via Equation (A.1) to obtain

$$\text{per-unit value (base 2)} = \text{per-unit value (base)} \frac{\text{base 1 value}}{\text{base 2 value}}. \tag{A.37}$$

A.1.5 Transformers

It was shown in Section 3.2 how a transformer could be represented by either the primary or the secondary equivalent circuit shown in Figure A.1. In these equivalent circuits the primary equivalent impedance Z_1 and the secondary equivalent impedance Z_2 are related by

$$Z_1 = n^2 Z_2, \tag{A.38}$$

where n is the nominal turns ratio. However, the primary and secondary base values are defined as

$$\begin{aligned} V_{\text{pb}} &= V_{1,\text{L}-\text{N}} & V_{\text{sb}} &= V_{2,\text{L}-\text{N}} \\ I_{\text{pb}} &= \frac{S_{3\phi}}{3V_{\text{pb}}} & I_{\text{sb}} &= \frac{S_{3\phi}}{3V_{\text{sb}}} \\ Z_{\text{pb}} &= \frac{V_{\text{pb}}}{I_{\text{pb}}} & Z_{\text{sb}} &= \frac{V_{\text{sb}}}{I_{\text{sb}}}, \end{aligned} \tag{A.39}$$

where

$$V_{\text{pb}} = n V_{\text{sb}}, \tag{A.40}$$

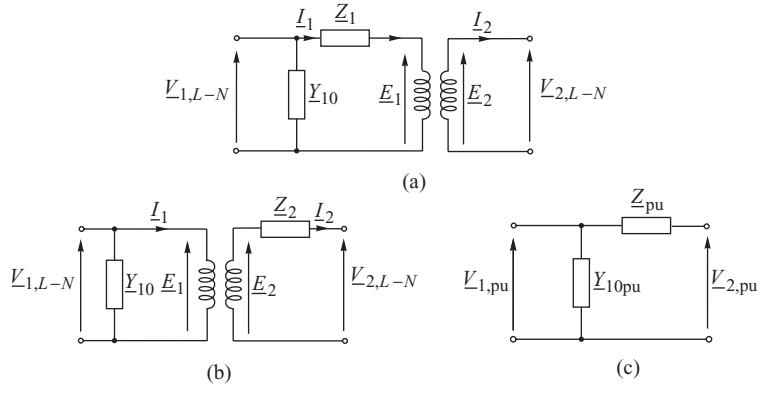

Figure A.1 Transformer equivalent circuit: (a) primary; (b) secondary; (c) per unit at nominal tap setting.

and implies that

$$I_{\text{pb}} = \frac{I_{\text{sb}}}{n}, \quad Z_{\text{pb}} = n^2 Z_{\text{sb}}. \tag{A.41}$$

Consequently, as 1 per unit on the high-voltage side of the transformer must be 1 per unit on the low voltage side and

$$Z_{\text{pu}} = \frac{Z_1}{Z_{\text{pb}}} = \frac{Z_2 n^2}{n^2 Z_{\text{sb}}} = \frac{Z_2}{Z_{\text{sb}}} = Z_{\text{pu}}, \tag{A.42}$$

the per-unit value of the primary and secondary equivalent impedance is the same so that the transformer at nominal taps can be represented by the per-unit equivalent shown in Figure A.1c. If the tap setting changes from nominal, the equivalent circuit is modified to that shown in Figure 3.8.

A.2 Partial Inversion

Consider the following block linear equation in which the variables have been grouped into two groups {R} and {E}:

$$\left[\begin{array}{c} \boldsymbol{x}_{\text{R}} \\ \hline \boldsymbol{x}_{\text{E}} \end{array}\right] = \left[\begin{array}{c|c} \boldsymbol{A}_{\text{RR}} & \boldsymbol{A}_{\text{RE}} \\ \hline \boldsymbol{A}_{\text{ER}} & \boldsymbol{A}_{\text{EE}} \end{array}\right] \left[\begin{array}{c} \boldsymbol{y}_{\text{R}} \\ \hline \boldsymbol{y}_{\text{E}} \end{array}\right]. \tag{A.43}$$

Expanding the equation gives

$$\boldsymbol{x}_{\text{R}} = \boldsymbol{A}_{\text{RR}} \boldsymbol{y}_{\text{R}} + \boldsymbol{A}_{\text{RE}} \boldsymbol{y}_{\text{E}}, \tag{A.44}$$

$$\boldsymbol{x}_{\text{E}} = \boldsymbol{A}_{\text{ER}} \boldsymbol{y}_{\text{R}} + \boldsymbol{A}_{\text{EE}} \boldsymbol{y}_{\text{E}}. \tag{A.45}$$

Simple manipulations result in

$$\boldsymbol{y}_{\text{E}} = -\boldsymbol{A}_{\text{EE}}^{-1} \boldsymbol{A}_{\text{ER}} \boldsymbol{y}_{\text{R}} + \boldsymbol{A}_{\text{EE}}^{-1} \boldsymbol{x}_{\text{E}}. \tag{A.46}$$

Substituting (A.46) into (A.44) gives

$$\boldsymbol{x}_{\text{R}} = \left(\boldsymbol{A}_{\text{RR}} - \boldsymbol{A}_{\text{RE}} \boldsymbol{A}_{\text{EE}}^{-1} \boldsymbol{A}_{\text{ER}}\right) \boldsymbol{y}_{\text{R}} + \boldsymbol{A}_{\text{RE}} \boldsymbol{A}_{\text{EE}}^{-1} \boldsymbol{x}_{\text{E}}. \tag{A.47}$$

Equations (A.46) and (A.47) can be written as

$$\left[\begin{array}{c} \boldsymbol{x}_{\text{R}} \\ \hline \boldsymbol{y}_{\text{E}} \end{array}\right] = \left[\begin{array}{c|c} \boldsymbol{A}_{\text{RR}} - \boldsymbol{A}_{\text{RE}} \boldsymbol{A}_{\text{EE}}^{-1} \boldsymbol{A}_{\text{ER}} & \boldsymbol{A}_{\text{RE}} \boldsymbol{A}_{\text{EE}}^{-1} \\ \hline -\boldsymbol{A}_{\text{EE}}^{-1} \boldsymbol{A}_{\text{ER}} & \boldsymbol{A}_{\text{EE}}^{-1} \end{array}\right] \left[\begin{array}{c} \boldsymbol{y}_{\text{R}} \\ \hline \boldsymbol{x}_{\text{E}} \end{array}\right]. \tag{A.48}$$

Comparing with (A.43), $\boldsymbol{y}_{\text{E}}$ has been moved to the left hand side of the equation and $\boldsymbol{x}_{\text{E}}$ to the right. This is referred to as the *partial inversion* of a matrix.

Equation (A.48) can be written as

$$\left[\begin{array}{c} \boldsymbol{x}_{\text{R}} \\ \hline \boldsymbol{y}_{\text{E}} \end{array}\right] = \left[\begin{array}{c|c} \boldsymbol{A}_{\text{R}} & \boldsymbol{B}_{\text{RE}} \\ \hline -\boldsymbol{B}_{\text{ER}} & \boldsymbol{C}_{\text{EE}} \end{array}\right] \left[\begin{array}{c} \boldsymbol{y}_{\text{R}} \\ \hline \boldsymbol{x}_{\text{E}} \end{array}\right], \tag{A.49}$$

where

$$\begin{aligned} \boldsymbol{A}_{\mathrm{R}} &= \boldsymbol{A}_{\mathrm{RR}} - \boldsymbol{A}_{\mathrm{RE}} \boldsymbol{A}_{\mathrm{EE}}^{-1} \boldsymbol{A}_{\mathrm{ER}} \\ \boldsymbol{B}_{\mathrm{RE}} &= \boldsymbol{A}_{\mathrm{RE}} \boldsymbol{A}_{\mathrm{EE}}^{-1} \\ \boldsymbol{B}_{\mathrm{ER}} &= \boldsymbol{A}_{\mathrm{EE}}^{-1} \underline{\boldsymbol{Y}}_{\mathrm{ER}} \\ \boldsymbol{C}_{\mathrm{EE}} &= \boldsymbol{A}_{\mathrm{EE}}^{-1}. \end{aligned} \tag{A.50}$$

In the particular case when $\boldsymbol{x}_{\mathrm{E}} = \boldsymbol{0}$ Equation (A.49) gives

$$\boldsymbol{x}_{\mathrm{R}} = \boldsymbol{A}_{\mathrm{R}} \boldsymbol{y}_{\mathrm{R}}. \tag{A.51}$$

These derived equations are useful when dealing with the transformation of the admittance and incremental network models.

A.3 Linear Ordinary Differential Equations

There are many good mathematical textbooks dealing with the solutions of ordinary differential equations. A well-written textbook aimed at engineers is Arnold (1992). This appendix contains the essential information regarding scalar linear differential equations necessary for understanding this textbook.

A.3.1 Fundamental System of Solutions

For real variables $x, t \in$ Real, the linear scalar homogeneous differential equation is of the form

$$\frac{\mathrm{d}^n x}{\mathrm{d}t^n} + a_1 \frac{\mathrm{d}^{n-1} x}{\mathrm{d}t^{n-1}} + \cdots + a_{n-2} \frac{\mathrm{d}^2 x}{\mathrm{d}t^2} + a_{n-1} \frac{\mathrm{d}x}{\mathrm{d}t} + a_n x = 0, \tag{A.52}$$

where $a_1, a_2, \ldots, a_n$ are constant coefficients.

Each function $x(t)$ that satisfies (A.52) is its solution. Without specifying some initial conditions, the solution of (A.52) is not unique and there may be an infinite number of solutions. For example, if function $x_1(t)$ is a solution then a solution is also any function $cx_1(t)$ where $c \neq 0$ is a constant. Additionally, if functions $x_1(t), x_2(t), x_3(t), \ldots$ are solutions then any linear combination of the functions $c_1 x_1(t) + c_2 x_2(t) + c_3 x_3(t) + \ldots$ is also a solution, because substituting that combination into (A.52) gives a sum of zeros, that is zero.

Solutions $x_1(t), x_2(t), x_3(t), \ldots$ are linearly independent if no solution can be expressed as a linear combination of the remaining solutions. For example, if $x_i(t), x_j(t), x_k(t), \ldots$ are linearly independent then there exist no constants $c_j, c_k, \ldots$ for which $x_i(t) = c_j x_j(t) + c_k x_k(t) + \ldots$ would hold.

The largest set of linearly independent solutions $x_1(t), x_2(t), x_3(t), \ldots, x_n(t)$ of Equation (A.52) is referred to as the *fundamental system of solutions*. Whether or not a given set of solutions is fundamental (i.e. the solutions are linearly independent) can be checked by investigating the

determinant of the matrix below, the columns of which contain individual solutions and their derivatives:

$$\det\ W = \det \begin{bmatrix} x_1 & x_2 & x_3 & \cdots & x_n \\ \dot{x}_1 & \dot{x}_2 & \dot{x}_3 & \cdots & \dot{x}_n \\ \ddot{x}_1 & \ddot{x}_2 & \ddot{x}_3 & \cdots & \ddot{x}_n \\ \dddot{x}_1 & \dddot{x}_2 & \dddot{x}_3 & \cdots & \dddot{x}_n \\ \vdots & \vdots & \vdots & \ddots & \vdots \end{bmatrix} \neq 0, \tag{A.53}$$

where $\dot{x} = \mathrm{d}x/\mathrm{d}t$, $\ddot{x} = \mathrm{d}^2x/\mathrm{d}t^2$, $\dddot{x} = \mathrm{d}^3x/\mathrm{d}t^3$, and so on, denote time derivatives. This determinant is referred to as the *Wronskian*, after the mathematician Jósef Wroński. It may be shown that solutions $x_1(t)$, $x_2(t)$, $x_3(t)$, …, $x_n(t)$ are linearly independent and form the fundamental system of solutions if, and only if, $\det\ W \neq 0$.

It follows then that a linear combination of the fundamental system of solutions of the form

$$x(t) = A_1x_1(t) + A_2x_2(t) + A_3x_3(t) + \cdots + A_nx_n(t) \tag{A.54}$$

is also a solution of Equation (A.52). Such a solution is referred to as the *general solution*. It is general because it contains all the fundamental solutions. Coefficients A_1, A_2, A_3, …, A_n are referred to as the *integration constants*.

For a linear equation the fundamental solutions are of the exponential form

$$x(t) = \mathrm{e}^{\lambda t}, \quad \frac{\mathrm{d}x}{\mathrm{d}t} = \lambda\mathrm{e}^{\lambda t}, \quad \frac{\mathrm{d}^2x}{\mathrm{d}t^2} = \lambda^2\mathrm{e}^{\lambda t}, \quad \frac{\mathrm{d}^3x}{\mathrm{d}t^3} = \lambda^3\mathrm{e}^{\lambda t}, \quad \text{and so on.} \tag{A.55}$$

Substituting (A.55) into Equation (A.52) gives

$$\lambda^n\mathrm{e}^{\lambda t} + a_1\lambda^{n-1}\mathrm{e}^{\lambda t} + \cdots + a_{n-2}\lambda^2\mathrm{e}^{\lambda t} + a_{n-1}\lambda\mathrm{e}^{\lambda t} + a_n\mathrm{e}^{\lambda t} = 0. \tag{A.56}$$

For each t, $\mathrm{e}^{\lambda t} \neq 0$ holds and Equation (A.56) may be simplified to the following form:

$$\lambda^n + a_1\lambda^{n-1} + \cdots + a_{n-2}\lambda^2 + a_{n-1}\lambda + a_n = 0. \tag{A.57}$$

This equation is referred to as the *characteristic equation*. It determines the values of λ for which the function $x(t) = \mathrm{e}^{\lambda t}$ is a solution of (A.52). The characteristic equation is an algebraic equation of nth order and it generally has n roots λ_1, λ_2, λ_3, …, λ_n. The roots of the characteristic equation form n solutions of the form

$$x_1(t) = \mathrm{e}^{\lambda_1 t}, \quad x_2(t) = \mathrm{e}^{\lambda_2 t}, \quad x_3(t) = \mathrm{e}^{\lambda_3 t}, \ldots, x_n(t) = \mathrm{e}^{\lambda_n t}. \tag{A.58}$$

The Wronskian of the solutions is

$$\det\ W = \det \begin{bmatrix} e^{\lambda_1 t} & e^{\lambda_2 t} & e^{\lambda_3 t} & \dots & e^{\lambda_n t} \\ \lambda_1 e^{\lambda_1 t} & \lambda_2 e^{\lambda_2 t} & \lambda_3 e^{\lambda_3 t} & \cdots & \lambda_n e^{\lambda_n t} \\ \lambda_1^2 e^{\lambda_1 t} & \lambda_2^2 e^{\lambda_2 t} & \lambda_3^2 e^{\lambda_3 t} & \cdots & \lambda_n^2 e^{\lambda_n t} \\ \lambda_1^3 e^{\lambda_1 t} & \lambda_2^3 e^{\lambda_2 t} & \lambda_3^3 e^{\lambda_3 t} & \cdots & \lambda_n^3 e^{\lambda_n t} \\ \vdots & \vdots & \vdots & \ddots & \vdots \end{bmatrix}. \tag{A.59}$$

Multiplying a matrix column by a number corresponds to multiplying the determinant of the matrix by that number. Hence the terms $e^{\lambda_1 t}$, $e^{\lambda_2 t}$, $e^{\lambda_3 t}$, and so on, can be extracted in front of the Wronskian (A.59). As

$$e^{\lambda_1 t} \cdot e^{\lambda_2 t} \cdot e^{\lambda_3 t} \cdot \ldots \cdot e^{\lambda_n t} = e^{(\lambda_1+\lambda_2+\lambda_3+\cdots+\lambda_n)t}, \tag{A.60}$$

Equation (A.59) can be expressed as

$$\det\ W = e^{(\lambda_1+\lambda_2+\lambda_3+\ldots+\lambda_n)t} \cdot \det \begin{bmatrix} 1 & 1 & 1 & \dots & 1 \\ \lambda_1 & \lambda_2 & \lambda_3 & \cdots & \lambda_n \\ \lambda_1^2 & \lambda_2^2 & \lambda_3^2 & \cdots & \lambda_n^2 \\ \lambda_1^3 & \lambda_2^3 & \lambda_3^3 & \cdots & \lambda_n^3 \\ \vdots & \vdots & \vdots & \ddots & \vdots \end{bmatrix}. \tag{A.61}$$

This determinant is made up of successive powers of the roots and is referred to as *Vandermonde's determinant*. It can be shown using mathematical induction that Vandermonde's determinant is equal to the sum of products of differences between the pairs of roots

$$\det \begin{bmatrix} 1 & 1 & 1 & \dots & 1 \\ \lambda_1 & \lambda_2 & \lambda_3 & \cdots & \lambda_n \\ \lambda_1^2 & \lambda_2^2 & \lambda_3^2 & \cdots & \lambda_n^2 \\ \lambda_1^3 & \lambda_2^3 & \lambda_3^3 & \cdots & \lambda_n^3 \\ \vdots & \vdots & \vdots & \ddots & \vdots \end{bmatrix} = \prod_{1 \le i \le j \le n} (\lambda_j - \lambda_i), \tag{A.62}$$

where

$$\prod_{1 \le i \le j \le n} (\lambda_j - \lambda_i) = (\lambda_n - \lambda_{n-1})(\lambda_n - \lambda_{n-2})(\lambda_n - \lambda_{n-3}) \ldots (\lambda_3 - \lambda_2)(\lambda_3 - \lambda_1)(\lambda_2 - \lambda_1). \tag{A.63}$$

Equation (A.62) is useful for a fast determination of Vandermonde's determinant. The proof can be found, for example, in Ogata (1967).

A.3.2 Real and Distinct Roots

The sufficient condition for Vandermonde's determinant given by (A.62), and therefore also the Wronskian given by (A.61), to be different from zero is that the roots of the characteristic equation are distinct:

$$\lambda_1 \neq \lambda_2 \neq \lambda_3 \neq \cdots \neq \lambda_n. \tag{A.64}$$

If this condition is satisfied, the functions given by (A.58) form the fundamental system of solutions of Equation (A.52). Hence the general solution (A.54) is

$$x(t) = A_1 e^{\lambda_1 t} + A_2 e^{\lambda_2 t} + A_3 e^{\lambda_3 t} + \cdots + A_n e^{\lambda_n t}. \tag{A.65}$$

When the integration constants $A_1, A_2, A_3, \ldots, A_n$ are not specified, the general solution gives an infinite number of solutions. The Cauchy problem consists of finding such a *particular solution* that satisfies the initial conditions for the solution and its derivatives: $x(t_0), \dot{x}(t_0), \ddot{x}(t_0), \dddot{x}(t_0), \ldots$. In order to solve the Cauchy problem, it is necessary to find such integration constants $A_1, A_2, A_3, \ldots, A_n$ for the general solution that the initial conditions are satisfied.

Often the initial conditions are assumed to be a non-zero value of the solution and zero values of its derivatives:

$$x(t_0) = \Delta x \neq 0, \quad \dot{x}(t_0) = 0, \quad \ddot{x}(t_0) = 0, \dddot{x}(t_0) = 0 \ \ldots. \tag{A.66}$$

Substituting function (A.65) and its derivatives calculated at time instant t_0 into (A.66) results in an algebraic equation

$$\left[\begin{array}{c|c|c|c|c} 1 & 1 & 1 & \ldots & 1 \\ \hline \lambda_1 & \lambda_2 & \lambda_3 & \cdots & \lambda_n \\ \hline \lambda_1^2 & \lambda_2^2 & \lambda_3^2 & \cdots & \lambda_n^2 \\ \hline \lambda_1^3 & \lambda_2^3 & \lambda_3^3 & \cdots & \lambda_n^3 \\ \hline \vdots & \vdots & \vdots & \ddots & \vdots \end{array}\right] \left[\begin{array}{c} A_1 \\ \hline A_2 \\ \hline A_3 \\ \hline A_4 \\ \hline \vdots \end{array}\right] = \left[\begin{array}{c} \Delta x \\ \hline 0 \\ \hline 0 \\ \hline 0 \\ \hline \vdots \end{array}\right]. \tag{A.67}$$

The matrix on the left hand side is Vandermonde's matrix. Equation (A.62) shows that under the assumption of distinct roots of the characteristic equation, the determinant of Vandermonde's matrix is different from zero, which means that the matrix is not singular and there is only one solution for the integration constants $A_1, A_2, A_3, \ldots, A_n$.

Example A3.1

Solve a third-order equation $\dddot{x} + 6\ddot{x} + 11\dot{x} + 6x = 0$ under the initial solutions given by (A.66).

The characteristic equation is $\lambda^3 + 6\lambda^2 + 11\lambda + 6 = 0$ with the distinct roots $\lambda_1 = -3, \lambda_2 = -2, \lambda_3 = -1$. The general solution (A.65) is of the form $x(t) = A_1 e^{-3t} + A_2 e^{-2t} + A_3 e^{-t}$. Equation (A.67) is

$$\begin{bmatrix} 1 & 1 & 1 \\ -3 & -2 & -1 \\ 9 & 4 & 1 \end{bmatrix} \begin{bmatrix} A_1 \\ A_2 \\ A_3 \end{bmatrix} = \begin{bmatrix} \Delta x \\ 0 \\ 0 \end{bmatrix} \quad \text{or} \quad \begin{bmatrix} A_1 \\ A_2 \\ A_3 \end{bmatrix} = \frac{1}{2} \begin{bmatrix} 2 & 3 & 1 \\ -6 & -8 & -2 \\ 6 & 5 & 1 \end{bmatrix} \begin{bmatrix} \Delta x \\ 0 \\ 0 \end{bmatrix}. \tag{A.68}$$

Hence $A_1 = \Delta x$, $A_2 = -3 \cdot \Delta x$, $A_3 = 3 \cdot \Delta x$. Finally, $x(t) = \Delta x \cdot (e^{-3t} - 3e^{-2t} + 3e^{-t})$.

For the dynamics considered in this book, of particular interest is a second-order scalar equation corresponding to the equation of motion for the synchronous generator (Section 5.4.6). Hence a solution to the second-order equation will now be discussed when the roots of the characteristic equation are initially assumed to be real.

Example A3.2

Solve the second-order equation $\ddot{x} - (\alpha_1 + \alpha_2)\dot{x} + \alpha_1\alpha_2 x = 0$ with the initial conditions given by (A.66).

The characteristic equation is $\lambda^2 - (\alpha_1 + \alpha_2)\lambda + \alpha_1\alpha_2 = 0$ with the distinct roots $\lambda_1 = \alpha_1, \lambda_2 = \alpha_2, \alpha_2 \neq \alpha_1$. The general solution (A.65) is $x(t) = A_1 e^{\alpha_1 t} + A_2 e^{\alpha_2 t}$. Equation (A.67) takes the form

$$\begin{bmatrix} 1 & 1 \\ \alpha_1 & \alpha_2 \end{bmatrix} \begin{bmatrix} A_1 \\ A_2 \end{bmatrix} = \begin{bmatrix} \Delta x \\ 0 \end{bmatrix} \quad \text{or} \quad \begin{bmatrix} A_1 \\ A_2 \end{bmatrix} = \frac{1}{\alpha_2 - \alpha_1} \begin{bmatrix} \alpha_2 & -1 \\ -\alpha_1 & 1 \end{bmatrix} \begin{bmatrix} \Delta x \\ 0 \end{bmatrix}. \tag{A.69}$$

Hence $A_1 = \Delta x \cdot \alpha_2/(\alpha_2 - \alpha_1)$ and $A_2 = -\Delta x \cdot \alpha_1/(\alpha_2 - \alpha_1)$.

Finally $x(t) = \Delta x \cdot [\alpha_2 e^{\alpha_1 t} - \alpha_1 e^{\alpha_2 t}]/(\alpha_2 - \alpha_1)$.

A.3.3 Repeated real roots

If condition (A.64) is not satisfied, and there are repeated real roots of the characteristic equation, then the fundamental system of equations can be built from those solutions that are linearly independent and correspond to distinct roots. Obviously there will then be fewer than n solutions corresponding to those roots, that is too few to solve the Cauchy problem of finding a particular solution for given initial conditions. In order to obtain a unique solution, one has to supplement the fundamental system of solutions by additional linearly independent solutions such that there is overall n solutions, where n is the order of the differential equation.

Let λ_i be a root of the characteristic equation repeated k times. Then one of the solutions belonging to the fundamental system of solutions corresponding to that root is of the form $x_{i1}(t) = e^{\lambda_i t}$. There are still $(k-1)$ missing linearly independent solutions which have to supplement the fundamental system of solutions. For a root λ_i repeated k times, a solution is formed in the following way:

$$x_{i_2}(t) = A_{i_2}(t) \cdot e^{\lambda_i t}, \quad x_{i_3}(t) = A_{i_3}(t) \cdot e^{\lambda_i t}, \ldots, x_{i_k}(t) = A_{i_k}(t) \cdot e^{\lambda_i t}, \tag{A.70}$$

where $A_{i_2}(t)$, $A_{i_3}(t), \ldots, A_{ik}(t)$ are the required functions chosen in such a way that the solutions are linearly independent. It can be shown (Arnold, 1992) that the required functions are orthogonal polynomials $t, t^2, t^3, \ldots, t^{k-1}$. The complete set of additional solutions corresponding to a root λ_i repeated k times is

$$x_{i1}(t) = e^{\lambda_i t}, \quad x_{i_2}(t) = t \cdot e^{\lambda_i t}, \quad x_{i_3}(t) = t^2 \cdot e^{\lambda_i t}, \ldots, x_{i_k}(t) = t^{k-1} \cdot e^{\lambda_i t}. \tag{A.71}$$

Obviously the complete set of fundamental solutions also contains the solutions corresponding to other roots.

Example A3.3

Solve a second-order equation $\ddot{x} - 2\alpha\dot{x} + \alpha^2 x = 0$ with the initial conditions given by (A.66).

The characteristic equation is $\lambda^2 - 2\alpha\lambda + \alpha^2 = 0$. It has two repeated roots $\lambda_1 = \lambda_2 = \alpha$. The fundamental system of solutions consists of the following functions: $e^{\alpha t}, t \cdot e^{\alpha t}$. The corresponding general solution is $x(t) = A_1 e^{\alpha t} + A_2 t e^{\alpha t}$.

Hence $\dot{x}(t) = \alpha A_1 e^{\alpha t} + A_2(1 + \alpha t) \cdot e^{\alpha t}$. Substituting the initial conditions $x(t_0) = \Delta x$ and $\dot{x}(t) = 0$ gives $A_1 = \Delta x$ and $\alpha A_1 + A_2(1 + \alpha t) = 0$, hence $A_2 = -\Delta x \cdot \alpha$. Finally $x(t) = \Delta x \cdot e^{\alpha t}(1 - \alpha t)$.

A.3.4 Complex and Distinct Roots

It is known from the theory of polynomials that if polynomial (A.57) with real coefficients $a_1, \ldots, a_{n-2}, a_{n-1}, a_n$ has complex roots then the roots form complex conjugate pairs λ_i, λ_i^* and so on.

Assume the following notation:

$$\lambda_i = \alpha_i + \mathrm{j}\Omega_i \quad \text{and} \quad \lambda_i^* = \alpha_i - \mathrm{j}\Omega_i. \tag{A.72}$$

Obviously the condition of distinct roots (A.64) is satisfied for this pair as $\lambda_i \neq \lambda_i^*$. Vandermonde's determinant can be expressed using (A.62) as

$$\prod_{1 \le i \le j \le n} (\lambda_j - \lambda_i) = (\lambda_n - \lambda_{n-1})(\lambda_n - \lambda_{n-2}) \ldots (\lambda_i - \lambda_i^*) \ldots (\lambda_3 - \lambda_2)(\lambda_3 - \lambda_1)(\lambda_2 - \lambda_1) \neq 0, \tag{A.73}$$

and it is different from zero because $(\lambda_i - \lambda_i^*) = \mathrm{j}2\Omega_i \neq 0$. This makes it possible to assume the following fundamental system of solutions:

$$\mathrm{e}^{\lambda_1 t}, \ldots, \mathrm{e}^{\lambda_i t}, \quad \mathrm{e}^{\lambda_i^* t}, \ldots, \mathrm{e}^{\lambda_n t}, \tag{A.74}$$

which contains exponential functions of λ_i and λ_i^*.

Using Equation (A.67) for given integration constants $A_1, \ldots, A_i, \ldots, A_n$ makes it possible to find the particular solution. As Vandermonde's matrix in Equation (A.67) and its determinant are complex, it may be expected that the integration constants in the fundamental set of solutions will also be complex, that is

$$x(t) = \ldots + A_i \mathrm{e}^{\lambda_i t} + B_i \mathrm{e}^{\lambda_i^* t} + \ldots, \tag{A.75}$$

where variables $x, t \in$ Real and the integration constants $A_i, B_i \in$ Complex. Differentiation of (A.75) gives

$$\dot{x}(t) = \ldots + \lambda_i A_i \mathrm{e}^{\lambda_i t} + \lambda_i^* B_i \mathrm{e}^{\lambda_i^* t} + \ldots. \tag{A.76}$$

Integration constants A_i, B_i can be calculated from the initial conditions assuming

$$\begin{aligned} x(t=0) &= \ldots + \Delta x_i + \ldots = \Delta x \\ \dot{x}(t=0) &= \ldots + 0 + \ldots = 0. \end{aligned} \tag{A.77}$$

Substituting these initial conditions into Equations (A.75) and (A.76) gives the following two simple equations: $A_i + B_i = \Delta x_i$ and $\lambda_i A_i + \lambda_i^* B_i = 0$. Solving these equations requires care because both A_i, B_i and λ_i, λ_i^* are complex numbers. Expressing the equation in matrix form gives

$$\begin{bmatrix} 1 & 1 \\ \lambda_i & \lambda_i^* \end{bmatrix} \begin{bmatrix} A_i \\ B_i \end{bmatrix} = \begin{bmatrix} \Delta x_i \\ 0 \end{bmatrix} \quad \text{or} \quad \begin{bmatrix} A_i \\ B_i \end{bmatrix} = \frac{1}{-\mathrm{j}2\Omega_i} \begin{bmatrix} \lambda_i^* & -1 \\ -\lambda_i & 1 \end{bmatrix} \begin{bmatrix} \Delta x_i \\ 0 \end{bmatrix}, \tag{A.78}$$

where, according to (A.72), Ω_i is the imaginary part of λ_i. Now one gets

$$\begin{aligned} A_i &= \Delta x \frac{1}{-\mathrm{j}2\Omega_i} \lambda_i^* = \Delta x \frac{\Omega_i + \mathrm{j}\alpha_i}{2\Omega_i} \\ B_i &= \Delta x \frac{1}{-\mathrm{j}2\Omega_i} (-\lambda_i) = \Delta x \frac{\Omega_i - \mathrm{j}\alpha_i}{2\Omega_i} = A_i^*. \end{aligned} \tag{A.79}$$

This shows that $B_i = A_i^*$. The general important conclusion is that for each pair of solutions $\mathrm{e}^{\lambda_i t}$ and $\mathrm{e}^{\lambda_i^* t}$ the integration constants resulting from the initial conditions form a complex conjugate

pair A_i, A_i^*. Hence the solutions of (A.75) is

$$x(t) = \ldots + A_i e^{\lambda_i t} + A_i^* e^{\lambda_i^* t} + \ldots \tag{A.80}$$

where

$$\begin{aligned} A_i e^{\lambda_i t} + A_i^* e^{\lambda_i^* t} &= A_i e^{\alpha_i t}(\cos \Omega_i t + \mathrm{j} \sin \Omega_i t) + A_i^* e^{\alpha_i t}(\cos \Omega_i t - \mathrm{j} \sin \Omega_i t) \\ &= e^{\alpha_i t}\left[(A_i + A_i^*) \cos \Omega_i t + \mathrm{j}(A_i - A_i^*) \sin \Omega_i t\right]. \end{aligned} \tag{A.81}$$

Obviously $(A_i + A_i^*) = 2 \operatorname{Re} A_i$ and $\mathrm{j}(A_i - A_i^*) = -2 \operatorname{Im} A_i$ are real numbers equal to the real and imaginary parts of the integration constant A_i, respectively. Hence Equation (A.81) is now

$$A_i e^{\lambda_i t} + A_i^* e^{\lambda_i^* t} = e^{\alpha_i t}\left[2 \operatorname{Re} A_i \cdot \cos \Omega_i t - 2 \operatorname{Im} A_i \cdot \sin \Omega_i t\right]. \tag{A.82}$$

Note that the left hand side of the equation contains operations on real numbers and the right hand side contains operations on imaginary numbers. This means that appropriate operations on complex numbers A_i, A_i^*, $e^{\lambda_i t}$, $e^{\lambda_i^* t}$ must result in the imaginary part of the term $A_i e^{\lambda_i t} + A_i^* e^{\lambda_i^* t}$ being equal to zero so that the overall result is a real number. This is an important observation leading to the conclusion that for the discussed case of complex conjugate pairs of roots, the particular solution is of the form

$$x(t) = \ldots + 2 \operatorname{Re} A_i \cdot e^{\alpha_i t} \cos \Omega_i t - 2 \operatorname{Im} A_i \cdot e^{\alpha_i t} \sin \Omega_i t + \ldots. \tag{A.83}$$

Hence it can be concluded that operations on complex numbers connected with looking for the particular solution are unnecessary because, instead of the fundamental system of solutions given by (A.74), one can consider a fundamental system of solutions of the form

$$e^{\lambda_1 t}, \ldots, e^{\alpha_i t} \cos \Omega_i t, \; e^{\alpha_i t} \sin \Omega_i t, \ldots, e^{\lambda_n t}, \tag{A.84}$$

consisting of real functions. As sine and cosine functions are orthogonal, the solutions $e^{\alpha_i t} \cos \Omega_i t$ and $e^{\alpha_i t} \sin \Omega_i t$ are linearly independent. This can be checked by calculating the Wronskian of the fundamental system of solutions (A.84) and the corresponding Vandermonde's determinant. The latter will contain terms proportional to $(\cos \Omega_i t - \sin \Omega_i t) \neq 0$.

These considerations lead to an important conclusion:

> Each complex conjugate pair of the roots λ_i, λ_i^* in the solution $x(t)$ of the differential equation (A.52) corresponds to real exponential functions $e^{\alpha_i t} \cos \Omega_i t$ and $e^{\alpha_i t} \sin \Omega_i t$ because the imaginary parts of the solutions corresponding to the pairs λ_i, λ_i^* cancel each other out.

There is another proof of the above statement using the theorem that if a complex function is a fundamental solution of a linear ordinary differential equation, then both the real and imaginary parts of that function also form the general solution. Proof of this can be found in a number of textbooks including Arnold (1992).

An examination of Equation (A.84) shows that the real roots λ_i of the characteristic equation will produce exponential terms of the form $e^{\lambda_i t}$ so that the roots are the reciprocals of time constants of the exponential terms. The complex conjugate root pairs $\lambda_i = \lambda_i^* = \alpha_i + \mathrm{j}\Omega_i$ of the characteristic equation will produce oscillatory terms $e^{\alpha_i t} \cos \Omega_i t$ and $e^{\alpha_i t} \sin \Omega_i t$. The imaginary parts of the roots are therefore equal to the frequencies of oscillation of each term and the real parts of the roots are the reciprocals of time constants of the exponential envelope of the oscillatory terms. The overall solution is stable if the real parts of all the roots are negative.

For the dynamics considered in this book, of particular interest is a second-order scalar equation corresponding to the equation of motion for the synchronous generator (Section 5.4.6), but now a solution to the second-order equation will be discussed when the roots of the characteristic equation are complex.

Example A3.4

Solve a second-order equation $\ddot{x} - 2\alpha\dot{x} + (\alpha^2 + \Omega^2)x = 0$ with the initial conditions given by (A.66).
The characteristic equation is $\lambda^2 - 2\alpha\lambda + (\alpha^2 + \Omega^2) = 0$. The roots are $\lambda_1 = \alpha + \mathrm{j}\Omega$ and $\lambda_2 = \lambda_1^* = \alpha - \mathrm{j}\Omega$. The fundamental system of solutions $\mathrm{e}^{\lambda_1 t}$, $\mathrm{e}^{\lambda_1^* t}$ results in the following Vandermonde's determinant:

$$\det \begin{bmatrix} 1 & 1 \\ \lambda_1 & \lambda_1^* \end{bmatrix} = \lambda_1^* - \lambda_1 = -\mathrm{j}2\Omega \neq 0, \tag{A.85}$$

which shows that the fundamental system of solutions was well chosen and the general solutions is of the form

$$x(t) = A_1 \mathrm{e}^{\lambda_1 t} + B_1 \mathrm{e}^{\lambda_1^* t}. \tag{A.86}$$

Equation (A.78) takes the form

$$\begin{bmatrix} 1 & 1 \\ \lambda_1 & \lambda_1^* \end{bmatrix} \begin{bmatrix} A_1 \\ B_1 \end{bmatrix} = \begin{bmatrix} \Delta x \\ 0 \end{bmatrix} \quad \text{or} \quad \begin{bmatrix} A_1 \\ B_1 \end{bmatrix} = \frac{1}{-\mathrm{j}2\Omega} \begin{bmatrix} \lambda_1^* & -1 \\ -\lambda_1 & 1 \end{bmatrix} \begin{bmatrix} \Delta x \\ 0 \end{bmatrix}. \tag{A.87}$$

Hence

$$A_1 = \Delta x \cdot \frac{\Omega + \mathrm{j}\alpha}{2\Omega} \quad \text{and} \quad B_1 = \Delta x \cdot \frac{\Omega - \mathrm{j}\alpha}{2\Omega} = A_1^*. \tag{A.88}$$

After substituting (A.88) into (A.86) simple algebra gives the following particular solution:

$$x(t) = \frac{\Delta x}{\Omega} \mathrm{e}^{\alpha t} [\omega \cos \Omega t - \alpha \sin \Omega t]. \tag{A.89}$$

Obviously the solution can be obtained in a simpler way by assuming at the outset the fundamental system of solutions given by (A.84), $\mathrm{e}^{\alpha t} \cos \Omega t$, $\mathrm{e}^{\alpha t} \sin \Omega t$, and the general solution

$$x(t) = C_1 \mathrm{e}^{\alpha t} \Omega \cos \omega t + C_2 \mathrm{e}^{\alpha t} \alpha \sin \Omega t. \tag{A.90}$$

Substituting the initial condition $x(t_0) = \Delta x$ leads to $C_1 = \Delta x / \Omega$. Differentiating (A.90) and substituting $\dot{x}(t_0) = 0$ gives $C_2 = -C_1$. Substituting the calculated constants $C_1 = -C_2 = \Delta x / \Omega$ into Equation (A.90) gives the solution given by (A.89).

The solution (A.89) contains an expression $[\Omega \cos \Omega t - \alpha \sin \Omega t]$. It corresponds to the cosine of angle differences: $\cos(\Omega t + \phi) = [\cos \Omega t \cos \phi - \sin \Omega t \sin \phi]$. In order to obtain that form exactly, it is necessary to transform Equation (A.89) in the following way:

$$x(t) = \frac{\Delta x}{\Omega} \mathrm{e}^{\alpha t} \sqrt{\Omega^2 + \alpha^2} \left[\frac{\Omega}{\sqrt{\Omega^2 + \alpha^2}} \cos \Omega t - \frac{\alpha}{\sqrt{\Omega^2 + \alpha^2}} \sin \Omega t \right], \tag{A.91}$$

where the expression in front of the square brackets was multiplied by $\sqrt{\Omega^2 + \alpha^2}$ while the components in the square brackets were divided by the same term. Assuming the notation

$$\sin \phi = \frac{\alpha}{\sqrt{\Omega^2 + \alpha^2}} \quad \text{and} \quad \cos \phi = \frac{\Omega}{\sqrt{\Omega^2 + \alpha^2}}, \tag{A.92}$$

it is easy to check that $\sin^2 \phi + \cos^2 \phi = 1$. With this definition of angle ϕ, Equation (A.91) becomes

$$x(t) = \frac{\Delta x}{\cos \phi} \mathrm{e}^{\alpha t} \cos(\Omega t + \phi). \tag{A.93}$$

This form of the second-order equation is convenient because Equation (A.93) clearly shows that the solution is in the form of a cosine function with exponentially decaying amplitude for $\alpha < 1$ and exponentially increasing amplitude for $\alpha > 1$ or a constant amplitude for $\alpha = 0$. Inspection of (A.93) shows that the solution satisfies the initial condition $x(t = 0) = \Delta x$.

Second-order equations represent many physical problems. It is convenient to express a second-order equation in the *standard form* investigated in the next example.

Example A3.5

Consider the standard form of a second-order equation $\ddot{x} + 2\zeta\Omega_{\text{nat}}\dot{x} + \Omega_{\text{nat}}^2 x = 0$ where Ω_{nat} is the *natural frequency of oscillations* and ζ is the *damping* ratio. The initial conditions are given by (A.66). The characteristic equation is $\lambda^2 + 2\zeta\Omega_{\text{nat}}\lambda + \Omega_{\text{nat}}^2 = 0$. When $\Delta = -4\Omega_{\text{nat}}^2(1 - \zeta^2) \geq 0$, that is the damping ratio $\zeta \geq 1$, the roots are real and the solution will contain the exponential terms discussed in Example A3.2 and Example A3.3. In this example the case of the *underdamped second-order system* will be discussed when $0 \leq \zeta < 1$. The characteristic equation will then have two roots forming a complex conjugate pair:

$$\lambda_{1,2} = -\zeta\Omega_{\text{nat}} \pm \text{j}\Omega_{\text{nat}}\sqrt{1 - \zeta^2} \quad \text{or} \quad \lambda_{1,2} = -\zeta\Omega_{\text{nat}} \pm \text{j}\Omega_{\text{d}}, \tag{A.94}$$

where $\Omega_{\text{d}} = \Omega_{\text{nat}}\sqrt{1 - \zeta^2}$ is the *damped frequency of oscillation* (in rad/s) as Ω_{nat} is the natural frequency of oscillations (in rad/s) when damping is neglected, that is when $\zeta = 0$ and $\lambda_{1,2} = \pm\text{j}\Omega_{\text{nat}}$. The solution $x(t)$ can be obtained in the same way as in the previous example or by using the solution (A.93) and substituting $\Omega = \Omega_{\text{d}}$ and $\alpha = -\zeta\Omega_{\text{nat}}$. Hence

$$x(t) = \frac{\Delta x}{\cos\phi} \text{e}^{-\zeta\Omega_{\text{nat}}t} \cos(\Omega_{\text{d}}t + \phi), \tag{A.95}$$

where $\phi = -\arcsin\zeta$.

A.3.5 Repeated Complex Roots

As shown previously, each complex conjugate pair of roots λ_i, λ_i^* corresponds to a solution (A.78) containing the terms $\text{e}^{\alpha_i t}\cos\Omega_i t$ and $\text{e}^{\alpha_i t}\sin\Omega_i t$. When the roots λ_i, λ_i^* are repeated k times then, as in (A.85), the general solution has to be complemented by the same terms multiplied by orthogonal polynomials $t, t^2, t^3, \ldots, t^{k-1}$. For a pair of complex roots repeated k times the following solutions are obtained:

$$\begin{aligned} &\text{e}^{\alpha_i t}\cos\Omega_i t, \quad t\cdot\text{e}^{\alpha_i t}\cos\Omega_i t, \quad t^2\cdot\text{e}^{\alpha_i t}\cos\Omega_i t, \ldots, t^{k-1}\cdot\text{e}^{\alpha_i t}\cos\Omega_i t \\ &\text{e}^{\alpha_i t}\sin\Omega_i t, \quad t\cdot\text{e}^{\alpha_i t}\sin\Omega_i t, \quad t^2\cdot\text{e}^{\alpha_i t}\sin\Omega_i t, \ldots, t^{k-1}\cdot\text{e}^{\alpha_i t}\sin\Omega_i t. \end{aligned} \tag{A.96}$$

Obviously the complete set of fundamental solutions also contains the solutions corresponding to other roots.

A.3.6 First-Order Complex Differential Equation

A particular case of a linear first-order differential equation is a homogeneous equation of the form $\dot{z} - \lambda z = 0$ where λ is a complex number. The equation can be rewritten as

$$\dot{z} = \lambda z. \tag{A.97}$$

According to the theory developed earlier the solution will be of the form

$$z(t) = \text{e}^{\lambda t} z_0, \tag{A.98}$$

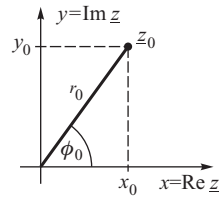

Figure A.2 Initial condition in the complex plane.

where $z_0 = z(t_0)$ is an initial condition (a complex number). Assume the following notation:

$$z(t) = x(t) + \mathrm{j}y(t), \quad z_0 = x_0 + \mathrm{j}y_0, \quad \lambda = \alpha + \mathrm{j}\Omega. \tag{A.99}$$

The solution will be interpreted in the complex plane of coordinates $x = \mathrm{Re}z$ and $y = \mathrm{Im}z$. Substituting (A.99) into (A.98) gives

$$x(t) + \mathrm{j}y(t) = \mathrm{e}^{(\alpha+\mathrm{j}\Omega)t}(x_0 + \mathrm{j}y_0),$$

or

$$x(t) + \mathrm{j}y(t) = \mathrm{e}^{\alpha t}(x_0 + \mathrm{j}y_0)(\cos\Omega t + \mathrm{j}\sin\Omega t).$$

Multiplying and ordering the terms gives

$$x(t) = \mathrm{e}^{\alpha t}(x_0\cos\Omega t - y_0\sin\Omega t), \tag{A.100a}$$
$$y(t) = \mathrm{e}^{\alpha t}(y_0\cos\Omega t + x_0\sin\Omega t). \tag{A.100b}$$

Figure A.2 shows that the initial condition $z_0 = x_0 + \mathrm{j}y_0$ is a point on the complex plane where

$$x_0 = r_0\cos\phi_0, \quad y_0 = r_0\sin\phi_0, \quad r_0 = \sqrt{x_0^2 + y_0^2}. \tag{A.101}$$

Substituting (A.101) into (A.100a) gives

$$x(t) = r_0\mathrm{e}^{\alpha t}(\cos\phi_0\cos\Omega t - \sin\phi_0\sin\Omega t), \tag{A.102a}$$
$$y(t) = r_0\mathrm{e}^{\alpha t}(\sin\phi_0\cos\Omega t + \cos\phi_0\sin\Omega t). \tag{A.102b}$$

Equations (A.102a,b) can be expressed as

$$x(t) = r_0\mathrm{e}^{\alpha t}\cos(\Omega t + \phi_0), \tag{A.103a}$$
$$y(t) = r_0\mathrm{e}^{\alpha t}\sin(\Omega t + \phi_0). \tag{A.103b}$$

Obviously the solutions $x(t)$ and $y(t)$ given by (A.103a, b) are proportional to the sine and cosine and are therefore shifted in time by $\pi/2$. Squaring and adding both sides of (A.103a, b) gives

$$r(t) = r_0\mathrm{e}^{\alpha t} \quad \text{where} \quad r(t) = \sqrt{[x(t)]^2 + [y(t)]^2}. \tag{A.103}$$

Again creating a complex number $z(t) = x(t) + \mathrm{j}y(t)$ from the solutions (A.103a, b) gives

$$z(t) = r_0\,\mathrm{e}^{\alpha t}[\cos(\Omega t + \phi_0) + \mathrm{j}\sin(\Omega t + \phi_0)] = r_0\,\mathrm{e}^{\alpha t}\mathrm{e}^{\mathrm{j}(\Omega t+\phi_0)} = r(t)\cdot\mathrm{e}^{\mathrm{j}(\Omega t+\phi_0)}. \tag{A.104}$$

Figure A.3 shows that function (A.105) describes a *logarithmic spiral* in the complex plane starting at a point (x_0, y_0) corresponding to the initial condition. The spiral rotates anticlockwise if $\Omega = \mathrm{Im}\lambda > 0$ and clockwise if $\Omega = \mathrm{Im}\lambda < 0$. For $\alpha = \mathrm{Re}\lambda < 0$ the spiral is converging towards the

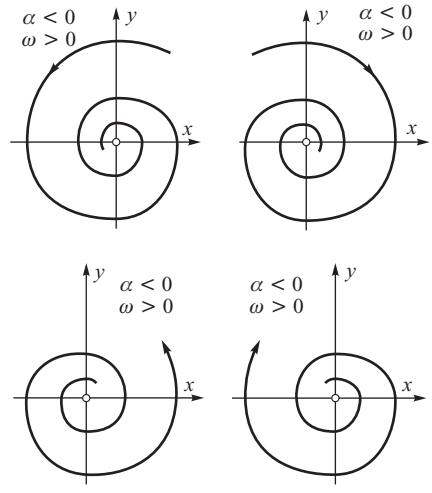

Figure A.3 Logarithmic spirals.

origin of coordinates while for $\alpha = \mathrm{Re}\lambda > 0$ the spiral is diverging. For $\alpha = \mathrm{Re}\lambda = 0$ the solution $z(t)$ corresponds to a circle in the complex plane.

Obviously for a conjugate value $\lambda^* = \alpha - \mathrm{j}\Omega = \alpha + \mathrm{j}(-\Omega)$ the imaginary part of λ^* has the opposite sign to λ. This means that the spiral corresponding to λ^* rotates in the opposite direction to the spiral corresponding to λ. Hence if a function is the sum of solutions for complex conjugate pairs λ, λ^* then the imaginary parts of the solutions will cancel each other out and the only remaining part will be the double real part of the spiral, that is

$$z_i(t) + z_j(t) = z_i(t) + z_i^*(t) = 2\mathrm{Re}z_i(t) = 2x(t) = 2r_0\, \mathrm{e}^{\alpha t} \cos(\Omega t + \phi_0). \tag{A.105}$$

This observation is important for the solution of matrix differential equations discussed in Section 12.1.

References

ABB (1991) An introduction to ABB series capacitors. *ABB Information Publication*.

Abe, S. and Isono, A. (1983) Determination of power system voltage stability. *Electrical Engineering in Japan*, **103** (3).

Acha, E., Fuerte-Esquivel, C.R. and Angeles-Camancho, C. (2004) *FACTS Modelling and Simulation in Power Networks*, John Wiley & Sons, Ltd, Chichester.

Ackermann, T. (2005) *Wind Power in Power Systems*, John Wiley & Sons, Ltd, Chichester.

Adibi, M.M., Hirsch, P.M. and Jordan, J.A. (1974) Solution methods for transient and dynamic stability. *Proceedings of the IEEE*, **62** (7), 951–8.

Adkins, B. (1957) *The General Theory of Electrical Machines*, Chapman and Hall.

A-eberle, *CPR-D Collapse Prediction Relay*, http://www.a-eberle.de.

Ahlgren, L., Johansson, K.E. and Gadhammar, A. (1978) Estimated life expenditure of turbine-generator shafts at network faults and risk for subsynchronous resonance in the Swedish 400 kV system. *IEEE Transactions on Power Apparatus and Systems*, **PAS-97** (6).

Ajjarapu, V. and Christy, C. (1992) The continuation power flow: a tool for steady-state voltage stability analysis. *IEEE Transactions on Power Systems*, **PWRS-7** (1), 416–423.

Akagi, H., Watanabe, E.H. and Aredes, M. (2007) *Instantaneous Power Theory and Application to Power Conditioning*, John Wiley & Sons, Inc.

Alsac, O., Stott, B. and Tinney, W.F. (1983) Sparsity oriented compensation methods for modified network solutions. *IEEE Transactions on Power Apparatus and Systems*, **PAS-102**, 1050–60.

Anderson, P.M., Agrawal, B.L. and Van Ness, J.E. (1990) *Subsynchronous Resonance in Power Systems*, IEEE Press.

Anderson, P.M. and Bose, A. (1983) Stability simulation of wind turbine systems. *IEEE Transactions on Power Applications and Systems*, **102**, 3791–5.

Anderson, P.M. and Fouad, A.A. (1977) *Power System Control and Stability*, The Iowa State University Press (2nd edn IEEE Press, 2003).

Arnold, W.I. (1992) *Ordinary Differential Equations*, Springer-Verlag.

Arrillaga, J. and Arnold, C.P. (1990) *Computer Analysis of Power Systems*, John Wiley & Sons, Ltd.

Arrillaga, J., Arnold, C.P. and Harker, B.J. (1983) *Computer Modelling of Electrical Power Systems*, John Wiley & Sons, Ltd.

Ashok Kumar, B.S.A., Parthasawathy, K., Prabhakara, F.S. and Khincha, H.P. (1970) Effectiveness of series capacitors in long distance transmission lines. *IEEE Transactions on Power Apparatus and Systems*, **PAS-89** (4), 941–50.

Athay, T., Podmore, R. and Virmani, S. (1979) A practical method for the direct analysis of transient stability. *IEEE Transactions on Power Apparatus and Systems*, **98** (2).

Balu, N.J. (1980) Fast turbine valving and independent pole tripping breaker applications for plant stability. *IEEE Transactions on Power Apparatus and Systems*, **PAS-99** (4).

Bellman, R. (1970) *Introduction to Matrix Analysis*, 2nd edn, McGraw-Hill.

Berg, G.L. (1973) Power system load representation. *IEE Proceedings*, **120**, 344–8.

© 2008 John Wiley & Sons, Ltd

Bernas, S. (1971) Zastepowanie grupy generatorow przy badaniu stabilnosci systemu elektroenergetycznego. *Prace Naukowe PW, Elektryka*, **17**.

Bialek, J. (1996) Tracing the flow of electricity. *IEE Proceedings – Generation, Transmission and Distribution*, **143** (4), 313–20.

Bialek, J. (2007) Why has it happened again? Comparison between the 2006 UCTE blackout and the blackouts of 2003. *IEEE PowerTech 2007, Lausanne*.

Bialek, J. and Grey, D.J. (1996) Application of clustering and factorisation tree techniques for parallel solution of sparse network equations. *IEE Proceedings – Generation, Transmission and Distribution*, **141** (6), 609–16.

Bölderl, P., Kulig, T. and Lambrecht, D. (1975) Beurteilung der Torsionsbeanspruchung in den Wellen von Turbosätzen bei wiederholt auftrenden Störungen im Laufe der Betriebszeit. *ETZ-A*, **96**, Heft 4.

Bourgin, F., Testud, G., Heilbronn, B. and Verseille, J. (1993) Present practices and trends on the French power system to prevent voltage collapse. *IEEE Transactions on Power Systems*, **PWRS-8** (3), 778–88.

Boyle, G. (2004) *Renewable Energy: Power for a Sustainable Future*, 2nd edn, Oxford University Press.

Brameller, A., Allan, R.N. and Hamam, Y.M. (1976) *Sparsity. Its Practical Application to System Analysis*, Pitman, London.

Breulmann, H., Grebe, E., Lösing, M. *et al.* (2000) *Analysis and Damping of Inter-Area Oscillations in the UCTE/CENTREL Power System.* CIGRE Paper No. 38–113.

Brown, H.E. (1975) *Solution of Large Networks by Matrix Methods*, John Wiley & Sons, Inc.

Brown, H.E., Shipley, R.B., Coleman, D. and Nied, R.B. (1969) A study of stability equivalents. *IEEE Transactions on Power Apparatus and Systems*, **PAS-88** (3).

Brown, P.G, de Mello, F.P., Lenfest, E.H. and Mills, R.J. (1970) Effects of excitation, turbine energy control and transmission on transient stability. *IEEE Transactions on Power Apparatus and Systems*, **PAS-89** (6).

Bumby, J.R. (1982) Torsional natural frequencies in the superconducting turbogenerator. *IEE Proceedings*, **129** (Pt C, 4), 141–51.

Bumby, J.R. (1983) *Superconducting Rotating Electrical Machines*, Clarendon Press, Oxford.

Bumby, J.R. and Wilson, J.M. (1983) Structural modes and undamped torsional natural frequencies of a superconducting turbogenerator rotor. *Journal of Sound and Vibration*, **87** (4), 589–602.

Cai, Y.Q. and Wu, C.S. (1986) A novel algorithm for aggregating coherent generating units. IFAC Symposium on Power System and Power Plant Control, Beijing, China.

Carpentier, J., Girard, R. and Scano, E. (1984) Voltage collapse proximity indicators computed from an optimal power flow. Proceedings of the 8th Power System Computing Conference, Helsinki, pp. 671–78.

Cegrell, T. (1986) *Power System Control Technology*, Prentice Hall International.

Chai, J.S. and Bose, A. (1993) Bottlenecks in parallel algorithms for power system stability analysis. *IEEE Transactions on Power Systems*, **PWRS-8** (1), 9–15.

Ching, Y.K. and Adkins, B.A. (1954) Transient theory of synchronous generators under unbalanced conditions. *IEE Proceedings*, **101** (Pt IV), 166–82.

Christiansen, P. (2003) A sea of turbines. *IEE Power Engineer*, **17** (1), 22–4.

Christie, R.D. and Bose, A. (1996) Load frequency control issues in power system operations after deregulation. *IEEE Transactions on Power Systems*, **PWRS-11** (3), 1191.

Chua, L.O. and Lin, P.-M. (1975) *Computer-Aided Analysis of Electronic Circuits*, Prentice Hall.

CIGRE Paper No. 37/38-01 (1994) Working Group 38.04: Ultra High Voltage Technology, *CIGRE Session*.

CIGRE Task Force 38-01-02 (1986) *Static VAR Compensators*.

CIGRE Technical Brochure No. 145: Modeling of power electronics equipment (FACTS) in load flow and stability programs, http://www.e-cigre.org.

CIGRE Technical Brochure No. 316: Defence plan against extreme contingencies, http://www.e-cigre.org.

CIGRE Technical Brochure No. 325: Review of on-line dynamic security assessment tools and techniques, http://www.e-cigre.org.

CIGRE Working Group 38.01 (1987) Planning against voltage collapse. *Electra*, 55–75.

Concordia, C. (1951) *Synchronous Machines. Theory and Performance*, John Wiley & Sons, Inc., New York.

Concordia, C. and Ihara, S. (1982) Load representation in power system stability studies. *IEEE Transactions on Power Apparatus and Systems*, **PAS-101** (4).

Contaxis, G. and Debs, A.S. (1977) Identification of external equivalents for steady-state security assessment. IEEE Power Summer Meeting, Paper F 77-526-7.

Crary, S.B. (1945, 1947) *Power System Stability*, Vols I, II, John Wiley & Sons, Inc., New York.

Cushing, E.W., Drechsler, G.E., Killgoar, W.P. *et al.* (1972) Fast valving as an aid to power system transient stability and prompt resynchronization and rapid reload after full load rejection. *IEEE Transactions on Power Apparatus and Systems*, **PAS-91** (2), 1624–36.

Dahl, O.G.C. (1938) *Electric Power Circuits – Theory and Applications*, McGraw-Hill, New York.

Dandeno, P. and Kundur, P. (1973) Non-iterative transient stability program including the effects of variable load voltage characteristics. *IEEE Transactions on Power Apparatus and Systems*, **PAS-92** (5).

Debs, A.S. (1988) *Modern Power System Control and Operation*, Kluwer Academic.

De Mello, F.P. and Concordia, C. (1969) Concepts of synchronous machine stability as affected by excitation control. *IEEE Transactions on Power Apparatus and Systems*, **PAS-88** (4), 316–29.

De Mello, R.W., Podmore, R. and Stanton, K.N. (1975) Coherency based dynamic equivalents: applications in transient stability studies. PICA Conference.

Di Caprio, U. and Marconato, R. (1975) A novel criterion for the development of multi-area simplified models oriented to on-line evaluation of power system dynamic security. Proceedings of the PSCC, Cambridge, UK.

Dimo, P. (1971) *L'analyse Nodale des Reseaux D'energie*, Eyrolles, Paris.

Dommel, H.W. and Sato, N. (1972) Fast transient stability solution. *IEEE Transactions on Power Apparatus and Systems*, **PAS-91** (4), 1643–50.

Dopazo, J.F., Dwarakonath, M.H., Li, J.J. and Sasson, A.M. (1977) An external system equivalent model using real-time measurements for system security evaluation. *IEEE Transactions on Power Apparatus and Systems*, **PAS-96**.

Duff, I.S., Erisman, A.M. and Reid, J.K. (1986) *Direct Methods for Sparse Matrices*, Oxford University Press.

Dunlop, R.D., Gutman, R. and Marchenko, R.P. (1979) Analytical development of loadability characteristic for EHV and UHV transmission lines. *IEEE Transactions on Power Apparatus and Systems*, **PAS-98**, 606–17.

Dy Liacco, T.E. (1968) *Control of Power Systems via Multi-Level Concept*, Report SRC-68-19, Case Western Reserve University.

Edelmann, H. (1963) *Berechung elektrischer Verbundnetze*, Springer-Verlag, Berlin.

Edelmann, H. (1974) Direkte Verfahren der Netzanalyse mit sparlichen Matritzen. *Nachrichtechnische Zeitschrift*, Heft 2–3.

Ekanayake, J., Holdsworth, L. and Jenkins, K. (2003a) Control of DFIG wind turbines. *IEE Power Engineer*, **17** (1), 28–32.

Ekanayake, J., Holdsworth, L., Wu, X. G. and Jenkins, K. (2003b) Dynamic modelling of doubly fed induction generator wind turbines. *IEEE Transactions on Power Systems*, **18** (2), 803–9.

El-Abiad, A.H. (1983) *Power System Analysis and Planning*, Hemisphere, Washington, DC and London.

Elgerd, O. (1982) *Electric Energy Systems Theory: An Introduction*, 2nd edn, McGraw-Hill, New York.

Elkraft Systems (2003) Power failure in Eastern Denmark and Southern Sweden on 23 September 2003.

EPRI (1991) Flexible AC Transmission Systems (FACTS). Scoping study, *EPRI Report EL-6943*, Final Report on RP3022-02 by GE.

EPRI (1999) *Decentralized Damping of Power Swings – Feasibility Study*, Final Report TR-112417.

Erlich, I., Kretschmann, J., Fortmann, J. *et al.* (2007) Modelling of wind turbines based on doubly-fed induction generators for power system stability studies. *IEEE Transactions on Power Systems*, **22** (3), 909–19.

Estanqueiro, A. (2007) A dynamic wind generation model for power system studies. *IEEE Transactions on Power Systems*, **22** (3), 920–8.

Fahlen, N.T. (1973) Series capacitors in power transmission: design and experience. International Conference on High Voltage DC and/or AC Power Transmission, London, IEE Conference Publication No. 107.

Fahlen, N.T. (1981) EHV series capacitor equipment protection and control. *IEE Proceedings*, **128** (Pt C).

Feng, X., Lubosny, Z. and Bialek, J.W. (2007) *Dynamic Equivalent of a Network with High Penetration of Distributed Generation*, IEEE PowerTech Conference.

Fouad, A.A. and Vittal, V. (1992) *Power System Transient Stability Analysis Using the Transient Energy Function Method*, Prentice Hall, Englewood Cliffs, NJ.

Garmond, A.J. and Podmore, R. (1978) Dynamic aggregation of generating unit models. *IEEE Transactions on Power Apparatus and Systems*, **PAS-97** (4).

Giles, R.L. (1970) *Layout of E.H.V. Substations*, Cambridge University Press, Cambridge.

Glebov [Glêbov], I.A. (1970) *Excitation systems of generators with controlled rectifiers*, Nauka, Leningrad (in Russian).

Gless, G.E. (1966) Direct method of Liapunov applied to transient power system stability. *IEEE Transactions on Power Apparatus and Systems*, **PAS-85** (2).

Glover, J.D. and Sarma, M. (1994) *Power System Analysis and Design*, 2nd edn, PWS, Boston.
Grainger, J.J. and Stevenson, W.D. (1994) *Power System Analysis*, McGraw-Hill.
Grebe, E., Handschin, E., Haubrich, H.J. and Traeder, G. (1979) Dynamische Langezeitstabilitat von Netzen. Elektrizitatswirtschaft, **78**, Heft 19.
Greenwood, A. (1971) *Electrical Transients in Power Systems*, Wiley-Interscience.
Gross, C.A. (1986) *Power System Analysis*, 2nd edn, John Wiley & Sons, Inc., New York.
Gubina, F., Bakic, K., Omahen, P., Hrovatin, J. and Jakl, F. (1994) Economical, planning and operational aspects of East-West power transmission over the Slovenian power network. 35th CIGRE Session, Paris.
Gubina, F., Omahen, P. and Machowski, J. (1987) Dynamic properties of a power system equivalent model for transient stability studies. 34th Congress on Electronics, MELECON'87, Rome, Italy, pp. 577–80.
Hacaturov [Hačaturov], A.A. (1969) *Asynchronous connection and re-synchronisation in electric power systems*, Energia, Moscow (in Russian).
Hammons, T.J. and Winning, D.J. (1971) Comparisons of synchronous machine models in the study of the transient behaviour of electrical power systems. *Proceedings of the IEE*, **118** (10).
Handschin, E. and Stephanblome, T. (1992) New SMES strategies as a link between network and power plant control. *International IFAC Symposium on Power Plants and Power System Control, Munich, Germany*.
Harkopf, T. (1978) Simulation of power system dynamics using trapezoidal rule and Newton's method. Proceedings of the PSCC Conference, Darmstadt.
Harris, M.R., Lawrenson, P.J. and Stephenson, J.M. (1970) *Per Unit Systems with Special Reference to Electrical Machines*, Cambridge University Press.
Hassenzahl, W.V. (1983) Superconducting magnetic energy storage. *Proceedings of the IEEE*, **71**, 1089–8.
Haubrich, H.J. and Fritz, W. (1999) *Study on Cross-Border Electricity Transmission Tariffs by order of the European Commission*, DG XVII/C1. Aachen.
Hicklin, J. and Grace, A. (1992) *Simulink*, MathWorks Inc.
Hill, D.J. (1993) Nonlinear dynamic load models with recovery for voltage stability studies. *IEEE Transactions on Power Systems*, **PWRS-8** (1), 166–76.
Hingorani, N.G. and Gyugyi, L. (2000) *Understanding FACTS. Concepts and Technology of Flexible AC Transmission Systems*, IEEE Press.
Holdsworth, L., Jenkins, N. and Strbac, G. (2001) *Electrical Stability of Large, Offshore Wind Farms*, IEE Conference on AC–DC Power Transmission.
Holdsworth, L., Wu, X.G., Ekanayake, J. and Jenkins, K. (2003) Comparison of fixed speed and doubly-fed induction wind turbines during power system disturbances. *IEE Proceedings – Generation, Transmission and Distribution*, **150** (3), 343–52.
Hughes, F.M., Anaya-Lara, O., Jenkins, N. and Strbac, G. (2006) A power system stabilizer for DFIG-based wind generation. *IEEE Transactions on Power Systems*, **21** (2).
Humpage, W.D. and Stott, B. (1965) Predictor-corrector methods of numerical integration in digital computer analysis of power system transient stability. *IEE Proceedings*, **112**, 1557–65.
Humpage, W.D., Wong, K.P. and Lee, Y.W. (1974) Numerical integration algorithms in power-system dynamic analysis. *IEE Proceedings*, **121**, 467–73.
Huwer, R. (1992) Robuste Power System Stabilizer für Mehrmaschinennetze, PhD Thesis, Universität Kaiserslautern.
IEEE Committee Report (1968) Computer representation of excitation systems. *IEEE Transactions on Power Apparatus and Systems*, **PAS-87** (6), 1460–4.
IEEE Committee Report (1969) Recommended phasor diagrams for synchronous machines. *IEEE Transactions on Power Apparatus and Systems*, **PAS-88** (11), 1593–610.
IEEE Committee Report (1973a) Excitation system dynamic characteristic. *IEEE Transactions on Power Apparatus and Systems*, **PAS-92** (1).
IEEE Committee Report (1973b) Dynamic models for steam and hydroturbines in power system studies. *IEEE Transactions on Power Apparatus and Systems*, **PAS-92** (6), 1904–15.
IEEE Committee Report (1973c) System load dynamics simulation effects and determination of load constants. *IEEE Transactions on Power Apparatus and Systems*, **PAS-92** (2), 600–9.
IEEE Committee Report (1981) Excitation system models for power system stability studies. *IEEE Transactions on Power Apparatus and Systems*, **PAS-100** (2), 494–509.
IEEE Committee Report (1991) Dynamic models for fossil fuelled steam units in power system studies. *IEEE Transactions on Power Systems*, **PWRS-6** (2), 753–61.

IEEE Committee Report (1992) Hydraulic turbine and turbine control models for system dynamic studies. *IEEE Transactions on Power Systems*, **PWRS-7** (1), 167–79.

IEEE Committee Report (1994) Static VAR compensator models for power flow and dynamic performance simulation. *IEEE Transactions on Power Systems*, **PWRS-9** (1), 229–40.

IEEE Power System Relaying Committee Report (1977) Out-of-step relaying for generators. *IEEE Transactions on Power Apparatus and Systems*, **PAS-96** (5), 1556–4.

IEEE Power System Relaying Comittee Power swing and out-of-step considerations on transmission lines. A report to the Power System Relaying Committee of IEEE Power Engineering Society. http://www133.pair.com/psrc/ (Published Reports/Line protections).

IEEE Std 122-1985. IEEE Recommended Practice for Functional and Performance Characteristics of Control Systems for Steam Turbine-Generators Units, IEEE Power Engineering Society.

IEEE Std 421.5-1992. IEEE Recommended Practice for Excitation System Models for Powers System Stability Studies, IEEE Power Engineering Society.

IEEE Task Force on Load Representation for Dynamic Performance (1993) Load representation for dynamic performance analysis. *IEEE Transactions on Power Systems*, **PWRS-8** (2), 472–82.

IEEE Task Force on Load Representation for Dynamic Performance (1995) Standard load models for power flow and dynamic performance simulation. *IEEE Transactions on Power Systems*, **PWRS-10** (3), 1302–12.

IEEE Working Group on Prime Mover and Energy Supply Models for System Dynamic Performance Studies (1994) Dynamic models for combined cycle power plants in power system studies. *IEEE Transaction on Power Systems*, **PWRS-9** (3), 1698–708.

IEEE Working Group Report of panel discussion (1986) Turbine fast valving to aid system stability: benefits and other considerations. *IEEE Transactions on Power Systems*, **PWRS-1** (2), 143–53.

Iliceto, F. and Cinieri, E. (1977) Comparative analysis of series and shunt compensation schemes for AC transmission systems. *IEEE Transactions on Power Apparatus and Systems*, **PAS-96** (1), 167–79.

Ilić, M. and Zaborszky, J. (2000) *Dynamics and Control of Large Electric Power Systems*, John Wiley & Sons, Inc., New York.

Ise, T., Murakami, Y. and Tsuji, K. (1986) Simultaneous active and reactive power control of superconducting magnetic storage using GTO converters. *IEEE Transactions on Power Delivery*, **PWRD-1** (1), 143–50.

Jancke, G., Fahlen, N. and Nerf, O. (1975) Series capacitors in power systems. *IEEE Transactions on Power Apparatus and Systems*, **PAS-94**, 915–25.

Januszewski, M. (2001) *Transient Stability Enhancement by Using FACTS Devices*, PhD Thesis, Warsaw University of Technology (in Polish).

Jones, C.V. (1967) *The Unified Theory of Electrical Machines*, Butterworth.

Kamwa, I. and Grondin, R. (1992) Fast adaptive scheme for tracking voltage phasor and local frequency in power transmission and distribution systems. *IEEE Transactions on Power Delivery*, **PWRD-7** (2), 789–95.

Kazovskij, Ė.Â., Danilêvič, Â.B., Kaŝarskij, Ė.G. and Rubisov, G.V. (1969) *Abnormal operating conditions of large synchronous machines*, Izdatelstvo Nauka, Leningradskoe Otdelenie, Leningrad (in Russian).

Kehlhofer, R. (1991) *Combined-Cycle Gas and Steam Turbine Power Plants*, The Fairmont Press, Librun, GA.

Kessel, P. and Glavitsch, H. (1986) Estimating the voltage stability of a power system. *IEEE Transactions on Power Delivery*, **PWRD-1** (3), 346–54.

Kimbark, E.W. (1995) *Power System Stability*, Vols I, II, III, John Wiley & Sons, Inc., New York, 1948, 1950, 1956, reprinted by IEEE in 1995.

Kirby, N.M., Xu, L., Luckett, M. and Siepmann, W. (2002) HVDC transmission for large offshore wind farms. *IEE Power Engineering Journal*, **16** (3), 135–41.

Kirchmayer, L.K. (1959) *Economic Control of Interconnected Systems*, John Wiley & Sons, Inc., New York.

Kuczyński, R., Paprocki, R. and Strzelbicki, J. (2005) Defence and restoration of the Polish power system. PSE-Operator, Konferencja Naukowa Rynek Energii (Conference Energy Market).

Kulicke, B. and Webs, A. (1975) Elektromechanisches Verhalten von Turbosetzen bei Kurzschlüssen in Kraftwerksnähe. *ETZ-A*, **96**, Heft 4.

Kumano, S., Miwa, Y., Kokai, Y. *et al.* (1994) Evaluation of transient stability controller system model. CIGRE Session 38-303.

Kundur, P. (1994) *Power System Stability and Control*, McGraw-Hill, New York.

Kundur, P., Lee, D.C. and Zein El-Din, H.M. (1981) Power system stabilizers for thermal units: analytical techniques and on-site validation. *IEEE Transactions on Power Apparatus and Systems*, **PAS-100**, 81–95.

Läge, K. and Lambrecht, D. (1974) Die Auswirkung dreipoliger Netzkurz-schlüsse mit Kurzschlussfortschaltung auf die mechanische Beansprachung von Turbosätzen. *ETZ-A*, **95**, Heft 10.

Lander, C.W. (1987) *Power Electronics*, 2nd edn, McGraw-Hill.

Larsen, E.V. and Swan, D.A. (1981) Applying power system stabilizers, Parts I, II, and III. *IEEE Transactions on Power Apparatus and Systems*, **PAS-100**, 3017–46.

Lee, D.C., Beaulieu, R.E. and Service, J.R.R. (1981) A power system stabilizer using speed and electrical power inputs - design and field experience. *IEEE Transactions on Power Apparatus and Systems*, **PAS-100**, 4151–67.

Lee, S.T.Y. and Schweppe, F.C. (1973) Distance measures and coherency recognition for transient stability equivalents. *IEEE Transactions on Power Apparatus and Systems*, **PAS-92** (5), 1550–7.

Leithead, W.E. (1992) Effective wind speed models for simple wind turbines simulations. Proceedings of the 14th Annual British Wind Energy Association Conference.

Leithead, W.E., Delasalle, S. and Reardon, D. (1991) Role and objectives of control for wind turbines. *IEE Proceedings C – Generation, Transmission and Distribution*, **138** (2), 135–48.

Löf, P.A., Hill, D.J., Arnborg, S. and Andersson, G. (1993) On the analysis of long term voltage stability. *Electric Power and Energy Systems*, **15** (4), 229–37.

Löf, P.A., Smed, T., Andersson, G. and Hill, D.J. (1992) Fast calculation of a voltage stability index. *IEEE Transactions on Power Systems*, **PWRS-7** (1), 54–64.

Lubosny, Z. and Bialek, J.W. (2007) Supervisory control of a wind farm. *IEEE Transactions on Power Systems*, **22** (2).

Lüders, G.A. (1971) Transient stability of multimachine power system via the direct method of Lyapunov. *IEEE Transactions on Power Apparatus and Systems*, **PAS-90** (1).

MacDonald, J. (1994) Present phase-angle regulating transformer technology. IEE Proceedings Colloquium Facts – the Key to Increased Utilisation of a Power System, pp. 61–2.

Machowski, J. (1985) Dynamic equivalents for transient stability studies of electrical power systems. *International Journal of Electrical Power and Energy Systems*, **7** (4), 215–23.

Machowski, J. and Bernas, S. (1989) *Stany nieustalone i stabilnosc systemu elektroenergetycznego*, Wydawnictwa Naukowo-Techniczne, Warszawa.

Machowski, J. and Białek, J. (2008) State-variable control of shunt FACTS devices using phasor measurements. *Electric Power System Research*, **78** (1), 39–48.

Machowski, J. and Nelles, D. (1992a) Optimal control of superconducting magnetic energy storage unit. *Electric Machines and Power Systems*, **20** (6).

Machowski, J. and Nelles, D. (1992b) Power system transient stability enhancement by optimal control of static VAR compensators. *International Journal of Electrical Power and Energy Systems*, **14** (5).

Machowski, J. and Nelles, D. (1993) Simple robust adaptive control of static VAR compensator. *European Transactions on Electric Power Engineering*, **3** (6).

Machowski, J. and Nelles, D. (1994) Optimal modulation controller for superconducting magnetic energy storage. *International Journal of Electrical Power and Energy Systems*, **16** (5).

Machowski, J., Bialek, J.W. and Bumby, J.R. (1997) *Power System Dynamics and Stability*, John Wiley & Sons, Ltd, Chichester.

Machowski, J., Cichy, A., Gubina, F. and Omahen, P. (1986) Modified algorithm for coherency recognition in large electrical power systems. IFAC Symposium on Power Systems and Power Plant Control, Beijing, China.

Machowski, J., Cichy, A., Gubina, F. and Omahen, P. (1988) External subsystem equivalent model for steady-state and dynamic security assessment. *IEEE Transactions on Power Systems*, **PWRS-3** (4).

Machowski, J., Gubina, F. and Omahen, P. (1986) Power system transient stability studies by Lyapunov method using coherency based aggregation. IFAC Symposium on Power Systems and Power Plant Control, Beijing, China.

Martin, H.F., Tapper, D.N. and Alston, T.M. (1976) Sustained fast valving applied to Tennessee Valley Authority's Watts Bar Nuclear Units. *Transactions of the ASME Journal of Engineering for Power*, Paper 76-JPGC-Pwr55.

Masters, G.M. (2004) *Renewable and Efficient Electric Power Systems*, Wiley–IEEE Press.

McDonald, J.D. (2003) *Electric Power Substations Engineering*, CRC Press.

McPherson, G. and Laramore, R.D. (1990) *Introduction to Electric Machines and Transformers*, 2nd edn, John Wiley & Sons, Inc., New York.

Miller, T.J.E. (1982) *Reactive Power Control in Electric Systems*, John Wiley & Sons, Inc., New York.

Moussa, H.A.M. and Yu, Y.N. (1972) Improving power system damping through supplementary governor control. PES Summer Meeting, Paper C 72 470-3.
Muller, S., Deicke, M. and De Donker, R.W. (2002) *Doubly fed induction generator systems*. IEEE Industry Applications Magazine, pp. 26–33.
Nagao, T. (1975) Voltage collapse at load ends of power systems. *Electrical Engineering in Japan*, **95** (4).
National Grid Company (NGC) (1994) *1994 Seven Year Statement*.
Nitta, T., Shirari, Y. and Okada, T. (1985) Power charging and discharging characteristics of SMES connected to artificial transmission line. *IEEE Transactions on Magnetics*, **21** (2).
Nogal, L. (2008) Application of wide area measurements to stability enhancing control of FACTS devices installed in tie-lines. PhD Thesis, Warsaw University of Technology (in Polish).
Ogata, K. (1967) *State Space Analysis of Control Systems*, Prentice Hall.
O'Kelly, D. (1991) *Performance and Control of Electrical Machines*, McGraw-Hill.
Olas, A. (1975) Synthesis of systems with prescribed trajectories. *Proceedings of Non-linear Vibrations*, **16**.
Omahen, P. (1991) Fast transient stability assessment using corrective PEBS method. Proceedings of 6th IEEE Mediterranean Electrotechnical Conference, Vol. 2, pp. 1408–11.
Omahen, P. (1994) *Unified Approach to Power System Analysis in its Multi-Time Scale Dynamic Response*. PhD Thesis, Warsaw University of Ethnology (in Polish).
Omahen, P. and Gubina, F. (1992) Simulations and field tests of a reactor coolant pump emergency start-up by means of remote gas units. *IEEE Transactions on Energy Conversion*, **EC-7** (4), 691–7.
Omahen, P. and Gubina, F. (1995) Experience with large power system dynamics model for security assessment. *CIGRE Power System Operation & Control Colloquium*, Johannesburg/Cape Town.
Pai, M.A. (1981) *Power System Stability: Analysis by the direct method of Lyapunov*, North-Holland, Amsterdam.
Pai, M.A. (1989) *Energy Function Analysis for Power System Stability*, Kluwer Academic.
Park, R.H. (1973) Fast turbine valving. *IEEE Transactions on Power Apparatus and Systems*, **PAS-92**, 1065–73.
Pavella, M., Ernst, D. and Ruiz-Vega, D. (2000) *Transient Stability of Power Systems: A Unified Approach to Assessment and Control*, Kluwer Academic.
Pavella, M. and Murthy, P.G. (1994) *Transient Stability of Power Systems. Theory and Practice*, John Wiley & Sons, Ltd.
Phadke, A.G. and Thorap, J.S. (1988) *Computer Relaying for Power Systems*, John Wiley & Sons, Inc.
Phadke, A.G., Thorap, J.S. and Adamiak, M.G. (1983) A new measurement technique for tracking voltage phasors, local system frequency and rate of change of frequency. *IEEE Transactions on Power Apparatus and Systems*, **PAS-102** (5).
Pissanetzky, S. (1984) *Sparse Matrix Technology*, Academic Press.
Podmore, R. (1978) Identification of coherent generators for dynamic equivalents. *IEEE Transactions on Power Apparatus and Systems*, **PAS-97**, 1344–54.
Press, W.H., Teukolsky, S.A., Vetterling, W.T. and Flannery, B.P. (1992) *Numerical Recipes in C: The Art of Scientific Computing*, 2nd edn, Cambridge University Press.
Racz, L.Z. and Bokay, B. (1988) *Power System Stability*, Kluwer Academic.
Rafian, M., Sterling, M.J.H. and Irving, M.R. (1987) Real time power system simulation. *IEE Proceedings*, **134** (Pt C, 3), 206–23.
Ramey, D.G. and Skooglund, J.W. (1970) Detailed hydrogovernor representation for system stability studies. *IEEE Transactions on Power Apparatus and Systems*, **PAS-89** (1), 106–12.
Rasolomampionona, D.D. (2000) Analysis of the power system steady-state stability: influence of the load characteristics. *Archives of Electrical Engineering*, **XLIX** (191-1).
Rasolomampionona, D.D. (2007) *Optimisation of parameters of TCPAR installed in tie lines with regard to their interaction with LFC*. Prace Naukowe Elektryka, z. 134 Publishing House of the Warsaw University of Technology (in Polish).
Riaz, M. (1974) Hybrid-parameter models of synchronous machines. *IEEE Transactions on Power Apparatus and Systems*, **PAS-93**, 849–58.
Rüdenberg, R. (1923) *Elektrische Schaltvorgänge und verwandte Störungserscheinungen in Starkstromanlagen*, Julius Springer, Berlin.
Rüdenberg, R. (1950) *Transient Performance of Electric Power Systems*, McGraw-Hill, New York.
Saccomanno, F. (2003) *Electric Power System Control: Analysis and Control*, Wiley–IEEE Press.
Schlueter, R.A., Ilu, T., Chang, J.C. *et al.* (1992) Methods for determining proximity to voltage collapse. *IEEE Transactions on Power Systems*, **PWRS-6** (2), 285–92.

Seshu, S. and Reed, M.B. (1961) *Linear Graphs and Electrical Networks*, Addison-Wesley.
Slootweg, J.G., de Hann, S.W.H., Polinder, H. and Kling, W.L. (2003) General model for representing variable speed wind turbines in power system dynamic simulations. *IEEE Transactions on Power Systems*, **18** (1), 144–51.
Slootweg, J.G., Polinder, H. and Kling, W.L. (2001) Dynamic modelling of a wind turbine with doubly fed induction generator. *Power Engineering Society Summer Meeting, IEEE paper 0-7803-7173-9/01*.
Song, Y.H. and Johns, A.T. (1999) *Flexible AC transmission systems (FACTS)*. IEE Power and Energy Series 30, IEE: London.
Stalewski, A., Goody, J.L.H. and Downes, J.A. (1980) Pole-slipping protection. 2nd International Conference on Developments in Power System Protection, IEE Conference Publication No. 185.
Stannard, N. and Bumby, J.R. (2007) Performance aspects of mains connected small scale wind turbines. *Proceedings of the IET – Generation, Transmission and Distribution*, **1** (2), 348–56.
Stott, B. (1974) Review of load flow calculation methods. *Proceedings of the IEEE*, **62**, 916–29.
Stott, B. (1979) Power system dynamic response calculations. *Proceedings of the IEEE*, **67**, 219–41.
Strang, G. (1976) *Linear Algebra and Its Applications*, Academic Press, New York.
Taylor, C.W. (1994) *Power System Voltage Stability*, McGraw-Hill.
Taylor, C.W., Haner, J.M., Hill, L.A. *et al.* (1983) A new out-of-step relay with rate of change of apparent resistance augmentation. *IEEE Transactions on Power Apparatus and Systems*, **PAS-102** (3).
Taylor, C.W., Haner, J.M. and Laughlin, T.D. (1986) Experience with the R-Rdot out-of-step relay. *IEEE Transactions on Power Delivery*, **PWRD-1** (2).
Tewerson, R.P. (1973) *Sparse Matrices*, Academic Press, New York.
Tinney, W.F., Brandwain, V. and Chan, S.M. (1985) Sparse vector methods. *IEEE Transactions on Power Apparatus and Systems*, **PAS-104**, 295–301.
Tinney, W.F. and Bright, J.M. (1986) Adaptive reductions for power equivalents. IEEE Power Winter Meeting, Paper 86 WM.
Tinney, W.F., Powell, W.L. and Peterson, N.M. (1973) Sparsity oriented network reduction. Proceedings of PICA Conference, Minneapolis, pp. 385–90.
Tinney, W.F. and Walker, J.W. (1967) Direct solutions of sparse network equations by optimally ordered triangular factorization. *Proceedings of the IEEE*, **55** (11), 1801–9.
Tiranuchit, A. and Thomas, R.J. (1988) A posturing strategy action against voltage instabilities in electric power systems. *IEEE Transactions on Power Systems*, **PWRS-3** (1), 87–93.
Troskie, H.J. and de Villiers, L.N.F. (2004) *Impact of Long Duration Faults on Out-Of-Step Protection*, ESCOM, South Africa.
UCTE (2007) Final Report. System Disturbance on 4 November 2006.
UCTE *Operation Handbook. Load Frequency Control and Performance*, Available at http://www.ucte.org/.
Ulyanov [Ul'ânov], S.A. (1952) *Short-circuits in electric power systems*, Moscow and Leningrad (in Russian).
Undrill, J.M. and Turner, A.E. (1971) Construction of power system electromechanical equivalents by modal analysis. *IEEE Transactions on Power Apparatus and Systems*, **PAS-90** (5).
Ungrad, H., Winkler, W. and Wiszniewski, A. (1995) *Protection Techniques in Electrical Energy Systems*, Marcel Dekker.
US–Canada Power System Outage Task Force (2004) Final Report on the August 14, 2003 Blackout in the United States and Canada.
Vaahedi, E., El-Kady, M.A., Libaque-Esaine, J.A. and Carvalho, V.F. (1987) Load models for large-scale stability studies from end-user consumption. *IEEE Transactions on Power Systems*, **PWRS-2** (4), 864–2.
Van Cutsem, T. (1991) A method to compute reactive power margins with respect to voltage collapse. *IEEE Transactions on Power Systems*, **PWRS-6**, 145–56.
Van Cutsem, T. and Vournas, C. (1998) *Voltage Stability of Electric Power Systems*, Springer-Verlag.
Van Der Hoven, I. (1957) Power spectrum of horizontal wind speed in the frequency range from 0.0007 to 900 cycles per hour. *American Journal of Meteorology*, **14**, 160–4.
Venikov [Vênikov], V.A. (1958) *Electromechanical transient processes in electric power systems*, Gosudarstvennoe Energeticeskoe Izdatelstvo, Moscow and Leningrad (in Russian).
Venikov [Vênikov], V.A. (1964) *Transient Phenomena in Electrical Power Systems*, Pergamon Press, Oxford.
Venikov [Vênikov], V.A. (1978a) *Transient electromechanical processes in electric power systems*, Vyssaa Skola, Moscow (in Russian).
Venikov [Vênikov], V.A. (1978b) *Transient Processes in Electrical Power Systems*, Mir, Moscow.

Venikov [Vênikov], V.A. (1985) *Transient electromechanical processes in electric power systems*, Vyssaa Skola, Moscow (in Russian).

Voropaj, N.I. (1975) Equivalencing of electric power systems under large disturbances. *Elektricestvo*, No. 9 (in Russian).

Vorley, D.H. (1974) *Numerical Techniques for Analysing the Stability of Large Power Systems*. PhD Thesis, University of Manchester.

Vournas, C.D., Nikolaidis, V.C. and Tassoulis, A.A. (2006) Postmortem analysis and data validation in the wake of the 2004 Athens Blackout. *IEEE Transactions on Power Systems*, **21** (3).

Wang, H.F., Hao, Y.S., Hogg, B.W. and Yang, Y.H. (1993) Stabilization of power systems by governor-turbine control. *Electrical Power & Energy Systems*, **15** (6), 351–61.

Wang, X. (1997) *Modal Analysis of Large Interconnected Power System*, Reihe 6: Energietechnik, Nr 380, VDI-Verlag, Düsseldorf.

Ward, J.B. (1949) Equivalent circuits for power flow studies. *AIEE Transactions on Power Apparatus and Systems*, **PAS-68**, 373–82.

Wasynczuk, O., Man, D.T. and Sullivan, J.P. (1981) Dynamic behaviour of a class of wind turbine generators during random wind fluctuations. *IEEE Transactions on Power Applications and Systems*, **PAS-100**, 2837–45.

Watson, W. and Coultes, M.E. (1973) Static exciter stabilizing signals on large generators – mechanical problems. *IEEE Transactions on Power Apparatus and Systems*, **PAS-92**, 204–11.

Weedy, B.M. (1980) *Underground Transmission of Electric Power*, John Wiley & Sons, Ltd, Chichester.

Weedy, B.M. (1987) *Electric Power Systems*, 3rd rev. edn, John Wiley & Sons, Ltd, Chichester.

Weisman, J. and Eckart, L.E. (1985) *Modern Plant Engineering*, Prentice Hall, Englewood Cliffs, NJ.

Welfonder, E. (1980) Regeldynamisches Zusammenvirken von Kraftwerken und Verbrauchern im Netzverbundbetrieb. *Elektrizitätswirtschaft*, **79**, Heft 20.

Westlake, A.J., Bumby, J.R. and Spooner, E. (1996) Damping the power angle oscillations of a permanent magnet synchronous generator with particular reference to wind turbine applications. *IEE Proceedings – Electric Power Applications*, **143** (3).

Willems, J.L. (1970) *Stability Theory of Dynamical Systems*, Nelson, London.

Wilson, D., Bialek, J.W. and Lubosny, Z. (2006) Banishing blackouts. *IEE Power Engineering Journal* **20** (2), 38–41.

Witzke, R.L., Kresser, J.V. and Dillard, J.K. (1953) Influence of AC reactance on voltage regulation of 6-phase rectifiers. *AIEE Transactions*, **72**, 244–53.

Wood, A.J. and Wollenberg, B.F. (1996) *Power Generation Operation and Control*, 2nd edn, John Wiley & Sons, Inc.

Wright, A. and Christopoulos, C. (1993) *Electrical Power System Protection*, Chapman and Hall, London.

Xiang, D., Ran, L., Tavner, P.J. and Yang, S. (2006) Control of a doubly fed induction generator in a wind turbine during grid fault ride-through. *IEEE Transactions on Energy Conversion*, **21** (2), 652–62.

Younkins, T.D., Chow, J.H., Brower, A.S. *et al.* (1987) Fast valving with reheat and straight condensing steam turbines. *IEEE Transactions on Power Systems*, **PWRS-2**, 397–405.

Yu, Y.N. (1983) *Electric Power System Dynamics*, Academic Press, New York.

Zdanov [Ždanov], P.S. (1948) *Stability of electric power systems*, Gosudarstvennoe Energeticeskoe Izdatelstvo, Moscow and Leningrad (in Russian).

Zdanov [Ždanov], P.S. (1979) *Stability problems of electric power systems*, Energia, Moscow (in Russian).

Zukov [Žukov], L.A. (1964) Simplified transformation of circuit diagrams of complex electric power systems. *Izvestia Akademii Nauk SSSR, Energetika i Transport*, No. 2 (in Russian).

Index

a,b co-ordinates, 115
Acceleration area, 185, 209, 211
AC exciter
  Rotating, 22, 466
  Static, 22, 468
Aggregation
  of generators, 567
  of nodes, 562–563
Air-gap flux, 80
Alert state, 10
Amortisseurs, 21, 146, 172
Angle of attack, 273
Angular momentum, 171
Annual energy demand, 15
Aperiodic mode, 504
Area control error (ACE), 343
Armature
  Leakage, 85, 136
  flux paths,134
  short circuit current, 133
  time constant, 133
  winding, 21
  reactance, 81, 85, 135
  reaction, 21, 79
Asynchronous
  operation, 210, 239, 245, 251
  torque, 172
Attenuation constant, 66
Automatic generator control (AGC), 336, 346
Auto-reclosing, 54, 212
Automatic voltage regulator (AVR)
  modelling, 462, 527
  load compensation, 23, 462
  limiters, 24, 200
  influence on fault current, 150
  influence on steady state stability, 196
  influence on transient stability, 216
  influence on voltage stability, 317
  modelling, 462, 526
Autotransformer, 37
Auxiliary services, 20

Backward swing, 400
Bang-bang control, 391, 397
Bandwidth of secondary control, 345
Betz limit, 266
Bias factors, 343, 366
Bifurcation point, 319
Blackouts, 323, 340
Blocking relay, 248
Boiler control, 475
  boiler-follows-turbine, 475
  turbine-follows-boiler, 475
  integrated, 475
Braking resistor, 45, 49, 391
Buchholz protection, 57
Busbars, 35
  protection, 57

Capacity factor, 269
Centre of power swing, 249
Classification of dynamics, 5
Characteristic equation, 192, 492, 517, 602
Characteristic impedance, 67
Charging current
  line, 66
  cable, 72
Classical model, 180, 456
Coherency, 567
  based equivalents, 573
  criterion, 571
  electromechanical, 566

© 2008 John Wiley & Sons, Ltd

Coherency (*Continued*)
exact, 567
recognition, 569
Combined cycle gas turbine (CCGT), 27
single shaft mode, 28
Combustion chamber, 27
Constant flux linkage, 127, 145, 153
Contingencies, 9
Controller
field-oriented, 289
vector, 289
Critical
disturbance, 4
fault clearing time, 210, 215, 230, 235
operating point, 176, 311
power demand, 310, 319
power state, 311
voltage, 311

Damped frequency, 611
Damper windings, 21,129, 136, 172, 186, 205
Damping
coefficient, 171, 175, 193
power, 172, 240
ratio, 193, 256, 262, 611
torque, 205
Danish concept, 270
Decentralized control, 341
DC excitation system, 20, 463
DC offset, 129
Declaration area, 189, 209, 229
Defence plan, 347
Diagonalization, 496
Dimo's method, 564
Direct method, 22, 230, 418
Disc averaging, 482
Discharge lighting, 105
Distance relay, 56
Distributed generation, 18
Distribution, 17, 19
Distribution transformer, 36
Disturbance
critical, 4
large, 207
small, 169
Dominant mode, 506
Droop, 32, 46, 336, 341
d,q axis, 76, 434
d,q to a,b transformation, 117, 436
0,d,q transformation, 436, 438

Economic dispatch, 336
Eigenvalues, 195, 491
Eigenvectors, 491
left and right hand, 492, 497
Electrical centre, 249
Electro-hydraulic governor, 29
Embedded generation, 18, 278
Emergency state, 10
Elimination of nodes, 230, 559
Energy function, 225
Environmental issues, 16
Exact coherency, 567
Excitation systems, 21, 384
load compensation, 23, 462
modelling, 462
Excitation transformer, 22, 40, 490
Extremis state, 9
Equal-area criteria, 184, 209, 228, 388, 400, 419
Equilibrium
point, 3, 176, 305, 339, 589
stable point, 178, 194, 306, 359
unstable point, 33, 178, 194, 306
Equivalents, 557

FACTS, 43, 119, 370, 391, 423,488
Fast-valving, 35, 244, 389
momentary, 389
sustained, 389
Fault
clearing, 166, 168
critical clearing time, 210, 215
shunts, 208
unbalanced, 211
Feedback control, 5
Fixed speed generator 269
Flux decrement145, 195, 215
Forward swing, 387, 400, 419, 423
Francis turbine, 476
Frequency collapse, 358, 363
Frequency control, 335
primary, 339, 346
secondary, 340, 346
tertiary, 345, 346
Frequency stiffness, 340
Fundamental system of solutions, 601

Gate turn-off thyristor, 44
Gas turbines, 26

Gauss-Seidel, 123
General solution, 602
Generating unit, 20
Generation characteristic, 336
Generator emfs, 78, 137, 143
  establishing initial values, 143
  subtransient, 140, 449
  steady-state, 99, 447
  transient, 142, 447
Generator equivalent circuits, 454
  steady-state, 143
  subtransient, 141, 143
  transient, 142, 143
Generator reactance, 136, 138
Generator transformer21, 36
Generator tripping, 392
  preventive, 393
  restitutive, 394
Governor control valves, 26, 389, 471, 473
Governor systems, 32, 480

Heat recovery boiler, 27
Hybrid network equations, 116
Hydraulic turbines, 28
  modelling, 476
  transfer function, 479

Ideally stiff load, 300
Impulse turbine, 29
Incremental model, 371, 577
Induction generator, 265
  doubly fed, 271
  fixed speed, 269
  variable speed, 271
Induction motor, 103, 282
  easy starting, 107
  equivalent circuit, 106
  heavy-starting, 107
  modelling, 485
  slip, 106, 486
  stalling voltage, 107
  torque-slip curve, 106
Inertia coefficient, 172
Inertia constant, 171
Infinite busbar, 146, 163, 167, 173
Integration constants, 604
Intercept valves, 26, 389, 472
Interconnected systems, 340, 344, 364
Interface error, 353
Internal power factor angle, 82
Islanded systems, 335, 361

Jacobian, 116

Kaplan turbine, 29

Line trap, 55
Leakage flux, 72, 76, 459
Leakage reactance, 81, 460
Load angle, 68, 118
Load characteristics, 104, 110
  effect of tap-changer, 111
  frequency, 104, 112, 358
  static, 110
  voltage, 105, 107, 108, 110
Load modelling, 104, 111, 485
  composite load, 104, 485
  constant current, 111
  constant power, 111
  constant impedance, 105, 111, 324
  exponential, 112
  frequency dependent, 112
  polynomial model, 111
  stiffness, 321
  voltage sensitivity, 105, 318
Load sensitivity
  frequency, 104, 339
  voltage, 104
Load shedding, 348, 360
Load reference set point, 39
Local measurements, 400, 410, 421, 428
Logarithmic spiral, 613
Lyapunov's first method, 513
Lyapunov's second (direct) method, 222, 407

Magnetizing reactance, 106, 274
Main stop valves, 34
Matrix
  factorization, 547, 553
  partial inversion, 543, 559, 600
Mechanical-hydraulic governor, 29, 470
Mechanical time constant, 171
Mho relay, 248, 250
Modal
  analysis, 513, 528, 570, 579
  matrix, 501
  reduction, 558
  variables, 501, 580, 587
Mode shape, 254, 509

Modulation controller, 47, 401, 404, 405
Multimachine systems, 220, 230, 307, 318, 352, 371, 491

Natural frequency, 193
  damped/undamped, 193, 256, 262
Natural load, 67
Negative damping, 187, 204, 218, 384, 422
Network equations, 113, 442, 450, 546, 553
Network feasibility, 299, 317
Network loadability, 300
Network splitting, 251
Network reduction, 557–558
Newton method, 123, 539, 551
Nodal admittance matrix, 75, 113
Nodal impedance matrix, 114
Nodal network equations, 113
Nodes: PV, PQ, slack, 122
Non-intervention rule, 342
Normal state, 10
Nose curves, 301
Numerical integration, 536

Off-nominal transformation ratio, 72, 74
Oscillatory mode, 504
Out-of-step protection (relaying), 244
Out-of-step tripping, 245
Overexcitation, 103
Overhead line, 68

Park's transformation, 438
Partial inversion, 543, 559, 600
Partially equidistant point, 590
Participation factor, 511
Particular solution, 606
Partitioned solution method, 541
Participation factor, 511, 588
Pelton Wheel, 28
Penstock, 28
Per unit systems, 439, 593
Pitch control, 237, 482
Phase angle regulator (TCPAR), 52, 370, 423
Phase constant, 66
Phase-shifting transformer , 40, 423, 488
Phasor
  Diagram, 86, 95, 141, 161, 180, 197, 288, 451
  measurement unit (PMU), 61
Physical reduction, 558
Point of common connection, 278
Pole-slip protection, 245, 249
Potier reactance, 460
Power angle, 92, 97, 101, 171
Power-angle characteristic
  classical, 183
  steady-state, 103
  transient, 179, 183, 209
Power capability curve, 91
Power conditioning system, 48
Power flow, 118
Power invariance, 595
Power line carrier, 55
Power swing, 185, 191, 215, 219
  detection, 248
Power system stability, 9
  angle, 9, 207
  voltage, 9, 299
  frequency, 9, 335
Power system stabilizer, 23, 47, 383, 429, 470
Power system structure, 19
Primary control, 339
Protection
  differential current, 54
  directional comparison, 55
  distance, 56
  local back-up, 43
  pole-slip, 244
  remote back-up, 54
Pull-out power, 177

Quadrature booster, 40, 52
q axis, 76

Rayleigh distribution, 268
Reactive power, 70, 91, 109, 305
Regulation power, 344, 362
Reheat stop valves, 26
Reliability of supply, 15
Reluctance power, 91
Reserve of secondary control, 345
Resynchronization, 237, 393
Rotation matrix, 441
Rotational
  voltage, 87, 486
  sampling, 482
Rotor angle, 101, 118, 170
Rotor screening, 135
Rotor swing, 184, 207, 218
Run-up control, 34
Roots
  distinct, 604
  repeated, 605

Saturation
characteristics, 458
factor, 459
parameter sensitivity, 461
Secondary control, 340
Security, 9
assessment, 10
dynamic, 11
small signal, 10
static, 10
transient, 11
voltage, 10
Self-excitation, 329
synchronous, 332
asynchronous, 333
Sensitivity analysis, 319, 510
Series capacitor, 41
thyristor controlled (TCSC), 50, 416
Series transformer, 40
Servomotor, 26, 473
Short circuit
current, 128, 134, 146, 149
in network, 167
power, 108, 396
reactance, 396
Shunt capacitor, 42, 45, 395
Shunt compensation, 41, 425
Shunt reactor, 25
Shut down wind speed, 267
Simulation methods
partitioned (alternating), 541
simultaneous (combined), 553
Slack bus (node), 122
Slip frequency, 271
Small signal stability, 491
Sparse matrix, 114, 547, 560
Speed deviation, 170
Speed measuring device, 26
Speeder gear, 29
Speed-droop
characteristic, 34, 336, 338
coefficient, 33
Speed reference set-point, 30
Speed ratio, 266
Spinning reserve, 337
Stability enhancement, 383
Stable equilibrium point, 181, 210, 227, 589
Stall control, 273
Standard form, 609
State
control, 370, 410
matrix, 500
space equation, 515
steady, 65, 135
subtransient, 125, 140
transient, 135, 141
variable, 3, 397, 500, 541
vector, 3, 500
Static compensator (STATCOM), 47, 395, 327, 488
Static VAR compensator (SVC), 45, 395, 488
Steady-state stability, 69, 177, 196, 491
condition, 190, 517
limit, 178
margin, 178
regulated system, 196
unregulated system, 177
Steam turbine, 25
cross-compound, 26
condenser, 26
modelling, 470
non-reheat, 25
overspeed control, 34
regulated characteristic
run-up control, 34
reheat, 25
stages, 25
tandem-compound, 25, 472
transfer function, 472
unregulated characteristic, 31
valves, 26, 389, 475
Step-up transformer, 18
Stiffness, 349, 344
Subtransmission network, 17
Subsynchronous resonance, 334
Substation, 21, 35
Subtransient reactance, 136
d axis, 136, 139
q axis, 137, 139
Subtransient saliency, 137, 148, 156
Subtransient time constant, 139
d axis, 139, 446
q axis, 139, 446
Superconducting magnetic energy storage (SMES), 49, 395
Supplementary control, 383
Surge impedance, 66
Surge impedance load (SIL), 67
Survival wind speed, 267
Swing equation, 169, 452, 514

Swing frequency, 189
Symmetrical components, 158
Synchronization, 163, 237
  condition, 239
  currents, 164, 238
  torque, 164, 238
Synchronous compensator, 42
Synchronous generator, 19
  emfs, 85, 95, 99
  equivalent circuits, 87, 100
  leakage flux, 76
  modelling, 433
  on no-load, 77
  parameters, 139
  power supplied to system, 102, 103
  protection, 57
  round-rotor, 76
  salient pole, 83
  saliency, 76
  steady state, 135
  subtransient, 135
  torque, 82, 88
  transient state, 135
Synchronous reactance, 82
  d axis, 85
  q axis, 85
Synchronous speed, 28, 77, 163, 170, 239
Synchronizing power
  steady state, 178
  transient, 184

Tap-changing transformers, 37
Tertiary control, 345
Thyristor, 43
  conventional, 43
  gate turn-off thyristor (GTO), 44
Tie-line, 17, 120, 342
  control, 336, 343
  oscillations, 364
Time constant, 128
  armature, 133
  d-axis, 133
  mechanical, 171
  q-axis, 138
Torque
  asynchronous, 172
  in round-rotor generator, 82
  in salient pole generator, 88
  mechanical, 171
  subtransient, 150
  synchronous, 82, 88
Torque angle, 83
Torsional oscillation, 253
Torsional fatigue, 237, 253, 263
Tower shadow, 482
Trajectory, 3, 223, 567, 591
Transfer
  admittance, 231, 561
  capability, 523
  equivalent network, 207, 560
Transformation matrix, 437
Transformer emf, 442
Transformers, 36
  booster, 40
  π equivalent, 73
  autotransformers, 41
  core loss, 72
  equivalent circuit, 73, 75
  excitation current, 73
  ideal, 73
  leakage flux, 72
  magnetization current, 72
  modelling, 74
  no-load test, 73
  off-nominal taps, 74
  phase shifting, 75
  short-circuit test, 73
  short-circuit voltage, 74
  tap-changing, 37
  three-winding transformers, 36
  two-winding transformers, 36
  unit transformer, 20
Transmission, 16
  angle, 66
Transmission lines, 65
  long, 66
  lossless, 67
  medium-length, 67
  short-length, 67
  π equivalent, 67
Transient droop, 479
Transient power angle, 178, 215
Transient reactance
  d axis, 136, 139, 444
  q axis, 138, 139, 444
Transient saliency, 179, 455
Transient stability, 9, 207
  margin, 210, 215
Transient time constant
  open-circuit, 139, 445
  short-circuit, 139, 445

Trumpet characteristic, 349
Turbine
  governor, 19, 34, 470
  modelling, 470
Turbogenerator, 20
Two-reaction theory, 84

Unbalanced faults, 211
Underexcitation, 103
Underdamped second – order system, 609
Underground cables, 35, 72
Unified power controller (UPFC), 52, 119, 423, 488
Uniform damping, 517
Unit transformer, 20
Unstable equilibrium point, 179, 195, 228, 589

Vandermonde's determinant, 603
Vector control, 289
Voltage collapse, 299, 310, 312
Voltage sensitivities, 104
Voltage-sensitive loads, 315
Voltage source converter, 47
Voltage stability, 9, 299
  criteria, 305
  index, 320
  proximity index, 320

Watt governor, 29
Water starting time, 474
Weibull distribution, 268
Wicket gates, 28
Wide area
  measurement system (WAMS), 58
  monitoring, 59
  measurement, protection, and control, (WAMPAC), 59, 378, 410
Wind
  power, 265
  shear, 482
  speed, 266, 482
  turbines, 265, 481
Wronskian, 603

Zhukov's method, 563